Antonio Luna
Joan C. Vilanova
L. Celso Hygino da Cruz Jr.
Santiago E. Rossi *Editors*

Functional Imaging in Oncology

Biophysical Basis and Technical Approaches

Volume 1

Springer

Functional Imaging in Oncology

Antonio Luna • Joan C. Vilanova
L. Celso Hygino da Cruz Jr.
Santiago E. Rossi
Editors

Functional Imaging in Oncology

Biophysical Basis and Technical Approaches - Volume 1

Springer

Editors
Antonio Luna
Chief of MRI
Health Time Group
Jaén
Spain

L. Celso Hygino da Cruz Jr.
Department of Radiology
CDPI and IRM
Rio de Janeiro, RJ
Brazil

Department of Radiology
University Hospitals
Case Western Reserve University
Cleveland, Ohio
USA

Santiago E. Rossi
Centro de Diagnóstico
Dr. Enrique Rossi
Buenos Aires
Argentina

Joan C. Vilanova
Chief of MRI
Clínica Girona - Hospital Sta. Caterina
Ass. Professor. University of Girona
Girona
Spain

ISBN 978-3-642-40411-5 ISBN 978-3-642-40412-2 (eBook)
DOI 10.1007/978-3-642-40412-2
Springer Heidelberg New York Dordrecht London

Library of Congress Control Number: 2013956428

Printed on acid-free paper

Springer is part of Springer Science+Business Media (www.springer.com)

To my parents for forming me into what I am today
With all my love to my Marias for their patience and support

Antonio

To my wife Cris for her patience and understanding; and to our daughter Cristina, and son Eduard, with love.

Kai

To my parents, Luiz Celso and Leonice, as well as to my wife Simone, for their support and understanding during the process of preparing this work.

Celso

To my friend and mentor Jeremy Erasmus
To my family and my wife Clara

Santiago

Foreword

Molecular and functional imaging can improve the diagnosis, treatment and outcomes in oncologic patients. The ability to non-invasively visualize, characterize and quantify biologic processes at the cellular, molecular and genetic level presents a new era in oncology. This book provides a practical approach to the different imaging techniques used to obtain and understand this functional information. The editors, Drs. Luna, Vilanova, Da Cruz and Rossi are well-renowned radiologists experienced in functional and molecular imaging. They have assembled an international group of acclaimed experts that complement their expertise and have written a two-volume tour de force on state-of-the-art functional imaging useful in the assessment and management of oncologic patients. This comprehensive review was a pleasure to read and will undoubtedly become an indispensable resource for clinicians-in-training as well as practicing radiologists and oncologists. The authors are adept at simplifying complexity and their ambitious effort provides a complete review of diffusion MRI, perfusion CT and MRI, dual-energy CT, spectroscopy, dynamic contrast-enhanced ultrasonography, and positron emission tomography (PET). The text is clearly written and complemented by numerous high-quality illustrations that highlight key features and major teaching points. The first volume explains the biologic basis of the functional imaging modalities and provides meaningful clinical insight and understanding of the techniques used in the imaging of angiogenesis, tumor metabolism and hypoxia. The second volume considers specific malignancies and the use and benefit of the different imaging modalities in the diagnosis, prediction of treatment outcome, and early evaluation of treatment response in oncologic patients. The chapters are concise and comprehensive enough for the reader to obtain a firm foundation in the essential aspects of the topic reviewed. In fact, both volumes 1 and 2 impart knowledge in an easy-to-read, concise, coherent format. It is impossible to over-applaud the clarity and well-written and structured format of these books. In summary, the authors have used their experience to write an excellent textbook and the scope, structure and attention to detail are superb. The topics are well focused and this wide-ranging review is an invaluable guide to functional imaging.

This is a thoughtful and well-developed book that is without doubt an excellent, comprehensive text of the essentials required to understand and use functional imaging.

Jeremy J. Erasmus
Professor, Chief of Thoracic Radiology
Department of Diagnostic Radiology
The University of Texas M.D. Anderson Cancer Center
Houston, TX, USA

Preface

In the last decades, comprehensive cancer care and research have both been critically dependent on imaging. The role of anatomical imaging with ultrasound, CT and MRI has grown progressively in the last decades. In this manner, the application of medical imaging to cancer patients has expanded from diagnosis and staging to screening, guide of treatment, therapeutic monitoring, detection of recurrence and prediction of treatment response. This change in the role of imaging has been due in part to the introduction of functional imaging with PET at the end of the last century, and posteriorly with other techniques such as advanced MRI sequences.

The recent advances in cellular biology, molecular biology and genetics have led to a better understanding of the biological bases of cancer. These advances in oncology biologics and the development of new biological therapies and treatment options have produced a paradigm shift in cancer treatment. In many clinical scenarios, cancer is now considered a chronic disease instead of an untreatable malignancy. Furthermore, the approach to cancer management is moving from treating the disease to personalized therapies. All these major changes need multidisciplinary teams where experts in biomedical imaging are – and will be – an important part of the puzzle. Very wide scales have to be covered by imaging, from the molecular and cellular level to organ to whole organism for clinical staging. In this manner, combined functional and anatomical imaging techniques are necessary to visualize and target different aspects of cancer. At this point, functional and molecular imaging might transform and improve all phases of cancer management.

Functional imaging using biomarkers can assess and quantify the biological characteristics of tumors by a wide range of techniques. In this manner, ultrasound can explore tumor angiogenesis by means of contrast-enhanced acquisitions and tissue elasticity using elastography. New CT approaches such as CT-perfusion and spectral energy CT have broadened the knowledge of tumor angiogenesis and tissue characteristics. Furthermore, MRI is now able to develop multiparametric studies of a tumor in a single study, being possible to analyze tumor cellularity, angiogenesis, hypoxia and metabolism simultaneously using diffusion-weighted, dynamic contrast-enhanced, BOLD and spectroscopic sequences, respectively. PET and multimodality (hybrid) imaging have also expanded their applications with the use of other metabolites different to 18-FDG. Therefore, it is possible to explore different cancer hallmarks, such as angiogenesis, metabolism, apoptosis, proliferation

or hypoxia. In addition, the development of new approaches such as optical imaging and nanocomposites, novel imaging probes for PET and MRI permit to target different molecular and cellular processes. All these developments are directed to the phenotyping of cancer by imaging techniques. The advances in functional and molecular imaging have laid to apply imaging as a cancer biomarker, to help direct cancer treatment in a way that is complementary to plans based on tissue- and blood-based biomarkers. The ability to measure in vivo cancer biology with functional imaging during treatment provides a unique opportunity to identify and select the therapy that is most likely to successfully treat an individual patient's cancer. Furthermore, in a very near future, new methodologies will deal with theranostics, looking for a combined and simultaneous diagnosis and treatment of the disease.

The purpose of this book is to provide a useful manual to be used by the wide range and variety of disciplines involved in the management of oncologic patients, including radiologists, nuclear medicine, oncologists, radiotherapist and the different medical specialists and nonmedical disciplines involved in the oncologic patient's care. We have tried to cover and provide all the extensive information related to the different imaging modalities in clinical use and research from the technical bases to clinical applications. For this purpose, the book is divided in two volumes. The first volume is focused on the biophysical basis and technical approaches of functional imaging techniques. This first volume is divided in four parts. The first part covers a general approach to cancer biology, imaging biomarkers and role of functional imaging in diagnosis and treatment. The three following parts that deal with the role of functional and molecular imaging in the study of cancer hallmark and review their technical basis and applications in clinical practice and research. This part of the book is organized by different imaging techniques in separate chapters to stress the importance of an adequate imaging technique and acquisition to optimize the performance of each technique. The second volume of the book is the largest, where the main types of cancers are addressed in different chapters and organized by system and organ. In each of these chapters, the role of functional imaging in the management of different tumor types is discussed.

This book has been possible due to the generous effort of all contributing authors. All of them, well-known experts in their respective fields, have shared with us their experience in cutting-edge topics. They have make possible to compile lots of new information in a surprisingly short period of time. Furthermore, it has been easy to coordinate such a great team, making editing of this book a learning and enjoyable process.

Finally, we would like to acknowledge the enormous support of Dr. Jeremy J. Erasmus in the first conception of this book and Dr. Roberto Garcia-Figueiras for his help in the organization of the contents.

We hope that this book can be helpful for all interested in cancer imaging, and readers may share some of the learning and enjoyment we had editing this book.

Jaén, Spain — Antonio Luna
Girona, Spain — Joan C. Vilanova
Rio de Janeiro, Brazil — L. Celso Hygino da Cruz Jr.
Buenos Aires, Argentina — Santiago E. Rossi

Contents

Volume 2 Clinical Applications

Part I

Clinical and Therapeutic Approach to Functional Oncological Imaging

Cancer Biology: What's Important for Imaging

1

José L. Vercher-Conejero, Zhenghong Lee, and Pablo R. Ros

Contents

J.L.Vercher-Conejero, MD
Clinical Area of Medical Imaging, Department of Nuclear Medicine, University and Polytechnic Hospital La Fe, Valencia, Spain

Department of Radiology, University Hospitals Case Medical Center, Case Western Reserve University, 11100 Euclid Avenue (BSH 5056), Cleveland, OH 44106, USA
e-mail: jlvercher@hotmail.com

Z. Lee, BS, MS, PhD
Department of Radiology, University Hospitals Case Medical Center, Case Western Reserve University, 11100 Euclid Avenue (BSH 5056), Cleveland, OH 44106, USA
e-mail: zhenghong.lee@case.edu

Department of Biomedical Engineering, Case Western Reserve University, Cleveland, OH, USA

P.R. Ros, MD, MPH, PhD (✉)
Department of Radiology, University Hospitals Case Medical Center, Case Western Reserve University, 11100 Euclid Avenue (BSH 5056), Cleveland, OH 44106, USA

University Hospitals Health System, Cleveland, OH, USA
e-mail: pablo.ros@uhhospitals.org

Abbreviations

ABL	Abelson gene
ADC	Apparent diffusion coefficient
AR	Androgen receptor
ATSM	diacetyl-bis(N4-methylthiosemicarbazone)
BLI	Bioluminescence
BOLD	Blood oxygen level dependent
CCD	Charge-coupled device
CEST	Chemical exchange saturation transfer
CML	Chronic myeloid leukemia
CT	Computer tomography imaging
DCE-MRI	Dynamic contrast-enhanced magnetic resonance imaging
DECT	Dual-energy computer tomography
DEN	Diethylnitrosamine
DOTA	1,4,7,10-tetraazacyclododecane-1,4,7,10-tetraacetic acid
DOTA-CTT	DOTA-Cys-Thr-Thr-His-Trp-Gly-Phe-Thr-Leu-Cys
DOTA-STT	DOTA-Ser-Thr-Thr-Gly-His-Phe-Trp-Thr-Leu-Ser

A. Luna et al. (eds.), *Functional Imaging in Oncology*,
DOI 10.1007/978-3-642-40412-2_1, © Springer-Verlag Berlin Heidelberg 2014

DWI	Diffusion-weighted imaging
ECM	Extracellular matrix
EGFR	Epidermal growth factor receptor gene
ESR	European Society of Radiology
EUS	Endoscopic ultrasound
FDG	Fluorodeoxyglucose
FDHT	Fluorodihydrotestosterone
FLT	Fluorothymidine
FMAU	1-(2′-deoxy-2′-fluoro-beta-D-arabinofuranosyl)thymine
FMISO	Fluoromisonidazole
fMRI	Functional magnetic resonance imaging
Gd	Gadolinium
GIST	Gastrointestinal stromal tumors
GLUT	Glucose transporters
H&E	Hematoxylin and eosin stain
HCR	Hepatocarcinogenesis reporter
Her2	Human epidermal growth factor receptor 2
IGT	Imaging-guided therapy
IVUS	Intravascular ultrasound
MDCT	Multidetector CT
MIP	Maximum intensity projection
ML10	2-(5- Fluoro-pentyl)-2-methyl malonic acid
MMPs	Matrix metalloproteinases
MRI or MR	Magnetic resonance imaging
MRS	Magnetic resonance spectroscopy
mTor	Mammalian target of rapamycin
NETs	Neuroendocrine tumors
NH3	Ammonia
NIR	Near-infrared region
OCT	Optical coherence tomography
OI	Optical imaging
PARACEST	Paramagnetic chemical exchange saturation transfer
PET	Positron emission tomography
PTSM	Pyruvaldehyde-bis(N4-ethylthiosemicarbazone)
RAS/ERK	Ras-extracellular signal-regulated kinase
Rb	Retinoblastoma protein
RbCl	Rubidium chloride
R-CHOP	Rituximab-cyclophosphamide hydroxydaunorubicin, Oncovin (vincristine), prednisone
RGD	Arginine-glycine-aspartate peptide
SPAIR	Spectral attenuated inversion recovery
SPECT	Single-photon emission tomography
SPIO	Superparamagnetic iron oxide
TK1	Thymidine kinase 1
US	Ultrasound
VEGF	Vascular endothelial growth factor

1.1 Introduction

1.1.1 Cancer Hallmarks and Tumor Microenvironment

In cancer, new pathways and oncogenic features are continuously discovered. Cancer cells show different characteristics among distinct tumor types allowing them to proliferate and metastasize to distant organs. In addition, cancer cells have distinguished characteristics from normal cells such as rapid proliferation, immortality, resistance to apoptosis, metastatic capacity, and resistance to immunologic blitz [1].

The main focus of cancer imaging is often directed to contrast the differences between neoplastic and normal tissues. From a targeting point of view, the phenotypic abnormalities could be grouped into two main categories: those typical of certain cells such as the existence, or not, of a particular malignant biomarker and those related to the tumor microenvironment including angiogenesis, perfusion, and hypoxia [1].

As *Hanahan and Weinberg* summarized in 2000 [2], the hallmarks of cancer could be categorized into six features needed to understand its biology. Recently, they introduced new elements to this complex mechanism as shown in Fig. 1.1 [3].

1.1.1.1 Sustaining Proliferative Signaling

One of the fundamental attributes of cancer cells is their capability to proliferate even with no associated signaling. This is what *Hanahan and Weinberg* called *sustaining proliferative signaling* and can be achieved by increasing the production of growth factors, stimulating normal cells to provide cancer ones with growth factors, activating protein in the downstream

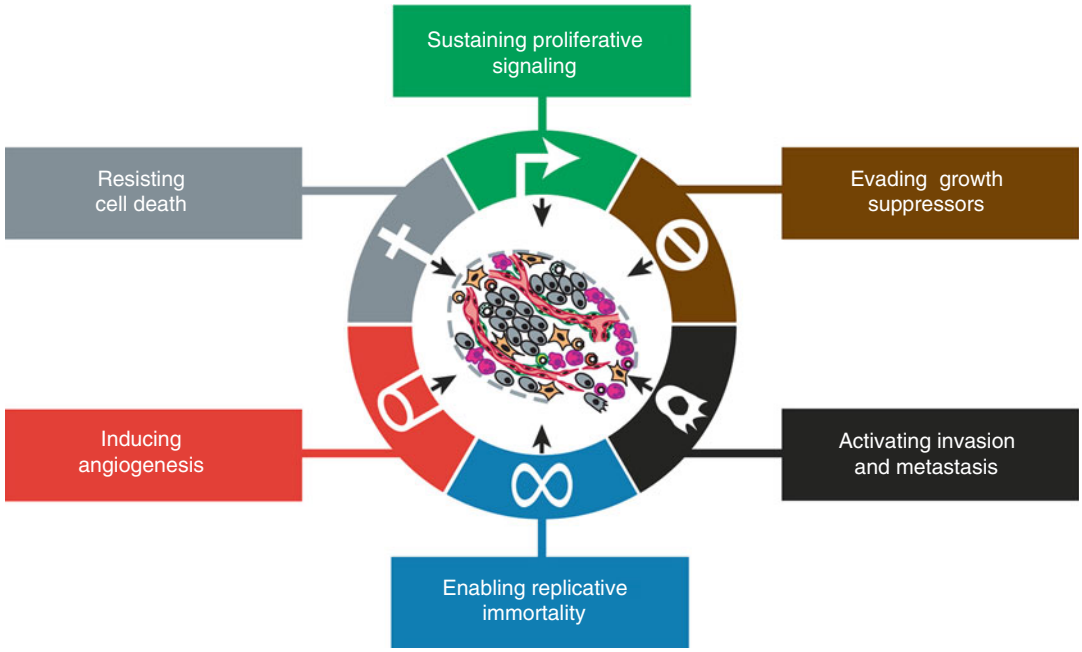

Fig. 1.1 The illustration shows the acquired biologic characteristics of malignant tissues proposed by Hanahan and Weinberg that has helped to understand the fingerprints of cancer cells (From Hanahan and Weinberg [3] with permission)

signaling pathway, and increasing the number of receptors on the cell or either modifying them to ease cancer cell signaling. In cancer cells, the process of intracellular communication may be taken over by specific mutations in otherwise normal genes, resulting in an abnormal gene called oncogene. Oncogenes generate abnormal genes products such as oncoproteins leading to a malignant cell behavior. These mutations may be produced in kinases, including EGFR mutations and c-Kit mutations, among others, that can disturb the signal transmitting function [1]. PI3K-Akt signaling, MAP-kinase pathway, mTOR pathway, cellular senescence, or oncogenes and tumor suppressor genes might contribute in this step [3]. This is key in targeted drug therapy as there is an interaction of membrane receptor-based tyrosine kinase and PI3K-Akt and RAS/ERK pathways and many drugs being used to inhibit signaling in different ways. Molecular-based imaging modalities have been used to image these molecular pathways. For example, some studies have demonstrated the extraordinary effect against gastrointestinal stromal tumors (GIST) of a tyrosine kinase inhibitor imatinib drug (Gleevec). GIST has been related to a transmembrane receptor, the oncogenic protein c-Kit. ^{18}F-fluorodeoxyglucose or ^{18}F-FDG, an analogue of glucose labeled with a positron emitter F-18, has been used in molecular imaging for assessing the therapeutic response of this drug in GIST patients. ^{18}F-FDG has shown the effect of blocking the specific tyrosine kinase activity associated with c-Kit [1]. Depending on the drug being used and its molecular target, a certain type of radiopharmaceutical can be applied to assess treatment response. For example, other tyrosine kinase inhibitor drugs, sunitinib and sorafenib, have been used in a type of kidney cancer. These drugs are targeting a specific angiogenic growth factor called vascular endothelial growth factor or VEGF. Other tracers such as ^{18}F-desatibib, ^{68}Ga-Fab'$_2$ herceptin, and ^{18}F-fluorodihydrotestosterone or ^{18}F-FDHT have been used to image different targets: mutant ABL in resistant chronic myeloid

leukemia (CML), Her2 in breast cancer, and androgen receptor (AR) in prostate cancer, respectively.

1.1.1.2 Evading Growth Suppressors

Cell proliferation in normal cells is a controlled process where many signals (pro- and anti-growth) coordinate the cycle phases. For example, the G_1 phase is the most vulnerable cell cycle vital due to the fact that it is at this point where extrinsic mitogenic signals may facilitate more mutations and therefore enable the development of cancer cells [4]. The rapid growth of malignant tissue can be measured by computed tomography imaging (CT) to evaluate changes in volume. Molecular imaging with specific tracers linked to proliferative processes such as the accelerated synthesis of DNA is more suited for this. Many tracers have been tested to image this mechanism. 2-^{18}F-fluorothymidine or ^{18}F-FLT is probably the most interesting and extensively used radiopharmaceutical in this setting. ^{18}F-FLT is a pyrimidine-based tracer taken by the cell via passive diffusion and facilitated transport by Na+-dependent carriers and then phosphorylated by thymidine kinase 1 (TK1) and finally trapped in the cell. In quiescent cells, TK1 activity is virtually absent, but in proliferating cells its activity is increased, particularly in the S phase of the cell cycle. This radiolabeled tracer has shown very promising results in monitoring response to treatment. In one study performed by Pio et al., 14 breast cancer patients were evaluated 2 weeks after the first cycle of treatment. Levels of the cancer antigen 27.29 (CA27.29), which is a soluble form of a mucin-like glycoprotein abundantly expressed on most carcinoma cells, showed very good correlation with ^{18}F-FLT uptake, as shown in Fig. 1.2 [5]. Another study evaluated ^{18}F-FLT in early response evaluation of high-grade non-Hodgkin lymphoma in 22 patients that were treated with combined immunochemotherapy (R-CHOP) or chemotherapy (CHOP) alone showing that a rapid reduction in FLT uptake was shown 7 days after initiation of therapy. However, there was no significant change in FLT uptake following the administration of rituximab alone [6].

The way antiproliferative signals usually work in normal cells is by inducing the G_0 phase or a postmitotic state [4]. However, most cancer cells evade these signals so they can proliferate. This characteristic is known as *evading growth suppressors* [3].

The two most representative tumor suppressors are p53 and the retinoblastoma protein (Rb) which regulate the cell cycle. While the protein p53 operates as a central control of apoptosis when there is a DNA damage, the Rb protein decides whether a cell should go or not through its cell cycle; in other words, it inhibits the pathway through the restriction checkpoint in G_1 [3, 7]. A protein such as p53 has been thought to participate in cancer cells metabolism as a modulator, especially by facilitating oxidative phosphorylation and reducing glycolysis. Therefore, when p53 is inactive due to a mutation, a process of glycolysis is then favored. This process can be studied with ^{18}F-FDG as this is a marker of glucose metabolism as some authors have shown a correlation between p53 and 18F-FDG [8–10]. When any of the tumor suppressors or processes is dysregulated, then the cycle progresses and consequently the cell proliferation is ongoing.

1.1.1.3 Activating Invasion and Metastasis

Another important cancer hallmark is *activating invasion and metastasis*, responsible for the spreading of neoplastic cells from the primary site into surrounding tissues and distant organs. It is believed, though not clear, that this process involves modifications in the cells so they can be attached to other cells and to the extracellular matrix (ECM) [3]. This may include different stages: local tissue invasion, intravasation, transition via blood and lymphatics, and colonization of foreign tissue [3]. Matrix metalloproteinases (MMPs) consist of a family if zinc-dependent endopeptidases for degrading ECM constituents, playing an important role in

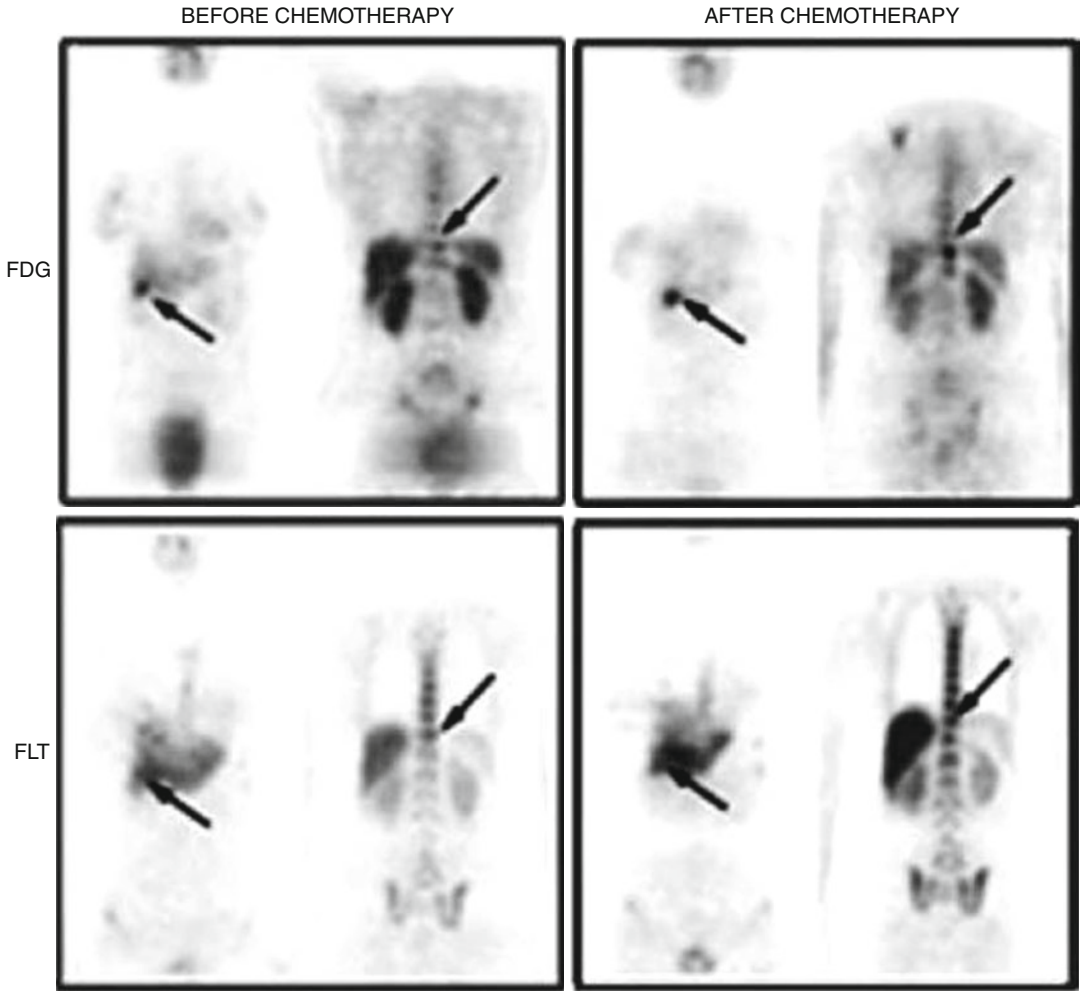

	FDG (avg. SUV)	FLT (avg. SUV)	CA 27.29 (U/mL)
Before Chemo.	2.6	4.9	40
After Chemo.	3.6	6.1	78
Difference	+1.0	+1.2	+38
%Change	+41.2%	+23.5%	+95%

Fig. 1.2 PET studies of a 43-year-old female with known metastatic breast carcinoma. ^{18}F-FDG-PET and ^{18}F-FLT-PET were performed before and after Aromasin treatment (an aromatase inhibitor). Both FDG and FLT studies show an increase of radiotracer uptake in the right kidney between the pre- and posttreatment scans. In addition, levels of tumoral biomarker CA27.29 also increased (From Pio et al. [5] with permission)

tumor invasion and metastases. The overproduction and uncontrolled function of MMPs have been correlated to many different tumors (brain, colon, melanoma, breast, etc.) [11]. Cross talk between cancer cells and cells of neoplastic stroma introduces the idea that metastatic process requires input from the surrounding tissue, so they do not originate from a cell-autonomous model [3, 12]. Imaging MMP expression with noninvasive imaging techniques such as PET, single-photon emission tomography (SPECT), and optical imaging may offer important information to predict metastatic potential of a tumor. Some synthetic sulfonamide-based MMP inhibitors including ^{64}Cu-DOTA-CTT, ^{64}Cu-DOTA-STT, and ^{123}I-CGS 27023A, among others, have been used as radiotracers to image overexpression of MMPs in tumors [11, 13].

1.1.1.4 Inducing Angiogenesis

The formation of new blood vessels, also called angiogenesis, is an essential process of tumor growth and metastatic dissemination [14]. Generally, angiogenesis is strongly controlled by a balance between stimulatory and inhibitory signaling molecules. However, when this balance is disrupted, a rapid proliferation of new vessels can happen, for instance, when a primary tumor releases angiogenic growth factors. The tumor-associated neovasculature is a multistep mechanism including signaling input from multiple angiogenic growth factors like VEGF, known as "angiogenic switch," and also the integrin signaling pathway [3]. Integrins are a group of cell adhesion molecules that are present on both neoplastic cells and newly formed vessels. Among the different integrin molecules already known, $\alpha_v\beta_3$ is the most studied in angiogenesis. Angiogenesis is therefore essential to the survival and growth of neoplastic tumors. *Inducing angiogenesis* eases tumor expansion mainly by delivering of oxygen and nutrients and production of growth factors for the cancer cell [14]. Angiogenesis has attracted some attention in therapy as a target for chemotherapeutic drugs. In fact, the first anti-angiogenic drug proven in humans was bevacizumab, a humanized monoclonal antibody which targets VEGF [15].

These processes can be imaged with radiolabeled tracers such as ^{64}Cu(DOTA)-VEGF$_{121}$ (targeting VEGF) or ^{18}F-galato-RGD (targeting integrin $\alpha_v\beta_3$) for PET imaging [16, 17]; ^{125}I-VEGF and ^{111}In-perfluorocarbon for SPECT imaging [18]; NP-RGD for SPECT imaging; RDG-Gd^{3+} for magnetic resonance imaging (MRI); RGD MBs and anti-VEGFR-2-Ab-microbubbles for ultrasound (US) or RGD-QD705; and QD-VEGF(DEE) for optical imaging (OI) [19].

1.1.1.5 Perfusion

The perfusion of tumors and their surrounding tissues is considered an essential physiological characteristic of tumor microenvironment as it is meant to be very important for planning and monitoring treatment response. Many imaging modalities including CT, MRI, and radionuclide techniques have shown their utility in understanding perfusion not only in oncology but also in heart pathologies (myocardium viability) and neurodegenerative disorders (dementia). Several tracers have been used to study blood flow, hypoxia, and neovascularization in primary tumors to investigate tumor perfusion. For example, ^{15}O-H_2O has turned out to be one of the most promising tracers to explain tumor perfusion in breast, kidney, colon, or lung cancer [20–22]; ^{62}Cu^{II}PTSM or other more commonly used PET perfusion imaging agents such as ^{82}Rb-RbCl, ^{13}N-NH_3, and ^{64}Ga-citrate have shown potential in brain, myocardium, and kidney, although with limitations [1]. Different CT techniques and novel MRI sequences are being used to learn more and quantify perfusion in neoplastic tissues and will be detailed in Sect. 1.2.

1.1.1.6 Resisting Cell Death

The programmed cell death (apoptosis) is a key process in cancer development and progression. In normal cells when an event such as an irreparable DNA damage is produced, they tend to switch on apoptosis. The ability of cancer cells to avoid apoptosis and continue with their proliferation is one of the fundamental features of cancer and is a major target of cancer therapy development [2, 3]. A signaling dysregulation in cancer cells promotes the overexpression of antiapoptotic

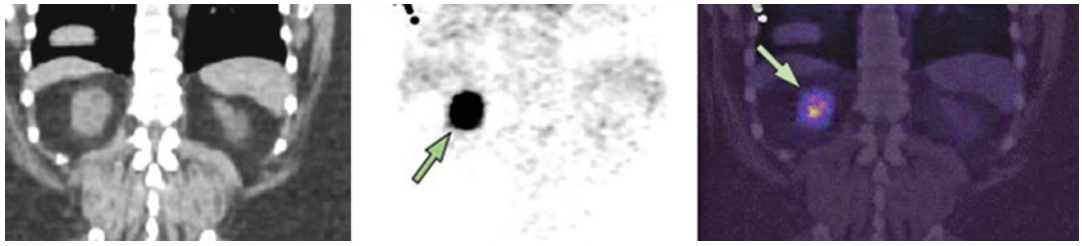

Fig. 1.3 Patient with a clear cell carcinoma scanned with ^{124}I-cG250 PET/CT (coronal CT, PET, and fused image) showing a focus of abnormal uptake (*arrow*) in the posterior portion of the right kidney (From Divgi et al. [37] with permission)

proteins and mutes the production of proapoptotic proteins [23]. Moreover, by altering the necrosis and normal cellular autophagy, cancer cells may *resist cell death* [3]. A radiolabeled molecule to image apoptosis called ^{18}F-ML10 has shown promising results in brain metastasis from non-small cell lung cancer patients treated with radiation therapy with promising results [24].

1.1.1.7 Hypoxia

Related to apoptosis, angiogenesis, tumor invasion, and metastasis, hypoxia is another very interesting feature that has impact on tumor environment. Hypoxia is a pathological condition defined as a reduction of tissue oxygenation and may lead to an insufficient supply of oxygen and nutrients to cells. In oncology, its severity will be dependent on the phenotype of cancer. For instance, cervical cancers are known to be highly hypoxic [1]. It has been exhibited in many studies that hypoxic neoplasias have worse prognosis for disease-free survival after treatment with chemotherapy as cytotoxicity aimed to be produced with certain anticancer drugs decreases in hypoxic tissues [25, 26]. Furthermore, hypoxic cells show significantly more resistance to radiotherapy treatment so affecting the radiation sensitivity [27–30]. Several hypoxia-selective PET tracers have been used with different results, but it is worth highlighting ^{18}F-fluoromisonidazole (^{18}F-MISO) and ^{64}Cu^{II}-ATSM which are being tested in many studies with interesting outcomes [31, 32]. ^{18}F-MISO has affinity for hypoxic cells with functional nitroreductase enzymes; therefore, it accumulates in activated cells but not in necrotic cells [33]. Many studies have shown excellent correlation between ^{18}F-MISO uptake and the oxygenation status of non-small cell lung neoplasms, head and neck cancer, gliomas, and cervical cancer [34].

Another interesting radiopharmaceutical is ^{124}I-cG250, an iodine-based radiolabeled tracer, which has shown the potential in evaluating hypoxia in certain tumors. cG250 is an antibody reacting against carbonic anhydrase-IX, which is overexpressed in hypoxic conditions, especially in clear cell renal carcinomas, the most common and aggressive renal tumor [35, 36]. *Divgi* et al. studied 26 patients with renal masses who were scheduled to undergo surgical resection. They concluded that PET with 124I-cG250 could identify accurately clear cell renal carcinoma; therefore, a negative PET scan would be highly predictive of a less aggressive phenotype helping surgical planning (Fig. 1.3) [37].

Dynamic contrast-enhanced and diffusion-weighted MRI sequences are also contributing in assessing hypoxia in tumor cells and the response of chemotherapy in these neoplasias [38–41].

1.1.1.8 Deregulating Cellular Energetics and Avoiding Immune Destruction

In addition to all those oncologic features, two new hallmarks have been recently introduced in oncology: *deregulating cellular energetics* and *avoiding immune destruction*, together with some enabling characteristics such as the *genome instability and mutation* generating random mutations and the *tumor-promoting inflammation* that favors tumor progression through various ways (Fig. 1.4) [3].

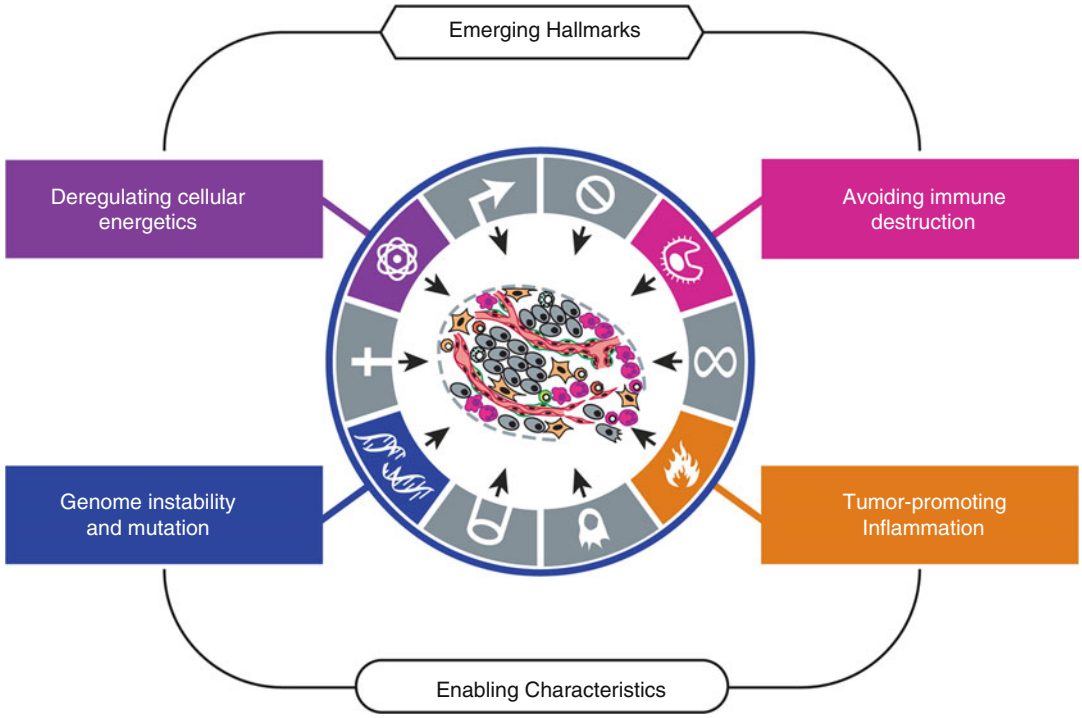

Fig. 1.4 The figure presents new proposed additional hallmarks that are thought to be involved in the pathogenesis of most cancers: one could have the ability to modify cellular metabolism by reprogramming or modifying it, while the other hallmark would be based on the capability of avoiding immunological destruction by cancer cells. In addition, the authors introduced two characteristics of neoplastic cells that could facilitate the acquisition of core and those emerging features: genomic instability and mutation, and inflammation, both of them enabling tumor progression (From Hanahan and Weinberg [3] with permission)

Cancer cells must make adjustments in their energy production in order to maintain the uncontrolled proliferation. Many mechanisms including using alternative metabolic pathways, adapting their glucose metabolism, and upregulating glucose transporters (GLUT) translate into an increase glucose uptake and utilization shown in many neoplasms, easily corroborated by molecular imaging, particularly by ^{18}F-FDG-PET [3, 42]. ^{18}F-FDG, as an analogue of glucose, is transported into cells by glucose transporter proteins and then phosphorylated by hexokinase to form FDG-6-phospate. However, it cannot be degraded via the glycolysis pathway nor dephosphorylated by glucose-6-phosphatase like glucose is. Therefore, FDG-6-phosphate gets trapped within the cell, and in this sense the more FDG there is in the cells, the greater the uptake in the tumor.

Many studies have suggested that a continuously active immune system recognizes and eliminates the majority of cancer cells before settling to form a tumor mass [3, 43, 44]. So the immune system is considered a fundamental process preventing tumor formation.

However, this is an unresolved issue because the role of the immune system is not yet clear. *Hanahan and Weinberg* and other authors introduced the concept of an elimination phase where the immune system recognizes and eliminates cancer cells. Then, the immune system is able to control the cancer cell growth but is not able to eliminate other cancer cells being in an equilibrium phase. Finally, tumor cells or clones not detected or destroyed by the immune system keep on growing [3, 45].

Each of the alterations that are produced in cancer cells of these hallmarks and tumor

microenvironment characteristics are associated with fundamental key molecules that might be targeted with certain probes or tracers and imaged.

1.1.2 Biomarkers

By definition, a biomarker is a biological molecule used as an imprint of a biological condition. It is a feature used to measure and evaluate, in an objective way, biological or pathogenic processes. Also it can be used as a treatment response marker, to detect or isolate a particular cell type or even a genetic level.

Biomarkers can be classified accordingly to the information gathered [46]:

(a) Histological (or biochemical) parameters obtained from biopsy or surgery tissue samples
(b) Biochemical parameters from blood or urine samples
(c) Anatomical, functional, or molecular parameters obtained with different imaging modalities

Therefore, biomarkers can be of tremendous value, being an essential piece of predictive and preventive medicine mainly in cardiology, neurology, and oncology, not only by adding understanding to these pathological processes but also by offering personalized therapy targeting cancer hallmarks [3].

Depending on what we want to image and/or treat, we have to acknowledge the target. Based on the hallmarks of cancer previously commented, many biomarkers have been studied including VEGF or integrin vectors for evaluating angiogenesis, radiolabeled glucose for the abnormal cellular energetics, thymidine analogues for proliferative signaling, receptor- [47] or enzyme-based [48] imaging, antibodies, selective anti-inflammatory drugs, telomerase inhibitors for the replicative immortality of cancer cells, and apoptotic markers, among endless others.

All of the many signaling targets have been made possible thanks to a numerous researchers by implementing translational studies from laboratory, preclinical, clinical, or population cohorts into clinical applications after an extensive testing in experimental models [49].

Imaging biomarkers, or molecular imaging, have many advantages including being considered a noninvasive method; it can be quantified [50, 51], is reliable, and offers reproducible data allowing multiparametric imaging. It represents a group of methods with specific probes, contrast agents, or MR pulse sequences [49] that image particular targets or pathways. All this infinitive information can be very useful to clinicians in the daily practice.

Besides cancer-related biomarkers, one of the fields where molecular imaging has an interesting impact is in cardiac studies. Vulnerable atherosclerotic plaque can be studied with coronary angiography by looking at the coronary lumen [52] requiring catheterization or at the coronary arterial wall with intravascular ultrasound (IVUS) [53, 54], though in these cases, it is considered to be an invasive imaging method. Other intravascular imaging techniques such as coronary computed tomography and cardiac magnetic resonance have been used for coronary and carotid lumen and wall [55] imaging. Optical coherence tomography (OI) [56] and near-infrared spectroscopy used for tissue spectral contrast [57] are being investigated.

In neurology, MRI and CT have been used to study brain infarction size and extent, lesion size, brain activity in multiple sclerosis and structural atrophy, and β-amyloid plaques with PET [58–60].

Section 1.2 of this chapter will briefly go through some of the molecular imaging techniques and its biomarkers and the unthinkable possibilities that imaging may offer in cancer biology.

1.2 Imaging Modalities: Molecular Imaging

Molecular imaging is a relatively "new" area that integrates molecular biology and state-of-the-art medical imaging, arisen in the last 15–20 years as a nexus between molecular biology and in vivo imaging. As already stated, it is defined

as a noninvasive technique able to visualize the natural microenvironment in real time, measure pharmacokinetics and pharmacodynamics of pharmaceuticals, and measure physiological or pathological inside living subjects at a cellular, molecular, or genetic level, among others [61–64].

Compared with conventional imaging techniques, molecular imaging has many advantages including 3D images of living organism thus enabling research into physiological or pathological situations such as signal transduction pathways, cell metabolism, and gene expression.

MI is a multidisciplinary branch of knowledge including molecular biology, genetics, biochemistry, physiology, physics, mathematics, pharmacology, immunology, and medicine [64]. Five imaging modalities are available for molecular imaging: CT, MRI, optical imaging, US, and radionuclide imaging which includes PET and SPECT.

Challenging problems remain to be solved such as the developing of new probes, translational research to the clinical arena, and multidisciplinary approach.

Each of the different imaging techniques has their different strengths and weaknesses that will be explained in the following section.

1.2.1 Computed Tomography

Computed tomography (CT) is based on the different attenuation levels in the tissues in the body produced by X-rays, thus resulting in an anatomic image. CT imaging has undergone an interesting evolution in the last few years. The development of high-resolution CT scans allows going deeper into a molecular level, a very important role in research studies [65, 66].

The main advantage of CT is probably its high spatial resolution (0.05 ~ 0.2 mm in preclinical studies and 0.5 ~ 1.0 mm in clinical studies). Availability, cost-effectiveness, fast acquisition time, excellent hard tissue imaging (bone), and relative simplicity are some of the advantages of CT imaging. On the other hand, some of the key limitations are exposure to ionizing radiation, limited soft tissue resolution, limited molecular imaging applications, and relatively low sensitivity (~10^{-3} mol/L). Recently, major improvements have been made to obtain significant dose reduction.

Due to the limited soft tissue resolution, CT contrasts have been developed for a better discrimination between normal and abnormal tissues. These are iodine-based contrast agents and are typically nonspecific [64, 67]. Also these contrast agents produce some renal toxicity so it cannot be used in all patients. For these reasons, a need for developing new contrast agents is being studied by many researches such as the use of targeted gold nanoparticles alone or even combined with 2-deoxy-D-glucose for a high-resolution anatomic and metabolic information of the subject scanned [68–72].

Some of the most significant and latest technological advances in CT are multislice CT, dual-energy CT, CT spectroscopy, photon counting imaging, and phase-contrast CT imaging, among others.

1.2.1.1 Multislice CT

Multislice CT came into the game with helical scanning and multi-detector CT (MDCT). The latter one can acquire an important number (recently up to 320-detector row MDCT) of tomographic slides in a very fast time [73, 74].

MDCT has the advantage of obtaining an enhanced spatial temporal resolution. Also the very short time that it takes to scan an individual avoids most of the motion artifacts produced by the patient. For this reason, it has become an important imaging tool for cardiac imaging [64].

Nonetheless, MDCT exposes the subject to higher radiation exposure [64, 75, 76].

1.2.1.2 Dual-Energy CT

Dual-energy CT (DECT) has shown a number of advantages compared to single-energy CT with energy-integrating detectors and is considered another advance in imaging. It consists of two separate X-ray tubes that can be operated at the same energy or at two different energies producing both the material decomposition images and monochromatic spectral images at energy levels

ranging from 40 to 140 keV [77]. The possibility of acquiring on the distinctive K-edge energies at the same time offers tissues to be characterized not by their attenuation values but by their composition. DECT or spectral CT is able to discriminate according to the difference in attenuation between two energies. K-edge imaging allows selective and quantitative imaging of administered contrast agents equipped with appropriate K-edge materials [69]. These features enable spectral CT a high spatiotemporal resolution and quantitative molecular imaging technology.

Photon counting detector splits the X-ray spectrum into several energy bins, and separate CT data are acquired in each energy bin. The CT data acquired in different energy bins are used for material decomposition, for example, calcium, uric acid renal stones [78], evaluating malignancies [79], differentiating hypervascular hepatic lesions [80], or even checking bone mineral density [81].

Photon counting may represent the most advanced form of spectral CT. Instead of separating the beam into merely high- and low-energy ranges, photon counting uses tight number of subranges or bins of the spectrum in order to form images based on the analysis of the spectral signature of tissues.

1.2.2 Magnetic Resonance Imaging

Magnetic resonance imaging (MRI) is a comprehensive molecular imaging without ionizing radiation, offering high temporal and spatial resolution and superb soft tissue contrast. By using a combination of powerful magnet and radiofrequencies, it displays anatomical and physiological information.

Other advantages of MRI include limitless depth of penetration, quantification data, and an ample clinical utility. An important disadvantage of MRI is its low sensitivity ($10^{-3} \sim 10^{-5}$ mol/L) [61], which lower than many other molecular imaging modalities [64] that can be very limiting due to the nonsignificant differences between atoms in high- and low-energy status.

However, efforts have been made to increase this low sensitivity by either increasing the magnetic field – 3.0 T in clinical environment and up to 7, 9.4, or even 11 T in the research field [82–84] – or hyperpolarizing atoms through dynamic nuclear polarization or by using the optical pumping technique enhancing significantly MR signals from different atoms [85, 86].

The contrast between different tissues seen on MRI is created by different relaxation times of each tissue. In order to achieve molecular imaging of disease biomarkers using MRI, targeted MRI contrast agents with high specificity and sensitivity (relaxivity) are required.

Beyond the most commonly used MRI sequences, novel techniques are being developed by many centers. By using advanced MRI sequences, supplemental information like functional or even metabolic information can be achieved besides anatomical images.

Dynamic contrast-enhanced magnetic resonance imaging (DCE-MRI) used a dynamic acquisition of T1-weighted MR images before, during, and after the administration of a contrast agent. A bolus of the appropriate contrast agent is injected into a vein, and rapid imaging techniques are then used to acquire serial images of a limited number of slices as the agent enters and leaves the tissue [87].

Contrast agents are usually gadolinium-based substances (Gd); nonetheless others such as superparamagnetic iron oxide (SPIO) have been tested [88]. These tend to shorten the T1 (Gd based) or T2 (SPIO based) relaxation times of protons causing measurable alterations in MR signal [64]. Some of the suggested uses of DCE-MRI are found in studying tumor microvascularization, lymphatics, and inflammation [64, 89].

Another new sequence that gradually is being incorporated into clinical routine is *diffusion-weighted imaging* (DWI) which is based on the restriction produced in the movement of water molecules in the interstitial space [90]. This is possible by detecting the apparent diffusion coefficient of tissue water (ADC). So in tissues with high cellularity, the movement of water molecules will be restricted showing low ADC, whereas tissues with low cellularity will show high ADC. DWI can be very useful when viable tissue is needed to be identified, for example, after an ischemic stroke, cancer imaging, or treatment response assessment [90, 91].

When needed functional information from MRI (fMRI), novel technique called *blood oxygen level dependent* (BOLD) has been introduced [92]. BOLD technique uses the endogenous deoxygenated hemoglobin to measure regional alterations, so higher levels of oxygenated blood will behave more intense on T2-weighted MRI images. It started mainly in neurology, to study brain functionality, cognition, memory, etc. [93, 94]. More clinical applications have been proven including the evaluation of differences in blood oxygen level in other tissues than brain and to evaluate the perfusion of tumors and response to treatment [92, 95, 96].

Magnetic resonance spectroscopy (MRS) cannot be considered a new technique because it has been used since 1950s [97–99], becoming an interesting element. MRS is based on applying electromagnetic pulses to a sample in an external magnetic field. Then, a tracer or probe is used to measure the results of the radiofrequency signals produced [64]. The inclusion of gradients that permits acquisition of positron data is the main difference between MRI and MSR. This is possible by creating a spectrum of peaks with the different *chemical shifts*, mainly lipids and metabolites, in a voxel of interest [64].

Commonly, MRS has been used for brain [100], breast, and prostate due to the good homogeneity of the magnetic field applied and the use of local acquisition coils with an outcome of a high signal-to-noise ratio. The spectral of metabolites used with MRS to study normal or abnormal physiology comprise choline, lactate, creatine, glutamate, lipids, and alanine.

To improve the sensitivity of MRS, a modified technique has been developed using a hyperpolarization enhancing the signal-to-noise ratio [101–103]. Hyperpolarized MRS has been performed with compound labeled with ^{13}C [104]. One that has shown promise is ^{13}C-pyruvate [85, 101] that plays a role in glycolysis and in preclinical studies such as ^{13}C-urea for perfusion imaging [105] and ^{13}C-fumarate for necrosis evaluation, among others [106]. For example, ^{13}C-fumarate can also be used for prostate cancer [107, 108].

Last but not least, new classes of MRI contrast agents working selectively by reducing the magnetization of the water signal with a minimal effect on its longitudinal signal, instead of the proton relaxation-based approach, have emerged as promising tool showing interesting information. Chemical exchange saturation transfer (CEST) and paramagnetic-CEST (PARACEST) contrast agents provide specific molecular and physiological information in oncology, mainly pH sensing [109–113].

1.2.3 Radionuclide Imaging

Radionuclide imaging is probably one of the earliest and cultivated molecular imaging modality, including positron emission tomography (PET) and single-photon emission computed tomography (SPECT).

Radionuclide imaging uses radionuclides combined with other elements to form chemical compounds or else combined with existing pharmaceutical compounds, to form what is called radiopharmaceuticals.

Radiopharmaceuticals or radiotracers can target specific organs or cellular receptors (Fig. 1.5) enabling the evaluation of biochemical changes, cellular physiology, cellular function and metabolism, and levels of molecular targets in an individual.

Through the years, advances in molecular imaging and radiochemistry have been used to develop new radiotracers or radiolabeled molecules to target different tissues, organs, or to even molecules rather than just anatomy.

Further, with the need of better anatomical information, hybrid modalities like SPECT/CT, SPECT/MRI, PET/CT (Fig. 1.6), and PET/MRI (Fig. 1.7) have been introduced into clinical practice offering not only molecular but also anatomical and functional information, all at once.

There are many advantages of using radionuclide imaging among which is its high sensitivity, quantitative capabilities, limitless depth of penetration, and clinical utility. In addition, the innumerable possibility of targeting a specific molecule, receptor, antibody, drug, etc., makes radionuclide imaging a unique tool for clinical, preclinical, and research studies.

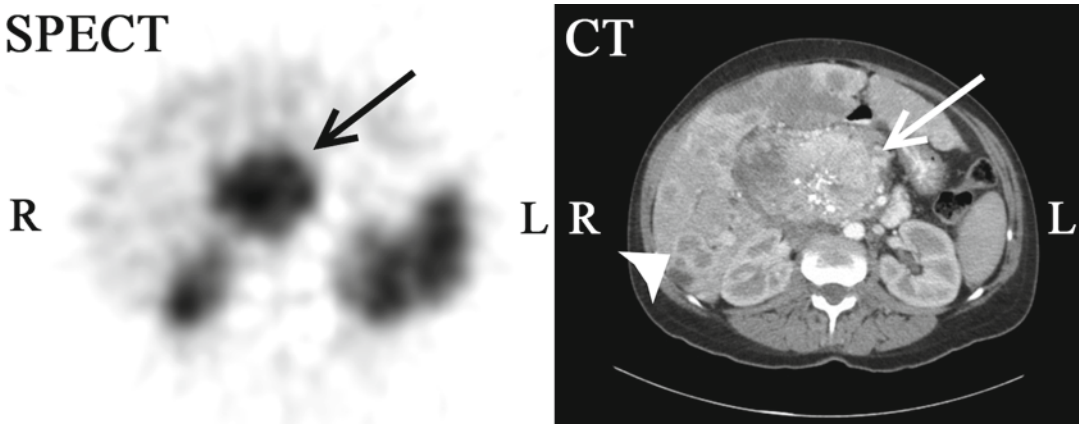

Fig. 1.5 ^{111}In-octreotide SPECT-CT scan of a 47-year-old female with a large abdominal mass. ^{111}In-octreotide, a somatostatin analogue labeled with indium-111 binds somatostatin receptors which are overexpressed in some neuroendocrine tumors (NETs). The study shows an abdominal rounded mass (*arrow*) with intense tracer uptake demonstrating a tumor expressing somatostatin receptors. Contrast-enhanced CT evidences a central large heterogeneous mass with gross calcifications. In addition, multiple ring-enhancing liver lesions (*arrowhead*) consistent with metastasis can be seen (Courtesy of Dr. Pilar Bello, Department of Nuclear Medicine, University and Polytechnic Hospital La Fe, Valencia, Spain)

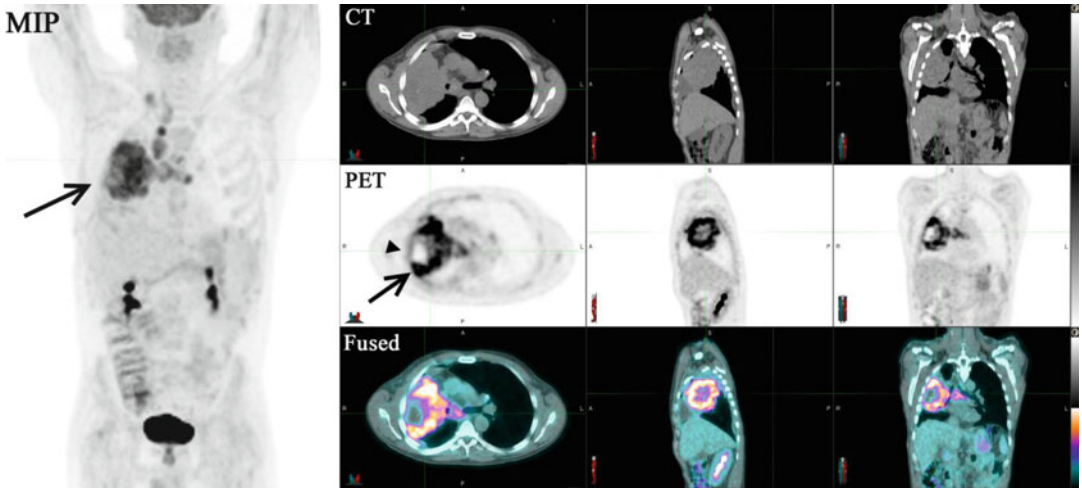

Fig. 1.6 ^{18}F-FDG-PET/CT (*top row*, CT; *middle row*, PET; *bottom row*, fused images) of a male with a recent diagnosis of small cell carcinoma of the lung. The PET study shows a highly intense heterogeneous abnormal tracer uptake (*arrow*) in the right mid-lung with several focal scattered areas of necrosis (*arrowheads*). The low-dose non-enhanced CT demonstrates a large rounded opacity occupying a large portion of the right lung extending contiguously into the right hilum with direct extension into adjacent lymph nodes. In addition, malignant intensity lymph nodes in the right supraclavicular fossa with extension into the precarinal and subcarinal space and anterior to the left bronchus are noticed

1.2.3.1 Single-Photon Emission Computed Tomography

The radionuclides used in single-photon emission computed tomography (SPECT) technology emit γ-rays during their decay. The most commonly used isotopes are ^{99m}technetium (^{99m}Tc), ^{111}indium (^{111}In), and ^{123}iodine (^{123}I). They all have relatively long half-life, thus obviating the

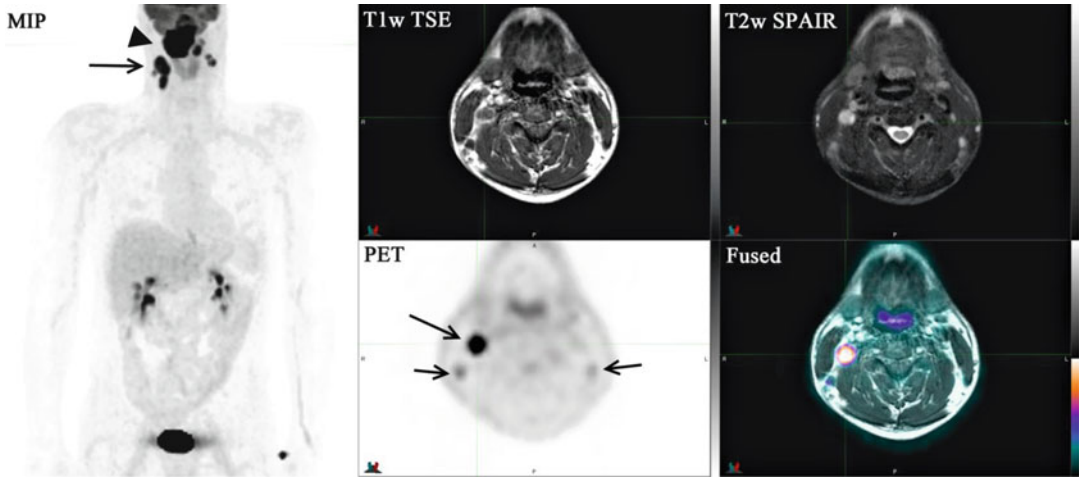

Fig. 1.7 ^{18}F-FDG PET/MRI (MIP image; *top row*, T1w TSE, T2w SPAIR; *bottom row*, PET, fused image) study of a 44-year-old male with a recently diagnosed invasive poorly differentiated squamous cell carcinoma of the nasopharynx. Large highly intense tracer uptake mass (*arrowhead*) involving the entire nasopharynx with extension to the skull base and involving the clivus which corresponds to the abnormal mass lesion identified in the MRI. Intense abnormal foci of tracer uptake are seen bilaterally in the posterior cervical region of the neck consistent with malignant lymphadenopathy (*arrows*)

need of a cyclotron on-site [61]. The SPECT gamma camera scanner is composed of the scintillator, photomultiplier tubes, and collimator, which rotate around the patient through multiple angles and directions to capture data and obtaining a tomographic reconstruction. SPECT is more affordable and thus more extensively used that PET cameras. However, SPECT is less sensitive than PET because γ-ray photons don't deliver adequate information regarding the origin of the photon, making impossible to define the line of response, as determined in PET [64].

Recent advances in improving sensitivity have been focused on high-resolution SPECT with pinhole scanners, different crystals used in the scintillators, etc. [114, 115]. Also, spatial resolution is lower than PET.

Hence, some disadvantages can be found on the ionizing radiation [116], like every RI modality, the limited spatial resolution already mentioned, and the lack of attenuation correction.

RI modalities such as SPECT or PET still lack spatial resolution compared with other imaging modalities so first, software fusion algorithm was developed to allow registration of functional and metabolic information gathered from RI with anatomical data from the CT or MRI, adding accuracy and precision to the studies [117]. As this has been expended, hybrid or multimodality systems have answered this demanding field by implementing CT or MRI components into the same gantry [118–121]. An additional benefit of combining SPECT with CT is the ability to be used not only for anatomical localization but also for attenuation correction [119, 122–124].

SPECT has limitless depth of penetration with an excellent sensitivity (though lower than PET), offering multiplexing capabilities. SPECT systems have the ability of distinguishing different radionuclides; therefore, it enables to image different targets simultaneously [125–127]. Furthermore, longer half-life period makes radiopharmaceuticals optimal for longitudinal studies.

Due to the enormous number of different radiopharmaceuticals designed for gamma cameras, it's impossible to line them up; however some remarkable ones are listed in Table 1.1 [64, 128–131].

1.2.3.2 Positron Emission Tomography

Contrary to SPECT agents, positron emission tomography (PET) agents use pharmaceuticals labeled with positron-emitting radionuclides

Table 1.1 SPECT radiopharmaceuticals (oncology related)

Radiopharmaceutical	Radiolabeling target	Applications
^{99m}Tc-MAA	Particles	Lung perfusion
^{99m}Tc-DTPA$_{aerosol}$	Particles	Lung ventilation
^{99m}Tc-DTPA	Chelates	Glomerular filtration, blood brain barrier disruption Renal function Brain tumors
^{99m}Tc-nanocolloid	Particles	Lymphatic drainage
^{99m}Tc-sulfur colloid	Particles	Reticuloendothelial function (bone marrow, liver and spleen imaging)
^{99m}Tc-MDP, ^{99m}Tc-HDP	Chelates	Bone formation
^{99m}Tc-sestamibi	Chelates	Blood flow, tumor viability Myocardial perfusion Breast cancer, parathyroid, etc.
^{67}Ga-citrate	Chelates	Tumor viability, capillary leakage Tumor imaging Infection imaging
^{99m}Tc-pertechnetate	As ions	Thyroid function
^{123}I-sodium iodine	As ions	Thyroid function
^{131}I-sodium iodine	As ions	Thyroid therapy
^{111}In-platelets	Cells	Cell incorporation (thrombus imaging)
^{99m}Tc-red blood cells$_{denaturated}$	Cells	Spleen imaging (accessory splenic tissue)
^{111}In-pentetrotide	Receptors	Somatostatin receptors (neuroendocrine tumors)
^{123}I-NP-59	Receptors	Cholesterol metabolism (adrenal dysfunction)
123I-MIBG	Receptors	Presynaptic adrenergic receptors (myocardial failure)
^{131}I-MIBG	Receptors	Cancer treatment (pheochromocytoma, neuroendocrine, neuroblastomas)
^{99m}Tc-CEA-Scan, IMMU-4 Fab'	Antibodies	Carcinoembryonic antigen – CEA (colorectal cancer)
^{99m}Tc-rituximab	Antibodies	CD20 molecules (oncology)
^{99m}Tc-annexin V	Proteins (phosphatidylserine)	Apoptosis imaging
^{99m}Tc-VEGF	Proteins	Angiogenesis imaging targeting vascular endothelial growth factor

produced mainly by particle accelerators also called cyclotrons but also can be produced by generators (rubidium 82).

PET cameras measure the signal produced by the radioactive decay of positron-emitting radioisotopes, such as ^{18}fluor (^{18}F), ^{11}carbon (^{11}C), ^{15}oxygen (^{15}O), ^{124}iodine (^{124}I), ^{68}galium (^{68}Ga), ^{82}rubidium (^{82}R), among many others. The annihilation of positrons is produced by colliding with an electron emitting two 511 keV photons thrown 180° apart in opposite direction. These photons are detected coincidently by scintillation crystals (different from the ones used for SPECT imaging due to the different energies). Then this signal is converted into an electrical signal and then into sinograms that will turn into tomographic images.

Key strengths of this technology include very high sensitivity ($10^{-11} \sim 10^{-12}$ mol/L) [64], limitless depth of penetration, and quantitative capabilities producing a broad impact in clinical and research application particularly in oncology, neurology, and cardiology [42, 117, 120, 132–134]. Many studies have proven the excellent utility of PET in detection, staging, radiotherapy planning, and treatment response assessment [134–145].

One of the major disadvantages of PET is that most of the radiotracers must be made with a cyclotron, and due to their relatively short half-life (hours, minutes, or even seconds), it's almost a requirement to have a cyclotron on-site or close to the facility hosting the system. Obviously, ionizing radiation, low spatial resolution, and difficult multiplexing capabilities are other disadvantages.

Like in SPECT imaging, the lack of anatomical reference and the long duration of the study since transmission images, besides emission images, have to be obtained for attenuation correction purposes have been compensated by merging PET either with CT or lately MRI [118, 146–153].

PET radiopharmaceuticals can target either metabolic-functional cell growth-related molecules such as glucose metabolism or other activities such as thymidine kinase, tissue oxygenation, cell death events, cell receptors, and specific tumor growth molecules.

Some of the most representative PET radiopharmaceuticals are shown in Table 1.2 [64, 128, 129, 132].

1.2.4 Optical Imaging

Optical imaging is an emerging molecular imaging modality, mainly based on genomics, proteomics, and optical technology. However, the visualization of tissues and cells using light waves has been used since decades ago [64].

Many approaches are being employed in optical imaging depending upon fluorescence, bioluminescence, absorption, or reflectance.

Fluorescence imaging may involve the use of genetically encoded fluorescence reporters or molecules that enable the visualization of molecular processes in living organism in real time [64]. Bioluminescence shows biological events in vivo such as gene expression and disease progression. Due to its high sensitivity, bioluminescence has been used to monitor tumor growth, metastases (Fig. 1.8), and response to treatment.

This technology requires what it is called charge-coupled device (CCD) camera and a source of filtered light. In order to increase the sensitivity, newer cameras named cool CCD have been utilized. Some advantages of optical imaging can be resumed in a very high sensitivity and specificity, multiplexing capabilities, and relatively safe (using low-energy photons) compared to RI techniques. On the other hand, it has a shallow penetration, which is not a problem in small animals in preclinical research, but it makes it very difficult for humans in a clinical environment, and the poor spatial resolution is the downside of this molecular imaging modality [61, 64].

Endogenous chromophores found in living organisms absorb the light. As increasing wavelength, light absorption and scattering decreases. Below ~700 nm these effects result in depthless penetration of few millimeters. Therefore, in the visible region of the spectrum, only superficial assessment of tissue features is possible. Once the wavelength increases above 900 nm approximately, water absorption may interfere with signal-to-background ratio. Since the absorption coefficient of tissue is lower in the near-infrared (NIR) region (700–900 nm), light can penetrate more deeply, up to some centimeters [155].

Some studies showed the use of NIR fluorophore in integrin imaging $\alpha v\beta 3$ in melanoma xenografts [156], other types of cancers [157], or even NIR fluorophore labeled with 2-deoxy-D-glucose [156, 158].

Other interesting clinical applications of optical imaging can be found in optical coherence tomography (OCT) which is a noninvasive, tomographic, biomicroscopic device that offers high-resolution, cross-sectional images of biological tissues in vivo and in real time. By generating false-color images, OCT provides both qualitative (morphology) and quantitative analysis of tissue structures based on the intensity of

Table 1.2 PET radiopharmaceuticals (oncology related)

Radiopharmaceutical	Radiolabeling target	Applications
^{18}F-FDG	Molecules	Glucose transporter I and hexokinase II (glucose metabolism)
^{18}F-FLT	Molecules	DNA synthesis, thymidine kinase-1 activity – cellular proliferation
^{18}F-MISO	Molecules	Viable oxygen/deficient cells (hypoxia)
^{18}F-FES	Receptors	Estrogen receptor activity (breast cancer)
^{18}F-NaF	Molecules	Osteogenic activity
^{18}F-Galacto-RGD	Peptides	Angiogenesis imaging targeting $\alpha\nu\beta3$ integrin
^{18}F-FET	Molecules	Amino acid transporter (brain tumors)
^{18}F-annexin V	Proteins	Apoptosis imaging
^{18}F-Fluorocholine ^{11}C-choline	Molecules	Cell proliferation
^{11}C-Acetate	Molecules	Fatty acid synthesis Oncology (prostate, bladder, renal) Myocardial infarction Ischemia
^{11}C-Methionine	Molecules	Amino acid transport (brain and pancreatic tumors)
^{11}C-Thymidine	Molecules	DNA synthesis, cell proliferation (brain tumors)
^{124}I-G250-mAb	Proteins (engineered)	Carbonic anhydrate-IX (oncology)
^{124}I-CA 19-9mAb	Antibodies	Carbohydrate tumor antigen CA19.9 (pancreatic cancer)
^{64}Cu-ATSM	Molecules	Viable oxygen-deficit cells (hypoxia)
^{64}Cu-DOTA-VEGF121	Proteins	Angiogenesis imaging targeting vascular endothelial growth factor
^{68}Ga-DOTATOC/ DOTANOC/ DOTATE	Receptors	Somatostatin receptors (neuroendocrine tumors)

the returned light. Traditionally, OCT was commercially sold to study ocular disorders including retinal or subretinal edema, retinopathy, multiple sclerosis, and more recently neoplastic diseases of the eye such as retinal and choroidal tumors [159–161]. *Rootman* et al. retrospectively studied 16 retinoblastoma patients with 22 intraocular lesions with OCT concluding that this technique could be applied for diagnosis of new lesions, monitoring response to laser therapy, and the identification of recurrences [160]. Besides ophthalmology, OCT has found wide applications in other medical specialties including dermatology, cardiology, and gastroenterology [162]. *Hatta* et al. studied the accuracy of preoperative staging of superficial esophageal squamous cell carcinomas in 123 patients by comparing high-resolution OCT and 20-MHz probe-type endoscopic ultrasound (EUS). The authors demonstrated that high-resolution OCT was more useful than EUS for preoperative staging of superficial esophageal squamous cell carcinoma [163].

Table 1.3 shows some examples of optical imaging probes [56, 155, 164–167].

1.2.5 Ultrasound

Ultrasound (US) is a very well-known and widely spread imaging modality that exploits the characteristics of high-frequency sound waves as they cross the biological tissue. Among the many advantages of this technology, it is worth mentioning that US is an relatively inexpensive

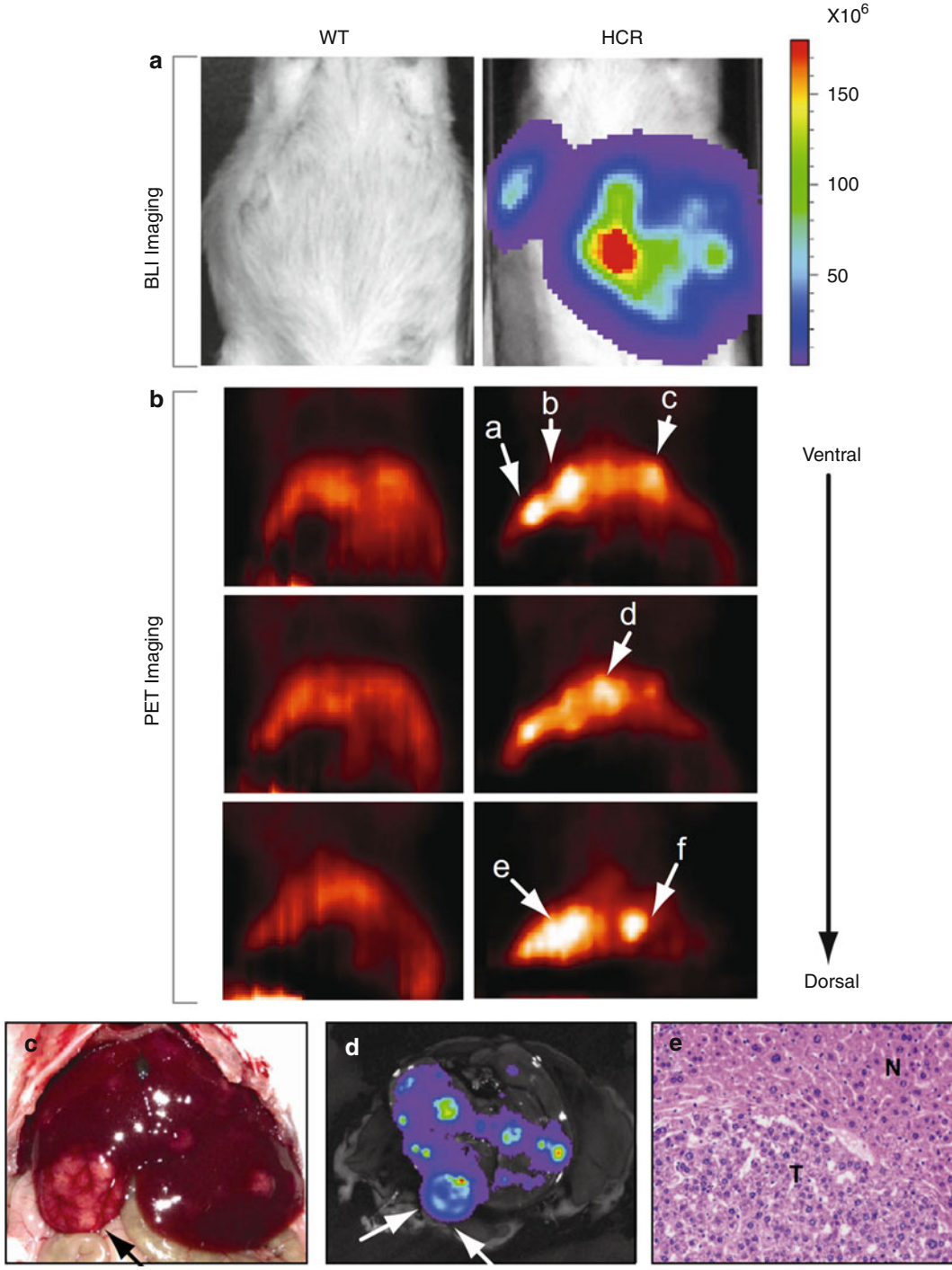

Fig. 1.8 Optical imaging and micro-PET of a neoplasia of the liver in mice after diethylnitrosamine (DEN) treatment, a classical hepatocarcinogen. (**a**) Bioluminescence (BLI) of a hepatocarcinogenesis reporter (HCR) mouse (*right*) compared with a wild-type control (*left*). On the right, BLI signals are observed. (**b**) Micro-PET using a substrate of thymidine kinase-based tracer labeled to a positron emitter, ^{18}F-FMAU, of the same mouse showing tracer uptake at different depths from the ventral surface of the liver. PET imaging is able to show multiple nodules at different depths and distinct patterns [**a**-**f**] within the tumor mass. (**c**) Multiple visible liver tumors are seen on the photograph, with Luc positive based on ex vivo BLI (**d**). Large tumor showed in **c** and **d** is pointed by *arrows*. (**e**) Typical tumor [T] and uniform nuclear morphology [N] in a H&E analysis. Most tumors were classified as benign hepatomas (From Lu et al. [154] with permission)

Table 1.3 Optical imaging probes (oncology related)

OI probe	Target	Applications
Fluorescence		
C(RGDyK)-Cy 5.5	Peptides	Angiogenesis imaging targeting αvβ3 integrin
Cy5.5-EGF	Peptides	Angiogenesis imaging targeting endothelial growth factor receptor (EGFR)
AB50-Cy5.5	Peptides	Caspase 3/7 – apoptosis imaging
ICG-Trastuzumab	Receptors	HER2 function
Bioluminescence		
Anti-CEA-Diabody-RLuc8	Antibodies	Carcinoembryonic antigen – CEA (colorectal cancer)

technique that may offer quantitative data, with a high temporal resolution, excellent sensitivity, and no ionizing radiation associated in a real-time practice. Moreover, US has an important value not only in diagnosis but also in therapeutics.

Unfortunately, it has a limited depth of penetration, not able to perform multiplexing studies, and due to its own characteristics, limited only to imaging soft tissues.

In the last years, US contrast agents have been developed adding to conventional US specificity and sensitivity depiction of molecular targets. For example, gas-filled microbubbles-based contrast agents coated with lipids or biopolymers have the ability for enhancing the reflection signal-to-noise ratio for blood [64, 168].

Although US contrast agents cannot provide specific molecular process information, new approaches including attaching these contrast agents to peptides or antibodies, for example, enable US to be used for molecular imaging purposes [64, 169].

It is expected that US as a molecular imaging modality will translate into clinical practice with new instruments such as endoscopes or new US contrast agents [64].

1.3 Imaging-Guided Therapy

Imaging-guided therapy (IGT) refers to a therapeutic procedure guided by any type of imaging modality. It corresponds to therapy based on the identification of a target, targeting the endpoint, monitoring the procedure, and follow-up. Obviously, these procedures are performed in environments with the proper equipment from radiology, nuclear medicine, radiotherapy, and surgery [170]. IGT uses the processed data acquired before, during, and after the therapy procedure making treatments (surgeries, radiotherapy, etc.) less invasive and more precise.

In order to perform a correct treatment, an exact localization not only of the target but also of the surrounding tissues, a correct placement of a catheter or probe into the aimed area, monitoring the changes during therapy, observing treatment response and efficacy, and controlling potential side effects are required.

Hence, the optimal features recommended for interventional therapy procedures include [170]:

1. Good target lesion/tissue contrast allowing a discrimination between the targeted structure and its surrounding
2. Real-time or near-real-time imaging
3. Interactive and multiplanar imaging capabilities
4. Therapy effects able to be observed for ablation therapy during and at the end of the procedure

Depending on the type of procedure to be performed, a certain imaging modality technique will be used. Mainly, three kinds of interventions can be done: vascular, percutaneous, or even open interventions. Probably, MRI can provide very good sensitivity and specificity and thus be recommended in percutaneous ablative therapy. However, if fast and accurate procedure is compulsory, CT fluoroscopy imaging can be the option to choose, at the expense of radiation exposure for the healthcare professional and the patient [170].

Table 1.4 Image guided therapy classification – image guided therapy working group (ESR)

IGT in Non-tumors	1. Transvascular/endovascular procedures
	Recanalization/revascularization by percutaneous balloon angioplasty, stent placement, aortic grafts, atherectomy, thrombectomy and thrombolysis
	Devascularization by placement of embolizing material as coils, particles and dedicated fluids
	Others including ablation of varices, renal artery radiofrequency ablation (RFA), reperfusion by fibrinolysis, intravascular drug-therapy, TIPS and transjugular biopsy, IVC filter placement, valvuloplasty
	2. Non-vascular procedures
	General, including puncture, drainage and evacuation. Placement of "assistance devices" such as fiducials
	Musculoskeletal: osteoplasty, kyphoplasty and placement of stabilization materials, intervertebral disc treatment
	Abdominal organs (mainly liver and kidney): drainage, instillation therapies and endoscopic procedures
	Central nervous system: neuronavigation procedures
IGT in Tumors	1. Transvascular procedures
	Embolization (bland, drug eluting, non-permanent)
	Chemo-ablative (including organ-selective perfusion), chemo-perfusion and chemo-embolization
	Radio-ablative (e.g. ^{90}Y-labeled microspheres, etc.)
	2. Non-vascular procedures
	Thermally ablative, such as radiofrequency ablation, microwave ablation, cryo-ablation and laser ablation
	Thermo-mechanical ablative, as highly intensive focused US
	Electro-ablative, as irreversible electroporation
	Chemo-ablative, such as ethanol injection
	3. Supportive conditions
	Pain therapy by instillation (drugs, alcohol and aceto-acid, implant-like substances such as cement) or thermal coagulation
	Others, such as port-a-caths
	4. Surgical procedures
	Intraoperative fluoroscopy-,. US-, CT- and MRI-guided, monitored and controlled procedures by either direct imaging of a target or probe placement.
	Intraoperative angiography under C-arm fluoroscopy or DSA (plus flat panel CT-like techniques) and related interventions.
	5. Radiation oncology
	Radiation treatment planning. Monitoring radiation therapy by navigator techniques and motions detection
	Fluoroscopic, US-, CT- or MRI-guided placement of fiducials and radiation catheters (brachytherapy, after loading).

The most common therapeutic interventions allude to diagnostic and interventional procedures: evacuation or decompression, revascularization, pain relief, emergency conditions, and palliative or curative tumor treatment, but also drug delivery [61, 64, 170–175].

Helmberger and Martí-Bonmatí et al. from the Image-Guided Therapy Working Group from the European Society of Radiology (ESR) recently published a statement regarding the actual status, addressing not only technical but also medicolegal and economical hot topics [170]. The Group recommended the following classification, though it is subject to change due to constant technical development (Table 1.4).

Some challenges still remain such as the impact IGT produces in regulatory medicolegal issues, together with radioprotection and technical

concerns. Imaging-guided therapy is proliferating among different medical specialties including surgery and cardiology. Therefore, training, radioprotection-related responsibilities, and a correct multidisciplinary integration should be a must.

Conclusion

This chapter discusses the promising future of molecular imaging in cancer imaging. It is also essential to understand the pathways in cancer biology, so potential research and clinical studies can be guided towards both diagnosis and assessment of treatment response and drug delivery. The development of new imaging technologies such as hybrid systems offering multiple and distinct, anatomical, functional, and metabolic information from a macroscopic to a molecular level opens an exciting journey. In addition, recent discoveries in biomarkers in combination with imaging are aimed to exploit the advantages of these modalities.

There is a need of a multidisciplinary approach in cancer imaging including biology, pharmacology, medicine, physics, genetics, and other fields to benefit the continual effort of fighting cancer.

References

1. Strauss HW. Nuclear oncology pathophysiology and clinical applications. Springer. 2013. Available via http://worldcat.org. http://www.springerlink.com/openurl.asp?genre=book&isbn=978-0-387-48893-6.
2. Hanahan D, Weinberg RA. The hallmarks of cancer. Cell. 2000;100(1):57–70.
3. Hanahan D, Weinberg RA. Hallmarks of cancer: the next generation. Cell. 2011;144(5):646–74.
4. Ringshausen I, et al. Cell cycle inhibition in malignant lymphoma: disease control by attacking the cellular proliferation machinery. Curr Drug Targets. 2006;7(10):1349–59.
5. Pio BS, et al. Usefulness of 3′-[F-18]fluoro-3′-deoxythymidine with positron emission tomography in predicting breast cancer response to therapy. Mol Imaging Biol. 2006;8(1):36–42.
6. Herrmann K, et al. Early response assessment using 3′-deoxy-3′-[18F]fluorothymidine-positron emission tomography in high-grade non-Hodgkin's lymphoma. Clin Cancer Res. 2007;13(12):3552–8.
7. Burkhart DL, Sage J. Cellular mechanisms of tumour suppression by the retinoblastoma gene. Nat Rev Cancer. 2008;8(9):671–82.
8. Kaira K, et al. Relationship between 18F-FDG uptake on positron emission tomography and molecular biology in malignant pleural mesothelioma. Eur J Cancer. 2012;48(8):1244–54.
9. Garcia Vicente AM, et al. 18F-FDG semi-quantitative parameters and biological prognostic factors in locally advanced breast cancer. Rev Esp Med Nucl Imagen Mol. 2012;31(6):308–14.
10. Crippa F, et al. Association between [18F]fluorodeoxyglucose uptake and postoperative histopathology, hormone receptor status, thymidine labelling index and p53 in primary breast cancer: a preliminary observation. Eur J Nucl Med. 1998;25(10):1429–34.
11. Sprague JE, et al. In vitro and in vivo investigation of matrix metalloproteinase expression in metastatic tumor models. Nucl Med Biol. 2006;33(2):227–37.
12. Qian BZ, Pollard JW. Macrophage diversity enhances tumor progression and metastasis. Cell. 2010;141(1):39–51.
13. Kopka K, et al. Synthesis and preliminary biological evaluation of new radioiodinated MMP inhibitors for imaging MMP activity in vivo. Nucl Med Biol. 2004;31(2):257–67.
14. Hicklin DJ, Ellis LM. Role of the vascular endothelial growth factor pathway in tumor growth and angiogenesis. J Clin Oncol. 2005;23(5):1011–27.
15. Ferrara N. Vascular endothelial growth factor: basic science and clinical progress. Endocr Rev. 2004;25(4):581–611.
16. Cai W, et al. PET of vascular endothelial growth factor receptor expression. J Nucl Med. 2006;47(12):2048–56.
17. Beer AJ, et al. Biodistribution and pharmacokinetics of the alphavbeta3-selective tracer 18F-galacto-RGD in cancer patients. J Nucl Med. 2005;46(8):1333–41.
18. Stollman T, et al. Scintigraphic imaging of VEGF-A expression with radiolabeled anti-VEGF monoclonal antibody. J Nucl Med Meeting Abstracts. 2007;48(MeetingAbstracts_2):24P-b.
19. Deshpande N, et al. Molecular ultrasound assessment of tumor angiogenesis. Angiogenesis. 2010;13(2):175–88.
20. Hentschel M, et al. Analysis of blood flow and glucose metabolism in mammary carcinomas and normal breast: a H2(15)O PET and 18F-FDG PET study. Nucl Med Commun. 2007;28(10):789–97.
21. Anderson H, et al. Measurement of renal tumour and normal tissue perfusion using positron emission tomography in a phase II clinical trial of razoxane. Br J Cancer. 2003;89(2):262–7.
22. de Langen AJ, et al. Use of H2(15)O-PET and DCE-MRI to measure tumor blood flow. Oncologist. 2008;13(6):631–44.
23. Ghobrial IM, et al. Targeting apoptosis pathways in cancer therapy. CA Cancer J Clin. 2005;55(3):178–94.
24. Reshef A, et al. Small-molecule biomarkers for clinical PET imaging of apoptosis. J Nucl Med. 2010;51(6):837–40.

25. Rebucci M, Michiels C. Molecular aspects of cancer cell resistance to chemotherapy. Biochem Pharmacol. 2013;85(9):1219–26.
26. Hashimoto K, et al. Expression of CD133 in the cytoplasm is associated with cancer progression and poor prognosis in gastric cancer. Gastric Cancer. 2013 Apr 5 [Epub ahead of print].
27. Tatum JL, et al. Hypoxia: importance in tumor biology, noninvasive measurement by imaging, and value of its measurement in the management of cancer therapy. Int J Radiat Biol. 2006;82(10):699–757.
28. Thomlinson RH, Gray LH. The histological structure of some human lung cancers and the possible implications for radiotherapy. Br J Cancer. 1955;9(4): 539–49.
29. Stegeman H, et al. Predictive value of hypoxia, proliferation and tyrosine kinase receptors for EGFR-inhibition and radiotherapy sensitivity in head and neck cancer models. Radiother Oncol. 2013;106(3):383–9.
30. Ogawa K, et al. Old but new methods in radiation oncology: hyperbaric oxygen therapy. Int J Clin Oncol. 2013;18(3):364–70.
31. Padhani A. PET imaging of tumour hypoxia. Cancer Imaging. 2006;6:S117–21.
32. Bourgeois M, et al. Contribution of [64Cu]-ATSM PET in molecular imaging of tumour hypoxia compared to classical [18F]-MISO–a selected review. Nucl Med Rev Cent East Eur. 2011;14(2):90–5.
33. Lee ST, Scott AM. Hypoxia positron emission tomography imaging with 18f-fluoromisonidazole. Semin Nucl Med. 2007;37(6):451–61.
34. Cheng J, et al. 18F-fluoromisonidazole PET/CT: a potential tool for predicting primary endocrine therapy resistance in breast cancer. J Nucl Med. 2013;54(3):333–40.
35. Zhang J. Recent advances in preoperative imaging of renal tumors. Curr Opin Urol. 2008;18(1):111–5.
36. Leung K. 124I-Chimeric monoclonal antibody G250. 2010 Apr 22 [Updated 2010 May 20]. In: Molecular Imaging and Contrast Agent Database (MICAD) [Internet]. Bethesda (MD): National Center for Biotechnology Information (US); 2004–2013. Available from: http://www.ncbi.nlm.nih.gov/books/NBK43528/.
37. Divgi CR, et al. Preoperative characterisation of clear-cell renal carcinoma using iodine-124-labelled antibody chimeric G250 (124I-cG250) and PET in patients with renal masses: a phase I trial. Lancet Oncol. 2007;8(4):304–10.
38. Ovrebo KM, et al. Assessment of hypoxia and radiation response in intramuscular experimental tumors by dynamic contrast-enhanced magnetic resonance imaging. Radiother Oncol. 2012;102(3):429–35.
39. Stoyanova R, et al. Mapping tumor hypoxia in vivo using pattern recognition of dynamic contrast-enhanced MRI data. Trans Oncol. 2012;5(6):437–47.
40. Halle C, et al. Hypoxia-induced gene expression in chemoradioresistant cervical cancer revealed by dynamic contrast-enhanced MRI. Cancer Res. 2012;72(20):5285–95.
41. Hompland T, et al. Connective tissue of cervical carcinoma xenografts: associations with tumor hypoxia and interstitial fluid pressure and its assessment by DCE-MRI and DW-MRI. Acta Oncol. 2013 Feb 27 [Epub ahead of print].
42. Chen K, Chen X. Positron emission tomography imaging of cancer biology: current status and future prospects. Semin Oncol. 2011;38(1):70–86.
43. Vajdic CM, van Leeuwen MT. Cancer incidence and risk factors after solid organ transplantation. Int J Cancer. 2009;125(8):1747–54.
44. Vajdic CM, et al. Cancer incidence before and after kidney transplantation. JAMA. 2006;296(23):2823–31.
45. Teng MW, et al. Immune-mediated dormancy: an equilibrium with cancer. J Leukoc Biol. 2008;84(4): 988–93.
46. European Society of Radiology. White paper on imaging biomarkers. InsightsImaging. 2010;1(2):42–5.
47. Wong DF, Pomper MG. Predicting the success of a radiopharmaceutical for in vivo imaging of central nervous system neuroreceptor systems. Mol Imaging Biol. 2003;5(6):350–62.
48. Foss CA, et al. Radiolabeled small-molecule ligands for prostate-specific membrane antigen: in vivo imaging in experimental models of prostate cancer. Clin Cancer Res. 2005;11(11):4022–8.
49. Pomper MG. Translational molecular imaging for cancer. Cancer Imaging. 2005;5 Spec No A:S16–26.
50. Marti Bonmati L, et al. Imaging biomarkers, quantitative imaging, and bioengineering. Radiologia. 2012; 54(3):269–78.
51. Revert Ventura AJ, et al. The heterogeneity of blood flow on magnetic resonance imaging: a biomarker for grading cerebral astrocytomas. Radiologia. 2012 Jun 25 [Epub ahead of print].
52. Ballantyne CM, et al. Effect of rosuvastatin therapy on coronary artery stenoses assessed by quantitative coronary angiography: a study to evaluate the effect of rosuvastatin on intravascular ultrasound-derived coronary atheroma burden. Circulation. 2008;117(19): 2458–66.
53. Tardif JC, et al. Effect of atherosclerotic regression on total luminal size of coronary arteries as determined by intravascular ultrasound. Am J Cardiol. 2006;98(1):23–7.
54. Nissen SE, et al. Effect of very high-intensity statin therapy on regression of coronary atherosclerosis: the ASTEROID trial. JAMA. 2006;295(13):1556–65.
55. Tardif J-C, et al. Imaging biomarkers in atherosclerosis trials. Circ Cardiovasc Imaging. 2011;4(3):319–33.
56. Pinto TL, Waksman R. Clinical applications of optical coherence tomography. J Interv Cardiol. 2006;19(6): 566–73.
57. Waxman S, et al. In vivo validation of a catheter-based near-infrared spectroscopy system for detection of lipid core coronary plaques: initial results of the SPECTACL study. JACC Cardiovasc Imaging. 2009;2(7):858–68.
58. Fennema-Notestine C, et al. Structural MRI biomarkers for preclinical and mild Alzheimer's disease. Hum Brain Mapp. 2009;30(10):3238–53.
59. Craig-Schapiro R, et al. Biomarkers of Alzheimer's disease. Neurobiol Dis. 2009;35(2):128–40.

60. Vercher-Conejero JL, et al. (2013) Amyloid PET/MRI in the Differential Diagnosis of Dementia. Clin Nucl Med.
61. Alberti C. From molecular imaging in preclinical/clinical oncology to theranostic applications in targeted tumor therapy. Eur Rev Med Pharmacol Sci. 2012;16(14):1925–33.
62. Weissleder R, Pittet MJ. Imaging in the era of molecular oncology. Nature. 2008;452(7187):580–9.
63. Weissleder R. Molecular imaging in cancer. Science. 2006;312(5777):1168–71.
64. James ML, Gambhir SS. A molecular imaging primer: modalities, imaging agents, and applications. Physiol Rev. 2012;92(2):897–965.
65. Jast J, Jasiuk I. Age-related changes in the 3D hierarchical structure of rat tibia cortical bone characterized by high resolution micro-CT. J Appl Physiol. 2013;114(7):923–33.
66. Duan J, et al. High-resolution micro-CT for morphologic and quantitative assessment of the sinusoid in human cavernous hemangioma of the liver. PLoS One. 2013;8(1):e53507.
67. Hyafil F, et al. Noninvasive detection of macrophages using a nanoparticulate contrast agent for computed tomography. Nat Med. 2007;13(5):636–41.
68. Wen S, et al. Multifunctional dendrimer-entrapped gold nanoparticles for dual mode CT/MR imaging applications. Biomaterials. 2013;34(5):1570–80.
69. Schirra CO, et al. Second generation gold nanobeacons for robust K-edge imaging with multi-energy CT. J Mater Chem. 2012;22(43):23071–7.
70. Shikhaliev PM. Photon counting spectral CT: improved material decomposition with K-edge-filtered x-rays. Phys Med Biol. 2012;57(6):1595–615.
71. Wang H, et al. Folic acid-modified dendrimer-entrapped gold nanoparticles as nanoprobes for targeted CT imaging of human lung adencarcinoma. Biomaterials. 2013;34(2):470–80.
72. Li J, et al. A novel functional CT contrast agent for molecular imaging of cancer. Phys Med Biol. 2010;55(15):4389–97.
73. Benedek T, et al. Multislice computed tomographic coronary angiography for quantitative assessment of culprit lesions in acute coronary syndromes. Can J Cardiol. 2013;29(3):364–71.
74. Kabasawa M, et al. Assessment of functional tricuspid regurgitation using 320-detector-row multislice computed tomography: risk factor analysis for recurrent regurgitation after tricuspid annuloplasty. J Thorac Cardiovasc Surg. 2012.
75. Sun Z, et al. Coronary CT angiography: current status and continuing challenges. Br J Radiol. 2012;85 (1013):495–510.
76. Sun Z. Multislice computed tomography angiography in the diagnosis of cardiovascular disease: 3D visualizations. Front Med. 2011;5(3):254–70.
77. Yu Y, et al. Hepatocellular carcinoma and focal nodular hyperplasia of the liver: differentiation with CT spectral imaging. Eur Radiol. 2013;23(6):1660–8.
78. Qu M, et al. Dual-energy dual-source CT with additional spectral filtration can improve the differentiation of non-uric acid renal stones: an ex vivo phantom study. AJR Am J Roentgenol. 2011;196(6):1279–87.
79. Graser A, et al. Single-phase dual-energy CT allows for characterization of renal masses as benign or malignant. Invest Radiol. 2010;45(7):399–405.
80. Lv P, et al. Differentiation of small hepatic hemangioma from small hepatocellular carcinoma: recently introduced spectral CT method. Radiology. 2011;259(3):720–9.
81. Zhang J, et al. Accurate measurement of bone mineral density using clinical CT imaging with single energy beam spectral intensity correction. IEEE Trans Med Imaging. 2010;29(7):1382–9.
82. Groebner J, et al. 7 Tesla compatible in-bore display for functional magnetic resonance imaging. MAGMA. 2013;26(4):371–5.
83. Burmeister HP, et al. Imaging of lamination patterns of the adult human olfactory bulb and tract: in vitro comparison of standard- and high-resolution 3T MRI, and MR microscopy at 9.4 T. Neuroimage. 2012;60(3):1662–70.
84. Chen J, et al. In vivo quantification of T1, T2, and apparent diffusion coefficient in the mouse retina at 11.74T. Magn Reson Med. 2008;59(4):731–8.
85. Albers MJ, et al. Hyperpolarized 13C lactate, pyruvate, and alanine: noninvasive biomarkers for prostate cancer detection and grading. Cancer Res. 2008;68(20):8607–15.
86. Gallagher FA, et al. Magnetic resonance imaging of pH in vivo using hyperpolarized 13C-labelled bicarbonate. Nature. 2008;453(7197):940–3.
87. Craciunescu OI, et al. DCE-MRI parameters have potential to predict response of locally advanced breast cancer patients to neoadjuvant chemotherapy and hyperthermia: a pilot study. Int J Hyperthermia. 2009;25(6):405–15.
88. Saritas EU, et al. Magnetic Particle Imaging (MPI) for NMR and MRI researchers. J Magn Reson. 2012;229:116–26.
89. Yu Y, et al. Quantitative analysis of clinical dynamic contrast-enhanced MR imaging for evaluating treatment response in human breast cancer. Radiology. 2010;257(1):47–55.
90. Malayeri AA, et al. Principles and applications of diffusion-weighted imaging in cancer detection, staging, and treatment follow-up. Radiographics. 2011;31(6):1773–91.
91. Thoeny HC, Ross BD. Predicting and monitoring cancer treatment response with diffusion-weighted MRI. J Magn Reson Imaging. 2010;32(1):2–16.
92. Jiang L, et al. Blood oxygenation level-dependent (BOLD) contrast magnetic resonance imaging (MRI) for prediction of breast cancer chemotherapy response: a pilot study. J Magn Reson Imaging. 2012;37(5):1083–92.
93. Chang C, et al. EEG correlates of time-varying BOLD functional connectivity. Neuroimage. 2013;15(72): 227–36.
94. Cantin S, et al. Impaired cerebral vasoreactivity to CO2 in Alzheimer's disease using BOLD fMRI. Neuroimage. 2011;58(2):579–87.

95. Falahpour M, et al. Subject specific BOLD fMRI respiratory and cardiac response functions obtained from global signal. Neuroimage. 2013;15(72):252–64.
96. Orringer DA, et al. Clinical applications and future directions of functional MRI. Semin Neurol. 2012;32(4):466–75.
97. Jardetzky O, Jardetzky CD. Proton magnetic resonance spectra of amino acids. J Biol Chem. 1958;233(2): 383–7.
98. Odeblad E. Some investigation with nuclear magnetic resonance on water associated with the vaginal cells. Acta Obstet Gynecol Scand. 1960;39:528–39.
99. Shafer PR, et al. Nuclear magnetic resonance spectroscopy: abnormal splitting of ethyl groups due to molecular assymetry. Proc Natl Acad Sci U S A. 1961;47(1):49–51.
100. Senaratne R, et al. Increased choline-containing compounds in the orbitofrontal cortex and hippocampus in euthymic patients with bipolar disorder: a proton magnetic resonance spectroscopy study. Psychiatry Res. 2009;172(3):205–9.
101. Vinding MS, et al. Dynamic nuclear polarization and optimal control spatial-selective (13)C MRI and MRS. J Magn Reson. 2013;227:57–61.
102. Schroeder MA, et al. Hyperpolarized 13C magnetic resonance reveals early- and late-onset changes to in vivo pyruvate metabolism in the failing heart. Eur J Heart Fail. 2013;15(2):130–40.
103. Santarelli MF, et al. How the signal-to-noise ratio influences hyperpolarized 13C dynamic MRS data fitting and parameter estimation. NMR Biomed. 2012;25(7):925–34.
104. Giovannetti G, et al. Hyperpolarized 13C MRS surface coil: design and signal-to-noise ratio estimation. Med Phys. 2010;37(10):5361–9.
105. Golman K, et al. Molecular imaging with endogenous substances. Proc Natl Acad Sci U S A. 2003;100(18):10435–9.
106. Shan L. Hyperpolarized [1,4-13C2]fumarate as an imaging agent of tumor cell death in vivo. In: Molecular Imaging and Contrast Agent Database (MICAD). Bethesda; 2004.
107. Chen AP, et al. Hyperpolarized C-13 spectroscopic imaging of the TRAMP mouse at 3T-initial experience. Magn Reson Med. 2007;58(6):1099–106.
108. Leung K. Hyperpolarized [1-13C]dehydroascorbic acid. In: Molecular Imaging and Contrast Agent Database (MICAD). Bethesda; 2004.
109. Hancu I, et al. CEST and PARACEST MR contrast agents. Acta Radiol. 2010;51(8):910–23.
110. Vinogradov E, et al. CEST: from basic principles to applications, challenges and opportunities. J Magn Reson. 2012;229:155–72.
111. Tee YK, et al. Evaluating the use of a continuous approximation for model-based quantification of pulsed chemical exchange saturation transfer (CEST). J Magn Reson. 2012;222:88–95.
112. Sheth VR, et al. Measuring in vivo tumor pHe with CEST-FISP MRI. Magn Reson Med. 2012;67(3): 760–8.
113. Takayama Y, et al. Ytterbium-based PARACEST agent: feasibility of CEST imaging on a clinical MR scanner. Magn Reson Med Sci. 2012;11(1):35–41.
114. Islamian JP, et al. Monte carlo study of the effect of collimator thickness on T-99m source response in single photon emission computed tomography. World J Nucl Med. 2012;11(2):70–4.
115. Deleye S, et al. Performance evaluation of small-animal multipinhole muSPECT scanners for mouse imaging. Eur J Nucl Med Mol Imaging. 2013;40(5): 744–58.
116. Camacho Lopez C, et al. Effective doses associated to the usual multimodal examinations in nuclear medicine. Rev Esp Med Nucl. 2011;30(5):276–85.
117. Histed SN, et al. Review of functional/anatomical imaging in oncology. Nucl Med Commun. 2012; 33(4):349–61.
118. Bouziotis P, et al. Radiolabeled iron oxide nanoparticles as dual-modality SPECT/MRI and PET/MRI agents. Curr Top Med Chem. 2012;12(23): 2694–702.
119. Lu SJ, et al. Value of SPECT/CT in the evaluation of knee pain. Clin Nnucl Med. 2013;38(6):e258–60.
120. Biermann M, et al. Is there a role for PET-CT and SPECT-CT in pediatric oncology? Acta Radiol. 2013.
121. Schaap J, et al. Incremental diagnostic accuracy of hybrid SPECT/CT coronary angiography in a population with an intermediate to high pre-test likelihood of coronary artery disease. Eur Heart J Cardiovasc Imaging. 2013;14(7):642–9.
122. Palmer MR, et al. Evaluation of relative renal function for patients who had undergone simultaneous liver-kidney transplants using Tc-99m-MAG3 scintigraphy with attenuation correction from anatomical images and SPECT/CT. Nucl Med Commun. 2011;32(8):738–44.
123. Bennewitz C, et al. Computer-aided evaluation of the anatomical accuracy of hybrid SPECT/spiral-CT imaging of lesions localized in the neck and upper abdomen. Nucl Med Commun. 2012;33(11): 1153–9.
124. Mathur S, et al. Clinical value of stress-only Tc-99m SPECT imaging: importance of attenuation correction. J Nucl Cardiol. 2013;20(1):27–37.
125. Fakhri GE. Ready for prime time? Dual tracer PET and SPECT imaging. Am J Nucl Med Mol Imaging. 2012;2(4):415–7.
126. Shcherbinin S, et al. Quantitative image reconstruction for dual-isotope parathyroid SPECT/CT: phantom experiments and sample patient studies. Phys Med Biol. 2012;57(15):4755–69.
127. Hijnen NM, et al. Dual-isotope 111In/177Lu SPECT imaging as a tool in molecular imaging tracer design. Contrast Media Mol Imaging. 2012;7(2):214–22.
128. Mankoff DA, et al. Tumor receptor imaging. J Nucl Med. 2008;49 Suppl 2:149S–63.
129. Elgazzar AH. The pathophysiologic basis of nuclear medicine. Springer-Verlag Berlin Heidelberg; 2006.
130. Buendia-Fuentes F, et al. Sympathetic reinnervation 1 year after heart transplantation, assessed using

iodine-123 metaiodobenzylguanidine imaging. Transplant Proc. 2011;43(6):2247–8.
131. Vercher-Conejero JL, et al. Abdominal splenosis: an often underdiagnosed entity. Rev Esp Med Nucl. 2011;30(2):97–100.
132. Vallabhajosula S, et al. A broad overview of positron emission tomography radiopharmaceuticals and clinical applications: what is new? Semin Nucl Med. 2011;41(4):246–64.
133. Gambhir SS. Molecular imaging of cancer with positron emission tomography. Nat Rev Cancer. 2002;2(9):683–93.
134. Czernin J, et al. PET/CT imaging: the incremental value of assessing the glucose metabolic phenotype and the structure of cancers in a single examination. Eur J Radiol. 2010;73(3):470–80.
135. Dunnwald LK, et al. Tumor metabolism and blood flow changes by positron emission tomography: relation to survival in patients treated with neoadjuvant chemotherapy for locally advanced breast cancer. J Clin Oncol. 2008;26(27):4449–57.
136. Yang W, et al. Imaging proliferation of (1)(8)F-FLT PET/CT correlated with the expression of microvessel density of tumour tissue in non-small-cell lung cancer. Eur J Nucl Med Mol Imaging. 2012;39(8): 1289–96.
137. Kubota K. From tumor biology to clinical Pet: a review of positron emission tomography (PET) in oncology. Ann Nucl Med. 2001;15(6):471–86.
138. Yanagawa M, et al. Evaluation of response to neoadjuvant chemotherapy for esophageal cancer: PET response criteria in solid tumors versus response evaluation criteria in solid tumors. J Nucl Med. 2012;53(6):872–80.
139. Graf N, et al. [18F]FLT is superior to [18F]FDG for predicting early response to antiproliferative treatment in high-grade lymphoma in a dose-dependent manner. Eur J Nucl Med Mol Imaging. 2013;40(1):34–43.
140. Ng SH, et al. Prospective study of [18F]fluorodeoxyglucose positron emission tomography and computed tomography and magnetic resonance imaging in oral cavity squamous cell carcinoma with palpably negative neck. J Clin Oncol. 2006;24(27): 4371–6.
141. Al-Ibraheem A, et al. Clinical applications of FDG PET and PET/CT in head and neck cancer. J Oncol. 2009;2009:208725.
142. Hustinx R, Lucignani G. PET/CT in head and neck cancer: an update. Eur J Nucl Med Mol Imaging. 2010;37(3):645–51.
143. Liao CT, et al. PET and PET/CT of the neck lymph nodes improves risk prediction in patients with squamous cell carcinoma of the oral cavity. J Nucl Med. 2011;52(2):180–7.
144. Zygogianni A, et al. A new role of PET/CT for target delineation for radiotherapy treatment planning for head and neck carcinomas. Hell J Nucl Med. 2012;15(2):139–43.
145. Johnson KA, et al. Appropriate use criteria for amyloid PET: a report of the Amyloid Imaging Task Force, the Society of Nuclear Medicine and Molecular Imaging, and the Alzheimer's Association. J Nucl Med. 2013;9(1):e-1–16.
146. Nakamoto Y, et al. Clinical value of image fusion from MR and PET in patients with head and neck cancer. Mol Imaging Biol. 2009;11(1):46–53.
147. Boss A, et al. Feasibility of simultaneous PET/MR imaging in the head and upper neck area. Eur Radiol. 2011;21(7):1439–46.
148. Ratib O, Beyer T. Whole-body hybrid PET/MRI: ready for clinical use? Eur J Nucl Med Mol Imaging. 2011;38(6):992–5.
149. Buchbender C, et al. Oncologic PET/MRI, part 1: tumors of the brain, head and neck, chest, abdomen, and pelvis. J Nucl Med. 2012;53(6):928–38.
150. Loeffelbein DJ, et al. PET-MRI fusion in head-and-neck oncology: current status and implications for hybrid PET/MRI. J Oral Maxillofac Surg. 2012;70(2): 473–83.
151. Mansi L, et al. PET/MRI and the revolution of the third eye. Eur J Nucl Med Mol Imaging. 2012;39(10):1519–24.
152. Platzek I, et al. PET/MRI in head and neck cancer: initial experience. Eur J Nucl Med Mol Imaging. 2013;40(1):6–11.
153. von Schulthess GK, et al. Clinical positron emission tomography/magnetic resonance imaging applications. Semin Nucl Med. 2013;43(1):3–10.
154. Lu X, et al. Alpha-fetoprotein-thymidine kinase-luciferase knockin mice: a novel model for dual modality longitudinal imaging of tumorigenesis in liver. J Hepatol. 2011;55(1):96–102.
155. Kovar JL, et al. A systematic approach to the development of fluorescent contrast agents for optical imaging of mouse cancer models. Anal Biochem. 2007;367(1):1–12.
156. Houston JP, et al. Quality analysis of in vivo near-infrared fluorescence and conventional gamma images acquired using a dual-labeled tumor-targeting probe. J Biomed Opt. 2005;10(5):054010.
157. Chen K, et al. RGD-human serum albumin conjugates as efficient tumor targeting probes. Mol imaging. 2009;8(2):65–73.
158. Kovar JL, et al. Characterization and performance of a near-infrared 2-deoxyglucose optical imaging agent for mouse cancer models. Anal Biochem. 2009;384(2):254–62.
159. Al-Mujaini A, et al. Optical coherence tomography: clinical applications in medical practice. Oman Med J. 2013;28(2):86–91.
160. Rootman DB, et al. Hand-held high-resolution spectral domain optical coherence tomography in retinoblastoma: clinical and morphologic considerations. Br J Ophthalmol. 2013;97(1):59–65.
161. Say EA, et al. Optical coherence tomography of retinal and choroidal tumors. J Ophthalmol. 2012; 2012:385058.
162. Vila PM, et al. Use of in vivo real-time optical imaging for esophageal neoplasia. Mt Sinai J Med. 2011;78(6):894–904.

163. Hatta W, et al. A prospective comparative study of optical coherence tomography and EUS for tumor staging of superficial esophageal squamous cell carcinoma. Gastrointest Endosc. 2012;76(3):548–55.
164. Sevick-Muraca EM, et al. Advancing the translation of optical imaging agents for clinical imaging. Biomed Opt Express. 2013;4(1):160–70.
165. Chen K, et al. Dual-modality optical and positron emission tomography imaging of vascular endothelial growth factor receptor on tumor vasculature using quantum dots. Eur J Nucl Med Mol Imaging. 2008;35(12):2235–44.
166. Zhu L, et al. Dynamic PET and optical imaging and compartment modeling using a dual-labeled cyclic RGD peptide probe. Theranostics. 2012;2(8): 746–56.
167. Cai W, Chen X. Multimodality molecular imaging of tumor angiogenesis. J Nucl Med. 2008;49 Suppl 2:113S–28.
168. Deshpande N, et al. Tumor angiogenic marker expression levels during tumor growth: longitudinal assessment with molecularly targeted microbubbles and US imaging. Radiology. 2011;258(3):804–11.
169. Deshpande N, et al. Molecular ultrasound imaging: current status and future directions. Clin Radiol. 2010;65(7):567–81.
170. Helmberger T, et al. Radiologists' leading position in image-guided therapy. Insights Imaging. 2013;4(1):1–7.
171. Sirsi SR, Borden MA. Advances in ultrasound mediated gene therapy using microbubble contrast agents. Theranostics. 2012;2(12):1208–22.
172. Schonberg SO, Wangler B. From molecular imaging markers to personalized image-guided therapy. Z Med Phys. 2013;23(1):1–2.
173. Riaz A, et al. Yttrium-90 radioembolization using TheraSphere in the management of primary and secondary liver tumors. Q J Nucl Med Mol Imaging. 2009;53(3):311–6.
174. Ghanaati H, et al. Imaging and imaging-guided interventions in the diagnosis and management of hepatocellular carcinoma (HCC)-review of evidence. Iran J Radiol. 2012;9(4):167–77.
175. Pacella CM, Papini E. Image-guided percutaneous ablation therapies for local recurrences of thyroid tumors. J Endocrinol Invest. 2013;36(1):61–70.

Imaging Biomarkers and Surrogate Endpoints in Oncology Clinical Trials

2

Richard G. Abramson and Thomas E. Yankeelov

Contents

R.G. Abramson, MD (✉)
Institute of Imaging Science,
Vanderbilt University, Nashville, TN, USA

Department of Radiology and Radiological Sciences,
Vanderbilt University Medical Center,
1161 Medical Center Drive,
Medical Center North, Suite CCC-1121,
Nashville, TN 37232-2675, USA

Vanderbilt-Ingram Cancer Center,
Vanderbilt University, Nashville, TN, USA
e-mail: richard.abramson@vanderbilt.edu

T.E. Yankeelov
Department of Radiology and Radiological Sciences,
Department of Biomedical Engineering,
Department of Physics and Department of Cancer Biology, Vanderbilt University, Institute of Imaging Science, 1161 21st Ave S, AA-1105 Medical Center North, Nashville, TN 37232-2310, USA

Vanderbilt-Ingram Cancer Center,
Vanderbilt University, Nashville, TN, USA
e-mail: thomas.yankeelov@vanderbilt.edu

Abbreviations

ACRIN	American College of Radiology Imaging Network
CI	Confidence interval
CR	Complete response
DCE-MRI	Dynamic contrast-enhanced magnetic resonance imaging
DFS	Disease-free survival
DW-MRI	Diffusion-weighted magnetic resonance imaging
ECOG	Eastern Cooperative Oncology Group

A. Luna et al. (eds.), *Functional Imaging in Oncology*,
DOI 10.1007/978-3-642-40412-2_2,

EGFR	Epidermal growth factor receptor
EMA	European Medicines Agency
FDA	U.S. Food and Drug Administration
FDG-PET	Fluorodeoxyglucose positron emission tomography
FLT-PET	Fluorodeoxythymidine positron emission tomography
HER2	Human epidermal growth factor receptor-2
IOM	Institute of Medicine
IWG	International Working Group
KRAS	V-Ki-ras2 Kirsten rat sarcoma viral oncogene homolog
MRI	Magnetic resonance imaging
NCI	National Cancer Institute
NIH	National Institutes of Health
ORR	Objective response rate
PD	Progressive disease
PERCIST	PET Response Criteria in Solid Tumors
PET	Positron emission tomography
PFS	Progression-free survival
PR	Partial response
QIBA	Quantitative Imaging Biomarker Alliance
QIN	Quantitative Imaging Network
RECIST	Response Evaluation Criteria In Solid Tumors
SD	Stable disease
TTP	Time to progression

2.1 Introduction

Interest in oncology biomarkers has surged over the past decade, fueled by scientific progress toward precision medicine and by the practical search for new efficiencies in the expensive and lengthy drug development process [1]. Biomarker use has the potential to help tailor care to patient subgroups, streamline the selection of candidate drug agents, and reduce the cost and duration of clinical trials. The statistical and methodological requirements for biomarker use are still evolving, however, and the scientific, industrial, and regulatory communities continue to struggle with issues of how to properly evaluate and utilize these tools.

This chapter discusses imaging biomarkers in oncology clinical trials. After reviewing definitions for biomarkers and related terms, we discuss the motivations underlying biomarker integration into oncology drug development and the use of imaging biomarkers across the oncology drug development continuum. We then briefly review current and emerging imaging biomarkers for cancer clinical trials. We conclude by providing a brief discussion of the evaluation of imaging biomarkers as surrogate endpoints, including the perspective from regulatory agencies.

2.2 Definitions

The surge in biomarker research over the past decade has brought some confusion with regard to competing definitions for biomarkers and related terms (Table 2.1). This chapter uses the Institute of Medicine (IOM)'s modification of the National Institutes of Health (NIH) Biomarkers Consensus Group definition of a biomarker as "a characteristic that is objectively measured and evaluated as an indicator of normal biological processes, pathogenic processes, or pharmacologic responses to an intervention" [2]. Oncology biomarkers are often divided conceptually into *prognostic biomarkers*, intended to forecast a likely disease course in the absence of treatment, and *predictive biomarkers*, intended to forecast a likely disease course in the presence of a specific treatment. Some authorities include a third category of *early response biomarkers* to draw particular attention to biomarkers that may reveal treatment response or failure earlier than conventional methods [3].

Any discussion of biomarkers in the context of oncology clinical trials must also include definitions of clinical and surrogate endpoints. The NIH Biomarkers Working Group defines a *clinical endpoint* as "a characteristic or variable that reflects how a patient feels, functions, or survives" [4]. Within a clinical trial, a clinical endpoint is a distinct measurement or analysis of

Table 2.1 Definitions

Term	Definition
Biomarker	A characteristic that is objectively measured and evaluated as an indicator of normal biological processes, pathogenic processes, or pharmacologic responses to an intervention
Prognostic biomarker	Intended to forecast a likely disease course in the absence of treatment
Predictive biomarker	Intended to forecast a likely disease course in the presence of a specific treatment
Early response biomarker	Intended to reveal treatment response or failure earlier than conventional methods
Clinical endpoint	A characteristic or variable that reflects how a patient feels, functions, or survives
Surrogate endpoint	A biomarker intended to substitute for a clinical endpoint
Biomarker evaluation	The overall process for confirming a biomarker's suitability as a surrogate endpoint
Analytical validation	The first component of biomarker evaluation in the IOM framework, describing objective demonstration that the biomarker can be accurately measured
Qualification	The second component of biomarker evaluation in the IOM framework, describing objective demonstration that the biomarker is associated with the clinical endpoint of concern
Utilization	The third component of biomarker evaluation in the IOM framework, describing subjective assessment of biomarker performance in the specific context of its proposed use

disease characteristics that reflects the effect of a therapeutic intervention. In general, survival has traditionally been the clinical endpoint of greatest interest in oncology trials [5].

A *surrogate endpoint* is defined as a biomarker that is intended to substitute for a clinical endpoint [4]. Surrogate endpoints are a subset of biomarkers. Using a biomarker as a surrogate endpoint implies that the biomarker has been through a rigorous, formal process to confirm its suitability as a substitute for a clinical endpoint. This confirmatory process has been described using a variety of different terms, including evaluation, qualification, and validation. In keeping with the IOM framework, we use the general term *biomarker evaluation* to refer to the overall process for confirming a biomarker's suitability as a surrogate endpoint. The IOM framework identifies three key components in the biomarker evaluation process: analytical validation, qualification, and utilization [2]. These three steps are discussed in more detail in Sect. 2.7.

2.3 Motivations Underlying Biomarker Integration into Oncology Drug Development

Despite its relatively recent emergence onto the research agenda, the biomarker concept is now invoked at all stages of oncology drug development, from early preclinical studies to late-stage clinical trials. The search for meaningful oncology biomarkers reflects both the growing importance of precision medicine and the increasing emphasis on finding ways to streamline the drug development process [6].

In the context of oncology drug development, precision (or personalized) medicine captures the notion of cancer as a heterogeneous group of diseases characterized by a diverse array of gene expression and activity patterns [7]. Tumor analysis at the molecular level offers the potential for identifying targets that may be variably expressed among different patients or even at different tumor sites in a single patient. Linking different cancer subtypes with the presence or absence of certain biomarkers may facilitate identification of tumors in which a targeted drug agent has a higher likelihood of success. Biomarker integration may thus promote optimization of therapeutic regimens for individual patients, with specific agents being selected only in tumor subtypes associated with a particular biomarker status, e.g., trastuzumab for

HER2-overexpressing breast cancers or cetuximab for EGFR-expressing colorectal cancers lacking a concomitant KRAS mutation.

Meanwhile, integration of biomarkers into preclinical studies and clinical trials offers the potential of reducing the length and expense of the drug development process, which by some estimates can require up to 10 years and one billion dollars [8]. In preclinical and early-stage clinical development, biomarker analysis may promote improved selection of patients for clinical trials by identifying patients who are more or less likely to benefit from therapy. Biomarkers may provide valuable early information on the presence or absence of drug efficacy that can be used to terminate less promising projects before they enter into more expensive later-stage testing [6]. Performing such studies in the preclinical setting also affords the opportunity to select appropriate imaging biomarkers for application in subsequent clinical trials employing the therapy under consideration.

For investigational agents that do proceed into late-stage clinical testing, biomarkers used as surrogate endpoints offer the prospect of smaller, less expensive, and more efficient clinical trials [9]. In particular, if a biomarker is deemed to be an acceptable substitute for survival, then trials can be designed and powered to demonstrate a significant change in the biomarker rather than the clinical endpoint, typically resulting in smaller patient accrual requirements and a dramatically shortened evaluation timeframe. Furthermore, traditional survival trials in many cancer types are becoming more difficult to analyze and interpret due to increasing patient life expectancies and the proliferation of therapeutic options, e.g., in metastatic breast cancer where patients may undergo multiple different lines of treatment extending over several years. It has been argued that in certain circumstances, biomarker-driven trials may offer "cleaner" assessments of drug efficacy than survival trials with fewer problems due to patient loss to follow-up, patients undergoing additional treatment after the investigational therapy, and patients experiencing intercurrent illness and death from other causes [9, 10].

2.4 Use of Imaging Biomarkers Across the Oncology Drug Development Continuum

An important concept to emphasize is that different imaging biomarkers might be appropriately deployed at different stages of the oncology drug development process. As the goals change from preclinical studies into early- and late-stage clinical trials, the requirements for biomarker evaluation and utilization also change.

2.4.1 Preclinical Studies

In the preclinical stages of the drug development process, key priorities include target identification and validation, identification of promising drug compound leads, and demonstration of target engagement as proof of concept. This process typically occurs first in in vitro studies of appropriate cell lines and then in preclinical in vivo animal studies and may initially involve high-throughput screening of thousands of candidate compounds to identify a handful of promising leads. The most sought-after imaging biomarkers during the preclinical stage will provide information on activity at the cellular and molecular levels. A comprehensive review of imaging biomarkers for preclinical drug development is beyond the scope of this chapter, which is focused on imaging biomarkers for human clinical trials.

2.4.2 Early- and Late-Stage Clinical Trials

Investigational agents undergo increasingly rigorous clinical testing as they progress along the path toward regulatory approval. Phase 1 and 2 studies are typically smaller trials designed to establish initial safety and dosing data and to demonstrate efficacy in small study populations. Phase 3 studies are typically much larger and more costly multisite trials aimed at collecting the necessary safety and efficacy data to support a marketing application to regulatory authorities.

Given the expense involved in proceeding from phase 2 into phase 3 testing, a key objective in early clinical trials is gathering sufficient preliminary efficacy data to inform a "go or no-go" decision on continuing into phase 3 studies.

The most relevant imaging biomarkers during clinical trials will be those that provide evidence of drug efficacy as well as those that select for patient subgroups in whom drug efficacy may be higher [11, 12]. In phase 1 and phase 2 trials, investigators may choose to incorporate biomarker endpoints from a constantly expanding menu of advanced imaging techniques, presumably selecting approaches that report on functional or compositional variables correlated with the mechanism of drug action. It is in this context that the advanced techniques described in this text are currently most relevant for demonstrating the efficacy of novel molecularly targeted agents. In phase 3 trials, the most important biomarkers will be those that are reproducible across large, multisite trials and those that have been rigorously confirmed as acceptable surrogate endpoints for survival. The requirements for imaging biomarkers may be more stringent for late-stage than for early-stage clinical trials because biomarker results from early-stage clinical trials are used primarily by the trial sponsor for internal decision making, while results from late-stage clinical trials will be scrutinized by outside regulatory authorities in the drug approval process.

2.5 Current Imaging Biomarkers for Oncology Clinical Trials

Imaging biomarkers for oncology clinical trials have evolved over the past 50 years, driven by the need for objective standards with which to perform "apples-to-apples" comparisons of treatment response both between patients within a clinical trial and between different clinical trials. Until recently, the majority of imaging biomarkers for oncology have centered on tumor size measurement and size measurement changes. This section briefly reviews the salient features and drawbacks of size-based imaging biomarkers, with an emphasis on the Response Evaluation Criteria for Solid Tumors (RECIST), the most commonly recognized and utilized standard for assessing response in solid malignancies. We also review the important criticisms of RECIST, and we describe incremental modifications of RECIST that have been deployed in various tumor types.

2.5.1 RECIST

Imaging-based tumor size measurement assessment guidelines for solid malignancies were first codified in the 1980 World Health Organization criteria [13] and were revised as the Response Evaluation Criteria in Solid Tumors (RECIST) in 2000 [14] and RECIST 1.1 in 2009 [15]. The Macdonald criteria for supratentorial malignant glioma were proposed in 1990 [16]. The International Working Group (IWG) or Cheson criteria for hematologic malignancies were first issued in 1999 [17] and were revised in 2007 [18]. These response assessment tools have enjoyed widespread utilization in the scientific, industrial, and regulatory communities, and new drug approval applications routinely include results using these imaging biomarkers to support efficacy claims.

RECIST was explicitly designed for use in phase 2 clinical trials (although it is used at other stages in drug development and even clinically) and is essentially a guideline for assessing tumor response and progression based on changes in anatomical tumor burden over time. RECIST specifies criteria for categorizing lesions on baseline (i.e., pretreatment) imaging as either "target" or "nontarget" lesions, with the former to be followed with successive quantitative size measurements and the latter to be followed qualitatively. At follow-up imaging (i.e., during treatment), lesion burden is reassessed in standardized fashion, with target lesions reevaluated as the sum of their unidimensional size measurements and nontarget lesions reevaluated subjectively according to changes perceived by the reviewer. At each imaging timepoint (typically a predetermined follow-up interval specified in the study protocol), patients are assigned one of four response

categories: complete response (CR), partial response (PR), stable disease (SD), or progressive disease (PD). These patient-level response categories can then be used to construct summary trial endpoints including objective response rate (ORR, i.e., the percentage of patients achieving either PR or CR), time to progression (TTP, i.e., average time until PD), and progression-free survival (PFS, i.e., average time until PD or death).

As present time, most clinical trial protocols for solid malignancies specify one or more of these RECIST-derived imaging biomarkers as endpoints for assessing efficacy of the investigational agent. Although ORR is still widely utilized, PFS and other "time-to-event" biomarkers are increasingly incorporated as primary efficacy endpoints, especially in late-stage randomized clinical trials [19]. Recent National Cancer Institute (NCI) task force recommendations have specifically encouraged the use of PFS as a primary efficacy endpoint in phase 2 clinical trials [20]. The ascendancy of PFS has paralleled the introduction of cytostatic agents into the therapeutic armamentarium; these agents, in contrast to traditional cytotoxic agents, result in cell cycle arrest rather than cell death and may be less likely to produce gross tumor shrinkage, although patients may benefit from a delay in tumor progression which would be captured in PFS but not in ORR.

2.5.2 Problems with Size-Based Biomarkers

How well do tumor size-based biomarkers perform for response assessment? In the phase 2 clinical trial setting, ORR is generally accepted as a valid indicator of antitumor efficacy because objective responses are infrequent in the absence of efficacious treatment [21]. There also exists a small but important literature linking objective tumor response to clinical survival benefit [22, 23], to success in later-stage clinical testing [24], and to future regulatory approval [25]. In general, however, tumor shrinkage is considered an unreliable surrogate for survival, one that may either overestimate or underestimate a drug's effect on the relevant clinical endpoint [15, 26] and one that may have a different correlation with survival in different tumor types or with different drug agents [25, 27]. PFS, meanwhile, has been correlated with survival only in certain tumor types (particular advanced colorectal and ovarian cancers) [28], and biostatisticians have cautioned against extrapolating survival associations even in these tumor types to novel anticancer therapies [27]. Although tumor size-based endpoints have become an important basis for oncology drug regulatory approval [21, 29], there have been several high-profile examples of authorities having granted accelerated approval to new anticancer drugs based on tumor size measurement data, only to rescind or narrow the approval as postmarketing data failed to show a survival benefit; notable examples include U.S. Food and Drug Administration (FDA) approvals of gefitinib (Iressa) for non-small cell lung cancer and, more recently, bevacizumab (Avastin) for metastatic breast cancer.

The shortcomings of RECIST have been well publicized [30, 31] and fall into two general categories: practical problems with its implementation and more fundamental objections to a size-based approach to response assessment. Practical problems with implementing RECIST include difficulties choosing target lesions representative of total tumor burden, the need to assess many lesions on a qualitative and subjective basis, and high intraobserver and interobserver variability for heterogeneous lesions or lesions with irregular borders [32]. Single-axis measurements as dictated by RECIST may not adequately capture size changes in nonspherical lesions or lesions with asymmetric growth. Lesions along curved surfaces, abutting other organs, or adjacent to other pathology may be difficult to measure by RECIST guidelines. Finally, the use of categorical rather than continuous response variables may sacrifice statistical power.

A more fundamental objection to RECIST is that an exclusive focus on tumor size may exclude other potentially meaningful features, including morphologic, compositional, and functional parameters that may provide a more comprehensive assessment of tumor status.

Tumor size change may lag weeks to months behind a tumor biological response or may never occur at all. Size measurement criteria may therefore underestimate or fail to capture antitumor efficacy, especially of newer targeted agents that produce a cytostatic rather than cytotoxic effect.

These considerations are motivating ongoing efforts within the oncologic imaging community to improve upon current tumor size measurement biomarkers. These efforts fall into two general categories: incremental modifications to size-based biomarkers and novel imaging techniques reporting on parameters other than tumor size.

2.5.3 Incremental Modifications to Tumor Size Measurement Techniques

Other important modifications of tumor size measurement techniques under current investigation include three-dimensional volumetric measurement approaches [33] and customized response assessment guidelines tailored to specific tumor types. Examples of the latter include the Choi criteria for gastrointestinal stromal tumors [34], the modified RECIST (mRECIST) criteria for hepatocellular carcinoma [35], and the immune-related response criteria (irRC) for melanoma immune modulator therapies [36].

In addition, the RECIST and IWG criteria themselves are dynamic systems that continue to evolve and incorporate new techniques. The most recent IWG criteria incorporate fluorodeoxyglucose positron emission tomography (FDG-PET) on a variable basis depending on the FDG avidity of the lymphoma subtype [18]. RECIST 1.1 also incorporates FDG-PET, albeit on a limited basis as an indicator of disease progression [15]. In general, despite much enthusiasm for the potential of metabolic imaging, response assessment guidelines have been slow to incorporate FDG-PET, especially for solid malignancies. This is due, at least in part, to the great challenge in optimizing and standardizing techniques to enable comparable results to be obtained by different vendors and institutions.

2.6 Emerging Techniques

The cancer imaging community is actively engaged in developing new oncologic imaging biomarkers based on advanced methods of tumor characterization. Development of new biomarker tools has proceeded across several different modalities, but in general all of the newer methods aim to interrogate for functional, molecular, or compositional changes that may report on tumor response earlier and/or with greater specificity than conventional methods. Emerging techniques providing candidate biomarkers include perfusion imaging (including dynamic contrast enhancement-MRI (DCE-MRI), perfusion CT, and microbubble contrast ultrasound techniques), diffusion imaging (including newer whole-body MR diffusion approaches), advanced imaging tools for molecular compositional analysis (including MR spectroscopy, magnetization transfer, and chemical exchange saturation transfer techniques), new elastography approaches (both MR and ultrasound based), and hybrid techniques facilitating registration of functional and anatomical information (including PET-CT and PET-MR). A brief introduction is presented here, but the reader is referred to other chapters in this volume for more detailed information on these techniques.

2.6.1 Imaging Methods Reporting on Vascular Status

When a malignant tumor reaches approximately 1–2 mm^3 in volume, it can no longer rely on the passive diffusion of metabolites from host tissue blood vessels in order to continue to proliferate, so new vasculature must develop in order for the tumor to continue to thrive [37, 38]. This process of neovascularization or angiogenesis is a signature of neoplasms and one of the principal potential targets for quantitative imaging [39]. In contrast to mature blood vessels that are the result of normal physiologic processes, tumor vessels produced by angiogenesis are characteristically leaky, fragile, and incompletely formed. It is believed that virtually all solid tumors are

dependent upon angiogenesis for survival [40] and many anti-angiogenic drugs are currently in clinical trials [41]. Thus, methods for imaging and quantitatively assessing this phenomenon are quite promising as biomarkers for application in preclinical and clinical studies.

Currently, one of the most widely employed methods for characterizing tumor neovasculature is DCE-MRI. (Other important methods for interrogating tumor vascularity include contrast-enhanced CT [42] and microbubble enhanced sonography [43].) Changes in the parameters obtained from DCE-MRI can be used to assess vascular changes within a tumor and, in particular, how a tumor is responding to treatment. The method is based on measurements and pharmacokinetic models of how a (typically) gadolinium based contrast agent perfuses through such vessels. Healthy vessels in normal tissues may be characterized by a range of parameters measuring blood flow, vessel permeability, and tissue volume fractions (i.e., fractions of a given sample of tissue that can be attributed to intravascular or extravascular space). These parameters are known to be different in vessels associated with tumors. Furthermore, as tumor blood vessels are known to change in response to anti-angiogenic drugs, the method provides a way of quantifying those changes. It is thus a plausible hypothesis that parameters measuring treatment induced changes in pathologic vessels will be predictive of response at an earlier time than changes in longest dimension. Indeed, many studies across a range of tumor types have shown just that.

2.6.2 Imaging Methods Reporting on Cell Density

Perhaps the most basic definition of cancer is that it is a set of diseases characterized by unregulated cell growth and proliferation. Furthermore, since many anticancer drugs have as their ultimate goal destruction of tumor cells, imaging methods sensitive to changes to tissue cellularity are of great importance. The typical application of histology and molecular biology in *living* systems is somewhat limited as it cannot provide a noninvasive deep tissue visualization of cells and molecules of interest. In particular, the visualization of cellular and molecular activity in animals normally requires the sacrifice and destruction of the organism to allow for analysis by histology and molecular biology. The development of cellular and molecular imaging techniques has begun to bridge this gap.

Two of the most promising methods for noninvasively probing tissue cellularity are diffusion-weighted magnetic resonance imaging (DW-MRI) to probe tissue cellularity and fluorodeoxythymidine-PET (FLT-PET) to image cell proliferation. DW-MRI exploits the microscopic thermally induced behavior of molecules moving in a random pattern, i.e., self-diffusion or Brownian motion. The rate of diffusion in cellular tissues is described by means of an apparent diffusion coefficient (ADC) that largely depends on the number and separation of barriers that a diffusing water molecule encounters. DW-MRI methods have been developed to map the ADC, and in well-controlled situations the variations in ADC have been shown to correlate inversely with tissue cellularity [44]. Many studies, both preclinical and clinical, have shown that exposure of tumors to chemotherapy leads to measurable increases in water diffusion in cases of favorable treatment response [45, 46].

FLT-PET exploits the increased uptake of thymidine in malignant tumors. Thymidine is a native nucleoside taken up by cells via surface nucleoside transporters and phosphorylated inside the cell by thymidine kinase 1 (TK1) into thymidine monophosphate. TK1 activity is upregulated during active DNA synthesis. FLT works in an analogous fashion: FLT is phosphorylated by TK1 into FLT monophosphate which is subsequently modified into FLT diphosphonate and triphosphonate by thymidylate kinase and diphosphate kinase, respectively. As FLT triphosphonate cannot be incorporated into the growing DNA chain, there will be an accumulation of FLT mono-, di-, and trisphosphate in such cells, thus

forming the basis of FLT-PET imaging of cell proliferation [47]. FLT-PET is thus a promising biomarker for cell proliferation in both preclinical and clinical studies.

2.6.3 Imaging Methods Reporting on Metabolic Events

The PET radiotracer most frequently used in clinical practice is fluorodeoxyglucose (FDG). As a glucose analogue, FDG is taken up by tumor cells via the GLUT1 and GLUT3 transporters and phosphorylated by hexokinase to FDG-6-phosphate. However, unlike glucose-6-phosphate, FDG-6-phosphate is not metabolized further in the glycolytic pathway and therefore remains trapped intracellularly because tumor cells do not have a significant amount of glucose-6-phosphatase to reverse this reaction. As the rate of glucose metabolism can differ significantly between healthy and malignant tissues, FDG can selectively accumulate in tumors, and quantification of this accumulation is a biomarker of tumor glucose metabolism. As discussed above, FDG-PET has been incorporated into the most recent response assessment guidelines for both solid and hematologic malignancies, but further incorporation into RECIST has been deferred pending development of further image acquisition and analysis standards. The PET community has taken bold steps in proposing a preliminary independent metabolic response standard, the PET Response Criteria in Solid Tumors (PERCIST) [48].

Magnetic resonance spectroscopy (MRS) can noninvasively provide data on the presence and relative concentrations of different metabolites in tumors [49]. MRS imaging (MRSI) extends this approach to provide spatial resolution of metabolite concentrations at the cost (typically) of increased scan time and reduced signal-to-noise ratios. These techniques have been employed for several decades to detect the altered metabolic signatures of cancer cells in both the diagnostic and prognostic settings. In particular, many malignancies demonstrate elevated levels of choline (due to increased membrane turnover in proliferating tumor cells) and lactate (due to increased anaerobic glycolysis).

2.7 Evaluation of Imaging Biomarkers as Surrogate Endpoints for Clinical Trials

As new imaging biomarkers advance to the point of possible adoption into clinical trials, investigators must contend with achieving the proper level of evaluation to assure that the biomarker is providing valuable information to its users. Just as different biomarkers might be appropriately deployed at different stages in the drug development process, there may be different requirements for biomarker evaluation depending on the intended use of the biomarker itself. In early-stage clinical studies, trial sponsors may determine for themselves whether an imaging biomarker is biologically relevant and has been sufficiently evaluated so as to be useful for internal decision making [6]. Conversely, if imaging biomarker data is to be collected for submission to regulatory authorities as part of a drug approval application, that biomarker data will be accepted as evidence of drug efficacy only if the biomarker has been previously evaluated and confirmed to be a valid or at least reasonably likely surrogate endpoint [21]. This section discusses the biomarker evaluation framework proposed by the IOM as it pertains to imaging biomarkers and surrogate endpoints for cancer clinical trials. We also briefly discuss the regulatory perspective.

2.7.1 The IOM Biomarker Evaluation Framework

The IOM framework establishes three discrete steps in the biomarker evaluation process: analytical validation, qualification, and utilization. *Analytical validation* involves demonstration that the biomarker can be reliably measured. For a biomarker to be analytically valid, its detection

and/or quantitative measurement must be accurate, reproducible across multiple clinical settings, and feasible over time [2]. Analytical validation of a biomarker includes generation of data on limits of detection, limits of quantification, and reference normal values.

A particular component of analytical validation that is underexplored, and critical to the acceptance of quantitative imaging biomarkers, is the repeatability and reproducibility of individual measures. Repeatability concerns variability in successive measurements (made by the same operator) and defines the difference between two scans that can be attributed to protocol and noise as opposed to true physiological changes. Reproducibility is defined as the degree of agreement between measurements made by different operators and is specified in several parameters including the 95 % confidence interval (CI) of the mean, which denotes the inter-user variability of the group mean parameter value. Measuring institutional repeatability and elaborating rigorous imaging protocols to ensure reproducibility are both important to inform comparisons between imaging sessions separated in time and are both crucial to enable calculation of the magnitude of observed effect required to conclude that a true biological change has occurred (e.g., in assessing the response of tumor to therapeutic intervention). Unfortunately, there is a fairly limited literature on the repeatability and reproducibility of quantitative imaging metrics. For example efforts in MRI or PET, the interested reader is referred to [50–54] and [55–57], respectively.

Qualification involves objective demonstration that the biomarker is associated with the clinical endpoint of concern. While the exact requirements for establishing this relationship have evolved over time and remain a subject of much debate and research, the current consensus is that qualification can be based on a "correlation approach": the biomarker should be prognostic for disease outcome in the absence of treatment, and the effect of intervention on the surrogate should be sufficiently correlated with the effect on the true endpoint [27]. With respect to the latter criterion, Prentice originally proposed that the biomarker must capture the full range of the treatment effect [58], but this requirement has been recognized as too strict to be practically useful and has been replaced with the criterion that the biomarker captures a substantial portion of the treatment effect, for example, more than 50 % [59]. Sargent et al. note that demonstrating correlation between a prospective biomarker and a clinical endpoint is not sufficient to qualify the biomarker, as such a correlation may be a result of prognostic factors influencing both the biomarker and clinical endpoint rather than the result of a similar treatment effect on both variables; rather, the true test for biomarker validity is whether it captures treatment effect at the trial level, as assessed by a meta-analysis of phase 3 trials in which both variables are measured [59].

A number of challenges exist for validation of imaging biomarkers using this statistical construct. First, even with a planned meta-analysis of several trials, it is difficult to obtain adequate power to show that a substantial portion of the treatment effect at the trial level is captured by the prospective biomarker [59]. Second, separate qualification of surrogate endpoints is required in the setting of different treatments; i.e., if a biomarker is qualified as a surrogate endpoint with respect to one treatment, it cannot be assumed that it is automatically qualified as a surrogate when evaluating a novel treatment with a different mechanism of action [27]. Third, this qualification approach assumes consensus on the appropriate clinical endpoint, which may not always be present. In particular, many observers have called attention to the difficulties in using overall survival as the primary clinical endpoint in solid tumors for which several lines of treatment may be available and have proposed instead that PFS may be a more appropriate endpoint for many phase 3 clinical trials [10].

Utilization involves assessment of biomarker performance in the specific context of its proposed use. From a pragmatic point of view, candidate biomarkers may be evaluated not solely on the basis of statistical qualification but also with respect to their biological plausibility and clinical usefulness [60]. Lassere has proposed

a formal schema for grading the surrogacy relationships between proposed biomarkers and clinical endpoints based on a weighted evaluation of biological, epidemiological, statistical, clinical trial, and risk-benefit evidence [61]. Even if an imaging biomarker is well correlated with clinical response, it may not demonstrate important drug side effects or toxicities [9]; the utilization component of the IOM framework therefore provides for a holistic assessment of a biomarker's usefulness for decision making.

2.7.2 The Regulatory Perspective

Regulatory considerations have had profound influence on the incorporation of imaging biomarkers into oncology clinical trials, especially during late-phase drug development. This section provides a brief history of how the regulatory perspective on imaging biomarkers has evolved, with a focus on the U.S. FDA. A detailed review of requirements from different agencies is beyond the scope of this chapter.

Two different routes are available for FDA approval of a new therapeutic agent: regular approval and accelerated approval. In the 1970s, before the creation of accelerated approval, the FDA commonly granted regular approval for cancer drugs based on ORR as determined either by imaging or by physical examination measurements. During the mid-1980s, however, the FDA determined that regular approval for cancer drugs should require more direct evidence of clinical benefit, particularly improved survival, improved quality of life, or improvement in an established surrogate for at least one of these [21]. Over the next decade, several endpoints were established as acceptable surrogates for clinical benefit, including improved disease-free survival (DFS) in selected adjuvant settings, durable CR in leukemia, and a high substantiated ORR in select solid tumors, provided that ORR data are considered alongside response duration, drug toxicity, and relief of tumor-related symptoms. It should be emphasized, therefore, that the requirement for established surrogacy of nonclinical endpoints did not eliminate drug approvals based on imaging biomarker data; indeed, improved ORR in conjunction with improvement in symptoms and adequate response duration has continued to support regular approval in several clinical settings [62].

The accelerated approval route was created in 1992, partially in response to public demand for quicker approval of new anticancer drugs. Accelerated approval allows for the consideration of surrogate endpoints that are "reasonably likely" to predict clinical benefit, a lower standard than that required for regular approval. A drug is approved under the accelerated approval regulations on the condition that the manufacturer conducts postmarketing studies to verify and describe the actual clinical benefit. If postmarketing studies fail to demonstrate clinical benefit, the drug may be removed from market under an expedited process. ORR has been the most commonly used nonclinical endpoint in support of accelerated approval [62].

A review of FDA cancer drug approvals between 1990 and 2002 showed that out of 71 total approvals, 57 were regular approvals and 14 were accelerated approvals. Thirty-nine out of the 57 regular approvals (68 %) were based on endpoints other than survival, mostly ORR but also DFS and TTP, occasionally but not always supplemented by evidence of relief of tumor-based symptoms. All 14 of the accelerated approvals were based on surrogate endpoints, again mostly ORR but also DFS and TTP [21].

Over the past decade, both the FDA and the European Medicines Agency (EMA) have hosted several workshops on biomarkers and surrogate endpoints in new drug development [63, 64]. The FDA has also established a public-private Biomarkers Consortium, including representation from the FDA, NIH, and pharmaceutical industry, seeking to identify and qualify new and existing biomarkers [65]. Both the FDA and EMA routinely issue guidance documents to industry on biomarker-related topics including methods of demonstrating drug efficacy [66], appropriate endpoints for cancer clinical trials [62], and considerations for adaptive design clinical trials [67].

Conclusion

Imaging biomarkers hold great potential for streamlining drug development and optimizing clinical care, but there is much to be done in order to develop, validate, and standardize emerging methods before they can be accepted as surrogate endpoints in multicenter trials. Ideally, biomarker development would be closely coupled with development of candidate compounds [11], but add-on costs have been a significant barrier, especially in clinical trials [68]. Part of the challenge has now been taken up by multiple government-industry partnerships, including the Quantitative Imaging Biomarker Alliance (QIBA), organized by the Radiological Society of North America (RSNA); the NCI's Quantitative Imaging Network (QIN); and the FDA and EMA biomarker consortia mentioned above. In the USA, the recent merging of the Eastern Cooperative Oncology Group (ECOG) with the American College of Radiology Imaging Network (ACRIN) provides an additional promising venue for advancing imaging biomarkers in oncology.

While traditional size-based imaging biomarkers will likely remain the dominant non-survival endpoints for the foreseeable future, major efforts are now being directed toward pushing response assessment beyond anatomical and morphological imaging to more fundamental metrics at the physiological, cellular, and molecular levels. These concepts will be developed more fully in subsequent chapters.

References

1. Institute of Medicine. A national cancer clinical trials system for the 21st century: reinvigorating the NCI cooperative group program. Washington, DC: National Academies Press; 2010.
2. Institute of Medicine. Evaluation of biomarkers and surrogate endpoints in chronic disease. Washington, DC: National Academies Press; 2010.
3. Hricak H. Oncologic imaging: a guiding hand of personalized cancer care. Radiology. 2011;259(3):633–40.
4. Group BDW. Biomarkers and surrogate endpoints: preferred definitions and conceptual framework. Clin Pharmacol Ther. 2001;69(3):89–95.
5. Wolff AC, et al. Research issues affecting preoperative systemic therapy for operable breast cancer. J Clin Oncol. 2008;26(5):806–13.
6. Richter WS. Imaging biomarkers as surrogate endpoints for drug development. Eur J Nucl Med Mol Imaging. 2006;33:S6–S10.
7. Varmus H. Ten years on–the human genome and medicine. N Engl J Med. 2010;362(21):2028–9.
8. Morgan S, et al. The cost of drug development: a systematic review. Health Policy. 2011;100(1):4–17.
9. Smith JJ, et al. Biomarkers in imaging: realizing radiology's future. Radiology. 2003;227(3):633–8.
10. Sargent DJ, Hayes DF. Assessing the measure of a new drug: is survival the only thing that matters? J Clin Oncol. 2008;26(12):1922–3.
11. Park JW, et al. Rationale for biomarkers and surrogate end points in mechanism-driven oncology drug development. Clin Cancer Res. 2004;10(11):3885–96.
12. Tan DS, et al. Biomarker-driven early clinical trials in oncology: a paradigm shift in drug development. Cancer J. 2009;15(5):406–20.
13. Miller AB, et al. Reporting results of cancer treatment. Cancer. 1981;47(1):207–14.
14. Therasse P, et al. New guidelines to evaluate the response to treatment in solid tumors. European Organization for Research and Treatment of Cancer, National Cancer Institute of the United States, National Cancer Institute of Canada. J Natl Cancer Inst. 2000;92(3):205–16.
15. Eisenhauer EA, et al. New response evaluation criteria in solid tumours: revised RECIST guideline (version 1.1). Eur J Cancer. 2009;45(2):228–47.
16. Macdonald DR, et al. Response criteria for phase II studies of supratentorial malignant glioma. J Clin Oncol. 1990;8(7):1277–80.
17. Cheson BD, et al. Report of an international workshop to standardize response criteria for non-Hodgkin's lymphomas. NCI Sponsored International Working Group. J Clin Oncol. 1999;17(4):1244.
18. Cheson BD, et al. Revised response criteria for malignant lymphoma. J Clin Oncol. 2007;25(5):579–86.
19. Kay A, et al. Randomized controlled trials in the era of molecular oncology: methodology, biomarkers, and end points. Ann Oncol. 2012;23(6):1646–51.
20. Seymour L, et al. The design of phase II clinical trials testing cancer therapeutics: consensus recommendations from the clinical trial design task force of the national cancer institute investigational drug steering committee. Clin Cancer Res. 2010;16(6):1764–9.
21. Johnson JR, et al. End points and United States Food and Drug Administration approval of oncology drugs. J Clin Oncol. 2003;21(7):1404–11.
22. Buyse M, et al. Relation between tumour response to first-line chemotherapy and survival in advanced colorectal cancer: a meta-analysis. Meta-Analysis Group in Cancer. Lancet. 2000;356(9227):373–8.

23. Paesmans M, et al. Response to chemotherapy has predictive value for further survival of patients with advanced non-small cell lung cancer: 10 years experience of the European Lung Cancer Working Party. Eur J Cancer. 1997;33(14):2326–32.
24. Sekine I, et al. Relationship between objective responses in phase I trials and potential efficacy of non-specific cytotoxic investigational new drugs. Ann Oncol. 2002;13(8):1300–6.
25. Goffin J, et al. Objective responses in patients with malignant melanoma or renal cell cancer in early clinical studies do not predict regulatory approval. Clin Cancer Res. 2005;11(16):5928–34.
26. Fleming TR, DeMets DL. Surrogate end points in clinical trials: are we being misled? Ann Intern Med. 1996;125(7):605–13.
27. Buyse M, et al. Biomarkers and surrogate end points–the challenge of statistical validation. Nat Rev Clin Oncol. 2010;7(6):309–17.
28. Booth CM, Eisenhauer EA. Progression-free survival: meaningful or simply measurable? J Clin Oncol. 2012;30(10):1030–3.
29. Sridhara R, et al. Review of oncology and hematology drug product approvals at the US Food and Drug Administration between July 2005 and December 2007. J Natl Cancer Inst. 2010;102(4):230–43.
30. Ratain MJ, Eckhardt SG. Phase II studies of modern drugs directed against new targets: if you are fazed, too, then resist RECIST. J Clin Oncol. 2004; 22(22):4442–5.
31. Tuma RS. Sometimes size doesn't matter: reevaluating RECIST and tumor response rate endpoints. J Natl Cancer Inst. 2006;98(18):1272–4.
32. Erasmus JJ, et al. Interobserver and intraobserver variability in measurement of non-small-cell carcinoma lung lesions: implications for assessment of tumor response. J Clin Oncol. 2003;21(13):2574–82.
33. Zhao B, et al. A pilot study of volume measurement as a method of tumor response evaluation to aid biomarker development. Clin Cancer Res. 2010;16(18): 4647–53.
34. Choi H, et al. Correlation of computed tomography and positron emission tomography in patients with metastatic gastrointestinal stromal tumor treated at a single institution with imatinib mesylate: proposal of new computed tomography response criteria. J Clin Oncol. 2007;25(13):1753–9.
35. Lencioni R, Llovet JM. Modified RECIST (mRECIST) assessment for hepatocellular carcinoma. Semin Liver Dis. 2010;30(1):52–60.
36. Wolchok JD, et al. Guidelines for the evaluation of immune therapy activity in solid tumors: immune-related response criteria. Clin Cancer Res. 2009;15(23):7412–20.
37. Folkman J. Role of angiogenesis in tumor growth and metastasis. Semin Oncol. 2002;29(6 Suppl 16):15–8.
38. Ribatti D, et al. The discovery of angiogenic factors: a historical review. Gen Pharmacol. 2000;35(5): 227–31.
39. Atri M. New technologies and directed agents for applications of cancer imaging. J Clin Oncol. 2006;24(20):3299–308.
40. Carmeliet P, Jain RK. Angiogenesis in cancer and other diseases. Nature. 2000;407(6801):249–57.
41. Verhoef C, et al. Angiogenesis inhibitors: perspectives for medical, surgical and radiation oncology. Curr Pharm Des. 2006;12(21):2623–30.
42. Koh TS, et al. Primary colorectal cancer: use of kinetic modeling of dynamic contrast-enhanced CT data to predict clinical outcome. Radiology. 2013;267(1):145–54.
43. Fleischer AC, et al. Sonographic depiction of microvessel perfusion: principles and potential. J Ultrasound Med. 2004;23(11):1499–506.
44. Anderson AW, et al. Effects of cell volume fraction changes on apparent diffusion in human cells. Mag Reson Imaging. 2000;18(6):689–95.
45. Galons JP, et al. Early increases in breast tumor xenograft water mobility in response to paclitaxel therapy detected by non-invasive diffusion magnetic resonance imaging. Neoplasia. 1999;1(2):113–7.
46. Lee KC, et al. Prospective early response imaging biomarker for neoadjuvant breast cancer chemotherapy. Clin Cancer Res. 2007;13(2 Pt 1):443–50.
47. Soloviev D, et al. [(18)F]FLT: an imaging biomarker of tumour proliferation for assessment of tumour response to treatment. Eur J Cancer. 2012;48(4): 416–24.
48. Wahl RL, et al. From RECIST to PERCIST: evolving considerations for PET response criteria in solid tumors. J Nucl Med. 2009;50 Suppl 1:122S–50S.
49. Griffiths JR, Glickson JD. Monitoring pharmacokinetics of anticancer drugs: non-invasive investigation using magnetic resonance spectroscopy. Adv Drug Deliv Rev. 2000;41(1):75–89.
50. Padhani AR, et al. Reproducibility of quantitative dynamic MRI of normal human tissues. NMR Biomed. 2002;15(2):143–53.
51. Yankeelov TE, et al. Repeatability of a reference region model for analysis of murine DCE-MRI data at 7T. J Magn Reson Imaging. 2006;24(5):1140–7.
52. Barnes SL, et al. Assessing the reproducibility of dynamic contrast enhanced magnetic resonance imaging in a murine model of breast cancer. Magn Reson Med. 2013;69(6):1721–34.
53. Dula AN, et al. Amide proton transfer imaging of the breast at 3 T: establishing reproducibility and possible feasibility assessing chemotherapy response. Magn Reson Med. 2013;70(1):216–24.
54. Alonzi R, et al. Reproducibility and correlation between quantitative and semiquantitative dynamic and intrinsic susceptibility-weighted MRI parameters in the benign and malignant human prostate. J Magn Reson Imaging. 2010;32(1):155–64.
55. Whisenant JG, et al. Reproducibility of static and dynamic (18)F-FDG, (18)F-FLT, and (18)F-FMISO MicroPET studies in a murine model of HER2+ breast cancer. Mol Imaging Biol. 2013;15(1):87–96.

56. Tseng JR, et al. Reproducibility of 3′-deoxy-3′-(18) F-fluorothymidine microPET studies in tumor xenografts in mice. J Nucl Med. 2005;46(11):1851–7.
57. Dandekar M, et al. Reproducibility of 18F-FDG microPET studies in mouse tumor xenografts. J Nucl Med. 2007;48(4):602–7.
58. Prentice RL. Surrogate endpoints in clinical trials: definition and operational criteria. Stat Med. 1989; 8(4):431–40.
59. Sargent DJ, et al. Validation of novel imaging methodologies for use as cancer clinical trial end-points. Eur J Cancer. 2009;45(2):290–9.
60. Green E, et al. Surrogate endpoint validation: statistical elegance versus clinical relevance. Stat Methods Med Res. 2008;17(5):477–86.
61. Lassere MN. The biomarker-surrogacy evaluation schema: a review of the biomarker-surrogate literature and a proposal for a criterion-based, quantitative, multidimensional hierarchical levels of evidence schema for evaluating the status of biomarkers as surrogate endpoints. Stat Methods Med Res. 2008; 17(3):303–40.
62. U.S. Food and Drug Administration. Guidance for industry: clinical trial endpoints for the approval of cancer drugs and biologics. Rockville, 2007.
63. Dis Markers. NIH-FDA conference: biomarkers and surrogate endpoints: advancing clinical research and applications. Abstracts. Dis Markers. 1998;14(4): 187–334.
64. European Medicines Agency. 2006 EMEA/EFPIA Workshop on Biomarkers. Available at: http://www.ema.europa.eu/ema/index.jsp?curl=pages/news_and_events/events/2009/11/event_detail_000077.jsp&mid=WC0b01ac058004d5c3. Accessed 23 Aug 2013.
65. The biomarkers consortium. Available at: http://www.biomarkersconsortium.org/. Accessed 23 Aug 2013.
66. U.S. Food and Drug Administration. Guidance for industry: providing clinical evidence of effectiveness for human drug and biological products. Rockville, 1998.
67. U.S. Food and Drug Administration. Guidance for industry: adaptive design clinical trials for drugs and biologics (draft guidance). Rockville, 2010.
68. Woodcock J. A framework for biomarker and surrogate endpoint use in drug development. Available at: www.fda.gov. Accessed 23 Aug 2013.

Role of Molecular Imaging in the Era of Personalized Medicine: A Review

3

Evis Sala, Hebert Alberto Vargas, Olivio F. Donati, Wolfgang A. Weber, and Hedvig Hricak

Contents

Please note: Dr. Donati's work was supported by the Swiss National Science Foundation and the Swiss Radiologic Society. The authors have no other funding support and no conflicts of interest to disclose.

E. Sala, MD, PhD • H.A. Vargas, MD • W.A. Weber, MD, PhD • H. Hricak, MD, PhD (✉)
Department of Radiology, Memorial Sloan-Kettering Cancer Center, 1275 York Avenue, room C-278, New York, NY 10065, USA
e-mail: salae@mskcc.org; vargasah@mskcc.org; weberw@mskcc.org; hricakh@mskcc.org

O.F. Donati, MD
Department of Radiology, Memorial Sloan-Kettering Cancer Center, 1275 York Avenue, room C-278, New York, NY 10065, USA

Institute of Diagnostic and Interventional Radiology, University Hospital Zurich, Raemistrasse 100, 8091, Zurich, Switzerland
e-mail: odonati@gmx.net

Abbreviations

ADC	Apparent diffusion coefficient
BOLD	Blood oxygen level dependent
^{11}C	Carbon-11
^{13}C	Carbon-13
CALGB	Cancer and leukemia group B
CT	Computed tomography
Cu	Copper-60/copper-64
DCE-MRI	Dynamic contrast-enhanced MRI
DNP	Dynamic nuclear polarization
DW-MRI	Diffusion-weighted MRI (also referred to as DWI)
EGFR	Epidermal growth factor receptor
EPR	Enhanced permeability and retention
F	Fluorine-18
FDG	Fluorodeoxyglucose
FET	Fluoroethyltyrosine
FLT	Fluoro-l-thymidine
FMISO	Fluoro-misonidazole [$^{60/64}$Cu] copper(II)-diactyl-bis(*N4-methyl-thiosemicarbazone* ($^{60/64}$Cu-ATSM)
HER2	Human epidermal growth factor receptor 2
ICG	Indocyanine green
K^{trans}	Volume transfer constant
MR/PET	Magnetic resonance/PET
MRI	Magnetic resonance imaging
MRSI	Magnetic resonance spectroscopic imaging
PET	Positron emission tomography
SPECT	Single-photon emission computed tomography

A. Luna et al. (eds.), *Functional Imaging in Oncology*,
DOI 10.1007/978-3-642-40412-2_3,

3.1 Introduction

Molecular imaging allows the visual representation, characterization, and quantification of biological processes at the cellular and subcellular levels within intact living organisms [1]. Although molecular imaging has existed for many years, thanks to advances in numerous fields, including molecular and cell biology, physics, engineering, and computer science, its scope has expanded dramatically over the past decade and is continuously growing. Not only are there now multiple imaging technologies created specifically for molecular imaging (e.g., SPECT, PET, and optical imaging modalities), there are also a plethora of methods to apply modalities originally created for anatomic imaging to directly or indirectly image biological processes; examples of the latter include the many forms of functional MRI, such as MR spectroscopic imaging (MRSI), diffusion-weighted MRI, and dynamic contrast-enhanced MRI [2–5].

MRSI allows the acquisition and spatial localization of metabolic data. In oncology, it is used to identify tumors based on their metabolic signatures [6]. For example, cancer in the brain may be detected based on changes in the relative concentrations of lactate, choline, and *N*-acetylaspartate [7]. The spatial and spectral resolution of MRSI, though limited, has been steadily increasing with improvements in software and MRI technology (e.g., higher magnetic field strengths).

DW-MRI, which measures water movement in biological tissues, is another promising technique for oncologic imaging that is quickly evolving [8, 9]. Within a highly cellular environment, water diffusion is restricted. Thus, solid tissues with high cellularity (e.g., tumor tissues, cytotoxic edema, abscess, and fibrosis) display higher DWI signal intensity and lower apparent diffusion coefficient (ADC) values than do less dense tissues [8–10]. Clinically, DW-MRI is used to detect, characterize, and stage tumors (Fig. 3.1); distinguish tumors from surrounding tissues; predict and monitor response to therapy; and evaluate tumor recurrence [11–14]. The development of stronger diffusion gradients, faster imaging sequences, and improvements in hardware have allowed DWI to be extended to whole-body imaging, which has been particularly useful in oncology [10].

To provide "multiparametric MRI," MRSI and DW-MRI are at times used in conjunction with each other or with dynamic contrast-enhanced MRI (DCE-MRI) [8]. For DCE-MRI, images are acquired repeatedly as a contrast agent passes through tissue, providing potentially useful information about blood flow and vascularization. With certain cancer treatments, changes in tumor vascularity that reflect treatment response may be visible on DCE-MRI before tumor size changes can be discerned on anatomic imaging. Thus, DCE-MRI appears to be a promising source of predictive biomarkers and has been used for early treatment response assessment in patients treated with anti-angiogenesis drugs, chemotherapy, and other therapies [15–19]. The role of DCE-MRI in clinical practice has been limited by the relatively small number of patients in many published trials, the use of widely varying acquisition techniques and modeled parameters, as well as the use of diverse disease endpoints. Current attempts to standardize DCE-MRI will help to address these issues in the future [8, 20].

Novel technologies for in vivo molecular imaging include new tools for Raman spectroscopy, which can distinguish specific molecular compositions based on the wavelengths of photons with which they have interacted [21]. In addition, equipment for a process called "dynamic nuclear polarization" (DNP) has just entered the clinical research arena [22]. MR signal is proportional to nuclear spin polarization (the difference in the fraction of nuclei aligned with or against an applied magnetic field); such polarization is typically very small, making it a challenge to image nuclei other than protons, which are readily apparent only because of their natural abundance in the body [22]. DNP makes it possible to image nuclei such as ^{15}N or ^{13}C rapidly and with high sensitivity by temporarily "hyperpolarizing" them [22]. After the administration of a hyperpolarized agent such as [1-^{13}C]pyruvate, the agent itself, as well as its metabolic products, can be depicted with MRI technology.

At present, PET (which is typically combined with CT to provide anatomical context) is the most versatile molecular imaging technology

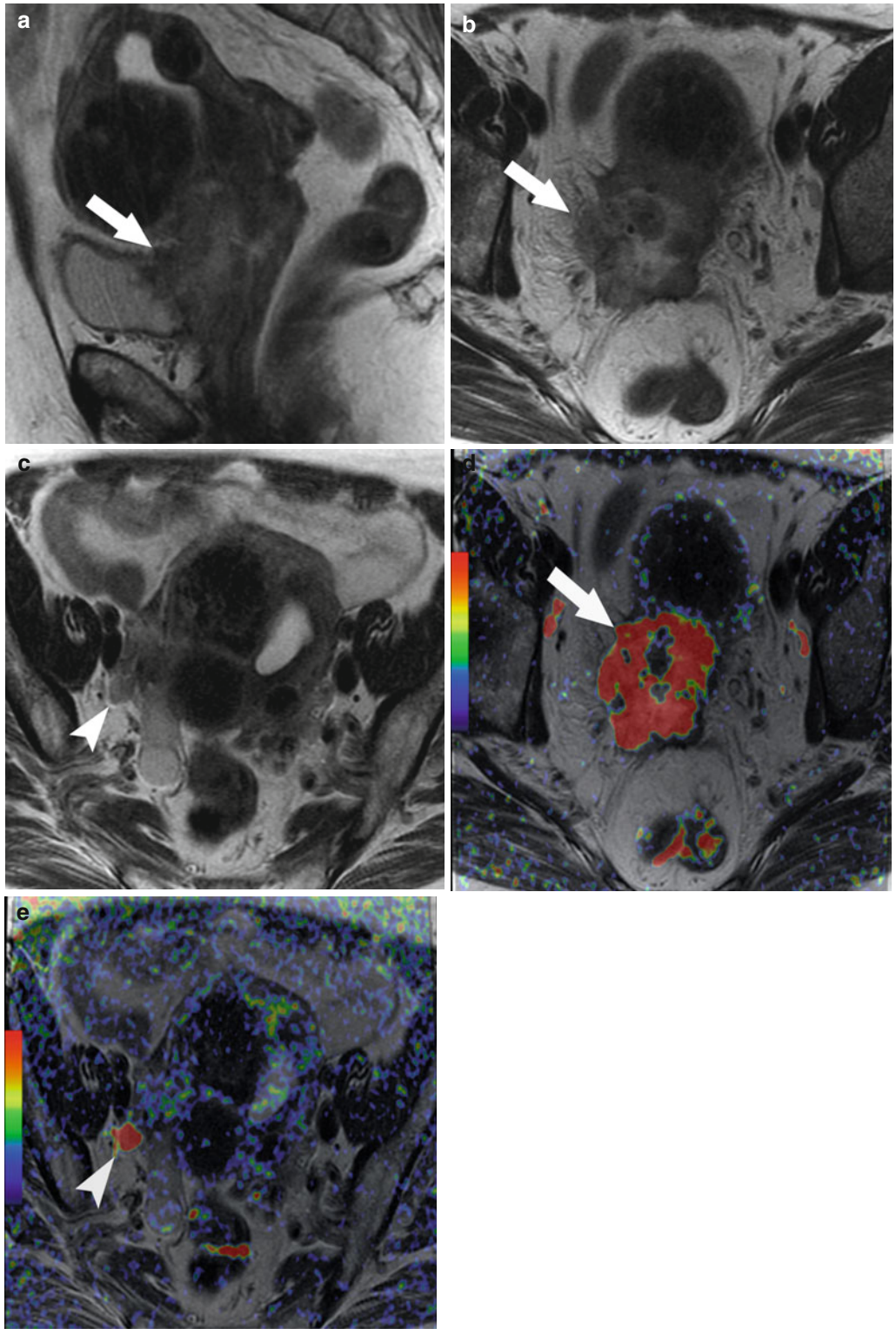

Fig. 3.1 Forty-four-year-old woman with stage IVA cervical cancer with pelvic lymph node metastasis. Sagittal (**a**) and axial (**b**, **c**) T2-weighted images demonstrate the tumor (*arrow*) invading the posterior bladder wall and an external iliac lymph node on the right (*arrowhead*). Fused diffusion-weighted and T2-weighted images (**d**, **e**) demonstrate restricted diffusion in the tumor (*arrow*) as well as in the metastatic lymph node (*arrowhead*)

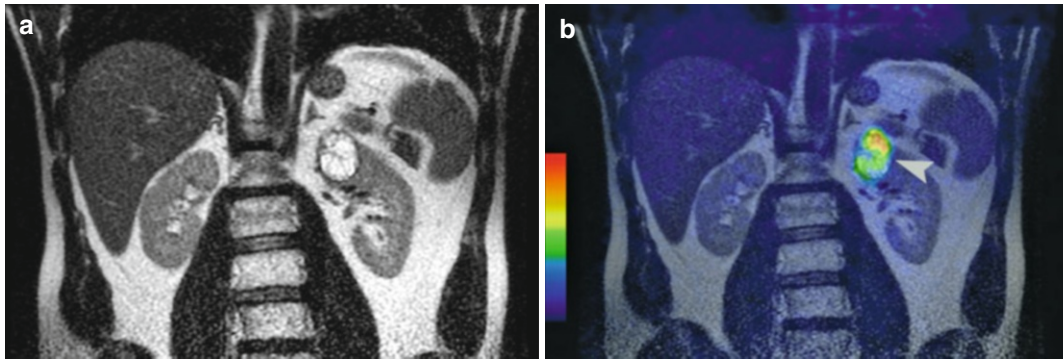

Fig. 3.2 Patient with clear cell carcinoma, Fuhrman grade II/IV. Coronal T2-weighted MR image (**a**) shows a renal mass at the left upper pole. Fused iodine-124-labeled cg250 PET/T2-weighted MR image (**b**) demonstrates tracer uptake within this renal mass (*arrowhead*). Pathology confirmed the presence of a clear cell carcinoma

available. Not only can it detect and quantify abnormal molecular activity throughout the body, it can be applied with a wide range of molecular imaging probes [23].

3.2 Current and Emerging Applications for Molecular Imaging in Oncology

The most important imaging modalities in oncology today are CT, MRI, and PET/CT. Compared to CT and PET/CT, MRI has important advantages, such as the lack of radiation exposure, high spatial and temporal resolution, superior soft tissue contrast, and the capacity for multiparametric imaging. Though it is still limited to the research setting, MRI with hyperpolarized molecules allows detailed studies of tumor metabolism not only in preclinical models but also in humans. MR/PET imaging (Fig. 3.2) offers the potential for robust, joint structural, functional, and molecular imaging assessment of a wide variety of tumors, as it allows PET techniques to be combined with the broad array of MRI techniques – including hyperpolarized MRI. As such, it promises to markedly enhance cancer detection and characterization, treatment planning, response prediction, and response assessment, and it could help optimize the development of new drugs by noninvasively providing in vivo quantitative data about their pharmacokinetics and pharmacodynamics [24]. Where possible, the substitution of MR/PET for PET/CT would also reduce radiation exposure, which is highly desirable for all patients and especially for pediatric patients and those who undergo multiple examinations.

3.2.1 Imaging in the Era of Genetic Medicine

Developing and validating quantitative imaging biomarkers that reflect underlying histologic and/or genomic features may provide a novel way of noninvasively assessing tumor heterogeneity and predicting drug response or resistance in oncology. The advent of molecularly targeted therapy and anti-angiogenic strategies has heightened the need for sensitive biomarkers for predicting treatment response and outcome, as resistance to chemotherapeutics and targeted therapies is common. Genetic intratumoral heterogeneity may contribute to treatment failure by initiating phenotypic diversity that introduces tumor sampling bias and enables drug resistance to emerge. In patients with primary and metastatic renal cell carcinoma, multiregion genetic analyses showed that spatially heterogeneous somatic mutations and chromosomal imbalances lead to phenotypic intratumoral diversity and that a single tumor biopsy specimen reveals a minority of the genetic aberrations present in an entire tumor [25]. Using phylogenic tree analysis to evaluate the relationships between tumor deposits in patients with

ovarian cancer, Cowin et al. [26] found substantial copy number differences between metastatic deposits within individual patients and identified signaling pathways plausibly linked to peritoneal dissemination and establishment of metastatic foci. Significantly greater genomic change was observed in patients who experienced relapse after responding to chemotherapy than in patients who were resistant from the outset, possibly reflecting the requirement for selection of a subpopulation of resistant cells in cases initially sensitive to treatment [26].

Morphological heterogeneity between and within tumors is readily apparent in clinical imaging; subjective expressions of these differences, such as spiculated, enhancing, and necrotic, are common descriptors in the imaging lexicon. In the past several years, imaging research has focused on quantifying these image features in an effort to understand their biological and clinical implications. More recently, in an approach referred to as "radiogenomics," quantitative shape, border, and texture analysis features (radiomics) obtained from CT, MRI, and PET have been correlated with genomic data and outcome data with the goal of developing robust biomarkers. Following extraction of more than 100 CT imaging features, Segal et al. [27] found that a subset of 14 features predicted 80 % of the gene expression pattern in hepatocellular carcinoma. A similar extraction of features from MRI of glioblastoma was able to predict protein expression patterns [28]. Radiomic features such as texture can predict response to therapy in renal cancer [29] and overall survival in primary [30] and metastatic colon cancer [31]. Analysis of heterogeneity on DCE-MRI and DW-MRI has been shown to improve diagnosis and assessment of prognosis for several tumor types [32–35]. Furthermore, measures of metabolic heterogeneity at baseline PET were able to predict response to chemoradiotherapy in patients with esophageal cancer [36].

Although radiomics analyses have shown a high degree of prognostic power, they are not spatially explicit. Radiomic features are generated over the entire tumor, using the assumption that tumors are heterogeneous but well mixed. However, it is readily apparent from DCE-MRI that perfusion can vary markedly within spatially distant tumor subregions that may represent distinct phenotypic habitats. Therefore, image-guided multiregional tumor analysis may be required to fully characterize tumor heterogeneity.

3.2.2 Contributions of Molecular Imaging in Treatment Selection and Planning

Optical imaging techniques have been developed to guide minimally invasive procedures (e.g., involving endoscopy or robotic techniques) as well as conventional surgical procedures. The use of fluorescence during routine endoscopic screening examinations in the gastrointestinal, bronchial, and urinary tracts is proving to be invaluable for detecting occult dysplastic lesions [37]. Furthermore, intraoperative optical imaging using fluorescence has been applied for tumor margin delineation and to identify malignant nodes. For example, optical imaging after the injection of indocyanine green (ICG) has been used to delineate tumors in patients with brain cancers as well as to map sentinel lymph nodes in patients with breast cancer [38, 39]. Recent research suggests that in ovarian cancer, tumor-specific intraoperative fluorescence imaging using a folate receptor-targeted fluorescent agent may improve intraoperative staging and allow more radical cytoreductive surgery [40].

Nanoparticle-based probes that contain more than one type of targeting component offer possibilities for applying multiple molecular imaging modalities in quick succession to improve gross tumor resection as well as subsequent fine margin resection. For instance, in studies using animal models, one probe tested allowed gliosarcomas to be identified by both preoperative MRI and intraoperative optical imaging [41], while another allowed visualization of glioma by MRI, photoacoustic imaging, and Raman imaging [42].

Molecular imaging can play an important role in radiotherapy planning. Higher radiation doses

can be selectively applied in areas of tumor that show high metabolic activity and are therefore likely to represent especially aggressive disease. For example, FDG-PET/CT-based radiation planning for lymph nodes has been found to change the radiotherapy field in 21–25 % of patients with lung cancer [43–45]. In a study of 41 patients with head and neck cancer, the radiation boost dose was markedly increased and targeted at the tumors with the highest FDG avidity [46]. The study indicated that a boost dose of 3.0 Gy/fraction to ≤10 cm^3 could be safely applied to the FDG-avid regions during the first 2 weeks of conventionally fractionated IMRT. A majority of local relapses occurred within the FDG-avid regions that had received elevated doses, suggesting that FDG avidity is a marker of the likelihood of relapse [46]. Randomized controlled trials comparing conventional and PET-based radiotherapy of locally advanced non-small cell lung cancer are ongoing (PETPLAN, NCT00697333; RTOG-1106, NCT01507428). These trials will investigate whether local control rates and side effects are improved by PET-based radiation treatment planning.

Fluoro-l-thymidine (FLT)-PET/CT can noninvasively measure tumor cell proliferation and can detect early radiotherapy response. For example, in head and neck cancer patients, rapidly decreasing FLT-PET SUVs have been observed during the course of radiotherapy. Conceivably, the radiation dose could be boosted in selected tumor areas with high proliferative activity identified by FLT-PET [47].

In organs such as the brain, where the accuracy of FDG-PET/CT is limited, MRS or PET with radiolabeled amino acids can provide an alternative means for guiding radiotherapy based on molecular information. The presence of metabolic abnormalities on MRS consistent with tumor outside of the target volume of Gamma knife radiosurgery is associated with significantly shorter overall survival [48]. Tumor volumes defined by PET with the radiolabeled amino acid analog fluoroethyltyrosine (FET) are markedly different from those defined by contrast enhancement or FLAIR signal abnormalities on MRI (Fig. 3.3) [49, 50]. A randomized controlled trial comparing amino-acid PET-based radiation treatment planning with MRI-based radiation treatment planning is ongoing (GLIAA, NCT01252459). This trial will determine whether progression-free survival is improved by PET-based radiotherapy.

Various techniques are available for imaging tumor hypoxia, which increases resistance to radiotherapy and chemotherapy [51, 52]. These techniques include PET with tracers such as [^{18}F]fluoro-misonidazole (FMISO), [^{18}F]fluoroazomycin-arabinofuranoside, or [$^{60/64}$Cu]copper(II)-diacetyl-bis(*N4-methylthiosemicarbazone* (ATSM), as well as blood oxygen level-dependent (BOLD) MR imaging, which detects hypoxia based on an increase in the transverse relaxation rate (R2*) of water caused by the paramagnetic effect of endogenous deoxyhemoglobin [53, 54]. Studies are ongoing that evaluate whether local control rates can be improved by applying higher radiation doses to hypoxic tumor subvolumes [55]. However, it remains an open question whether the size and location of hypoxic volumes remains stable in untreated tumors and during radiotherapy.

Imaging of hypoxia has also shown promise for guiding the use of chemotherapeutic drugs that specifically act on hypoxic tumors (Fig. 3.4): The hypoxia-selective drug tirapazamine was not beneficial in unselected head and neck cancer patients but only in the subgroup of patients with FMISO-PET-positive tumors [56, 57] .

3.2.3 The Role of Molecular Imaging in Treatment Follow-Up

It is essential to be able to detect and localize residual and recurrent cancers so that timely and appropriate salvage therapy can be administered. However, posttreatment changes (e.g., loss of normal anatomy or the formation of scar tissue) often hamper the identification of such cancers by conventional cross-sectional imaging. By adding metabolic to morphologic information, molecular imaging can help to distinguish recurrent or residual disease. The use of FDG-PET for further evaluation of patients with clinically suspected tumor

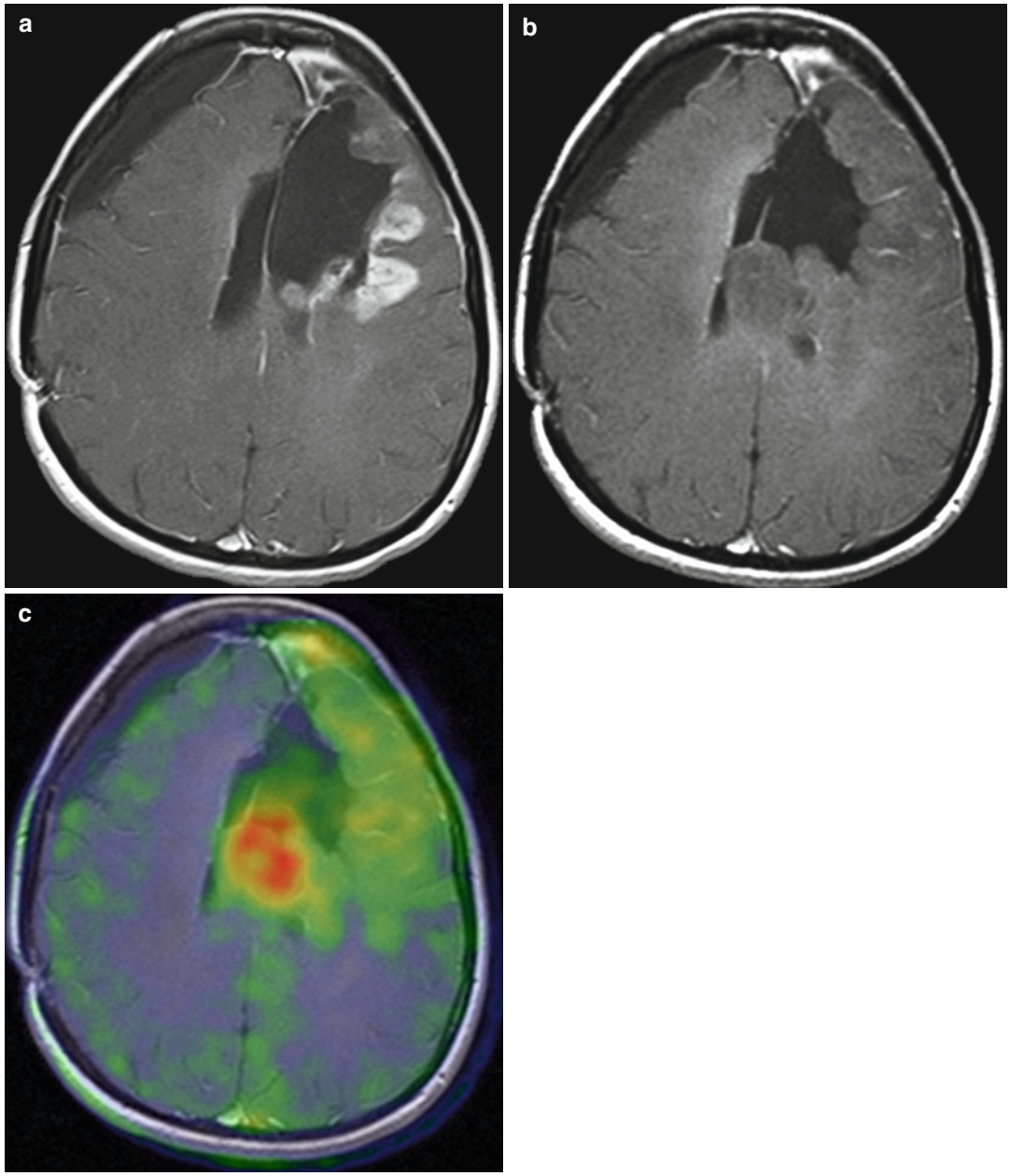

Fig. 3.3 Value of PET with ^{18}F-fluoroethyltyrosine (^{18}F-FET) in recurrent glioblastoma. T1-weighted MRI (**a**) shows a left frontal contrast-enhancing lesion, lateral to the resection defect. After 2 months of treatment with bevacizumab, T1-weighted MRI (**b**) shows a marked reduction of contrast enhancement but a growing tumor mass. ^{18}F-FET PET demonstrates metabolically active, viable tumor tissue in the left frontal lobe as well as adjacent to the left ventricle (**c**), illustrating the ability of ^{18}F-FET PET to depict the infiltrative growth of brain tumors

recurrence is well established in many malignancies including head and neck squamous cell carcinomas, lung cancer, rectal cancer, and ovarian cancer. In these patients PET/CT can guide local therapeutic strategies such as resection of solitary liver metastases [49, 58–63]. However, the role FDG-PET for surveillance in asymptomatic patients needs further study. In patients with a low

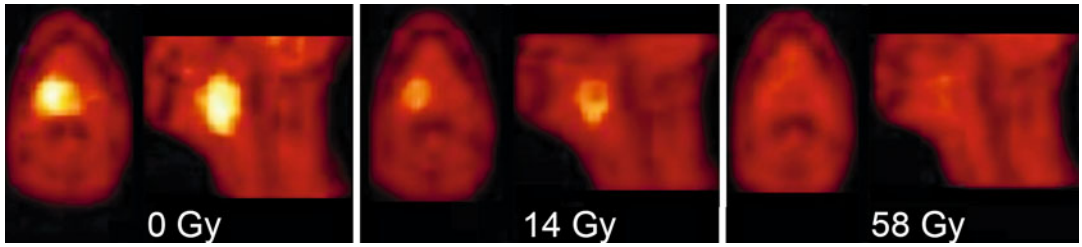

Fig. 3.4 Monitoring of tumor hypoxia in oropharyngeal cancer during radiotherapy with 18F-fluoro-misonidazole (^{18}F-FMISO) PET (axial and sagittal PET images are shown). The untreated tumor (0 Gy, *left*) shows high tracer uptake indicating the presence of hypoxia. During treatment (14 Gy, *middle*, and 58 Gy *right*) there is a rapid decrease of FMISO uptake consistent with resolution of hypoxia

risk of recurrence, the positive predictive value of FDG-PET may be too low to be clinically useful. Conversely, it has not been proven in randomized trials that early detection of asymptomatic recurrences by FDG-PET improves outcome.

MRS can also be a useful supplement to anatomic imaging in the search for recurrence. Studies have demonstrated its ability to help differentiate locally recurrent prostate cancer from benign and necrotic tissue after radiation treatment (Fig. 3.5) [65], hormone deprivation therapy [66], and cryosurgery [67]. DW-MRI and DCE-MRI are also very useful in evaluating local recurrence of prostate cancer and have been incorporated in routine clinical practice (Fig. 3.6) [68, 69].

For detection of lymph node and bone metastases, PET/CT with radiolabeled choline ([^{11}C] choline) or choline analogs ([^{18}F]choline or [^{18}F] fluoroethylcholine) (Fig. 3.7) has been found to yield promising results in patients with recurrent prostate cancer [70–72]. Choline PET/CT can detect metastatic prostate cancer at low PSA levels and may guide local therapies such as secondary lymph node dissection [70, 71].

The use of FDG-PET to monitor tumor response to therapy is well established in Hodgkin's lymphoma (Fig. 3.8) and aggressive non-Hodgkin's lymphomas. In these diseases, response status is now predominantly dependent on the FDG-PET findings. PET is also increasingly used in lymphomas and many solid tumors to determine tumor response early in the course of therapy.

PET-guided response-adapted therapy has been most extensively studied in Hodgkin's lymphoma and diffuse large B-cell lymphoma. Several studies have shown that tumor response after two to three cycles of chemotherapy is strongly predictive of progression-free survival [73]. Thus, treatment may be intensified in patients without a metabolic response on PET or de-escalated in patients with a favorable response on PET.

Response-adapted therapies are also being explored in solid tumors. In esophageal cancer quantitative changes in tumor FDG uptake after 2 weeks of preoperative chemotherapy were shown to be predictive of histopathologic response and progression-free and overall survival. Based on these data, a phase II study evaluated response-adapted therapy in patients with locally advanced distal esophageal cancer [74]. In patients for whom PET failed to show a metabolic response, neoadjuvant chemotherapy was stopped after 2 weeks of therapy and immediate surgical resection was performed. In contrast, patients with a metabolic response on PET received the full 3 months of preoperative chemotherapy. The results of the study indicated that response-adapted therapy is feasible and enriches the histopathologic response rate in the group of patients classified as metabolic responders. These patients demonstrated excellent progression-free and overall survival. In the group of metabolic nonresponders, progression-free survival and overall survival were not inferior to historic controls who were treated with 3 months of chemotherapy irrespective of their response on PET. Ongoing studies are evaluating whether outcome of metabolic nonresponders can be improved by changing chemotherapy early in the course of treatment (CALGB-80803, NCT01333033).

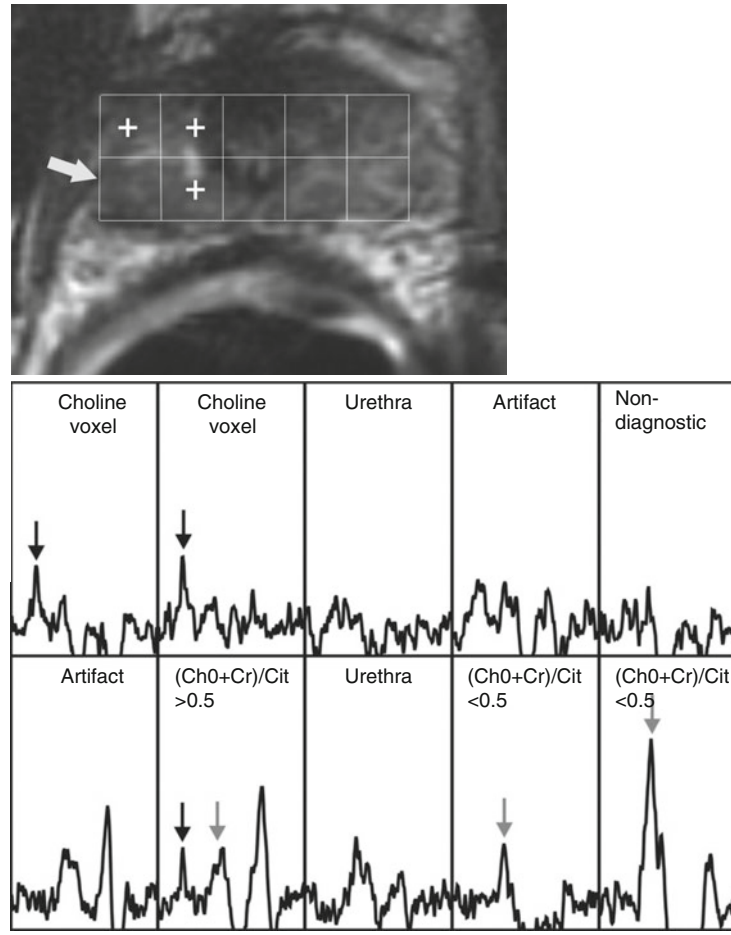

Fig. 3.5 Local prostate cancer recurrence after external beam radiation therapy, detected with MR imaging and MR spectroscopy. This 63-year-old patient had increasing PSA levels 66 months after completion of external beam radiation therapy. (**a**) Transverse T2-weighted MR image (4000/96, 14-mm field of view, 3.0-mm section thickness, no intersection gap, 256 × 192 matrix, and four signals acquired) with overlaid MR spectroscopic grid; spectra obtained in the prostate apex are shown in (**b**). A suspicious focal nodular region of reduced signal intensity at T2-weighted MR imaging was observed on the right side (*arrow* in **a**) (Adapted and reprinted from Pucar et al. [64])

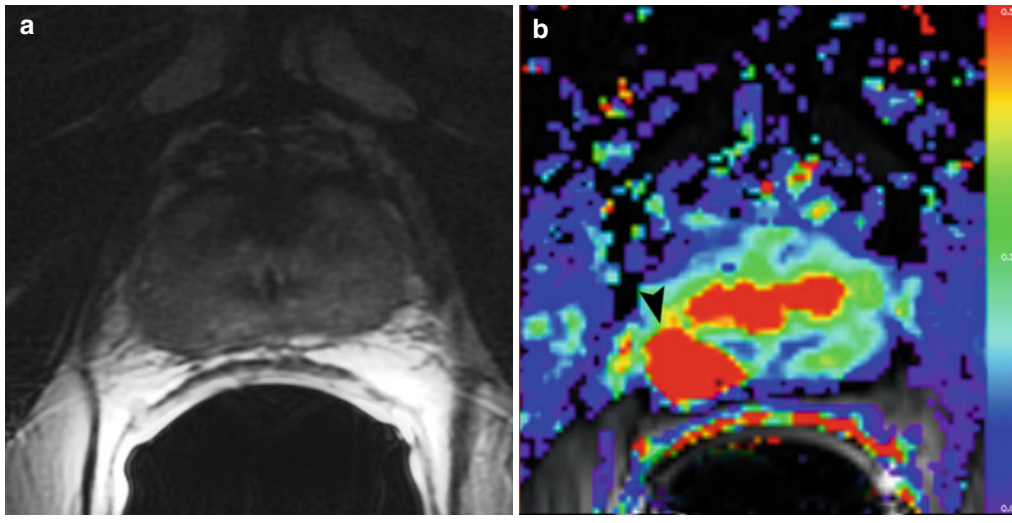

Fig. 3.6 Sixty-nine-year-old patient with biopsy-proven prostate cancer (Gleason score 3+4) in the right mid-gland. The cancer is not clearly visible on the T2-weighted image (**a**). On the parametric map of K^{trans} (**b**), the ADC map (**c**, $b = 0$, 1,000 mm^2/s), and on the fused presentation of the T2-weighted image and the K^{trans} parametric map (**d**), the tumor (*arrowheads*) is clearly identifiable. Note the hypointense peripheral zone on the T2-weighted image (**a**) caused by post-radiation changes (Reprinted from Donati et al. [68])

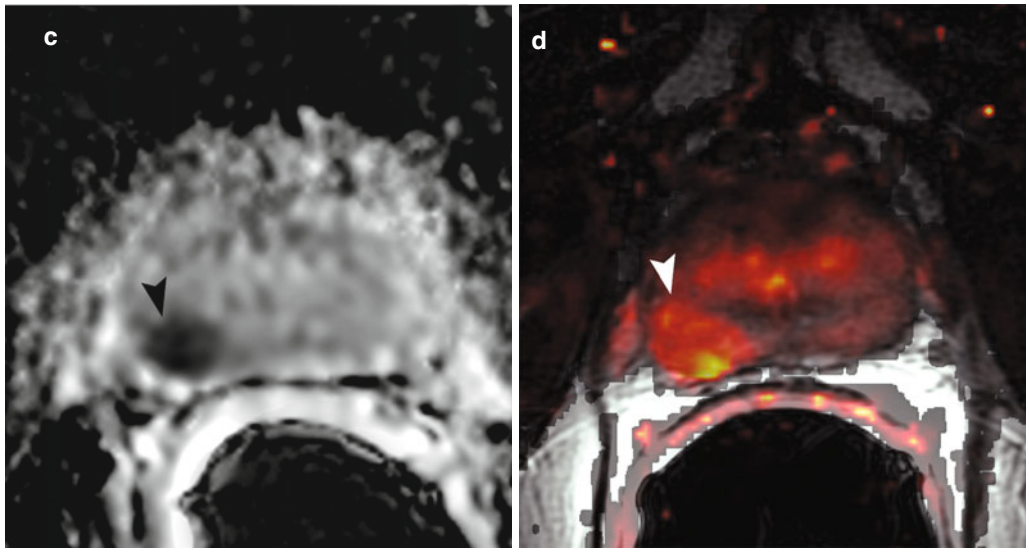

Fig. 3.6 (continued)

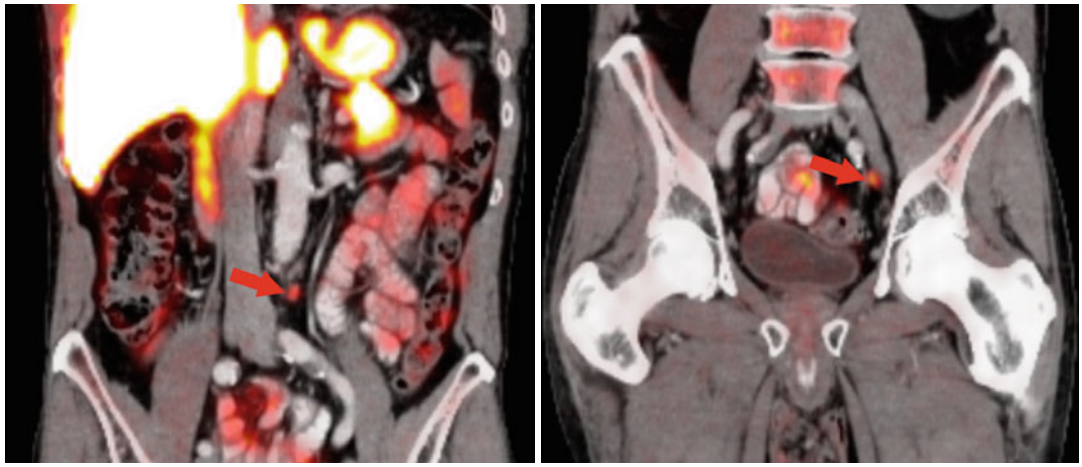

Fig. 3.7 Detection of lymph node metastases of prostate cancer (Gleason score 8) by ^{18}F-fluoroethylcholine PET/CT. The PET/CT images show focal uptake in normal-sized lymph nodes in the left common iliac and the left paraaortic areas (*red arrows*)

A novel approach to study tumor metabolism during therapy is MRI with hyperpolarized, ^{13}C-labeled, metabolic substrates. For example, animal studies have suggested that by detecting changes in lactate levels, such metabolic imaging may be useful for monitoring tumor response to therapy for lymphoma and brain tumors [22, 75]. Hyperpolarized [1-^{13}C]pyruvate has also been found to distinguish early-stage prostate cancer from late-stage prostate cancer based on lactate levels [22]. The first clinical trial of MRI with hyperpolarized [1-^{13}C] pyruvate was recently conducted in patients with prostate cancer.

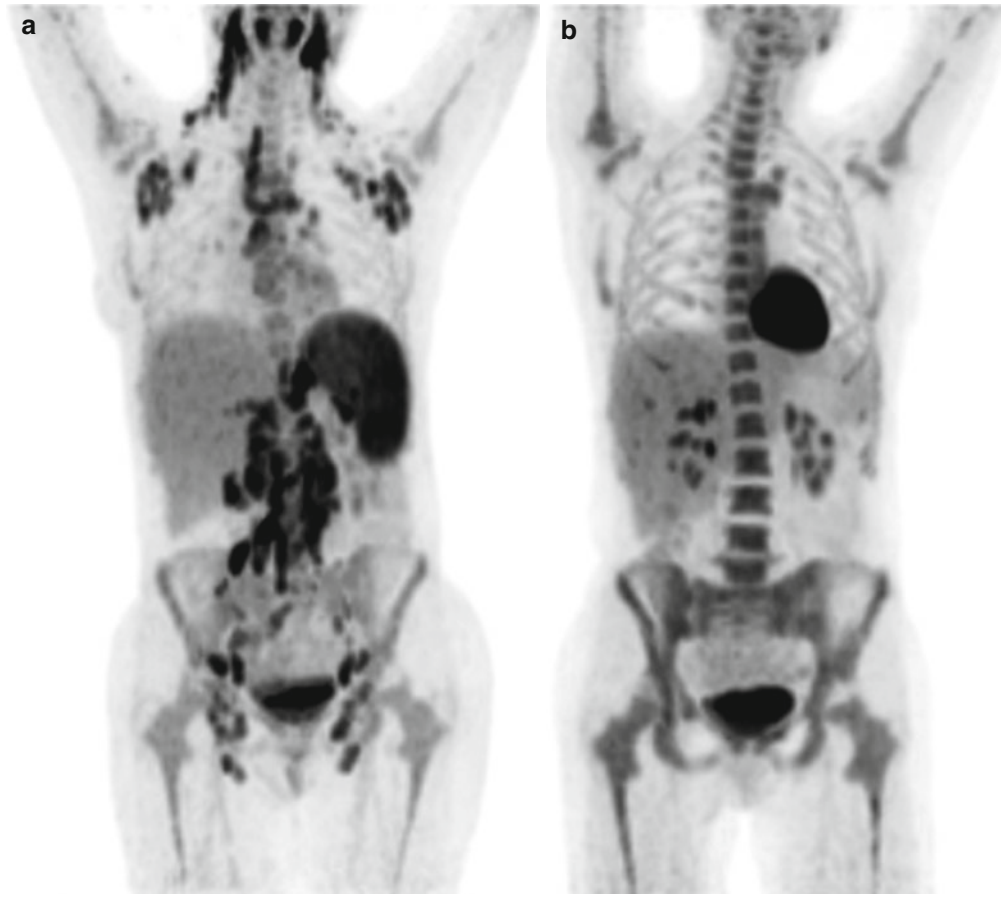

Fig. 3.8 ^{18}F-FDG-PET in Hodgkin's lymphoma before (**a**) and after (**b**) two cycles of chemotherapy. The maximum intensity projection images demonstrate a complete metabolic response indicating a favorable response to chemotherapy

3.3 Molecular Imaging in Drug Development

Many novel cancer drugs bind to specific targets, such as protein kinase domains or cell surface antigens. It is possible to convert these therapeutics into molecular imaging probes by radiolabeling. Examples include erlotinib, a drug which inhibits EGFR and has a remarkable inhibitory effect on lung cancers with a mutated form of the EGFR kinase domain, and trastuzumab, an anti-Her-2 antibody [76, 77]. However, it can be challenging to develop imaging based on this approach because the unspecific binding of the drug may be greater than the specific binding, especially for small molecules targeting intracellular targets. For androgen and estrogen receptors, specific ligands are available that allow noninvasive imaging of receptor expression as well as monitoring of therapies that target these two classes of receptors [78–80].

3.4 Theranostics

Theranostics describes the use of a diagnostic test to assess the presence of a molecular target in order to determine the suitability–and in some

cases guide the application–of a particular therapy. While the term "theranostics" is new, the concept has been used for many years in nuclear medicine for diagnosis and therapy of thyroid disorders. In fact, the first report of radioiodine treatment of metastatic thyroid cancer from 1946 used measurement of radioiodine uptake by the metastasis to guide therapy with radioiodine.

Theranostics can be practiced by performing in vitro testing and selecting in vivo therapy based on the test results [81]. The most established examples of this approach are probably HER-2 testing of breast cancer tissue before the administration of trastuzumab and determination of the presence of EGFR kinase mutations before therapy of non-small cell lung cancer with erlotinib or gefitinib [82, 83]. A fundamental limitation of this in vitro diagnostic–in vivo therapeutic approach is the fact that only a small sample of the tumor can be tested in vitro. Frequently this sample has also been obtained at the time of initial therapy and may not reflect the biology of metastatic disease at the time of recurrence. Considering the well-known genetic instability and heterogeneity of most malignant tumors, a whole-body imaging approach to detect the presence or absence of a molecular marker in all metastatic lesions has many advantages compared to the in vitro diagnostic approach. Such an approach is currently being studied clinically in patients with castration-resistant metastatic prostate cancer. In this disease androgen receptor imaging with FDHT PET/CT can be used for the selection and monitoring of treatment with an androgen receptor antagonist [80]. The most sophisticated theranostic approach is perhaps one that combines in vivo diagnosis with therapy. Receptor-targeting radiopeptides have been developed for imaging and treating tumors that overexpress peptide receptors. The biodistribution and tumor uptake of these peptides can be assessed noninvasively by imaging, and radiation doses to tumor and normal organs can be determined. Based on these data patients can be selected for radiopeptide therapy and the amount of radioactivity that can be safely administered can be determined. Imaging can then be used to monitor tumor response to therapy (Fig. 3.9) and detect disease recurrence [84]. Agents that enable similar theranostic approaches are also being developed using nanoparticles [85]. These particles can accumulate in malignant tumors by a very common characteristic of malignancy – the enhanced permeability and retention (EPR) effect that is caused by the immature tumor vasculature. Uptake can be increased and made more specific by linking the particles to ligands, antibody fragments, peptides, or small molecules. A specific advantage of nanoparticles as compared to antibodies or peptides is that they can easily be designed to permit multimodality imaging, for example, when a particle that can be detected optically is labeled with a radionuclide that is it detectable by PET [85, 86]. The production of multivalent and multiparametric nanoparticles loaded with different targeting moieties, contrast agents, and drugs may permit the design of highly personalized therapies [87].

3.5 Integrated Diagnostics

While molecular imaging-based diagnostics and theranostics have several important strengths, a fundamental limitation is their restricted capacity for multiparametric characterization. Using the techniques of modern genetics, it has become feasible to assess the expression of thousands of genes simultaneously and to sequence the whole genome of cancer cells. Compared to this depth of information, the capabilities of PET and SPECT, as well as those of MRI and optical imaging, are currently very limited. This is unlikely to change fundamentally in the foreseeable future. Conversely, the fundamental strengths of molecular imaging are the capacity for whole-body imaging and noninvasive monitoring of changes over time. Because in vitro and in vivo tests can provide different, complementary types of information, the integration of in vivo molecular imaging approaches with in vitro tests is expected to be of great value for advancing cancer care [85, 88]. The goal of such integrated diagnostics is to maximize the patient-specific information that can be used to design optimal,

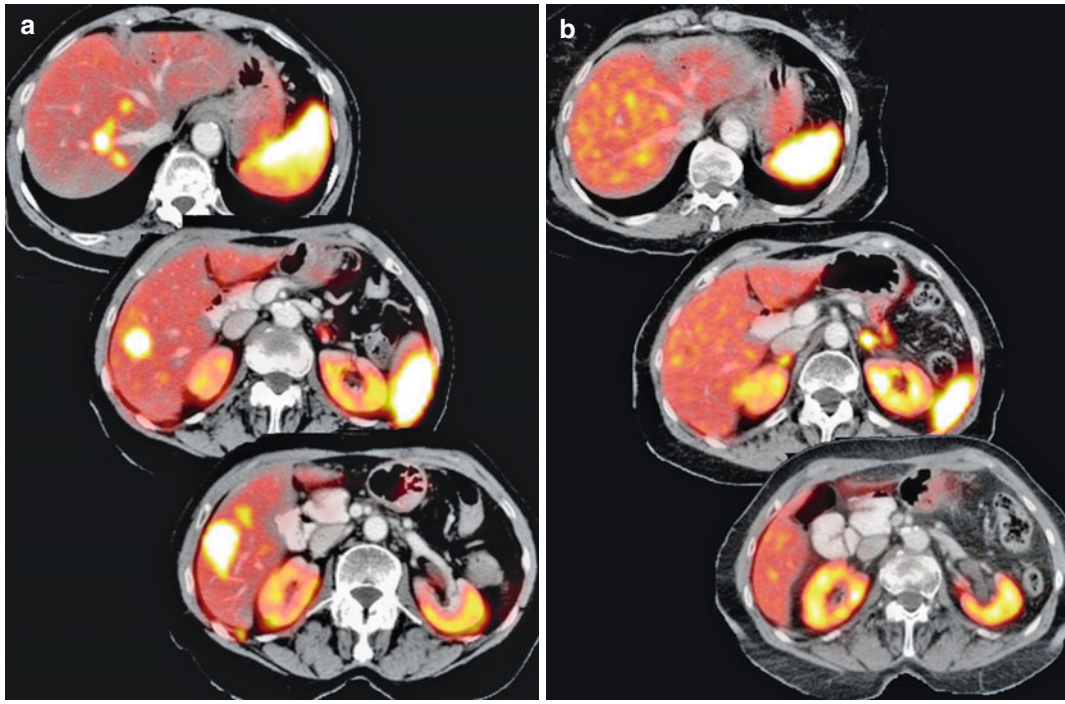

Fig. 3.9 ^{68}Ga-DOTA-TATE PET/CT before (**a**) and after (**b**) therapy with ^{177}Lu-DOTA-TATE. There is almost complete resolution of the multiple liver metastases

personalized therapies. This should include morphologic, functional, and molecular data and will require close collaborations between imaging disciplines, genetics, and pathology.

3.6 Summary

Molecular imaging is already contributing to improvements in cancer care, and its importance will continue to grow as the new paradigm of molecularly based medicine takes hold. The spectrum of molecular imaging tools that are currently available or emerging is wide, ranging from handheld optical imaging tools to whole-body scanners; existing techniques are continuously evolving, and new ones are constantly being developed. As a result, there is scarcely any aspect of oncology that is likely to remain uninfluenced by molecular imaging in the future. Perhaps the most important strength of molecular imaging for advancing cancer care is its ability to evaluate entire tumors in vivo, thus capturing the heterogeneity of tumor biology both within and between tumor deposits in the same patient. This ability makes it invaluable for selecting, planning, and adjusting therapies, as well as for advancing the understanding of disease processes and the development and testing of new treatments.

References

1. Massoud TF, Gambhir SS. Molecular imaging in living subjects: seeing fundamental biological processes in a new light. Genes Dev. 2003;17(5):545–80.
2. Kircher MF, et al. Noninvasive cell-tracking methods. Nat Rev Clin Oncol. 2011;8(11):677–88.
3. Kircher MF, Willmann JK. Molecular body imaging: MR imaging, CT, and US. Part II. Applications. Radiology. 2012;264(2):349–68.
4. Kircher MF, Willmann JK. Molecular body imaging: MR imaging, CT, and US. Part I. Principles. Radiology. 2012;263(3):633–43.
5. Weissleder R, Pittet MJ. Imaging in the era of molecular oncology. Nature. 2008;452(7187):580–9.
6. Negendank W. Studies of human tumors by MRS: a review. NMR Biomed. 1992;5(5):303–24.

7. Glunde K, et al. MRS and MRSI guidance in molecular medicine: targeting and monitoring of choline and glucose metabolism in cancer. NMR Biomed. 2011;24(6):673–90.
8. Hegde JV, et al. Multiparametric MRI of prostate cancer: an update on state-of-the-art techniques and their performance in detecting and localizing prostate cancer. J Magn Reson Imaging. 2013;37(5):1035–54.
9. Padhani AR, et al. Diffusion-weighted magnetic resonance imaging as a cancer biomarker: consensus and recommendations. Neoplasia. 2009;11(2):102–25.
10. Koh DM, Collins DJ. Diffusion-weighted MRI in the body: applications and challenges in oncology. AJR Am J Roentgenol. 2007;188(6):1622–35.
11. Guo Y, et al. Differentiation of clinically benign and malignant breast lesions using diffusion-weighted imaging. J Magn Reson Imaging. 2002;16(2):172–8.
12. Choi EK, et al. Node-by-node correlation between MR and PET/CT in patients with uterine cervical cancer: diffusion-weighted imaging versus size-based criteria on T2WI. Eur Radiol. 2009;19(8):2024–32.
13. Partridge SC, et al. Differential diagnosis of mammographically and clinically occult breast lesions on diffusion-weighted MRI. J Magn Reson Imaging. 2010;31(3):562–70.
14. Mardor Y, et al. Pretreatment prediction of brain tumors' response to radiation therapy using high b-value diffusion-weighted MRI. Neoplasia. 2004;6(2):136–42.
15. Barrett T, et al. DCE and DW MRI in monitoring response to androgen deprivation therapy in patients with prostate cancer: a feasibility study. Magn Reson Med. 2012;67(3):778–85.
16. Gollub MJ, et al. Dynamic contrast enhanced-MRI for the detection of pathological complete response to neoadjuvant chemotherapy for locally advanced rectal cancer. Eur Radiol. 2012;22(4):821–31.
17. Jensen LR, et al. Diffusion-weighted and dynamic contrast-enhanced MRI in evaluation of early treatment effects during neoadjuvant chemotherapy in breast cancer patients. J Magn Reson Imaging. 2011;34(5):1099–109.
18. Kim JH, et al. Dynamic contrast-enhanced 3-T MR imaging in cervical cancer before and after concurrent chemoradiotherapy. Eur Radiol. 2012;22(11):2533–9.
19. Padhani AR, Leach MO. Antivascular cancer treatments: functional assessments by dynamic contrast-enhanced magnetic resonance imaging. Abdom Imaging. 2005;30(3):324–41.
20. Leach MO, et al. Imaging vascular function for early stage clinical trials using dynamic contrast-enhanced magnetic resonance imaging. Eur Radiol. 2012; 22(7):1451–64.
21. Zavaleta CL, et al. Raman's "effect" on molecular imaging. J Nucl Med. 2011;52(12):1839–44.
22. Kurhanewicz J, et al. Analysis of cancer metabolism by imaging hyperpolarized nuclei: prospects for translation to clinical research. Neoplasia. 2011;13(2):81–97.
23. Hricak H, et al. Global trends in hybrid imaging. Radiology. 2010;257(2):498–506.
24. Torigian DA, et al. PET/MR imaging: technical aspects and potential clinical applications. Radiology. 2013;267(1):26–44.
25. Gerlinger M, et al. Intratumor heterogeneity and branched evolution revealed by multiregion sequencing. N Engl J Med. 2012;366(10):883–92.
26. Cowin PA, et al. LRP1B deletion in high-grade serous ovarian cancers is associated with acquired chemotherapy resistance to liposomal doxorubicin. Cancer Res. 2012;72(16):4060–73.
27. Segal E, et al. Decoding global gene expression programs in liver cancer by noninvasive imaging. Nat Biotechnol. 2007;25(6):675–80.
28. Zinn PO, et al. Radiogenomic mapping of edema/cellular invasion MRI-phenotypes in glioblastoma multiforme. PLoS One. 2011;6(10):e25451.
29. Goh V, et al. Assessment of response to tyrosine kinase inhibitors in metastatic renal cell cancer: CT texture as a predictive biomarker. Radiology. 2011;261(1):165–71.
30. Ng F, et al. Assessment of primary colorectal cancer heterogeneity by using whole-tumor texture analysis: contrast-enhanced CT texture as a biomarker of 5-year survival. Radiology. 2013;266(1):177–84.
31. Miles KA, et al. Colorectal cancer: texture analysis of portal phase hepatic CT images as a potential marker of survival. Radiology. 2009;250(2):444–52.
32. Canuto HC, et al. Characterization of image heterogeneity using 2D Minkowski functionals increases the sensitivity of detection of a targeted MRI contrast agent. Magn Reson Med. 2009;61(5):1218–24.
33. Kyriazi S, et al. Metastatic ovarian and primary peritoneal cancer: assessing chemotherapy response with diffusion-weighted MR imaging – value of histogram analysis of apparent diffusion coefficients. Radiology. 2011;261(1):182–92.
34. Rose CJ, et al. Quantifying spatial heterogeneity in dynamic contrast-enhanced MRI parameter maps. Magn Reson Med. 2009;62(2):488–99.
35. Yang X, Knopp MV. Quantifying tumor vascular heterogeneity with dynamic contrast-enhanced magnetic resonance imaging: a review. J Biomed Biotechnol. 2011;2011:732848.
36. Tixier F, et al. Intratumor heterogeneity characterized by textural features on baseline 18F-FDG PET images predicts response to concomitant radiochemotherapy in esophageal cancer. J Nucl Med. 2011;52(3): 369–78.
37. Taruttis A, Ntziachristos V. Translational optical imaging. AJR Am J Roentgenol. 2012;199(2):263–71.
38. Haglund MM, et al. Enhanced optical imaging of human gliomas and tumor margins. Neurosurgery. 1996;38(2):308–17.
39. Troyan SL, et al. The FLARE intraoperative near-infrared fluorescence imaging system: a first-in-human clinical trial in breast cancer sentinel lymph node mapping. Ann Surg Oncol. 2009;16(10):2943–52.
40. van Dam GM, et al. Intraoperative tumor-specific fluorescence imaging in ovarian cancer by folate recep-

tor-alpha targeting: first in-human results. Nat Med. 2011;17(10):1315–9.
41. Kircher MF, et al. A multimodal nanoparticle for preoperative magnetic resonance imaging and intraoperative optical brain tumor delineation. Cancer Res. 2003;63(23):8122–5.
42. Kircher MF, et al. A brain tumor molecular imaging strategy using a new triple-modality MRI-photoacoustic-Raman nanoparticle. Nat Med. 2012; 18(5):829–34.
43. Bradley JD, et al. Positron emission tomography in limited-stage small-cell lung cancer: a prospective study. J Clin Oncol. 2004;22(16):3248–54.
44. Kamel EM, et al. Whole-body (18)F-FDG PET improves the management of patients with small cell lung cancer. J Nucl Med. 2003;44(12):1911–7.
45. van Loon J, et al. 18FDG-PET based radiation planning of mediastinal lymph nodes in limited disease small cell lung cancer changes radiotherapy fields: a planning study. Radiother Oncol. 2008;87(1):49–54.
46. Madani I, et al. Positron emission tomography-guided, focal-dose escalation using intensity-modulated radiotherapy for head and neck cancer. Int J Radiat Oncol Biol Phys. 2007;68(1):126–35.
47. Troost EG, et al. 18F-FLT PET/CT for early response monitoring and dose escalation in oropharyngeal tumors. J Nucl Med. 2010;51(6):866–74.
48. Chan AA, et al. Proton magnetic resonance spectroscopy imaging in the evaluation of patients undergoing gamma knife surgery for Grade IV glioma. J Neurosurg. 2004;101(3):467–75.
49. Grosu AL, et al. An interindividual comparison of O-(2-[18F]fluoroethyl)-L-tyrosine (FET)- and L-[methyl-11C]methionine (MET)-PET in patients with brain gliomas and metastases. Int J Radiat Oncol Biol Phys. 2011;81(4):1049–58.
50. Pauleit D, et al. O-(2-[18F]fluoroethyl)-L-tyrosine PET combined with MRI improves the diagnostic assessment of cerebral gliomas. Brain. 2005;128(Pt 3):678–87.
51. Kurihara H, et al. Radiolabelled agents for PET imaging of tumor hypoxia. Curr Med Chem. 2012;19(20):3282–9.
52. Tachibana I, et al. A prospective clinical trial of tumor hypoxia imaging with 18F-fluoromisonidazole positron emission tomography and computed tomography (F-MISO PET/CT) before and during radiation therapy. J Radiat Res. 2013 [Epub ahead of print].
53. Figueiras RG, et al. Novel oncologic drugs: what they do and how they affect images. Radiographics. 2011;31(7):2059–91.
54. Krohn KA, et al. Molecular imaging of hypoxia. J Nucl Med. 2008;49 Suppl 2:129S–48.
55. Zips D, et al. Exploratory prospective trial of hypoxia-specific PET imaging during radiochemotherapy in patients with locally advanced head-and-neck cancer. Radiother Oncol. 2012;105(1):21–8.
56. Rischin D, et al. Prognostic significance of [18F]-misonidazole positron emission tomography-detected tumor hypoxia in patients with advanced head and neck cancer randomly assigned to chemoradiation with or without tirapazamine: a substudy of Trans-Tasman Radiation Oncology Group Study 98.02. J Clin Oncol. 2006;24(13):2098–104.
57. Rischin D, et al. Tirapazamine, cisplatin, and radiation versus cisplatin and radiation for advanced squamous cell carcinoma of the head and neck (TROG 02.02, HeadSTART): a phase III trial of the Trans-Tasman Radiation Oncology Group. J Clin Oncol. 2010;28(18):2989–95.
58. Caulo A, et al. Integrated imaging of non-small cell lung cancer recurrence: CT and PET-CT findings, possible pitfalls and risk of recurrence criteria. Eur Radiol. 2012;22(3):588–606.
59. Even-Sapir E, et al. Detection of recurrence in patients with rectal cancer: PET/CT after abdominoperineal or anterior resection. Radiology. 2004;232(3):815–22.
60. Ho AS, et al. Impact of positron emission tomography/computed tomography surveillance at 12 and 24 months for detecting head and neck cancer recurrence. Cancer. 2013;119(7):1349–56.
61. Prakash P, et al. Role of PET/CT in ovarian cancer. AJR Am J Roentgenol. 2010;194(6):W464–70.
62. Ruers TJ, et al. Improved selection of patients for hepatic surgery of colorectal liver metastases with (18)F-FDG PET: a randomized study. J Nucl Med. 2009;50(7):1036–41.
63. Yi JS, et al. 18F-FDG PET/CT for detecting distant metastases in patients with recurrent head and neck squamous cell carcinoma. J Surg Oncol. 2012;106(6): 708–12.
64. Pucar D, et al. Prostate cancer: correlation of MR imaging and MR spectroscopy with pathologic findings after radiation therapy-initial experience. Radiology. 2005;236:545–53.
65. Pickett B, et al. Use of MRI and spectroscopy in evaluation of external beam radiotherapy for prostate cancer. Int J Radiat Oncol Biol Phys. 2004;60(4):1047–55.
66. Mueller-Lisse UG, et al. Localized prostate cancer: effect of hormone deprivation therapy measured by using combined three-dimensional 1H MR spectroscopy and MR imaging: clinicopathologic case-controlled study. Radiology. 2001;221(2):380–90.
67. Parivar F, et al. Detection of locally recurrent prostate cancer after cryosurgery: evaluation by transrectal ultrasound, magnetic resonance imaging, and three-dimensional proton magnetic resonance spectroscopy. Urology. 1996;48(4):594–9.
68. Donati OF, et al. Multiparametric prostate MR imaging with T2-weighted, diffusion-weighted, and dynamic contrast-enhanced sequences: are all pulse sequences necessary to detect locally recurrent prostate cancer after radiation therapy? Radiology. 2013;268(2):440–50.
69. Westphalen AC, et al. Multiparametric 3T endorectal MRI after external beam radiation therapy for prostate cancer. J Magn Reson Imaging. 2012;36(2): 430–7.
70. Giovacchini G, et al. [11C]choline positron emission tomography/computerized tomography for early

detection of prostate cancer recurrence in patients with low increasing prostate specific antigen. J Urol. 2013;189(1):105–10.
71. Jilg CA, et al. Salvage lymph node dissection with adjuvant radiotherapy for nodal recurrence of prostate cancer. J Urol. 2012;188(6):2190–7.
72. Plathow C, Weber WA. Tumor cell metabolism imaging. J Nucl Med. 2008;49 Suppl 2:43S–63.
73. de Geus-Oei LF, et al. FDG-PET/CT based response-adapted treatment. Cancer Imaging. 2012;12(2):324–35.
74. Lordick F, et al. PET to assess early metabolic response and to guide treatment of adenocarcinoma of the oesophagogastric junction: the MUNICON phase II trial. Lancet Oncol. 2007;8(9):797–805.
75. Day SE, et al. Detecting tumor response to treatment using hyperpolarized 13C magnetic resonance imaging and spectroscopy. Nat Med. 2007;13(11):1382–7.
76. Dijkers EC, et al. Biodistribution of 89Zr-trastuzumab and PET imaging of HER2-positive lesions in patients with metastatic breast cancer. Clin Pharmacol Ther. 2010;87(5):586–92.
77. Memon AA, et al. PET imaging of patients with non-small cell lung cancer employing an EGF receptor targeting drug as tracer. Br J Cancer. 2011;105(12):1850–5.
78. Beattie BJ, et al. Pharmacokinetic assessment of the uptake of 16beta-18F-fluoro-5alpha-dihydrotestosterone (FDHT) in prostate tumors as measured by PET. J Nucl Med. 2010;51(2):183–92.
79. Linden HM, et al. Fluoroestradiol positron emission tomography reveals differences in pharmacodynamics of aromatase inhibitors, tamoxifen, and fulvestrant in patients with metastatic breast cancer. Clin Cancer Res. 2011;17(14):4799–805.
80. Scher HI, et al. Antitumour activity of MDV3100 in castration-resistant prostate cancer: a phase 1–2 study. Lancet. 2010;375(9724):1437–46.
81. Ozdemir V, et al. Shifting emphasis from pharmacogenomics to theranostics. Nat Biotechnol. 2006;24(8):942–6.
82. Hricak H. Oncologic imaging: a guiding hand of personalized cancer care. Radiology. 2011;259(3):633–40.
83. Weber WA, et al. Technology insight: novel imaging of molecular targets is an emerging area crucial to the development of targeted drugs. Nat Clin Pract Oncol. 2008;5(1):44–54.
84. Ambrosini V, et al. Radiopeptide imaging and therapy in Europe. J Nucl Med. 2011;52 Suppl 2:42S–55.
85. Kircher MF, et al. Molecular imaging for personalized cancer care. Mol Oncol 2012;6(2):182–195.
86. Welch MJ, et al. The advantages of nanoparticles for PET. J Nucl Med. 2009;50(11):1743–6.
87. Li KC, et al. Combined vascular targeted imaging and therapy: a paradigm for personalized treatment. J Cell Biochem Suppl. 2002;39:65–71.
88. Krestin GP, et al. Integrated diagnostics: proceedings from the 9th biennial symposium of the International Society for Strategic Studies in Radiology. Eur Radiol. 2012;22(11):2283–94.

Radiotherapy and Imaging

4

Ursula Nestle and Anca-Ligia Grosu

Contents

Abbreviations

AA-PET	Amino acid PET
CT	Computed tomography
CTV	Clinical target volume
FDG	Fluoro-deoxyglucose
GTV	Gross tumor volume
IMRT	Intensity-modulated radiation therapy
MRI	Magnetic resonance imaging
OAR	Organ at risk
PET	Positron emission tomography
PTV	Planning target volume
RT	Radiotherapy
SRT, SBRT	Stereotactic (body) radiotherapy
SUV	Standardized uptake value
TNM	Tumor staging system

4.1 Introduction

During the last 20 years, an impressing technical progress has led to a new definition of radiation oncology. Today, the radiation oncologist is a main contributor to curative treatment in virtually all cancers. Radiotherapy is a very effective local treatment in the primary, neoadjuvant, and adjuvant treatment situation of cancer patients (Table 4.1). Radiotherapy alone, also enhanced by chemotherapy, is a curative treatment option in primary tumors of the brain, head and neck, lung, esophagus, prostate, bladder, uterus, anal canal, and skin. In the neoadjuvant setting, radiotherapy

U. Nestle (✉) • A.-L. Grosu
Department for Radiation Oncology,
University of Freiburg Medical Center,
Robert Koch Strasse 3, D-79106 Freiburg, Germany
e-mail: ursula.nestle@uniklinik-freiburg.de

A. Luna et al. (eds.), *Functional Imaging in Oncology,*
DOI 10.1007/978-3-642-40412-2_4,

Table 4.1 Examples for the curative or locally curative role of radiotherapy in interdisciplinary treatment concepts for oncologic patients

Tumor/location	Radiotherapy indications (by rising stage)[a]	Other components of multimodal therapy	Aim of treatment	Main imaging modality used[b]
Glioma	Adjuvant RT/RCT Definitive RT/RCT	Resection Chemotherapy	Cure	MRI
Brain metastases	Radiosurgery SFRT	Resection Chemotherapy	Local control	MRI
Head and neck cancer	Definitive RT Adjuvant RT/RCT Definitive RCT	Resection Chemotherapy	Cure	MRI CT FDG-PET
Breast cancer	Adjuvant RT	Resection Endocrine therapy Chemotherapy	Cure	Mammography CT
Lung cancer	SBRT Neoadjuvant RT Adjuvant RT Definitive RCT	Resection Chemotherapy	Cure	CT FDG-PET
Lung metastases	SBRT	Resection Chemotherapy	Local control	CT FDG-PET
Esophagus carcinoma	Definitive RT (brachytherapy) Neoadjuvant RCT Definitive RCT	Resection Chemotherapy	Cure	CT FDG-PET
Liver metastases	SBRT	Resection Chemotherapy	Local control	MRI
Rectal cancer	Adjuvant RT Neoadjuvant RT	Resection Chemotherapy	Cure	CT MRI
Prostate cancer	Definitive RT Adjuvant RT RT of recurrence	Resection Endocrine therapy	Cure	CT MRI
Gynecologic tumors	Definitive RT Adjuvant RCT Definitive RCT (all including brachytherapy)	Resection Chemotherapy	Cure	CT MRI

[a]*RT* radiotherapy, *RCT* radiochemotherapy, *SBRT* stereotactic body radiotherapy
[b]*CT* computed tomography, *MRI* magnetic resonance tomography, *PET* positron emission tomography

is, e.g., the standard treatment for rectal cancer and operable tumors of the lung, esophagus, and sarcoma. In the adjuvant situation, radiotherapy is essential for the cure of breast cancer and after resection of tumors of the head and neck, lung, esophagus, stomach, prostate, and uterus. Radiotherapy is furthermore a relevant treatment option in lymphoma and pediatric tumors. In addition, increasingly effective palliation can safely be achieved by radiation treatment, e.g., for locally advanced tumors of the head and neck, chest, and pelvis as well as for metastases in the brain, bone, lung, and liver.

The technical progress of recent years has been made possible by advancing computational resources leading to improved planning and application technologies and by congenial engineering developments like multi-leaf collimators and on-site positioning control. However, all these developments would not have been possible without medical imaging (Fig. 4.1). By the 1980s, CT was integrated into radiotherapy planning [1].

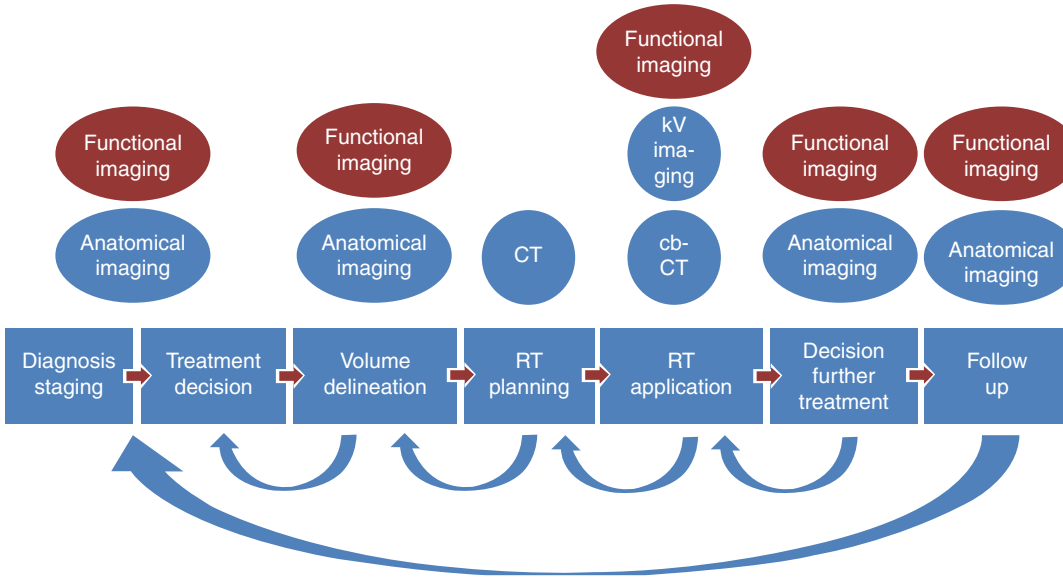

Fig. 4.1 Role of imaging in the radiotherapy process: the *arrows* showing the various feedback slopes triggered by often imaging based information

While the first intentions were rather aimed at better geometrical and physical treatment planning (until today, CT tissue density data are used for the calculation of beam attenuation within the patient), it became obvious very soon that the (patho)anatomical informations could also be used for target definition and normal tissue identification. This has triggered the development of modern target volume concepts and planning techniques. Today, we have highly precise technologies of treatment planning an delivery available, e.g., intensity-modulated radiation therapy (IMRT) and stereotactic radiotherapy (SRT, SBRT), which enable safe high-dose treatment of precisely defined target volumes with simultaneous sparing of normal tissues [2]. IMRT techniques enable the radiation oncologist to spare organs like the spinal cord or the parotid glands while giving therapeutic radiation doses to neighboring tumors, e.g., in the head and neck area [3]. It is possible to spare the rectum and the bladder while giving high-dose curative treatment to prostate cancer [4] and to cure benign tumors of the base of the skull with a minimum of neurological late sequelae [5]. Stereotactic radiotherapy of brain metastases preserves the quality of life of many of cancer patients without neuropsychological toxicity [6, 7], while stereotactic radiotherapy of localized lung cancers in inoperable patients has improved the prognosis of this patient group on an epidemiologically measurable scale [8].

Modern IMRT techniques have also opened the door to the application of various dose levels within one treatment. Practical implementations are simultaneously integrated boost techniques, where, e.g., the macroscopic tumor and the areas of assumed microscopic spread are covered by high- and intermediate-dose ranges (Fig. 4.2) [9]. Beyond this, the so-called dose painting has become possible, where radiotherapy adaptation within a given target can be defined by biological properties of certain sub-volumes. Using IMRT, e.g., hypoxic regions within a tumor assumed to be radioresistant, might be treated with dose prescriptions on the basis of hypoxia-PET imaging [10]. This is a very interesting field for the use of molecular imaging techniques for radiotherapy. First studies in the head and neck tumors presently address this option [11]; however, clinical outcome data have to be awaited before introducing these techniques into clinical practice.

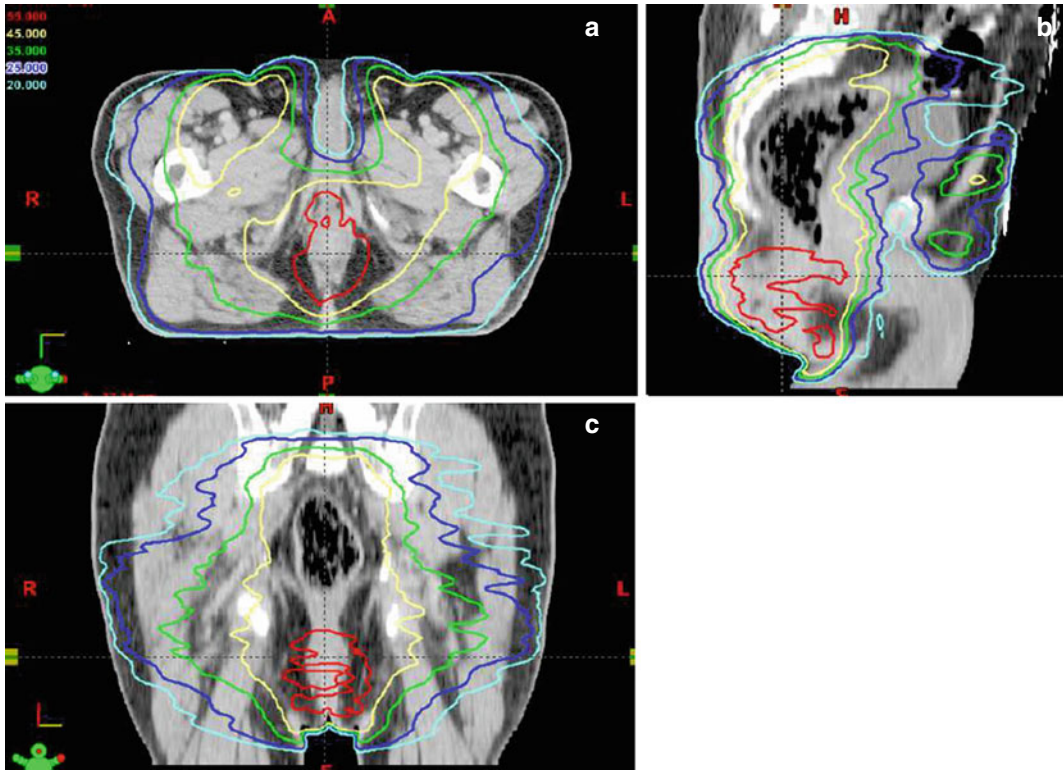

Fig. 4.2 IMRT-based simultaneous integrated boost technique: three-plane view (**a**, **b**, **c**) of an RT-treatment plan for the curative simultaneous radiochemotherapy of a patient with anal cancer. 54 Gy are given to the primary tumor and 45 Gy to the nodal CTV. Note the high dose prescribed to the primary tumor (*red* isodoses) is given simultaneously to the medium-dose treatment to the adjuvant nodal areas (*yellow* isodoses)

The new particle beam technologies like proton and heavy ion therapies promise even better dose distributions. Due to their physical properties, the treatment dose can be delivered to a very confined area with perfect sparing especially of the normal tissues behind the target. However, being very sensitive to the physical properties of the tissue, these methods also rely on imaging as a prerequisite for successful treatment planning and delivery [12].

Re-irradiation has been largely avoided in the past, due to the risk of severe normal tissue toxicity. But with a more precise definition and 3D dose documentation together with growing clinical and radiobiological knowledge, re-irradiation can now also be given more frequently, provided that restaging reveals localized tumor progression and the area of progression can be defined clearly (Fig. 4.3) [13–17].

Overall, in the light of all these new possibilities, accurate staging and depiction of the geometry of malignant spread are a prerequisite for effective and precise radiotherapy applications. While very high doses are given inside of target volumes, a rather low exposure is often achieved in their direct neighborhood (Fig. 4.4). Technical and interpretational imaging errors may directly translate to impaired local tumor control and/or increased risk for normal tissue toxicity. Furthermore, erroneous interpretation of posttreatment changes may lead to unnecessary interventions and patient discomfort.

This chapter will go through the relevant applications of imaging in radiotherapy and aims at increasing the awareness of the reader about radiotherapy specific questions and requirements for molecular imaging.

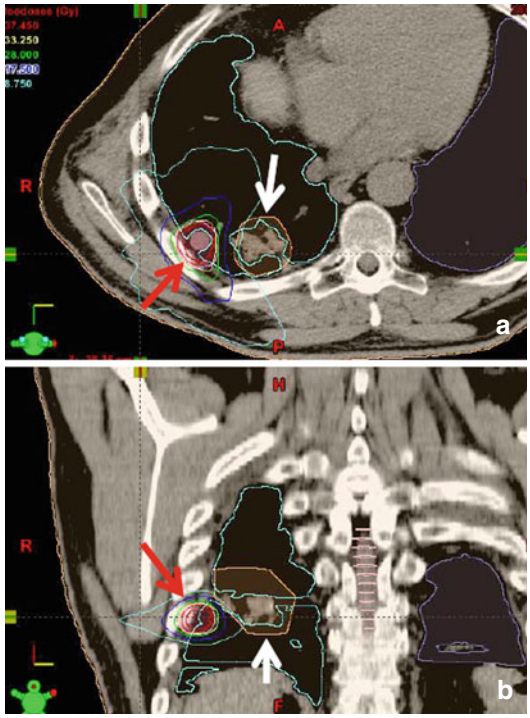

Fig. 4.3 Re-irradiation of a patient with metachronous pulmonary metastases of colon cancer in axial (**a**) and coronal (**b**) plane. The actual target volume of IMRT-SBRT to a metastasis near the thoracic wall (*red arrow*) lies in direct neighborhood of the former treatment volume (*white arrow*) now showing post-RT fibrosis. The IMRT technique enables the avoidance of the former high-dose area (*light blue* isodose)

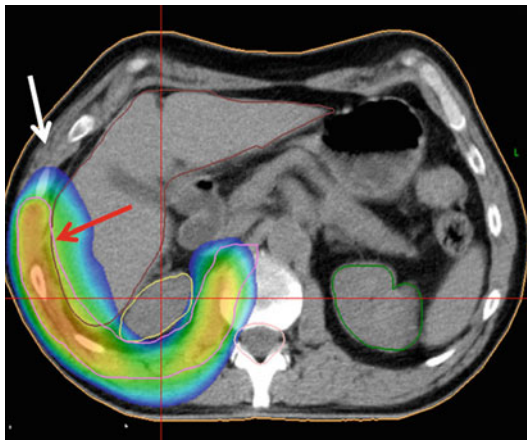

Fig. 4.4 IMRT plan of a patient with pleural mesothelioma. Note that high-dose areas (*red arrow*) are very confined to the PTV (*pink* contour), while the neighboring thoracic wall (*white arrow*) and the right kidney (*yellow* contour) receive far lower doses. In case of erroneous target volume delineation, the risk for a local recurrence in the *white arrow* area would be high

4.2 Diagnosis/Staging

Imaging is mandatory in the process of diagnosis and staging of tumors, as this is a prerequisite for interdisciplinary guideline-based treatment decisions. The decision for the appropriate radiotherapy concept cannot be made without adequate imaging. Obviously, a local aggressive treatment with curative option like stereotactic radiotherapy will only be of benefit for the patient in a metastasis-free situation. During initial evaluation of the benefit of improved staging, several groups reported that the detection of unexpected metastases by FDG-PET often led to a palliative rather than a curative concept with less unnecessary interventions in incurable situations [18–22]. However, the early accurate diagnosis of patients in an oligo-metastatic situation has also led to the discussion of new locally curative treatment concepts for this population, and first data on long-term survivors have been published [23]. The advances in molecular imaging, e.g., the use of FDG-PET/CT for solid tumors, have therefore significantly improved patient care (Fig. 4.5). It has been shown, that the mere fact, to have performed a FDG PET during the staging of a cancer patient can be a prognostic factor by itself [24].

Although histology is a prerequisite for oncologic decision making, there may be certain situations in which the decision for radiotherapy can be based on imaging alone, e.g., repeated chest CT + FDG-PET/CT in medically inoperable patients with small lung cancers. Although controversially discussed, it has been shown that missing histology in cases with clear imaging based diagnosis is prognostically irrelevant [25].

In contrast, further information derived from imaging may be of prognostic significance. Beyond TNM staging information, data derived from molecular imaging like SUVmax, metabolic volume [26], imaging assessed tumor hypoxia [27], perfusion parameters and MRI-spectroscopic parameters [28], have been shown to predict outcome. Like prognostic indices based on pretreatment data (lymphoma, breast cancer scores), these factors might be used to stratify treatments in the future. However, such concepts will need to be tested in clinical trials before general use.

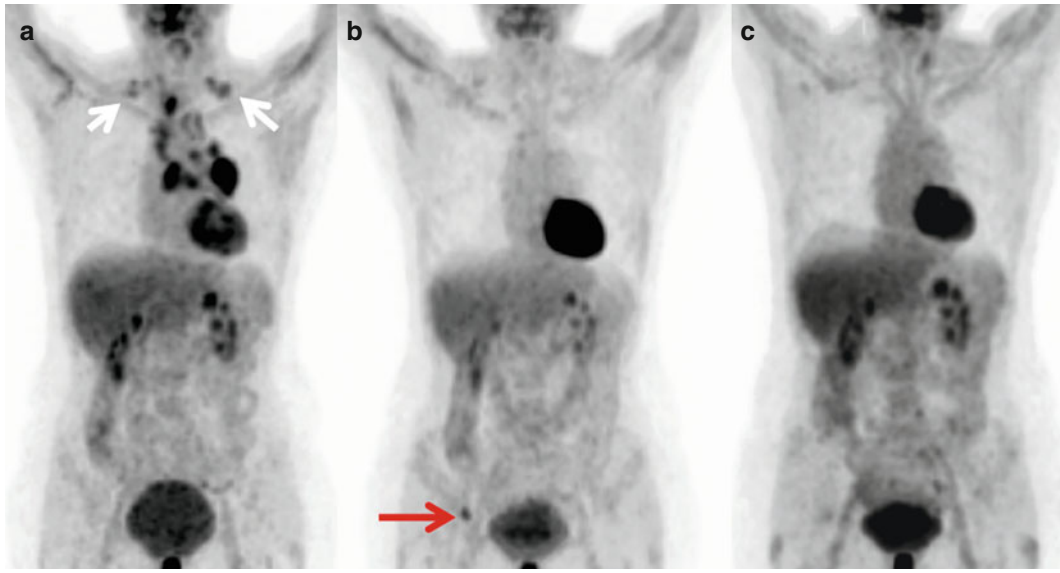

Fig. 4.5 Serial FDG-PET-CT whole body scans (MIPs) showing long-term survival after FDG-PET-based treatment of a 50-year-old woman with non-small cell lung cancer. (**a**) Initial situation with T3 N3 M0 NSCLC (supraclavicular spread, *white arrows*) before combined radiochemotherapy. (**b**) Complete metabolic remission of the thoracic tumor 9 months later with diagnosis of a solitary bone metastasis (*red arrow*). (**c**) Complete metabolic remission 15 months after radiotherapy of the metastasis and bisphosphonate treatment. The patient is alive without recurrence 3 years after initial presentation

In this context, it is important to know that the timing of imaging for radiotherapy needs to be discussed together with the initial treatment decision. In many cases, radiotherapy treatment volumes will relate to initial tumor spread, irrespective of whether radiotherapy will be given as initial treatment or in a later, e.g., adjuvant, situation or after (induction) chemotherapy. Consequently the radiotherapy portals may need to include all pretreatment tumor spread. As systemic treatment may lead to early decrease of signals from molecular imaging, the lack of a pretreatment scan may cause an undertreatment of the patient [29]. On the other hand, tumor progression may be present between initial staging and onset of radiotherapy. Hence, if imaging is to be used for the planning of primary radiotherapy or radiochemotherapy, it may be necessary to repeat scans. This has been shown impressively by the Melbourne group, who reported on a 32 % risk of progression in FDG-PET within 24 days after initial staging of locally advanced lung cancer [30].

After a decision for radiotherapy has been made, the specific interest of the radiation oncologist for further development of his treatment concept lies in the geometry of the disease. Firstly, the local situation of the primary tumor is highly relevant for the choice of radiotherapy techniques and achievable doses. Here, molecular imaging, e.g., amino acid PET may help in giving the correct topography of brain tumors [31] or FDG-PET in the delineation of primary or recurrent head and neck tumors [32].

Secondly, nodal staging is a crucial topic for radiotherapy concepts of many solid tumors. In the primary radiotherapy and/or radiochemotherapy of most cases with head and neck tumors, lung and esophageal cancer, upper abdominal malignancies, and pelvic tumors, a certain radiation dose will be given to macroscopically unaffected nodal areas, and this adjuvant radiotherapy of nodal regions is a main contributor for treatment toxicity. Obviously, the diagnosis of macroscopic nodal involvement will influence this treatment decision. Furthermore, the accuracy of the staging method used may influence the target of radiotherapy. A prominent example is the omission of large mediastinal target volumes in the primary radiochemotherapy for lung cancer after the advent of FDG-PET [33]. In the change of adjuvant concepts, beyond diagnostic accuracy,

several other factors have to be respected: aim of the treatment, clinical problem, precision of actual target volume concepts, achievable doses to the macroscopic tumor leading to the chance of cure, risk profile for surrounding normal tissues, and the amount of dose compromise caused by radiotherapy of adjuvant nodal areas. The appreciation of these factors may lead to different concepts, for example, due to remaining diagnostic uncertainties and normal tissue profiles in relation to the chance of cure, FDG-PET-based staging did not lead to the omission of adjuvant nodal treatment in the head and neck tumors or in the neoadjuvant radiotherapy of rectal cancer [34]. However, future clinical studies will lead to the elaboration of new target volume concepts for many tumors based on new (molecular) imaging methods after their thorough diagnostic workup.

4.3 Treatment Planning and Application

Radiotherapy has the aim to kill tumor cells while sparing normal tissues as much as possible. Necessary tumor doses and tolerance doses as well as fractionation regimes have been elaborated through decades of clinical and radiobiological research. However, the above-mentioned new technologies pose new questions to tumor and normal tissue dosage concepts. While in the conventionally fractionated 3D-radiotherapy area, tumors tended to show slow mass shrinkage and normal tissues exhibited locally well-confined areas of radiation-induced changes, the hypofractionated high-dose treatment in SRT/SBRT may cause necrosis and "overkill" [35], while IMRT and the volumetric arc techniques may lead to diffuse low-dose irradiation of less confined volumes [36] with new profiles and geometries of radiation-induced normal tissue changes.

Overall, for radiotherapy treatment planning, there are basically two fields of interest: the identification of the topography and geometry of diseased tissue and the correct segmentation of the anatomy of normal tissues.

For decades, the International Commission on Radiation Units and Measurements (ICRU) has defined evolving standard definitions for radiotherapy target volumes. Their recent recommendations [37] include (Fig. 4.6):

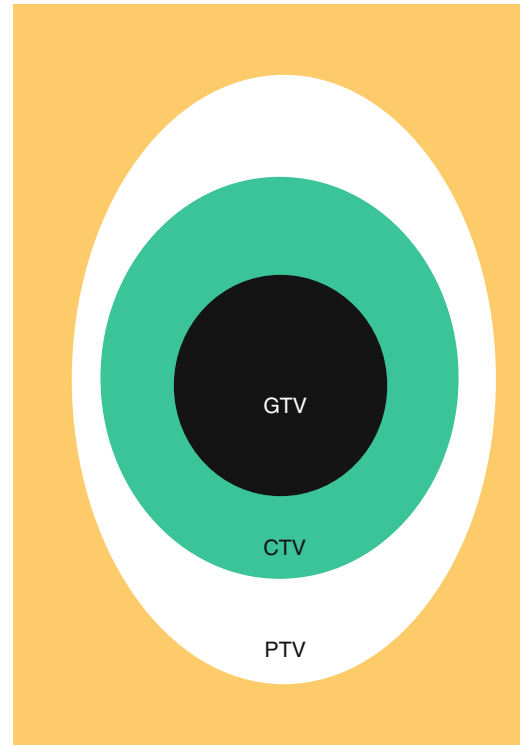

Fig. 4.6 Schematic illustration of ICRU target volumes. *GTV* gross tumor volume, *CTV* clinical target volume, *PTV* planning target volume

- The gross tumor volume (GTV), being gross demonstrable extend and location of the malignant growth, irrespective of the method used for its detection.
- The clinical target volume (CTV), being a volume that contains a demonstrable GTV and/or subclinical malignant disease that must be eliminated.
- The planning target volume (PTV) including the CTV and the surrounding margin. It is a geometrical concept used for treatment planning and defined to ensure that the prescribed dose is actually delivered to the CTV with a clinically acceptable probability.
- The organs-at-risk (OAR) tissues, which if irradiated could suffer significant morbidity and thus might influence the treatment planning and/or the dose prescription.

Besides the impact of imaging on CTV concepts (see above), anatomical and molecular imaging will mainly be used for the definition of the GTV. Here, the approach of the treating

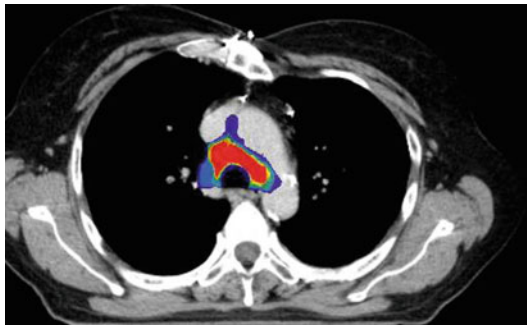

Fig. 4.7 Interobserver variability in target volume delineation: representative axial slice showing a mediastinal target volume (to contain left and right UICC/AJCC lymph node stations 4) anatomically delineated by seven different radiation oncologists using the same protocol and atlas. The *colors* mark the number of observers having included the respective area into their CTV from *dark blue* (1 observer) to *red* (all observers)

physician towards the imaging used differs significantly from that of the diagnostic radiologist. While the latter aims at reporting the correct diagnosis, supplemented by data relevant for staging, the radiation oncologist, who then knows diagnosis and staging, seeks for information on the geometrical spread of the tumor. Hence, his focus will be on the exact borders of the tumor and the detailed anatomy of neighboring normal tissues in order to provide satisfactory dose coverage.

The target volume delineation performed by the treating physician is one of the weakest links in the radiotherapy chain, being characterized by a severe interobserver variability (Fig. 4.7) [38]. In target volume delineation, the imaging modality applied and the methods used may have as significant an impact as the expertise and education of the staff involved [39]. Therefore, there is a strong need for diagnostic knowledge in radiation oncology and for interdisciplinary research and communication between imaging specialists and radiation oncologists. A molecular imaging method is of interest for the delineation of gross tumor volume, if it shows a higher sensitivity and specificity for tumor tissue in comparison to CT and anatomical MRI. This is the case for FDG-PET, e.g., in lung cancer [29], head and neck cancer [32], gynecological cancers, and gastrointestinal malignancies; for amino acid PET (AA PET) in brain tumors [31, 40]; for choline PET in prostate cancer [41]; and for somatostatin-receptor PET in neuroendocrine tumors. Beyond the depiction of primary tumors, PET may be of great help in RT planning for tumor recurrence or progression after initial treatment (see below).

It should be emphasized that imaging used for radiotherapy planning must be co-registered accurately with the anatomical reference for treatment application, i.e., the planning CT [42]. This is best achieved by scanning the patient in planning position (Fig. 4.8). If such image data are not available, diagnostic images should be viewed side by side in order to avoid the delineation of false volumes caused by incorrect fusion. Current recommendations do also not advocate nonrigid (i.e., elastic) image fusion for RT planning purposes, as these techniques have not been evaluated for their safety in this context [42].

Several studies showed a reduction of interobserver variability by the use of molecular imaging, mainly FDG-PET, in various tumors [43–45]. However, a significant variability remains, mainly caused by the blurry appearance of PET images. PET-based GTV delineation needs some practice and may be assisted by clinical protocols and/or automatic or semiautomatic image segmentation.

In order to reach standardization, several groups have developed (semi)automatic methods for the generation of PET-based gross tumor volumes (GTVs). Unfortunately, there is no consensus on a commonly accepted method and the application of different methods to the same lesion will lead to significantly different volumes [46, 47]. Therefore, automatic methods should only be used after institutional evaluation and calibration [48]. Although new initiatives promise future solutions of this problem [49, 50], presently the safest and most practical solution for PET-based tumor volumes may be the joint delineation by the radiation oncologist together with the nuclear medicine physician [42].

Historic [51] and recent [31, 41] examples for the possible benefit of PET-based radiotherapy planning in lung cancer, brain tumors, and prostate cancer are given in Figs. 4.9, 4.10, and 4.11.

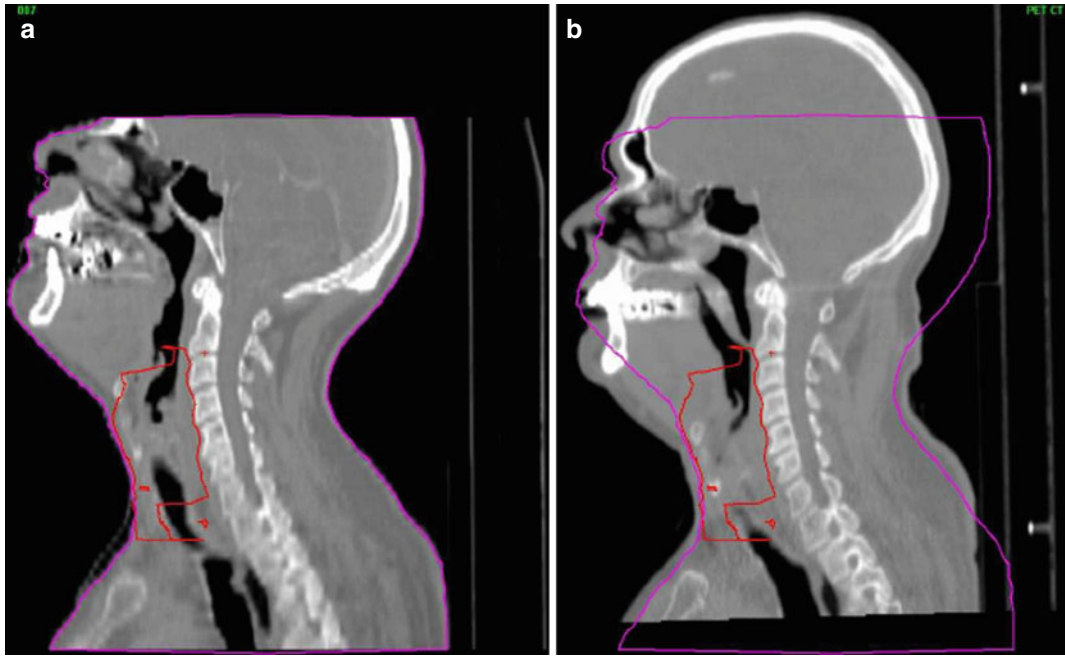

Fig. 4.8 Importance of patient position for target volume delineation. (**a**) Sagittal reconstruction of the planning CT scan of a patient with laryngeal cancer in radiotherapy treatment position secured by positioning aid (mask), CTV marked in red. (**b**) Sagittal reconstruction of CT from the PET/CT scanner of the same patient without positioning aid, rigid image fusion with respect to the cervical spine. Note that the anatomical position of the larynx significantly changes its relation to the *red* CTV contour (Courtesy W. Vogel, Amsterdam)

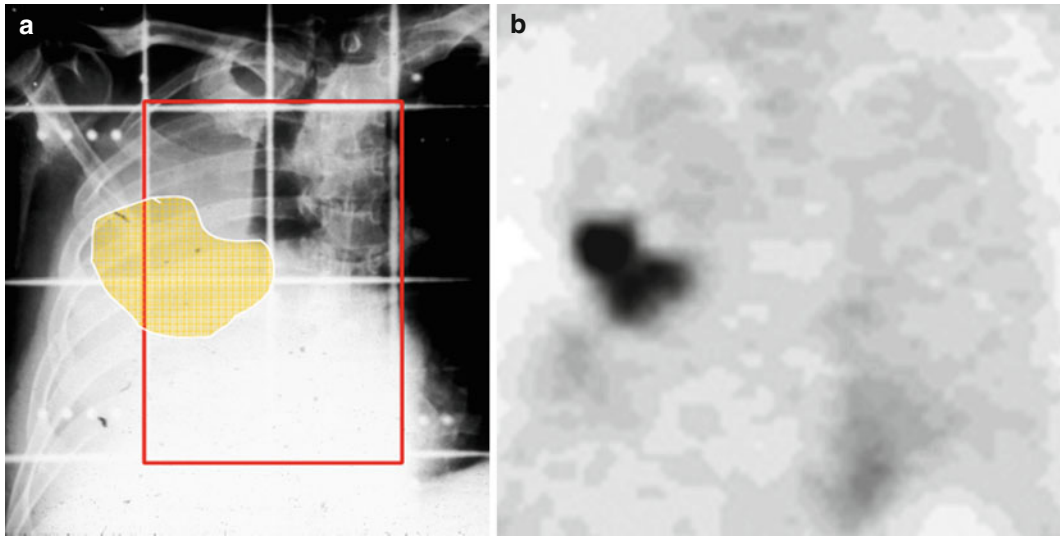

Fig. 4.9 Historical case of a patient with complete atelectasis of the right lung treated by external beam radiotherapy in August 1997 (anterior/posterior fields in simulator planned 2D technique) with the aim of reopening the right main bronchus. (**a**) Simulation film with *rectangular* anterior treatment portal marked in *red*. (**b**) Corresponding coronal slice of non-attenuation-corrected FDG-PET of the same patient showing large FDG accumulation from mediastinum to thoracic wall (FDG accumulation marked in *orange* on simulator film for orientation). Note that large parts of the tumors are not covered by the treatment portal, while a large volume of normal tissue is given radiotherapy

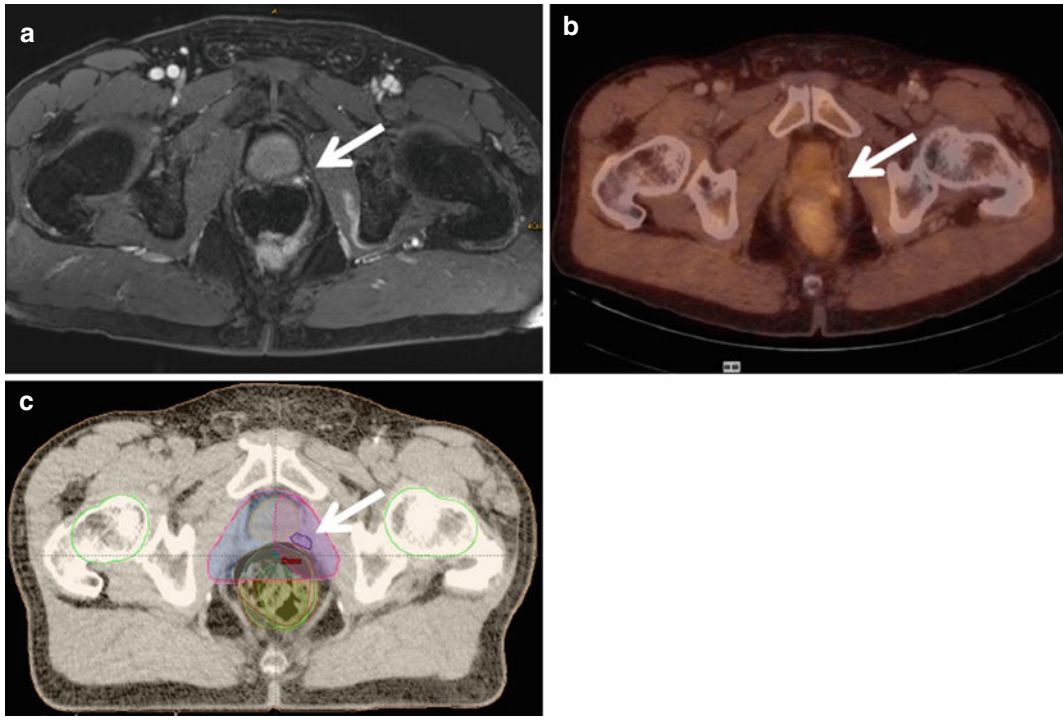

Fig. 4.10 Imaging for radiotherapy planning of a patient with PSA recurrence of prostate cancer, 3 years after radical prostatectomy. (**a**) MRI scan (contrast-enhanced fatsat T1 sequence) with focal contrast enhancement (*arrow*) in the lateral aspect of the prostatic fossa. (**b**) 18-F-choline PET/CT showing corresponding focally increased choline uptake (*arrow*). (**c**) Radiotherapy planning CT with corresponding GTV (dark blue contour, *arrow*) and surrounding PTV (*pink* color wash) for boost irradiation of macroscopic recurrence

Concerning movements, there are multiple methods to assess and account for organ motion during radiotherapy [52]. All of them involve imaging. Overall, respiratory movements must be accounted for in the chest and upper abdomen, while different organ fillings cause movements in the pelvis. Respiratory movements cause significant displacements in lung tumors but also in mediastinal structures like esophageal tumors and lymph nodes as well as in the upper abdomen involving not only the liver but also kidneys and the retroperitoneum. In conventional radiotherapy, these movements are accounted for by adding a population-based margin to the CTV. However, it has been shown that these margins often fail, especially when the planning CT has not been acquired with respect to motional status, e.g., depicting the snapshot of an extreme breathing position [33]. Therefore, with the advent of high-precision technologies, the concepts of gating (irradiation only during certain parts of the breathing phase) and tracking (beam following the target) have been explored along with various implant, breath-hold, and patient feedback technologies. Target volume concepts include the definition of the internal target volume (ITV; Fig. 4.12), which again can be reduced using certain statistical methods according to the probability of tumor presence. All these methods rely on initial 4D imaging, mainly acquired by CT; some of the methods also need in-room monitoring of patient's breathing. To date, none of the available methods can be regarded as standard. However, an institutional policy for movement compensation is needed for any kind of high-precision radiotherapy in chest and upper abdomen. In this context, the use of 4D PET and/or cine-MRI techniques is of high interest and a field of intensive research.

Concerning pelvic movements, in the context of radiotherapy of the prostate and the bladder,

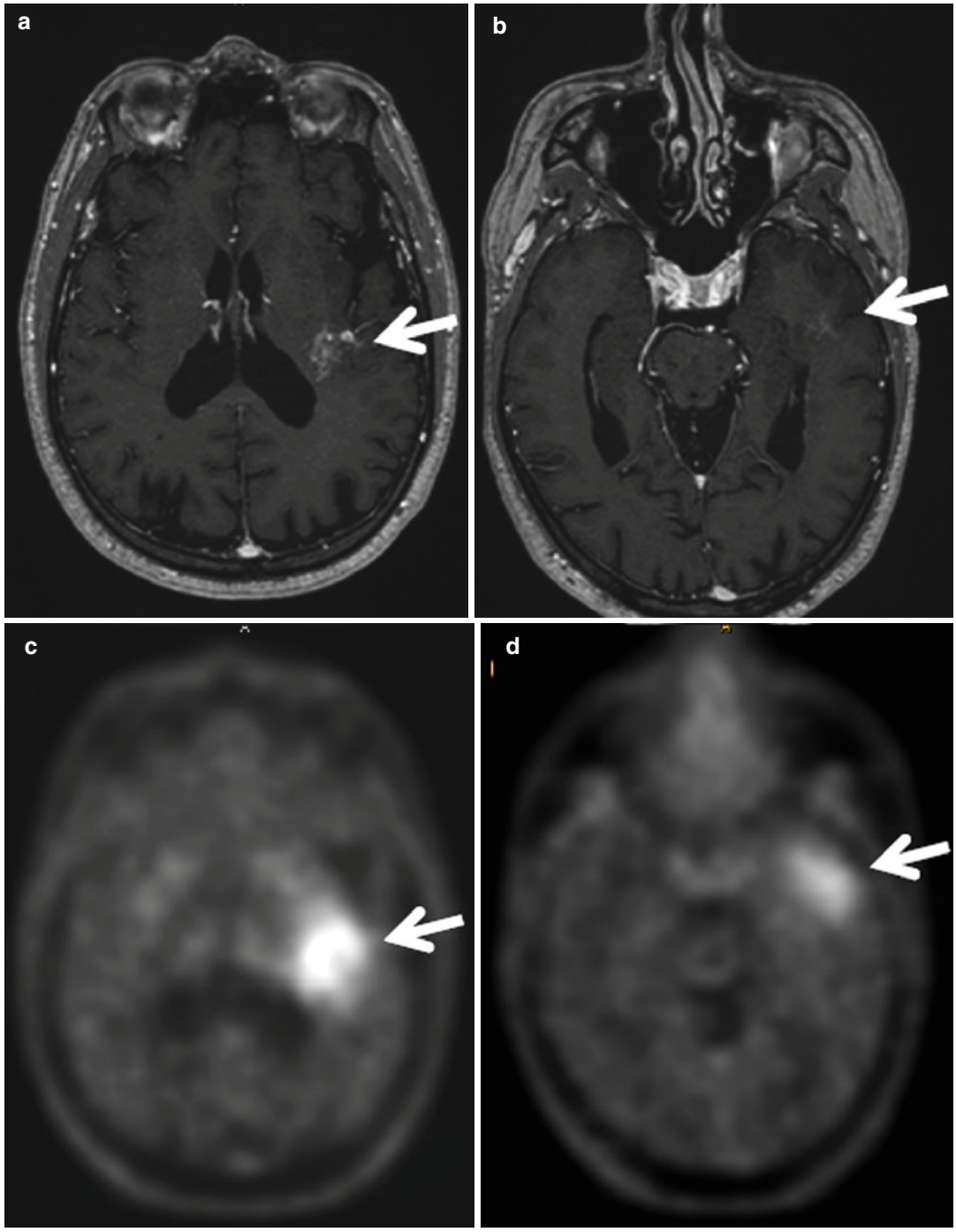

Fig. 4.11 Imaging for radiotherapy planning of a patient with recurrent glioblastoma. (**a**, **b**) Two axial slices of the MRI scan (contrast-enhanced T1 sequence) with areas of pathological contrast enhancement (*white arrows*). (**c**, **d**) Two corresponding slices of the 18-F-ethyltyrosine PET scan with significantly increased uptake (*arrows*) far beyond the area of MRI contrast enhancement leading to increase of the target volume (not shown)

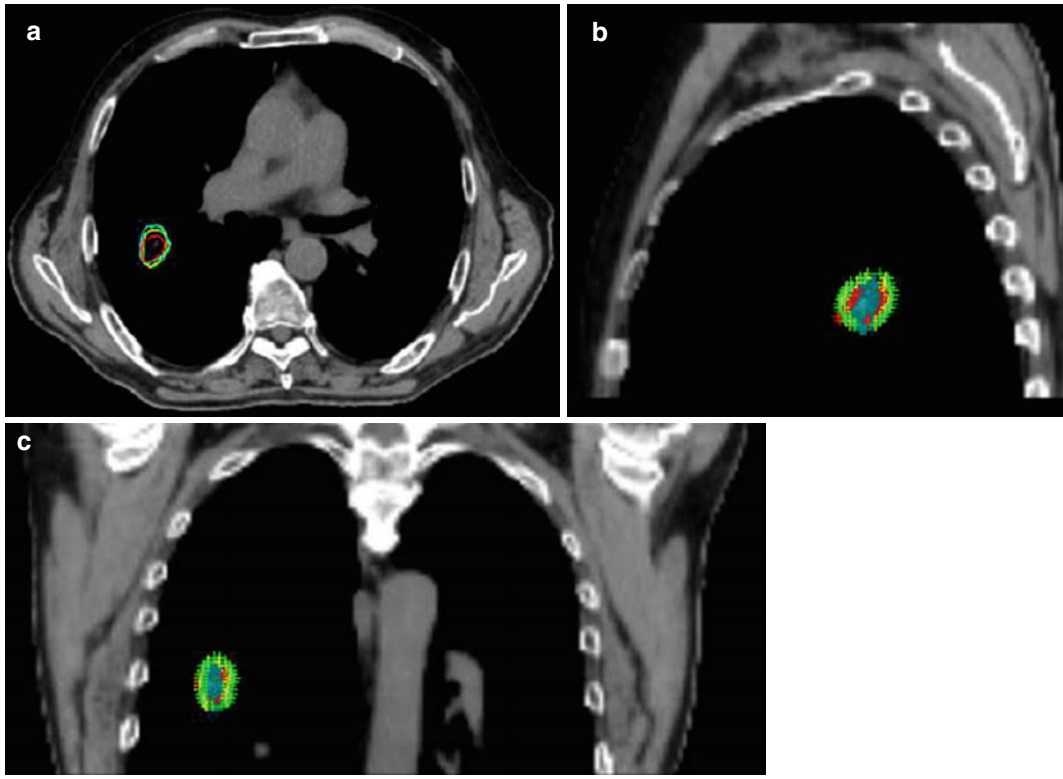

Fig. 4.12 Internal target volume (ITV) composed from three CTVs (*red*, *yellow*, and *green* contours) of different breathing positions in a patient scheduled for stereotactic radiotherapy of the lung

the filling of bladder and rectum are accounted for. This is a focus of the so-called adaptive radiotherapy (ART), i.e., the re-optimization of treatment plans by modification of initial planning parameters, which is closely connected to image-guided radiotherapy (IGRT, see below) [53]. Ideally, a treatment plan can be chosen daily according to the respective varying anatomy [54]. Obviously, such an approach will involve daily on-site CT imaging.

The irradiation of normal tissues is an important topic in the context of radiotherapy. While some normal tissues (e.g., bone, skin, connective tissue) are rather radioresistant and tolerate therapeutic doses when given in a fractionated treatment, others are more radiosensitive (e.g., lung, kidney, nerve tissue) and therefore need special attention. Beyond the issue of tolerance doses, there are differences in the character of radiation reactions: "parallel" normal tissues (e.g., liver, lung), where radiation-induced damage of a small volume may not harm the patient, while "serial" tissues (e.g., spinal cord, esophagus) may completely lose their function, when only a small volume is affected by severe radiotherapy toxicity. With respect to this in a time of rising doses and precision, it is clear that in order to ensure maximum normal tissue sparing, the relevant normal tissues within the area to be treated need to be thoroughly delineated. This is a prerequisite for the use of modern treatment planning, e.g., IMRT optimization. Differences in NT delineation may directly affect treatment plans [55].

Therefore, a lot of effort is presently being invested in the use of atlas-based automatic anatomical normal tissue delineations. While some groups have shown the possibility and benefit of the integration of functional normal tissue data (e.g., lung perfusion) [56] into the planning process, molecular imaging methods are not widely used for the characterization of normal tissues for radiotherapy planning. This is a field of future research and improvement.

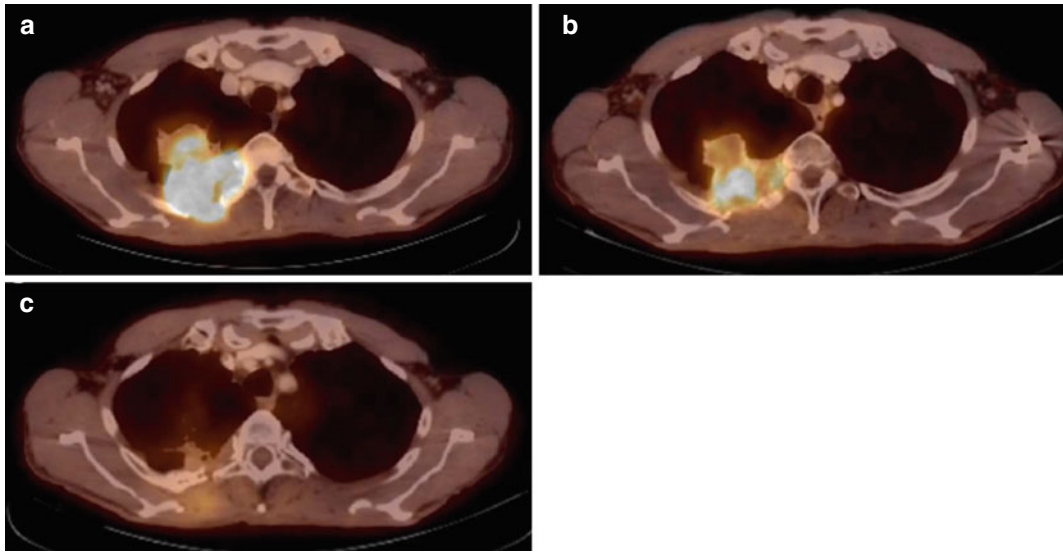

Fig. 4.13 Early response FDG-PET/CT predicting late CT response in a patient with locally advanced NSCLC. (**a**) Axial fused FDG-PET/CT depicting the large tumor invading the thoracic wall before radiochemotherapy. (**b**) Corresponding slice of FDG-PET/CT 2 weeks after start of treatment showing significant decrease of FDG accumulation without relevant morphologic changes in CT. (**c**) Corresponding slice of FDG-PET/CT 11 months later showing a nearly complete metabolic and very good morphologic tumor remission

In the technical process of modern radiotherapy application, imaging plays a major role. Modern linear accelerators provide the possibility to acquire plain X-ray or 3D datasets (e.g., cone beam CT) with the possibility to match anatomically to the planned position and automatically reposition the patient before treatment. This "image-guided radiotherapy" (IGRT) is one of the tools for highly precise treatment delivery [57]. However, as IGRT is based on anatomical landmarks, molecular imaging does not play a role in this context. Furthermore, the basic use of anatomical correlation in treatment planning and delivery shows the need for a high-quality co-registration of molecular imaging data with anatomy if used for radiotherapy.

4.4 Response Assessment

4.4.1 Detection of Recurrence

Besides IGRT and anatomical ART, molecular imaging during treatment is a focus of present research. It has been shown that the reduction of FDG uptake (Fig. 4.13) and the remainder of FDG accumulations during radiochemotherapy, e.g., of lung cancer, is predictive for the outcome after treatment [58]. As it is clear that the achievement of a complete tumor remission is related to prognosis [59], ongoing studies investigate, if a boost to highly FDG active regions within the tumor improves outcome [11]. Other groups address the behavior of hypoxic areas (Fig. 4.14) during radiotherapy with the aim of dose modification to improve outcome [60]. As in the context of systemic treatment, the early assessment of tumor response is also an interesting conceptual topic for radiotherapy, ongoing clinical studies investigate, if the assessment of response during radiotherapy (e.g., by FDG- or FLT-PET, by apoptosis imaging or perfusion and diffusion MRI) may lead to treatment modifications, e.g., to changes in the dose prescription or possibly to the re-discussion of consecutive treatments, e.g., to the omission of surgery in patients well responding to radiation [61]. Still, the multicenter standardization of response measures is a challenge. However, the result of these trials may lead to solid interdisciplinary concepts and stress the

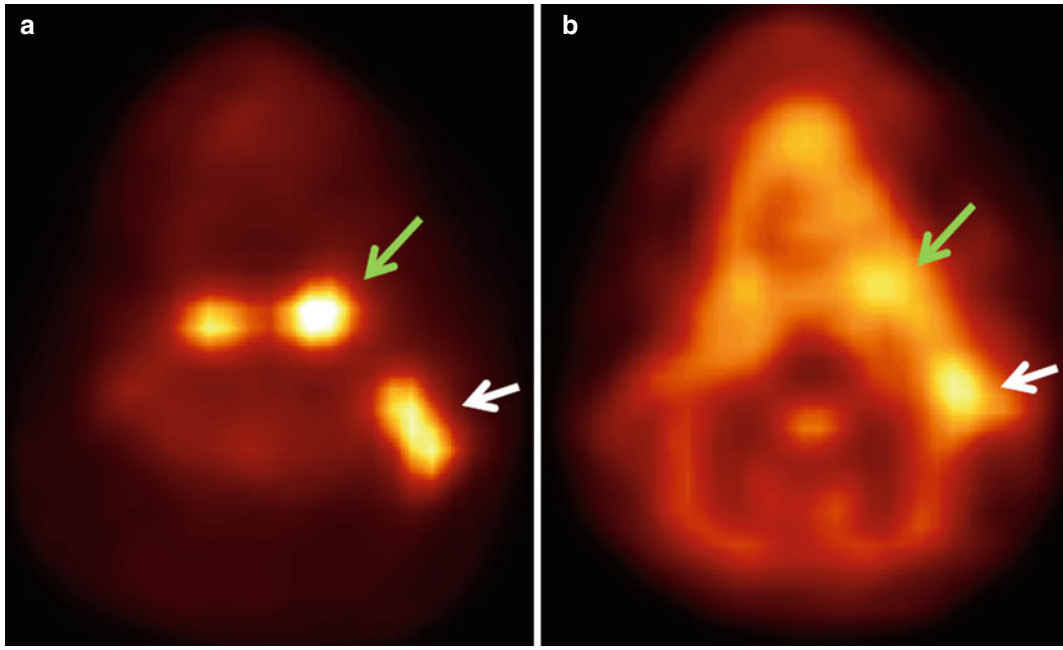

Fig. 4.14 Hypoxia imaging in a patient with locally advanced oropharyngeal carcinoma. (**a**) Axial slice of FDG-PET scan showing pathologic FDG uptake in the primary tumor (*green arrow*) and a cervical lymph node (*white arrow*). (**b**) Corresponding slice of 18-F-MISO PET scan. Note the relatively low tracer uptake in the primary tumor (*green arrow*) as compared to the uptake of the lymph node (*white arrow*)

importance of imaging during and after radiotherapy.

Of high interest is furthermore the monitoring of normal tissue changes during radiotherapy by molecular imaging. DeRuysscher and colleagues found a correlation of the FDG uptake in normal lung with radiation-induced lung disease after treatment [62]. Other authors found a similar correlation and furthermore a correlation of normal tissue changes with tumor remission [63]. However, all these data need further investigations before they may become part of treatment concepts.

After completion of radiotherapy or radiochemotherapy, imaging will be used to assess response and to detect recurrences. For lung cancer, a clear survival advantage has been shown for complete metabolic responders as assessed by FDG-PET [63–66]. The high predictive value of FDG-PET in the differential diagnosis of posttreatment changes and tumor recurrence has also been shown in the head and neck tumors [67]. Other applications include the imaging characterization of early and late normal tissue reactions. As the correct diagnosis of radiation-induced normal tissue changes is closely related to the treatment geometry, this field again requires the close collaboration between diagnostic radiologists and radiation oncologists. Problems are often caused by radiation-induced inflammatory changes in normal tissues. These may severely hamper imaging assessment of tumor response in anatomical as well as in molecular imaging (Fig. 4.15). However, thorough image analysis beyond merely measuring the SUV, e.g., including image patterns and the knowledge about the former radiotherapy dose distribution will often lead to correct diagnoses. Molecular imaging has been shown to be of help in the differential diagnosis between treatment-related changes

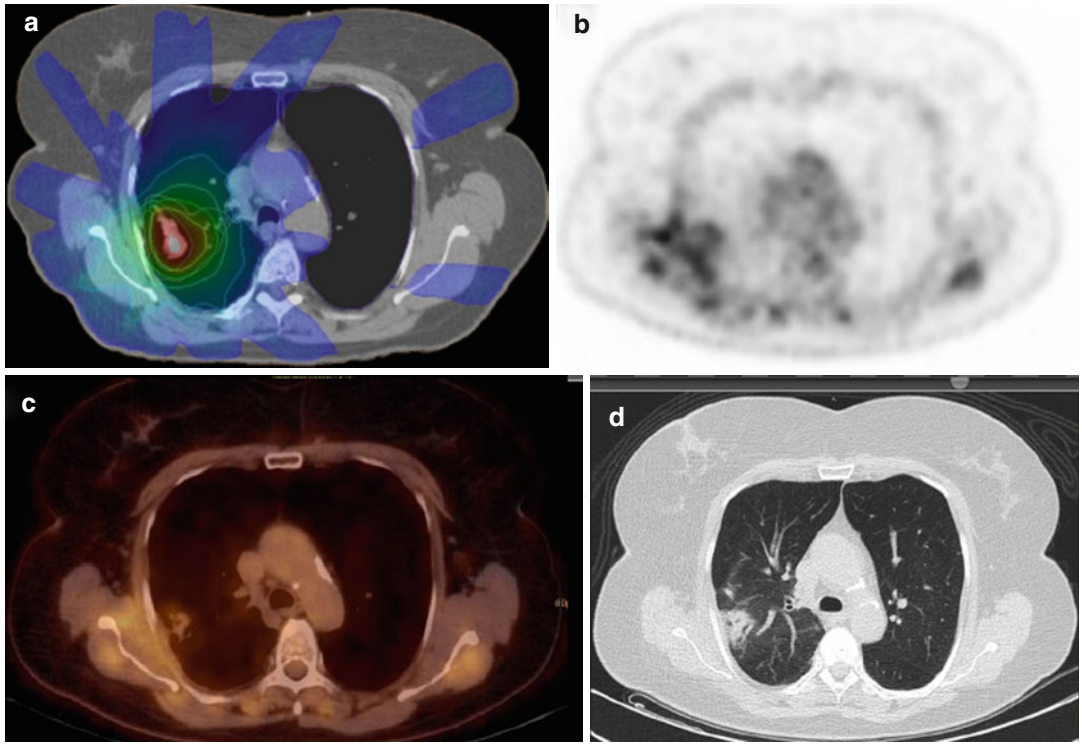

Fig. 4.15 Imaging after SBRT in a patient with localized NSCLC UICC stage I. (**a**) Isodose distribution of SBRT treatment. (**b–d**) FDG-PET/CT (**b**: FDG-PET, **c**: fused image, **d**: CT) 1 year after treatment showing diffusely increased uptake within the former high-dose area corresponding to focal radiation-induced changes of lung and thoracic wall

and recurrence, e.g., perfusion MRI and amino acid PET in the differential diagnosis of radionecrosis versus recurrent glioma [68].

Conclusion

Imaging is an indispensable part of radiotherapy practice. With the development of effective high-precision technologies, the requirements for pre-, interim, and posttreatment imaging and the fields of their application have increased. For the most effective use of imaging in radiation oncology, the interdisciplinary exchange on concepts, technologies, and mutual demands between the specialists involved is required and best ensured by close collaboration and joint research.

References

1. Goitein M. Computed tomography in planning radiation therapy. Int J Radiat Oncol Biol Phys. 1979;5(3):445–7.
2. Brahme A. Optimization of stationary and moving beam radiation therapy techniques. Radiother Oncol. 1988;12(2):129–40.
3. Chao KS. Protection of salivary function by intensity-modulated radiation therapy in patients with head and neck cancer. Semin Radiat Oncol. 2002;12(1 Suppl 1):20–5.
4. Bauman G, et al. Intensity-modulated radiotherapy in the treatment of prostate cancer. Clin Oncol (R Coll Radiol). 2012;24(7):461–73.
5. Minniti G, et al. Radiotherapy and radiosurgery for benign skull base meningiomas. Radiat Oncol. 2009;4:42.
6. Nieder C, et al. Presentation, patterns of care, and survival in patients with brain metastases: What has changed in the last 20 years? Cancer. 2011;117(11):2505–12.

7. Prokic V, et al. Whole brain irradiation with hippocampal sparing and dose escalation on multiple brain metastases: a planning study on treatment concepts. Int J Radiat Oncol Biol Phys. 2013; 85(1):264–70.
8. Palma D, et al. Impact of introducing stereotactic lung radiotherapy for elderly patients with stage I non-small-cell lung cancer: a population-based time-trend analysis. J Clin Oncol. 2010;28(35):5153–9.
9. Jin JY, et al. Advances in treatment techniques: arc-based and other intensity modulated therapies. Cancer J. 2011;17(3):166–76.
10. Ling CC, et al. Towards multidimensional radiotherapy (MD-CRT): biological imaging and biological conformality. Int J Radiat Oncol Biol Phys. 2000; 47(3):551–60.
11. van Elmpt W, et al. The PET-boost randomised phase II dose-escalation trial in non-small cell lung cancer. Radiother Oncol. 2012;104(1):67–71.
12. Mohan R, Bortfeld T. Proton therapy: clinical gains through current and future treatment programs. Front Radiat Ther Oncol. 2011;43:440–64.
13. Mantel F, et al. Stereotactic body radiation therapy in the re-irradiation situation – a review. Radiat Oncol. 2013;8:7.
14. Ramey SJ, Marshall DT. Re-irradiation for salvage of prostate cancer failures after primary radiotherapy. World J Urol. 2012 [Epub ahead of print].
15. Chen AM, et al. Practical considerations in the re-irradiation of recurrent and second primary head-and-neck cancer: who, why, how, and how much? Int J Radiat Oncol Biol Phys. 2011;81(5):1211–9.
16. Ammirati M, et al. The role of retreatment in the management of recurrent/progressive brain metastases: a systematic review and evidence-based clinical practice guideline. J Neurooncol. 2010;96(1):85–96.
17. Nieder C, et al. Improvement, clinical course, and quality of life after palliative radiotherapy for recurrent glioblastoma. Am J Clin Oncol. 2008;31(3): 300–5.
18. Abramyuk A, et al. Modification of staging and treatment of head and neck cancer by FDG-PET/CT prior to radiotherapy. Strahlenther Onkol. 2013;189(3): 197–201.
19. Barber TW, et al. 18F-FDG PET/CT has a high impact on patient management and provides powerful prognostic stratification in the primary staging of esophageal cancer: a prospective study with mature survival data. J Nucl Med. 2012;53(6):864–71.
20. Davey K, et al. The impact of 18-fluorodeoxyglucose positron emission tomography-computed tomography on the staging and management of primary rectal cancer. Dis Colon Rectum. 2008;51(7):997–1003.
21. Gregory DL, et al. Effect of PET/CT on management of patients with non-small cell lung cancer: results of a prospective study with 5-year survival data. J Nucl Med. 2012;53(7):1007–15.
22. Klaeser B, et al. Therapeutic impact of 2-[fluorine-18] fluoro-2-deoxy-D-glucose positron emission tomography in the pre- and postoperative staging of patients with clinically intermediate or high-risk breast cancer. Ann Oncol. 2007;18(8):1329–34.
23. De Ruysscher D, et al. Radical treatment of non-small-cell lung cancer patients with synchronous oligometastases: long-term results of a prospective phase II trial (Nct01282450). J Thorac Oncol. 2012;7(10):1547–55.
24. Eschmann SM, et al. FDG PET for staging of advanced non-small cell lung cancer prior to neoadjuvant radio-chemotherapy. Eur J Nucl Med Mol Imaging. 2002;29(6):804–8.
25. Lagerwaard FJ, et al. Outcomes of stereotactic ablative radiotherapy in patients with potentially operable stage I non-small cell lung cancer. Int J Radiat Oncol Biol Phys. 2012;83(1):348–53.
26. Lin Y, et al. Prognostic value of preoperative metabolic tumor volumes on PET-CT in predicting disease-free survival of patients with stage I non-small cell lung cancer. Anticancer Res. 2012;32(11):5087–91.
27. Thorwarth D, et al. Combined uptake of [18F]FDG and [18F]FMISO correlates with radiation therapy outcome in head-and-neck cancer patients. Radiother Oncol. 2006;80(2):151–6.
28. Peet AC, et al. Functional imaging in adult and paediatric brain tumours. Nat Rev Clin Oncol. 2012;9(12):700–11.
29. Nestle U, et al. Practical integration of [18F]-FDG-PET and PET-CT in the planning of radiotherapy for non-small cell lung cancer (NSCLC): the technical basis, ICRU-target volumes, problems, perspectives. Radiother Oncol. 2006;81(2):209–25.
30. Everitt S, et al. High rates of tumor growth and disease progression detected on serial pretreatment fluorodeoxyglucose-positron emission tomography/computed tomography scans in radical radiotherapy candidates with nonsmall cell lung cancer. Cancer. 2010;116(21):5030–7.
31. Grosu AL, Weber WA. PET for radiation treatment planning of brain tumours. Radiother Oncol. 2010;96(3):325–7.
32. Gregoire V, Chiti A. Molecular imaging in radiotherapy planning for head and neck tumors. J Nucl Med. 2011;52(3):331–4.
33. De Ruysscher D, et al. European Organisation for Research and Treatment of Cancer recommendations for planning and delivery of high-dose, high-precision radiotherapy for lung cancer. J Clin Oncol. 2010; 28(36):5301–10.
34. Gregoire V, et al. PET-based treatment planning in radiotherapy: a new standard? J Nucl Med. 2007;48 Suppl 1:68S–77.
35. van Baardwijk A, et al. Is high-dose stereotactic body radiotherapy (SBRT) for stage I non-small cell lung cancer (NSCLC) overkill? A systematic review. Radiother Oncol. 2012;105(2):145–9.
36. Bezjak A, et al. Intensity-modulated radiotherapy in the treatment of lung cancer. Clin Oncol (R Coll Radiol). 2012;24(7):508–20.
37. Gregoire V, Mackie TR. State of the art on dose prescription, reporting and recording in Intensity-

Modulated Radiation Therapy (ICRU report No. 83). Cancer Radiother. 2011;15(6–7):555–9.
38. Weiss E, Hess CF. The impact of gross tumor volume (GTV) and clinical target volume (CTV) definition on the total accuracy in radiotherapy theoretical aspects and practical experiences. Strahlenther Onkol. 2003;179(1):21–30.
39. Horan G, et al. "Two are better than one": a pilot study of how radiologist and oncologists can collaborate in target volume definition. Cancer Imaging. 2006;6: 16–9.
40. Grosu AL, et al. An interindividual comparison of O-(2-[18F]fluoroethyl)-L-tyrosine (FET)- and L-[methyl-11C]methionine (MET)-PET in patients with brain gliomas and metastases. Int J Radiat Oncol Biol Phys. 2011;81(4):1049–58.
41. Rischke HC, et al. Treatment of recurrent prostate cancer following radical prostatectomy: the radiation-oncologists point of view. Q J Nucl Med Mol Imaging. 2012;56(5):409–20.
42. Thorwarth D, et al. Integration of FDG-PET/CT into external beam radiation therapy planning: technical aspects and recommendations on methodological approaches. Nuklearmedizin. 2012;51(4):140–53.
43. Schreurs LM, et al. Impact of 18-fluorodeoxyglucose positron emission tomography on computed tomography defined target volumes in radiation treatment planning of esophageal cancer: reduction in geographic misses with equal inter-observer variability: PET/CT improves esophageal target definition. Dis Esophagus. 2010;23(6):493–501.
44. Steenbakkers RJ, et al. Reduction of observer variation using matched CT-PET for lung cancer delineation: a three-dimensional analysis. Int J Radiat Oncol Biol Phys. 2006;64(2):435–48.
45. Grosu AL, et al. 11C-methionine PET improves the target volume delineation of meningiomas treated with stereotactic fractionated radiotherapy. Int J Radiat Oncol Biol Phys. 2006;66(2):339–44.
46. Zaidi H, El Naqa I. PET-guided delineation of radiation therapy treatment volumes: a survey of image segmentation techniques. Eur J Nucl Med Mol Imaging. 2010;37(11):2165–87.
47. Nestle U, et al. Comparison of different methods for delineation of 18F-FDG PET-positive tissue for target volume definition in radiotherapy of patients with non-Small cell lung cancer. J Nucl Med. 2005;46(8):1342–8.
48. Schaefer A, et al. Multi-centre calibration of an adaptive thresholding method for PET-based delineation of tumour volumes in radiotherapy planning of lung cancer. Nuklearmedizin. 2012;51(3):101–10.
49. Shepherd T, et al. Comparative study with new accuracy metrics for target volume contouring in PET image guided radiation therapy. IEEE Trans Med Imaging. 2012;31(11):2006–24.
50. Zito F, et al. The use of zeolites to generate PET phantoms for the validation of quantification strategies in oncology. Med Phys. 2012;39(9):5353–61.
51. Nestle U, et al. 18F-deoxyglucose positron emission tomography (FDG-PET) for the planning of radiotherapy in lung cancer: high impact in patients with atelectasis. Int J Radiat Oncol Biol Phys. 1999; 44(3):593–7.
52. Wolthaus JW, et al. Comparison of different strategies to use four-dimensional computed tomography in treatment planning for lung cancer patients. Int J Radiat Oncol Biol Phys. 2008;70(4):1229–38.
53. Ghilezan M, et al. Adaptive radiation therapy for prostate cancer. Semin Radiat Oncol. 2010;20(2): 130–7.
54. Meijer GJ, et al. High precision bladder cancer irradiation by integrating a library planning procedure of 6 prospectively generated SIB IMRT plans with image guidance using lipiodol markers. Radiother Oncol. 2012;105(2):174–9.
55. Li XA, et al. Variability of target and normal structure delineation for breast cancer radiotherapy: an RTOG Multi-Institutional and Multiobserver Study. Int J Radiat Oncol Biol Phys. 2009;73(3):944–51.
56. Munawar I, et al. Intensity modulated radiotherapy of non-small-cell lung cancer incorporating SPECT ventilation imaging. Med Phys. 2010;37(4):1863–72.
57. Jaffray DA. Image-guided radiotherapy: from current concept to future perspectives. Nat Rev Clin Oncol. 2012;9(12):688–99.
58. Aerts HJ, et al. Identification of residual metabolic-active areas within NSCLC tumours using a pre-radiotherapy FDG-PET-CT scan: a prospective validation. Lung Cancer. 2012;75(1):73–6.
59. MacManus MP, et al. Imaging with F-18 FDG PET is superior to Tl-201 SPECT in the staging of non-small cell lung cancer for radical radiation therapy. Australas Radiol. 2001;45(4):483–90.
60. Thorwarth D, Alber M. Implementation of hypoxia imaging into treatment planning and delivery. Radiother Oncol. 2010;97(2):172–5.
61. Haustermans K, et al. The ESTRO Breur Lecture 2010: toward a tailored patient approach in rectal cancer. Radiother Oncol. 2011;100(1):15–21.
62. De Ruysscher D, et al. Increased (18)F-deoxyglucose uptake in the lung during the first weeks of radiotherapy is correlated with subsequent Radiation-Induced Lung Toxicity (RILT): a prospective pilot study. Radiother Oncol. 2009;91(3):415–20.
63. Hicks RJ, et al. Early FDG-PET imaging after radical radiotherapy for non-small-cell lung cancer: inflammatory changes in normal tissues correlate with tumor response and do not confound therapeutic response evaluation. Int J Radiat Oncol Biol Phys. 2004;60(2): 412–8.
64. Eschmann SM, et al. Repeat 18F-FDG PET for monitoring neoadjuvant chemotherapy in patients with stage III non-small cell lung cancer. Lung Cancer. 2007;55(2):165–71.
65. Hellwig D, et al. Value of F-18-fluorodeoxyglucose positron emission tomography after induction therapy of locally advanced bronchogenic carcinoma. J Thorac Cardiovasc Surg. 2004;128(6):892–9.
66. Pottgen C, et al. Value of 18F-fluoro-2-deoxy-D-glucose-positron emission tomography/computed

tomography in non-small-cell lung cancer for prediction of pathologic response and times to relapse after neoadjuvant chemoradiotherapy. Clin Cancer Res. 2006;12(1):97–106.
67. Abgral R, et al. Does 18F-FDG PET/CT improve the detection of posttreatment recurrence of head and neck squamous cell carcinoma in patients negative for disease on clinical follow-up? J Nucl Med. 2009; 50(1):24–9.
68. Galldiks N, et al. Role of O-(2-(18)F-fluoroethyl)-L-tyrosine PET for differentiation of local recurrent brain metastasis from radiation necrosis. J Nucl Med. 2012;53(9):1367–74.

New Therapies and Functional-Molecular Imaging

5

Roberto García-Figueiras and Anwar R. Padhani

Contents

Abbreviations

AAT	Antiangiogenesis therapy
ADC	Apparent diffusion coefficient
AR	Androgen receptor
BC	Breast cancer
BF	Blood flow
BM	Bone marrow
CRT	Chemoradiotherapy
DCE-MRI	Dynamic contrast-enhanced MRI
DCE-US	Dynamic contrast-enhanced ultrasound
DWI	Diffusion-weighted imaging
DW-MRI	Diffusion-weighted magnetic resonance imaging
EGFR	Epidermal growth factor receptor
FDG	^{18}F-2-fluoro-2-deoxy-D-glucose
FLT	^{18}F-3-deoxy-3-fluorothymidine
FMI	Functional and molecular imaging
G-CSF	Granulocyte colony-stimulating factor
HIF-1a	Hypoxia-inducible factor-1a
K^{trans}	Transfer constant
MFMI	Multiparametric functional-molecular imaging
MTT	Mean transit time
MVD	Microvessel density
PARP	polyADP-ribose polymerase

R. García-Figueiras, MD (✉)
Department of Radiology, Hospital Clínico,
Complexo Hospitalario Universitario de Santiago de Compostela, Choupana s/n,
Santiago de Compostela 15706, Spain
e-mail: roberto.garcia.figueiras@sergas.es

A.R. Padhani, MB, BS, FRCP, FRCR
Department of Radiology,
Paul Strickland Scanner Centre,
Mount Vernon Cancer Centre, Rickmansworth Rd,
Northwood, Middlesex, HA6 2RN, UK
e-mail: anwar.padhani@stricklandscanner.org.uk

A. Luna et al. (eds.), *Functional Imaging in Oncology*,
DOI 10.1007/978-3-642-40412-2_5,

PC	Prostate cancer
pCR	Pathological complete response
PCT	Perfusion CT
PET	Positron emission tomography
RC	Renal cancer
SUV	Standardized uptake value
VDAs	Vascular disruptive agents
VEGF	Vascular endothelial growth factor
WB-MRI	Whole-body magnetic resonance imaging

5.1 Introduction

Over the last decade, the molecular and genetic causes underlying cancer development have been unraveled through major advances in genomics, proteomics, and metabolomics. It is now clear that "tumorigenesis" is a complex, multistep, multipath process that is many years in the making. Genetic content and tumor microenvironment determine the appearance of key features expressed by the malignant tumor phenotype [1, 2]. The major characteristics of cancer are caused by deregulation of cell control pathways, such as uncontrolled proliferation via sustained proliferative signaling, evading growth suppressors, resisting cell death and enabled replicative immortality together with sustained angiogenesis, and activating invasion and metastasis formation. Underlying these hallmarks is genome instability, which generates the genetic diversity that facilitates their acquisition and inflammation, which promotes the development of multiple hallmark functions [1, 2].

Advances in our understanding of cancer hallmarks have created great expectations on translating these discoveries into effective treatments for patients. The central pillars of cancer therapy have historically been surgery, radiotherapy, chemotherapy, and hormonal manipulations; but recently there has been an emergence of a wide range of novel oncologic therapies (NOTs) including drugs designed to target and disrupt specific biological pathways such as antiangiogenic drugs; vascular disruptive agents; drugs interfering with tumor cell surface growth signalling (EGFR-Her2 or KIT receptors); drugs affecting pathways mediating downstream effects of EGFR, ALK, and c-KIT (PI3K/Akt/mTOR and RAS-RAF-MAPK pathways); novel hormonal therapies (HT); immunotherapy (IT); advanced forms of radiation therapy (stereotactic radiation therapy); and interventional techniques (such as embolization or ablation) [3–7].

Currently, imaging influences every step of routine cancer patient care; and developments in functional and molecular imaging (FMI) capabilities have further transformed our perceptions of the expressed cancer phenotype. FMI techniques, such as positron emission tomography (PET), dynamic contrast medium-enhanced MRI (DCE-MRI) and CT (DCE-CT), diffusion-weighted MRI (DW-MRI), and magnetic resonance spectroscopic imaging (MRSI), are important tools for the assessment of tumor hallmarks providing quantitative biomarkers for the noninvasive assessment for tumors in vivo [6–13]. Imaging approaches probing physiological and molecular processes complement detailed structural imaging information. In this chapter, we describe the role of clinically available FMI techniques in the evaluation of novel therapy approaches.

5.2 Cancer Hallmarks and New Oncologic Therapies

Preclinical discoveries had changed our understanding of key biological processes that are altered in tumors including angiogenesis, metabolism, proliferation, and invasiveness [1]. Translating improved understanding in cancer genetic changes to new therapies has opened up the possibility of high-precision/personalized cancer therapy based on tumor genotype-specific features. This new therapeutic approach has been shown to be successful with clinical approval by regulatory authorities for a number of new drugs such as imatinib, directed against breakpoint cluster region-abelson (BCR-ABL) for chronic myeloid leukemia (CML) or against mutant c-KIT for gastrointestinal stromal tumor (GIST), erlotinib and gefitinib directed against mutant epidermal growth factor receptor (EGFR) for non-small cell lung cancer (NSCLC), crizotinib directed against echinoderm microtubule-associated protein like 4-anaplastic lymphoma

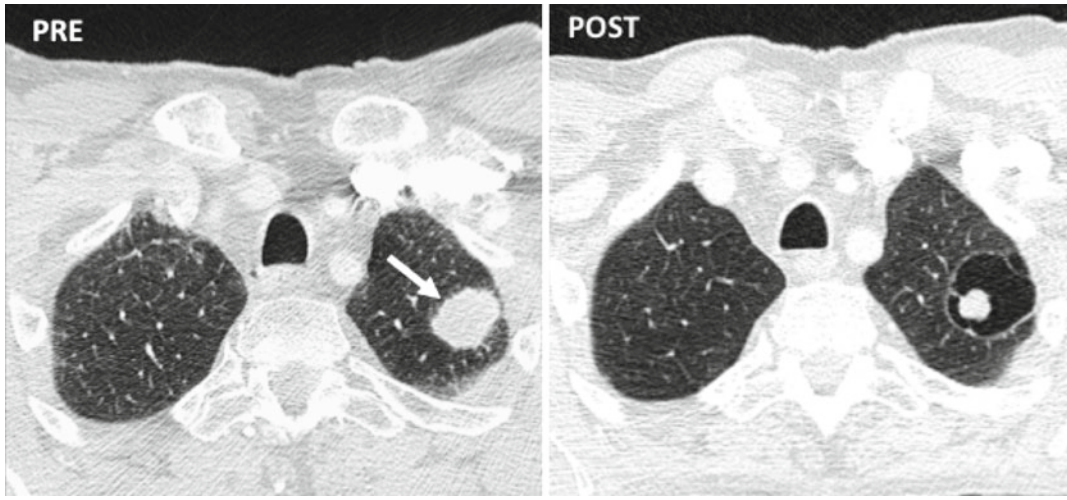

Fig. 5.1 Lung carcinoma in a 53-year-old man treated with VEGFR agent combined with platinum-based chemotherapy. New therapies may induce central necrosis and cavity formation. Tumor response assessment would change if one took into account loss of tumor volume as a result of cavitation because RECIST does not capture this feature. Pre-therapy CT shows a lung mass in the left upper lobe (*arrow*). Post-therapy CT images demonstrate extensive cavitation

kinase (EML4-ALK) for NSCLC, polyADP-ribose polymerase (PARP) inhibitors in breast and ovarian cancers, and vemurafenib directed against mutant B-type Raf kinase (BRAF) for melanoma [3, 6].

For the successful development and clinical deployment of NOTs, it is increasingly important to develop imaging techniques that improve decision making when using and evaluating these therapies. Understanding the relationship between tumor hallmarks, therapy effects and imaging findings is essential to demonstrate clinical effectiveness of novel therapeutic approaches (Fig. 5.1). Specifically FMI techniques will increasingly be used because they are able to depict time-varying alternations in tumor physiology, biochemistry, and microenvironment in response to therapy [6–13].

5.2.1 Tumor Angiogenesis

Neoangiogenesis, the formation of new blood vessels, is a critical event in tumor growth [14]. Angiogenesis is a multistep process regulated by pro- and antiangiogenic factors. In cancer, genetic mutations, inflammatory processes, and hypoxia are able to tilt and sustain the angiogenic balance towards a pro-angiogenic form [14–16]. Angiogenesis is initiated when cells experience low oxygen tensions and develop adaptive responses mediated by the hypoxia-inducible factor-1a (HIF-1a), which activates the expression of vascular endothelial growth factor (VEGF), the key central mediator of tumor angiogenesis. Upregulation of VEGF pathways has been shown in many different tumors [14–17]. Other angiogenic activators such as placental growth factor (PlGF), fibroblast growth factor (FGF), hepatocyte growth factor (HGF), and matrix metalloproteinases also facilitate the tumor angiogenic process.

Tumor angiogenesis is sustained and uncontrolled and lacks remodelling, ultimately resulting in the development of a heterogeneous and disorganized network of tortuous and dilated vessels with characteristically show increased microvessel permeability. Tumor microvessel hyperpermeability to macromolecules is a direct contributor to raised hydrostatic interstitial fluid pressure which itself acts as a barrier to successful therapy [18].

Structural microvessel abnormalities also exacerbate the already precarious oxygen supply to tumors causing further tumor hypoxia [14–19]. Tumors attempt to overcome oxygen deficiency by further overexpressing pro-angiogenic factors

thus creating a vicious feedback cycle of hypoxia-abnormal angiogenesis. This abnormal cycling via HIF-1a also promotes the development an aggressive tumor phenotype prone to spread via metastasis pathways [2].

Tumor angiogenesis is a proven target for anticancer therapy (ACT). In this setting, two distinct approaches for antiangiogenesis therapy (AAT) in tumors have emerged: inhibition of growth factors/signalling pathways necessary for endothelial cells growth and proliferation and therapies that directly target the established tumor vasculature. In the latter group, we can include vascular disruptive agents (VDAs) but also radiotherapy. Antiangiogenic target therapies act via the inhibition of angiogenesis often mediated by VEGF-action blockade. In the short term, they may also act through vascular normalization, which results in reduction in interstitial fluid pressure and temporary improved tumor oxygenation. VDAs selectively target endothelial cells and pericytes of the tumor vasculature [18] producing an acute vascular shutdown and tumor necrosis but have not yet been approved for clinical use [6, 7, 16–21]. Radiation-induced tumor cell death is usually attributed to DNA damage to tumor cells, thus triggering cell death by apoptosis and/or necrosis. However, radiation may also cause damage to endothelial cells. Stereotactic radiotherapy (SRT), which maximizes radiation dose/fraction, can lead to rapid endothelial apoptosis and to the obliteration of the tumor vasculature [21].

5.2.2 Tumor Metabolism and Proliferation

Different intracellular pathways are involved in tumor proliferation and metabolic activity regulation. The majority of human epithelial cancers are noted for upregulation of cell surface receptors capable of activation by growth factors including those of the epidermal growth factor receptor (EGFR) family, such as EGFR and HER2 [22, 23]. Given the importance of the EGFR pathway in cancer development, both anti-EGFR monoclonal antibodies and small-molecule EGFR tyrosine kinase receptor inhibitors (TKIs) have been developed. KIT receptor also plays critical oncogenic roles in a broad spectrum of hematologic and solid tumors controlling various cellular processes such as proliferation and differentiation, apoptosis, and metabolic tumor activity [24]. Imatinib mesylate inhibits KIT kinase activity and represents the front-line drug for the treatment of unresectable and advanced gastrointestinal stromal tumors (GISTs). Beside this, a variety of human malignancies have anaplastic lymphoma kinase (ALK) translocations. In lung cancers, the presence of a fusion gene, EML4-ALK, activates ALK overexpression, which contributes to increased cell proliferation and survival signalling via a number of intracellular pathways. Lung cancer cell lines harboring ALK gene rearrangements are sensitive to ALK inhibitor crizotinib [25, 26].

Different pathways mediate downstream effects of EGFR, ALK, or KIT pathways, including the phosphoinositide-3-kinase/Akt/mammalian target of rapamycin (mTOR) (PI3K/AKT/mTOR) pathway, which activates cellular survival signals [27], and the RAS-RAF-MAPK pathway [28] that affects cell proliferation, tumor invasion, and metastasis. Downstream pathways are also viable oncologic targets. Several drugs such as everolimus or temsirolimus specifically target the downstream signalling pathway PI3K/Akt/mTOR in renal carcinoma [27]. This strategy has merit for breast cancer also [29]. Beside this, approximately 40–60 % of malignant melanomas contain a BRAF mutation. The RAS family members act as critical mediators in cellular growth and survival. BRAF inhibitors have shown notable activity in patients with melanoma with BRAF gene mutations [28].

Hormonal therapy (HT) constitutes a different type of therapy for modulating tumor proliferation. Steroid hormone growth factors interact with nuclear receptors to activate the transcription of genes whose products stimulate the growth and viability of hormone-dependent malignancies [30, 31]. HT blocks the effects of hormones in tumors, mainly in breast cancer (BC) and in prostate tumors. A number of novel hormonal therapies have recently been introduced for the treatment of metastatic breast and prostate cancers including drugs targeting the

endogenous production of estrogen/testosterone and selective estrogen/androgen receptor degraders (SERDs/SARDs).

5.2.3 Tumor Invasiveness

The receptor tyrosine kinase MET and its ligand, hepatocyte growth factor (HGF), regulate multiple cellular processes that stimulate cell proliferation, invasion and angiogenesis. Abnormal MET activation and causes por clinical outcomes. Abnormal MET activation correlates with poor prognosis in patients with cancer. Thus, MET has emerged as an attractive target for cancer therapy. Several MET inhibitors have been introduced into the clinic [32]. Cabozantinib (XL184) is a small-molecule kinase inhibitor with potent activity towards MET and VEGF receptor 2. It is currently being evaluated in a number of tumor types with encouraging results in prostate cancer (PC) [33, 34].

5.2.4 Avoid Immune Surveillance

Tumor cells are able to evade immune recognition and suppress immune reactivity despite the fact that many tumors elicit a strong immune response [35]. Nevertheless, the immune system can respond to some types of tumors that display highly immunogenic cancer cell-related antigens. It is also possible to activate the immune system into an antitumor state [5]. Immunotherapy has been successfully introduced into the clinic for treatment of metastatic prostate and breast tumors, lymphoma, and melanoma.

5.3 Assessment of New Oncologic Therapies by Functional and Molecular Imaging

When considering therapy effects on tumors, there appear to be differences in imaging observations between therapies [6–13, 36–41]. In each case, imaging findings appear to depend on anatomic sites and on interactions between specific tissue microstructure and the mechanism of action of therapy given. Traditional oncologic therapies, such as chemotherapy or radiotherapy, do not selectively attack malignant cells, but affect proliferating cells regardless of their malignant status. These therapies cause cellular lysis often via necrosis or apoptotic mechanisms. Tumor cell loss will lead to difference changes depending on the imaging technique applied. On DW-MRI, cellular lysis results in increased water diffusion, which increases apparent diffusion coefficient (ADC) values [36–38]. Chemotherapy and radiotherapy have also been shown to have an indirect antivascular effect via tumor cell killing and subsequent withdrawal of angiogenic cytokines; the latter is needed as a survival factor for immature vessels. On DCE imaging, a favorable tumor response to chemotherapy results in decreases in the rate and magnitude of enhancement for a number of tumor types [38, 39]. Such decreases in DCE-MRI kinetic parameters may be delayed after radiation therapy when an initial hyperemic response is often seen [42]. Concomitantly, FDG-PET shows reductions in glucose metabolism activity of tumors in response to therapy [40]. Applying this knowledge to novel biologic targeted drugs, hormonal therapy, advanced forms of radiation therapy, and interventional techniques, such as embolization or ablation, is not always straightforward. These aspects are considered more fully below.

5.3.1 Antiangiogenic and Antivascular Therapies

The structure and function of tumor vasculature is distinct compared to normal vessels. Malignant tumors show vessels with spatial heterogeneity, chaotic structure, and increased perfusion, capillary permeability to macromolecules, and volume of extravascular-extracellular space [41]. These abnormalities of new tumor vessels permit distinction of malignant vascularity from benign vascularity using FI techniques. In clinical practice, indirect measurements of angiogenesis can be performed noninvasively using different imaging techniques, including dynamic

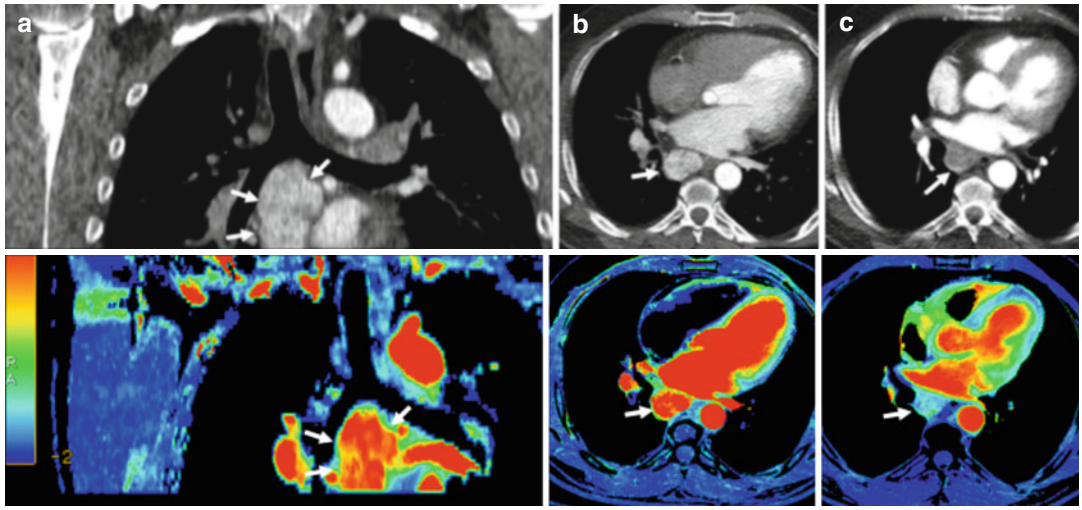

Fig. 5.2 Renal carcinoma with metastatic mediastinal lymph nodes treated with an anti-VEGFR agent. Pretherapy coronal (**a**) and axial (**b**) reformatted conventional CT images (*top row*) and perfusion blood volume (BV) parametric maps (*bottom row*) show a conglomerate of hypervascular metastatic nodes in the subcarinal area (*arrows*). Perfusion BV parametric maps show high BV suggesting intense active angiogenesis. Functional map evidences a mean BV value = 43.9 mil/100 g. (**c**) Posttherapy with an anti-VEGFR agent (**c**), axial CT image and perfusion BV parametric map show early angiogenic tumor response with marked decrease in tumor enhancement and BV value (*arrows*). Functional map evidences a mean BV value = 10.2 mil/100 g

contrast-enhanced MRI (DCE-MRI), dynamic susceptibility-enhanced MRI (DSC-MRI), diffusion MRI (intravoxel incoherent motion), PET with oxygen-labeled water, perfusion CT (PCT), and dynamic microbubble-enhanced ultrasound; but DCE imaging with CT and MRI seems to be the most useful clinical tools [39, 41, 43–46]. DCE techniques are based on the acquisition of serial images through a region of interest before, during, and after the intravenous injection of a contrast agent. DCE images can be analyzed by quantitative model-dependent or semiquantitative (non-model-dependent) means to obtain different functional parameters, which can be related to vascular properties: blood flow (BF), blood volume (BV), microvessel permeability, extraction fraction, and plasma and interstitial volumes [38, 39, 44, 45] (Fig. 5.2a–c). Data acquisition and analysis are comparable despite inherent differences between imaging techniques in signal production and mechanism of tissue contrast enhancement [47].

DCE parameters allow the monitoring of changes in tumor vascularity. Many of the calculated kinetic parameters have physiological significance, are repeatable, and have clear clinical uses in diagnosis, guiding therapy, predicting patient outcome, and evaluating response to different therapies [6, 39, 43–45]. The effects of antiangiogenic drugs and VDAs on DCE kinetic parameters have been found to be similar with the dominant effect of successful therapy being reductions in BF and permeability. However, there are clear differences in the timing of the onset and duration of vascular changes. The effects of AAT are not immediate, arising at least 1–2 days post-drug administration. On the other hand, VDAs cause rapid shutdown of the vasculature within minutes to hours of drug administration, and reversibility of effects can be visible in the short term (24–48 h) [6, 39, 43, 48]. The vascular pruning of "normalization" induced by AAT can be detected on DCE by a combination of findings including reductions in vascular permeability and leakage space and regional increases in BF [18, 19, 49].

There is a clear need to establish thresholds for change that can be considered as significant for change and response. For example, in DCE-MRI, a reduction in transfer constant (K^{trans})

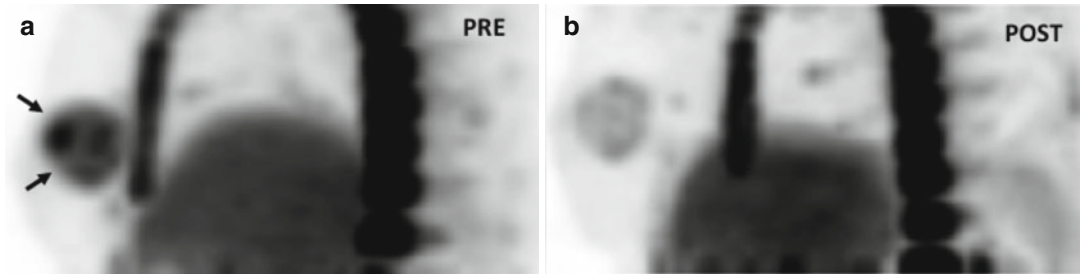

Fig. 5.3 FLT-PET in a patient with HER-2-positive locally advanced breast cancer treated with chemotherapy and anti-EGFR agent. Pre-therapy (**a**). Sagittal FLT-PET image shows an increased uptake in the breast (*arrows*) corresponding to tumor involvement. SUV max = 5.6. Post-therapy (**b**). Sagittal FLT-PET image 9 days post-therapy shows early decreased FLT uptake in the breast. SUV max = 2.5 (Courtesy of JA Richter, MD, PhD. Department of Nuclear Medicine, Clínica Universitaria de Navarra, Pamplona, Spain)

of >40 % is usually considered a true difference caused by drug effect [50], while Petralia et al. [51] evidenced using PCT that decreases between scans of patients with hepatocellular carcinoma of more than 35 % for BF and 43 % for BV, or an increase of more than 55 % for mean transit time, could be considered beyond the analysis variability. Such thresholds often seem to depend on anatomic regions being evaluated but also on imaging acquisition parameters and on analysis [52]. It should be remembered that thresholds for true changes are not necessarily the same as thresholds for change that result in clinically significant alterations in tumor vasculature when in generally larger reductions in vascular kinetic parameters are needed. Finally, there has been an emerging interest in the development of imaging biomarkers for identifying patients who will likely respond favorably to inhibition of angiogenesis. However, no validated imaging biomarker signature has yet emerged [53, 54]. What is known is that the greater the magnitude of enhancement, the greater is the change following AAT. However, the latter observation has not translated into a predictive imaging biomarker of AAT [55].

DW-MRI may also; evaluate AAT directed towards VEGF pathway. These agents cause reductions in tumor ADC values, secondary to antivascular effects (reducted tissue perfusion) and via reductions of the extravascular-extracellular space secondary to vascular normalization and the lowering of vascular permeability. Reductions of ADC values due to reduction of tissue perfusion are not always notable using antiangiogenic and antivascular therapies. On the contrary, succesful treatment with AVT increases ADC values can be detected, particularly when causes significant tumor necrosis [37, 38]. PET has also been used to evaluate the effects of AAT. There seem to be no systematic effects on FDG uptake [41, 56]. However, AAT induces tumor hypoxia, which causes increased HIF-1a levels. HIF produces an upregulation of cell membrane glucose transporters and secondary increases in FDG uptake by tumors. Finally, direct PET-perfusion measurements of BV and BF or direct PET imaging of angiogenesis may allow a specific PET evaluation of angiogenesis in the clinic [41].

5.3.2 Target Therapies Blocking Tumor Proliferation

FDG-PET has demonstrated efficacy in the assessment of tumor response to anti-EGFR/HER-2 drugs [57–59]. However, tumor proliferation changes may be directly evaluated using ^{18}F-3-deoxy-3-fluorothymidine (FLT)-PET (Fig. 5.3a, b). This thymidine analogue is retained within cells by thymidine kinase 1 (TK1); the latter is specifically active during DNA synthesis. Intracellular trapping of ^{18}F-FLT that presumably gives a measure of the TK1 activity is increased in malignant cells and correlated with cellular proliferation [58, 59]. In

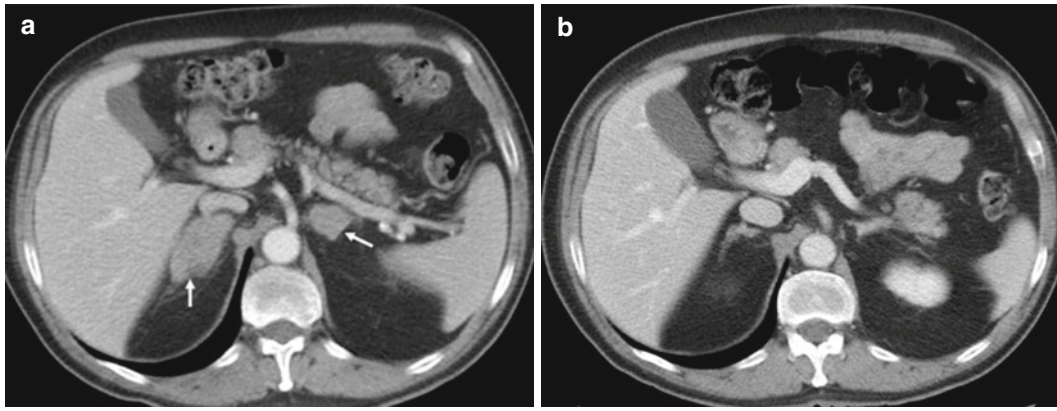

Fig. 5.4 (**a**) Non-small cell lung carcinoma with adrenal metastases in a 53-year-old man treated with an ALK inhibitor. Pre-therapy (**a**). CT image shows bilateral adrenal metastatic deposits (*arrows*). Post-therapy (**b**). CT image shows a marked response with almost complete resolution of the adrenal masses

this setting, preclinical observations have found that FLT-PET but not FDG-PET imaging may be a robust early indicator of erlotinib response in EGFR-dependent tumor models [60, 61]. However, on the contrary, different studies found that a marked decrease in FDG uptake preceded changes in FLT uptake and cell death in gefitinib-sensitive cell lines [62] and that the results of FDG scans were more informative than FLT scans in NSLC patients [63]. A practical limitation for using FLT in NSCLC patients is that FLT has relatively low uptake compared with FDG in many lesions [63]. It is anticipated that direct PET imaging of EGFR/HER2 expression and activity will eventually be able to predict which patients will likely respond to therapy and monitor tumor response [64].

There is very limited evaluation of EGFR inhibitors with perfusion techniques [6, 39]. DCE-MRI did not show a significant change in quantitative parameters in patients with advanced colorectal cancer treated with vandetanib (an inhibitor of VEGFR, EGFR, and RET signalling pathways) [65] or with nasopharyngeal cancer treated with combined therapy including cetuximab [66]. There are no published reports on the DW-MRI evaluation of anti-EGFR/HER-2 agents. It seems rational to expect increases in ADC values with therapies that cause cell death [37, 38]; however, the magnitude of ADC increases will depend on the mechanism of cell death (necrotic versus apoptotic) and whether there is an inflammatory response to tumor cell kill.

5.3.2.1 Anti-ALK Drugs

Genetic alterations of ALK are associated with a number of cancers, including anaplastic large cell lymphoma (ALCL) and a subset of NSCLC (Fig. 5.4a, b). Small-molecule inhibitors of ALK kinase activity have been developed in the recent years, and crizotinib (combined c-MET and ALK inhibitor) has been clinically approved [25, 67]. There are scarce reports in the literature of the use of FMI in ALK-positive tumors, which suggest the possible role of FDG-PET for detecting response to crizotinib [26, 68].

5.3.2.2 Drugs Inhibiting c-KIT Pathway

Drugs targeting c-KIT pathway has been mainly focused in GISTs treated with imatinib. FDG-PET has a significant value in assessing treatment response to imatinib in GIST patients with dramatic decreases in glucose metabolism in responder patients. FDG-PET allows an early assessment of treatment response and is a strong predictor of clinical outcome [69] (Fig. 5.5). Further evaluation of new candidate markers of treatment response, such as quantitative perfusion or DW-MRI, may be the key for optimized

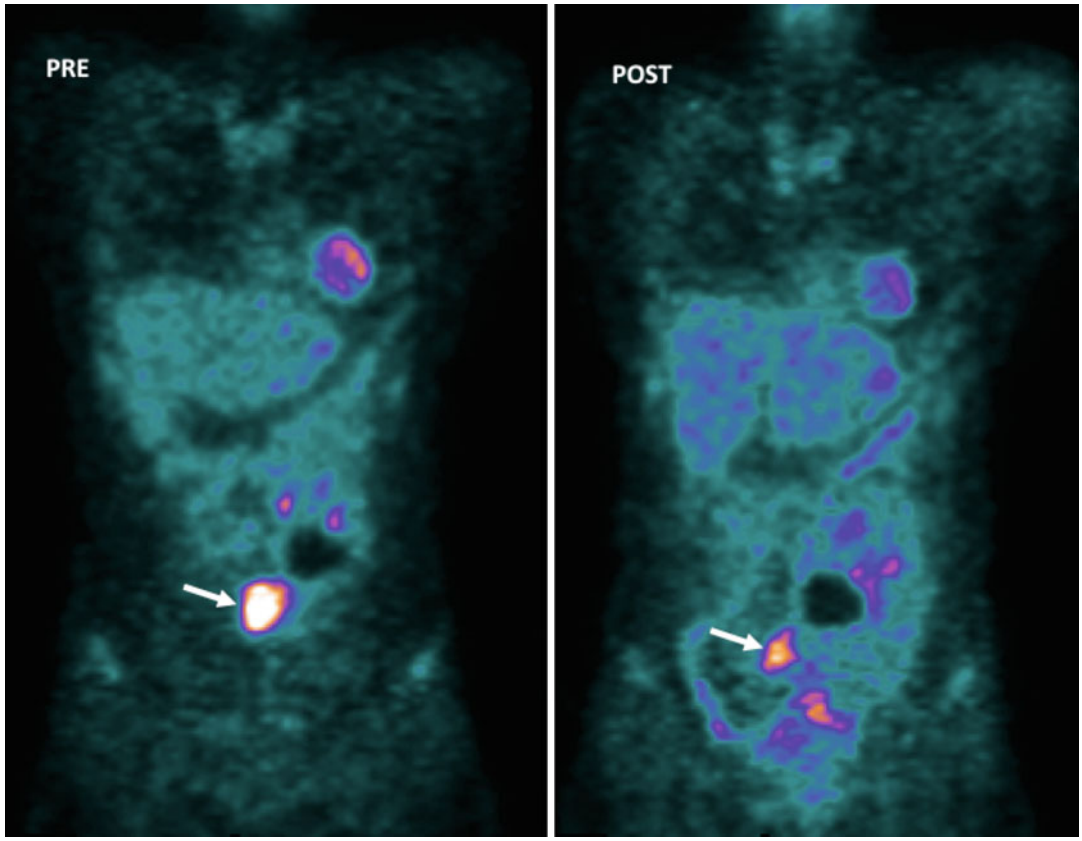

Fig. 5.5 GISTs in a 53-year-old woman. Pre-therapy. Coronal MIP FDG-PET image (*left*) shows an FDG-avid mass (*arrow*). PET image obtained 72 h after therapy with imatinib mesylate shows an early partial response with a decrease in tumor uptake (*arrow-right*)

monitoring of targeted therapies in GIST. In this setting, preliminary results show that DW-MRI may predict tumor response. A low pre-therapy ADC and marked ADC increase at 1 week after therapy is associated with good response [70].

5.3.2.3 Pathways Mediating Downstream Effects of EGFR, ALK, and c-KIT

PI3K/Akt/mTOR Pathway

PI3K/Akt/mTOR pathway is a commonly used pipeline for many growth stimuli and regulates key tumor processes by promoting protein synthesis, glucose metabolism, cellular migration, cell survival, and angiogenesis [27]. PI3K/Akt/mTOR pathway inhibitors include rapamycin and its analogues (everolimus and temsirolimus), which target a distal pathway component, mTOR. FDG-PET studies show decreases in metabolic activity and tumor proliferation with mTOR inhibitors [71–73]. mTOR signalling plays a specific role in the control of angiogenic pathways in renal cancer. mTOR inhibitors act by reducing the levels of HIF-1a. However, HIF-2 alpha is most active in the subtype of clear cell cancers, explaining the limited response of these tumors to mTOR inhibitors [74].

RAS-RAF-MAPK

The BRAF proto-oncogene activates RAF/MEK/ERK signaling, a major driver of carcinogenesis in various malignancies, most notably in melanoma [28]. The BRAF inhibitor, vemurafenib, has been approved for the treatment of metastatic melanoma in patients harboring

$BRAF^{V600}$ mutations. Tumors containing RAS mutations displayed enhanced FDG uptake, and vemurafenib reduces FDG uptake in tumors with $BRAF^{V600}$ mutation that are successfully treated. On the other hand, FDG may predict acquired drug resistance. An increase in FDG uptake observed of a specific lesion in a patient on vemurafenib treatment suggests the development of drug resistance [75, 76].

5.3.3 Drugs Inhibiting Tumor Invasiveness: The MET Pathway

There is a limited experience evaluating the HGF/MET pathway using FMI. However, although FLT-PET is not a direct measure of MET activity itself, preliminary results suggest the possibility of FLT-PET as a clinical biomarker for monitoring tumor response to MET inhibition with crizotinib [77]. On the contrary, no significant change in DCE-MRI parameters was observed after 7 days of tivantinib treatment [78]. Recently, it has been noted that metastatic PC patients treated with the c-MET inhibitor XL-184 (cabozantinib) show dramatic decreases in bone scan agent technetium-99m-methylene diphosphonate. It is not clear why such dramatic changes in technetium uptake in the majority of patients is accompanied by only a littel proportion of patients responding clinically to therapy [34]. However, a possible explanation could be based on the overexpression of MET within bone osteoblasts and osteoclasts, which action could be inhibited by cabozantinib. Skeletal uptake of technetium-99m occurs as a function of skeletal osteogenic activity, being consequently affected by cabozantinib. This observation serves as a reminder that changes seen on FMI may represent bystander effects on adjacent tissue within or beside tumor masses and should not only be ascribed to antitumor targeting action.

5.3.4 Hormonal Therapy

Steroid hormones play important roles in hormone-receptor-positive BC and PC due to their effects on cell growth, differentiation, and function. These hormone effects are mediated via activation of cell surface receptors, which are often upregulated. Hormonal therapy (HT) represents a powerful therapeutic option in hormone-receptor-positive breast and prostate cancers (Fig. 5.6). Androgen deprivation therapy (ADT) has shown antivascular and metabolic effects in PC. HT reduces perfusion and permeability of both malignant tumors and normal prostate gland within a month after starting therapy [79, 80]. Metabolic glandular atrophy reduces citrate peaks in tumor and in normal glandular tissues, but there is only slow loss of choline and creatine in tumor foci on H-MRSI [80]. These data seem to be contradicted by Røe et al. [81] who showed an increased tumor vascularization after ADT. Initial data using DW-MRI evaluation in PC treated with HT suggests minimum change in ADC values, although there is limited experience in this field [80, 82].

Metastatic BC and PC frequently remain confined to the skeleton. In these tumors, metastatic disease is often first treated with HT. FDG-PET shows only a limited value in evaluating bone response in metastatic PC, because osteoblastic bone lesions only show low FDG uptake [83]. However, FDG-PET scans tend to be positive in higher-grade disease, and baseline specific uptake values (SUV) do correlate with prognosis in some tumor types. In BC, tamoxifen and aromatase inhibitors demonstrated a paradoxical increases in tumor FDG uptake at early time points after treatment in some patients, the so-called metabolic flare. FDG metabolic flare has been correlated with positive tumor response to HT in BC and if observed is associated with better overall survival [84].

A number of tumor-specific PET tracers have been evaluated for their ability to predict and monitor bony therapy response, including ^{18}F-FES (fluoroestradiol) for BC and ^{18}F-FDHT (fluorodihydrotestosterone) for PC [85]. These ligands report on tumor cell expression of estrogen and androgen receptors. ^{18}F-DHT uptakes have been correlated with androgen receptor (AR) expression levels in castrate-resistant prostate cancer, and it has been noted that spatial distribution of ^{18}F-DHT is often different to that of ^{18}FDG scans.

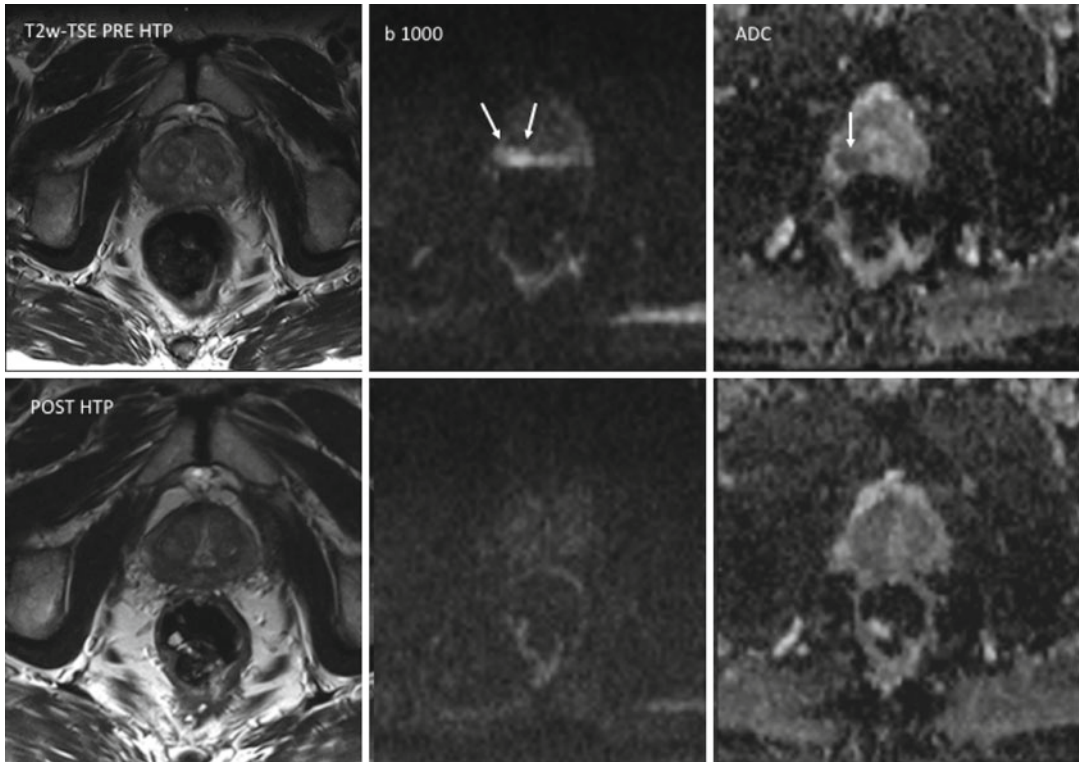

Fig. 5.6 Prostate cancer in a 72-year-old man. T2-weighted TSE, b1000 diffusion-weighted imaging (DWI), and ADC map obtained pre-therapy (*top row*) and before hormonal therapy (HTP) (*bottom row*). Images show a focal area in the right peripheral zone with increased signal on b1000 DWI and low ADC values (mean, 0.83 × 10–3 mm^2/s) (*arrows*). ADC maps obtained 3 months after hormonal therapy (*bottom row*) show increased ADC values (mean, 1.32 × 10–3 mm^2/s) in the same area. The tumor is not depicted on b1000 DWI

As a result, different imaging phenotypes are recognizable at the patient and lesion level (AR predominant, glycolysis predominant, and AR/glycolysis concordant). This differential expression related to the total tumor burden maybe a predictive biomarker for response to novel therapeutics targeting these receptors and their intracellular pathways (SERDs/SARDs).

The effect of hormonal on metastatic bone disease in BC and PC patients is incompletely described. In our experience, decreases in bone marrow disease signal intensity on high-b-value images are generally observed with successful treatments. Effective tumor cell death should result in greater water diffusivity manifested as higher ADC values [36–38, 86, 87]. However, the extent of ADC increases seems to depend on the type of treatment given with greater ADC increases for cytotoxic chemotherapy and radiation. These treatments cause tumor cell death via a number of mechanisms (apoptosis, necrosis, mitotic catastrophe, autophagy, and senescence), many of which lead to tumor necrosis with an inflammatory component [36–38, 86, 87]. When patients are treated successfully with HTs, ADC value increases seem to be less marked possibly because cell death is less likely to be associated with inflammation [87].

5.3.5 Immunotherapy

Ipilimumab, an anti-CTLA-4-blocking antibody, is licensed for the treatment of melanoma (Fig. 5.7) and is currently undergoing trials for the treatment of lung cancer and castrate-resistant PC. Therapy assessment of soft tissue disease using this treatment is problematic because initial increases in tumor burden or the appearance of new lesions can be seen. That is, RECIST criteria

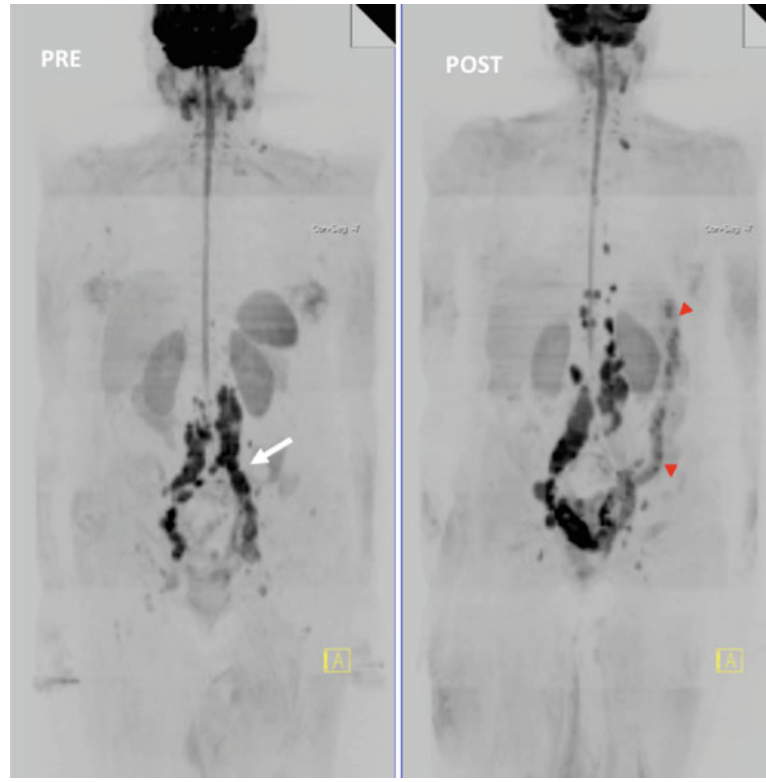

Fig. 5.7 Whole-body MRI (WB-MRI) tumor evaluation in a 68-year-old female with melanoma treated with ipilimumab. WB-MRI images pre (*left*)- and post (*right*)-administration of ipilimumab. Note background bone marrow atrophy. Post-therapy exam evidenced disease progression (nodes are bigger and more regions are involved) but left common iliac region (*white arrow*) responded. The patient also had colitis (*red arrowheads*). The anti-CTLA4 antibody, ipilimumab, may cause severe side effects. Diarrhea due to immune-related colitis is the most frequent serious toxicity and, if untreated, may lead to intestinal perforation

cannot be readily applied for therapy assessments. Novel criteria for the evaluation of antitumor responses with immunotherapeutic agents are required. New morphologic criteria have recently been suggested [88], but these remain unsatisfactory for clinical use at the individual patient level.

The role of FMI techniques to monitor the therapy effects of immunotherapy (IT) is limited. FDG-PET findings may be confusing, because both activated immune cells and cancer cells show increased glucose analogue uptake. Beside this, IT may produce different immune-mediated toxicities that may mimic malignancy. For example, ipilimumab may produce FDG-avid uptake secondary to immune-mediated toxicities such as colitis [89]. To address these PET limitations, novel PET radiotracers and other techniques that can demonstrate and quantify antigens, receptors, and enzymes specifically expressed by immune cells are under development [90, 91]. Their clinical applicability is unlikely to be forthcoming in the near term.

In past, interferon has been a standard-of-care therapy for metastatic renal cancer. However, interferon showed a relatively weak antiangiogenic effect in clinical practice with any significant association between changes in tumor perfusion and progression-free survival in these patients [92]. Thalidomide also modulates immune responses which also causes potent inhibition of angiogenesis. Faria et al. [93] showed that decreases in BF in CT perfusion in renal cancer were significantly associated with clinical benefit.

Caution is mandatory in the evaluation of cancer patients when the granulocyte colony-stimulating factor (G-CSF) is used to moderate the degree of neutropenia occurring because of chemotherapy. This therapy stimulates the BM to produce granulocytes and stem cells and also stimulates the proliferation and function of neutrophils (a part of the immune system). G-CSF increases BM cellularity and causes increased BM signal intensity on high-b-value diffusion-weighted images (Fig. 5.8). This

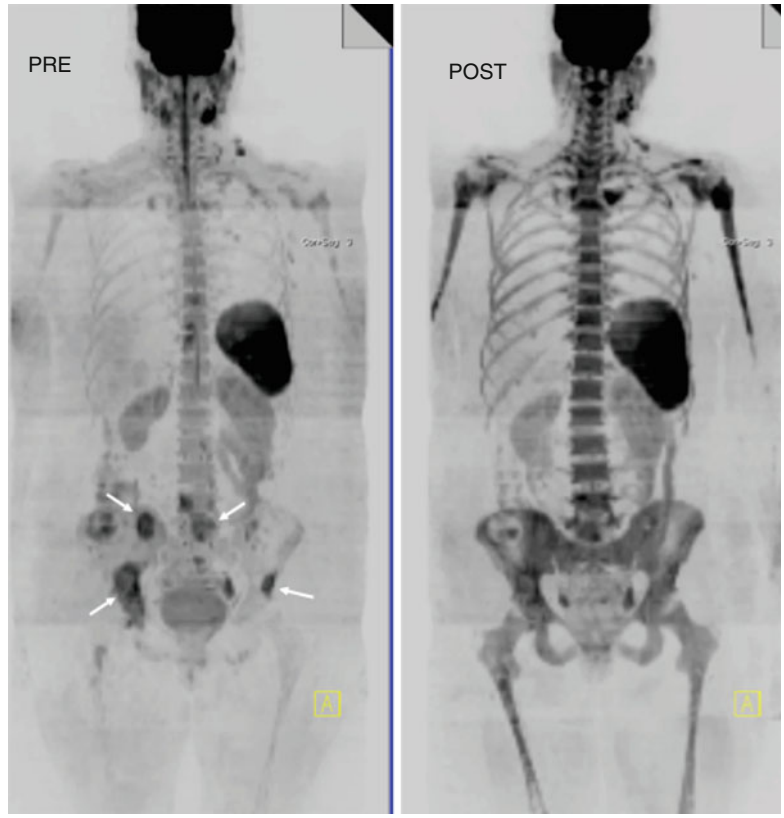

Fig. 5.8 Bone marrow hyperplasia induced by chemotherapy with G-CSF therapy. Whole-body MRI (WB-MRI) images in a 50-year-old woman with metastatic breast cancer before and after 3 cycles of chemotherapy and granulocyte colony stimulating factor (G-CSF) given to prevent neutropenia. Inverted grey-scale 3D-maximum intensity projection WB-MRI (b900) images pre- and post-G-CSF. *Left image* shows multiple bone metastases (some of them marked with *arrows*). *Right image* after 3 cycles of chemotherapy shows increases in signal intensity of the bone marrow leading to the decreased visibility of the bone metastases. The splenic size has also increased. The increased signal intensity of the background bone marrow should not be misinterpreted as malignant progression

phenomenon is observed in normal adult red-marrow areas (spine, vertebrae, pelvis, sternum, ribs) and in areas with reconversion of yellow marrow to red marrow (proximal limb bones) [37]. This finding may be confused to disease progression on WB-DWI. In order to avoid this problem, signal intensity changes should be correlated with ADC values and with appearances on other MR imaging sequences.

5.3.6 New Radiation Therapy Techniques

A number of preclinical and a few clinical studies have evaluated the effects of external beam radiation therapy with DCE-MRI and DW-MRI. Initial increases in rate and magnitude of enhancement corresponding to the recognized acute hyperemic response mediated via release of cytokines including VEGF are well documented in the DCE literature. However, RT causes necrosis or cellular lysis, which leads to late decreases in the rate and magnitude of enhancement. New radiation techniques such as SRT deliver very high individual doses of radiation to ablate small, well-defined tumors. With this technique, there are also hyperacute hyperemic, but rapid decreases in kinetic parameters secondary to acute vascular collapse have been shown by DCE-CT [94, 95].

Preclinical studies show that ADC increases occur rapidly in tumors that are radiosensitive, with changes visible as early as 24–72 h after a single large fraction of radiation [96]. Such increases in ADC values are not seen in squamous cell cancer, which are relatively radioresistant unless concomitant chemotherapy is given [97]. Increases in ADC values appear to occur incrementally in fractionated regimens with the greatest increases visible at the end of therapy [98]. These increases seem to be related to two

different features: tumor cell death and tissue edema secondary to inflammation and increased microvessel leakiness. Early increases in ADC values (1–3 weeks) have also been noted for squamous cell head and neck cancers, brain gliomas, locally advanced rectal cancer, and uterine cervical cancers treated with CRT [99–101]. In fact, a number of clinical studies have shown that the failure of tumor ADC values to increase in response to radiation or CRT results in a poorer response to therapy [99, 102]. At present, the temporal evolution of changes in ADC in response to CRT has not yet firmly established.

5.3.7 Interventional Techniques

There are relatively few studies evaluating with FMI the effects of radiofrequency ablation (RFA) on tumors and surrounding tissues. An animal study showed modest increases in ADC values and reductions in glucose uptake 2–3 days after therapy. Ablated areas did show heterogeneous appearances on ADC maps reflecting treatment effects, such as interstitial edema, hemorrhage, carbonization, necrosis, and fibrosis [37, 38]. Tumors treated with RFA show large decreases in FDG uptake in tumor bed and a persistent peripheral FDG uptake indicating inflammation. Perhaps, new imaging techniques such as perfusion CT may provide an opportunity for improved assessment of the post-therapy tumor bed [103].

The effects of high-intensity focused ultrasound (HIFU) have been investigated on uterine fibroids using contrast medium enhancement and DW-MRI. Initial reductions in ADC values within ablated tissues were observed in combination with decreasing contrast enhancement. At 6-month follow-up, areas of decreased contrast agent uptake persisted, but the signal intensity on DW images appeared heterogeneous within treated regions. Increasing ADC values were presumed to reflect cell loss and liquefactive necrosis [37, 38]. Transarterial chemoembolization (TACE) causes an early reduction of ADC values after therapy (within the first few hours), after which consistent rises in ADC values occur, coinciding with the development of cystic and necrotic changes [37, 38]. Kamel et al. [104] observed that reductions in the degree of enhancement were seen immediately on DCE-MRI images after chemoembolization and were sustained over the observation period. However, increases in ADC values became most apparent after 1–2 weeks but had returned to the baseline values by 4 weeks.

5.3.8 Development of New Therapeutic Agents in Cancer

Currently, many therapeutic agents are under development, including anti-hypoxia agents, proteasome inhibitors, agents that counteract tumor glycolysis, antiangiogenic therapy based on integrin αvβ3 inhibitors, or agents that target drug resistance. Among these, anti-hypoxia drugs and agents targeting drug resistance may represent the most attractive future oncologic therapies [105–108]. Hypoxia and intrinsic or acquired drug resistance are key obstacles to successful cancer treatment. However, there are limited data on in vivo imaging evaluation of these agents in clinical practice [107, 108]. Finally, proteasome inhibitors have a significant antiproliferative and proapoptotic activity on patients with multiple myeloma [109, 110]. Myeloma plasma cells synthesize large quantities of immunoglobulin. The buildup of excess protein triggers a number of downstream signal transduction cascades. Myeloma cells are reliant on protein handling pathways for their survival. Bortezomib targets the ubiquitin-proteasome pathway, which plays a critical role in important processes for tumor cell growth and survival. FMI techniques, such as whole-body magnetic resonance imaging (WB-MRI) or FDG-PET/CT, are increasingly used to evaluate multiple myeloma and to monitor therapeutic response (Fig. 5.9a, b) [111, 112].

5.4 New Perspectives

Imaging techniques that assess tumor hallmarks have gained credence for response assessment alongside standard response criteria with the emergence of novel therapies as promising strategies for

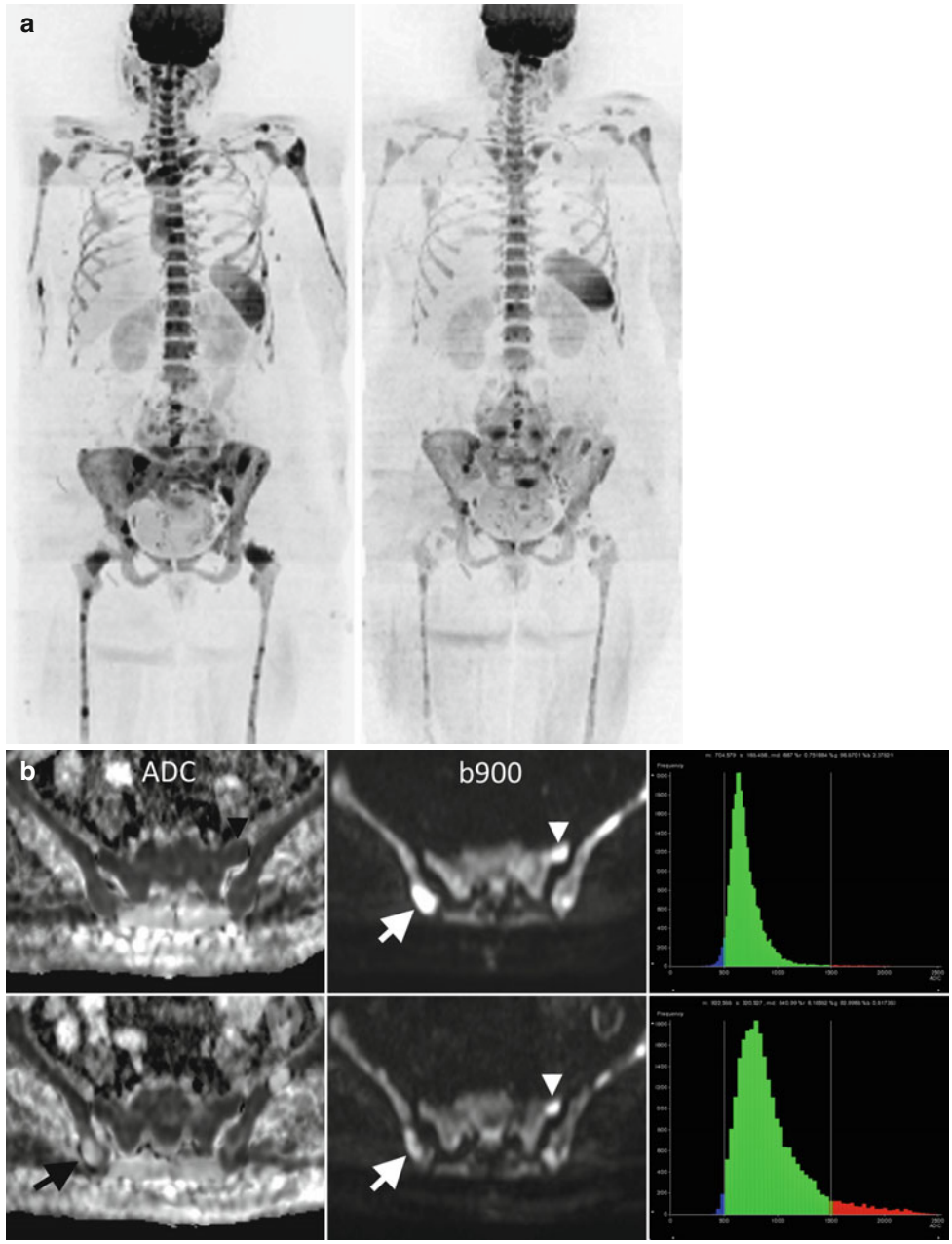

Fig. 5.9 Myeloma treated with proteasome inhibitors. A 46-year-old female with relapsed multiple myeloma. Imaging findings pre-therapy and post 3 cycles of chemotherapy (bortezomib, doxorubicin, and dexamethasone). (**a**) Diffusion-weighted b900 3D maximum intensity projection (MIP) images (inverted scale) show that there is a decrease in intensity in the background bone marrow signal and in the size and signal intensity of many focal lesions. However, many small focal lesions (both sides of the pelvis and in the proximal femora) have persistent high signal intensity consistent with an incomplete response to therapy. (**b**) Axial apparent diffusion coefficient (*ADC*) maps, b900 images, and ADC histograms before (*top row*) and after therapy. Many lesions show decreases in signal intensity on b900 images (*white arrows*) accompanied by increases in ADC values (*black arrow*) – these are responding lesions. Some lesions show no change in appearances (*arrow head*) indicating persistent active disease. ADC histograms of the whole pelvis volumen of interest prescribed on the pre-therapy scan applied to the posttreatment scan after image registration. There is some increase in the number of pixels with ADC values greater than 1,500 $\mu m^2/s$ (*red*), but the majority of pixels remain below. The patient ultimately relapsed with plasma cell leukemia

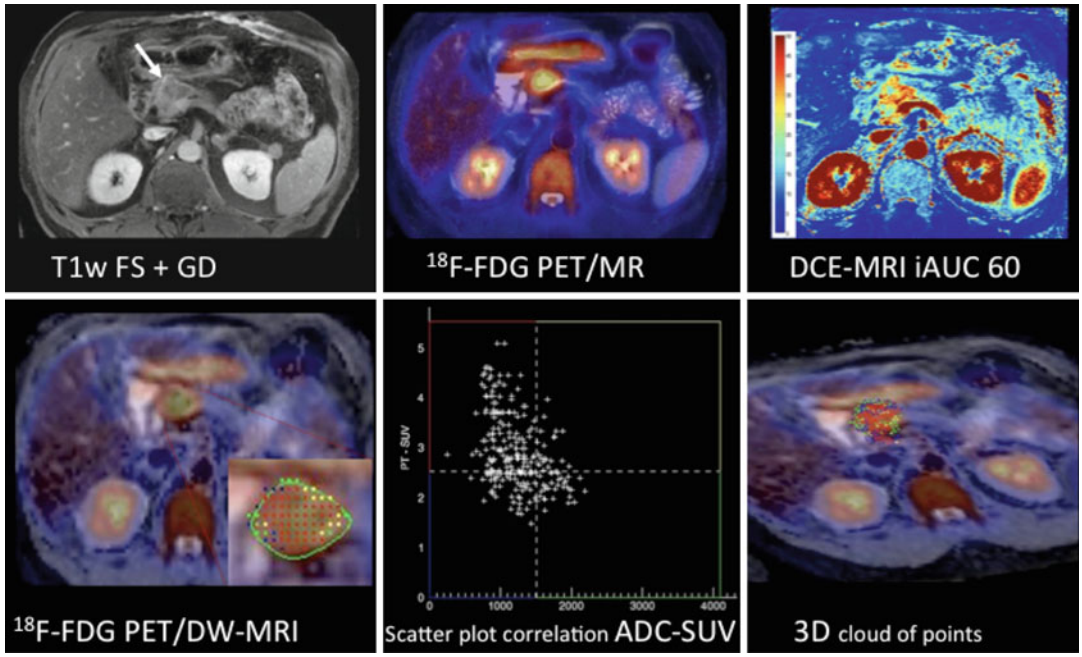

Fig. 5.10 PET/MR multiparametric tumor evaluation in a patient with pancreatic cancer (*arrow*). Contrast-enhanced T1-weighed fat-saturation, fused image superimposing axial contrast-enhanced T1-weighed fat-saturation MR image and ^{18}F-FDG-PET, DCE-MRI, and fused image superimposing ADC parametric map and ^{18}F-FDG-PET. PET/MRI evaluation shows high metabolic activity in the tumor, while in the DCE-MRI, high perfusion is mainly depicted at the tumor periphery. In the scatter plot for voxel-by-voxel analysis (Anima M3P) of different imaging signals (SUV and ADC), you can see a inverse correlation of SUV and ADC, with most areas in the tumor showing high FDG uptake and low ADC values (coded in *red*). A combined analysis has a synergistic effect and tells us more about tumor aggressiveness, patient prognosis, and tumor biology in general as compared to simple ROI analysis of single parameters individually (Courtesy of A Beer, MD, PhD. Department or Nuclear Medicine, Technische Universität München, Munich, Germany)

cancer treatment [6–13]. FMI has begun to mature technologically as shown by the numerous studies focused on technical optimization, reproducibility, validation, biological correlation, and clinical uses. FMI techniques may provide useful quantitative imaging parameters for tumor evaluation, including prognostic parameters that allow for a better patient stratification for therapy and tumor response assessment [113, 114]. But, in this role, there are several challenges that FMI needs to continue to address. We need imaging biomarkers to be able to identify patients who are likely to respond to a given therapy, as well as for measuring patient response to therapy. These two measures are necessary for selecting the right therapy for the right patient. There are several challenges to the widespread implementation of FMI techniques as cancer response biomarker [6, 113–115]. First, there is often a lack of standard approaches to data collection and analysis. Second, measurements of reproducibility are needed if one is to use quantitative FMI parameters for the assessment of therapy response. Biologic parameters are subject to random and systematic errors including the natural biologic variability of parameters, the variability inherent in the measuring instruments, and additional errors induced by appraisers or analysis techniques. Third, new user-friendly software tools for image analysis and data visualization are needed in order to be able to integrate/cross-correlate data analyses. Fourth, based on current data, the time course of changes in tumors secondary to therapy is yet to be fully defined for the entire range of therapies/therapy combinations. Finally, future studies that include good quality prospective validation correlating FMI parameters to outcome end points

in the trial setting are needed to take imaging forward as a biomarker in oncology. It must be understood that tumors are genetically and phenotypically heterogeneous, and they may vary in their responses to therapies. That is why multiplexed/multiparametric imaging evaluations will be needed to unravel the underlying biology [115] (Fig. 5.10). In this scenario, discordant results between techniques are likely to be biologically meaningful, representing the actual tumor phenotype. There is a real opportunity to advance multiparametric imaging with the emergence of new imaging technologies in both hardware (e.g., PET-MRI scanners) and software. These advances offer new opportunities for improving patient care towards increased precision and ultimately personalization.

Conclusion

In conclusion, our understanding of the complexity of cancer hallmarks, their evaluation using imaging, and their modification by NOTs is incomplete. The potential of FMI, which allows the visualization of fundamental biomolecular and cellular processes, remains unrealized. Much of the hope in "personalized medicine" in oncology is based on it. New FMI techniques offer insights into tumor hallmarks, and imaging features should allow us to answer key questions relating to prognosis, identification of therapeutic targets for selecting patients for a given therapy, individualized response assessments, definition of new response criteria, and early prediction of clinical outcome.

Disclosures Roberto García Figueiras: Nothing to disclose.
Anwar R Padhani
Consultant, F. Hoffmann-La Roche Ltd Consultant, IXICO Limited Advisory Board, Acuitus Medical Ltd Advisory Board, Bayer AG Advisory board, Siemens AG

References

1. Hanahan D, Weinberg RA. The hallmarks of cancer: the next generation. Cell. 2011;144(5):646–74.
2. Gillies RJ, et al. Evolutionary dynamics of carcinogenesis and why targeted therapy does not work. Nat Rev Cancer. 2012;12:487–93.
3. Nagahiro S. Present status and problems on molecular targeted therapy of cancer. Cancer Res Treat. 2012;44(1):1–10.
4. Ikushima H. Radiation therapy: state of the art and the future. J Med Invest. 2010;57(1–2):1–11.
5. Weiner LM. Cancer immunotherapy: the end game begins. N Engl J Med. 2008;358(25):2664–5.
6. Figueiras RG, et al. Novel oncologic drugs: what they do and how they affect images. Radiographics. 2011;31(7):2059–91.
7. Desar IM, et al. Beyond RECIST: molecular and functional imaging techniques for evaluation of response to targeted therapy. Cancer Treat Rev. 2009;35(4):309–21.
8. Gillies RJ, et al. The biology underlying molecular imaging in oncology: from genome to anatome and back again. Clin Radiol. 2010;65(7):517–21.
9. Marcus CD, et al. Imaging techniques to evaluate the response to treatment in oncology: current standards and perspectives. Crit Rev Oncol Hematol. 2009;72(3):217–38.
10. Stephen RN, Gillies RJ. Promise and progress for functional and molecular imaging of response to targeted therapies. Pharm Res. 2007;24(6):1172–85.
11. Pysz MA, et al. Molecular imaging: current status and emerging strategies. Clin Radiol. 2010;65(7):500–16.
12. Gallagher FA. An introduction to functional and molecular imaging with MRI. Clin Radiol. 2010;65(7):557–66.
13. Atri M. New technologies and directed agents for applications of cancer imaging. J Clin Oncol. 2006;24(20):3299–308.
14. Kerbel RS. Tumor angiogenesis. N Engl J Med. 2008;358(19):2039–49.
15. Sullivan LA, Brekken RA. The VEGF family in cancer and antibody-based strategies for their inhibition. MAbs. 2010;2(2).
16. Ferrara N. Vascular endothelial growth factor as a target for anticancer therapy. Oncologist. 2009;9 Suppl 1:2–10.
17. Jahangiri A, Aghi MK. Biomarkers predicting tumor response and evasion to anti-angiogenic therapy. Biochim Biophys Acta. 1825;1:86–100.
18. Goel S, et al. Normalization of the vasculature for treatment of cancer and other diseases. Physiol Rev. 2011;91(3):1071–121.
19. Jain RK. Normalization of tumor vasculature: an emerging concept in antiangiogenic therapy. Science. 2005;307(5706):58–62.
20. Hinnen P, Eskens FA. Vascular disrupting agents in clinical development. Br J Cancer. 2007;96(8):1159–65.
21. Kolesnick R, Fuks Z. Radiation and ceramide-induced apoptosis. Oncogene. 2003;22(37):5897–906.
22. Ciardiello F, Tortora G. EGFR antagonists in cancer treatment. N Engl J Med. 2008;358(11):1160–74.
23. Jones KL, Buzdar AU. Evolving novel anti-HER2 strategies. Lancet Oncol. 2009;10(12):1179–87.

24. Sleijfer S, et al. Drug insight: gastrointestinal stromal tumors (GIST) – the solid tumor model for cancer-specific treatment. Nat Clin Pract Oncol. 2008;5(2):102–11.
25. Yuan Y, et al. Novel targeted therapeutics: inhibitors of MDM2, ALK and PARP. J Hematol Oncol. 2011;4:16.
26. Gambacorti-Passerini C, Messa C. Crizotinib in anaplastic large-cell lymphoma. N Engl J Med. 2011; 364:775–6.
27. Yuan R, et al. Targeting tumorigenesis: development and use of mTOR inhibitors in cancer therapy. J Hematol Oncol. 2009;2:45.
28. El-Osta H, et al. BRAF mutations in advanced cancers: clinical characteristics and outcomes. PLoS One. 2011;6(10):e25806.
29. Baselga J, et al. Everolimus in postmenopausal hormone-receptor – positive advanced breast cancer. N Engl J Med. 2012;366(6):520–9.
30. El Saghir NS, et al. Treatment of metastatic breast cancer: state-of-the-art, subtypes and perspectives. Crit Rev Oncol Hematol. 2011;80(3):433–49.
31. Mottet N, et al. EAU guidelines on prostate cancer. Part II: treatment of advanced, relapsing, and castration-resistant prostate cancer. Eur Urol. 2011; 59(4):572–83.
32. Peters S, Adjei AA. MET: a promising anticancer therapeutic target. Nat Rev Clin Oncol. 2012; 9(6):314–26.
33. Yakes FM, et al. Cabozantinib (XL184), a novel MET and VEGFR2 inhibitor, simultaneously suppresses metastasis, angiogenesis, and tumor growth. Mol Cancer Ther. 2011;10(12):2298–308.
34. Smith DC, et al. Cabozantinib in patients with advanced prostate cancer: results of a phase II randomized discontinuation trial. J Clin Oncol. 2013; 31(4):412–9.
35. Cavallo F, et al. 2011: the immune hallmarks of cancer. Cancer Immunol Immunother. 2011;60(3):319–26.
36. Koh DM, Padhani AR. Diffusion-weighted MRI: a new functional clinical technique for tumour imaging. Br J Radiol. 2006;79:633–5.
37. Padhani AR, Koh DM. Diffusion MR imaging for monitoring of treatment response. Magn Reson Imaging Clin N Am. 2011;19(1):181–209.
38. Li SP, Padhani AR. Tumor response assessments with diffusion and perfusion MRI. J Magn Reson Imaging. 2012;35(4):745–63.
39. García-Figueiras R, et al. CT perfusion in oncologic imaging: a useful tool? AJR Am J Roentgenol. 2013;200(1):8–19.
40. Bussink J, et al. PET-CT for radiotherapy treatment planning and response monitoring in solid tumors. Nat Rev Clin Oncol. 2011;8(4):233–42.
41. Turkbey B, et al. Imaging of tumor angiogenesis: functional or targeted? AJR Am J Roentgenol. 2009; 193(2):304–13.
42. Harvey CJ, et al. Functional CT imaging of the acute hyperemic response to radiation therapy of the prostate gland: early experience. J Comput Assist Tomogr. 2001;25(1):43–9.
43. Leach MO, et al. Assessment of antiangiogenic and antivascular therapeutics using MRI: recommendations for appropriate methodology for clinical trials. Br J Radiol. 2003;76 Spec No 1:S87–91.
44. O'Connor JP, et al. Dynamic contrast-enhanced imaging techniques: CT and MRI. Br J Radiol. 2011;84 Spec No 2:S112–20.
45. Miles KA. Molecular imaging with dynamic contrast-enhanced computed tomography. Clin Radiol. 2010;65(7):549–56.
46. Deshpande N, et al. Molecular ultrasound assessment of tumor angiogenesis. Angiogenesis. 2010;13(2):175–88.
47. Hudson JM, et al. Contrasting the vascular response to sunitinib as measured by DCE-CT, DCE-MRI, and DCE-US. J Clin Oncol. 2013;31(suppl 6):abstr 378.
48. Galbraith SM, et al. Combretastatin A4 phosphate has tumor antivascular activity in rat and man as demonstrated by dynamic magnetic resonance imaging. J Clin Oncol. 2003;21(15):2831–42.
49. Batchelor TT, et al. AZD2171, a pan-VEGF receptor tyrosine kinase inhibitor, normalizes tumor vasculature and alleviates edema in glioblastoma patients. Cancer Cell. 2007;11:83–95.
50. Jackson A, et al. Imaging tumor vascular heterogeneity and angiogenesis using dynamic contrast-enhanced magnetic resonance imaging. Clin Cancer Res. 2007;13:3449–59.
51. Petralia G, et al. Quantification of variability in breath-hold perfusion CT of hepatocellular carcinoma: a step toward clinical use. Radiology. 2012; 265(2):448–56.
52. Ng CS, et al. Reproducibility and comparison of DCE-MRI and DCE-CT perfusion parameters in a rat tumor model. Technol Cancer Res Treat. 2012;11(3):279–88.
53. Jain RK, et al. Biomarkers of response and resistance to antiangiogenic therapy. Nat Rev Clin Oncol. 2009;6:327–38.
54. Duda DG, et al. Biomarkers of antiangiogenic therapy: how do we move from candidate biomarkers to valid biomarkers? J Clin Oncol. 2010;28:183–5.
55. Fournier LS, et al. Metastatic renal carcinoma: evaluation of antiangiogenic therapy with dynamic contrast-enhanced CT. Radiology. 2010;256(2):511–8.
56. Azad NS, et al. Dual targeting of vascular endothelial growth factor (VEGF) with sorafenib and bevacizumab: clinical and translational results. J Clin Oncol. 2007;18S Abstract.
57. Patel CN, et al. FDG PET/CT in oncology: "raising the bar". Clin Radiol. 2010;65(7):522–35.
58. Nanni C, et al. Non FDG PET. Clin Radiol. 2010; 65(7):536–48.
59. Groves AM, et al. Non-[18F]FDG PET in clinical oncology. Lancet Oncol. 2007;8(9):822–30.

60. Cullinane C, et al. An in vivo tumor model exploiting metabolic response as a biomarker for targeted drug development. Cancer Res. 2005;65:9633–6.
61. Atkinson DM, et al. Using fluorodeoxythymidine to monitor anti-EGFR inhibitor therapy in squamous cell carcinoma xenografts. Head Neck. 2008; 30(6):790–9.
62. Su H, et al. Monitoring tumor glucose utilization by positron emission tomography for the prediction of treatment response to epidermal growth factor receptor kinase inhibitors. Clin Cancer Res. 2006; 12:5659–67.
63. Mileshkin L, et al. Changes in 18F-fluorodeoxyglucose and 18F-fluorodeoxythymidine positron emission tomography imaging in patients with non-small cell lung cancer treated with erlotinib. Clin Cancer Res. 2011;17(10):3304–15.
64. Cai W, et al. Multimodality imaging of the HER-kinase axis in cancer. Eur J Nucl Med Mol Imaging. 2008;35(1):186–208.
65. Mross K, et al. DCE-MRI assessment of the effect of vandetanib on tumor vasculature in patients with advanced colorectal cancer and liver metastases: a randomized phase I study. J Angiogenes Res. 2009; 1:5.
66. Ma BB, et al. A phase II study of concurrent cetuximab-cisplatin and intensity- modulated radiation therapy (IMRT) in locoregionally advanced nasopharyngeal carcinoma (NPC) with correlation using dynamic contrast-enhanced magnetic resonance imaging (DCE-MRI) [abstr]. J Clin Oncol. 2008; 26(Suppl):6055.
67. Camidge DR, Doebele RC. Treating ALK-positive lung cancer – early successes and future challenges. Nat Rev Clin Oncol. 2012;9(5):268–77.
68. Ou SHI, et al. Rapid and dramatic radiographic and clinical response to an ALK inhibitor (crizotinib, PF02341066) in an ALK translocation-positive patient with non-small cell lung cancer. J Thorac Oncol. 2010;5:2044–6.
69. Treglia G, et al. 18F-Fluorodeoxyglucose positron emission tomography in evaluating treatment response to imatinib or other drugs in gastrointestinal stromal tumors: a systematic review. Clin Imaging. 2012;36(3):167–75.
70. Tang L, et al. Gastrointestinal stromal tumors treated with imatinib mesylate: apparent diffusion coefficient in the evaluation of therapy response in patients. Radiology. 2011;258(3):729–38.
71. Honer M, et al. Anti-angiogenic/vascular effects of the mTOR inhibitor everolimus are not detectable by FDG/FLT-PET. Transl Oncol. 2010;3(4): 264–75.
72. Ma WW, et al. [18F]fluorodeoxyglucose positron emission tomography correlates with Akt pathway activity but is not predictive of clinical outcome during mTOR inhibitor therapy. J Clin Oncol. 2009; 27(16):2697–704.
73. Aide N, et al. 18F-FLT PET as a surrogate marker of drug efficacy during mTOR inhibition by everolimus in a preclinical cisplatin-resistant ovarian tumor model. J Nucl Med. 2010;51(10):1559–64.
74. Shinagare AB, et al. Genitourinary imaging: part 2, role of imaging in medical management of advanced renal cell carcinoma. AJR Am J Roentgenol. 2012; 199(5):W554–64.
75. Baudy AR, et al. PET is a good biomarker of both early response and acquired resistance in BRAFV600 mutant melanomas treated with vemurafenib and the MEK inhibitor GDC-0973. EJNMMI Res. 2012; 2(1):22.
76. McArthur GA, et al. Marked, homogeneous, and early [18F]fluorodeoxyglucose-positron emission tomography responses to vemurafenib in BRAF-mutant advanced melanoma. J Clin Oncol. 2012;3 0(14):1628–34.
77. Cullinane C, et al. Differential (18)F-FDG and 3′-deoxy-3′-(18)F-fluorothymidine PET responses to pharmacologic inhibition of the c-MET receptor in preclinical tumor models. J Nucl Med. 2011; 52(8):1261–7.
78. Adjei AA, et al. Early clinical development of ARQ 197, a selective, non-ATP-competitive inhibitor targeting MET tyrosine kinase for the treatment of advanced cancers. Oncologist. 2011;16:788–99.
79. Alonzi R, et al. Antivascular effects of neoadjuvant androgen deprivation for prostate cancer: an in vivo human study using susceptibility and relaxivity dynamic MRI. Int J Radiat Oncol Biol Phys. 2011;80(3):721–7.
80. Mueller-Lisse UG, et al. Time-dependent effects of hormone-deprivation therapy on prostate metabolism as detected by combined magnetic resonance imaging and 3D magnetic resonance spectroscopic imaging. Magn Reson Med. 2001;46:49–57.
81. Røe K, et al. Vascular responses to radiotherapy and androgen-deprivation therapy in experimental prostate cancer. Radiat Oncol. 2012;7:75.
82. Nemoto K, et al. Changes in diffusion-weighted images for visualizing prostate cancer during antiandrogen therapy: preliminary results. Urol Int. 2010;85(4):421–6.
83. Fogelman I, et al. Positron emission tomography and bone metastases. Semin Nucl Med. 2005;35: 135–42.
84. Dehdashti F, et al. PET-based estradiol challenge as a predictive biomarker of response to endocrine therapy in women with estrogen-receptor-positive breast cancer. Breast Cancer Res Treat. 2009;113(3): 509–17.
85. Mankoff DA, et al. Tumor receptor imaging. J Nucl Med. 2008;49 Suppl 2:149S–63.
86. Padhani AR, et al. Assessing the relation between bone marrow signal intensity and apparent diffusion coefficient in diffusion-weighted MRI. AJR Am J Roentgenol. 2013;200(1):163–70.

87. Padhani AR, Gogbashian A. Bony metastases: assessing response to therapy with whole-body diffusion MRI. Cancer Imaging. 2011;11 Spec No A:S129–45.
88. Wolchok JD, et al. Guidelines for the evaluation of immune therapy activity in solid tumors: immune-related response criteria. Clin Cancer Res. 2009; 15(23):7412–20.
89. Bronstein Y, et al. Radiologic manifestations of immune-related adverse events in patients with metastatic melanoma undergoing anti-CTLA-4 antibody therapy. AJR Am J Roentgenol. 2011;197(6): W992–1000.
90. Tumeh PC, et al. PET imaging of cancer immunotherapy. J Nucl Med. 2008;49(6):865–8.
91. Lucignani G, et al. Molecular imaging of cell-mediated cancer immunotherapy. Trends Biotechnol. 2006;24(9):410–8.
92. Ng CS, et al. Perfusion CT in patients with metastatic renal cell carcinoma treated with interferon. AJR Am J Roentgenol. 2010;194:166–71.
93. Faria SC, et al. CT quantification of effects of thalidomide in patients with metastatic renal cell carcinoma. AJR Am J Roentgenol. 2007;189:378–85.
94. Guan LM, et al. Early changes measured by CT perfusion imaging in tumor microcirculation following radiosurgery in rat C6 brain gliomas. J Neurosurg. 2011;114(6):1672–80.
95. Cai J, et al. A rabbit irradiation platform for outcome assessment of lung stereotactic radiosurgery. Int J Radiat Oncol Biol Phys. 2009;73(5):1588–95.
96. Lee SC, et al. Early detection of radiation therapy response in non-Hodgkin's lymphoma xenografts by in vivo 1H magnetic resonance spectroscopy and imaging. NMR Biomed. 2010;23(6):624–32.
97. Hamstra DA, et al. Diffusion magnetic resonance imaging: an imaging treatment response biomarker to chemoradiotherapy in a mouse model of squamous cell cancer of the head and neck. Transl Oncol. 2008;4:187–94.
98. Larocque MP, et al. Monitoring T2 and ADC at 9.4 T following fractionated external beam radiation therapy in a mouse model. Phys Med Biol. 2010; 55(5):1381–93.
99. Galban CJ, et al. A feasibility study of parametric response map analysis of diffusion-weighted magnetic resonance imaging scans of head and neck cancer patients for providing early detection of therapeutic efficacy. Transl Oncol. 2009;2(3): 184–90.
100. Hamstra DA, et al. Evaluation of the functional diffusion map as an early biomarker of time-to-progression and overall survival in high-grade glioma. Proc Natl Acad Sci U S A. 2005;102(46):16759–64.
101. Liu Y, et al. Diffusion-weighted imaging in predicting and monitoring the response of uterine cervical cancer to combined chemoradiation. Clin Radiol. 2009;64(11):1067–74.
102. Hamstra DA, et al. Functional diffusion map as an early imaging biomarker for high-grade glioma: correlation with conventional radiologic response and overall survival. J Clin Oncol. 2008;26(20): 3387–94.
103. Rasmussen F, Madsen HHT. Imaging follow-up of RF ablation of lung tumours. Cancer Imaging. 2011;11:S123–8.
104. Kamel IR, et al. Unresectable hepatocellular carcinoma: serial early vascular and cellular changes after transarterial chemoembolization as detected with MR imaging. Radiology. 2009;250(2):466–73.
105. Boyle RG, Travers S. Hypoxia: targeting the tumour. Anticancer Agents Med Chem. 2006;6(4):281–6.
106. Denny WA. Hypoxia-activated prodrugs in cancer therapy: progress to the clinic. Future Oncol. 2010;6(3):419–28.
107. Padhani AR, et al. Imaging oxygenation of human tumours. Eur Radiol. 2007;17(4):861–72.
108. Dizdarevic S, Peters AM. Imaging of multidrug resistance in cancer. Cancer Imaging. 2011;11: 1–8.
109. Crawford LJ, et al. Proteasome inhibitors in cancer therapy. J Cell Commun Signal. 2011;5(2):101–10.
110. Aronson LI, Davies FE. DangER: protein ovERload. Targeting protein degradation to treat myeloma. Haematologica. 2012;97(8):1119–30.
111. Terpos E, et al. Advances in imaging and the management of myeloma bone disease. J Clin Oncol. 2011;29(14):1907–15.
112. Padhani AR, et al. Whole-body diffusion-weighted MR imaging in cancer: current status and research directions. Radiology. 2011;261(3):700–18.
113. Bayouth JE, et al. Image-based biomarkers in clinical practice. Semin Radiat Oncol. 2011;21(2): 157–66.
114. Rudin M. Imaging readouts as biomarkers or surrogate parameters for the assessment of therapeutic interventions. Eur Radiol. 2007;17(10):2441–57.
115. Padhani AR, Miles KA. Multiparametric imaging of tumor response to therapy. Radiology. 2010;256(2):348–64.

Medical Image Computing for Oncology: Review and Clinical Examples

6

Zhong Xue and Stephen T.C. Wong

Contents

Abbreviations

AFINITI	Assisted Follow-up in NeuroImaging of Therapeutic Intervention
BWH	Brigham Women's Hospital
CT	Computed tomography
CTL	Cytotoxic T-lymphocytes
DICOM	Digital Imaging and Communications in Medicine
EBV	Epstein Barr virus
FCM	Fuzzy C-means
FDG	Fluorodeoxyglucose
FFD	Free-Form Deformations
FLAI	Fluid-attenuated inversion recovery
GBM	Glioblastoma multiforme
GUI	Graphical user interface
HD	Hodgkin's disease
ITK	Insight Toolkit
LINA	Longitudinal Image Navigation and Analysis
LMP	Latent membrane protein
MRI	Magnetic resonance imaging
NHL	Non-Hodgkin's lymphoma
PACS	Picture Archiving and Communication Systems
PFS	Progression free survival
PICE	Prior Information Constrained Evolution
QI	Quantitative Index
ROI	Region of Interest
ROI	Regions of interest
SMD	Statistical model of deformation
SUV	Standard uptake value

Z. Xue • S.T.C. Wong (✉)
Department of Systems Medicine and Bioengineering, The Methodist Hospital Research Institute, Weill Cornell Medical College, Houston, TX 77030, USA
e-mail: stwong@tmhs.org

A. Luna et al. (eds.), *Functional Imaging in Oncology*,
DOI 10.1007/978-3-642-40412-2_6, © Springer-Verlag Berlin Heidelberg 2014

6.1 Introduction

Medical imaging captures images of the human body or organs for clinical purposes or medical science. Preclinical imaging can visualize living animals for research purposes. Various imaging modalities have long been crucial to the researcher in observing morphometric and functional changes of tumor within different organs at tissue, cellular, or molecular levels. Longitudinal data in animals also respond to physiological or environmental changes during drug discovery. Imaging modalities that are noninvasive and in vivo have become especially important to study human and animals. Broadly speaking, techniques such as high-frequency micro-ultrasound, magnetic resonance imaging (MRI), and computed tomography (CT) are usually used for anatomical imaging, while optical imaging (fluorescence and bioluminescence), positron emission tomography (PET), and single-photon emission computed tomography (SPECT) are usually used for molecular visualizations.

Medical imaging is routinely used for cancer diagnosis and monitoring. Commonly used modalities include digital radiography, fluoroscopy, CT, MRI, ultrasound, and PET. Mammography is one of the successful imaging modality used for screening breast cancer regularly and uses low-energy X-rays (usually around 30 kVp) to examine the human breast. On the other hand, because CT and MRI are sensitive to different tissue properties, the appearance of the images obtained with the two modalities differs markedly but can be used for diagnosis and follow-up studies. In CT, X-rays must be blocked by some form of dense tissue to create an image, so the image quality for soft tissues is poor. On the other hand, in MRI, while any nucleus with a net nuclear spin can be used, the proton of the hydrogen atom remains the most widely used, especially in the clinical setting, because it is so ubiquitous and returns a strong signal. It reconstructs soft-tissue image and presents better contrast than CT.

Nuclear medicine acts as an important tool both in diagnostic imaging and in treatment of disease and may also be referred to as molecular imaging and therapeutics. Different from the typical concept of anatomical radiology, nuclear medicine enables assessment of physiology and molecular activities in vivo. This function-based approach to medical evaluation has useful applications in most subspecialties, such as oncology, neurology, and cardiology. Scintigraphy, SPECT, and PET are used to detect regions of biologic activity that may be associated with disease. PET uses coincidence detection to image functional processes. Short-lived positron-emitting isotope, such as 18F, is incorporated with an organic substance such as glucose, creating F18-fluorodeoxyglucose, which can be used as a marker of metabolic utilization. Images of activity distribution throughout the body can show rapidly growing tissue, like tumor, metastasis, or infection. PET images can be viewed in comparison to computed tomography scans to determine an anatomical correlate. Modern scanners may integrate PET, allowing PET/CT or PET/MRI to optimize the image reconstruction involved with positron imaging. This is performed on the same equipment without physically moving the patient off of the gantry. The resultant hybrid of functional and anatomical imaging information is a useful tool in noninvasive diagnosis and patient management.

Although many algorithms and methods of image analysis have been reported, validated, and are freely available on line, very few have been engineered or integrated into medical image workflow for clinical trials or routine clinical use. This gap has seriously limited the impact that computational algorithms and methods developed by the medical imaging research community have made to advance image-based clinical trials and translational research. It is interesting to organize and manage medical imaging datasets as well as their quantitative results generated by the manual or semiautomated image analysis tools to support safer and more effective "targeted" therapy that goes beyond the capability of existing image management systems, such as picture archiving and communication systems (PACS) [1, 2].

An integrated medical imaging computing system is designed to enhance efficacy and reduce error in the interpretation and monitoring of cancer therapy responses. The system provides physicians and researchers with automated tools and integrated information needed to allow sensitive, reproducible, quantitative assessment of longitudinal changes in response to therapeutic intervention. The primary goal is to introduce the tools and techniques resulting from imaging informatics research into real-life settings in clinical care, supporting the imaging follow-up studies and clinical trials in cancer therapy. The FDA requires imaging findings to be reproducible so that an independent reviewer can draw the same conclusion or derive the same computed measurements as those included in a trial submission. As a result, a unified architecture is required for a DICOM-based imaging data management platform that supports heterogeneous image capture environments and modalities. Automated markups and computations are recommended to facilitate reproducibility, but manual segmentation or annotations are often needed to compute the imaging findings. A common vocabulary or lexicon server is often included in the integrated image computing system for generating diagnosis and treatment reports and specifying the imaging protocols.

The data scheme includes image data, metadata definitions from image analysis such as regions of interest (ROIs) or lesions, standard uptake value (SUV) for each ROI, image segmentation labels, as well as longitudinal deformation fields among serial images, and associated metadata such as treatment outcome, radiology report, patient information, and other clinical data if any. The data model is instantiated via a relational database in which metadata are stored in tables as specified by the scheme and image data (raw and processed) are stored in a trusted file system indexed by the pointers stored in the database tables. The metadata is archived in a structured way to support advanced statistical analysis and modeling.

6.2 Tumor Segmentation: Examples from Glioblastoma Multiforme

6.2.1 Introduction

Despite the best available standard therapies, including surgery, radiation, and chemotherapy, the survival in patients diagnosed with glioblastoma multiforme (GBM) remains dismal at 14 months [3]. Newer therapeutic strategies aiming at targeting specific molecules are being developed and tested in clinical trials [4]. Temozolomide chemoradiation has significantly prolonged survival but produces pseudoprogression that is difficult or impossible to distinguish from recurrence in 30–50 % of patients [3, 5]. In addition, antiangiogenic therapies have been used in combination with conventional chemotherapy in patients with recurrent GBM, demonstrating radiographic response rates of 35–50 % [6–8]. These agents improve significantly patient quality of life but alter the pattern of recurrence by a potent effect on tumor permeability, suppressing enhancement within a solid tumor with a resulting increase in the frequency of infiltrative recurrence [9].

These therapy-induced alterations in the natural history and imaging appearance of treated GBM have made imaging follow-up by conventional MRI difficult, which motivates widespread ongoing research to discover additional imaging biomarkers and has led to a revision in response criteria. Although the most commonly used imaging criteria for evaluating treatment response are still based on measurement of enhancing tumor (the Macdonald Criteria) [10], the increase in infiltrative recurrence and the difficulty in distinguishing recurrence from progression has led to proposal of a new criteria for tumor response that includes abnormality on T2-weighted or fluid-attenuated inversion recovery (FLAIR) images as additional markers for progression (the RANO criteria) [11]. The RANO criteria also recommend the use of volumetric measurements of enhancing tumor because reliance on cross

product diameters is problematic and highly operator dependent in cases of irregularly shaped tumor, multifocal tumor, or tumor with cystic or necrotic components. Recently, volumetric measures were found comparable [12] or superior [13, 14] to linear diameter measures as indicators of tumor evaluation.

Volumetric methods have the advantage of more reproducibly and precisely measuring the size of tumor and are being increasingly used in clinical settings. For example, volumetric measurements of both the enhancing and non-enhancing tumor have been correlated to progression-free survival (PFS) and overall survival (OS) [9, 15]. To date, the major barrier to widespread adoption of these methods in clinical neuro-oncology has been that manual and assisted manual segmentation methods are quite time consuming for the operator. Due to presence of heterogeneous signal intensity in necrotic or cystic tumor and at the margin of infiltrative tumors, it is difficult to segment a tumor by hand, and the development of automatic or semiautomatic software tools that can provide efficient volumetric measurement and assist longitudinal shape analysis for follow-up studies could provide significant benefit.

Tumor segmentation algorithms are classified into voxel-based or deformable shape model-based methods. Fuzzy clustering methods (voxel-based) are among the more popular approaches [16–20], and they classify each voxel into one of either the normal brain tissues (gray matter, white matter, and CSF) or tumor tissues. The algorithm developed by Philips et al. [20] can differentiate clinically vital boundaries of tumor and edema from hemorrhage in multimodal MRI. The performance of multimodal intensity-based clustering can be limited by overlapping of intensity between tumor and normal tissues [21, 22]. To account for this, additional features such as multidimensional intensity vectors have been designed for the clustering. Clark et al. [23] has integrated knowledge-based techniques and multimodality clustering to segment GBM tumors. Fletcher-Heath et al. [19] presented the first tumor segmentation for non-enhancing MR data, including T1, T2, and proton density-weighted images, to track tumor size over time. Prastawa et al. [24, 25] designed a knowledge-based tumor segmentation algorithm that learns voxel-intensity distributions from normal brain and detects outlying tumor voxels. Kaus et al. developed a spatially varying statistical classification algorithm using a template to moderate the segmentation obtained by statistical classification [26, 27].

A second class of algorithms uses deformable shape models to segment tumor from normal brain. These methods are derived from the traditional Snake model [28] that uses surfaces to match tumor boundaries. The concept of these techniques is the use of energy function and various shape models: the external energy derived from the matching degree between the shape and the image features is used to distinguish tumor from normal tissues, and the internal energy is used to constrain the tumor shape. In order to adjust for the change of topology, implicit models such as level sets [29–34] can be used. Intensity distributions within and outside tumor region have been used for level set segmentation [35–37].

Voxel-based segmentation algorithms can better adapt the segmented tumor shape to local image, and deformable model-based segmentation schemes are more robust but generally need proper initialization. To take the advantages of both algorithms, we propose an AFINITI (Assisted Follow-up in NeuroImaging of Therapeutic Intervention) pipeline for segmenting MR images by combining them. In the first stage, the voxel-based segmentation using the FSL FAST [38, 39] is performed automatically for initial tumor segmentation from T1-weighted images. The T2-weighted images are also automatically segmented and combined with the T1 segmentation results. Then, a level-set-based segmentation is used to refine the segmentation results with minimal manual input by embedding the major functions of ITK-SNAP [40]. These tools are integrated into one pipeline with a single GUI. We validate the AFINITI pipeline by applying the software to 26 clinical GBM cases by comparing the results with those obtained using manual segmentation.

6.2.2 Methods

Serial MRI scans from 26 patients with diagnosis of GBM at Brigham and Women's Hospital (BWH) between 2004 and 2009 who had interpretable high-resolution MR scans were retrieved from BWH's PACS. All MRI scans were performed on 1.5 or 3 T MRI scanners. The imaging protocol contained at least an axial 3D SPGR T1-weighted series covering the whole brain acquired at a 5–10-min delay after the intravenous administration of 0.1–0.2 mmol/kg gadopentetate dimeglumine contrast agent and an axial 2D T2-weighted MR sequences. The slice thickness in all cases was between 1.0 and 1.5 mm for 3D SPGR sequences and 6 mm for the 2D FSE T2-weighted sequences. The typical 1.5 T 3D SPGR parameters were set as TR = 25 ms, TE = 6 ms, FOV = 200 × 240 mm, and Matrix = 224 × 224.

Manual segmentation was performed under the supervision of two practicing faculty neuroradiologists by a research associate trained in neuroanatomy and neuroimaging, and the final segmentations were reviewed and corrected jointly by the two neuroradiologists to minimize the bias among raters. Segmentation was performed using the public domain tool, ITK-SNAP, by manually tracing the boundary between the areas of abnormal enhancement and normal tissue on the 3D SPGR images, excluding non-enhancing, presumably necrotic or cystic, portions of tumor but including areas of heterogeneous enhancement felt to represent tumor.

The goal of AFINITI is to enhance efficacy and reduce errors in the interpretation of neuroimaging follow-up studies for several common indications and provide the interpreting and referring physicians with automated tools and augmented information needed to allow sensitive, reproducible, quantitative assessment of longitudinal changes in brains in response to therapeutic intervention. We have seamlessly implemented the state-of-the-art neuroimaging tools into the AFINITI image computing pipeline to facilitate clinical quantification of GBM [41]. The graphical user interface (GUI) for implementing and visualizing the image processing modules was developed based on the ITK-SNAP framework. Additional modules were added to assist users in selecting input images, specifying and adjusting segmentation parameters, as well as examining, editing, and saving results. To make the software user-friendly, it takes DICOM series inputs for processing. DICOM series with overlapping ROIs were written with modified DICOM tags as the outputs so that the results can be presented on different viewing workstations and distinguished from the original images. The AFINITI software pipeline was written in C++and MS DOS batch scripting languages. The major tools embedded in the AFINITI pipeline included preprocessing, the FSL FAST, and the modified level set method in the ITK-SNAP package.

In the AFINITI pipeline, we integrated the FAST tool [42] for initial brain tumor segmentation. The preprocessing step mainly strips skulls from T1-weighted images and co-registers T1-weighted images to T2-weighted images. A deformable brain image registration was used to automatically align the skull-stripped template image onto each individual image to remove the skulls. We classified the tissues into not only the normal tissue types (WM, GM, and CSF) but also active tumor tissues [16–20]. Figure 6.1 shows the preprocessing procedure while Fig. 6.2 presents an example of segmentation using FAST. It can be seen that the segmentation results can be noisy with many small vascular spots in normal tissues that were classified as tumor tissue.

To reduce the false-positive spots, we developed a T2 mapping method to remove them. As shown in Fig. 6.3b, the T2-weighted image (Fig. 6.3a) was first registered onto the T1-weighted image with initial segmentation of FAST overlap. A low-bound intensity thresholding was then applied to the registered T2-weighted image, and only high-intensity regions covering all the segmented tumor regions but not the false-positive regions were kept. Combining the T1 and T2 segmentation results and performing morphological shape corrections, we obtained the final automatic tumor segmentation. Then, the tumor can be automatically selected by using morphological operations. Therefore, regions with small volumes or flat shapes were deleted

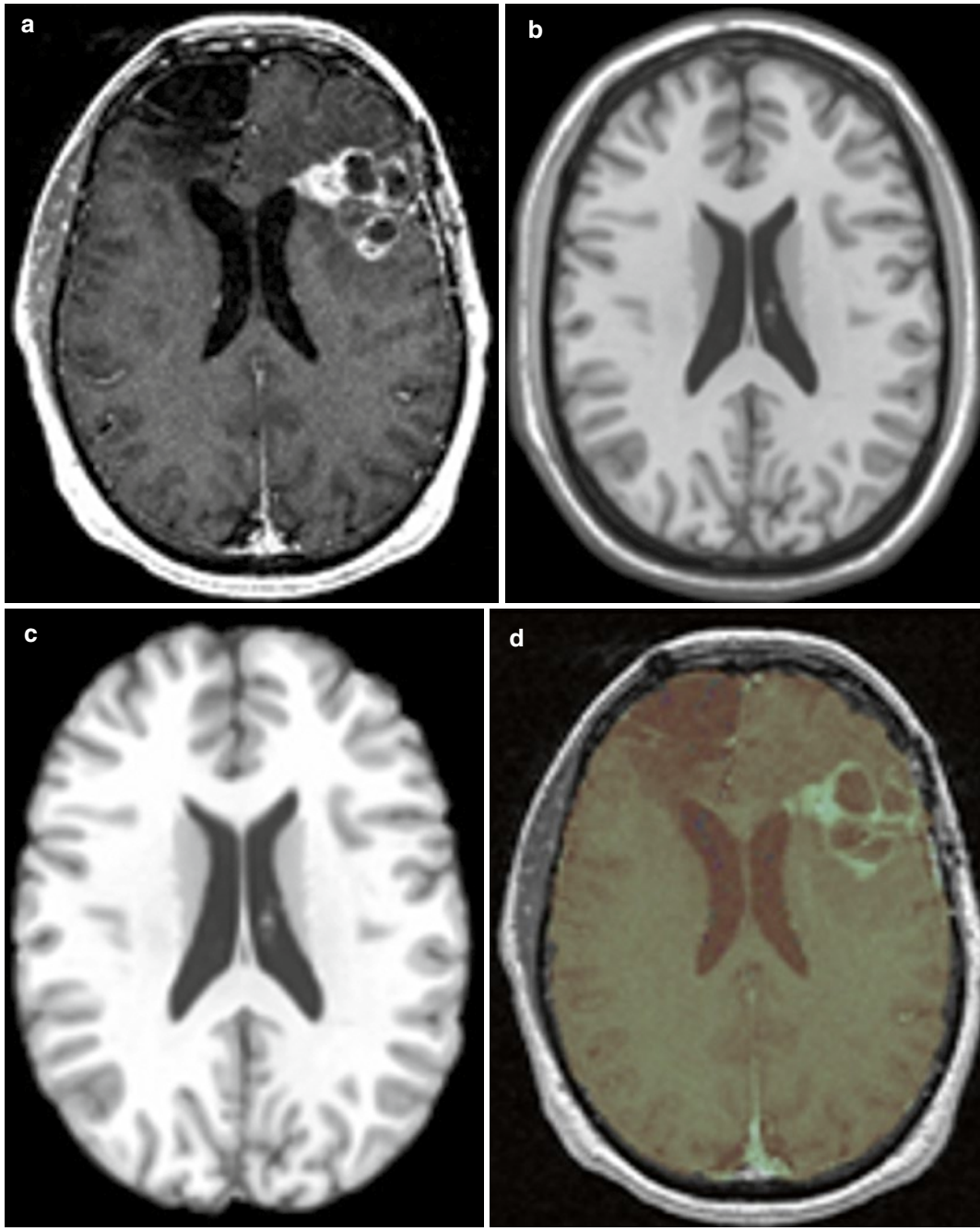

Fig. 6.1 Registration-based skull stripping method. (**a**) Original image to be processed; (**b**) the template image; (**c**) the segmented brain region of the template image; (**d**) overlapping the brain region onto the original image [41]

by applying 3D open operation. If the tumor seed points are provided, a region grow operation will be performed to further remove false-positive regions. Figure 6.3e illustrates the final automatic segmentation of the tumor.

After automatic segmentation, level-set-based segmentation can be further performed to interactively refine the results by visualization and manual correction [43]. These tasks were accomplished by embedding ITK-SNAP into our

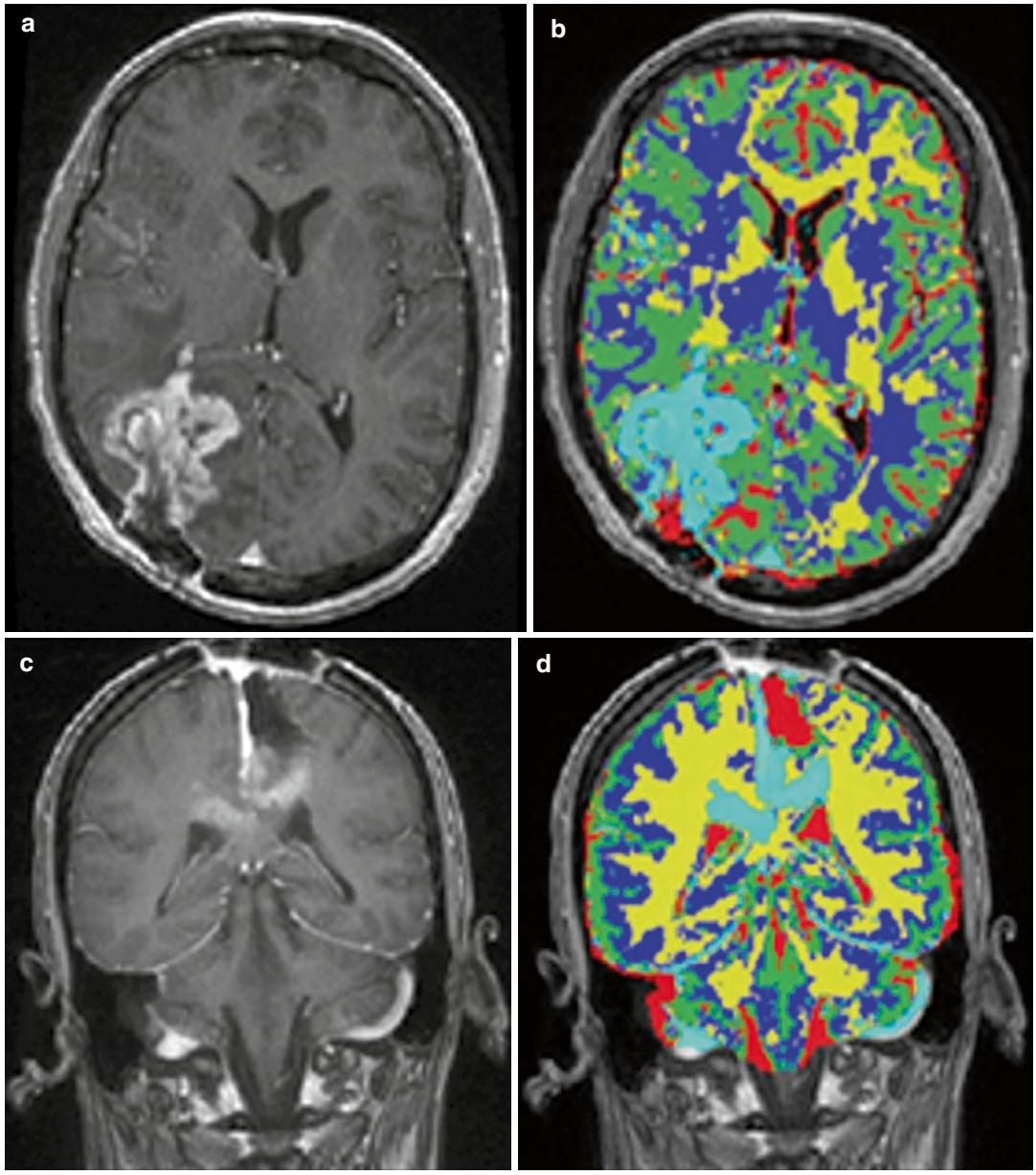

Fig. 6.2 Some examples of tumor segmentation results after FAST. (**a**, **c**) Input images; (**b**, **d**) FAST segmentation results [41]

software pipeline. ITK-SNAP is a software application used to segment structures in 3D medical images. It provides semiautomatic segmentation using level set methods, as well as manual delineation and image navigation.

Finally, after the segmented tumor result is accepted, the tumor volume, tumor center point location, and the overlapping of the segmented tumor region on the original images were automatically generated in the original DICOM format using a new series number. According to the current neuroradiology workflow, the new data series can be uploaded to a PACS server so that radiologists can interpret the images of GBM patients by referring to the segmentation results.

6.2.3 Results

All the GBM tumor patient cases were processed using the proposed AFINITI pipeline. Of all 26 cases, 24 were visually inspected and found satisfactory by the participating neuroradiologists, and two cases were further refined using the second step, namely, level-set-based

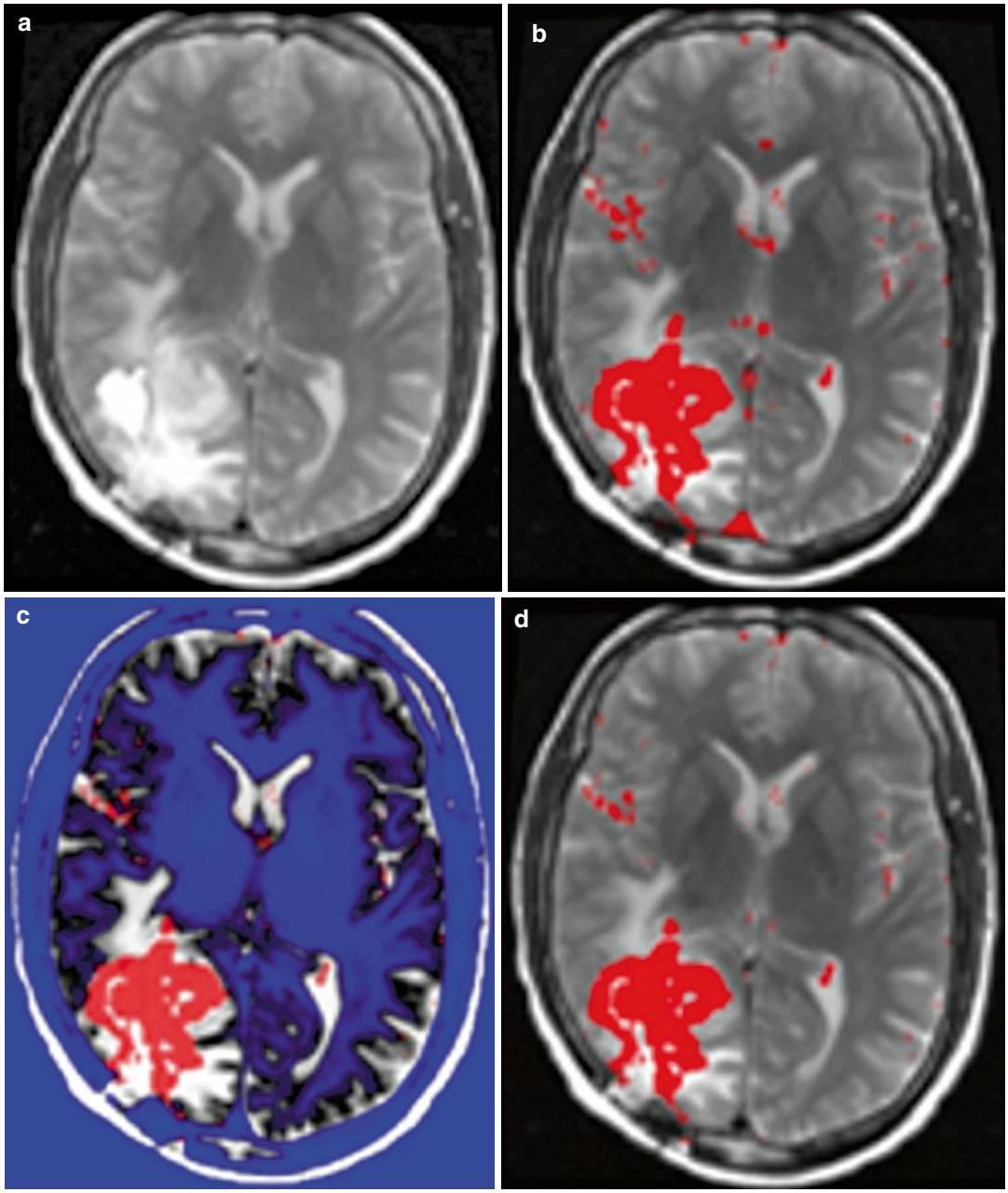

Fig. 6.3 An illustration of the combined T1 and T2 segmentation. (**a**) T2 image registered onto T1 image; (**b**) overlaying the segmentation result from T1 image onto T2 image; (**c**) thresholding T2 image (*blue* shows the ROI filtered out); by adjusting the threshold, we can eliminate the enhanced big vessels close to the tumor; (**d**) after applying T2 thresholding, the majority of false-positive spots were removed; and (**e**) other isolated spots are removed using morphological operations [41]

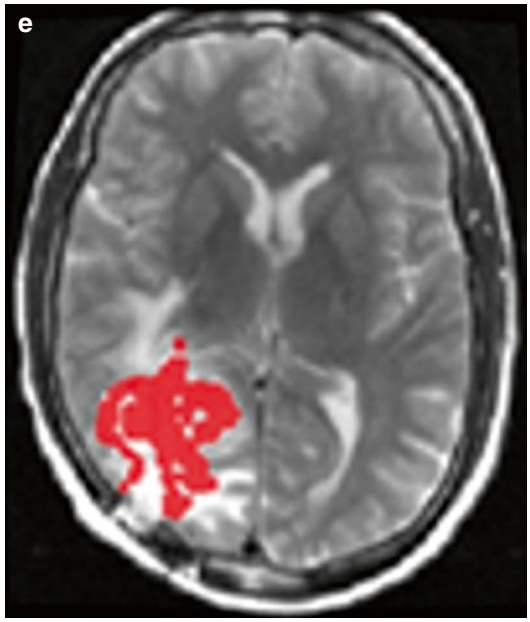

Fig. 6.3 (continued)

refinement. The average time for the two cases using level-set-based refinement was approximately 4 min. Quantitative measurements from manual segmentation and from AFINITI were compared. Denoting the results of AFINITI as set A and those of manual segmentation as M, the ratio of the intersection versus the union, i.e., $|A \cap M|/|A \cup M|$, was calculated. Figure 6.4 shows the correlation between AFINITI and manual segmentation, and the Pearson correlation coefficient for all the 26 cases is 0.96.

Figure 6.5 shows the original images, the manual and AFINITI segmentation results, and the overlapping images of these two cases. The tumor sizes measured from AFINITI were generally smaller than those obtained from manual segmentation, suggesting that human raters tend to over-segment tumor. During manual selection of the tumor regions, the bright enhanced regions were marked while the small dark regions inside and close to the tumor boundary were not

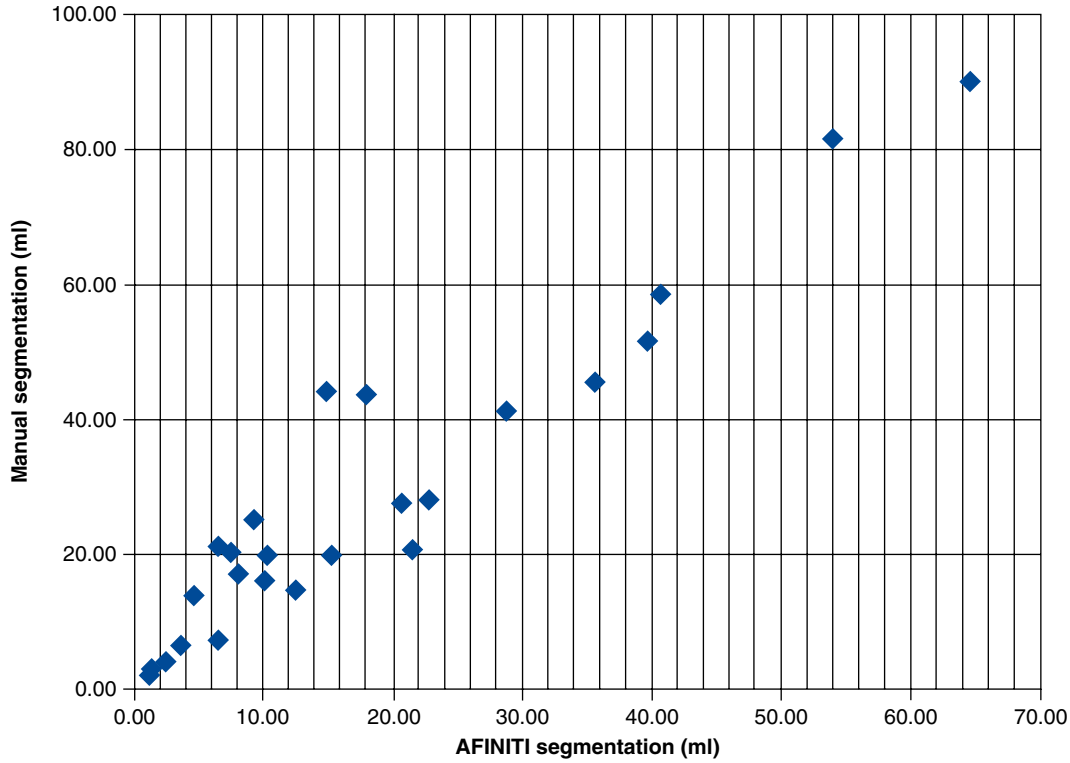

Fig. 6.4 Correlation of the segmentation results [41]

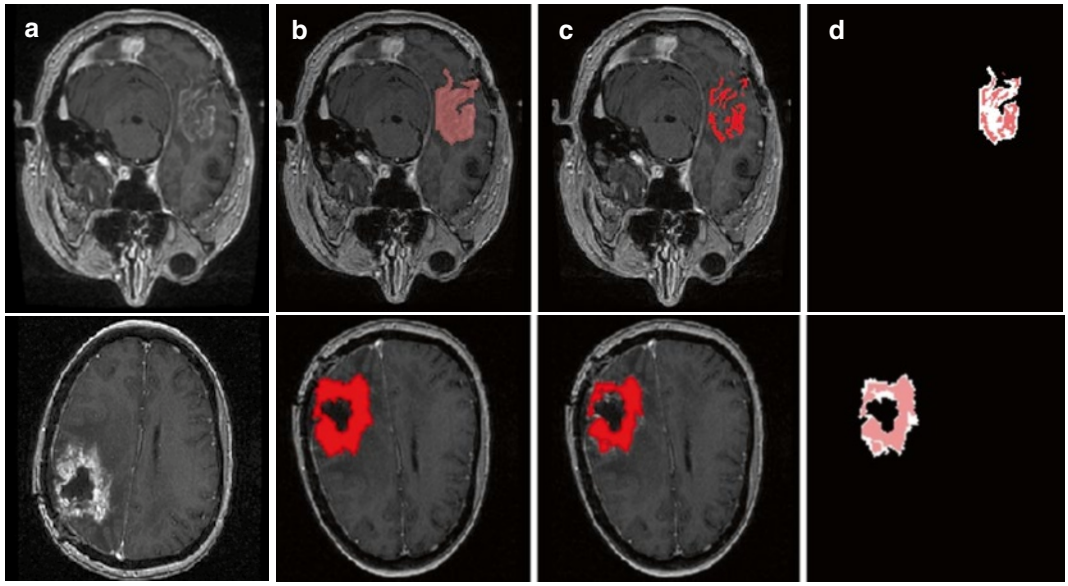

Fig. 6.5 Difference between manual and semiautomatic segmentations: (**a**) original image; (**b**) manual segmentation; (**c**) semiautomatic segmentation; (**d**) difference between manual segmentation (background *white shape*) and semiautomatic segmentation (highlighted *red shape*) [41]

selected. Therefore, although AFINITI results generated a more detailed boundary of the tumor (Fig. 6.5c), the volumes were slightly smaller. Considering the Pearson correlation coefficient between AFINITI and manual results, they are highly correlated, suggesting comparable performance for the proposed automatic tumor segmentation pipeline.

We also compared AFINITI segmentation against voxel-based segmentation (FSL FAST). Because the segmentation results of the voxel-based segmentation lacked spatial continuity (see Fig. 6.2d for example), they were further processed with tumor selection and morphological operation for the comparison. No manual interaction was involved in any of the 26 cases for the FAST algorithm. The student *T*-Test of the Jaccard indexes of AFINITI and voxel-based results (p-value = 0.0071) showed the advantage of AFINITI. To further evaluate the agreement and systematic differences between segmentation methods and manual segmentation, the Bland-Altman plots of the volume measures between AFINITI and manual results, and between FAST and manual results, were shown in Fig. 6.6. The horizontal axis is the average of the volume measure, and the vertical axis indicates the difference between manual and automatic measures (manual – automatic). It can be seen that FAST generated relatively large errors as compared to AFINITI. Meanwhile, as stated in the above discussions, AFINITI tends to yield less volume because of the detailed segmentation of enhanced tumor regions (see Fig. 6.5 for details).

Finally, it is worth noting that the automatic process of AFINITI took approximately 20 min for each dataset using a workstation with 1.86G Hz Intel Core 2 CPU and 2 GB RAM, and the average interactive refinement process took approximately 4 min of operator time. In contrast, the time required for manual segmentation of the dataset varied considerably, depending on the attributes of the tumor, ranging from 30 to 90 min. In the proposed clinical workflow, the scanned data would be first automatically routed to the AFINITI workstation for data processing prior to study interpretation, and the segmented AFINITI output would be transferred as a new additional series of images onto the PACS server along with the quantitative measurement of the tumor. The interpreting radiologists would examine the overlays to confirm the accuracy of

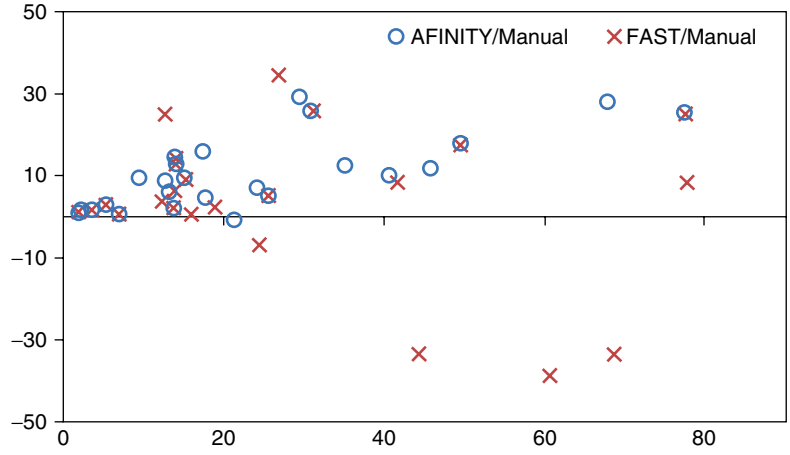

Fig. 6.6 Bland-Altman plots of the volume measures between AFINITI and manual results and between FAST and manual results, respectively [41]

automatic segmentation and incorporate the volumetric output into the clinical report as part of the standard workflow.

Evaluation of the software by comparison of volumetric output with manual segmentation of the same clinical dataset showed a significant linear correlation and high degree of overlapping. Although the process time used for manual operation was not rigorously evaluated, use of the system reduced clinical operator time required for segmentation and quantitation from approximately 30–90 min per case to less than 4 min in the roughly 8 % of cases that required correction and to less than 1 min in the majority of cases where the AFINITI output did not require correction. It is not clear how the average processing time using software based on the AFINITI method would compare with currently available commercial software for assisted manual segmentation. Clearly, recently released commercial tools would be expected to substantially decrease operator time compared with the open-source tools used in this study, but it seems unlikely that even these tools could achieve a lower average operator time for segmentation and quantitation than what the AFINITI method provides. The software package was evaluated using the typical clinical MRI data, although ideally the robustness of the algorithm can be tested with different protocols. Due to the availability of manual results, we did not compare the accuracy for different groups of protocols. This could be a future work by using clinical studies from multiple scanners.

Nevertheless, the fraction of cases that require operator correction are clearly an area that requires further development, possibly with incorporation of additional data types. In addition, the processing time of 20 min is significant, although, since this is proposed to occur offline prior to expert interpretation, it is not a critical problem for current diagnostic imaging workflow. This processing speed and the user-friendliness of the graphical interface need to be further improved for full clinical translation of the methods presented as will production of FDA-approved software tools. Both of these improvements and full translation will require product development resources that are beyond the scope of our lab, so we are releasing the AFINITI software pipeline free of charge on our website http://www.cbi-tmhs.org/AFINITI/ in the hope that other groups will be able to extend our work and that its availability will motivate the development of fully translatable clinical tools.

An additional significant weakness is that 2D input data was used for the T2-weighted image analysis, which has large separation between slice thickness (5 ~ 6 mm). 3D T2-weighted whole brain image data was not available routinely at the time that the initial datasets were acquired for this study, but because of rapid progress in 3.0 T MRI, they are now routinely available for clinical brain imaging. Adaptation of the software to perform segmentation on high-resolution 3D T2-weighted image datasets is important because inclusion of such datasets would allow automated

assessment of infiltrative progression as required for use of the recently proposed RANO criteria for brain tumor follow-up and would allow automated computation of recently proposed image metrics such at rNTR that may be more predictive of patient outcome [9].

The automatic tumor delineation pipeline could be applied in clinics by first automatically routing the scanned data to the AFINITI workstation for automatic data processing prior to study interpretation. After this, the segmented AFINITI output will be superimposed on the original MRI images, and new images are generated with new series numbers under the same patient ID. The data are then transferred onto the PACS server along with the quantitative measurement of the tumor. The interpreting radiologists would examine the overlay images together with the original sequences for diagnosis and for incorporating the volumetric measures into the clinical report as part of the standard workflow.

Currently, after segmentation, quantitative measures of tumor can be obtained, relieving the tedious work load for manual segmentation. The quantitative measures can be used in a follow-up study that precisely gives the temporal changes for tumor evaluation. In the long run, we foresee that computational image analysis could provide more detailed measures after segmentation, such as heterogeneity measures, transition from enhanced tumor to necrosis, and transition from enhanced tumor to edema. Generally, in contrast-enhanced MR images, GBM consists of enhancing tumor, necrosis, and non-enhancing tumor, including edema. In multimodal MR, enhanced tumor can be clearly seen from T1 post-contrast images but non-enhanced tumor often overlaps with edema by visual assessment. Quantitative segmentation is thus important to segment GBM in detail and to help neuroradiologists determine the tumor margin and determine the aggressiveness of GBM.

6.2.4 Improvement of Level Set Segmentation to 4D

The GBM segmentation can also be improved for semiautomatic segmentation of brain tumor from T1 images in serial MR images, called prior information constrained evolution (PICE) [43]. First, PICE uses a level set framework not only based on image gradient but also based on intensity distribution inside and outside brain tumor, which is estimated using nonparametric density estimation. Then, we show that this framework can be extended to tumor segmentation for longitudinal images so that the prior distribution consists of the intensity distribution in the current image can also contain information obtained from other time-point images. For a single-time-point image, the evolution of the level set is based on the image gradient and the intensity distribution of the current image. For serial images, the prior information obtained from the images of the same patient at other time points is added to the level set evolution for more longitudinally consistent segmentation. In experiments we compared PICE with the traditional level set method in 3-D. In addition, we also illustrate that it can be easily extended to 4-D images, which facilitates follow-up studies of brain tumor treatments. Using longitudinal glioblastoma data from five patients, we showed the advantages of the proposed algorithm.

The proposed method aims to segment brain tumor semiautomatically from T1-weighted MR brain images. Our approach is a combination of the image gradient information and the image intensity information in the level set formulation. In level set methods, the basic idea is that a contour C can be represented by the zero-level set of a higher dimensional function $\phi:\Omega\rightarrow R$ in the image domain Ω. The embedding function can be defined as the signed distance function (SDF) with $\phi<0$ inside the contour and $\phi>0$ outside the contour. The contour is propagated by evolving the embedding function ϕ according to an appropriate partial differential equation (PDE). The PDE can be directly derived from the energy function $E(\phi)$ defined on the space of the image domain.

6.2.4.1 3-D PICE

For tumor segmentation from single-time-point 3-D images, gradient and intensity distribution of brain tumor can be combined in the evolution with the energy function:

$$E(\phi) = \int_{\Omega} v\left|\nabla H(\phi)\right| \mathrm{d}x + \alpha E_{\mathrm{g}} + \beta E_{\mathrm{p}}, \quad (6.1)$$

where the first term guarantees a smooth zero-level set function and the second term E_g is the gradient term ensuring that the image gradients along the zero-level set are larger than others. The last term E_p is the intensity prior term used to constrain the intensity distribution inside and outside tumor. The level set function can be calculated by minimizing the energy function $E(\phi)$. The gradient term E_g is defined as follows:

$$E_{\mathrm{g}}(\phi) = \int_{\Omega} g\delta(\phi)\left|\nabla\phi\right| \mathrm{d}x, \quad (6.2)$$

where δ is the Dirac function, g is the boundary indicator function $g = 1/1 + |\nabla G * I(x)|^2$, and G is the Gaussian function. $I(x)$ is the image intensity at voxel x. It can be seen that this energy term can be minimized when the zero-level set matches the boundaries in image I. For the prior intensity information, in the Bayesian framework, this can be computed by maximizing the posterior distribution:

$$P(\phi|I) = P(I|\phi)P(\phi), \quad (6.3)$$

where $P(I|\phi)$ is the conditional distribution of image intensities given the current zero-level set ϕ. $P(\phi)$ is the shape prior. Because in tumor segmentation the shape prior is unknown, the energy term E_p can be calculated as

$$E_p = -\int_{\Omega} \log P(I|\phi) \mathrm{d}x, \quad (6.4)$$

Using the Heaviside step function $H()$, the energy term ends up with

$$E_p = -\int_{\Omega} \big(H(\phi)\log P_{\mathrm{out}}(I|\phi) + (1 - H(\phi))\log P_{\mathrm{in}}(I|\phi)\big)\mathrm{d}x, \quad (6.5)$$

where $P_{in}(I|\phi)$ and $P_{out}(I|\phi)$ are the conditional distribution of image intensities inside and outside of the zero-level set function. It can be seen that the difference of this method with other methods is that it combines both boundary information and intensity distribution in one evolution and uses nonparametric density estimation for distribution estimation.

6.2.4.2 4-D PICE

In this section we show that PICE can be easily extended for 4-D tumor segmentation. One of the important applications of tumor segmentation is follow-up study, wherein longitudinal changes are the important measures. Although registration of longitudinal images is necessary for this application, the accuracy is not very important since we only need to establish correspondence of tumor, not the tumor boundaries. Thus the image intensity information of the tumor at different time points can then be used for tumor segmentation. Notice that the tumor shapes can be different and the intensity information might be more consistent. Intuitively our rationale is that by correlating the intensity distribution among different time points, the segmentation criteria tend to be the same at different time points and thus yield relatively stable segmentation results across different time points.

Specifically E_p in Eq. (6.1) needs to consider not only the intensity information from the current time-point image but also the intensity distribution from other time-point images. Therefore, Eq. (6.3) can be rewritten as

$$P(\phi|I,\tilde{\phi},\tilde{I}) = P(I|\phi,\tilde{\phi},\tilde{I})P(\phi|\tilde{\phi},\tilde{I}), \quad (6.6)$$

where $\tilde{\phi}$ and $\tilde{I}$ reflect the segmentation results and the images at other time points. In Eq. (6.6), $P(\phi|\tilde{\phi},\tilde{I})$ can be omitted since we do not want to enforce any temporal shape constraints on the longitudinal tumor shapes. However, for the same patient, our rationale is that the intensity information within the brain tumor might be longitudinally similar which can help to improve the longitudinal consistency in segmenting tumors in different time points. Based on this observation, Eq. (6.6) becomes

$$P(I|\phi,\tilde{\phi},\tilde{I}) \quad P(I|\phi)P(I|\tilde{\phi},\tilde{I}), \quad (6.7)$$

where the constraints of image information from other time-point images can be reflected by the prior probability $P(I|\tilde{\phi},\tilde{I})$ and $P(I|\phi)$ is the same as Eq. (6.3). The prior probability is divided into two parts: inside the tumor and outside the tumor or ϕ. We use the histograms of the inside and outside as the prior information

obtained from other time-point segmentation results. So $P(I|\tilde{\phi},\tilde{I})$ can be written as

$$P(I|\tilde{\phi},\tilde{I})=P(h_{\text{in}},h_{\text{out}}|\tilde{h}_{\text{in}},\tilde{h}_{\text{out}})=P(h_{\text{in}}|\tilde{h}_{\text{in}})p(h_{\text{out}}|\tilde{h}_{\text{out}}),$$

assuming that the two conditional distributions are independent and can be separated. In this work for convenience of calculation, we only consider the histogram inside the tumor, $P(I|\tilde{\phi},\tilde{I})=P(h_{in}|\tilde{h}_{in})$, since the selection of corresponding regions outside tumor is ad hoc. Thus the energy function $E(\phi)$ in Eq. (6.1) can be written as

$$\begin{aligned}E(\phi) &= \nu\int_{\Omega}|\nabla H(\phi)|dx+\alpha\int_{\Omega}g\delta(\phi)|\nabla\phi|dx\\ &\quad-\beta\int_{\Omega}(\log(P(I|\phi))+\log(P(h_{\text{in}}|\tilde{h}_{\text{in}})))dx,\end{aligned} \tag{6.8}$$

where h_{in} represents the histogram of image intensity inside the tumor at the current time point and $\tilde{h}_{\text{in}}$ is the histogram of image inside $\tilde{\phi}$ at another time point. This term involves the information in other time points and can be calculated as

$$\begin{aligned}\frac{\partial P(h_{in}|\tilde{h}_{in})}{\partial\phi} &= \delta(\phi)\int\text{sign}(F(y)\\ &\quad-F_i)(y)(H(y-I(x))\\ &\quad-F(y))\text{dy},\end{aligned} \tag{6.9}$$

where y is the range of intensity, such as [0,…, 255]. $F(y)$ is the integrate of histogram of image in the current time point. This term ensures that the tumor intensity distributions at different time points for the same patients are similar. Notice that $P(h_{\text{in}}|\tilde{h}_{\text{in}})$ can be calculated not only from one image but also from multiple images at different time points.

In order to achieve the proposed algorithm, image registration is necessary for serial images of the same patient. Given a series of MRI images I_n, $n=1,\ldots,N$, all the subsequent images were first globally aligned onto the space of the baseline by applying the rigid registration in FLIRT. This is accurate enough to build the correspondence among the tumor regions at different time points.

6.2.4.3 Results

The experiment consists of two parts. One is the segmentation of GBM from single-time-point images. Another one is the serial image segmentation. The dataset contains the MRI image from five patients, and every patient has two time-point images. For each patient, the images are either longitudinal images before resection or those after resection. Currently the proposed PICE does not apply to the longitudinal data containing both images before and after resection. The MRI images of each patient are acquired on a 1.5 T GE signal MR scanner. Images are T1 modality with a high resolution of $256\times256\times124$ or $192\times256\times128$. The voxel size is $0.94\times0.94\times1.50$ mm^3.

In our experiments, we found that the traditional level set method can derive good results if the tumor intensity is homogeneous, e.g., when the tumor is brighter than the tissues around it, and it did not work well when both bright and dark regions are present in the tumor, i.e., it can't handle the inhomogeneous tumor due to complexity of edges. In comparison, using the same seed points inside the tumor, the results from PICE show that it can segment tumor well from single-time-point 3-D MRI images, even the intensity of the tumor vary complex. Figure 6.7 gives an example. Quantitatively, for all the ten testing images, compared to the manually marked ground truth, the volumetric ratios of the automatically segmented tumors with respect to the manual tumors are $98.3\pm.2$ % for PICE and 87.8 ± 4.7 % for the traditional level set algorithm. It can be seen that PICE obtains very accurate segmentation results and significantly improves the performance of the traditional level set method ($p<0.05$).

The PICE algorithm was then used to segment tumor from longitudinal images. Figure 6.8 shows the segmentation results of a patient at different time points using 4-D PICE. Quantitatively, in terms of volumetric ratios of the segmented tumors with respect to the manual results, they are actually very similar to those of the 3-D cases, and we did not find significant differences between them. In fact, the improvement might be in the subtle temporal stability in tumor follow-up study, and two time points are limited to test this factor. More tests will be done after sufficient data are collected.

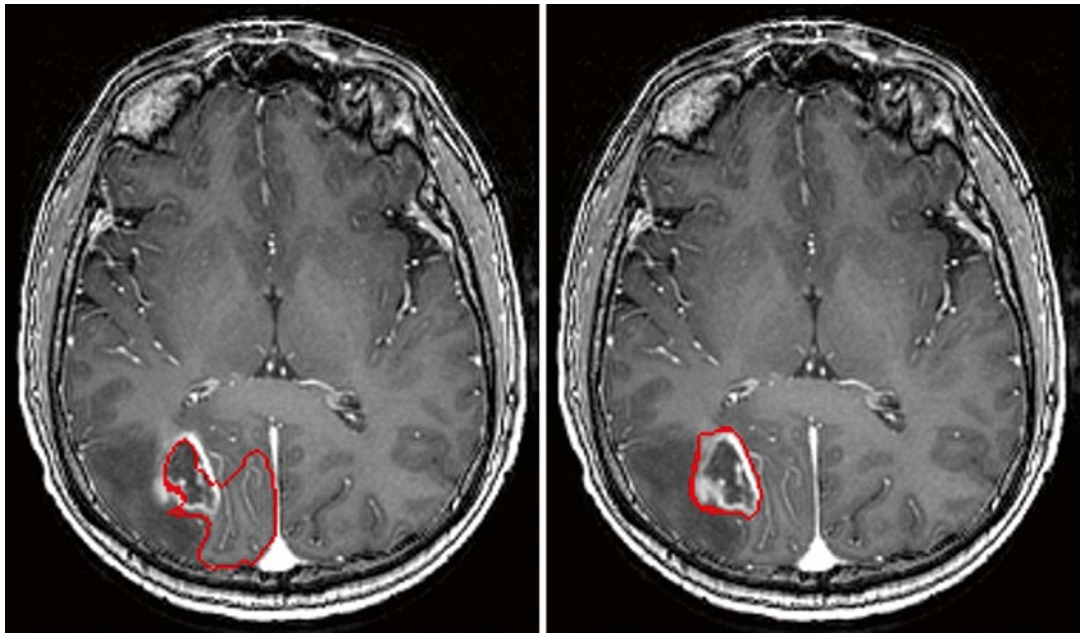

Fig. 6.7 Example of the segmentation results by traditional level set method (*left*) and PICE (*right*). The *red* contour is the boundary of the segmentation result [43]

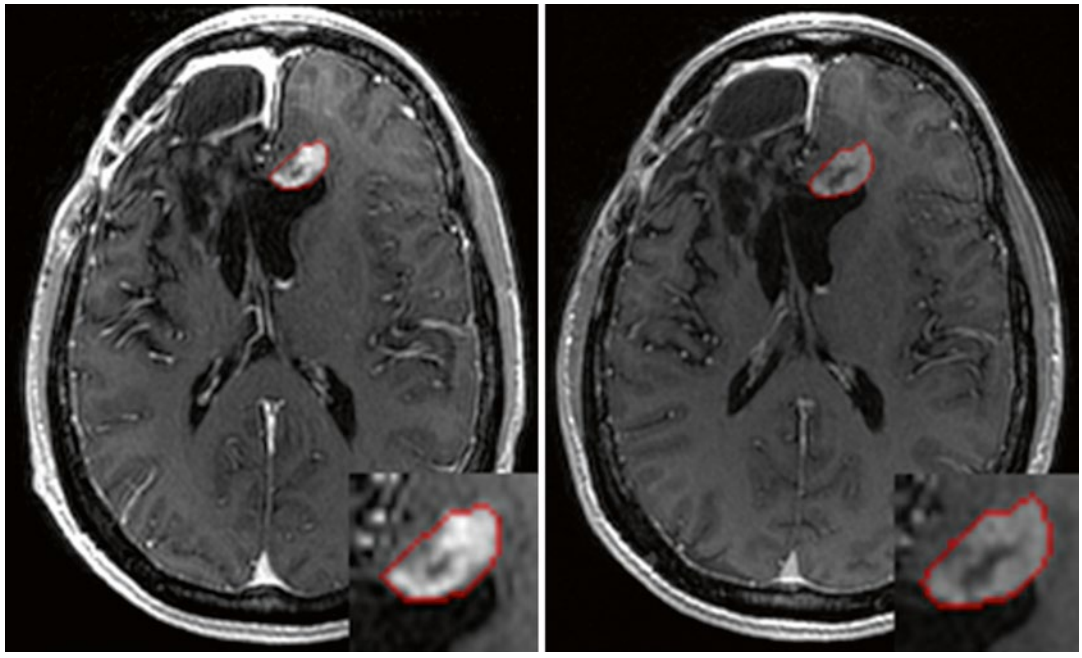

Fig. 6.8 Segmentation results illustrated on globally aligned images. *Left* is the result at time point 1; *right* is the result at time point 2 [43]

6.2.5 Concluding Remarks on AFINITI for GBM Applications

We presented an image computing pipeline for GBM segmentation and demonstrated its applicability to clinical data. The software adopts the current state-of-the-art tumor segmentation algorithms and combines the advantages of the traditional voxel-based and deformable shape-based segmentation methods. This provides automatic tumor segmentation based on both T1- and T2-weighted MR brain data, with graphical and numerical output that can be visualized and interactively refined using the embedded GUI based on the ITK-SNAP framework. Finally, the software was incorporated into a conventional PACS-based MRI interpretation workflow. Validation of results using clinical GBM data showed high correlation between the AFINITI results and manual annotation and suggested significant reduction in operator time for performing volumetric quantitation of GBM. The AFINITI pipeline is freely available from our public website (see http://www.cbi-tmhs.org/Projects/AFINITI/).

6.3 Tumor Follow-Up Study: Examples of PET/CT Dual-Modality Imaging

6.3.1 Introduction

Lymphoma is a hematologic malignancy of lymphocyte origin, accounting for approximately 5 % of all cancers in the United States [44]. Classically, lymphomas are classified as Hodgkin's disease (HD) or non-Hodgkin's lymphoma (NHL) with several subclassification schemes to describe various cellular, genetic, and clinical subtypes [45]. Treatment for lymphoma is dependent on its type and stage, as well as the age and general clinical status of patients. For most early-stage lymphomas, standard first-line therapy for lymphoma includes chemotherapy with or without radiation therapy [46]. Immunotherapy and hematopoietic stem-cell transplantation have added to the oncologic armamentarium particularly for patients with aggressive or advanced disease. Adoptive immunotherapeutic approaches using genetically modified cytotoxic T lymphocytes (CTL) with engineered tumor-antigen-recognizing receptors have shown promising preclinical and clinical results to date [47–50]. The Epstein-Barr virus (EBV) is known to be associated with a high percentage (up to 40 %) of HD and NHL [51]. Thus, viral-expressed proteins represent highly specific antigen targets. Recently engineered CTLs that recognize an EBV protein, called LMP2, can produce complete responses in HD and NHL patients [52].

Accurate monitoring of patients undergoing adoptive CTL therapy is critical for evaluating response and disease recurrence. The diagnostic gold standard, tissue biopsy, is both invasive and logistically difficult to perform on all patients at specific time intervals. Treatment responses are currently assessed by a canonical approach that integrates clinical examination, laboratory findings, and imaging data. The preferred imaging technique is PET/CT, which combines metabolic information using the positron-emitting sugar analog, [F-18]-fluorodeoxyglucose (FDG), with morphologic changes in tumor size acquired from conventional CT [53–59]. Relative FDG uptake in lesions of active high-grade lymphomas is typically high thus allowing for semiquantitative assessment of disease status [60]. However, interpretation of PET/CT studies is dependent on non-standardized criteria for assessing relative tumor metabolism and methods for measuring mass lesions, both of which are manually performed and calculated. Moreover, diagnostic PET/CT scans acquired at periodic intervals generate a massive amount of data, which require manual selection of regions of interest (ROI) for comparative and quantitative analyses. Currently clinical investigators are hampered by the absence of validated quantitative methods for evaluating therapy response in a comprehensive format. For example, in assessing longitudinal PET/CT imaging data, oncologists generally refer patients to radiologists or nuclear medicine physicians, who then generate interpretations in their standard reporting format. However, conventional diagnostic reports generally do not describe all

detectable lesions, and there is usually no quantitative longitudinal comparison. Furthermore, the presence of the adoptively transferred T cells at disease sites may give false-positive results on PET requiring prolonged follow-up on imaging. Thus there is an urgent need to develop robust methods and tools for quantitative assessment of therapeutic response.

Several methods have been developed to evaluate the treatment response in patients with lymphoma [61–68]. Although computer-aided methods for lymphoma segmentation [69, 70] and longitudinal CT analysis exist [71], these methods apply global affine transformation or pairwise free-form deformable registration for processing longitudinal image data, and there is a lack of longitudinal stability in the quantitative analysis. Traditional pairwise [72, 73] and groupwise [74] image registration algorithms have been used for image alignment; however, the pairwise algorithms warp each image separately and often cause relatively unstable measures of the serial images because no temporal information of the serial images has been used in the registration procedure. Groupwise image registration methods simultaneously process multiple images but consider the images as a group, not a time series. Thus the temporal information has not been used efficiently. For longitudinal images, the relationship between temporally neighboring images is much more important than that of the images with larger time intervals.

In this work the recently developed joint serial image registration and segmentation algorithm for longitudinal CT data [75] is used in the computer-assisted quantitative analysis for lymphoma treatment monitoring. This longitudinal image navigation and analysis (LINA) software tool [76] facilitates the quantitative evaluation of treatment outcomes for lymphoma patients using a computer-assisted serial image analysis approach and automatically constructs the longitudinal correspondences along serial images for each individual patient. In this way, it is possible to automatically determine ROIs in the serial images after defining them at each time point using a semiautomated segmentation algorithm.

In experiments, we applied the proposed methodology to the datasets of patients with lymphoma in the clinical trial investigating LMP-specific CTLs in patients with relapsed EBV-positive lymphoma (ClinicalTrials.gov Identifier: NCT00671164). Two sets of experiments were performed to validate the method. In the first experiment, we tested the accuracy of the registration method using simulated serial lung CT images with known ground truth about the deformation. The results show that the average error using the longitudinal deformable registration on ten randomly simulated images was 3.3 mm. The second experiment calculated the errors of all the maximum of standardized uptake value (SUVmax) within each ROI determined by LINA and the semiautomatic/manual segmentation method, respectively. For all the ROIs of the nine patients studied in this section, the mean error of SUVmax between the automatic and the semiautomatic segmentation results was 0.02. Based on these measures, the longitudinal quantitative index curves showing treatment responses using the proposed method are also consistent with the semiautomatic method. Implementing the proposed serial image quantification approach into the LINA pipeline can therefore supply more accurate, complete, and intuitive assessments of the treatment responses in patients with lymphoma after CTL therapy.

6.3.2 Methods

PET/CT serial images of nine patients in the clinical trial (ClinicalTrials.gov Identifier: NCT00671164), administering LMP-specific cytotoxic T lymphocytes to patients with relapsed EBV-positive lymphoma, were acquired in an integrated PET/CT system (GE Discovery ST) with conventional dosing of ^{18}F-FDG (0.21 mCi/kg). Serial images of each patient consisted of two to six complete PET/CT datasets obtained at multiple time points. The resolution of CT images was 0.98 mm × 0.98 mm × 3.75 mm, and that of PET was 5.47 mm × 5.47 mm × 3.75 mm. The clinical protocol was approved by the Food and Drug Administration, the Recombinant

DNA Advisory Committee and the hospitals' Institutional Review Boards. Nine patients had active disease at the time of CTL therapy. Tumor samples had been established as EBV+ve, using immunohistochemistry for LMP-1, in situ hybridization for EBER, or both [77].

We developed an image computing tool (called LINA: longitudinal image navigation and analysis) to semiautomatically segment the lesions, to automatically calculate the longitudinal deformations for each image series, and to map the ROIs from one time point onto all other time points. Both the volumetric shape changes and longitudinal quantitative PET measures of each ROI can be visualized using LINA. The detailed steps are introduced in detail as follows. After global co-registration of the PET and CT images at each time point, ROIs and liver were segmented using a level set-based semiautomatic method. Longitudinal deformations of the serial data were automatically calculated. Then, any semiautomatically segmented ROI at one time point can be automatically mapped onto other time-point images to facilitate quantitative analysis.

After acquiring PET/CT scans, the first step is a global co-registration between reconstructed PET and CT images. Precise identification of the lymphoma region also requires the aid of CT images, which supply information regarding the precise anatomical structure and the lymphoma boundary. To facilitate their interpretation, it is necessary to co-register PET and CT images, thereby relating the metabolic activity (uptake pattern) from the PET scan to the morphologic information from the CT scan. Thus the combined imaging improves the accuracy of assessing pathologic versus physiologic uptake.

PET/CT images were co-registered based on maximization of normalized mutual information (NMI) using a global optimization method developed by Jenkinson et al. [78]. Affine transformation and trilinear interpolation were used in the multi-resolution implementation of the algorithm by combining a fast local optimization Powell's method [79]. Denoting the transformation between the CT I_t and PET P_t images at time point t as A_t, a voxel v in the CT image will correspond to voxel $u = A_t(v)$ in the PET image. All these transformation matrices were stored for constructing the longitudinal correspondences among the PET images by combining with the longitudinal.

To quantitatively analyze the treatment response in lymphoma patients, who received adoptive CTL therapy, ROIs of mass lesions needed to be visually identified in PET/CT images. These ROIs included lymph nodes and other lymphoid organs with increased PET activity. In our application, we segment two types of ROIs: (1) shapes or boundaries of ROIs that are clearly detectable, e.g., discrete lymph nodes, and (2) ROIs without discernable boundaries. We therefore used a level set-based semiautomatic ROI segmentation for this study. For the ROIs with clear boundaries on CT, we used the image boundary-based level set algorithm [80] to extract the ROI shapes with a proper initialization; for ROIs without discernable boundaries, manual segmentation will be used if the level set method fails.

Even with the help of the semiautomatic segmentation tool, the extraction of lymphoma regions is laborious, especially for patients requiring extensive serial imaging with a relatively large number of mass lesions (ROIs) in many sets of PET/CT images. Moreover, in order to calculate the longitudinal PET activity changes of each ROI, it is also necessary to construct their temporal correspondences. Generally, the images taken at the first time point are chosen as the baseline datasets, and the ROIs (possible lymphoma mass region and liver region) are semiautomatically segmented or manually marked from the fused PET/CT images at the baseline. Since the longitudinal deformations among each image series are known, these segmented ROIs can be deformed onto the images at other time points so that all corresponding ROIs in the follow-up images can be automatically extracted. Similarly, any new ROI that is only observable in a follow-up image can also be marked or segmented, which can then be automatically mapped onto the baseline and other time-point images.

We recently developed a serial CT image registration algorithm [75] to automatically align all the CT images of the same patient at different time points to automatically calculate the longitudinal correspondences. For serial image registration, the relationship between temporally neighboring images is much more important than that of the images with larger time intervals, since both anatomical structure and tissue properties of neighboring images tend to be more similar for neighboring images than others; moreover these temporal changes might be characterized using specific physical processes models. Therefore, we formulated the serial image registration so that the registration of the current time-point image is related to not only the previous but also the following images (if available). Given a series of CT images I_t, $t=0,1,\ldots,T$ (I_0 is usually called the baseline), all the subsequent images were first globally aligned onto the space of the baseline by applying the rigid registration in Insight Toolkit (ITK). Thus matrix $R_{0\to t}$ or R_t will reflect the transformation from time point 0 to time point t. In addition to the global transformation, we needed to estimate the deformations from the baseline onto each image, i.e., $\mathbf{f}_{0\to t}$ or simply denoted as $\mathbf{f}_t$. For the current CT image I_t, if the deformation of its previous image I_{t-1}, $\mathbf{f}_{t-1}$, and that of the next image I_{t+1}, $\mathbf{f}_{t+1}$, are known, the deformation $\mathbf{f}_t$ can be calculated by jointly considering both the previous and the next images and by minimizing:

$$E_t=\sum_{v\in\Omega}\left\{\left|e\left[I_t\left(\mathbf{f}_t\left(R_t\left(v\right)\right)\right)\right]-e\left[I_0\left(v\right)\right]\right|^2+\sum_{i=-1,1}\left|e\left[I_t\left(\mathbf{f}_t\left(R_t\left(v\right)\right)\right)\right]-e\left[I_{t+i}\left(\mathbf{f}_{t+i}\left(R_{t+i}\left(v\right)\right)\right)\right]\right|^2\right\} \tag{6.10}$$

where $e[]$ is the operator for calculating the features around each voxel of the image and Ω is the image domain. In this work, the feature vector for each voxel consisted of the image intensity, gradient magnitude, and the fuzzy membership functions obtained by performing a FCM algorithm on the images (assuming three tissue types: bone, low-intensity and high-intensity tissues), i.e., $e[v]=[I(v),\ |\nabla I(v)|\ ,\ \mu_{v,1},\ \mu_{v,2},\ \mu_{v,3}]$. Since the cubic B-Spline was used to model the deformation field, the continuity and smoothness was guaranteed; thus the regularization term of the deformation field was omitted. Further, we used a topological regularization step to ensure that the Jacobian determinants of the deformations fields were positive. In this way the topology of the deformation field did not change from one image onto the subsequent images. The serial image registration algorithm then iteratively refines the deformation field $\mathbf{f}_t$ of each time-point image by minimizing the energy function in Eq. (6.1) and performs 4-D clustering of the image series until convergence. Notice that in the first iteration, since the registration results for neighboring images were not available, only the first term of Eq. (6.1) was used, which is essentially a pairwise FFD [81].

After global co-registration and longitudinal deformable registration, correspondences among the CT image series were constructed, and all the ROIs segmented at one time-point image were automatically mapped onto other time points. Suppose an ROI r_0 has been obtained from the baseline CT image, the corresponding region in the baseline PET image will be $A_0(r_0)$. The corresponding region in the PET image at time t will be $r_t=A_t[\mathbf{f}_t(R_t(r_0))]$, where the global transformation from time point 0 to time point t, R_t, is first applied, followed by a deformable transformation $\mathbf{f}_t$, and finally the deformed ROI is transformed onto the PET space at time point t using A_t. If the ROI is not segmented at the baseline, it can also be automatically mapped onto other time points in a similar way. The reason that we combine the global transformations between CT and PET images, the global transformations between the baseline CT image and other time-point images, as well as the longitudinal deformation fields for the globally aligned CT images for mapping the ROI is that no interpolation on the PET images needs to be performed in order to obtain accurate SUV measures from PET images.

Our next step is to quantify the signals in PET image, given each region r_t at time t. In PET imaging, a radioactive material (e.g., FDG) is systemically administered by intravenous injection and allowed a period of cellular uptake of the compound (up to 40 min). Following this period, the patient is scanned in an instrument that detects positron annihilation 511 keV photons. FDG accumulates in cell through a mechanism involving glucose transport and phosphorylation by hexokinase, rending it trapped inside cells. Thus FDG concentration is proportional to the first biochemical steps in glucose metabolism. One widely applied semiquantitative method for measuring FDG activity is the maximum of standardized uptake value (SUV) [82–87], which relates the value of activity concentration found in a certain tissue to the injected activity per the patient body weight. The SUV of a voxel v in region r_t is calculated using attenuation-corrected images, injected dose of FDG and FMT, patient's body weight, and the cross calibration factor between PET and dose calibration [88] and is defined as follows:

$$\mathrm{SUV}(v) = \frac{\text{Radioactive concentration at } v\,(\mathrm{MBq/g})}{\text{Injected dose}\,(\mathrm{MBq})/\text{Patient body weight}\,(\mathrm{g})}. \tag{6.11}$$

As expected, higher SUV corresponds to greater metabolic activity. There is some evidence [86, 89] suggesting that an SUV greater than 2.5 indicates metastatic disease identified as suspected tumor sites. However, due to the interindividual differences and diffusion ability of radioactivity at different time points, a relative SUV value in an ROI should be compared with those in normal brain, liver, or heart organ region. Therefore, it is suggested that quantitative evaluation to determine the response to therapy in patients with lymphoma needs to refer to the SUV in normal and tumor tissue since different image reconstruction, processing techniques, patient conditions, and dose of radioactive drug may affect the specific numerical value of the SUV.

In our study, the ratio of maximum of SUV in an ROI versus the mean SUV of a liver region is employed as the quantitative index (QI) to quantify the therapeutic effect, which can be expressed by the following equation:

$$QI(r_t) = \frac{\mathrm{SUV}_{\max}}{\mathrm{SUV}_{\mathrm{mean}}} = \frac{\max_{v \in r_t}\{\mathrm{SUV}(v)\}}{\mathrm{mean}\left(\mathrm{SUV}\left(\mathrm{liver}_t\right)\right)}. \tag{6.12}$$

6.3.3 Results and Discussion

The LINA toolkit has been applied to lymphoma patient follow-up studies in the experiments. Patients included six men and three women. The median age was 29 (range 20–63). The total number of lesions identified on imaging was 34, and the mean number of lesions per patient was3.7 (range, 1–7 lesions). In the first experiment, we evaluated the accuracy of the longitudinal registration algorithm using chest lung CT images, and in the second experiment, the quantitative follow-up results of the proposed method are compared with the manual results.

The proposed longitudinal deformable registration algorithm has been evaluated by using randomly simulated lung CT images. First, for each series of the sample images, the demon's algorithm [90] was used to register the subsequent images onto the first time-point image. Then, one sample image was selected as the template image, and all the other first time-point images of other subjects were deformed onto the template space using the same deformable registration algorithm. Finally, the statistical model for the spatially warped/normalized temporal deformations was calculated, which was then used to randomly generate the longitudinal deformation of the template image. In this section, the statistical model of deformation (SMD) presented in [91] was used to train such a model. In this experiment we used the chest CT images obtained from The Methodist Hospital as our datasets, one image was selected as the template, and other 19 images were selected as the training samples. After applying the algorithm on the ten randomly simulated images, the registration

errors with the ground truth were calculated reflecting the accuracy of the registration. The results showed that the mean registration error (resolution 0.98 mm × 0.98 mm × 3.75 mm) was 3.3 mm. In general, the registration errors were found in less than the largest voxel spacing of the simulated images.

In the second experiment, we compared the proposed automatic ROI mapping based on longitudinal registration with the semiautomatic/manual segmentation methods for ROI. First, the FLIRT program [92] was used to co-register the PET/CT images at same time point. For each CT image, a radiologist delineated all the ROIs using our semiautomatic segmentation tools or manually. In the automatic ROI mapping method, the segmented ROIs from the baseline were automatically mapped onto all the CT images in the follow-up time points. Finally, the SUVs of each ROI were calculated in the original PET image space by transforming the corresponding regions to PET, so that no interpolation of the PET images is performed.

For a dataset with PET (image size 128 × 128 × 300) and CT (image size 512 × 512 × 300), the average time for co-registration was about 8 min on HP xw4400 workstation by using the FLIRT program. The time for deformable registration of two CT images was dependent on the sub-volume to be registered. For sub-volumes cut from the CT with size 256 × 256 × 70, the calculation time is less than 200 s.

We compared the results of automatic ROI mapping with the original semiautomatic/manual segmentation results, using SUV values of each region. The mean of the relative squared differences between two SUVmax values for all the regions of all the patients is calculated as follows:

$$error = \sum_{i \in N} \frac{\left(\mathrm{SUV}_{\max}(r_i) - \mathrm{SUV}_{\max}(\check{r}_i)\right)^2}{\left(\mathrm{SUV}_{\max}(r_i)\right)^2} \Big/ N, \tag{6.13}$$

where r_i and $\check{r}_i$ denote the segmentation results using the semiautomatic/manual segmentation and the proposed automatic mapping for the ith, respectively. N is the total number of ROIs under evaluation. For all the ROIs of the nine patients we studied, this average normalized squared difference is 0.02. Therefore, the computer-assisted quantitative analysis method obtains similar results with the "gold standard."

First, the semiautomatic and manual ROI segmentation are illustrated in Figs. 6.9 and 6.10, respectively. From Fig. 6.9a we can visually identify the region of interest, and then manual points are initialized inside the lymph nodes (Fig. 6.9b), and the algorithm automatically extracts the boundaries of the lymph nodes as shown in Fig. 6.9c. When the boundaries of an ROI are blurry, the level set algorithm normally leaks into a larger region, and a manual segmentation of the ROI is then applied. From Fig. 6.10a we identified a region of interest, but from the initial point shown in Fig. 6.10b, the level set segmentation leaks into a larger region in the CT image. Therefore manual segmentation of the ROI is necessary. Figure 6.10c shows the manually marked region.

It is worth noting that the PET signal can also be used to facilitate the segmentation process. For example, the level set evolution can stop to grow when the PET signal is weak. However, since the PET signal is the one that we need to measure, if the selection of ROI is dependent on the PET signal itself, it will introduce biased quantitative calculation. Thus in this study we used the strategy that the ROIs are only selected from the CT images.

Based on the proposed algorithm, a longitudinal imaging navigation and computing tool are developed. The key functions include a sophisticated data management system to facilitate quantitative longitudinal studies and statistical analysis, an exceptional 4-D viewer of longitudinal images with underlying longitudinal deformations and 4-D ROIs, and the quantitative results for the follow-up study of each patient. In this section, we introduce the visualization of some results. Compared to the radiological reports, the new tool will provide a platform for comprehensive dataset management.

Figure 6.11 shows an example with four time points, where lymph nodes can be clearly segmented. The first row shows the fused PET/CT images, where lymphoma region has obvious high intensity. The segmentation results

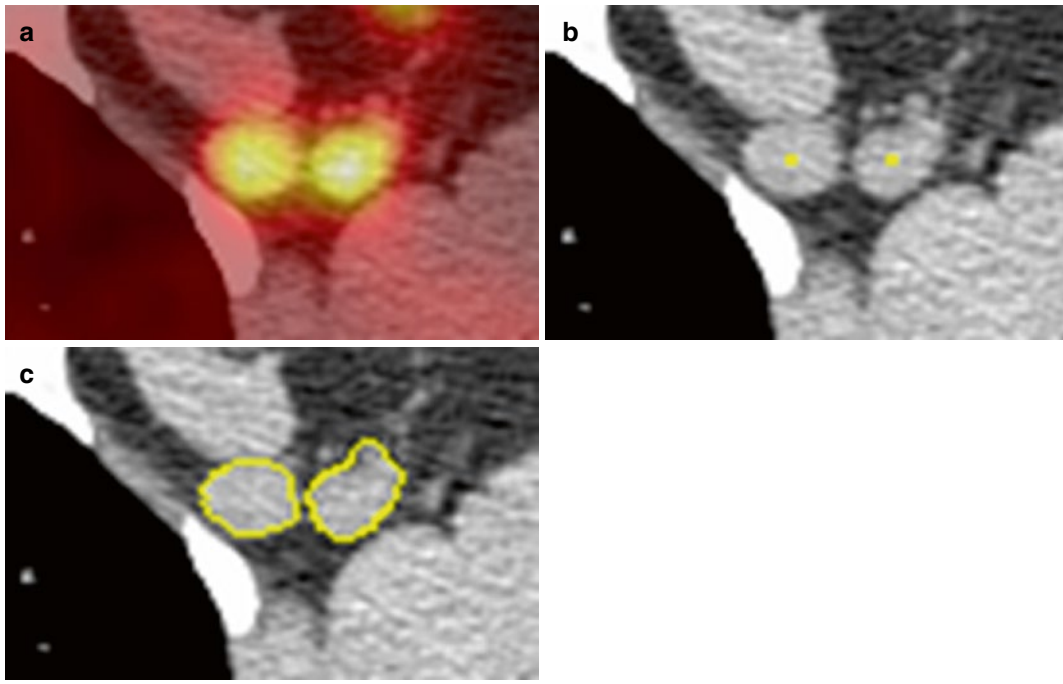

Fig. 6.9 Illustration of semiautomatic lymph node segmentation using level set method. (**a**) The region of interest is first identified by overlapping the PET with the CT; (**b**) an initial point is then manually marked for each lymph node from CT image; and (**c**) the level set method is applied to automatically extract the lymph nodes [76]

are shown in the second row, and the yellow curves illustrate the semiautomatic lymph node segmentation results. For the follow-up CT images, we applied the serial image registration algorithm and warped the baseline image onto each subsequent CT image shown in row 3. Correspondingly, the ROI at baseline can be transformed onto these CT images, shown as the green contours in row 3. At each follow-up time point, the warped baseline image appears similar to the CT image captured at that time point. By using the automatically mapped ROIs, SUV and QI measurements can be automatically generated for each case. These data can be used to quantitatively assess metabolic activity in specific lesions over multiple imaging datasets which is critical for evaluating therapy response. From the QI values given, we can see the positive response of the treatment quantitatively.

After calculation of QI (the ratio of maximal SUV of lesion to the mean SUV of the liver), they can be plotted longitudinally and supplied as quantitative response of treatment. Figure 6.12 shows some results in our datasets. Each figure shows the plots of QIs of all ROIs of one patient. For the same longitudinally corresponding ROI, we used lines with the same color to link them, and solid line shows the semiautomatic/manual results and dashed lines indicate the results of the automatic mapping results. The big solid circle markers indicate that semiautomatic/manual segmentations at that time point are automatically mapped onto other time points for automatic SUV calculation.

Figure 6.12a, b show two examples where semiautomatic segmentation of ROI is performed from the baseline. By comparing the solid lines with the dashed lines, it can be seen that the longitudinal QI values obtained by using both methods are in reasonable agreement. The longitudinal change of QI of each ROI indicates that these ROIs are obvious response to treatment within the first five and a half months, while the

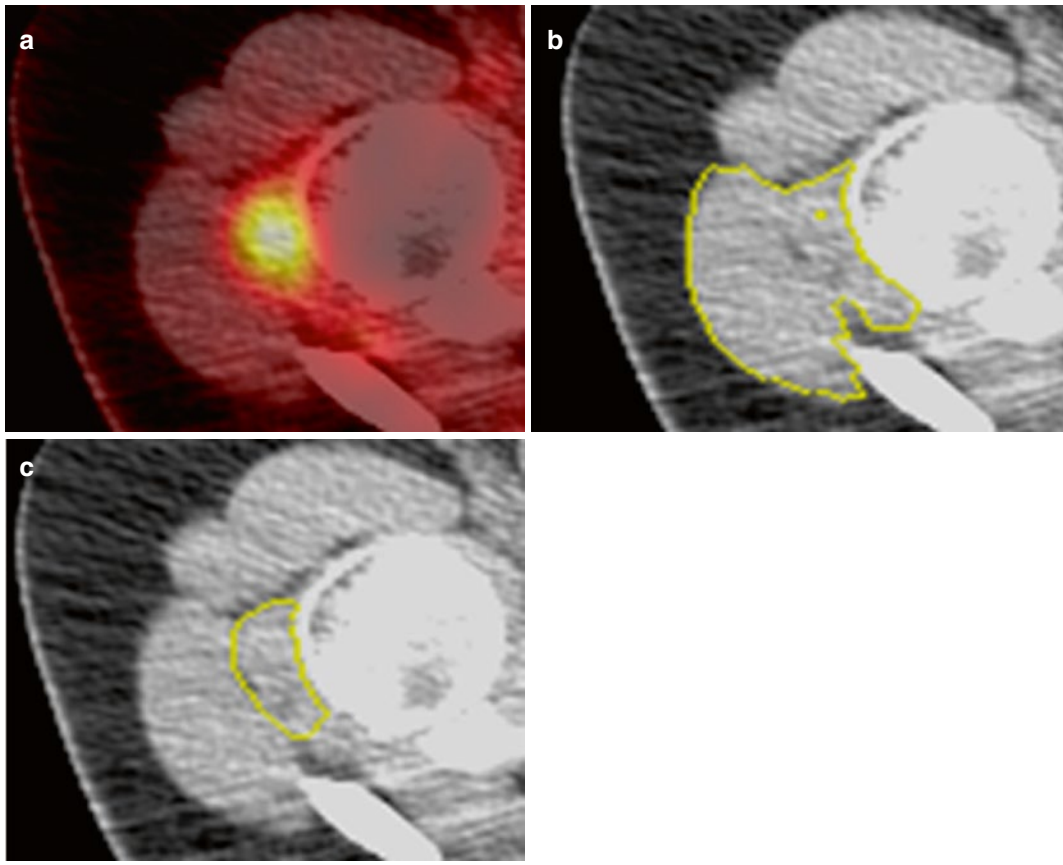

Fig. 6.10 An illustration of manual segmentation of ROI where boundaries are not clearly discernable, in which the semiautomatic method has failed. (**a**) The ROI is first identified by overlapping the PET with the CT; (**b**) the level-set segmentation leaks into a larger region in the CT image; and (**c**) the region of interest is then manually marked on the CT image by referring to (a) [76]

situation might become worse between 5.5 and 8.5 months. Figure 6.12c, d show two examples where it might be difficult to identify some ROIs in the images. Figure 6.12c shows the results of one patient with four ROIs at five time points, in which it is difficult to identify the ROIs at the fifth time point except for one. All the lesions are determined from the baseline image and the computer-assisted method can determine the corresponding lesions for all the follow-up studies, while it is difficult to even manually mark the lesion for some scans. The results show that our method can delineate other three ROIs at the fifth time point by using serial CT registration, which assists oncologist to quantitatively evaluate the treatment response. In Fig. 6.12d, two ROIs can be detected at the first time point (blue and red circle point indication), and the other two ROIs indicated by green and magenta circle points can be identified at the second time point. By using the proposed computer-assisted quantitative approach, we can automatically calculate the SUV values of along the image series and hence prove a comprehensive quantitative evaluation of the treatment outcomes of lymphoma. Figure 6.12c, d indicate that our proposed method enables to provide pro- and post-perspective analysis for treatment outcomes of lymphoma.

From the experimental results, one can see clearly that this method has the following advantages. Since lymphomas are often gathered together in some patients, it is difficult to map one-to-one

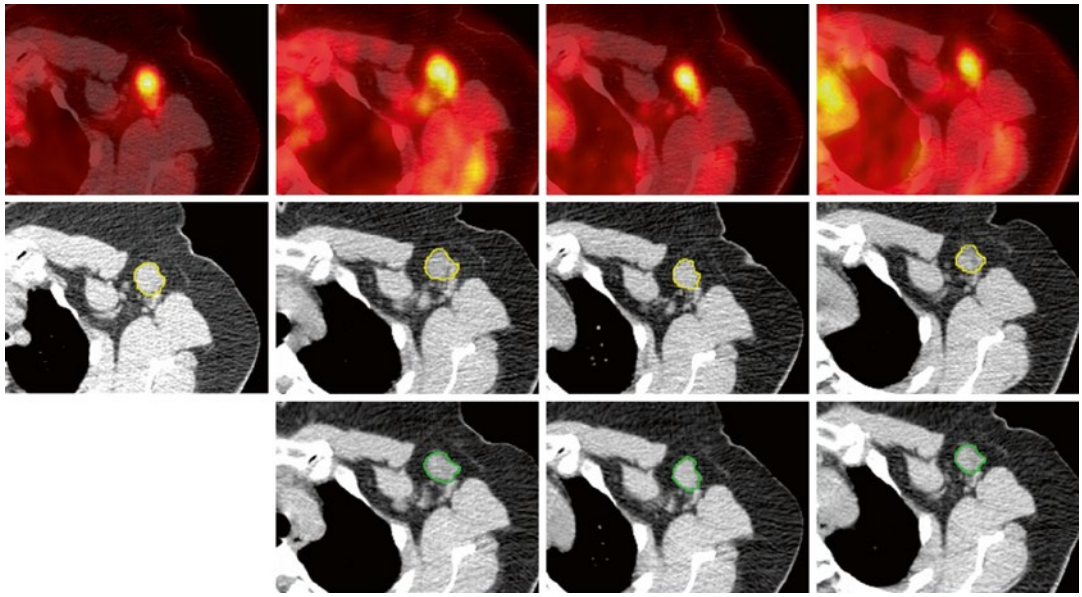

Fig. 6.11 Comparison of the semiautomatic segmentation of lymph node and the automatically mapped shapes. *Row* 1: Fused PET/CT images at different time points; *Row* 2: semiautomatically segmented lymph nodes; *Row* 3: the warped baseline CT image and the corresponding ROIs at subsequent time points. It can be seen that the QI of ROI decreases along with time/treatment [76]

correspondence among the lymphoma regions segmented by hand at different time points. Our method is able to automatically segmented ROIs from follow-up CT images by using ROI mapping based on the longitudinal correspondences, and it is more efficient to accomplish the goal of quantitative analysis; the novel analysis tool enables us to show the longitudinal image data with ROI in 4D. The volume and QI of ROIs can be visualized in time sequence. The plots of QI supply a quantitative evaluation means for treatment response of lymphoma. All these functions simplify the analysis and improve the efficiency of analysis.

In our experiments, the only one error occurred when the lesion size is small (<12 mm). There are several factors affecting this error. First, the precision of PET/CT co-registration will undoubtedly affect the accuracy of SUV calculation of lymphoma region especially when the lesion is small and does not have clear boundary from CT images. Another factor is that whether the automatically mapped ROIs are accurate enough to cover the PET peak region. Based on our validation of the algorithms, the matching accuracy for longitudinal CT series is about 3.3 mm for resolution $0.98 \times 0.98 \times 3.75$ mm, and it is less than one voxel size. Therefore, in the case where lesion size is small (<12 mm), we applied a relatively large ROI to cover the whole PET peak spot, i.e., grow the accurate ROI by 3.75 mm in all directions. In this way, all the 34 lesions can be successfully analyzed using our computer-assisted quantitative analysis tool.

6.4 Future Trends

Medical image computing has been widely used in clinical and preclinical assessment of cancer. This chapter presents the components and techniques of medical image computing and describes two representative applications in oncology, namely, one assists the neuroimaging follow-up during GBM Therapeutic

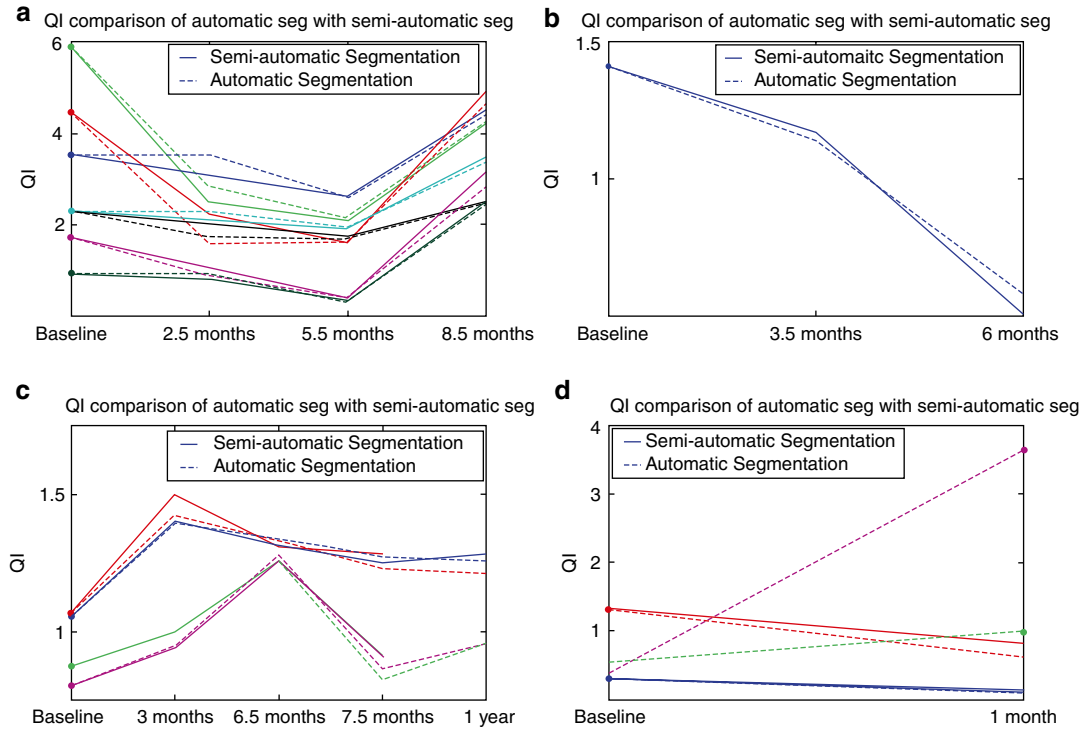

Fig. 6.12 Plots of longitudinal QI values of different patients for both semiautomatic segmentation method and the proposed computer-assisted method. (**a**) Six lesions, four time points; (**b**) one lesion, three time points; (**c**) four lesions, five time points; and (**d**) four lesions, two time points. In (**a**, **b**) all the lesions are determined from the baseline image, and no other new lesion is identified in follow-up studies; in (**c**), all the lesions are determined from the baseline image, and the computer-assisted method can determine the corresponding lesions for all the follow-up studies, while it is difficult to even manually mark the lesion for some scans; in (**d**), new lesions are identified at follow-up studies, and they can be mapped to the baseline using the proposed approach [76]

Intervention and the other enables computer-assisted quantitative analysis for lymphoma treatment monitoring. Among all the imaging modalities, ex vivo and in vivo microscopy and medical imaging are mostly used in research and clinics, respectively. The former can capture cellular and tissue-level morphometry and molecular activities while the latter images organ- and tissue-level properties. One notable trend is to combine the macro- and microscale imaging information that would help better diagnose, subtype, and quantify the formulation, progression, and mechanism of various types of cancers. Imaging is also commonly used for drug discovery, starting from microscopic imaging in vitro and then quantifying the therapeutic response in tissue and tumor level.

Acknowledgements The research is supported by NLM G08-LM008937, CPRIT RR100627, and JS Dunn Research Foundation. The authors would like to thank the contribution of Tiancheng He, Ph.D.; Po Su, M.E.; Ying Zhu, M.Sc.; Yong Zhang, Ph.D.; XinGao, Ph.D.; and Hai Li, Ph.D. in the development of AFINITI and LINA systems, as well as Geoffrey Young, M.D., of Brigham and Women's Hospital in the consultation of AFINITI and Stephen Gottschalk and Catherine Bollard, M.D., of Texas Children Hospital in the consultation of LINA.

References

1. Wong ST, Huang HK. Design methods and architectural issues of integrated medical image data base systems. Comput Med Imaging Graph. 1996;20(4):285–99. Epub 1996/07/01.
2. Wong ST, et al. Design and applications of a multimodality image data warehouse framework. J Am Med Inform Assoc. 2002;9(3):239–54. Epub 2002/04/25.

3. Stupp R, et al. Radiotherapy plus concomitant and adjuvant temozolomide for glioblastoma. N Engl J Med. 2005;352(10):987–96.
4. Van Meir EG, et al. Exciting new advances in neuro-oncology: the avenue to a cure for malignant glioma. Cancer J Clin. 2010;60(3):166–93.
5. Topkan E, et al. Pseudoprogression in patients with glioblastoma multiforme after concurrent radiotherapy and temozolomide. Am J Clin Oncol. 2012;35(3):284–9.
6. Pope WB, et al. MRI in patients with high-grade gliomas treated with bevacizumab and chemotherapy. Neurology. 2006;66(8):1258–60.
7. Vredenburgh JJ, et al. Phase II trial of bevacizumab and irinotecan in recurrent malignant glioma. Clin Cancer Res. 2007;13(4):1253–9.
8. Vredenburgh JJ, et al. Bevacizumab plus irinotecan in recurrent glioblastoma multiforme. J Clin Oncol. 2007;25(30):4722–9.
9. Norden AD, et al. Bevacizumab for recurrent malignant gliomas: efficacy, toxicity, and patterns of recurrence. Neurology. 2008;70(10):779–87.
10. Macdonald DR, et al. Response criteria for phase II studies of supratentorial malignant glioma. J Clin Oncol. 1990;8(7):1277–80.
11. Wen PY, et al. Updated response assessment criteria for high-grade gliomas: response assessment in neuro-oncology working group. J Clin Oncol. 2010;28(11):1963–72.
12. Galanis E, et al. Validation of neuroradiologic response assessment in gliomas: measurement by RECIST, two-dimensional, computer-assisted tumor area, and computer-assisted tumor volume methods. Neuro Oncol. 2006;8(2):156–65.
13. Sorensen AG, et al. Comparison of diameter and perimeter methods for tumor volume calculation. J Clin Oncol. 2001;19(2):551–7.
14. Gladwish A, et al. Evaluation of early imaging response criteria in glioblastoma multiform. Radiat Oncol. 2011;6:1–7.
15. Ellingson BM, et al. Quantitative volumetric analysis of conventional MRI response in recurrent glioblastoma treated with bevacizumab. Neuro Oncol. 2011;13(4):401–9.
16. Corso JJ, et al. Efficient multilevel brain tumor segmentation with integrated Bayesian model classification. IEEE Trans Med Imaging. 2008;27(5):629–40.
17. Vaidyanathan M, et al. Monitoring brain tumor response to therapy using MRI segmentation. Magn Reson Imaging. 1997;15(3):323–34.
18. Vaidyanathan M, et al. Comparison of supervised MRI segmentation methods for tumor volume determination during therapy. Magn Reson Imaging. 1995;13(5):719–28.
19. Fletcher-Heath LM, et al. Automatic segmentation of non-enhancing brain tumors in magnetic resonance images. Artif Intell Med. 2001;21(1–3):43–63.
20. Phillips 2nd WE, et al. Application of fuzzy c-means segmentation technique for tissue differentiation in MR images of a hemorrhagic glioblastoma multiforme. Magn Reson Imaging. 1995;13(2):277–90.
21. Moonis G, et al. Estimation of tumor volume with fuzzy-connectedness segmentation of MR images. AJNR Am J Neuroradiol. 2002;23(3):356–63.
22. Emblem KE, et al. Automatic glioma characterization from dynamic susceptibility contrast imaging: brain tumor segmentation using knowledge-based fuzzy clustering. J Magn Reson Imaging. 2009;30(1):1–10.
23. Clark MC, et al. Automatic tumor segmentation using knowledge-based techniques. IEEE Trans Med Imaging. 1998;17(2):187–201.
24. Prastawa M, et al. A brain tumor segmentation framework based on outlier detection. Med Image Anal. 2004;8(3):275–83.
25. Prastawa M, et al. Automatic brain tumor segmentation by subject specific modification of atlas priors. Acad Radiol. 2003;10(12):1341–8.
26. Kaus MR, et al. Automated segmentation of MR images of brain tumors. Radiology. 2001;218(2):586–91.
27. Warfield SK, et al. Adaptive, template moderated, spatially varying statistical classification. Med Image Anal. 2000;4(1):43–55.
28. Kass M, et al. Snakes: active contour models. Int J Comput Vis. 1988;1:321–31.
29. Rivest-Henault D, Cheriet M. Unsupervised MRI segmentation of brain tissues using a local linear model and level set. Magn Reson Imaging. 2011;29(2):243–59.
30. Wang L, et al. Level set segmentation of brain magnetic resonance images based on local Gaussian distribution fitting energy. J Neurosci Methods. 2010;188(2):316–25.
31. Chen Y, et al. An improved level set method for brain MR images segmentation and bias correction. Comput Med Imaging Graph. 2009;33(7):510–9.
32. Hu S, Collins DL. Joint level-set shape modeling and appearance modeling for brain structure segmentation. Neuroimage. 2007;36(3):672–83.
33. Cheng L, et al. A generalized level set formulation of the Mumford-Shah functional for brain MR image segmentation. Inf Process Med Imaging. 2005;19:418–30.
34. Vese LA, Chan TF. A multiphase level set framework for image segmentation using the Mumford and Shah model. Int J Comput Vis. 2002;50(3):271–93.
35. Cheng LS, et al. A generalized level set formulation of the Mumford-Shah functional with shape prior for medical image segmentation. Comput Vis Biomed Image Appl Proc. 2005;3765:61–71.
36. Dydenko I, et al. A level set framework with a shape and motion prior for segmentation and region tracking in echocardiography. Med Image Anal. 2006;10(2):162–77.
37. Rousson M, Cremers D. Efficient kernel density estimation of shape and intensity priors for level set segmentation. Med Image Comput Comput Assist Interv. 2005;8(Pt 2):757–64.

38. Smith SM, et al. Advances in functional and structural MR image analysis and implementation as FSL. Neuroimage. 2004;23 Suppl 1:S208–19.
39. Woolrich MW, et al. Bayesian analysis of neuroimaging data in FSL. Neuroimage. 2009;45(1 Suppl): S173–86.
40. Yushkevich PA, et al. User-guided 3D active contour segmentation of anatomical structures: significantly improved efficiency and reliability. Neuroimage. 2006;31(3):1116–28.
41. Zhu Y, et al. Semi-automatic segmentation software for quantitative clinical brain glioblastoma evaluation. Acad Radiol. 2012;19(8):977–85.
42. Zhang Y, et al. Segmentation of brain MR images through a hidden Markov random field model and the expectation-maximization algorithm. IEEE Trans Med Imaging. 2001;20(1):45–57.
43. Xue X, et al., editors. PICE: prior information constrained evolution for 3-D and 4-D brain tumor segmentation. In: IEEE International Symposium on Biomedical Imaging; Rotterdam, The Netherlands. 2010.
44. Jemal A, et al. Cancer statistics, 2008. CA Cancer J Clin. 2008;58(2):71–96.
45. Morton LM, et al. Proposed classification of lymphoid neoplasms for epidemiologic research from the Pathology Working Group of the International Lymphoma Epidemiology Consortium (InterLymph). Blood. 2007;110(2):695–708.
46. Hoppe R, et al. Hodgkin lymphoma. Philadelphia: Lippincott Williams & Wilkins; 2007.
47. Bollard CM, et al. Cytotoxic T lymphocyte therapy for Epstein-Barr virus + Hodgkin's disease. J Exp Med. 2004;200(12):1623–33.
48. Dudley ME, Rosenberg SA. Adoptive-cell-transfer therapy for the treatment of patients with cancer. Nat Rev. 2003;3(9):666–75.
49. Yee C, et al., editors. Adoptive T cell therapy using antigen-specific CD8+ T cell clones for the treatment of patients with metastatic melanoma: in vivo persistence, migration, and antitumor effect of transferred T cells. Proc Natl Acad Sci USA. 2002;99(25):16168–173.
50. Straathof KC, et al. Treatment of nasopharyngeal carcinoma with Epstein-Barr virus–specific T lymphocytes. Blood. 2005;105(5):1898–904.
51. Heslop HE, et al. Long-term restoration of immunity against Epstein-Barr virus infection by adoptive transfer of gene-modified virus-specific T lymphocytes. Nat Med. 1996;2(5):551–5.
52. Bollard CM, et al. Complete responses of relapsed lymphoma following genetic modification of tumor-antigen presenting cells and T-lymphocyte transfer. Blood. 2007;110(8):2838–45.
53. Antoch G, et al. A radiologist's perspective on dual-modality PET/CT: optimized CT scanning protocols and their effect on PET quality. J Nucl Med. 2002;43(5):307.
54. Bar-Shalom R, et al. Clinical performance of PET/CT in evaluation of cancer: additional value for diagnostic imaging and patient management. J Nucl Med. 2003;44(8):1200–9.
55. Coleman RE, et al. Concurrent PET/CT with an integrated imaging system: Intersociety dialogue from the joint working group of the American College of Radiology, the Society of Nuclear Medicine, and the Society of Computed Body Tomography and Magnetic Resonance. J Nucl Med. 2005;46(7): 1225–39.
56. Ell PJ. The contribution of PET/CT to improved patient management. Br J Radiol. 2006;79(937): 32–6.
57. Farma JM, et al. PET/CT fusion scan enhances CT staging in patients with pancreatic neoplasms. Ann Surg Oncol. 2008;15(9):2465–71.
58. Sironi S, et al. Integrated FDG PET/CT in patients with persistent ovarian cancer: correlation with histologic findings. Radiology. 2004;233(2):433–40.
59. Schiepers C, et al. PET for staging of Hodgkin's disease and non-Hodgkin's lymphoma. Eur J Nucl Med Mol Imaging. 2003;30 Suppl 1:S82–8.
60. Ngeow JY, et al. High SUV uptake on FDG-PET/CT predicts for an aggressive B-cell lymphoma in a prospective study of primary FDG-PET/CT staging in lymphoma. Ann Oncol. 2009;20(9):1543–7.
61. Kostakoglu L, Goldsmith SJ. F-18-FDG PET evaluation of the response to therapy for lymphoma and for breast, lung, and colorectal carcinoma. J Nucl Med. 2003;44(2):224–39.
62. Kuo PH, et al. FDG-PET/CT for the evaluation of response to therapy of cutaneous T-cell lymphoma to vorinostat (suberoylanilide hydroxamic acid, SAHA) in a phase II trial. Mol Imaging Biol. 2008; 10(6):306–14.
63. De Barsy C, et al. Whole-body FDG PET imaging as a method for staging and early assessment of treatment response in pediatric patients with lymphoma. J Nucl Med. 2003;44(5):346.
64. Eich HT, et al. FDG-PET for treatment response assessment in advanced stage Hodgkin lymphoma - report on the 2nd interim analysis of GHSG trial HD15. Strahlenther Onkol. 2008;184:11.
65. Moulin-Romsee G, et al. Cost-effectiveness of early treatment response assessment by PET in non-Hodgkin lymphoma. Eur J Nucl Med Mol Imaging. 2007;34:S242-S.
66. Pregno P, et al. Response assessment in aggressive non Hodgkin lymphoma disease: predictive value of mid-treatment evaluation by 18-FDG-positron emission tomography/computed tomography (PET). Ann Oncol. 2008;19:249–50.
67. Pregno P, et al. Predictive value of response assessment with mid-treatment evaluation of 18-FDG-positron emission tomography/complited tomography (PET) in aggressive non Hodgkin lymphoma (NHL). Haematol Hematol J. 2007;92:59–60.
68. Stroobants S, et al. PET-CT for treatment response assessment in lymphoma. Haematol Hematol J. 2007;92:20.

69. Yan JY, et al. Automated matching and segmentation of lymphoma on serial CT examinations. Med Phys. 2007;34(1):55–62.
70. Pekar V, et al., inventors; Koninklijke Philips Electronics N.V., assignee. 3D image segmentation. NLMay 2009. US patent No. 20060159341-A1.
71. Sofka M, Stewart CV. Location registration and recognition (LRR) for longitudinal evaluation of corresponding regions in CT volumes. Med Image Comput Comput Assist Interv Int Conf Med Image Comput Comput Assist Interv. 2008;11(Pt 2):989–97.
72. Duncan J, Ayache N. Medical image analysis: progress over two decades and the challenges ahead. IEEE Trans Pattern Anal Mach Intell. 2000;22:85–106.
73. Rueckert D, et al. Nonrigid registration using free-form deformations: application to breast MR images. IEEE Trans Med Imaging. 1999;18(8):712–21.
74. Marsland S, et al. A minimum description length objective function for group-wise non-rigid image registration. Image Vis Comput. 2008;26(3):333–46.
75. Xue Z, et al. Joint registration and segmentation of serial lung CT images for image-guided lung cancer diagnosis and therapy. Comput Med Imaging Graph. 2010;34(1):55–60.
76. Gao X, et al. Computer-assisted quantitative evaluation of therapeutic responses for lymphoma using serial PET/CT imaging. Acad Radiol. 2010; 17(4):479–88.
77. Roskrow MA, et al. Epstein-Barr virus (EBV)-specific cytotoxic T lymphocytes for the treatment of patients with EBV-positive relapsed Hodgkin's disease. Blood. 1998;91(8):2925–34.
78. Jenkinson M, Smith S. A global optimisation method for robust affine registration of brain images. Med Image Anal. 2001;5(2):143–56.
79. Press WH, et al. Numerical recipes in C. Cambridge, UK: Cambridge Univ. Press; 1992.
80. Paragios N, et al. Gradient vector flow fast geometric active contours. IEEE Trans Pattern Anal Mach Intell. 2004;26(3):402–7.
81. Rueckert D, et al. Automatic construction of 3-D statistical deformation models of the brain using nonrigid registration. IEEE Trans Med Imaging. 2003;22(8):1014–25.
82. Ceresoli G, et al. Positron emission tomography with F18-fluorodeoxyglucose (FDG-PET) in malignant pleural mesothelioma (MPM): prediction of response to chemotherapy by quantitative assessment of standard uptake value (SUV). Lung Cancer. 2005; 49:S219-S.
83. Keyes JW. Suv – standard uptake or silly useless value. J Nucl Med. 1995;36(10):1836–9.
84. Luo J. Estimate standard uptake value (SUV) in F18FDG PET tumor imaging. Med Phys. 2006; 33(6):2014–5.
85. Mahan S, Ramsey C. Automatic generation of standard uptake value (SUV) isolines for treatment planning. Med Phys. 2003;30(6):1429.
86. Panizo CM, et al. The maximum standard uptake value (SUVmax) of PET/CT correlates with lymphoma aggressivity. Ann Oncol. 2008;19:250.
87. Suzuki O, et al. Standardization of PET standard uptake value for delineating GTV in integrated PET-CT of head and neck cancer. Int J Radiat Oncol Biol Phys. 2008;72(1):S409–S.
88. Thie JA. Understanding the standardized uptake value, its methods, and implications for usage. J Nucl Med. 2004;45(9):1431–4.
89. Rosenberg SA. National-cancer-institute sponsored study of classifications of non-hodgkins lymphomas - summary and description of a working formulation for clinical usage. Cancer. 1982;49(10):2112–35.
90. Vercauteren T, et al. Non-parametric diffeomorphic image registration with the demons algorithm. Med Image Comput Comput Assist Interv Int Conf Med Image Comput Comput Assist Interv. 2007; 10(Pt 2):319–26.
91. Xue Z, et al. Statistical representation of high-dimensional deformation fields with application to statistically constrained 3D warping. Med Image Anal. 2006;10(5):740–51.
92. Jenkinson M. FLIRT. v5.5 ed. University of Oxford. http://www.fmrib.ox.ac.uk/fsl/flirt/index.html. 2008.

Part II

Imaging of Cancer Hallmarks

Imaging Angiogenesis

7

Alan Jackson and James P.B. O'Connor

Contents

Abbreviations

($IAUC_{60}$)	Initial area under the contrast agent concentration-time curve of the first 60 s after contrast agent arrival
ANG-1	Angiopoetin-1
ASL	Arterial spin labelling
CC-TCC	Contrast concentration time course curves
CEUS	Contrast enhanced ultrasound
DCE-MRI	Dynamic contrast enhanced MRI
DCT	Dynamic CT
DOTA	Tetraacetic acid
DRCE-MRI	Dynamic Relaxivity Contrast Enhanced MRI
DSCE-MRI	Dynamic susceptibility contrast enhanced MRI
EC	Endothelial cells
ECM	Extracellular matrix
FGFs	Fibroblast growth factors
GBM	Glioblastoma
HIF-2α	Hypoxia-inducible factor-2α
IB	Imaging biomarkers
K^{trans}	Transfer contrast coefficient
MMP	Matrix metalloproteinases
MVD	Microvascular density
PHD2	Prolyl-hydroxylase domain 2
PlGF	Placental growth factor
rCBV	Cerebral blood volume
RGD	Arginine-glycine-aspartic acid
TKI	Tyrosine-kinase inhibitor
VEGF	Vascular endothelial growth factor
v_p	Vascular fraction
V_D	Volume of distribution

A. Jackson, PhD, MBChB, FRCR, FRCP, FBIR (✉)
Wolfson Molecular Imaging Centre,
University of Manchester, 27 Palatine Rd,
Withington, Manchester M20 3LJ, UK
e-mail: alan.jackson@manchester.ac.uk

J.P.B. O'Connor, PhD, FRCR
Imaging Sciences Research Group,
The University of Manchester,
Stopford Building, Oxford Road,
Manchester M13 9PT, UK

Department of Radiology,
The Christie NHS Foundation Trust, Wilmslow Road,
Manchester M20 4BX, UK
e-mail: james.o'connor@manchester.ac.uk

A. Luna et al. (eds.), *Functional Imaging in Oncology*,
DOI 10.1007/978-3-642-40412-2_7, © Springer-Verlag Berlin Heidelberg 2014

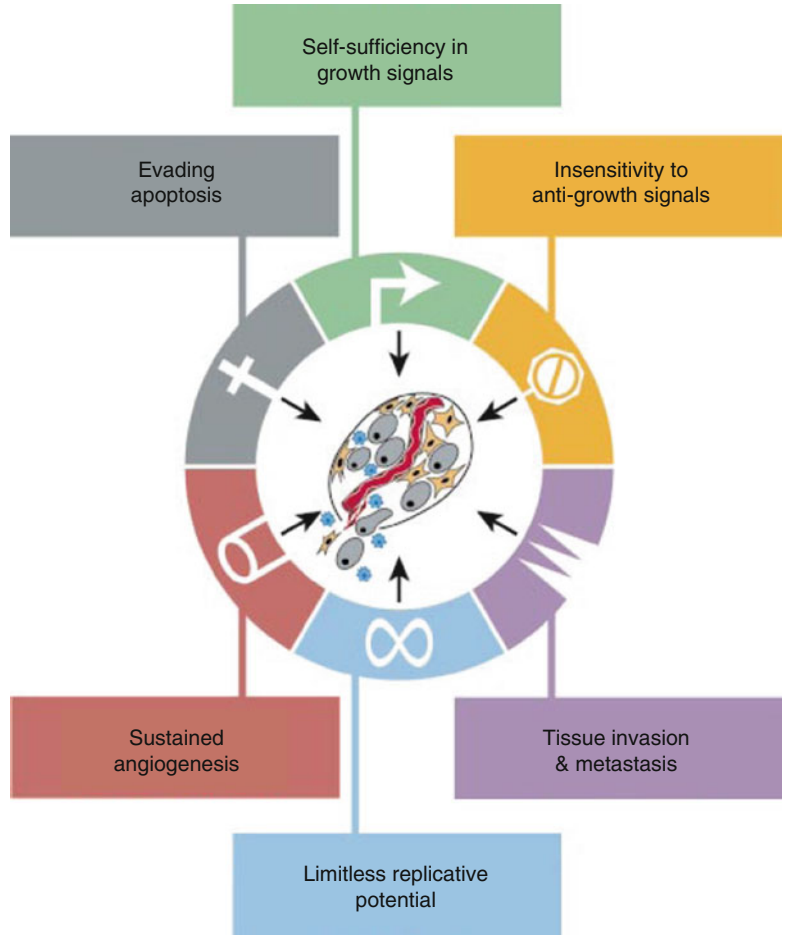

Fig. 7.1 The hallmarks of cancer (From Hanahan and Weinberg [1] with permission)

7.1 Introduction

The ability to sustain angiogenesis and develop independent vascular supply is one of the classic hallmarks of the cancer cell [1] (Fig. 7.1). The complex biological signalling mechanisms that underlie the angiogenic process have been the target of unprecedented research interest for the past 30 years. The understandable hope of early pioneers in the field that inhibition of vessel growth would provide a "magic bullet" to target multiple tumours has proven to be unfounded. However, our knowledge of the angiogenic process and the signalling mechanisms involved in it continues to evolve, leading to the development of novel antiangiogenic therapeutic strategies. The spatial heterogeneity of the tumour microenvironment and of the biological mechanisms involved in the angiogenic process has led to considerable interest in the development of quantitative imaging biomarkers (IB) that can be utilised both in clinical applications and in clinical studies of therapeutic strategies with antiangiogenic intent. In this chapter we will briefly review the relevant biology of the angiogenic process and the rationale behind the development of novel antiangiogenic cancer therapies. We will then explore the range of relevant imaging biomarkers and their potential strengths and weaknesses for future clinical and research applications.

7.2 The Biology of Angiogenesis

Tumour development and growth is dependent on development of new blood vessels to meet increasing demands for nutrient delivery and

waste removal. This process of neovascularisation is called angiogenesis. The biology of angiogenesis is complex and continues to be a source of active research [2]. In tumour tissue, the process of angiogenesis is controlled by a number of angiogenic signalling mechanisms mediated by small molecules or cytokines. These may be released by tumour cells or by hypoxic or inflammatory tissue. Some knowledge of the angiogenic process is essential to understand the development of imaging-based biomarkers, and a brief, relatively simplified, description is presented here and illustrated in Fig. 7.2. Readers are referred to specific detailed reviews for further information regarding the biological processes involved in angiogenesis [2].

In healthy vessels endothelial cells (ECs) form a monolayer interconnected by junctional molecules, which include claudins and VE-cadherin. ECs are covered in a sheath of pericytes that actively suppress endothelial proliferation and which, together with EC, form a common basement membrane. Pericytes produce a range of signalling molecules including vascular endothelial growth factor (VEGF), angiopoetin-1 (ANG-1), fibroblast growth factors (FGFs), NOTCH and chemokines which support endothelial cell repair. EC can also respond directly to dissolved oxygen concentration and have receptors for hypoxia-inducible factors such as prolyl-hydroxylase domain 2 (PHD2) and hypoxia-inducible factor-2α (HIF-2α) which support a mechanism to enable remodelling of vessels to optimise oxygen delivery.

Under hypoxic and hypoglycaemic conditions, tumour cells will release pro-angiogenic signalling molecules including VEGF, ANG-2, FGFs and chemokines into the local microenvironment. When normal vessels are exposed to pro-angiogenic signals, pericytes detach from the basement membrane by the action of matrix metalloproteinases (MMPs), and tight junctions between endothelial cells loosen with increase in the permeability of the endothelial membrane. There is then extravasation of plasma proteins, which are involved in formation of an early extracellular matrix (ECM). Integrin signalling stimulates migration of EC onto this ECM, which in turn stimulates further release of pro-angiogenic signalling molecules. Growth of new vessels is an ordered process that involves a single EC, known as the tip cell. Neighbouring ECs, known as stalk cells, divide under the influence of NOTCH, placental growth factor (PlGF) and FGDFs to form an elongated vascular stalk that then develops a patent lumen in response to VEGF and a range of other signalling molecules. New vessels fuse with existing vasculature to initiate blood flow, and the new vessels develop pericyte coverage, reform EC tight junctions and develop new basement membranes.

7.3 Antiangiogenic Therapies

The development of imaging biomarkers to study the process of angiogenesis has been a major area of imaging research development. This was largely driven by the anticipation that antiangiogenic small molecules would provide an effective therapeutic intervention which, by targeting a common biological mechanism, would be effective across a range of cancer types. In practice, compared to initial expectations, therapeutic benefits of antiangiogenic agents have been rather disappointing [3]. Development of resistance to antiangiogenic therapy is relatively common [4], and some agents have proven toxic when combined with chemotherapy [5, 6]. Worryingly, some evidence is beginning to suggest that antiangiogenic therapy may cause cancer cells to become increasingly malignant in behaviour [7, 8]. Nonetheless, anti-VEGF targeting agents such as bevacizumab [9] have shown significant benefit and are licensed for use in a number of clinical settings (metastatic colorectal cancer, metastatic non-squamous non-small-cell lung cancer, glioblastoma (GBM) and metastatic renal cancer) although anti-VEGF agents are used as a monotherapy only in GBM. Agents which target the TKI pathways to block pro-angiogenic signalling have also been approved for use in a number of clinical applications [10] (Table 7.1).

Although the initial hopes for antiangiogenic therapy have not been entirely fulfilled, enormous

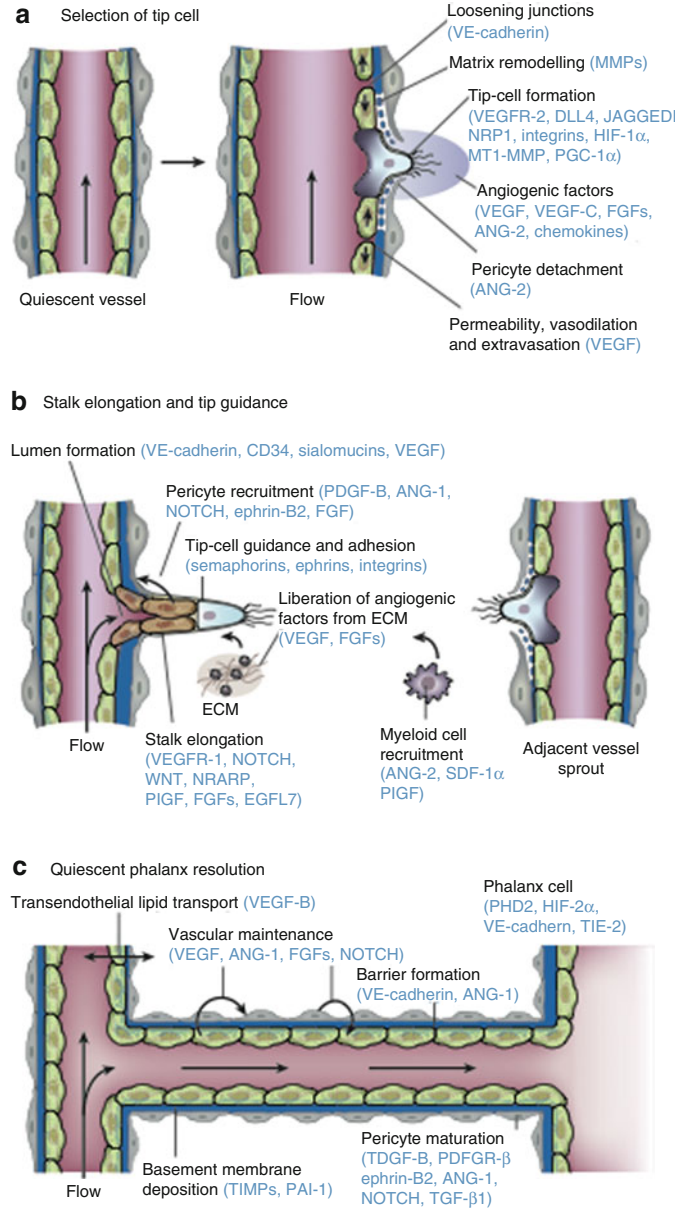

Fig. 7.2 The consecutive steps of blood vessel branching are shown, with the key molecular players involved denoted in parentheses. (**a**) After stimulation with angiogenic factors, the quiescent vessel dilates, and an endothelial cell tip cell is selected (*DLL4* and *JAGGED*1) to ensure branch formation. Tip-cell formation requires degradation of the basement membrane, pericyte detachment and loosening of endothelial cell junctions. Increased permeability permits extravasation of plasma proteins (such as fibrinogen and fibronectin) to deposit a provisional matrix layer and proteases remodel pre-existing interstitial matrix, all enabling cell migration. For simplicity, only the basement membrane between endothelial cells and pericytes is depicted, but in reality, both pericytes and endothelial cells are embedded in this basement membrane. (**b**) Tip cells navigate in response to guidance signals (such as semaphorins and ephrins) and adhere to the extracellular matrix (mediated by integrins) to migrate. Stalk cells behind the tip cell proliferate, elongate and form a lumen, and sprouts fuse to establish a perfused neovessel. Proliferating stalk cells attract pericytes and deposit basement membranes to become stabilised. Recruited myeloid cells such as tumour-associated macrophages (TAMs) and TIE-2-expressing monocytes (TEMs) can produce pro-angiogenic factors or proteolytically liberate angiogenic growth factors from the ECM. (**c**) After fusion of neighbouring branches, lumen formation allows perfusion of the neovessel, which resumes quiescence by promoting a phalanx phenotype, re-establishment of junctions, deposition of basement membrane, maturation of pericytes and production of vascular maintenance signals. Other factors promote transendothelial lipid transport (From Carmeliet and Jain [2] with permission)

Table 7.1 Summary of phase II and III trials of anti-vascular agents

Drug	Approved indication	Improvement in RR (%)	Improvement in PFS (months)	Improvement in OS (months)
Bevacizumab	Metastatic colorectal cancer (with chemotherapy)	10	4.4	4.7[a]
		0	1.4	1.4[a]
		7.8	2.8	2.5[a]
		14.1	2.6	2.1[b]
	Metastatic non-squamous NSCLC (with chemotherapy)	20	1.7	2.0[a]
		10.3–14.0	0.4–0.6	NR[a]
	Metastatic breast cancer (with chemotherapy)[c]	15.7	5.9	NS[a]
		9–18	0.8–1.9	NS[a]
		11.8–13.4	1.2–2.9	NS[a]
		9.9	2.1	NS[b]
	Recurrent GBM (monotherapy)	Currently only phase II data reported		
	Metastatic RCC (with IFN-α)	18	4.8	NS[a]
		12.4	3.3	NS[a]
Sunitinib	Metastatic RCC	35	6.0	4.6[a]
Sorafenib	Metastatic RCC	8	2.7	NS[b]
	Unresectable HCC	1	NS	2.8[a]
		2	1.4	2.3[a]
Pazopanib	Metastatic RCC	27	5.0	NR[a,b]

From Carmeliet and Jain [2] with permission
For reference, see http://clinicaltrials.gov
Antiangiogenic therapies currently approved by the US Food and Drug Administration (FDA) for treatment of malignancies. Per indication, the results of various trials are shown. The data show the improvement observed after the addition of the anti-VEGF therapy
GBM glioblastoma multiforme, *HCC* hepatocellular carcinoma, *IFN* interferon, *NR* not reported, *NS* not significant, *NSCLC* non-small-cell lung carcinoma, *OS* overall survival, *PFS* progression-free survival, *RCC* renal cell carcinoma, *RR* response rate
[a]First-line therapy
[b]Second-line therapy
[c]The FDA recommended the withdrawal of bevacizumab for breast cancer in December 2010; this is under appeal, with a hearing expected in June 2011. However, bevacizumab is approved for metastatic breast cancer in Europe, except in the United Kingdom

resource continues to be applied to the development of improved agents by increasing understanding of the modes of action, mechanisms of resistance and the principles that underlie the identification of optimised combination therapies [11–15]. Multiple mechanisms of resistance have been identified relating to changes occurring in tumour cells, EC or other cells in the tumour stroma. Some tumours, such as pancreas, are simply hypovascular by nature and therefore less sensitive to antiangiogenic strategies. Production of other pro-angiogenic signalling molecules can render tumours VEGF independent. Hypoxia in the native tumour or induced by vessel loss after antiangiogenic therapy can also promote mutations supporting development of hypoxia-resistant tumour cells and alternate pro-angiogenic mechanisms. Furthermore, there is some evidence, in GBM, that tumour stem cells can differentiate into EC via a process which is relatively insensitive to VEGF blockade [16].

7.4 Imaging Angiogenesis

Recognition of the importance of the angiogenic process led to substantial research efforts to identify tissue, soluble and imaging biomarkers that could be used clinically and in preclinical and clinical research. Imaging biomarkers have specific potential benefits that make them highly attractive. Quantitative imaging investigations can be performed non-invasively, can be repeated on a number of occasions to examine therapeutic

responses and, most importantly, provide unique spatial data that allows investigation of heterogeneous tumour biology in vivo. In addition, the nature of antiangiogenic therapies and the sheer number of potential candidate compounds available made, and continue to make, the design of clinical outcome trials challenging. Development of panels of appropriate biomarkers to allow phenotypic classification, early response prediction and detection of biological activity in early, pre-phase 1, clinical trials became increasingly important.

Early development focused on the identification of biomarkers that quantified aspects of microvascular structure such as vascular fraction, endothelial permeability and blood flow. These biomarkers now have wide clinical application and are also routinely employed in clinical trials of antiangiogenic therapies. However, more recently there has been significant interest in developing biomarkers that target other aspects of the angiogenic process leading to the description of an increasingly wide range of PET-based molecular imaging agents.

7.4.1 Biomarkers of Perfusion and the Vascular Microenvironment

The technical details associated with the various imaging techniques are covered in considerable detail in earlier chapters. However, it is worth reviewing the characteristics and potential benefits of the quantitative imaging methods that now form an integral component of many or most antiangiogenic drug trials. Early approaches focused on the known histological features of angiogenic tissue. Classically, histochemical staining studies had identified the importance of the density of new vessels (microvascular density; MVD) measured on stained tissue. Although it is associated with a number of technical problems, MVD has been shown to relate to malignancy and outcome in a number of tumours and is routinely used in histological studies [17]. Many early imaging studies focused on identifying surrogate biomarkers of MVD mainly using dynamic contrast-enhanced MRI (DCE-MRI) with technical development commonly occurring in brain tumours due to favourable signal-to-noise characteristics and a lack of physiological motion. Most early studies used T_2*-weighted acquisitions, often referred to as dynamic susceptibility contrast-enhanced MRI (DSCE-MRI), since susceptibility effects produce larger proportional signal changes in normal grey and white matter and, at that time, system architecture made rapid dynamic acquisitions with T_2* weighting easier than T_1 weighting. A proportional cerebral blood volume (rCBV) estimation is easily obtained from this data assuming that technical problems associated with contrast leakage are appropriately dealt with [18]. By scaling to normal white matter or pure vascular tissues (large veins), rCBV can be normalised to produce absolute values (CBV) which have shown close agreement with histological assessment of MVD in a number of cancer types and show similar correlations with tumour grade, aggressiveness and survival data [19–21].

Most early antiangiogenic agents targeted VEGF or VEGF signalling. Since VEGF produces rapid and significant increases in the permeability of the endothelial membrane, considerable work was directed towards the quantification of permeability by measurement of MR contrast agent leakage. Unfortunately, measurement of contrast agent leakage using T_2* dynamic images is problematic, and the adoption of T_1-weighted dynamic sequences, often referred to as dynamic relaxivity contrast-enhanced MRI (DRCE-MRI), received increasing attention. DRCE-MRI data can be acquired on most standard clinical MR imaging systems; however, dynamic signal intensity changes can vary between systems due to differences in acquisition sequence design, receiver gain settings and other technical variables. Early studies attempted to minimise these sources of variation by the use of simple, normalised, metrics such as the maximal rate of change of signal intensity or the ratio of pre- and post-contrast signal intensity. However, a desire for better standardisation across imaging systems and for greater physiological specificity led to the development and

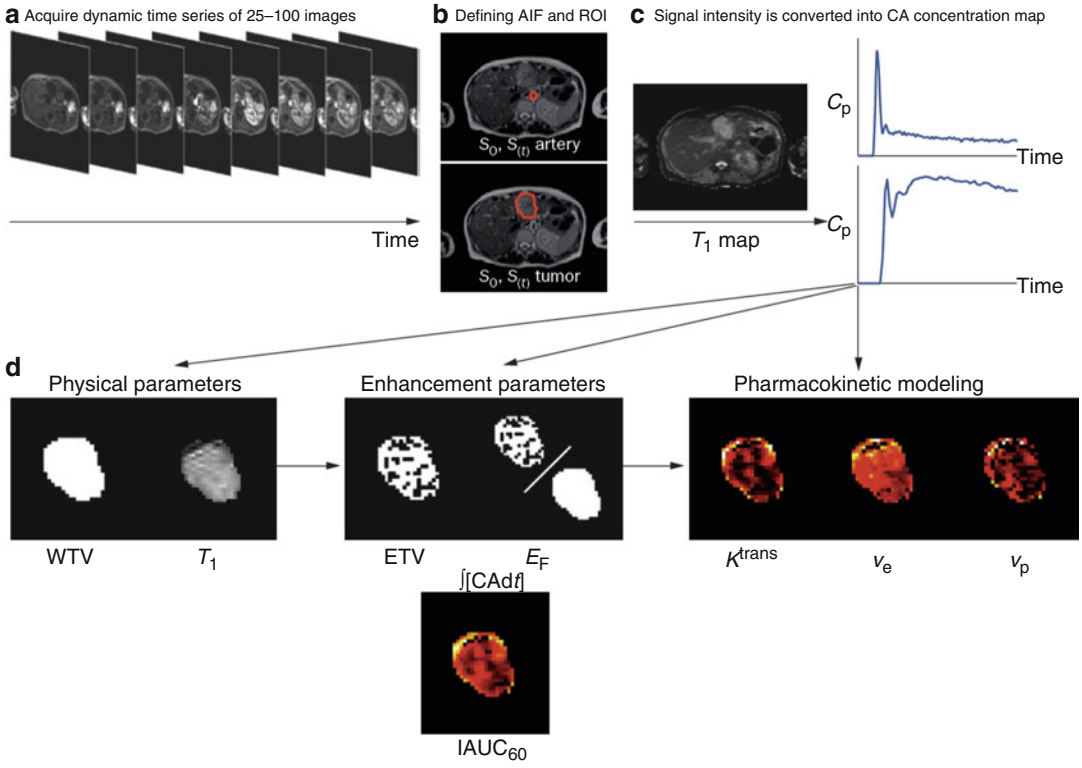

Fig. 7.3 DCE-MRI data acquisition and analysis. (**a**) Multiple images (typically 25–100) are acquired as a bolus of contrast agent passes through tissue capillaries; (**b**) the region of interest for a tumour and the feeding vessel arterial input function are defined; and (**c**) signal intensity values for each voxel are converted into contrast agent concentration using a map of T_1 values. These steps allow calculation of (**d**) WTV and T_1 values. Next, voxels are classified as enhancing or not after which parameters based on the amount and proportion of enhancement can be defined, along with the $IAUC_{60}$. Finally, a pharmacokinetic model may be applied to derive parameters such as K^{trans}. Abbreviations: $\int$[CA]dt area under the contrast agent–time curve, *AIF* arterial input function, *Cp* contrast–agent concentration in plasma, *CA* contrast agent, *DCE-MRI* dynamic contrast-enhanced MRI, E_F enhancing fraction, *ETV* enhancing tumour volume, $IAUC_{60}$ initial area under concentration agent–time curve at 60 s, K^{trans} volume transfer constant between plasma and the extracellular extravascular leakage space, *ROI* region of interest, *S* signal, T_1 longitudinal relaxation time, v_e volume of extracellular extravascular leakage space, v_p blood plasma volume, *WTV* whole tumour volume (From O'Connor et al. [25] with permission)

widespread application of pharmacokinetic analytical approaches [22]. Signal intensity changes are used together with direct measurements of baseline T_1 values to calculate contrast concentration time course curves (CC-TCC). These can then be analysed using simple pharmacokinetic models to derive variables which have, in theory, both relative independence from variations resulting from differences in scanning equipment and sequence implementation and also offer increased physiological specificity. Most studies use a modified version of the original Toft's pharmacokinetic model that produces estimates of vascular fraction (v_p), extravascular extracellular space fraction (v_e) and the transfer contrast coefficient (K^{trans}) [23, 24] (Fig. 7.3).

Table 7.2 lists the parameters which can be extracted by the application of pharmacokinetic models and which are believed to be of value in clinical trials of novel therapies [26].

The K^{trans} value will be affected by blood flow and by the permeability surface area product of the endothelium (P.S). It rapidly became evident that the VEGF inhibition was indeed associated with rapid and profound reductions in K^{trans} [25, 27, 28]. However, it must be noted

Table 7.2 Imaging biomarkers used in studies of anti-vascular agents

Parameter definition		Unit	Notes
Primary end points			
K^{trans}	Volume transfer constant between plasma and the EES	min^{-1}	Composite measure of permeability, capillary surface area and flow
$IAUC_{60}$	Initial area under concentration agent-time curve at 60 s	mmol min	Similar measure to K^{trans}, but also influenced by v_e
Alternative functional biomarkers[a]			
k_{ep}	Rate constant between EES and plasma	min^{-1}	NA
v_e	Volume of EES per unit volume of tissue	NA	NA
v_p	Blood plasma volume	NA	Relatively poor reproducibility
F	Blood flow	ml/g min^{-1}	Temporal resolution achieved in most studies is too slow
PS	Permeability surface area product per unit mass of tissue	ml/g min^{-1}	Temporal resolution achieved in most studies is too slow
Alternative biophysical measurements[b]			
WTV	Whole tumor volume	mm^3	Easy to measure
ETV	Enhancing tumor volume	mm^3	Easy to measure
E_F	Enhancing fraction (ETV: WTV ratio)	none	Easy to measure
T_1	Longitudinal relaxation time	ms	Easy to measure

Parameters derived from DCE-MRI: As recommended by Leach et al. [26]
Abbreviations: *DCE-MRI* dynamic contrast-enhanced MRI, *EES* extracellular extravascular leakage space, *NA* not applicable
[a]Require pharmacokinetic modelling
[b]Do not require pharmacokinetic modelling

that pharmacokinetic analyses have been far less popular in clinical practice where simple semi-quantitative metrics have become well established in many areas of oncology including prostate [29–31], breast [32–43], pancreatic [44], cervical [45], colonic [46] and rectal cancers [21, 47], bone sarcoma [48] and brain tumours [49, 50]. This clinical preference for semi-quantitative metrics reflects the complexity of pharmacokinetic analysis. The requirement to measure baseline T_1 values and to identify a representative arterial input function (LIF) together with potential confusion concerning the choice of the most appropriate pharmacokinetic model make the use of semi-quantitative metrics far more attractive in a busy clinical environment. However, semi-quantitative metrics are capable of providing significant insight into the angiogenic status of tumour microvasculature which is, in most cases, comparable to pharmacokinetic parameters (Fig. 7.4).

With the development of rapid multi-slice CT acquisitions, it was natural that the analytical approaches taken with DCE-MRI would be applied to CT data. Dynamic CT (DCT) has a number of potential advantages over MRI. The main one of these is that the concentration of contrast agent is directly linearly related to the measured attenuation value [51]. This makes measurements of semi-quantitative parameters and the application pharmacokinetic models more simple and alleviates many of the problems associated with multicentre studies in MRI (Fig. 7.5) [52–54].

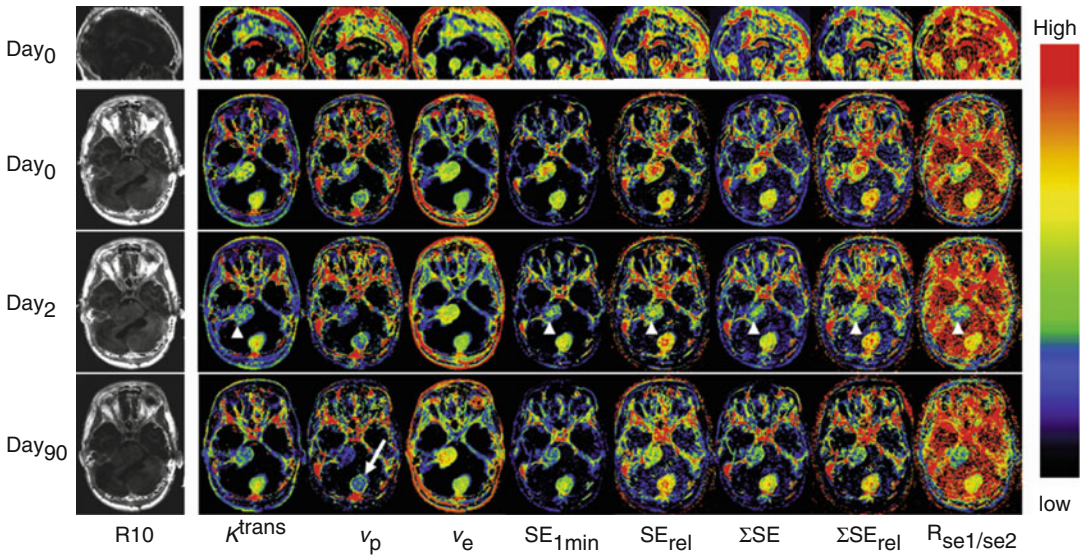

Fig. 7.4 Axial view of central slices of 3D longitudinally co-registered kinetic and semi-quantitative parametric maps obtained in 26-year-old woman, who has type II neurofibromatosis with a progressive VS (*arrow heads*) and an occipital located meningioma (*arrow*) undergoing treatment with bevacizumab. Images show comparisons of pharmacokinetic leak derived parameters K^{trans}, v_p and v_e with semi-quantitative parameters (before and 2 and 90 days after the start of treatment): (1) *absolute signal enhancement* (SE_{1min}), (2) *relative signal enhancement* (SE_{rel}) which uses a baseline value for normalisation in order to reduce the dependence on biological and imaging system variables, (3) *the sum of SE over a fixed postinjection duration* (*SE*), (4) *the sum of* SE_{rel} *over a fixed postinjection duration* (SE_{rel}) and (5) *signal enhancement ratio*, commonly defined as the ratio of early to late contrast enhancement ratio, e.g. $R_{se1/se2} = (SI_{1\ min\ post} - SI_{pre})/(SI_{5\ min\ post} - SI_{pre})$

The main problem with DCT is of course the radiation dose that is significant and limits the application of the technique into clinical trials requiring repeated imaging measurements.

The development of microbubble contrast agents led to the development of contrast-enhanced ultrasound (CEUS) which allows imaging of vessels with diameters of 50–100 μm using a combination of intravascular contrast and Doppler sonography. However, CEUS is limited by the presence of appropriate sonographic windows and is extremely operator dependent.

Although DRCE-MRI rapidly became an key component of many antiangiogenic studies, a number of other specific IB have been developed for angiogenesis. Some of these reflect recognition that novel antiangiogenic strategies may well not show changes in endothelial permeability but may affect other parts of the angiogenic process. One example of this is the recognition that antiangiogenic agents change the branching structure of the angiogenic vascular tree so that it more closely resembles normal vascular tissue [55]. This process, named normalisation, produces a change in the balance of vessel sizes within the tissue which can be detected by examining the differences in contrast-induced signal change on T_2- and T_2*-weighted images [56]. A number of studies used this approach to develop a vessel normalisation index which showed significant changes in response to tyrosine kinase inhibitors (Fig. 7.6) [57, 58].

Changes in vessel structure induced by antiangiogenic therapy can also be expected to produce changes in blood flow and blood flow velocity which can, in theory, be detected by arterial spin labelling. The ability to study antiangiogenic effects without the use of gadolinium-based contrast media is attractive, and a number of groups have examined the feasibility of ASL showing both treatment-induced changes and evidence that these changes can be

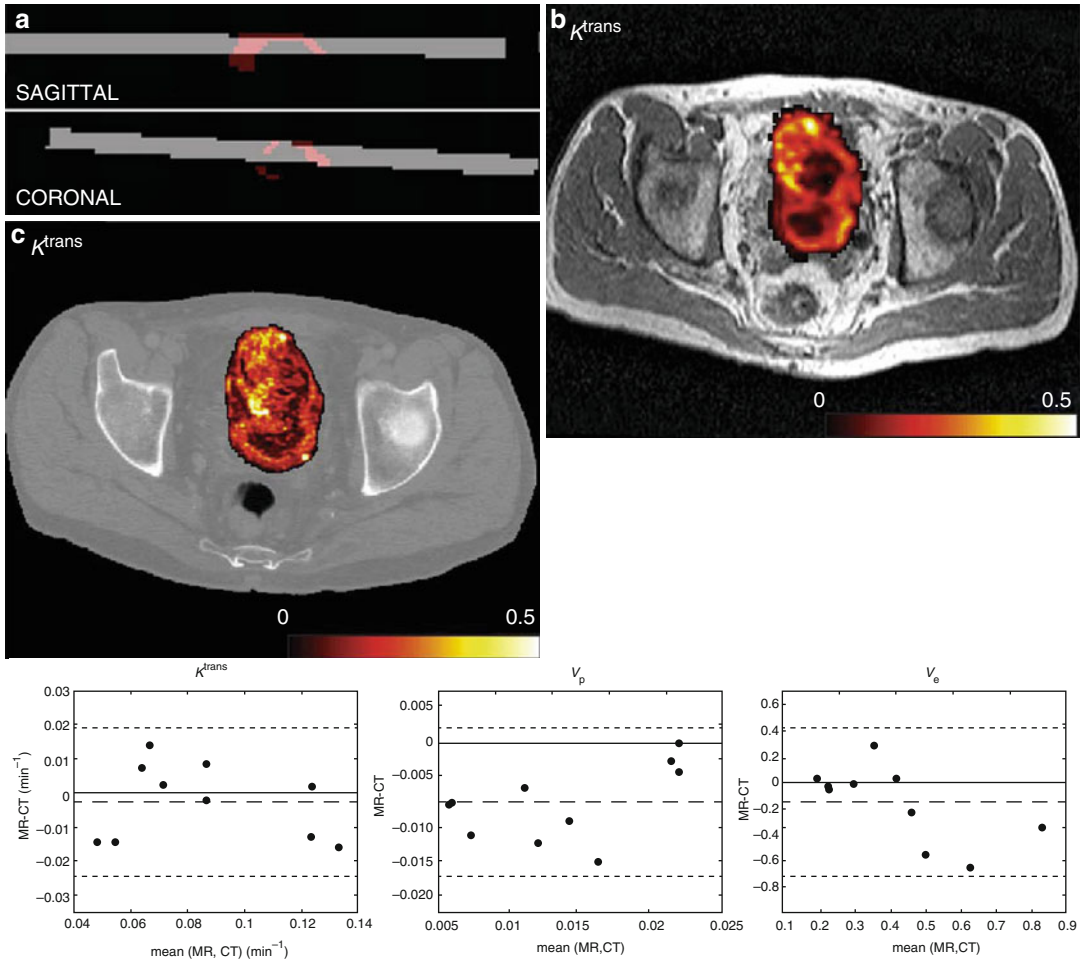

Fig. 7.5 (**a**) CT volume (*grey*) backtransformed into MR space and intersecting tumour ROI (*red*), sagittal and coronal views in a patient with bladder cancer. (**b**) Example of K^{trans} map for DCE-MRI overlaid onto T_2-weighted anatomical image after affine transformation to CT space. (**c**) Example of K^{trans} map for DCE-CT at native resolution overlaid onto image from dynamic CT set. Colour scale in min^{-1}. (**d**) Bland–Altman plots for the median values of K^{trans} (in min^{-1}), v_p and v_e (both unitless). The *dashed lines* indicate the mean difference, and the dotted lines indicate the limits of agreement (From Naish et al. [52] with permission)

used as early predictors of therapeutic response (Fig. 7.7) [60, 61].

A small number of studies have been performed using PET-based biomarkers to measure flow and vascular fraction. The most commonly employed method is ^{15}O-water which allows direct measurement of tissue perfusion and the volume of distribution (V_D) for water sometimes called the exchanging water space. This parameter is poorly understood but appears to represent the proportion of tissue that is available for perfusion by water and is predicted to be low in areas of fat or necrosis [59]. Measurements of tumour perfusion using ^{15}O-water appear to show high reproducibility within an interclass correlation coefficient of 0.95 in one study of patients with lung tumours [62]. However, V_D appears to be rather more variable. Early clinical applications of ^{15}O-water measurements have been relatively limited but have demonstrated a relationship between flow measurements and the angiographic vascularity of liver metastases, changes induced by combined nicotinamide and carbogen administration in colorectal liver metastases and increased perfusion in patients with malignant breast disease [63–66]. ^{15}O-water

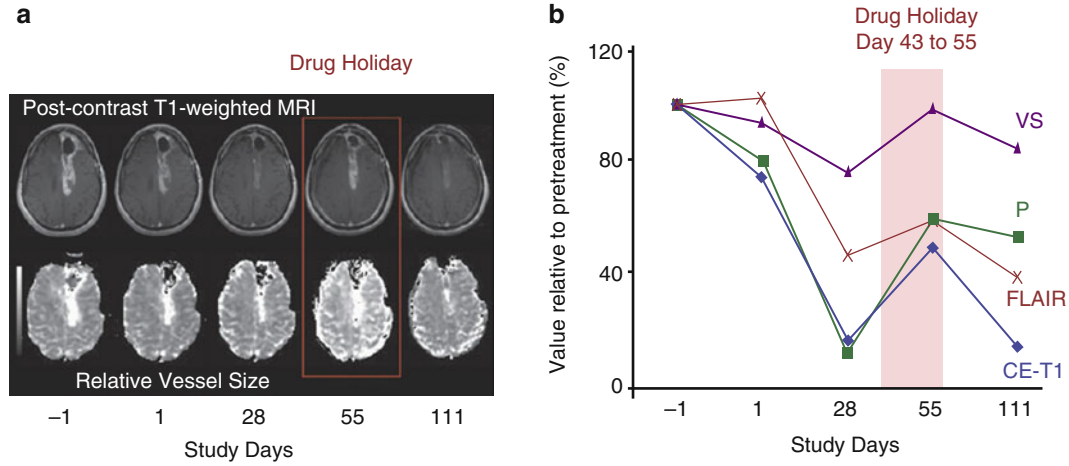

Fig. 7.6 Reversibility of normalisation: (**a**) vascular and volume changes as a function of time in a patient with glioblastoma multiforme who did not take drug from days 43–56 and was imaged on day 55 (shown as drug holiday). T_1-weighted anatomic images after intravenous administration of gadolinium-DTPA. Note that at day 55, there is a rebound in tumour enhancement, which decreases again after restarting the drug as seen on follow-up imaging on day 110. In this patient, maps of relative vessel size also show fluctuation with the drug holiday and resumption of AZD2171 treatment. (**b**) Measurements of imaging parameters confirm the reversibility of vascular normalisation by drug interruption followed by renormalisation after AZD2171 is resumed. (*VS* vessel size, *P* endothelial permeability, *CE-T1* contrast-enhanced T_1-weighted sequence) (From Batchelor et al. [57] with permission)

perfusion measurements have also been used in a limited number of studies of conventional chemotherapy and antiangiogenic therapies. Anderson and colleagues used a combination of ^{15}O-water to measure flow and ^{15}O-carbon monoxide to measure regional blood volume in 12 patients with renal carcinoma treated with razoxane, an oral agent with mixed cytotoxic and antiangiogenic activity [67]. They found that perfusion of renal tumours was lower than normal kidney but demonstrated no significant changes in tumour perfusion or blood volume in response to drug. There were also no significant changes in a group of four patients who showed disease progression at follow-up. A study of six patients receiving thalidomide for androgen-independent prostate cancer showed an inverse correlation between prostate-specific antigen and blood flow suggesting that response to antiangiogenic agents is associated with improved tumour circulation [68]. Although PET-based methods for measurement of flow and blood volume are readily available, they have been seldom used. This presumably reflects the radiation dose and relative complexity of the approach compared to the increasingly reliable DCE-MRI techniques.

7.4.2 DCE-MRI in Clinical Trials

DCE-MRI techniques have now been used in over 100 early-phase clinical trials of anti-vascular therapies [25]. Despite this, the role of DCE-MRI in decision-making or drug development and the design of trials using T_1-weighted DCE-MRI remains relatively controversial. The earliest trials of anti-vascular agents were reported approximately 10 years ago. Many used semi-quantitative parameters similar to those used in clinical breast cancer evaluation, but as discussed above, the majority of studies have relied on pharmacokinetic analysis most commonly using the modified Toft's model [69], and a number of consensus workshops have proposed the selection of $IAUC_{60}$ and K^{trans} as the preferred DCE-MRI endpoints in clinical trials [26, 70].

By the end of 2011, 86 DCE-MRI studies reporting 1,604 patients had evaluated single-agent anti-vascular therapies. Fifty-nine of these used inhibitors of VEGF or VEGFR [25], 16 used vascular targeting agents and 11 used agents with other postulated anti-vascular activities. In some studies, clinical benefit was associated with

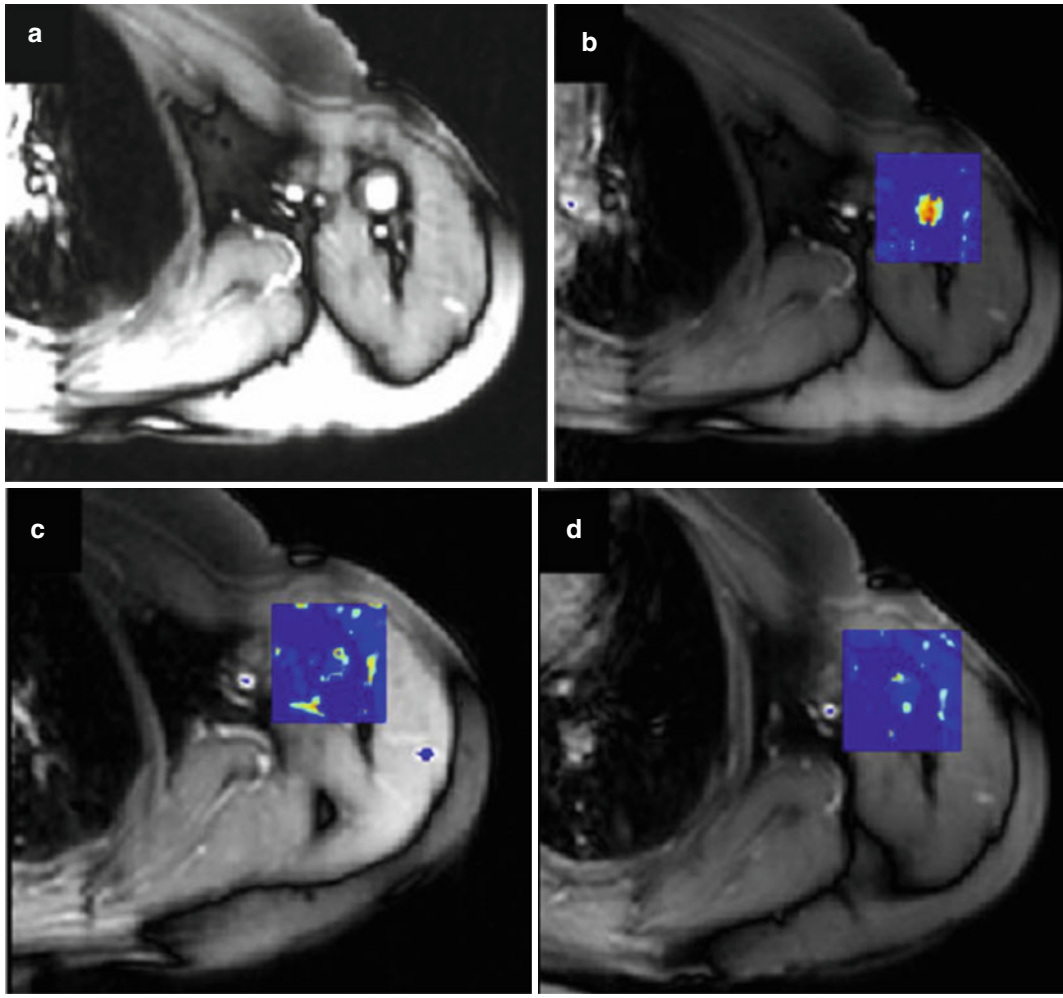

Fig. 7.7 (**a**–**d**) Forty-five-year-old female patient presenting with IgG lambda-secreting multiple myeloma. The patient was treated with bortezomib and showed a good response to therapy. For anatomical orientation one M0 image is given without coloured perfusion overlays (**a**). At baseline examination (**b**), tumour perfusion was measured at 358 ml min^{-1} 100 g^{-1}. Three weeks after onset of bortezomib therapy, myeloma perfusion dropped to 143 ml min^{-1} 100 g^{-1}(**c**). Another 5 weeks later, tumour perfusion was decreased to 74 ml min^{-1} 100 g^{-1}(**d**) (From Laking and Price [59])

clear early reduction in $IAUC_{60}$ and/or K^{trans} with VEGF, VEGFR and tyrosine kinase-targeted agents. In contrast, drugs with little demonstrable clinical benefit showed minimal or insignificant reductions in these parameters. Examples of this include three trials of semaxanib (targeting VEGFR) in 46 patients [71–73] and three trials of vandetanib (targeting VEGFR and EGFR) in 41 patients [74–76] in which $IAUC_{60}$ and K^{trans} did not change with drug treatment.

Unfortunately, reductions in K^{trans} reported in studies of vatalanib, a VEGFR inhibitor, [77–80] were similar to those seen with inhibitors of VEGF such as bevacizumab, cediranib, sorafenib and fosbretabulin. However, vatalanib has failed to demonstrate a survival benefit in phase III trials in patients with colorectal cancer when used in combination with cytotoxic agents [81]. Thus, anti-vascular drug activity (measured by DCE-MRI in studies of monotherapy) in phase I and phase II trials does not guarantee success of an anti-vascular agent in combination regimens in phase III testing [82]. Various studies have also suggested utility of DCE-MRI-based metrics in optimising drug dose, particularly in identifying a therapeutic window between the biologically active dose which produces DCE-MRI

parameter change and the clinical maximum tolerated dose. It has also been suggested that DCE-MRI parameters may help with dose scheduling [83]. However, some vascular targeting agents have shown complex non-linear relationships between drug dose and vascular response [25].

It is important to note that significant changes in other DCE-MRI-derived parameters have been reported in a large number of clinical trials. Tumour volume considered as a continuous variable or graded in such a way to take account of relatively small reductions has been demonstrated as a common response to both VEGF/VEGFR targeting and TKI inhibitors. Similarly the T_1 parameter, which is calculated routinely to allow contrast concentration calculations, has also shown significant change in response to antiangiogenic agents which has been taken to indicate drug-induced changes in free fluid within the tumour [25, 27]. Blood plasma volume (v_p) and fractional extravascular extracellular space volume (v_e) are commonly not reported in clinical trial data. However, 13/86 studies of antiangiogenic monotherapy that did include calculations of v_p demonstrated large statistically significant reductions in response to bevacizumab, cediranib, sorafenib and sunitinib [25].

These findings, taken in combination, suggest that DCE-MRI metrics do provide useful guidance in drug development and early-phase clinical studies. However, emerging evidence clearly indicates a multi-parametric analysis of DCE-MRI data offers greater insight into the mechanism of drug actions than studies that use only a single parameter such as K^{trans}.

7.4.3 Molecular Biomarkers

Our understanding of the angiogenic process continues to increase at an almost exponential rate. Numerous novel therapeutic targets are identified and candidate compounds screened for activity in preclinical models. It is increasingly clear that the established imaging biomarkers available for clinical trials are severely limited. Although, as we have seen, DCE-MRI provides valuable and reliable information; it describes only selected elements of the tumours microvascular environment. Increasingly, there is a demand for biomarkers that can quantify specific molecular processes associated with angiogenesis to provide a more comprehensive toolkit for preclinical and clinical studies. The development of novel PET radiotracers has received extensive attention, and a number of promising molecular imaging agents, targeting the angiogenic process, have been assessed in preclinical and early-phase clinical studies. There is an extensive literature regarding the potential targets for the development of molecular markers [84–90]; however, we will focus here on the three best-developed and most promising approaches: (1) imaging of VEGF receptors, (2) imaging of integrin expression and (3) imaging of matrix metalloproteinases.

7.5 Imaging VEGF

VEGF is a potent regulator of neovascularisation both in healthy tissue development and cancer. Variations in mRNA splicing result in at least seven isoforms of VEGF with varying receptor binding affinities. There are two VEGF receptor tyrosine kinases, VEGFR-1 and the VEGFR-2, that are principally expressed on EC. Elevated levels of VEGF have been described as a poor prognostic sign in cancer and correlate with increased metastatic behaviour [91]. VEGF imaging has been accomplished using radiolabelled antibodies or antibody fragments. The first imaging was performed using radiolabelled bevacizumab in mice [92]; however, the antibody showed poor immune reactivity, and maximum uptake did not occur until 4–7 days postinjection. The first human VEGF imaging used HuMV883, a humanised version of a mouse monoclonal anti-VEGF antibody (MV833) that has antitumour activity against a number of human tumour xenografts. Imaging in patients with solid tumours using radiolabelled HuMV833, after treatment with the antibody, demonstrated heterogeneity of distribution and clearance both between patients and individual tumours [28]. 111In-labelled bevacizumab was later used to image VEGF in colorectal cancer patients with liver metastases. Although 9 of 12 patients with metastatic lesions were detected, no correlation was found between the level of antibody accumulation and expression of VEGF in post-resection analysis [93].

An alternative approach to image VEGF expression is the use of radiolabelled soluble forms of VEGF, like VEGF121. One preclinical study using ^{64}Cu-DOTA-VEGF121 demonstrated prominent uptake in small highly vascularised U87MG grafts but lower uptake in less well-vascularised large tumours [94]. This led to a follow-up study which demonstrated that the VEGFR-2 expression is regulated in a narrow window of tumour sizes which may imply that repeated VEGFR-targeted studies might help in the management of angiogenic therapies [95]. More recently, Nagengast and colleagues [96] developed 89Zr-ranibizumab for potential use as non-invasive biomarker of VEGF signalling. Ranibizumab, a monoclonal antibody fragment (Fab) derivative of bevacizumab, used to treat macular degeneration, has a higher affinity than bevacizumab for all soluble and matrix bound human VEGF-A isoforms. In contrast to ^{18}F-FDG and ^{15}O-water PET, VEGF-PET demonstrated dynamic changes within the tumour during sunitinib treatment with a strong decline in signal in the tumour centre and only minimal reduction in tumour rim, with a pronounced rebound after sunitinib discontinuation. VEGF-PET results corresponded closely with tumour growth and immunohistochemical vascular and tumour markers.

7.6 Integrin Imaging

Integrins are heterodimeric membrane receptors comprised of an α and a β subunit that mediate interactions between cells. To date, 18 different α and 8 different β subunits have been identified, forming 24 different integrin receptors [97]. A common property of many integrins is their interaction with the arginine–glycine–aspartic acid (RGD) sequence found in extracellular matrix proteins like vitronectin, fibrinogen, thrombospondin and fibronectin. The most extensively studied of these in the angiogenic process is the integrin αvβ3 which is highly expressed on the surface of activated EC. However, integrins are commonly expressed on the surface of tumour cells, and the interpretation of the signal obtained from integrin imaging can therefore be complex [98]. The first integrin-specific PET tracer used in humans was [^{18}F] galacto-RGD. The initial study of mixed tumour types demonstrated wide variability of tumour uptake with high background in the kidneys, liver, spleen and bowel. Immunohistological examination of resected tissue demonstrated that the number of αvβ3-positive vessels per field of view correlated highly with tumour uptake of [^{18}F]galacto-RGD [99]. A similar correlation between uptake and immunohistochemical staining was also demonstrated in a later, larger study [100].

The use of [^{18}F]galacto-RGD in a mixed tumour population of 19 patients produced a detection rate the malignant lesions of 79 % whilst in a study of 12 patients with squamous cell carcinoma of the head and neck the detection rate was 83 % in primary tumours but lower in lymph node metastasis [101]. In 16 patients with breast cancer, all primary lesions were identified, and no false-positive lesions were seen, but once again sensitivity for lymph node metastases was lower (37 %) [102].

A number of modifications designed to improve the pharmacokinetic properties of RGD peptides have been described. A recent approach is the development of multimeric tracers since RGD interactions are thought to be based on multivalent interactions with clusters of integrin membrane proteins. These tracers are designed to more effectively identify tumours in areas of high physiologic integrin expression, such as the liver, spleen and bowel. Direct comparison of monomeric, dimeric and tetrameric cyclic RGD tracers conjugated with DOTA and radiolabelled with [103]. In in mice with SK-RC-52 renal cell carcinoma xenografts demonstrated tumour uptake of the tetramer which exceeded that of both the dimer and the monomer [104] and a ^{64}Cu-DOTA-RGD octamer demonstrated higher uptake than tetramer versions in human glioblastoma tumour grafts [105].

One significant alternate integrin-specific tracer is [^{18}F]fluciclatide which has been developed by GE Healthcare and is becoming

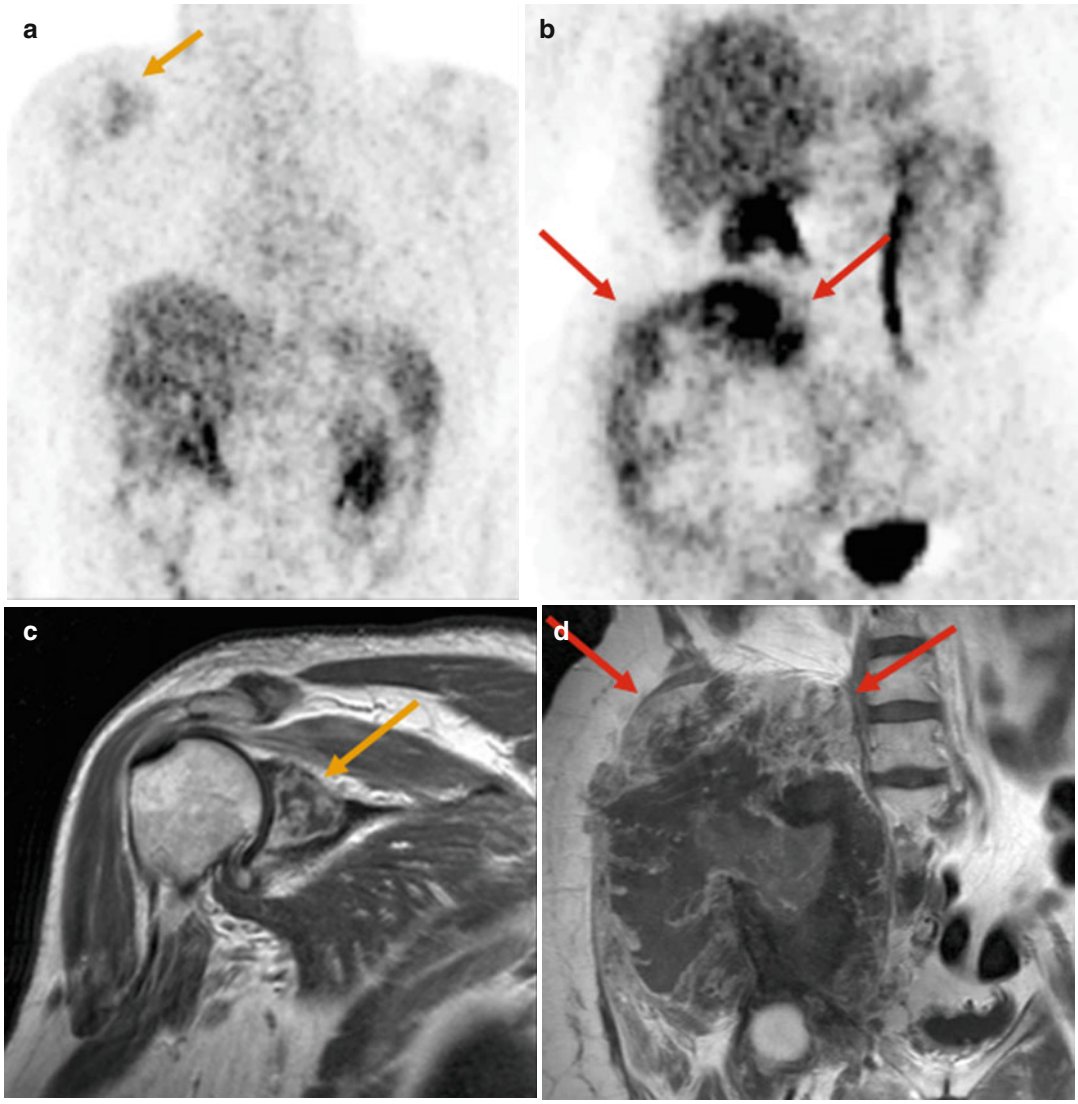

Fig. 7.8 *Upper row* galacto- RGD PET coronal, 60 min p.i. *Lower row* MRI post-Gd-DTPA coronal. Whereas the well-differentiated G1 chondrosarcoma in the right shoulder and the dedifferentiated G3 chondrosarcoma in the right pelvis both show contrast enhancement in MRI, the G3 tumour shows intense tracer uptake (especially in the upper parts of the tumour), but the G1 tumour shows only faint tracer uptake (Reproduced from Gaertner et al. [107])

widely available. This commercially available tracer shows different binding affinities with the highest affinity for αvβ5 (IC50 0.1 nM), followed by integrin αvβ3 (IC50 11.1 nM). A study in human glioma heterografts treated with sunitinib demonstrated a therapy-induced reduction in tumour uptake over a 2-week period. This correlated with a reduction in tumour MVD suggesting that this agent is capable of demonstrating vascular responses transgenic inhibition prior to the occurrence of significant volumetric changes [106].

The potential role of integrin imaging in the clinical environment remains uncertain. Observations of associations between integral expression and tumour progression in melanoma and tumour grade in sarcoma have suggested potential clinical utility (Fig. 7.8).

Similarly, preclinical studies have demonstrated that integrin αvβ3 has an important role in promoting aggression and metastatic potential in breast cancer and glioma. These observations suggest specific potential clinical utility for integral imaging, particularly in the selection of patients for antiangiogenic therapies. This is supported by a study using integrated imaging in metastatic colorectal carcinoma in the liver where increased uptake correlated with a partial response to therapy [107].

7.7 Imaging Matrix Metalloproteinases

MMPs are a group of extracellular proteins that disrupt the components of the extracellular matrix and basement membrane. The family includes a wide range of over 20 MMPs that play roles in angiogenesis but also in tissue development and wound healing [108]. Many of the MMPs are expressed by malignant cells and are involved in angiogenesis and metastatic dissemination, but MMP-2 and MMP-9 are most commonly present in malignant tissue [109]. In 1999 Koivunen and colleagues discovered a peptide known as CTT that inhibits MMP-2 and MMP-9 activity and prevents tumour growth and metastasis [103, 110]. In-radiolabelled CTT uptake correlated with both normal and tumour tissue MPP activity [103], but its application to imaging is limited by poor tumour uptake [111]. Alternative approaches to image MMP activity by labelling small molecular MMP inhibitors have been developed but also suffer from poor tumour contrast and high levels of non-specific activity [112, 113].

Conclusions

Angiogenesis has provided one of the most important therapeutic targets for the treatment of cancer for nearly 20 years. Despite a greater investment in the study of the process and the development of associated therapeutic approaches, current antiangiogenic therapies offer only modest benefits in limited clinical applications. The development and validation of novel antiangiogenic therapies and, more importantly, the development of combination therapies are likely to rely increasingly on accurate identification of patients who are likely to respond. Imaging biomarkers currently offer the most promising approaches to this kind of personalised medicine and will continue to be of vital importance in drug development, clinical trial and clinical settings. Although at the present time DCE-MRI techniques remain the backbone of antiangiogenic imaging, there is a clear and increasing need for improved imaging biomarkers which will lead to increasing applications of molecular imaging techniques.

References

1. Hanahan D, Weinberg RA. The hallmarks of cancer. Cell. 2000;100(1):57–70.
2. Carmeliet P, Jain RK. Molecular mechanisms and clinical applications of angiogenesis. Nature. 2011;473(7347):298–307.
3. Cook KM, Figg WD. Angiogenesis inhibitors: current strategies and future prospects. CA Cancer J Clin. 2010;60(4):222–43.
4. Jain RK, et al. Biomarkers of response and resistance to antiangiogenic therapy. Nat Rev Clin Oncol. 2009;6(6):327–38.
5. Chen HX, Cleck JN. Adverse effects of anticancer agents that target the VEGF pathway. Nat Rev Clin Oncol. 2009;6(8):465–77.
6. Verheul HM, Pinedo HM. Possible molecular mechanisms involved in the toxicity of angiogenesis inhibition. Nat Rev Cancer. 2007;7(6):475–85.
7. Ebos JM, et al. Accelerated metastasis after short-term treatment with a potent inhibitor of tumor angiogenesis. Cancer Cell. 2009;15(3):232–9.
8. Paez-Ribes M, et al. Antiangiogenic therapy elicits malignant progression of tumors to increased local invasion and distant metastasis. Cancer Cell. 2009;15(3):220–31.
9. Shih T, Lindley C. Bevacizumab: an angiogenesis inhibitor for the treatment of solid malignancies. Clin Ther. 2006;28(11):1779–802.
10. Gotink KJ, Verheul HM. Anti-angiogenic tyrosine kinase inhibitors: what is their mechanism of action? Angiogenesis. 2010;13(1):1–14.
11. Oklu R, et al. Angiogenesis and current antiangiogenic strategies for the treatment of cancer. J Vasc Interv Radiol. 2010;21(12):1791–805; quiz 1806.
12. Tejpar S, et al. Overcoming resistance to antiangiogenic therapies. Oncologist. 2012;17(8):1039–50.

13. Bocci G, Loupakis F. The possible role of chemotherapy in antiangiogenic drug resistance. Med Hypotheses. 2012;78(5):646–8.
14. Helfrich I, et al. Resistance to antiangiogenic therapy is directed by vascular phenotype, vessel stabilization, and maturation in malignant melanoma. J Exp Med. 2010;207(3):491–503.
15. Cao Y, et al. Improvement of antiangiogenic cancer therapy by understanding the mechanisms of angiogenic factor interplay and drug resistance. Semin Cancer Biol. 2009;19(5):338–43.
16. Wang R, et al. Glioblastoma stem-like cells give rise to tumour endothelium. Nature. 2010;468(7325):829–33.
17. Nico B, et al. Evaluation of microvascular density in tumors: pro and contra. Histol Histopathol. 2008;23(5):601–7.
18. Jackson A, et al. Abnormalities in the recirculation phase of contrast agent bolus passage in cerebral gliomas: comparison with relative blood volume and tumor grade. AJNR Am J Neuroradiol. 2002; 23(1):7–14.
19. Tynninen O, et al. MRI enhancement and microvascular density in gliomas. Correlation with tumor cell proliferation. Invest Radiol. 1999;34(6):427–34.
20. Yao WW, et al. Rectal cancer: 3D dynamic contrast-enhanced MRI; correlation with microvascular density and clinicopathological features. Radiol Med. 2011;116(3):366–74.
21. Zhang XM, et al. 3D dynamic contrast-enhanced MRI of rectal carcinoma at 3T: correlation with microvascular density and vascular endothelial growth factor markers of tumor angiogenesis. J Magn Reson Imaging. 2008;27(6):1309–16.
22. Jackson A. Analysis of dynamic contrast enhanced MRI. Br J Radiol. 2004;77(Spec No 2):S154–66.
23. Tofts PS, Kermode AG. Measurement of the blood–brain barrier permeability and leakage space using dynamic MR imaging. 1. Fundamental concepts. Magn Reson Med. 1991;17(2):357–67.
24. Jackson A, et al. Dynamic contrast-enhanced magnetic resonance imaging in oncology. Berlin: Springer; 2005.
25. O'Connor JP, et al. Dynamic contrast-enhanced MRI in clinical trials of antivascular therapies. Nat Rev Clin Oncol. 2012;9(3):167–77.
26. Leach MO, et al. The assessment of antiangiogenic and antivascular therapies in early-stage clinical trials using magnetic resonance imaging: issues and recommendations. Br J Cancer. 2005;92(9): 1599–610.
27. O'Connor JP, et al. Quantifying antivascular effects of monoclonal antibodies to vascular endothelial growth factor: insights from imaging. Clin Cancer Res. 2009;15(21):6674–82.
28. Jayson GC, et al. Molecular imaging and biological evaluation of HuMV833 anti-VEGF antibody: implications for trial design of antiangiogenic antibodies. J Natl Cancer Inst. 2002;94(19):1484–93.
29. Engelbrecht MR, et al. Discrimination of prostate cancer from normal peripheral zone and central gland tissue by using dynamic contrast-enhanced MR imaging. Radiology. 2003;229(1):248–54.
30. Padhani AR, et al. Dynamic contrast enhanced MRI of prostate cancer: correlation with morphology and tumour stage, histological grade and PSA. Clin Radiol. 2000;55(2):99–109.
31. Rouviere O, et al. Characterization of time-enhancement curves of benign and malignant prostate tissue at dynamic MR imaging. Eur Radiol. 2003; 13(5):931–42.
32. Arasu VA, et al. Can signal enhancement ratio (SER) reduce the number of recommended biopsies without affecting cancer yield in occult MRI-detected lesions? Acad Radiol. 2011;18(6):716–21.
33. Jansen SA, et al. Normal parenchymal enhancement patterns in women undergoing MR screening of the breast. Eur Radiol. 2011;21(7):1374–82.
34. Jansen SA, et al. The diverse pathology and kinetics of mass, nonmass, and focus enhancement on MR imaging of the breast. J Magn Reson Imaging. 2011;33(6):1382–9.
35. Li KL, et al. Invasive breast cancer: predicting disease recurrence by using high-spatial-resolution signal enhancement ratio imaging. Radiology. 2008;248(1):79–87.
36. Partridge SC, et al. Association between serial dynamic contrast-enhanced MRI and dynamic 18F-FDG PET measures in patients undergoing neoadjuvant chemotherapy for locally advanced breast cancer. J Magn Reson Imaging. 2010;32(5): 1124–31.
37. Hattangadi J, et al. Breast stromal enhancement on MRI is associated with response to neoadjuvant chemotherapy. AJR Am J Roentgenol. 2008;190(6): 1630–6.
38. Gribbestad IS, et al. Comparative signal intensity measurements in dynamic gadolinium-enhanced MR mammography. J Magn Reson Imaging. 1994;4(3):477–80.
39. Williams TC, et al. Breast MR imaging: computer-aided evaluation program for discriminating benign from malignant lesions. Radiology. 2007; 244(1):94–103.
40. Flickinger FW, et al. Differentiation of benign from malignant breast masses by time-intensity evaluation of contrast enhanced MRI. Breast disease: tissue characterization with Gd-DTPA enhancement profiles. Radiology. 1990;174:491–4.
41. Su MY, et al. Correlation of dynamic contrast enhancement MRI parameters with microvessel density and VEGF for assessment of angiogenesis in breast cancer. J Magn Reson. 2003;18(4):467–77.
42. Brown J, et al. Magnetic resonance imaging screening in women at genetic risk of breast cancer: imaging and analysis protocol for the UK multicentre Study. UK MRI Breast Screening Study Advisory Group. Magn Reson Imaging. 2000; 18(7):765–76.
43. Kuhl CK, et al. Dynamic breast MR imaging: are signal intensity time course data useful for

differential diagnosis of enhancing lesions? Radiology. 1999;211(1):101–10.
44. Akisik MF, et al. Pancreatic cancer: utility of dynamic contrast-enhanced MR imaging in assessment of antiangiogenic therapy. Radiology. 2010; 256(2):441–9.
45. Zahra MA, et al. Semiquantitative and quantitative dynamic contrast-enhanced magnetic resonance imaging measurements predict radiation response in cervix cancer. Int J Radiat Oncol Biol Phys. 2009;74(3):766–73.
46. Florie J, et al. Dynamic contrast-enhanced MRI of the bowel wall for assessment of disease activity in Crohn's disease. AJR Am J Roentgenol. 2006; 186(5):1384–92.
47. de Lussanet QG, et al. Dynamic contrast-enhanced magnetic resonance imaging of radiation therapy-induced microcirculation changes in rectal cancer. Int J Radiat Oncol Biol Phys. 2005;63(5):1309–15.
48. Dyke JP, et al. Osteogenic and Ewing sarcomas: estimation of necrotic fraction during induction chemotherapy with dynamic contrast-enhanced MR imaging. Radiology. 2003;228(1):271–8.
49. Narang J, et al. Differentiating treatment-induced necrosis from recurrent/progressive brain tumor using nonmodel-based semiquantitative indices derived from dynamic contrast-enhanced T1-weighted MR perfusion. Neuro Oncol. 2011;13(9):1037–46.
50. Lavini C, et al. Model-based, semiquantitative and time intensity curve shape analysis of dynamic contrast-enhanced MRI: a comparison in patients undergoing antiangiogenic treatment for recurrent glioma. J Magn Reson Imaging. 2011;34(6):1303–12.
51. Bains LJ, et al. Tracer kinetic analysis of dynamic contrast-enhanced MRI and CT bladder cancer data: a preliminary comparison to assess the magnitude of water exchange effects. Magn Reson Med. 2010;64(2):595–603.
52. Naish JH, et al. Comparison of dynamic contrast-enhanced MRI and dynamic contrast-enhanced CT biomarkers in bladder cancer. Magn Reson Med. 2011;66(1):219–26.
53. Messiou C, et al. Advanced solid tumors treated with cediranib: comparison of dynamic contrast-enhanced MR imaging and CT as markers of vascular activity. Radiology. 2012;265(2):426–36.
54. Fournier LS, et al. Metastatic renal carcinoma: evaluation of antiangiogenic therapy with dynamic contrast-enhanced CT. Radiology. 2010;256(2):511–8.
55. Jain RK. Normalizing tumor vasculature with anti-angiogenic therapy: a new paradigm for combination therapy. Nat Med. 2001;7(9):987–9.
56. Schmainda KM, et al. Characterization of a first-pass gradient-echo spin-echo method to predict brain tumor grade and angiogenesis. AJNR Am J Neuroradiol. 2004;25(9):1524–32.
57. Batchelor TT, et al. AZD2171, a pan-VEGF receptor tyrosine kinase inhibitor, normalizes tumor vasculature and alleviates edema in glioblastoma patients. Cancer Cell. 2007;11(1):83–95.
58. Sorensen AG, et al. A "vascular normalization index" as potential mechanistic biomarker to predict survival after a single dose of cediranib in recurrent glioblastoma patients. Cancer Res. 2009; 69(13):5296–300.
59. Laking G, Price P. Radionuclide imaging of perfusion and hypoxia. Eur J Nucl Med Mol Imaging. 2010;37 Suppl 1:S20–9.
60. De Bazelaire C, et al. Arterial spin labeling blood flow magnetic resonance imaging for the characterization of metastatic renal cell carcinoma(1). Acad Radiol. 2005;12(3):347–57.
61. Fenchel M, et al. Early response assessment in patients with multiple myeloma during anti-angiogenic therapy using arterial spin labelling: first clinical results. Eur Radiol. 2010;20(12):2899–906.
62. de Langen AJ, et al. Reproducibility of tumor perfusion measurements using 15O-labeled water and PET. J Nucl Med. 2008;49(11):1763–8.
63. Hoekstra CJ, et al. Measurement of perfusion in stage IIIA-N2 non-small cell lung cancer using H(2)(15)O and positron emission tomography. Clin Cancer Res. 2002;8(7):2109–15.
64. Yamaguchi A, et al. Correlation between angiographically assessed vascularity and blood flow in hepatic metastases in patients with colorectal carcinoma. Cancer. 2000;89(6):1236–44.
65. Hentschel M, et al. Analysis of blood flow and glucose metabolism in mammary carcinomas and normal breast: a H2(15)O PET and 18F-FDG PET study. Nucl Med Commun. 2007;28(10):789–97.
66. Gupta N, et al. Carbogen and nicotinamide increase blood flow and 5-fluorouracil delivery but not 5-fluorouracil retention in colorectal cancer metastases in patients. Clin Cancer Res. 2006;12(10):3115–23.
67. Anderson H, et al. Measurement of renal tumour and normal tissue perfusion using positron emission tomography in a phase II clinical trial of razoxane. Br J Cancer. 2003;89(2):262–7.
68. Kurdziel KA, et al. Using positron emission tomography 2-deoxy-2-[18F]fluoro-D-glucose, 11CO, and 15O-water for monitoring androgen independent prostate cancer. Mol Imaging Biol. 2003;5(2): 86–93.
69. Tofts PS, et al. Quantitative analysis of dynamic Gd-DTPA enhancement in breast tumors using a permeability model. Magn Reson Med. 1995; 33(4):564–8.
70. Leach MO, et al. Imaging vascular function for early stage clinical trials using dynamic contrast-enhanced magnetic resonance imaging. Eur Radiol. 2012;22(7):1451–64.
71. Medved M, et al. Semiquantitative analysis of dynamic contrast enhanced MRI in cancer patients: variability and changes in tumor tissue over time. J Magn Reson Imaging. 2004;20(1):122–8.
72. O'Donnell A, et al. A phase I study of the angiogenesis inhibitor SU5416 (semaxanib) in solid tumours, incorporating dynamic contrast MR pharmacodynamic end points. Br J Cancer. 2005;93(8):876–83.

73. Dowlati A, et al. Novel phase I dose de-escalation design trial to determine the biological modulatory dose of the antiangiogenic agent SU5416. Clin Cancer Res. 2005;11(21):7938–44.
74. Miller KD, et al. A multicenter phase II trial of ZD6474, a vascular endothelial growth factor receptor-2 and epidermal growth factor receptor tyrosine kinase inhibitor, in patients with previously treated metastatic breast cancer. Clin Cancer Res. 2005;11(9):3369–76.
75. Annunziata CM, et al. Vandetanib, designed to inhibit VEGFR2 and EGFR signaling, had no clinical activity as monotherapy for recurrent ovarian cancer and no detectable modulation of VEGFR2. Clin Cancer Res. 2010;16(2):664–72.
76. Mross K, et al. DCE-MRI assessment of the effect of vandetanib on tumor vasculature in patients with advanced colorectal cancer and liver metastases: a randomized phase I study. J Angiogenes Res. 2009;1:5.
77. Morgan B, et al. Dynamic contrast-enhanced magnetic resonance imaging as a biomarker for the pharmacological response of PTK787/ZK 222584, an inhibitor of the vascular endothelial growth factor receptor tyrosine kinases, in patients with advanced colorectal cancer and liver metastases: results from two phase I studies. J Clin Oncol. 2003;21(21): 3955–64.
78. Mross K, et al. Phase I clinical and pharmacokinetic study of PTK/ZK, a multiple VEGF receptor inhibitor, in patients with liver metastases from solid tumours. Eur J Cancer. 2005;41(9):1291–9.
79. Thomas AL, et al. Phase I study of the safety, tolerability, pharmacokinetics, and pharmacodynamics of PTK787/ZK 222584 administered twice daily in patients with advanced cancer. J Clin Oncol. 2005;23(18):4162–71.
80. Drevs J, et al. A phase IA, open-label, dose-escalating study of PTK787/ZK 222584 administered orally on a continuous dosing schedule in patients with advanced cancer. Anticancer Res. 2010; 30(6):2335–9.
81. Hecht JR, et al. Randomized, placebo-controlled, phase III study of first-line oxaliplatin-based chemotherapy plus PTK787/ZK 222584, an oral vascular endothelial growth factor receptor inhibitor, in patients with metastatic colorectal adenocarcinoma. J Clin Oncol. 2011;29(15):1997–2003.
82. Ellis LM. Antiangiogenic therapy: more promise and, yet again, more questions. J Clin Oncol. 2003;21(21):3897–9.
83. Jonker DJ, et al. A phase I study to determine the safety, pharmacokinetics and pharmacodynamics of a dual VEGFR and FGFR inhibitor, brivanib, in patients with advanced or metastatic solid tumors. Ann Oncol. 2011;22(6):1413–9.
84. Eder M, et al. ScVEGF-PEG-HBED-CC and scVEGF-PEG-NOTA conjugates: comparison of easy-to-label recombinant proteins for [68Ga]PET imaging of VEGF receptors in angiogenic vasculature. Nucl Med Biol. 2010;37(4):405–12.
85. Fedorova A, et al. The development of peptide-based tools for the analysis of angiogenesis. Chem Biol. 2011;18(7):839–45.
86. Matusiak N, et al. Probes for non-invasive matrix metalloproteinase-targeted imaging with PET and SPECT. Curr Pharm Des. 2013;19(25): 4647–72.
87. Michalski MH, Chen X. Molecular imaging in cancer treatment. Eur J Nucl Med Mol Imaging. 2011;38(2):358–77.
88. Niu G, Chen X. PET imaging of angiogenesis. PET Clin. 2009;4(1):17–38.
89. Saga T, et al. Molecular imaging of cancer: evaluating characters of individual cancer by PET/SPECT imaging. Cancer Sci. 2009;100(3):375–81.
90. Stacy MR, et al. Targeted molecular imaging of angiogenesis in PET and SPECT: a review. Yale J Biol Med. 2012;85(1):75–86.
91. Ferrara N. Vascular endothelial growth factor: basic science and clinical progress. Endocr Rev. 2004;25(4):581–611.
92. Nagengast WB, et al. In vivo VEGF imaging with radiolabeled bevacizumab in a human ovarian tumor xenograft. J Nucl Med. 2007;48(8):1313–9.
93. Scheer MG, et al. Imaging liver metastases of colorectal cancer patients with radiolabelled bevacizumab: lack of correlation with VEGF-A expression. Eur J Cancer. 2008;44(13):1835–40.
94. Cai W, et al. PET of vascular endothelial growth factor receptor expression. J Nucl Med. 2006;47(12):2048–56.
95. Chen K, et al. Quantitative PET imaging of VEGF receptor expression. Mol Imaging Biol. 2009;11(1):15–22.
96. Nagengast WB, et al. VEGF-PET imaging is a noninvasive biomarker showing differential changes in the tumor during sunitinib treatment. Cancer Res. 2011;71(1):143–53.
97. Takada Y, et al. The integrins. Genome Biol. 2007;8(5):215.
98. Desgrosellier JS, Cheresh DA. Integrins in cancer: biological implications and therapeutic opportunities. Nat Rev Cancer. 2010;10(1):9–22.
99. Haubner R, et al. [18F]galacto-RGD: synthesis, radiolabeling, metabolic stability, and radiation dose estimates. Bioconjug Chem. 2004;15(1):61–9.
100. Beer AJ, et al. Positron emission tomography using [18F]Galacto-RGD identifies the level of integrin alpha(v)beta3 expression in man. Clin Cancer Res. 2006;12(13):3942–9.
101. Beer AJ, et al. [18F]galacto-RGD positron emission tomography for imaging of alphavbeta3 expression on the neovasculature in patients with squamous cell carcinoma of the head and neck. Clin Cancer Res. 2007;13(22 Pt 1):6610–6.
102. Beer AJ, et al. Patterns of alphavbeta3 expression in primary and metastatic human breast cancer as shown by 18F-Galacto-RGD PET. J Nucl Med. 2008;49(2):255–9.
103. Hanaoka H, et al. Chemical design of a radiolabeled gelatinase inhibitor peptide for the imaging of

gelatinase activity in tumors. Nucl Med Biol. 2007;34(5):503–10.
104. Liu S, et al. Evaluation of a (99m)Tc-labeled cyclic RGD tetramer for noninvasive imaging integrin alpha(v)beta3-positive breast cancer. Bioconjug Chem. 2007;18(2):438–46.
105. Li ZB, et al. (64)Cu-labeled tetrameric and octameric RGD peptides for small-animal PET of tumor alpha(v)beta(3) integrin expression. J Nucl Med. 2007;48(7):1162–71.
106. Battle MR, et al. Monitoring tumor response to antiangiogenic sunitinib therapy with 18F-fluciclatide, an 18F-labeled alphaVbeta3-integrin and alphaV beta5-integrin imaging agent. J Nucl Med. 2011;52(3):424–30.
107. Gaertner FC, et al. Radiolabelled RGD peptides for imaging and therapy. Eur J Nucl Med Mol Imaging. 2012;39 Suppl 1:S126–38.
108. Galis ZS, Khatri JJ. Matrix metalloproteinases in vascular remodeling and atherogenesis: the good, the bad, and the ugly. Circ Res. 2002;90(3):251–62.
109. Pellikainen JM, et al. Expression of matrix metalloproteinase (MMP)-2 and MMP-9 in breast cancer with a special reference to activator protein-2, HER2, and prognosis. Clin Cancer Res. 2004; 10(22):7621–8.
110. Koivunen E, et al. Tumor targeting with a selective gelatinase inhibitor. Nat Biotechnol. 1999;17(8): 768–74.
111. Sprague JE, et al. In vitro and in vivo investigation of matrix metalloproteinase expression in metastatic tumor models. Nucl Med Biol. 2006; 33(2):227–37.
112. Zheng QH, et al. Synthesis and preliminary biological evaluation of MMP inhibitor radiotracers [11C] methyl-halo-CGS 27023A analogs, new potential PET breast cancer imaging agents. Nucl Med Biol. 2002;29(7):761–70.
113. Gaertner FC, et al. Molecular imaging of alphavss3 expression in cancer patients. Q J Nucl Med Mol Imaging. 2010;54(3):309–26.

Imaging of Tumor Metabolism: MR Spectroscopy

8

Asif Rizwan and Kristine Glunde

Contents

A. Rizwan
Division of Cancer Imaging Research,
The Russell H. Morgan Department of Radiology and Radiological Science, The Johns Hopkins University School of Medicine, Traylor Building, Room 310A, 720 Rutland Avenue,
Baltimore, MD 21205, USA
e-mail: arizwan2@jhmi.edu

K. Glunde (✉)
Division of Cancer Imaging Research,
The Russell H. Morgan Department of Radiology and Radiological Science, The Johns Hopkins University School of Medicine, Traylor Building, Room 212, 720 Rutland Avenue,
Baltimore, MD 21205, USA

Sidney Kimmel Comprehensive Cancer Center,
Baltimore, MD 21231, USA
e-mail: kglunde@mri.jhu.edu

Abbreviations

3-APP	3-aminopropyl phosphonate
5-FC	5-fluorocytosine
5-FU	5-fluorouracil
AKT	Protein kinase B
AMPK	Adenosine monophosphate-activated protein kinase
Asp-NAT	Aspartate *N*-acetyltransferase
ATP	Adenosine-5′-triphosphate
CA	Carbonic anhydrase
CCL-103F	1-(2-hydroxy-3-hexaflu–oroisopro-poxy-propyl)-2-nitroimidazole
CCT	CTP–phosphocholinecytidylyl-transferase
CDP-Eth	Cytidine diphosphate ethanolamine

A. Luna et al. (eds.), *Functional Imaging in Oncology,*
DOI 10.1007/978-3-642-40412-2_8, © Springer-Verlag Berlin Heidelberg 2014

CEST	Chemical exchange saturation transfer
CF3PM	5,6-dimethyl-4-[3-(2-nitro1-imidazolyl)-propylamino]-2-trifluoromethylpyrimidine hydrochloride
Cho	Free choline
CHPT	Cholinephosphotransferase
CHT	High-affinity choline transporter
CK	Choline kinase
CLT	Choline transporter-like proteins
CoA	Coenzyme A
Cr	Creatine
CSI	Chemical shift imaging
CTP	Cytidine triphosphate
DNP	Dynamic nuclear polarization
FGF	Fibroblast growth factor
FID	Free induction decay
FNuct	Fluoronucleotides
Gln	Glutamine
Glu	Glutamate
Glx	Sum of Glu and Gln
GPC	Glycerophosphocholine
GPE	Glycerophosphoethanolamine
HIF	Hypoxia-inducible factor
HR-NMR	High-resolution NMR
HSQC	Heteronuclear single-quantum correlation spectroscopy
IEPA	2-imidazole-1-yl-3-ethoxycarbonyl propionic acid
IgG	Immunoglobulin
IL	Interleukin
JNK	c-Jun N-terminal kinase
LDH	Lactate dehydrogenase
MAP	Mitogen-activated protein
MCT	Monocarboxylate transporters
MRS	Magnetic resonance spectroscopy
MS	Multiple sclerosis
mTOR	Mammalian target of rapamycin
NAA	*N*-acetylaspartate
NADH	Reduced form of nicotinamide adenine dinucleotide
NaTFA	Sodium trifluoroacetate
NDP	Nucleoside diphosphate
NMR	Nuclear magnetic resonance
NTP	Nucleoside triphosphate
OCTN	Organic cation/carnitine transporters
PA	Phosphatidic acid
PC	Phosphocholine
PCA	Perchloric acid
PCr	Phosphocreatine
PDE	Phosphodiester
PEMT	Phosphatidylethanolamine *N*-methyltransferase
pHe	pH extracellular
pHi	PH intracellular
Pi	Pnorganic phosphate
PI3K	Phosphatidylinositol 3-kinases
PLA	Phospholipase A
PME	Phosphomonoester
PPM	Parts per million
PtdCho	Phosphatidylcholine
PtdEth	Phosphatidylethanolamine
RF	Radio frequency
RIF	Radiation-induced fibrosarcoma
RINEPT	Refocused insensitive nuclei enhanced by polarization transfer
RTK	Receptor tyrosine kinase
SelMQC	Selective multiple-quantum coherence filter
TCA	Tricarboxylic acid
tCho	Total choline
tCr	Total creatine
TP53	Tumor protein 53
TRAMP	Transgenic adenocarcinomas of mouse prostate
VHL	Von Hippel–Lindau
Yb-DO3A-oAA	Ytterbium-1,4,7,10-tetraazacyclododecane-1,4,7-tetraacetic acid

8.1 Introduction

Cancer is a disease in which abnormal cells divide uncontrolled without effective cell cycle regulation to regulate their growth and homeostasis [1, 2]. The American Cancer Society has stated that half of all men and one-third of all women in the United States will develop cancer during their lifetime [1]. It is estimated that 1,638,910 new cancer cases and 577,190 cancer-related

deaths occurred in the United States in 2012 [3]. Abnormal metabolism is an important feature of cancers cells, and it results in a variety of phenotypes in cancers cells [4, 5]. In addition, this altered metabolism in cancer cells may also play an important role in resistance to chemotherapies, and it offers new molecular targets for anticancer therapy [4, 5]. Therefore, understanding how different cancer cells adjust and regulate their metabolism is essential for understanding cancer, tumor microenvironment, and metastatic spread and for successfully treating cancer. Magnetic resonance spectroscopy (MRS) enables us to measure and visualize distributions of metabolites in tumors [6, 7]. This book chapter describes studies of tumor metabolism using MRS methods in cultured cells, in tumor models ex vivo and in vivo, as well as advanced MRS techniques that can identify specific markers of tumor metabolic changes.

8.2 Tumor Metabolism and Oncogenes

Cancer cells typically have a high proliferation rate, and as a result, many metabolic pathways, such as glycolysis, the tricarboxylic acid (TCA) cycle, oxidative phosphorylation, the pentose phosphate pathway, and the synthesis of nucleotides and lipids, are modified to promote nutrient uptake and to meet the high demand for bioenergetics and biosynthesis precursors [8, 9]. The major energy sources utilized by cancer cells are glucose and glutamine [5, 8]. In normal cells, glucose is mostly metabolized through glycolysis, which produces pyruvate. In the presence of oxygen, pyruvate enters the mitochondria. Pyruvate is then converted to acetyl-CoA and enters the TCA cycle. Each TCA cycle generates three molecules of NADH (reduced form of nicotinamide adenine dinucleotide), which donate their electrons to the electron transport chain to drive adenosine-5′-triphosphate (ATP) synthesis. Collectively, these processes are known as cellular respiration. There is some disagreement, but most reports conclude that 36 molecules of ATP are produced from each molecule of glucose during respiration [10]. In contrast to normal mammalian cells, cancer cells prefer glycolysis to cellular respiration, even in the presence of oxygen [1, 2]. This phenomenon is known as Warburg effect [11]. Pyruvate is converted to lactate instead of entering the TCA cycle, and NADH is oxidized to NAD^+ to allow glycolysis to continue. Most cancer cells also use glutamine, besides glucose, for metabolism, protein synthesis, and nucleotide base synthesis and as a precursor for other amino acids [12, 13]. Abnormal choline phospholipid metabolism is another metabolic hallmark of cancer cells [14, 15]. The choline metabolite profile of cancer cells is characterized by elevated phosphocholine (PC), which is often accompanied by elevated glycerophosphocholine (GPC). The enzymes directly causing this elevation include choline kinase alpha, phospholipase C, phospholipase D, and phospholipases A2 [15, 16].

A number of oncogenes [17] and tumor suppressor genes [18] drive cancer cell metabolism such as hypoxia-inducible factors (HIFs), myc, NF-κB, Ras, phosphatidylinositol 3-kinases (PI3K), Akt (protein kinase B), receptor tyrosine kinases (RTKs), mitogen-activated protein (MAP) kinases, mammalian target of rapamycin (mTOR), adenosine monophosphate-activated protein kinase (AMPK), tumor protein 53 (TP53), and Von Hippel–Lindau (VHL) [15, 19, 20]. These oncogenes and tumor suppressor genes display complex reciprocal interactions with several metabolic pathways [15, 19, 20]. A deeper understanding of the pathways that connect oncogenes or tumor suppressor genes to the metabolic reprogramming of cancer cells will hopefully reveal new targets for anticancer treatment, which can be monitored by detecting the metabolic end product of the targeted pathway.

8.3 Fundamentals of Magnetic Resonance Spectroscopy

Here, we briefly introduce metabolic MRS techniques and their applications. Some of the key nuclei and their applications are also summarized in Table 8.1. The nuclear magnetic resonance

Table 8.1 MR-detectable metabolites and their applications in tumor metabolism

Nucleus	Detected metabolite or signal	Application to tumor metabolism
^{1}H	Cho, GPC, PC, tCho [7, 15]	Choline phospholipid metabolism
	Alanine, lactate, pyruvate [6, 27, 117]	Glycolysis
	Triacylglycerides (–CH_2–**CH_2**–CH_2–), (**CH_3**–CH_2–), (–**CH**=CH–), (–CH=CH–**CH_2**–CH=CH–) [132]	Mobile lipids
	Cr, PCr, tCr [158]	Energy metabolism
	Citrate, fumarate, Gln, Glu, Glx, succinate [27, 285]	TCA cycle
	2-Hydroxyglutarate [173, 174]	Mutated isocitrate dehydrogenase 1
	IEPA [192, 193], Yb-DO3A-oAA [199]	Extracellular pH (pHe)
	N-Acetylaspartate [145, 146]	Marker of neuronal health
^{19}F	5-Fluorouracil (5-FU) [227], 5-fluorocytosine (5-FC) [233]	Anticancer drug pharmacokinetics
	Fluorinated nitroimidazoles (CF3PM, CCL-103F) [235–238]	Tumor hypoxia
^{31}P	3-APP [200, 201]	Tumor pHe
	Chemical shift difference between Pi and PCr or NTP [200]	Tumor pHi
	PC,GPC, PME, PDE [7, 204, 216, 217, 286, 287]	Choline phospholipid metabolism
	PE, GPE, PME, PDE [7, 204, 216, 217]	Ethanolamine phospholipid metabolism
	NTPs, NDPs, PCr, Pi [7, 204, 216, 217]	Energy metabolism
^{13}C	^{13}C-labeled substrates ([1-^{13}C] glucose, [U-^{13}C] glucose, [3-^{13}C] pyruvate, [3-^{13}C] lactate, [4-^{13}C] α-ketoglutarate) [244, 249, 250]	Metabolic flux, enzyme activities
	Hyperpolarized ^{13}C-labeled substrates ([1-^{13}C] pyruvate, [1-^{13}C] lactate, [1-^{13}C] glutamine) [47, 103, 262]	Metabolic flux, enzyme activities
	Hyperpolarized bicarbonate [279]	Tumor pH

Abbreviations: *3-APP* 3-Aminopropyl phosphonate, *IEPA* 2-imidazole-1-yl-3-ethoxycarbonyl propionic acid, *CCL-103F* 1-(2-hydroxy-3-hexafluoroisopropoxy-propyl)-2-nitroimidazole, *CF3PM* 5,6-dimethyl-4-[3-(2-nitro-1-imidazolyl)-propylamino]-2-trifluoromethylpyrimidine hydrochloride, *Cho* Choline, *Cr* Creatine, *Glu* Glutamate, *Gln* Glutamine, *Glx* Sum of Glu and Gln, *GPC* glycerophosphocholine, *NDP* nucleoside diphosphate, *NTP* nucleoside triphosphate, *PC* phosphocholine, *PCr* phosphocreatine, *PDE* phosphodiester, *Pi* inorganic phosphate, *PME* phosphomonoester, *tCho* total choline, *tCr* total creatine, *Yb-DO3A-oAA* ytterbium-1,4,7,10-tetraazacyclododecane-1,4,7-tetraacetic acid

(NMR) signal is based on the fact that the nuclei have magnetic properties that can be exploited to generate information about their chemical properties [21–24]. MR-active nuclei have odd numbers of protons, neutrons, or both, and they possess a magnetic moment. Commonly employed MRS metabolic measurements are from ^{1}H, ^{19}F, ^{31}P, and ^{13}C, in descending order of sensitivity [7]. In the presence of an external magnetic field B_0, the magnetic moments from these nuclei will align either with or against B_0, and they will precess at a resonant frequency, ω_0.

Detection of these magnetic moments is possible after excitation with a radio-frequency (RF) pulse transmitted by an RF coil at the resonant frequency of the nuclei of interest. During excitation, the nuclei will be promoted to the less favorable higher energy state after absorbing the energy from the RF pulse. After each excitation pulse, one must wait for the spins to return to the equilibrium, which is a process termed relaxation. The motion of the magnetic moments during relaxation generates RF signals whose intensities depend on the concentration of the nuclei and on two rate constants that govern the relaxation times of the magnetization: (1) the exponentially decaying spin–lattice or longitudinal relaxation time T1 and (2) the exponentially decaying spin–spin or transverse relaxation time T2 [25]. The detected free

induction decay (FID) of these RF signals can be Fourier transformed to generate a frequency domain spectrum that contains peaks from different metabolites [26].

The local electron distributions in a molecule can shield the nuclei of interest to various degrees from the applied magnetic field B_0. Thus, MRS signals are typically shifted in the frequency domain and thereby provide information about the chemical environment of the nuclear spin, such as chemical bonds, chemical structure, and neighboring nuclei. This difference in resonance frequency is known as chemical shift. Chemical shifts of nuclei are expressed as parts per million (ppm) and are typically reported relative to a reference frequency.

In vivo MRS can be either localized (single- or multi-voxel) or non-localized. Single-voxel localization gives signal from a defined volume to minimize signal contributions from neighboring tissues. Multi-voxel MR spectra provide spatial information about the distribution of the metabolites. Chemical shift imaging (CSI) can be utilized for obtaining 1-dimensional (1D), 2D, or 3D spectra from the tissue of interest. Phase encoding gradients are incorporated in CSI to generate a grid of MR spectra. Non-localized MRS provides signals from the entire sensitive region of the coil that detects the RF signal. Non-localized MRS is often used for metabolites with very short T2 relaxation, as it requires minimizing the time delay between excitation and acquisition [27].

Metabolites extracted from cancer cells, tumor tissues, or body fluids such as plasma and urine can be analyzed by high-resolution NMR spectroscopy (HR-NMR) [28]. A number of different extraction techniques exist for this purpose such as the perchloric acid (PCA) method, which extracts water-soluble metabolites [29]. The dual-phase extraction method utilizes a chloroform/methanol/water extraction and will yield the simultaneous extraction of water-soluble metabolites and organic solvent-soluble lipid components from the same sample [29]. These extracts can be measured by HR-NMR, which analyzes the different metabolites either by pattern recognition or by quantifying their concentrations [27].

8.4 Commonly Used MR-Active Nuclei for Investigating Tumor Metabolism

Proton or ^{1}H NMR is the most commonly used NMR nucleus with 99.99 % natural abundance of the ^{1}H isotope. In vivo ^{1}H MRS is dominated by the water signal and therefore may require suppressing it. ^{1}H MRS data can be analyzed by either utilizing the water signal as a concentration reference or by calculating the ratio of the signals from certain metabolites [6, 7, 27]. Some of the commonly measured metabolites in ^{1}H MRS and HR-NMR include choline-containing compounds, lactate, lipids, *N*-acetylaspartate, creatine and phosphocreatine, glutamate and glutamine, myoinositol, alanine, and citrate [6, 7, 30]. Moreover, ^{1}H MRS can also be utilized to measure tumor pH and tumor oxygen consumption [6, 31].

The ^{19}F nucleus has 100 % natural abundance and mammalian tissue contains no endogenous MR-visible ^{19}F. As a result, there is no background ^{19}F MR signal that can interfere with that from administered ^{19}F-containing compounds. A number of ^{19}F-containing chemotherapeutic agents such as 5-fluorouracil (5-FU) can be used to map the drug distribution and metabolism of the administered compound [32, 33]. The sensitivity of ^{19}F chemical shifts due to the local environment is higher than that of ^{1}H as the ^{19}F nucleus is typically surrounded by nine electrons rather than a single electron as is the case with ^{1}H [34]. Examples of ^{19}F MRS applications include measurements of tumor pH, oxygen content, and tumor glucose consumption, as well as anticancer drug pharmacokinetics [32, 33, 35–37].

^{31}P MRS can be used as a noninvasive tool for measuring the relative intracellular concentrations of several ^{31}P-containing metabolites such as inorganic phosphate (Pi), phosphocreatine (PCr), adenosine triphosphate (ATP), phosphomonoesters (PMEs) such as phosphocholine (PC) and phosphoethanolamine (PE), and phosphodiesters (PDEs) such as glycerophosphocholine (GPC) and glycerophosphoethanolamine

(GPE) [38–41]. The acid dissociation constant p*K*a of *P*i is in the physiological range. As the electron distribution and shielding of the ^{31}P atom changes with changes in pH, it is possible to detect the change in pH-dependent chemical shift from *P*i with ^{31}P MRS.

With only 1.1 % natural abundance of the ^{13}C isotope, ^{13}C MRS of endogenous metabolites is less sensitive than ^{1}H. However, it is possible to administer ^{13}C-labeled substrates and follow the incorporation of the ^{13}C-label from the substrate into other molecules with ^{13}C MRS [42–45]. For example, glycolytic rates can be measured by assessing the uptake and metabolism of ^{13}C-labeled glucose in cancer cells or in tumor models in animals [6]. One of the most important innovations in recent years is the development of automated dynamic nuclear polarization equipment for hyperpolarizing ^{13}C nuclei, which can be used to measure metabolic fluxes through select enzyme-catalyzed steps with up to 10,000-fold improved sensitivity [46–52]. However, this technique requires hyperpolarized substrates with long T1 relaxation times [46]. Therefore, compounds such as pyruvate are particularly attractive for hyperpolarization as the T1 relaxation time for the C1 position of hyperpolarized [1-^{13}C] pyruvate is long (40 s at 14.1 T) [50].

Other nuclei such as ^{23}Na and ^{2}H have some limited applications for MRS. ^{23}Na MRS, with 100 % natural abundance of the ^{23}Na isotope, offers the advantage of noninvasive measurements of the sodium content in tumors. Increased sodium concentrations have been found in brain tumors relative to that in normal brain structures [51]. Tumor blood flow can be measured using ^{2}H MRS by noninvasively measuring the uptake of D_2O solution [53].

8.4.1 ^{1}H MRS of Choline Phospholipid Metabolism

Choline is an essential nutrient [54] and can be found in a wide variety of foods such as egg yolk, seeds, legumes, vegetables, kidney, and liver. The liver can synthesize phosphatidylcholine (PtdCho) from phosphatidylethanolamine (PtdEth), which is catalyzed by the enzyme phosphatidylethanolamine *N*-methyltransferase (PEMT) [55, 56]. PEMT gene expression is induced by estrogen, and hence, most men and postmenopausal women need to consume choline in their diet [55]. Choline is essential for the structure and function of all living cells [15, 57]. It is required for the synthesis of phospholipids to form cell membranes and enable membrane signaling, for the synthesis of acetylcholine to function as neurotransmitter, for the synthesis of lipoproteins to enable lipid transport, and as a source of methyl groups [54]. Activated choline phospholipid metabolism is characterized by increased levels of phosphocholine (PC) and total choline-containing compounds (tCho), and most tumor types investigated so far display an activated choline phospholipid metabolism, which is driven by oncogenic signaling [15, 58–62]. Increasing proliferation with growth hormones did not increase the PC and tCho levels in normal cells [63].

PC is a precursor and a breakdown product of PtdCho. PtdCho together with other phospholipids such as PtdEth and neutral lipids forms the cellular lipid bilayer membranes and regulates membrane integrity. The increased PC and tCho levels in tumors are caused by overexpression and activation of multiple choline transporters and enzymes in choline phospholipid metabolism of cancer cells [15]. The transport of free extracellular choline into cancer cells is assisted by four types of choline-transporting membrane systems, namely, high-affinity choline transporters (CHTs), choline transporter-like proteins (CTLs), organic cation transporters (OCTs), and organic cation/carnitine transporters (OCTNs) [15, 64–67]. Cancer cells display an increased expression of these choline-transporting systems [15, 16], which results in an increased rate of choline transport into cancer cells, eventually leading to increased PC levels [68–70].

Intracellular choline is converted to PC by the enzyme choline kinase (CK) [71], and this enzyme is highly active in tumors of the lung, ovary, colon, cervix, breast, and prostate [72, 73]. Choline kinase α (CKα) expression and activity is linked with cancer cell proliferation and can be a potential marker for cancer prognosis [15]. Another source for the elevated intracellular

choline compounds in cancer cells is an increased activity of phospholipase D (PLD), which hydrolyses PtdCho to phosphatidic acid (PA) and choline. Increased PLD expression and activity was reported in breast cancer [74], gastric cancer [75], ovarian cancer [76], and melanoma [77] cells. Higher expression of PLD is associated with a higher invasive potential of human breast cancer cells [78]. Other enzymes, such as phospholipase A2 (PLA2), lysophospholipase, GPC phosphodiesterase, and diacylglycerol cholinephosphotransferase 1 (CHPT1), are also important in altering the metabolite levels of PC, GPC, and choline [15]. Metastatic breast tumors have a significantly higher expression of PLA2 enzymes compared to nonmetastatic breast tumors in humans [79]. Figure 8.1a shows choline phospholipid metabolism in a cancer cell with the oncogenic signaling pathways that drive alterations in enzyme activity or expression within choline phospholipid metabolism [15].

There is evidence for the oncogenic potential of CKα as its activation potentiates Rho-A-induced malignant transformation and metastasis [80]. Furthermore, enzymes in choline phospholipid metabolism can be regulated by other oncogenic signaling pathways [81] such as Ras [82–85] and the PI3K/AKT pathway [84, 86] (Fig. 8.1a). One of the downstream kinases of Ras is the mitogen-activated protein kinase (MAPK) family member c-Jun *N*-terminal kinase (JNK). JNK phosphorylates and inhibits CTP–phosphocholine cytidylyltransferase (CCT) [87]. Since cytidine triphosphate (CTP) catalyzes the rate-limiting step in PtdCho biosynthesis in cells, JNK kinases work as negative regulators of phospholipid synthesis (Fig. 8.1a).

In breast [63] and ovarian [88] cancers, malignant transformation leads to a GPC to PC switch in the choline phospholipid metabolite profile, leading to a lower GPC/PC ratio in these cancers compared with respective normal tissue (Fig. 8.1b). ^{1}H MR spectra in Fig. 8.1b–d show elevated PC and tCho in tumor cells (Fig. 8.1b), in tumor biopsy extracts (Fig. 8.1c), and in a tumor in vivo (Fig. 8.1d) [63, 89–91]. Prostate cancer cells exhibit significantly higher PC as well as GPC levels compared with normal prostate epithelial and stromal cells [88]. ^{1}H MRS can detect these metabolic changes in tumor tissue biopsies or cancer cells ex vivo. ^{1}H NMR spectra of cell extracts reveal three water-soluble choline metabolites such as free choline (Cho), GPC, and PC between 3.2 and 3.3 ppm. The tCho ^{1}H MRS peak detected in in vivo MRS consists of overlapping signals from Cho, PC, and GPC, which is due to the broad-line widths typically obtained in in vivo MRS because of less homogeneous magnetic fields in live tissues. Therefore, a single tCho peak is detected instead of individual Cho, PC, and GPC peaks. Clinical trials are currently in progress to optimize ^{1}H MRS for in vivo applications to resolve the tCho peak into its constituent resonances by using higher magnetic field strengths and post-processing means projected to optimize spectral resolution.

8.4.2 ^{1}H MRS of Lactate Metabolism

In cellular metabolism, pyruvate is mainly obtained from glucose and glutamine metabolism [92–94]. The lactate dehydrogenase A (LDH-A) enzyme catalyzes the reversible conversion of pyruvate to lactate [95]. This reversible reaction also results in the generation of NAD^{+}, which helps to continue further glycolysis [96]. Almost all eukaryotic cells have LDH isoenzymes, reflecting the significance of this metabolic step. In the presence of oxygen, the accumulated lactate can be converted back to pyruvate by LDH-B, which is further oxidized to CO_2 and H_2O in the TCA cycle [96, 97]. Each TCA cycle generates three molecules of NADH, which transfer their electrons to the electron transport chain to drive ATP synthesis. These processes together are known as cellular respiration, producing around 36 molecules of ATP from each molecule of glucose [10]. In contrast to normal mammalian cells, cancer cells prefer glycolysis to cellular respiration, even in the presence of oxygen. Warburg [11] first described the accumulation of lactate in tumor cells and its association with aerobic glycolysis (Fig. 8.2a). Activation of oncogenic signaling by PI3K/AKT, Ras, Myc, and PTEN mutation enhances aerobic glycolysis (Fig. 8.2a). The glycolytic enzyme LDH-A converts pyruvate to lactate, concomitantly oxidizing NADH to NAD^{+} and thereby promoting further glycolytic flux (Fig. 8.2a).

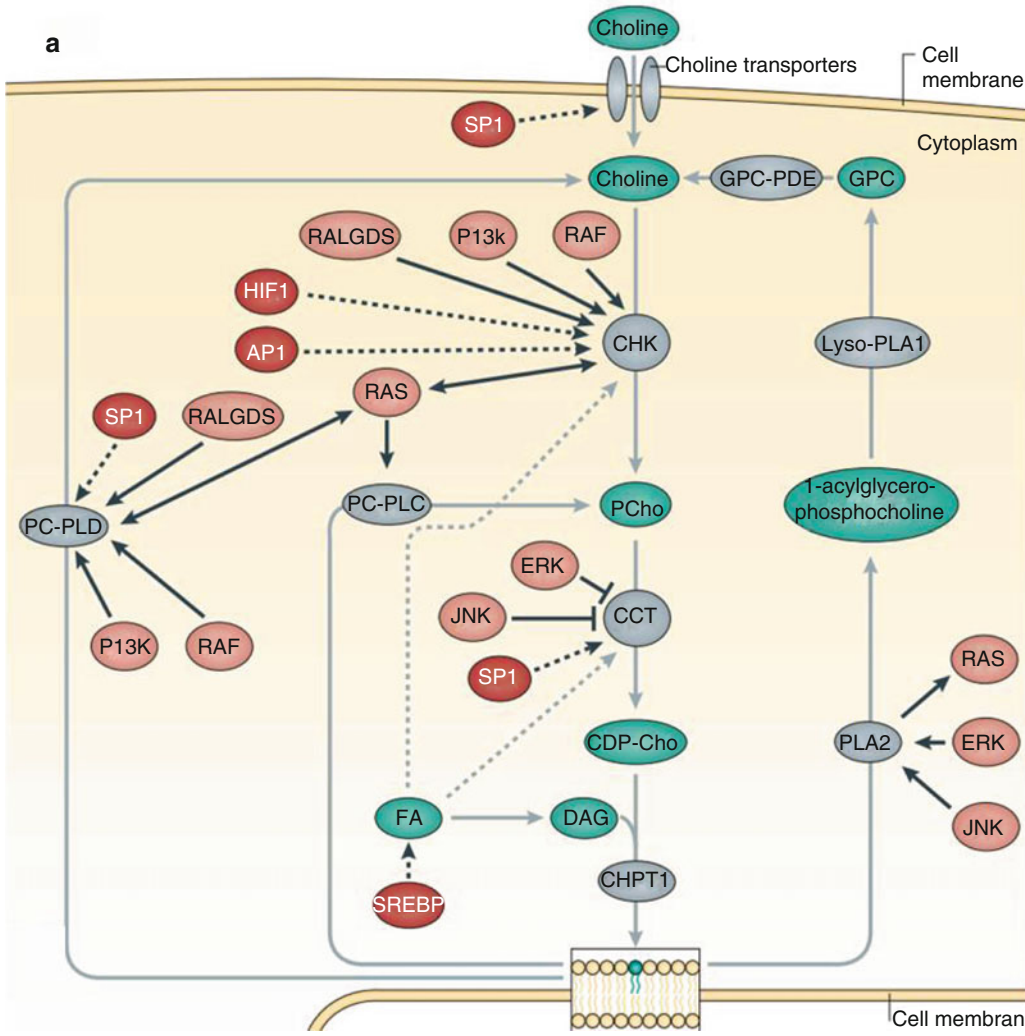

Fig. 8.1 ^{1}H MRS of choline phospholipid metabolism. (**a**) Pathways of choline phospholipid metabolism in mammalian cells. *Gray arrows* represent choline metabolic pathways, *dashed gray arrows* indicate the regulation of enzyme activity in choline metabolism, and *black arrows* indicate connections to oncogenic signaling pathways. *Solid black arrows* indicate increased or decreased enzyme activity, and *dashed black arrows* indicate increased gene transcription. *AP1* activator protein 1, *CHK* choline kinase, *CHPT1* diacylglycerol cholinephosphotransferase 1, *CCT* CTP–phosphocholine cytidylyltransferase, *DAG* diacylglycerol, *FA* fatty acid, *GPC* glycerophosphocholine, *HIF-1* hypoxia-inducible factor-1, *JNK* JUN N-terminal kinase, *PC-PLC* phosphatidylcholine-specific phospholipase C, *PC-PLD* phosphatidylcholine-specific phospholipase D, *PLA2* phosphatidylcholine-specific phospholipase A2, *PC* phosphocholine, *PtdCho* phosphatidylcholine, *RALGDS* RAL GTPase guanine nucleotide dissociation stimulator, *RTK* receptor tyrosine kinase, *SREBP* sterol regulatory element binding protein (Adapted with kind permission from Glunde et al. [15]). (**b**) Expanded high-resolution ^{1}H NMR spectra of the choline region of breast cancer cells. The spectra were obtained from extracts of highly aggressive triple-negative human MDA-MB-231 breast cancer cell, weakly aggressive estrogen receptor positive human MCF-7 breast cancer cells, and nonmalignant human mammary epithelial MCF-12A cells grown in culture. (**c**) High-resolution ^{1}H NMR spectra of biopsy extracts. Biopsy extracts from a low-grade astrocytoma and a high-grade glioblastoma showed a higher concentration of PC in the high-grade tumor, while the GPC peak dominated the choline metabolite profile in low-grade tumors (Adapted from Elsevier, Malet-Martino and Holzgrabe [89]). (**d**) Water-suppressed ^{1}H MR spectra from normal muscle and a glioblastoma xenograft in vivo. Representative ^{1}H MR spectra from a normal quadriceps muscle of a mouse (*top panel*) and a human glioblastoma U87MG tumor xenograft grown in the same mouse (*bottom panel*) show that the tumor contains an elevated total choline signal at 3.2 ppm as compared to the muscle (Kindly permitted by the Zhu et al. [91])

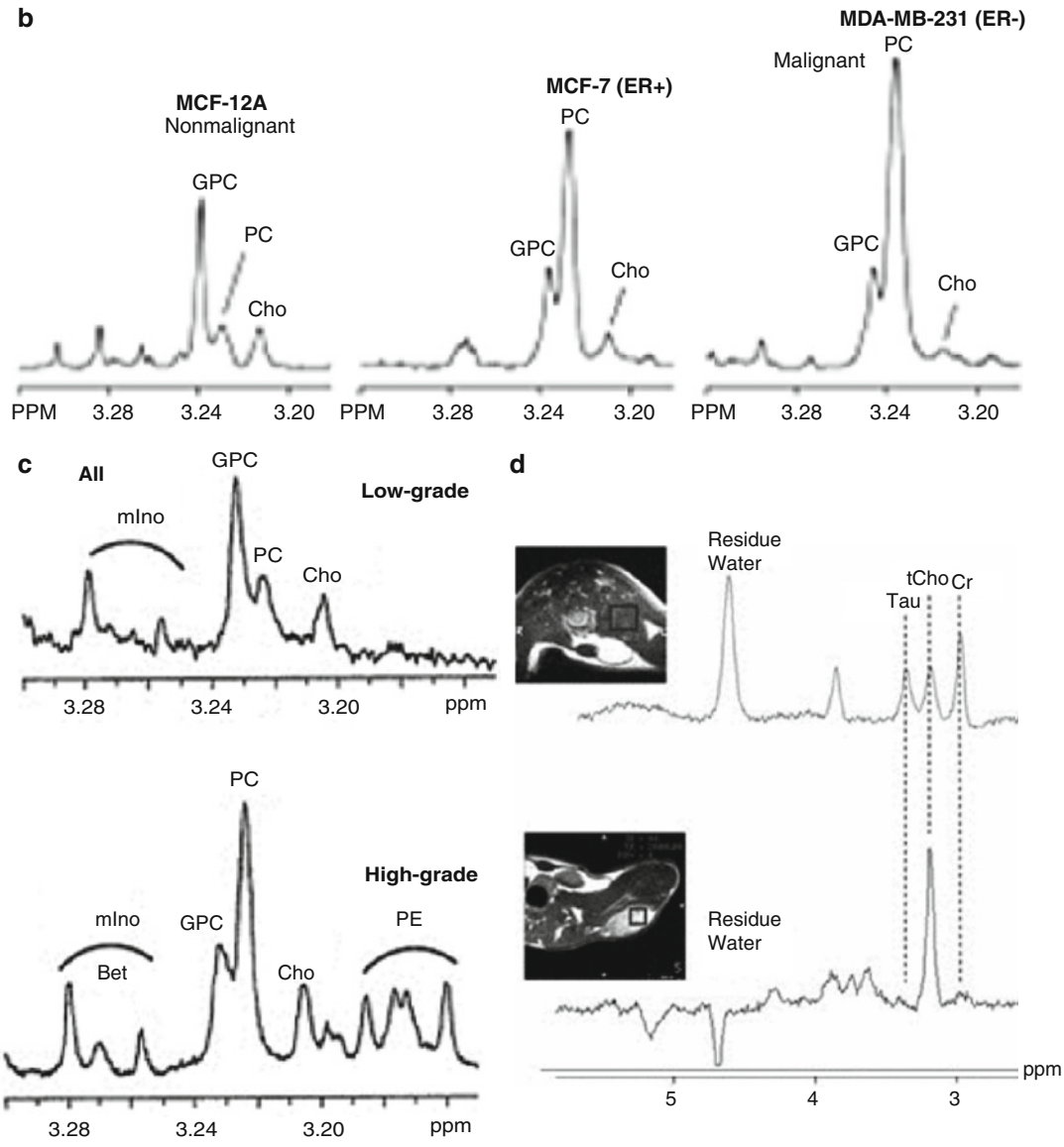

Fig. 8.1 (continued)

LDH-A expression and high tumor lactate are required for the progression of many tumors [98–100]. Lactate levels in primary tumors are associated with the development of metastases, and lactate can be used as a biomarker of cancer prognosis and treatment efficacy [96]. Cervical cancer biopsies showed a relationship between high tumor lactate and reduced survival [101]. Similar results have been reported in head and neck cancers [102], brain tumors [103], breast cancer [96, 104], prostate cancer [103], and rectal adenocarcinomas [105]. Lactate can promote angiogenesis in wounds [106], collagen deposition by fibroblasts [107], and revascularization and tissue repair through redox mechanisms [108]. Lactate is able to trigger the release of vascular endothelial growth factor (VEGF) from macrophages [109, 110]. Lactate can

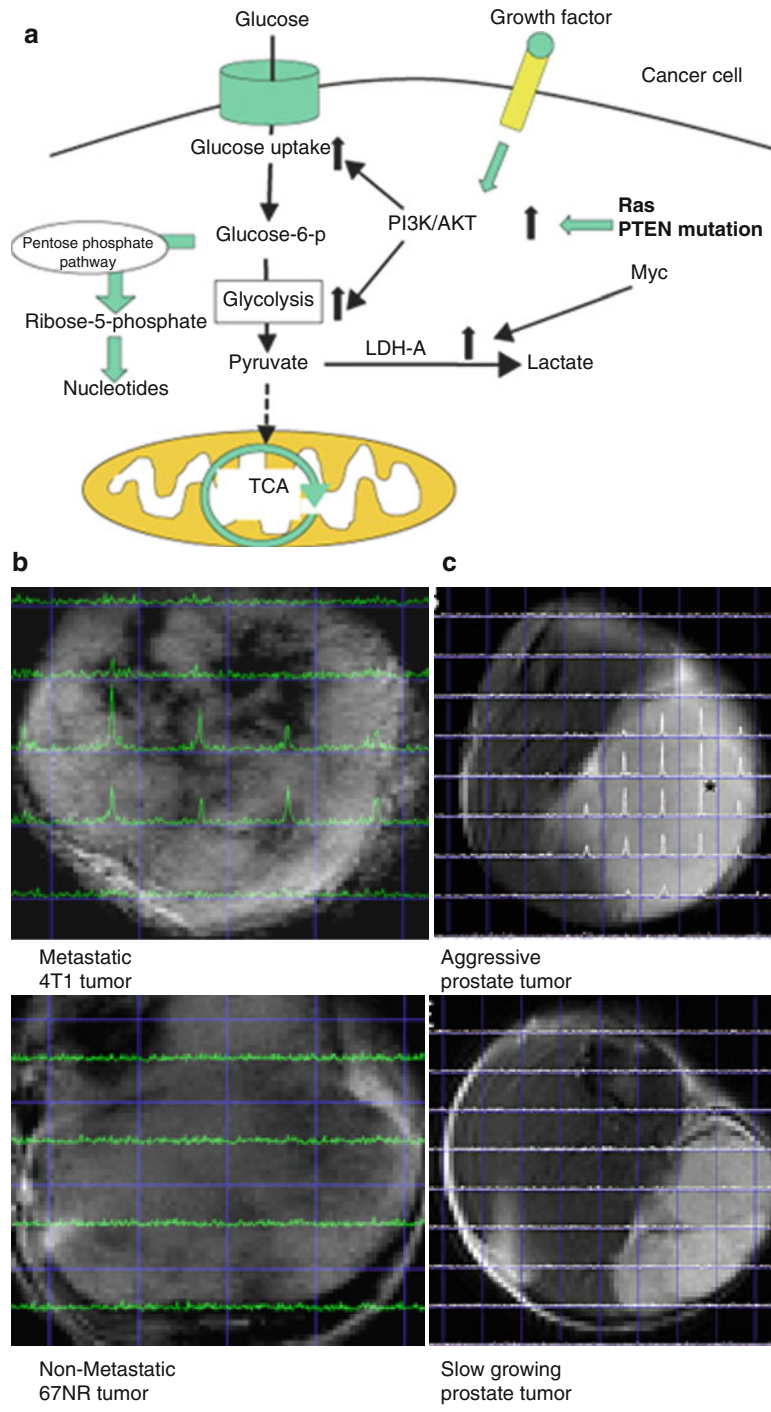

Fig. 8.2 ^{1}H MRS of lactate metabolism. (**a**) Aerobic glycolysis in cancer cells. Cancer cells heavily depend on aerobic glycolysis as their major source of ATP. The PI3K/AKT pathway and PTEN mutations enhance glycolytic enzyme activities. The Ras and Myc oncogenes also stimulate glycolysis. Increased lactate dehydrogenase A (LDH-A) expression further enhances glycolysis (Adapted with kind permission from Elsevier, Sato [90]). (**b**) Tumor lactate and metastases. Metastatic murine 4 T1 breast tumors have a significantly higher lactate concentration than nonmetastatic isogenic murine 67NR breast tumors (Kindly permitted by the Serganova et al. [96]). (**c**) Tumor lactate and aggressiveness. Lactate MRS spectra in Dunning faster-growing (*upper panel*) and Dunning slow-growing (*lower panel*) rat prostate tumors suggest that the presence of lactate may be a feature of cancer aggressiveness (Adapted with kind permission from Yaligar et al. [122])

stimulate nuclear factor-kappa B (NF-κB) and interleukin-8 (IL-8) production in endothelial cells [111] and activate hypoxia-inducible factor-1 (HIF-1) in oxidative tumor cells [112].

Quantitative measurement of lactate by ^{1}H MRS in vivo is difficult because of its low concentrations (5–10 mmol) compared to water (~55 mol). In addition, there is an overlap of the

^{1}H resonances originating from the CH_3 groups of lactate with the CH_2 groups of mobile lipids. This overlap with intense co-resonant lipid peaks makes it difficult to separate the lactate signal. Therefore, the detection of tumor lactate concentrations using conventional MRS techniques such as PRESS [113] and STEAM [114] is a challenging task. To remove the lipid signals, spectral editing techniques, such as spin-echo (SE) J-difference spectroscopy [115] and selective multiple-quantum coherence filter (SelMQC) [6, 116–119], have been developed. Recently, Hadamard slice encoding (HadSelMQC) was added to the SelMQC sequence to obtain a lactate signal from particular locations within large tumors [120, 121].

Preclinical ^{1}H MRS studies have demonstrated a significantly higher amount of lactate in metastatic breast tumors compared to nonmetastatic breast tumors in a mouse model [96] (Fig. 8.2b). The presence of lactate was also shown to be a marker of aggressive prostate tumors in rats [122] (Fig. 8.2c). A decrease in lactate concentration in tumors is a reliable and sensitive indicator of response to several types of chemotherapy or radiotherapy as seen by ^{1}H MRS measurements [123]. For example, the lactate concentration in RIF-1 sarcomas in mouse models decreased by 60 % within 24 h after administration of a single dose of cyclophosphamide [124]. A decrease in lactate levels has also been observed in a fibrosarcoma tumor model in mouse after 5-FU chemotherapy treatment [125].

8.4.3 ^{1}H MRS of Mobile Lipid Metabolism

Lipids comprise 4–16 % of the total mass in each cell. These lipids are polar phospholipids and neutral lipids such as triacylglycerides (TG) and cholesterol esters (CE) [126]. Lipids are mostly limited to bilayer membranes such as the plasma membrane and membranes of the Golgi, endoplasmic reticulum, and various other cellular organelles. However, for MR visibility, the lipid compound must possess sufficient rotational molecular freedom in order to motionally narrow MR line shape [127]. Hence, ^{1}H MR-visible lipid signals in vivo or in intact cells are limited to isotropically tumbling and relatively nonrestricted lipid molecules [126], such as triacylglycerides and cholesterol esters in neutral lipid droplets, and not from the lipids in membrane bilayers. MR-visible lipids are therefore often called mobile lipids.

Most cancer cells have a high concentration of mobile lipids, which are visible in ^{1}H MRS [128]. The ^{1}H MR signal from mobile lipids is mainly comprised of a narrow signal at 1.3 ppm, which arises from methylene groups ($-CH_2-\mathbf{CH_2}-CH_2-$), and at 0.9 ppm, which arises from methyl groups ($\mathbf{CH_3}-CH_2-$). These methylene and methyl signals originate from fatty acyl chains of triacylglycerides that form mobile lipid droplets in the cytoplasm or in the extracellular space [30, 129]. The lactate ^{1}H MRS signal overlaps with the lipid CH_2 signal [130] at 1.3 ppm and therefore requires spectral editing to separate the methylene signals from the lactate signal [116, 119, 131]. Other resonances arise from mobile polyunsaturated fatty acyl chains at 5.3 ~ 5.4 ppm ($-C\mathbf{H}=CH-$) or 2.8 ppm ($-CH=CH-C\mathbf{H}^2-CH=CH-$) [127]. However, the presence of the water signal at 4.7 ppm may interfere with the detection of the lipid signal at 5.4 ppm [129]. An example of mobile lipid ^{1}H MR spectra of intact NIH-3 T3 fibroblasts at 9.4 T is shown in Fig. 8.3a where *ras*-transfection inhibited mobile lipid formation and/or facilitated their extrusion from the cell [130].

Increased mobile lipid signals were found under conditions of stress associated with acidic environments [132]. Accumulation of triacylglycerides in tumor cells has been related to hypoxia [133], initiation of growth arrest and apoptosis [134], differentiation [135], and mitochondrial degeneration [136]. ^{1}H MRS showed that Taxol- and Adriamycin-resistant immortalized human K562 myelogenous leukemia cells have lower fatty acid methylene/methyl ratios and higher tCho/methyl ratios than drug-sensitive cells [137]. Drug-resistant variants of human MCF-7 mammary carcinoma and human LoVo colon adenocarcinoma cells have a higher mobile lipid signal intensity than their respective drug-sensitive counterparts (Fig. 8.3b, c), even though

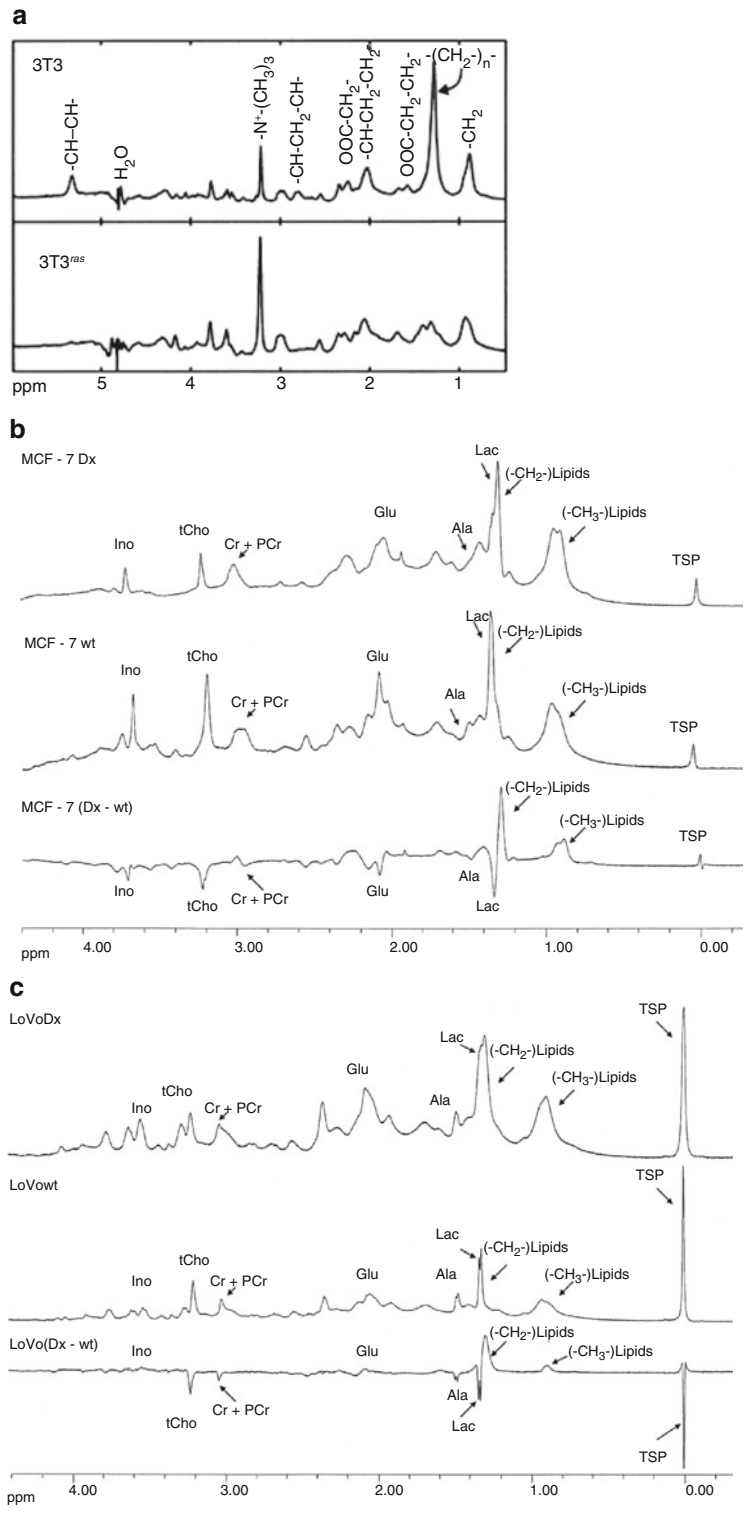

Fig. 8.3 ^{1}H MRS of lipid metabolism. (**a**) ^{1}H MR spectra of mobile lipids. Mobile lipid signals from 3 T3 fibroblasts (*top*) and Ras-transformed 3 T3 fibroblasts (*bottom*) are shown including the assignment of the major mobile lipid signals. Ras-transformation inhibited mobile lipid formation and/or facilitated their extrusion from the cells (Adapted with kind permission from Elsevier, Ferretti et al. [130]). (**b**, **c**) Mobile lipids and multidrug resistance. The mobile lipid profiles of human MCF-7 mammary carcinomas (**b**) and human LoVo colon adenocarcinomas (**c**) were compared for drug-sensitive (*wt*) and drug-resistant (*Dx*) tumor cells. The results show that drug-resistant cells (Dx) have a higher mobile lipid intensity compare to drug-sensitive cells (wt) as evident from the difference spectra on the *bottom* (Dx – wt) (Kindly permitted by Elsevier, Santini et al. [138])

the sensitive and resistant cells of each pair grow in a similar manner [138]. This suggests that mobile lipids may play an important role in drug resistance.

8.4.4 ^{1}H MRS of *N*-Acetylaspartate Metabolism

The amino acid derivative *N*-acetylaspartate (NAA) is the second most abundant amino acid compound in the human central nervous system (CNS) after glutamate [139, 140]. The nervous system-specific enzyme aspartate *N*-acetyltransferase (Asp-NAT) synthesizes NAA in mitochondria by acetylating the amino group of aspartate using acetyl-CoA [141, 142]. The NAA pool is dynamically regulated by continuous intercompartmental cycling between neurons and oligodendrocytes [140]. The functions of NAA include osmoregulation and generation of the neurotransmitter glutamate, which is why NAA is a well-accepted marker of neuronal health [140, 143]. Its concentration has been reported to decline in most CNS disorders and multiple sclerosis (MS) lesions [144]. Typical ^{1}H NMR spectra of brain tissue contain NAA as one of the best visible peaks at 2.02 ppm [145, 146]. The presence of NAA and a high NAA/creatine ratio indicate normal brain tissue [147]. Normal brain or low-grade gliomas have a relatively high concentration of NAA and a low level of tCho and lactate, and lipid signals are absent [148]. A progressive decrease in the NAA signal and an elevation in tCho level indicate the development of high-grade gliomas [145, 148, 149]. ^{1}H MRS studies of normal rat brain and rat brain with F98 gliomas, E367 neuroblastomas, and RN6 schwannomas at 10–15 days post inoculation demonstrate an absence of signals from NAA in the tumor resulting from the destruction or displacement of neuronal tissue by the tumor [149] (Fig. 8.4).

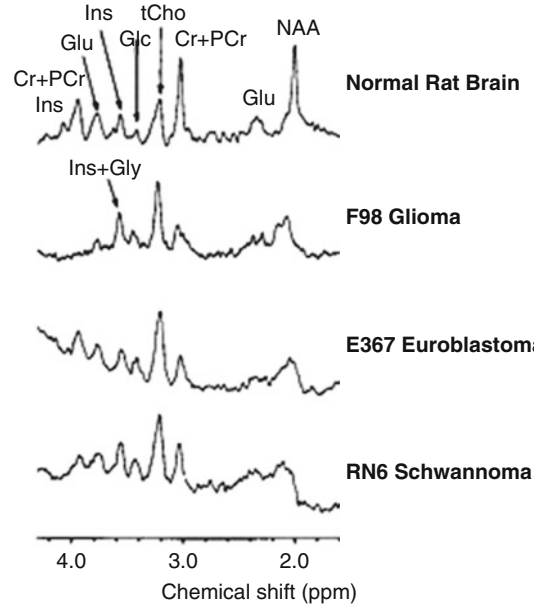

Fig. 8.4 ^{1}H MRS detecting *N*-acetylaspartate (*NAA*), creatine (*Cr*), and phosphocreatine (*PCr*). F98 gliomas, E367 neuroblastomas, and RN6 schwannomas in rat brain show an absence of NAA signal and a loss of total creatine, resulting from the destruction or displacement of neuronal tissue by the tumor (Adapted with permission from Gyngell et al. [149])

8.4.5 ^{1}H MRS of Creatine Metabolism

Creatine (Cr) is a marker of energy metabolism, which upon phosphorylation is utilized as an energy reservoir in cells with high-energy demand. Tissues with excitable cells, such as the skeletal muscle, brain, heart, and retina, require the instantaneous availability of a large amount of energy that cannot be provided by ATP alone [150]. Phosphocreatine (PCr) is the only high-energy phosphate-containing compound in vertebrates that acts as a reserve for high-energy phosphates, donating phosphoryl groups for ATP synthesis when supplies are low [150, 151]. Cr is taken up with the diet, and it can also be synthesized from the amino acids arginine, glycine, or methionine in the liver, pancreas, and kidneys [150, 152, 153]. Cr is transported through the blood and taken up by cells through active creatine transporters [154]. Creatine kinase (CK) catalyzes the reversible phosphorylation of Cr to PCr, thereby hydrolyzing ATP to ADP and vice versa [155]. While CK expression is enhanced [156], the total creatine (tCr, sum of combined Cr and PCr signals) concentration is decreased [157] in most tumors when compared to their nonmalignant tissues of origin.

The ^{1}H MRS tCr peak, which can be detected at 3.05 ppm, consists of Cr and PCr, which cannot be resolved in vivo at magnetic field strengths of 9.4 T and below [158]. tCr is frequently used for calculating metabolite ratios such as the tCho:tCr and the NAA:tCr ratio for the evaluation of tumor progression [159]. Several studies have reported an increased tCho:tCr and a decreased NAA:tCr ratio in fast-growing gliomas [159]. After radiotherapy, a significantly higher tCho:tCr ratio was detected in recurrent brain tumors as compared to areas of radiation injury [160]. In preclinical studies of F98 gliomas, E367 neuroblastomas, and RN6 schwannomas in rat brains, a loss of tCr was observed in tumor tissue as compared to normal rat brain tissue [149] (Fig. 8.4).

8.4.6 ^{1}H MRS of Glutamate and Glutamine Metabolism

The plasma concentration of glutamine (Gln) is about 2.5 mM and it is the most abundant free amino acid in plasma [161]. Gln provides the respiratory fuel for rapidly proliferating enterocytes and lymphocytes, regulates the acid–base balance through the production of ammonia, and is a precursor of nucleic acids, nucleotides, amino sugars, and proteins [162]. Gln is abundant in the milk protein casein, as well as in plants and animal meat [163]. Gln is a major source of nitrogen and carbon in tumors, and it provides metabolic intermediates in the synthesis of nucleic acids, proteins, and hexosamines during tumor growth [164]. Moreover, glutamine can be deamidated by glutaminase (GLS) to form glutamate (Glu), and the expression of glutaminases is regulated by c-Myc and p53 [164]. Several cancer cells heavily depend on glutamate for the production of ATP by oxidizing glutamate-derived α-ketoglutarate [165] and for the biosynthesis of glutathione (GSH), a primary antioxidant of the cell [164, 166]. Thus, glutamine metabolism is potentially important in predicting both the presence of specific transforming mutations in tumors and the sensitivity to therapeutic agents designed to target glutamine utilization [164, 167].

Glu and Gln are often referred to as Glx, which represents the sum of the unresolved Glu and Gln peaks. In ^{1}H MRS, the Glx signals arise in two resonance frequency ranges, namely, between 2.33–2.44 and 3.75–3.77 ppm [168]. Using short echo time (TE) ^{1}H MRS, it is possible to detect the Glx signal, but it is difficult to quantify Glx from these spectra because of the uneven baseline of short TE spectra [168]. However, at high magnetic field, e.g., 7 T, it is possible to differentiate the C4 proton resonances of Glu, Gln, and GSH at 2.35, 2.45, and 2.55 ppm, respectively, by using TE-optimized point-resolved spectroscopy (PRESS) [166]. ^{1}H MRS of human serous ovarian carcinoma SKOV3 xenografts showed an increase of the myoinositol (Ins) signal and a decrease of the Glx signal during tumor progression [169] (Fig. 8.5a).

Isocitrate dehydrogenase (IDH) catalyzes the oxidative decarboxylation of isocitrate and produces α-ketoglutarate (α-KG) [170]. Mutations in the isocitrate dehydrogenase genes IDH1 and IDH2 frequently occur in several human cancers such as gliomas and acute myeloid leukemia, which results in a loss of α-KG and gain of 2-hydroxyglutarate (2-HG) [170–172]. Hence, the detection of 2-HG by ^{1}H MRS in tumors can be utilized to predict possible IDH1/IDH2 gene mutations in cancer [173, 174]. This requires the use of localized adiabatic selective refocusing (LASER) correlation spectroscopy (COSY) to extract the 2-HG metabolite spectra from the overlapping Gln and Glu resonances [174]. The 2-HG peak is clearly visible in 2D LASER-COSY spectra from a patient with an anaplastic astrocytoma with a point mutation in arginine 132 (R132) of the IDH1 enzyme [174] (Fig. 8.5a). Conversely, a patient with a primary glioblastoma containing wild-type IDH1 and the brain of a healthy volunteer with wild-type IDH1 did not display any 2-HG signal [174] (Fig. 8.5b).

8.4.7 ^{1}H MRS of Tumor pH

Several studies have demonstrated that solid tumors have an intracellular pH (pHi) of around 7.2, whereas the extracellular pH (pHe) of tumors is acidic with pHe values between 6.2

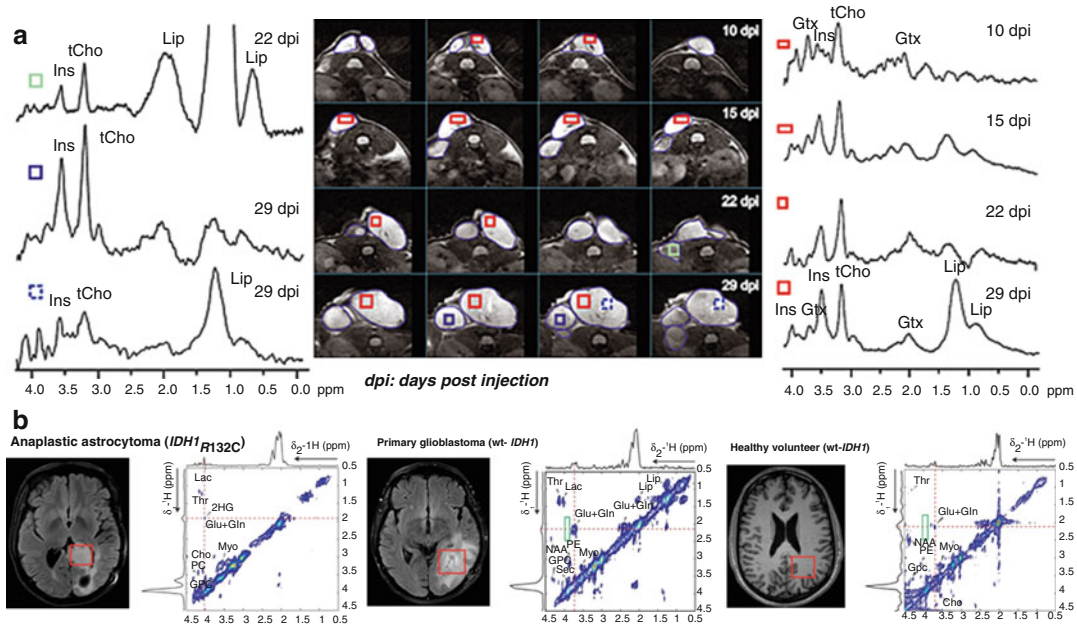

Fig. 8.5 ^{1}H MRS of glutamate (Glu), glutamine (Glu), and 2-hydroxyglutarate (2HG). (**a**) ^{1}H MR spectra from subcutaneous SKOV3A tumors in mice show an increase in the myoinositol (*Ins*) signal and a decrease in the glutamine plus glutamate (*Glx*) signal during tumor growth (Kindly permitted by Canese et al. [169]). (**b**) 2D LASER-COSY spectra in humans in vivo at 3 T show a 2-hydroxyglutarate (2HG) peak (*green rectangle*) in an astrocytoma patient with mutated isocitrate dehydrogenase 1 (IDH1, mutated at R132C), but not in a primary glioblastoma patient with wild-type IDH1 (wt-IDH1), and a healthy volunteer with wt-IDH1 (Adapted with kind permission from Andronesi et al. [174])

and 6.9 [175, 176]. The acidic pH in the tumor microenvironment affects cell cycle progression, proliferation, and differentiation in cancer cells, as well as tumor treatment response [175, 177–179]. In addition, environmental acidity affects the oncogenic expression of several genes and may lead to a more aggressive tumor phenotype [175, 177]. Tumor acidity also plays a critical role in the promotion of cancer cell invasiveness and metastatic capacity [180, 181]. When cancer cells form tumors, blood vessels are required for the expansion of the tumor beyond a diameter of 1–2 mm [182, 183]. Similar to normal angiogenesis, a tumor triggers the sprouting of new blood vessels from preexisting blood vessels in the vicinity of the tumor [184]. Members of the fibroblast growth factor (FGF) and vascular endothelial growth factor (VEGF) families are the most common angiogenic factors that promote angiogenesis, which is also the case in tumors [181]. Tumor-induced neovascular networks, however, are abnormal in structure, inhomogeneous, and chaotic and may be dilated and nonfunctional, which results in inadequate nutrient and oxygen supply to some parts of the tumor [181, 182, 184]. This abnormal tumor vasculature causes various regions of tumors to be transiently or chronically hypoxic [31, 177]. Hypoxia can promote glycolysis instead of cellular respiration, thereby further enhancing lactic acid production [96, 175, 177]. As described by Warburg, tumor cells maintain a high glycolytic rate even in the presence of sufficient oxygen [11]. Thus, glycolysis and lactate production are a major part of tumor cell metabolism in normoxic as well as in hypoxic tumor regions [1]. The abnormal and partially nonfunctional vasculature of tumors prevents an efficient clearance of lactate, protons, and other acidic compounds from the extracellular tumor microenvironment, thereby contributing to the low tumoral pHe [1, 98, 185, 186].

To avoid acid-induced apoptosis, tumor cells have developed mechanisms to actively export the surplus protons and lactic acid, which leads to the acidification of the extracellular environment while keeping pHi within a tolerable range [177]. Monocarboxylate transporters (MCTs) are important cellular pH regulators in cancer cells, and several members of the MCT family have been characterized as H^+/lactate symporters that can export lactic acid from the cells [187]. In addition during hypoxia, HIF-1 will induce membrane-bound carbonic anhydrase (CA) IX and XII expression in tumors [188]. CA IX and XII contribute to the extrusion of hydrogen ions and to cytoplasmic alkalization in an acidic tumor microenvironment [188].

One of the first methods that was employed to measure tissue pH was microelectrodes [189]. Microelectrodes are invasive, can destroy cell membrane integrity, and mostly sense H^+ ions in the extracellular space of tissues. The use of ^{1}H MRS would allow pH measurements of small volumes noninvasively. The measurement of tumor pH by MRS and magnetic resonance imaging (MRI) has been demonstrated in several studies, in which either endogenous metabolites were detected or exogenous agents were administered to assess tumor pH. Several extrinsic probes were developed for ^{1}H MRS measurements of tumor pH such as imidazoles, i.e., 2-imidazole-1-yl-3-ethoxycarbonyl propionic acid (IEPA), and aromatic compounds [190–193]. ^{1}H MRSI of breast and brain tumor xenografts showed that the imidazole resonance arises in the 8–9 ppm region where no endogenous, potentially interfering signals are detected [191, 192]. The C2 carbon in the imidazole ring is pH sensitive. Using intraperitoneally injected IEPA in an MDA-MB-435 tumor xenograft-bearing mouse, the pHe was found to be heterogeneous and acidic ($6.44 < \text{pHe} < 6.79$) (Fig. 8.6) [192]. Endogenous imidazoles, such as histidine, can also be measured to derive pHi in vivo by using ^{1}H MRS [194]. It is possible to orally administer histidine in humans to increase their histidine concentration in the brain and subsequently generate a pH map of the normal brain [194]. Gadolinium-based compounds, whose relaxivity is pH dependent, also present the opportunity to image tissue pH in vivo.

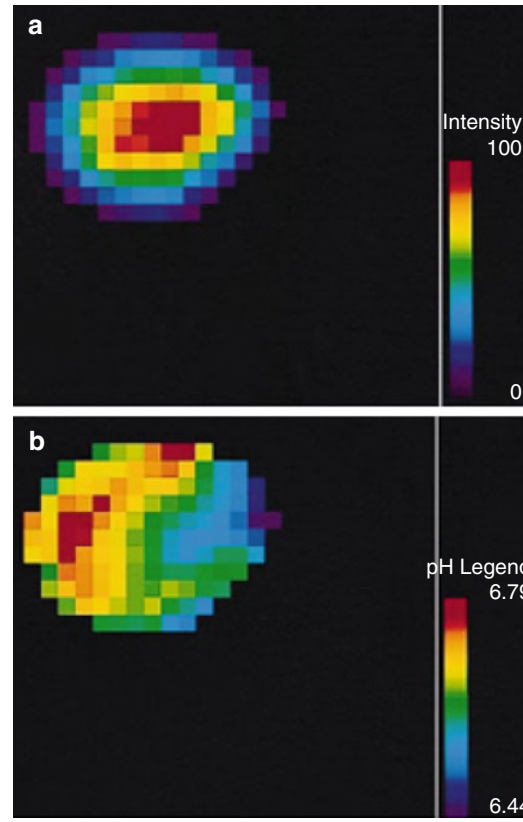

Fig. 8.6 ^{1}H MRS of tumor pHe measured by intraperitoneally injected 2-imidazole-1-yl-3-ethoxycarbonyl propionic acid (IEPA). (**a**) Intensity map of the H2-resonance of IEPA and (**b**) corresponding pHe map in a representative MDA-MB-435 tumor xenograft (Adapted with kind permission from van Sluis et al. [192])

A single injection of dysprosium-DOTP52 with gadolinium-DOTA-4AmP52 was used to generate a pH map of rat brains with gliomas [195].

A relatively new MRS approach to measure pH is to utilize chemical exchange saturation transfer (CEST), which is based on the chemical exchange of exchangeable protons with water protons for signal enhancement [196, 197]. In ^{1}H CEST imaging, the exogenous or endogenous compounds that give contrast contain exchangeable protons or other moieties that can be selectively saturated [196–198]. After the transfer of the saturation to the water signal, the compounds can be indirectly detected through the decrease in the water signal. Paramagnetic CEST agents, for example, Yb-DO3A-oAA (ytterbium-1,4,7,10-tetraazacyclododecane-1,4,7-tetraacetic acid),

can be utilized to measure pHe in MCF-7 breast tumor xenografts in mice [199].

8.4.8 ^{31}P MRS of Tumor pH

^{31}P MRS can simultaneously measure pHi from the chemical shift of endogenous inorganic phosphate (Pi) and pHe from the chemical shift of exogenous indicators, such as 3-aminopropyl phosphonate (3-APP) [200, 201]. Tumor pHi as measured by ^{31}P MRS can be derived from the chemical shift difference between the Pi signal and the signal of an endogenous reference molecule such as PCr or NTP [200]. The limitation of this method is that it assumes that Pi is only found in the intracellular space, which is not entirely true as there can be a minor contribution to the Pi signal from extracellular Pi [200]. The chemical shift of the ^{31}P nucleus in 3-APP is pH sensitive, making it a good indicator of pHe. The use of 3-APP for measuring pHe is nontoxic, and it is neither internalized nor metabolized by the cells [201]. A robust calibration equation for in vivo pHe measurement from the chemical shift of 3-APP has been reported [201]. Intraperitoneal injection of 3-APP in mice has been applied to the measurement of pHe in several tumor models such as radiation-induced fibrosarcoma (RIF-1) tumors with a pHe of 6.66, human MCF-7 breast tumor xenografts with a pHe of 7.11, and human colon adenocarcinoma xenografts with a pHe of 6.79 [201–203].

8.4.9 ^{31}P MRS of Phospholipid Metabolism

^{31}P-containing choline phospholipid metabolites such as PC at 3.9 ppm and GPC at 0.5 ppm and ethanolamine phospholipid metabolites such as PE at 4.5 ppm and GPE at −1.2 ppm can be detected with ^{31}P MRS, using a reference compound such as methylene diphosphonic acid set to 18 ppm [7]. ^{31}P MRS also detects energy metabolites such as PCr, NTP, and NDP, as well as Pi [204]. In vivo ^{31}P MR spectra typically show a phosphomonoester (PME) signal of unresolved PC and PE resonances and a phosphodiester (PDE) signal of unresolved GPC and GPE resonances [7].

^{1}H MRS has been more widely used in the clinical setting than ^{31}P MRS to assess the level of choline phospholipid metabolites in tumors because of the higher sensitivity of ^{1}H MRS as compared to ^{31}P MRS and because of the more frequent availability of ^{1}H MRS than ^{31}P MRS on commercial MR scanners. Nevertheless, clinical ^{31}P MRS at high magnetic field is currently being pursued due to several advantages of using the ^{31}P nucleus [204, 205]. For example, the MR signal intensity from the tCho signal detected by ^{1}H MRS is four orders of magnitude smaller than the signals from the surrounding lipids, while with ^{31}P MRS, no lipid signals at all are observed from tissue [204]. ^{31}P MRS has been shown to reliably detect PC, GPC, PE, and GPE at 1.5 T or higher magnetic field in several human diseases, thereby providing information on both PtdCho and PtdEth metabolism [205], and not only PtdCho metabolism as with ^{1}H MRS. Polarization transfer methods such as RINEPT (refocused insensitive nuclei enhanced by polarization transfer) can increase the sensitivity of the ^{31}P MR signal from PC, GPC, PE, and GPE by more than twofold [205].

PtdCho and PtdEth, which account for more than 50 % of total phospholipid in mammalian cells, are generated by distinct but partially overlapping pathways [206, 207]. PtdEth is synthesized by the consecutive actions of ethanolamine kinase, which phosphorylates free Eth to form PE; phosphoethanolamine cytidylyltransferase, which uses PE to form high-energy cytidine diphosphate ethanolamine (CDP-Eth); and diacylglycerol ethanolaminephosphotransferase, which catalyzes the formation of PtdEth from CDP-Eth [206, 207]. The biosynthetic pathway of PtdCho utilizes parallel enzymes such as CK, CCT, and CHPT (Fig. 8.1a), which use choline instead of ethanolamine [206]. The enzymes for these two distinct biosynthetic pathways of PtdEth and PtdCho synthesis can overlap significantly [206]. Several isoforms of choline kinase are also able to phosphorylate ethanolamine [208–211], and several phosphotransferases can use both CDP-choline and CDP-ethanolamine for the synthesis of PtdCho and PtdEth [206, 208–211]. Although choline phospholipid metabolism has been

extensively studied, ethanolamine phospholipid metabolism has received much less attention, in particular at the molecular level. Using ^{31}P MRS of liver extracts, higher Eth levels and a lower rate of PtdEth synthesis were found in lymphomatous mouse livers as compared to control livers [212]. However, the rate of PtdCho synthesis in lymphomatous mouse livers was similar to that in control mouse livers [212]. Several cancer cells and tumors display abnormal ethanolamine phospholipid metabolism, including breast cancer [213], prostate cancer [214], and brain tumors [215].

^{31}P MRS can be used noninvasively to monitor the modulation of phospholipid metabolite levels, such as PC, after treatments that target enzymes in phospholipid metabolism, such as inhibitors [216] or shRNA [217] targeting choline kinase alpha. Treatment with the choline kinase alpha inhibitor MN58b significantly reduced the PC levels in human MDA-MB-231 breast and human HT29 colon cancer cells [216]. MN58b reduced the tumor growth, which was accompanied by a reduction in phosphomonoesters (PME) as detected by ^{31}P MRS in MDA-MB-231 and HT29 tumor xenografts [216]. Ex vivo ^{31}P MRS analyses of the same MN58b-treated tumor extracts showed a significant reduction in PC when compared to nontreated tumors, confirming that the decreases in PME in vivo resulted from a decrease in PC [216]. The use of lentiviral vector to deliver choline kinase alpha-specific shRNA to MDA-MB-231 tumors in mice demonstrated a reduction of PC and PME in ^{31}P MR spectra in vivo, as well as reduced tumor growth, proliferation, and necrosis following treatment [217].

Changes in tumor phospholipid metabolism can also be employed as a surrogate marker for assessing the tumor response to treatment with new anticancer drugs that target oncogenic pathways such as histone deacetylation [218]. Histone acetylation has an essential role in transcription, replication, and repair of DNA, and it is regulated by the opposing effects of two families of enzymes, which are histone acetyltransferases and histone deacetylases (HDACs) [219]. The HDAC inhibitors LAQ824 and SAHA prevent angiogenesis, cause cell cycle arrest, and induce apoptosis in cancer cells [218]. Significant increases in PC were observed in cancer cells following treatment with HDAC inhibitors [220]. In vivo studies showed a significant increase in PME/total phosphorus signal in LAQ824-treated HT29 tumor xenografts [220]. Figure 8.7 shows that inhibition of HDAC by LAQ824 was associated with increased PME and PC levels [220]. This ^{31}P MRS study demonstrated that the rise in PC and PME upon HDAC inhibition may be used as a surrogate marker for tumor response after treatment with HDAC inhibitors [220].

8.4.10 ^{31}P MRS of Tumor Energy Metabolism

^{31}P MRS is able to detect the energy status of tumors and cancer cells, which can be deduced from the cellular or tumoral levels of NTP, nucleoside diphosphate (NDP), PCr, and Pi. As described above, cancer cells are distinctively metabolically reprogrammed, displaying abnormal activities in glycolysis, TCA cycle, and oxidative phosphorylation to generate NTP to meet the energy requirements for cell proliferation. A shortage of cellular NTP levels could influence the functioning of growth factor receptors [221]. As mentioned above, the high-energy phosphate PCr can act as a reserve for ATP synthesis when ATP supplies are low. AMP-activated protein kinase (AMPK), which acts as an energy sensor protein, monitors shifts in the cellular AMP and ADP to ATP ratio [222]. Failure to maintain adequate ATP levels in cancer cells promotes apoptosis ***via*** AMPK activation [222]. Another source of cellular energy is inorganic polyphosphate (poly P) which is a polymer of Pi molecules that are linked by phosphoanhydride bonds [223]. Poly P also serves as a reserve to replenish the necessary pool of Pi [223]. Relative concentrations of intracellular high-energy ^{31}P-containing metabolites and their breakdown products such as NTPs, NDPs, PCr, and Pi can be estimated by ^{31}P MRS techniques [224, 225]. Figure 8.7 shows in vitro and in vivo ^{31}P MR spectra from human HT29 colon adenocarcinoma cells, displaying typical ^{31}P MR signals from PME, Pi, PDE, PCr, NTP**γ**/NDP**γ** (combined nucleotide di- and triphosphates), NDP**α**/NTP**α** (combined nucleotide di- and triphosphates), NAD, and NTP**β** [220]. Hence, ^{31}P MRS can be employed to estimate the metabolic status of tumors

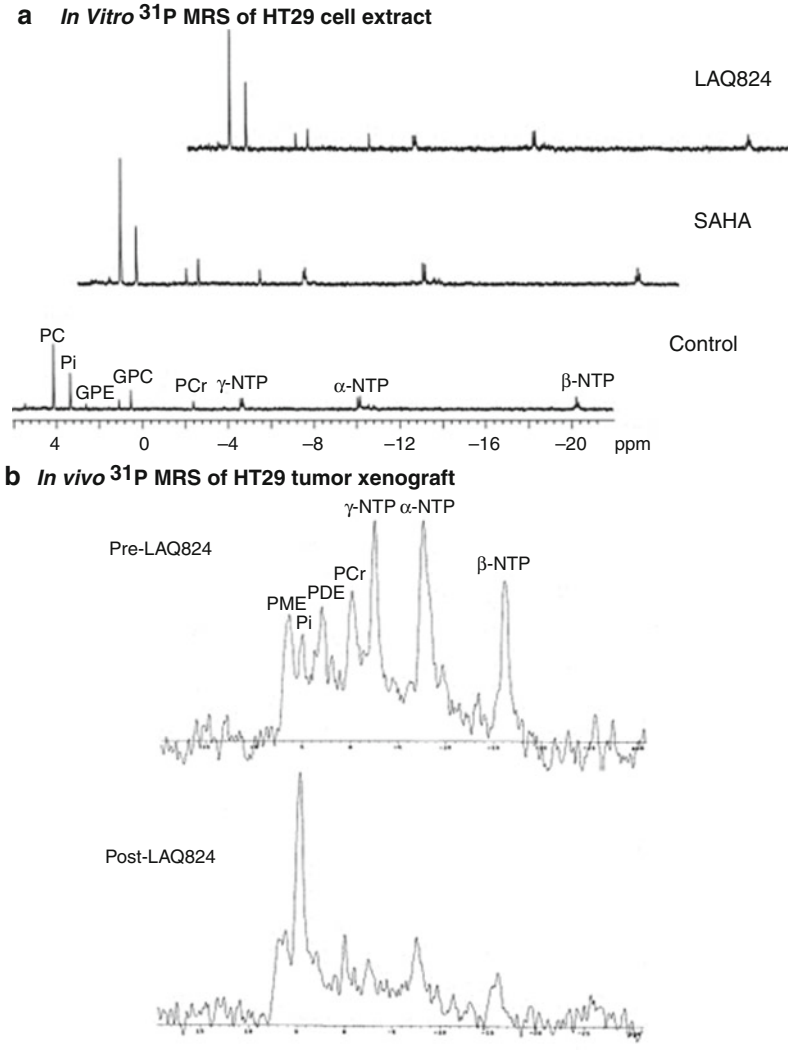

Fig. 8.7 Inhibition of HDAC by LAQ824 or SAHA is associated with changes in choline phospholipid metabolism. (**a**) In vitro ^{31}P MRS of an HT29 cell extract treated with vehicle (*bottom panel*), 34 μM SAHA (*middle panel*), and 350 nM LAQ824 (*top panel*) for 24 h. Peak assignments: phosphocholine (*PC*), glycerophosphocholine (*GPC*), glycerophosphoethanolamine (*GPE*), inorganic phosphate (*Pi*), phosphocreatine (*PCr*), and nucleoside triphosphates (*α-*, *β-*, *λ-NTP*). (**b**) In vivo ^{31}P MR spectra of a HT29 tumor before (*top panel*) and after (*bottom panel*) LAQ824 treatment (25 mg/kg i.p. for 2 days) are shown. Peak assignments: phosphomonoesters (*PME*), phosphodiesters (*PDE*), inorganic phosphate (*Pi*), phosphocreatine (*PCr*), and nucleoside triphosphates (*α-*, *β-*, *λ-NTP*) (Adapted with kind permission from Chung et al. [220])

and cancer cells. Since energy metabolism also depends on the supply of glucose and oxygen to the cells, ^{31}P MRS can be utilized to estimate tissue blood supply, hypoxic cell fraction, and radiation treatment response [7, 224].

8.4.11 ^{19}F MRS of Tumor Metabolism

^{19}F MRS is an important means for observing biological processes in a complex system. The distinct advantages of ^{19}F MRS are its large chemical shift range, high gyromagnetic ratio (40 MHz/T), and negligible endogenous ^{19}F MR signal [203, 226]. These advantages of ^{19}F MRS result in a high signal-to-noise ratio when a fluorinated compound is introduced as a contrast agent. A number of ^{19}F MRS studies using fluorinated compounds and therapeutic agents have focused on metabolism and pharmacokinetics in vivo and in excised tumor tissues. For example, the anticancer drug 5-fluorouracil (5-FU, 5-fluoro-1H,3H-pyrimidine- 2,4-dione), a pyrimidine analogue, irreversibly inhibits thymidylate synthase, which kills cancer cells [227]. Figure 8.8a summarizes the main metabolic pathways of 5-FU. Following administration of 5-FU, the fluorinated compounds that can be detected by ^{19}F MRS include free 5-FU, fluoro-ureido-propionic acid, fluoro-beta-alanine

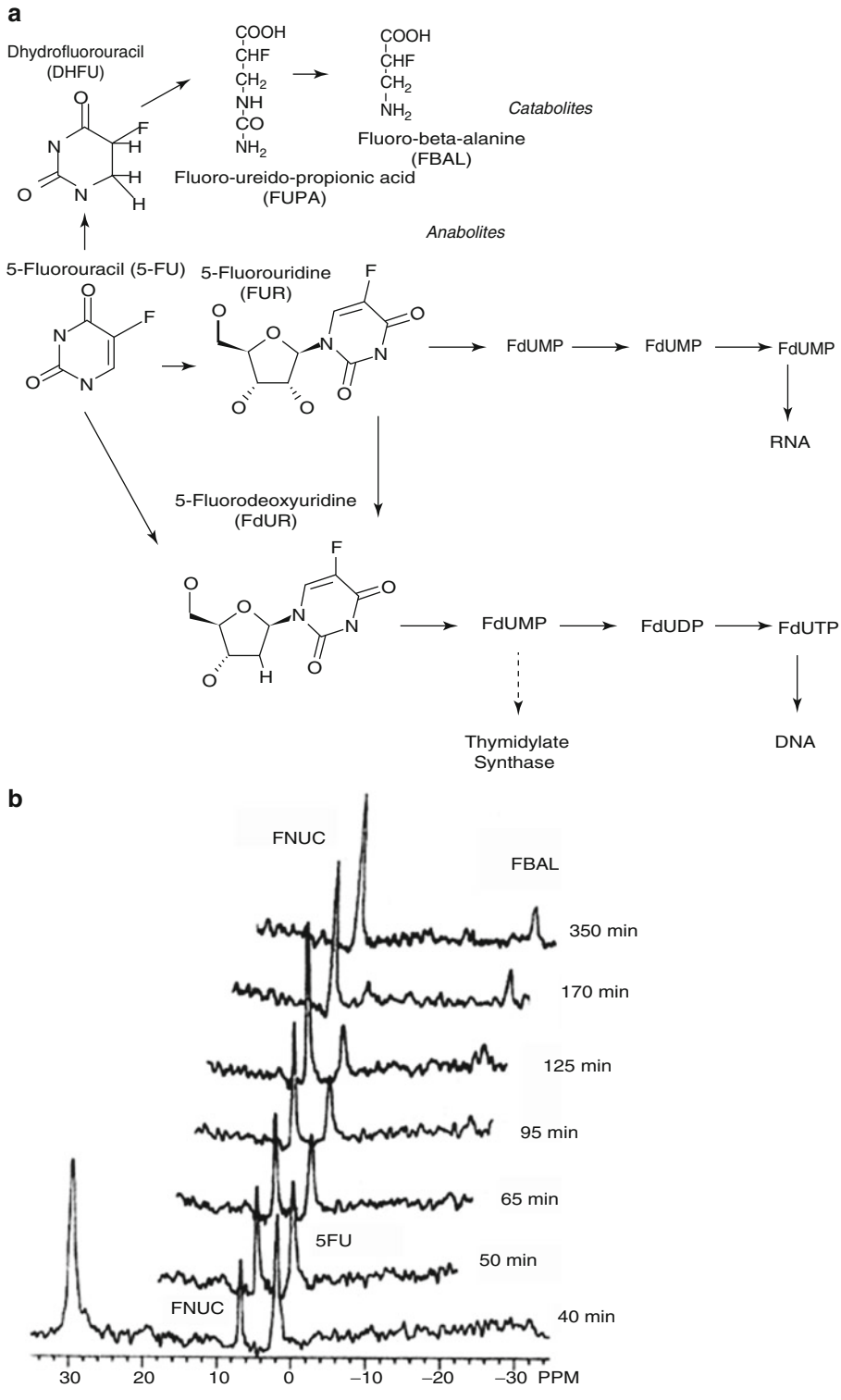

Fig. 8.8 ^{19}F MRS of 5-fluorouracil metabolism in a tumor model. (**a**) Metabolic pathways of 5-fluorouracil (5-FU) and (**b**) ^{19}F MR spectra of 5-FU, fluoro-beta-alanine (*FBAL*), and fluoronucleotides (*FNUC*) in vivo. The spectra were detected from a representative Walker 256 carcinoma grown in a rat (Adapted with kind permission from Elsevier, Wolf et al. [228])

(FBAL), and peaks in the nucleoside/nucleotide region [228]. Several ^{19}F MRS studies have revealed the pharmacokinetics of 5-FU in tumors in vivo [229, 230]. ^{19}F MRS showed an accumulation and slow disappearance of 5-FU in subcutaneous Yoshida sarcoma and drug-induced liver tumors in rats [229]. Noninvasive detection of the cytotoxic fluoronucleotides (FNuct) can be used to predict 5-FU cytotoxicity in tumors [231] (add reference). 5-FU and all its metabolites can diffuse out of cells, except for FNuct, which are trapped within the cells because of their charged phosphate groups. For example, the cytotoxicity of FNuct was measured in vivo by ^{19}F MRS in Walker carcinosarcomas in rats [231]. Figure 8.8b shows that the ^{19}F spectra of 5-FU, FBAL, and fluoronucleosides/fluoronucleotides (FNUC) as well as a reference compound can be clearly detected in a Walker 256 carcinoma grown in a rat as measured in vivo at 4.7 T [228]. Similarly, fluorinated proteins such as bovine serum albumin, gammaglobulin, and purified immunoglobulin (IgG) have been developed by selective trifluoroacetylation using ***S***-ethyl trifluorothioacetate [232]. They can be utilized as ^{19}F MRS probes for optimizing the delivery of antineoplastic agents to tumors [232]. ^{19}F MRS was also employed to study the conversion of 5-fluorocytosine (5-FC) to 5-fluorouracil (5-FU) by cytosine deaminase in human HCT116 colon tumor xenografts in mice [233, 234]. In conclusion, ^{19}F MRS of ^{19}F-labeled anticancer drugs can noninvasively monitor drug pharmacokinetics and treatment outcome.

^{19}F-labeled probes have been developed to monitor tumor hypoxia. It is important for the development of ^{19}F-labeled hypoxia-sensing probes that they do not lose their ^{19}F-nuclei during their hypoxia-mediated metabolism. For example, fluorinated nitroimidazole derivatives such as CF3PM (5,6-dimethyl-4-[3-(2-nitro-1-imidazolyl)-propylamino]-2-trifluoromethylpyrimidine hydrochloride) and CCL-103 F (1-(2-hydroxy-3-hexafluoroisopropoxy-propyl)-2-nitroimidazole) can be used to measure hypoxia in vivo [235–239]. These fluorinated 2-nitroimidazole compounds are metabolized by cells under hypoxic conditions, in which cellular reductases cause nitroimidazoles to undergo one electron reductions to form reactive species [235, 240, 241]. Within the hypoxic cells, the probes were mainly associated with the endoplasmic reticulum, the nucleus, and the cytoplasmic side of intracellular vesicles [235, 240, 241]. Compared to the washout of the parent 2-nitroimidazole compound, the washout of adducts was slower [236]. Hence, the degree of hypoxia within a given tumor can be measured from the time course of residual 2-nitroimidazole compound in this tumor [236]. These fluorinated nitroimidazole probes have been utilized to measure hypoxia in preclinical studies. For example, CF3PM has been used in SCCVII squamous carcinomas in mice, and CCI-103 F in Dunning R3227 prostate cancer and Walker 256 tumors in rats [235, 239, 242].

^{19}F MRS can be useful for observing intracellular and extracellular tumor pH [33]. Probes for in vivo tumor pH measurement with ^{19}F MRS include ZK-150471 (3-[*N*-(4-fluoro-2-trifluoromethylphenyl)-sulfamoyl]-propionic acid) and fluorinated vitamin B6 derivatives (6-fluoropyridoxol and 6-fluoropyridoxamine) [203, 243]. pH values are typically calculated from tumor ^{19}F MR spectra obtained following administration of ZK-150471 or a fluorinated vitamin B6 derivative by comparing their chemical shift with that of a sodium trifluoroacetate (NaTFA) standard [203, 243]. The cell-impermeable probe ZK-150471 has been shown to measure pHe in murine RIF01 fibrosarcomas, murine Lettre tumors, and human HT29 tumor xenografts in mice [203].

8.4.12 ^{13}C MRS of ^{13}C-Labeled Glucose and Lactate Metabolism

Glucose is necessary for energy-producing metabolic processes and for the synthesis of macromolecular products. As described above, increased glucose uptake and enhanced glycolysis are metabolic hallmarks of cancer and can therefore serve as indicators of malignant transformation. ^{13}C-labeled glucose and ^{13}C-labeled lactate detection with ^{13}C MRS provides a noninvasive and quantitative method

to assess glucose delivery to the tumor, glycolysis, and lactate clearance from the tumor [244–246]. ^{13}C MRS with the use of ^{13}C-labeled glucose can be used to monitor glucose metabolism in cancer cells in culture and in tumor models in vivo and hence can be employed to study the kinetics of glycolysis alterations occurring with malignant transformation of tumor cells [244, 247, 248]. The natural abundance of the ^{13}C isotope is only 1.1 %, which allows us to measure the rates of ^{13}C-label incorporation into metabolites by ^{13}C MRS following infusion or injection of ^{13}C-enriched substrates [244]. As ^{13}C-labeled tracers are not radioactive, they can be safely infused or injected in preclinical and clinical applications to study intermediary metabolism, enzyme activity, and metabolic regulation [249]. Extracts of surgically resected tissues from animal models or patients infused or injected with ^{13}C-labeled glucose and extracts of cancer cells incubated with ^{13}C-labeled glucose can also be analyzed ex vivo [244].

Glycolytic use of [1-^{13}C] glucose will incorporate the ^{13}C isotope into the C3 position of pyruvate [249] and then into the C4 position of α-ketoglutarate in the TCA cycle [249]. From [4-^{13}C] α-ketoglutarate, the isotope is transferred to the cellular glutamate pool by exchange reactions through amino acid transaminases and mitochondrial and cytosolic transporters [249]. Since the rate of exchange between pyruvate and glutamate is many times faster than the TCA cycle, the glutamate pool acts as a trap for ^{13}C-label [249]. Maximum enrichment of the pyruvate pool can be achieved by using uniformly labeled glucose with ^{13}C-labels in all six carbons of glucose ([U-^{13}C] glucose) instead of singly labeled glucose. Increased glycolytic rates in cancer cells typically generate a high concentration of ^{13}C-labeled lactate [96].

^{13}C MRS experiments with ^{13}C-labeled glucose can be employed to simultaneously measure the consumption of [1-^{13}C] glucose and the formation of [3-^{13}C] lactate and thus enable the measurement of the kinetic parameters for glucose delivery to the tumor, tumor glycolysis, and lactate clearance from the tumor [250]. For example, a ^{13}C MRS study using [1-^{13}C] glucose revealed that treatment with the antiestrogen tamoxifen reduced the glycolytic rate and lactate clearance by twofold but did not affect other parameters in human MCF-7 breast tumor xenografts [250]. High-resolution ^{13}C MRS of RIF-1 tumor extracts demonstrated that their TCA cycle activity was significantly increased at 24 h following treatment with cyclophosphamide [251]. In the same tumor model, an in vivo study showed that following [1-^{13}C] glucose injection, [3-^{13}C] lactate levels reached steady state within 50 min, whereas [3-^{13}C] alanine increased continuously [252], which is shown in Fig. 8.9. Volume-localized ^{13}C MRS with ^{1}H-^{13}C cross polarization was applied to detect the conversion of [1-^{13}C] glucose to [3-^{13}C] lactate in C3H mouse mammary carcinomas in vivo [253]. This study also showed that tumor oxygenation decreased with increasing glycolytic rate in vivo [253]. In vitro studies using two-dimensional heteronuclear single-quantum correlation spectroscopy (HSQC) and labeled [U-^{13}C] glucose show that human embryonic kidney HEK293T cells produced a high level of ^{13}C-glycine derived from [U-^{13}C] glucose, whereas H1299 lung cancer cells produced relatively low and nontumorigenic MCF-10A mammary epithelial cells no ^{13}C-labeled glycine [254]. These ^{13}C MRS experiments suggest that in some cancer cells, glycolytic carbons can be diverted into glycine metabolism through phosphoglycerate dehydrogenase (PHGDH), which contributes to the pathogenesis of some cancers [254].

8.4.13 ^{13}C MRS of Choline Metabolism

As discussed above, high concentrations of tCho- and choline-containing metabolites are detected in a variety of malignancies [15]. Free intracellular choline (Cho) can be acetylated to synthesize the neurotransmitter acetylcholine, phosphorylated for the synthesis of PC and PtdCho, and oxidized to produce the methyl donors betaine and S-adenosylmethionine. In vitro and in vivo ^{13}C MRS studies with ^{13}C-labeled methionine in 9 L rat gliomas revealed a significant amount of

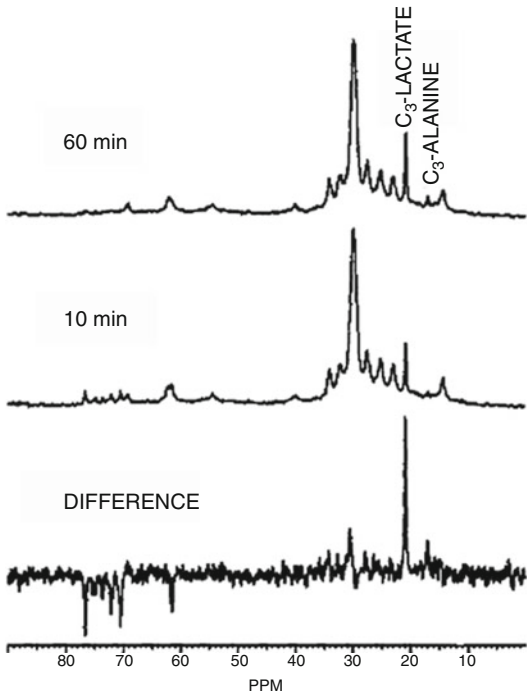

Fig. 8.9 ^{13}C MRS of ^{13}C-labeled glucose and lactate metabolism. The spectra were obtained at 10 and at 60 min following injection of [1-^{13}C] glucose in mice bearing RIF-1 tumors. It shows a net increase of [3-^{13}C] lactate and [3-^{13}C] (Adapted with kind permission from Constantinidis et al. [252])

de novo choline synthesis most likely from the liver, while in vitro experiments with the 9 L rat glioma cell line demonstrated that these cells were unable to synthesize choline de novo [255]. Similarly, ^{13}C- labeled choline in combination with ^{13}C MRS has been utilized to study choline metabolism, specifically to follow the label of ^{13}C in the Kennedy pathway [16, 256]. ^{13}C MRS studies following administration of [1,2-^{13}C] choline revealed that [1,2-^{13}C] choline was rapidly taken up and phosphorylated in MCF-7 breast cancer cells and tumors [257]. Increased PC, and total choline-containing metabolites, and decreased GPC were observed in human MDA-MB-231 breast cancer cells compared with nonmalignant human MCF-12A mammary epithelial cells using [1,2-^{13}C]-labeled choline with ^{13}C MRS [16]. Microarray analyses from the same cell lines demonstrate overexpression of choline kinase and phospholipase C [16]. Using [1,2-^{13}C]-labeled choline with ^{13}C MRS also demonstrated a twofold higher rate of choline transport and a tenfold higher rate of PC and betaine synthesis in human MCF-7 breast cancer cells compared to human mammary epithelial cells [258]. These results suggest that a combination of enhanced choline transport, increased choline kinase activity, and increased catabolism mediated by increased phospholipase C activity drive the activated choline phospholipid metabolism in the breast cancer cells [16, 257, 258].

8.4.14 Hyperpolarized ^{13}C MRS of Tumors

The use of hyperpolarized ^{13}C substrates has revolutionized the use of metabolic MRS in vivo as it has dramatically increased the signal-to-noise ratio obtained for these ^{13}C-labeled substrates compared to their non-hyperpolarized counterparts [50, 259–261]. The principle of hyperpolarization is explained in the following. The nuclear spins of MR-active nuclei are oriented either parallel or antiparallel to the external magnetic field B_0, and hence, the total spins are in a superposition of these two states known as Zeeman states [259]. The population difference between these two states, which is defined as the polarization P, generates the MR signal. The polarization is proportional to the magnetic field strength and the gyromagnetic ratio of the nucleus. The population difference can be increased by several orders of magnitude with a method known as hyperpolarization where nuclei are forced to be in a nonequilibrium distribution among Zeeman levels with respect to the thermal equilibrium [262]. Parahydrogen-induced polarization [263], optical pumping of noble gases [264], dynamic nuclear polarization (DNP) [265], or brute force [266] can create a hyperpolarized agent. Since the goal of using hyperpolarization is to image metabolism in real time, it is essential that hyperpolarized compounds are soluble in aqueous solution and have a sufficiently long relaxation time so that they can be transported, be administered, and have adequate time to go through metabolic reactions [259, 267].

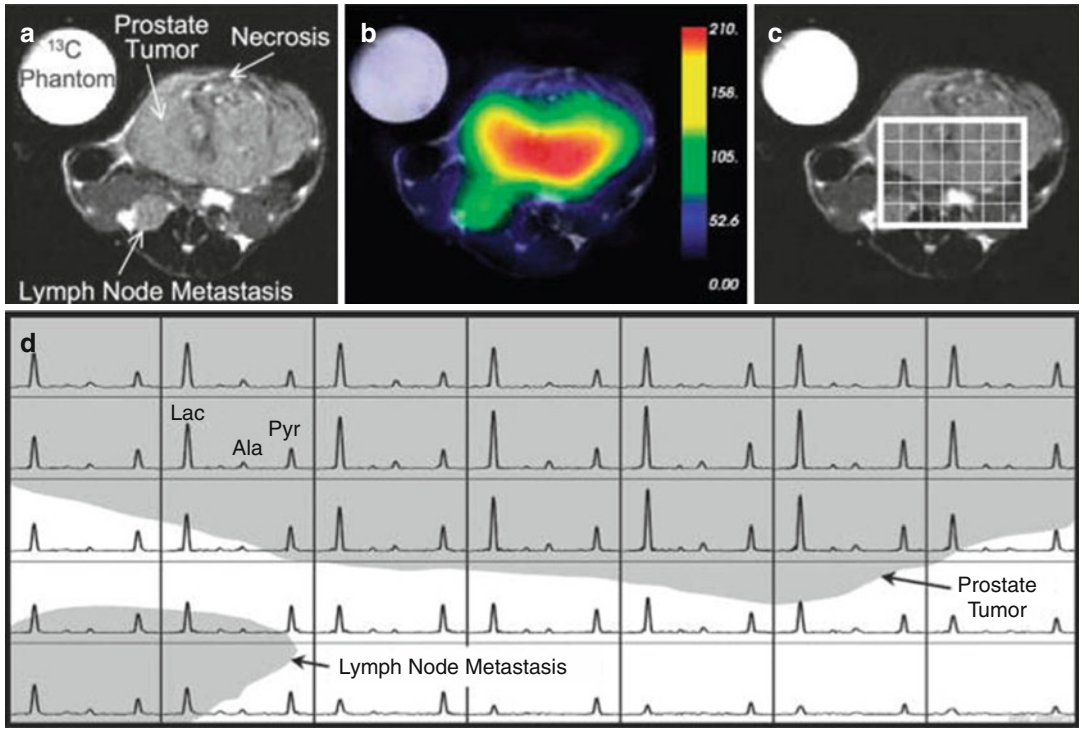

Fig. 8.10 Hyperpolarized ^{13}C MRS using [1-^{13}C] pyruvate. Hyperpolarized [1-^{13}C] pyruvate MRS in transgenic adenocarcinoma of mouse prostate (TRAMP) tumors demonstrates higher hyperpolarized [1-^{13}C] lactate and [1-^{13}C] alanine levels with cancer progression. (**a**) T_2-weighted proton image shows the primary tumor and lymph node metastasis. (**b**) The hyperpolarized ^{13}C lactate image following the injection of hyperpolarized [1-^{13}C] pyruvate. (**c**) After spatially zero filling and voxel shifting, a subset of the spectral grid was selected and (**d**) displayed (Adapted from the Albers et al. [103])

[1-^{13}C] Pyruvate is the most widely studied hyperpolarized substrate because of its relatively long T1 relaxation time, good solubility in water, fast transport across the cell membrane, and rapid metabolism [268]. There are three main metabolic pathways for pyruvate: (1) It can be converted to [1-^{13}C] lactate by lactate dehydrogenase (LDH), (2) it can undergo transamination with glutamate to form [1-^{13}C] alanine, or (3) it can be irreversibly oxidized to acetyl-CoA in mitochondria, which releases $^{13}CO_2$ in the form of $H_2{}^{13}CO_3^-$ in the mitochondria [50, 268]. Hyperpolarized ^{13}C MRS of pyruvate in cancer has the potential for clinical translation in cancer diagnosis and in monitoring the efficacy of anticancer treatments [52]. For example, the PI3K/Akt/mTOR signaling pathway plays a critical role in cancer cell proliferation, differentiation, metabolism, and survival and is currently being explored as a target for anticancer therapy [269, 270]. Hyperpolarized lactate levels produced from hyperpolarized pyruvate through LDH activity were significantly reduced when PI3K was inhibited with LY294002 in GS-2 glioblastoma and in MDA-MB-231 breast tumor xenografts [52]. The hyperpolarized lactate-to-pyruvate ratio was also reduced in mTOR-targeted therapy by everolimus in glioblastomas in mice [47]. Similarly, it was shown in EL4 mouse lymphomas that the pyruvate-to-lactate flux was inhibited within 24 h of etoposide chemotherapy due to loss of coenzyme NAD(H) [260]. Reduced levels of hyperpolarized lactate were produced from hyperpolarized [1-^{13}C] pyruvate in rat C6 gliomas between 24 and 96 h post-radiotherapy [271]. Hyperpolarized [1-^{13}C] pyruvate in transgenic adenocarcinomas of mouse prostate (TRAMP) resulted in elevated hyperpolarized lactate and alanine with cancer progression [103]. Figure 8.10 shows representative hyperpolarized ^{13}C MR spectra from a TRAMP mouse with a

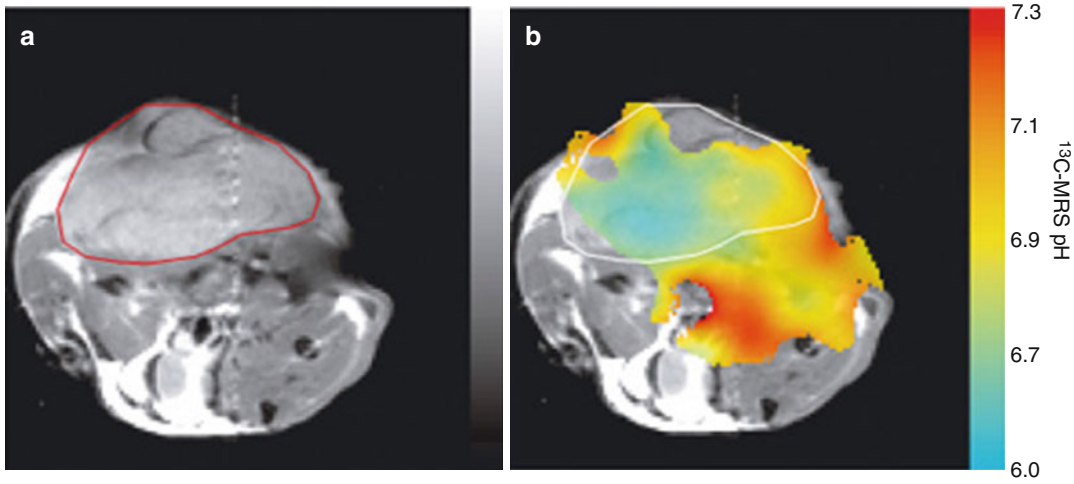

Fig. 8.11 Hyperpolarized ^{13}C bicarbonate MRSI. Tumor pH was measured in a representative mouse EL4 lymphoma in vivo with hyperpolarized bicarbonate. (**a**) Proton MR image of a subcutaneously implanted EL4 tumor in mouse and (**b**) the pH map [279]. (Adapted with kind permission from Gallagher et al. [279])

high-grade tumor and metastasis in the right periaortic lymph node [103].

Other hyperpolarized molecules of interest include bicarbonate, glutamine, fumarate, succinate, lactate, and choline, among others [103, 259, 261, 267, 272–274]. Using hyperpolarized [1-^{13}C] lactate as a substrate enables observing the conversion of hyperpolarized lactate to pyruvate, in addition to detecting secondary conversions to hyperpolarized alanine and bicarbonate through pyruvate [275]. Increased choline metabolites have been observed in tumors in both clinical and preclinical studies [61]. Hyperpolarized [1,1,2,2-D(4), 2-(13) C] choline chloride provides a new tool for studying choline metabolism as the chemical shift of the ^{13}C position is able to differentiate choline, acetylcholine, PC, and betaine [274].

Malignant transformation also leads to the activation of glutaminase, which converts glutamine to glutamate to fuel cancer cell metabolism [276]. In addition, glutamine protects cells against oxidative stress and complements glucose for the production of macromolecules [13]. Therefore, imaging glutamine metabolism will have a significant impact on understanding tumor progression and will potentially allow monitoring of treatment response. The conversion of hyperpolarized [5-^{13}C] glutamine to [5-^{13}C] glutamate has been confirmed in human hepatocellular (HepG2) cancer cells and human glioma cells (SF188-Bcl-xL) in vitro [277, 278].

Cellular pH is highly regulated in mammalian cell, which is in part through extracellular buffering by bicarbonate (HCO_3^-) [279]. HCO_3^- is able to counteract changes in pH through interconversion with CO_2 through the enzyme carbonic anhydrase [280]. As discussed above, tumor pHe is lower than normal tissue pHe due to increased aerobic glycolysis, reduced buffering, and abnormal perfusion [31]. Following intravenous injection of hyperpolarized bicarbonate ($H^{13}CO_3^-$) in vivo, it is possible to measure tumor pHe from the ratio of the signal intensities of $H^{13}CO_3^-$ and $^{13}CO_2$ [279]. Using this probe, it was shown that subcutaneously implanted mouse EL4 lymphomas displayed a low interstitial pH compared to the surrounding tissue (Fig. 8.11) [279].

Since hyperpolarized glucose has a very short T1 (<1 s), its pentose analogue fructose (T1 ~ 16 s) offers an alternative tool to investigate downstream glycolytic processes [273]. Fructose can enter glycolysis through phosphorylation by fructokinases [281]. The C_2 position of fructose has a relatively long relaxation time when hyperpolarized (~16 s at 37 °C), in addition to a high solution state polarization (~12 %) [273]. MRSI of hyperpolarized [2-^{13}C] fructose revealed a higher uptake and increased metabolism of fructose in mouse prostate tumors of

TRAMP mice relative to surrounding normal tissue [273]. Acetate, in the form of acetyl-CoA, is produced in cells from the catabolism of sugars, fats, and proteins [282–284]. The TCA cycle utilizes acetyl-CoA and reduces NAD^+ to NADH, which is fed into oxidative phosphorylation [283, 284]. Hyperpolarized [1-^{13}C] acetate can be used for in vivo imaging of the cellular TCA cycle rate [261]. Production of malate from fumarate is a sensitive marker of cellular necrosis [272]. It was shown that following intravenous injection of hyperpolarized [1,4-$^{13}C_2$] fumarate, hyperpolarized [1,4-$^{13}C_2$] malate production was 2.4-fold higher in etoposide-treated mouse EL4 lymphomas compared to untreated lymphomas due to tumor cell necrosis, making this approach a powerful tool for monitoring treatment outcome [272].

Conclusions

In conclusion, preclinical multinuclear MRS of tumors offers a wide spectrum of diverse tools to assess endogenous tumor metabolism, the physiological tumor microenvironment characterized by hypoxia and acidic pHe, drug delivery and drug metabolism, and response to chemotherapeutic and molecularly targeted anticancer treatments. Preclinical MRS has helped tremendously in gaining a better understanding of tumors as living organs in vivo as it provides the powerful ability to measure metabolic processes noninvasively. Research studies that have combined MRS of tumor models in vivo with metabolic and molecular measurements performed ex vivo and/or in cultures from the same cell or tumor models have provided molecular insights that have guided clinical MRS settings, treatment strategies, as well as treatment monitoring. Multinuclear MRS, where different nuclei are measured in the same tumor, offers unprecedented possibilities of multiplexing the metabolic readout from tumors in vivo. The continuing push of MR technology towards higher magnetic field strengths offers new possibilities for increasing the sensitivity of MRS measurements in research studies and eventually in patients. In addition, smart approaches have been developed for increasing the sensitivity of MRS by polarization transfer methods such as RINEPT [205] or by chemical exchange with highly abundant water molecules such as done in CEST [196–198]. In the age of molecular imaging and molecular medicine, it is also possible to combine in vivo MRS and MRI with other imaging modalities either sequentially or in novel hybrid instruments, such as MR–PET or MR–optical scanners, to further improve the sensitivity and molecular specificity of cancer detection and treatment monitoring.

References

1. Hanahan D, Weinberg RA. Hallmarks of cancer: the next generation. Cell. 2011;144(5):646–74.
2. Hanahan D, Weinberg RA. The hallmarks of cancer. Cell. 2000;100(1):57–70.
3. Siegel R, et al. Cancer statistics, 2012. CA Cancer J Clin. 2012;62(1):10–29.
4. Dang CV, et al. Therapeutic targeting of cancer cell metabolism. J Mol Med (Berl). 2011;89(3):205–12.
5. Vander Heiden MG. Targeting cancer metabolism: a therapeutic window opens. Nat Rev Drug Discov. 2011;10(9):671–84.
6. He Q, et al. Magnetic resonance spectroscopic imaging of tumor metabolic markers for cancer diagnosis, metabolic phenotyping, and characterization of tumor microenvironment. Dis Markers. 2003;19(2–3):69–94.
7. Glunde K, Bhujwalla ZM. Metabolic tumor imaging using magnetic resonance spectroscopy. Semin Oncol. 2011;38(1):26–41.
8. Vander Heiden MG, et al. Understanding the Warburg effect: the metabolic requirements of cell proliferation. Science. 2009;324(5930):1029–33.
9. Deberardinis RJ, et al. Brick by brick: metabolism and tumor cell growth. Curr Opin Genet Dev. 2008;18(1):54–61.
10. Semenza GL. Targeting HIF-1 for cancer therapy. Nat Rev Cancer. 2003;3(10):721–32.
11. Warburg O. On the origin of cancer cells. Science. 1956;123(3191):309–14.
12. Daye D, Wellen KE. Metabolic reprogramming in cancer: unraveling the role of glutamine in tumorigenesis. Semin Cell Dev Biol. 2012;23(4):362–9.
13. DeBerardinis RJ, Cheng T. Q's next: the diverse functions of glutamine in metabolism, cell biology and cancer. Oncogene. 2009;29(3):313–24.
14. Ackerstaff E, et al. Choline phospholipid metabolism: a target in cancer cells? J Cell Biochem. 2003;90(3):525–33.

15. Glunde K, et al. Choline metabolism in malignant transformation. Nat Rev Cancer. 2011; 11(12):835–48.
16. Glunde K, et al. Molecular causes of the aberrant choline phospholipid metabolism in breast cancer. Cancer Res. 2004;64(12):4270–6.
17. Stehelin D, et al. DNA related to the transforming gene(s) of avian sarcoma viruses is present in normal avian DNA. Nature. 1976;260(5547):170–3.
18. Harris H, et al. Suppression of malignancy by cell fusion. Nature. 1969;223(5204):363–8.
19. Jones RG, Thompson CB. Tumor suppressors and cell metabolism: a recipe for cancer growth. Genes Dev. 2009;23(5):537–48.
20. Levine AJ, Puzio-Kuter AM. The control of the metabolic switch in cancers by oncogenes and tumor suppressor genes. Science. 2010;330(6009): 1340–4.
21. Rabi II, et al. The molecular beam resonance method for measuring nuclear magnetic moments. Phys Rev. 1939;55(6):526.
22. Bloch F, et al. Nuclear induction. Phys Rev. 1946;70(7–8):460–74.
23. Bloembergen N, et al. Relaxation effects in nuclear magnetic resonance absorption. Phys Rev. 1948;73(7):679.
24. Damadian R, et al. Field focusing nuclear magnetic resonance (FONAR): visualization of a tumor in a live animal. Science. 1976;194(4272):1430–2.
25. Bloembergen N, et al. Nuclear magnetic relaxation. Nature. 1947;160(4066):475.
26. Ernst RR, Anderson WA. Application of Fourier transform spectroscopy to magnetic resonance. Rev Sci Instrum. 1966;37(1):93–102.
27. McIntyre DJ, et al. Magnetic resonance spectroscopy of cancer metabolism and response to therapy. Radiat Res. 2012;177(4):398–435.
28. Pople JA, et al. High resolution NMR spectroscopy. New York: McGraw-Hill; 1959.
29. Le Belle JE, et al. A comparison of cell and tissue extraction techniques using high-resolution 1H-NMR spectroscopy. NMR Biomed. 2002;15(1):37–44.
30. Gillies RJ, Morse DL. In vivo magnetic resonance spectroscopy in cancer. Annu Rev Biomed Eng. 2005;7:287–326.
31. Gillies RJ, et al. pH imaging. A review of pH measurement methods and applications in cancers. IEEE Eng Med Biol Mag. 2004;23(5):57–64.
32. Aboagye EO, et al. Intratumoral conversion of 5-fluorocytosine to 5-fluorouracil by monoclonal antibody-cytosine deaminase conjugates: noninvasive detection of prodrug activation by magnetic resonance spectroscopy and spectroscopic imaging. Cancer Res. 1998;58(18):4075–8.
33. Ruiz-Cabello J, et al. Fluorine (19F) MRS and MRI in biomedicine. NMR Biomed. 2010;24(2):114–29.
34. Gerig JT. Fluorine NMR of proteins. Prog Nucl Magn Reson Spectrosc. 1994;26:293–370.
35. Klomp DW, et al. Optimization of localized 19F magnetic resonance spectroscopy for the detection of fluorinated drugs in the human liver. Magn Reson Med. 2003;50(2):303–8.
36. Martino R, et al. Fluorine nuclear magnetic resonance, a privileged tool for metabolic studies of fluoropyrimidine drugs. Curr Drug Metab. 2000;1(3):271–303.
37. Yu JX, et al. 19F: a versatile reporter for non-invasive physiology and pharmacology using magnetic resonance. Curr Med Chem. 2005;12(7):819–48.
38. Bhujwalla ZM, et al. Metabolic heterogeneity in RIF-1 tumours detected in vivo by 31P NMR spectroscopy. NMR Biomed. 1990;3(5):233–8.
39. Daly PF, et al. Phospholipid metabolism in cancer cells monitored by 31P NMR spectroscopy. J Biol Chem. 1987;262(31):14875–8.
40. Street JC, et al. 13C and 31P NMR investigation of effect of 6-aminonicotinamide on metabolism of RIF-1 tumor cells in vitro. J Biol Chem. 1996;271(8):4113–9.
41. Vaupel P, et al. Correlations between 31P-NMR spectroscopy and tissue O2 tension measurements in a murine fibrosarcoma. Radiat Res. 1989;120(3):477–93.
42. Cohen SM, et al. Effects of ethanol on alanine metabolism in perfused mouse liver studied by 13C NMR. Proc Natl Acad Sci U S A. 1979;76(10):4808–12.
43. Fung BM. Carbon-13 and proton magnetic resonance of mouse muscle. Biophys J. 1977;19(3):315–9.
44. Shen J, et al. Determination of the rate of the glutamate/glutamine cycle in the human brain by in vivo 13C NMR. Proc Natl Acad Sci U S A. 1999;96(14):8235–40.
45. Horowitz BL, et al. MR of intracranial epidermoid tumors: correlation of in vivo imaging with in vitro 13C spectroscopy. AJNR Am J Neuroradiol. 1990;11(2):299–302.
46. Ardenkjaer-Larsen JH, et al. Increase in signal-to-noise ratio of >10,000 times in liquid-state NMR. Proc Natl Acad Sci U S A. 2003;100(18):10158–63.
47. Chaumeil MM, et al. Hyperpolarized 13C MR spectroscopic imaging can be used to monitor Everolimus treatment in vivo in an orthotopic rodent model of glioblastoma. Neuroimage. 2011;59(1):193–201.
48. Dafni H, et al. Hyperpolarized 13C spectroscopic imaging informs on hypoxia-inducible factor-1 and myc activity downstream of platelet-derived growth factor receptor. Cancer Res. 2010;70(19):7400–10.
49. Harrison C, et al. Comparison of kinetic models for analysis of pyruvate-to-lactate exchange by hyperpolarized 13 C NMR. NMR Biomed. 2012;25(11):1286–94.
50. Merritt ME, et al. Hyperpolarized 13C allows a direct measure of flux through a single enzyme-catalyzed step by NMR. Proc Natl Acad Sci U S A. 2007;104(50):19773–7.
51. Ouwerkerk R, et al. Tissue sodium concentration in human brain tumors as measured with 23Na MR imaging. Radiology. 2003;227(2):529–37.
52. Ward CS, et al. Noninvasive detection of target modulation following phosphatidylinositol

3-kinase inhibition using hyperpolarized 13C magnetic resonance spectroscopy. Cancer Res. 2010;70(4):1296–305.
53. Burney IA, et al. Effect of vasoactive drugs on tumour blood flow as determined by 2H nuclear magnetic resonance spectroscopy. Acta Oncol. 1995;34(3): 367–71.
54. Zeisel SH, da Costa KA. Choline: an essential nutrient for public health. Nutr Rev. 2009;67(11):615–23.
55. Resseguie M, et al. Phosphatidylethanolamine N-methyltransferase (PEMT) gene expression is induced by estrogen in human and mouse primary hepatocytes. FASEB J. 2007;21(10):2622–32.
56. Zeisel SH. Choline: critical role during fetal development and dietary requirements in adults. Annu Rev Nutr. 2006;26:229–50.
57. Zeisel SH, Blusztajn JK. Choline and human nutrition. Annu Rev Nutr. 1994;14:269–96.
58. Negendank W. Studies of human tumors by MRS: a review. NMR Biomed. 1992;5(5):303–24.
59. Podo F. Tumour phospholipid metabolism. NMR Biomed. 1999;12(7):413–39.
60. Ronen SM, Leach MO. Imaging biochemistry: applications to breast cancer. Breast Cancer Res. 2001;3(1):36–40.
61. Glunde K, Serkova NJ. Therapeutic targets and biomarkers identified in cancer choline phospholipid metabolism. Pharmacogenomics. 2006;7(7): 1109–23.
62. Ramirez de Molina A, et al. Expression of choline kinase alpha to predict outcome in patients with early-stage non-small-cell lung cancer: a retrospective study. Lancet Oncol. 2007;8(10):889–97.
63. Aboagye EO, Bhujwalla ZM. Malignant transformation alters membrane choline phospholipid metabolism of human mammary epithelial cells. Cancer Res. 1999;59(1):80–4.
64. Hara T, et al. Choline transporter as a novel target for molecular imaging of cancer. Mol Imaging. 2006;5(4):498–509.
65. Koepsell H, et al. Organic cation transporters. Rev Physiol Biochem Pharmacol. 2003;150:36–90.
66. Okuda T, et al. Identification and characterization of the high-affinity choline transporter. Nat Neurosci. 2000;3(2):120–5.
67. O'Regan S, et al. An electric lobe suppressor for a yeast choline transport mutation belongs to a new family of transporter-like proteins. Proc Natl Acad Sci U S A. 2000;97(4):1835–40.
68. Eliyahu G, et al. Phosphocholine as a biomarker of breast cancer: molecular and biochemical studies. Int J Cancer. 2007;120(8):1721–30.
69. Katz-Brull R, Degani H. Kinetics of choline transport and phosphorylation in human breast cancer cells; NMR application of the zero trans method. Anticancer Res. 1996;16(3B):1375–80.
70. Kouji H, et al. Molecular and functional characterization of choline transporter in human colon carcinoma HT-29 cells. Arch Biochem Biophys. 2009;483(1):90–8.
71. Wittenberg J, Kornberg A. Choline phosphokinase. J Biol Chem. 1953;202(1):431–44.
72. Marchan R, et al. Choline-releasing glycerophosphodiesterase EDI3 links the tumor metabolome to signaling network activities. Cell Cycle. 2012;11(24):4499–506.
73. Stewart JD, et al. Choline-releasing glycerophosphodiesterase EDI3 drives tumor cell migration and metastasis. Proc Natl Acad Sci U S A. 2012;109(21):8155–60.
74. Zhong M, et al. Phospholipase D prevents apoptosis in v-Src-transformed rat fibroblasts and MDA-MB-231 breast cancer cells. Biochem Biophys Res Commun. 2003;302(3):615–9.
75. Uchida N, et al. Phospholipase D activity in human gastric carcinoma. Anticancer Res. 1999;19(1B):671–5.
76. Iorio E, et al. Alterations of choline phospholipid metabolism in ovarian tumor progression. Cancer Res. 2005;65(20):9369–76.
77. Oka M, et al. Protein kinase C alpha associates with phospholipase D1 and enhances basal phospholipase D activity in a protein phosphorylation-independent manner in human melanoma cells. J Invest Dermatol. 2003;121(1):69–76.
78. Foster DA, Xu L. Phospholipase D in cell proliferation and cancer. Mol Cancer Res. 2003;1(11):789–800.
79. Yamashita S, et al. Overexpression of group II phospholipase A2 in human breast cancer tissues is closely associated with their malignant potency. Br J Cancer. 1994;69(6):1166–70.
80. Ramirez de Molina A, et al. Choline kinase is a novel oncogene that potentiates RhoA-induced carcinogenesis. Cancer Res. 2005;65(13):5647–53.
81. Warden CH, et al. Acid-soluble precursors and derivatives of phospholipids increase after stimulation of quiescent Swiss 3T3 mouse fibroblasts with serum. Biochem Biophys Res Commun. 1980;94(2):690–6.
82. Lacal JC, et al. Novel source of 1,2-diacylglycerol elevated in cells transformed by Ha-ras oncogene. Nature. 1987;330(6145):269–72.
83. Macara IG. Elevated phosphocholine concentration in ras-transformed NIH 3T3 cells arises from increased choline kinase activity, not from phosphatidylcholine breakdown. Mol Cell Biol. 1989;9(1):325–8.
84. Ramirez de Molina A, et al. Regulation of choline kinase activity by Ras proteins involves Ral-GDS and PI3K. Oncogene. 2002;21(6):937–46.
85. Warden CH, Friedkin M. Regulation of choline kinase activity and phosphatidylcholine biosynthesis by mitogenic growth factors in 3T3 fibroblasts. J Biol Chem. 1985;260(10):6006–11.
86. Wang T, et al. Choline transporters in human lung adenocarcinoma: expression and functional implications. Acta Biochim Biophys Sin (Shanghai). 2007;39(9):668–74.
87. Ryan AJ, et al. c-Jun N-terminal kinase regulates CTP:phosphocholine cytidylyltransferase. Arch Biochem Biophys. 2006;447(1):23–33.

88. Ackerstaff E, et al. Detection of increased choline compounds with proton nuclear magnetic resonance spectroscopy subsequent to malignant transformation of human prostatic epithelial cells. Cancer Res. 2001;61(9):3599–603.
89. Malet-Martino M, Holzgrabe U. NMR techniques in biomedical and pharmaceutical analysis. J Pharm Biomed Anal. 2011;55(1):1–15.
90. Sato N. Central role of mitochondria in metabolic regulation of liver pathophysiology. J Gastroenterol Hepatol. 2007;22 Suppl 1:S1–6.
91. Zhu M, et al. Reproducibility of total choline/water ratios in mouse U87MG xenograft tumors by 1H-MRS. J Magn Reson Imaging. 2012;36(2):459–67.
92. Gatenby RA, Gillies RJ. Why do cancers have high aerobic glycolysis? Nat Rev Cancer. 2004;4(11):891–9.
93. Costello LC, Franklin RB. 'Why do tumour cells glycolyse?': from glycolysis through citrate to lipogenesis. Mol Cell Biochem. 2005;280(1–2):1–8.
94. Samudio I, et al. Mitochondrial uncoupling and the Warburg effect: molecular basis for the reprogramming of cancer cell metabolism. Cancer Res. 2009;69(6):2163–6.
95. Stambaugh R, Post D. Substrate and product inhibition of rabbit muscle lactic dehydrogenase heart (H4) and muscle (M4) isozymes. J Biol Chem. 1966;241(7):1462–7.
96. Serganova I, et al. Metabolic imaging: a link between lactate dehydrogenase a, lactate, and tumor phenotype. Clin Cancer Res. 2011;17(19):6250–61.
97. Granchi C, et al. Inhibitors of lactate dehydrogenase isoforms and their therapeutic potentials. Curr Med Chem. 2010;17(7):672–97.
98. Fantin VR, et al. Attenuation of LDH-A expression uncovers a link between glycolysis, mitochondrial physiology, and tumor maintenance. Cancer Cell. 2006;9(6):425–34.
99. Le A, et al. Inhibition of lactate dehydrogenase A induces oxidative stress and inhibits tumor progression. Proc Natl Acad Sci U S A. 2010;107(5):2037–42.
100. Seth P, et al. On-target inhibition of tumor fermentative glycolysis as visualized by hyperpolarized pyruvate. Neoplasia. 2011;13(1):60–71.
101. Walenta S, et al. High lactate levels predict likelihood of metastases, tumor recurrence, and restricted patient survival in human cervical cancers. Cancer Res. 2000;60(4):916–21.
102. Brizel DM, et al. Elevated tumor lactate concentrations predict for an increased risk of metastases in head-and-neck cancer. Int J Radiat Oncol Biol Phys. 2001;51(2):349–53.
103. Albers MJ, et al. Hyperpolarized 13C lactate, pyruvate, and alanine: noninvasive biomarkers for prostate cancer detection and grading. Cancer Res. 2008;68(20):8607–15.
104. Gatza ML, et al. Analysis of tumor environmental response and oncogenic pathway activation identifies distinct basal and luminal features in HER2-related breast tumor subtypes. Breast Cancer Res. 2011;13(3):R62.
105. Walenta S, et al. Metabolic classification of human rectal adenocarcinomas: a novel guideline for clinical oncologists? J Cancer Res Clin Oncol. 2003;129(6):321–6.
106. Fraisl P, et al. Regulation of angiogenesis by oxygen and metabolism. Dev Cell. 2009;16(2):167–79.
107. Green H, Goldberg B. Collagen and cell protein synthesis by an established mammalian fibroblast line. Nature. 1964;204:347–9.
108. Hunt TK, et al. Aerobically derived lactate stimulates revascularization and tissue repair via redox mechanisms. Antioxid Redox Signal. 2007;9(8):1115–24.
109. Constant JS, et al. Lactate elicits vascular endothelial growth factor from macrophages: a possible alternative to hypoxia. Wound Repair Regen. 2000;8(5):353–60.
110. Xiong M, et al. Production of vascular endothelial growth factor by murine macrophages: regulation by hypoxia, lactate, and the inducible nitric oxide synthase pathway. Am J Pathol. 1998;153(2):587–98.
111. Vegran F, et al. Lactate influx through the endothelial cell monocarboxylate transporter MCT1 supports an NF-kappaB/IL-8 pathway that drives tumor angiogenesis. Cancer Res. 2011;71(7):2550–60.
112. De Saedeleer CJ, et al. Lactate activates HIF-1 in oxidative but not in Warburg-phenotype human tumor cells. PLoS One. 2012;7(10):e46571.
113. Bottomley PA. Spatial localization in NMR spectroscopy in vivo. Ann N Y Acad Sci. 1987;508:333–48.
114. Frahm J, et al. Localized high-resolution proton NMR spectroscopy using stimulated echoes: initial applications to human brain in vivo. Magn Reson Med. 1989;9(1):79–93.
115. Rothman DL, et al. Homonuclear 1H double-resonance difference spectroscopy of the rat brain in vivo. Proc Natl Acad Sci U S A. 1984;81(20):6330–4.
116. He Q, et al. Proton detection of choline and lactate in EMT6 tumors by spin-echo-enhanced selective multiple-quantum-coherence transfer. J Magn Reson B. 1996;112(1):18–25.
117. He Q, et al. Single-scan in vivo lactate editing with complete lipid and water suppression by selective multiple-quantum-coherence transfer (Sel-MQC) with application to tumors. J Magn Reson B. 1995;106(3):203–11.
118. Freeman DM, et al. A double quantum coherence transfer proton NMR spectroscopy technique for monitoring steady-state tumor lactic acid levels in vivo. Magn Reson Med. 1990;14(2):321–9.
119. Thakur SB, et al. In vivo lactate signal enhancement using binomial spectral-selective pulses in selective MQ coherence (SS-SelMQC) spectroscopy. Magn Reson Med. 2009;62(3):591–8.
120. Mellon EA, et al. Detection of lactate with a hadamard slice selected, selective multiple quantum coherence, chemical shift imaging sequence (HDMD-SelMQC-CSI) on a clinical MRI scanner: application to tumors and muscle ischemia. Magn Reson Med. 2009;62(6):1404–13.

121. Pickup S, et al. Lactate imaging with Hadamard-encoded slice-selective multiple quantum coherence chemical-shift imaging. Magn Reson Med. 2008;60(2):299–305.
122. Yaligar J, et al. Lactate MRSI and DCE MRI as surrogate markers of prostate tumor aggressiveness. NMR Biomed. 2011;25(1):113–22.
123. Plathow C, Weber WA. Tumor cell metabolism imaging. J Nucl Med. 2008;49 Suppl 2:43S–63.
124. Poptani H, et al. Detecting early response to cyclophosphamide treatment of RIF-1 tumors using selective multiple quantum spectroscopy (SelMQC) and dynamic contrast enhanced imaging. NMR Biomed. 2003;16(2):102–11.
125. Aboagye EO, et al. Detection of tumor response to chemotherapy by 1H nuclear magnetic resonance spectroscopy: effect of 5-fluorouracil on lactate levels in radiation-induced fibrosarcoma 1 tumors. Cancer Res. 1998;58(5):1063–7.
126. Hakumaki JM, Kauppinen RA. 1H NMR visible lipids in the life and death of cells. Trends Biochem Sci. 2000;25(8):357–62.
127. Delikatny EJ, et al. MR-visible lipids and the tumor microenvironment. NMR Biomed. 2011;24(6):592–611.
128. Mannechez A, et al. Proton NMR visible mobile lipid signals in sensitive and multidrug-resistant K562 cells are modulated by rafts. Cancer Cell Int. 2005;5(1):2.
129. Hakumaki JM, et al. 1H MRS detects polyunsaturated fatty acid accumulation during gene therapy of glioma: implications for the in vivo detection of apoptosis. Nat Med. 1999;5(11):1323–7.
130. Ferretti A, et al. Biophysical and structural characterization of 1H-NMR-detectable mobile lipid domains in NIH-3T3 fibroblasts. Biochim Biophys Acta. 1999;1438(3):329–48.
131. Melkus G, et al. Short-echo spectroscopic imaging combined with lactate editing in a single scan. NMR Biomed. 2008;21(10):1076–86.
132. Rosi A, et al. (1H) MRS studies of signals from mobile lipids and from lipid metabolites: comparison of the behavior in cultured tumor cells and in spheroids. NMR Biomed. 2004;17(2):76–91.
133. Mylonis I, et al. Hypoxia causes triglyceride accumulation by HIF-1-mediated stimulation of lipin 1 expression. J Cell Sci. 2012;125(Pt 14):3485–93.
134. Heerdt BG, et al. Initiation of growth arrest and apoptosis of MCF-7 mammary carcinoma cells by tributyrin, a triglyceride analogue of the short-chain fatty acid butyrate, is associated with mitochondrial activity. Cancer Res. 1999;59(7):1584–91.
135. Namiot Z, et al. Gastric cancer with special references to WHO and Lauren's classifications: glycogen and triacylglycerol concentrations in the tumor. Neoplasma. 1989;36(3):363–8.
136. Calabrese C, et al. Biochemical alterations from normal mucosa to gastric cancer by ex vivo magnetic resonance spectroscopy. Cancer Epidemiol Biomarkers Prev. 2008;17(6):1386–95.
137. Le Moyec L, et al. Proton nuclear magnetic resonance spectroscopy reveals cellular lipids involved in resistance to adriamycin and taxol by the K562 leukemia cell line. Cancer Res. 1996;56(15):3461–7.
138. Santini MT, et al. The relationship between 1H-NMR mobile lipid intensity and cholesterol in two human tumor multidrug resistant cell lines (MCF-7 and LoVo). Biochim Biophys Acta. 2001;1531(1–2):111–31.
139. Tallan HH, et al. N-acetyl-L-aspartic acid in brain. J Biol Chem. 1956;219(1):257–64.
140. Baslow MH. N-acetylaspartate in the vertebrate brain: metabolism and function. Neurochem Res. 2003;28(6):941–53.
141. Goldstein FB. Biosynthesis of N-acetyl-L-aspartic acid. Biochim Biophys Acta. 1959;33(2):583–4.
142. Benuck M, D'Adamo Jr AF. Acetyl transport mechanisms. Metabolism of N-acetyl-L-aspartic acid in the non-nervous tissues of the rat. Biochim Biophys Acta. 1968;152(3):611–8.
143. Clark JF, et al. N-acetylaspartate as a reservoir for glutamate. Med Hypotheses. 2006;67(3):506–12.
144. Rigotti DJ, et al. Whole-brain N-acetylaspartate as a surrogate marker of neuronal damage in diffuse neurologic disorders. AJNR Am J Neuroradiol. 2007;28(10):1843–9.
145. Law M, et al. Glioma grading: sensitivity, specificity, and predictive values of perfusion MR imaging and proton MR spectroscopic imaging compared with conventional MR imaging. AJNR Am J Neuroradiol. 2003;24(10):1989–98.
146. Mehta V, Namboodiri MA. N-acetylaspartate as an acetyl source in the nervous system. Brain Res Mol Brain Res. 1995;31(1–2):151–7.
147. Ishimaru H, et al. Differentiation between high-grade glioma and metastatic brain tumor using single-voxel proton MR spectroscopy. Eur Radiol. 2001;11(9):1784–91.
148. Bulik M, et al. Potential of MR spectroscopy for assessment of glioma grading. Clin Neurol Neurosurg. 2012;115(2):146–53.
149. Gyngell ML, et al. Proton MR spectroscopy of experimental brain tumors in vivo. Acta Neurochir Suppl (Wien). 1994;60:350–2.
150. Wallimann T, et al. Intracellular compartmentation, structure and function of creatine kinase isoenzymes in tissues with high and fluctuating energy demands: the 'phosphocreatine circuit' for cellular energy homeostasis. Biochem J. 1992;281(Pt 1):21–40.
151. Prabhakar G, et al. Phosphocreatine restores high-energy phosphates in ischemic myocardium: implication for off-pump cardiac revascularization. J Am Coll Surg. 2003;197(5):786–91.
152. da Silva RP, et al. Creatine synthesis: hepatic metabolism of guanidinoacetate and creatine in the rat in vitro and in vivo. Am J Physiol Endocrinol Metab. 2009;296(2):E256–61.
153. Ohtsuki S, et al. The blood–brain barrier creatine transporter is a major pathway for supplying

creatine to the brain. J Cereb Blood Flow Metab. 2002;22(11):1327–35.
154. Murphy R, et al. Creatine transporter protein content, localization, and gene expression in rat skeletal muscle. Am J Physiol Cell Physiol. 2001;280(3):C415–22.
155. Baird MF, et al. Creatine-kinase- and exercise-related muscle damage implications for muscle performance and recovery. J Nutr Metabol. 2012;2012:960363.
156. Shatton JB, et al. Creatine kinase activity and isozyme composition in normal tissues and neoplasms of rats and mice. Cancer Res. 1979;39 (2 Pt 1):492–501.
157. Lowry OH, et al. Diversity of metabolic patterns in human brain tumors–I. High energy phosphate compounds and basic composition. J Neurochem. 1977;29(6):959–77.
158. Sartorius A, et al. Proton magnetic resonance spectroscopic creatine correlates with creatine transporter protein density in rat brain. J Neurosci Methods. 2008;172(2):215–9.
159. Meyerand ME, et al. Classification of biopsy-confirmed brain tumors using single-voxel MR spectroscopy. AJNR Am J Neuroradiol. 1999;20(1):117–23.
160. Weybright P, et al. Differentiation between brain tumor recurrence and radiation injury using MR spectroscopy. AJR Am J Roentgenol. 2005;185(6):1471–6.
161. Brosnan JT. Interorgan amino acid transport and its regulation. J Nutr. 2003;133(6 Suppl 1):2068S–72.
162. Lacey JM, Wilmore DW. Is glutamine a conditionally essential amino acid? Nutr Rev. 1990;48(8):297–309.
163. Li X, et al. Composition of amino acids in feed ingredients for animal diets. Amino Acids. 2011;40(4):1159–68.
164. Rajagopalan KN, DeBerardinis RJ. Role of glutamine in cancer: therapeutic and imaging implications. J Nucl Med. 2011;52(7):1005–8.
165. Reitzer LJ, et al. Evidence that glutamine, not sugar, is the major energy source for cultured HeLa cells. J Biol Chem. 1979;254(8):2669–76.
166. Choi C, et al. Improvement of resolution for brain coupled metabolites by optimized (1)H MRS at 7T. NMR Biomed. 2010;23(9):1044–52.
167. Zhao Y, et al. Targeting cellular metabolism to improve cancer therapeutics. Cell Death Dis. 2013;4:e532.
168. McKnight TR. Proton magnetic resonance spectroscopic evaluation of brain tumor metabolism. Semin Oncol. 2004;31(5):605–17.
169. Canese R, et al. Characterisation of in vivo ovarian cancer models by quantitative 1H magnetic resonance spectroscopy and diffusion-weighted imaging. NMR Biomed. 2011;25(4):632–42.
170. Xu W, et al. Oncometabolite 2-hydroxyglutarate is a competitive inhibitor of alpha-ketoglutarate-dependent dioxygenases. Cancer Cell. 2011; 19(1):17–30.
171. Losman JA, et al. (R)-2-hydroxyglutarate is sufficient to promote leukemogenesis and its effects are reversible. Science. 2013;339:1621–5.
172. Koivunen P, et al. Transformation by the (R)-enantiomer of 2-hydroxyglutarate linked to EGLN activation. Nature. 2012;483(7390):484–8.
173. Choi C, et al. 2-hydroxyglutarate detection by magnetic resonance spectroscopy in IDH-mutated patients with gliomas. Nat Med. 2012;18(4): 624–9.
174. Andronesi OC, et al. Detection of 2-hydroxyglutarate in IDH-mutated glioma patients by in vivo spectral-editing and 2D correlation magnetic resonance spectroscopy. Sci Transl Med. 2012;4(116):116ra4.
175. Zhang X, et al. Tumor pH and its measurement. J Nucl Med. 2010;51(8):1167–70.
176. Paradise RK, et al. Acidic extracellular pH promotes activation of integrin alpha(v)beta(3). PLoS One. 2011;6(1):e15746.
177. Song CW, et al. Influence of tumor pH on therapeutic response. In: Cancer drug resistance. New Jersey: Humana Press; 2006. p. 21–42.
178. Gerweck LE, Seetharaman K. Cellular pH gradient in tumor versus normal tissue: potential exploitation for the treatment of cancer. Cancer Res. 1996;56(6):1194–8.
179. McCarty MF, Whitaker J. Manipulating tumor acidification as a cancer treatment strategy. Altern Med Rev. 2010;15(3):264–72.
180. Robey IF, Martin NK. Bicarbonate and dichloroacetate: evaluating pH altering therapies in a mouse model for metastatic breast cancer. BMC Cancer. 2011;11:235.
181. Zetter BR. Angiogenesis and tumor metastasis. Annu Rev Med. 1998;49:407–24.
182. Folkman J. Tumor angiogenesis: therapeutic implications. N Engl J Med. 1971;285(21):1182–6.
183. Folkman J, et al. Isolation of a tumor factor responsible for angiogenesis. J Exp Med. 1971;133(2):275–88.
184. Papetti M, Herman IM. Mechanisms of normal and tumor-derived angiogenesis. Am J Physiol Cell Physiol. 2002;282(5):C947–70.
185. Griffin JL, Shockcor JP. Metabolic profiles of cancer cells. Nat Rev Cancer. 2004;4(7):551–61.
186. Griffiths JR. Are cancer cells acidic? Br J Cancer. 1991;64(3):425–7.
187. Halestrap AP, Meredith D. The SLC16 gene family-from monocarboxylate transporters (MCTs) to aromatic amino acid transporters and beyond. Pflugers Arch. 2004;447(5):619–28.
188. Chiche J, et al. Hypoxia-inducible carbonic anhydrase IX and XII promote tumor cell growth by counteracting acidosis through the regulation of the intracellular pH. Cancer Res. 2009;69(1):358–68.
189. Cheng X-F, Wu R-H. MR-based methods for pH measurement in brain tumors: current status and clinical potential. In: Abujamra AL, editor. Diagnostic techniques and surgical management of brain tumors. Intech; New York: 2011. p 287–302.

190. Raghunand N. Tissue pH measurement by magnetic resonance spectroscopy and imaging. Methods Mol Med. 2006;124:347–64.
191. Garcia-Martin ML, et al. Mapping extracellular pH in rat brain gliomas in vivo by 1H magnetic resonance spectroscopic imaging: comparison with maps of metabolites. Cancer Res. 2001;61(17):6524–31.
192. van Sluis R, et al. In vivo imaging of extracellular pH using 1H MRSI. Magn Reson Med. 1999;41(4):743–50.
193. Gil S, et al. Imidazol-1-ylalkanoic acids as extrinsic 1H NMR probes for the determination of intracellular pH, extracellular pH and cell volume. Bioorg Med Chem. 1994;2(5):305–14.
194. Vermathen P, et al. Administration and (1)H MRS detection of histidine in human brain: application to in vivo pH measurement. Magn Reson Med. 2000;43(5):665–75.
195. Martinez GV, et al. Imaging the extracellular pH of tumors by MRI after injection of a single cocktail of T1 and T2 contrast agents. NMR Biomed. 2011;24(10):1380–91.
196. Ward KM, Balaban RS. Determination of pH using water protons and chemical exchange dependent saturation transfer (CEST). Magn Reson Med. 2000;44(5):799–802.
197. Ward KM, et al. A new class of contrast agents for MRI based on proton chemical exchange dependent saturation transfer (CEST). J Magn Reson. 2000;143(1):79–87.
198. van Zijl PC, Yadav NN. Chemical exchange saturation transfer (CEST): what is in a name and what isn't? Magn Reson Med. 2011;65(4):927–48.
199. Liu G, et al. Imaging in vivo extracellular pH with a single paramagnetic chemical exchange saturation transfer magnetic resonance imaging contrast agent. Mol Imaging. 2012;11(1):47–57.
200. Stubbs M, et al. An assessment of 31P MRS as a method of measuring pH in rat tumours. NMR Biomed. 1992;5(6):351–9.
201. Gillies RJ, et al. 31P-MRS measurements of extracellular pH of tumors using 3-aminopropylphosphonate. Am J Physiol. 1994;267(1 Pt 1):C195–203.
202. Raghunand N, et al. Plasmalemmal pH-gradients in drug-sensitive and drug-resistant MCF-7 human breast carcinoma xenografts measured by 31P magnetic resonance spectroscopy. Biochem Pharmacol. 1999;57(3):309–12.
203. Ojugo AS, et al. Measurement of the extracellular pH of solid tumours in mice by magnetic resonance spectroscopy: a comparison of exogenous (19)F and (31)P probes. NMR Biomed. 1999;12(8):495–504.
204. Klomp DW, et al. 31P MRSI and 1H MRS at 7 T: initial results in human breast cancer. NMR Biomed. 2011;24(10):1337–42.
205. Klomp DW, et al. Efficient 1H to 31P polarization transfer on a clinical 3T MR system. Magn Reson Med. 2008;60(6):1298–305.
206. Gibellini F, Smith TK. The Kennedy pathway–De novo synthesis of phosphatidylethanolamine and phosphatidylcholine. IUBMB Life. 2010;62(6):414–28.
207. Kennedy EP, Weiss SB. The function of cytidine coenzymes in the biosynthesis of phospholipides. J Biol Chem. 1956;222(1):193–214.
208. Henneberry AL, McMaster CR. Cloning and expression of a human choline/ethanolaminephosphotransferase: synthesis of phosphatidylcholine and phosphatidylethanolamine. Biochem J. 1999;339(Pt 2):291–8.
209. Lykidis A. Comparative genomics and evolution of eukaryotic phospholipid biosynthesis. Prog Lipid Res. 2007;46(3–4):171–99.
210. Gallego-Ortega D, et al. Differential role of human choline kinase alpha and beta enzymes in lipid metabolism: implications in cancer onset and treatment. PLoS One. 2009;4(11):e7819.
211. Kent C. Eukaryotic phospholipid biosynthesis. Annu Rev Biochem. 1995;64:315–43.
212. Dixon RM, Tian M. Phospholipid synthesis in the lymphomatous mouse liver studied by 31P nuclear magnetic resonance spectroscopy in vitro and by administration of 14C-radiolabelled compounds in vivo. Biochim Biophys Acta. 1993;1181(2):111–21.
213. Zhu L, Bakovic M. Breast cancer cells adapt to metabolic stress by increasing ethanolamine phospholipid synthesis and CTP:ethanolaminephosphate cytidylyltransferase-Pcyt2 activity. Biochem Cell Biol. 2012;90(2):188–99.
214. Swanson MG, et al. Quantification of choline- and ethanolamine-containing metabolites in human prostate tissues using 1H HR-MAS total correlation spectroscopy. Magn Reson Med. 2008;60(1):33–40.
215. Albert DH, Anderson CE. Fatty acid composition at the 2-position of ether-linked and diacyl ethanolamine and choline phosphoglycerides of human brain tumors. Lipids. 1977;12(9):722–8.
216. Al-Saffar NM, et al. Noninvasive magnetic resonance spectroscopic pharmacodynamic markers of the choline kinase inhibitor MN58b in human carcinoma models. Cancer Res. 2006;66(1):427–34.
217. Krishnamachary B, et al. Noninvasive detection of lentiviral-mediated choline kinase targeting in a human breast cancer xenograft. Cancer Res. 2009;69(8):3464–71.
218. Kristeleit R, et al. Histone modification enzymes: novel targets for cancer drugs. Expert Opin Emerg Drugs. 2004;9(1):135–54.
219. Legube G, Trouche D. Regulating histone acetyltransferases and deacetylases. EMBO Rep. 2003;4(10):944–7.
220. Chung YL, et al. Noninvasive magnetic resonance spectroscopic pharmacodynamic markers of a novel histone deacetylase inhibitor, LAQ824, in human colon carcinoma cells and xenografts. Neoplasia. 2008;10(4):303–13.
221. Fang M, et al. The ER UDPase ENTPD5 promotes protein N-glycosylation, the Warburg effect, and proliferation in the PTEN pathway. Cell. 2010;143(5):711–24.

222. Nieminen AI, et al. Myc-induced AMPK-phospho p53 pathway activates Bak to sensitize mitochondrial apoptosis. Proc Natl Acad Sci U S A. 2013;110(20):E1839–48.
223. Pavlov E, et al. Inorganic polyphosphate and energy metabolism in mammalian cells. J Biol Chem. 2010;285(13):9420–8.
224. Okunieff PG, et al. Tumor size dependent changes in a murine fibrosarcoma: use of in vivo 31P NMR for non-invasive evaluation of tumor metabolic status. Int J Radiat Oncol Biol Phys. 1986;12(5):793–9.
225. Gadian DG, Radda GK. NMR studies of tissue metabolism. Annu Rev Biochem. 1981;50:69–83.
226. Deutsch CJ, Taylor JS. Intracellular pH as measured by 19F NMR. Ann N Y Acad Sci. 1987;508:33–47.
227. Longley DB, et al. 5-fluorouracil: mechanisms of action and clinical strategies. Nat Rev Cancer. 2003;3(5):330–8.
228. Wolf W, et al. 19F-MRS studies of fluorinated drugs in humans. Adv Drug Deliv Rev. 2000;41(1):55–74.
229. Harada M, et al. In-vivo 19F-MRS study of 5-fluorouracil (5-FU) metabolism on tumors. Gan To Kagaku Ryoho. 1991;18(1):75–80.
230. van Laarhoven HW, et al. Carbogen breathing differentially enhances blood plasma volume and 5-fluorouracil uptake in two murine colon tumor models with a distinct vascular structure. Neoplasia. 2006;8(6):477–87.
231. McSheehy PM, et al. Enhanced 5-fluorouracil cytotoxicity and elevated 5-fluoronucleotides in the rat Walker carcinosarcoma following methotrexate pretreatment: a 19F-MRS study in vivo. Br J Cancer. 1992;65(3):369–75.
232. Mehta VD, et al. Fluorinated proteins as potential 19F magnetic resonance imaging and spectroscopy agents. Bioconjug Chem. 1994;5(3):257–61.
233. Dresselaers T, et al. Non-invasive 19F MR spectroscopy of 5-fluorocytosine to 5-fluorouracil conversion by recombinant *Salmonella* in tumours. Br J Cancer. 2003;89(9):1796–801.
234. Li C, et al. Conjugation of poly-L-lysine to bacterial cytosine deaminase improves the efficacy of enzyme/prodrug cancer therapy. J Med Chem. 2008;51(12):3572–82.
235. Papadopoulou MV, et al. Novel non-invasive probes for measuring tumor-hypoxia by 19F-magnetic resonance spectroscopy (19F-MRS). Studies in the SCCVII/C3H murine model. Anticancer Res. 2006;26(5A):3259–63.
236. Papadopoulou MV, et al. Novel fluorinated hypoxia-targeted compounds as Non-invasive probes for measuring tumor-hypoxia by 19F-magnetic resonance spectroscopy (19F-MRS). Anticancer Res. 2006;26(5A):3253–8.
237. Cline JM, et al. Distribution of the hypoxia marker CCI-103F in canine tumors. Int J Radiat Oncol Biol Phys. 1994;28(4):921–33.
238. Ljungkvist AS, et al. Changes in tumor hypoxia measured with a double hypoxic marker technique. Int J Radiat Oncol Biol Phys. 2000;48(5):1529–38.
239. Raleigh JA, et al. Fluorescence immunohistochemical detection of hypoxic cells in spheroids and tumours. Br J Cancer. 1987;56(4):395–400.
240. Aboagye EO, et al. The novel fluorinated 2-nitroimidazole hypoxia probe SR-4554: reductive metabolism and semiquantitative localisation in human ovarian cancer multicellular spheroids as measured by electron energy loss spectroscopic analysis. Br J Cancer. 1995;72(2):312–8.
241. Aboagye EO, et al. Bioreductive metabolism of the novel fluorinated 2-nitroimidazole hypoxia probe N-(2-hydroxy-3,3,3-trifluoropropyl)-2-(2-nitroimidazolyl) acetamide (SR-4554). Biochem Pharmacol. 1997;54(11):1217–24.
242. Kwock L, et al. Evaluation of a fluorinated 2-nitroimidazole binding to hypoxic cells in tumor-bearing rats by 19F magnetic resonance spectroscopy and immunohistochemistry. Radiat Res. 1992;129(1):71–8.
243. Mason RP. Transmembrane pH gradients in vivo: measurements using fluorinated vitamin B6 derivatives. Curr Med Chem. 1999;6(6):481–99.
244. Maher EA, et al. Metabolism of [U-13 C]glucose in human brain tumors in vivo. NMR Biomed. 2012;25(11):1234–44.
245. Marin-Valencia I, et al. Glucose metabolism via the pentose phosphate pathway, glycolysis and Krebs cycle in an orthotopic mouse model of human brain tumors. NMR Biomed. 2012;25(10):1177–86.
246. Kurhanewicz J, et al. Current and potential applications of clinical 13C MR spectroscopy. J Nucl Med. 2008;49(3):341–4.
247. Gaglio D, et al. Oncogenic K-Ras decouples glucose and glutamine metabolism to support cancer cell growth. Mol Syst Biol. 2011;7:523.
248. Post JF, et al. 13C NMR studies of glucose metabolism in human leukemic CEM-C7 and CEM-C1 cells. Magn Reson Med. 1992;23(2):356–66.
249. Rothman DL, et al. In vivo nuclear magnetic resonance spectroscopy studies of the relationship between the glutamate-glutamine neurotransmitter cycle and functional neuroenergetics. Philos Trans R Soc Lond B Biol Sci. 1999;354(1387):1165–77.
250. Rivenzon-Segal D, et al. Glycolysis as a metabolic marker in orthotopic breast cancer, monitored by in vivo (13)C MRS. Am J Physiol Endocrinol Metab. 2002;283(4):E623–30.
251. Poptani H, et al. Cyclophosphamide treatment modifies tumor oxygenation and glycolytic rates of RIF-1 tumors: 13C magnetic resonance spectroscopy, Eppendorf electrode, and redox scanning. Cancer Res. 2003;63(24):8813–20.
252. Constantinidis I, et al. In vivo 13CNMR spectroscopy of glucose metabolism of RIF-1 tumors. Magn Reson Med. 1991;20(1):17–26.
253. Nielsen FU, et al. Effect of changing tumor oxygenation on glycolytic metabolism in a murine C3H mammary carcinoma assessed by in vivo nuclear magnetic resonance spectroscopy. Cancer Res. 2001;61(13):5318–25.

254. Locasale JW, et al. Phosphoglycerate dehydrogenase diverts glycolytic flux and contributes to oncogenesis. Nat Genet. 2011;43(9):869–74.
255. Gillies RJ, et al. In vitro and in vivo 13C and 31P NMR analyses of phosphocholine metabolism in rat glioma cells. Magn Reson Med. 1994;32(3):310–8.
256. Ronen SM, Degani H. The application of 13C NMR to the characterization of phospholipid metabolism in cells. Magn Reson Med. 1992;25(2):384–9.
257. Katz-Brull R, et al. Choline metabolism in breast cancer; 2H-, 13C- and 31P-NMR studies of cells and tumors. MAGMA. 1998;6(1):44–52.
258. Katz-Brull R, et al. Metabolic markers of breast cancer: enhanced choline metabolism and reduced choline-ether-phospholipid synthesis. Cancer Res. 2002;62(7):1966–70.
259. Golman K, et al. Molecular imaging using hyperpolarized 13C. Br J Radiol. 2003;76(Spec No 2):S118–27.
260. Day SE, et al. Detecting tumor response to treatment using hyperpolarized 13C magnetic resonance imaging and spectroscopy. Nat Med. 2007; 13(11):1382–7.
261. Ross BD, et al. Hyperpolarized MR imaging: neurologic applications of hyperpolarized metabolism. AJNR Am J Neuroradiol. 2009;31(1):24–33.
262. Rizi RR. A new direction for polarized carbon-13 MRI. Proc Natl Acad Sci U S A. 2009; 106(14):5453–4.
263. Bowers CR, Weitekamp DP. Transformation of symmetrization order to nuclear-spin magnetization by chemical reaction and nuclear magnetic resonance. Phys Rev Lett. 1986;57(21):2645–8.
264. Goodson BM. Nuclear magnetic resonance of laser-polarized noble gases in molecules, materials, and organisms. J Magn Reson. 2002;155(2):157–216.
265. Abragam A, Goldman M. Principles of dynamic nuclear polarisation. Rep Prog Phys. 2001;41(3):395.
266. Frossati G. Polarization of ^{3}He, D_2 (and possibly ^{129}Xe) using cryogenic techniques. Nucl Instrum Meth A. 1998;402(2):479–83.
267. Schroeder MA, et al. Hyperpolarized magnetic resonance: a novel technique for the in vivo assessment of cardiovascular disease. Circulation. 2011; 124(14):1580–94.
268. Kurhanewicz J, et al. Analysis of cancer metabolism by imaging hyperpolarized nuclei: prospects for translation to clinical research. Neoplasia. 2011;13(2):81–97.
269. Bunney TD, Katan M. Phosphoinositide signalling in cancer: beyond PI3K and PTEN. Nat Rev Cancer. 2010;10(5):342–52.
270. Morgensztern D, McLeod HL. PI3K/Akt/mTOR pathway as a target for cancer therapy. Anticancer Drugs. 2005;16(8):797–803.
271. Day SE, et al. Detecting response of rat C6 glioma tumors to radiotherapy using hyperpolarized [1–13C] pyruvate and 13C magnetic resonance spectroscopic imaging. Magn Reson Med. 2011;65(2): 557–63.
272. Gallagher FA, et al. Production of hyperpolarized [1,4-13C2]malate from [1,4-13C2]fumarate is a marker of cell necrosis and treatment response in tumors. Proc Natl Acad Sci U S A. 2009; 106(47):19801–6.
273. Keshari KR, et al. Hyperpolarized [2-13C]-fructose: a hemiketal DNP substrate for in vivo metabolic imaging. J Am Chem Soc. 2009;131(48):17591–6.
274. Allouche-Arnon H, et al. A hyperpolarized choline molecular probe for monitoring acetylcholine synthesis. Contrast Media Mol Imaging. 2011; 6(3):139–47.
275. Chen AP, et al. Feasibility of using hyperpolarized [1-13C]lactate as a substrate for in vivo metabolic 13C MRSI studies. Magn Reson Imaging. 2008;26(6):721–6.
276. Wang JB, et al. Targeting mitochondrial glutaminase activity inhibits oncogenic transformation. Cancer Cell. 2010;18(3):207–19.
277. Gallagher FA, et al. 13C MR spectroscopy measurements of glutaminase activity in human hepatocellular carcinoma cells using hyperpolarized 13C-labeled glutamine. Magn Reson Med. 2008;60(2):253–7.
278. Qu W, et al. Facile synthesis [5-(13)C-4-(2)H(2)]-L-glutamine for hyperpolarized MRS imaging of cancer cell metabolism. Acad Radiol. 2011; 18(8):932–9.
279. Gallagher FA, et al. Magnetic resonance imaging of pH in vivo using hyperpolarized 13C-labelled bicarbonate. Nature. 2008;453(7197):940–3.
280. Meldrum NU, Roughton FJ. Carbonic anhydrase. Its preparation and properties. J Physiol. 1933;80(2):113–42.
281. Rutledge AC, Adeli K. Fructose and the metabolic syndrome: pathophysiology and molecular mechanisms. Nutr Rev. 2007;65(6 Pt 2):S13–23.
282. Engel FL. The influence of the endocrine glands on fatty acid and ketone body metabolism. AMA Arch Intern Med. 1957;100(1):18–33.
283. Modica-Napolitano JS, et al. Mitochondria and human cancer. Curr Mol Med. 2007;7(1):121–31.
284. Modica-Napolitano JS, Singh KK. Mitochondria as targets for detection and treatment of cancer. Expert Rev Mol Med. 2002;4(9):1–19.
285. Lodi A, Ronen SM. Magnetic resonance spectroscopy detectable metabolomic fingerprint of response to antineoplastic treatment. PLoS One. 2011; 6(10):e26155.
286. Bottomley PA, et al. Human in vivo phosphate metabolite imaging with 31P NMR. Magn Reson Med. 1988;7(3):319–36.
287. Griffiths JR, et al. 31P-NMR studies of a human tumour in situ. Lancet. 1983;1(8339):1435–6.

Imaging of Tumour Metabolism: 18-FDG PET

9

Michael Lin and Divesh Kumar

Contents

Abbreviations

2-DG	2-deoxy-D-glucose
BAT	Brown adipose tissue
BMB	Bone marrow biopsy
CI	Conventional imaging
CRC	Colorectal cancer
CRT	Chemoradiation
CWU	Conventional work-up
DTC	Differentiated thyroid cancer
EBUS-TBNA	Endobronchial ultrasound guided transbronchial needle aspiration
EGFR	Epidermal growth factor receptor
EUS	Endoscopic ultrasound
F-18	Fluorine-18
FDG	Fluoro-D-glucose
GLUT	Glucose transport proteins
HCC	Hepatocellular carcinoma
HD	Hodgkin's disease
HNSCC	Head and neck squamous cell cancers
LABC	Locally advanced breast cancer
LARC	Locally advanced rectal cancer
MTV	Metabolic tumour volume
NHL	Non-Hodgkin's lymphoma
NPV	Negative predictive value
NSCLC	Non-small cell lung cancer
OS	Overall survival
PFS	Progression-free survival
RCT	Randomised controlled trial
RT	Radiotherapy
SPN	Solitary pulmonary nodule
SUV	Standardized uptake value
TLG	Total lesion glycolysis

M. Lin (✉) • Divesh Kumar
Department of Nuclear Medicine and PET, Liverpool Hospital, Ground Floor, New Clinical Building, Sydney, NSW, Australia
e-mail: michael.lin@swsahs.nsw.gov.au; divesh.kumar@sswahs.nsw.gov.au

A. Luna et al. (eds.), *Functional Imaging in Oncology*,
DOI 10.1007/978-3-642-40412-2_9,

TOF	Time-of-flight
TRG	Tumor regression grade
VEGF	Vascular endothelial growth factor

9.1 Basic Concepts of FDG PET in Oncology

9.1.1 2-Deoxy-2-[18F]fluoro-D-Glucose (^{18}F-FDG)

9.1.1.1 Historical Aspects

The conceptual design and synthesis of 2-deoxy-2-[18F]fluoro-D-glucose began several years before the first ^{18}F-FDG was synthesised for human injection. Bessell and colleagues [1] first described FDG in an unlabelled form (nonradioactive) and demonstrated that it is a good substrate for hexokinase. This hypothesis was tested using labelled carbon-14 and autoradiography studies. Biodistribution and toxicity studies in animals were conducted as there was no data to support the human administration of labelled or unlabelled form of FDG [2, 3].

The first synthesis of ^{18}F-FDG for human studies took place in the late 1970s. The scientists at the National Institutes of Health, the University of Pennsylvania and Brookhaven National Laboratory developed ^{18}F-FDG as a tool for mapping glucose metabolism in the human brain [4], and images obtained with non-positron emission tomography (i.e. positron computed tomography) demonstrated its concentration in the brain [5] (Fig. 9.1). Major technological advancements have now made it easier to synthesise and image ^{18}F-FDG, which is routinely used in the fields of clinical oncology, neurology and cardiology.

9.1.1.2 Fluorine-18 (F-18)

Fluorine-18 (F-18) is a useful positron-emitting radioisotope that has rapidly become the isotope of choice for labelling biomolecules. The F-18 radioisotope is produced using a cyclotron. The most common method used to produce the isotope is using enriched oxygen water target (oxygen-18). In the cyclotron, the hydrogen ions are accelerated and pushed onto a carbon foil and converted to protons. The protons impact the enriched oxygen-18 target which produce the radioisotope [6] and is used to radiolabel biomolecules with high specific activity. With a half-life of 109.8 min, F-18 radiolabelled isotopes such as ^{18}F-FDG are desirable for research and clinical use without the need for an on-site cyclotron facility.

The decay of F-18 is primarily positron emission with an energy of approximately 0.633 MeV [7]. When injected intravenously, the emitted positrons travel a few millimetres in tissue before combining with negatively charged electrons, converting mass into energy and releasing two high-energy (511 keV) photons (gamma rays), which are emitted at approximately 180° to each other (Fig. 9.2). The simultaneous detection of these photons by the PET scanner is then used to construct a three-dimensional image of the sequence of events [7].

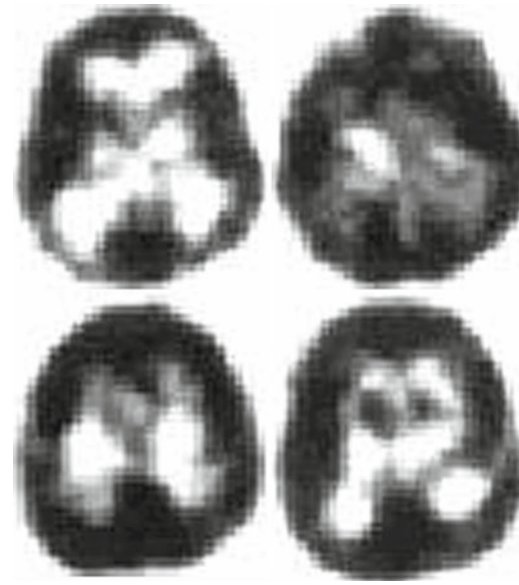

Fig. 9.1 Early whole-brain tomographic FDG images of brain function in a normal volunteer reveal high concentration of the agent in cortical and subcortical grey matter. The brain images were obtained with positron computed tomography (PCT)

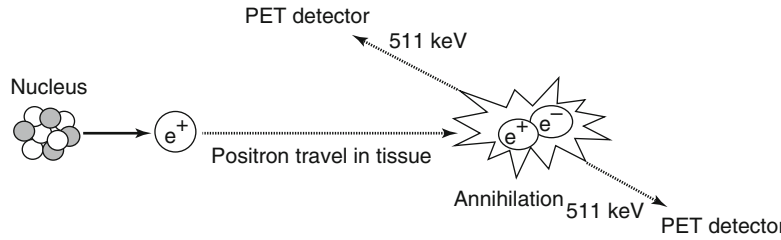

Fig. 9.2 A positron emission tomography scanner is used to detect photons emitted by the annihilation event of an electron and positron. The photons have identical energies (511 keV) and emitted simultaneously at approximately 180° in opposite directions. The near-simultaneous detection by PET of these high-energy photons is known as annihilation coincidence detection

9.1.1.3 2-Deoxy-D-Glucose

2-Deoxy-D-glucose (2-DG) is a glucose molecule which has the 2-hydroxyl group replaced by hydrogen, so that it cannot undergo further glycolysis (Fig. 9.3). Glucose hexokinase traps this substance in most cells (with the exception of the liver and kidney) making it a good marker for tissue glucose consumption and hexokinase activity [8]. This is exploited in oncologic imaging where many cancers have elevated glucose utilisation and upregulated hexokinase levels. 2-DG labelled with carbon-14 has been a popular ligand for laboratory research in animal models, where distribution is assessed by tissue slicing followed by autoradiography [9]. 2-DG has also been used in targeted optical imaging for fluorescent in vivo imaging. In PET, fluorodeoxyglucose is used where one of the two hydrogens of 2-deoxy-D-glucose is replaced with the positron-emitting isotope F-18 (Fig. 9.4) allowing distribution of the tracer to be imaged [10].

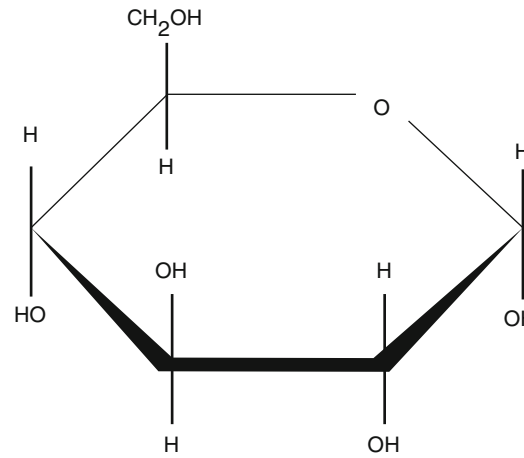

Fig. 9.3 Structure of 2-deoxy-D-glucose (2-DG)

9.1.1.4 Positron Emission Tomography

The limited anatomical resolution of PET is overcome by the advent of combined PET and computed tomography (CT) scanners (PET-CT) in a single gantry. This landmark development allows the fusion of functional and precise anatomical information for the first time with a significant improvement in diagnostic confidence and accuracy. As a result, over the past decade, PET-CT has replaced PET-alone systems. The introduction of Time-of-Flight (TOF) technology for PET further improves lesion detection as a result of innovation in scanner detectors (scintillators) and enhanced accuracy in localising the annihilation event (Fig. 9.2). More recently PET combined with magnetic resonance imaging (MRI) (PET-MRI) [11] is also making a transition from a research tool into the clinical domain.

9.1.1.5 FDG Production

The production of FDG is a multistep process that begins with a particle accelerator such as a cyclotron which produces the [F-18] fluoride radionuclide. The most common reaction is through proton irradiation by the $^{18}O(p, n)$ 18F

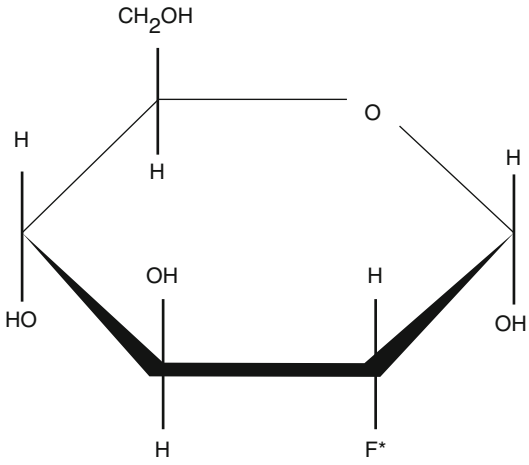

Fig. 9.4 Structure of 2-deoxy-2-fluoro-D-glucose (18F-FDG). The *asterisk* indicates the location of the hydroxyl group for 2-DG which is replaced by the radioactive isotope fluorine-18 (F-18) to enable detection by PET

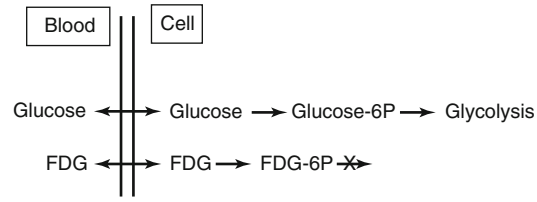

Fig. 9.5 Diagram of FDG metabolism in comparison with glucose. Whereupon glucose undergoes glycolysis to generate energy, FDG phosphorylated by hexokinase enzyme does not undergo further metabolism and is trapped within the cells. This results in increased tracer uptake and retention within metabolically active tissues. Since malignant cells have enhanced glucose metabolism, FDG allows this process to be imaged and mapped by PET

reaction on a pressurised oxygen-18-enriched water target [12]. After irradiation the radioactive [F-18] fluoride is transferred to a radiopharmaceutical production laboratory or clean room for further transformation into FDG. The [F-18] fluoride is pumped from the cyclotron to a FDG synthesiser unit housed in a lead-shielded hot cell. The hot cell provides an environment of air classification compatible for pharmaceutical manufacturing and to protect the operator from ionising radiation. Several automated chemical manipulations are then carried out leading to a product which is ultimately formulated into a physiological injectable solution. The final product is subjected to either sterilising filtration or steam sterilisation, quality control analysis and quality assurance checks before released for injection into humans [13].

9.1.2 FDG Metabolism in Tumours

FDG is a glucose analogue and, just like glucose, is actively transported into the cell mediated by a group of structurally related glucose transport proteins (GLUT). Once internalised, glucose and FDG are both phosphorylated by hexokinase as the first step towards glycolysis. Glucose continues along the glycolytic pathway for energy production, whereas FDG cannot enter glycolysis (Fig. 9.5) and becomes effectively trapped intracellularly as FDG-6-phosphate and steadily accumulates [14–16].

Published by Otto Warburg in 1927, glucose metabolism is enhanced in cancer cells [17] and displays an over-expression of GLUT, particularly GLUT-1 and GLUT-3, as well as higher levels of hexokinase isoforms type I and II [18, 19]. Cancer cells are highly metabolically active and favour the more inefficient anaerobic pathway adding to the already increased glucose demands. The increase in glycolysis has been proposed as a metabolic strategy of tumour cells to ensure survival and growth in environments with low oxygen concentration [16]. Tumour cells also have low levels of the dephosphorylation enzyme glucose-6-phosphatase which catalyses glucose-6-phosphate and FDG-6-phosphate. These combined mechanisms form the basis whereupon tumour cells take up and retain higher levels of FDG when compared to normal tissue.

9.1.3 Normal Physiologic FDG Distribution and Benign Variants

There is high physiologic FDG uptake in the cerebral cortex and basal ganglia of the brain where glucose is the main substrate for

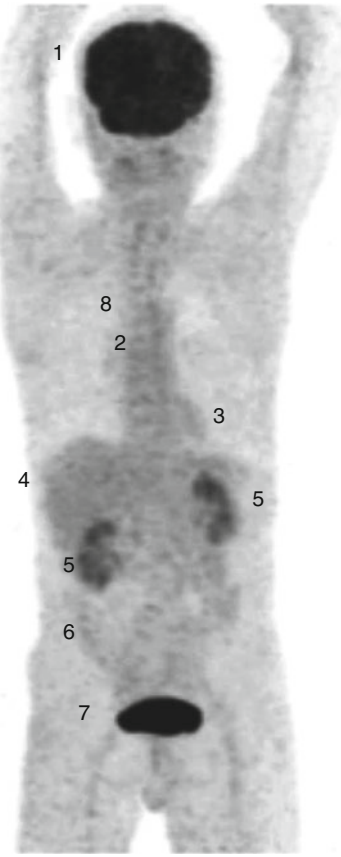

Fig. 9.6 Whole-body FDG PET (maximum intensity projection image) of a patient showing normal biodistribution following injection of 370 MBq of FDG and scanned at 60 min. There is intense FDG accumulation in the cerebral cortex (*1*) and mild FDG uptake in the bone marrow (*2*), myocardium (*3*), liver (*4*) and in large bowel (*6*). Tracer excretion is seen in the kidneys (*5*) and intensely in the bladder (*7*). There is minimal FDG activity in the lungs (*8*)

metabolism (Fig. 9.6). Normal biodistribution of FDG in other tissues includes mediastinal blood pool activity, liver, spleen and bone marrow with variable uptake in salivary glands, skeletal muscle, and gastrointestinal tract especially the stomach and colon. FDG accumulation in myocardium depends on substrate availability, and in a fasting patient where insulin levels are low, free fatty acid is the predominant substrate and glucose utilisation is usually low. FDG is not reabsorbed by renal tubules, and therefore a high percentage of the administered dose is excreted via the kidneys and bladder [20]. Urinary tracer pooling along the ureters is commonly seen and, in patients who had undergone urinary diversion surgery, may sometimes cause uncertainty in scan interpretation.

In males, testicular FDG uptake is normally mild to moderate in intensity, symmetric and diffuse in pattern, and the degree of uptake is dependent on age [21]. Physiologic FDG activity in the ovaries can be observed in premenopausal women during ovulation and within corpus luteum cysts [22] and in the uterus at mid-cycle and during the menstrual flow phase [23]. Diffuse FDG uptake can be seen in normal breasts due to proliferative glandular tissue and at the nipples, and high FDG uptake can also be observed in lactating breasts [22].

Normal diffuse homogeneous thymic activity is seen in children with an inverted "V" shape configuration on the coronal views [22]. Increased FDG uptake can be expected at sites of muscle activation (e.g. skeletal muscles following strenuous activity, lingual and mastication muscles from chewing, symmetric vocal cord uptake during phonation).

FDG is not cancer specific and will accumulate in areas with high levels of metabolism and glycolysis. Increased FDG uptake in adipose tissue observed on PET is well recognised, and an inverse relationship between the frequency of FDG uptake in brown adipose tissue (BAT) and the environmental temperature has been demonstrated [24]. BAT regulates thermogenesis and its activation is seen more frequently in winter months. Although BAT can significantly interfere with scan interpretation on PET-alone systems where it can be indistinguishable from uptake within pathological lymphadenopathy (Fig. 9.7), the problem is mitigated with PET-CT with the accurate localisation of tracer uptake to fat tissue on the corresponding CT images. Activated BAT may also account for a less common benign variant of focal increased cardiac FDG accumulation observed in lipomatous hypertrophy of the interatrial septum [25].

Prominent diffuse bowel uptake, especially in the large bowel, is commonly seen in patients on metformin therapy [26] (Fig. 9.8).

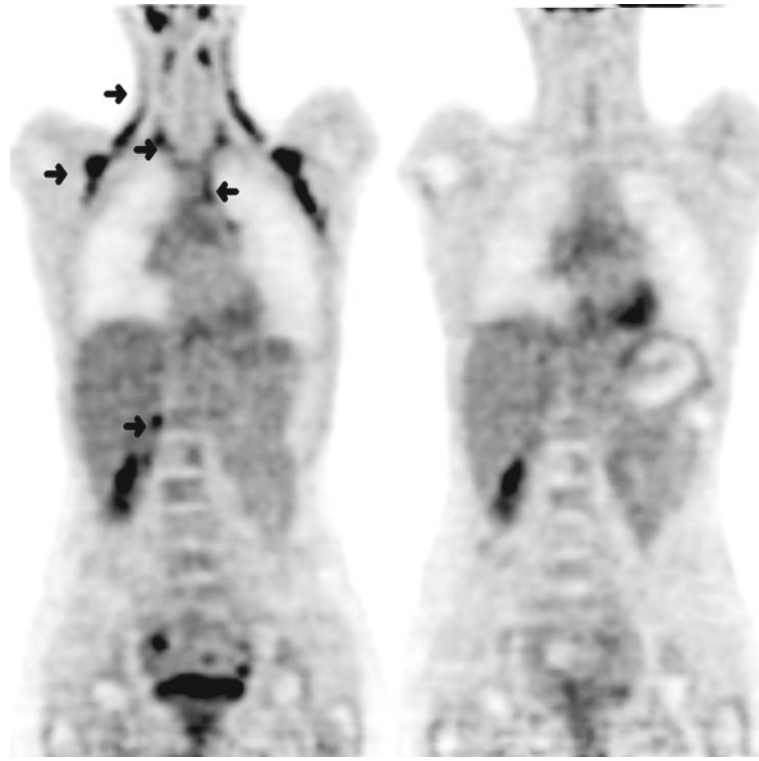

Fig. 9.7 (*Left*) Coronal FDG PET images of a 27-year-old woman with Hodgkin's disease and a typical distribution of activated brown adipose tissue (BAT). There was intense FDG uptake in a symmetric pattern in the cervical, supraclavicular, axillary and paraspinal regions, left anterior superior mediastinum and in the right perinephric region (*arrows*). A repeat scan (*Right*) 1 week later with oral diazepam as premedication demonstrated resolution of these areas of uptake confirming the presence of activated BAT observed on the initial scan

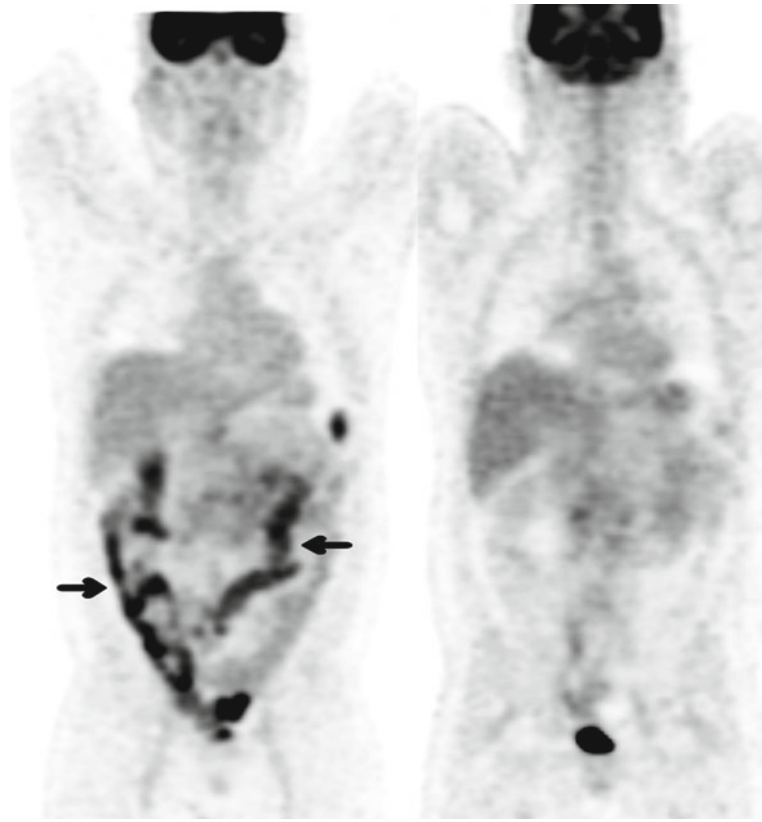

Fig. 9.8 (*Left*) Coronal FDG PET image of a 43-year-old man with newly diagnosed lymphoma in the abdomen. He has a history of type 2 diabetes on metformin therapy. The scan demonstrated moderate to intense diffuse FDG uptake throughout the bowel most markedly in the colon (*arrows*). (*Right*) A repeat PET scan a few days later after withholding metformin for 72 h showed resolution of reactive bowel uptake and better visualisation of the known sites of intra-abdominal lymphoma. There was physiological urinary tracer excretion in the bladder and normal FDG accumulation in the brain, myocardium and liver

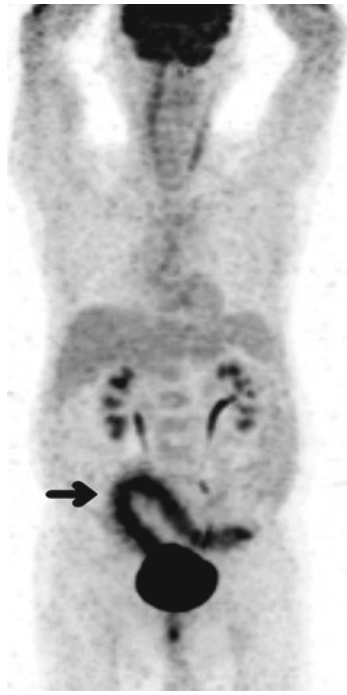

Fig. 9.9 A 77-year-old man underwent FDG PET scan for further investigation of chronic diarrhoea and abdominal pain. Colonoscopy findings were not specific and a gastrointestinal malignancy remained a possible diagnosis. Maximum intensity projection PET image showed intense segmental tracer accumulation along the sigmoid colon and rectum (*arrow*) with marked mucosal thickening, pericolonic inflammatory changes and mesenteric stranding on CT scan (not shown) consistent with an inflammatory process. On the rest of the PET image, there was prominent linear neck muscle uptake and physiologic tracer excretion in the kidneys, ureters and bladder. There was normal FDG accumulation in the brain, myocardium and liver. At surgery and histopathology, ischaemic colitis secondary to mesenteric panniculitis was found

The underlying mechanism is thought to be due to an increase in glucose use by the intestine from upregulation of glucose transporters. Because the use of metformin could potentially mask significant colonic lesions, some investigators have suggested ceasing this medication prior to FDG PET [27]. One study which comprised 138 diabetic patients found that 2 days of discontinuation of metformin was sufficient in reducing high intestinal uptake [28]. Although discontinuation of metformin therapy does reduce intestinal FDG accumulation, this has to be balanced against potential hyperglycemia which could render the PET images suboptimal due to substrate competition between glucose and FDG.

There are a large number of benign conditions that can cause false-positive results when interpreting FDG PET oncology scans. Active inflammation and infection can cause positive uptake due to increased FDG accumulation in macrophages and leucocytes [29]. In patients who have recently undergone treatment such as radiotherapy (RT), post-therapy inflammation can be difficult to differentiate from residual malignancy. Intense pleural uptake from talc pleurodesis is frequently seen and may be indistinguishable from superimposed pleural malignancy. In active colitis intense segmental bowel uptake can be observed (Fig. 9.9).

Reactive focal FDG uptake is often seen at sites of subcutaneous/intramuscular injections (Fig. 9.10), tissue repair from recent surgery, biopsy or acute fractures (Fig. 9.11) [30], and a detailed clinical history from the patient should be recorded. Granulomatous disorders such as

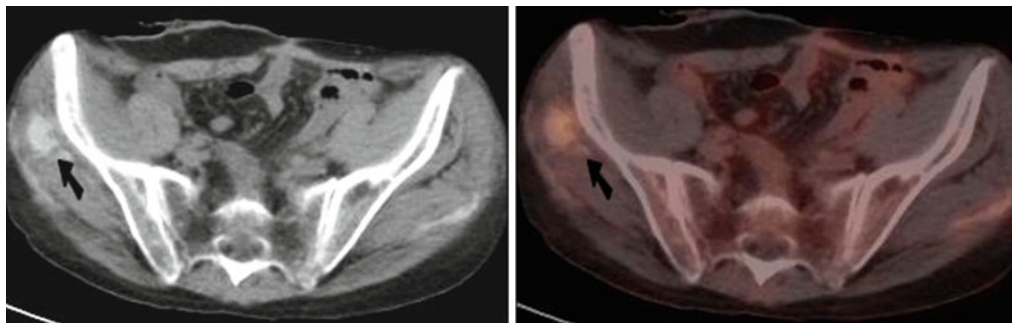

Fig. 9.10 Transaxial CT (*Left*) and combined FDG PET-CT (*Right*) of the pelvis. There was focal increased FDG uptake at the site of recent intramuscular iron injection associated with soft tissue calcification in the right gluteus medius muscle (*arrows*). There was also a linear area of mild uptake on the contralateral side due to a previous injection

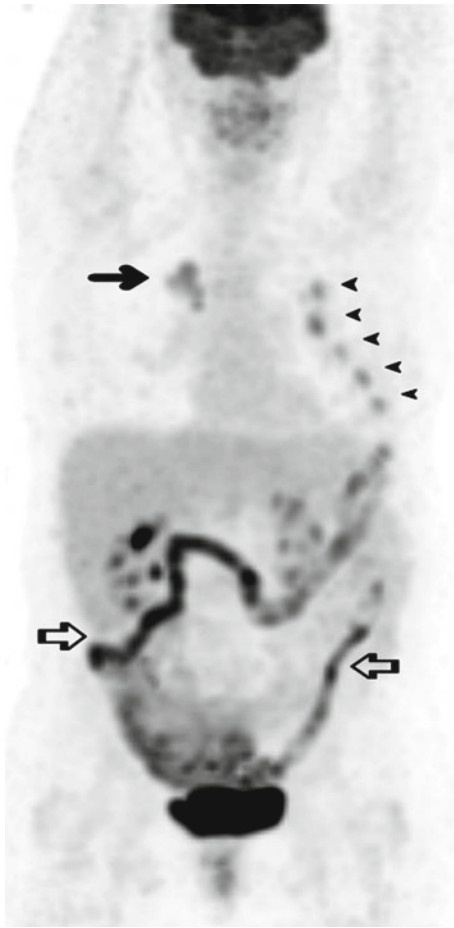

Fig. 9.11 A 67-year-old woman presented for a FDG PET scan to further characterise an irregular 37 mm pulmonary mass in the upper lobe of the right lung. On PET the mass demonstrated moderately increased FDG accumulation (*arrow*) as well as adjacent focal uptake at the right pulmonary hilum consistent with primary lung cancer with ipsilateral hilar lymph node metastasis. There were multiple foci of increased uptake at the left second to sixth ribs anteriorly (*arrowheads*) in a consecutive pattern, some of which corresponded to callus formation on CT scan (not shown) consistent with rib fractures. Further history from the patient revealed recent trauma from an accidental fall onto her left side. There was also moderate to intense diffuse bowel uptake (*open arrows*) secondary to metformin therapy

tuberculosis and sarcoidosis (Fig. 9.12) as well as chronic inflammatory disorders such as pneumoconiosis are also confounders and not infrequent causes of false-positive PET results. These conditions can lead to increased FDG uptake and mimic malignancy especially within pulmonary hilar and mediastinal lymph nodes and can pose a diagnostic challenge when interpreting PET oncology scans.

9.1.4 Standardised Uptake Value

In clinical practice, FDG PET scans are interpreted visually and semi-quantitatively using the standardised uptake value (SUV). SUV is a relatively simple, reproducible and well-established index for quantifying glucose utilisation by measuring the activity of tracer in the lesion or organ corrected for the patient's weight and dose of FDG injected. Although there are many limitations and factors affecting SUV measurements and hence subject to variability [31–33], several popular indices are used in the clinical setting which includes maximum SUV (SUV_{max}), mean SUV (SUV_{mean}) and SUV corrected for lean body mass (SUV_{lean}). SUV measurements are increasingly incorporated in clinical trials in providing an objective assessment of therapy response on serial PET scans. While useful, it is important to be aware of the limitations of this parameter and potential over-reliance during clinical decision making [34].

Other PET imaging biomarkers that have attracted significant interest recently are the determination of the metabolic tumour volume (MTV) and total lesion glycolysis (TLG). MTV is estimated by delineating the region of interest (e.g. tumour) using either a fixed SUV cut-off or region growing up to a prefixed percentage of the SUV_{max}, whereas TLG is derived by multiplying the MTV by the mean SUV. These PET parameters have shown to be useful prognostic markers in certain solid tumours [35]. In a study of 328 patients with non-small cell lung cancer (NSCLC), the prognosis of patients could be stratified using median whole-body MTV [36]. For MTV ≤65.7 ml the median overall survival (OS) was 41.1 months, compared with 9.5 months for those with a median MTV of >65.7 ml. Both MTV and TLG were shown to be independent prognostic factors after adjusting for age, gender, treatment intent, histology and stage and were better prognostic markers than whole-body SUV_{max} and SUV_{mean}.

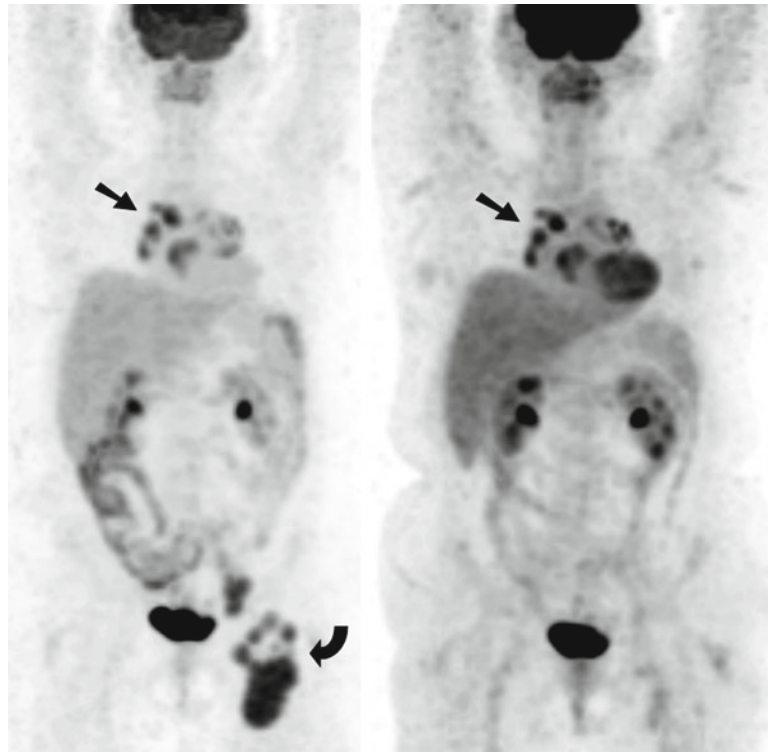

Fig. 9.12 Sarcoidosis as a mimic of malignancy. A 56-year-old woman with newly diagnosed diffuse large B-cell non-Hodgkin's lymphoma (NHL) underwent a staging FDG PET scan (*Left*). There was intense FDG uptake within multiple lymph nodes in the left groin (*curved arrow*) at the sites of biopsy proven NHL, as well as moderate to intense foci at the pulmonary hila and mediastinum bilaterally which were more marked on the right side (*arrow*). Following completion of chemotherapy, a repeat FDG PET (*Right*) was undertaken which demonstrated marked metabolic response at the sites of lymphoma in the left groin; however, the uptake in the pulmonary hila and mediastinum was relatively unchanged. There was physiologic FDG accumulation in the brain, oropharynx, myocardium, liver, spleen, kidneys and bladder and along bowel loops. As a result of the difference in metabolic response on PET and in order to exclude refractory lymphoma, a mediastinoscopy and biopsy of the mediastinal lymphadenopathy were arranged. Histology of the right paratracheal lymph nodes revealed granulomatous inflammation consistent with sarcoidosis and no malignancy was found

9.2 Clinical Applications of FDG PET in Oncology

9.2.1 FDG PET in the Diagnosis of Malignancy and Characterisation of Tumours

9.2.1.1 Solitary Pulmonary Nodule

In the initial evaluation of a solitary pulmonary nodule (SPN), FDG PET is the most accurate imaging modality. Incidental pulmonary nodules are increasingly detected especially with improvement in the sensitivity of modern CT scanners and often pose a management dilemma. The risk of malignancy is dependent on the individual patient, and the use of FDG PET is incorporated in management guidelines [37]. For an accurate assessment, the size of the nodule should be at least 8 mm, below which PET is less reliable due to partial volume effects (i.e. the degree of tracer accumulation in small lesions which are near the resolution limits of the imaging equipment may be underestimated) and respiratory motion. Malignant SPN generally has a higher FDG uptake than benign lesions. By considering clinically relevant information and

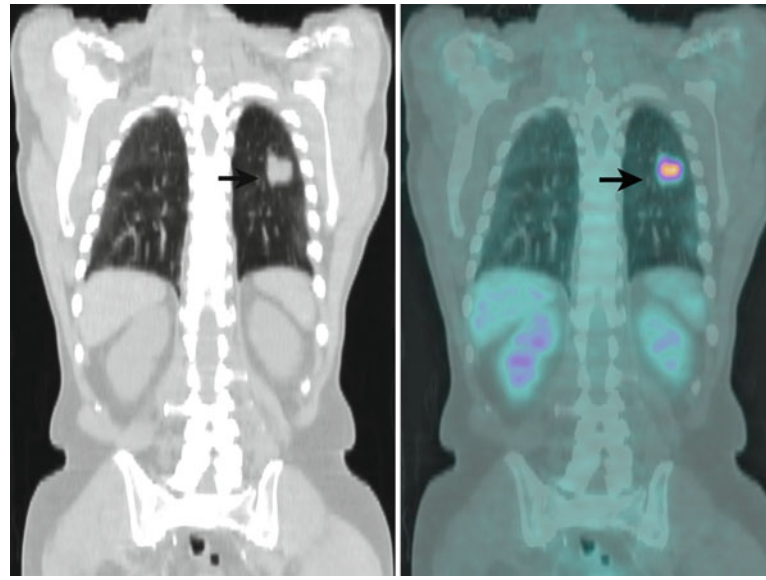

Fig. 9.13 Coronal CT (*Left*) and combined FDG PET-CT (*Right*) images of the lungs of a 78-year-old man who presented for further characterisation of an irregular 34 mm solitary pulmonary mass in the lower lobe of the left lung (*arrows*). SUV_{max} of the lesion on PET was 7.3. In view of the PET findings, the patient underwent surgery, and a T2N0 poorly differentiated squamous cell carcinoma confined to lung parenchyma was resected

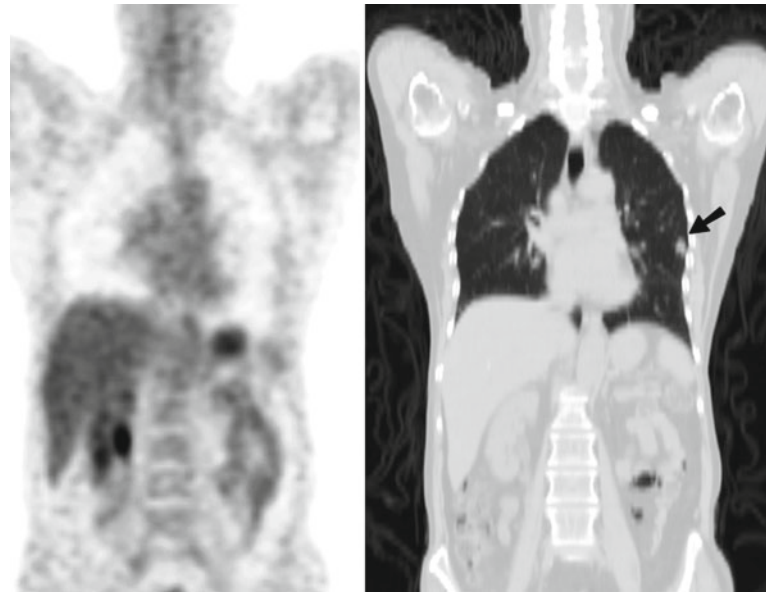

Fig. 9.14 Coronal PET (*Left*) and CT (*Right*) images of a 58-year-old woman who presented for further characterisation of an irregular 10 mm solitary pulmonary nodule in the lower lobe of the left lung (*arrow*). The lesion had faint FDG uptake on PET with an SUV_{max} of 1.1. The patient underwent surgery, and a T1N0 bronchoalveolar carcinoma was removed

the pretest probability for malignancy, the addition of PET can risk-stratify and identify patients who would benefit from an invasive strategy [38]. Although false-positive results can occur (e.g. inflammation, infection or sarcoidosis), a nodule with a SUV_{max} of more than 2.5 is generally considered malignant until proven otherwise [39] (Fig. 9.13). The converse, however, is not necessarily true. Since the degree of FDG uptake depends on size and proliferative activity, false-negative results can occur in small nodules or in malignancy with low metabolic rates (e.g. carcinoid or bronchoalveolar carcinoma) (Fig. 9.14). In a study by Hashimoto and colleagues [40], the probability of malignancy in any visually evident lesion (SUV between 1.0

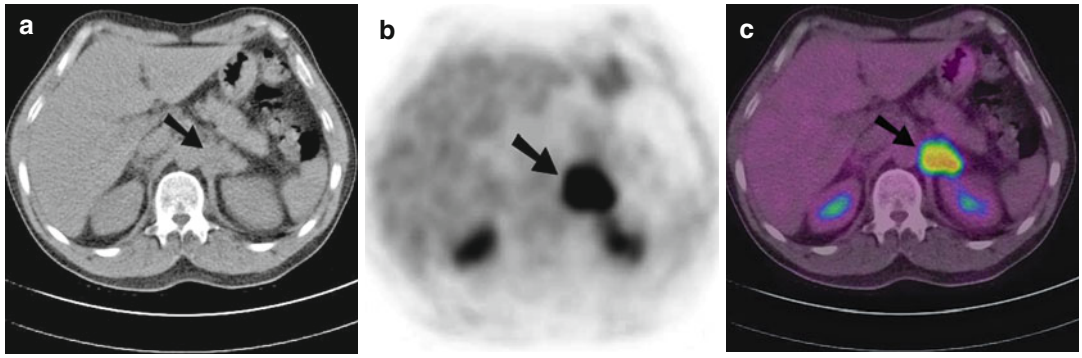

Fig. 9.15 Transaxial CT (**a**), FDG PET (**b**) and combined PET-CT (**c**) images of the upper abdomen of a 55-year-old man with adenocarcinoma of unknown origin. Bilateral adrenal enlargement with abnormal increased FDG was noted. The right adrenal gland measured 30 mm with an SUV_{max} of 4.4 on PET (not shown). There was also intense FDG uptake within a 35 mm left adrenal mass with an SUV_{max} of 10.0 (*arrows*), and the level of uptake was significantly above that of background hepatic parenchymal activity. The SUV ratio of the left adrenal gland/liver was 5.3. The patient died 7 months after the PET scan

and 2.5) was reported at 60 %, and most lesions (15 out of 16 lesions) were ≥10 mm on CT. Some authors are of the opinion that nodules can only be regarded as benign if they are completely negative on PET [41].

9.2.1.2 Brain Tumours

The use of FDG PET in brain tumours was the first oncological application. The initial clinical data emerged in the early 1980s when Di Chiro and colleagues demonstrated the efficacy in grading and predicting prognosis in primary brain tumours [42]. However FDG crosses the blood–brain barrier, and scan interpretation is hampered by high cerebral glucose consumption and consequently high physiologic tracer activity in the grey matter. Therefore FDG when utilised alone is not ideal in neuro-oncology. Moreover FDG PET may not differentiate benign and malignant cerebral lesions with sufficient accuracy [43]. Where FDG PET may be helpful is in determining the grade of the primary brain tumour at diagnosis (high vs. low grade), detection of malignant transformation of low-grade tumours (e.g. anaplastic transformation) and to provide prognostic information [44]. FDG PET can also contribute in targeting a site for biopsy by identifying the most metabolically active component of a lesion discriminating active tumour from surrounding oedema.

9.2.1.3 Adrenal Lesions

In patients with malignancy, FDG PET has demonstrated a sensitivity of 83 %, specificity of 85 % and a negative predictive value (NPV) of 93 % in the evaluation of adrenal masses of at least 10 mm in size [45]. Various semi-quantitative parameters have also been used such as SUV threshold or adrenal-to-liver ratios [46, 47]. In a cohort of 150 patients with various malignancies, by using a SUV cut-off of 3.1, FDG PET correctly classified most adrenal lesions with a PPV of 89 % and a NPV of 99 % [46] (Fig. 9.15). The reference standard used in this study was mostly imaging follow-up. Nine out of one hundred and seventy-five adrenal masses were misclassified where a small percentage of adrenal adenomas had an SUV of more than 3.1. When the unenhanced CT information of the PET-CT was interpreted in conjunction with PET using attenuation values less than or equal to 10 HU for diagnosing an adenoma, only three masses (1.7 %) were misclassified. PET was found to be useful even for small lesions defined as less than 15 mm. In patients with no history of malignancy, there is limited data showing the incremental benefit of adding PET. In a study comprising 37 patients with no previous history of cancer, active malignancy or elevated hormonal secretion, FDG PET

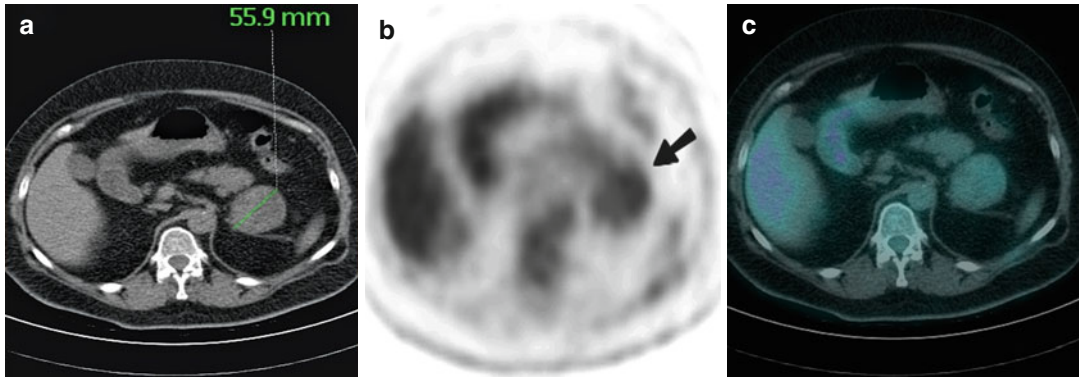

Fig. 9.16 Transaxial CT (**a**), FDG PET (**b**) and combined PET-CT (**c**) images of a 53-year-old woman with no history of malignancy who presented with a 55.9 mm left adrenal mass. At the site of the mass on CT, there was mild heterogeneous FDG uptake on PET (*arrow*) with an SUV_{max} of 2.6 (the level of uptake was less than background hepatic parenchymal activity) favouring a benign aetiology. There were no other abnormalities identified on PET. At surgery, a large benign adrenocortical adenoma was removed

was useful in characterising tumours following inconclusive CT or MRI results [48] (Fig. 9.16). A high NPV of 93 % was found in another study using visual analysis of adrenal FDG uptake less than hepatic uptake as criteria for a benign lesion [49].

9.2.1.4 Liver Tumours

Normal hepatic parenchyma demonstrates moderate physiologic FDG uptake, and as a result, the sensitivity for liver tumours is compromised due to poor contrast between lesion and background. There is currently no strong evidence to support FDG PET for diagnosing malignancy in hepatic lesions in patients with no history of cancer. The application is further diminished due to the variable degree of glucose metabolism in hepatocellular carcinoma (HCC). In one study, only 55 % of HCC (mean diameter of 57 mm; range 15–200 mm) demonstrated FDG uptake above normal background liver activity [50]. High levels of glucose-6-phosphatase in these tumours which lead to dephosphorylation of FDG are thought to account for this. Another PET tracer ^{11}C-acetate has been used in conjunction with FDG for the detection of HCC with some success [51]. FDG avidity correlated with the degree of cellular differentiation and tumour grade, and increased FDG uptake is more likely to be exhibited by tumours which are poorly differentiated. Well-differentiated HCC tends to show a reverse pattern with negative uptake on FDG PET but positive uptake with ^{11}C-acetate.

9.2.2 FDG PET in Staging Malignancy

9.2.2.1 Non-small Cell Lung Cancer

The role of FDG PET is well established in staging many malignancies. There is extensive evidence for NSCLC where PET-CT is more accurate than conventional methods [52], cost-effective [53] and incorporated into the diagnostic algorithm in management guidelines [54–56] (Fig. 9.17). The benefit in NSCLC has now been demonstrated and supported by several randomised controlled trials (RCT) where the addition of PET [57] or PET-CT [58] to conventional workup (CWU) at staging prevents unnecessary surgery in NSCLC (Fig. 9.18). In a multicentre RCT with 188 patients, the investigators demonstrated the addition of PET resulted in a 51 % relative reduction in futile thoracotomy and avoided unnecessary surgery in 1 out of 5 patients [57]. For mediastinal nodal staging with PET (Fig. 9.19), a meta-analysis of 44 studies published between 1994 and 2006 showed a pooled sensitivity and specificity of 74 and 85 %, respectively, whereas for CT, sensitivity and specificity of 51 and 85 %,

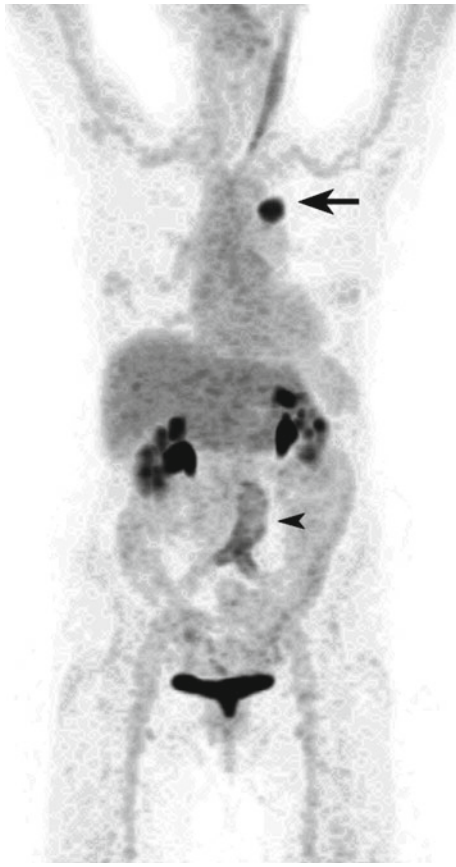

Fig. 9.17 Maximum intensity projection (MIP) image of an 80-year-old woman who underwent a FDG PET scan to stage newly diagnosed lung cancer in the apical segment of the left lower lobe. The primary demonstrated intense FDG uptake with a SUV_{max} of 17 (*arrow*), and PET did not reveal metastatic disease. There was also mild diffuse linear-increased FDG accumulation surrounding the asymptomatic aortobifemoral vascular graft (*arrowhead*). There was prominent muscle activation along the left sternocleidomastoid muscle as well as physiologic tracer excretion in both kidneys and bladder. The patient subsequently underwent surgery with a curative intent, and a T2aN0 moderately differentiated adenocarcinoma was resected which was confined to the lung parenchyma

respectively, were reported [54]. A RCT of 189 patients who underwent invasive mediastinal staging either with mediastinoscopy, endoscopic ultrasound (EUS) fine-needle aspiration or endobronchial ultrasound-guided transbronchial needle aspiration (EBUS-TBNA) regardless of PET-CT or CT findings showed in patients without enlarged lymph nodes and a PET-negative mediastinum, patients could proceed directly to surgery in view of the low false-negative results [59]. However in patients with enlarged lymph nodes irrespective of PET findings, further staging investigation is required. For mediastinal lymph node positivity on PET-CT, confirmation should be sought before a decision on operability is made as false-positive FDG uptake in mediastinal lymph nodes can occur in inflammatory or interstitial lung diseases (e.g. tuberculosis, anthracosis, silicosis, sarcoidosis) and can mimic or coexist with metastatic disease.

PET is increasingly incorporated in treatment planning for NSCLC especially in RT planning. The integration of structural and metabolic information on PET-CT in contouring allows a tumouricidal dose to be delivered to malignancy (primary and involved lymph nodes) and at the same time, sparing toxicity to surrounding organs by delivering the lowest RT dose to the smallest volume of normal tissue. This is especially relevant in the context of post-obstruction atelectasis where the boundary between collapsed lung and tumour is not distinguishable on anatomical imaging alone. The advent of 4-dimensional (4D) PET-CT imaging where image acquisition is "timed" in relation to the different phases of the respiratory cycle further improves the accuracy in defining the target volume [60]. Whether this improvement in contouring translates to superior patient outcomes will depend on future data regarding long-term follow-up of these patients.

9.2.2.2 Lymphoma

In aggressive lymphomas, FDG PET has replaced conventional imaging such as gallium scintigraphy. FDG PET leads to a change in stage in 10–40 % cases, especially upstaging by detecting additional lesions [61]. Results from the Australian PET Data Collection also suggested superiority in low-grade subtypes [62]. For bone marrow assessment, PET complements biopsy, and the accuracy depends on the histology of the disease. In a meta-analysis ($n=587$), the sensitivity of PET was 76 % in aggressive lymphomas and 30 % for indolent subtypes [63]. Since the iliac crest is often chosen as the

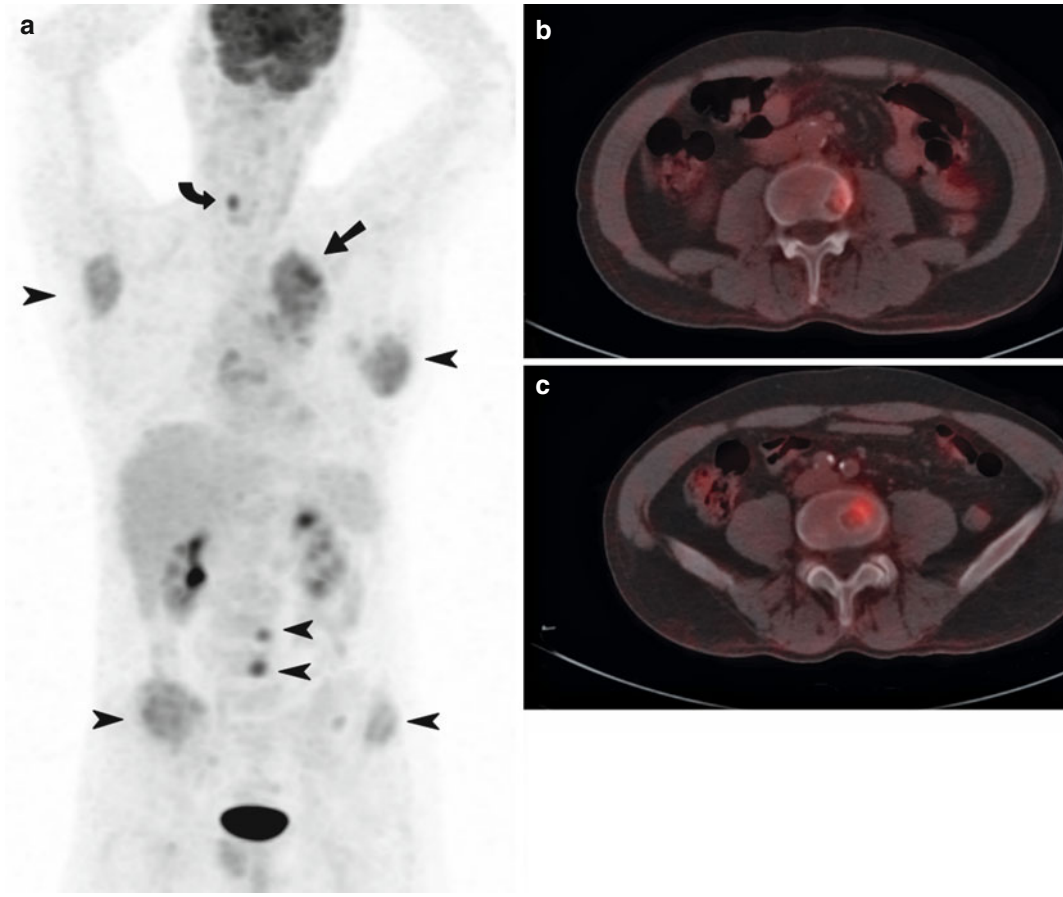

Fig. 9.18 Staging non-small cell lung cancer. A 55-year-old man who presented with coughing, a hoarse voice and significant weight loss underwent a staging FDG PET-CT scan for newly diagnosed adenocarcinoma of the left lung. The patient was staged as T2N2M0 on conventional imaging, and the initial management plan was for radical treatment with a curative intent. On PET (**a**), the primary mass in the left upper lobe (*arrow*) demonstrated moderate FDG uptake ($SUV_{max} = 5.4$) with evidence of mediastinal invasion. There was also widespread metastatic disease within the bones (*arrowheads*) with extension into adjacent soft tissues in the scapulae and ilium. There was normal FDG accumulation in the brain, liver and testicles and physiologic urinary tracer excretion in the kidneys and bladder. Selected transaxial combined PET-CT images (**b**, **c**) showing abnormal focal FDG uptake within lytic lesions at the vertebral bodies of L3 and L4, respectively. Focal-increased FDG uptake was also observed at the right vocal cord (*curved arrow*) representing compensatory supraphysiologic activation as a result of left recurrent laryngeal nerve compression. Following PET, the patient's management was changed to palliative chemotherapy with carboplatin and gemcitabine and subsequently palliative radiotherapy to the spine. The patient passed away 7 months after the PET scan

site for bone marrow biopsy (BMB) which in turn may not be involved by lymphoma, PET-CT can reduce false-negative BMB by locating the site of bone marrow infiltration prior to sampling where an accuracy of 100 % has been reported [64]. BMB is invasive and insensitive owing to sampling error, and some investigators have debated the need for routine BMB in patients with Hodgkin's disease (HD) in the era of staging PET-CT [65–68]. Whether PET-CT obviates the need of BMB very much depends on the histological subtype of lymphoma and the pattern of FDG uptake in bone marrow. Where focal or multifocal uptake predicts marrow infiltration with a high degree of accuracy (Fig. 9.20), a diffuse pattern may be secondary to marrow hyperplasia or diffuse lymphomatous infiltration.

Some investigators have demonstrated a correlation between cellular proliferation and

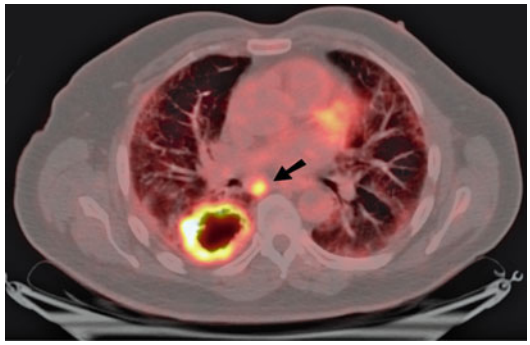

Fig. 9.19 Preoperative staging non-small cell lung cancer with FDG PET. A 67-year-old man with pulmonary fibrosis underwent a staging FDG PET-CT scan for newly diagnosed moderately differentiated squamous cell carcinoma of the right lung. On PET-CT, the primary mass in the right lower lobe measured 57 mm with a rim of intense FDG uptake ($SUV_{max} = 18$) and central photopaenia consistent with necrosis. There was focal intense uptake within a 24 mm subcarinal lymph node with a SUV_{max} of 12 (*arrow*) consistent with metastatic disease which was confirmed and resected during surgery

SUV measurements and the ability to differentiate indolent from aggressive non-Hodgkin's lymphoma (NHL) [69] and grade I/II from grade III follicular NHL [70]. However there is a significant overlap in the range of SUV in different subtypes of NHL, and no definite SUV threshold has been identified where a certain tumour phenotype can be predicted with sufficient accuracy.

9.2.2.3 Oesophageal Cancer

In a meta-analysis comparing EUS, CT and PET in staging oesophageal and gastro-oesophageal junction cancers, EUS was more sensitive but less specific than CT and PET for regional lymph node metastases [71]. For distant metastases, PET is superior. In a prospective trial of 129 patients, PET led to a high-impact change in management (change in treatment modality or intent) in 35 % of patients and from curative to palliative intent in 20 % [72].

9.2.2.4 Gastric Cancer

For gastric cancer the role of staging FDG PET is evolving and is currently not yet recommended as part of routine clinical practice [73]. The detection of the primary can be confounded by prominent physiologic uptake in the stomach and may partly explain the mixed results. The

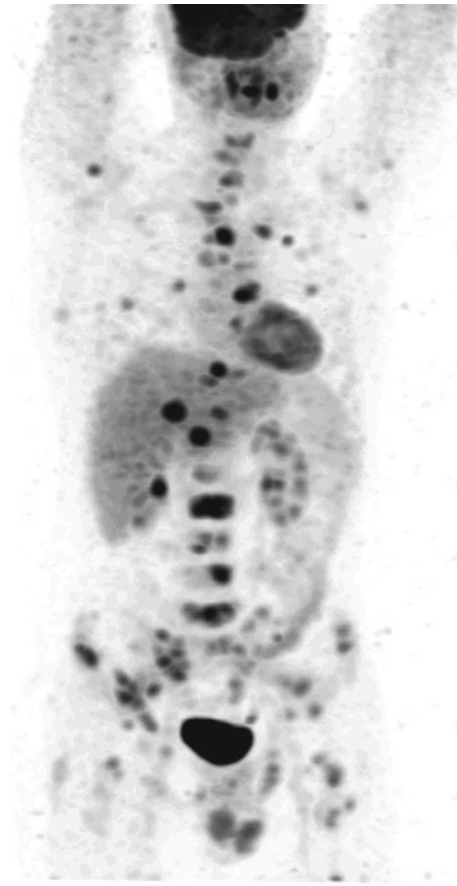

Fig. 9.20 Staging newly diagnosed lymphoma in a 40-year-old male with ALK negative anaplastic large cell NHL. Whole-body FDG PET (maximum intensity projection image) showed intense focal FDG activity in multiple liver lesions, left lung and extensively in multiple skeletal sites consistent with stage IV disseminated disease. Bone marrow biopsy of L2 vertebra at the site of the most intense FDG uptake confirmed bone marrow involvement. There was normal FDG accumulation in the brain and myocardium and physiologic urinary tracer excretion in the kidneys and bladder

sensitivity is lowest for non-intestinal diffuse subtypes and in those containing signet ring cells and rich in mucin. A positive correlation between accuracy of nodal staging and FDG avidity in the primary also exists [74]. In our experience, PET is useful in detecting distant metastatic disease in approximately 8 % of cases not identified on conventional imaging [75] (Fig. 9.21) and may have incremental value in selected patients (e.g. T3 or T4 tumours of non-signet ring cell histology). We have also found positive uptake in lymph nodes on FDG PET independently pre-

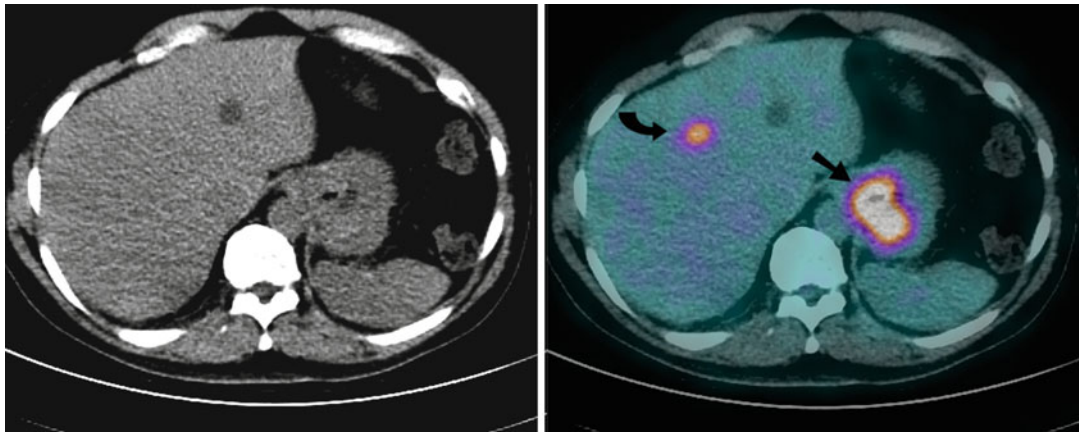

Fig. 9.21 A 67-year-old man with newly diagnosed fungating poorly differentiated gastric adenocarcinoma who underwent preoperative FDG PET-CT scan for staging. Axial CT (*Left*) and combined FDG PET-CT (*Right*) images demonstrated intense focal uptake at the site of the primary (*arrow*), within a perigastric lymph node (not shown) and in segment IV of the liver (*curved arrow*). An incidental hepatic cyst with no increased FDG uptake was noted medial to this lesion. A diagnostic contrast-enhanced CT scan did not demonstrate any significant abnormality within the liver, and an attempted fine-needle aspiration (FNA) biopsy of the hepatic lesion seen on PET failed to reveal malignancy. The patient proceeded to gastric resection following which there was progression of the liver lesion that was previously identified on preoperative PET-CT. A repeat FNA confirmed metastatic disease at this lesion, and multiple large hepatic metastases were seen on CT scan 5 months following surgery despite adjuvant chemotherapy

dicts poor survival and may potentially be useful in stratifying patients with poor prognosis for upfront additional treatments such as biological therapy with trastuzumab, RT or participation in clinical trials [76].

9.2.2.5 Colorectal Cancer

FDG PET for the initial staging of colorectal cancer (CRC) is currently not recommended as a routine investigation [77]. However, PET can contribute towards decision making in cases with potentially resectable synchronous metastases and in patients with suspected but inconclusive distant metastatic disease on conventional imaging. In these patients, PET can alter treatment intent (e.g. palliative vs. curative) or preclude surgical management by detecting unsuspected metastases [78, 79].

9.2.2.6 Breast Cancer

For locally advanced breast cancer (LABC), staging PET has an incremental role in addition to conventional staging by detecting unsuspected extra-axillary and distant metastases [80]. In a recent prospective study of 117 patients with inflammatory and noninflammatory LABC, FDG PET-CT showed positivity in all the primary tumours and outperformed conventional imaging for bone, distant lymph node and liver metastases [81]. Overall, FDG PET-CT changed the disease stage in 61 patients (52 %) however its use is limited in early breast cancer (Stage I and II) and cannot replace invasive axillary staging (e.g. sentinel lymph node biopsy) [82].

9.2.2.7 Urothelial Malignancy

FDG is suboptimal in primary staging of urological malignancies due to urinary excretion of the tracer thereby masking tumour detection. The detection of most prostate carcinoma and renal cell cancer is also hampered by a low rate of glucose metabolism as well as non-specific FDG uptake in benign conditions such as prostatitis and benign prostatic hypertrophy. More suitable derivatives include choline which is incorporated into cell membrane phospholipids, or acetate involved in cytoplasmic lipid synthesis [83].

9.2.3 FDG PET in Monitoring Therapy Response

Heterogeneity in tumour behaviour is a major challenge in clinical oncology, and monitoring response to therapy allows patients to be stratified and treatment regimen to be optimised. By identifying therapy failure early leads to discontinuation of futile treatment, and a switch to an alternative management strategy aims to improve patient outcomes. In contrast, low-risk patients showing early response may qualify for a less aggressive regimen and avoid potential unnecessary treatment related toxicities (e.g. second malignancy from radiation therapy) and expense. Before PET, assessment of therapeutic efficacy is based on changes in the size of tumour (e.g. RECIST criteria- Response Evaluation Criteria in Solid Tumours) [84]. Such crude anatomic-based systems have well-recognised limitations. A tumour that has reduced in size may contain malignancy, and conversely a residual mass may represent post-therapy inflammation, fibrosis or necrosis with no viable malignant cells. Since metabolic activity precedes volumetric changes, imaging tumour biomarkers such as FDG as a surrogate for therapeutic response, in particular early during the treatment schedule seems ideal. This is increasingly incorporated into drug development trials where response on PET is used to indicate therapy success. Despite clear advantages, standardisation of instrumentation, scanning parameters and interpretative criteria is mandatory so that inter- and intra-observer variability can be minimised [32, 85]. Since SUV is dependent on many factors [32, 33] and if PET-CT metrics are used to compare baseline and follow-up studies, rigorous standardisation and consistency in imaging parameters and scanning conditions is crucial to allow meaningful and reproducible results.

9.2.3.1 Early Work

One of the earliest studies using sequential FDG PET to assess early treatment efficacy was conducted by Richard Wahl and colleagues in 11 women with locally advanced breast cancers [86]. They demonstrated that in patients who responded to treatment, there was a rapid and significant decrease in tumour glucose metabolism which preceded any reduction in tumour size. Conversely, no significant decrease in FDG uptake in terms of SUV after three cycles of treatment was observed in nonresponding patients.

9.2.3.2 Rectal Cancer

For locally advanced rectal cancer (LARC), neoadjuvant RT or combined chemoradiation (CRT) has become the standard of care. A number of studies have shown the ability of serial FDG PET-CT performed before and after neoadjuvant therapy to predict pathologic response in the primary tumour [87–89]. Melton and colleagues demonstrated a sensitivity of 85.7 % and specificity of 84.6 % for identifying patients who have complete pathological response or microscopic residual disease [87]. By using a cut-off value of 43 % reduction in SUV_{max} to separate metabolic responders and nonresponders, PET-CT performed as early as 2 weeks after starting neoadjuvant CRT predicted histopathological tumour regression grade (TRG) [89]. Metabolic response is also prognostic [90, 91]. Five-year overall survival (OS) in 88 subjects with stage II and III rectal cancer was 91 % in patients with a negative PET performed 7 weeks after CRT and 72 % in those with a positive PET [90].

9.2.3.3 Oesophageal Cancer

The feasibility of early metabolic response assessment by PET influencing clinical decisions is shown in prospective studies such as the MUNICON (Metabolic response evalUatioN for Individualisation of neoadjuvant Chemotherapy in oesOphageal and esophagogastric adeNocarcinoma) I and II trials [92, 93] (Fig. 9.22). In this study, chemotherapy was discontinued in metabolic nonresponders after 2 weeks of neoadjuvant treatment and proceeded to have surgery early, whereas metabolic responders continued chemotherapy for a maximum duration of 12 weeks prior to tumour resection. The investigators showed there was no histological response in metabolic nonresponders, and early discontinuation of chemotherapy had no negative consequences [92].

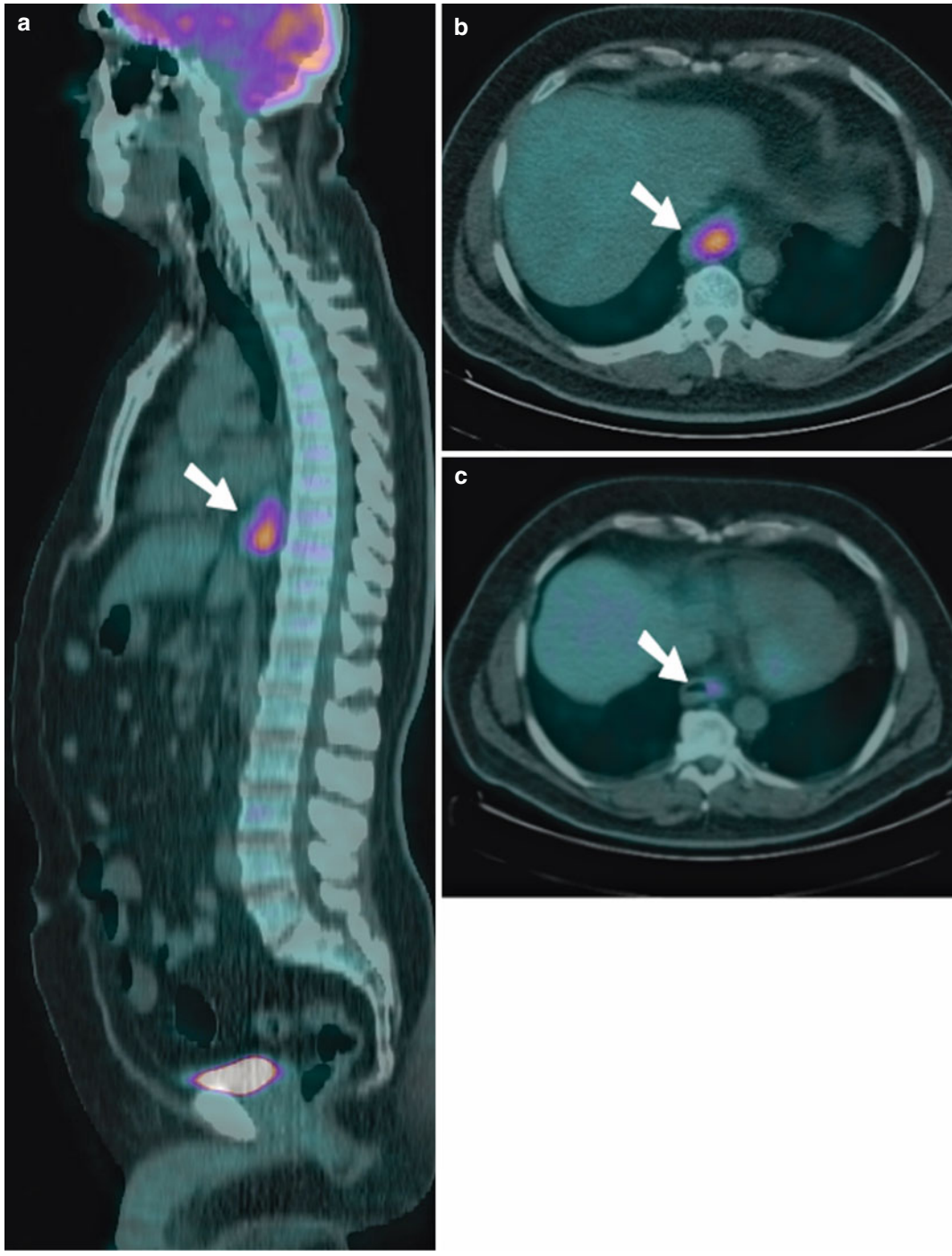

Fig. 9.22 (**a**) Sagittal and (**b**) axial staging FDG PET-CT images of a 59-year-old man with newly diagnosed squamous cell carcinoma of the distal thoracic oesophagus (*arrows*). The primary demonstrated intense focal FDG uptake with a SUV_{max} of 8.6. No other sites of disease were identified on PET. He underwent three cycles of neoadjuvant chemotherapy, and a follow-up scan was undertaken to assess treatment response. (**c**) Posttreatment axial PET-CT images showed a significant metabolic response at the primary site (*arrow*) with a reduction in the extent and degree of FDG uptake. There was a 60 % reduction in metabolic activity at the primary with mild to moderate residual uptake with a SUV_{max} of 3.4. The patient proceeded to surgery, and an Ivor-Lewis oesophagogastrectomy was performed

9.2.3.4 FDG PET and Targeted Therapy

As cellular pathways in carcinogenesis are unravelled (e.g. apoptosis, angiogenesis), cancer therapeutics are increasingly personalised. Biological therapy such as vascular endothelial growth factor (VEGF) and epidermal growth factor receptor (EGFR) inhibitors targeting various signalling pathways is a relatively recent addition to the armamentarium of anticancer drugs. These drugs induce cytostasis and may not lead to a substantial reduction in tumour size, and response is often under-estimated by anatomical means. A lack of progression despite an absence of tumour shrinkage may in fact indicate treatment success, and therefore metabolic response better reflects therapeutic efficacy compared with conventional imaging. This was shown with the tyrosine kinase inhibitor imatinib mesylate (Glivec) in gastrointestinal stromal tumour (GIST) where early treatment and lasting tumour responses were identified and predicted with FDG PET as early as 24 h after starting treatment, preceding morphological changes on CT by a median of 7 weeks [94]. More recently in patients with NSCLC receiving the EGFR inhibitor, erlotinib, patients with progressive metabolic disease on early follow-up PET at 14 days showed a significantly shorter time to progression (47 vs. 119 days) and OS (87 vs. 828 days) compared with patients having stable metabolic disease, partial or complete responses [95]. In a phase I dose-escalating trial evaluating the BRAF kinase inhibitor vemurafenib in metastatic melanoma, it was found there was a dose-dependent reduction in FDG uptake in patients at 15 days after starting treatment as well as a trend towards longer progression-free survival (PFS) in patients with a greater reduction in SUV_{max} [96].

9.2.3.5 FDG PET and Local Ablative Therapy

Following local ablative therapies with selective internal radiation using ^{90}Yttrium microspheres or radiofrequency ablation for hepatic metastases, PET is more accurate in monitoring treatment response since anatomical modalities are often unable to differentiate between residual tumour and perilesional post-therapy changes due to tumour necrosis, cystic degeneration or haemorrhage [97, 98].

9.2.3.6 Lymphoma

In lymphoma, there is intense research interest in the role of FDG PET to evaluate treatment response and is the subject of many ongoing prospective trials. The goal is to achieve an optimal balance between effective treatment and toxicity (e.g. avoiding long-term toxicity by eliminating RT to the mediastinum in favourable patients) and reliably identify those who need an escalation of therapy. This is especially important in subsets of patients with good prognosis or early stage disease where standard treatment can achieve cure in more than 90 % of cases.

Response Assessment at the End of Treatment

PET is helpful in differentiating tumour recurrence from fibrosis in the setting of a residual mass and is recommended after completion of first-line therapy [99]. For aggressive lymphomas, two meta-analyses have supported the predictive value of FDG PET performed at the completion of therapy [100, 101]. A meta-analysis of 15 studies comprising 705 patients revealed a pooled sensitivity and specificity for detecting residual disease of 84 and 90 % in HD and 72 and 100 % in aggressive NHL, respectively [101]. PET performed at the completion of therapy has a high NPV. In a German trial (HD15 trial of the German Hodgkin Study Group) of advanced HD patients with residual masses larger than 2.5 cm after completing 6–8 cycles of BEACOPP chemotherapy (bleomycin, etoposide, adriamycin, cyclophosphamide, vincristine, procarbazine and prednisone), PFS was 96 % in PET-negative patients where consolidation RT was omitted. A NPV of 94 % was achieved defined as the proportion of PET-negative patients without progression, relapse or RT within 12 months of follow-up [102]. The preliminary data suggests that omitting RT in patients with complete metabolic response following intensive BEACOPP chemotherapy does not appear to have a significant impact on short-term outcome. On the other hand, positive PET findings would warrant histopathological confirmation before instigating a change in therapy (Fig. 9.23).

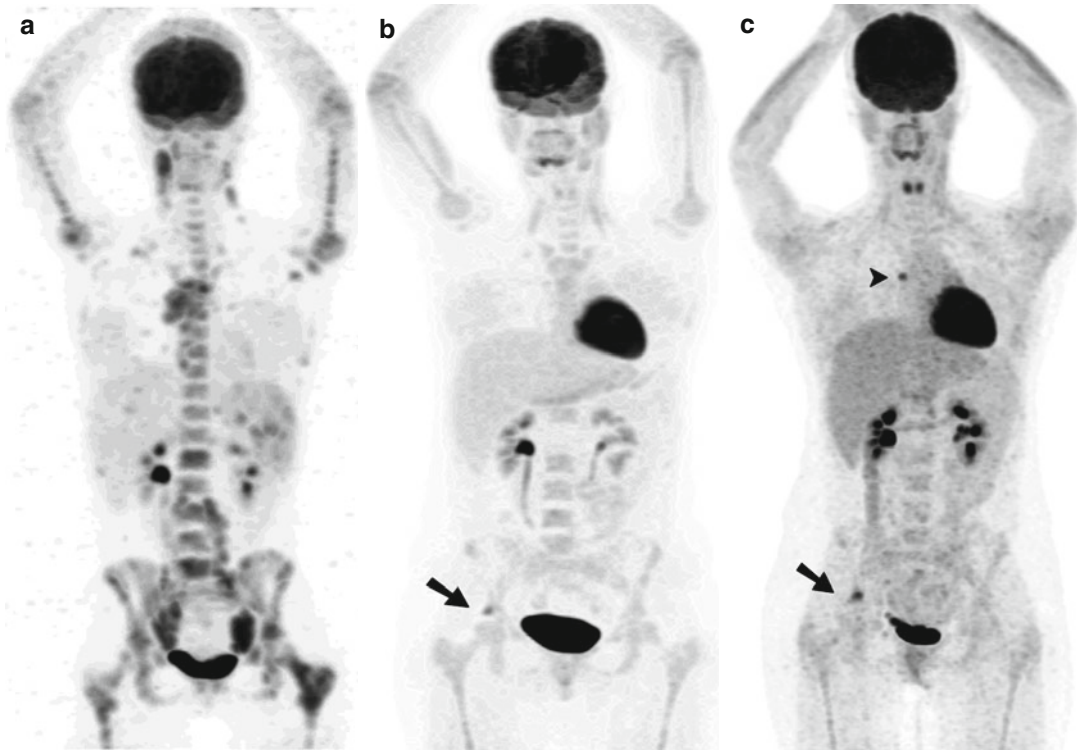

Fig. 9.23 (**a**) FDG PET of a 23-year-old woman with nodular sclerosing Hodgkin's disease (NSHD) involving multiple lymph node groups above and below the diaphragm most marked in the mediastinum and neck, left para-aortic and pelvic regions, spleen and extensively in the skeleton consistent with disseminated stage IV disease. She received ABVD (doxorubicin, bleomycin, vinblastine, dacarbazine) chemotherapy and was reassessed with PET scans after four cycles (**b**) and following completion of treatment (**c**). There was persistent focal-increased FDG accumulation at the right anterior aspect of the acetabulum (*arrows*) on both follow-up PET scans, and in addition, there was focal increased uptake at the right anterior mediastinum (*arrowhead*) suspicious for refractory disease (**c**). On the rest of the follow-up scans, there was resolution of the widespread abnormal areas of uptake seen on staging PET. As a result of the PET findings, mediastinoscopy and biopsy of the lymph node at the right anterior mediastinum was performed which revealed refractory NSHD. The patient subsequently underwent salvage chemotherapy and stem cell transplantation

Response Assessment at Interim of Treatment

PET scanning performed during mid-treatment is highly prognostic in aggressive lymphoma, and a negative scan predicts superior PFS and OS independent of other prognostic factors [103–105]. In a trial of 260 patients with advanced HD, a positive and negative interim PET after 2 cycles of ABVD (doxorubicin, bleomycin, vinblastine, dacarbazine) chemotherapy has a 2-year PFS of 95 and 13 %, respectively [105] (Fig. 9.23). Similarly in aggressive NHL Zinzani and colleagues demonstrated a 4-year PFS of 75 and 18 %, respectively, for positive and negative interim PET and a statistically significant difference in OS between the two groups [106]. Despite its prognostic ability, one of the main issues is the standardisation of interim scan interpretation. The visual criteria originally developed in London at Guy's and St Thomas's Hospitals and recently validated [107], the Deauville 5-point scale using the mediastinum and liver as reference background draws us towards a consensus on interim PET reporting [108] (Fig. 9.23). While risk-adaptive treatment strategy either through escalation or de-escalation based on metabolic response seems instinctive and will very likely translate into superior patient outcomes, we eagerly await the results of many ongoing prospective trials evaluating interim

PET response-guided strategies [109, 110] prior to its adoption into routine clinical practice. Interim PET should currently be performed in the context of clinical trials.

9.2.4 FDG PET in the Assessment of Recurrent Malignancy

9.2.4.1 Colorectal Cancer

FDG PET is useful in the detection and evaluation of a wide range of recurrent malignancies. One of the most common indications with substantial evidence is in the evaluation of recurrent CRC [111–115]. Metastasectomy in CRC is potentially curative; however, a significant proportion of patients have unresectable disease at surgery or relapse shortly following surgery reflecting suboptimal preoperative imaging workup and patient selection. The superiority of PET compared with CT is in the sensitivity for detecting unsuspected extrahepatic metastases. Pawlik and colleagues [116] found a 55 % reduction in futile laparotomy rate in PET-screened patients, and adding PET to conventional preoperative assessment avoided one in six unnecessary laparotomies in a phase III trial [117]. PET-screened patients also had better 5-year survival following hepatic resection compared with historical controls most likely as a result of better patient selection [118]. In patients with a rise in carcinoembryonic antigen (CEA) levels, PET is more sensitive than multi-detector CT scan in identifying the site of CRC recurrence [119] (Fig. 9.24).

9.2.4.2 Gynaecological Malignancy

Recurrent cervical cancer has a poor prognosis if not limited to the pelvis. Radiation therapy and pelvic exenteration are options for local recurrent disease, and conventional imaging (CI) is often unable to differentiate between post-radiation or surgical changes and malignancy. In a study of 40 patients, FDG PET was more accurate and sensitive than CI in detecting recurrence, and in patients with an isolated elevated tumour marker (squamous cell carcinoma antigen) level, PET-CT showed a recurrence with a sensitivity of 100 %, whereas CI was falsely negative in all cases [120]. The addition of PET information led to a change in treatment plan in more than half the patients and predicted patient outcome. In suspected recurrent ovarian cancer, PET plays a role in early detection and in determining whether the disease is localised or disseminated. Based on elevated CA-125 levels, anatomical imaging or clinical symptoms, a study showed that PET-CT identified additional sites of disease in more than two-thirds of patients mostly at lymph node regions below the diaphragm or peritoneal disease not detected by CI [121]. PET-CT results had a high impact on management in nearly 50 % of subjects where the modality of treatment was changed.

9.2.4.3 Head and Neck Squamous Cell Cancer

In head and neck squamous cell cancers (HNSCC) after treatment with RT with or without chemotherapy, a meta-analysis of 27 studies reported a pooled sensitivity, specificity, PPV and NPV of 94, 82, 75 and 95 % for detecting recurrence at the primary site and 74, 88, 49 and 96 % for detecting nodal recurrence in the neck [122]. The sensitivity is greater for scans performed at 10 weeks or more after treatment, and to avoid false-positive findings due to posttreatment inflammation, PET should ideally be performed 10–12 weeks after the end of therapy. A negative PET highly predicts the absence of disease and potentially obviates neck dissections despite residual nodal abnormalities on CT [123]. Routine surveillance FDG PET at 12 months after treatment has also been shown to detect asymptomatic local and distant recurrences with an accuracy of 90 % [124].

9.2.4.4 Recurrent Thyroid Cancer

A switch in tumour biology is the basis for utilising FDG PET in recurrent thyroid cancer. A proportion of patients with differentiated thyroid cancer (DTC) dedifferentiate and progress over time where there is a loss of sodium-iodine symporter function and reduction in iodine trapping and a corresponding upregulation in glucose transporter (GLUT) expression and positivity on FDG PET. This manifests clinically when patients present with elevated serum thyroglobulin levels following thyroidectomy despite a negative

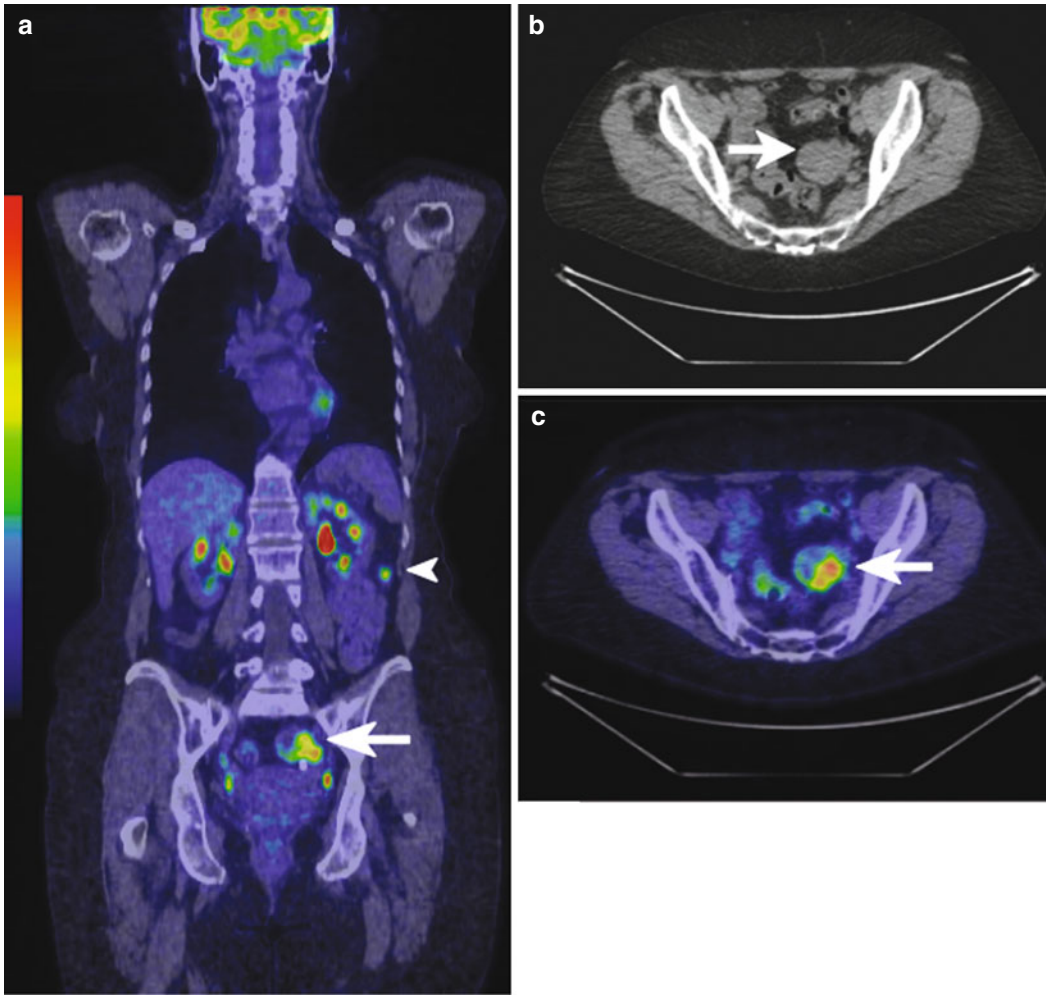

Fig. 9.24 A 58-year-old woman previously underwent a laparoscopic subtotal colectomy for a moderately differentiated T4N1 adenocarcinoma of the proximal descending colon followed by adjuvant FOLFOX (fluorouracil, folinic acid, oxaliplatin) chemotherapy. On routine clinical follow-up 18 months after surgery, a raised serum CEA level of 19 μg/l was detected (normal range: 0–5.0) which rose to 51 μg/l within 2 months. Diagnostic CT scan of the chest, abdomen and pelvis did not demonstrate any significant abnormalities to suggest metastatic disease. FDG PET-CT for further evaluation was then undertaken. (**a**) Coronal-fused PET-CT, (**b**) transaxial CT and (**c**) fused PET-CT images revealed intense focal FDG uptake within a partly cystic left ovarian mass (*arrows*) and focal increased uptake within a 13 mm peritoneal nodule (*arrowhead*) lateral to the lower pole of the left kidney in the left paracolic gutter. In the rest of the scan, there was normal physiologic FDG uptake in the brain, myocardium and liver and urinary tracer excretion in the kidneys and distal ureters. Following PET, the patient underwent laparoscopic exploration with removal of a metastatic Krukenberg tumour in the left ovary and was considered for further cycles of chemotherapy

radioiodine (I-131 or I-123) surveillance scan. PET scanning in this setting is recommended by the American Thyroid Association [125]. A meta-analysis of 17 studies in 571 patients showed a pooled sensitivity of 88 % for detecting recurrence in this setting, and not surprisingly, even better results with PET-CT [126]. A mixed pattern can be observed where some metastatic lesions show I-131 uptake indicating the presence of intact sodium-iodine symporter function, while dedifferentiated lesions show FDG avidity. It has been shown that FDG-positive metastatic disease is more resistant to high-dose radioiodine therapy [127], and therefore the use of diagnostic tests can

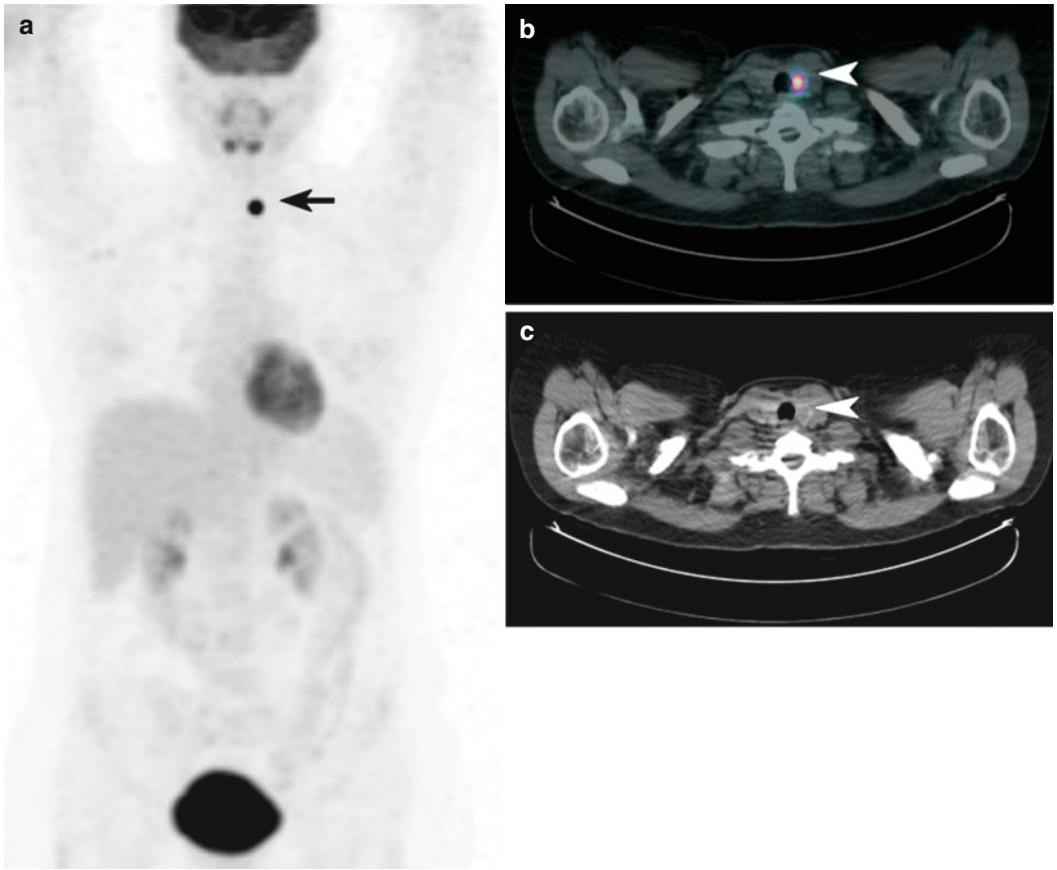

Fig. 9.25 A 38-year-old woman with widespread lymphadenopathy and suspected lymphoma underwent a FDG PET-CT scan for further investigation. (**a**) Maximum intensity projection (MIP) PET and (**b**) fused axial PET-CT images revealed intense focal FDG uptake within the left lobe of thyroid with a SUV_{max} of 17.4 (*arrow* and *arrowhead*), localising to (**c**) a 13 mm hypodense thyroid nodule with small areas of calcification on the concurrent low-dose CT scan (*arrowhead*). There was very mild increased FDG accumulation within morphologically normal lymph nodes in the right axilla, and faintly in a single normal lymph node in the left axilla (not shown) favouring either reactive changes or low-level inflammation. Following PET-CT, the patient underwent a fine-needle aspiration biopsy under ultrasound guidance of the left thyroid lesion seen on PET-CT and later a hemithyroidectomy which confirmed a benign follicular adenoma

help identify patients who are better suited for a specific treatment – an example of theranostic medicine.

9.2.5 The Detection of Synchronous Neoplasms on FDG PET and the Role of PET in Screening

9.2.5.1 Incidental Benign Lesions on FDG PET

As discussed previously, FDG is not a tumour-specific tracer and false-positive results can occur. In a review by Metser and colleagues [128], benign, non-physiological uptake of FDG was encountered in more than 25 % of PET-CT studies. The majority of benign lesions found were inflammatory in nature, and the rest comprised various benign tumours or tumour-like conditions (e.g. pituitary adenoma, fibroadenoma of the breast, neurofibroma, thyroid adenoma (Fig. 9.25) and multi-nodular goitre, pheochromocytoma (Fig. 9.26), hibernoma and various skeletal conditions including enchondroma, fibrous dysplasia and Paget's disease).

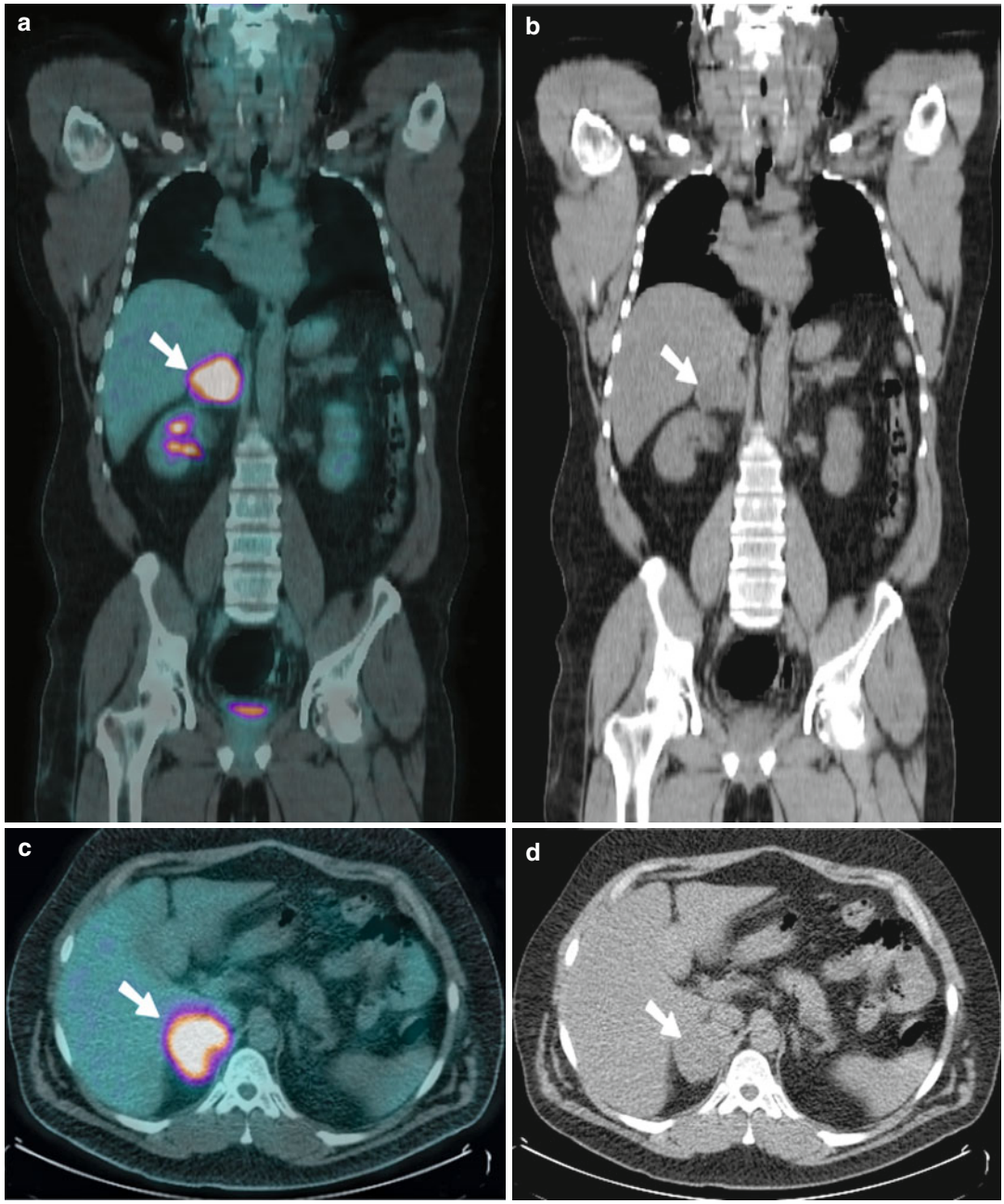

Fig. 9.26 A 36-year-old man with newly diagnosed pheochromocytoma. (**a**, **c**) Fused PET-CT images and (**b**, **d**) CT images revealed intense focal FDG uptake within a right adrenal mass with a SUV_{max} of 17 (*arrows*). The patient also underwent a metaiodobenzylguanidine (MIBG) scan labelled with radioiodine (^{123}I) which demonstrated concordant intense MIBG uptake at the site of the tumour. There were no other sites of disease identified on PET or MIBG scan. At surgery, a 58×54 mm pheochromocytoma was removed with no evidence of malignant features

9.2.5.2 Synchronous Malignancy or Premalignant Lesions on FDG PET

Synchronous primary malignancy or an incidental premalignant condition detected on PET is not rare. They are usually uncovered when the location of abnormal uptake that is regarded as unusual for metastatic disease from the known cancer is further investigated. In one series of 2,360 subjects who underwent PET-CT, unexpected malignancy and premalignant lesions were found in nearly 2 % of patients; the majority of which originated from the thyroid, colon, lung and breast [129].

Unexpected focal colonic uptake on FDG PET is found in approximately 0.6–3.7 % of patients [130]. A considerable proportion of these patients have clinically significant abnormalities such as a premalignant polyp or carcinoma when further investigations are carried out. Therefore colonoscopy in suitable patients (i.e. non-palliative) in a timely manner to exclude sinister causes seems worthwhile (Fig. 9.27) [130].

Incidental focal increased FDG uptake in the thyroid has been reported to occur between 1.1 and 2.9 % of patients undergoing PET scans [131]. Thyroid malignancy is found in approximately a third of these patients with such a finding [132, 133] although the intensity of FDG uptake in terms of SUV_{max} does not seem to predict histology with sufficient accuracy to obviate a biopsy (Figs. 9.28 and 9.29). In one series, in patients who were found to have intercurrent thyroid malignancy, more than half had non-papillary and intermediate to high-risk histopathology [132].

A synchronous malignancy found on FDG PET also impacts on management decisions. In 649 patients with NSCLC who underwent staging FDG PET scans, unexpected second primary malignancies and premalignant dysplastic colorectal polyps were found in about 3 % of patients [134]. In those with a second primary cancer, 3 out of 11 patients (27 %) had a high-impact change in management from an initial curative intent to palliative.

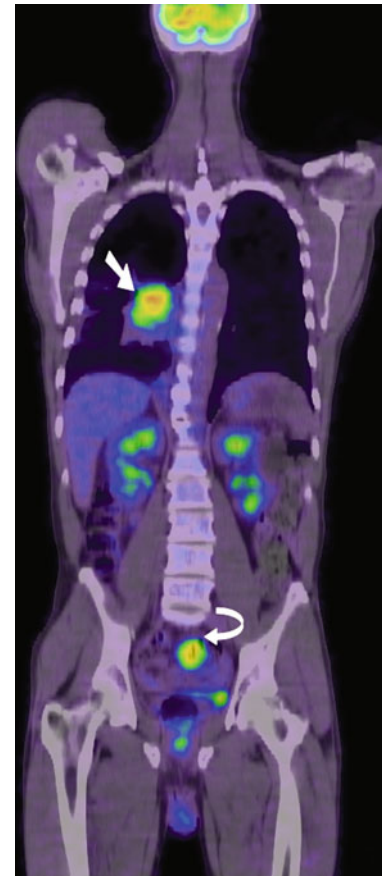

Fig. 9.27 A 58-year-old man with newly diagnosed non-small cell lung cancer underwent a staging PET-CT scan. The known primary malignancy at the right pulmonary hilum demonstrated intense focal FDG uptake (*arrow*) with extension into the mediastinum. There was low-level ill-defined uptake surrounding this consistent with associated atelectasis. However, there was also unsuspected focal intense FDG uptake at the rectosigmoid junction (*curved arrow*) suspicious for a synchronous premalignant lesion such as a dysplastic polyp or a colorectal cancer. There was normal urinary FDG pooling in the bladder inferior to this as well as tracer excretion in both kidneys. Colonoscopy and subsequent surgery confirmed a synchronous large circumferential moderately differentiated adenocarcinoma

9.2.5.3 FDG PET and Screening

Whole-body screening for cancer using PET in the healthy population is a contentious issue. In a study of 155,456 healthy Japanese volunteers over a 4-year period, positive findings on FDG

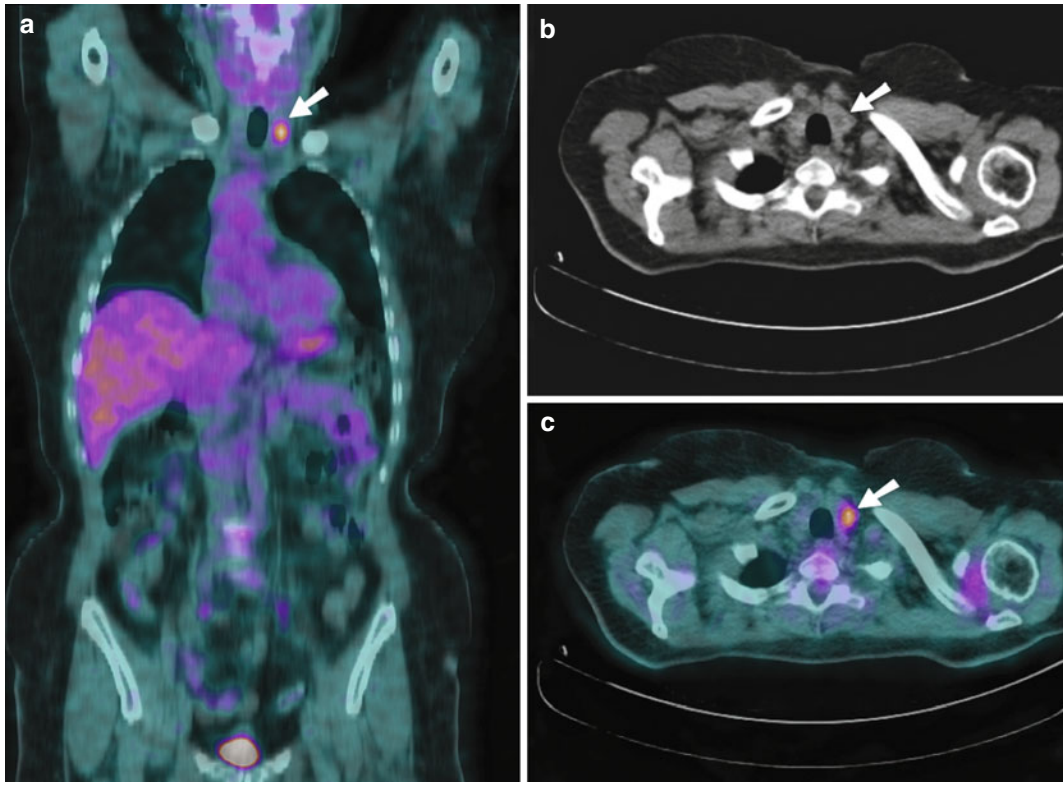

Fig. 9.28 FDG PET-CT scan of a 61-year-old woman with suspected colorectal liver metastasis. (**a**, **c**) Coronal- and transaxial-fused PET-CT images showing moderate focal FDG uptake with a SUV_{max} of 4.0 (*arrow*) at the inferior pole of the left lobe of the thyroid corresponding to a (**b**)16 mm rounded lesion of mixed density on CT scan (*arrow*). There was no abnormal focal increased FDG accumulation seen in the liver to suggest metastatic disease. Since the thyroid gland would be an unusual site for metastatic disease from colorectal origin and instead more likely to represent an intercurrent pathology, a fine-needle aspiration biopsy under ultrasound guidance of the PET-avid lesion in the left lobe of the thyroid was performed which revealed a benign follicular adenoma

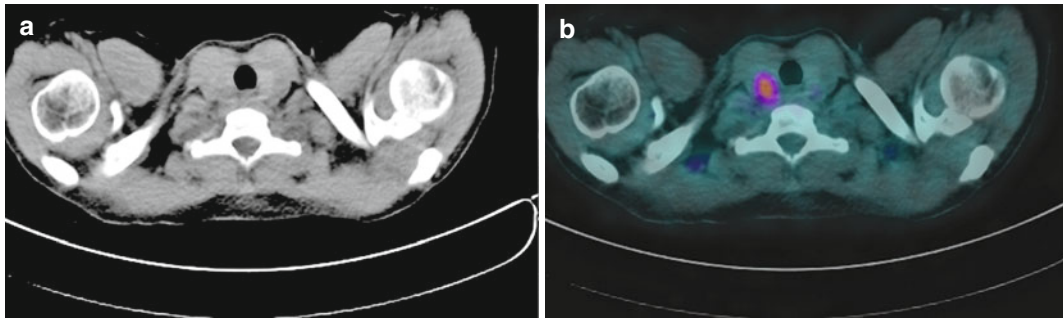

Fig. 9.29 FDG PET-CT scan of a 45-year-old woman with a solitary 10 mm lung nodule in the right upper lobe for further characterisation. Transaxial (**a**) CT and (**b**) fused PET-CT images showing moderate focal FDG uptake with a SUV_{max} of 4.3 in the right mid-pole of thyroid. At surgery, a T2N0 22 mm papillary thyroid cancer was found. The lung nodule in the right upper lobe (not shown) did not demonstrate FDG uptake consistent with a benign aetiology. In both these examples, the intensity of FDG uptake at the thyroid lesions is similar

PET or PET-CT were found in 78 % of patients detected with cancers comprising about 1 % of the total screened cases [135]. Despite the scale of this survey, no firm conclusions or recommendation can be drawn. While screening with PET may have a potential role in high-risk individuals, routine screening in the low-risk healthy population is currently not cost effective or clinically justified [136].

9.3 Summary

Molecular imaging using PET-CT has been one of the revolutionary developments in cancer imaging. To date FDG remains the most widely used radiotracer for PET. Applied to the study of glucose metabolism in malignancy, we are able to understand and unravel part of the molecular signature and biology of tumours non-invasively. Owing to its huge clinical success, FDG PET is incorporated into routine clinical practice. Its major advantage compared with conventional methods in providing an accurate assessment of treatment efficacy, by identifying responding and nonresponding patients early during their treatment schedule, sees PET central to decision making in many ongoing risk-adapted clinical trials. Using PET metrics in defining treatment end points also accelerates the development and approval of new drugs against cancer that is crucial in the rapidly evolving field of cancer therapeutics. Despite the expansion and increasing availability of specific PET probes targeting other molecular pathways in oncogenesis, FDG remains a stalwart of PET and the cornerstone in the ongoing refinement of personalised cancer medicine.

References

1. Bessell E, et al. The use of deoxyfluoro-D-glucopyranoses and related compounds in a study of yeast hexokinase specificity. Biochem J. 1972; 128(2):199–204.
2. Gallagher BM, et al. Radiopharmaceuticals XXVII. 18F-labeled 2-deoxy-2-fluoro-d-glucose as a radiopharmaceutical for measuring regional myocardial glucose metabolism in vivo: tissue distribution and imaging studies in animals. J Nucl Med. 1977; 18(10):990–6.
3. Som P, et al. A fluorinated glucose analog, 2-fluoro-2-deoxy-D-glucose (F-18): nontoxic tracer for rapid tumor detection. J Nucl Med. 1980;21(7):670–5.
4. Fowler JS. Design and synthesis of 2-deoxy-2-[18F] fluoro-D-glucose (18FDG). In: Welch M, Redvanly C, editors. Handbook of radiopharmaceuticals, radiochemistry and applications. Chichester: Wiley; 2003. p. 307–21.
5. Kuhl DE, et al. The Mark IV system for radionuclide computed tomography of the brain. Radiology. 1976;121(2):405–13.
6. Snyder SE, Kilbourn MR. Chemistry of fluorine-18 radiopharmaceuticals. In: Handbook of radiopharmaceuticals. Chichester: Wiley; 2003. p.195–227.
7. Tucker R, et al. Impact of fluorine-18 fluorodeoxyglucose positron emission tomography on patient management: first year's experience in a clinical center. J Clin Oncol. 2001;19(9):2504–8.
8. Sols A, Crane RK. Substrate specificity of brain hexokinase. J Biol Chem. 1954;210(2):581–95.
9. Sokoloff L. Mapping of local cerebral functional activity by measurement of local cerebral glucose utilization with [14C]deoxyglucose. Brain. 1979;102(4):653–68.
10. Ido T, et al. Labeled 2-deoxy-D-glucose analogs. 18F-labeled 2-deoxy-2-fluoro-D-glucose, 2-deoxy-2-fluoro-D-mannose and 14C-2-deoxy-2-fluoro-D-glucose. J Label Compd Radiopharm. 1978;14(2): 175–83.
11. VonSchulthess GK, et al. Clinical positron emission tomography/magnetic resonance imaging applications. Semin Nucl Med. 2013;43(1):3–10.
12. Ruth T, Wolf A. Absolute cross section for the production of 18F via the 18O(p, n)18F reaction. Radiochim Acta. 1979;26(21):21–4.
13. International Atomic Energy Agency. Cyclotron produced radionuclides: guidance on facility design and production of [18F] flurodeoxyglucose (FDG). In: IAEA radioisotopes and radiopharmaceuticals ed. Vienna: International Atomic Energy Agency; 2012.
14. Gallagher BM, et al. Metabolic trapping as a principle of radiopharmaceutical design: some factors resposible for the biodistribution of [18F] 2-deoxy-2-fluoro-D-glucose. J Nucl Med. 1978;19(10):1154–61.
15. Silverman M, et al. Specificity of monosaccharide transport in dog kidney. Am J Physiol. 1970;218(3): 743–50.
16. Plathow C, Weber WA. Tumor cell metabolism imaging. J Nucl Med. 2008;49 Suppl 2:43S–63.
17. Warburg O, et al. The metabolism of tumours in the body. J Gen Physiol. 1927;8(6):519–30.
18. Haberkorn U, et al. FDG uptake, tumor proliferation and expression of glycolysis associated genes in animal tumor models. Nucl Med Biol. 1994;21(6):827–34.
19. Pauwels EK, et al. FDG accumulation and tumor biology. Nucl Med Biol. 1998;25(4):317–22.

20. Cook GJ, et al. Normal physiological and benign pathological variants of 18-fluoro-2-deoxyglucose positron-emission tomography scanning: potential for error in interpretation. Semin Nucl Med. 1996; 26(4):308–14.
21. Kitajima K, et al. Normal uptake of 18F-FDG in the testis: an assessment by PET/CT. Ann Nucl Med. 2007;21(7):405–10.
22. Shammas A, et al. Pediatric FDG PET/CT: Physiologic uptake, normal variants, and benign conditions. Radiographics. 2009;29(5):1467–86.
23. Chander S, et al. Physiologic uterine uptake of FDG during menstruation demonstrated with serial combined Positron Emission Tomography and Computed Tomography. Clin Nucl Med. 2002;27(1):22–4.
24. Kim S, et al. Temporal relation between temperature change and FDG uptake in brown adipose tissue. Eur J Nucl Med Mol Imaging. 2008;35:984–9.
25. Fukuchi K, et al. Benign variations and incidental abnormalities of myocardial FDG uptake in the fasting state as encountered during routine oncology positron emission tomography studies. Br J Radiol. 2007;80:3–11.
26. Gontier E, et al. High and typical 18F-FDG bowel uptake in patients treated with metformin. Eur J Nucl Med Mol Imaging. 2008;35(1):95–9.
27. Özülker T, et al. Clearance of the high intestinal 18F-FDG uptake associated with metformin after stopping the drug. Eur J Nucl Med Mol Imaging. 2010; 37(5):1011–7.
28. Oh J-R, et al. Impact of medication discontinuation on increased intestinal FDG accumulation in diabetic patients treated with metformin. Am J Roentgenol. 2010;195(6):1404–10.
29. Zhuang H, et al. Applications of fluorodeoxyglucose-PET imaging in the detection of infection and inflammation and other benign disorders. Radiol Clin North Am. 2005;43(1):121–34.
30. Shon IH, Fogelman I. F-18 FDG positron emission tomography and benign fractures. Clin Nucl Med. 2003;28(3):171–5.
31. de Langen AJ, et al. Repeatability of 18F-FDG uptake measurements in tumors: a metaanalysis. J Nucl Med. 2012;53(5):701–8.
32. Boellaard R. Need for standardization of 18F-FDG PET/CT for treatment response assessments. J Nucl Med. 2011;52:93S–100.
33. Huang SC. Anatomy of SUV. Standardized uptake value. Nucl Med Biol. 2000;27(7):643–6.
34. Weiss GJ, Korn RL. Interpretation of PET Scans: do not take SUVs at face value. J Thorac Oncol. 2012; 7(12):1744–6.
35. de Wiele C, et al. Predictive and prognostic value of metabolic tumour volume and total lesion glycolysis in solid tumours. Eur J Nucl Med Mol Imaging. 2013;40(2):290–301.
36. Zhang H, et al. Independent prognostic value of whole-body metabolic tumor burden from FDG-PET in non-small cell lung cancer. Int J Comput Assist Radiol Surg. 2013;8(2):181–91.
37. MacMahon H, et al. Guidelines for management of small pulmonary nodules detected on CT scans: a statement from the Fleischner Society. Radiology. 2005;237(2):395–400.
38. Grgic A, et al. Risk stratification of solitary pulmonary nodules by means of PET using 18F-fluorodeoxyglucose and SUV quantification. Eur J Nucl Med Mol Imaging. 2010;37:1087–94.
39. Fletcher JW, et al. A comparison of the diagnostic accuracy of 18F-FDG PET and CT in the characterization of solitary pulmonary nodules. J Nucl Med. 2008;49(2):179–85.
40. Hashimoto Y, et al. Accuracy of PET for diagnosis of solid pulmonary lesions with 18F-FDG uptake below the standardized uptake value of 2.5. J Nucl Med. 2006;47(3):426–31.
41. Fisher RE, Fletcher JW. PET for the evaluation of solitary pulmonary nodules/REPLY. J Nucl Med. 2009;50(2):326–7.
42. Di Chiro G, et al. Glucose utilization of cerebral gliomas measured by [18F] fluorodeoxyglucose and positron emission tomography. Neurology. 1982; 32(12):1323–9.
43. Lin M, et al. Neurosyphilitic gumma on F18-2-fluoro-2-deoxy-D-glucose (FDG) positron emission tomography: an old disease investigated with a new technology. J Clin Neurosci. 2009;16(3):410–2.
44. Chen W. Clinical applications of PET in brain tumors. J Nucl Med. 2007;48:1468–81.
45. Vikram R, et al. Utility of PET/CT in differentiating benign from malignant adrenal nodules in patients with cancer. Am J Roentgenol. 2008;191(5):1545–51.
46. Metser U, et al. ^{18}F-FDG PET/CT in the evaluation of adrenal masses. J Nucl Med. 2006;47(1):32–7.
47. Jana S, et al. FDG-PET and CT characterization of adrenal lesions in cancer patients. Eur J Nucl Med Mol Imaging. 2006;33(1):29–35.
48. Tessonnier L, et al. Does 18F-FDG PET/CT add diagnostic accuracy in incidentally identified non-secreting adrenal tumours? Eur J Nucl Med Mol Imaging. 2008;35(11):2018–25.
49. Ansquer C, et al. 18F-FDG PET/CT in the characterization and surgical decision concerning adrenal masses: a prospective multicentre evaluation. Eur J Nucl Med Mol Imaging. 2010;37(9):1669–78.
50. Khan MA, et al. Positron emission tomography scanning in the evaluation of hepatocellular carcinoma. J Hepatol. 2000;32(5):792–7.
51. Ho C-L, et al. (11)C-Acetate PET imaging in hepatocellular carcinoma and other liver masses. J Nucl Med. 2003;44(2):213–21.
52. Wu Y, et al. Diagnostic value of fluorine 18 fluorodeoxyglucose positron emission tomography/computed tomography for the detection of metastases in non–small-cell lung cancer patients. Int J Cancer. 2013;132(2):E37–47.
53. Søgaard R, et al. Preoperative staging of lung cancer with PET/CT: cost-effectiveness evaluation alongside a randomized controlled trial. Eur J Nucl Med Mol Imaging. 2011;38(5):802–9.

54. Silvestri GA, et al. Noninvasive staging of non-small cell lung cancer. ACCP evidenced-based clinical practice guidelines (2nd edition). Chest. 2007;132(3 Suppl):178S–201.
55. Crinò L, et al. Early stage and locally advanced (non-metastatic) non-small-cell lung cancer: ESMO clinical practice guidelines for diagnosis, treatment and follow-up. Ann Oncol. 2010;21 Suppl 5: v103–15.
56. Working party of the Australian Cancer Network, The Cancer Council Australia, and Clinical Oncological Society of Australia. Clinical practice guidelines for the prevention, diagnosis and management of lung cancer. The Cancer Council Australia and Australian Cancer Network, Sydney. 2004.
57. van Tinteren H, et al. Effectiveness of positron emission tomography in the preoperative assessment of patients with suspected non-small-cell lung cancer: the PLUS multicentre randomised trial. Lancet. 2002;359(9315):1388–92.
58. Fischer B, et al. Preoperative staging of lung cancer with combined PET-CT. N Engl J Med. 2009; 361(1):32–9.
59. Fischer BM, et al. Multimodality approach to mediastinal staging in non-small cell lung cancer. Faults and benefits of PET-CT: a randomised trial. Thorax. 2011;66(4):294–300.
60. Mac Manus MP, Hicks RJ. The role of Positron Emission Tomography/Computed Tomography in Radiation Therapy Planning for patients with lung cancer. Semin Nucl Med. 2012;42(5):308–19.
61. Schiepers C, et al. PET for staging of Hodgkin's disease and non-Hodgkin's lymphoma. Eur J Nucl Med Mol Imaging. 2003;30(1):S82–8.
62. Scott A, et al. Positron emission tomography changes management, improves prognostic stratification and is superior to gallium scintigraphy in patients with low-grade lymphoma: results of a multicentre prospective study. Eur J Nucl Med Mol Imaging. 2009;36(3):347–53.
63. Pakos EE, et al. 18F-FDG PET for evaluation of bone marrow infiltration in staging of lymphoma: a meta-analysis. J Nucl Med. 2005;46(6): 958–63.
64. Schaefer N, et al. Bone involvement in patients with lymphoma: the role of FDG-PET/CT. Eur J Nucl Med Mol Imaging. 2007;34(1):60–7.
65. Cheson BD. Hodgkin lymphoma: protecting the victims of our success. J Clin Oncol. 2012;30(36): 4456–7.
66. El-Galaly TC, et al. Routine bone marrow biopsy has little or no therapeutic consequence for positron emission tomography/computed tomography–staged treatment-naive patients with Hodgkin lymphoma. J Clin Oncol. 2012;30:4508–14.
67. Moulin-Romsee G, et al. 18F-FDG PET/CT bone/bone marrow findings in Hodgkin's lymphoma may circumvent the use of bone marrow trephine biopsy at diagnosis staging. Eur J Nucl Med Mol Imaging. 2010;37(6):1095–105.
68. Richardson SE, et al. Routine bone marrow biopsy is not necessary in the staging of patients with classical Hodgkin lymphoma in the 18F-fluoro-2-deoxyglucose positron emission tomography era. Leuk Lymphoma. 2012;53(3):381–5.
69. Schöder H, et al. Intensity of 18Fluorodeoxyglucose uptake in positron emission tomography distinguishes between indolent and aggressive non-Hodgkin's lymphoma. J Clin Oncol. 2005;23(21):4643–51.
70. Tang B, et al. Correlating metabolic activity with cellular proliferation in follicular lymphomas. Mol Imaging Biol. 2009;11(5):296–302.
71. van Vliet EPM, et al. Staging investigations for oesophageal cancer: a meta-analysis. Br J Cancer. 2008;98(3):547–57.
72. Chatterton BE, et al. Positron emission tomography changes management and prognostic stratification in patients with oesophageal cancer: results of a multicentre prospective study. Eur J Nucl Med Mol Imaging. 2009;36(3):354–61.
73. Lutz MP, et al. Highlights of the EORTC St. Gallen International Expert Consensus on the primary therapy of gastric, gastroesophageal and oesophageal cancer – differential treatment strategies for subtypes of early gastroesophageal cancer. Eur J Cancer. 2012;48(16):2941–53.
74. Kim S-K, et al. Assessment of lymph node metastases using 18F-FDG PET in patients with advanced gastric cancer. Eur J Nucl Med Mol Imaging. 2006;33(2):148–55.
75. Karikios DJ, et al. The role of ^{18}F-fluorodeoxyglucose positron emission tomography/computed tomography (^{18}FDG PET-CT) in the preoperative staging of gastric cancer: A retrospective review at a single institution. [Abstract]. Asia–Pac J Clin Oncol 2011; 7(Suppl. 4):118.
76. Coupe N, et al. Staging FDG PET predicts survival in gastric cancer and its potential impact on management decisions. Asia-Pac J Clin Oncol 2012; 8(Suppl. 2):49.
77. Schmoll HJ, et al. ESMO Consensus Guidelines for management of patients with colon and rectal cancer. A personalized approach to clinical decision making. Ann Oncol. 2012;23(10):2479–516.
78. Park IJ, et al. Efficacy of PET/CT in the accurate evaluation of primary colorectal carcinoma. Eur J Surg Oncol. 2006;32(9):941–7.
79. Llamas-Elvira J, et al. Fluorine-18 fluorodeoxyglucose PET in the preoperative staging of colorectal cancer. Eur J Nucl Med Mol Imaging. 2007;34(6): 859–67.
80. Fuster D, et al. Preoperative staging of large primary breast cancer with [18F]fluorodeoxyglucose positron emission tomography/computed tomography compared with conventional imaging procedures. J Clin Oncol. 2008;26(29):4746–51.
81. Groheux D, et al. 18F-FDG PET/CT in staging patients with locally advanced or inflammatory breast cancer: comparison to conventional staging. J Nucl Med. 2013;54(1):5–11.

82. Pritchard KI, et al. Prospective study of 2- [18F] fluoro-deoxyglucose positron emission tomography in the assessment of regional nodal spread of disease in patients with breast cancer: an Ontario Clinical Oncology Group study. J Clin Oncol. 2012;30(12):1274–9.
83. Powles T, et al. Molecular positron emission tomography and PET/CT imaging in urological malignancies. Eur Urol. 2007;51(6):1511–21.
84. Eisenhauer EA, et al. New response evaluation criteria in solid tumours: revised RECIST guideline (version 1.1). Eur J Cancer. 2009;45(2):228–47.
85. Wahl RL, et al. From RECIST to PERCIST: evolving considerations for PET response criteria in solid tumors. J Nucl Med. 2009;50 Suppl 1:122S–50.
86. Wahl RL, et al. Metabolic monitoring of breast cancer chemohormonotherapy using positron emission tomography: initial evaluation. J Clin Oncol. 1993;11(11):2101–11.
87. Melton G, et al. Efficacy of preoperative combined 18-fluorodeoxyglucose positron emission tomography and computed tomography for assessing primary rectal cancer response to neoadjuvant therapy. J Gastrointest Surg. 2007;11(8):961–9.
88. Guerra L, et al. Change in glucose metabolism measured by 18F-FDG PET/CT as a predictor of histopathologic response to neoadjuvant treatment in rectal cancer. Abdom Imaging. 2011;36(1):38–45.
89. Janssen MHM, et al. Accurate prediction of pathological rectal tumor response after two weeks of preoperative radiochemotherapy using 18F-fluorodeoxyglucose-positron emission tomography-computed tomography imaging. Int J Radiat Oncol Biol Phys. 2010;77(2):392–9.
90. Capirci C, et al. Long-term prognostic value of 18F-FDG PET in patients with locally advanced rectal cancer previously treated with neoadjuvant radiochemotherapy. Am J Roentgenol. 2006; 187(2):W202–8.
91. Kalff V, et al. Findings on 18F-FDG PET scans after neoadjuvant chemoradiation provides prognostic stratification in patients with locally advanced rectal carcinoma subsequently treated by radical surgery. J Nucl Med. 2006;47(1):14–22.
92. Lordick F, et al. PET to assess early metabolic response and to guide treatment of adenocarcinoma of the oesophagogastric junction: the MUNICON phase II trial. Lancet Oncol. 2007;8(9):797–805.
93. zum Büschenfelde CM, et al. 18F-FDG PET-guided salvage neoadjuvant radiochemotherapy of adenocarcinoma of the esophagogastric junction: the MUNICON II trial. J Nucl Med. 2011;52(8):1189–96.
94. Stroobants S, et al. 18FDG-Positron emission tomography for the early prediction of response in advanced soft tissue sarcoma treated with imatinib mesylate (Glivec). Eur J Cancer. 2003;39(14):2012–20.
95. Benz MR, et al. 18F-FDG PET/CT for monitoring treatment responses to the epidermal growth factor receptor inhibitor Erlotinib. J Nucl Med. 2011;52(11):1684–9.
96. McArthur GA, et al. Marked, homogeneous, and early [18F]fluorodeoxyglucose–positron emission tomography responses to vemurafenib in BRAF-mutant advanced melanoma. J Clin Oncol. 2012; 30(14):1628–34.
97. Lin M, et al. Treatment response in liver metastases following 90Y SIR-spheres: an evaluation with PET. Hepatogastroenterology. 2007;54:910–2.
98. Travaini L, et al. Role of [18F]FDG-PET/CT after radiofrequency ablation of liver metastases: preliminary results. Eur J Nucl Med Mol Imaging. 2008; 35(7):1316–22.
99. Juweid ME, et al. Use of positron emission tomography for response assessment of lymphoma: Consensus of the Imaging Subcommittee of International Harmonization Project in lymphoma. J Clin Oncol. 2007;25(5):571–8.
100. Terasawa T, et al. 18F-FDG PET for posttherapy assessment of Hodgkin's disease and aggressive non-Hodgkin's lymphoma: a systematic review. J Nucl Med. 2008;49(1):13–21.
101. Zijlstra J, et al. 18F-Fluoro-deoxyglucose positron emission tomography for post-treatment evaluation of malignant lymphoma: a systematic review. Haematologica. 2006;91:522–9.
102. Kobe C, et al. Positron emission tomography has a high negative predictive value for progression or early relapse for patients with residual disease after first-line chemotherapy in advanced-stage Hodgkin lymphoma. Blood. 2008;112(10):3989–94.
103. Mikhaeel NG, et al. FDG-PET after two to three cycles of chemotherapy predicts progression-free and overall survival in high-grade non-Hodgkin lymphoma. Ann Oncol. 2005;16(9):1514–23.
104. Spaepen K, et al. Early restaging positron emission tomography with 18F-fluorodeoxyglucose predicts outcome in patients with aggressive non-Hodgkin's lymphoma. Ann Oncol. 2002;13(9):1356–63.
105. Gallamini A, et al. Early interim 2-[18F]fluoro-2-deoxy-D-glucose positron emission tomography is prognostically superior to international prognostic score in advanced-stage Hodgkin's lymphoma: a report from a Joint Italian-Danish study. J Clin Oncol. 2007;25(24):3746–52.
106. Zinzani PL, et al. Midtreatment 18F-fluorodeoxyglucose positron-emission tomography in aggressive non-Hodgkin lymphoma. Cancer. 2011;117(5):1010–8.
107. Barrington S, et al. Concordance between four European centres of PET reporting criteria designed for use in multicentre trials in Hodgkin lymphoma. Eur J Nucl Med Mol Imaging. 2010;37(10):1824–33.
108. Meignan M, et al. Report on the third international workshop on interim positron emission tomography in lymphoma held in Menton, France, 26–27 September 2011 and Menton 2011 Consensus. Leuk Lymphoma. 2012;53(10):1876–81.
109. Aridgides P, et al. PET response-guided treatment of Hodgkin's lymphoma: a review of the evidence and active clinical trials. Adv Hematol. 2011.

110. Hutchings M, Barrington SF. PET/CT for therapy response assessment in lymphoma. J Nucl Med. 2009;50 Suppl 1:21S–30.
111. Huebner RH, et al. A meta-analysis of the literature for whole-body FDG PET detection of recurrent colorectal cancer. J Nucl Med. 2000;41(7):1177–89.
112. Scott AM, et al. PET changes management and improves prognostic stratification in patients with recurrent colorectal cancer: results of a multicenter prospective study. J Nucl Med. 2008;49(9):1451–7.
113. Kalff V, et al. The clinical impact of 18F-FDG PET in patients with suspected or confirmed recurrence of colorectal cancer: a prospective study. J Nucl Med. 2002;43(4):492–9.
114. Deleau C, et al. Clinical impact of fluorodeoxyglucose-positron emission tomography scan/computed tomography in comparison with computed tomography on the detection of colorectal cancer recurrence. Eur J Gastroenterol Hepatol. 2011;23:275–81.
115. Lin M, et al. Positron emission tomography and colorectal cancer. Crit Rev Oncol Hematol. 2011;77(1):30–47.
116. Pawlik T, et al. Trends in nontherapeutic laparotomy rates in patients undergoing surgical therapy for hepatic colorectal metastases. Ann Surg Oncol. 2009;16(2):371–8.
117. Ruers TJM, et al. Improved selection of patients for hepatic surgery of colorectal liver metastases with 18F-FDG PET: a randomized study. J Nucl Med. 2009;50(7):1036–41.
118. Fernandez FG, et al. Five-year survival after resection of hepatic metastases from colorectal cancer in patients screened by positron emission tomography with F-18 fluorodeoxyglucose (FDG-PET). Ann Surg. 2004;240:438–47.
119. Metser U, et al. Assessment of tumor recurrence in patients with colorectal cancer and elevated carcinoembryonic antigen level: FDG PET/CT versus contrast-enhanced 64-MDCT of the chest and abdomen. Am J Roentgenol. 2010;194(3):766–71.
120. Pallardy A, et al. Clinical and survival impact of FDG PET in patients with suspicion of recurrent cervical carcinoma. Eur J Nucl Med Mol Imaging. 2010; 37(7):1270–8.
121. Fulham MJ, et al. The impact of PET-CT in suspected recurrent ovarian cancer: a prospective multi-centre study as part of the Australian PET Data Collection Project. Gynecol Oncol. 2009;114(3):462–8.
122. Isles MG, et al. A systematic review and meta-analysis of the role of positron emission tomography in the follow up of head and neck squamous cell carcinoma following radiotherapy or chemoradiotherapy. Clin Otolaryngol. 2008;33(3):210–22.
123. Porceddu SV, et al. Results of a prospective study of positron emission tomography–directed management of residual nodal abnormalities in node-positive head and neck cancer after definitive radiotherapy with or without systemic therapy. Head Neck. 2011;33(12):1675–82.
124. Abgral R, et al. Does ^{18}F-FDG PET/CT improve the detection of posttreatment recurrence of head and neck squamous cell carcinoma in patients negative for disease on clinical follow-up? J Nucl Med. 2009; 50(1):24–9.
125. Cooper DS, et al. Revised American Thyroid Association management guidelines for patients with thyroid nodules and differentiated thyroid cancer. Thyroid. 2009;19(11):1167–214.
126. Dong M-J, et al. Value of 18F-FDG-PET/PET-CT in differentiated thyroid carcinoma with radioiodine-negative whole-body scan: a meta-analysis. Nucl Med Commun. 2009;30(8):639–50.
127. Wang W, et al. Resistance of [18F]-Fluorodeoxyglucose-avid metastatic thyroid cancer lesions to treatment with high-dose radioactive iodine. Thyroid. 2001;11(12):1169–75.
128. Metser U, Even-Sapir E. Increased 18F-fluorodeoxyglucose uptake in benign, nonphysiologic lesions found on whole-body positron emission tomography/computed tomography (PET/CT): accumulated data from four years of experience with PET/CT. Semin Nucl Med. 2007;37(3):206–22.
129. Even-Sapir E, et al. The presentation of malignant tumours and pre-malignant lesions incidentally found on PET-CT. Eur J Nucl Med Mol Imaging. 2006;33(5):541–52.
130. Lin M, et al. Management of patients following detection of unsuspected colon lesions by PET imaging. Clin Gastroenterol Hepatol. 2011;9:1025–32.
131. Katz SC, Shaha AR. PET-associated incidental neoplasms of the thyroid. J Am Coll Surg. 2008; 207:259–64.
132. Wong C, et al. The clinical significance and management of incidental focal FDG uptake in the thyroid gland on positron emission tomography/computed tomography (PET/CT) in patients with non-thyroidal malignancy. Acta Radiol. 2011;52:899–904.
133. Bogsrud TV, et al. The value of quantifying 18F-FDG uptake in thyroid nodules found incidentally on whole-body PET–CT. Nucl Med Commun. 2007;28(5):373–81.
134. Lin M, Ambati C. The management impact of clinically significant incidental lesions detected on staging FDG PET-CT in patients with non-small cell lung cancer (NSCLC): an analysis of 649 cases. Lung Cancer. 2012;76(3):344–9.
135. Minamimoto R, et al. The current status of an FDG-PET cancer screening program in Japan, based on a 4-year (2006–2009) nationwide survey. Ann Nucl Med. 2013;27(1):46–57.
136. Hillman BJ. Screening for cancer with high technology imaging tests. J Clin Oncol. 2009;27(11): 1740–1.

Imaging of Tumor Metabolism: PET with Other Metabolites

10

Chi-Lai Ho, Sirong Chen, and Man-Ki Cheung

Contents

Abbreviations

^{18}F-DOPA	F-18-fluoro-L-phenylalanine
^{18}F-FAC	^{18}F-acetate
^{18}F-FLT	^{18}F-fluorothymidine
acetyl-CoA	Acetyl-coenzyme A
APUD	Amine Precursor Uptake and Decarboxylation
EGF	Endothelial growth factors
FAS	Fatty acid synthetase
FNH	Focal Nodular Hyperplasia
HCC	Hepatocellular carcinoma
MGUS	Monoclonal gammopathy of undetermined significance
NET	Neuroendocrine tumors
NSCLC	Non-small cell lung carcinoma
PSA	Prostate-specific antigen
RCC	Renal cell carcinoma
SREBPs	Sterol regulatory element-binding proteins
SUV	Standardized uptake value
TCA	Tricarboxylic acid cycle
TK1	Thymidine kinase 1

As the research of metabolic imaging is expanding, the clinical applications of radiolabeled substrates have also been increasing. Apart from glycolysis, other biochemical processes including amino acid synthesis, peptide and nucleic acid sequencing, lipid metabolism, signal transduction, and neurotransmitter-receptor interactions are also known to represent various forms of metabolic changes possibly found in tumor cells. In the literature, there are increasing amount of research studies

C.-L. Ho, MD (✉) • S. Chen, PhD
M.-K. Cheung, PhD
Department of Nuclear Medicine and PET,
Hong Kong Sanatorium and Hospital, 2 Village Road,
Happy Valley, Hong Kong, China
e-mail: garrettho@hksh.com; sirongchen@hksh.com;
jackycheung@hksh.com

A. Luna et al. (eds.), *Functional Imaging in Oncology*,
DOI 10.1007/978-3-642-40412-2_10, © Springer-Verlag Berlin Heidelberg 2014

on non-^{18}F-FDG PET radiopharmaceuticals targeted for specific biochemical processes other than glycolysis. This chapter discusses on the basic biochemistry of non-^{18}F-FDG PET tracers and how a good understanding of the underlying metabolic pathways of individual tracers leads to various clinical applications, particularly in the improvement of tumor detection, diagnosis, and patient management. Specific discussion is focused on ^{11}C-acetate, ^{18}F-acetate, ^{11}C-choline, ^{18}F-choline, ^{11}C-methionine, ^{18}F-DOPA, ^{18}F-FLT, and Gallium-68 (^{68}Ga)-labeled somatostatin analogs, primarily because these PET tracers have been investigated in greater biochemical and pharmaceutical details. Some have already been clinically confirmed useful, while others have great potentials to add to our understanding and to guide our research development on tumor metabolism and growth.

10.1 ^{11}C-Acetate and ^{18}F-Acetate

10.1.1 ^{11}C-Acetate

10.1.1.1 Tumor Metabolism

Acetate acts as a probe of cellular metabolism through conversion into acetyl-coenzyme A (acetyl-CoA), the key intermediate precursor for various catabolic and anabolic biochemical pathways, and is important in cellular membrane function [1]. The use of ^{11}C-labeled acetate in biochemical research was initially for the study of myocardial metabolism two to three decades ago [2–5] but was later extended to oncological PET investigations.

Apart from glucose, fatty acids are another category of important source of energy for many organisms. They also play key roles as biochemical modifiers in a number of protein synthesis and reactions. A substantial subset of tumor cells convert acetate into fatty acids through β-oxidation by a key enzyme known as fatty acid synthetase (FAS), which is overexpressed in some cancer cells [1, 6–10]. FAS is an anabolic enzyme that catalyzes the terminal steps in the de novo biosynthesis of fatty acids. Growth factors such as endothelial growth factors (EGF) are able to stimulate FAS mRNA, protein, and activity [11, 12]. The first step of fatty acid synthesis is carboxylation of acetyl-CoA to form malonyl-CoA, the carbon source of the fatty acyl chain. Acetyl-CoA carboxylase catalyzes a two-step reaction as summarized below:

$$\mathrm{HCO_{3^-}} + \mathrm{ATP} + \mathrm{acetyl\text{-}CoA} = \mathrm{ADP} + \mathrm{P_i} + \mathrm{malonyl\text{-}CoA}. \quad (10.1)$$

Elongation of fatty acid chain occurs via four recurring reactions beginning with condensation between malonyl-CoA and acetyl-CoA through acyl carrier protein thioesters. The end product is palmitate, a 16-carbon fatty acid chain:

$$\mathrm{CH_3CO\text{-}CoA} + 7\mathrm{HOOCCH_2CO\text{-}CoA} + 14\,\mathrm{NADPH} + 14\mathrm{H^+} = \mathrm{CH_3\left(CH_2\right)_{14}COOH} + 7\mathrm{CO_2} + 8\mathrm{CoASH} + 14\,\mathrm{NADP^+} + 6\mathrm{H_2O} \quad (10.2)$$

During the synthesis process, six specific subunits of enzyme activities, collectively known as FAS, are involved. Fatty acids are degraded in the mitochondrial matrix via the β-oxidation pathway.

10.1.1.2 Application

Prostate Cancer

^{11}C-acetate has a distinct advantage over ^{18}F-FDG in the evaluation of urological diseases because, unlike ^{18}F-FDG, it does not have urinary excretion [13–16]. One of the first applications of ^{11}C-acetate in oncology focused on its use in prostate cancer. Swinnen et al. [17, 18] demonstrated that in a prostate cancer cell line (LNCaP), FAS expression is markedly elevated by androgens via an indirect pathway involving sterol regulatory element-binding proteins (SREBPs) [1, 19]. In 2002, Oyama et al. [14] reported a 100 % sensitivity of ^{11}C-acetate PET for the 22 patients with histologically proven prostate adenocarcinoma.

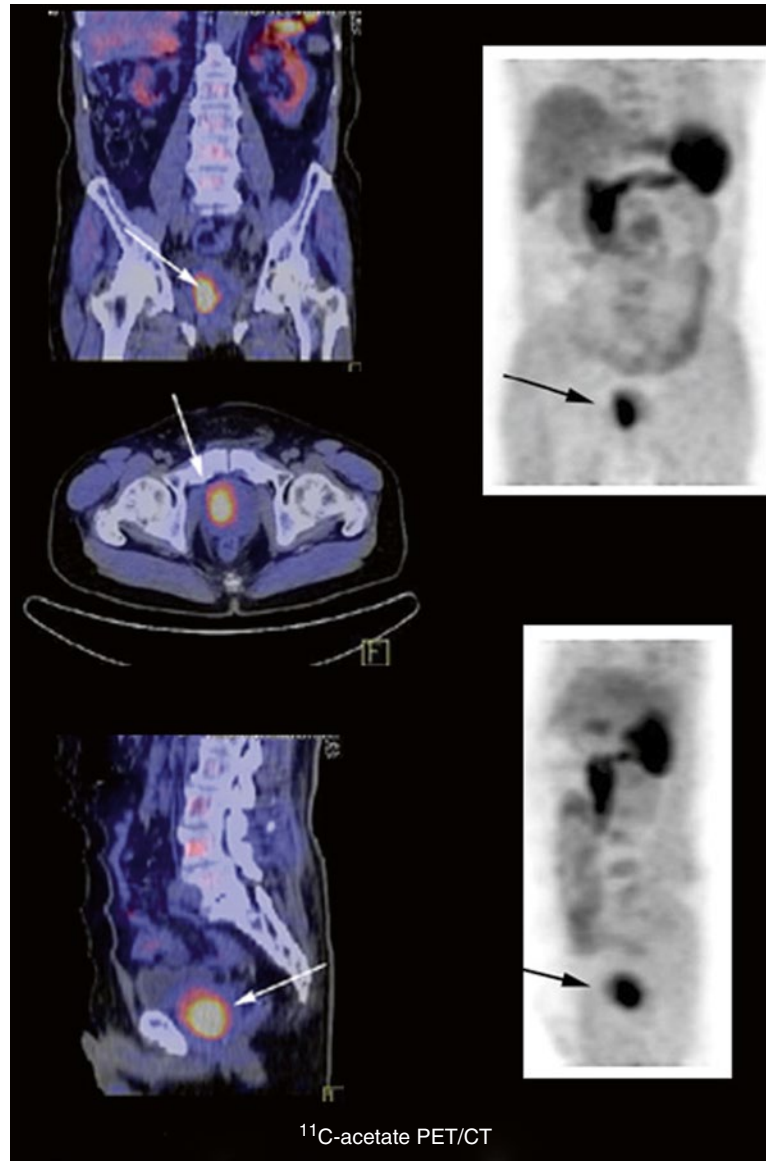

Fig. 10.1 A recurrent prostate carcinoma (*arrows*) shows focally increased metabolism on ^{11}C-acetate PET/CT

In a study by Kotzerke et al. [20] for a cohort of patients with increasing prostate-specific antigen (PSA) levels after complete prostatectomy, ^{11}C-acetate PET was able to detect local recurrence in 15 out of 18 patients. Albrecht et al. [21] reported that even in patients having only slightly increased PSA levels, ^{11}C-acetate PET detected 6/6 patients suspected of prostate cancer recurrence. Figure 10.1 shows the ^{11}C-acetate PET/CT image of a patient with recurrent prostate carcinoma but without increased PSA concentration. ^{11}C-acetate PET is particularly effective in the evaluation of lymph node involvement and distant metastases and significantly affects patient management [20, 22, 23]. In a report by Fricke et al. [24], sensitivity of ^{11}C-acetate PET in detection of bone metastasis from prostate malignancy was ~83 %.

Renal Cell Carcinoma

Apart from prostate carcinoma, ^{11}C-acetate PET studies were also performed on other urological malignancies, including renal cell carcinoma

(RCC) [13, 25] and bladder cancer [26]. In 1995, Shreve and his co-workers were the first to use dynamic ^{11}C-acetate PET to characterize renal tumors [13]. By analysis with kinetic modeling, they found that ^{11}C-acetate clearance rate was reduced in RCC cancer cells compared to normal renal parenchyma. With dynamic acquisition beyond 10 min after intravenous ^{11}C-acetate administration, retention of ^{11}C-acetate within a lesion greater than normal renal parenchyma was found in 3 RCCs of clear cell subtype. However, after this preliminary study by Shreve, there have been very little data in the following decade to further confirm or support its clinical value for the evaluation of RCC, while some data were even quite negative [27].

In 2009, Oyama et al. [28] and his co-workers reported that the sensitivity of ^{11}C-acetate PET in detecting RCC was 70 % (14/20). The majority of the RCC lesions in this study belonged to the clear cell subtype, but they did not mention the grade of differentiation of these lesions nor had they performed parallel ^{18}F-FDG PET for comparison. Greater details on the use of dual-tracer (^{11}C-acetate and ^{18}F-FDG) PET/CT to evaluate the metabolic characters of different subtypes of RCC and how to differentiate them from angiomyolipoma, especially fat-poor angiomyolipoma, were studied by Ho et al. [25, 29]. Their study consisted of 58 patients, 10 with angiomyolipoma and 48 with RCC. All angiomyolipoma showed negative avidity for ^{18}F-FDG but marked avidity for ^{11}C-acetate, which was significantly higher than that of RCC (^{11}C-acetate lesion-to-kidney SUV_{max} ratio = 4.11 ± 0.53 vs 2.00 ± 0.71, $P < 0.05$). With Receiver Operator Characteristic Curve (ROC) analysis, their preliminary finding was that ^{11}C-acetate SUV_{max} ratio ≥3.71 could differentiate angiomyolipoma (including fat-poor angiomyolipoma) from RCC with a sensitivity of 93.8 % (15/16) and specificity of 98.0 % (49/50). Different RCC subtypes/grades (25 low- and 11 high-grade clear cell, 7 chromophobe, 4 papillary, and 1 collecting duct) were found to have different dual-tracer metabolic pattern, with an overall RCC detection sensitivity of 90 % (45/50). High-grade clear cell RCC was more avid for ^{18}F-FDG and low-grade was more avid for ^{11}C-acetate (Fig. 10.2) [25]. All chromophobe RCC were avid only for ^{11}C-acetate but not ^{18}F-FDG while papillary RCC were primarily the opposite (Fig. 10.3) [25]. Collecting duct RCC showed markedly increased uptake of ^{18}F-FDG but negative on ^{11}C-acetate PET. Four RCC cases negative by dual-tracers were of low-grade clear cell RCC. "Primary RCC being ^{18}F-FDG avid" was the only independent predictor of RCC recurrence in 3 years ($P < 0.05$), with a median disease-free survival of 22 months. The diagnostic criteria of ^{11}C-acetate SUV_{max} ratio ≥3.71 and negative ^{18}F-FDG uptake for angiomyolipoma can also be applied to multicentric angiomyolipoma. In a case report by the same authors on a patient with a left kidney mass and regional hypermetabolic retroperitoneal lymph nodes, all lesions showed markedly increased ^{11}C-acetate metabolism (lesion-to-kidney SUV_{max} ratio = 4.4–4.9) but no abnormal ^{18}F-FDG uptake (Fig. 10.4) [29]. Both the renal mass and regional lymph nodes were pathologically confirmed as "multicentric low-fat angiomyolipoma with lymph node involvement," whose prognosis is significantly different from "RCC with lymph node metastases" [29].

Hepatocellular Carcinoma

Hepatocellular carcinoma (HCC) is one of the leading cancers in many Asian countries and is ranked even higher in the list of cancer deaths in the last few years. However, it is reported that 30–50 % of primary HCC are not ^{18}F-FDG avid or are only mildly avid [30–34]. The underlying biochemical reason is that an enzyme, known as glucose-6-phosphatase, is present in abundance within the normal liver cells and in certain types of HCC. This leads to dephosphorylation of ^{18}F-FDG-6-phosphate and "leakage" of ^{18}F-FDG back to the circulation. This is in contrary to many forms of malignant tumors in which ^{18}F-FDG-6-phosphate is "metabolically trapped" because either the phosphatase enzyme itself or its activity is very low or negligible, and

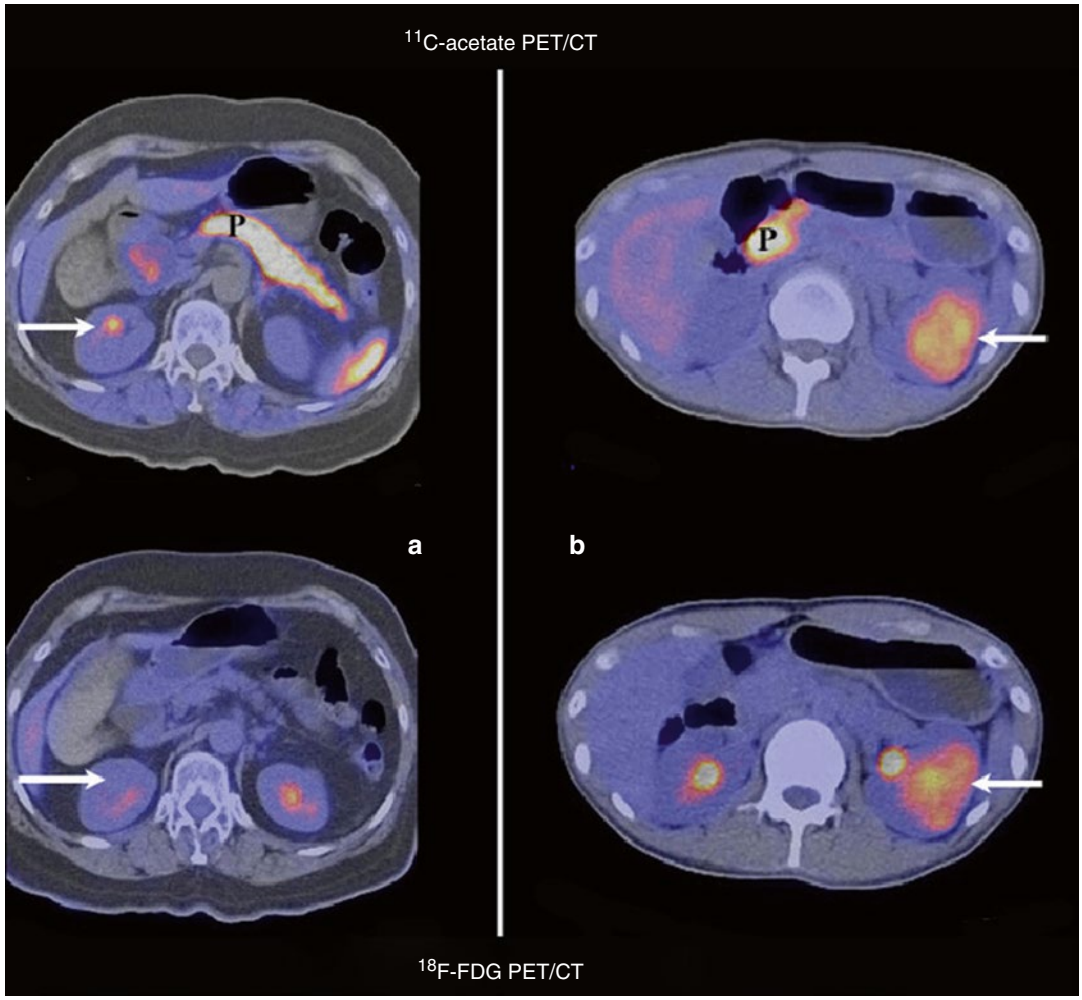

Fig. 10.2 (**a**) A 1-cm low-grade RCC of clear cell subtype (*arrows*) is moderately avid for ^{11}C-acetate PET/CT (*upper row*) but completely negative for ^{18}F-FDG (*lower row*). (**b**) A 3.5 cm high-grade RCC of clear cell subtype of left kidney (*arrows*) shows increased ^{11}C-acetate (*upper row*) and ^{18}F-FDG (*lower row*) metabolism on dual-tracer PET/CT. *P* pancreas

^{18}F-FDG-6-phosphate cannot be further metabolized by the second enzyme, an isomerase. Recent research has found encouraging results in the use of ^{11}C-acetate for the detection of HCC and to assess its kinetics and uptake characteristics in HCC [35–40]. In the first study using ^{11}C-acetate as the PET tracer for HCC [35], 57 patients with liver masses (39 HCCs, 3 cholangiocarcinomas, 10 liver secondaries, 2 focal nodular hyperplasia [FNH], 1 adenoma, and 2 hemangiomas) were investigated. ^{11}C-acetate PET was found to have a sensitivity of 87 % in the detection of HCC, while ^{18}F-FDG PET had a sensitivity of 47 %. However, the more important finding by this research group is that ^{11}C-acetate is complementary to ^{18}F-FDG, so that there was mutual coverage of the false-negative lesions in one tracer by the other. The combined sensitivity by the two tracers is 100 % in their study based on a group of patients with intermediate HCC lesion size (3.5 ± 1.9 cm) [35]. They found that the individual tracer avidity depends on the

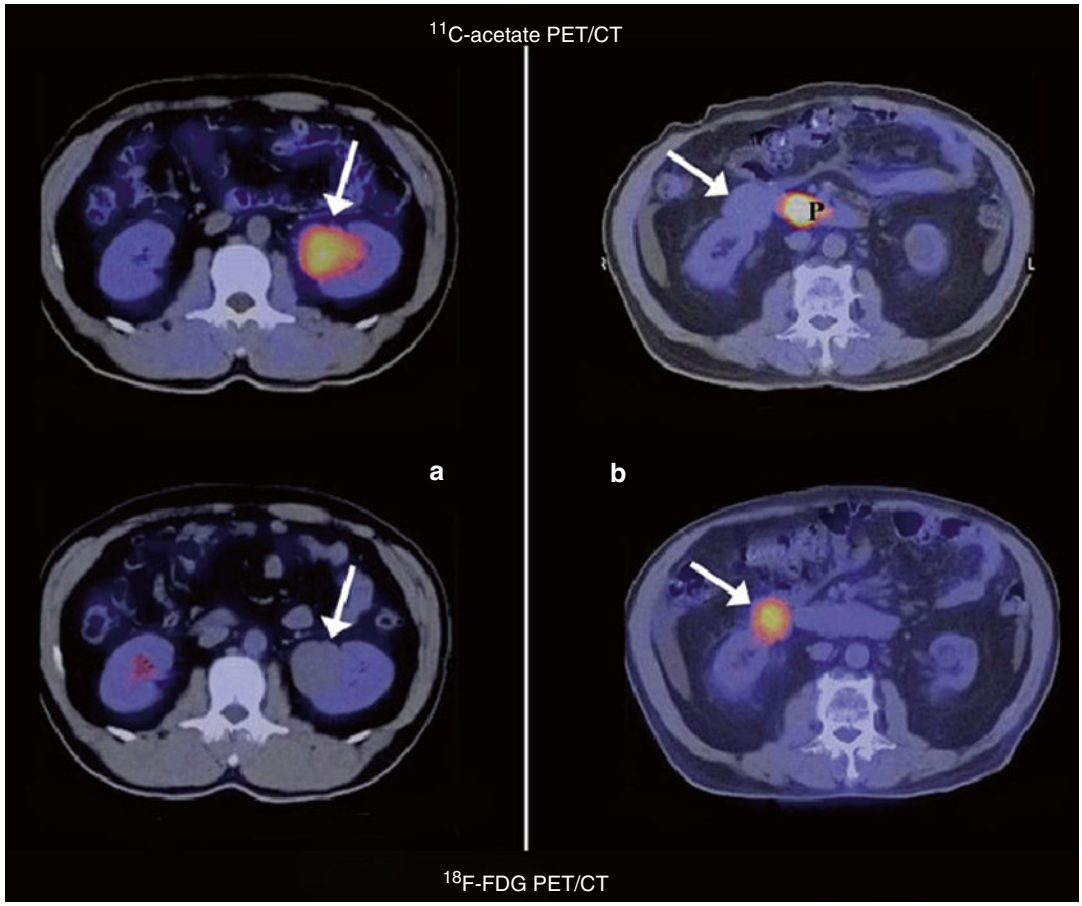

Fig. 10.3 PET/CT of (**a**) a RCC of chromophobe subtype (*arrows*) shows increased ^{11}C-acetate (*upper row*) but negative ^{18}F-FDG metabolism (*lower row*); (**b**) a RCC of papillary subtype (*arrows*) shows increased ^{18}F-FDG (*lower row*) but negative ^{11}C-acetate metabolism (*upper row*). *P* pancreas

degree of differentiation of the HCC cell types. Well-differentiated HCC tends to show negative uptake on ^{18}F-FDG PET but positive uptake on ^{11}C-acetate PET (Fig. 10.5), while poorly differentiated HCC has the opposite tracer uptake pattern. The HCC cell types of intermediate differentiation tend to show dual-tracer avidities. Their results illustrate the relationship between functional concordance and morphological change. As HCC cells form in the early stage of development, they have similar or little morphological difference when compared with normal hepatocytes and therefore were likely to possess less alteration in metabolic or enzymatic properties. As a result, well-differentiated HCC behaves metabolically or enzymatically similar to normal hepatocytes. However, as the tumor cells become morphologically more dedifferentiated when they replicate and grow, their metabolic preference or enzyme systems will likewise depart from the original status. Poorly differentiated HCC may then obtain its energy source from the glycolytic pathway with no difference from other ^{18}F-FDG-avid malignancies.

Since smaller tumors are likely to be well differentiated in their early development, a specific group of HCC lesions smaller than 2 cm (mean size: 1.5 ± 0.3 cm) was specifically evaluated by the same group of researchers [41]. They found that the sensitivity of ^{11}C-acetate PET in the detection of small HCC was 86.8 %, similar to that of HCC with intermediate size. The only

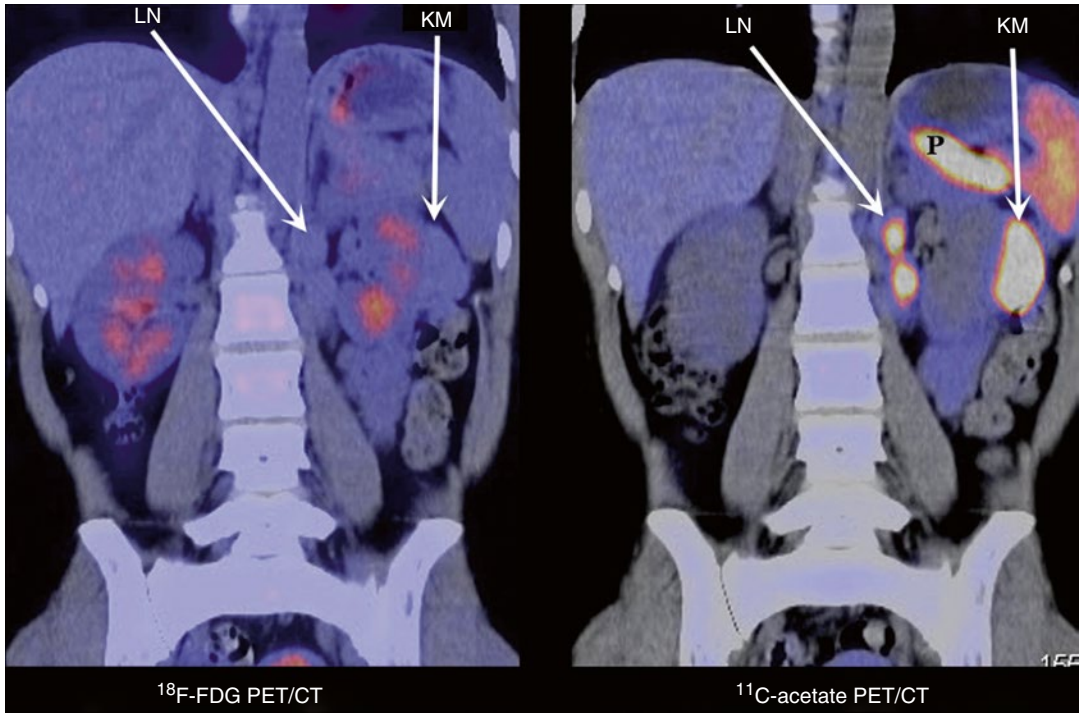

Fig. 10.4 ^{11}C-acetate and ^{18}F-FDG PET/CT of multicentric fat-poor angiomyolipoma with lymph node involvement. *KM* kidney mass, *LN* a chain of para-aortic nodes, *P* pancreas

difference was that there was a shift from the proportion of lesions positive for both tracers (34.5 % for intermediate HCC; 18.4 % for small HCC) to a larger proportion of lesions positive for ^{11}C-acetate only (52.7 % for intermediate HCC; 68.4 % for small HCC). This is in agreement with the initial observation that the smaller tumors are usually well differentiated in their early development, and they tend to be more often detected by ^{11}C-acetate PET rather than ^{18}F-FDG PET (Fig. 10.6).

^{11}C-acetate is reasonably specific for HCC in the evaluation of liver masses since it is not the preferred substrate of energy source in a number of neoplastic entities such as hemangioma, cholangiocarcinoma [42], metastatic carcinomas from colon, breast, pancreas, and lung, as well as carcinoid tumors. Pure cholangiocarcinoma (cholangioadenocarcinoma) is primarily avid for ^{18}F-FDG (Fig. 10.7) with mean lesion-to-liver SUV_{max} ratio of 4.1 ± 0.9 [42]. When both tracers are positive, the underlying pathology is more likely to be mixed, such as cholangio-HCC, or a poorly to moderately differentiated HCC. Two benign pathologic entities possessing pure ^{11}C-acetate avidity include hepatic angiomyolipoma and FNH. Hepatic angiomyolipoma is a potential false-positive in using ^{11}C-acetate PET for evaluation of a liver mass when the lesion has a low-fat content, so-called "fat-poor" angiomyolipoma, though common in the kidney, is rare in the liver [43]. It is a diagnostic pitfall when it is fat-poor and at the same time small in size. If a fat-poor angiomyolipoma is of reasonable size (say 2 cm or more), it is usually not a diagnostic problem since angiomyolipoma has a very high utilization of ^{11}C-acetate and is statistically distinguishable from the majority of well-differentiated HCC. FNH, on the other hand, has a wider variability in the degree of ^{11}C-acetate metabolic intensity from minimal to moderate (Fig. 10.8). The lesion activity margins are, however, usually less well defined or blurred. An inner nidus of hypometabolism representing the central scar can be theoretically present but most of the time not visualized. When FNH is

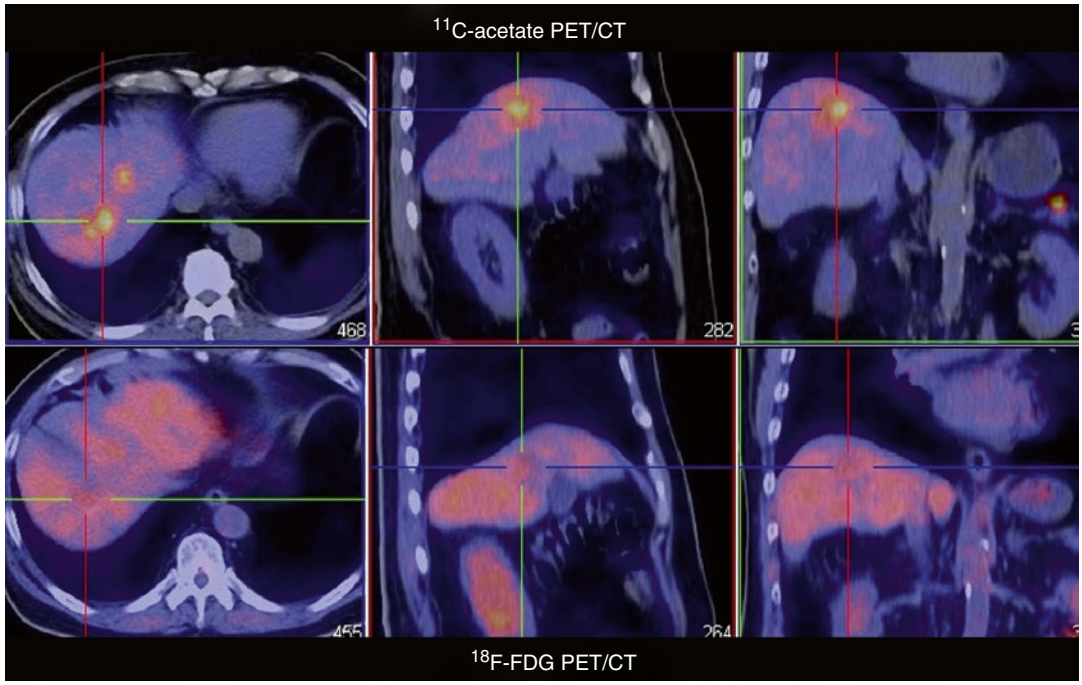

Fig. 10.5 Multicentric well-differentiated HCC shows increased uptake of ^{11}C-acetate (*upper row*) but is negative on ^{18}F-FDG (*lower row*) PET/CT

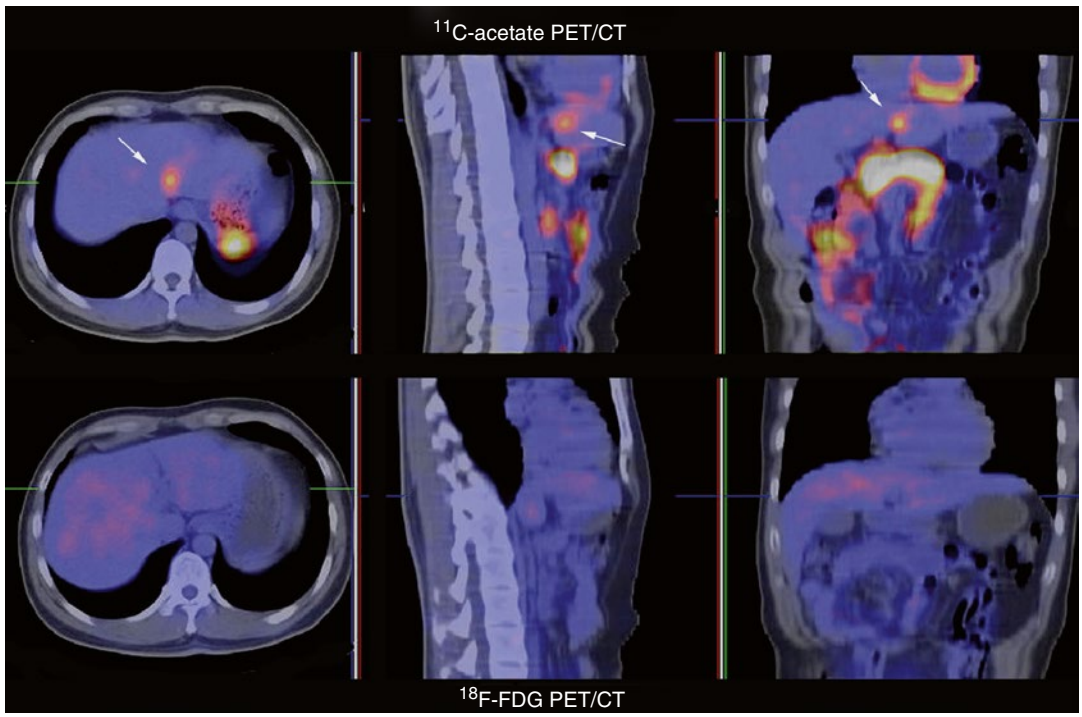

Fig. 10.6 A small well-differentiated HCC (*arrows*), nodule size of 1,6 cm, shows increased ^{11}C-acetate metabolism (*upper row*) but is negative on ^{18}F-FDG (*lower row*) PET/CT

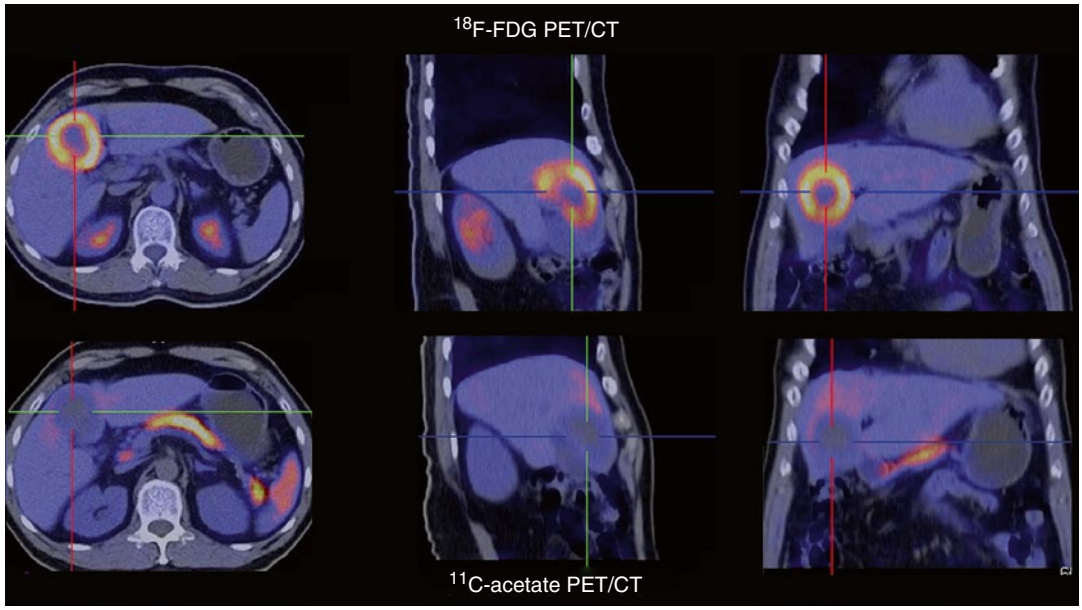

Fig. 10.7 Dual-tracer PET/CT of a cholangiocarcinoma shows markedly increased ^{18}F-FDG metabolism (*upper row*) but no abnormal ^{11}C-acetate activity (*lower row*)

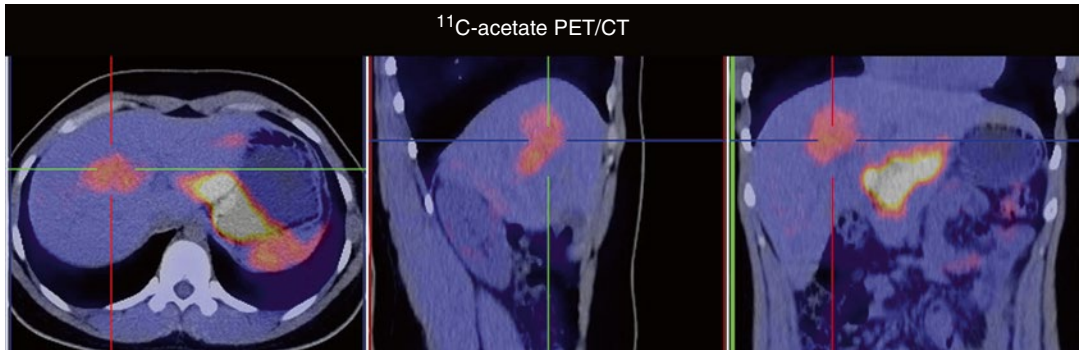

Fig. 10.8 A FNH lesion shows mildly increased ^{11}C-acetate metabolism with ill-defined margins

suspected, ^{99m}Tc-sulfur colloid SPECT/CT study should be performed. A positive (normal or increased activity) scan indicates intact Kupffer cell function, which is almost pathognomonic for FNH. Both hepatic angiomyolipoma and FNH do not show abnormal (increased or decreased) ^{18}F-FDG metabolism.

The complementary nature of ^{11}C-acetate and ^{18}F-FDG is seen not just in primary HCC tumors but is also demonstrated in metastatic HCC lesions. In 2007, Ho et al. [44] used both ^{11}C-acetate and ^{18}F-FDG for the detection of HCC metastases in correlation with the dual-tracer avidity of their corresponding primary HCC. It was found that ^{18}F-FDG had the highest sensitivity of 88 % in the detection of HCC metastasis when the primary HCC tumor was also ^{18}F-FDG avid. On the other hand, when the primary HCC was ^{11}C-acetate avid, ^{18}F-FDG had the lowest sensitivity of 67 %. Therefore, the sensitivity of ^{18}F-FDG PET in detecting metastatic lesions is quite dependent on the primary tracer avidity, which reflects the degree of cellular differentiation of the primary HCC tumor. Extrahepatic metastases

secondary to HCC commonly involve the lung and abdominal lymph nodes [44–46]. However, bone is not so often a rare site of metastasis as it seemed to be since it can occur as the first and only site of metastatic involvement in about 12 % of HCC patients with metastasis [47]. ^{11}C-acetate PET is reported to demonstrate an incremental value of 23 % (7/30) over ^{18}F-FDG in the detection of bone metastasis.

Following the initial study by Ho et al. [35], a number of research groups have also confirmed the usefulness of ^{11}C-acetate in the detection of HCC, especially well-differentiated cell types [48–50]. In an animal study of woodchuck models, acetyl-CoA synthetase activity was found elevated in HCC as compared to normal woodchuck liver [51]. In 2009, Yun et al. [52] was also able to show that the patterns of ^{18}F-FDG and ^{11}C-acetate uptake were complementary to each other in both human HCC and HCC cell lines. FAS expression was seen in cells with high ^{18}F-FDG or ^{11}C-acetate uptake, suggesting the presence of increased glucose- or acetate-dependent lipid synthesis. Acetyl-CoA synthetase activity is upregulated to facilitate ^{11}C-acetate uptake and acetate-dependent lipid synthesis for the growth of cancer cells with a low-glycolysis phenotype.

Lung and Brain Cancers

Besides urological and liver cancers, ^{11}C-acetate PET has also been investigated for assessment of other malignancies, such as brain tumor [53–56] and certain types of lung carcinoma [57, 58] such as bronchioloalveolar cell carcinoma, and well-differentiated adenocarcinoma. Yamamoto's group investigated the usefulness of ^{11}C-acetate PET in evaluating brain glioma in 15 patients (5/15 grade II, 3/15 grade III, and 7/15 glioblastoma) before treatment [54]. They found that the sensitivity for the detection of brain glioma by ^{11}C-acetate PET was 90 % and that the mean ^{11}C-acetate SUV in high-grade gliomas (IV) was significantly higher than that in low-grade glioma (II). Tsuchida and his co-workers in 2008 also published their results regarding ^{11}C-acetate PET on glioma [53]. They found significant difference in ^{11}C-acetate uptake between high-grade and low-grade glioma. They concluded that ^{11}C-acetate can be considered as a promising tracer in studying the grading of glioma. ^{11}C-acetate PET was also reported positive in detection of astrocytoma (26 patients) [55].

Multiple Myeloma

Multiple myeloma, a malignant disease of plasma B cells associated with bone marrow infiltration, is the most common primary bone malignancy. It causes no symptoms until it has reached an advanced stage [59]. ^{18}F-FDG PET [60–62] was adopted widely in the recent years for the detection of multiple myeloma since they could identify myeloma sites in a considerable amount of patients with negative radiography findings. However, ^{18}F-FDG PET has a false-negative rate of ~40 % [63]. ^{11}C-acetate PET has been reported to show promising results in the detection of bone metastases from prostate carcinoma, RCC and HCC, as already discussed above. The common denominator of these metastatic bone lesions is that they are all known to have an osteolytic pattern of bone destruction. As multiple myeloma lesions are typically "punched out" on radiographic skeletal survey, there are preliminary data in the literature investigating on the potential diagnostic value of ^{11}C-acetate PET on multiple myeloma [64, 65]. The first study [64] reported their results on 15 symptomatic untreated myeloma patients. ^{11}C-acetate PET identified 12/15 (80 %), while ^{18}F-FDG detected 9/15 (60 %) symptomatic myeloma patients, and the 2 tracers were complementary to each other with an overall sensitivity of 87 % (13/15). Figure 10.9 shows the dual-tracer PET/CT images of a stage I myeloma patient. ^{11}C-acetate PET/CT shows that the myeloma lesions are avidly demonstrated while they are all negative by ^{18}F-FDG PET. ^{11}C-acetate PET was also shown to have great potential for assessment of tumor response during the early course of treatment, which is a distinct advantage over other structural imaging modalities. In the second study by the same group of researchers [65], results on a larger group of patients (37 patients: 17 new myeloma, 1 monoclonal gammopathy of undetermined significance [MGUS], 2 smoldering myeloma, 6 myeloma in remission, and 11

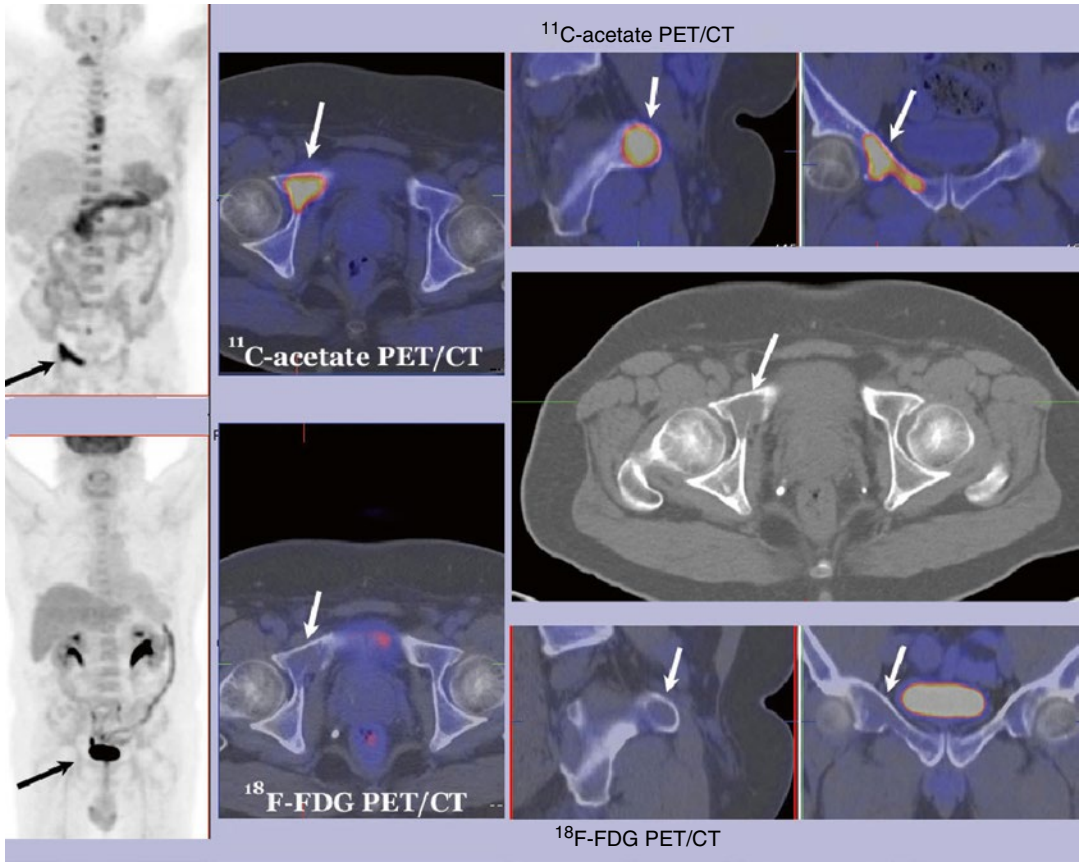

Fig. 10.9 ^{11}C-acetate PET/CT shows focally increased uptake over C4, C7, T8, L1, right acetabulum and superior pubic ramus (*arrows*), left scapula, 2 foci in manubrium, and sternum but without corresponding increased ^{18}F-FDG metabolism in a patient with stage I multiple myeloma

relapsed myeloma) were reported. They showed that ^{11}C-acetate PET had a similar sensitivity of 82.4 % for untreated myeloma patients, with an incremental value of 58.8 % over ^{18}F-FDG alone. Figure 10.10 shows the dual-tracer (^{11}C-acetate and ^{18}F-FDG) PET/CT of a patient with stage III diffuse myeloma. Their data reported that ^{11}C-acetate PET was able to identify myeloma bone lesions in 10/11 patients with relapsing myeloma. Diagnosis by ^{11}C-acetate PET was more confident than ^{18}F-FDG in terms of lesion tracer avidity and number of bone lesions. The highest lesion activity in each patient had mean ^{11}C-acetate $SUV_{max} = 12.9 \pm 4.9$ vs ^{18}F-FDG $SUV_{max} = 9.0 \pm 5.1$ ($P < 0.05$). Nine patients with indolent/inactive disease were true negative on ^{11}C-acetate PET: MGUS, smoldering myeloma and myeloma in remission. A single case report has also noted that ^{11}C-acetate PET incidentally showed an ^{11}C-acetate avid myeloma lesion initially suspected to be metastatic from HCC in a patient with known HCC disease [66].

10.1.2 ^{18}F-Acetate

The numerous studies on ^{11}C-acetate have demonstrated that it can be used in cardiology and oncology with no contraindications apart from pregnancy and the necessity of a scanner capable of fast and efficient data acquisition. Despite its limited availability, this tracer can surely be considered to be a promising one, because of its versatility and capacity to even detect non-^{18}F-FDG-avid neoplasms.

For PET centers that do not have on-site cyclotrons, the use of ^{11}C-acetate is limited by the short,

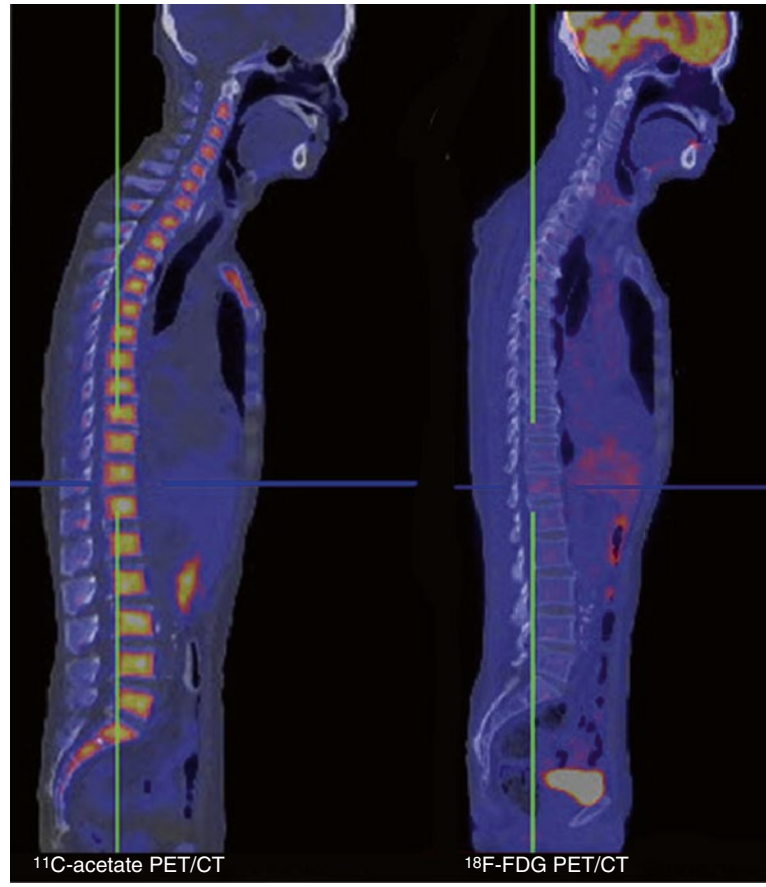

Fig. 10.10 Dual-tracer PET/CT shows generalized accentuated ^{11}C-acetate activity (*left*) in axial marrow but negative ^{18}F-FDG uptake (*right*) in a patient diagnosed of diffuse multiple myeloma

20 min, radioactive half-life of ^{11}C. Therefore, acetate analogs labeled with positron emitters having a longer half-life are needed. One of the potential radiopharmaceuticals proposed in the literature is ^{18}F-acetate (^{18}F-FAC) [67–70]. In 2012, a PET/CT study [71] was designed to evaluate the whole-body biodistribution and tumor uptake characteristics of ^{18}F-FAC in human subjects as compared to ^{11}C-acetate. The biodistribution of ^{18}F-FAC in humans (Fig. 10.11) [71], however, was shown to be different from animal studies as reported in the literature [69, 70, 72, 73]. As proposed by Ponde et al. [69], this was suspected to be related to "species differences." Their study showed that there were urinary activities in baboon but not in rodents. Referring to the pioneer data available in literature, there was indeed strong evidence of species-related biodistribution, toxicity, and excretion differences in regard to nonradioactive fluoroacetate [74]. The biodistribution of ^{18}F-FAC PET showed no significant difference at 20 min and 1 h (Fig. 10.11). There was diffuse activity in the heart, great vessels, liver, and spleen. No urinary activity was seen in the kidneys or urinary bladder, and there was no significant marrow uptake on both sets of ^{18}F-FAC PET studies, suggesting little to no defluorination at least in 1 h of study. There was variable amount of activity in the colon, suggesting that the mode of excretion was likely to be bowel-predominant, which agreed with the findings of previous research groups [69, 70, 75]. Comparing with the ^{18}F-FAC data, the biodistribution of ^{11}C-acetate in the human subject was statistically very different from those of the ^{18}F-FAC. Figure 10.12 [71] shows the ^{11}C-acetate PET images of a large HCC extensively involving the left lobe and segments V–VIII of right lobe intensely avid for ^{11}C-acetate; however, no hypermetabolic lesions were identified on ^{18}F-FAC PET images.

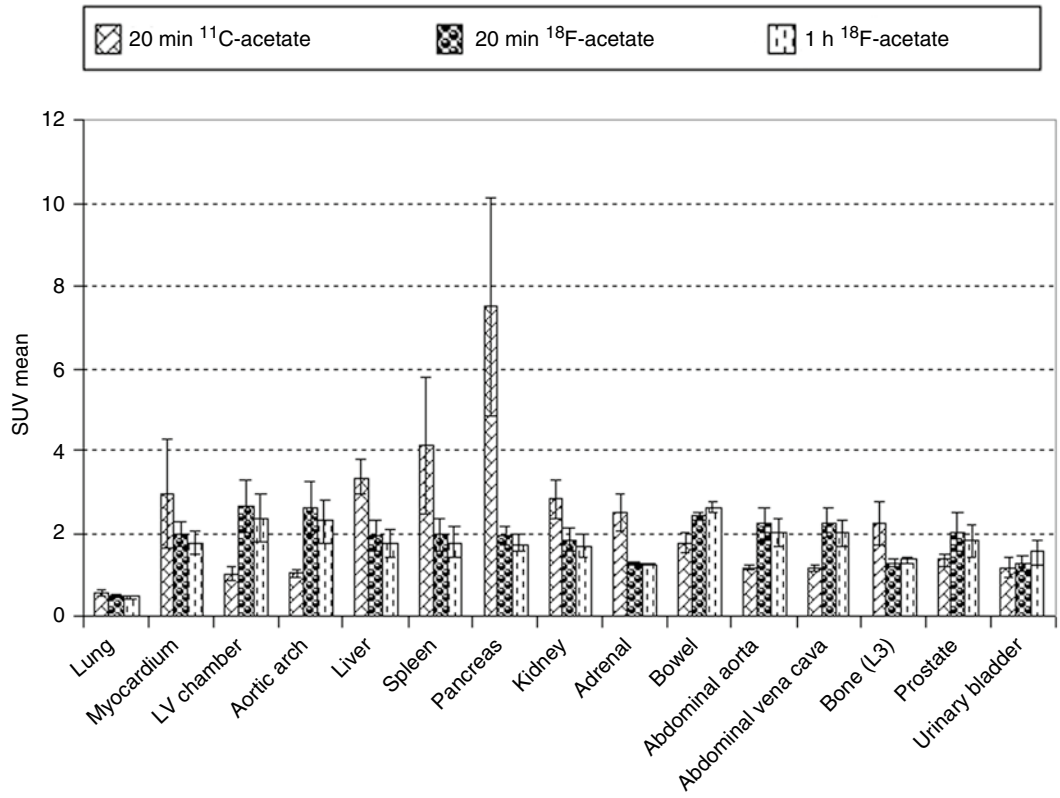

Fig. 10.11 The biodistribution spectrum of ^{18}F-acetate at 20 min and 60 min and ^{11}C-acetate at 20 min in the non-tumor parts of the major organs of five human subjects with known primary and metastatic HCC disease

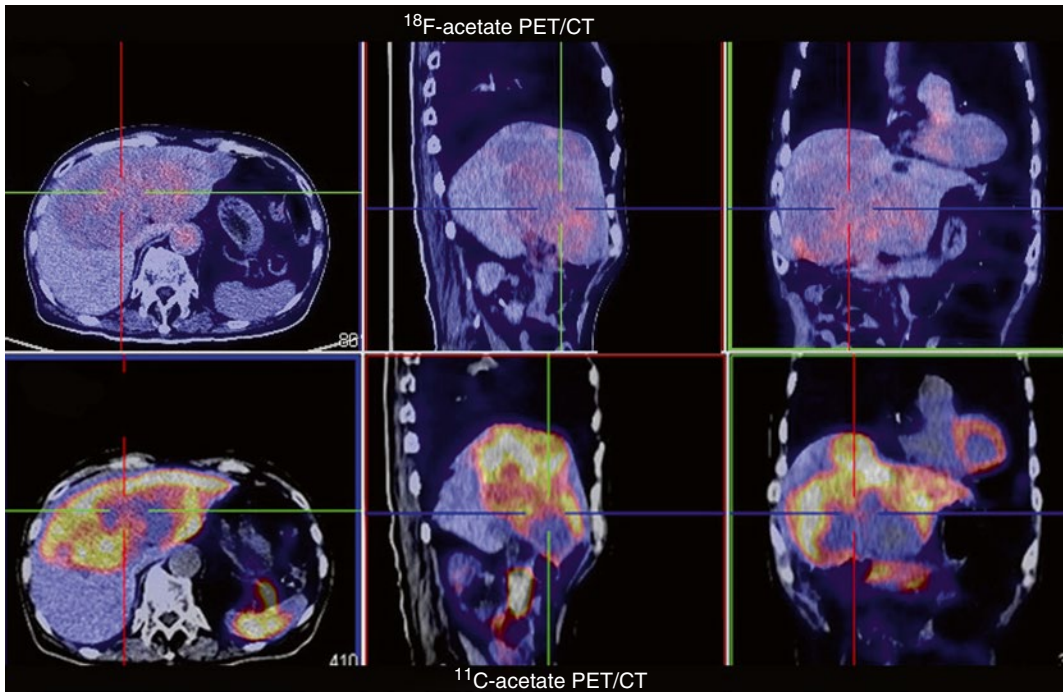

Fig. 10.12 A huge HCC lesion with marked avidity for ^{11}C-acetate but is negative on ^{18}F-acetate PET/CT

Analysis from known biochemical data shows that FAC initially behaves similarly to acetate. Within the mitochondria, it is converted into fluoroacetyl-CoA in the TCA cycle, and then metabolized by citrate synthase to fluorocitrate. However, different from normal ^{11}C-citrate, fluorocitrate binds strongly with the enzyme aconitase and inhibits further oxidative metabolism in the rest of TCA cycle. Because of this strong fluorocitrate-aconitase binding and subsequent metabolic blockage, two major effects different from ^{11}C-citrate are noted. One is impaired clearance of trapped ^{18}F-fluorocitrate from the cells [76]; the other is failure of transport to the cytosol for conversion back to acetyl-CoA and lipid synthesis. The above discussion explains why there is slow clearance of ^{18}F-FAC in the human body. The "blood-pool"-like pattern of ^{18}F-FAC retention on the PET images and negative uptake by the primary and metastatic HCC lesions can all be explained from the standpoint of biochemistry. ^{18}F-FAC is therefore not recommended for use as an alternative tracer for HCC in place of ^{11}C-acetate in human subjects. It is well known that variations in enzyme system, subtype, and abundance are highly species dependent. And this is also the reason for the manifestation of variation in tolerance to the toxic effects of a single substance between species or even among different routes of administration within the same species.

10.2 ^{11}C-Choline and ^{18}F-Choline

10.2.1 ^{11}C-Choline

10.2.1.1 Tumor Metabolism

Choline is involved in methyl group metabolism and lipid transport and is a component of a number of important biological compounds including membrane phospholipids (lecithin, sphingomyelin, and plasmalogen), neurotransmitter (acetylcholine), and platelet activating factor [77].

Haubrich et al. [78] found in animal studies that the major radiolabeled choline activity in brain and other organs measured soon after intravenous injection of choline was biochemically incorporated as phosphorylcholine, an intermediate involved in phospholipid synthesis. Most normal brain cells and neurogenic tumor cells are characterized by the predominance of phosphorylcholine synthesis [79–81]. Phospholipid is the main component of cell membrane production.

10.2.1.2 Application

After intravenous ^{11}C-choline injection, blood clearance of this tracer is very rapid and its biological distribution in tissues reaches a steady state in 5 min. Figure 10.13 shows the PET/CT image of a patient with a left parietal metastatic brain lesion, which is markedly avid for ^{11}C-choline. Unlike ^{18}F-FDG, the background brain uptake of ^{11}C-choline is very low, while the tumor-to-background ratio is very high. It is because ^{11}C-choline cannot penetrate the blood–brain barrier except when it is disrupted. The radioactive choline is rapidly incorporated into tumor cells and phosphorylated to become phosphorylcholine and finally integrated into a phospholipid, namely, phosphatidylcholine [79, 82]. This high ^{11}C-choline uptake correlates with the MRS findings when high content of choline-containing compounds are found in the brain tumors [83, 84].

Besides brain tumors, ^{11}C-choline PET has been investigated for its application in differentiating between lung cancer and tuberculosis as suggested by Hara and associates [85]. They reported that both cancer and tuberculosis have high uptake of ^{18}F-FDG, but the latter has a significantly less degree of ^{11}C-choline uptake compared with the former. However, lung cancer is known to present with a wide spectrum of ^{18}F-FDG metabolic intensities according to cell types and grades of differentiation, while tuberculosis may also metabolize ^{18}F-FDG at various rates depending on the balance between its virulence and the host resistance. Squamous cell carcinoma and high-grade or poorly differentiated adenocarcinomas usually have very high ^{18}F-FDG avidity. Low-grade adenocarcinomas and bronchioloalveolar cell carcinomas have little or no significant activity with either ^{18}F-FDG or ^{11}C-choline. Thus, a low ^{11}C-choline uptake cannot reliably differentiate between low-grade malignancy and low-virulence tuberculosis.

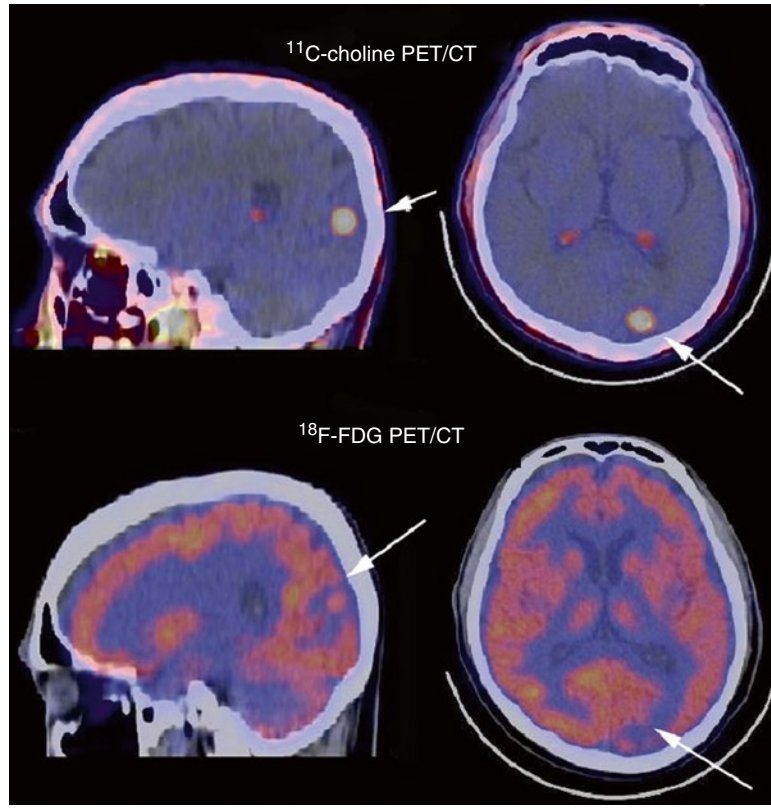

Fig. 10.13 A 50-year-old patient was treated by *X*-knife radiosurgery for brain metastases from lung carcinoma origin. Follow-up ^{18}F-FDG PET/CT 2 years later is unremarkable (*lower row*), but ^{11}C-choline PET/CT shows focally increased ^{11}C-choline activity (*arrows*) at left posterior parietal brain consistent with metastasis (*upper row*)

Prostate carcinoma is another example of tumors having limitations in using ^{18}F-FDG PET for detection due to the low uptake of this tracer by the tumor and the presence of intense excretory tracer activities in the urinary bladder. Gleason score and Ki67 labeling index are known to correlate with tumor cell proliferation in prostate carcinoma [86, 87]. However, its biologic aggressiveness may not be a major factor reflected by choline metabolism in prostate carcinoma [88, 89]. Nonetheless, the efficacy of ^{11}C-choline for localizing primary or metastatic prostate cancer has been studied [22, 90–92]. ^{11}C-choline metabolism is also mildly increased in benign hyperplasia and chronic prostatitis; although lower than a substantial fraction of segments with prostate carcinoma, foci of low ^{11}C-choline activity cannot reliably differentiate between benign causes and low-grade malignancy. In monitoring tumor recurrence after radical prostatectomy, serial serum evaluation of PSA concentration is essential [93–95]. ^{11}C-choline PET has been found valuable in patients suspected of recurrence because of elevated PSA level after prostatectomy, particularly important in differentiating between local and distant disease and subsequent management [96, 97].

10.2.2 ^{18}F-Fluorocholine

The use of ^{11}C-choline is limited only to PET centers that have onsite cyclotrons because of its short half-life (20 min). To facilitate the use of this tracer by other sites with PET scanners only, the development of ^{18}F-fluorocholine (half-life of 110 min) becomes necessary. The feasibility use of ^{18}F-fluorocholine PET for evaluation of prostate cancer has been investigated in details during its early development with respect to tracer kinetics, biochemistry and synthesis, and initial results compared with ^{18}F-FDG [98–101]. ^{18}F-fluorocholine can provide higher resolution images as a result of its shorter positron

length path. DeGrado et al. [102] compared the pharmacokinetics data of ^{18}F-fluorocholine with that of ^{11}C-choline reported by Roivainen et al. [103]. He suggested that ^{11}C-choline was converted by an oxidative metabolism to ^{11}C-betaine followed by subsequent clearance of betaine from the tissue. But ^{18}F-fluorocholine lacked tissue clearance and was metabolically trapped.

Efficacy of ^{18}F-fluorocholine PET has been reported for localization of primary or metastatic prostate carcinoma, as well as disease recurrence in patients after radical treatment [98, 104–107]. In a retrospective study of 156 patients with recurrent prostate carcinoma [108], ^{18}F-fluorocholine PET/CT was reported to have an important impact on the therapeutic strategy.

^{18}F-fluorocholine PET/CT, though less specific and sensitive when compared with ^{11}C-acetate, might serve as an alternative to ^{11}C-acetate in some PET centers for evaluation of prostate cancers and HCC [109, 110], owing to its longer ^{18}F half-life and thus being able to deliver to PET imaging centers without an on-site cyclotron.

10.3 ^{11}C-Methionine

10.3.1 Tumor Metabolism

Another target for functional tumor imaging is to evaluate increased protein metabolism in cancer cells by the use of radiolabeled amino acids. ^{11}C-methionine is the most popular PET tracers used to study amino acid metabolism, through either protein synthesis or amino acid transport across cell membranes. Amino acid transportation is always accompanied by a counter transport process, i.e., a second amino acid using the sodium-dependent transporter system to supply the malignant cells with sufficient nutrients for energy, protein synthesis, and proliferation. The sodium-dependent transporter system such as system A is normally overexpressed in neoplastic cells [111]. ^{11}C-methionine in gliomas is due to increase in the transport to the tumor across the blood–brain barrier [112–115], which is mediated by the sodium-independent L-amino acid carrier in the luminal membrane of endothelial cells, to meet the demands of the accelerated protein and RNA synthesis in malignant tumors [116].

Inflammatory cells in general have a lower protein metabolism relative to glucose metabolism; therefore, imaging with labeled amino acids is less confounded by uptake in inflammatory tissues than is ^{18}F-FDG, viz., more tumor specific.

10.3.2 Application

^{11}C-methionine PET is a useful tool in the diagnosis of brain tumors [117–119]. Similar to ^{11}C-acetate, the background uptake of labeled amino acids in normal brain tissue is low, providing good contrast to the tumors with increased protein metabolism [120]. Figure 10.14 shows the difference in tumor-to-background uptake ratios between ^{11}C-methionine and ^{18}F-FDG PET/CT in a patient with a glioblastoma at the right entorhinal cortex, hippocampus, and subiculum. The advantage in diagnosis is clearly illustrated by the ^{11}C-methionine PET/CT. On detection of primary brain tumors, Ogawa et al. [121] reported that the sensitivity for ^{11}C-methionine PET in 32 patients was 97 % with high-grade tumors and 61 % with low-grade tumors. Mosskin et al. [122] found a patient-based sensitivity of 84 % in a group of patients having stereotactic biopsy proof of pathology. Five patients, however, were false-positive with increased ^{11}C-methionine uptake in non-tumor tissue. Mildly increased ^{11}C-methionine uptake has been reported in inflammation and necrosis [123]. Despite the presence of limitations, clinically useful data have been reported, such as in differentiation between skull base meningiomas and benign neuromas [124] and between glioma and nonneoplastic lesions in patients suspected of brain tumors [125].

The diagnostic performance of PET using ^{11}C-methionine in detecting parathyroid adenoma has been investigated [126–129]. ^{11}C-methionine PET may be helpful in patients with diagnosis of primary hyperparathyroidism when conventional imaging techniques are negative or inconclusive in localizing a parathyroid adenoma [128, 130, 131]. A study of 47 patients with head and neck tumors

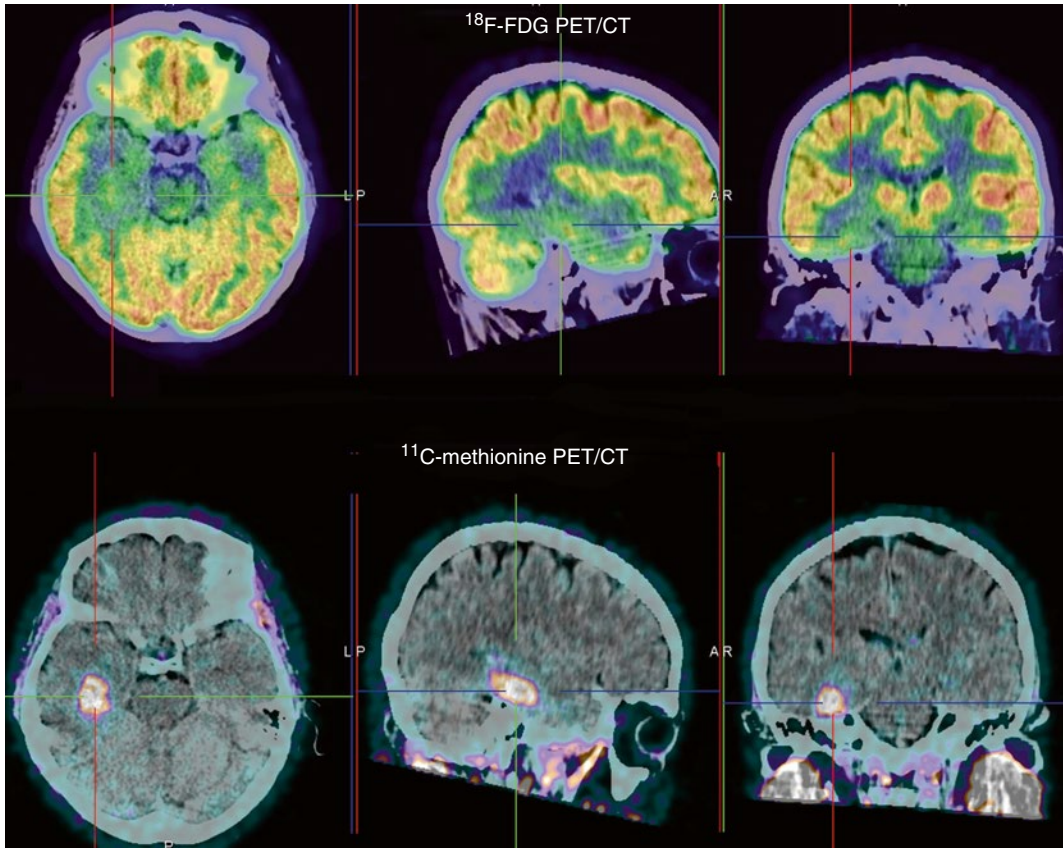

Fig. 10.14 A glioblastoma at the right entorhinal cortex, hippocampus, and subiculum shows increased ^{11}C-methionine metabolism ($SUV_{max} = 4.33$) but only minimally increased ^{18}F-FDG activity

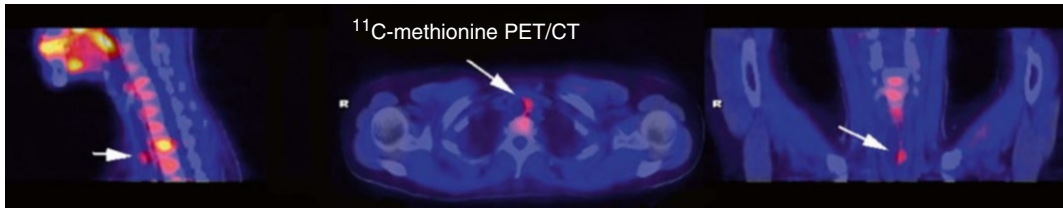

Fig. 10.15 Regional ^{11}C-methionine PET/CT of a recurrent medullary thyroid cancer (*arrows*) in a patient presented with elevated Calcitonin after thyroidectomy

reported that the sensitivity for detection of malignant tumors larger than 1 cm in size by ^{11}C-methionine PET was 91 % [132]. The types of tumor positive on ^{11}C-methionine PET included squamous cell carcinoma, lymphoma, adenocystic carcinoma, lymphoepithelioma, adenocarcinoma, transitional cell carcinoma, and plasmacytoma. As shown in Fig. 10.15, ^{99m}Tc-sestamibi SPECT/CT, CT, MRI, and ^{18}F-FDG PET/CT were all negative in a patient with increased calcitonin after thyroidectomy for medullary carcinoma. A solitary small nodule with increased ^{11}C-methionine uptake was found at the left paratracheal region. Biopsy of the nodule under CT guidance confirmed metastatic medullary carcinoma and the patient underwent further exploration and resection afterwards.

In addition to head and neck cancers, Leskinen-Kallio and associates also reported on

14 patients with suspected breast cancers. They found a positive correlation of ^{11}C-methionine with a large S-phase fraction, reflecting the proliferative rate of malignant breast cancer cells. Both primary and metastatic breast cancer can be effectively imaged but tumors less than 2 cm were negative and the high uptakes in liver and marrow were the known limitations of this tracer in metastatic survey [133].

10.4 ^{18}F-DOPA

10.4.1 Tumor Metabolism

Labeled amino acids or amino acid analogs constitute another important class of PET tracers for tumor imaging of the brain and neuroendocrine pathologies. 3,4-dihydroxy-6-F-18-fluoro-L-phenylalanine (^{18}F-DOPA) is an amino acid analog that is taken up across the blood–brain barrier by a neutral amino acid transporter [134]. It has good image contrast, showing high uptake in tumor tissue and low uptake in the normal brain tissue. The uptake of ^{18}F-DOPA follows the same pathway as that of ^{11}C-methionine [125, 135] for brain tumors. In imaging of neuroendocrine tumors (NET), the NET cells arising from the Amine Precursor Uptake and Decarboxylation (APUD) stem cells show increased ^{18}F-DOPA (an amine precursor) utilization [136]. After intravenous administration, ^{18}F-DOPA is transported to the NET cells via a sodium-independent L-type amino acid transporter [137]. As the enzyme aromatic amino acid decarboxylase is upregulated in these NET cells, ^{18}F-DOPA is converted to ^{18}F-fluorodopamine. It is then transported into the cytoplasmic neurosecretory granules via vesicular monoamine transporter for storage [138, 139]. Some ^{18}F-fluorodopamine is subject to enzymatic degradation in the cytosol and the metabolites leave the cell via diffusion [140]. The degraded products are metabolically active catecholamine such as dopamine, norepinephrine, and epinephrine, which are secreted by the NET cells in the body.

Carbidopa is an inhibitor known to inhibit peripheral conversion of ^{18}F-DOPA into ^{18}F-fluorodopamine [139, 141]. Premedication with carbidopa half an hour before ^{18}F-DOPA injection increases the uptake of the tracer by the tumor and decreases the competitive uptake by the pancreas.

10.4.2 Application

Uptake of ^{18}F-DOPA by brain tumors has been reported to be quite similar to that of ^{11}C-methionine [125, 135]. In a study [142] of 15 patients with newly diagnosed or previously treated low-grade gliomas (WHO grade I or II), ^{18}F-DOPA was positive in all cases of primary and recurrent low-grade gliomas and negative in the patients in remission.

Functional imaging of NETs is challenging because they represent a group of heterogeneous neoplasms originating from various anatomical locations, possessing a variety of biochemical or receptor derangements, and very often of small size at initial presentation. ^{18}F-FDG PET has never been used on a routine basis for imaging of NETs, whereas the diagnostic sensitivity seems to be low for NETs because they usually possess a low proliferation index, slow growth rate, and low glucose consumption [143, 144]. As described above, NET can be detected by the use of biochemical probes for the APUD pathway by ^{18}F-DOPA PET/CT [145–147]. Figure 10.16 shows ^{18}F-DOPA PET/CT images of a pheochromocytoma at the left adrenal gland, with the tumor being markedly avid for the ^{18}F-DOPA tracer. Figure 10.17 shows ^{18}F-DOPA PET/CT images of liver metastasis from pancreatic NET with significantly increased ^{18}F-DOPA uptake.

The presence of prominent molecular biomarkers means that treatment of NET with peptide receptor radionuclide therapy is feasible. In particular, ^{111}indium-labeled somatostatin receptor scintigraphy (^{111}In-SRS) has a wider usage and more frequent acceptance in centers without PET facilities support. SRS is essential to establish the usefulness of therapy with somatostatin analogs for NET; however, it is less desirable for monitoring treatment response during the early stage of treatment due to the frequent occurrence

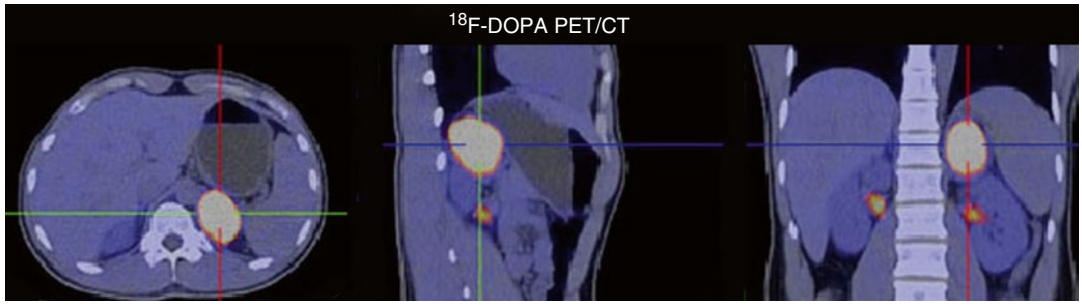

Fig. 10.16 ^{18}F-DOPA PET/CT of a pheochromocytoma of the left adrenal gland

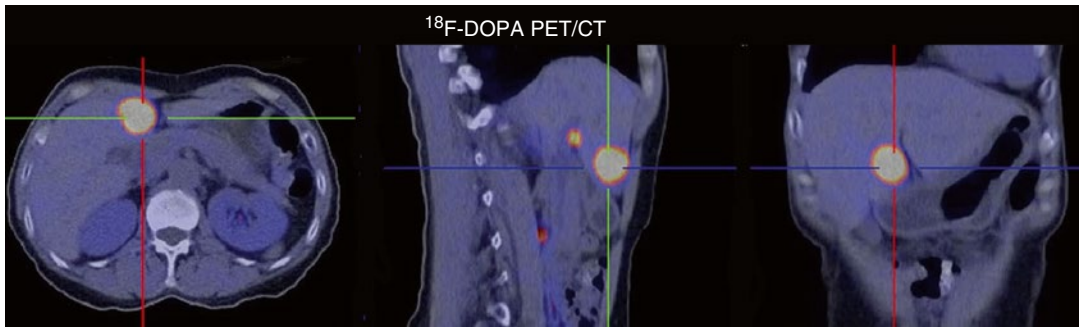

Fig. 10.17 ^{18}F-DOPA PET/CT shows a metastatic liver lesion in a patient with pancreatic neuroendocrine tumor

of upregulation of somatostatin receptors. NET tumor cells may increase the amount of receptors to partially compensate for the treatment effects although tumor metabolism has been attenuated. Other than monitoring therapy, ^{18}F-DOPA PET/CT also performs better than SRS in diagnosis and staging of NETs. On the other hand, in situations where NET lesions have low expression of somatostatin receptors or in cases of nonspecific NET cell types, ^{18}F-DOPA should be the preferred tracer for imaging.

Carcinoid tumors are generally considered as slow growing NETs. ^{18}F-DOPA PET/CT has a high sensitivity (>80 %) for detection of carcinoid tumors [146, 148, 149]. In a study [150] of 21 documented carcinoid patients, ^{18}F-DOPA PET/CT identified carcinoid tumors in 20 patients (patient-based sensitivity: 95 %). The region-based sensitivities of ^{18}F-DOPA PET/CT, CT, SRS, and CT + SRS were 95, 61, 62, and 71 %, respectively, and lesion-based sensitivities were 96, 69, 50, and 72 %, respectively.

10.5 ^{18}F-FLT

10.5.1 Tumor Metabolism

As ^{3}H-thymidine is regarded as the gold standard to measure cell proliferation in vivo, ^{11}C-thymidine has been proposed as a radiotracer for PET imaging of tumor proliferation [151, 152]. However, its metabolic instability circumvents the routine clinical use of this tracer for tumor imaging. 3′-deoxy-3′-^{18}F-fluorothymidine (^{18}F-FLT) is a pyrimidine nucleoside, a structural analog of thymidine and could reflect tumor cell proliferation with high tumor specificity. ^{18}F-FLT permeates the cell membrane by a facilitated transport by sodium-dependent carriers as well as by passive diffusion [153, 154]. Thymidine kinase 1 (TK1) is an enzyme expressed during the DNA synthesis phase of the cell cycle [155–161]. TK1 activity is much higher in proliferating cells than in quiescent cells [159, 162–164]. After membrane transport, ^{18}F-FLT is phosphorylated by TK1 to become ^{18}F-FLT monophosphate and accumulates in the cytosol of the

cells [159]. ^{18}F-FLT acts as a chain terminator [165] because ^{18}F substitution in the 3′-position results in markedly decreased affinity for the pyrimidine transporter [166] and reduced affinity for TK1 as compared to natural thymidine [167]. There is, in fact, only a very small amount of DNA being incorporated with ^{18}F-FLT in cancer cells via the salvage pathway of DNA synthesis [168].

10.5.2 Application

^{18}F-FDG uptake is not tumor specific. Various forms of inflammatory lesions also take up ^{18}F-FDG, and they represent a major cause of false-positive results. In a side-by-side comparative study between ^{18}F-FLT and ^{18}F-FDG PET of a rodent model with induced inflammation [169], ^{18}F-FDG accumulated in the inflamed muscle with higher uptake than the contralateral healthy thigh, while ^{18}F-FLT PET showed symmetric muscle activities in bilateral thighs. ^{18}F-FLT uptake has been shown to reflect the activity of TK1 [170–172], therefore, ^{18}F-FLT uptake correlates strongly with Ki67 index ($r = 0.84 \sim 0.89$, $P < 0.001$) [173–175].

^{18}F-FLT PET has been used for investigation of the diagnosis of primary breast cancer and locoregional metastases. In a study [176] of 12 patients with 14 primary breast cancer lesions (T2–T4), 13 lesions demonstrated focally increased ^{18}F-FLT uptake and 7 out of 8 patients with histologically proven axillary lymph node metastases showed focally increased ^{18}F-FLT uptake. ^{18}F-FLT PET is useful for assessment of proliferation activity and diagnosis in brain glioma [174], lymphoma [172], lung cancer [175, 177] and HCC [178]. Vesselle et al. [175] reported that ^{18}F-FLT PET may play a significant role in the evaluation of indeterminate pulmonary lesions, in the prognostic assessment of resectable non-small cell lung carcinoma (NSCLC) and possibly in the evaluation of NSCLC response to chemotherapy. In 2003, Buck et al. [177] examined 26 patients (18 malignant and 8 benign tumors) with pulmonary nodules on CT using both ^{18}F-FDG and ^{18}F-FLT PET. ^{18}F-FDG PET was found to have a slightly better sensitivity than ^{18}F-FLT (17/18 vs 16/18), while ^{18}F-FLT PET was significantly more specific than ^{18}F-FDG (8/8 vs 4/8) for the detection of lung malignancies. In a pilot study [178] for imaging of proliferation and detection of HCC with ^{18}F-FLT PET, the proliferation marker MIB-1 positively correlated with the mean SUV ($r = 0.66$, $P = 0.02$) of HCC and the sensitivity was 69 % (11/16).

In general, ^{18}F-FLT uptake correlates significantly better with the proliferative activity of a variety of tumors than ^{18}F-FDG. ^{18}F-FLT may be regarded as the more superior PET tracer in specificity for assessment of tumor characterization, growth rate, therapeutic response [179], and outcome. For primary tumor diagnosis, ^{18}F-FLT PET may be less sensitive than ^{18}F-FDG but more accurate for differentiation from benign entities.

10.6 ^{68}Ga-Labeled Somatostatin Analogs

10.6.1 Tumor Metabolism

For neuroendocrine tumors with overexpression of somatostatin receptors (subtypes 1–5 or SSTR1-5) [180–182] on the tumor cell surface, radiolabeled somatostatin analogs such as ^{111}In-octreotide, ^{68}Ga-tetraazacyclododecane-tetraacetic acid-octreotide (DOTATOC), ^{68}Ga-DOTA-octreotate (DOTATATE) [183, 184], and ^{68}Ga-Lanreotide or ^{68}Ga-DOTA-1-NaI3-octreotide (DOTANOC) [183] may all have strong binding affinity to these receptors. All four kinds of ^{68}Ga-labeled somatostatin analogs have different affinities for different receptor subtypes. For instance, DOTATOC and DOTATATE are able to induce SSTR2 internalization; DOTA-lanreotide binds SSTR5 selectively; DOTANOC shows a high affinity for SSTR2, 3 and 5 [185–187]. Therefore, NET imaging with radiolabeled somatostatin analogs depends strongly on both receptor density and affinity.

10.6.2 Application

^{68}Ga-DOTATOC, ^{68}Ga-DOTANOC, and ^{68}Ga-DOTATATE PET not only offer high sensitivity for the diagnosis of NETs, they also

have proven value in staging by detection of regional and distant metastases, as well as in guidance and monitoring of treatment [188–190]. Owing to the high resolution of PET, ^{68}Ga-DOTATOC has a sensitivity of >90 %, which is significantly higher than that of traditional ^{111}In-SRS [191–193]. In a comparative study [194] of ^{68}Ga-DOTATATE and ^{18}F-FDG PET/CT on 38 consecutive patients with a diagnosis of primary or recurrent NET, the sensitivity of ^{68}Ga-DOTATATE PET/CT was 82 % and that of ^{18}F-FDG PET/CT was 66 %. The sensitivity of combined ^{68}Ga-DOTATATE and ^{18}F-FDG PET/CT was 92 %. ^{68}Ga-DOTATATE PET/CT is especially superior to ^{18}F-FDG for evaluation of well-differentiated NET. ^{68}Ga-DOTATOC PET/CT is more useful as a functional tool than the structural information from CT and MRI in planning radiotherapy and is especially useful for detection of osseous infiltration [195]. In the evaluation of prostate cancer and related bone metastases, DOTATOC-affine somatostatin receptors (subtypes 2 and 5) can be visualized with ^{68}Ga-DOTATOC PET/CT [196].

The large number of published data on a variety of cancer cells with different biochemical requirement for energy consumption, replication, and growth demonstrate a clear interest in the research of non-^{18}F-FDG PET tracers. An understanding of their metabolic pathways and related biochemical reactions is the key to the success of development in functional evaluation of these tumors.

References

1. Swinnen JV, et al. Stimulation of tumor-associated fatty acid synthase expression by growth factor activation of the sterol regulatory element-binding protein pathway. Oncogene. 2000;19:5173–81.
2. Henes CG, et al. Assessment of myocardial oxidative metabolic reserve with positron emission tomography and carbon-11 acetate. J Nucl Med. 1989;30:1489–99.
3. Sun KT, et al. Compartment model for measuring myocardial oxygen consumption using [1-11C]acetate. J Nucl Med. 1997;38:459–66.
4. Sun KT, et al. Simultaneous measurement of myocardial oxygen consumption and blood flow using [1-carbon-11]acetate. J Nucl Med. 1998;39:272–80.
5. Brown MA, et al. Validity of estimates of myocardial oxidative metabolism with carbon-11 acetate and positron emission tomography despite altered patterns of substrate utilization. J Nucl Med. 1989;30:187–93.
6. Soloviev D, et al. PET imaging with 11C-acetate in prostate cancer: a biochemical, radiochemical and clinical perspective. Eur J Nucl Med Mol Imaging. 2008;35:942–9.
7. Beynen AC, et al. The effects of lactate and acetate on fatty acid and cholesterol biosynthesis by isolated rat hepatocytes. Int J Biochem. 1982;14:165–9.
8. Ferezou J, et al. Evidence for different isotopic enrichments of acetyl-CoA used for cholesterol synthesis in the liver and intestine: a study in the rat by mass fragmentography after intravenous infusion of [13C]acetate. Biochim Biophys Acta. 1986;875:227–35.
9. Yoshimoto M, et al. Characterization of acetate metabolism in tumor cells in relation to cell proliferation: acetate metabolism in tumor cells. Nucl Med Biol. 2001;28:117–22.
10. Swinnen JV, et al. Fatty acid synthase drives the synthesis of phospholipids partitioning into detergent-resistant membrane microdomains. Biochem Biophys Res Commun. 2003;302:898–903.
11. Swinnen JV, et al. Androgen regulation of the messenger RNA encoding diazepam-binding inhibitor/acyl-CoA-binding protein in the human prostatic adenocarcinoma cell line LNCaP. Mol Cell Endocrinol. 1994;104:153–62.
12. Swinnen JV, et al. Androgen regulation of the messenger RNA encoding diazepam-binding inhibitor/acyl-CoA-binding protein in the rat. Mol Cell Endocrinol. 1996;118:65–70.
13. Shreve P, et al. Carbon-11-acetate PET imaging in renal disease. J Nucl Med. 1995;36:1595–601.
14. Oyama N, et al. 11C-acetate PET imaging of prostate cancer. J Nucl Med. 2002;43:181–6.
15. Dimitrakopoulou-Strauss A, Strauss LG. PET imaging of prostate cancer with 11C-acetate. J Nucl Med. 2003;44:556–8.
16. Oyama N, et al. 11C-acetate PET imaging of prostate cancer: detection of recurrent disease at PSA relapse. J Nucl Med. 2003;44:549–55.
17. Swinnen JV, Verhoeven G. Androgens and the control of lipid metabolism in human prostate cancer cells. J Steroid Biochem Mol Biol. 1998;65:191–8.
18. Swinnen JV, et al. Androgens stimulate fatty acid synthase in the human prostate cancer cell line LNCaP. Cancer Res. 1997;57:1086–90.
19. Swinnen JV. Increased lipogenesis in steroid-responsive cancer cells: mechanisms of regulation, role in cancer cell biology and perspectives on clinical applications. Verh K Acad Geneeskd Belg. 2001;63:321–33.
20. Kotzerke J, et al. Carbon-11 acetate positron emission tomography can detect local recurrence of prostate cancer. Eur J Nucl Med Mol Imaging. 2002;29:1380–4.
21. Albrecht S, et al. (11)C-acetate PET in the early evaluation of prostate cancer recurrence. Eur J Nucl Med Mol Imaging. 2007;34:185–96.

22. Kotzerke J, et al. Intraindividual comparison of [11C]acetate and [11C]choline PET for detection of metastases of prostate cancer. Nuklearmedizin. 2003;42:25–30.
23. Reske SN, et al. PET and PET/CT in relapsing prostate carcinoma. Urologe A. 2006;45:1240, 1242–1244, 1246–1248, 1250.
24. Fricke E, et al. Positron emission tomography with 11C-acetate and 18F-FDG in prostate cancer patients. Eur J Nucl Med Mol Imaging. 2003; 30:607–11.
25. Ho CL, et al. Dual-tracer PET/CT in renal angiomyolipoma and subtypes of renal cell carcinoma. Clin Nucl Med. 2012;37:1075–82.
26. Schoder H, et al. Initial results with (11)C-acetate positron emission tomography/computed tomography (PET/CT) in the staging of urinary bladder cancer. Mol Imaging Biol. 2012;14:245–51.
27. Kotzerke J, et al. [1-(11)C]acetate uptake is not increased in renal cell carcinoma. Eur J Nucl Med Mol Imaging. 2007;34:884–8.
28. Oyama N, et al. 11C-Acetate PET imaging for renal cell carcinoma. Eur J Nucl Med Mol Imaging. 2009;36:422–7.
29. Ho CL, et al. 11C-acetate PET/CT in multicentric angiomyolipoma of the kidney. Clin Nucl Med. 2011;36:407–8.
30. Okazumi S, et al. Evaluation of liver tumors using fluorine-18-fluorodeoxyglucose PET: characterization of tumor and assessment of effect of treatment. J Nucl Med. 1992;33:333–9.
31. Khan MA, et al. Positron emission tomography scanning in the evaluation of hepatocellular carcinoma. J Hepatol. 2000;32:792–7.
32. Schroder O, et al. Limited value of fluorine-18-fluorodeoxyglucose PET for the differential diagnosis of focal liver lesions in patients with chronic hepatitis C virus infection. Nuklearmedizin. 1998; 37:279–85.
33. Delbeke D, et al. Evaluation of benign vs malignant hepatic lesions with positron emission tomography. Arch Surg. 1998;133:510–5; discussion 515–6.
34. Trojan J, et al. Fluorine-18 FDG positron emission tomography for imaging of hepatocellular carcinoma. Am J Gastroenterol. 1999;94:3314–9.
35. Ho CL, et al. 11C-acetate PET imaging in hepatocellular carcinoma and other liver masses. J Nucl Med. 2003;44:213–21.
36. Chen S, Feng D. Noninvasive quantification of the differential portal and arterial contribution to the liver blood supply from PET measurements using the 11C-acetate kinetic model. IEEE Trans Biomed Eng. 2004;51:1579–85.
37. Chen S, et al. Tracer kinetic modeling of 11C-acetate applied in the liver with positron emission tomography. IEEE Trans Med Imaging. 2004;23:426–32.
38. Chen S, et al. Functional imaging techniques for the evaluation of hepatocellular carcinoma using dynamic 11C-acetate PET imaging. Curr Med Imaging Rev. 2006;2:205–14.
39. Chen S, Feng D. Evaluation of hepatocellular carcinoma with dynamic 11C-acetate PET: a dual-modeling method. IEEE Trans Nucl Sci. 2008; 55:999–1007.
40. Chen S, Feng D. Novel parameter estimation methods for 11C-acetate dual-input liver model with dynamic PET. IEEE Trans Biomed Eng. 2006;53:967–73.
41. Ho CL, et al. 11C acetate and 18F FDG PET-CT imaging in hepatocellular carcinoma less than 2 cm. J Nucl Med. 2005;46:46.
42. Ho CL, et al. 11C-acetate and 18F-FDG PET/CT characteristics for a cohort of asymptomatic patients with non-specific CT/MR findings subsequently diagnosed of intrahepatic cholangiocarinoma. J Nucl Med. 2011;52:95P.
43. Ho CL, et al. Education and imaging. Hepatobiliary and pancreatic: imaging for hepatic angiomyolipoma. J Gastroenterol Hepatol. 2010;25:1589.
44. Ho CL, et al. Dual-tracer PET/CT imaging in evaluation of metastatic hepatocellular carcinoma. J Nucl Med. 2007;48:902–9.
45. Katyal S, et al. Extrahepatic metastases of hepatocellular carcinoma. Radiology. 2000;216:698–703.
46. Kawaoka T, et al. FDG positron emission tomography/computed tomography for the detection of extrahepatic metastases from hepatocellular carcinoma. Hepatol Res. 2009;39:134–42.
47. Ho CL, et al. PET/CT characteristics of isolated bone metastases in hepatocellular carcinoma. Radiology. 2011;258:515–23.
48. Li S, et al. Comparison of (11)C-acetate positron emission tomography and (67)Gallium citrate scintigraphy in patients with hepatocellular carcinoma. Liver Int. 2006;26:920–7.
49. Park JW, et al. A prospective evaluation of 18F-FDG and 11C-acetate PET/CT for detection of primary and metastatic hepatocellular carcinoma. J Nucl Med. 2008;49:1912–21.
50. Salem N, et al. PET imaging of hepatocellular carcinoma with 2-deoxy-2[18F]fluoro-D-glucose, 6-deoxy-6[18F] fluoro-D-glucose, [1-11C]-acetate and [N-methyl-11C]-choline. Q J Nucl Med Mol Imaging. 2009;53:144–56.
51. Kuang Y, et al. A colorimetric assay method to measure acetyl-CoA synthetase activity: application to woodchuck model of hepatitis virus-induced hepatocellular carcinoma. J Biochem Biophys Methods. 2007;70:649–55.
52. Yun M, et al. The importance of acetyl coenzyme A synthetase for 11C-acetate uptake and cell survival in hepatocellular carcinoma. J Nucl Med. 2009;50:1222–8.
53. Tsuchida T, et al. Grading of brain glioma with 1-11C-acetate PET: comparison with 18F-FDG PET. Nucl Med Biol. 2008;35:171–6.
54. Yamamoto Y, et al. 11C-acetate PET in the evaluation of brain glioma: comparison with 11C-methionine and 18F-FDG-PET. Mol Imaging Biol. 2008;10:281–7.

55. Liu RS, et al. PET imaging of brain astrocytoma with 1-11C-acetate. Eur J Nucl Med Mol Imaging. 2006;33:420–7.
56. Liu RS, et al. 1-11C-acetate versus 18F-FDG PET in detection of meningioma and monitoring the effect of gamma-knife radiosurgery. J Nucl Med. 2010;51:883–91.
57. Higashi K, et al. 11C-acetate PET imaging of lung cancer: comparison with 18F-FDG PET and 99mTc-MIBI SPET. Eur J Nucl Med Mol Imaging. 2004;31:13–21.
58. Nomori H, et al. 11C-acetate can be used in place of 18F-fluorodeoxyglucose for positron emission tomography imaging of non-small cell lung cancer with higher sensitivity for well-differentiated adenocarcinoma. J Thorac Oncol. 2008;3:1427–32.
59. Boccadoro M, Pileri A. Diagnosis, prognosis, and standard treatment of multiple myeloma. Hematol Oncol Clin North Am. 1997;11:111–31.
60. Castellani M, et al. The prognostic value of F-18 fluorodeoxyglucose bone marrow uptake in patients with recent diagnosis of multiple myeloma: a comparative study with Tc-99m sestamibi. Clin Nucl Med. 2010;35:1–5.
61. Mahfouz T, et al. 18F-fluorodeoxyglucose positron emission tomography contributes to the diagnosis and management of infections in patients with multiple myeloma: a study of 165 infectious episodes. J Clin Oncol. 2005;23:7857–63.
62. Hillner BE, et al. Relationship between cancer type and impact of PET and PET/CT on intended management: findings of the national oncologic PET registry. J Nucl Med. 2008;49:1928–35.
63. Shortt CP, et al. Whole-body MRI versus PET in assessment of multiple myeloma disease activity. AJR Am J Roentgenol. 2009;192:980–6.
64. Ho CL, et al. Preliminary assessment of 11C-acetate and 18F-FDG PET/CT for the diagnosis and management of multiple myeloma. J Nucl Med. 2011;52:110P.
65. Ho CL, et al. Added value of 11C-acetate PET/CT to 18F-FDG for the management of myeloma. J Nucl Med. 2012;53:155P.
66. Lee SM, et al. Incidental finding of an 11C-acetate PET-positive multiple myeloma. Ann Nucl Med. 2010;24:41–4.
67. Jeong JM, et al. Synthesis of no-carrier-added [18F] fluoroacetate. J Labelled Comp Radiopharm. 1997;34:395–9.
68. Sun LQ, et al. New approach to fully automated synthesis of sodium [18F]fluoroacetate – a simple and fast method using a commercial synthesizer. Nucl Med Biol. 2006;33:153–8.
69. Ponde DE, et al. 18F-fluoroacetate: a potential acetate analog for prostate tumor imaging–in vivo evaluation of 18F-fluoroacetate versus 11C-acetate. J Nucl Med. 2007;48:420–8.
70. Richter S, et al. [18F]fluoroacetate and radiopharmacological characterization in rats and tumor-xenografted mice. Curr Radiopharm. 2008;1:103–9.
71. Ho CL, et al. [18F]fluoroacetate positron emission tomography for hepatocellular carcinoma and metastases: an alternative tracer for [11C]acetate? Mol Imaging. 2012;11:229–39.
72. Nishii R, et al. Pharmacokinetics, metabolism, biodistribution, radiation dosimetry, and toxicology of (18)F-fluoroacetate ((18)F-FACE) in non-human primates. Mol Imaging Biol. 2012;14(2):213–24.
73. Lindhe O, et al. [(18)F]fluoroacetate is not a functional analogue of [(11)C]acetate in normal physiology. Eur J Nucl Med Mol Imaging. 2009; 36:1453–9.
74. Peters R. Some metabolic aspects of fluoroacetate especially related to fluorocitrate. Ciba Found Symp. 1971;2:55–76.
75. Matthies A, et al. Imaging of prostate cancer metastases with 18F-fluoroacetate using PET/CT. Eur J Nucl Med Mol Imaging. 2004;31:797.
76. Goncharov NV, et al. Toxicology of fluoroacetate: a review, with possible directions for therapy research. J Appl Toxicol. 2006;26:148–61.
77. Canty DJ, Zeisel SH. Lecithin and choline in human health and disease. Nutr Rev. 1994;52:327–39.
78. Haubrich DR, et al. Distribution and metabolism of intravenously administered choline[methyl- 3-H] and synthesis in vivo of acetylcholine in various tissues of guinea pigs. J Pharmacol Exp Ther. 1975; 193:246–55.
79. George TP, et al. Phosphatidylcholine biosynthesis in cultured glioma cells: evidence for channeling of intermediates. Biochim Biophys Acta. 1989; 1004:283–91.
80. Yavin E. Regulation of phospholipid metabolism in differentiating cells from rat brain cerebral hemispheres in culture. Patterns of acetylcholine phosphocholine, and choline phosphoglycerides labeling from (methyl-14C)choline. J Biol Chem. 1976;251:1392–7.
81. Hara T, et al. PET imaging of brain tumor with [methyl-11C]choline. J Nucl Med. 1997;38:842–7.
82. Liscovitch M, et al. Differential regulation of phosphatidylcholine biosynthesis by 12-O-tetradecanoylphorbol-13-acetate and diacylglycerol in NG108-15 neuroblastoma x glioma hybrid cells. J Biol Chem. 1987;262:17487–91.
83. Alger JR, et al. Metabolism of human gliomas: assessment with H-1 MR spectroscopy and F-18 fluorodeoxyglucose PET. Radiology. 1990;177:633–41.
84. Fulham MJ, et al. Mapping of brain tumor metabolites with proton MR spectroscopic imaging: clinical relevance. Radiology. 1992;185:675–86.
85. Hara T, et al. Uptake rates of 18F-fluorodeoxyglucose and 11C-choline in lung cancer and pulmonary tuberculosis: a positron emission tomography study. Chest. 2003;124:893–901.
86. Breeuwsma AJ, et al. In vivo uptake of [11C]choline does not correlate with cell proliferation in human prostate cancer. Eur J Nucl Med Mol Imaging. 2005;32:668–73.

87. Farsad M, et al. Detection and localization of prostate cancer: correlation of (11)C-choline PET/CT with histopathologic step-section analysis. J Nucl Med. 2005;46:1642–9.
88. Reske SN, et al. Imaging prostate cancer with 11C-choline PET/CT. J Nucl Med. 2006; 47:1249–54.
89. Richter JA, et al. Dual tracer 11C-choline and FDG-PET in the diagnosis of biochemical prostate cancer relapse after radical treatment. Mol Imaging Biol. 2010;12:210–7.
90. Picchio M, et al. [11C]Choline PET/CT detection of bone metastases in patients with PSA progression after primary treatment for prostate cancer: comparison with bone scintigraphy. Eur J Nucl Med Mol Imaging. 2012;39:13–26.
91. Kotzerke J, et al. Experience with carbon-11 choline positron emission tomography in prostate carcinoma. Eur J Nucl Med. 2000;27:1415–9.
92. de Jong IJ, et al. Preoperative staging of pelvic lymph nodes in prostate cancer by 11C-choline PET. J Nucl Med. 2003;44:331–5.
93. Grall J, Corbel L. PSA and benign prostatic hyperplasia. Ann Urol (Paris). 2004;38 Suppl 2:S43–5.
94. Scattoni V, et al. Detection of lymph-node metastases with integrated [11C]choline PET/CT in patients with PSA failure after radical retropubic prostatectomy: results confirmed by open pelvic-retroperitoneal lymphadenectomy. Eur Urol. 2007;52: 423–9.
95. Rinnab L, et al. Evaluation of [11C]-choline positron-emission/computed tomography in patients with increasing prostate-specific antigen levels after primary treatment for prostate cancer. BJU Int. 2007;100:786–93.
96. Reske SN, et al. [11C]choline PET/CT imaging in occult local relapse of prostate cancer after radical prostatectomy. Eur J Nucl Med Mol Imaging. 2008;35:9–17.
97. de Jong IJ, et al. 11C-choline positron emission tomography for the evaluation after treatment of localized prostate cancer. Eur Urol. 2003;44:32–8; discussion 38–9.
98. Graute V, et al. Relationship between PSA kinetics and [18F]fluorocholine PET/CT detection rates of recurrence in patients with prostate cancer after total prostatectomy. Eur J Nucl Med Mol Imaging. 2012;39:271–82.
99. Hara T, et al. Development of (18) F-fluoroethylcholine for cancer imaging with PET: synthesis, biochemistry, and prostate cancer imaging. J Nucl Med. 2002;43:187–99.
100. Beheshti M, et al. Detection of bone metastases in patients with prostate cancer by 18F fluorocholine and 18F fluoride PET-CT: a comparative study. Eur J Nucl Med Mol Imaging. 2008;35:1766–74.
101. Beheshti M, et al. 18F choline PET/CT in the preoperative staging of prostate cancer in patients with intermediate or high risk of extracapsular disease: a prospective study of 130 patients. Radiology. 2010;254:925–33.
102. DeGrado TR, et al. Pharmacokinetics and radiation dosimetry of 18F-fluorocholine. J Nucl Med. 2002;43:92–6.
103. Roivainen A, et al. Blood metabolism of [methyl-11C]choline; implications for in vivo imaging with positron emission tomography. Eur J Nucl Med. 2000;27:25–32.
104. Beheshti M, et al. The use of F-18 choline PET in the assessment of bone metastases in prostate cancer: correlation with morphological changes on CT. Mol Imaging Biol. 2009;11:446–54.
105. Kwee SA, et al. Localization of primary prostate cancer with dual-phase 18F-fluorocholine PET. J Nucl Med. 2006;47:262–9.
106. Pelosi E, et al. Role of whole-body 18F-choline PET/CT in disease detection in patients with biochemical relapse after radical treatment for prostate cancer. Radiol Med. 2008;113:895–904.
107. Bauman G, et al. 18F-fluorocholine for prostate cancer imaging: a systematic review of the literature. Prostate Cancer Prostatic Dis. 2012;15: 45–55.
108. Soyka JD, et al. Clinical impact of 18F-choline PET/CT in patients with recurrent prostate cancer. Eur J Nucl Med Mol Imaging. 2012;39:936–43.
109. Talbot JN, et al. Detection of hepatocellular carcinoma with PET/CT: a prospective comparison of 18F-fluorocholine and 18F-FDG in patients with cirrhosis or chronic liver disease. J Nucl Med. 2010;51:1699–706.
110. Talbot JN, et al. PET/CT in patients with hepatocellular carcinoma using [(18)F]fluorocholine: preliminary comparison with [(18)F]FDG PET/CT. Eur J Nucl Med Mol Imaging. 2006;33:1285–9.
111. Bading JR, et al. System A amino acid transport in cultured human tumor cells: implications for tumor imaging with PET. Nucl Med Biol. 1996; 23:779–86.
112. Bergstrom M, et al. Comparison of the accumulation kinetics of L-(methyl-11C)-methionine and D-(methyl-11C)-methionine in brain tumors studied with positron emission tomography. Acta Radiol. 1987;28:225–9.
113. Christensen HN. Role of amino acid transport and countertransport in nutrition and metabolism. Physiol Rev. 1990;70:43–77.
114. Knudsen GM, et al. Asymmetrical transport of amino acids across the blood–brain barrier in humans. J Cereb Blood Flow Metab. 1990; 10:698–706.
115. Sanchezdel Pino MM, et al. Neutral amino acid transport characterization of isolated luminal and abluminal membranes of the blood-brain barrier. J Biol Chem. 1995;270:14913–8.
116. Schober O, et al. Non selective transport of [11C-methyl]-L-and D-methionine into a malignant glioma. Eur J Nucl Med. 1987;13:103–5.
117. Derlon JM, et al. [11C]L-methionine uptake in gliomas. Neurosurgery. 1989;25:720–8.
118. Ogawa T, et al. Clinical value of PET with 18F-fluorodeoxyglucose and L-methyl-11C-methionine

for diagnosis of recurrent brain tumor and radiation injury. Acta Radiol. 1991;32:197–202.
119. Ogawa T, et al. Carbon-11-methionine PET evaluation of intracerebral hematoma: distinguishing neoplastic from non-neoplastic hematoma. J Nucl Med. 1995;36:2175–9.
120. Chung JK, et al. Usefulness of 11C-methionine PET in the evaluation of brain lesions that are hypo- or isometabolic on 18F-FDG PET. Eur J Nucl Med Mol Imaging. 2002;29:176–82.
121. Ogawa T, et al. Cerebral glioma: evaluation with methionine PET. Radiology. 1993;186:45–53.
122. Mosskin M, et al. Positron emission tomography with 11C-methionine of intracranial tumours compared with histology of multiple biopsies. Acta Radiol Suppl. 1986;369:157–60.
123. Kubota K, et al. Differential diagnosis of AH109A tumor and inflammation by radioscintigraphy with L-[methyl-11C]methionine. Jpn J Cancer Res. 1989;80:778–82.
124. Nyberg G, et al. PET-methionine of skull base neuromas and meningiomas. Acta Otolaryngol. 1997;117:482–9.
125. Herholz K, et al. 11C-methionine PET for differential diagnosis of low-grade gliomas. Neurology. 1998;50:1316–22.
126. Otto D, et al. Pre-operative localisation of hyperfunctional parathyroid tissue with 11C-methionine PET. Eur J Nucl Med Mol Imaging. 2004;31:1405–12.
127. Beggs AD, Hain SF. Use of co-registered 11C-methionine PET and computed tomography for the localisation of parathyroid adenomas. Eur J Nucl Med Mol Imaging. 2003;30:1602.
128. Beggs AD, Hain SF. Localization of parathyroid adenomas using 11C-methionine positron emission tomography. Nucl Med Commun. 2005;26:133–6.
129. Tang BN, et al. Accurate pre-operative localization of pathological parathyroid glands using 11C-methionine PET/CT. Contrast Media Mol Imaging. 2008;3:157–63.
130. Caldarella C, et al. Diagnostic performance of positron emission tomography using (11)C-methionine in patients with suspected parathyroid adenoma: a meta-analysis. Endocrine. 2013;43(1):78–83.
131. Cook GJ, et al. [11C]Methionine positron emission tomography for patients with persistent or recurrent hyperparathyroidism after surgery. Eur J Endocrinol. 1998;139:195–7.
132. Leskinen-Kallio S, et al. Imaging of head and neck tumors with positron emission tomography and [11C]methionine. Int J Radiat Oncol Biol Phys. 1994;30:1195–9.
133. Leskinen-Kallio S, et al. Uptake of 11C-methionine in breast cancer studied by PET. An association with the size of S-phase fraction. Br J Cancer. 1991;64:1121–4.
134. Schiepers C, et al. 18F-FDOPA kinetics in brain tumors. J Nucl Med. 2007;48:1651–61.
135. Becherer A, et al. Brain tumour imaging with PET: a comparison between [18F]fluorodopa and [11C] methionine. Eur J Nucl Med Mol Imaging. 2003;30:1561–7.
136. Minn H, et al. 18F-FDOPA: a multiple-target molecule. J Nucl Med. 2009;50:1915–8.
137. Fiebrich HB, et al. Total 18F-dopa PET tumour uptake reflects metabolic endocrine tumour activity in patients with a carcinoid tumour. Eur J Nucl Med Mol Imaging. 2011;38:1854–61.
138. Koopmans KP, et al. Molecular imaging in neuroendocrine tumors: molecular uptake mechanisms and clinical results. Crit Rev Oncol Hematol. 2009;71:199–213.
139. Neels OC, et al. Manipulation of [11C]-5-hydroxytryptophan and 6-[18F]fluoro-3,4-dihydroxy-L-phenylalanine accumulation in neuroendocrine tumor cells. Cancer Res. 2008;68:7183–90.
140. Eisenhofer G, et al. Understanding catecholamine metabolism as a guide to the biochemical diagnosis of pheochromocytoma. Rev Endocr Metab Disord. 2001;2:297–311.
141. Plathow C, Weber WA. Tumor cell metabolism imaging. J Nucl Med. 2008;49 Suppl 2:43S–63.
142. Tripathi M, et al. Comparative evaluation of F-18 FDOPA, F-18 FDG, and F-18 FLT-PET/CT for metabolic imaging of low grade gliomas. Clin Nucl Med. 2009;34:878–83.
143. Adams S, et al. Metabolic (PET) and receptor (SPET) imaging of well- and less well-differentiated tumours: comparison with the expression of the Ki-67 antigen. Nucl Med Commun. 1998;19:641–7.
144. Belhocine T, et al. Fluorodeoxyglucose positron emission tomography and somatostatin receptor scintigraphy for diagnosing and staging carcinoid tumours: correlations with the pathological indexes p53 and Ki-67. Nucl Med Commun. 2002;23:727–34.
145. Becherer A, et al. Imaging of advanced neuroendocrine tumors with (18)F-FDOPA PET. J Nucl Med. 2004;45:1161–7.
146. Hoegerle S, et al. Whole-body 18F dopa PET for detection of gastrointestinal carcinoid tumors. Radiology. 2001;220:373–80.
147. Cheng T, et al. Dual-tracer (18F-FDG and 18F-DOPA) PET/CT in evaluation of neuroendocrine tumors: an Asian study. J Nucl Med. 2011;52:167P.
148. Koopmans KP, et al. Improved staging of patients with carcinoid and islet cell tumors with 18F-dihydroxy-phenyl-alanine and 11C-5-hydroxy-tryptophan positron emission tomography. J Clin Oncol. 2008;26:1489–95.
149. Koopmans KP, et al. Staging of carcinoid tumours with 18F-DOPA PET: a prospective, diagnostic accuracy study. Lancet Oncol. 2006;7:728–34.
150. Yakemchuk VN, et al. PET/CT using (1)(8) F-FDOPA provides improved staging of carcinoid tumor patients in a Canadian setting. Nucl Med Commun. 2012;33:322–30.
151. Martiat P, et al. In vivo measurement of carbon-11 thymidine uptake in non-Hodgkin's lymphoma using positron emission tomography. J Nucl Med. 1988;29:1633–7.

152. Mankoff DA, et al. Kinetic analysis of 2-[11C]thymidine PET imaging studies: validation studies. J Nucl Med. 1999;40:614–24.
153. Belt JA, et al. Nucleoside transport in normal and neoplastic cells. Adv Enzyme Regul. 1993;33:235–52.
154. Mackey JR, et al. Functional nucleoside transporters are required for gemcitabine influx and manifestation of toxicity in cancer cell lines. Cancer Res. 1998;58:4349–57.
155. Arner ES, et al. Selective assays for thymidine kinase 1 and 2 and deoxycytidine kinase and their activities in extracts from human cells and tissues. Biochem Biophys Res Commun. 1992;188:712–8.
156. Langen P, et al. 3′-Deoxy-3′-fluorothymidine, a new selective inhibitor of DNA-synthesis. Acta Biol Med Ger. 1969;23:759–66.
157. Matthes E, et al. Phosphorylation, anti-HIV activity and cytotoxicity of 3′-fluorothymidine. Biochem Biophys Res Commun. 1988;153:825–31.
158. Munch-Petersen B, et al. Diverging substrate specificity of pure human thymidine kinases 1 and 2 against antiviral dideoxynucleosides. J Biol Chem. 1991;266:9032–8.
159. Sherley JL, Kelly TJ. Regulation of human thymidine kinase during the cell cycle. J Biol Chem. 1988;263:8350–8.
160. Kong XB, et al. Comparisons of anti-human immunodeficiency virus activities, cellular transport, and plasma and intracellular pharmacokinetics of 3′-fluoro-3′-deoxythymidine and 3′-azido-3′-deoxythymidine. Antimicrob Agents Chemother. 1992;36:808–18.
161. Mier W, et al. [18F]FLT; portrait of a proliferation marker. Eur J Nucl Med Mol Imaging. 2002;29:165–9.
162. Sakamoto S, et al. Relative activities of thymidylate synthetase and thymidine kinase in human mammary tumours. Anticancer Res. 1993;13:205–7.
163. Romain S, et al. DNA-synthesis enzyme activity: a biological tool useful for predicting anti-metabolic drug sensitivity in breast cancer? Int J Cancer. 1997;74:156–61.
164. Boothman DA, et al. Enhanced expression of thymidine kinase in human cells following ionizing radiation. Int J Radiat Oncol Biol Phys. 1994;30:391–8.
165. Been LB, et al. [18F]FLT-PET in oncology: current status and opportunities. Eur J Nucl Med Mol Imaging. 2004;31:1659–72.
166. Gati WP, et al. Structural modifications at the 2′- and 3′-positions of some pyrimidine nucleosides as determinants of their interaction with the mouse erythrocyte nucleoside transporter. Biochem Pharmacol. 1984;33:3325–31.
167. Eriksson S, et al. Comparison of the substrate specificities of human thymidine kinase 1 and 2 and deoxycytidine kinase toward antiviral and cytostatic nucleoside analogs. Biochem Biophys Res Commun. 1991;176:586–92.
168. Seitz U, et al. Evaluation of pyrimidine metabolising enzymes and in vitro uptake of 3′-[(18)F]fluoro-3′-deoxythymidine ([(18)F]FLT) in pancreatic cancer cell lines. Eur J Nucl Med Mol Imaging. 2002;29:1174–81.
169. van Waarde A, et al. Selectivity of 18F-FLT and 18F-FDG for differentiating tumor from inflammation in a rodent model. J Nucl Med. 2004;45:695–700.
170. Rasey JS, et al. Validation of FLT uptake as a measure of thymidine kinase-1 activity in A549 carcinoma cells. J Nucl Med. 2002;43:1210–7.
171. van Westreenen HL, et al. Comparison of 18F-FLT PET and 18F-FDG PET in esophageal cancer. J Nucl Med. 2005;46:400–4.
172. Wagner M, et al. 3′-[18F]fluoro-3′-deoxythymidine ([18F]-FLT) as positron emission tomography tracer for imaging proliferation in a murine B-Cell lymphoma model and in the human disease. Cancer Res. 2003;63:2681–7.
173. Hatakeyama T, et al. 11C-methionine (MET) and 18F-fluorothymidine (FLT) PET in patients with newly diagnosed glioma. Eur J Nucl Med Mol Imaging. 2008;35:2009–17.
174. Chen W, et al. Imaging proliferation in brain tumors with 18F-FLT PET: comparison with 18F-FDG. J Nucl Med. 2005;46:945–52.
175. Vesselle H, et al. In vivo validation of 3′deoxy-3′-[(18)F]fluorothymidine ([(18)F]FLT) as a proliferation imaging tracer in humans: correlation of [(18)F]FLT uptake by positron emission tomography with Ki-67 immunohistochemistry and flow cytometry in human lung tumors. Clin Cancer Res. 2002;8:3315–23.
176. Smyczek-Gargya B, et al. PET with [18F]fluorothymidine for imaging of primary breast cancer: a pilot study. Eur J Nucl Med Mol Imaging. 2004;31:720–4.
177. Buck AK, et al. Imaging proliferation in lung tumors with PET: 18F-FLT versus 18F-FDG. J Nucl Med. 2003;44:1426–31.
178. Eckel F, et al. Imaging of proliferation in hepatocellular carcinoma with the in vivo marker 18F-fluorothymidine. J Nucl Med. 2009;50:1441–7.
179. Kishino T, et al. Usefulness of 3′-deoxy-3′-18F-fluorothymidine PET for predicting early response to chemoradiotherapy in head and neck cancer. J Nucl Med. 2012;53:1521–7.
180. Reisine T, Bell GI. Molecular biology of somatostatin receptors. Endocr Rev. 1995;16:427–42.
181. Kwekkeboom DJ, et al. Peptide receptor radionuclide therapy in patients with gastroenteropancreatic neuroendocrine tumors. Semin Nucl Med. 2010;40:78–88.
182. Reubi JC, et al. Somatostatin receptor sst1-sst5 expression in normal and neoplastic human tissues using receptor autoradiography with subtype-selective ligands. Eur J Nucl Med. 2001;28:836–46.
183. Wild D, et al. DOTA-NOC, a high-affinity ligand of somatostatin receptor subtypes 2, 3 and 5 for

labelling with various radiometals. Eur J Nucl Med Mol Imaging. 2003;30:1338–47.
184. Win Z, et al. The possible role of 68Ga-DOTATATE PET in malignant abdominal paraganglioma. Eur J Nucl Med Mol Imaging. 2006;33:506.
185. Reubi JC, et al. Affinity profiles for human somatostatin receptor subtypes SST1-SST5 of somatostatin radiotracers selected for scintigraphic and radiotherapeutic use. Eur J Nucl Med. 2000; 27:273–82.
186. Al-Nahhas A, et al. What can gallium-68 PET add to receptor and molecular imaging? Eur J Nucl Med Mol Imaging. 2007;34:1897–901.
187. Cescato R, et al. Internalization of sst2, sst3, and sst5 receptors: effects of somatostatin agonists and antagonists. J Nucl Med. 2006;47:502–11.
188. Hofman MS, et al. High management impact of Ga-68 DOTATATE (GaTate) PET/CT for imaging neuroendocrine and other somatostatin expressing tumours. J Med Imaging Radiat Oncol. 2012; 56:40–7.
189. Oh S, et al. Effect of peptide receptor radionuclide therapy on somatostatin receptor status and glucose metabolism in neuroendocrine tumors: intraindividual comparison of Ga-68 DOTANOC PET/CT and F-18 FDG PET/CT. Int J Mol Imaging. 2011; 2011:524130.
190. Prasad V, Baum RP. Biodistribution of the Ga-68 labeled somatostatin analogue DOTA-NOC in patients with neuroendocrine tumors: characterization of uptake in normal organs and tumor lesions. Q J Nucl Med Mol Imaging. 2010;54:61–7.
191. Gabriel M, et al. 68Ga-DOTA-Tyr3-octreotide PET in neuroendocrine tumors: comparison with somatostatin receptor scintigraphy and CT. J Nucl Med. 2007;48:508–18.
192. Buchmann I, et al. Comparison of 68Ga-DOTATOC PET and 111In-DTPAOC (Octreoscan) SPECT in patients with neuroendocrine tumours. Eur J Nucl Med Mol Imaging. 2007;34:1617–26.
193. Froeling V, et al. Impact of Ga-68 DOTATOC PET/CT on the diagnosis and treatment of patients with multiple endocrine neoplasia. Ann Nucl Med. 2012;26(9):738–43.
194. Kayani I, et al. Functional imaging of neuroendocrine tumors with combined PET/CT using 68Ga-DOTATATE (DOTA-DPhe1, Tyr3-octreotate) and 18F-FDG. Cancer. 2008;112:2447–55.
195. Nyuyki F, et al. Potential impact of (68) Ga-DOTATOC PET/CT on stereotactic radiotherapy planning of meningiomas. Eur J Nucl Med Mol Imaging. 2010;37:310–8.
196. Luboldt W, et al. Visualization of somatostatin receptors in prostate cancer and its bone metastases with Ga-68-DOTATOC PET/CT. Mol Imaging Biol. 2010;12:78–84.

Current Clinical Imaging of Hypoxia with PET and Future Perspectives

11

Mareike Roscher, Carmen Wängler, Stefan O. Schönberg, and Björn Wängler

Contents

Abbreviations

ACRIN	American College of Radiology Imaging Network
ATSM	Diacetyl-bis(N^4-methylthiosemicarbazone)
BOLD	Blood oxygen level dependent
CAIX	Carbonic anhydrase IX
CT	Computed tomography
DAHANCA	Danish Head and Neck Cancer Group
EF5	2-(2-nitro-1H-imidazol-1-yl)-*N*-(2,2,3,3,3-[^{18}F]pentafluoropropyl)-acetamide
EPR	Electron paramagnetic resonance
FAZA	Fluoroazomycin arabinoside
FDG	Fluorodeoxyglucose
FETA	Fluoroetanidazole
FETNIM	Fluoroerythronitroimidazole
FMISO	Fluoromisonidazole
GLUT-1	Glucose transporter-1
IAZA	Iodoazomycinarabinoside
GTV	Gross tumor volume
HIF-1	Hypoxia-inducible transcription factor-1
HNC	Head and neck cancer
IMRT	Intensity-modulated radiation therapy

M. Roscher • B. Wängler (✉)
Institute of Clinical Radiology and Nuclear Medicine, Medical Faculty Mannheim of Heidelberg University, Molecular Imaging and Radiochemistry, Theodor-Kutzer-Ufer 1-3, 68167 Mannheim, Germany
e-mail: mareike.roscher@medma.uni-heidelberg.de; bjoern.waengler@medma.uni-heidelberg.de

C. Wängler
Institute of Clinical Radiology and Nuclear Medicine, Medical Faculty Mannheim of Heidelberg University, Biomedical Chemistry, Theodor-Kutzer-Ufer 1-3, 68167 Mannheim, Germany
e-mail: carmen.waengler@medma.uni-heidelberg.de

S.O. Schönberg
Institute of Clinical Radiology and Nuclear Medicine, University Medical Center Mannheim, Medical Faculty Mannheim of Heidelberg University, Theodor-Kutzer-Ufer 1-3, 68167 Mannheim, Germany
e-mail: stefan.schoenberg@umm.de

A. Luna et al. (eds.), *Functional Imaging in Oncology*,
DOI 10.1007/978-3-642-40412-2_11,

MISO	Misonidazole
MRI	Magnetic resonance imaging
NSCLC	Non-small cell lung cancer
PET	Positron Emission Tomography
p.i.	Post injection
PTSM	Pyruvaldehyde-bis (N^4-methyl thiosemicarbazone)

11.1 Introduction

Hypoxia is a characteristical pathophysiological property of most tumors and occurs as a consequence of inadequate blood supply [1]. If tumors reach a diameter of a few millimeters, for instance, in locally advanced lesions or in rapidly growing tumors, the oxygen supply generally stays persistently behind the requirements of the tumor despite neovascularization [2]. This reflects the structural and functional disorganization of tumor vasculature resulting in disturbed microcirculation (acute hypoxia) and intercapillary distances that are beyond the diffusion range of oxygen (chronic hypoxia) [3, 4]. Thus, the classification of chronic and acute hypoxia is of limited validity [5] as the blood flow as well as the capacity of hemoglobin to deliver oxygen to cells may vary resulting in changing partial pressures for O_2. Additionally, also the nutrients and the pH can change in hypoxic tissues [3]. Hypoxic areas are distributed heterogeneously within a given tumor population regarding incidence and severity [4, 6]. Tumor hypoxia could be shown to be an adverse prognostic and predictive factor in several different entities like cervical cancer, soft tissue sarcoma, and head and neck cancer [5, 7] as it leads to alterations in the (patho) physiome of cells.

Biochemists define hypoxia as O_2-limited electron transport [8], whereas clinicians define it as a state of reduced O_2 availability or decreased O_2 partial pressure restricting or even abolishing functions of organs, tissues, and cells [9, 10]. The use of the term hypoxia in this context describes the clinical definition of hypoxia reflecting the imbalance between cellular O_2 consumption rate and O_2 supply to the cells [5, 6].

Since the beginning of the twentieth century, the role of hypoxia in tumor resistance is known as molecular oxygen could be shown to be a critical determinant of the response of cells to radiation [11, 12]. Oxygen plays a pivotal role in radiation therapy, a process known as oxygen enhancement effect. "Normal," oxygenated tissues display an oxygen partial pressure of about 45–50 mmHg (5 mmHg correspond to ~0.7 % O_2 in the gas phase or 7 μM in solution). If the O_2 partial pressure is reduced to values less than 25–30 mmHg, the sensitivity of cells is progressively limited. Oxygen is a potent radiosensitizer resulting from its high electron affinity. After absorbing the energy from ionizing radiation, free radicals are formed leading to DNA damage or modifications in other biologic molecules within the cells. Under hypoxic conditions, up to three times higher doses are required to achieve the same cytotoxic effects as under normoxic conditions [13, 14]. Additionally, many chemotherapies are oxygen dependent as they lead to the generation of free oxygen radicals such as doxorubicin and bleomycin. On top, the biologic alterations resulting from hypoxia as the effects on cell cycle or alterations in proteome hamper the success of chemotherapeutic treatments (as reviewed in [5]). In addition and due to the disturbed microcirculation or the increased expression of multidrug resistance transporters (e.g., P-glycoprotein), the exposure of cells to chemotherapeutics might be reduced [15, 16].

Thus, hypoxia can either result in impaired growth and cell death or act as a factor leading to malignant progression and increased therapy resistance [7, 17–19]. In the latter case, hypoxia is a strong selection pressure for cells inducing a vicious circle of hypoxia and subsequent malignant progression [6]. Hereby, it compromises many biological functions [1], for example, the cell cycle progression arresting the cells in G_1/S phase or lengthening the G_1 phase disproportionately [20–22], promoting genomic instability and thereby increasing the mutation rate [6, 23]. Furthermore, gene expression and proteomic profiles are changed with an increase in transcription and translation of survival and growth factors, angiogenic molecules, chaperones, and proteins involved in tumor invasiveness facilitating metastasis of the tumor and leading to a more

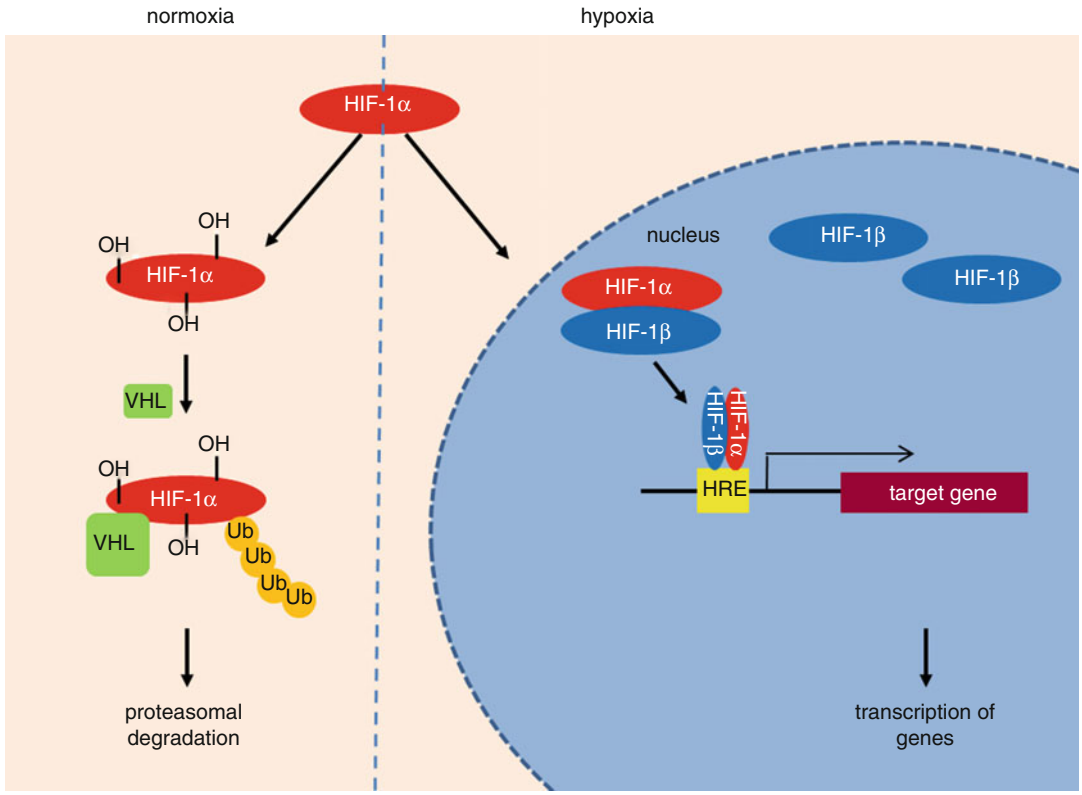

Fig. 11.1 Schematic pathways of hypoxia-inducible factor-1 (HIF-1). HIF-1α is under normoxic conditions enzymatically hydroxylated enabling the tumor suppressor von Hippel-Lindau (VHL) to bind. This leads to the ubiquitination and proteasomal degradation of HIF-1α. If the cell, however, turns hypoxic, HIF-1α is no longer hydroxylated. VHL cannot interact with the HIF-1α increasing the half-life of the molecule. HIF-1α can enter the nucleus and as heterodimer with HIF-1β bind to hypoxia-responsive element (HRE) domains on the DNA resulting in the transcription of more than 100 target genes involved among others in angiogenesis, glucose metabolism, metastasis, and pro-survival pathways

malignant phenotype resistant to cell death and altered metabolism [24, 25]. For instance, the higher expression of the glucose transporter-1 (GLUT-1) that can be a result of hypoxia correlates with a poorer outcome in breast cancer, head and neck cancer (HNC), and non-small cell lung cancer (NSCLC) [26–28], while carbonic anhydrase IX (CAIX) is implicated to play a role in tumor cell survival and invasiveness [29, 30]. The best characterized molecule which alters the signaling pathways during hypoxia is the hypoxia-inducible transcription factor-1 (HIF-1) (Fig. 11.1). This heterodimer consisting of HIF-1α and HIF-1β binds in its reduced state to hypoxia responsive elements on the DNA increasing the transcription of genes responsible for angiogenesis, erythropoiesis, energy metabolism, and glucose transport into the cell. Consequently, cell survival and oxygen supply is supported [31]. Under normoxic conditions, HIF-1α is rapidly ubiquitinated and degraded with a half-life of about 10 min, whereas it is stabilized under hypoxic conditions [31]. Additionally, also the expression of HIF-1 can be enhanced. High levels of HIF-1α could be shown to be associated with a poorer treatment response and clinical outcome in breast cancer, HNC, as well as in NSCLC and stomach cancer [32–37] making it an attractive candidate for drug targeting [38, 39]. The alterations in hypoxic cells might explain delayed recurrences, dormant micrometastases, and growth retardation in large tumor masses [5].

Studies using oxygen microelectrodes, several different MRI and electron paramagnetic

resonance (EPR) approaches, and detection of exogenous (e.g., misonidazole, 2-(2-nitro-1H-imidazol-1-yl)-N-(2,2,3,3,3-[^{18}F] pentafluoropropyl)-acetamide(EF5), or pimonidazole) or endogenous [e.g., HIF-1, CAIX, GLUT-1] molecular markers of cellular hypoxia with immunohistochemical or noninvasive imaging techniques all show that hypoxia is a common feature of tumors in patients presenting for therapy, as well as in animal tumors.

As hypoxia is associated with radiation- and chemoresistance (especially if the tumor areas include tumor-initiating stem cells), it does need not only to be detected in tumors but ideally also to be quantified with the help of predictive biomarkers [4]. Several invasive and noninvasive methods for measuring hypoxia are already established or in development – each with its own advantages and limitations. The question which technique is superior for a clinical or experimental setting depends on the available applications, on the degree of invasiveness, and the resolution required. So far the "gold standard" is intratumoral polarographic measurement of O_2 partial pressures which is not appropriate for monitoring the development within the tumor mass during treatment due to its invasiveness. Furthermore, this technique is limited in its application because only random measurements at some sites within a tumor can be performed. Minimally invasive tools such as serum-based diagnostics and global gene signatures are under investigation [4]. Additionally, also the blood oxygen level-dependent (BOLD) effect can be measured via MRI noninvasively as well using paramagnetic deoxyhemoglobin and diamagnetic oxyhemoglobin as an endogenous hypoxia marker (Chap. 12). Hence, this method depends on the perfusion of tumor tissue with red cells, a prerequisite which is not always fulfilled [7]. Next to magnetic resonance imaging (MRI), especially PET imaging has emerged as a promising noninvasive tool to detect and monitor tumor oxygenation. Deeper insights into anatomical and biological information about the tumor might be revealed using PET/CT after applying sensitizer adducts which on top allows to more precisely estimate the location of the hypoxic areas and the quantification of hypoxia levels [40].

11.2 PET Tracers Used in Hypoxia Imaging

The imaging of hypoxia with PET has several advantages as the measurements allow a repeated noninvasive whole tumor assessment in vivo. This is one of the major advantages as an estimation of the temporal and spatial distribution of hypoxia can be monitored in the course of a treatment [41]. Nevertheless, hypoxia tracers have to meet several characteristics: they have to be retained specifically in hypoxic cells via an oxygen-specific mechanism with a fast blood clearance to reach appropriate concentrations even in perfusion-limited regions and to generate low concentrations of nonspecific metabolites. Furthermore, hypoxia tracers should allow a repeatable, simple, nontoxic, and fast assessment of local oxygen levels with a high spatial resolution. Another objective in measuring tumor hypoxia via PET is to ensure the reproducibility of the tracer distribution and thresholding irrespective of the operator interpreting the data. The tracers which are currently in use give promising results but do not fulfill all of these requirements [42] which is the reason for the ongoing development of novel tracers with improved imaging properties.

Most of the different hypoxia tracers for PET imaging used so far are bioreductive molecules which will be described in the following sections. Among these, the halogenated PET nitroimidazole agents labeled with F-18 and I-124 have a quite long history, whereas Cu-diacetyl-bis(N^4-methylthiosemicarbazone) (Cu-ATSM) has only recently been proposed for PET imaging [43].

The major caveat of using PET imaging for hypoxia is that it is usually only a loco- or even microregional effect with patches of cells dispersed throughout the tumor. As the resolution of PET scanners is limited due to the physical characteristics of the used radionuclides and the varying spatial resolutions of 2–4 mm that can

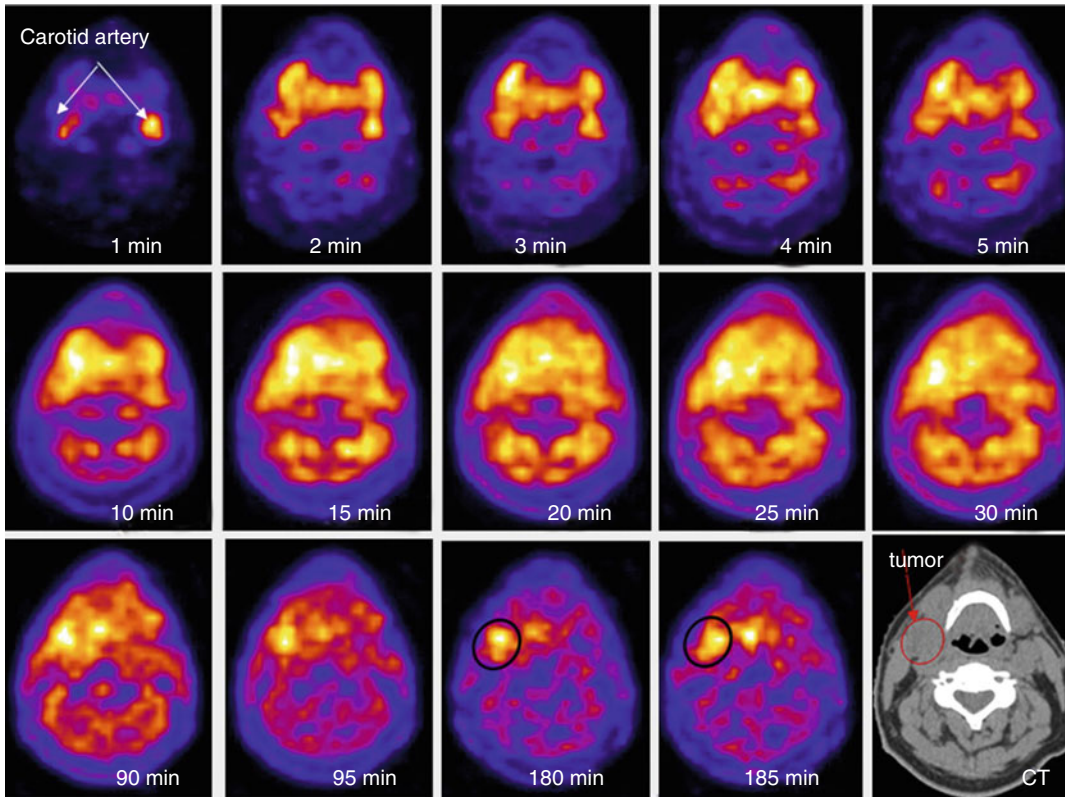

Fig. 11.2 Optimized characterization of tracer uptake in tumors applying dynamic PET scans. Compared to static PET scans allowing the assessment of standardized uptake values, dynamic scans can provide additional data about the movement and rate of uptake of the applied PET tracer allowing for a more complete diagnosis. After injection of [^{18}F]FMISO in a patient with HNC, the dynamic PET scan was applied as a function of time: the first five images taken were of 1 min duration and then 5 frames with 5 min duration followed. The patient was reimaged at 90 min and 180 min after injection. The distribution of [^{18}F]FMISO can be tracked from the initial blood pool to the specific accumulation within the tumors. The images were co-registered with low-dose CT scan (*last image*) Reprinted with kind permission of SNMMI from: Carlin and Humm [44])

be achieved by standard clinical scanners, the exact level of hypoxia and its distribution are difficult to locate and quantify so far. In consequence, partial volumes are averaged, giving rise to statistical uncertainties. Hence, the suboptimal signal-to-noise ratio is a concern for the clinical use. These limitations might at least partially be overcome by dynamic imaging employing a kinetic modeling approach (Fig. 11.2). In contrast to single-time-point PET images, dynamic hypoxia PET can distinguish between tumor hypoxia and circulating radiotracer [44]. Dynamic scans, however, are expensive, complex to analyze, and cause inconvenience to patients [45].

11.2.1 [^{18}F]Fluorodeoxyglucose

[^{18}F]Fluorodeoxyglucose ([^{18}F]FDG) is the most commonly used PET tracer in clinical routine for oncologic imaging as it allows a sensitive but unspecific detection of many tumors. In hypoxic cells, the mitochondrial ATP synthesis drops; the cells stimulate the Pasteur effect. Furthermore, HIF-1 stimulates the expression of GLUT-1 transporting FDG into the cells [46]. However, the Warburg epigenetic phenotype in normoxic tumor cells leads to a higher uptake of FDG in cells decreasing the possibility to detect hypoxia in malignant tissues. Furthermore, several preclinical and clinical studies could show

that there is no or only a weak correlation between uptake of hypoxia tracers and retention of FDG [47–53]. According to the studies undertaken so far, the use of [^{18}F]FDG as biomarker for hypoxia remains questionable. Therefore, a number of hypoxia-specific PET tracers have been developed.

11.2.2 Nitroimidazole-Based PET Radiotracers

In the 1970s, nitroimidazoles were discovered as clinical radiosensitizers and first proposed as reducible hypoxia markers in 1979 by Chapman [54, 55]. These molecules mimic the effects of oxygen leading to the sensitization of hypoxic cells to radiation. Nevertheless, if high concentrations of nitroimidazoles were applied which could restore the sensitivity of cells, toxic effects could be observed [56]. For PET imaging very low amounts of the tracers are applied (<15 μg) which do not result in any pharmacologic side effects. One major advantage of nitroimidazoles is that they are less than 5 % protein bound and are therefore distributed efficiently throughout the body even if the blood flow is reduced [57, 58]. On top, they can be applied in immunohistochemistry as well as in PET applications allowing for variable detection techniques of hypoxic tissues, e.g., prior to and after a resection of the tumor.

Nitroimidazoles consist of an imidazole ring with a nitro group at the 2′ position and an additional side chain with different residues at the 1′ position which alters the pharmacokinetic properties of the individual molecules (Fig. 11.3, Table 11.1). In vivo, the NO_2 group can be reduced to NH_2 if it undergoes a 6-electron intracellular modification: comparable to O_2 although with less affinity, the nitro function of nitroimidazoles can accept electrons from the respiratory chain reducing it to the radical anion $–NO_2^-$ (Fig. 11.4). Cellular reductases such as xanthine oxidases with a nitroreductase activity catalyze this reaction and are assumed not to be a limiting factor in this process [59]. In the presence of oxygen, the reactive radical intermediate is reoxidized, as oxygen can accept the electrons from the nitro radical and the parent nitroimidazole can leave the cell via passive diffusion. Under hypoxic conditions, however, the nitroimidazole is further reduced. If a second electron is accepted, the nitroimidazole is irreversibly reduced to an nitroso (–N = O) group. Additional reduction steps lead to the generation of an hydroxylamine (-NHOH)

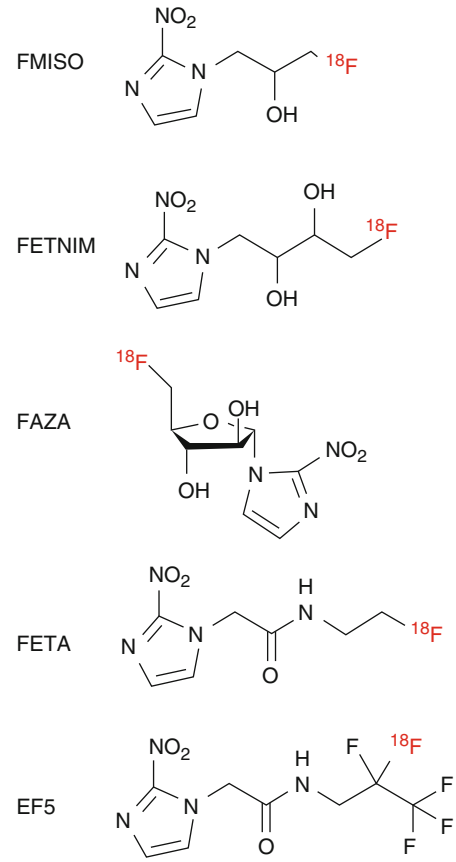

Fig. 11.3 Structure of nitroimidazole-based PET hypoxia imaging agents

Table 11.1 Partition coefficients of different nitroimidazoles. The octanol/water partition coefficient depends on the contained alkyl chain

Nitroimidazole	Alkyl chain	Partition coefficient
FMISO	$–CH_2CHOCH_2F$	0.44
FETNIM	$–CH_2CHOHCHOHCH_2F$	0.17
FETA	$–CH_2CONHCH_2CH_2F$	0.16
EF5	$–CH_2CONHCH_2CF_2CF_3$	5.7

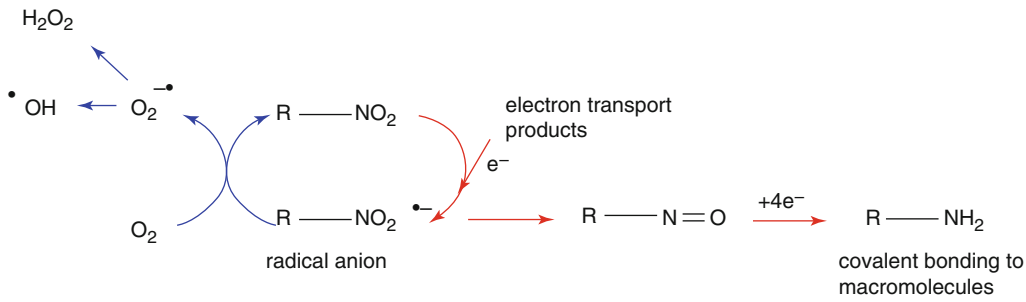

Fig. 11.4 Mechanism of nitroimidazole retention in hypoxic cells. Nitroimidazoles are reduced by electrons to form radical anions. If oxygen is available, the anion reacts preferentially with this electron acceptor, turning the tracer in its parent state. However, if O_2 is not present, the radical anion accepts another electron to produce nitroso- and hydroxylamine intermediates which are sequentially reduced to amines which are cellularly retained. The reactions taking place under normoxic conditions are presented with *blue arrows*, whereas hypoxic reactions are marked with *red arrows*

functionality. This highly reactive hydroxylamine can bind covalently to thiols of macromolecules in the hypoxic cells [38, 60]. Hence, the molecule is entrapped and accumulates within the cells [7, 61, 62]. Due to the dependence of the reactions on electrons from the respiratory chain as well as on the enzymatic activity of nitroreductases, only hypoxic vital cells can be detected. The first observations of nitroimidazole retention within cell spheroids in vitro as well as in tumor models in vivo support this hypothesis [55, 63]. The rate of nitroimidazole accumulation correlates with the degree of hypoxia within the cells allowing for the distinction between normoxia and hypoxia.

To date, several different fluorinated and iodinated nitroimidazole derivates have been developed and tested, a selection of which will be discussed here. As no systematic analysis of all 2-nitroimidazole tracers in the same tumor model or patient group has been undertaken so far, it is difficult to state which tracer is superior to the others in identifying tumor hypoxia.

11.2.2.1 [^{18}F]Fluoromisonidazole ([^{18}F]FMISO)

[^{18}F]Fluoromisonidazole ([^{18}F]FMISO) (Fig. 11.3) is the best evaluated and most widely used hypoxia tracer which can be considered as gold standard for PET imaging of hypoxia. The group around Janet Rasey at the University of Washington was the first to propose noninvasive imaging of hypoxia. They pioneered the synthesis of [^{18}F]FMISO and demonstrated its feasibility in vivo [57, 64]. The radiosynthesis of [^{18}F]FMISO is possible using a commercially available precursor molecule and an automated radiosynthesis protocol. 90–120 min after application, PET measurements result in the best contrast, whereas the early delivery of [^{18}F]FMISO depends on the blood flow [42]. The tracer accumulates specifically in hypoxic tissues, and the images obtained unambiguously reflect the regional oxygen partial pressure [61, 65]. The clearance of [^{18}F]FMISO from the blood is relatively slow and the tracer distributes via free diffusion in tissues. A reasonable tumor-to-blood cutoff value of $\geq$1.2 is in general used to distinguish normoxia from locoregional hypoxia, and the detection of hypoxia is only possible in viable cells due to the dependency on enzymatic pathways [66]. Even if the blood flow is reduced to one-third, hypoxia and the absence of hypoxia can be detected. The metabolization of [^{18}F]FMISO is mainly hepatobiliary but the tracer is also in part excreted via the kidneys resulting in a radiation exposure of patients which is equal or comparable to other radiopharmaceuticals [65, 67, 68].

[^{18}F]FMISO can diffuse freely across the blood-brain barrier as it is highly lipophilic and has no protein-binding capacity. As the signal is independent of other factors (altered glucose concentration, pH, and glutathione), [^{18}F]FMISO harbors several advantages for imaging [69].

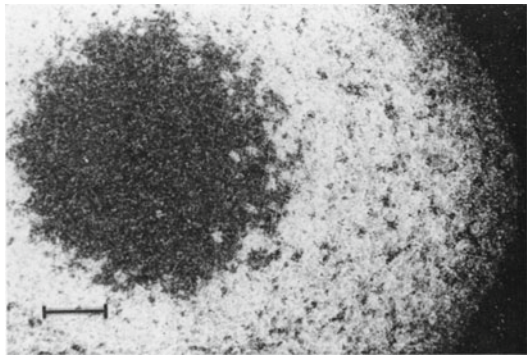

Fig. 11.5 Uptake of [^{14}C]MISO in cellular spheroids. The cell line EMT-6/UW was grown until spheroids of 1 mm were obtained. These were incubated for 8 h with [^{14}C]MISO and autoradiographs were taken. The uptake of [^{14}C]MISO can be observed in a band of cells surrounding a necrotic core in the center of the spheroid. The normoxic cells in the rim of the spheroid do not accumulate the tracer (The figure was reprinted with kind permission of Radiation Research from Rasey et al. [63])

Furthermore, this nitroimidazole derivative is reduced at any hypoxic site and entrapped within the cells. One major disadvantage of [^{18}F]FMISO is the low signal-to-noise ratio resulting in images of limited contrast due to the poor washout [70]. This problem can be overcome by calculating the tumor-to-blood ratio taking a venous blood sample during PET imaging.

The first studies on the uptake of [^{18}F]FMISO were performed in vitro with multicellular spheroids. In these aggregates of cells mimicking small tumors, hypoxia could be visualized and quantitatively measured. In Chinese hamster lung V79 spheroids after 4 h of incubation with [^{3}H]misonidazole ([^{3}H]MISO), and [^{14}C]MISO autoradiographs revealed a necrotic center followed by highly tracer-accumulating cells surrounded by the well-oxygenated periphery demonstrating the dependence of tracer entrapment on cell viability (Fig. 11.5) [63]. In monolayer preparations of adult rat myocytes, the relationship between the oxygen concentration and [^{3}H]FMISO binding was studied [71]. In comparison to normoxic controls, the [^{3}H]FMISO retention after 3 h was about 26 times higher under anoxic conditions; in hypoxic cells the uptake was increased about 15-fold. In a hepatic artery occlusion model in pigs, in vivo

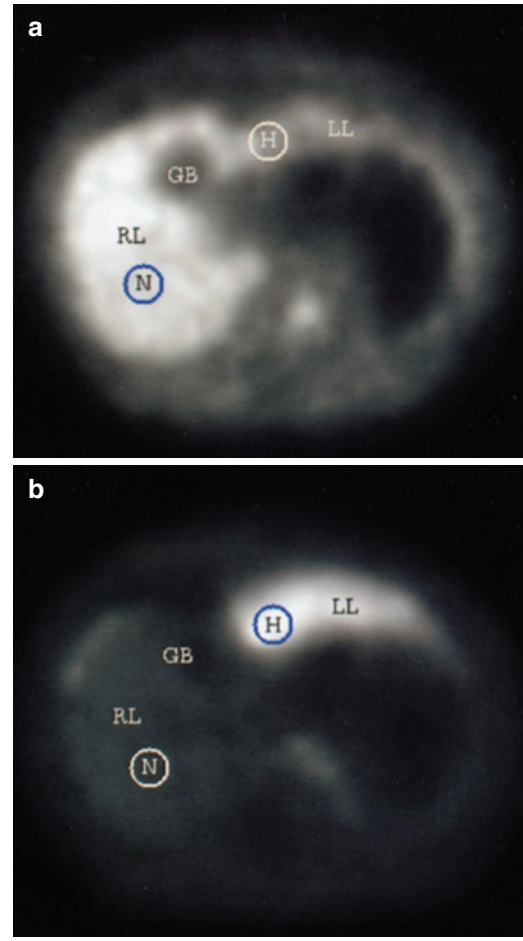

Fig. 11.6 Detection of hypoxia by [^{18}F]FMISO. In domestic pigs liver tissue hypoxia was induced by segmental arterial hepatic occlusion. 3 h after injection of [^{18}F]FMISO, dynamic PET scans were performed to measure the specific retention of the tracer within the hypoxic liver segments. This correlated directly to the severity of tissue hypoxia. (**a**) In the first minutes, [^{18}F]FMISO displayed high activity in the normally perfused right liver lobe (perfusion), (**b**) while the specific retention in the hypoxic left liver lobe can be observed in later time points (165–180 min). No activity was detected in the gallbladder (*GB*). The circular ROIs indicate normal and hypoxic areas as measured with polarographic electrode measurements before and after PET scanning (The figure was reprinted with kind permission of Springer Science+Business Media from: Piert et al. [72])

hypoxia-dependent [^{18}F]FMISO entrapment was shown (Fig. 11.6) [72]. The [^{18}F]FMISO accumulation in flow-impaired hepatic segments was about three to four times higher than in normal-flow segments. Polarographic elec-

trode measurements confirmed the correlation between [^{18}F]FMSIO uptake and oxygen levels within the tissues.

In vivo, further preclinical studies comparing the results of polarographic measurements and [^{18}F]FMISO accumulation have been reported. In a rat tumor model, a good correlation of both parameters could be observed [73], while in C3H mammary cancer xenografts, no correlation was found between the two methods [74]. This might be due to the fact that necrotic tissues with low oxygen levels can be identified as hypoxic using the electrode assessment but do not retain [^{18}F]FMISO due to the lack of entrapment of the tracer. A general differentiation between mice with hypoxic and nonhypoxic tumors was possible.

The uptake of [^{18}F]FMISO was also analyzed in comparative studies with immunohistochemical staining techniques. The exogenous hypoxia marker pimonidazole and the endogenous hypoxia marker CAIX were compared to [^{18}F]FMISO in a rhabdomyosarcoma rat xenograft [75]. The detected hypoxic volumes were significantly correlated underlining the value of [^{18}F]FMISO PET to detect hypoxia. Two further studies were undertaken by Troost and colleagues in several xenograft models [76, 77]. They found a correlation between [^{18}F]FMISO PET and pimonidazole immunochemistry.

In order to analyze the regional variation in hypoxia within a single tumor which might result from differences in [^{18}F]FMISO delivery as well as the oxygen levels in more detail in vivo, studies within one tumor were undertaken [78]. Four hours after injection of [^{18}F]FMISO, the freely diffusible blood flow tracer C-14-iodoantipyrine – that has the same partition coefficient as [^{18}F]FMISO – was applied to mice. The tumors were dissected into central and peripheral regions, and additional samples were taken from several healthy organs. The tumors generally exhibited a low blood flow, whereas a high blood flow was shown in lungs and kidneys. No correlation between regional flow and [^{18}F]FMISO entrapment in individual tumors was found which was also detected for normal tissues. This effect was also observed in larger animals where a very low blood flow was independent of the [^{18}F]FMISO retention [58].

Several clinical studies compared the correlation between measurements of partial oxygen pressures and [^{18}F]FMISO accumulation as well. In patients with HNC, positive correlations could be found between the two methods [79, 80].

The first study showing the feasibility of [^{18}F]FMISO was performed to detect hypoxia in three glioma patients (Fig. 11.7) [81]. Rasey and colleagues could identify hypoxic areas in a variety of tumors prior to treatment [82]. They concluded that human tumor hypoxia is widely prevalent and highly variable inter- and intraindividually.

In clinical studies, it could be shown that the uptake of [^{18}F]FMISO correlated with a poor prognosis for patients in HNC and glioblastoma. In patients with HNC 83 % of the tumors have hypoxic subvolumes which were in most cases distributed in single confluent areas, whereas only 22 % were diffusely dispersed [83]. For the patients with HNC, a differentiation between responders and nonresponders to radiotherapy was possible with nonresponders having a higher retention of [^{18}F]FMISO although the tumor accumulation varied [49]. A further criterion to differentiate between the two groups was that responders had an initially lower perfusion followed by accumulation of [^{18}F]FMISO, whereas the nonresponders showed an initial high perfusion followed by a rapid washout. In glioma patients, the volume and intensity of the detected hypoxia determined prior to radiotherapy showed a strong correlation with a shortened time to progression and overall survival (Fig. 11.8) [84]. For soft tissue tumors, however, [^{18}F]FMISO might possibly not be the tracer of choice due to large fractions of necrotic tissue within the tumor lesions [85]. Nevertheless, further studies are required to verify this hypothesis.

In different settings using [^{18}F]FMISO, intensity-modulated radiation therapy (IMRT) has been applied and could show next to interindividual differences reproducible results and the feasibility of an imaging-based planning of radiotherapy resulting in a locoregional management of tumors (Fig. 11.9) [86, 87]. Furthermore, in a first study using [^{18}F]FMISO PET, the

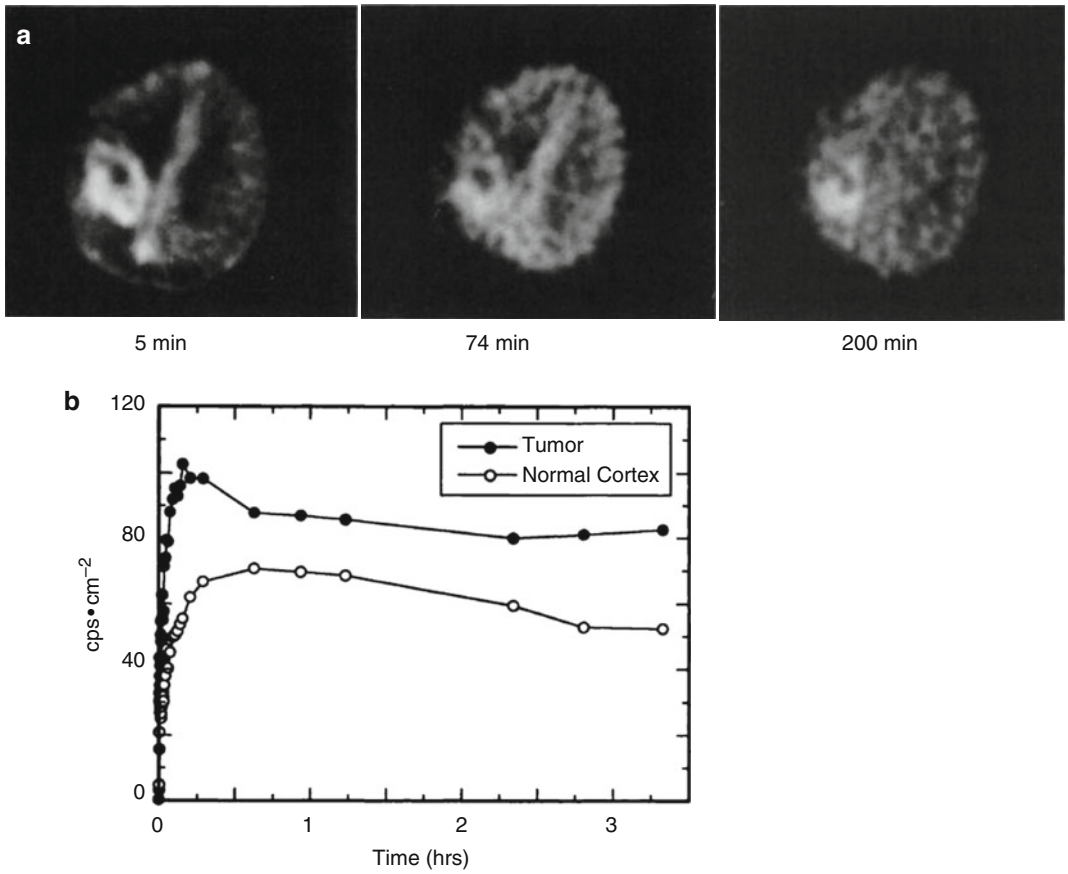

Fig. 11.7 The first clinical PET scans using [^{18}F]FMISO in a patient with malignant glioma. (**a**) 5 min after injecting [^{18}F]FMISO, a first tumor activity could be detected. At later time points the uptake in the cortex could be observed although being very slow, indicating a slow passage of tracer across the intact blood-brain barrier. Nevertheless, the activity within the lesion remains higher. (**b**) The time-activity curve for the tumor parallels at about 40 min the curve for the cortical region and the increases to the end of the scanning. These first studies underline the importance of [^{18}F]FMISO for PET imaging of hypoxia (Reprinted by permission of SNMMI from: Valk et al. [81])

response to hypoxia-activated chemotherapy using tirapazamine in patients with advanced HNC could be predicted [88].

One preclinical study evaluated the uptake of [^{18}F]FAZA and [^{18}F]FDG in different cancer cell lines. Whereas [^{18}F]FAZA showed an increased retention in hypoxic cells in comparison to normoxic cells, the entrapment of [^{18}F]FDG was reduced which could also be shown in tumor xenografts [47]. In clinical studies, similar observations have been reported. In comparison to polarographic measurements, [^{18}F]FDG could not differentiate hypoxic from normoxic HNC tissues, whereas [^{18}F]FMISO uptake correlated with the partial pressure of oxygen [50, 80]. Further studies compared the retention of [^{18}F]FMISO and [^{18}F]FDG in patients with HNC, sarcoma, breast cancer, and NSCLC as well as glioma [48–53]. Each of these resulted in no correlation between [^{18}F]FDG uptake and hypoxia (Fig. 11.10). Some studies, however, could show a correlation of [^{18}F]FDG and [^{18}F]FMISO uptake in HNC [52, 89] and brain tumors [90] which calls for further elucidation.

In summary, [^{18}F]FMISO has been validated in several different studies for various tumor types. It could be shown to result in variable but significant levels of hypoxia and to be a prognostic indicator with increasing importance [91].

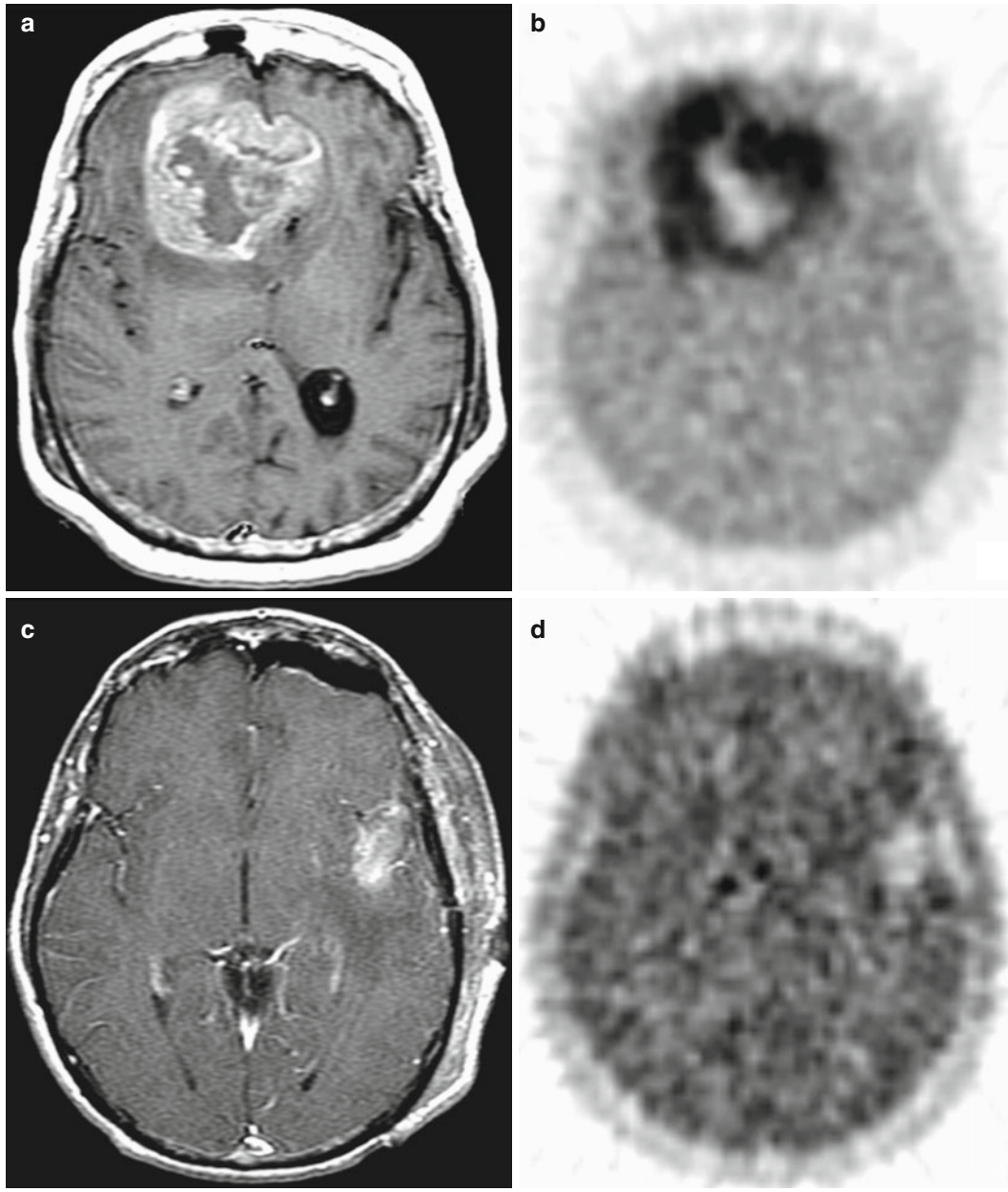

Fig. 11.8 [^{18}F]FMISO accumulation has a predictive value. In patients with glioblastoma multiforme, the [^{18}F]FMISO uptake was assessed 2 h p.i. using PET scans before radiotherapy. Tumor-to-blood ratios >1.2 defined the hypoxic value. The burden of hypoxic tissue within the tumor is inversely related to time to tumor progression and survival. (**a**, **c**) The MRI T1Gd images of two patients show the overall tumor size and its localization in the brain. (**b**, **d**) [^{18}F]FMISO uptake in the hypoxic areas of the glioma. Especially in patient 1, the high uptake of [^{18}F]FMISO can be observed as well as the necrotic center with no retention of the PET tracer (Reprinted with kind permission from AACR from Spence et al. [84])

However, it shows a slow accumulation in hypoxic tumors, a low tumor-to-background ratio, and a significant non-oxygen-dependent metabolism [61].

Next to [^{18}F]FMISO several alternative nitroimidazoles have been developed and tested to optimize the pharmaco- and biokinetics in regard to a faster blood clearance, less nonspecific

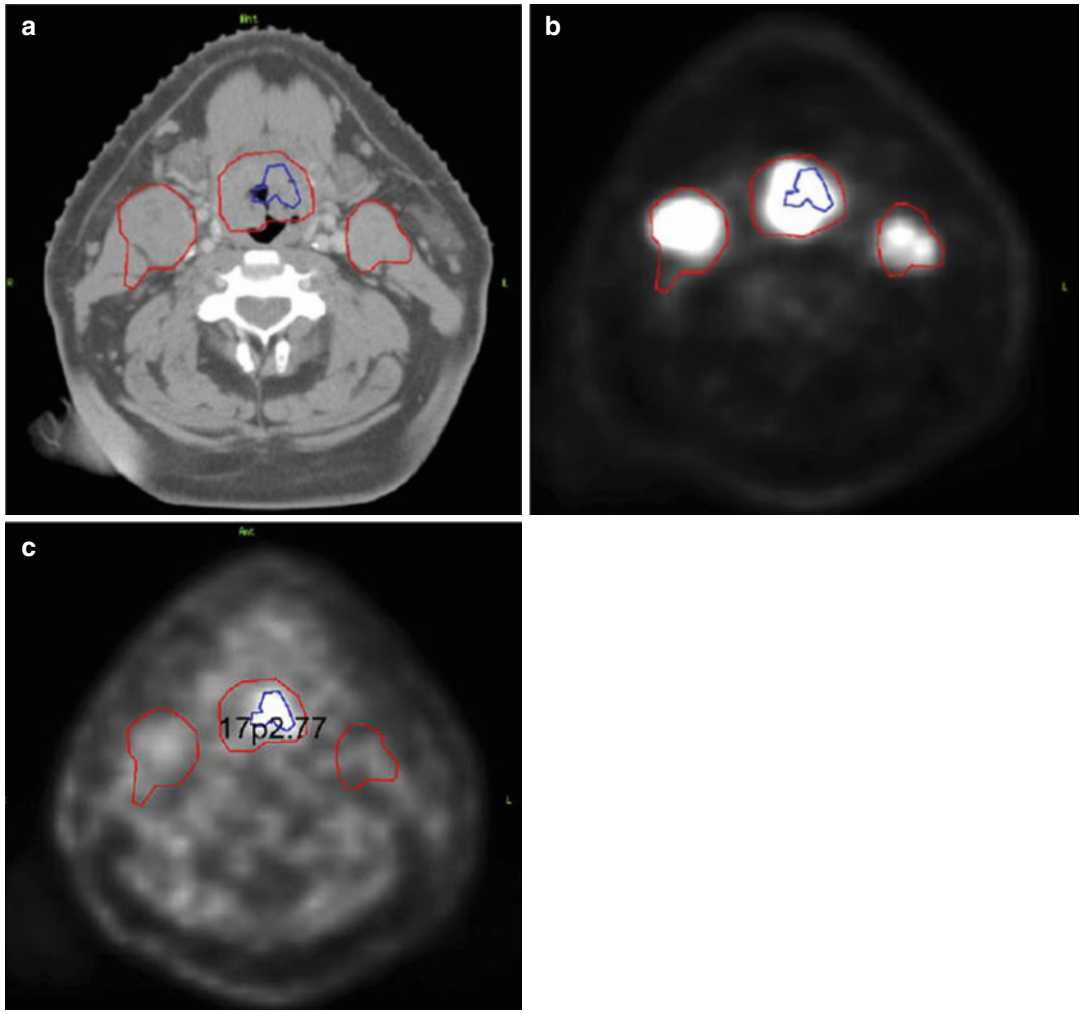

Fig. 11.9 Feasibility of [^{18}F]FMISO PET/CT guided dose-painting IMRT. In HNC patients, the dose escalation to radioresistant hypoxic zones was aimed at while sparing the surrounding normal tissue. The gross tumor volume (GTV) was delineated and the corresponding hypoxic areas determined by [^{18}F]FDG PET/CT and [^{18}F]FMISO PET/CT image fusion showing (**a**) a CT axial slice, (**b**) an [^{18}F]FDG-PET axial scan, and (**c**) an [^{18}F]FMISO PET axial slice. This study underlines the importance of multiparametric analyses of tumors for optimizing treatment schemes and to enhance the locoregional control of tumors (Reprinted with permission from Elsevier from Lee et al. [86])

retention, or fewer metabolites of the PET agents. These new agents have to prove to be superior to [^{18}F]FMISO in order to gain acceptance [65].

11.2.2.2 [^{18}F]Fluoroerythronitroimidazole ([^{18}F]FETNIM)

[^{18}F]Fluoroerythronitroimidazole ([^{18}F]FETNIM) (Fig. 11.3) was first described and evaluated by Yang et al. in 1995 [92]. In mammary tumor-bearing rats, their studies indicated that [^{18}F]FETNIM has significantly higher tumor-to-blood and tumor-to-muscle ratios than [^{18}F]FMISO at 4 h post injection (p.i.). The pharmacokinetic properties of [^{18}F]FETNIM show a low peripheral metabolism and only very little defluorination. The metabolites were hypothesized to be trapped within hypoxic cells [93]. In mice implanted with CH3 mammary carcinomas, [^{18}F]FETNIM was investigated in comparison to [^{18}F]FMISO under different oxygenation conditions [94]. These studies revealed that [^{18}F]FETNIM accumulation correlates with the oxygenation status in the

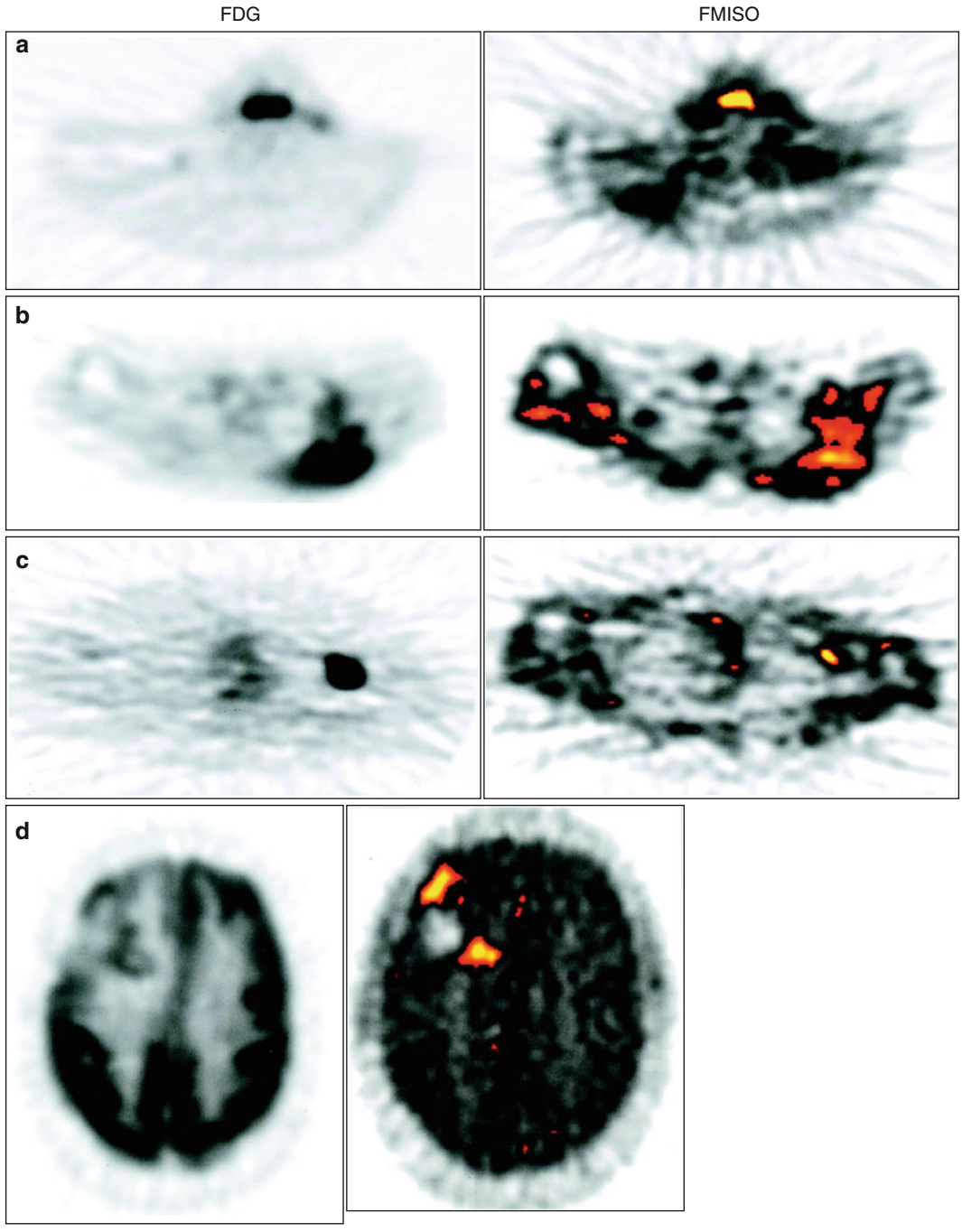

Fig. 11.10 Relationship between regional hypoxia and glucose metabolism in different tumor entities comparing [^{18}F]FMISO and [^{18}F]FDG uptake. Patients with different tumors ranging from those with a high prevalence of hypoxia (HNC, glioma) to those that are less frequently hypoxic (breast cancer) were analyzed for the accumulation of [^{18}F]FMISO (*right column*) and [^{18}F]FDG (*left column*) via PET scans. Representative images for both tracers show only a minor correlation between the overall tumor maximum standardized uptake value for FDG and hypoxic volume in patients with (**a**) HNC, (**b**) liposarcoma of the left posterior shoulder, (**c**) axillary metastases from left breast cancer, and (**d**) glioma of the right frontal region. Significant differences among the different tumor types could be observed, indicating discordance between hypoxia and glucose metabolism (Reprinted with kind permission by AACR from Rajendran et al. [52])

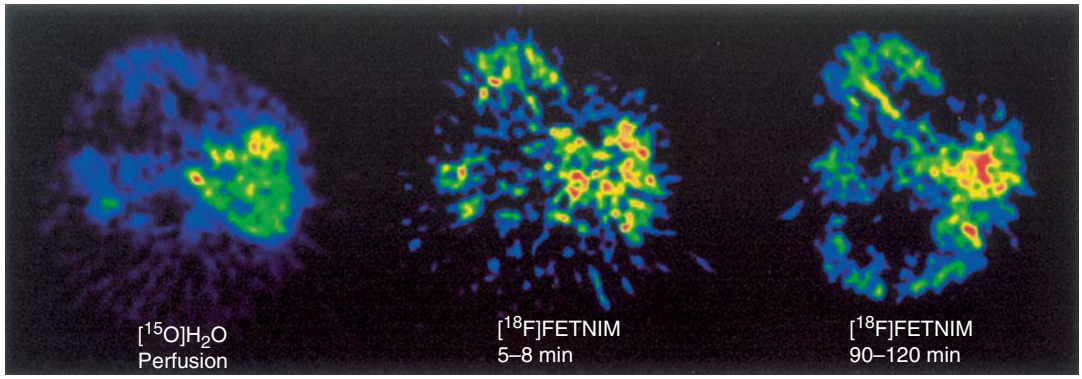

Fig. 11.11 [18F]FETNIM uptake depends on the tumor perfusion. The tumor perfusion (assessed by $[^{15}O]H_2O$ PET scan, *left*) of a patient with left hypopharyngeal tumor (HNC) was compared with a dynamic PET scan of [18F]FETNIM after 5–8 min (*middle*) and 90–120 min (*right*). The different pattern of [18F]FETNIM distribution in the early and late phases of the dynamic study depends on the perfusion of the tumor: At higher blood flow, the entrapment of [18F]FETNIM reflects the oxygenation well. The tissue-to-plasma ratios reached a steady-state level at 60 min p.i. in both tumor tissue and muscle indicating that the tissue-to-plasma ratio may provide best results using only a few late time points (The figure was reprinted with kind permission by Springer Science+Business Media from Lehtiö et al. [96])

tumors. In contrast to [18F]FMISO, however, [18F]FETNIM displayed a more favorable biodistribution with a low background signal in normoxic tissues [94]. This can be attributed to the higher hydrophilicity of [18F]FETNIM, enabling a higher tumor-to-background ratio. Clinical studies on [18F]FETNIM were performed with HNC patients in Finland, University of Turku. In these studies, it was shown that the early uptake of [18F]FETNIM was highly variable and depending on perfusion as demonstrated by $[^{15}O_2]H_2O$ PET [95]. To monitor hypoxia, the tumor-to-plasma ratio provided the best results (Fig. 11.11) [96]. Especially at high blood flows, [18F]FETNIM accumulation reflects the oxygenation status well and thus should be well suited for hypoxia imaging in tissues with high blood flow. Assessing the radiotherapy response in 21 patients with HNC, a high uptake of [18F]FETNIM was shown to be related to a poor overall survival [97] underlining the predictive value of this hypoxia tracer. Also a preliminary study for 26 patients with NSCLC and a further with 16 cervical carcinoma patients provided evidence that [18F]FETNIM PET imaging is a valuable method to estimate hypoxia within tumors and to predict the overall survival of patients [98, 99].

Despite the promising results of [18F]FETNIM, further studies are required to validate this PET tracer as a noninvasive imaging agent for PET imaging. Furthermore, it remains to be determined whether the use of this PET tracer presents any advantages over the use of [18F]FMISO.

11.2.2.3 [18F]Fluoroazomycin Arabinoside ([18F]FAZA)

[18F]Fluoroazomycin arabinoside [18F]FAZA (Fig. 11.3) exhibits superior pharmacokinetics compared to [18F]FMISO resulting from its reduced lipophilicity. This enables a faster clearance and hence a better contrast in imaging [100]. Additionally, [18F]FAZA can diffuse faster into cells so that this tracer is more readily available for hypoxic alteration [101, 102]. These observations are in line with a comparative study for [18F]FMISO and [18F]FAZA in mouse xenograft models where [18F]FAZA revealed better biokinetics with a higher tumor-to-muscle ratio and an oxygen-dependent uptake mechanism [103]. In contrast, a study published by Sorger et al. led to the conclusion that while [18F]FAZA indicates reduced oxygen levels comparable to [18F]FMISO in vitro, in vivo in a Walker 256 rat sarcoma model [18F]FMISO displayed a slightly higher uptake and tumor-to-muscle ratio [104]. To prove the superiority of [18F]FAZA over [18F]FMISO, more studies have to be undertaken. A further animal study with three squamous cell

carcinomas and one fibrosarcoma with differing characteristics regarding vascularization, hypoxia, and necrosis compared [^{18}F]FAZA uptake with Eppendorf electrode measurements and the hypoxia marker pimonidazole [105]. In vivo, the hypoxia selectivity of [^{18}F]FAZA could be proven in this study as well as in a study published by Tran et al. comparing OxyLite, EPR oximetry, and [^{19}F]MRI relaxometry [106].

Applying a chemoradiotherapy with tirapazamine – a prodrug activated to a toxic radical in hypoxic cells – the predictive value of [^{18}F]FAZA was investigated in a breast cancer xenograft-bearing tumor mouse model [107]. A high tumor accumulation of [^{18}F]FAZA was found to be an adverse indicator for tumor progression. Furthermore, [^{18}F]FAZA uptake could also predict the success of chemoradiotherapy, whereby the application of tirapazamine in hypoxic tumors could efficiently improve the therapeutic effect depending on the degree of hypoxia. The authors conclude that [^{18}F]FAZA prior to treatment might be a way to personalize tumor therapies involving radiation [107]. In these tumor-bearing mice also the reproducibility of hypoxia PET scans could be demonstrated. Therefore, pretreatment imaging is a valuable and reliable tool for treatment schemes targeting or modifying hypoxia [108].

In clinical studies, the feasibility of [^{18}F]FAZA was determined in 11 untreated HNC patients and 14 advanced rectal cancer patients [109, 110]. The quality of images achieved was adequate and the imaging feasible. The imaging for clinical static PET was performed 2 h p.i. and the recommended threshold was 1.5. [^{18}F]FAZA tumor uptake differed inter- and intraindividually; thus, further studies were undertaken to evaluate [^{18}F]FAZA in clinical settings. A study including 50 patients with different tumor entities confirmed the previously obtained data of [^{18}F]FAZA as feasible hypoxia tracer providing an adequate image quality [111]. The results of the DAHANCA (Danish Head and Neck Cancer Group) 24 trial including 50 patients revealed that in HNC patients receiving radiotherapy, [^{18}F]FAZA PET/CT was a prognostic factor regarding disease-free survival. Significant differences could be found between patients with and without hypoxic areas within their tumors [112].

Furthermore, the role of [^{18}F]FAZA PET imaging was analyzed in order to characterize hypoxia in the course of radiation treatment planning (Fig. 11.12) [83]. Eighteen patients with advanced squamous cell HNC were monitored, and the [^{18}F]FAZA uptake measurements were feasible for radiation treatment planning and IMRT (Sect. 11.4).

[^{124}I]iodoazomycinarabinoside ([^{124}I]IAZA) is an iodinated [^{18}F]FAZA analogue. As iodine has a longer half-life (4.18 days) than ^{18}F (110 min), it was suggested that imaging at later time points might reveal advantages in imaging results. However, this could not be shown [100]. Instead, a deiodination of the molecule was suggested as a significant thyroid uptake was observed.

11.2.2.4 [^{18}F]Fluoroetanidazole ([^{18}F]FETA)

[^{18}F]Fluoroetanidazole ([^{18}F]FETA) (Fig. 11.3) was first synthesized by Tewson in 1997 [113]. This nitroimidazole tracer has a decreased lipophilicity and superior biokinetics than [^{18}F]FMISO. In vivo, it turned out to be stable to nonhypoxic degradation and showed less metabolites in blood and urine compared to [^{18}F]FMISO. Preclinical studies with different tumor models showed that the uptake of [^{18}F]FETA correlates with the oxygen partial pressure within the tumor and a decrease in tracer uptake after carbogen breathing [114, 115]. The clinical potential of this promising PET hypoxia tracer has so far not been analyzed.

11.2.2.5 2-(2-Nitro-1H-imidazol-1-yl)-*N*-(2,2,3,3,3-[^{18}F]pentafluoropropyl)-acetamide ([^{18}F]EF5)

Next to the mono-fluorinated 2-nitroimidazoles also fluoroalkylacetamide derivatives which are more highly fluorinated have been developed and named as EF1 [116], EF3 [117], and EF5 [118]. Among these, 2-(2-nitro-1H-imidazol-1-yl)-*N*-(2,2,3,3,3-[^{18}F]pentafluoropropyl)-acetamide (EF5) (Fig. 11.3) was originally developed as an agent for biopsy stainings and has only recently been introduced as PET tracer to monitor hypoxia. The biological half-life of this molecule is improved because of its enhanced lipophilicity [119]. So far, EF5 is the most stable 2-nitroimidazole reported [43].

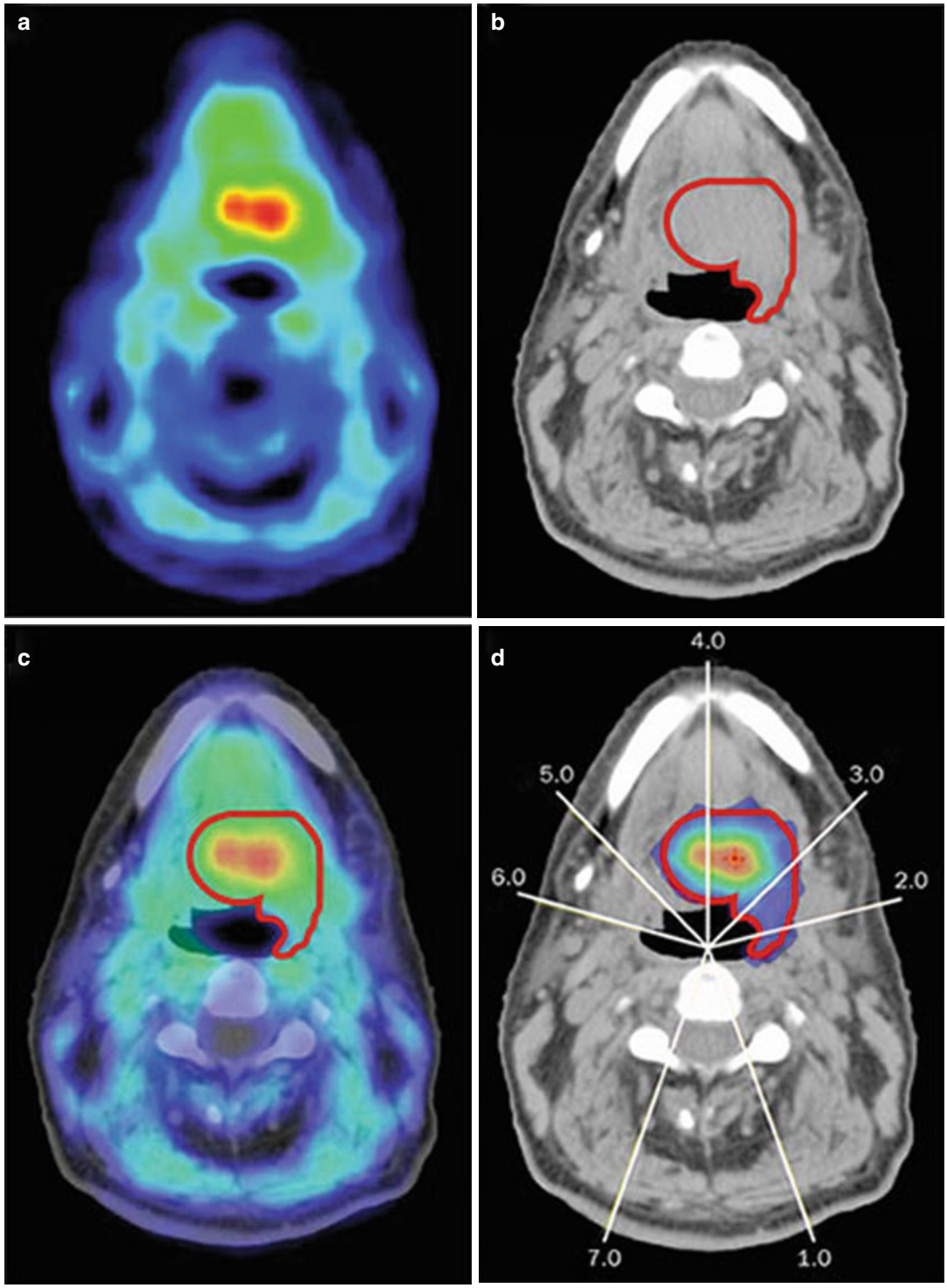

Fig. 11.12 Use of [^{18}F]FAZA PET scans for dose painting. (**a**) The PET scan shows the uptake of [^{18}F]FAZA in an HNC patient with squamous cell carcinoma indicating hypoxic areas, (**b**) while the CT scan can be used to determine the GTV and hence for treatment planning and dose calculation. (**c**) If the PET and CT scans are fused, the exact localization of the hypoxic areas within the tumor can be determined and (**d**) dose distribution for dose-painting IMRT can be planned. The white lines indicate the direction of the radiation treatment fields resulting in the different doses for therapy (*blue*: 63 Gy, *red*: 98 Gy) (Reprinted by permission from Macmillan Publishers Ltd: Horsman, 2012, © 2012, Nature Publishing group [45])

The major limitation of this promising agent is the more complex labeling chemistry based on electrophilic fluorination that hampers its availability in comparison to the nucleophilic displacement reactions used in the radiosynthesis of the mono-fluorinated 2-nitroimidazoles [120].

The first human trial was performed on 15 HNC patients whereby the feasibility of [^{18}F]EF5 could be demonstrated. In a time course analysis, Komar et al. demonstrated a blood-flow-dependent initial distribution which showed to be hypoxia-specific at later time points. The best results were found performing the PET scan 3 h p.i. with a tumor-to-muscle cutoff value of 1.5 (Fig. 11.13) [121]. Additionally, [^{18}F]EF5 reveals a predictive value as an increased tumor uptake

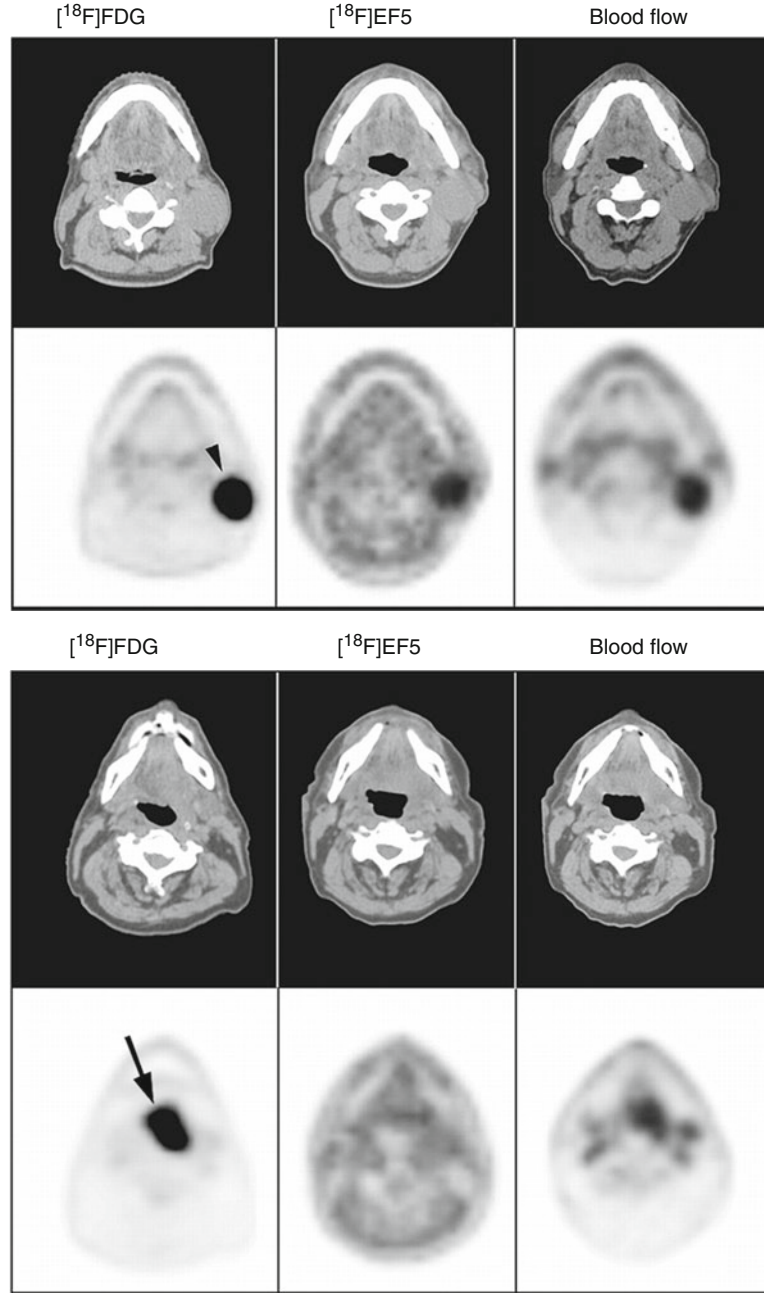

Fig. 11.13 Comparison of PET/CT scans for [^{18}F]EF5, [^{18}F]FDG, and [^{15}O]H_2O. In three squamous cell HNC patients, the three tracers [^{18}F]EF5, [^{18}F]FDG, and [^{15}O]H_2O were applied and PET/CT scans performed. The measurement of blood flow was followed by an [^{18}F]EF5 PET/CT scan. The [^{18}F]FDG scan was performed separately. The primary and metastatic lesions are visible on the blood flow and the [^{18}F]FDG scans. [^{18}F]EF5 PET was measured 3 h p.i. This tracer detects hypoxia well in HNC patients. Voxel-by-voxel analysis of co-registered blood flow and [^{18}F]EF5 revealed a distinct pattern of hypoxia with a tumor-to-muscle ratio of 1.5 at 3 h for clinically significant hypoxia. The three tracers did not show a significant correlation although a negative relationship between [^{15}O]H_2O and [^{18}F]EF5 could be detected. While *arrows* indicate primary tumors, *arrowheads* point to metastatic lesions (Reprinted by permission of SNMMI from: Komar et al. [121])

Fig. 11.13 (continued)

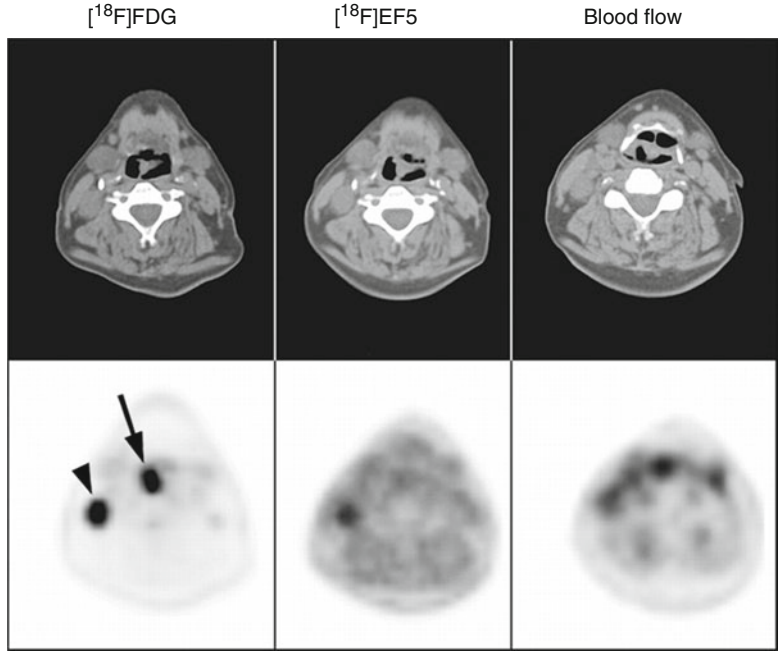

correlates with higher grade tumors and a high prevalence of metastasis formation [122, 123].

A comparative study with [18F]EF3 and [18F]FDG was performed in patients with HNC [119]. No correlation in the uptake of the two tracers could be observed underlining the difference of the hypoxia-specific [18F]EF3 and the tumor-sensitive [18F]FDG.

11.2.3 Cu-Diacetyl-bis(N4-methylthiosemicarbazone) (Cu-ATSM)

An alternative agent with great promise for PET hypoxia imaging is Cu-diacetyl-bis(N4-methylthiosemicarbazone) (Cu-ATSM) developed from the blood perfusion agent Cu-pyruvaldehyde-bis(N4-methylthiosemicarbazone) (Cu-PTSM) [124]. Cu-ATSM consists of the chelator diacetyl-bis(N4-methylthiosemicarbazone) complexing a copper(II) ion (Fig. 11.14). The precursor can be rapidly labeled with a variety of copper isotopes. The four positron-emitting radioisotopes Cu-60 ($t_{1/2}$ 0.4 h), Cu-61 ($t_{1/2}$ 3.32 h), Cu-62 ($t_{1/2}$ 0.16 h), and Cu-64 ($t_{1/2}$ 12.7 h) can be used flexibly for PET imaging [125] and

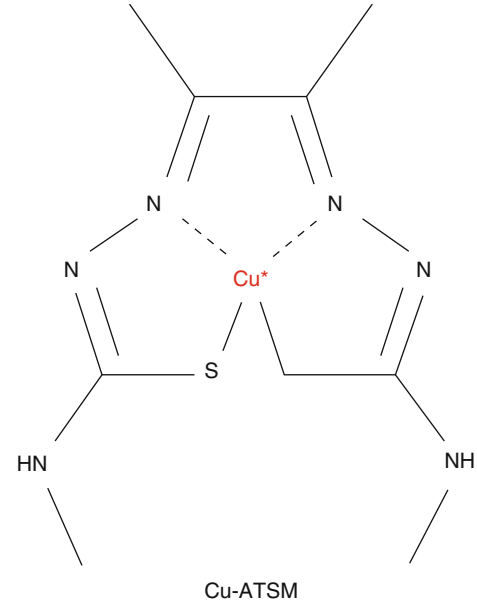

Fig. 11.14 Structure of Cu-ATSM. The highlighted Cu ion (Cu*) is a representation of the radioactive isotopes Cu-60, Cu-61, Cu-62, and Cu-64

serial imaging can be performed in short intervals to monitor reperfusion using the short-lived radionuclides [69]. Cu-ATSM is retained in higher extent (up to tenfold) than [18F]FMISO

within hypoxic cells as demonstrated for EMT6 breast cancer cells [126]. The neutral lipophilic molecule is highly membrane permeable and can pass normoxic cells metabolically unchanged due to its relatively low redox potential. Cu(II)-ATSM is retained comparable to the nitroimidazoles in hypoxic tissues following its reduction to [Cu(I)-ATSM]$^-$ due to its negative charge. The exact mechanism of how Cu-ATSM is entrapped within cells is however not completely understood. It is suggested that the reduction of Cu(II) ATSM is a reversible process in the presence of oxygen. Furthermore, it is hypothesized that Cu(I) might dissociate slowly and irreversibly from the complex which could explain the only partial washout of copper isotopes after the reoxygenation of cells [127].

Several studies have been undertaken to preclinically evaluate the value of Cu-ATSM in hypoxia imaging. An in vivo glioma xenograft model demonstrated the correlation of Cu-ATSM and partial oxygen pressure within the tumor in comparison to polarographic electrode measurements [128]. Due to its high background clearance, Cu-ATSM results in a higher signal-to-noise ratio [129] although also an unspecific retention could be observed [130]. Compared to nitroimidazoles, Cu-ATSM showed higher tumor uptakes resulting in high-quality images at 20 min p.i. [126, 128]. A study comparing [^{18}F]EF5 with [^{64}Cu]ATSM in fibrosarcomas, 9L glioma, and animal R3230 mammary adenocarcinomas demonstrated Cu-ATSM to be a valuable hypoxia marker in some tumor types but not for all [130]. In some tumor cell lines like FSA rat fibrosarcoma [130], R3327-AT rat prostatic [131], and SCCVII murine squamous cell carcinoma [132], no significant correlation between hypoxia and tracer accumulation could be observed. This intertumoral selectivity remains one of the main challenges for the use of Cu-ATSM as a general hypoxia marker. Different hypotheses exist concerning the varying retention within hypoxic cells. On the one hand, different redox potentials might explain for the differences as well as the pH within the cells [133], and on the other hand, it is presumed that Cu(I) dissociating from Cu-ATSM might be transported out of the tumor cells as the copper transporter ATP7B could be shown to be overexpressed in several human malignancies, e.g., in breast, ovarian, and gastric cancer [134].

[^{60}Cu]ATSM has been validated for its use especially for cervical and lung cancers. The appropriate threshold to discriminate between hypoxia and normoxic tissue was determined to be 3.5 after a dynamic imaging for 60 min in 14 patients with biopsy-proven cervical cancer [135]. These results could be confirmed in a second study with 38 patients with cervical cancer [136]. The uptake of [^{60}Cu]ATSM furthermore proved to be predictive for progression-free survival and overall survival. In both studies no correlation with FDG uptake could be observed. The ACRIN (American College of Radiology Imaging Network) trial 6682 is currently ongoing with the aim to assess the potential of [^{64}Cu]ATSM as predictive biomarker for treatment outcome in cervical cancer in 100 female participants [44].

In further clinical settings, the predictive role for [^{60}Cu]ATSM could be demonstrated. In an initial study with 14 patients with biopsy-proven non-small cell lung cancer, the [^{60}Cu]ATSM uptake correlated with the therapy response to radiation or chemotherapy, discriminating responders from nonresponders (Fig. 11.15) [137]. In 2008, Dietz and collaborators showed in a pilot study that [^{60}Cu]ATSM may be predictive of survival and tumor response to neoadjuvant chemoradiotherapy in patients with locally invasive primary or node-positive rectal cancer [138]. Semiquantitatively, the tumor uptake of the PET tracer was determined using the tumor-to-muscle ratio. If this ratio exceeded 2.6, patients had a worse prognosis regarding the overall and progression-free survival. An increase of the molecular hypoxia markers VEGF, EGFR, COX-2, and CAIX, an increase in apoptosis, as well as a poor outcome could be shown to be associated with [^{60}Cu]ATSM uptake in cervical cancer patients [135].

Also for IMRT, Cu-ATSM imaging via PET/CT might prove feasible as shown by Chao and collaborators for patients with HNC [139].

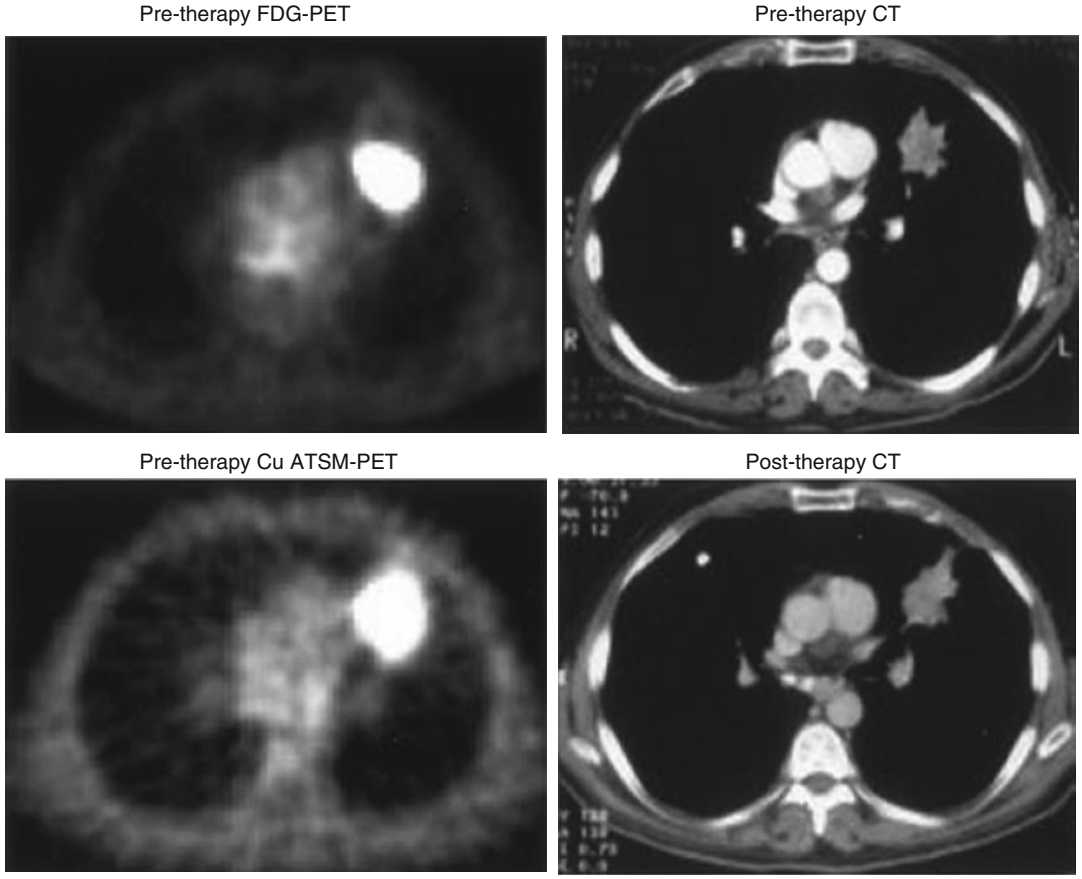

Fig. 11.15 Feasibility of [^{60}Cu]ATSM in clinical imaging of NSCLC for predicting the response to therapy. The pre-therapy [^{18}F]FDG-PET scan (*upper left*) and the CT scan (*upper right*) of this NSCLC patient representing the results of a nonresponder confirm the existence of the tumor in the lingular mass. The uptake of [^{60}Cu]ATSM was analyzed prior to therapy using PET scan (*lower left*) and compared to tumor response to therapy. Nonresponders had a tumor-to-muscle ratio of ≥3.0. The PET results were correlated with a follow-up PET scan 3 months after chemotherapy. The patient died 15 months after diagnosis due to progressive disease. [^{18}F]FDG uptake and responsiveness to therapy as well as [^{18}F]FDG and [^{60}Cu]ATSM uptake did not correlate significantly (The figure was reprinted with kind permission by Springer Science+Business Media from Dehdashti et al. [137])

In summary, Cu-ATSM holds promise for the future PET imaging irrespective of the applied copper isotope [140]. Due to its small molecular weight and high membrane permeability, it shows a high diffusion rate into cells where it is rapidly reduced and retained in case of hypoxia. Cu-ATSM might also respond to other adverse conditions within the tumor indicating that Cu-ATSM might be a more general biomarker for poor treatment response [44]. Furthermore, Cu-ATSM exhibits a high tumor-to-background ratio as it is cleared fast from the blood. Positive results in future clinical applications are thus to be expected [61].

11.2.4 Anti-Carbonic Anhydrase IX (CAIX) Antibodies

Another strategy for the detection of hypoxia via PET depends on the radiolabeling of anti-carbonic anhydrase IX (CAIX) antibodies. One

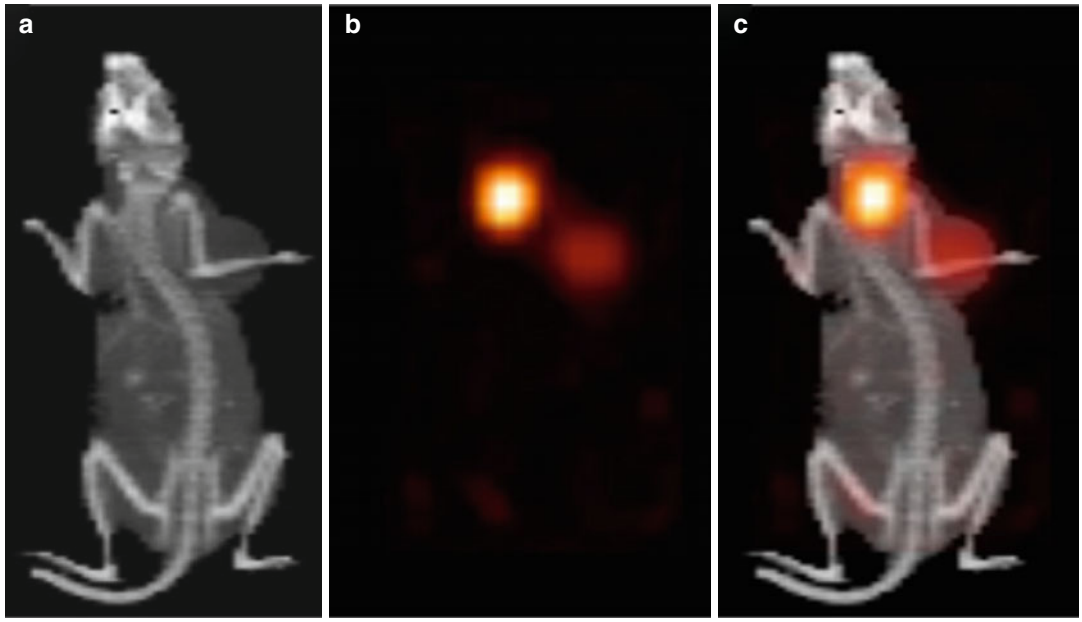

Fig. 11.16 Uptake of the anti-CAIX antibody [^{124}I] cG250 in xenografted RCC. At day 3 p.i., [^{124}I]cG250 accumulates with a maximal trend towards correlation to the partial oxygen pressure within the xenografted RCC SK-RC 52 in balb/c nude mice. (**a**) The CT scan visualizes the localization of the xenograft in the right shoulder region, (**b**) whereas the localization of [^{124}I]cG250 can be observed in the PET scan. Liberated [^{124}I] is retained in the thyroid. (**c**) The co-registered [^{124}I]cG250 PET/CT scan demonstrates the better imaging of multiparametric assessments (Reprinted with permission by Elsevier from Lawrentschuk et al. [147])

of the downstream targets of the transcription factor HIF-1α is CAIX which is upregulated under hypoxic conditions and hence an intrinsic hypoxia-related (endogenous) cell marker [141, 142]. This enzyme is displayed on the cell surface of hypoxic cells [141], while normoxic cells of the gastric mucosa, bile ducts, and small intestine show only a basal expression of CAIX. After determination of the CAIX levels within hypoxic areas, the treatment of patients with CAIX-targeted therapeutics could also be favorable.

A study with fragments of the anti-CAIX antibody cG250 was undertaken in order to investigate the assessment of tumor hypoxia in a tumor xenograft model of a human HNC and to determine the spatial correlation between radiotracer to the microscopic distribution of the cells [143]. The [^{89}Zr]cG250(Fab′)$_2$ uptake correlated significantly and rapidly after injection with the immunohistochemical staining for CAIX expression, and tumors could be clearly visualized by PET after 4 h. 24 h p.i., the tumor uptake was already reduced, displaying presumably the fast pharmacodynamics of the tracer. In comparison to pimonidazole staining, however, the signal of the antibody fragments was reduced.

As a significant molecular marker, 87–100 % of the clear cell subtype of renal cell carcinoma (RCC) express CAIX [144–146]. Hence, a further study to detect hypoxia in a human xenograft model of RCC was undertaken with [^{124}I]cG250 [147]. All tumors analyzed developed hypoxia and the antibody localized in excellent manner within the tumors as measured by PET/CT correlating to the obtained data of polarographic O_2 microelectrode probes (Fig. 11.16). However, no significant correlation between the expression of CAIX and hypoxia could be found. This might be due to the fact that CAIX is also involved in angiogenesis which occurs throughout the tumor.

As these results for the antibody and fragments of cG250 are holding great promise, further studies are warranted to verify their value in the imaging of hypoxia.

11.3 Integrin-Specific PET Tracers: An Indirect Marker for Tumor Hypoxia?

Angiogenesis is a central hallmark of tumors reaching a size of more than ~1 mm^3 [148]. Hypoxia leads to angiogenesis as the transcription factor HIF-1 upregulates the expression of VEGF, PDGFB, and other critical angiogenic growth factors [149]. Angiogenesis is a potential target for cancer diagnosis and therapy, and hence, research focuses on it on a basal, translational, and clinical level. Integrin $\alpha_v\beta_3$ playing a central role in angiogenesis is expressed on the surface of activated endothelial cells and is furthermore also under the control of HIF-1 [150]. Therefore, integrin-targeted PET tracers like RGD derivatives labeled with ^{18}F and ^{68}Ga might also be useful in hypoxia detection. The data obtained from studies trying to correlate the distribution of hypoxia and integrin markers did not come to conclusive results [151, 152]. One major drawback of this angiogenesis imaging is that integrins can be detected on all cells throughout the tumor and that they are not hypoxia-specific. Further research is required to clarify the connection of hypoxia and angiogenesis. Nevertheless, the imaging of these two parameters might help tailoring individual tumor therapies.

11.4 Treatment Planning in Therapy After Hypoxia PET Imaging

Although limited in treatment response, hypoxic areas within tumors harbor the opportunity for tumor selective therapies including prodrugs activated by hypoxia, hypoxia-specific gene therapy, or targeting molecules upon which hypoxic cell survival depends [153]. Ideally, the development of novel bioreductive therapeutics with a paired diagnostic value will be forced [4]. Oncology has to exploit this highly validated target for therapy [4]. Furthermore, in radiation therapy IMRT can be applied after determining hypoxic areas within a tumor enabling dose escalation during radiation therapies. In a so-called dose-painting process, the dose delivered to the hypoxic tissues can be individually adapted in order to overcome radiation resistance depending on the severity of hypoxia [154]. Dose painting describes the administration of a nonuniform radiation dose distribution in the target volume which is based on functional or molecular images [155]. Yet the feasibility of IMRT has to be evaluated in clinical settings.

The main goal of radiation therapies is to destroy in a local treatment all tumor cells and to achieve a complete remission. The sparing of healthy tissues while destroying a maximum of the tumor via dose escalation is another objective aiming at a greater tumor control with lower side effects. The dependence of radiation resistance on hypoxia is well known and might be overcome by dose escalation in the hypoxic areas after detection. Currently no study describes the improvement of outcome after enhancing the radiation dose to hypoxic tissues. For treatment planning in radiation therapy, PET imaging exhibits some limitations which have to be overcome. Usually, clinical PET scanners have a resolution of about 2–4 mm, while the hypoxic areas within a tumor can exhibit dimensions of some 100 μm [105, 156]. Therefore, only "partial volume effects" can be measured as one voxel might contain regions of normoxia as well as extreme hypoxia (Fig. 11.17). Additionally, also background noise, patient movements, and the tumor as dynamic system itself might modulate the intensities leading to irregularities and ambiguities in the PET signal. At a subvoxel scale the severity of hypoxia and the resulting level of radiosensitivity cannot be determined. Therefore, multiparametric imaging combining MRI (BOLD) with PET as well as dynamic imaging might yield a better and synergistically optimized representation of the actual tumor biology [41]. Another unresolved question so far is the influence of increased radiation applied to the tissues. Nevertheless, dose painting seems to be a realistic and attractive concept which needs to be clinically proven.

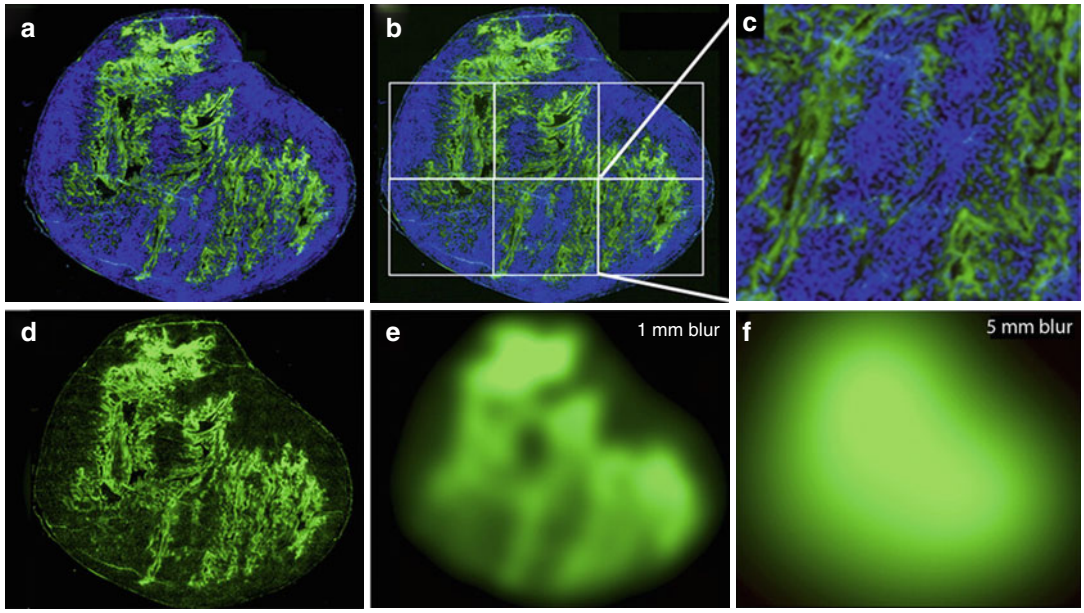

Fig. 11.17 Comparison of the resolution of hypoxia detection using immunohistochemistry to PET imaging. (**a**) A histologic section of a tumor was stained with the hypoxia marker pimonidazole (*green*) and the vascular perfusion marker Hoechst 33342 (*blue*) demonstrating the dispersed hypoxic areas within the tumor. (**b**) The superimposition of the same image with six 5 mm^2 regions represents the resolution of a clinical PET scanner (**c**) where single regions can be magnified and analyzed. (**d**–**f**) If for the same image stained solely with pimonidazole a Gaussian blur of 1 mm (**e**) and 5 mm (**f**) is applied, the resolution of clinical PET scanners is obtained. These pictures clearly indicate the dependence of voxel values on the maximum uptake of tracer and the hypoxic fraction of voxels. The signals are averaged. If the spatial resolution is increased, the hypoxic areas can be visualized with a higher reliability playing an important role in radiotherapy planning using IMRT (Reprinted by permission of SNMMI from Carlin and Humm [44])

Conclusion

Several PET tracers for the noninvasive detection of hypoxia have been developed and investigated to predict the outcome and identify patients with an impaired prognosis due to hypoxia. The application of hypoxia tracers for PET and PET/CT provides so far a useful and informative value for the prognosis of rectal and cervical carcinoma, NSCLC, glioma, and head and neck tumors. Unfortunately, the imaging contrast in comparison to [^{18}F]FDG is relatively low and impedes the analysis. The establishment and validation of hypoxia PET tracers is still under development, and the clinical use of these agents depends on how reliable their predictive value will prove to be. Nevertheless, PET, PET/CT, and PET/MRI offer the potential to optimize and individualize the treatments of patients suffering from hypoxic cancers. The risk stratification of newly diagnosed tumors as well as tailored treatment could be possible using dose escalation and dose painting in radiotherapy as well as hypoxia-activated drugs. The road to personalized medicine requires molecular imaging beyond tumor detection as also the characterization of the tumor on a functional level is of critical importance.

References

1. West JB. Respiratory physiology – the essentials. Baltimore/London/Los Angeles: Williams & Wilkins; 1999.
2. Helmlinger G, et al. Interstitial pH and pO2 gradients in solid tumors in vivo: high-resolution measurements reveal a lack of correlation. Nat Med. 1997;3:177–82.
3. Vaupel P, et al. Blood flow, tissue oxygenation, pH distribution, and energy metabolism of murine mammary adenocarcinomas during growth. Adv Exp Med Biol. 1989;248:835–45.

4. Wilson WR, Hay MP. Targeting hypoxia in cancer therapy. Nat Rev Cancer. 2011;11:393–410.
5. Höckel M, Vaupel P. Tumor hypoxia: definitions and current clinical, biologic, and molecular aspects. J Natl Cancer Inst. 2001;93:266–76.
6. Vaupel P, Harrison L. Tumor hypoxia: causative factors, compensatory mechanisms, and cellular response. Oncologist. 2004;9 Suppl 5:4–9.
7. Vaupel P, Mayer A. Hypoxia in cancer: significance and impact on clinical outcome. Cancer Metastasis Rev. 2007;26:225–39.
8. Boyer PD, et al. Oxidative phosphorylation and photophosphorylation. Annu Rev Biochem. 1977;46: 955–66.
9. Honig CR. Modern cardiovascular physiology. Boston/Toronto: Little and Brown; 1988.
10. Zander R, Vaupel P. Proposal for using a standardized terminology on oxygen transport to tissue. Adv Exp Med Biol. 1985;191:965–70.
11. Crabtree HG, Cramer W. The action of radium on cancer cells. II. Some factors determining the susceptibility of cancer cells to radium. Proc R Soc Lond B. 1933;113:238–50.
12. Schwarz G. Desensibilisierung gegen Röntgen- und Radiumstrahlen. Münchener Med Wochenschau. 1909;24:1–2.
13. Gray LH, et al. The concentration of oxygen dissolved in tissues at the time of irradiation as a factor in radiotherapy. Br J Radiol. 1953;26:638–48.
14. Hall EJ. Radiobiology for the radiologist. Philadelphia: Lippincott; 1994.
15. Comerford KM, et al. Hypoxia-inducible factor-1-dependent regulation of the multidrug resistance (MDR1) gene. Cancer Res. 2002;62:3387–94.
16. Thews O, et al. Hypoxia-induced extracellular acidosis increases p-glycoprotein activity and chemoresistance in tumors in vivo via p38 signaling pathway. Adv Exp Med Biol. 2011;701:115–22.
17. Riva C, et al. Cellular physiology and molecular events in hypoxia-induced apoptosis. Anticancer Res. 1998;18:4729–36.
18. Shimizu S, et al. Prevention of hypoxia-induced cell death by Bcl-2 and Bcl-xL. Nature. 1995;374: 811–3.
19. Soengas MS, et al. Apaf-1 and caspase-9 in p53-dependent apoptosis and tumor inhibition. Science. 1999;284:156–9.
20. Giaccia AJ. Hypoxic stress proteins: survival of the fittest. Semin Radiat Oncol. 1996;6:46–58.
21. Koch CJ, et al. The effect of hypoxia on the generation time of mammalian cells. Radiat Res. 1973;53:43–8.
22. Pettersen EO, Lindmo T. Inhibition of cell-cycle progression by acute treatment with various degrees of hypoxia: modifications induced by low concentrations of misonidazole present during hypoxia. Br J Cancer. 1983;48:809–17.
23. Yuan J, Glazer PM. Mutagenesis induced by the tumor microenvironment. Mutat Res. 1998;400: 439–46.
24. Harris AL. Hypoxia – a key regulatory factor in tumour growth. Nat Rev Cancer. 2002;2:38–47.
25. Pennacchietti S, et al. Hypoxia promotes invasive growth by transcriptional activation of the met protooncogene. Cancer Cell. 2003;3:347–61.
26. Kang SS, et al. Clinical significance of glucose transporter 1 (GLUT1) expression in human breast carcinoma. Jpn J Cancer Res. 2002;93:1123–8.
27. Kunkel M, et al. Overexpression of Glut-1 and increased glucose metabolism in tumors are associated with a poor prognosis in patients with oral squamous cell carcinoma. Cancer. 2003;97:1015–24.
28. Younes M, et al. Overexpression of Glut1 and Glut3 in stage I nonsmall cell lung carcinoma is associated with poor survival. Cancer. 1997;80:1046–51.
29. Parkkila S, et al. Carbonic anhydrase inhibitor suppresses invasion of renal cancer cells in vitro. Proc Natl Acad Sci U S A. 2000;97:2220–4.
30. Robertson N, et al. Role of carbonic anhydrase IX in human tumor cell growth, survival, and invasion. Cancer Res. 2004;64:6160–5.
31. Weinberg RA. The biology of cancer. New York/Abingdon: Garland Science; 2007.
32. Aebersold DM, et al. Expression of hypoxia-inducible factor-1alpha: a novel predictive and prognostic parameter in the radiotherapy of oropharyngeal cancer. Cancer Res. 2001;61:2911–6.
33. Bos R, et al. Levels of hypoxia-inducible factor-1alpha independently predict prognosis in patients with lymph node negative breast carcinoma. Cancer. 2003;97:1573–81.
34. Griffiths EA, et al. Hypoxia-inducible factor-1alpha expression in the gastric carcinogenesis sequence and its prognostic role in gastric and gastro-oesophageal adenocarcinomas. Br J Cancer. 2007;96:95–103.
35. Swinson DE, et al. Hypoxia-inducible factor-1 alpha in non small cell lung cancer: relation to growth factor, protease and apoptosis pathways. Int J Cancer. 2004;111:43–50.
36. Trastour C, et al. HIF-1alpha and CA IX staining in invasive breast carcinomas: prognosis and treatment outcome. Int J Cancer. 2007;120:1451–8.
37. Vleugel MM, et al. Differential prognostic impact of hypoxia induced and diffuse HIF-1alpha expression in invasive breast cancer. J Clin Pathol. 2005;58:172–7.
38. Jubb AM, et al. Assessment of tumour hypoxia for prediction of response to therapy and cancer prognosis. J Cell Mol Med. 2010;14:18–29.
39. Semenza GL. Targeting HIF-1 for cancer therapy. Nat Rev Cancer. 2003;3:721–32.
40. Krause BJ, et al. PET and PET/CT studies of tumor tissue oxygenation. Q J Nucl Med Mol Imaging. 2006;50:28–43.
41. Thorwarth D, Alber M. Implementation of hypoxia imaging into treatment planning and delivery. Radiother Oncol. 2010;97:172–5.
42. Astner ST, et al. Imaging of tumor physiology: impacts on clinical radiation oncology. Exp Oncol. 2010;32:149–52.

43. Lapi SE, et al. Positron emission tomography imaging of hypoxia. PET Clin. 2009;4:39–47.
44. Carlin S, Humm JL. PET of hypoxia: current and future perspectives. J Nucl Med. 2012;53:1171–4.
45. Horsman MR, et al. Imaging hypoxia to improve radiotherapy outcome. Nat Rev Clin Oncol. 2012;9:674–87.
46. Semenza GL. HIF-1: upstream and downstream of cancer metabolism. Curr Opin Genet Dev. 2010;20:51–6.
47. Busk M, et al. Cellular uptake of PET tracers of glucose metabolism and hypoxia and their linkage. Eur J Nucl Med Mol Imaging. 2008;35:2294–303.
48. Cherk MH, et al. Lack of correlation of hypoxic cell fraction and angiogenesis with glucose metabolic rate in non-small cell lung cancer assessed by 18F-fluoromisonidazole and 18F-FDG PET. J Nucl Med. 2006;47:1921–6.
49. Eschmann SM, et al. Prognostic impact of hypoxia imaging with 18F-misonidazole PET in non-small cell lung cancer and head and neck cancer before radiotherapy. J Nucl Med. 2005;46:253–60.
50. Gagel B, et al. [18F] fluoromisonidazole and [18F] fluorodeoxyglucose positron emission tomography in response evaluation after chemo-/radiotherapy of non-small-cell lung cancer: a feasibility study. BMC Cancer. 2006;6:51.
51. Rajendran JG, et al. [(18)F]FMISO and [(18)F]FDG PET imaging in soft tissue sarcomas: correlation of hypoxia, metabolism and VEGF expression. Eur J Nucl Med Mol Imaging. 2003;30:695–704.
52. Rajendran JG, et al. Hypoxia and glucose metabolism in malignant tumors: evaluation by [18F]fluoromisonidazole and [18F]fluorodeoxyglucose positron emission tomography imaging. Clin Cancer Res. 2004;10:2245–52.
53. Thorwarth D, et al. Combined uptake of [18F]FDG and [18F]FMISO correlates with radiation therapy outcome in head-and-neck cancer patients. Radiother Oncol. 2006;80:151–6.
54. Chapman JD. Hypoxic sensitizers – implications for radiation therapy. N Engl J Med. 1979;301:1429–32.
55. Chapman JD, et al. A marker for hypoxic cells in tumours with potential clinical applicability. Br J Cancer. 1981;43:546–50.
56. Brown JM. Clinical trials of radiosensitizers: what should we expect? Int J Radiat Oncol Biol Phys. 1984;10:425–9.
57. Grunbaum Z, et al. Synthesis and characterization of congeners of misonidazole for imaging hypoxia. J Nucl Med. 1987;28:68–75.
58. Martin GV, et al. Noninvasive detection of hypoxic myocardium using fluorine-18-fluoromisonidazole and positron emission tomography. J Nucl Med. 1992;33:2202–8.
59. Prekeges JL, et al. Reduction of fluoromisonidazole, a new imaging agent for hypoxia. Biochem Pharmacol. 1991;42:2387–95.
60. Tatum JL, et al. Hypoxia: importance in tumor biology, noninvasive measurement by imaging, and value of its measurement in the management of cancer therapy. Int J Radiat Biol. 2006;82:699–757.
61. Mees G, et al. Molecular imaging of hypoxia with radiolabelled agents. Eur J Nucl Med Mol Imaging. 2009;36:1674–86.
62. Whitmore GF, Varghese AJ. The biological properties of reduced nitroheterocyclics and possible underlying biochemical mechanisms. Biochem Pharmacol. 1986;35:97–103.
63. Rasey JS, et al. Comparison of binding of [3H]misonidazole and [14C]misonidazole in multicell spheroids. Radiat Res. 1985;101:473–9.
64. Rasey JS, et al. Characterization of radiolabeled fluoromisonidazole as a probe for hypoxic cells. Radiat Res. 1987;111:292–304.
65. Krohn KA, et al. Molecular imaging of hypoxia. J Nucl Med. 2008;49 Suppl 2:129S–48.
66. Padhani A. PET imaging of tumour hypoxia. Cancer Imaging. 2006;6:S117–21.
67. Graham MM, et al. Fluorine-18-fluoromisonidazole radiation dosimetry in imaging studies. J Nucl Med. 1997;38:1631–6.
68. Overgaard J. Clinical evaluation of nitroimidazoles as modifiers of hypoxia in solid tumors. Oncol Res. 1994;6:509–18.
69. Padhani AR, et al. Imaging oxygenation of human tumours. Eur Radiol. 2007;17:861–72.
70. Nunn A, et al. Nitroimidazoles and imaging hypoxia. Eur J Nucl Med. 1995;22:265–80.
71. Martin GV, et al. Fluoromisonidazole. A metabolic marker of myocyte hypoxia. Circ Res. 1990;67:240–4.
72. Piert M, et al. Introducing fluorine-18 fluoromisonidazole positron emission tomography for the localisation and quantification of pig liver hypoxia. Eur J Nucl Med. 1999;26:95–109.
73. Chang J, et al. A robotic system for 18F-FMISO PET-guided intratumoral pO2 measurements. Med Phys. 2009;36:5301–9.
74. Bentzen L, et al. Assessment of hypoxia in experimental mice tumours by [18F]fluoromisonidazole PET and pO2 electrode measurements. Influence of tumour volume and carbogen breathing. Acta Oncol. 2002;41:304–12.
75. Dubois L, et al. Evaluation of hypoxia in an experimental rat tumour model by [(18)F]fluoromisonidazole PET and immunohistochemistry. Br J Cancer. 2004;91:1947–54.
76. Troost EG, et al. Imaging hypoxia after oxygenation-modification: comparing [18F]FMISO autoradiography with pimonidazole immunohistochemistry in human xenograft tumors. Radiother Oncol. 2006;80:157–64.
77. Troost EG, et al. Correlation of [18F]FMISO autoradiography and pimonidazole [corrected] immunohistochemistry in human head and neck carcinoma xenografts. Eur J Nucl Med Mol Imaging. 2008;35:1803–11.
78. Rasey JS, et al. Quantifying hypoxia with radiolabeled fluoromisonidazole: pre-clinical and clinical

studies. In: Machulla H-J, editor. The imaging of hypoxia. Dordrecht: Kluwer Academic Publishers; 1999.
79. Gagel B, et al. pO(2) Polarography versus positron emission tomography ([(18)F] fluoromisonidazole, [(18)F]-2-fluoro-2′-deoxyglucose). An appraisal of radiotherapeutically relevant hypoxia. Strahlenther Onkol. 2004;180:616–22.
80. Zimny M, et al. FDG – a marker of tumour hypoxia? A comparison with [18F]fluoromisonidazole and pO2-polarography in metastatic head and neck cancer. Eur J Nucl Med Mol Imaging. 2006;33:1426–31.
81. Valk PE, et al. Hypoxia in human gliomas: demonstration by PET with fluorine-18-fluoromisonidazole. J Nucl Med. 1992;33:2133–7.
82. Rasey JS, et al. Quantifying regional hypoxia in human tumors with positron emission tomography of [18F]fluoromisonidazole: a pretherapy study of 37 patients. Int J Radiat Oncol Biol Phys. 1996;36:417–28.
83. Grosu AL, et al. Hypoxia imaging with FAZA-PET and theoretical considerations with regard to dose painting for individualization of radiotherapy in patients with head and neck cancer. Int J Radiat Oncol Biol Phys. 2007;69:541–51.
84. Spence AM, et al. Regional hypoxia in glioblastoma multiforme quantified with [18F]fluoromisonidazole positron emission tomography before radiotherapy: correlation with time to progression and survival. Clin Cancer Res. 2008;14:2623–30.
85. Bentzen L, et al. Tumour oxygenation assessed by 18F-fluoromisonidazole PET and polarographic needle electrodes in human soft tissue tumours. Radiother Oncol. 2003;67:339–44.
86. Lee NY, et al. Fluorine-18-labeled fluoromisonidazole positron emission and computed tomography-guided intensity-modulated radiotherapy for head and neck cancer: a feasibility study. Int J Radiat Oncol Biol Phys. 2008;70:2–13.
87. Lin Z, et al. The influence of changes in tumor hypoxia on dose-painting treatment plans based on 18F-FMISO positron emission tomography. Int J Radiat Oncol Biol Phys. 2008;70:1219–28.
88. Rischin D, et al. Prognostic significance of [18F]-misonidazole positron emission tomography-detected tumor hypoxia in patients with advanced head and neck cancer randomly assigned to chemoradiation with or without tirapazamine: a substudy of Trans-Tasman Radiation Oncology Group Study 98.02. J Clin Oncol. 2006;24:2098–104.
89. Jansen JF, et al. Noninvasive assessment of tumor microenvironment using dynamic contrast-enhanced magnetic resonance imaging and 18F-fluoromisonidazole positron emission tomography imaging in neck nodal metastases. Int J Radiat Oncol Biol Phys. 2010;77:1403–10.
90. Cher LM, et al. Correlation of hypoxic cell fraction and angiogenesis with glucose metabolic rate in gliomas using 18F-fluoromisonidazole, 18F-FDG PET, and immunohistochemical studies. J Nucl Med. 2006;47:410–8.
91. Lee ST, Scott AM. Hypoxia positron emission tomography imaging with 18f-fluoromisonidazole. Semin Nucl Med. 2007;37:451–61.
92. Yang DJ, et al. Development of F-18-labeled fluoroerythronitroimidazole as a PET agent for imaging tumor hypoxia. Radiology. 1995;194:795–800.
93. Grönroos T, et al. Pharmacokinetics of [18F] FETNIM: a potential marker for PET. J Nucl Med. 2001;42:1397–404.
94. Grönroos T, et al. Comparison of the biodistribution of two hypoxia markers [18F]FETNIM and [18F] FMISO in an experimental mammary carcinoma. Eur J Nucl Med Mol Imaging. 2004;31:513–20.
95. Lehtiö K, et al. Imaging of blood flow and hypoxia in head and neck cancer: initial evaluation with [(15) O]H(2)O and [(18)F]fluoroerythronitroimidazole PET. J Nucl Med. 2001;42:1643–52.
96. Lehtiö K, et al. Quantifying tumour hypoxia with fluorine-18 fluoroerythronitroimidazole ([18F] FETNIM) and PET using the tumour to plasma ratio. Eur J Nucl Med Mol Imaging. 2003;30:101–8.
97. Lehtiö K, et al. Imaging perfusion and hypoxia with PET to predict radiotherapy response in head-and-neck cancer. Int J Radiat Oncol Biol Phys. 2004;59:971–82.
98. Li L, et al. Comparison of 18F-fluoroerythronitro imidazole and 18F-fluorodeoxyglucose positron emission tomography and prognostic value in locally advanced non-small-cell lung cancer. Clin Lung Cancer. 2010;11:335–40.
99. Vercellino L, et al. Hypoxia imaging of uterine cervix carcinoma with (18)F-FETNIM PET/CT. Clin Nucl Med. 2012;37:1065–8.
100. Reischl G, et al. Imaging of tumor hypoxia with [124I]IAZA in comparison with [18F]FMISO and [18F]FAZA – first small animal PET results. J Pharm Pharm Sci. 2007;10:203–11.
101. Kumar P, et al. Fluoroazomycin arabinoside (FAZA): synthesis, 2H and 3H-labelling and preliminary biological evaluation of a novel 2-nitroimidazole marker of tissue hypoxia. J Label Compd Radiopharm. 1999;42:3–16.
102. Kumar P, et al. Microwave-assisted (radio) halogenation of nitroimidazole-based hypoxia markers. Appl Radiat Isot. 2002;57:697–703.
103. Piert M, et al. Hypoxia-specific tumor imaging with 18F-fluoroazomycin arabinoside. J Nucl Med. 2005;46:106–13.
104. SorgerD,etal.[18F]Fluoroazomycinarabinofuranoside (18FAZA) and [18F]fluoromisonidazole (18FMISO): a comparative study of their selective uptake in hypoxic cells and PET imaging in experimental rat tumors. Nucl Med Biol. 2003;30:317–26.
105. Busk M, et al. Imaging hypoxia in xenografted and murine tumors with 18F-fluoroazomycin arabinoside: a comparative study involving microPET, autoradiography, PO2-polarography, and fluorescence microscopy. Int J Radiat Oncol Biol Phys. 2008;70:1202–12.
106. Tran LB, et al. Hypoxia imaging with the nitroimidazole 18F-FAZA PET tracer: a comparison with

OxyLite, EPR oximetry and 19F-MRI relaxometry. Radiother Oncol. 2012;105:29–35.
107. Beck R, et al. Pretreatment 18F-FAZA PET predicts success of hypoxia-directed radiochemotherapy using tirapazamine. J Nucl Med. 2007;48: 973–80.
108. Busk M, et al. PET hypoxia imaging with FAZA: reproducibility at baseline and during fractionated radiotherapy in tumour-bearing mice. Eur J Nucl Med Mol Imaging. 2013;40:186–97.
109. Havelund BM, et al. Tumour hypoxia imaging with 18F-fluoroazomycinarabinofuranoside PET/CT in patients with locally advanced rectal cancer. Nucl Med Commun. 2013;34:155–61.
110. Souvatzoglou M, et al. Tumour hypoxia imaging with [18F]FAZA PET in head and neck cancer patients: a pilot study. Eur J Nucl Med Mol Imaging. 2007;34:1566–75.
111. Postema EJ, et al. Initial results of hypoxia imaging using 1-alpha-D: -(5-deoxy-5-[18F]-fluoroarabinofuranosyl)-2-nitroimidazole (18F-FAZA). Eur J Nucl Med Mol Imaging. 2009;36:1565–73.
112. Mortensen LS, et al. FAZA PET/CT hypoxia imaging in patients with squamous cell carcinoma of the head and neck treated with radiotherapy: results from the DAHANCA 24 trial. Radiother Oncol. 2012;105:14–20.
113. Tewson TJ. Synthesis of [18F]fluoroetanidazole: a potential new tracer for imaging hypoxia. Nucl Med Biol. 1997;24:755–60.
114. Barthel H, et al. In vivo evaluation of [18F]fluoroetanidazole as a new marker for imaging tumour hypoxia with positron emission tomography. Br J Cancer. 2004;90:2232–42.
115. Rasey JS, et al. Characterization of [18F]fluoroetanidazole, a new radiopharmaceutical for detecting tumor hypoxia. J Nucl Med. 1999;40:1072–9.
116. Evans SM, et al. Noninvasive detection of tumor hypoxia using the 2-nitroimidazole [18F]EF1. J Nucl Med. 2000;41:327–36.
117. Christian N, et al. Determination of tumour hypoxia with the PET tracer [18F]EF3: improvement of the tumour-to-background ratio in a mouse tumour model. Eur J Nucl Med Mol Imaging. 2007;34:1348–54.
118. Ziemer LS, et al. Noninvasive imaging of tumor hypoxia in rats using the 2-nitroimidazole 18F-EF5. Eur J Nucl Med Mol Imaging. 2003;30:259–66.
119. Koch CJ, et al. Pharmacokinetics of EF5 [2-(2-nitro-1-H-imidazol-1-yl)-N-(2,2,3,3,3-pentafluoropropyl) acetamide] in human patients: implications for hypoxia measurements in vivo by 2-nitroimidazoles. Cancer Chemother Pharmacol. 2001;48:177–87.
120. Dolbier Jr WR, et al. [18F]-EF5, a marker for PET detection of hypoxia: synthesis of precursor and a new fluorination procedure. Appl Radiat Isot. 2001;54:73–80.
121. Komar G, et al. 18F-EF5: a new PET tracer for imaging hypoxia in head and neck cancer. J Nucl Med. 2008;49:1944–51.
122. Evans SM, et al. Comparative measurements of hypoxia in human brain tumors using needle electrodes and EF5 binding. Cancer Res. 2004;64:1886–92.
123. Evans SM, et al. EF5 binding and clinical outcome in human soft tissue sarcomas. Int J Radiat Oncol Biol Phys. 2006;64:922–7.
124. Wood KA, et al. [(64)Cu]diacetyl-bis(N(4)-methylthiosemicarbazone) – a radiotracer for tumor hypoxia. Nucl Med Biol. 2008;35:393–400.
125. Vavere AL, Lewis JS. Cu-ATSM: a radiopharmaceutical for the PET imaging of hypoxia. Dalton Trans. 2007; (43):4893–4902
126. Lewis JS, et al. Evaluation of 64Cu-ATSM in vitro and in vivo in a hypoxic tumor model. J Nucl Med. 1999;40:177–83.
127. Dearling JL, et al. Copper bis(thiosemicarbazone) complexes as hypoxia imaging agents: structure-activity relationships. J Biol Inorg Chem. 2002;7:249–59.
128. Lewis JS, et al. Tumor uptake of copper-diacetyl-bis(N(4)-methylthiosemicarbazone): effect of changes in tissue oxygenation. J Nucl Med. 2001;42:655–61.
129. Fujibayashi Y, et al. Comparative studies of Cu-64-ATSM and C-11-acetate in an acute myocardial infarction model: ex vivo imaging of hypoxia in rats. Nucl Med Biol. 1999;26:117–21.
130. Yuan H, et al. Intertumoral differences in hypoxia selectivity of the PET imaging agent 64Cu(II)-diacetyl-bis(N4-methylthiosemicarbazone). J Nucl Med. 2006;47:989–98.
131. Burgman P, et al. Cell line-dependent differences in uptake and retention of the hypoxia-selective nuclear imaging agent Cu-ATSM. Nucl Med Biol. 2005;32:623–30.
132. Matsumoto K, et al. The influence of tumor oxygenation on hypoxia imaging in murine squamous cell carcinoma using [64Cu]Cu-ATSM or [18F]fluoromisonidazole positron emission tomography. Int J Oncol. 2007;30:873–81.
133. Bowen SR, et al. Characterization of positron emission tomography hypoxia tracer uptake and tissue oxygenation via electrochemical modeling. Nucl Med Biol. 2011;38:771–80.
134. Katano K, et al. The copper export pump ATP7B modulates the cellular pharmacology of carboplatin in ovarian carcinoma cells. Mol Pharmacol. 2003;64:466–73.
135. Grigsby PW, et al. Comparison of molecular markers of hypoxia and imaging with (60)Cu-ATSM in cancer of the uterine cervix. Mol Imaging Biol. 2007;9:278–83.
136. Dehdashti F, et al. Assessing tumor hypoxia in cervical cancer by PET with 60Cu-labeled diacetyl-bis(N4-methylthiosemicarbazone). J Nucl Med. 2008;49:201–5.
137. Dehdashti F, et al. In vivo assessment of tumor hypoxia in lung cancer with 60Cu-ATSM. Eur J Nucl Med Mol Imaging. 2003;30:844–50.
138. Dietz DW, et al. Tumor hypoxia detected by positron emission tomography with 60Cu-ATSM as a

predictor of response and survival in patients undergoing neoadjuvant chemoradiotherapy for rectal carcinoma: a pilot study. Dis Colon Rectum. 2008;51:1641–8.
139. Chao KS, et al. A novel approach to overcome hypoxic tumor resistance: Cu-ATSM-guided intensity-modulated radiation therapy. Int J Radiat Oncol Biol Phys. 2001;49:1171–82.
140. Lewis JS, et al. An imaging comparison of 64Cu-ATSM and 60Cu-ATSM in cancer of the uterine cervix. J Nucl Med. 2008;49:1177–82.
141. Pastorekova S, et al. Tumor-associated carbonic anhydrases and their clinical significance. Adv Clin Chem. 2006;42:167–216.
142. Wykoff CC, et al. Hypoxia-inducible expression of tumor-associated carbonic anhydrases. Cancer Res. 2000;60:7075–83.
143. Hoeben BA, et al. PET of hypoxia with 89Zr-labeled cG250-F(ab′)2 in head and neck tumors. J Nucl Med. 2010;51:1076–83.
144. Liao SY, et al. Identification of the MN/CA9 protein as a reliable diagnostic biomarker of clear cell carcinoma of the kidney. Cancer Res. 1997;57:2827–31.
145. Murakami Y, et al. MN/CA9 gene expression as a potential biomarker in renal cell carcinoma. BJU Int. 1999;83:743–7.
146. Uemura H, et al. MN/CA IX/G250 as a potential target for immunotherapy of renal cell carcinomas. Br J Cancer. 1999;81:741–6.
147. Lawrentschuk N, et al. Investigation of hypoxia and carbonic anhydrase IX expression in a renal cell carcinoma xenograft model with oxygen tension measurements and (1)(2)(4)I-cG250 PET/CT. Urol Oncol. 2011;29:411–20.
148. Folkman J. Angiogenesis. Annu Rev Med. 2006;57:1–18.
149. Rey S, Semenza GL. Hypoxia-inducible factor-1-dependent mechanisms of vascularization and vascular remodelling. Cardiovasc Res. 2010;86:236–42.
150. Cowden Dahl KD, et al. Hypoxia-inducible factor regulates alphavbeta3 integrin cell surface expression. Mol Biol Cell. 2005;16:1901–12.
151. Langen KJ, Eschmann SM. Correlative imaging of hypoxia and angiogenesis in oncology. J Nucl Med. 2008;49:515–6.
152. Picchio M, et al. Intratumoral spatial distribution of hypoxia and angiogenesis assessed by 18F-FAZA and 125I-Gluco-RGD autoradiography. J Nucl Med. 2008;49:597–605.
153. Brown JM, Wilson WR. Exploiting tumour hypoxia in cancer treatment. Nat Rev Cancer. 2004;4:437–47.
154. Ling CC, et al. Towards multidimensional radiotherapy (MD-CRT): biological imaging and biological conformality. Int J Radiat Oncol Biol Phys. 2000;47:551–60.
155. Bentzen SM, Gregoire V. Molecular imaging-based dose painting: a novel paradigm for radiation therapy prescription. Semin Radiat Oncol. 2011;21:101–10.
156. Busk M, et al. Resolution in PET hypoxia imaging: voxel size matters. Acta Oncol. 2008;47:1201–10.

MRI Hypoxia Measurements

12

Stefanie Remmele, Ralph P. Mason,
and James P.B. O'Connor

Contents

Abbreviations

BOLD	Blood oxygen-level dependent
ESR	Electron spin resonance
FLOOD	Flow and blood oxygenation level dependent sequence
FREDOM	Fluorocarbon Relaxometry using Echo planar imaging for Dynamic Oxygen Mapping
HFB	Hexafluorobenzene
HiSS	High spectral and spatial resolution
HMDSO	Hexamethyldisiloxane
OE-MRI	Oxygen-enhanced MRI
PFCs	Perfluorocarbons
TOLD	Tissue Oxygen Level Dependant contrast MRI

S. Remmele, PhD (✉)
Department of Biomedical Engineering,
University of Applied Sciences, Landshut,
Landshut 84036, Germany
e-mail: sremmele@fh-landshut.de

R.P. Mason, PhD, CSci, CChem, FRSC
Department of Radiology,
The University of Texas Southwestern Medical Center,
5323 Harry Hines Boulevard, Dallas, TX, USA
e-mail: ralph.mason@utsouthwestern.edu

J.P.B. O'Connor, PhD, FRCR
Imaging Sciences Research Group,
The University of Manchester,
Stopford Building, Oxford Road,
Manchester, M13 9PT, UK

Department of Radiology,
The Christie NHS Foundation Trust, Wilmslow Road,
Manchester, M20 4BX, UK
e-mail: james.o'connor@manchester.ac.uk

12.1 Introduction

12.1.1 Clinical Relevance of Hypoxia Imaging

Tumor hypoxia promotes cell division and invasion, angiogenesis, and inflammation and increases the metastatic risk [1–3]. Furthermore, tumor hypoxia is not only related to aggressive growth but also to an elevated resistance to a number of tumor treatment strategies like radiation, chemotherapy, thermal ablation, and photodynamic therapies [2, 4–10].

Accordingly, intensive laboratory and clinical efforts to overcome tumor hypoxia have been

A. Luna et al. (eds.), *Functional Imaging in Oncology*,
DOI 10.1007/978-3-642-40412-2_12,

made [11, 12]. Indeed, a threefold increase in radioresistance has been demonstrated when cells are irradiated under hypoxic conditions compared with normoxia, i.e., an oxygen partial pressure (pO_2) of >15 Torr for a given single radiation dose [13, 14]. The presence of hypoxic cells in human tumors is considered one of the principal reasons for the failure of radiation therapy. Wouters and Brown further showed the "intermediate" level of cell oxygenation between hypoxic and fully oxygenated was most predictive for the outcome of fractionated radiation [15]. Thus, they stressed the need to "measure tumor oxygenation in a manner that reflects the true oxygenation status of all the tumor cells, not just the ones most refractory to the effects of ionizing radiation." Knowledge of tissue oxygenation, therefore, predicts the radiation response and regional tumor control [6].

12.1.2 Overview of MRI Methods to Measure the Oxygenation of Tumors

Much effort has been spent on the development of noninvasive oxygenation measurements with MRI [16, 17]. Many approaches exploit the effect of oxygen on the relaxation properties of tissue. In these examinations, short values of the reversible transverse relaxation time T_2^* (high $R_2^* = 1/T_2^*$ values) are related to low blood oxygenation due to the paramagnetic nature of deoxygenated blood [18]. There is at least one study that exploits the longitudinal relaxation time T_1 or R_1 relaxivity of "free," i.e., dissolved oxygen molecules [19] to measure the concentration of oxygen in CSF [20]. In order to separate the effect of oxygen on the relaxation parameters from other influences, methods have been devised that derive oxygenation measures from the change of the relaxation parameters in response to oxygen-enhanced breathing challenges [21–32]. The results of these approaches are qualitative in nature but do not require any dedicated hardware or contrast agents other than conventional anesthesia gases.

Direct pO_2 values can be obtained by ^{19}F imaging methods (Sect. 12.3) [17]. These techniques exploit the change of the longitudinal relaxation rate R_1 of perfluorocarbon (PFC) reporter molecules. The approach provides quantitative oxygenation measurements, but requires specific hardware (dual-tuned coils, multi-nuclei system). By analogy proton MRI oximetry in small animals was demonstrated using hexamethyldisiloxane (HMDSO) as a reporter [33–36]. The contrast agents are not yet clinically available. Another contrast-agent-dependent MR oximetry method makes use of the Overhauser effect, combining the advantages of MRI with the oxygen sensitivity of electron spin resonance (ESR) techniques [37]. Again, this method is able to provide 3D representation of pO_2 but using specific hardware and experimental contrast agents.

In addition, biomarkers of perfusion derived from dynamic contrast-enhanced MRI (DCE-MRI) have been shown in some studies to relate to genetic profiles of hypoxia [38], oxygen tension [39], and histological measurement of hypoxic fraction [40–42] with first promising results in cervix cancer patients [43, 44]. However, tissue oxygen tension and hypoxia are affected not only by oxygen delivery (perfusion) but also by diverse factors including hemoglobin saturation, vascular geometry, and consumption (oxidative phosphorylation). Therefore, DCE-MRI measurement of perfusion provides at best indirect estimates of hypoxia and in some circumstances bare little relationship to hypoxia at all [45].

12.2 MRI Hypoxia Methods

12.2.1 Relating R_2^* and R_1 to Oxygenation

In 1990 Ogawa introduced the blood-oxygen-level-dependent imaging (BOLD) technique [18]. He showed that deoxygenated hemoglobin is paramagnetic and the susceptibility difference between blood and the surrounding tissue causes magnetic field gradients around the vessels (Fig. 12.1). These microscopic field inhomogeneities result in a shortening of T_2^* (increase of R_2^*) and thus in a signal loss in T_2^*-weighted

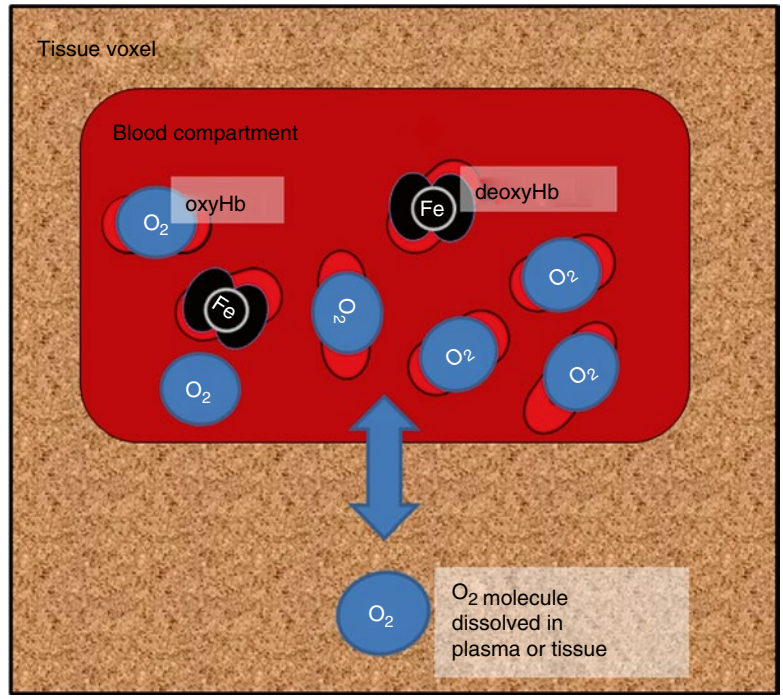

Fig. 12.1 The oxygen transport from the lung to every cell of the body is described by two mechanisms. Most of the oxygen molecules bind to hemoglobin (Hb), whereas the minority of oxygen molecules dissolve in blood plasma and tissue fluids [46]. Deoxygenated hemoglobin (deoxyHb) and dissolved oxygen molecules are paramagnetic, increasing the R_2* and R_1 relaxation rates [18, 19]

images. Since then, various groups investigated T_2*-weighted signals and quantitative T_2* or R_2* values as markers for tissue oxygenation [22, 31, 32, 47–50].

In pure blood, R_2* can be approximated by a simple linear or quadratic function dependent on the concentration of deoxygenated hemoglobin the deoxyHb concentration (i.e. [deoxyHb]) and thus the blood-oxygen saturation (sO_2) and the hematocrit level (Hct) [51]. In tissue, direct correlation of sO_2 or even pO_2 with R_2* is poor, though there are distinct trends [22, 32, 47, 50]. The deoxyHb fraction causes a frequency shift that is also dependent on the hematocrit (Hct), the volume fraction of the deoxygenated blood (dBV_f), the vessel architecture, and the oxygen saturation in deoxyHb containing vessels (*Y*):

$$\delta\omega \sim dBV_f \cdot \Delta\chi_0 \cdot Hct \cdot (1 - Y) \cdot B0 \quad (12.1)$$

A variety of approaches (qBOLD) attempt to quantify the frequency shift from the difference in gradient and spin echo signals [48, 52–55]. This adds new uncertainties, since this difference is also influenced by macroscopic field inhomogeneities, T_2, and – depending on the sequence – also by water diffusion. Accordingly, preliminary results are encouraging, but the complexity of the model and the examination is hampering the clinical translation of the approach [56].

Likewise, the longitudinal relaxation time T_1 (or rate $R_1 = 1/T_1$) has been investigated as oxygen marker. Notably, R_1 scales with the concentration of "free," i.e., dissolved oxygen molecules (i.e. [O_2]) [19, 57]. This has been applied to oximetry of well-defined microenvironments such as vitreous humor [58], but the separation of the pO_2 effects on R_1 from other tissue-related effects by simple quantification of R_1 is not straightforward, and native T_1 mapping has not yet been utilized to assess the oxygenation of tumors.

12.2.2 Oxygen-Enhanced MRI

In the attempt to separate the influence of oxygenation on the MR relaxation rates from other sources, different groups have investigated the change of the relaxation rates R_2* and R_1 during changes of oxygenation (e.g., induced by inhalation of oxygen) as a

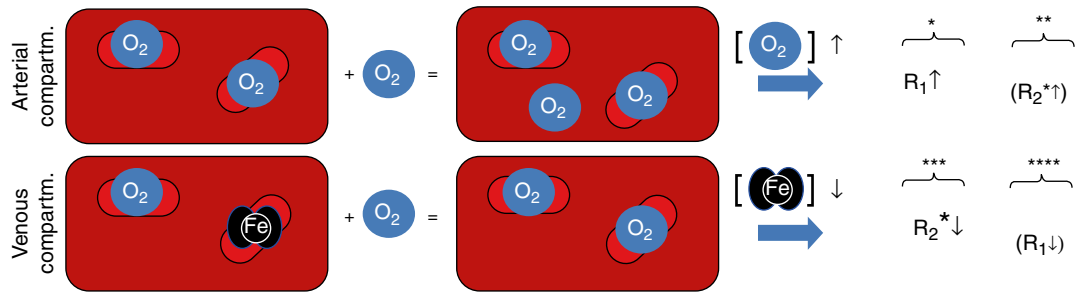

Fig. 12.2 Simplified schematic of the effect of an oxygen breathing challenge on the relaxation rates R_2* and R_1 (neglecting flow). The size of arrows and letters indicate the strength of the effect (*See Young et al. [57], **see Schwarzbauer and Deichmann [59], ***see Ogawa et al. [18], and ****see Blockley et al. [60])

marker for blood or tissue oxygenation, respectively. In response to oxygen breathing, the additional oxygen molecules bind to hemoglobin and dissolve in plasma and tissue fluids. In arterial blood, the fraction change of the deoxyHb concentration (i.e. [deoxyHb]) and thus R_2* is negligible, but [O_2] changes significantly due to a sixfold pO_2 increase, causing an R_1 increase. In venous blood pO_2 doubles causing significant decrease in deoxyHb, which results in a strong R_2* drop, whereas [O_2], and thus R_1, barely changes (Fig. 12.2). Breathing oxygen thus alters R_1 and R_2*, depending on the composition of a voxel but also dependent on blood flow and volume changes [61].

12.2.2.1 Oxygen-Enhanced MRI Using BOLD Contrast and R_2* Quantification

The interest in R_2*-weighted OE-MRI was mainly driven by clinical and preclinical results from the 1990s showing that the BOLD response to carbogen (abbrev. Cb and consisting of 95 % O_2 and 5 % CO_2) breathing differed between tumors and normal tissue [49, 62–64] (Fig. 12.3).

Since then, BOLD MRI has been frequently investigated as a monitoring tool to assess the tumor response to vasomodulation, e.g., using respiratory challenges (Cb) or drugs [21–26, 31, 32, 65–67]. Although here MRI is not directly used to measure tumor hypoxia, it is still a helpful tool in the planning of therapies that aim at elevating the oxygen tension of tissue and by this alleviate the effect of hypoxia on the radioresistance of tumors. Preliminary work showed a good correlation between the changes in pO_2 and BOLD measures [22, 32, 67] during Cb breathing (Fig. 12.4), whereas the relationship between the native pO_2 of tissue and the BOLD changes remains unclear.

On the other hand, there is preliminary but promising evidence – based on basic and mostly preclinical research – that the R_2* response to Cb is determined by vascular function and architecture [16, 23] and predicts the responsiveness of a tumor to a radiation treatment [31].

Various scanning techniques have been investigated for oxygen-enhanced BOLD measurements. R_2*-weighted gradient-echo signal intensities are not only sensitive to changes of R_2* and [deoxyHb] but also to changes of inflow and R_1, particularly when using short TR and high flip angles [61]. Likewise, the quantitative ΔR_2* estimate can be derived from the logarithmic ratio of the signal intensities at two different time points (e.g., before and during oxygen breathing). The excellent temporal resolution of single gradient-echo sequences, however, makes them well suited for dynamic volumetric experiments. With multi-gradient-echo sequences and a multi-echo fit, it is possible to separate the R_2* changes at the expense of either spatial or temporal resolution. Alternatively, R_2* can also be derived from the line width of the water resonance peak using spectroscopic imaging. Using high spectral and spatial resolution (HiSS) MRI in a preclinical study, it was shown that the percentage difference in the height and integral of the water peak best correlates with the changes of pO_2 during Cb breathing [21, 65, 67, 68]. Dynamic sampling of the R_2* response is advisable since the kinetics of the response to an oxygen challenge depends on the underlying vasoreactivity and may differ

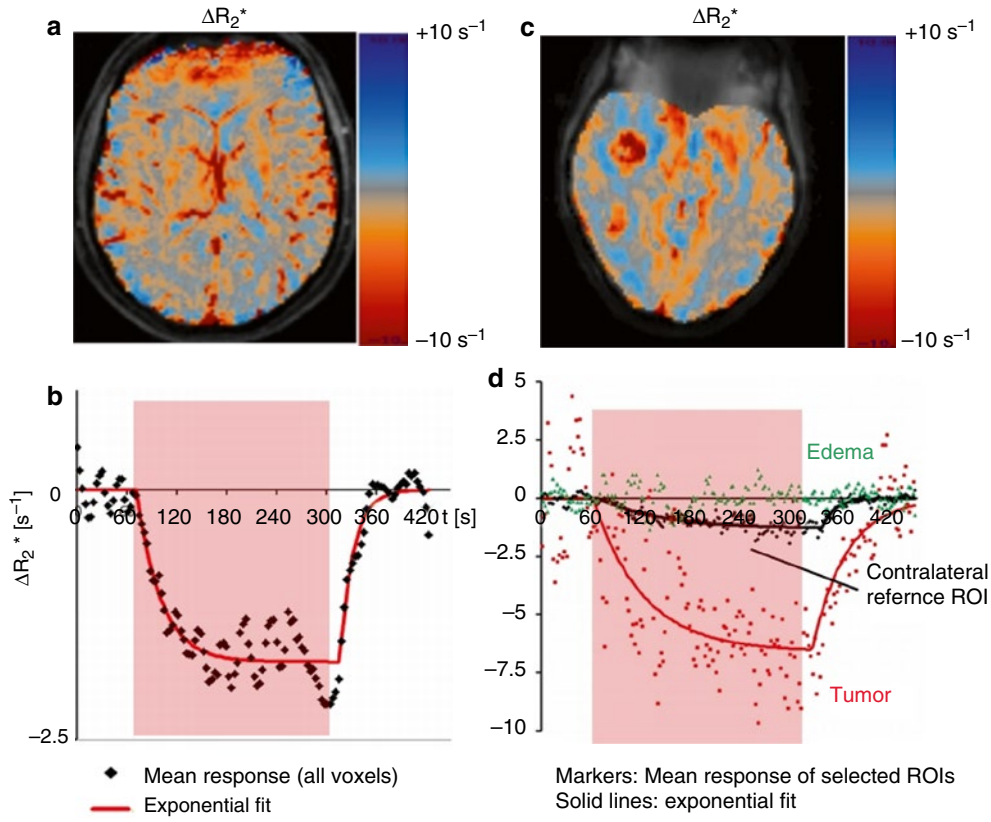

Fig. 12.3 ΔR_2^* response overlays (**a**, **c**) and response curves (**b**, **d**) obtained in a healthy volunteer (*left*) and a patient (*right*). The response curves represent the average response from all voxels within a ROI. In the volunteer, all voxels are selected; in the patient, ROIs representing enhancing tumor and edema are selected manually. The R_2^* response amplitude differs between normal and tumor tissue (**c**). The response in healthy brain parenchyma is well represented by a piecewise exponential function (**b**). The response in the pathological tissue is more complex (**d**) (Data: courtesy of Dr. Petra Mürtz, Prof. H. H. Schild, University of Bonn, Germany)

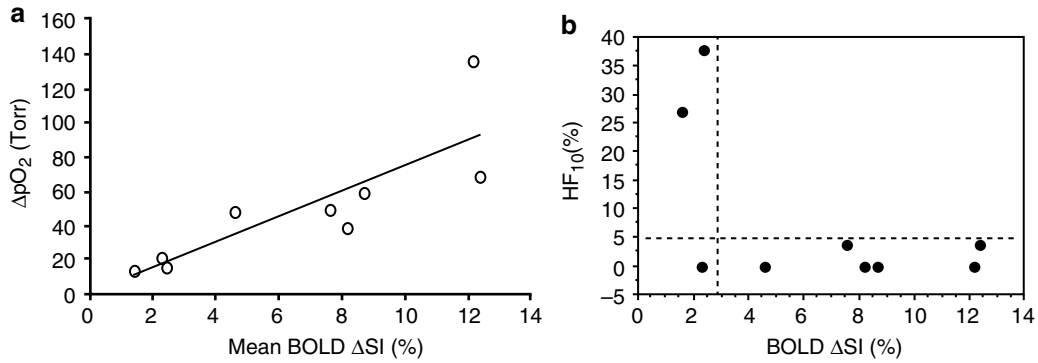

Fig. 12.4 Relationships between pO_2 and BOLD responses to oxygen challenge. (**a**) A significant linear correlation was found between mean increase in tissue pO_2 (ΔpO_2) and mean spin echo planar BOLD signal increase in nine 13762NF rat breast tumors with respect to oxygen breathing challenge ($r^2 < 0.7$; $p < 0.001$). (**b**) Comparison of the final hypoxic fraction (HF_{10}) with oxygen breathing as a function of BOLD signal response (ΔSI) suggests strong predictive value. For most tumors (6 of 9) a large BOLD response coincided with low residual HF_{10}. A small BOLD response indicated a large residual hypoxic fraction in 2 of 3 tumors (Reproduced with permission from Zhao et al. [32]

between normal and pathological tissue (Fig. 12.3). The optimal timing of any single pre and post measurement is thus hardly predictable. In normal tissue, the R_2* response to an oxygen-enhanced block challenge is well described by piecewise exponential functions [28], and in pathological tissue diverse kinetics have been observed [26].

12.2.2.2 Oxygen-Enhanced MRI Using TOLD Contrast and R_1 Quantification

In T_1-weighted oxygen-enhanced MRI (OE-MRI) sometimes referred to as TOLD (Tissue-Oxygen-Level-Dependant contrast MRI), molecular oxygen is inhaled in the form of either pure oxygen (100 % O_2) or as an admixture of oxygen (typically 90–98 % O_2) and a small percentage of carbon dioxide (typically 2–5 % CO_2). It has been recognized for several decades that when molecular oxygen is dissolved in blood and tissue plasma, the longitudinal relaxation rates of protons (termed R_1) are increased [57, 69], but this contrast mechanism has only been exploited more recently enabled by improvements in MRI scanner hardware and analysis methods. Initial clinical interest has centered on how this tissue contrast mechanism may map regional oxygen tension in normal and diseased lungs [70–72]. Subsequent research has also addressed how this technique may detect, quantify, and map oxygen delivery from the lungs via the blood stream [73] to healthy tissues [20, 74–77] and to tumors [78, 79]. As the method simply uses medical oxygen (or Cb) and standard MRI equipment, with no investigational tracers or devices, it is readily translatable between animal models and humans.

Initial preclinical experiments showed small, but significant increases in tumor R_1 in squamous cell cancer murine models on challenge with 100 % oxygen at both hyperbaric conditions [80] and normal pressure [78]. Similarly, significant increased in tumor R_1 has been reported in the well-vascularized tumor tissue in Dunning R3327 rat tumors [81], GH3 murine prolactinomas [82], orthotopic murine U87 glioblastoma breathing Cb [83], and in the peripheral zones of the rabbit VX2 carcinoma model induced both by 100 % oxygen and by various admixtures of hyperoxic gas containing up to 9 % CO_2 [84]. In this latter study, elevated pO_2 was detected using invasive measurements with the OxyLite system. Weak but significant positive relationship between tumor blood flow (measured by DCE-MRI) and magnitude of R_1 increase induced by 100 % oxygen was found.

Consistent data has been provided in three clinical studies of T_1-weighted OE-MRI. An initial report of three patients with non-small cell lung cancer recorded small increases in tumor R_1 following Cb inhalation [85]. Subsequent study in patients with various solid tumors including ovarian, cervical, and gastrointestinal tract cancers showed increases in tumor R_1 induced by 100 % oxygen that had some spatial mismatch with perfusion measured by DCE-MRI [79]. Finally, similar data have been reported in well-vascularized regions of human glioblastoma multiforme [86].

These preclinical and clinical data suggest that in well-vascularized tumors, breathing hyperoxic gas causes an increase in tumor R_1 due to an increased concentration of oxygen dissolved within the tissue plasma. However, not all tumor regions are well oxygenated with near-complete hemoglobin saturation, and little or no increase in tumor R_1 has been reported in some models, for example, in sublines of the Dunning R3327 rat model where larger tumors, and those tumors with poor vascularization, showed distinctly different behavior from the significant changes detected in small well-vascularized lesions [81]. One explanation for these data is that negligible excess oxygen is delivered to some tumor regions and cannot be detected in the plasma and tissue fluid within those tumor regions.

More recently, it has been proposed that the signal changes observed in T_1-weighted OE-MRI may be more subtle than first thought and may provide binary distinction of those tissue regions that are hypoxic and those that are normoxic. Decrease in R_1 following oxygen inhalation in tumors has previously been reported [61, 87], and this may reflect hypoxic tumor regions with suboptimal hemoglobin saturation that show reduced blood R_1 as oxygen molecules bind to

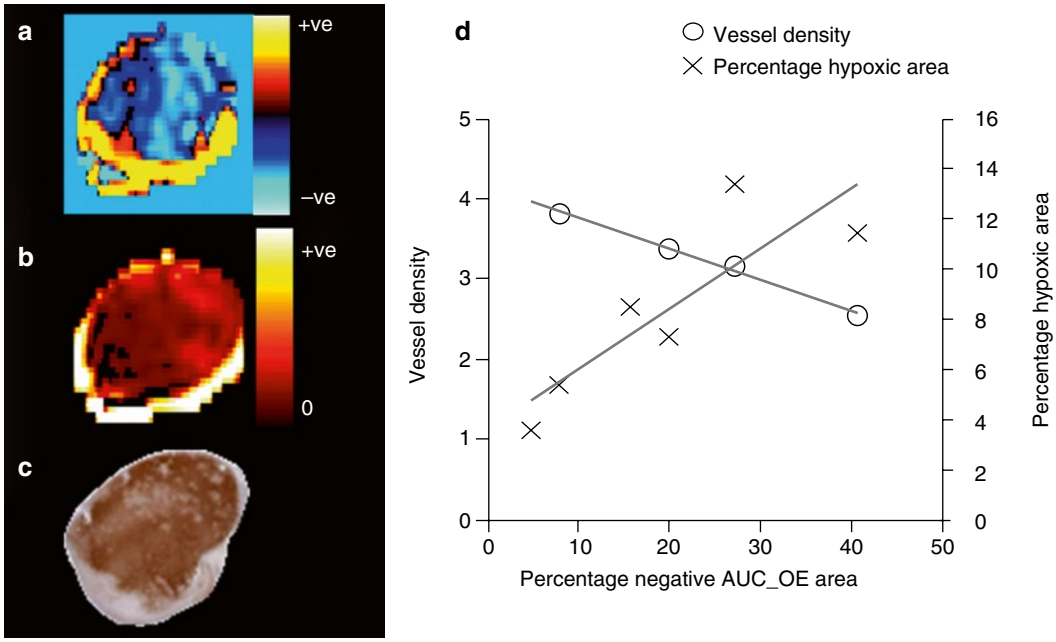

Fig. 12.5 T_1-weighted OE-MRI and relationship to histology in a U87 glioblastoma model. (**a**) OE-MRI shows areas of increased and decreased R_1 (s^{-1}). The negative R_1 corresponds to (**b**) negligible perfusion on DCE-MRI and (**c**) hypoxic tumor on pimonidazole staining. In distinction, a well-perfused vascular rim shows increase in R_1. (**d**) In a cohort of six tumors, the percentage of the tumor with negative R_1 changes in the area under the curve (AUC) correlated strongly with the percentage of tumor hypoxic area. There was also negative correlation between negative R_1 changes and vessel density measured by CD31 (Data from Linnik et al. [86])

deoxygenated hemoglobin molecules and increase the ratio of oxygenated to deoxygenated hemoglobin [60, 88]. Thus, reduction in tumor R_1 may identify those hypoxic regions where available deoxygenated hemoglobin species bind excess delivered tissue oxygen.

Several studies have evaluated how T_1-weighted OE-MRI affects tumor voxels that correspond to hypoxic regions. In a subcutaneous murine U87 glioma model, both increase and decrease in R_1 were measured. Increase in R_1 corresponded to well-perfused tumor regions, whereas decrease in R_1 corresponded to poorly perfused areas (Fig. 12.5). Moreover, the decrease in R_1 correlated positively with hypoxic fraction measured by pimonidazole staining [86]. Regional decrease in R_1 has also been reported in two studies of human glioblastoma [86, 87] that correspond to poor perfusion and slower R_2*.

It should be stressed that while T_1-weighted OE-MRI shows promise as a noninvasive method of mapping tumor oxygenation status and identifying tumor hypoxia, the technique is in its infancy and has yet to be validated in multiple animal models and then qualified in clinical data.

12.2.2.3 Simultaneous Approaches

Limitations of the BOLD and TOLD approaches encompass the lack of specificity in the absence of a response. In case of BOLD measurements, this could be either due to the absence of blood or due to a high native blood oxygenation (absence of deoxyHb) [4]. In the case of TOLD, again, a negligible change can be either due to the absence of any O_2 delivery or due to a high native deoxyHb concentration and a predominant binding of the additional O_2 molecules to hemoglobin. Preliminary studies demonstrate that the joint measurement of R_1 and R_2* overcomes this lack of specificity as shown in Fig. 12.6 [82, 86, 87, 89].

Steady-state short-TR gradient-echo sequences can be used to simultaneously estimate R_2* (from the gradient-echo signal at TE)

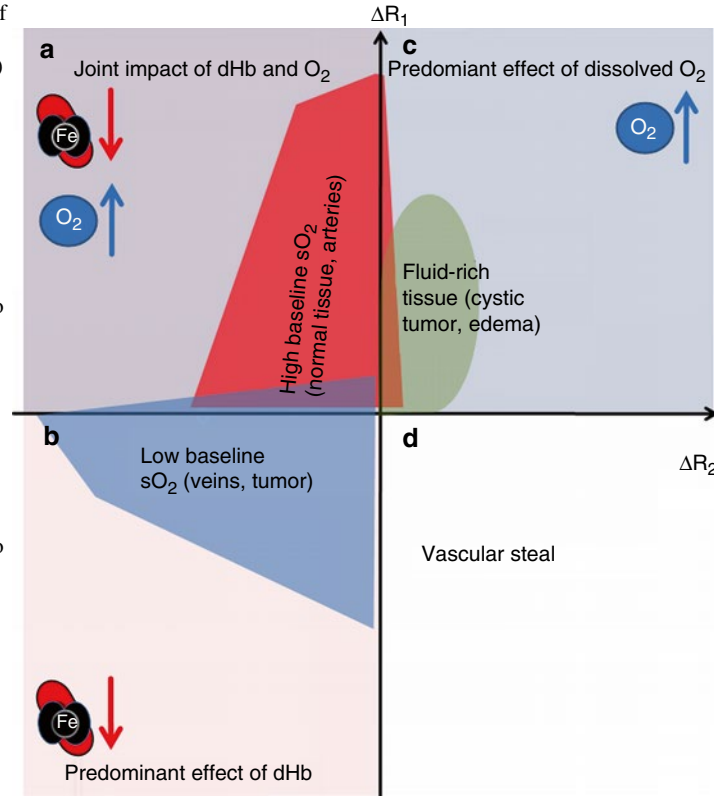

Fig. 12.6 Schematic representation of tumor R_1 and R_2* induced changes following oxygen or Cb inhalation. (**a**) In regions that are well oxygenated, excess dissolved oxygen will increase the plasma and tissue fluid R_1 but will have negligible effect on hemoglobin (Hb) saturation (hence small effect on R_2*). (**b**) In distinction, hypoxic regions with suboptimal oxygen saturation will show preferential binding of excess oxygen molecules to deoxygenated Hb molecules, which reduces the content of paramagnetic deoxyHb, shortening both R_2* and R_1. (**c**) In the absence of deoxyHb (e.g., fluids like in cystic tumor regions or edema), the excess oxygen in solution prolongs both R_1 and R_2*. (**d**) Non-oxygenation-related R_2* increase and R_1 decrease, presumably related to vascular steal (Figure adapted from Remmele et al. [87])

and R_1 (from the T_1-weighted signal intensity at TE = 0 ms) [87]. Using high flip angles, slice-selective sequences and without outer signal suppression the signal at TE = 0 ms are primarily influenced by inflow. Such a sequence has thus been investigated as simultaneous flow and blood oxygenation level dependent sequence (FLOOD) [90, 91]. In combination with lower flip angles and inflow suppression, the sequence becomes sensitive to both changes of deoxyHb, via R_2*, and changes of dissolved oxygen molecules via R_1. This approach has been used to detect tissue of non-normoxic characteristics in cerebral tumors [87, 92] (Fig. 12.7).

12.2.2.4 Conclusion on Oxygen-Enhanced MRI

The use of standard anesthesia gases and conventional MR sequences makes T_2*- and T_1-weighted OE-MRI a promising approach towards qualitative oxygenation assessment in clinical oncology. Future work needs to clarify the choice of gas inhaled (100 % oxygen vs. Cb) and the analysis methods employed (which biomarker should be derived). Since physiological changes other than oxygen dynamics can alter the tissue relaxation properties, not all signal changes can be ascribed to the presence of molecular oxygen or deoxyHb in a voxel, and this raises questions over whether an increase in tissue R_1 or R_2* can be calibrated into a measurement of tissue pO_2. Well-designed histological and histographic experiments are required to understand the precise meaning of the signal changes in tumors with a range of vascular and hypoxic status.

12.2.3 ^{19}F MR Imaging

BOLD and TOLD MRI have the great advantage of exploiting endogenous contrast, either intrinsic or induced by inhaled oxygen. However,

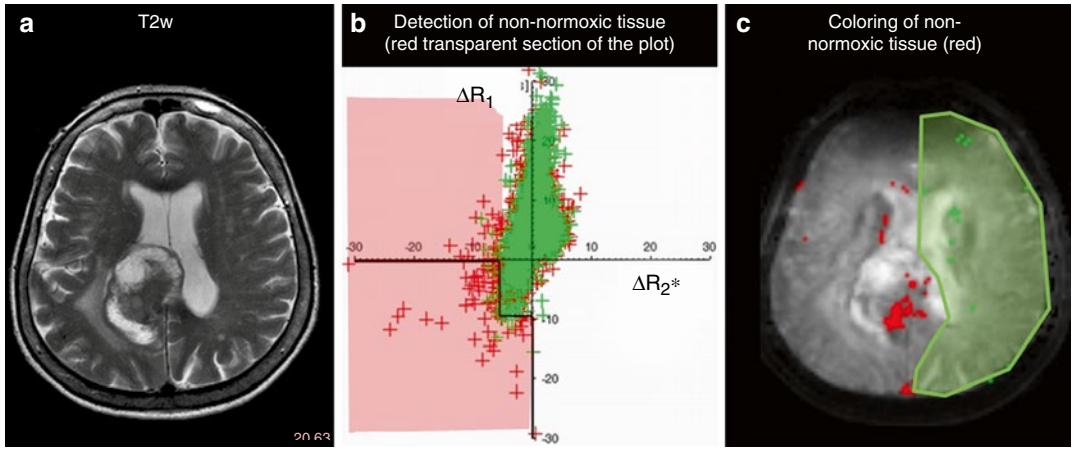

Fig. 12.7 Detection of tissue voxels with non-normoxic characteristics based on the simultaneous measurement of R_1 and R_2* in response to Cb. (**a**) T_2-weighted image of a patient with a brain metastasis. (**b**) Non-normoxic voxels are detected based on the position in the ΔR_1 over ΔR_2* scatter plot respective to the position of voxels from a reference region (*green*). (**c**) Coloring of non-normoxic voxels (*red*) and the selected reference voxels (*green*) as overlay on an R_2*-weighted image (Figure adapted from Remmele et al. [87])

except in well-defined tissue milieux such as vitreous humor of the eye [58, 93], CSF [94] or major blood vessels [95], they do not provide quantitative oximetry. Quantitative in vivo MR oximetry has been demonstrated based on the relaxation rates of perfluorocarbons (PFCs) using ^{19}F MRI, as pioneered by Thomas et al. [17, 96]. Dynamic pO_2 measurements may be achieved within minutes from multiple locations within a tissue with a precision of 1–3 Torr in relatively hypoxic regions [17].

PFCs exhibit very high gas solubility, are essentially inert, and are nontoxic. For oximetry the most crucial property is the ideal liquid–gas interaction with oxygen, obeying Henry's law and providing a linear dependence of the ^{19}F spin–lattice relaxation rate $R_1 = A + B\ pO_2$ (e.g., Fig. 12.8), as reviewed previously [17, 96, 98]. The relationship has been reported across the whole range of pO_2 values including hyperbaric conditions [99]. However, there is additional sensitivity to magnetic field and temperature, necessitating appropriate calibration curves [100–102]. PFCs are exceedingly hydrophobic so that oxygen sensitivity is independent of most environmental components, such as metal ion concentrations, pH, and proteins, and therefore calibration curves established in vitro may be applied in vivo [100, 103–105]. MR oximetry has been demonstrated using various PFCs: initially perfluorotributylamine and perfluorooctyl bromide were favored, but these multi-resonant reporters have been largely replaced by hexafluorobenzene (HFB) and perfluoro-15-crown-5 ether (15C5) [17, 106].

Hexafluorobenzene has many virtues as a reporter including high sensitivity to pO_2, minimal sensitivity to temperature, a single ^{19}F resonance, and ready availability [17, 101]. HFB does exhibit a particularly long T_1 reaching 12 s under anoxic conditions at 4.7 T, potentially making data acquisition slow [17, 107]. To provide effective temporal resolution for dynamic measurements, Zhao et al. developed *FREDOM* (Fluorocarbon Relaxometry using Echo planar imaging for Dynamic Oxygen Mapping) [17], which typically provides pO_2 maps in 6.5 min [107]. Recently Gallez et al. implemented a Look-Locker sequence generating maps in 90 s under similar conditions [108]. Tumor oximetry using HFB has been presented in various tumors growing in rats and mice [32, 107, 109–120]. Extensive intratumoral heterogeneity has been

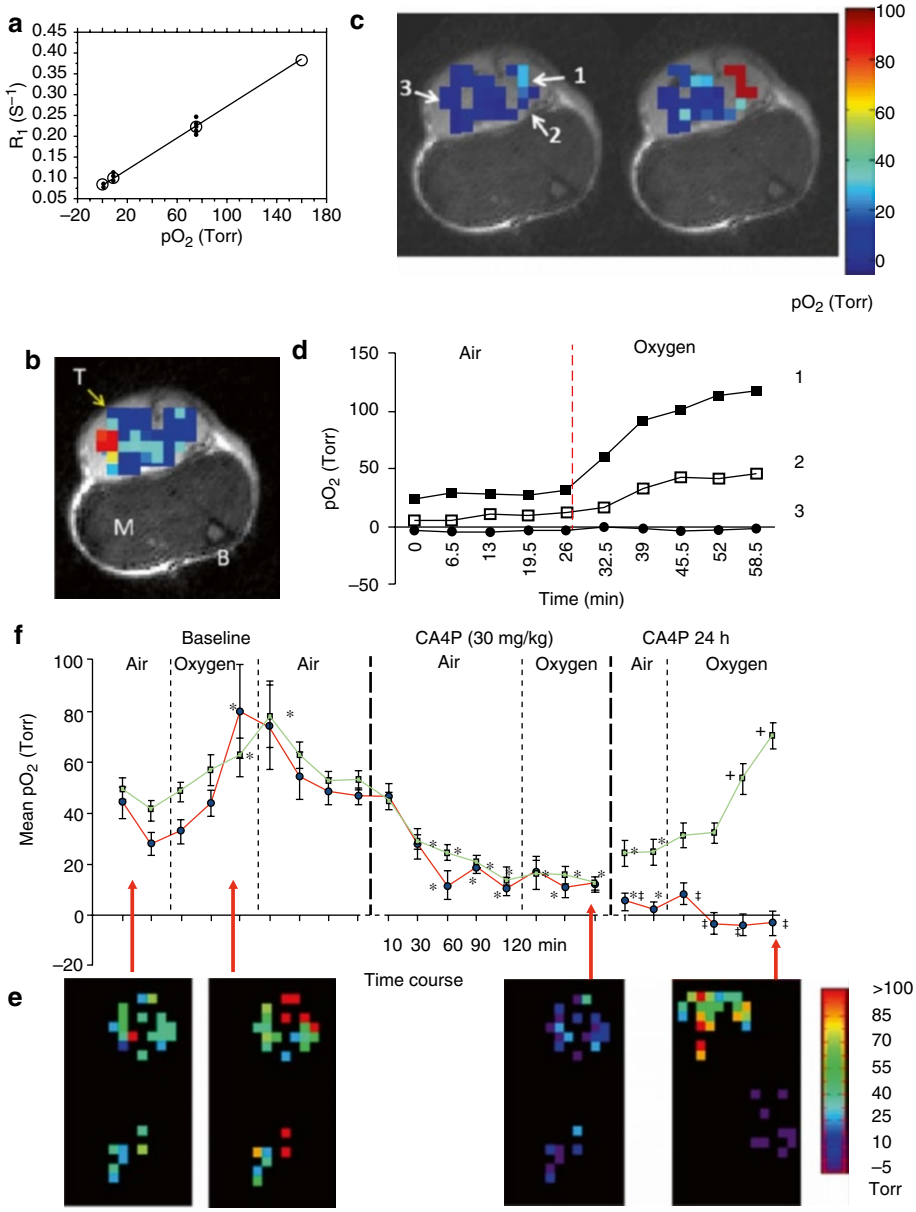

Fig. 12.8 Quantitative oximetry using ^{19}F NMR. (a) The ^{19}F NMR spin–lattice relaxation rate (R_1) of HFB (hexafluorobenzene) shows a linear response to pO_2: at 37 °C and 4.7 T, R_1 (s^{-1}) = 0.0835 × 0.001876pO_2 (Torr) (Adapted from Zhao et al. [17]). (**b**) HFB (50 µl) was injected directly into a Dunning prostate R3327-AT1 tumor (~0.7 cm^3) growing in the thigh of a rat in a fan pattern to provide well-distributed signal throughout a plane of the tumor, as shown in the ^{19}F signal density map overlaid on a high-resolution T_2*W image (*M* muscle, *B* bone marrow, *T* tumor). (**c**) pO_2 maps were obtained using FREDOM, while the anesthetized rat breathed air (*left*) and after about 30 min oxygen breathing (*right*) revealing pO_2 heterogeneity. (**d**) Dynamic changes in pO_2 for three specific voxels (indicated by *arrows* in (c) upon oxygen breathing). Voxels 1 and 2 showed significant pO_2 enhancement ($p<0.01$) [Rami Hallac (2012), Unpublished data]. (**e**) Acute response to vascular-disrupting agent observed by FREDOM in a representative subcutaneous 13762NF rat breast tumor. pO_2 maps indicated two separated groups of voxels representing central and peripheral tumor regions. Twenty-five individual voxels were traceable from the pretreated baseline to 2 h after administration of the vascular-disrupting agent combretastatin (CA4P, Zybrestat®), and further measurements were possible 24 h posttreatment. Significant decrease in pO_2 was evident for all the individual voxels after CA4P, and pO_2 no longer responded to oxygen inhalation after 2 h. The 24 h maps showed improved pO_2 and significant response to oxygen breathing in the peripheral region, but not in the central region. (**f**) Mean pO_2 curves are shown for the peripheral (□) and central (●) voxels of this tumor. *$p<0.05$ from baseline air, +$p < 0.05$ from 24 h air, ‡$p<0.05$ from periphery (Data and or figures adapted from Zhao et al. [97])

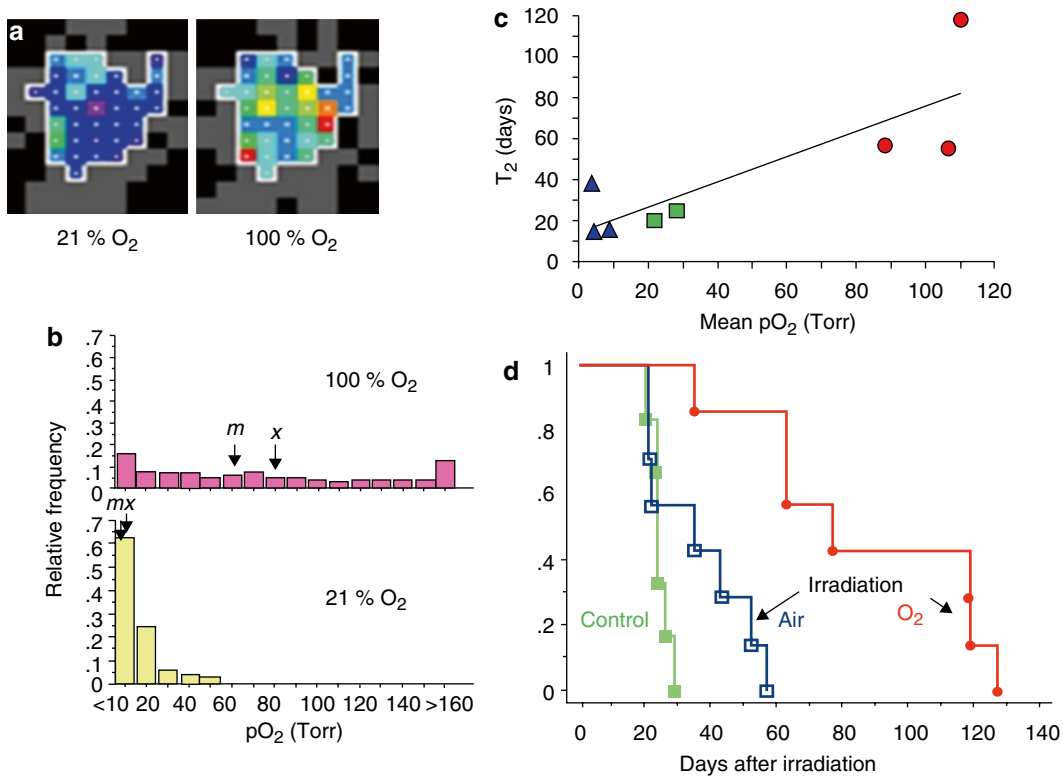

Fig. 12.9 Modulating tumor hypoxia to enhance radiation response. (**a**) pO_2 maps obtained using FREDOM in a large Dunning prostate R3327-HI tumor (3.5 cm^3) following direct injection of HFB (45 µl) using 32G needle. The tumor exhibited considerable hypoxia, but some regions were better oxygenated (mean $pO_2 = 3.3 \pm 1.0$ (SE) Torr; median $pO_2 = 5.4$ Torr; range 0–56 Torr), while anesthetized rat breathed air (21 % O_2). Switching to oxygen inhalation essentially eliminated all hypoxia in this tumor as seen in map obtained 16–24 min after switching gas; mean $pO_2 = 63.8 \pm 2.1$ Torr ; median $pO_2 = 56.4$ Torr; range 7.6–262 Torr. (**b**) Histograms showing pO_2 distributions in regions of a group of five large tumors [size range 3.1–5.9 cm^3]. During air breathing considerable hypoxia was observed, but this was significantly modified when rats breathed O_2: *arrows* indicate mean (*x*) and median (*m*) pO_2's. (**c**) Tumor volume doubling time (T2) following irradiation (single dose of 30 Gy = half the TCD50) showed a strong correlation with estimated pO_2 (it was actually measured using FREDOM on the previous day, while rat breathed relevant gas). *Blue triangles* represent large tumors breathing air during irradiation, *while red circles* represent large tumors on rats breathing oxygen during irradiation. *Green squares* represent two small tumors with air breathing. (**d**) Kaplan–Meier hazard plots indicate T2 for large R3327-HI tumors. Tumors on rats breathing air during irradiation showed little benefit over controls. By contrast, a significant growth delay (51 days; $p < 0.01$) was observed in large HI tumors, when rats breathed oxygen 30 min prior to and during irradiation [119–121]

reported (see, e.g., Fig. 12.9a, b) with hypoxic fractions ranging from $HF_{10} = 16$ % in small Dunning prostate R3327-H tumors to 83 % in large R3327-AT1 tumors on anesthetized rats breathing air, commensurate with the "gold standard" Eppendorf electrode system [114]. While deposition of reporter molecule requires needle insertion into the tissue, just as with needle electrodes, ^{19}F oximetry has the great advantage of allowing repeat noninvasive pO_2 measurements (e.g., Figs. 12.8c and 12.9a, b). The use of a fine sharp needle (e.g., 32 gauge) and small volumes of reporter molecule (typically, 10–100 µl) makes the approach minimally invasive.

^{19}F MR oximetry is particularly useful for evaluating acute response to interventions, most commonly hyperoxic gas breathing challenges,

(e.g., Figs. 12.8 and 12.9) [17, 32, 107, 117–123], since these are predicted to modulate tumor hypoxia. pO_2 distributions and measurements at individual locations have been reported to be highly reproducible and generally quite stable under baseline conditions (Figs. 12.8d) [117, 118, 123].

Perfluorocarbon may be injected into a single location providing local pO_2 by spectroscopy with spatial discrimination by virtue of the discrete site of injection [101]. However, recognizing tumor heterogeneity [3, 114] it is preferable to distribute the PFC, so as to sample diverse regions and provide a representation of the whole tumor [17] (Figs. 12.8 and 12.9).

The greatest strength is the ability to examine differential local tissue behavior to interventions. In most tumors, regions which are well oxygenated show substantial response to hyperoxic gas breathing, while initially hypoxic regions (<5 Torr) are generally quite unresponsive to acute interventions (Fig. 12.8) [101, 118, 121]. However specific tumor types show different behavior with significant response of even quite hypoxic regions to breathing oxygen [111, 118–120]. Notably, large Dunning prostate R3327-HI tumors showed extensive hypoxia, which was essentially eliminated by breathing oxygen (Fig. 12.9) [118, 120, 123]. Such modulation has been correlated with improved response to high-dose radiation, and a direct relationship was observed between pO_2 at time of irradiation and subsequent tumor volume doubling time (Fig. 12.9c) [109, 120].

Other ^{19}F MR oximetry studies have examined tumor pO_2 response to castration [115], pharmaceutical drugs, or experimental agents, notably vasoactive agents such as hydralazine [121] and vascular-disrupting agents, such as combretastatin (e.g., Fig. 12.8e, f), anti-VCAM1-tTF (truncated tissue factor) coaguligand, and arsenic trioxide [97, 110, 113, 124].

Direct intratumoral injection of reporter molecule into subcutaneous tumors allows immediate interrogation of regions of interest. Oximetry based on direct injection into tissues has been reported in diverse tissues allowing measurement of oxygenation in the retina [125–127]; cerebral, interstitial, and ventricular spaces [128]; the brain, kidney, liver, gut, and muscle [35, 36, 129, 130]; and diverse tumors [17, 32, 97, 101, 107, 108, 110, 112, 115–120, 131]. Early observations, and many current implementations, have used systemic delivery of perfluorocarbon emulsions (PFCEs). These were originally developed as synthetic blood substitutes and may be administered intravenously (IV). Following IV infusion, a typical PFCE circulates with a vascular half-life of 12 h, and several reports examined tissue vascular pO_2, while PFC remained in the blood [103, 132–135]. The particulate nature of PFCEs leads to extensive macrophage uptake and sequestration in the reticuloendothelial system [136]. Therefore oximetry is particularly efficient in the liver and spleen with reports examining pO_2 response to oxygen breathing challenge or the influence of von Hippel-Lindau (VHL) expression and inactivation in transgenic mice [137–141]. Many PFCs show long-term tissue retention (perfluorotripropylamine is reported to have a half-life of 65 days in the liver [142]) allowing noninvasive oximetry in vivo over a period of weeks. Systemic delivery of reporter molecules does tend to bias measurements towards well-perfused tumor regions, and thus initial measurements may approach arterial pO_2 [143, 144], but the approach has allowed long-term assessment of hypoxiation accompanying tumor growth (Fig. 12.10).

Any technique has optimal applications and potential limitations. Currently, ^{19}F remains esoteric on human scanners, and thus alternative approaches may be better suited to translational oximetry. The need for a reporter molecule also raises issues of FDA approval, and thus ^{19}F MR oximetry is probably most suitable for quantitative work in small animals. It is also highly suitable for comparison with and/or validation of other methods, such as BOLD and TOLD, as discussed in other sections of this chapter.

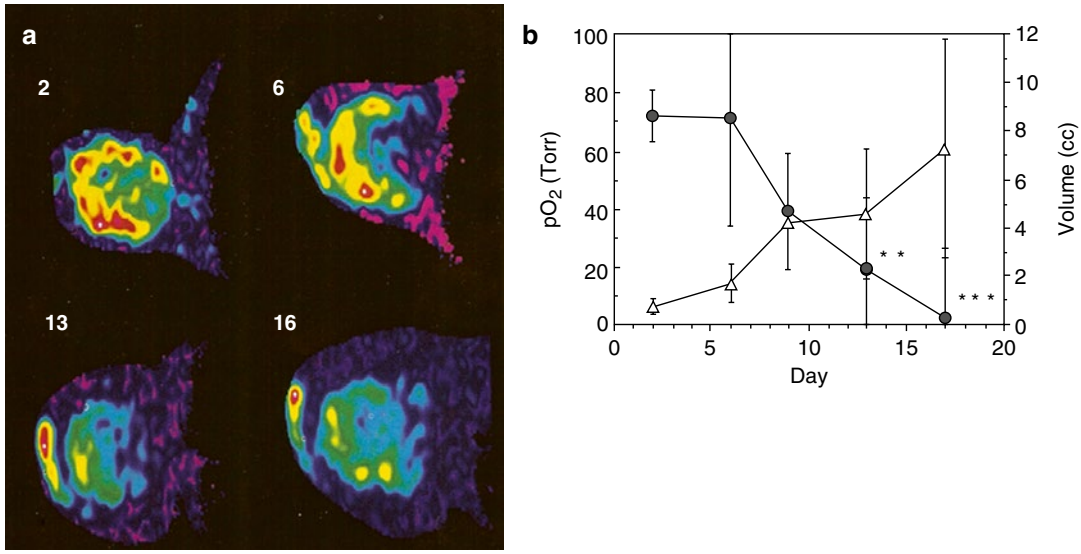

Fig. 12.10 Tumor hypoxiation accompanying growth. (**a**) Oxypherol blood substitute emulsion was administered intravenously to a rat bearing a Dunning prostate tumor R3327-AT1 and became sequestered in tissue. Following vascular clearance ^{19}F MRI was used to determine the distribution of perfluorocarbon, which is overlaid on tumor outline from correlated proton MRI. Fluorine-19 spectroscopic relaxometry was used to measure pO_2 in the tumor with repeated measurements over a period of 3 weeks revealing the variation in local pO_2 during tumor growth. Perfluorocarbon initially resided in the vascularized peripheral region of the tumor, and pO_2 was found to be about 75 Torr in the small tumor (diameter about 1 cm). As the tumor grew, the sequestered PFC retained its original distribution, but when the tumor had doubled in size, the residual PFC was predominantly in the core of the tumor and the pO_2 of this region was 0 Torr indicating central tumor hypoxia. (**b**) Variation in mean pO_2 for a group of six tumors over 16 days showing significant hypoxiation of the tissue $*p<0.05$; $**p<0.002$, $***p<0.001$ (Figures reproduced from Mason et al. [144])

12.3 Summary and Future Perspective

Hypoxia is one of the key parameters in oncology, and the assessment of tumor hypoxia with MRI has thus been, and still is, a matter of extensive research. Table 12.1 summarizes the MR oxygenation methods discussed in this chapter. Whereas native relaxometry approaches are limited in specificity, oxygen-enhanced R_2* and R_1 have a considerable promise as molecular imaging techniques to qualitatively interrogate tumor oxygen delivery and hypoxia. The prerequisite for their clinical acceptance and success, however, is either a full understanding of the underlying hemodynamic and oxygenation-related mechanisms or a proven relevance in a large patient study, e.g., correlating OE-MRI results with radiation outcome. The clinical acceptance of ^{19}F methods might be hampered by the need for dedicated transmit and receive MR technology as well as for approved and commercially attractive contrast agents. On the other hand, the ability of ^{19}F MRI to deliver quantitative pO_2 measures makes it a strong and important tool for oncologic and pharmaceutical research.

Table 12.1 Summary of methods for MR oxygenation measurements

	Method	Effect	Oxygen measure	Pro	Contra	References
Sect. 12.2.1	Native R_2*	Tissue R_2* is a function of sO_2 (and to a minor degree also of $[O_2]$)	Qualitative	Contrast agent free Simple and time efficient Does not require specific hardware	Poor specificity	[22, 47, 50]
	Native R_2* and signal modeling	R_2* is a function of sO_2 but also of the Hct level, the blood volume, R_2, blood flow, ΔB_0, etc.	(Semi-) quantitative	Delivers quantitative sO_2 estimate Does not require specific hardware	Requires additional measurements Limited accuracy	[48, 52, 53, 55]
	Dynamic native R_2*	Low-frequency fluctuations in R_2* over time may be correlated to acute hypoxia	Qualitative	Contrast agent free Simple Does not require specific hardware	Time consuming	[145]
	Native R_1	The R_1 of tissue fluids is a function of the concentration of oxygen molecules (and to a minor degree also of [deoxyHb])	Qualitative	Contrast agent free Simple and time efficient Does not require specific hardware	Poor specificity Not yet applied in oncology	[20, 58, 93–95]
Sect. 12.2.2	OE- R_2*	ΔR_2*- and R_2*-weighted signal intensities in response to oxygen breathing scales with baseline [deoxyHb]	Qualitative	Increases specificity compared to native R_2* mapping	Requires delivery of oxygen-enriched air to patients Limited specificity for high sO_2, low blood volume, steal	[21–32, 49, 62–68, 146–150]
	OE-R_2* with HiSS	See OE-BOLD. T_2* quantified by height and width of water peak	Qualitative	Higher R_2* accuracy than using multi-gradient-echo	Lower spatial or temporal resolution than using multi-gradient-echo	[21, 65, 67, 68]
	OE- R_1	ΔR_1* and R_1-weighted signal intensities in response to oxygen breathing scales with $\Delta[O_2]$ during oxygen breathing	Qualitative	Increases specificity compared to native R_1 mapping	Requires delivery of oxygen-enriched air to patients Limited specificity for low sO_2, low blood volume, steal	[75, 76, 78, 79, 81]
	Combined OE-R_2* and OE-R_1 with inflow suppression	See above	Qualitative (detection of areas with low oxygenation)	Increases specificity of either OE-R_2* or OE-R_1	Requires delivery of oxygen-enriched air to patients	[82, 86, 87, 89, 92, 151]

Sect. 12.2.3	^{19}F MRI + reporter	O_2 induced R_1 relaxation of PFC reporter: direct dynamic pO_2 maps	Quantitative pO_2	Has been correlated with radiation response in preclinical studies	Requires reporter molecule and delivery Requires ^{19}F MRI equipment	[17, 108–110, 112, 117–120, 129, 130, 139, 152–158]
See Sect. 12.1	^{1}H MRI + reporter	O_2 induced R_1 relaxation of siloxane reporter: direct dynamic pO_2 maps	Quantitative pO_2	^{1}H MRI	Requires H_2O and fat suppression	[34–36]
	Hypoxia	Bioreduction of nitroimidazoles	Quantitative hypoxia (with assumptions)	Hypoxia as opposed to pO_2	Contrast agent, variable nitroreductase expression	[154, 159–161]
	DCE-MRI	Exploiting expected correlation of oxygenation and perfusion	Qualitative and indirect	Often part of the experiment anyway (in research studies)	Only indirect hypoxia marker (via perfusion)	[38–44]
	Overhauser and ESR	Electron spin relaxation in the presence of O_2	Quantitative	Quantitative pO_2	Dedicated hardware and contrast agents	[162, 163]

Acknowledgements Investigations were supported in part by funds from the NIH NCI (R01 CA139043; 1U24 CA126608; P30 CA142543; P41 RR02584). S. Remmele would also like to thank her partners at the University of Bonn, Germany, and Dr. Petra Mürtz in particular, for the fruitful collaboration, their helpful advice, and support.

References

1. Avni R, et al. Hypoxic stress and cancer: imaging the axis of evil in tumor metastasis. NMR Biomed. 2011;24:569–81.
2. Gillies RJ. MRI of the tumor microenvironment. J Magn Reson Imaging. 2002;16:430–50.
3. Vaupel P, Mayer A. Hypoxia in cancer: significance and impact on clinical outcome. Cancer Metastasis Rev. 2007;26:225–39.
4. Baudelet C, Gallez B. Current issues in the utility of blood oxygen level dependent MRI for the assessment of modulations in tumor oxygenation. Curr Med Imaging Rev. 2005;1:229–43.
5. Fyles A, et al. Tumor hypoxia has independent predictor impact only in patients with node-negative cervix cancer. J Clin Oncol. 2002;20:680–7.
6. Gatenby RA, et al. Oxygen distribution in squamous-cell carcinoma metastases and its relationship to outcome of radiation-therapy. Int J Radiat Oncol Biol Phys. 1988;14:831–8.
7. Gross S, et al. Monitoring photodynamic therapy of solid tumors online by BOLD-contrast MRI. Nat Med. 2003;9:1327–31.
8. Overgaard J. Hypoxic radiosensitization: adored and ignored. J Clin Oncol. 2007;25:4066–74.
9. Teicher BA. Hypoxia and drug resistance. Cancer Metastasis Rev. 1994;13:139–68.
10. Yetkin FZ, Mendelsohn D. Hypoxia imaging in brain tumors. Neuroimaging Clin N Am. 2002;12:537–52.
11. Kaanders JH, et al. Accelerated radiotherapy with carbogen and nicotinamide (ARCON) for laryngeal cancer. Radiother Oncol. 1998;48:115–22.
12. Kaanders JH, et al. ARCON: a novel biology-based approach in radiotherapy. Lancet Oncol. 2002;3:728–37.
13. Brown JM, Wouters BG. Comments on hyperbaric oxygen and carbogen/nicotinamide with fractionated radiations. Radiat Res. 1997;148:526–7.
14. Gray L, et al. The concentration of oxygen dissolved in tissues at time of irradiation as a factor in radiotherapy. Br J Radiol. 1953;26:638–48.
15. Wouters BG, Brown JM. Cells at intermediate oxygen levels can be more important than the "hypoxic fraction" in determining tumor response to fractionated radiotherapy. Radiat Res. 1997;147:541–50.
16. Neeman M, Dafni H. Structural, functional, and molecular MR imaging of the microvasculature. Annu Rev Biomed Eng. 2003;5:29–56.
17. Zhao D, et al. Measuring changes in tumor oxygenation. Methods Enzymol. 2004;386:378–418.
18. Ogawa S, et al. Oxygenation-sensitive contrast in magnetic-resonance image of rodent brain at high magnetic-fields. Magn Reson Med. 1990;14:68–78.
19. Chiarotti G, et al. Proton relaxation in pure liquids and in liquids containing paramagnetic gases in solution. Nuovo Cimento. 1955;1:863–73.
20. Zaharchuk G, et al. Noninvasive oxygen partial pressure measurement of human body fluids in vivo using magnetic resonance imaging. Acad Radiol. 2006;13:1016–24.
21. Al-Hallaq HA, et al. MRI measurements correctly predict the relative effects of tumor oxygenating agents on hypoxic fraction in rodent BA1112 tumors. Int J Radiat Oncol Biol Phys. 2000;47:481–8.
22. Baudelet C, Gallez B. How does blood oxygen level-dependent (BOLD) contrast correlate with oxygen partial pressure (pO_2) inside tumors? Magn Reson Med. 2002;48:980–6.
23. Baudelet C, et al. Determination of the maturity and functionality of tumor vasculature by MRI: correlation between BOLD-MRI and DCE-MRI using P792 in experimental fibrosarcoma tumors. Magn Reson Med. 2006;56:1041–9.
24. Dunn JF. Changes in oxygenation of intracranial tumors with carbogen: a BOLD MRI and EPR oximetry study. J Magn Reson Imaging. 2002;16:511–21.
25. Müller A. Intracranial tumor response to respiratory challenges at 3.0 T: impact of different methods to quantify changes in the MR relaxation rate R_2*. J Magn Reson Med. 2010;32:17–23.
26. Müller A. Analysing the response in R_2* relaxation rate of intracranial tumors to hyperoxic and hypercapnic respiratory challenges: initial results. Eur Radiol. 2011;21:786–98.
27. Mürtz P, et al. Changes in the MR relaxation rate R(2)* induced by respiratory challenges at 3.0 T: a comparison of two quantification methods. NMR Biomed. 2010;23:1053–60.
28. Remmele S, et al. Quantification of the magnetic resonance signal response to dynamic (C)O(2)-enhanced imaging in the brain at 3 T: R(2)* BOLD vs. balanced SSFP. J Magn Reson Imaging. 2010;31:1300–10.
29. Rijpkema M, et al. Effects of breathing a hyperoxic hypercapnic gas mixture on blood oxygenation and vascularity of head-and-neck tumors as measured by magnetic resonance imaging. Int J Radiat Oncol Biol Phys. 2002;53:1185–91.
30. Rijpkema M, et al. BOLD MRI response to hypercapnic hyperoxia in patients with meningiomas: correlation with Gadolinium-DTPA uptake rate. Magn Reson Imaging. 2004;22:761–7.
31. Rodrigues LM, et al. Tumor R_2* is a prognostic indicator of acute radiotherapeutic response in rodent tumors. J Magn Reson Imaging. 2004;19:482–8.
32. Zhao DW, et al. Comparison of H-1 blood oxygen level-dependent (BOLD) and F-19 MRI to investi-

gate tumor oxygenation. Magn Reson Med. 2009; 62:357–64.
33. Gulaka PK, et al. Hexamethyldisiloxane-based nanoprobes for ^{1}H MRI oximetry. NMR Biomed. 2011;24:1226–34.
34. Kodibagkar VD, et al. A novel ^{1}H NMR approach to quantitative tissue oximetry using hexamethyldisiloxane. Magn Reson Med. 2006;55:743–8.
35. Kodibagkar VD, et al. Physical principles of quantitative nuclear magnetic resonance oximetry. Front Biosci. 2008;13:1371–84.
36. Kodibagkar VD, et al. Proton Imaging of Siloxanes to map Tissue Oxygenation Levels (PISTOL): a tool for quantitative tissue oximetry. NMR Biomed. 2008;21:899–907.
37. Krishna MC, et al. Electron paramagnetic resonance imaging of tumor pO(2). Radiat Res. 2012;177: 376–86.
38. Halle C, et al. Hypoxia-induced gene expression in chemoradioresistant cervical cancer revealed by dynamic contrast-enhanced MRI. Cancer Res. 2012;72:5285–95.
39. Ceelen W, et al. Noninvasive monitoring of radiotherapy-induced microvascular changes using dynamic contrast enhanced magnetic resonance imaging (DCE-MRI) in a colorectal tumor model. Int J Radiat Oncol Biol Phys. 2006;64:1188–96.
40. Donaldson SB, et al. Perfusion estimated with rapid dynamic contrast-enhanced magnetic resonance imaging correlates inversely with vascular endothelial growth factor expression and pimonidazole staining in head-and-neck cancer: a pilot study. Int J Radiat Oncol Biol Phys. 2011;81:1176–83.
41. Egeland TA, et al. Assessment of fraction of radiobiologically hypoxic cells in human melanoma xenografts by dynamic contrast-enhanced MRI. Magn Reson Med. 2006;55:874–82.
42. Ovrebo KM, et al. Assessment of hypoxia and radiation response in intramuscular experimental tumors by dynamic contrast-enhanced magnetic resonance imaging. Radiother Oncol. 2012;102:429–35.
43. Cooper RA, et al. Tumor oxygenation levels correlate with dynamic contrast-enhanced magnetic resonance imaging parameters in carcinoma of the cervix. Radiother Oncol. 2000;57:53–9.
44. Lyng H, et al. Assessment of tumor oxygenation in human cervical carcinoma by use of dynamic Gd-DTPA-enhanced MR imaging. J Magn Reson Imaging. 2001;14:750–6.
45. Gulliksrud K, et al. Quantitative assessment of hypoxia in melanoma xenografts by dynamic contrast-enhanced magnetic resonance imaging: intradermal versus intramuscular tumors. Radiother Oncol. 2010;97:233–8.
46. Law R, Bukwirwa H. 2008. The physiology of oxygen delivery. Update in anaesthesia. http://update.anaesthesiologists.org/wp-content/uploads/2008/12/Oxygen-Delivery.pdf. Accessed Feb 2013.
47. Chopra S, et al. Comparing oxygen-sensitive MRI (BOLD R_2*) with oxygen electrode measurements: a pilot study in men with prostate cancer. Int J Radiat Biol. 2009;85:805–13.
48. Christen T, et al. Is T2* enough to assess oxygenation? Quantitative blood oxygen level-dependent analysis in brain tumor. Radiology. 2012;262: 495–502.
49. Griffiths JR, et al. The response of human tumors to carbogen breathing, monitored by Gradient-Recalled Echo Magnetic Resonance Imaging. Int J Radiat Oncol Biol Phys. 1997;39:697–701.
50. Hoskin PJ, et al. Hypoxia in prostate cancer: correlation of bold-MRI with pimonidazole immunohistochemistry – initial observations. Int J Radiat Oncol Biol Phys. 2007;68:1065–71.
51. Spees WM, et al. Water proton MR properties of human blood at 1.5 Tesla: magnetic susceptibility, T(1), T(2), T*(2), and non-Lorentzian signal behavior. Magn Reson Med. 2001;45:533–42.
52. An HY, Lin WL. Quantitative measurements of cerebral blood oxygen saturation using magnetic resonance imaging. J Cereb Blood Flow Metab. 2000;20:1225–36.
53. Christen T, et al. Evaluation of a quantitative blood oxygenation level-dependent (qBOLD) approach to map local blood oxygen saturation. NMR Biomed. 2011;24:393–403.
54. Fujita N, et al. Quantitative mapping of cerebral deoxyhemoglobin content using MR imaging. Neuroimage. 2003;20:2071–83.
55. He X, Yablonskiy DA. Quantitative BOLD: mapping of human cerebral deoxygenated blood volume and oxygen extraction fraction: default state. Magn Reson Med. 2007;57:115–26.
56. Bryan RN. Science to practice: is T2* enough to assess oxygenation? Radiology. 2012;262:375–7.
57. Young IR, et al. Enhancement of relaxation rate with paramagnetic contrast agents in NMR imaging. J Comp Tomogr. 1981;5:543–7.
58. Berkowitz BA, et al. Measuring the human retinal oxygenation response to a hyperoxic challenge using MRI: Eliminating blinking artifacts and demonstrating proof of concept. Magn Reson Med. 2001;" 46:412–6.
59. Schwarzbauer C, Deichmann R. Vascular component analysis of hyperoxic and hypercapnic BOLD contrast. Neuroimage. 2012;59:2401–12.
60. Blockley NP, et al. Field strength dependence of R_1 and R_2* relaxivities of human whole blood to ProHance, Vasovist, and deoxyhemoglobin. Magn Reson Med. 2008;60:1313–20.
61. Howe FA, et al. Issues in flow and oxygenation dependent contrast (FLOOD) imaging of tumors. NMR Biomed. 2001;14:497–506.
62. Karczmar GS, et al. Effects of hyperoxia on T_2* and resonance frequency weighted magnetic resonance images of rodent tumors. NMR Biomed. 1994; 7:3–11.
63. Kuperman VY, et al. Changes in T_2*-weighted images during hyperoxia differentiate tumors from normal tissue. Magn Reson Med. 1995;33:318–25.

64. Robinson SP, et al. Magnetic resonance imaging techniques for monitoring changes in tumor oxygenation and blood flow. Semin Radiat Oncol. 1998;8:197–207.
65. Al-Hallaq HA, et al. Using high spectral and spatial resolution bold MRI to choose the optimal oxygenating treatment for individual cancer patients. Adv Exp Med Biol. 2003;530:433–40.
66. Jordan BF, et al. Changes in tumor oxygenation/perfusion induced by the no donor, isosorbide dinitrate, in comparison with carbogen: monitoring by EPR and MRI. Int J Radiat Oncol Biol Phys. 2000;48:565–70.
67. Al-Hallaq HA, et al. Correlation of magnetic resonance and oxygen microelectrode measurements of carbogen-induced changes in tumor oxygenation. Int J Radiat Oncol Biol Phys. 1998;41:151–9.
68. Al-Hallaq HA, et al. Spectrally inhomogeneous BOLD contrast changes detected in rodent tumors with high spectral and spatial resolution MRI. NMR Biomed. 2002;15:28–36.
69. Akber SF. Correlation between oxygen tension and spin–lattice relaxation rate in tumors. Eur J Radiol. 1989;9:56–9.
70. Edelman RR, et al. Noninvasive assessment of regional ventilation in the human lung using oxygen-enhanced magnetic resonance imaging. Nat Med. 1996;2:1236–9.
71. Jakob PM, et al. Assessment of human pulmonary function using oxygen-enhanced T(1) imaging in patients with cystic fibrosis. Magn Reson Med. 2004;51:1009–16.
72. Ohno Y, et al. Oxygen-enhanced MR ventilation imaging of the lung: preliminary clinical experience in 25 subjects. AJR Am J Roentgenol. 2001;177:185–94.
73. Kershaw LE, et al. Measurement of arterial plasma oxygenation in dynamic oxygen-enhanced MRI. Magn Reson Med. 2010;64:1838–42.
74. Jones RA, et al. Imaging the changes in renal T-1 induced by the inhalation of pure oxygen: a feasibility study. Magn Reson Med. 2002;47:728–35.
75. O'Connor JPB, et al. Organ-specific effects of oxygen and carbogen gas inhalation on tissue longitudinal relaxation times. Magn Reson Med. 2007;58:490–6.
76. O'Connor JPB, et al. Comparison of normal tissue R-1 and R-2* modulation by oxygen and carbogen. Magn Reson Med. 2009;61:75–83.
77. Tadamura E, et al. Effect of oxygen inhalation on relaxation times in various tissues. JMagn Reson Imaging. 1997;7:220–5.
78. Matsumoto K, et al. MR assessment of changes of tumor in response to hyperbaric oxygen treatment. Magn Reson Med. 2006;56:240–6.
79. O'Connor JPB, et al. Preliminary study of oxygen-enhanced longitudinal relaxation in MRI: a potential novel biomarker of oxygenation changes in solid tumors. Int J Radiat Oncol Biol Phys. 2009;75:1209–15.
80. Kinoshita Y, et al. Preservation of tumor oxygen after hyperbaric oxygenation monitored by magnetic resonance imaging. Br J Cancer. 2000;82:88–92.
81. Pacheco-Torres J, et al. DOCENT-dynamic oxygen challenge evaluated by NMR T_1 and T_2* of tumors. Proc Int Soc Magn Reson Med. 2008;16:abstract 450.
82. Burrell JS, et al. Exploring ΔR_2* and ΔR_1 as imaging biomarkers of tumor oxygenation. J Magn Reson Imaging (IMRI). 2013;38:429–34.
83. Zhou H, et al. Integrated MRI approaches to interrogate tumor oxygenation and vascular perfusion of orthotopic brain tumors in a mouse model. Proc Int Soc Magn Reson Med. 2010;18:abstract 2793.
84. Winter JD, et al. Quantitative MRI assessment of VX2 tumor oxygenation changes in response to hyperoxia and hypercapnia. Phys Med Biol. 2011;56:1225.
85. Arnold JFT, et al. Quantitative regional oxygen transfer imaging of the human lung. J Magn Reson Imaging. 2007;26:637–45.
86. Linnik IV, et al. Noninvasive tumor hypoxia measurement using magnetic resonance imaging in murine U87 glioma xenografts and in patients with glioblastoma. doi: 10.1002/mrm.24826. Magn Res Med. 2013;(in press).
87. Remmele S, et al. Novel MR method to detect non-normoxic tissue based on cluster analysis of the dynamic R_2* and R_1 response to a hyperoxic respiratory challenge. Proc Int Soc Magn Reson Med. 2012;20.
88. Silvennoinen MJ, et al. Comparison of the dependence of blood R_2 and R_2* on oxygen saturation at 1.5 and 4.7 Tesla. Magn Reson Med. 2003;49:47–60.
89. Remmele S, et al. Classification of tissue oxygenation properties based on simultaneous dynamic ΔR_1 and ΔR_2* D(C)O2E-MRI. Proc Int Soc Magn Reson Med. 2011;19:abstract 4270.
90. Howe FA, et al. Flow and oxygenation dependent (FLOOD) contrast MR imaging to monitor the response of rat tumors to carbogen breathing. Magn Reson Imaging. 1999;17:1307–18.
91. Robinson SP, et al. Tumor response to hypercapnia and hyperoxia monitored by FLOOD magnetic resonance imaging. NMR Biomed. 1999;12:98–106.
92. Remmele S, et al. Dynamic and simultaneous MR measurement of R_1 and R_2* changes during respiratory challenges for the assessment of blood and tissue oxygenation. Magn Reson Med. 2013;70(1):136–46.
93. Roberts R, et al. alpha-Lipoic acid corrects late-phase supernormal retinal oxygenation response in experimental diabetic retinopathy. Invest Ophthalmol Vis Sci. 2006;47:4077–82.
94. Zaharchuk G, et al. Measurement of cerebrospinal fluid oxygen partial pressure in humans using MRI. Magn Reson Med. 2005;54:113–21.
95. Wright GA, et al. Estimating oxygen saturation of blood in vivo with MR imaging at 1.5 T. J Magn Reson Imaging. 1991;1:275–83.
96. Thomas SR. The biomedical applications of Fluorine-19 NMR. In: Partain CL, Price RR, Patton

JA, Kulkarni MV, James AEJ, editors. Magnetic resonance imaging. London: W.B. Saunders Co; 1988. p. 1536–52.
97. Zhao D, et al. Tumor physiological response to combretastatin A4 phosphate assessed by MRI. Int J Radiat Oncol Biol Phys. 2005;62:872–80.
98. Mason RP. Non-invasive physiology: ^{19}F NMR of perfluorocarbon. Artif Cells Blood Substit Immobil Biotechnol. 1994;22:1141–53.
99. Delpuech J-J, et al. Fluorocarbons as oxygen carriers. I. An NMR study of oxygen solutions in hexafluorobenzene. J Chem Phys. 1979;70:2680–7.
100. Mason RP, et al. In vivo oxygen tension and temperature: simultaneous determination using ^{19}F spectroscopy of perfluorocarbon. Magn Reson Med. 1993;29:296–302.
101. Mason RP, et al. Hexafluorobenzene: a sensitive ^{19}F NMR indicator of tumor oxygenation. NMR Biomed. 1996;9:125–34.
102. Shukla HP, et al. A comparison of three commercial perfluorocarbon emulsions as high field NMR probes of oxygen tension and temperature. J Magn Reson Series B. 1995;106:131–41.
103. Eidelberg D, et al. ^{19}F imaging of cerebral blood oxygenation in experimental middle cerebral artery occlusion: preliminary results. J Cereb Blood Flow Metab. 1988;8:276–81.
104. Lai C-S, et al. Effect of oxygen and the spin label TEMPO-Laurate on ^{19}F and proton relaxation rates of the perfluorochemical blood substitute FC-43 emulsion. J Magn Reson. 1984;57:447–52.
105. Thomas SR, et al. Evaluation of the influence of the aqueous-phase bioconstituent environment on the F-19 T1 of perfluorocarbon blood substitute emulsions. J Magn Reson Imaging. 1994;4:631–5.
106. Yu J-X, et al. New frontiers and developing applications in ^{19}F NMR. Prog NMR Spectrosc. 2013;70:25–49.
107. Hunjan S, et al. Tumor oximetry: demonstration of an enhanced dynamic mapping procedure using fluorine-19 echo planar magnetic resonance imaging in the Dunning prostate R3327-AT1 rat tumor. Int J Radiat Oncol Biol Phys. 2001;49:1097–108.
108. Jordan BF, et al. Rapid monitoring of oxygenation by ^{19}F magnetic resonance imaging: Simultaneous comparison with fluorescence quenching. Magn Reson Med. 2009;61:634–8.
109. Bourke VA, et al. Correlation of radiation response with tumor oxygenation in the dunning prostate R3327-AT1 tumor. Int J Radiat Oncol Biol Phys. 2007;67:1179–86.
110. Diepart C, et al. Arsenic trioxide treatment decreases the oxygen consumption rate of tumor cells and radiosensitizes solid tumors. Cancer Res. 2012;72:482–90.
111. Krohn KA, et al. Molecular imaging of hypoxia. J Nucl Med. 2008;49:129S–48148.
112. Magat J, et al. Noninvasive mapping of spontaneous fluctuations in tumor oxygenation using F-19 MRI. Med Phys. 2010;37:5434–41.
113. Mason RP, et al. Quantitative assessment of tumor oxygen dynamics: molecular imaging for prognostic radiology. J Cell Biochem. 2002;87(suppl):45–53.
114. Mason RP, et al. Multimodality imaging of hypoxia in preclinical settings. Q J Nucl Med Mol Imaging. 2010;54:259–80.
115. McNab JA, et al. Tissue oxygen tension measurements in the Shionogi model of prostate cancer using F-19 MRS and MRI. Magn Reson Mater Phys Biol Med. 2004;17:288–95.
116. Song Y, et al. Dynamic breast tumor oximetry: the development of prognostic radiology. Technol Cancer Res Treat. 2002;1:471–8.
117. Xia M, et al. Tumor oxygen dynamics measured simultaneously by near infrared spectroscopy and ^{19}F magnetic resonance imaging in rats. Phys Med Biol. 2006;51:45–60.
118. Zhao D, et al. Differential oxygen dynamics in two diverse Dunning prostate R3327 rat tumor sublines (MAT-Lu and HI) with respect to growth and respiratory challenge. Int J Radiat Oncol Biol Phys. 2002;53:744–56.
119. Zhao D, et al. Tumor oxygen dynamics: correlation of in vivo MRI with histological findings. Neoplasia. 2003;5:308–18.
120. Zhao D, et al. Correlation of tumor oxygen dynamics with radiation response of the dunning prostate R3327-HI tumor. Radiat Res. 2003;159:621–31.
121. Zhao D, et al. Prognostic radiology: quantitative assessment of tumor oxygen dynamics by MRI. Am J Clin Oncol. 2001;24:462–6.
122. Kim JG, et al. Interplay of tumor vascular oxygenation and tumor pO_2 observed using NIRS, oxygen needle electrode, and ^{19}F MR pO_2 mapping. J Biomed Opt. 2003;8:53–62.
123. Zhao D, et al. Tumor oxygen dynamics with respect to growth and respiratory challenge: investigation of the Dunning prostate R3327-HI tumor. Radiat Res. 2001;156:510–20.
124. Mason RP, et al. Oxygenation in a human tumor xenograft: manipulation through respiratory challenge and anti-body directed infarction. In: Dunn JF, Swartz HM, editors. Oxygen transport to tissue XXII proceedings of the 27th annual meeting of the International Society on Oxygen Transport to Tissue. New York: Kluwer Acad; 2003. p. 197–204.
125. Berkowitz BA, et al. Oxygen kinetics in the vitreous substitute perfluorotributylamine – a F-19 NMR-study in vivo. Invest Ophthalmol Vis Sci. 1991;32:2382–7.
126. Wilson CA, et al. Measurement of preretinal pO_2 in the vitrectomized human eye using ^{19}F NMR. Arch Ophthalmol. 1992;110:1098–100.
127. Zhang W, et al. Role of hypoxia during normal retinal vessel development and in experimental retinopathy of prematurity. Invest Ophthalmol Vis Sci. 2003;44:3119–23.
128. Duong TQ, et al. Effect of hyperoxia, hypercapnia, and hypoxia on cerebral interstitial oxygen tension

and cerebral blood flow. Magn Reson Med. 2001;45:61–70.
129. Liu S, et al. Quantitative tissue oxygen measurement in multiple organs using ^{19}F MRI in a rat model. Magn Reson Med. 2011;66:1722–30.
130. Mignion L, et al. Hexafluorobenzene in comparison with perfluoro-15-crown-5-ether for repeated monitoring of oxygenation using ^{19}F MRI in a mouse model. Magn Reson Med. 2013;69:248–54.
131. McIntyre DJO, et al. Tumor oxygenation measurements by ^{19}F MRI of perfluorocarbons. Curr Sci. 1999;76:753–62.
132. Fishman JE, et al. Oxygen-sensitive ^{19}F NMR imaging of the vascular system *in vivo*. Magn Reson Imaging. 1987;5:279–85.
133. Fishman JE, et al. *In vivo* measurements of vascular oxygen tension in tumors using MRI of a fluorinated blood substitute. Invest Radiol. 1989;24:65–71.
134. Giraudeau C, et al. High sensitivity ^{19}F MRI of a perfluorooctyl bromide emulsion: application to a dynamic biodistribution study and oxygen tension mapping in the mouse liver and spleen. NMR Biomed. 2012;25:654–60.
135. Noth U, et al. In vivo measurement of partial oxygen pressure in large vessels and in the reticuloendothelial system using fast ^{19}F-MRI. Magn Reson Med. 1995;34:738–45.
136. Kaufman RJ. Medical oxygen transport using perfluorochemicals. In: Goldstein J, editor. Biotechnology of blood. New York: Butterworth-Heinemann; 1991. p. 127–58.
137. Barker BR, et al. Oxygen tension mapping by ^{19}F echo planar NMR imaging of sequestered perfluorocarbon. J Magn Reson Imaging. 1994;4:595–602.
138. Bellemann ME, et al. Quantification and visualization of oxygen partial pressure in vivo by ^{19}F NMR imaging of perfluorocarbons. Biomed Tech. 2002;47:451–4.
139. Dardzinski BJ, Sotak CH. Rapid tissue oxygen tension mapping using ^{19}F Inversion-recovery Echo-planar imaging of Perfluoro-15-crown-5-ether. Magn Reson Med. 1994;32:88–97.
140. Holland SK, et al. Imaging oxygen tension in liver and spleen by ^{19}F NMR. Magn Reson Med. 1993;29:446–58.
141. Kucejova B, et al. Uncoupling hypoxia signaling from oxygen sensing in the liver results in hypoketotic hypoglycemic death. Oncogene. 2011;30:2147–60.
142. Mattrey RF, Long DC. Potential role of PFOB in diagnostic imaging. Invest Radiol. 1988;23:s298–301.
143. Baldwin NJ, et al. *In situ* ^{19}F MRS measurement of RIF-1 tumor blood volume: corroboration by radioisotope-labeled [^{125}I]-albumin and correlation to tumor size. Magn Reson Imaging. 1996;14:275–80.
144. Mason RP, et al. Non-invasive determination of tumor oxygen tension and local variation with growth. Int J Radiat Oncol Biol Phys. 1994;29:95–103.
145. Baudelet C, et al. Physiological noise in murine solid tumors using T_2*-weighted gradient-echo imaging: a marker of tumor acute hypoxia? Phys Med Biol. 2004;49:3389–411.
146. Hallac RR, et al. Oxygenation in cervical cancer and normal uterine cervix assessed using blood oxygenation level-dependent (BOLD) MRI at 3T. NMR Biomed. 2012;25:1321–30.
147. Jiang L, et al. Blood oxygenation level-dependent (BOLD) contrast magnetic resonance imaging (MRI) for prediction of breast cancer chemotherapy response: a pilot study. J Magn Reson Imaging. 2013;37:1083–92.
148. Karczmar GS, et al. Magnetic resonance measurement of response to hyperoxia differentiates tumors from normal tissue and may be sensitive to oxygen consumption. Invest Radiol. 1994;29(2):161–3.
149. Robinson SP, et al. Noninvasive monitoring of carbogen-induced changes in tumor blood flow and oxygenation by functional magnetic resonance imaging. Int J Radiat Oncol Biol Phys. 1995;33:855–9.
150. Robinson SP, et al. The response to carbogen breathing in experimental tumour models monitored by gradient-recalled echo magnetic resonance imaging. Br J Cancer. 1997;75:1000–6.
151. Ding Y, et al. Simultaneous measurement of TOLD and BOLD effects in abdominal tissue oxygenation level studies. doi: 10.1002/jmri.24006. J Magn Reson Imaging. 2013;38(5):1230–6.
152. Baete SH, et al. An oxygen-consuming phantom simulating perfused tissue to explore oxygen dynamics and ^{19}F MRI oximetry. Magn Reson Mater Phys Biol Med. 2010;23:217–26.
153. Fan XB, et al. Effect of carbogen on tumor oxygenation: combined fluorine-19 and proton MRI measurements. Int J Radiat Oncol Biol Phys. 2002;54:1202–9.
154. Robinson SP, Griffiths JR. Current issues in the utility of ^{19}F nuclear magnetic resonance methodologies for the assessment of tumor hypoxia. Phil Trans Biol Sci. 2004;359:987–96.
155. Thomas SR, et al. In vivo pO_2 imaging in the porcine model with perfluorocarbon F-19 NMR at low field. Magn Reson Imaging. 1996;14:103–14.
156. Diepart C, et al. In vivo mapping of tumor oxygen consumption using ^{19}F MRI relaxometry. NMRBiomed. 2011;24(5):458–63.
157. Kadayakkara DKK, et al. In Vivo Observation of Intracellular Oximetry in Perfluorocarbon-Labeled Glioma Cells and Chemotherapeutic Response in the CNS Using Fluorine-19 MRI. Magn Reson Med. 2010;64(5):1252–9.
158. Mignion L, et al. Hexafluorobenzene in comparison with perfluoro-15-crown-5-ether for repeated monitoring of oxygenation using ^{19}F MRI in a mouse model. Magn Reson Med 2012:epub

159. Pacheco-Torres J, et al. Imaging tumor hypoxia by magnetic resonance methods. NMR Biomed. 2011;24:1–16.
160. Procissi D, et al. In vivo F-19 magnetic resonance spectroscopy and chemical shift imaging of trifluoro-nitroimidazole as a potential hypoxia reporter in solid tumors. Clin Cancer Res. 2007;13:3738–47.
161. Rojas-Quijano FA, et al. Synthesis and characterization of a hypoxia-sensitive MRI probe. Chemistry. 2012;18:9669–76.
162. Golman K, et al. Dynamic in vivo oxymetry using overhauser enhanced MR imaging. J Magn Reson Imaging. 2000;12:929–38.
163. Krishna MC, et al. Overhauser enhanced magnetic resonance imaging for tumor oximetry: coregistration of tumor anatomy and tissue oxygen concentration. Proc Natl Acad Sci U S A. 2002;99:2216–21.

Part III

Functional Imaging Techniques in Clinical Use

Overview of Functional MR, CT, and US Imaging Techniques in Clinical Use

13

Ewelina Kluza, Doenja M.J. Lambregts, and Regina G.H. Beets-Tan

Contents

Abbreviations

^{1}H	Proton
^{1}H-MRS	Proton magnetic resonance spectroscopy
2D	Two-dimensional
3D	Three-dimensional
A	Initial amplitude of MRI signal enhancement
ADC	Apparent diffusion coefficient
AIF	Arterial input function
ASL	Arterial spin labeling
ATP	Adenosine-5′-triphosphate
C	Carbon-13
CEUS	Contrast-enhanced ultrasonography
CNS	Central nervous system
CT	Computed tomography
DCE-MRI	Dynamic contrast-enhanced
DCUS	Double contrast-enhanced ultrasound
DSC	Dynamic-susceptibility contrast
DWI	Diffusion-weighted magnetic resonance imaging
EES	Extracellular extravascular space
Gd	Gadolinium
Gd-DOTA	Gadolinium tetraazacyclododecanetetraacetate
Gd-DTPA	Gadolinium diethylenetriamine pentaacetate
Gd-HP-DO3A	Gadolinium hydroxypropyltetraazacyclododecane triacetate

E. Kluza, PhD • D.M.J. Lambregts, MD, PhD
R.G.H. Beets-Tan, MD, PhD (✉)
Department of Radiology, GROW School of Oncology and Developmental Biology, Maastricht University Medical Center, 5800, 6202 AZ Maastricht, The Netherlands
e-mail: e.kluza@maastrichtuniverity.nl; d.lambregts@mumc.nl; r.beets-tan@mumc.nl

A. Luna et al. (eds.), *Functional Imaging in Oncology*,
DOI 10.1007/978-3-642-40412-2_13,

IAUC	Initial area under the contrast agent concentration–time curve
IRF	Impulse residue function
k^{ep}	Exchange rate constant
K^{trans}	Endothelial transfer coefficient
mM	Millimolar
mm^2	Square millimeter
MMCAs	Macromolecular contrast agents
MRI	Magnetic resonance imaging
MRS	Magnetic resonance spectroscopy
MRSI	Magnetic resonance spectroscopic imaging
MTT	Mean transit time
MVD	Microvessel density
Na	Sodium
NTP	Nucleoside triphosphates
P	Phosphorus
P MRS	Phosphor magnetic resonance spectroscopy
P_i	Inorganic phosphor
rBF	Relative blood flow
rBV	Relative blood volume
s	Second
T1	Longitudinal relaxation time
T2	Transverse relaxation time
T2*	Relaxation time caused by spin–spin interactions and local magnetic field inhomogeneities
tCho	Choline compounds (total choline)
tCr	Creatine compounds (total creatine)
TTP	Time to peak
USPIOs	Ultrasmall iron oxide particles
UTP	Uridine-5′-triphosphate
v_e	Extravascular extracellular space fractional volume

13.1 Introduction

Functional and molecular imaging enable visualization of tumor pathophysiology, providing information on the cellularity, vascular function, metabolism, and molecular biology of the tumor tissue. Functional imaging combines information on tumor morphology with quantified information on underlying tissue characteristics (imaging biomarkers). Among all functional imaging technologies, magnetic resonance imaging (MRI) is emerging as one of the most promising, because of its versatility, noninvasiveness, and lack of exposure to ionizing radiation.

In this chapter, we will address the various functional imaging techniques (MRI, CT, and ultrasonography) with respect to its technical principles and possible applications in clinical practice. Among the vascular imaging technologies, dynamic contrast-enhanced magnetic resonance imaging (DCE-MRI) received the largest attention in the clinics, and therefore, DCE-MRI is the focus of our review. We will explain DCE-MRI using low molecular weight and macromolecular contrast agents as well as alternative technology for vascular MR imaging: arterial spin labeling (ASL) and dynamic-susceptibility contrast (DSC-MRI). We will also discuss vascular imaging technology with CT and contrast-enhanced ultrasonography (CEUS). Diffusion-weighted MRI (DWI-MRI), its principles and its ability to probe the tumor cellularity, will be addressed as well as metabolic imaging with magnetic resonance spectroscopy (MRS). Metabolic imaging with nuclear techniques has been the focus of the previous chapter and is outside the scope of this chapter.

13.2 Vascular Imaging

Noninvasive vascular imaging strategies enable characterization of the vasculature in the entire tumor volume and permit the longitudinal follow-up of a patient. Importantly, and in contrast to histopathological methods, they assess the functional status of tumor vessels, which appears to be diagnostically more relevant than morphological/structural information. The majority of the vascular imaging methods use contrast agents to highlight the vascular bed and quantify its functional features. The quantitative vascular measurement method has been proposed as the potential surrogate maker of therapeutic response. However, its true diagnostic relevance needs to be further evaluated in clinical trials.

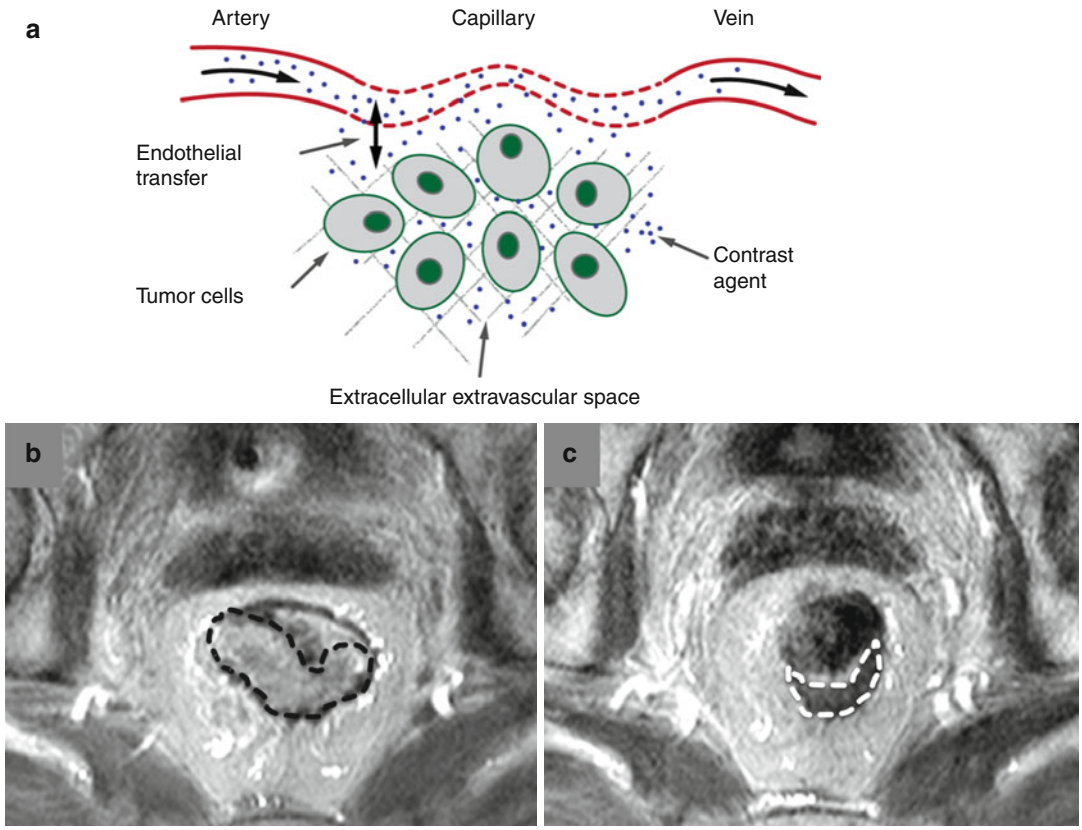

Fig. 13.1 (**a**) Schematic illustration of the DCE-MRI technique in tumor tissue. Intravenously injected MRI contrast agent arrives from arteries in the capillary bed of the tumor tissue and extravasates into the tumor extracellular space. The kinetics of MR signal changes observed in the tumor can be analyzed qualitatively or quantitatively to provide characterization of tissue perfusion, capillary permeability, exchange kinetics, and the volume of extracellular extravascular space. *Lower panel* displays contrast-enhanced T1w images of a slice through the pelvis of a patient with rectal tumor before (**b**) and after chemoradiotherapy (**c**). The primary tumor, which is delineated with the *blacked dashed line*, displays high enhancement (**b**), whereas residual tissue after chemoradiotherapy, defined by the *white dashed line*, is poorly enhancing (**c**)

13.2.1 Dynamic Contrast-Enhanced MRI

Dynamic contrast-enhanced MRI (DCE-MRI) with low molecular weight contrast agents is the most widely applied vascular imaging method in the clinical setting. In DCE-MRI, the vascular function is assessed indirectly by monitoring the pharmacokinetics of an intravenously administered contrast agent with dynamic T_1-weighted scan. Gadolinium (Gd) chelates, commonly used for this purpose, are small hydrophilic molecules characterized by short circulation half-life of typically less than half an hour. Examples of these contrast agents are Gd-DTPA (Magnevist), Gd-HP-DO3A (ProHance), and Gd-DOTA (Dotarem). After systemic injection, these agents are rapidly distributed throughout the body, passing through the endothelium of normal vessels, with the exception of those of the central nervous system (CNS). However, in pathological processes such as a brain tumor, which are associated with the disturbance of blood–brain barrier, Gd chelates are able to accumulate in the affected regions of the CNS as well. After reaching the tissue, the agent remains in the extracellular space during a short period with a concentration plateau, regulated by equal influx and efflux rates, and then followed by the washout phase. The schematic representation of DCE-MRI principles on the tissue level is displayed in the Fig. 13.1a.

Although Gd chelates are able to pass the normal endothelium, generating contrast in normal tissue, specific features of tumor vessels enable their differentiation from the surrounding tissue. The degree of signal enhancement depends on the tissue perfusion, the arterial input function (AIF, i.e., the concentration–time course of contrast agent in the artery supplying the tissue), the capillary surface area, the capillary permeability, and the volume fraction of the extracellular extravascular space (EES). The hyperpermeability and, usually, large volume of the tumor vascular bed are key factors, which contribute to strong DCE-MRI contrast in the tumor (Fig. 13.1b). However, after (chemo)radiotherapy, this high enhancement may decrease considerably as a result of the replacement of well-vascularized tumor by poorly vascularized scar tissue (Fig. 13.1c). The magnitude and dynamics of contrast enhancement can be expressed either in a qualitative or in a (semi)quantitative manner. The former method involves the visual assessment of an obviously enhancing tumor area, and it is commonly performed in the radiological practice. Furthermore, the temporal profile of tumor enhancement can be assigned into one of three qualitative categories: (1) progressive enhancement pattern (washin), which shows continuous increase in signal intensity throughout time; (2) persistent enhancement pattern, displaying initial uptake followed by plateau phase; and (3) washout pattern, which has a relatively rapid uptake followed by reduction in enhancement towards the latter time points [1]. This method is predominantly exploited in breast cancer diagnostics and considers the type three enhancement pattern as strongly suggestive of malignancy. Importantly, DCE-MRI can deliver quantitative and (patho)physiologically meaningful vascular parameters. In order to assess these kinetic parameters, signal changes following the administration of a Gd chelate should be converted into the contrast agent concentration–time curves. To this aim, baseline T_1 values are measured in the tumor before DCE-MRI acquisition or the reference tissue method is applied [2]. Alternatively, unconverted relative MR signal intensity curves can serve the determination of semiquantitative kinetic parameters. The descriptive or semiquantitative kinetic parameters, such as the initial amplitude of MRI signal enhancement (A), initial area under the contrast agent concentration–time curve (IAUC), and initial slope or time to peak (TTP) of the concentration–time curve, are derived without using pharmacokinetic modeling. These parameters are straightforward; however, they are highly influenced by the experimental setup [3]. In contrast, pharmacokinetic parameters, such as the endothelial transfer coefficient (K^{trans}), the exchange rate constant (k^{ep}), and the EES fractional volume (v_e), assessed by using mathematical models to fit the data [4], are considered to be more physiologically meaningful, and they are less sensitive to the experimental conditions [3]. An example of the sensitivity of K^{trans} and k^{ep} to chemoradiotherapy-induced changes in the tumor vasculature is displayed in Fig. 13.2.

An important feature of the tumor vasculature is its heterogeneity. Therefore, pixel-by-pixel analysis of DCE-MRI data is the preferred method, providing parameter maps [5]. The analysis of the parameter distribution provided better prediction of the therapeutic response in breast cancer patients [6] and tumor recurrence after radiotherapy in patients with cervical carcinoma [7], as compared to mean or median value.

Dynamic contrast-enhanced MRI with macromolecular contrast agents is a novel vascular imaging method, which exploits macromolecular contrast agents (MMCAs) to assess the tissue vascular characteristics. The pharmacokinetic properties of MMCAs differ considerably from those of the low molecular weight Gd chelates. Their macromolecular size, ranging from a few to a few hundred nanometers, does not allow them to cross the endothelial layer of normal vessels. Moreover, generally, they are designed as long-circulating agents with a blood circulation half-life of the order of several hours. In the tumor microenvironment, the enhanced endothelial permeability enables extravasation of macromolecular agents. However, this process is much slower than in the case of low molecular weight

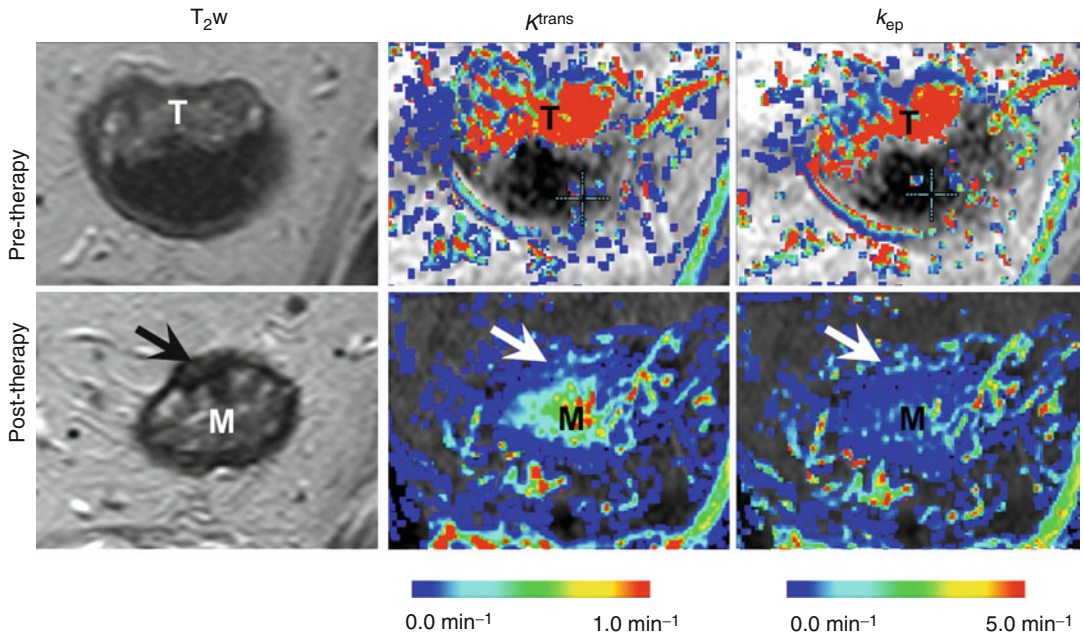

Fig. 13.2 DCE-MRI assessment of chemoradiotherapy-induced changes in the tumor vasculature. Representative T2-weighted images (T_2w) and maps of the endothelial transfer coefficient (K^{trans}) and the exchange rate constant (k^{ep}) obtained for a rectal cancer patient at the primary staging (*upper panel*) and after 8 weeks' interval following the neoadjuvant chemoradiotherapy (*lower panel*). The tumor location in the pre-therapy state is indicated by "T." In the *lower panel*, *arrows* point to the potential residual tumor tissue after chemoradiotherapy, whereas the symbol "M" indicates the edematous mucosa. Both types of pharmacokinetic maps show a dramatic decrease in the parameter values after chemoradiotherapy, which indicates the vascular regression

contrast agents. Therefore, the separate assessment of vascular parameters, such as blood volume and vascular permeability, is considered to be more accurate [8]. So far, neither of the MMCAs is routinely used in the oncological diagnostics. Examples of MMCAs that have entered clinical trials include the Gd-cascade polymer (Gadomer-17) and P792 (Vistarem). Furthermore, an interesting group of MMCAs are Gd complexes, which bind reversibly to endogenous albumin, such as Gd-BOPTA (MultiHance) or gadofosveset (AngioMARK/Vasovist/Ablavar). Ultrasmall iron oxide particles (USPIOs), such as feruglose (Clariscan) or ferumoxtran-10 (Resovist S), belong to the MMCAs as well. Delayed imaging after intravenous injection with USPIOs has been employed to detect metastatic spread in lymph nodes, liver, and bone marrow [9, 10]. Interestingly, in addition to the blood volume and vascular permeability, the USPIO-based readout also provides estimates of the vessel diameter [11], which can serve as a valuable marker of the antiangiogenic effects.

Dynamic-susceptibility contrast (DSC) MRI, also known as bolus-tracking MRI, is a dynamic MRI method that provides estimates of perfusion and other hemodynamic parameters. It exploits T2* sequences to monitor the passage of contrast material through a capillary bed, which presents as decrease in MR signal intensity [12]. The degree of signal loss is dependent on the vascular concentration of the contrast agent and microvessel size and volume. DSC-MRI can therefore provide quantitative indicatives of relative blood volume (rBV), relative blood flow (rBF), and mean transit time (MTT) derived from the first pass of contrast agent through the microcirculation [13]. DSC-MRI is most reliably used for normal brain and non-enhancing brain lesions, e.g.,

low-grade gliomas, because the contrast medium is retained within the intravascular space [13, 14]. In contrast, it cannot readily be applied to areas of marked blood–brain barrier breakdown or to extracranial tumors with very leaky blood vessels. This is because the T1 enhancing effects of Gd chelates can counteract the T2* signal lowering effects, resulting in falsely low blood volume values in very leaky vessels [15]. A solution to overcoming this problem is to use non-gadolinium susceptibility contrast agents, which have a strong T2* effect but a weak T1 effect. The signal loss observed with T2*-weighted sequences has been used qualitatively in clinical studies to characterize liver, breast, and brain tumors [16–18].

13.2.2 Noninvasive Vascular MR Imaging

Arterial spin labeling (ASL) is a completely noninvasive vascular MR method, which exploits arterial water as an endogenous tracer. It is therefore very desired for the longitudinal patient follow-up. Importantly, ASL yields absolute measurements of blood flow at high spatial and temporal resolution [19]. In ASL, the proton spins of the arterial water are magnetically labeled, i.e., undergo either saturation or inversion, prior to reaching the imaged volume. Blood flowing into the imaging slice exchanges with tissue water, altering the tissue magnetization. A perfusion-weighted image can be generated by the subtraction of a "labeled" image from a control image, in which spin labeling has not been performed. ASL has been clinically applied in the assessment of cerebral blood flow in various pathological states, including cerebrovascular disease, neurodegenerative disease, and epilepsy. In oncology, the ASL application has been mainly limited to brain tumors [20, 21]. In extracranial tumors, however, technical challenges limit the ability to label the supplying vessels of the tumor [22]. Moreover, it is sometimes difficult to differentiate the tumor-feeding artery. Nevertheless, some preclinical and clinical studies have shown potential of ASL for cancer diagnosis and therapy evaluation at peripheral locations [23, 24].

13.2.3 Perfusion CT

Computed tomography (CT) is currently one of the most commonly used imaging modalities because of widespread availability, reasonable costs, fast image acquisition, whole-body 3D coverage, and high spatial resolution. On the other hand, CT has several important disadvantages, including the use of ionizing radiation, poor soft tissue contrast, and limited functional information. In clinical oncology, contrast-enhanced CT plays an important role, being the imaging method of choice for monitoring of pulmonary, hepatic, mediastinal, and retroperitoneal lymph node metastases [25]. Perfusion CT, a dynamic contrast-enhanced CT method, also aspires for the position in cancer diagnostics, by generating (patho)physiologically relevant hemodynamic parameters. Although perfusion CT can be readily incorporated into existing CT protocols, clinical experience has largely comprised preliminary studies and few large-scale clinical trials have been performed [26].

A perfusion CT measurement consists of a dynamic series of images acquired before, during, and after an intravenous bolus of iodinated contrast material. The first pass of contrast agent through the vascular system typically comprises the first 45–60 s post-contrast. Over time, increasing amounts of contrast material pass into the extravascular space until equilibrium is reached at approximately 2 min post-contrast. The resulting temporal changes in contrast enhancement can be used to assess a range of parameters that reflect the functional status of the tissue vasculature. As a consequence of the two-compartment kinetics of a contrast agent, there are two categories of (patho)physiological data that are obtained from perfusion CT data. The intravascular phase of enhancement provides estimation of the perfusion, i.e., blood flow per unit volume or mass of tissue, and the relative blood volume. The extravascular phase can be used to evaluate vascular permeability exploiting the fact that tumor blood

vessels are abnormally permeable to circulating molecules [27].

Vascular function of the imaged tissue can be expressed by means of semiquantitative and quantitative parameters. Semiquantitative parameters, such as the enhancement peak or enhancement rate, are obtained from tumor time–attenuation curves and have been shown to correlate with MVD in lung and renal cancer [28, 29]. Compartmental analysis and deconvolution represent the two most widely used quantitative analysis methods for determination of perfusion and other vascular parameters from dynamic CT data. Compartmental analysis for first-pass studies considers the intravascular and extravascular spaces as a single compartment, which can be done prior to the moment when contrast medium appears in the draining veins of the tissue of interest. Perfusion is calculated either from the maximal slope of the tissue concentration–time curve or from its peak height, normalized to the arterial input function. A two-compartment model is used for measurements of capillary permeability and blood volume [27]. Deconvolution method uses arterial and tissue time–attenuation curves to calculate the impulse residue function (IRF) for the tissue of interest, where the IRF is a theoretical tissue curve that would be obtained from an instantaneous arterial input [27]. Compartmental analysis and deconvolution methods have both been validated against other reference standards both in animals and humans, showing high accuracy and reproducibility [30–32].

13.2.4 Contrast-Enhanced Ultrasonography (CEUS)

Contrast-enhanced ultrasonography (CEUS) imaging emerges as the most popular medical imaging modality, which can be attributed to the low cost per examination and high safety profile. Due to poor scattering of ultrasonic waves by blood, the US contrast agents have been developed to assess the functional tissue status. The US contrast agents consist of micron-sized gas bubbles encapsulated in biodegradable shells. In contrast to both CT- and MRI-based methods, CEUS enables the visualization of tissue capillary network. This unique feature is due to a high sensitivity of US to very small amounts of contrast agent, even to a single bubble. Furthermore, because sonography is a dynamic method that is performed in real time, the tissue perfusion properties can be deduced from both the influx and washout of the contrast media. In addition, signals from the microbubbles enable the visualization of slow flow in microscopic vessels. CEUS is now routinely used for diagnosis, particularly for the detection and characterization of various liver tumors [33]. More detailed description of the methodological principles of CEUS and its clinical applicability can be found in the recent review by Postema and Gilja [34]. In addition to conventional CEUS, double contrast-enhanced ultrasound (DCUS) has been recently developed to improve the assessment of gastric cancer [35]. In clinical application of this methodology, the use of an oral US contrast agent reveals the three-layered structure of the gastric wall, while the application of an intravenous contrast reveals the dynamic features of tumor vascularity. DCUS is considered as superior to the traditional staging methods for gastric cancer since it can assess the depth of tumor penetration and the presence of lymph node metastases. In addition, a few research groups proposed blood flow measurements by Doppler ultrasonography for therapy monitoring in different malignancies [36–38].

13.3 Cellular Viability/Density Imaging with Diffusion MRI

Diffusion-weighted MR imaging (DWI) is a technique that is increasingly gaining ground within the field of oncology. The contrast in DWI is derived from differences in the microscopic movement ("diffusion") of water protons between different tissues. The degree of water diffusion is mainly dependent on a tissue's cellular density, the presence of intact cell membranes, and the viscosity of fluids. In tissues with a dense cellular structure, with many intact cell membranes, or within fluids with a highly viscous content,

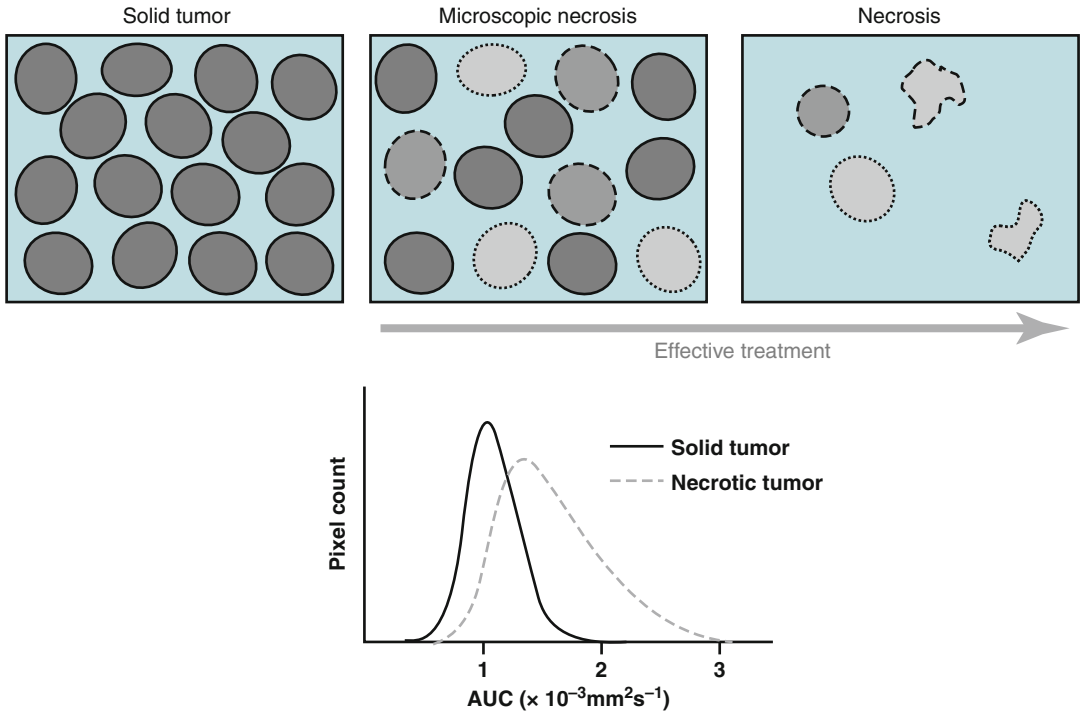

Fig. 13.3 Schematic representation of therapy-induced changes in tumor cellularity and water mobility measured as an apparent diffusion coefficient (ADC). The increase in extracellular space and membrane permeability associated with cell death (*upper panel*) results in greater water mobility, which is observed as a shift of tumor ADC distribution towards higher ADC values (*lower panel*). (Inspired by [39])

the movement of water protons is restricted. In contrast, the loss of cellularity, e.g., as a result of chemotherapy, is associated with an increase in the water diffusion and can be measured by DWI (Fig. 13.3) [39]. Diffusion weighting is typically obtained by applying two bipolar diffusion sensitizing gradients to a T2-weighted spin echo sequence. The gradient duration, the amplitude, and the interval between the two gradients together determine the degree of diffusion weighting (referred to as the "b-value"). On high b-value (e.g., b800–1000) diffusion images, the signal from most soft tissues is suppressed, and the only signal that remains is that of high cellular structures, such as malignant tumors, but also some normal anatomical structures such as nerves and lymphoid tissues. Traditionally, DWI was mainly used in neurologic imaging to detect areas of brain ischemia, an indication for which DWI has proven itself invaluable. In the early years, body DWI was not deemed feasible due to artifacts caused by limitations in the scan technique, the presence of air-filled spaces (lungs, bowels), and respiratory motion. Nowadays, however, these limitations have been largely overcome, and extracranial applications of DWI are rapidly emerging. One of the current cornerstones of DWI is the evaluation of malignancies. Numerous studies have shown the value of diffusion for the detection of malignant tumors within specific organs such as the liver and prostate [40, 41] but also in the whole-body setting to assess the extent of disease in patients with lymphoma or to screen for metastases from, for example, prostate and breast cancer [42, 43]. One of the main strengths of DWI is that it not only allows for a visual assessment but also enables the acquisition of quantitative data. When plotting the degree of signal attenuation obtained at two or more b-values logarithmically, the slope

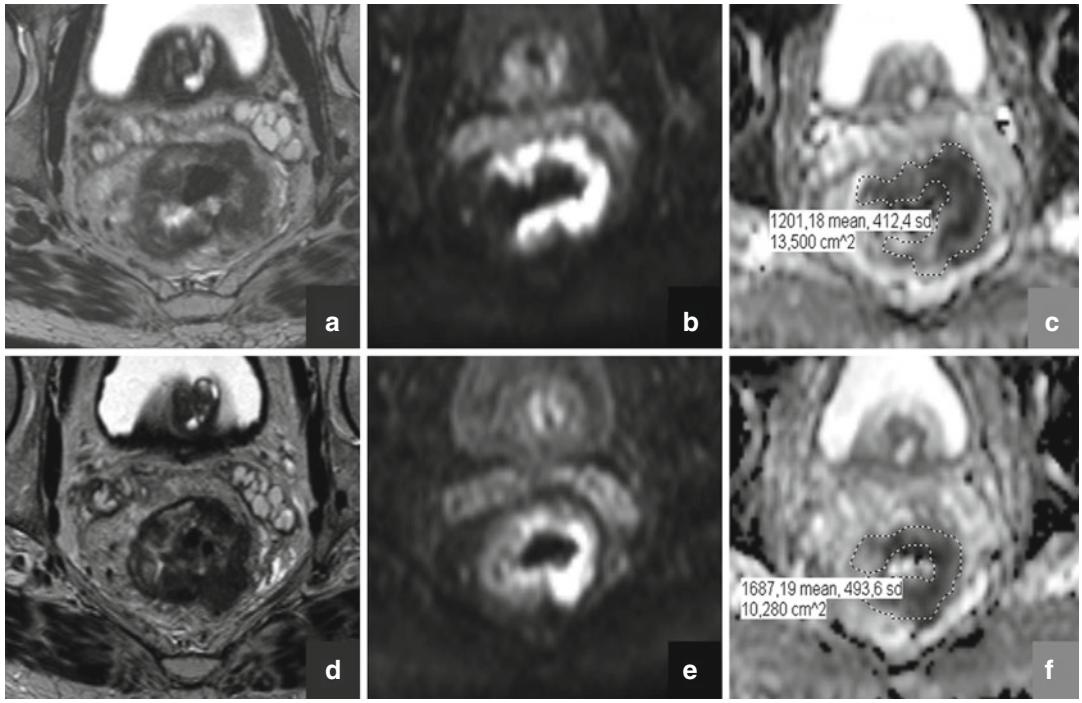

Fig. 13.4 Early therapy assessment by diffusion-weighted imaging (DWI). Example of a patient with a rectal tumor at primary staging (**a**–**c**) and early during neoadjuvant treatment, after 2 weeks of chemoradiotherapy (**d**–**f**). On T2-weighted MRI before treatment (**a**), a circular T3 tumor is visible. After 2 weeks of treatment (**d**), no apparent changes in tumor shape, signal intensity, or volume can yet be detected. On high b-value (b1000) DWI before treatment (**b**), the tumor is easily detectable because its high signal intensity – indicating restricted diffusion – makes it stand out compared to the suppressed signal of the surrounding tissues. After 2 weeks of treatment (**e**), changes in the DWI signal can already be observed. When analyzing changes in the tumor's mean apparent diffusion coefficient (ADC) measurements – the quantitative measure of diffusion – a clear increase in ADC from $1{,}200\times10^{-6}$ mm^2/s before treatment (**c**) to $1{,}687\times10^{-6}$ mm^2/s after 2 weeks of treatment (**f**) can be observed, indicating that DWI and in particular ADC measurements may be used as an early marker of tumor response

of this line can be used as a quantitative measure of diffusion: the "apparent diffusion coefficient" (ADC). ADC has been shown a useful parameter to help distinguish between benign and malignant lesions. For example, in the liver study, it has been shown that the ADC of metastatic lesions (1.05×10^{-3} mm^2/s) and hepatocellular carcinoma (1.22×10^{-3} mm^2/s) was significantly lower compared to benign lesions such as focal nodular hyperplasia (1.40×10^{-3} mm^2/s), hemangiomas (1.92×10^{-3} mm^2/s), and cysts (3.02×10^{-3} mm^2/s) [44]. Moreover, ADC has been suggested as a potential imaging biomarker to assess and monitor the behavior of tumors after onset of cancer treatment. When a tumor responds to treatment, this is reflected by a change in its cellular microstructure, which can readily be detected as a change in its diffusion characteristics (Fig. 13.4). The use of ADC as an imaging biomarker is an appealing option; because DWI is a noninvasive technique, acquisition is relatively fast and can easily be incorporated into any clinical MRI protocol. Moreover, DWI does not require the use of exogenous contrast agents or ionizing radiation. Hence, the use of ADC as a noninvasive tumor biomarker is now frequently being explored, and successful results have been reported in various types of malignancies such as colorectal cancer, primary and metastatic liver tumors, bone tumors, and lymphoma [45–48].

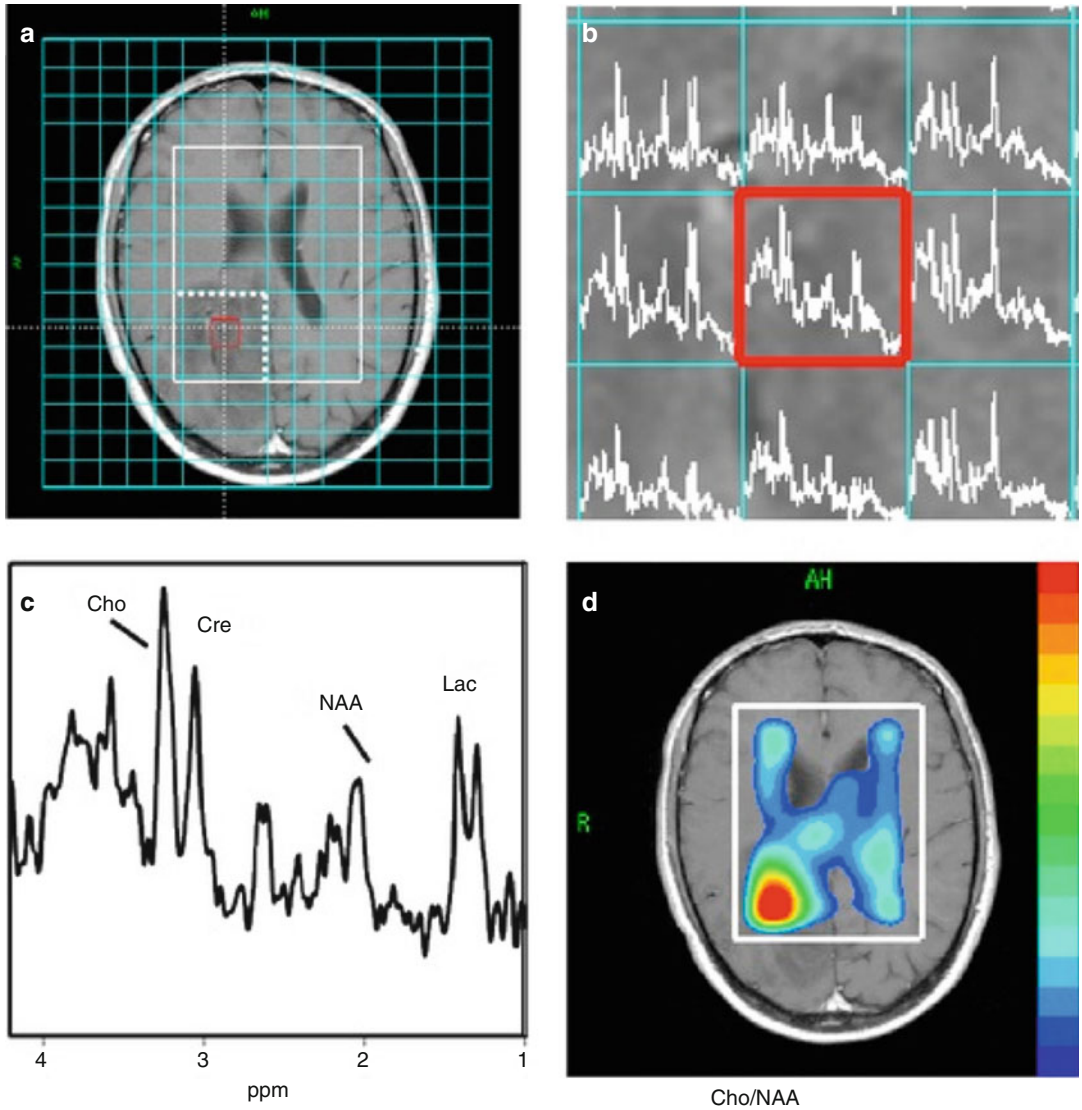

Fig. 13.5 Magnetic resonance spectroscopic imaging (MRSI) data obtained from a patient with a brain tumor (low-grade oligodendroglioma). (**a**) MR image with volume of interest in white and two-dimensional MRSI grid in blue. Spectra are only acquired from the MRSI voxels inside the volume of interest. The *dotted line* in (**a**) indicates the MRSI voxels shown in (**b**). (**b**) Part of the spectral image showing MRSI voxels with their corresponding spectra. (**c**) Enlargement of the spectrum obtained from the voxel indicated in *red* in (b) and (c). The spectrum shows a typical pattern for a low-grade brain tumor with increased choline, decreased NAA, and the doublet of lactate. (**d**) Metabolite map showing the intensity distribution of the ratio of choline to NAA over the volume of interest with the highest intensity indicated in red at the position of the tumor (Reproduced with permission [51])

13.4 Metabolic Imaging with Magnetic Resonance Spectroscopy

Magnetic resonance spectroscopy (MRS) provides chemical information on the tissue metabolic profile. In contrast to conventional MRI, which detects the presence of mainly water and lipids, MRS generally depicts the resonance spectra of various chemical compounds to obtain a metabolite fingerprint of the tumor. MRS is not restricted to proton (^{1}H) detection but also carbon (^{13}C), phosphorus (^{31}P), and sodium (^{23}Na), which are present in several compounds

that play a role in tumor metabolism. The specific property that enables detection of the aforementioned nuclei is the so-called chemical shift, which causes unique resonance frequencies for nuclei of different molecular groups. Specific spectral profiles, which can be observed in an MR spectrum, reflect the identity of biomolecules present at the studied location. A particular advantage of MRS is that it provides quantitative data as the intensity of spectral signals is related to the concentration of these compounds. In practice, the detection of molecules is restricted to those present at the concentration higher than 0.1–1 mM [49]. Therefore, new strategies are being explored to enhance the sensitivity of MRS with hyperpolarization of endogenous or exogenous compounds [50]. Following the intravenous administration, the metabolic conversion of a hyperpolarized compound can be monitored by fast high-resolution MRSI to provide real-time metabolic information.

^{1}H-MRS plays a prominent role in clinical applications, particularly in brain, breast, and prostate cancer [49]. This is because ^{1}H nuclei are present in most metabolites and can be detected with high sensitivity. Moreover, $^{1H\text{-}MRS}$ can be employed relatively easily on clinical MRI scanners. MRS is used to assess metabolism in either single or multiple selected locations (metabolic mapping). ^{1}H-MRS of a single voxel is the most common way to assess metabolic information. A multivoxel or spectroscopic imaging approach (MRSI) has been developed to assess the metabolic heterogeneity of tumor tissue. In this way, a large tissue volume can be selected, which is divided into small voxels (Fig. 13.5). Subsequently, a 2D or 3D spatial map can be reconstructed from signals in spectra of each voxel. ^{1}H-MRS has uncovered abnormal levels of several metabolites, reflecting changes in the metabolism and physiology due to neoplastic growth. The most characteristic for brain tumors is an increase in the choline compound (Cho) level and decrease in the total creatine (tCr) as compared to normal brain tissue (Fig. 13.5) [51]. Moreover, in MR spectra of brain tumors, a lactate signal can be also observed. In prostate tumors, the proton signal of tCho has been frequently reported as increased compared to the healthy prostate tissue [52]. In contrast, the citrate peak displayed relatively low level. ^{1}H-MRS can be used to characterize breast lesions through differences in the ratio of fat and water signals [53, 54] or the intensity of signal from Cho [55, 56]. Anticancer therapy may alter the tumor metabolic profile, depending on the level of response. For example, the complete regression of nodal lesion of head and neck carcinoma has been accompanied by the disappearance of the primarily observed Cho peak (Fig. 13.6) [57].

In vivo ^{31}P MRS has shown great promise as a tool for cancer research and the clinical management of solid tumors. ^{31}P MRS can detect phosphorylated compounds in vivo, which are present at greater than roughly 100 mM concentration, including metabolites such as nucleoside triphosphates (NTP: ATP, UTP, and similar compounds), phosphocreatine, inorganic phosphor (P_i), and a variety of phosphomonoester and phosphodiester compounds [58]. In breast cancer, ^{31}P MRS studies have shown phosphomonoester and diester peaks attributable to enhanced levels of phosphoethanolamine and (glycero)phosphocholine [59]. The enhanced levels of these metabolites were also found in other tumor types, including brain [60] and soft tissue tumors [61].

Conclusions

Functional imaging provides information on underlying tumor pathophysiology; cellularity, vascular function, metabolism, and molecular biology of the tumor tissue. Functional imaging combined with conventional morphological imaging gives us comprehensive information on tumor heterogeneity and risk profile. Among all functional imaging technologies, functional MRI is emerging as one of the most promising in oncology because of its versatility and lack of radiation exposure. Dynamic contrast-enhanced MRI (DCE-MRI) with micro or macromolecular contrast, arterial spin labeling (ASL) and dynamic-susceptibility contrast (DSC) MRI are promising techniques to evaluate the tumor vasculature but still under investigation. Diffusion-weighted MRI (DWI-MRI) is increasingly used in clinical practice to characterize

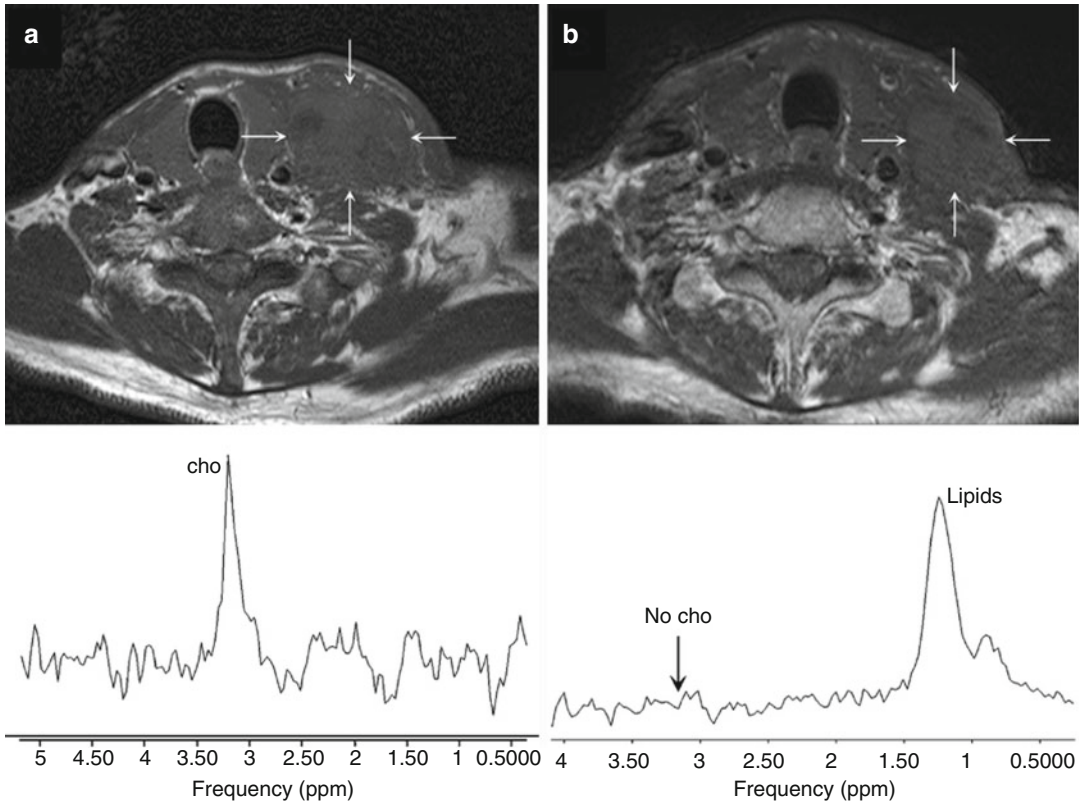

Fig. 13.6 MR images and ^{1}H MRS spectra from a metastatic neck node which showed no residual cancer posttreatment (*arrows*). (**a**) The spectrum with lipids removed shows an intense total choline (*Cho*) peak before the patient underwent treatment. (**b**) Posttreatment spectroscopy performed at the same location shows no detectable Cho in the unprocessed spectrum in the posttreatment mass (Reproduced with permission [57])

lesions. Metabolic imaging with magnetic resonance spectroscopy (MRS) has its application in brain, breast and prostate cancer imaging. Despite its potential functional imaging is not yet widely used in practice. One of the reasons is a weak evidence still that proves its value. So far evidence is from small single center studies. Apart from that we face several challenges. First, we need to standardize the imaging protocols, the acquisition of data, the data processing methods and methods of analysis. Second, we need to know the reproducibility of such a measurement, the intra- and intervendor as well as the intra- and interobserver variability. Third, it is important to understand the natural variation of each individual biomarker and know whether the change that we observe can truly be ascribed to changes induced by treatment. Software programs for smooth integration into diagnostic PACS systems and (radiation) treatment planning systems need to be developed. And most importantly, the most effective functional imaging biomarkers should be incorporated in clinical outcome trials to understand its true value in cancer medicine. Only then we will know whether functional imaging is of true value in cancer treatment.

References

1. Kuhl CK, et al. Dynamic breast MR imaging: are signal intensity time course data useful for differential diagnosis of enhancing lesions? Radiology. 1999; 211:101–10.
2. Kovar DA, et al. A new method for imaging perfusion and contrast extraction fraction: input functions derived from reference tissues. J Magn Reson Imaging. 1998;8:1126–34.
3. Leach MO, et al. The assessment of antiangiogenic and antivascular therapies in early-stage clinical trials

using magnetic resonance imaging: issues and recommendations. Br J Cancer. 2005;92:1599–610.
4. Tofts PS, et al. Estimating kinetic parameters from dynamic contrast-enhanced T_1-weighted MRI of a diffusible tracer: standardized quantities and symbols. J Magn Reson Imaging. 1999;10:223–32.
5. Jackson A, et al. Imaging tumor vascular heterogeneity and angiogenesis using dynamic contrast-enhanced magnetic resonance imaging. Clin Cancer Res. 2007;13:3449–59.
6. Chang YC, et al. Angiogenic response of locally advanced breast cancer to neoadjuvant chemotherapy evaluated with parametric histogram from dynamic contrast-enhanced MRI. Phys Med Biol. 2004;49:3593–602.
7. Mayr NA, et al. Pixel analysis of MR perfusion imaging in predicting radiation therapy outcome in cervical cancer. J Magn Reson Imaging. 2000;12: 1027–33.
8. Daldrup-Link HE, Brasch RC. Macromolecular contrast agents for MR mammography: current status. Eur Radiol. 2003;13:354–65.
9. Michel SCA, et al. Preoperative breast cancer staging: MR imaging of the axilla with ultrasmall superparamagnetic iron oxide enhancement. Radiology. 2002;225:527–36.
10. Hudgins PA, et al. Ferumoxtran-10, a superparamagnetic iron oxide as a magnetic resonance enhancement agent for imaging lymph nodes: a phase 2 dose study. AJNR Am J Neuroradiol. 2002;23:649–56.
11. Tropres I, et al. Vessel size imaging. Magn Reson Med. 2001;45:397–408.
12. Edelman RR, et al. Cerebral blood flow: assessment with dynamic contrast-enhanced T2*-weighted MR imaging at 1.5 T. Radiology. 1990;176:211–20.
13. Rempp KA, et al. Quantification of regional cerebral blood flow and volume with dynamic susceptibility contrast-enhanced MR imaging. Radiology. 1994; 193:637–41.
14. Wenz F, et al. Effect of radiation on blood volume in low-grade astrocytomas and normal brain tissue: quantification with dynamic susceptibility contrast MR imaging. Am J Roentgenol. 1996;166: 187–93.
15. Padhani AR. Functional MRI for anticancer therapy assessment. Eur J Cancer. 2002;38:2116–27.
16. Ichikawa T, et al. Characterization of hepatic lesions by perfusion-weighted MR imaging with an echoplanar sequence. Am J Roentgenol. 1998;170:1029–34.
17. Kuhl CK, et al. Breast neoplasms: T2* susceptibility-contrast, first-pass perfusion MR imaging. Radiology. 1997;202:87–95.
18. Kvistad KA, et al. Differentiating benign and malignant breast lesions with T2*-weighted first pass perfusion imaging. Acta Radiol. 1999;40:45–51.
19. Borogovac A, Asllani I. Arterial Spin Labeling (ASL) fMRI: advantages, theoretical constraints, and experimental challenges in neurosciences. Int J Biomed Imaging. 2012;2012:818456.
20. Warmuth C, et al. Quantification of blood flow in brain tumors: comparison of arterial spin labeling and dynamic susceptibility-weighted contrast-enhanced MR imaging. Radiology. 2003;228:523–32.
21. Wolf RL, et al. Grading of CNS neoplasms using continuous arterial spin labeled perfusion MR imaging at 3 Tesla. J Magn Reson Imaging. 2005;22:475–82.
22. Barrett T, et al. MRI of tumor angiogenesis. J Magn Reson Imaging. 2007;26:235–49.
23. Schor-Bardach R, et al. Does arterial spin-labeling MR imaging-measured tumor perfusion correlate with renal cell cancer response to antiangiogenic therapy in a mouse model? Radiology. 2009;251:731–42.
24. Schmitt P, et al. Quantitative tissue perfusion measurements in head and neck carcinoma patients before and during radiation therapy with a non-invasive MR imaging spin-labeling technique. Radiother Oncol. 2003;67:27–34.
25. D'Ippolito G, et al. CT and MRI in monitoring response: state-of-the-art and future developments. Q J Nucl Med Mol Imaging. 2011;55:603–19.
26. Miles KA, Griffiths MR. Perfusion CT: a worthwhile enhancement? Br J Radiol. 2003;76:220–31.
27. Miles KA, et al. Application of CT in the investigation of angiogenesis in oncology. Acad Radiol. 2000; 7:840–50.
28. Swensen SJ, et al. Lung nodule enhancement at CT: prospective findings. Radiology. 1996;201:447–55.
29. Jinzaki M, et al. Double-phase helical CT of small renal parenchymal neoplasms: correlation with pathologic findings and tumor angiogenesis. J Comput Assist Tomogr. 2000;24:835–42.
30. Cenic A, et al. A CT method to measure hemodynamics in brain tumors: validation and application of cerebral blood flow maps. AJNR Am J Neuroradiol. 2000;21:462–70.
31. Hattori H, et al. Tumor blood flow measured using dynamic computed tomography. Invest Radiol. 1994; 29:873–6.
32. Wintermark M, et al. Simultaneous measurement of regional cerebral blood flow by perfusion CT and stable xenon CT: a validation study. AJNR Am J Neuroradiol. 2001;22:905–14.
33. Claudon M, et al. Guidelines and good clinical practice recommendations for contrast enhanced ultrasound (CEUS) – update 2008. Ultraschall Med. 2008;29:28–44.
34. Postema M, Gilja OH. Contrast-enhanced and targeted ultrasound. World J Gastroenterol. 2011;17: 28–41.
35. Huang P, et al. Double contrast-enhanced ultrasonography evaluation of preoperative Lauren classification of advanced gastric carcinoma. Arch Med Sci. 2011;7:287–93.
36. van der Woude HJ, et al. Treatment of high-grade bone sarcomas with neoadjuvant chemotherapy: the utility of sequential color Doppler sonography in predicting histopathologic response. Am J Roentgenol. 1995;165:125–33.
37. Singh S, et al. Color Doppler ultrasound as an objective assessment tool for chemotherapeutic response in advanced breast cancer. Breast Cancer. 2005; 12:45–51.

38. Lassau N, et al. Prognostic value of angiogenesis evaluated with high-frequency and colour Doppler sonography for preoperative assessment of primary cutaneous melanomas: correlation with recurrence after a 5 year follow-up period. Cancer Imaging. 2006;6:24–9.
39. Ross BD, et al. Evaluation of cancer therapy using diffusion magnetic resonance imaging. Mol Cancer Ther. 2003;2:581–7.
40. Coenegrachts K, et al. Improved focal liver lesion detection: comparison of single-shot diffusion-weighted echoplanar and single-shot T2 weighted turbo spin echo techniques. Br J Radiol. 2007;80:524–31.
41. Katahira K, et al. Ultra-high-b-value diffusion-weighted MR imaging for the detection of prostate cancer: evaluation in 201 cases with histopathological correlation. Eur Radiol. 2011;21:188–96.
42. Kwee TC, et al. Whole-body MRI, including diffusion-weighted imaging, for the initial staging of malignant lymphoma: comparison to computed tomography. Invest Radiol. 2009;44:683–90.
43. Gutzeit A, et al. Comparison of diffusion-weighted whole body MRI and skeletal scintigraphy for the detection of bone metastases in patients with prostate or breast carcinoma. Skeletal Radiol. 2010;39(4):333–43.
44. Bruegel M, et al. Characterization of focal liver lesions by ADC measurements using a respiratory triggered diffusion-weighted single-shot echo-planar MR imaging technique. Eur Radiol. 2008;18:477–85.
45. Cui Y, et al. Apparent diffusion coefficient: potential imaging biomarker for prediction and early detection of response to chemotherapy in hepatic metastases. Radiology. 2008;248:894–900.
46. Sun YS, et al. Locally advanced rectal carcinoma treated with preoperative chemotherapy and radiation therapy: preliminary analysis of diffusion-weighted MR imaging for early detection of tumor histopathologic downstaging. Radiology. 2010;254:170–8.
47. Lin C, et al. Whole-body diffusion-weighted imaging with apparent diffusion coefficient mapping for treatment response assessment in patients with diffuse large B-cell lymphoma: pilot study. Invest Radiol. 2011;46:341–9.
48. Horger M, et al. Whole-body diffusion-weighted MRI with apparent diffusion coefficient mapping for early response monitoring in multiple myeloma: preliminary results. AJR Am J Roentgenol. 2011;196:W790–5.
49. Heerschap A. In vivo MRS in clinical oncology. In: Shields AF, Price P, editors. In vivo imaging of cancer therapy. Totowa: Humana Press Inc.; 2007.
50. Kurhanewicz J, et al. Analysis of cancer metabolism by imaging hyperpolarized nuclei: prospects for translation to clinical research. Neoplasia. 2011;13:81–97.
51. van der Graaf M. In vivo magnetic resonance spectroscopy: basic methodology and clinical applications. Eur Biophys J. 2010;39:527–40.
52. Kurhanewicz J, Vigneron DB. Advances in MR spectroscopy of the prostate. Magn Reson Imaging Clin N Am. 2008;16:697–710, ix–x.
53. Chu DZ, et al. Proton NMR of human breast tumors: correlation with clinical prognostic parameters. J Surg Oncol. 1987;36:1–4.
54. Sijens PE, et al. Human breast cancer in vivo: H-1 and P-31 MR spectroscopy at 1.5 T. Radiology. 1988; 169:615–20.
55. Bradamante S, et al. High-resolution 1H NMR spectroscopy in the diagnosis of breast cancer. Magn Reson Med. 1988;8:440–9.
56. Katz-Brull R, et al. Clinical utility of proton magnetic resonance spectroscopy in characterizing breast lesions. J Natl Cancer Inst. 2002;94:1197–203.
57. King AD, et al. Monitoring of treatment response after chemoradiotherapy for head and neck cancer using in vivo 1H MR spectroscopy. Eur Radiol. 2010;20:165–72.
58. Steen RG. Response of solid tumors to chemotherapy monitored by in vivo 31P nuclear magnetic resonance spectroscopy: a review. Cancer Res. 1989;49:4075–85.
59. Leach MO, et al. Measurements of human breast cancer using magnetic resonance spectroscopy: a review of clinical measurements and a report of localized 31P measurements of response to treatment. NMR Biomed. 1998;11:314–40.
60. Segebarth CM, et al. MR image-guided P-31 MR spectroscopy in the evaluation of brain tumor treatment. Radiology. 1987;165:215–9.
61. Shinkwin MA, et al. Integrated magnetic resonance imaging and phosphorus spectroscopy of soft tissue tumors. Cancer. 1991;67:1849–58.

Diffusion-Weighted MR Imaging

14

Henry H. Tam and Dow-Mu Koh

Contents

Abbreviations

ADC	Apparent diffusion coefficient
AP	Anterior-posterior
CT	Computed tomography
D	Tissue diffusivity
D^*	Pseudodiffusion coefficient
DDC	Distributed diffusion coefficient
DWIBS	Diffusion weighted imaging with body signal suppression
DW-MRI	Diffusion weighted MRI
EPI	Echo-planar imaging
^{18}F	^{18}Fluorine
FDG	Fluoro-2-deoxy-D-glucose
fDM	Functional diffusion map
f_V	Fractional volume of flowing water molecules within the capillaries
GRAPPA	Generalized Autocalibrating Partially Parallel Acquisition
IR	Inversion recovery
IVIM	Intravoxel incoherent motion
MPG	Motion probing gradients
PET	Positron emission tomography
ROI	Region of interest
SENSE	Sensitivity encoding
SNR	Signal-to-noise ratio
SPAIR	Spectral attenuated inversion recovery
TR	Repetition time
α	Stretching parameter

H.H. Tam, MBBS, BSc (Hons), FRCR (✉)
D.-M. Koh, MBBS, MD, MRCP, FRCR
Department of Radiology,
Royal Marsden Hospital, Surrey, UK
e-mail: henry.tam@outlook.com;
dowmukoh@icr.ac.uk

A. Luna et al. (eds.), *Functional Imaging in Oncology*,
DOI 10.1007/978-3-642-40412-2_14,

MRI is an attractive imaging modality in oncology owing to its lack of ionising radiation and exquisite soft tissue contrast. While conventional MRI provides invaluable morphological information, it gives little functional information. Diffusion-weighted MRI (DW-MRI) derives its contrast from the movement of water molecules in the tissue microenvironment and thus provides an insight into tissue cellularity and architecture.

Einstein formalised the mathematical description of Brownian motion in 1905 [1], but it was not until 1965 that water diffusion in nuclear magnetic resonance (NMR) was studied and described by Stejskal and Tanner [2]. It took another 20 years for DW-MRI to be employed clinically [3]. Among the first clinical application, DW-MRI was used to evaluate ischaemic stroke [4, 5]. Its utility soon broadened to include brain tumours [6–8], and the technological advances in the last decade have enabled its use in extracranial malignancies [9–16]. DW-MRI is quick to perform and non-invasive and can be applied for lesion detection, disease characterisation and assessment of treatment response. Quantitative measurements derived from DW-MRI are potential imaging biomarkers to predict likelihood of treatment response and prognosis in oncology.

In this chapter, we will review the principles of DW-MR imaging, its technical considerations, image interpretation and its broad application in oncology. Discussions related to DW-MRI in specific diseases will be reviewed in subsequent chapters.

14.1 Principles of DWI

The pioneers of NMR recognised the effect of diffusion on signal intensity [17]. Carr and Purcell [18] performed the first diffusion sensitive NMR experiment by applying a constant magnetic gradient in a spin-echo sequence. They observed that the phase shifts accumulated by static molecules before the 180° pulse were cancelled by phase shifts in the opposite direction after the 180° pulse, thereby preserving phase coherence and signal strength; conversely, with water molecules that randomly move through a gradient field, e.g. diffusion, the spins are not refocused by the 180° pulse resulting in phase dehiscence and signal loss.

Torrey in 1956 [19] showed that the Bloch equations for magnetisation can be modified to include diffusion effects. This was applied by Stejskal and Tanner [2] using a spin-echo sequence with an additional pair of diffusion-sensitive motion-probing gradient (MPG) pulses of equal magnitude before and after the 180° refocusing pulse (Fig. 14.1). This scheme forms the basis of DW-MRI sequences in clinical use today.

DW-MRI acquisition speed can be improved by using single-shot echo-planar imaging (EPI) where the whole k-space making up an image is filled within one repetition time (TR). Acquisition speed is further improved by parallel imaging methods such as SENSE and GRAPPA [20], which reduces the echo-train length. As EPI is sensitive to susceptibility artefacts [21], non-EPI techniques such as single-shot turbo spin-echo have also been used [22]. However, these are typically associated with longer acquisition times, making them less practical in a clinical setting.

14.2 *b*-Values and Apparent Diffusion Coefficient (ADC)

The rate of diffusion of any molecule depends on the particle size, the medium viscosity and the temperature, which can be described using the diffusion coefficient, D, with the unit mm^2/s.

In a DW-MRI study, the amount of signal attenuation from each voxel after application of the MPGs is related to the strength of the MPGs and D,

$$\frac{S}{S_0} = \exp\left[-\gamma^2 G^2 \delta^2 \left(\Delta - \frac{\delta}{3}\right) D\right] \quad (14.1)$$

where S_0 is the baseline signal with no diffusion weighting; S the signal after applying diffusion weighting; γ, G, Δ and δ the gyromagnetic ratio, strength of the diffusion gradients, time interval between the diffusion gradients and duration of the gradient, respectively; and D the diffusion coefficient. The parameters G, Δ or δ can be varied, although on clinical scanners only the gradient amplitude, G, is usually changed. In the above equation, the term $\gamma^2 G^2 \delta^2 \left(\Delta - \frac{\delta}{3}\right)$ can be

summarised as the *b*-value, *b*, with unit s/mm^2 [23]. Thus,

$$S(b) = S_0 e^{-Db} \tag{14.2}$$

By performing imaging using at least two *b*-values, it is possible to quantify the diffusion coefficient, *D*, for each imaged voxel

$$D = \frac{1}{(b_2 - b_1)} \ln\left[\frac{S(b_1)}{S(b_2)}\right] \tag{14.3}$$

In tissues, in vivo water movement is influenced by various factors such as pressure gradient, ionic and osmotic gradients, capillary perfusion and bulk tissue movements. Furthermore, the motion of water is impeded by microstructures such as cell membranes and macromolecules. Thus, the measurement of diffusion coefficient, *D*, in tissues is only an estimation of pure water diffusivity and is termed apparent diffusion coefficient (ADC).

Figure 14.2 illustrates what one might expect to see in a DW-MRI study. With increasing diffusion weighting, there is progressive signal loss from the imaged voxels. ADC represents the rate of signal loss with increasing *b*-values; therefore if the signal intensity (in logarithmic scale) is plotted against the *b*-value, the slope of the resulting line represents the ADC. The steeper the slope, the higher the ADC value. The ADC value of each

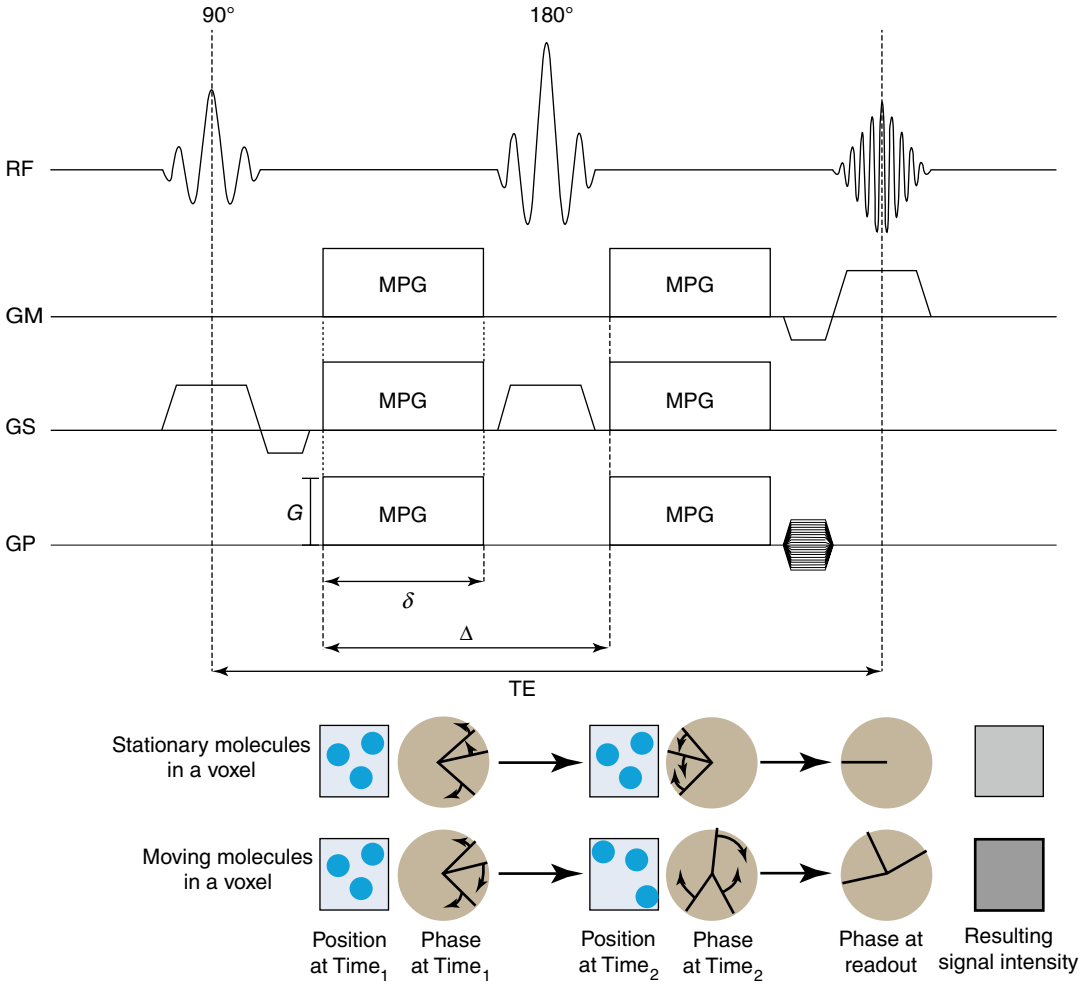

Fig. 14.1 Pulse sequence timing diagram of basic diffusion-weighted sequence formed by adding a pair of motion-probing gradients (MPGs) to a spin-echo sequence. *G*, Δ and *δ* (strength of the MPGs, time interval between the MPGs and duration of the MPGs) are adjustable parameters which influence the diffusion weighting

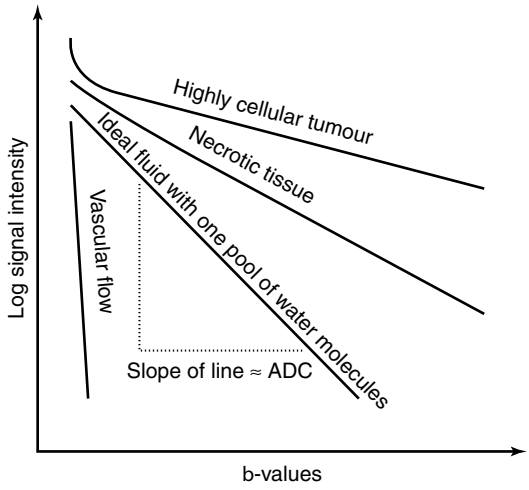

Fig. 14.2 Schematic diagram of signal attenuation of different tissue types with increasing diffusion weighting. The rate of signal loss (i.e. the slope of a line on this plot) is the ADC. Note the initial steep part of the curve seen in solid tissue (e.g. tumour), indicating the presence of a fast-moving pool of water. In tissue, this is due to pseudodiffusion, i.e. perfusion and inherent water diffusion associated with microcapillaries. If there is only one pool of water molecules, the resulting plot should be a straight line

voxel can be displayed as greyscale or pseudocolour on the image matrix as an ADC map.

In voxels where there is one pool of randomly moving water molecules, the rate of signal attenuation is mono-exponential and the logarithmic plot of signal intensity against *b*-values is a straight line (Fig. 14.2). Fitting a line onto the data points on this plot using Eq. (14.3) would yield an ADC value that is a very close approximation to the true value. Such an approach is known as a mono-exponential fit as the equation contains a single exponential. However, as demonstrated in early clinical experiments, the ADC curves tend to have an initial rapid attenuation at the low *b*-value ranges ($b = 0$–100 s/mm^2) and a slower rate of attenuation at the higher *b*-value ranges. This has led Le Bihan et al. [23] to conclude that there exists two or more pools of randomly moving water molecules moving at different rates within tissues. Under such circumstances, ADCs derived from a mono-exponential fit would not adequately account for tissue behaviour. As such, various approaches have been developed to account for the non-mono-exponential attenuation of signal in tissues.

14.3 Pseudodiffusion and Intravoxel Incoherent Motion (IVIM)

As well as diffusion of water molecules within tissues, bulk water movement in randomly orientated capillaries (i.e. perfusion) can also cause phase dispersion at DW-MRI. The resulting loss of signal is akin to that seen in true diffusion and has been termed pseudodiffusion [23]. As capillary flow is significantly faster compared with water diffusion in tissue, signal loss per unit increase in *b*-value is also greater, meaning that signal loss from the majority of perfusing water molecules occurs at relatively low *b*-values ($b = 0$–100 s/mm^2). If the low *b*-values are included in a mono-exponential calculation of ADC, the value of ADC would be overestimated, i.e. the ADC would suggest a higher diffusion rate than can be accounted for by tissue water. Since the effect of perfusion on ADC is particularly marked at low *b*-value ranges, a means to desensitise the effect of perfusion has been suggested by calculating ADC from the higher *b*-value ranges ($b > 100$ s/mm^2), to produce a perfusion insensitive ADC. In contrast, an ADC value calculated using a full range of *b*-values is variably perfusion sensitive ADC [24–26] (Fig. 14.3), depending on the number and range of *b*-values used for its calculation.

A more sophisticated approach accounting for pseudodiffusion has been proposed by Le Bihan et al. [23, 27, 28]. In this approach, water molecules in random motion are said to exhibit intravoxel incoherent motion (IVIM), which include water molecules undergoing true diffusion and those moving within randomly orientated capillaries (perfusion). The contribution of true diffusion and perfusion towards signal loss are written as two separate terms in the equation modified from (14.2),

$$S(b) = (1 - f_V)e^{-bD} + f_V e^{-bD^*} \qquad (14.4)$$

where f_V is the fractional volume of flowing water molecules within the capillaries (therefore, $(1 - f_V)$ denotes the fraction of water molecules undergoing true diffusion); D is the tissue diffusion coefficient, uninfluenced by movement of water molecules within the capillaries; D^* is the pseudodiffusion coefficient that represents the

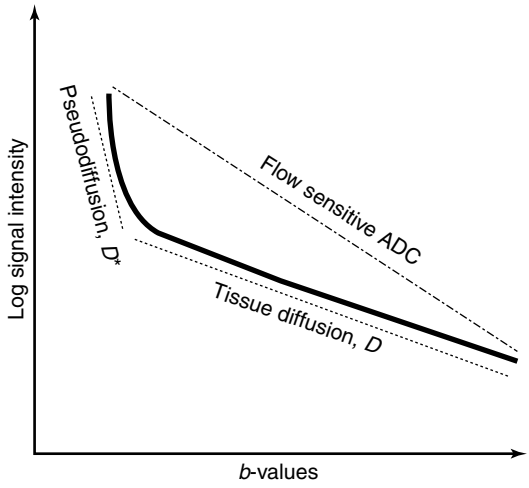

Fig. 14.3 Schematic DW-MRI signal plot of a generic soft tissue demonstrating perfusion and diffusion effects. If the rate of signal loss (ADC) is calculated from all *b*-values, the resulting ADC is sensitive to flow and overestimates the true diffusivity. In tissues with significant perfusion fraction, tissue diffusion can be more accurately approximated using the bi-exponential model or by omitting the low *b*-values in the ADC calculation

amount of non-diffusional random movements of water molecules, e.g. perfusion, plus the diffusion of these water molecules. As discussed in the above section, there is minimal contribution from pseudodiffusion at the higher *b*-values, thus the term $f_V e^{-bD^*}$ becomes negligible at the higher *b*-value ranges. By performing the DW-MRI study with a range of *b*-values, including $b=0$ s/mm^2, a number of *b*-values between 0 and 100 s/mm^2 and higher *b*-values, it is possible to solve the bi-exponential equation (14.4) for D, D^* and f_V. ADC can be approximated as

$$ADC \approx D + \frac{f_V}{b} \qquad (14.5)$$

Using the IVIM model, it is therefore possible to attribute a fast component of tissue water diffusivity to perfusion by deriving D^* and f_V (Fig. 14.3). Indeed, studies comparing intravascular tracer and DW-MRI with IVIM modelling have shown good correlation between tissue blood volume and f_V and between relative blood flow and D^* [29, 30]. Of note is that a tissue may have high D^* but low f_V values, as the two vascular properties are not related. However, as the pseudodiffusion coefficient, D^*, is influenced by physiological processes other than perfusion, e.g. glandular secretion and renal tubular flow, there remains controversy regarding the reliability of IVIM-derived perfusion parameters in secretory organs such as the salivary glands and kidneys [31–33].

14.4 Other Non-mono-exponential Diffusion Models

Another approach to account for the non-mono-exponential attenuation of the water signal in tissue is the stretched-exponential model [34], which does not necessitate *a priori* knowledge of the number of diffusion pools. The amount of signal loss after application of MPGs is described as thus

$$\frac{S}{S_0} = \exp\left\{-\left(b \times DDC\right)^{\alpha}\right\} \qquad (14.6)$$

where DDC is the distributed diffusion coefficient, a surrogate for ADC, and α is the stretching parameter which describes the deviation of the curve from a mono-exponential line. $\alpha=1$ describes perfect alignment with the mono-exponential line consistent with a single diffusion pool, whereas a value of $\alpha<1$ suggests the presence of a distribution of different diffusion rates within the imaged voxel. Hence, α is also known as a heterogeneity index. One limitation of the stretched-exponential model is that unlike the IVIM model, it is difficult to correlate the term of α with a specific biological underpinning.

There are other phenomenological diffusion models (e.g. Gaussian, Kurtosis) that are used in research, but these are beyond the scope of discussion in this chapter.

14.5 Technical Implementation

14.5.1 General Considerations

DW-MRI is made possible within a clinically acceptable time frame with EPI and parallel imaging. However, T2* effects of the tissues causes signal attenuation on EPI and is sensitive to B0, leading to reduced signal-to-noise ratio (SNR). This can be improved by increasing the slice thickness, increasing the number of signal averages,

Table 14.1 Single-shot DW-EPI parameters in clinical examination of the abdomen and pelvis

	Abdomen	LFOV pelvis	SFOV pelvis
Field of view (mm)	380	380	220–280
RFOV	80	80	80
Number of slices	26–33	40–48	18
Slice thickness (mm)	6–7	6	5
Slice gap (mm)	10 %	10 %	10 %
Matrix	104–112/256	104–112/256	112/256
Foldover direction	AP	AP	AP
TE (ms)	66–70	66	66–70
TR (ms)	5,000	5,600–7,400	2,500–3,100
PI factor	2	2	2
Fat saturation	SPAIR	IR/SPAIR	SPAIR
EPI factor	59–104	59–104	75–112
Signal averages	4–5	4	4–8
Bandwidth (Hz/Px)	1,800	1,800	1,800
b-values (s/mm^2)	0,100,500,750	0,900	0,300,750
Acquisition time (min)	4.5	2.5	3

Adapted from Koh and Theony [93]
AP anterior-posterior, *IR* inversion recovery, *SPAIR* spectral attenuated inversion recovery

increased pixel size or large field of view (FOV), shorter echo-times, optimising receiver bandwidth and use of parallel imaging techniques.

Another problem in DW-MRI is chemical shift artefacts from fat which can be particularly pronounced on DW-MRI images due to the narrow bandwidth used in phase encoding. As the bandwidth per pixel in DW-MRI is 10–30 Hz compared to the fat-water chemical shift frequency of 220 Hz, signal displacement up to 10–15 pixels can be seen (approximately 6 cm if a pixel size of 4 mm is used). Ensuring optimal fat signal suppression is therefore critical in DW-MRI.

With increasing availability of 3.0 T scanners, there is a potential to improve image quality with the theoretical doubling of SNR compared to a 1.5 T system. However, at higher field strength, susceptibility artefacts are accentuated and become more problematic. Chemical shift artefacts can also be more profound.

14.5.2 DW-MRI in the Body

Breathing-related artefacts are an additional consideration in body DW-MRI. This problem can be dealt with in three approaches [35]: (1) breath-hold imaging, (2) navigator echo respiratory-triggered imaging and (3) free breathing.

Breath-hold DW-MRI acquisition time is typically <20 s per breath hold and the full dataset is acquired in a few breath holds. It may improve conspicuity of small lesions but has the disadvantage of limited *b*-values per breath hold, increased sensitivity to susceptibility artefacts (due to long echo train) and reduced SNR. Images are also prone to degradation by other uncontrolled physiological motions such as vessel/cardiac pulsation and peristalsis.

In navigator echo respiratory-triggered imaging [36], the position of the diaphragm is tracked by a pencil-beam excitation prepulse placed between the liver and lung. Compared with breath-hold imaging, navigator DW-MRI shows higher SNR and lesion to liver contrast ratio [37]. In a modified sequence using navigator echo to track pixel displacement without respiratory gating, image sharpness is improved compared with free-breathing technique with minimal increase in acquisition time [38, 39].

Free-breathing technique uses multiple signal averaging to overcome the effect of motion. Because of the increased number of acquisitions, it has better SNR compared with breath-hold imaging and allows more *b*-values to be acquired. It is also possible to use thinner slices in free breathing, thereby allowing for multiplanar manipulation of the images. ADC obtained using free-breathing technique has been found to be

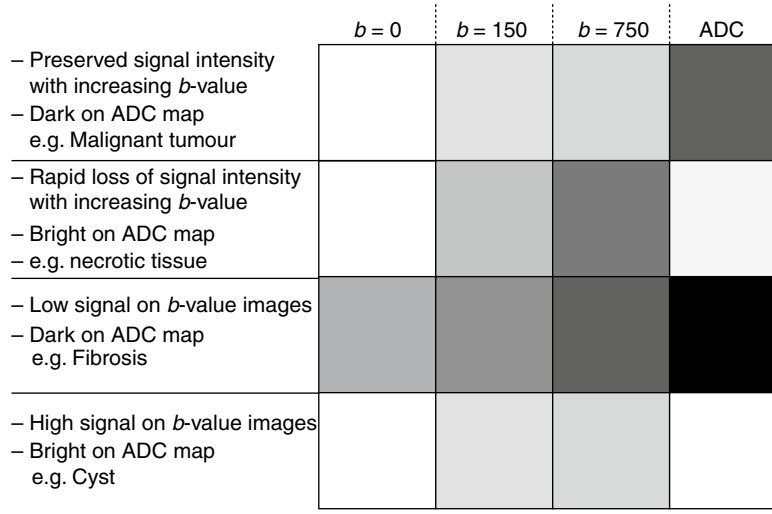

Fig. 14.4 Four common signal intensity patterns observed on the *b*-value images and ADC maps at DWI

reproducible and not dissimilar to values obtained using other acquisition techniques [40, 41]. Typical image acquisition protocols used for body DW-MRI are shown in Table 14.1.

14.6 Image Interpretation

Interpretation of DW-MRI and its accompanying ADC maps can be performed qualitatively by visual assessment or quantitatively by numerical analysis of regions of interest (ROIs) on the ADC maps. When visually assessing the DW-MRI images, the images should be interpreted together with the ADC map and other morphological MR images to avoid misinterpretation. Likewise, when quantitatively analysing the ADC map, the source diffusion-weighted images and other morphological images should be assessed for any artefacts, which may bias the ADC estimates.

Most DW-MRI studies will yield observations that fit into one of the following four categories (Fig. 14.4) as below.

1. *Lesions with relatively preserved signal intensity with increasing b-values and dark on ADC maps* (Fig. 14.5). This indicates impeded diffusion within the lesion and may result from increase in cellular density and/or increased tortuosity of the extracellular space. Malignancy is the prime example of pathology, which may give rise to this picture. Other pathologies that may lead to this imaging appearance include active inflammation [42] and abscess [43].
2. *Lesions showing rapidly decreasing signal intensity with increasing b-values and bright on ADC maps* (Fig. 14.6). This occurs in lesions with relatively unimpeded diffusion, e.g. cysts, necrotic tissues and vasogenic oedema without accompanying rise of cellularity. Careful interpretation of the DW-MRI and morphological images may reveal clues as to the true nature of the lesion. In simple cysts, it would be unusual to observe perilesional diffusion impediment or complex internal structure; conversely, one might expect to see a rim of tissue with impeded diffusion in necrotic tumour, which represents viable disease.
3. *Lesions showing low signal intensity on both the b-value images and ADC map* (Fig. 14.7). This can be observed in regions of inherent low signal on the fat-suppressed T2-weighted image (e.g. fat and fibrosis) or may be secondary to imaging artefacts (including processes that result in susceptibility effects in the local magnetic field such as haemorrhage, iron deposition and dense calcifications). Note, however, that fibrosis can exhibit a range of signal intensities and ADC values and is yet to be fully characterised.
4. *Lesions showing relatively preserved signal intensity with increasing b-values and bright on ADC map* (Fig. 14.8). This results from "T2 shine-through" effects and will be discussed in the next section.

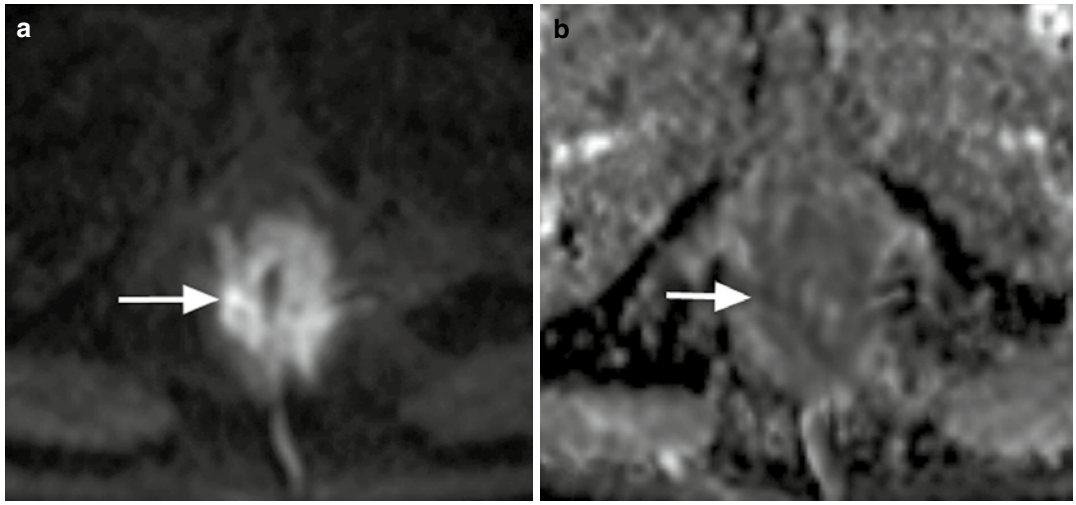

Fig. 14.5 A man with carcinoma of the anus. (**a**) $b = 900$ s/mm^2 DWI image shows abnormal high signal and thickening of the anal canal (*arrow*). (**b**) ADC map returns low signal intensity and ADC values (*arrow*)

Quantitatively, the ADC values of a lesion can be measured by drawing regions of interest (ROI). This may help in lesion characterisation as malignant disease often has lower ADC values and can provide a quantitative measure for tumour response assessment. When defining a region of interest, it is preferable to do so first on the high *b*-value images and then copy the ROI to the ADC map at the equivalent body position, as disease boundaries can be difficult to define on the ADC maps.

14.7 Potential Pitfalls in Interpreting DW-MRI

14.7.1 Using Signal Intensity on *b*-Value Images

The basis for disease identification using *b-value* images depends on differential signal between the disease and background tissue. Hence, potential pitfalls may arise from lesions with intrinsically long T2 relaxation times (T2 shine-through effect), susceptibility effects that destroy the diffusion signal and disease occurring at anatomical locations in the body that normally shows high signal intensity (e.g. brain, salivary glands, spinal cord, lymph nodes, spleen, testes, ovaries and peripheral zone of the prostate).

14.7.1.1 T2 Shine-Through

Any tissues/lesions with sufficiently long T2 relaxivity, e.g. fluid within a simple cyst, can show high signal intensity on the high *b*-value image even though diffusion may not be impeded in such tissues/lesions. Fortunately, T2 shine-through can be distinguished from true impeded diffusion by corroborating the signal intensity to its ADC value. A lesion with T2 shine-through will show high ADC value (Fig. 14.8). Additionally, on long echo time T2-weighted sequence, a T2 shine-through lesion will also show very high signal intensity relative to a lesion with true impeded diffusion.

14.7.1.2 Susceptibility Artefacts

Any local field inhomogeneity would create susceptibility artefacts, which lower the signal intensity of the affected voxels (Fig. 14.9). In the context of oncological imaging, this may be due to paramagnetic materials, such as blood products, calcifications, iron or other metallic deposits, resulting in lower signal intensity and ADC values. However, strong focal perturbation of the B0 magnetic field can lead to spurious areas of high signal intensity on the *b*-value images, which should not be interpreted as disease. Natural locales of field inhomogeneity (air-bone interface of the paranasal sinuses, interface between bowel gas and bowel wall) can limit the utility of EPI-DW-MRI in these regions, particularly at 3.0 T.

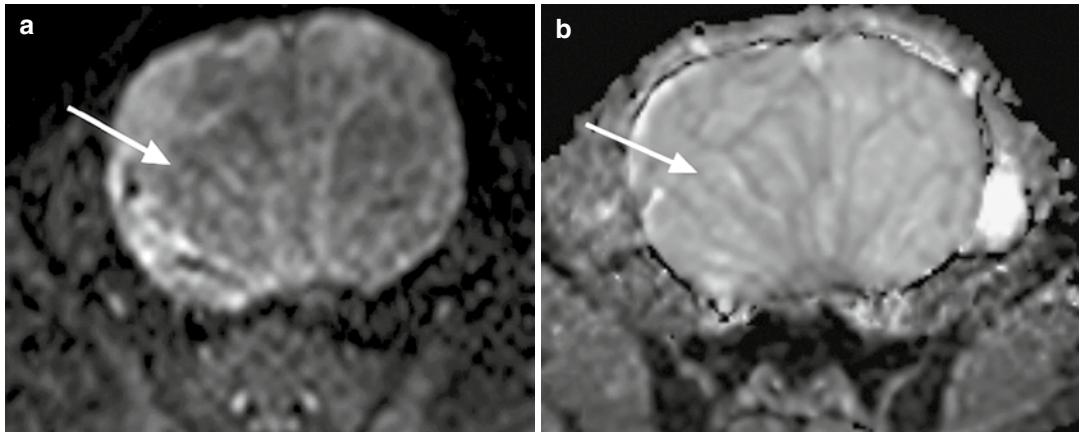

Fig. 14.6 A woman with cystadenoma of the ovary. (**a**) The cystic area within the lesion shows signal loss on the $b=750$ s/mm^2 image (*arrow*) compared with the internal septi which remains relatively high signal. (**b**) The cystic area returns high ADC values on the ADC map (*arrow*)

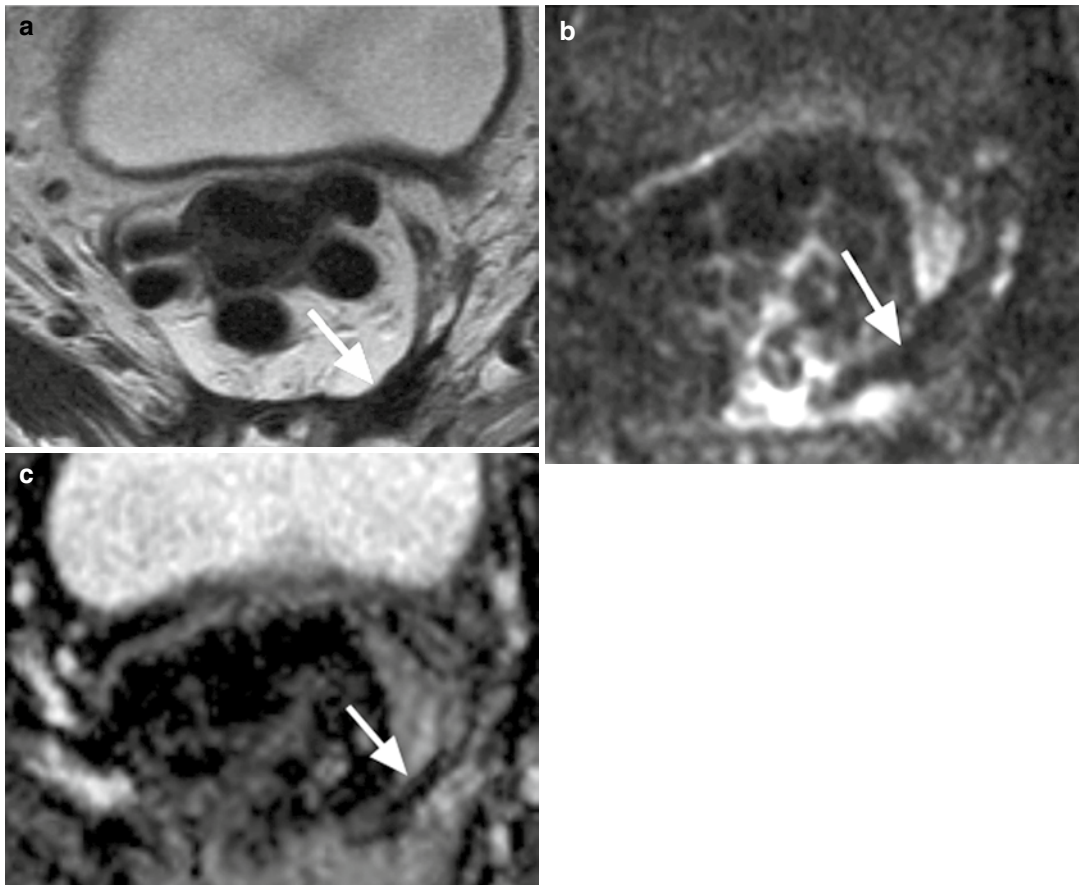

Fig. 14.7 A man with previous low anterior resection for rectal cancer. (**a**) T2-weighted MRI shows low signal intensity change in the presacral area (*arrow*) consistent with fibrosis. (**b**) This shows low signal intensity on the $b=900$ s/mm^2 image (*arrow*) and (**c**) also returns predominantly low ADC value (*arrow*)

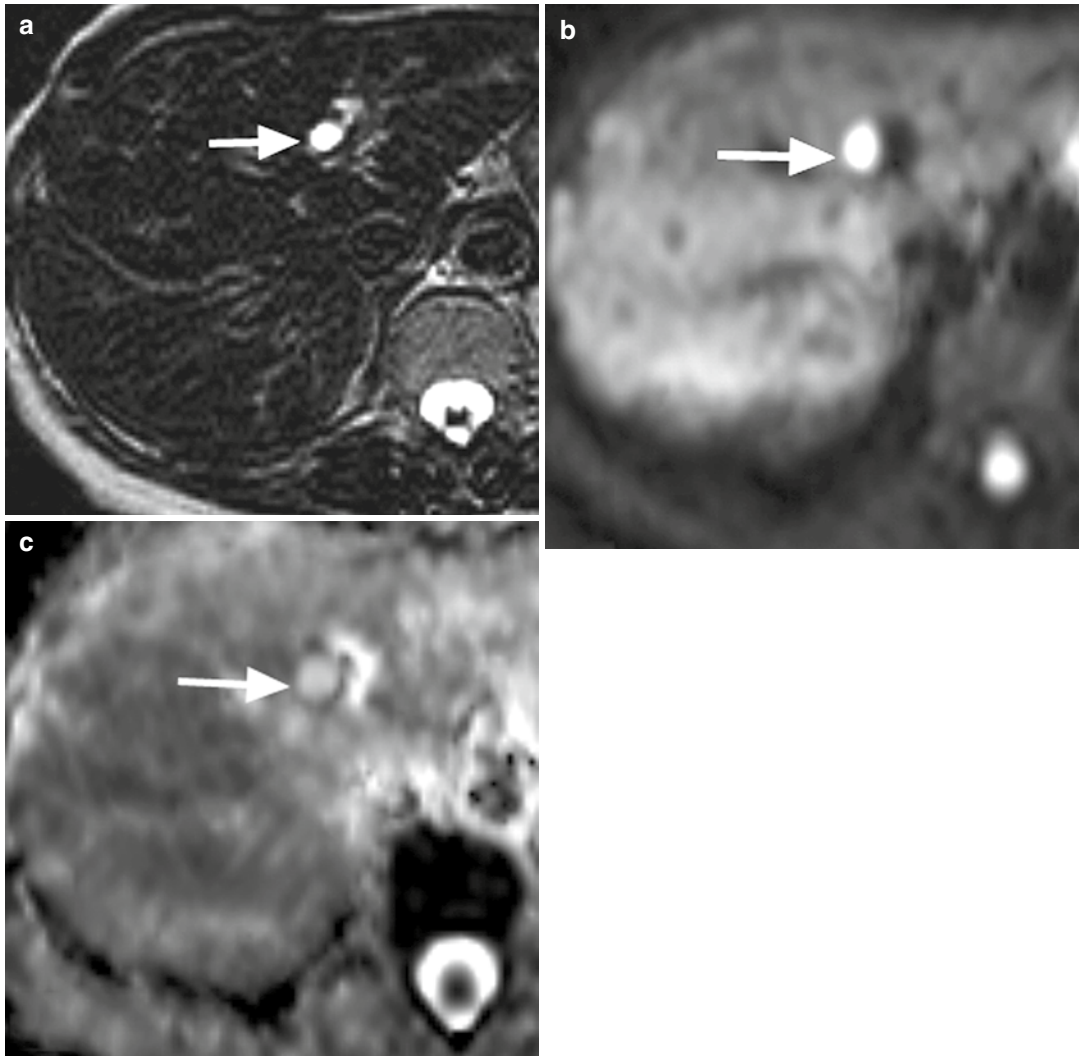

Fig. 14.8 A 40-year-old man with a cyst in the left lobe of the liver. (**a**) T2-weighted image obtained with long echo time (TE = 240 ms) shows a 1 cm high signal intensity cyst in left hepatic lobe (*arrow*). (**b**) The cyst remains high signal on the $b = 750$ s/mm^2 image due to its long T2 relaxation time (*arrow*). (**c**) Note the high ADC value of cyst confirming T2 shine-through effect (*arrow*)

14.7.2 Using ADC Values

Artefacts that distort the *b*-value images can lead to spurious ADC estimation.

Motion-induced voxel misregistration may be reduced by "tracking" motion with ECG gating or navigator control, but these methods are time-consuming. Hence, even though free-breathing diffusion will result in signal averaging between voxels, multiple signal averaging can improve confidence in the measurement of ADC values. Studies have shown that in the abdomen, using free-breathing acquisition can result in a good ADC measurement reproducibility of about 14 % [44, 45] and that ADC values obtained as such may be more reproducible than breath-hold or respiratory-triggered scans [40].

Another source of ADC measurement error is Eddy currents, which leads to image distortion, thus changing the alignment of voxels when calculating ADC producing a spurious result. Effects from Eddy currents cannot be eliminated entirely but may be largely mitigated by shielding of the various conducting elements of the scanner, use of shaped MPG (pre-emphasis), twice refocused spin echo,

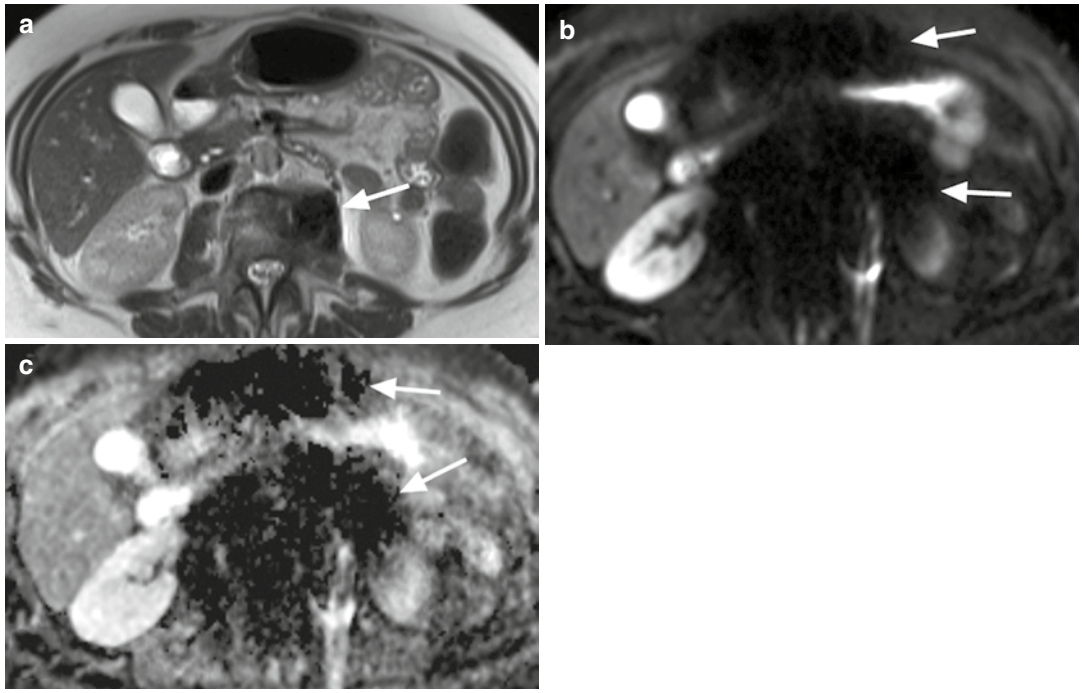

Fig. 14.9 A 45-year-old man with history of spinal surgery. (**a**) Turbo spin-echo T2-weighted imaging shows susceptibility artefacts arising from surgical screws in the spine (*arrow*). (**b**) Echo-planar DWI is highly sensitive to magnetic field inhomogeneity, inducing more pronounced susceptibility artefacts at imaging (*arrows*) and obscuring normal structures. (**c**) These areas with artefacts lead to spurious ADC values (*arrows*) and cannot be assessed

actively screened gradients and software-based post-processing [21].

Finally, ADC may be underestimated in the kidney after intravenous gadolinium-based contrast medium injection [46], although the same study found no effects of gadolinium on liver, pancreas or spleen. If there is substantial accumulation of contrast material within an organ after contrast administration, it may be prudent to perform DW-MRI sequences prior to contrast administration.

14.7.3 False-Positive and False-Negative Results in Disease Assessment

As the inference of pathology on DW-MRI relies on impeded diffusion, there are benign conditions that may mimic malignant pathologies, e.g. hepatic adenoma/focal nodular hyperplasia [47] (Fig. 14.10) and abscesses [43]. Conversely, there are malignant conditions that show relatively unimpeded diffusion, which can be misinterpreted as normal tissues, e.g. well-differentiated hepatocellular carcinoma [48] or mucinous carcinoma (Fig. 14.11). Hypercellular red marrow, e.g. young patients or those with bone marrow hyperplasia following granulocyte colony stimulating factor (G-CSF) stimulation, is also hyperintense on high *b*-value images and may be confused for diffuse marrow infiltration. Normal lymph nodes can show impeded diffusion and may be difficult to differentiate from malignant nodes based on diffusion characteristics.

14.8 Clinical Application in the Body

The application of DW-MRI in the body has largely been in oncology, although the technique has also been applied to evaluate infective and inflammatory conditions. In oncology, malignant tissues tend to exhibit impeded diffusion, resulting in relative preservation of

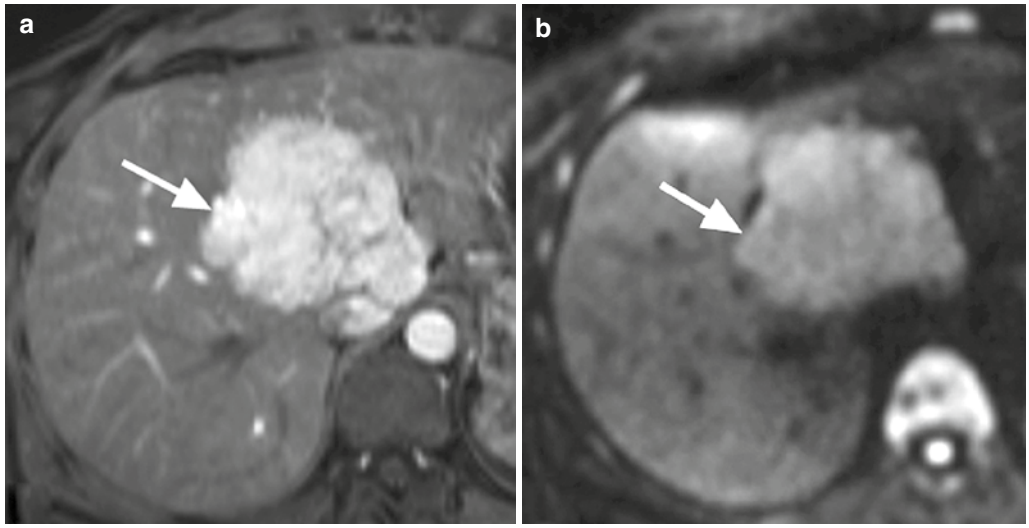

Fig. 14.10 A hepatic lesion (**a**) with preserved signal on DWI (*arrow*). (**b**) The lesion shows near uniform enhancement in the arterial phase (*arrow*), with a suggestion of central scar, consistent with focal nodular hyperplasia. Lesion was unchanged for 12 months at follow-up

signal intensity relative to normal tissues with increasing *b-values* (i.e. bright on DW-MRI) and return low ADC values [49–54]. The broad areas of applying oncological applications are summarised below.

14.8.1 Disease Detection

DW-MRI has been shown to improve lesion detection compared with conventional MR imaging, CT imaging and even PET imaging. The technique has been shown to be of particular value for detecting liver metastases, peritoneal disease, prostate cancer and bone metastases.

In the liver, using DW-MRI improves disease detection, either on its own or in combination with contrast-enhanced imaging [47, 55–59]. However, in the cirrhotic liver, the success of DW-MRI in detecting hepatocellular carcinoma appears more variable [60].

In ovarian cancer, peritoneal deposits as small as 5 mm may be prognostically important [61]. However, CT scans often miss such small lesions, with sensitivity in the region of 10–20 % for deposits <1 cm [62]. DW-MRI has a high diagnostic sensitivity in this context (Fig. 14.12) [63], which can be comparable to ^{18}F-FDG-PET/CT [64].

In the male pelvis, the addition of DW-MRI to a T2-weighted sequence improves the detection of prostate carcinoma [65, 66]. However, the sensitivity of DW-MRI (± other sequences) in detecting transitional zone lesion remains poor [67, 68]. DW-MRI may also identify index lesions for targeted biopsy and improve diagnostic yield in previously biopsy-negative patients [69–71].

DW-MRI is superior for detecting non-sclerotic bone metastasis compared to other imaging methods [72]. Other studies have shown comparable results between whole-body DW-MRI and nuclear medicine bone scintigraphy in the detection of bone metastases [73]. Indeed, some authors have suggested the use of whole-body DW-MRI as a one-stop staging investigation replacing body CT and bone scintigraphy [74].

14.8.2 Disease Characterisation

The ADC values of benign lesions are generally higher than malignant lesions. In the liver [47, 75], the most commonly used threshold for distinguishing malignant from benign lesion is 1.47–1.63 mm^2/s with reasonably high diagnostic accuracies, below which the lesions are considered malignant. The lack of standardisation in scanning protocols in the literature has hampered

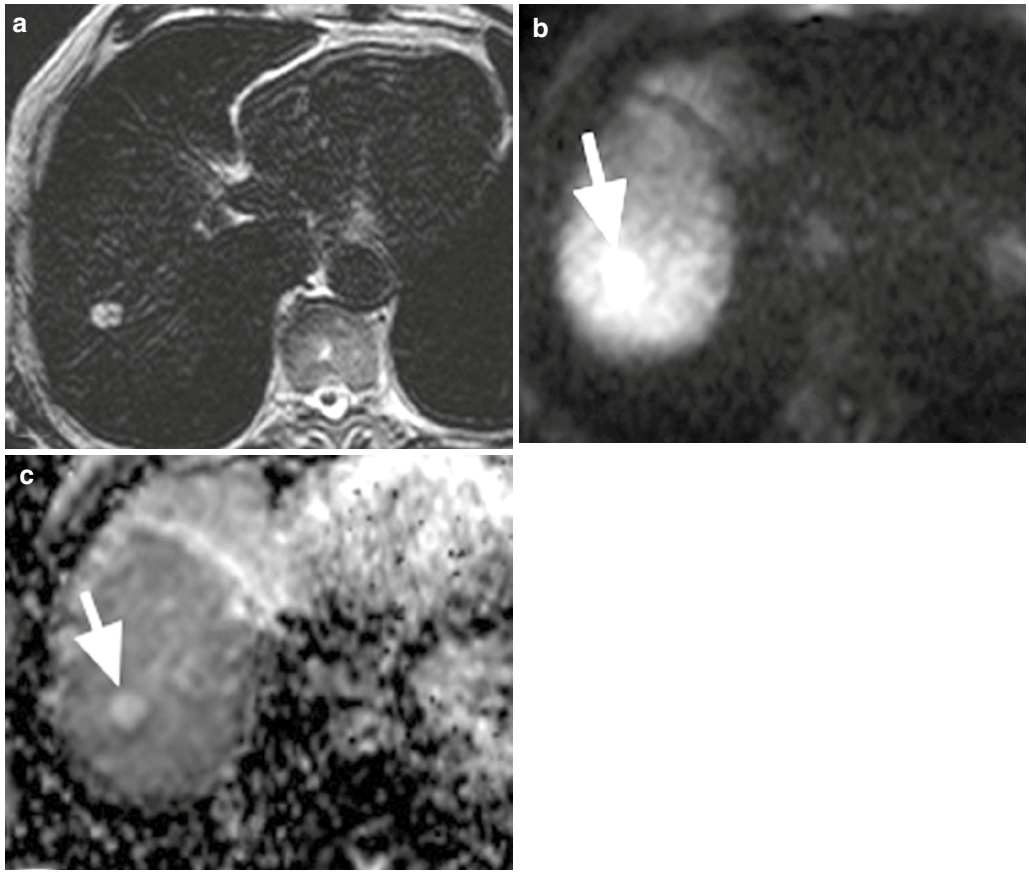

Fig. 14.11 Mucinous metastasis to right lobe of liver from rectal cancer. (**a**) T2-weighted imaging at long echo time (TE = 240 ms) shows hyperintense lesion (*arrow*) in right lobe of liver. (**b**) Lesion demonstrates T2-shine-through effect and appears as high signal on $b = 750$ s/mm^2 image (*arrow*). (**c**) The metastasis returns relatively high ADC values (*arrow*)

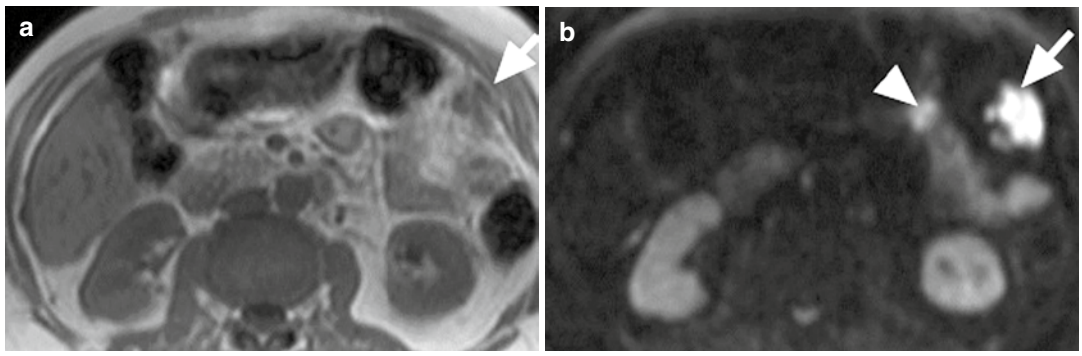

Fig. 14.12 Peritoneal disease. (**a**) On the T1-weighted image, the peritoneal disease in the left flank is more difficult to discern (*arrow*) compared with (**b**) the $b = 900$ s/mm^2 image, where the lesion appears markedly hyperintense compared with background (*arrow*). Note also the site of serosal disease involving a loop of small bowel (*arrowhead*)

the clinical use of ADC cut-off values for lesion characterisation. A further problem in using ADC for lesion characterisation is the significant overlap of ADC values between malignant and non-malignant lesions, making it difficult to use ADC values alone to prospectively classify lesions.

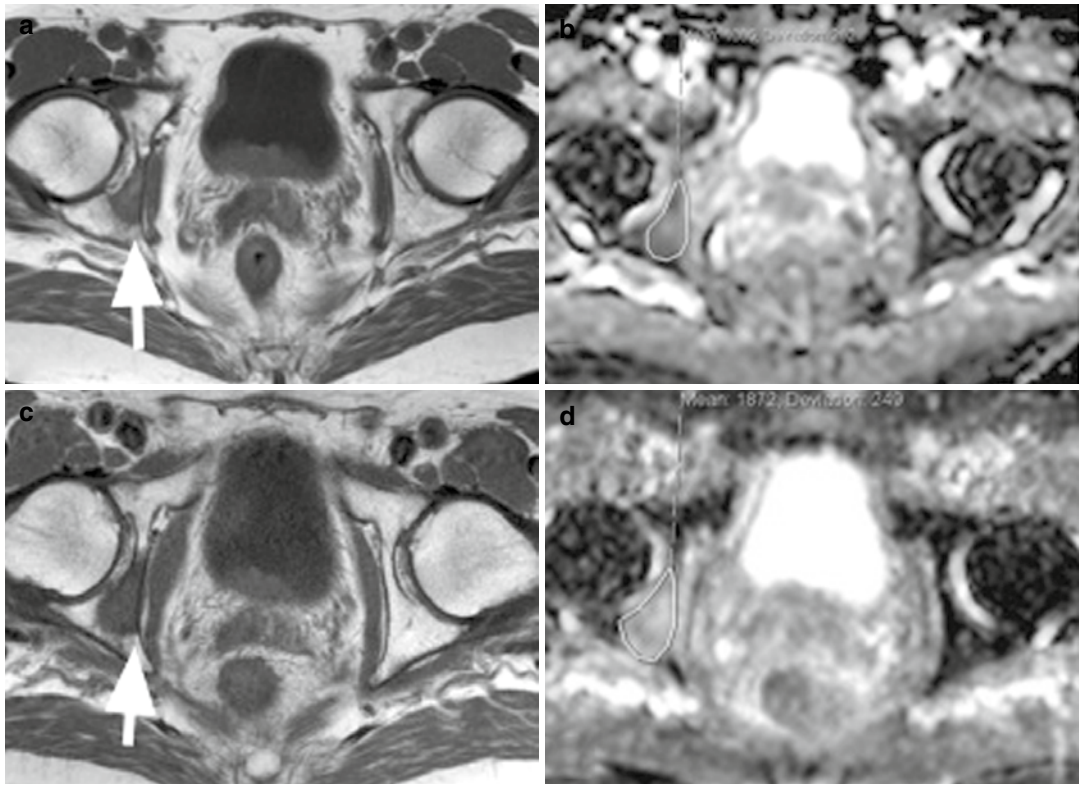

Fig. 14.13 Pretreatment (**a**) T1-weighted image and (**b**) ADC map showing metastasis in the right acetabulum (*arrow*), which returns a mean ADC value of 1.00×10^{-3} mm²/s. After 8 weeks of chemotherapy, (**c**) T1-weighted and (**d**) ADC map shows no appreciable change on T1-weighted imaging (*arrow*), but the lesion ADC has increased by more than 80 % to 1.87×10^{-3} mm²/s, in keeping with responding disease

14.8.3 Response Assessment

Studies have shown a rise in tumour ADC following treatment in breast cancer [76], colorectal liver metastases [77, 78], prostate cancer including bone disease (Fig. 14.13) [79–82] and cervical cancer [83]. Such a change occurs from days to months after treatment, depending on tumour type. However, the exact temporal relationship between treatment and ADC changes has not been systematically documented.

As well as comparing pre- and post-treatment mean ADCs in areas of body that are less prone to physiological motion, e.g. brain, head and neck and bones, it may be possible to analyse the change in ADC on a voxel-by-voxel basis. In this approach, the pre-treatment ADC map is spatially co-registered with the post-treatment ADC map, and the resulting difference in ADC value of each voxel can be colour-coded and displayed in a functional diffusion map (fDM) [84].

14.8.4 Prognosis

There is emerging evidence that parameters derived from DW-MRI, e.g. ADC values, may provide prognostic information. For example, Vandecaveye et al. showed that a smaller magnitude of change of ADC at 2 and 4 weeks post-radiotherapy in head and neck SCC was associated with locoregional recurrence at 2 years [85]. A low ADC value in pancreatic cancer also predicts for a faster rate of progression [86]. The efficacy of DW-MRI in disease prognostication requires further validation in multicentre prospective studies.

14.8.5 Whole-Body DW-MRI

Whole-body DW-MRI, more commonly known as DWIBS (diffusion-weighted imaging with body signal suppression), is a technique described by Takahara et al. [87] in the 2000s. By

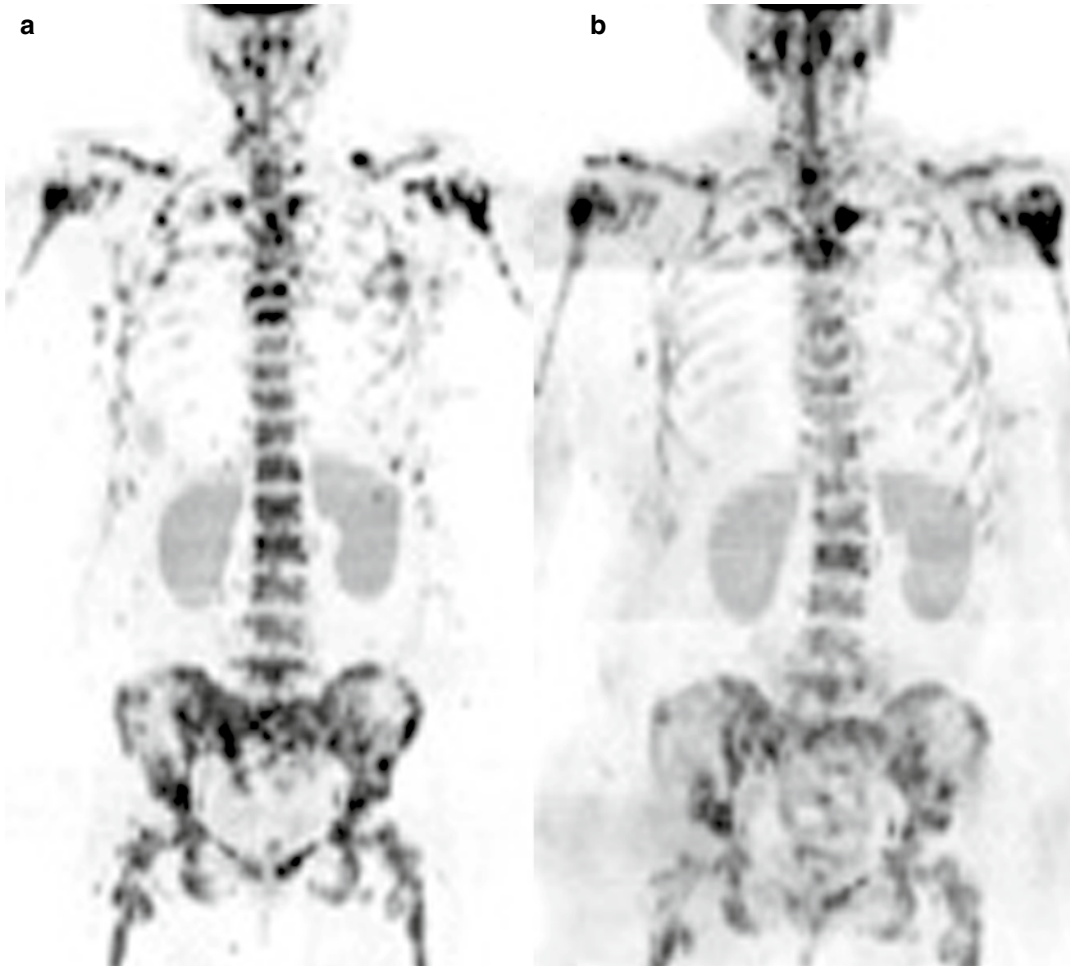

Fig. 14.14 Whole-body diffusion-weighted MR imaging. Inverted greyscale maximum intensity projections (MIPs) of axially acquired DWI from the skull base to mid-thigh level in a patient with metastatic prostate cancer, obtained (**a**) before and (**b**) after treatment with a novel therapeutic agent. Note widespread low signal intensity marrow infiltration on pretreatment imaging, which becomes less pronounced after treatment. Whole-body DWI produces "at-a-glance" images, which are being evaluated for assessing tumour response to treatment

combining axial image stacks and using maximum intensity projections, the resultant images can be displayed using an inverted greyscale to produce images that superficially resemble PET imaging (Fig. 14.14). Readers are referred to the articles by Takahara et al. [87] and Kwee et al. [88] for an overview of the technical aspect of DWIBS.

The evidence supporting the clinical use of DWIBS is growing. DWIBS has been shown to be comparable to ^{18}F-FDG-PET/CT in the staging of non-small cell lung cancer [89, 90] and has potential for staging lymphoma [91, 92]. Another area of oncology where DWIBS can make an impact is response assessment, especially in bones, which is being investigated (Fig. 14.14).

Acknowledgements The authors would like to thank Mr. David J. Collins (Institute of Cancer Research, London) for his insight and helpful comments on the physics and technical aspect of this chapter.

References

1. Einstein A. Investigations on the theory of the brownian movement. Mineola: Dover Publications Inc.; 2003.
2. Stejskal EO, Tanner JE. Spin diffusion measurements: spin echoes in the presence of a time-dependent field gradient. J Chem Phys. 1965;42(1):288–92.
3. Le Bihan D, Breton E. Imagerie de diffusion in-vivo par résonance. C R Acad Sci. 1985;301(15):1109–12.

4. Le Bihan D, et al. Diffusion MR imaging: clinical applications. AJR Am J Roentgenol. 1992; 159(3):591–9.
5. Provenzale JM, Sorensen AG. Diffusion-weighted MR imaging in acute stroke: theoretic considerations and clinical applications. AJR Am J Roentgenol. 1999;173(6):1459–67.
6. Le Bihan D, et al. Diffusion and perfusion magnetic resonance imaging in brain tumours. Top Magn Reson Imaging. 1993;5(1):25–31.
7. Knopp MV, et al. Functional neuroimaging in the assessment of CNS neoplasms. Eur Radiol. 1997;7 Suppl 5:209–15.
8. Schaefer PW, et al. Diffusion-weighted MR imaging of the brain. Radiology. 2000;217(2):331–45.
9. Koh DM, Sohaib A. Diffusion-weighted imaging of the male pelvis. Radiol Clin North Am. 2012;50(6):1127–44.
10. Koyama T, Togashi K. Functional MR imaging of the female pelvis. J Magn Reson Imaging. 2007; 25(6):1101–12.
11. Maeda M, Maier SE. Usefulness of diffusion-weighted imaging and the apparent diffusion coefficient in the assessment of head and neck tumours. J Neuroradiol. 2008;35(2):71–8.
12. Balci NC, et al. Diffusion-weighted magnetic resonance imaging of the pancreas. Top Magn Reson Imaging. 2009;20(1):43–7.
13. Sugita R, et al. Diffusion-weighted MRI in abdominal oncology: clinical applications. World J Gastroenterol. 2010;16(7):832–6.
14. Lin C, et al. Whole-body diffusion-weighted magnetic resonance imaging with apparent diffusion coefficient mapping for staging patients with diffuse large B-cell lymphoma. Eur Radiol. 2010;20(8): 2027–38.
15. Iacconi C. Diffusion and perfusion of the breast. Eur J Radiol. 2010;76(3):386–90.
16. Costa FM, et al. Diffusion-weighted magnetic resonance imaging for the evaluation of musculoskeletal tumours. Magn Reson Imaging Clin N Am. 2011; 19(1):159–80.
17. Hahn EL. Spin echoes. Phys Rev. 1950;80(4):580–94.
18. Carr HY, Purcell EM. Effects of diffusion on free precession in nuclear magnetic resonance experiments. Phys Rev. 1954;94(3):630–8.
19. Torrey HC. Bloch equations with diffusion terms. Phys Rev. 1956;104(3):563–5.
20. Larkman DJ, Nunes RG. Parallel magnetic resonance imaging. Phys Med Biol. 2007;52(7):R15–55.
21. Le Bihan D, et al. Artefacts and pitfalls in diffusion MRI. J Magn Reson Imaging. 2006;24(3):478–88.
22. Jindal M, et al. A systematic review of diffusion-weighted magnetic resonance imaging in the assessment of postoperative cholesteatoma. Otol Neurotol. 2011;32(8):1243–9.
23. Le Bihan D, et al. MR imaging of intravoxel incoherent motions: application to diffusion and perfusion in neurologic disorders. Radiology. 1986;161(2): 401–7.
24. Thoeny HC, et al. Diffusion-weighted MR imaging of kidneys in healthy volunteers and patients with parenchymal diseases: initial experience. Radiology. 2005;235(3):911–7.
25. Thoeny HC, et al. Effect of vascular targeting agent in rat tumour model: dynamic contrast-enhanced versus diffusion-weighted MR imaging. Radiology. 2005;237(2):492–9.
26. Koh DM, Collins DJ. Diffusion-weighted MRI in the body: applications and challenges in oncology. AJR Am J Roentgenol. 2007;188(6):1622–35.
27. Le Bihan D. Intravoxel incoherent motion perfusion MR imaging: a wake-up call. Radiology. 2008; 249(3):748–52.
28. Le Bihan D, et al. Separation of diffusion and perfusion in intravoxel incoherent motion MR imaging. Radiology. 1988;168(2):497–505.
29. Wirestam R, et al. Perfusion-related parameters in intravoxel incoherent motion MR imaging compared with CBV and CBF measured by dynamic susceptibility-contrast MR technique. Acta Radiol. 2001;42(2):123–8.
30. Powers TA, et al. Renal artery stenosis: in vivo perfusion MR imaging. Radiology. 1991;178(2):543–8.
31. Yoshino N, et al. Salivary glands and lesions: evaluation of apparent diffusion coefficients with split-echo diffusion-weighted MR imaging – initial results. Radiology. 2001;221(3):837–42.
32. Zhang L, et al. Functional evaluation with intravoxel incoherent motion echo-planar MRI in irradiated salivary glands: a correlative study with salivary gland scintigraphy. J Magn Reson Imaging. 2001;14(3): 223–9.
33. Muller MF, et al. Can the IVIM model be used for renal perfusion imaging? Eur J Radiol. 1998; 26(3):297–303.
34. Bennett KM, et al. Characterization of continuously distributed cortical water diffusion rates with a stretched-exponential model. Magn Reson Med. 2003;50(4):727–34.
35. Naganawa S, et al. Diffusion-weighted imaging of the liver: technical challenges and prospects for the future. Magn Reson Med Sci. 2005;4(4):175–86.
36. Bruegel M, et al. Characterization of focal liver lesions by ADC measurements using a respiratory triggered diffusion-weighted single-shot echo-planar MR imaging technique. Eur Radiol. 2008;18(3): 477–85.
37. Taouli B, et al. Diffusion-weighted imaging of the liver: comparison of navigator triggered and breathhold acquisitions. J Magn Reson Imaging. 2009; 30(3):561–8.
38. Ivancevic MK, et al. Diffusion-weighted MR imaging of the liver at 3.0 Tesla using TRacking Only Navigator echo (TRON): a feasibility study. J Magn Reson Imaging. 2009;30(5):1027–33.
39. Takahara T, et al. Diffusion-weighted magnetic resonance imaging of the liver using tracking only navigator echo: feasibility study. Invest Radiol. 2010; 45(2):57–63.

40. Kwee TC, et al. Comparison and reproducibility of ADC measurements in breathhold, respiratory triggered, and free-breathing diffusion-weighted MR imaging of the liver. J Magn Reson Imaging. 2008;28(5):1141–8.
41. Choi JS, et al. Comparison of breathhold, navigator-triggered, and free-breathing diffusion-weighted MRI for focal hepatic lesions. J Magn Reson Imaging. 2013;38(1):109–18.
42. Oto A, et al. Active Crohn's disease in the small bowel: evaluation by diffusion weighted imaging and quantitative dynamic contrast enhanced MR imaging. J Magn Reson Imaging. 2011;33(3):615–24.
43. Yoshida S, et al. Female urethral diverticular abscess clearly depicted by diffusion-weighted magnetic resonance imaging. Int J Urol. 2008;15(5):460–1.
44. Braithwaite AC, et al. Short- and midterm reproducibility of apparent diffusion coefficient measurements at 3.0-T diffusion-weighted imaging of the abdomen. Radiology. 2009;250(2):459–65.
45. Koh DM, et al. Reproducibility and changes in the apparent diffusion coefficients of solid tumours treated with combretastatin A4 phosphate and bevacizumab in a two-centre phase I clinical trial. Eur Radiol. 2009;19(11):2728–38.
46. Wang CL, et al. Effect of gadolinium chelate contrast agents on diffusion weighted MR imaging of the liver, spleen, pancreas and kidney at 3 T. Eur J Radiol. 2011;80(2):e1–7.
47. Parikh T, et al. Focal liver lesion detection and characterization with diffusion-weighted MR imaging: comparison with standard breath-hold T2-weighted imaging. Radiology. 2008;246(3):812–22.
48. Muhi A, et al. High-b-value diffusion-weighted MR imaging of hepatocellular lesions: estimation of grade of malignancy of hepatocellular carcinoma. J Magn Reson Imaging. 2009;30(5):1005–11.
49. Guo Y, et al. Differentiation of clinically benign and malignant breast lesions using diffusion-weighted imaging. J Magn Reson Imaging. 2002;16(2):172–8.
50. Erdem G, et al. Diffusion-weighted images differentiate benign from malignant thyroid nodules. J Magn Reson Imaging. 2010;31(1):94–100.
51. Razek AA, et al. Role of apparent diffusion coefficient values in differentiation between malignant and benign solitary thyroid nodules. AJNR Am J Neuroradiol. 2008;29(3):563–8.
52. Razek AA, et al. Role of diffusion-weighted magnetic resonance imaging in characterization of renal tumours. J Comput Assist Tomogr. 2011;35(3):332–6.
53. Onur MR, et al. Role of the apparent diffusion coefficient in the differential diagnosis of gastric wall thickening. J Magn Reson Imaging. 2012;36(3):672–7.
54. Gourtsoyianni S, et al. Respiratory gated diffusion-weighted imaging of the liver: value of apparent diffusion coefficient measurements in the differentiation between most commonly encountered benign and malignant focal liver lesions. Eur Radiol. 2008;18(3):486–92.
55. Bruegel M, et al. Diagnosis of hepatic metastasis: comparison of respiration-triggered diffusion-weighted echo-planar MRI and five t2-weighted turbo spin-echo sequences. AJR Am J Roentgenol. 2008;191(5):1421–9.
56. Zech CJ, et al. Black-blood diffusion-weighted EPI acquisition of the liver with parallel imaging: comparison with a standard T2-weighted sequence for detection of focal liver lesions. Invest Radiol. 2008;43(4):261–6.
57. Nasu K, et al. Hepatic metastases: diffusion-weighted sensitivity-encoding versus SPIO-enhanced MR imaging. Radiology. 2006;239(1):122–30.
58. Coenegrachts K, et al. Focal liver lesion detection and characterization: comparison of non-contrast enhanced and SPIO-enhanced diffusion-weighted single-shot spin echo echo planar and turbo spin echo T2-weighted imaging. Eur J Radiol. 2009;72(3):432–9.
59. Koh DM, et al. Detection of colorectal hepatic metastases using MnDPDP MR imaging and diffusion-weighted imaging (DWI) alone and in combination. Eur Radiol. 2008;18(5):903–10.
60. Wu LM, et al. A pooled analysis of diffusion-weighted imaging in the diagnosis of hepatocellular carcinoma in chronic liver diseases. J Gastroenterol Hepatol. 2013;28(2):227–34.
61. Chi DS, et al. What is the optimal goal of primary cytoreductive surgery for bulky stage IIIC epithelial ovarian carcinoma (EOC)? Gynecol Oncol. 2006;103(2):559–64.
62. de Bree E, et al. Peritoneal carcinomatosis from colorectal or appendiceal origin: correlation of preoperative CT with intraoperative findings and evaluation of interobserver agreement. J Surg Oncol. 2004;86(2):64–73.
63. Fujii S, et al. Detection of peritoneal dissemination in gynecological malignancy: evaluation by diffusion-weighted MR imaging. Eur Radiol. 2008;18(1):18–23.
64. Soussan M, et al. Comparison of FDG-PET/CT and MR with diffusion-weighted imaging for assessing peritoneal carcinomatosis from gastrointestinal malignancy. Eur Radiol. 2012;22(7):1479–87.
65. Tan CH, et al. Diffusion-weighted MRI in the detection of prostate cancer: meta-analysis. AJR Am J Roentgenol. 2012;199(4):822–9.
66. Wu LM, et al. The clinical value of diffusion-weighted imaging in combination with T2-weighted imaging in diagnosing prostate carcinoma: a systematic review and meta-analysis. AJR Am J Roentgenol. 2012;199(1):103–10.
67. Yoshizako T, et al. Usefulness of diffusion-weighted imaging and dynamic contrast-enhanced magnetic resonance imaging in the diagnosis of prostate transition-zone cancer. Acta Radiol. 2008;49(10):1207–13.
68. Hoeks CM, et al. Transition zone prostate cancer: detection and localization with 3-T multiparametric MR imaging. Radiology. 2013;266(1):207–17.
69. Park BK, et al. Lesion localization in patients with a previous negative transrectal ultrasound biopsy and

persistently elevated prostate specific antigen level using diffusion-weighted imaging at three Tesla before rebiopsy. Invest Radiol. 2008;43(11):789–93.
70. Portalez D, et al. Prospective comparison of T2w-MRI and dynamic-contrast-enhanced MRI, 3D-MR spectroscopic imaging or diffusion-weighted MRI in repeat TRUS-guided biopsies. Eur Radiol. 2010;20(12):2781–90.
71. Hambrock T, et al. Prospective assessment of prostate cancer aggressiveness using 3-T diffusion-weighted magnetic resonance imaging-guided biopsies versus a systematic 10-core transrectal ultrasound prostate biopsy cohort. Eur Urol. 2012;61(1):177–84.
72. Eiber M, et al. Whole-body MRI including diffusion-weighted imaging (DWI) for patients with recurring prostate cancer: technical feasibility and assessment of lesion conspicuity in DWI. J Magn Reson Imaging. 2011;33(5):1160–70.
73. Gutzeit A, et al. Comparison of diffusion-weighted whole body MRI and skeletal scintigraphy for the detection of bone metastases in patients with prostate or breast carcinoma. Skeletal Radiol. 2010;39(4):333–43.
74. Lecouvet FE, et al. Can whole-body magnetic resonance imaging with diffusion-weighted imaging replace Tc 99m bone scanning and computed tomography for single-step detection of metastases in patients with high-risk prostate cancer? Eur Urol. 2012;62(1):68–75.
75. Taouli B, et al. Evaluation of liver diffusion isotropy and characterization of focal hepatic lesions with two single-shot echo-planar MR imaging sequences: prospective study in 66 patients. Radiology. 2003;226(1):71–8.
76. Sharma U, et al. Longitudinal study of the assessment by MRI and diffusion-weighted imaging of tumour response in patients with locally advanced breast cancer undergoing neoadjuvant chemotherapy. NMR Biomed. 2009;22(1):104–13.
77. Koh DM, et al. Predicting response of colorectal hepatic metastasis: value of pretreatment apparent diffusion coefficients. AJR Am J Roentgenol. 2007;188(4):1001–8.
78. Cui Y, et al. Apparent diffusion coefficient: potential imaging biomarker for prediction and early detection of response to chemotherapy in hepatic metastases. Radiology. 2008;248(3):894–900.
79. Song I, et al. Assessment of response to radiotherapy for prostate cancer: value of diffusion-weighted MRI at 3 T. AJR Am J Roentgenol. 2010;194(6):W477–82.
80. Reischauer C, et al. Bone metastases from prostate cancer: assessing treatment response by using diffusion-weighted imaging and functional diffusion maps – initial observations. Radiology. 2010; 257(2):523–31.
81. Barrett T, et al. DCE and DW MRI in monitoring response to androgen deprivation therapy in patients with prostate cancer: a feasibility study. Magn Reson Med. 2012;67(3):778–85.
82. Foltz WD, et al. Changes in apparent diffusion coefficient and T(2) relaxation during radiotherapy for prostate cancer. J Magn Reson Imaging. 2013; 37(4):909–16.
83. Harry VN, et al. Diffusion-weighted magnetic resonance imaging in the early detection of response to chemoradiation in cervical cancer. Gynecol Oncol. 2008;111(2):213–20.
84. Moffat BA, et al. Functional diffusion map: a noninvasive MRI biomarker for early stratification of clinical brain tumour response. Proc Natl Acad Sci U S A. 2005;102(15):5524–9.
85. Vandecaveye V, et al. Predictive value of diffusion-weighted magnetic resonance imaging during chemoradiotherapy for head and neck squamous cell carcinoma. Eur Radiol. 2010;20(7):1703–14.
86. Niwa T, et al. Advanced pancreatic cancer: the use of the apparent diffusion coefficient to predict response to chemotherapy. Br J Radiol. 2009;82(973): 28–34.
87. Takahara T, et al. Diffusion weighted whole body imaging with background body signal suppression (DWIBS): technical improvement using free breathing, STIR and high resolution 3D display. Radiat Med. 2004;22(4):275–82.
88. Kwee TC, et al. Diffusion-weighted whole-body imaging with background body signal suppression (DWIBS): features and potential applications in oncology. Eur Radiol. 2008;18(9):1937–52.
89. Sommer G, et al. Preoperative staging of non-small-cell lung cancer: comparison of whole-body diffusion-weighted magnetic resonance imaging and 18F-fluorodeoxyglucose-positron emission tomography/computed tomography. Eur Radiol. 2012;22(12):2859–67.
90. Ohno Y, et al. Non-small cell lung cancer: whole-body MR examination for M-stage assessment – utility for whole-body diffusion-weighted imaging compared with integrated FDG PET/CT. Radiology. 2008;248(2):643–54.
91. Abdulqadhr G, et al. Whole-body diffusion-weighted imaging compared with FDG-PET/CT in staging of lymphoma patients. Acta Radiol. 2011;52(2): 173–80.
92. van Ufford HM, et al. Newly diagnosed lymphoma: initial results with whole-body T1-weighted, STIR, and diffusion-weighted MRI compared with 18F-FDG PET/CT. AJR Am J Roentgenol. 2011;196(3):662–9.
93. Koh DM, Theony HC. Diffusion-weighted MR imaging. Berlin, Germany: Springer-Verlag; 2010.

Perfusion CT: Principles, Technical Aspects and Applications in Oncology

15

Olwen Westerland and Vicky Goh

Contents

Abbreviations

AIF	Arterial input function
BF	Regional blood flow
BV	Blood volume
CT	Computed tomography
$CTDI_{vol}$	CT Dose Index by volume
DCE-CT	Dynamic contrast enhanced CT
DLP	Dose length product
DNA	DeoxyriboNucleic Acid
EF	Extraction Fraction
18F-FDG	Fluoro-deoxy-glucose
HCC	Hepatocellular carcinoma
K_{trans}	Transfer constant
MTT	Mean transit time
MVD	Microvessel density
NSCLC	Non small cell lung cancer
PET	Positron emission tomography
PS	Permeability surface area product
ROI	Region of interest
VEGF	Vascular endothelial growth factor

O. Westerland
Division of Imaging Sciences and Biomedical Engineering, King's College London, London, UK

Department of Radiology, Guy's and St Thomas' NHS Foundation Trust, London, UK

V. Goh (✉)
Division of Imaging Sciences and Biomedical Engineering, King's College London, London, UK

Department of Radiology, St Thomas' Hospital, Lambeth Palace Road, London, SE1 7EH, UK
e-mail: vicky.goh@kcl.ac.uk

A. Luna et al. (eds.), *Functional Imaging in Oncology*,
DOI 10.1007/978-3-642-40412-2_15,

15.1 Introduction

Assessment of the functional vasculature of a tissue or organ of interest by dynamic contrast-enhanced CT techniques is based on intravenous contrast agent kinetics. In clinical practice low-molecular-weight (<1 kDa) iodinated contrast agents are used, which have negligible serum protein binding. Their distribution in the body is similar to that of extracellular fluid. Following a bolus intravenous injection of contrast agent, the contrast agent distributes rapidly within the vascular system. As the contrast agent transits through a vascular bed, it passes from the intravascular to the extravascular-extracellular compartment, with the exception of the brain, retina and testis. The rate at which this occurs is determined by a number of factors including the rate of tissue delivery, vessel surface area and the permeability of these vessels which will differ between pathological and normal tissue. There is subsequent return of contrast agent from the extravascular-extracellular compartment back into the intravascular compartment, and the contrast agent is excreted usually by the kidneys. Typically there is insignificant passage of contrast agent into the intracellular compartment (<1 %). By taking advantage of the differences in contrast agent kinetics between pathological and normal tissues or organs, this provides tissue- or organ-specific information of the functional vasculature.

By assessing the dynamic changes in vessel and tissue or organ enhancement over time following intravenous administration of an iodinated contrast agent, both qualitative and quantitative parameters may be assessed. Qualitative parameters refer to descriptors of the enhancement time curves. These include curve shape, time to peak enhancement, peak enhancement or area under the enhancement time curve. These parameters will be influenced by technical and patient factors including contrast agent dose, contrast agent rate of administration and cardiac output. Quantitative parameters are derived from kinetic modelling of the enhancement time curves and are more physiologically based. These include regional blood flow, blood volume and extraction fraction or permeability surface area product (Table 15.1). These parameters may be obtained in a robust manner and may provide relevant clinical information to the clinician and enable treatment effects on the vasculature to be assessed [1].

Table 15.1 Definition of vascular parameters

Vascular parameter	Definition
Regional blood flow (BF)	Flow rate of whole blood through the vasculature of a defined tissue volume or mass
Regional blood volume (BV)	Volume of flowing whole blood within the functioning vasculature of a defined tissue volume or mass
Extraction fraction (EF)	Fraction of the whole blood contrast agent that is transferred to the extravascular-extracellular space during a single passage of the contrast agent
Permeability surface area product (PS)	Product of permeability and total surface area of capillary endothelium in a unit volume or mass of tissue and reflects the total diffusional flux across the capillaries

Regional blood flow, blood volume and vascular leakage parameters within the tumour are interrelated but may vary with the underlying tumour environment. For example, areas of high blood flow, blood volume and leakage may reflect well-perfused areas with presence of shunting and areas of angiogenesis; low blood flow, blood volume and low-leakage areas may represent areas of poor vascularisation ± necrosis; low blood flow, blood volume and high-leakage areas may represent poor perfusion areas with angiogenesis.

15.2 Biological Correlates of Tumour Vascular Parameters

Tumour vascular parameters derived via kinetic modelling provide physiological information regarding regional blood flow and thus the delivery of oxygen and nutrients to the tumour; regional tumour blood volume, which reflects functional ‘vascular density’; and vascular

leakage from the capillaries or neovessels. In general tumours demonstrate higher vascularisation than normal tissues. These parameters may also provide a surrogate measure of tumour angiogenesis and perfusion-related hypoxia.

15.2.1 The Tumour Vasculature

The development of a viable tumour blood supply is essential to support tumour growth and proliferation [2]. This may occur through sprouting from pre-existing vessels (vasculogenesis), de novo vascular formation through recruitment of circulating endothelial progenitor cells and vessel co-option. The tumour microenvironment including hypoxia, glucose deprivation and low pH plays an important role in the initiation of tumour angiogenesis via the activation of oncogenes and/or inactivation of tumour suppressor genes [3].

In terms of morphology, the tumour vasculature appears functionally distinct and spatially heterogeneous. The vasculature lacks the usual hierarchical branching pattern and in general demonstrates greater vessel density at the tumour periphery. The vessels themselves are thin and tortuous, characterised by a relatively high endothelial cell proliferation rate, incomplete endothelium, relative absence of smooth muscle or pericyte investiture and hyper-permeability resulting in high interstitial fluid pressure.

15.2.2 Immunohistochemistry Correlates of Dynamic Contrast-Enhanced CT

Microvessel density (MVD) and vascular endothelial growth factor (VEGF) are commonly used immunohistological measures of angiogenesis. In a number of cancers including lung, renal, gastrointestinal and pancreatic cancer, associations have been found between MVD and VEGF and various perfusion CT parameters. Most of the evidence relates to lung cancer. Typically these correlations have been moderate: histological analysis has been varied based on different number of 'hotspot' counts or from random areas of the whole tumour. There have also been negative studies, in part reflecting the heterogeneity of analyses and immunohistological biomarkers used [4].

With respect to the lung, peak CT enhancement in patients with solitary pulmonary nodules has been correlated significantly with both MVD and VEGF, irrespective of the benign or malignant nature of the nodules [5]. In patients with operable NSCLC, either CT peak enhancement, blood flow, blood volume or permeability surface area product has been shown to demonstrate a moderate correlation with MVD: Li et al. showed that CT regional blood flow correlated with CD34 expression ($r = 0.715$; $P = <0.001$) assessed in 6 tumour regions: central (3) and peripheral (3) [6]. Ma et al. showed that CT peak enhancement and regional blood flow correlated with CD34 expression assessed in 5 hotspots in VEGF positive but not VEGF negative tumours [7]. Similarly Sauter et al. have found that there is a moderate correlation between extraction fraction and blood flow and CD34 [8], while Spira et al. have found a positive association between MVD and blood flow and volume [9]. Peak enhancement, blood flow and relative blood volume have also been shown to be significantly higher in VEGF positive compared to VEGF negative tumours [7, 10].

There have also been several pathological correlative studies in other abdominally sited cancers. In renal cell cancer an initial study in 24 patients showed a moderate correlation ($r = 0.60$) between peak enhancement and hotspot MVD (CD34) Wang et al. [11]. More recently a further small study ($n = 10$) where patients with renal cell cancer underwent volumetric perfusion CT prior to surgery has confirmed that regional blood flow and blood volume correlated significantly with MVD (CD34; $r = 0.600$–0.829); however, K^{trans} only demonstrated moderate correlations with MVD in non-necrotic areas ($r = 0.550$) [12].

Moderate correlations ($r = 0.42$) between regional blood volume and hotspot MVD (CD34) have been found in gastric adenocarcinoma [13].

Similarly in colorectal cancer, moderate correlations between regional blood volume and permeability surface area product and non-hotspot MVD (CD34) have been shown [14]. In pancreatic adenocarcinoma moderate correlations ($r = 0.49$) have also been found between MVD and peak enhancement in the arterial phase [15].

Perfusion CT parameters may also inform on the presence of perfusion-related hypoxia. In lung cancer blood volume measurements have also been found to be negatively correlated to an exogenous marker of hypoxia (pimonidazole: $r = -0.48$) [16]. However, one of the challenges of clinico-pathological correlative studies is the comparison of in vivo with ex vivo findings. Tacelli et al. have showed that areas of low regional tumour BV but high PS have higher CD34 expression (assessed in 3 hotspots in the non-necrotic tumour portion) than areas of high regional tumour BV and high PS: 72.1 versus 47.9, $P = 0.038$ [17], which they postulated could be related to the degree of tumour interstitial pressure.

15.3 Technical Aspects

15.3.1 Patient Preparation

As with any contrast-enhanced CT study, patients should be well hydrated and have a normal renal function. For studies involving abdominal organs such as the liver, pancreas and bowel, recent food intake may affect organ perfusion, and patient fasting may be appropriate. If an oral contrast agent is required, water is preferred to positive contrast agents. An anti-peristaltic drug (e.g. glucagon or hyoscine-N-butyl bromide) is advisable for DCE-CT studies of the bowel and/or pelvis.

Keeping the patient well informed concerning the CT acquisition will improve the quality of the study. Clear instructions should be given, for example, regarding the need to stay still, breathing instructions for breath-held studies, cessation of swallowing during the acquisition for head and neck studies and potential effects induced by the contrast agent including a hot flush.

Table 15.2 Recommended volume of contrast agent

Iodine concentration (mg/mL)	Volume (mL)
300	40–60
350	35–50
370	32–48
400	30–45

From [1]

15.3.2 Contrast Agent Administration

The dose and manner in which contrast agents are administered will influence parameter quantification. Kinetic modelling benefits from a bolus injection of contrast agent and an injection rate of at least 4 mL/s via a large bore intravenous cannula, usually sited in the antecubital fossa. Injection rates beyond 10 mL/s appear to confer no additional benefit for quantification. The total injected iodine dose should be within the range of 12–18 g. It is important that the iodine concentration administered is not less than 300 mg/mL. If iodine concentrations are >350 mg/mL, the contrast agent must be warmed to body temperature prior to injection, as the higher viscosity will slow the actual injection rate. The volume of contrast agent will depend on the iodine concentration used (Table 15.2) [1].

15.3.3 CT Data Acquisition

With current state-of-the-art technology, an entire organ such as the brain, lungs, liver, spleen or kidney may be encompassed with a high spatial resolution and a high temporal acquisition sampling rate. A typical CT acquisition is shown in Fig. 15.1.

To ensure accurate quantification, a sampling rate of 2 s or less should be used. For the initial perfusion phase, an acquisition duration of 45 s is adequate; for the interstitial phase at least 5 additional time points are recommended, the sampling rate ranging from 5 to 15 s depending on the kinetic model applied [1]. The change in blood vessel and tumour enhancement during this time, which is related to the passage of intravenous contrast agent between the intravascular and extravascular-extracellular space, provides

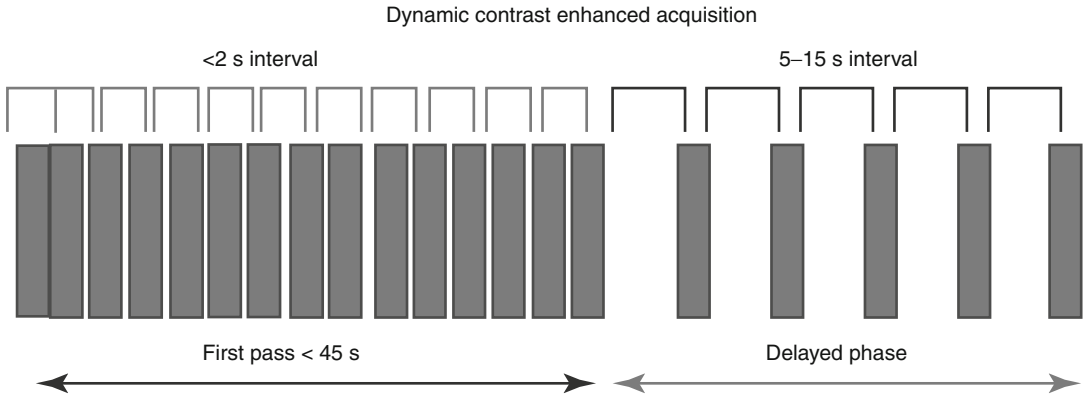

Fig. 15.1 Schema showing typical perfusion CT acquisition for tumour evaluation

Table 15.3 Summary of the commonly applied kinetic models

Kinetic model	Compartments	Parameter measured	Assumptions
Johnson-Wilson distributed parameter	Dual	BF, BV, MTT, PS	Constrained IRF
Patlak	Dual	EF, BV	One way transfer Well-mixed compartments
Maximum slope	Single	BF	No venous outflow

BF regional blood flow, *BV* regional blood volume, *MTT* mean transit time, *PS* permeability surface area product, *EF* extraction fraction

the necessary data for quantification. As the concentration of iodine within blood vessels and tissues is proportional to the resultant increase in attenuation, temporal changes in attenuation can be analysed using standard kinetic models without prior conversion to iodine concentration.

15.3.4 Image Processing

15.3.4.1 Motion Correction and Image Registration

For target lesions located in motion susceptible sites, breath-holding during the first-pass study will reduce motion artefact and voxel displacement. For longer duration studies, motion correction/image registration may compensate for motion artefact, and this is incorporated into commercial software platforms, for example, based on a non-rigid deformable registration technique [18].

15.3.4.2 Quantification of Vascular Parameters

The vascular parameters which can be quantified include regional blood flow (BF), blood volume and extraction fraction or permeability surface area product.

Different mathematical models may be applied to derive these. Commonly used tracer kinetic modelling include (1) maximum initial slope, (2) Patlak and (3) distributed parameter analysis (Table 15.3).

In practice quantification using commercial platforms requires a region of interest (ROI) to be placed within an input artery (to generate an arterial input function, AIF) and for the lesion(s) of interest. From the arterial and tissue enhancement time curve that are displayed by the software, quantitative parametric maps are generated (Fig. 15.2).

While volume-of-interest analysis, encompassing the whole tumour, may be the least susceptible to observer error and experience and provide a global evaluation of perfusion and angiogenesis; this may not best reflect the heterogeneity within a tumour, particularly if this demonstrates areas of necrosis, calcification or haemorrhage, as these are 'averaged' in the process (Fig. 15.3).

In practice it is important to choose an appropriate target lesion(s). Ideally this should be

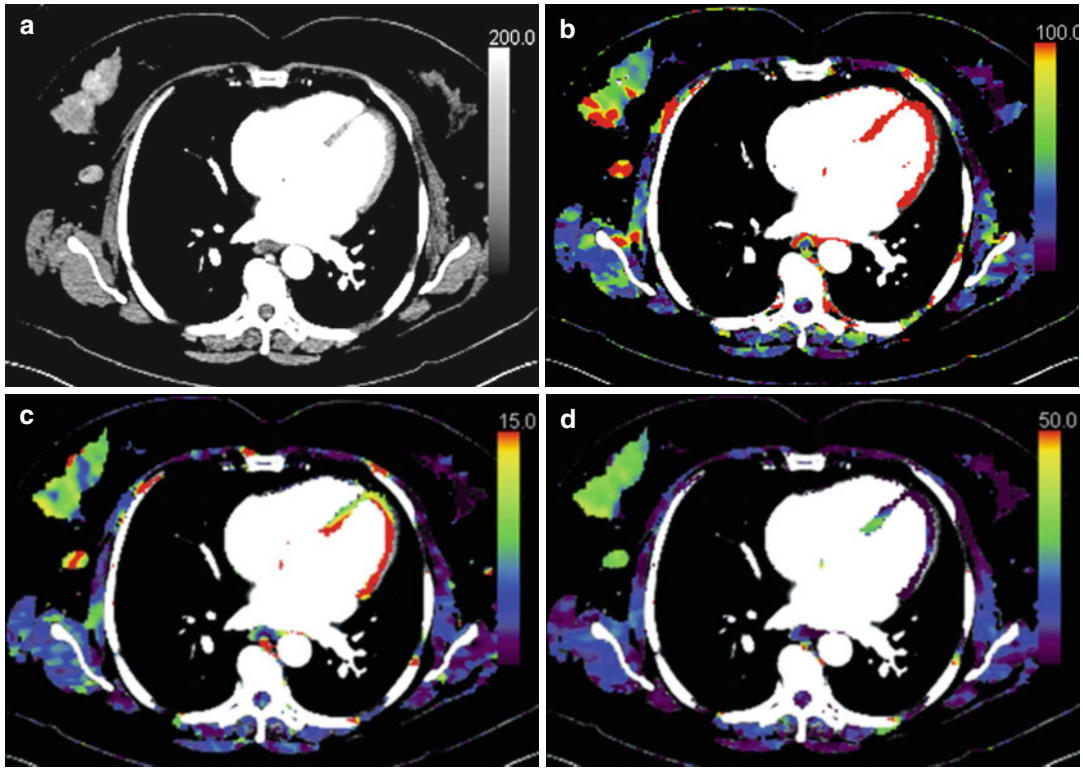

Fig. 15.2 Perfusion CT image of a right breast cancer (**a**) and corresponding parametric maps of regional blood flow (**b**), blood volume (**c**) and extraction fraction (**d**) are shown. The tumour demonstrates heterogeneous blood flow and blood volume

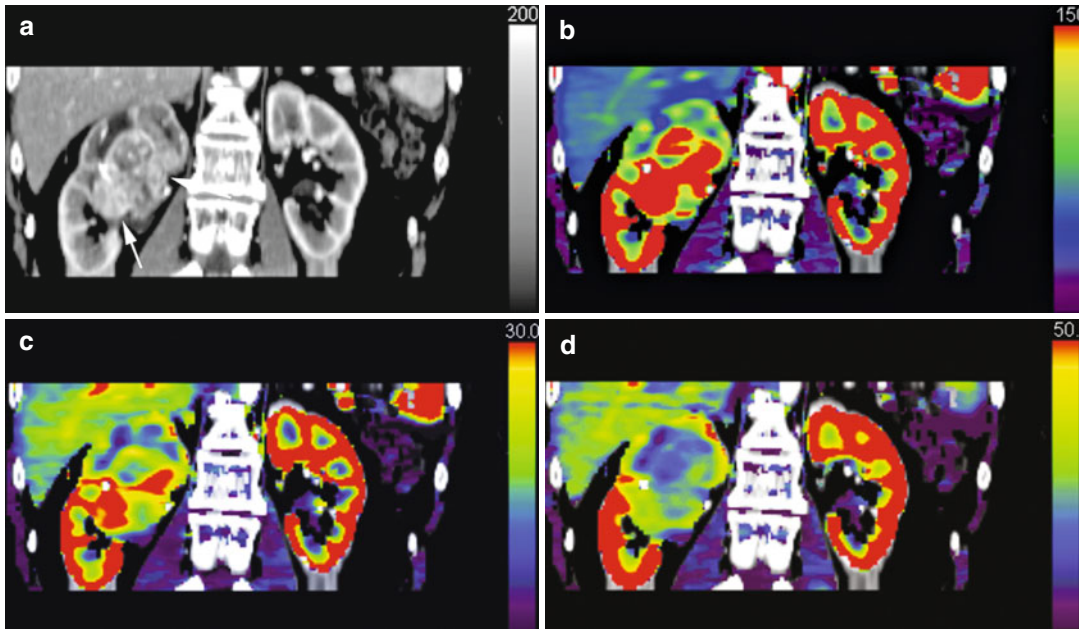

Fig. 15.3 Dynamic contrast-enhanced CT (**a**) and corresponding parametric maps of a large heterogeneous renal cancer are shown: regional blood flow (**b**), regional blood volume (**c**) extraction fraction (**d**)

>2 cm and not in close proximity to large vessels (e.g. superior vena cava or aorta), heart or diaphragm in order to reduce artefacts. For lesions located in motion susceptible sites, breath-holding techniques (± initial hyperventilation) and/or the use of motion correction/image registration will reduce motion artefacts. For target lesions located within the bowel, the use of a standard anti-peristaltic (Buscopan or glucagon) will reduce the motion related to peristalsis. It is also important to select an appropriate artery to derive the AIF. The vessel chosen must be of sufficient size to prevent partial voluming occurring secondarily due to pulsation or movement artefact (including peristalsis) or laminar flow within the vessel. If this is the case, this will influence and change the arterial time-attenuation curve. It is assumed that the arterial time-attenuation curve of the artery in the field of view is identical to the vessel supplying the tumour. This is only valid if there is no obstructive process or other significant feeding vessels.

15.4 Clinical Implementation

15.4.1 Quality Assurance and Quality Control

The ready availability of perfusion CT software on commercial reporting workstations has facilitated clinical implementation. However, in addition to standard quality assurance that tests the performance of the CT scanner, quality control procedures should be in place for perfusion CT, particularly where longitudinal studies are planned and robust quantification is required, for example, in the clinical trial setting [1]. Quality control refers to the processes needed to maintain quality. Standardisation of acquisition, analysis and reporting protocols should be implemented, where possible. These acquisition, radiation dose, data processing and reporting protocols should be recorded for each patient allowing audit to be undertaken. The use of phantom calibration, assessment of image quality (contrast to noise ratio) and, in clinical trials, central data review should be undertaken of at least 10 % of the dataset.

15.4.2 Radiation Dose

The cancer risk associated with perfusion CT has to be balanced against the potential benefits derived from quantification of tumour vascularity. Imaging should comply with the ALARA (*A*s *L*ow *A*s *R*easonably *A*chievable) principle. The radiation dose of a perfusion CT acquisition is dependent on the temporal frequency of the acquisition, volume of coverage, kilovoltage and milliampere selected [19]. The risk significance of a radiation exposure from DCE-CT will depend to some extent on the clinical circumstance. The risk of radiation exposure from perfusion CT, for example, will be relatively inconsequential in the context of radiation therapy.

The CT acquisition should be tailored to the research or clinical question or clinical context. A maximal acceptable dose should be assigned for the acquisition ensuring that satisfactory signal:noise characteristics can be obtained. In general it is good practice to ensure that a maximum effective dose of 20 mSv for a volume of tissue measuring 4 cm in the cranio-caudal direction is not exceeded [1]. The effective dose is obtained by multiplying the dose length product (DLP, $mGy \cdot cm$) provided by the CT scanner and the appropriate conversion factor ($mSvmGy^{-1} \cdot cm^{-1}$). The DLP and CT Dose Index by volume ($CTDI_{vol}$) of DCE-CT studies should be recorded in the patient record.

15.4.3 Measurement Reproducibility

Good measurement reproducibility is essential for the clinical application of any technique. Ideally the coefficient of variation should be less than 20 % [20]. This is particularly pertinent in oncological imaging for response assessment, where the differences in repeated measurements have to be smaller than the expected therapeutic effect. Usually, the more straightforward a

measurement, the easier it should be to reproduce. With perfusion CT techniques, measurement reproducibility has been shown to be acceptable, with a coefficient variation of 13.2–35 % which has been reported for the cranial circulation of both animals and humans [21, 22] and coefficients of variation ranging from 14 to 24 % for tumours [23–25].

It is also important in the context of repeated measurements that intra- and interobserver variability are limited. In general intraobserver is better than interobserver agreement [26], in concordance with other studies of observer agreement using traditional morphological measures of response [27]. Where appropriate a single observer should analyse serial examinations in the same patient.

The tumour location, the tumour size, the acquisition protocol, the software programme and positioning of the arterial and tumour ROIs by individuals all contribute to observer variation [28]. For perfusion CT coefficients of variation have ranged from 2.5–9.5 % [29] to 14–20.8 % [30] in cranial studies and 3–13 % in a study of squamous cancers of the extracranial head and neck [31].

15.5 Clinical Applications

In oncological practice its main role remains the evaluation of the effectiveness of drugs which target the tumour vasculature, particularly in the context of clinical trials [32]. However, by reflecting perfusion and angiogenesis and exploiting the differences in perfusion parameters between tumour and normal tissues, perfusion CT may also assist lesion characterisation, delineation of tumour extent, tumour phenotyping and prognostication.

15.5.1 Response Assessment

Quantitative parameters derived from perfusion CT may be used to monitor the effects of a variety of treatments. These include chemotherapy with standard and novel agents (anti-angiogenic drugs, vascular disrupting agents, immunotherapy), radiotherapy and interventional oncologic procedures such as embolisation of the tumour vascular supply or radiofrequency ablation. Early evidence has shown that a common long-term effect of treatment is a reduction in perfusion CT parameters following treatment completion, although in the short term, there may be a variable vascular effect related to the therapeutic mechanism of action (Table 15.4).

With standard chemotherapy, which affects actively replicating cells via DNA damage or interruption of DNA repair, this effect is thought to reflect the loss of angiogenic cytokine support following cell death [33]. With anti-angiogenic therapies, differing vascular effects may be seen depending on mechanism of action of the drug under investigation and timing of the scan. An initial effect may be a decrease in vascular permeability and reduction in interstitial fluid pressure, with normalisation of function of the vasculature resulting in a transient increase in tumour blood flow [34]. In the longer term, with subsequent pruning of the vasculature, a reduction in regional blood flow, blood volume and vascular permeability may be elicited. With vascular disrupting agents, which target the proliferating immature vasculature ± the mature vasculature, a rapid shutdown in tumour vascularisation may occur that is usually transient and reversible within 24–48 h. This may be followed by a rebound re-vascularisation [35]. With radiotherapy, the acute effects are related to an initial inflammatory effect; the permeability is related to microvascular damage, which can lead to tumour shrinkage [36] (Figs. 15.4 and 15.5). With interventional procedures perfusion CT parameters may provide evidence of effective treatment or the need for further procedural attempts for optimal therapeutic effect [37].

In early phase clinical trials, these quantitative parameters may provide insight into drug pharmacodynamics [38]. Tumour angiogenesis is an attractive target for anticancer therapy. For drug development, results from such trials may inform on ‘go-no-go’ pharma decisions, as well as appropriate dosages to be taken into further stages. In recent years different therapeutic agents have

Table 15.4 The acute and chronic vascular effects of therapy measured by perfusion CT

	Perfusion CT parameter		
Therapy	Blood flow	Blood volume	Vascular leakage
Cytotoxic chemotherapy: short-term effects	Unchanged	Unchanged	Unchanged
Cytotoxic chemotherapy: long-term effects	Decrease	Decrease	Decrease Unchanged
Anti-angiogenics: short-term effects	Increase Unchanged	Increase Unchanged	Decrease
Anti-angiogenics: long-term effects	Decrease	Decrease	Decrease
Vascular disrupting agents: short-term effects	Decrease	Decrease	Decrease
Vascular disrupting agents: long-term effects	Increase Unchanged	Increase Unchanged	Increase Unchanged
Radiotherapy: short-term effects	Increase	Increase	Increase
Radiotherapy: long-term effects	Decrease	Decrease	Decrease
Interventional: radiofrequency ablation	Decrease	Decrease	Decrease
Interventional: TACE	Decrease Absent	Decrease Absent	Decrease Absent

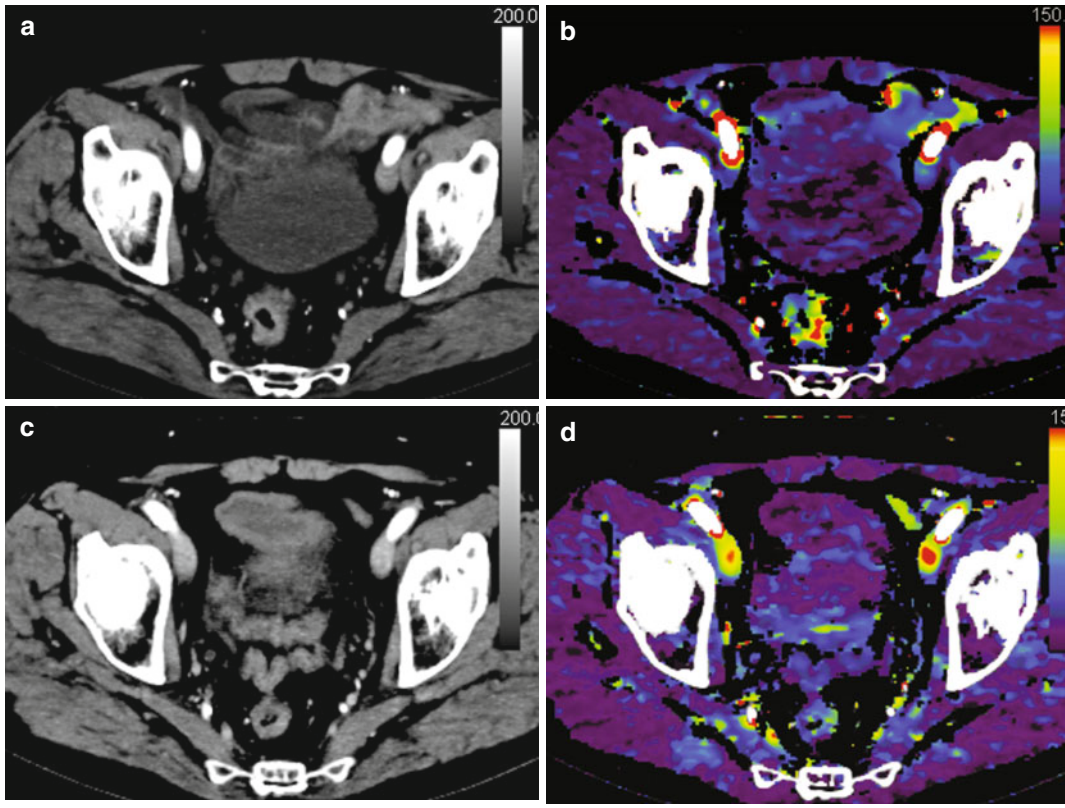

Fig. 15.4 Axial image (**a**) and regional blood flow map (**b**) of a rectal cancer. Following neoadjuvant chemoradiation there is tumour shrinkage (**c**) and decrease in blood flow (**d**)

been developed and licensed including antibodies targeting vascular endothelial growth factor (e.g. bevacizumab) and small molecule tyrosine kinase inhibitors (e.g. sunitinib, sorafenib, pazopanib). These agents have been shown to be effective in clinical trials in several cancers

including metastatic colorectal cancer [39], metastatic renal cell cancer [40, 41] and hepatocellular cancer [42] with a modest improvement in objective benefit (progression-free survival or overall survival).

15.5.2 Perfusion CT as a Prognostic and Predictive Biomarker

This remains an exploratory area for perfusion CT but clinically promising as tumour angiogenesis and tumour hypoxia may be adverse prognostic factors. A few studies have addressed if perfusion CT can provide additional information to current tumour staging strategies. Some correlative studies have assessed if perfusion CT parameters may reflect tumour type, grade or stage in a number of tumour types including hepatocellular cancer [43], non-small cell lung cancer [7, 44, 45] and colorectal cancer [46, 47]. In hepatocellular cancer; higher-grade cancers have been shown to have higher perfusion measurements than in lower-grade hepatocellular cancers [43]. There have been conflicting results in surgically confirmed non-small cell lung cancer with some studies showing no relationship while others reporting differences in measurements between adenocarcinomas, squamous cell, large cell and

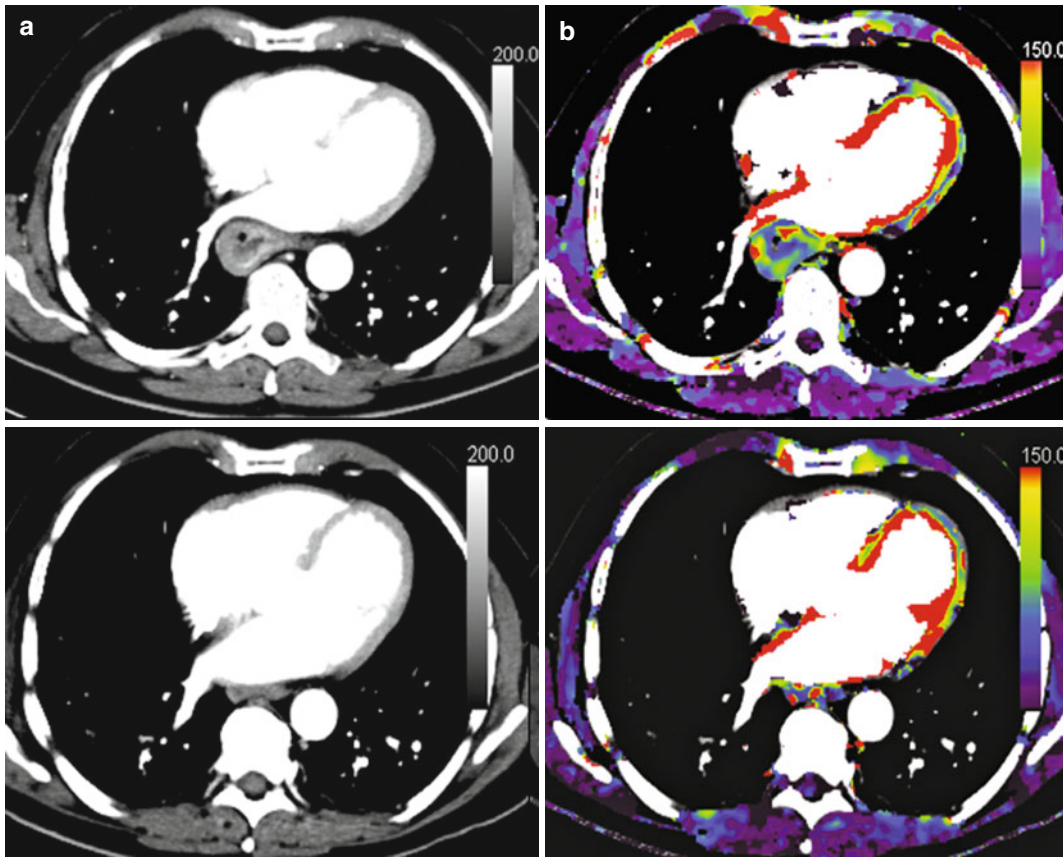

Fig. 15.5 Axial images of an oesophageal cancer before (*top row*) and after treatment (*bottom row*). Following definitive chemoradiation there has been a good response with a reduction in tumour size (**a**) and tumour vascularisation: regional blood flow (**b**) and extraction fraction (**c**)

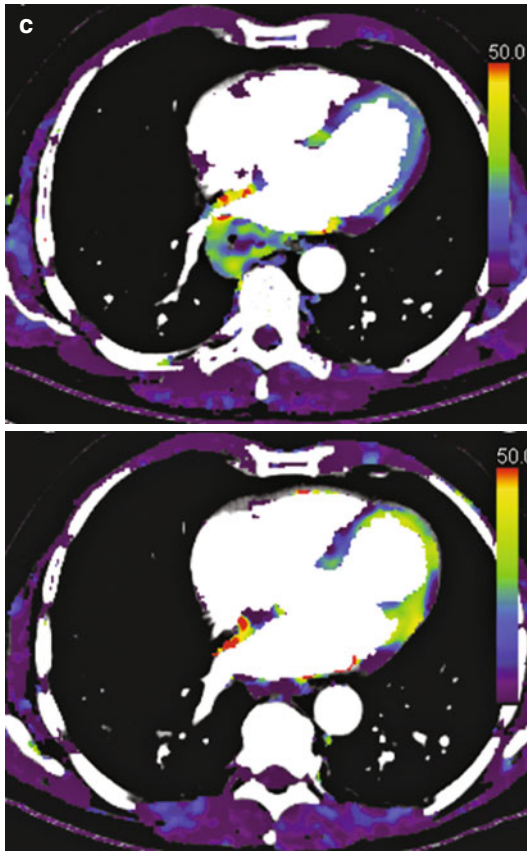

Fig. 15.5 (continued)

small cell carcinomas. In primary colorectal tumours, permeability surface area product is increased in patients with metastatic disease compared with tumours without evidence of metastases at staging [46]. With a correlation between permeability surface area product and microvessel density [14], this finding supports the theory that greater angiogenesis in colorectal cancer may be associated with a higher likelihood of metastatic disease.

Perfusion CT parameters have also shown promise in terms of predicting outcome at staging. Regional blood flow, as a marker of overall tumour perfusion and an indirect marker of hypoxia, may be an important prognostic biomarker. A study in primary oesophageal cancer treated with chemoradiation found that overall survival was lower in patients with lower baseline blood flow [47]. A rectal cancer study has also produced similar results [48]. This is consistent with our current understanding of tumour biology, which proposes that tumour hypoxia may be associated with a more aggressive tumour type and found in other cancers including extracranial head and neck cancers [49] and cervical cancer [44, 50].

In a small study of colorectal cancer patients treated with surgery and followed up until presentation with metastatic disease, baseline regional blood flow was found to be substantially lower in patients who developed subsequent metastases in comparison to patients who remain disease-free [46].

Perfusion CT parameters have also shown promise as a predictive biomarker at staging. It is hypothesised that a higher regional blood flow ensures better tumour oxygenation and potentially increases radiosensitivity and enables better delivery of the chemotherapeutic agents. Several studies have shown that tumours which have a lower regional blood flow are more likely to be poor responders to chemotherapy and radiotherapy treatment. This was shown to be the case in renal cell carcinoma, where the baseline enhancement blood flow and blood volume were significantly lower in patients who did not respond to treatment [51, 52]. This is also the case for head and neck SCC where lower regional blood flow values are associated with a higher failure rate [49, 53, 54]. This has also been shown for anti-angiogenic therapy, where higher baseline quantitative parameters are associated with a higher response rate [55, 56]. With locoregional procedures, such as laser-induced thermotherapy for lung tumours [57] and radiofrequency ablation or transarterial chemoembolisation for liver tumours [37, 58], perfusion CT may predict for technical success immediately after treatment. Hegenscheid et al. have suggested that lung tumours with perfusion measurements that do not change after therapy are likely to have progressive disease [57].

15.5.3 Perfusion CT for Lesion Characterisation and Phenotyping

Apart from its role in response assessment, perfusion CT techniques may aid lesion characterisation and augment assessment of tumour biology, providing an imaging 'phenotype' either as a single modality [9] or when combined with 18F-FDG-PET-CT [59, 60, 61], where perfusion parameters are combined with metabolic parameters. As mentioned previously, there are usually significant differences in tumour and normal tissue vascularisation related to the structural and functional differences in tumour and normal vessels, although there may be overlap in the vascular characteristics of inflammation and cancer. There are exceptions, for example, pancreatic tumours where lower perfusion is typically observed in first-pass studies compared to the normal pancreatic parenchyma [62–64]. A similar reduction in vascularisation is also seen in inflammatory pancreatitis [65, 66]; and chronic pancreatitis [65, 67], with the potential to differentiate between pancreatic adenocarcinoma and mass-forming chronic pancreatitis [68], which demonstrates higher perfusion than cancer.

In the lung both semi-quantitative and quantitative measures may improve the characterisation of solitary pulmonary nodules. Malignant lesions typically have a higher rate of enhancement and analysis of the enhancement time curves shows faster washout compared with benign lesions. Absence of enhancement is a strong predictor of benignity [69]; using a threshold of 15HU or greater, sensitivity, specificity and accuracy for malignancy can be 98, 58 and 77 %, respectively [69]. In terms of quantitative parameters, Zhang et al. found in 65 patients with solitary pulmonary nodules that the mean perfusion value of malignant SPNs was significantly higher than benign nodules (70 vs. 10 mL/min/100 mL, respectively) [70]. Similarly Sitartchouk et al. found that perfusion and blood volume were significantly higher in malignant than benign solitary pulmonary nodules [71]. However, inflammatory nodules also demonstrate elevated perfusion values, reducing specificity [72]. The addition of vascular permeability measurements has the potential to improve differentiation of malignant and inflammatory nodules: Ma et al. found that permeability was significantly higher in cancer compared with inflammatory nodules [7].

In the context of cirrhosis, perfusion CT has the potential to improve detection and characterisation of hepatocellular carcinoma. In a rat model of HCC, Fournier et al. demonstrated that DCE-CT allowed for early tumour detection: arterial blood flow was high with a sensitivity and specificity of detection of 86 and 65 %, respectively, within 11 weeks of tumour induction even though only 7 % was visible by eye [73]. HCC typically shows an increase in arterial liver perfusion [74, 75] with higher perfusion in well-differentiated tumours [76].

In the colon, assessment of regional blood volume, blood flow and vascular permeability may help in distinguishing colon cancer from diverticular disease. Their features may overlap in terms of clinical symptoms and morphological imaging, and distinction between colon cancers and diverticular disease based on these characteristics can be challenging, particularly as up to 30 % of colon cancers are coincident with diverticular disease. Vascular parameters such as regional blood flow, blood volume and permeability surface area product are highest in cancer: regional blood flow and blood volume had a sensitivity of 80 % and specificity of 75 and 70 % for differentiating cancer from acute diverticulitis, which is better than that achieved using established CT morphological criteria [77].

Perfusion CT techniques have also been applied to characterise lymph nodes, where it may potentially provide additional information to size, and aid differentiation between malignant and benign lymph nodes either as a single modality [78] or combined with 18F-FDG-PET/CT [61, 79, 80]. These have included the assessment of mediastinal lymph nodes in lung cancer [61], squamous cell cancer (SCC) of the head and neck [78] and in breast cancer [81]. Metastatic nodes typically demonstrate higher perfusion than benign nodes (Fig. 15.6).

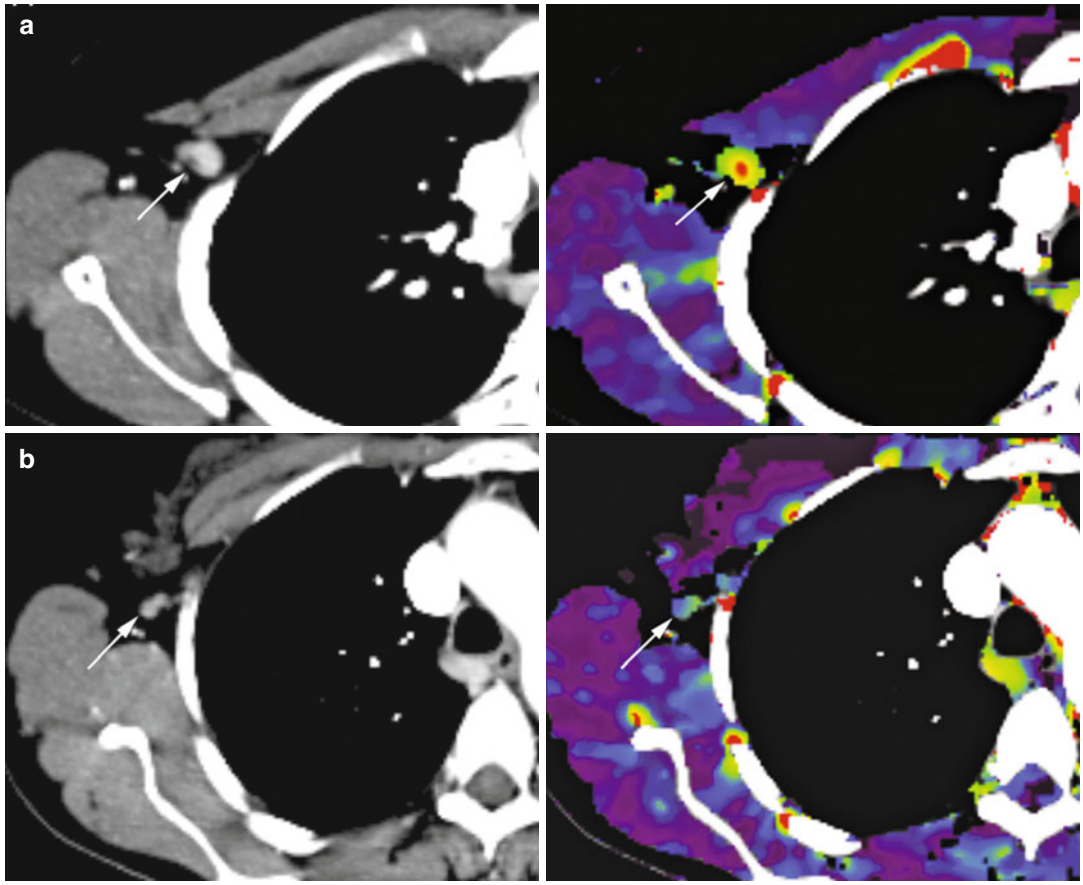

Fig. 15.6 Perfusion characteristics of nodes (*arrows*): a malignant node (**a**) associated with primary breast cancer (not shown) demonstrates higher blood volume than a benign node (**b**)

15.6 Summary

In conclusion, perfusion CT is a robust technique for imaging the functional tumour vasculature. With current state-of-the-art technology, whole-organ regional blood flow, blood volume and vascular leakage can be investigated: this can encompass more than a single target lesion. In clinical trials, it may provide evidence of vascular response in early phase trials, though further validation studies are required for these measurements to be surrogate endpoints in phase III clinical trials. Perfusion CT also has a growing role in wider clinical practice for the assessment of locoregional therapy and anti-angiogenic therapy for agents licensed for clinical use. Perfusion CT may aid lesion characterisation and has shown potential as a prognostic and predictive biomarker. As technological improvements in CT continue to evolve, this will further extend clinical applications.

References

1. Miles KA, et al. Experimental Cancer Medicine Centre Imaging Network Group. Current status and guidelines for the assessment of tumour vascular support with dynamic contrast-enhanced computed tomography. Eur Radiol. 2012;22:1430–41.
2. Folkman J. The role of angiogenesis in tumour growth. Semin Cancer Biol. 1992;3:65–71.
3. Hanahan D, Folkman J. Patterns and emerging mechanisms of the angiogenic switch during tumourigenesis. Cell. 1996;86:353–64.

4. Goh V, et al. Assessment of the metabolic flow phenotype of primary colorectal cancer: correlations with microvessel density are influenced by the histological scoring method. Eur Radiol. 2012;22:1687–92.
5. Yi CA, et al. Solitary pulmonary nodules: dynamic enhanced multidetector row CT study and comparison with vascular endothelial growth factor and microvessel density. Radiology. 2004;233:191–9.
6. Li Y, et al. Peripheral lung carcinoma: correlation of angiogenesis and first-pass perfusion parameters of 64-detector row CT. Lung Cancer. 2008;61:44–53.
7. Ma SH, et al. Peripheral pulmonary nodules: relationship between multi-slice spiral CT perfusion imaging and tumor angiogenesis and VEGF expression. BMC Cancer. 2008;8:186.
8. Sauter AW, et al. Multifunctional profiling of non-small cell lung cancer using 18F-FDG PET/CT and volume perfusion CT. J Nucl Med. 2012;53:521–9.
9. Spira D, et al. Assessment of tumor vascularity in lung cancer using Volume Perfusion CT (VPCT) with histopathologic comparison: a further step toward an individualized tumor characterization. J Comput Assist Tomogr. 2013;37:15–21.
10. Tateishi U, et al. Lung tumors evaluated with FDG-PET and dynamic CT: the relationship between vascular density and glucose metabolism. J Comput Assist Tomogr. 2002;26:185–90.
11. Wang JH, et al. Dynamic CT evaluation of tumor vascularity in renal cell carcinoma. AJR Am J Roentgenol. 2006;186:1423–30.
12. Reiner CS, et al. Computed tomography perfusion imaging of renal cell carcinoma: systematic comparison with histopathological angiogenic and prognostic markers. Invest Radiol. 2013;48:183–91.
13. Yao J, et al. Gastric adenocarcinoma: can perfusion CT help to noninvasively evaluate tumor angiogenesis? Abdom Imaging. 2011;36:15–21.
14. Goh V, et al. Colorectal tumor vascularity: quantitative assessment with multidetector CT – do tumor perfusion measurements reflect angiogenesis? Radiology. 2008;249:510–7.
15. Hattori Y, et al. Enhancement patterns of pancreatic adenocarcinoma on conventional dynamic multidetector row CT: correlation with angiogenesis and fibrosis. World J Gastroenterol. 2009;15:3114–21.
16. Mandeville HC, et al. Operable non-small cell lung cancer: correlation of volumetric helical dynamic contrast-enhanced CT parameters with immunohistochemical markers of tumor hypoxia. Radiology. 2012;264:581–9.
17. Tacelli N, et al. Assessment of non-small cell lung cancer perfusion: pathologic-CT correlation in 15 patients. Radiology. 2010;257:863–71.
18. Saddi KA, et al. Large deformation registration of contrast-enhanced images with volume preserving constraint. In: Pluim JPW, Reinhardt JM, editors. Proceedings of SPIE: medical imaging 2007—image processing, vol. 6512. Bellingham: International Society for Optical Engineering; 2007. p. 651203.
19. Goh V, et al. Radiation dose from volumetric helical perfusion CT of the thorax, abdomen or pelvis. Eur Radiol. 2011;21:974–81.
20. Goh V, et al. Reproducibility of dynamic contrast-enhanced MRI: why we should care. Radiology. 2013;266:698–700.
21. Cenic A, et al. A CT method to measure hemodynamics in brain tumors: validation and application of cerebral flow maps. AJNR Am J Neuroradiol. 2000;21:462–70.
22. Nabavi DG, et al. Quantitative assessment of cerebral hemodynamics using CT: stability, accuracy, and precision studies in dogs. J Comput Assist Tomogr. 1999;23:506–15.
23. Goh V, et al. Quantitative assessment of tissue perfusion using MDCT: comparison of colorectal cancer and skeletal muscle measurement reproducibility. AJR Am J Roentgenol. 2006;187:164–9.
24. Ng QS, et al. Quantitative assessment of lung cancer perfusion using MDCT: does measurement reproducibility improve with greater tumor volume coverage? AJR Am J Roentgenol. 2006;187:1079–84.
25. Purdie TG, et al. Functional CT imaging of angiogenesis in rabbit VX2 soft-tissue tumor. Phys Med Biol. 2001;46:3161–75.
26. Ng QS, et al. Lung cancer perfusion at multi-detector row CT: reproducibility of whole tumor quantitative measurements. Radiology. 2006;239:547–53.
27. Erasmus JJ, et al. Inter- and intra-observer variability in measurement of non-small cell carcinoma lung lesions: implications for assessment of tumor response. J Clin Oncol. 2003;21:2574–82.
28. Goh V, et al. Quantitative assessment of colorectal cancer tumor vascular parameters by using perfusion CT: influence of tumor region of interest. Radiology. 2008;247:726–32.
29. Sanelli PC, et al. Reproducibility of postprocessing of quantitative CT perfusion maps. AJR Am J Roentgenol. 2007;188:213–8.
30. Fiorella D, et al. Assessment of the reproducibility of postprocessing dynamic CT perfusion data. AJNR Am J Neuroradiol. 2004;25:97–107.
31. Bisdas S, et al. Functional CT of squamous cell carcinoma in the head and neck: repeatability of tumor and muscle quantitative measurements, inter- and intra-observer agreement. Eur Radiol. 2008;18:2241–50.
32. Goh V, et al. Computed tomography perfusion imaging for therapeutic assessment: has it come of age as a biomarker in oncology? Invest Radiol. 2012;47:2–4.
33. Lissoni P, et al. Chemotherapy and angiogenesis in advanced cancer: vascular endothelial growth factor (VEGF) decline as predictor of disease control during taxol therapy in metastatic breast cancer. Int J Biol Markers. 2000;15:308–11.
34. Jain RK. Normalization of tumor vasculature: an emerging concept in antiangiogenic therapy. Science. 2005;307:58–62.

35. Hinnen P, Eskens FA. Vascular disrupting agents in clinical development. Br J Cancer. 2007;96: 1159–65.
36. Garcia-Barros M, et al. Tumour response to radiotherapy regulated by endothelial cell apoptosis. Science. 2003;300:1155–9.
37. Chen G, et al. Computed tomography perfusion in the evaluating the therapeutic effect of transarterial chemoembolization for hepatocellular carcinoma. World J Gastroenterol. 2008;14:5738–43.
38. Parulekar WR, Eisenhauer EA. Phase I trial design for solid tumour studies of targeted non-cytotoxic agents: theory and practice. J Natl Cancer Inst. 2004;96:990–7.
39. Hurwitz H, et al. Bevacizumab plus irinotecan, fluorouracil, and leucovorin for metastatic colorectal cancer. N Engl J Med. 2004;350:2335–42.
40. Escudier B, et al. Sorafenib in advanced clear-cell renal-cell carcinoma. N Engl J Med. 2007;356:125–34.
41. Motzer RJ, et al. Sunitinib versus interferon alfa in metastatic renal-cell carcinoma. N Engl J Med. 2007;356:115–24.
42. Llovet JM, et al. Sorafenib in advanced hepatocellular carcinoma. N Engl J Med. 2008;359:378–90.
43. Sahani DV, et al. Advanced hepatocellular carcinoma: CT Perfusion of liver and tumor tissue-initial experience. Radiology. 2007;243:736–43.
44. Li XS, et al. The value of perfusion CT in predicting the short term response to synchronous radiochemotherapy for cervical squamous cancer. Eur Radiol. 2012;22:617–24.
45. Tateishi U, et al. Contrast-enhanced dynamic computed tomography for the evaluation of tumor angiogenesis in patients with lung carcinoma. Cancer. 2002;95:835–42.
46. Goh V, et al. Can perfusion CT assessment of primary colorectal adenocarcinoma blood flow at staging predict for subsequent metastatic disease? A pilot study. Eur Radiol. 2009;19:79–89.
47. Hayano K, et al. Perfusion CT can predict response to chemoradiation therapy and survival in oesophageal squamous cell carcinoma: initial results. Oncol Rep. 2007;18:901–8.
48. Hayano K, et al. Quantitative measurement of blood flow using perfusion CT for assessing clinicopathological features and prognosis in patients with rectal cancer. Dis Colon Rectum. 2009;52:1624–9.
49. Hermans R, et al. Tumor perfusion rate determined non-invasively by dynamic computed tomography predicts outcome in head-and-neck cancer after radiotherapy. Int J Radiat Oncol Biol Phys. 2003;57:1351–6.
50. Haider MA, et al. Assessment of the tumor microenvironment in cervix cancer using dynamic contrast enhanced CT, interstitial fluid pressure and oxygen measurements. Int J Radiat Oncol Biol Phys. 2005;62:1100–7.
51. Fournier LS, et al. Metastatic renal carcinoma: evaluation of anti-angiogenic therapy with dynamic contrast enhanced CT. Radiology. 2010;256:511–8.
52. Han KS, et al. Pretreatment assessment of tumor enhancement on contrast-enhanced computed tomography as a potential predictor of treatment outcome in metastatic renal cell carcinoma patients receiving antiangiogenic therapy. Cancer. 2010;116:2332–42.
53. Bisdas S, et al. Response and progression-free survival in oropharynx squamous cell carcinoma assessed by pretreatment perfusion CT: comparison with tumor volume measurements. AJNR Am J Neuroradiol. 2009;30:793–9.
54. Bisdas S, et al. Outcome prediction after surgery and chemoradiation of squamous cell carcinoma in the oral cavity, oropharynx, and hypopharynx: use of baseline perfusion CT microcirculatory parameters vs. tumor volume. Int J Radiat Oncol Biol Phys. 2009;73:1313–8.
55. Jiang T, et al. Monitoring response to antiangiogenic treatment and predicting outcomes in advanced HCC using image biomarkers, CT perfusion, tumor density, and tumor size (RECIST). Invest Radiol. 2012;47:11–7.
56. Wang J, et al. Tumor response in patients with advanced non-small cell lung cancer: perfusion CT evaluation of chemotherapy and radiation therapy. AJR Am J Roentgenol. 2009;193:1090–6.
57. Hegenscheid K, et al. Assessing early vascular changes and treatment response after laser-induced thermotherapy of pulmonary metastases with perfusion CT: initial experience. AJR Am J Roentgenol. 2010;194:1116–23.
58. Ippolito D, et al. Hepatocellular carcinoma treated with transarterial chemoembolization: dynamic perfusion-CT in the assessment of residual tumor. World J Gastroenterol. 2010;16:5993–6000.
59. Goh V, et al. The flow-metabolic phenotype of primary colorectal cancer: assessment by integrated 18F-FDG PET/perfusion CT with histopathologic correlation. J Nucl Med. 2012;53:687–92.
60. Ippolito D, et al. Feasibility of perfusion CT technique integrated into conventional (18)FDG/PET-CT studies in lung cancer patients: clinical staging and functional information in a single study. Eur J Nucl Med Mol Imaging. 2013;40:156–65.
61. Sauter AW, et al. Correlation between [(18)F] FDG PET/CT and volume perfusion CT in primary tumours and mediastinal lymph nodes of non-small-cell lung cancer. Eur J Nucl Med Mol Imaging. 2013;40:677–84.
62. Delrue L, et al. Assessment of tumor vascularization in pancreatic adenocarcinoma using 128-slice perfusion computed tomography imaging. J Comput Assist Tomogr. 2011;35:434–8.
63. Kandel S, et al. Whole-organ perfusion of the pancreas using dynamic volume CT in patients with primary pancreas carcinoma: acquisition technique, post-processing and initial results. Eur Radiol. 2009; 19:2641–6.
64. Klauss M, et al. Computed tomography perfusion analysis of pancreatic carcinoma. J Comput Assist Tomogr. 2012;36:237–42.

65. Delrue L, et al. Tissue perfusion in pathologies of the pancreas: assessment using 128-slice computed tomography. Abdom Imaging. 2012;37:595–601.
66. Tsuji Y, et al. Perfusion CT is superior to angiography in predicting pancreatic necrosis in patients with severe acute pancreatitis. J Gastroenterol. 2010;45:1155–62.
67. Arikawa S, et al. Assessment of chronic pancreatitis: use of whole pancreas perfusion with 256-slice computed tomography. Pancreas. 2012. [Epub ahead of print].
68. Lu N, et al. 64-slice CT perfusion imaging of pancreatic adenocarcinoma and mass-forming chronic pancreatitis. Acad Radiol. 2011;18:81–8.
69. Swensen SJ, et al. Lung nodule enhancement at CT: multicenter study. Radiology. 2000;214:73–80.
70. Zhang M, Kono M. Solitary pulmonary nodules: evaluation of blood flow patterns with dynamic CT. Radiology. 1997;205:471–8.
71. Sitartchouk I, et al. Computed tomography perfusion using first pass methods for lung nodule characterization. Invest Radiol. 2008;43:349–58.
72. Ohno Y, et al. Differentiation of malignant and benign pulmonary nodules with quantitative first-pass 320-detector row perfusion CT versus FDG PET/CT. Radiology. 2011;258:599–609.
73. Fournier LS, et al. Early modifications of hepatic perfusion measured by functional CT in a rat model of hepatocellular carcinoma using a blood pool contrast agent. Eur Radiol. 2004;14:2125–33.
74. Ippolito D, et al. Perfusion computed tomographic assessment of early hepatocellular carcinoma in cirrhotic liver disease: initial observations. J Comput Assist Tomogr. 2008;32:855–8.
75. Ippolito D, et al. Perfusion CT in cirrhotic patients with early stage hepatocellular carcinoma: assessment of tumor-related vascularization. Eur J Radiol. 2010;73:148–52.
76. Ippolito D, et al. Quantitative assessment of tumour associated neovascularisation in patients with liver cirrhosis and hepatocellular carcinoma: role of dynamic-CT perfusion imaging. Eur Radiol. 2012;22:803–11.
77. Goh V, et al. Differentiation between diverticulitis and colorectal cancer: quantitative CT perfusion measurements versus morphologic criteria–initial experience. Radiology. 2007;242:456–62.
78. Trojanowska A, et al. Squamous cell cancer of hypopharynx and larynx – evaluation of metastatic nodal disease based on computed tomography perfusion studies. Eur J Radiol. 2012;81(5):1034–9.
79. Bisdas S, et al. Whole-tumor perfusion CT parameters and glucose metabolism measurements in head and neck squamous cell carcinomas: a pilot study using combined positron-emission tomography/CT imaging. AJNR Am J Neuroradiol. 2008;29:1376–81.
80. Veit-Haibach P, et al. Combined PET/CT-perfusion in patients with head and neck cancers. Eur Radiol. 2013;23:163–73.
81. Liu Y, et al. Accuracy of computed tomography perfusion in assessing metastatic involvement of enlarged axillary lymph nodes in patients with breast cancer. Breast Cancer Res. 2007;9:R40.

Perfusion Imaging by Magnetic Resonance

16

Javier Sánchez González, Antonio Luna, and L. Celso Hygino da Cruz Jr.

Contents

Abbreviations

AIF	Arterial Input Function
ASL	Arterial Spin Labeling
AUC	Area Under the Curve
BBB	Blood-Brain Barrier
BOLD	Blood Oxygen Dependent-Level
BV	Blood Volume
C(t)	Contrast Concentration in the Tissue
CA(t)	Contrast Concentration in the Feeding Arteries
CASL	Continuous ASL
CBF	Cerebral Blood Flow
CBV	Cerebral Blood Volume
D	Diffusion Coefficient
D^*	Pseudodiffusion Coefficient
DCE	Dynamic Contrast Enhanced
DSC	Dynamic Susceptibility Contrast
DWI	Diffusion-Weighted Imaging
EPI	Echo Planar Imaging
EPISTAR	Echo-Planar MR Imaging and Signal Targeting with Alternating Radio Frequency
f^v	Perfusion Fraction
FAIR	Flow Alternating Inversion Recovery
GE	Gradient Echo
IVIM	Intravoxel Incoherent Motion
k^{ep}	Transfer rate of the blood from the extravascular-extracellular space to the vessel

J. Sánchez González, PhD (✉)
MR Clinical Scientist, Philips Healthcare, Iberia, Spain
e-mail: javier.sanchez.gonzalez@philips.com

A. Luna, MD
Chief of MRI, Health Time Group, Jaén, Spain

Assistant professor of Radiology, University Hospitals, Case Western Reserve University, Cleveland, Ohio, USA
e-mail: aluna70@htime.org

L.C.H. da Cruz Jr., MD
Department of Radiology, CDPI and IRM, Rio de Janeiro, RJ, Brazil
e-mail: celsohygino@hotmail.com

Javier Sánchez Gónzalez is a full-time employee of Philips Healthcare

A. Luna et al. (eds.), *Functional Imaging in Oncology,*
DOI 10.1007/978-3-642-40412-2_16, © Springer-Verlag Berlin Heidelberg 2014

K^{trans}	Transfer rate of the blood from the vessels to the extravascular-extracellular space
MT	Magnetization Transfer
MTT	Mean Transit Time
NAA	N-Acetyl-Aspartate
PASL	Pulsed ASL
PET	Positron Emission Tomography
rCBF	Relative Cerebral Blood Flow
rCBV	Relative Cerebral Blood Volume
RCC	Renal Cell Carcinoma
RF	Radiofrequency
SE	Spin Echo
SENSE	Sensitivity Encoding for fast MRI
SPECT	Single Photon Emission Tomography
SPGR	Spoiled Gradient Echo
SSh-EPI	Single-shot Echo-Planar Imaging
TE	Echo Time
TIC	Time Signal Intensity Curve
TR	Repetition Time
TRUS	Trans Rectal UltraSound
v_e	Extracellular Extravascular Volume
v_p	Capillary Vascular Plasma volume
VSI	Vessel Size Imaging
WHO	World Health Organization
3D SPGR	3D T1-weighted spoiled gradient-echo

16.1 Introduction

Perfusion lies in the domain of the physiology trying to provide information about how efficiently the blood is providing oxygen and nutrients to the tissue and how effectively it is removing waste products from the tissue. To accomplish these objectives, fresh blood must be provided to the tissue from inflowing arteries and deoxygenated blood must be removed through the venous system.

Quantitative analysis of perfusion can be evaluated from a simplified point of view when a single organ, with a single blood supply, such as the kidney, is analyzed. If it is assumed that the organ is uniformly perfused and that the total blood is completely "used" in the capillary bed, in order to measure the blood flow into the organ, it is just necessary to quantify the total amount of contrast that reaches the organ and the organ mass (to present perfusion measurements in the usual units of ml/min/100 g). This intuitive understanding of perfusion becomes more complex when one attempts to determine the spatial distribution of perfusion within an organ and to map it as an image.

Three main approaches are used for MR perfusion studies, two of which are analogous to radioisotope tracer studies and use similar methods for analysis of the flow dynamics. One approach acquires a series of rapid T1-weighted imaging studies following the bolus administration of a gadolinium-chelated contrast agent, and an increase in tissue signal occurs as the contrast agent infuses the extravascular spaces of the tissue. This type of techniques is known as dynamic contrast-enhanced (DCE) MRI. On this approach, perfusion defects are visualized as a lack of signal increase for the affected region of tissue.

The second approach is useful if the contrast agent remains in the blood vessels, such as in cerebral tissue with an intact blood–brain barrier (BBB). In this situation, there is not any transfer of contrast agent to the extravascular space, producing minor signal variation due to T1 effect. In this case, the paramagnetic nature of the contrast agent during the arrival increases the local susceptibility, causing increased T2* dephasing of nearby tissues. Serial T2*-weighted gradient-echo (GE) or echo-planar sequences (EPI) are acquired, and the well-perfused tissue exhibits a reduction of signal relative to the pre-contrast images or the poorly perfused tissues. These techniques are known as dynamic susceptibility contrast (DSC) MRI.

These first two approaches rely on an intravenous contrast injection while the third approach does not use contrast media to highlight the flowing spins. Instead, two sets of images are acquired. One set is acquired following an MR tagging strategy, such as applying an inversion pulse in those spins that flow to the territory of interest, whereas the other set of images, obtained in basal conditions, is used as a reference. The difference image shows signal primarily from the moving spins providing perfusion information of the organ. This technique is known as arterial spin labeling (ASL).

In addition, other recent approaches of perfusion estimation have been developed with MRI.

The analysis of diffusion with intravoxel incoherent motion (IVIM) model of signal decay, permits to obtain information related with tissue blood flow through parameters, such us perfusion fraction (f_V) or the pseudodiffusion coefficient (D^*) (see Chap. 14). This technique is now beginning to be tested in the analysis of tumor perfusion, and there is limited reported data. Blood oxygen dependent-level (BOLD) MRI is a rapid noninvasive method for assessing regional tissue oxygen concentration using the paramagnetic properties of deoxyhemoglobin as an endogenous contrast agent. Therefore, BOLD MRI is also valid to estimate tissue perfusion. We will obviate this technique in the chapter as it was extensively reviewed in Chap. 12.

In this chapter we will focus on the existing techniques to evaluate perfusion information with MRI. In each case, we will describe the whole necessary process from image acquisition to image post-processing and analysis to get accurate perfusion information. In addition, a succinct review of current clinical applications of all these techniques in the brain and body is performed, with emphasis in the most appropriate MRI technique to perform according to the clinical situation.

16.2 Contrast-Based Techniques

16.2.1 Image Acquisition

16.2.1.1 Dynamic Susceptibility Contrast MRI

In anatomical regions like the brain, where under normal conditions the bolus of contrast does not pass (leakage) to the extravascular space due to the presence of the BBB, there is a minor signal variation due to T1 effect during DCE-MRI acquisition. In this case it is necessary to look for other mechanism of contrast. In this sense, gadolinium-based contrast agents increase the local susceptibility at arrival due to their paramagnetic nature. This susceptibility variation produce increased T2* dephasing of nearby tissues that can be monitoring using a dynamic T2- or T2*-weighted sequence. This procedure is known as DSC-MRI. Rapid imaging using relaxivity or susceptibility effects can be used to generate a contrast concentration time curve from the first pass of the contrast bolus. This allows the use of well-established analysis techniques to produce measures of relative cerebral blood volume (rCBV) and mean transit time (MTT). Using these parameters, it is then possible to calculate relative cerebral blood flow (rCBF) using the central volume theorem (rCBF = rCBV/MTT).

Acquisition strategies based of T2 [1] and T2* [2, 3] sequences have been proposed for DSC-MRI acquisition to evaluate the susceptibility variation produced by the first pass of contrast injection (Fig. 16.1). In all cases, image readout is normally based on single-shot echo-planar imaging (SSh-EPI) to increase the time resolution of these experiments, using a long TE for a strong weighting in T2 effects. Normally, spin-echo (SE) sequences have a TE of 100 ms while gradient-echo (GE) sequences use a TE around 35 ms.

Although, both types of image weighting (T2 and T2*) are sensible to contrast concentration, it has been described a different behavior depending on the vessel size. On one hand, SE-based maps show a stronger capillary weighting and suppression of large vessels, making that the gray-to-white matter ratio determined with the SE method is in better agreement with previous positron emission tomography (PET) and single photon emission tomography (SPECT) studies than the GE results. On the other hand, GE techniques are also sensible to large vessel perfusion [4]. For brain tumor aggressiveness differentiation, GE techniques have shown higher rCBV in aggressive tumors compared to SE sequences. In addition, equivalent dispersion levels have been found on both techniques [5].

Based on the different behavior of both acquisition techniques depending on vessel size, imaging techniques has been proposed to be able to measure the radius of the vessel. These techniques are known as vessel size imaging (VSI). Although a deep explanation of these techniques is out of the scope of this chapter, two different acquisition approaches have been proposed in the literature. The main difference between both approaches relies on the used contrast and the associated acquisition approach. The first

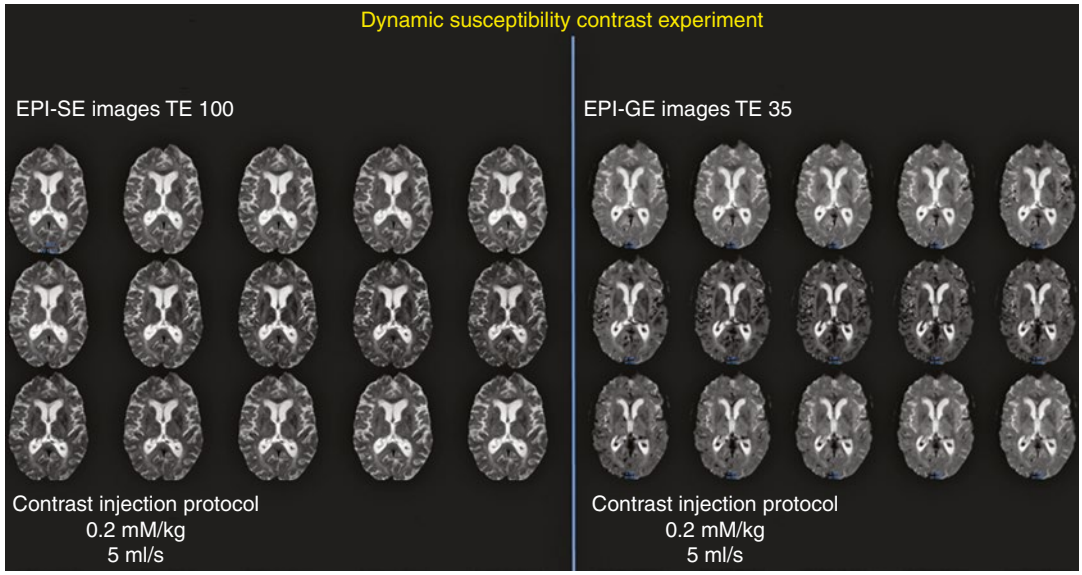

Fig. 16.1 T2- and T2*-weighted echo-planar MR image of the same slice show decreased signal intensity of brain parenchyma while bolus of paramagnetic contrast material passing through the tissues. The reduction of signal intensity is greater within the gray matter than in the white matter. In GE T2* acquisition this signal drop can be appreciated in all territories, especially in great vessels. Conversely, in SE T2-weighted images this signal drop is more pronounced in gray matter than in great vessels

approach use a super-paramagnetic contrast agent and R2 and R2* mapping techniques for the estimation of relaxation difference when the contrast is distributed in the parenchyma [6]. The second approach benefits from the first pass of gadolinium combined with a dynamic acquisition where GE- and SE-weighted images are acquired at the same time [7].

For quantitative flow results using DSC-MRI experiments, it is necessary to convert T2 changes in contrast concentration using the following equation:

$$\frac{1}{\mathrm{T2}(t)} = \frac{1}{\mathrm{T2}(0)} + r\mathrm{C}(t), \qquad (16.1)$$

where r represents the T2 relaxativity constant of the contrast, and T2(t) and T2(0) represents the T2 during the contrast passage and at the baseline. A detailed analysis of the conventional MRI signal shows that the $S(t)$ can be expressed as:

$$\mathrm{S}(t) = \mathrm{S}_0(\mathrm{T1})e^{-\frac{\mathrm{TE}}{\mathrm{T2,T2^*}(t)}}, \qquad (16.2)$$

where S_0 (T1) represents the fully T2 or T2* relaxed signal that takes into account T1 saturation effects, $S(t)$ represents the signal evolution during contrast injection, TE represents the echo time of the sequence, and T2(t) or T2*(t) the relaxation constant that will be affected by the changes in contrast concentration during the first pass of contrast. Under the assumption that there is no signal change due to T1 relaxation, S_0 (T1) remains constant during the experiment and the contrast concentration can be obtained as:

$$\Delta R2(t), \Delta R^*2(t) = -\frac{1}{\mathrm{TE}}\ln\left(\frac{S(t)}{S(0)}\right). \qquad (16.3)$$

In the case where there is also a signal variation due to T1 effects, Eq. 16.3 cannot be applied. A clear example is when the BBB is broken and the contrast goes to the extravascular-extracellular space and is accumulated along the experiment also producing faster T1 relaxation. Imaging sequences sensitive to susceptibility effects will demonstrate a decrease in signal due to contrast passage. However, unless the

sequence is insensitive to relaxivity effects, this will cause elevation of signal intensity (T1 shine-through), which may result in underestimation of rCBV [8, 9].

In order to avoid T1 effects in the signal, two different approaches have been suggested. The most common one is to inject a pre-bolus of contrast before the DSC-MRI experiment [10]. With this injection, those brain regions with broken BBB accumulates enough contrast, producing less variation due to T1 effects during the second contrast injection of the DSC-MRI experiment. This approach is combined with acquisition strategies less sensible to T1 effect, with small excitation flip angles, normally lower than 35º [10]. The second approach is to acquire dual-echo sequences [11] with a segmented EPI sequence that allows T2 and T2* estimation for each dynamic acquisition and, it does not need to refer to different dynamic acquisitions to get the relaxativity variation due to contrast concentration. Moreover, this technique allows to distinguish between T2 and T1 effect during the acquisition and, therefore, to obtain not only the conventional DSC-MRI parameters, but also the extraction fraction of the contrast to the extravascular space.

16.2.1.2 Dynamic Contrast-Enhanced MRI

The most common method to measure perfusion is known as DCE-MRI, where a dynamic imaging technique is used to monitor the time variation signal change in the tissue due to an intravenous injection of a bolus of paramagnetic tracer. The first DCE-MRI experiments were performed at mid-1980s [12, 13], but true perfusion weighting was only obtained when this signal variation could be followed at the equivalent time scale of tracer dynamics [14, 15]. Since this is the time scale of typical tracer transit times through the capillary bed, the tracer is essentially intravascular during the first pass of the bolus, providing pure perfusion weighting.

Depending on the image information that will be extracted from the images, the acquisition strategy needs to be defined. On one hand, in many clinical applications, it is sufficient to acquire a limited number of images at the baseline and during contrast pass through the tissue of interest, in order to measure the maximum enhancement and contrast washout and roughly study the enhancement pattern. This approach does not require a very high-temporal resolution acquisition, and for this reason, this approach is usually performed in most of the clinical abdominal MRI.

On the other hand, the evaluation of the whole hemodynamic perfusion information derived from DCE-MRI exams relies on the quantitative capability of the MRI techniques to provide an accurate contrast concentration along time not only in the tissue -$C(t)$- but also in the feeding arteries -$C_A(t)$-. This requirement imposes some limitation in the temporal resolution that need to be fulfilled, establishing a framework for MRI techniques applied in DCE-MRI studies.

On MRI, intravenous tracers produce a competitive T1 and T2 relaxation mechanism when used in clinical environment. Normally, T1 effects are the most relevant relaxation mechanism associating signal changes during the MRI acquisition. At the same time, the contrast arrival also presents T2* effect, especially in the feeding arteries, that needs to be reduced in order to avoid underestimation of contrast concentration in the $C_A(t)$.

Most of the sequences applied in DCE-MRI are either 2D or 3D gradient-echo sequences. The earliest approaches used a 2D sequence with a limited number of slices to achieve the high-temporal resolution required for perfusion MRI. However, since the introduction of parallel imaging and acceleration schemes for dynamic imaging [16, 17], fast 3D acquisition has become feasible and is gradually replacing 2D approaches in current practice. Moreover, 3D acquisition is less sensible to B1 artifacts reducing slice profile error of the 2D acquisition. For this reason this section will be focused on the 3D approach (Fig. 16.2), but deeper analysis of MRI techniques applied to DCE-MRI can be found elsewhere [18].

For accurate flow estimation, it is necessary to estimate the contrast concentration for every dynamic acquisition. To get this concentration it

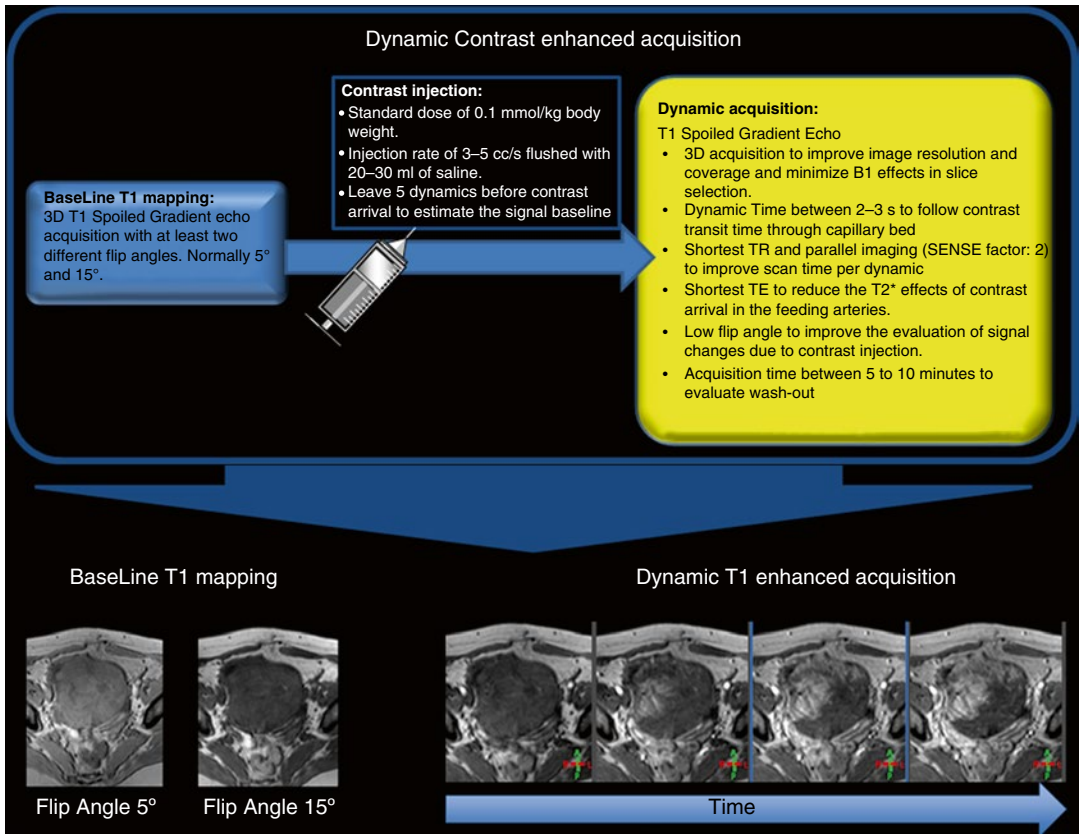

Fig. 16.2 Schematic representation of a DCE-MRI acquisition including the baseline T1 mapping, the injection protocol, and the dynamic acquisition

is possible to use the well-known T1 relation described by:

$$\frac{1}{\mathrm{T1}(t)} = \frac{1}{\mathrm{T}_{10}} + \mathrm{r}_1 C, \tag{16.4}$$

where T1(t) represents the T1 variation trough dynamic acquisition due to contrast concentration, T_{10} represents the T1 of the tissue at the baseline, r_1 represents T1 relaxativity of the contrast agent, and C represents the unknown contrast concentration. From Eq. 16.4 contrast concentration can be easily estimated if T_{10} and T1(t) are known. The easiest way to estimate this baseline T_{10} value of the tissue is acquiring a 3D T1-weighted spoiled gradient-echo (3D SPGR) acquisition with different flip angles, maintaining equal all other acquisition parameters. The optimum selection of the applied flip angle to estimate T1 values can be chosen depending on the expected T1 value [19]. The final estimated T1 value is obtained fitting the signal intensity of the images acquired with different flip angles to:

$$S = \frac{S_0 \left(1 - \mathrm{E}_1\right) \sin\left(\alpha\right)}{1 - E_1 \cos\left(\alpha\right)}, \qquad E_1 = e^{-\frac{\mathrm{TR}}{\mathrm{T}_{10}}} \tag{16.5}$$

where α represents the applied flip angle in each acquisition, S_0 represents the T1 fully relaxed signal that takes into account T2 effects, and TR represents the repetition time of the sequence.

Dynamic acquisition is also performed using a 3D SPGR acquisition strategy. The sampling rate of this sequence should be sufficient to follow the transient of the contrast through the capillary bed that is typical between 3 and 5 s. In order to

achieve this dynamic time, the shortest possible TR is chosen and parallel acquisition techniques are normally applied. To minimize the $T2^*$ effects due to contrast arrival, especially in the $C_A(t)$ estimation, the shortest possible echo time (TE) is preferable. To improve the visualization of the contrast concentration variations, it is desirable to define an optimum flip angle according to a defined range of contrast concentration and the other image parameter [20]. Finally, the number of dynamic acquisitions is chosen to cover the whole hemodynamic process, according to the enhancement pattern of the tissue, but a 5 min acquisition is normally sufficient to evaluate the tissue wash out.

16.2.2 Image Analysis

16.2.2.1 Motion Compensation

As an alternative to motion compensation approaches on the acquisition level, or complementary to them, motion correction may be performed on the post-processing level [21]. Technically, the major difficulty in DCE-MRI compared to similar problems in medical imaging is the changing signal intensities during bolus passage. The challenge for a (semi) automatic motion correction technique is to distinguish these changes from those due to motion, and the development of robust techniques remains an open problem. For an ROI-based analysis, the most straightforward approach is to redraw or modify the ROI for every individual dynamic acquisitions. The process is tedious and time consuming, difficult to automatize [22], and is not suitable for a pixel analysis. An alternative approach is based on co-registration techniques, which aim to match motion-affected images to a reference image by a rigid or nonrigid deformation of the image [23–25]. Co-registration is attractive in theory, as it fully removes motion effects and reconstructs the data that would be measured in the absence of motion. However, it is computationally challenging and usually requires expert intervention especially in those body organs where the displacement is different depending on the organ position.

16.2.2.2 Image Quantification

Different strategies can be applied to extract quantitative parameters from perfusion studies. The simplest approach uses curve descriptor like contrast arrival time (time when the contrast arrive to a pixel), time to peak (time for the maximum signal intensity), or area under the curve (AUC, integral of the contrast concentration time curve for a specific time interval definition).

On the other hand, once the contrast concentration is obtained from each dynamic acquisition, the tracer kinetic theory provides a relation between those quantities and thus forms the basis for determining the tissue status from the measured concentrations in the tissue $C(t)$ and the feeding artery $C_A(t)$. This theory establishes a relation between both quantities that follows:

$$C(t) = F_p C_A(t) \otimes R(t), \qquad (16.6)$$

where F_p is the flow of the blood plasma in the tissue, and $R(t)$ is normally called residue function and represents the fraction left in the tissue at time t of a dose injected at time $t=0$, and $\otimes$ represent the convolution operator. The residual function $R(t)$ is the relative amount of contrast in the VOI in an idealized perfusion experiment, where a unit area bolus is instantaneously injected and subsequently washed out by the perfusion.

The blood volume (BV) can be estimated as:

$$V = k_H F_p(t) \int R(\tau - t')\,dt', \qquad (16.7)$$

where the k_H represents a correction factor that takes into account the extracellular behavior of the contrast.

Following the central volume theorem, the passage of contrast can also be measured with DSC-MRI through the MTT, expressed as $MTT = V/F_p$ which gives a measure of the washout time of the blood in the volume of interest. In the case of cerebral perfusion, F_p is known as CBF and the contrast volume is known as CBV (Fig. 16.3).

One step further in this theory is the pharmacokinetic modeling of the residue function in terms of the hemodynamic parameters. The

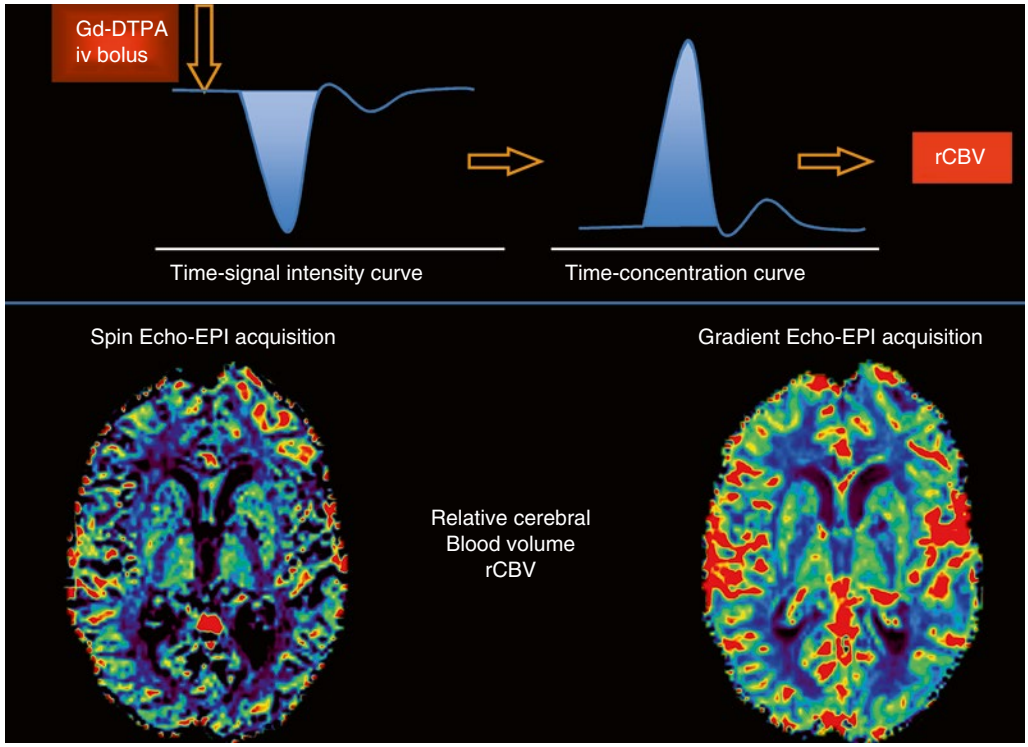

Fig. 16.3 Time-signal intensity curve demonstrates decreased signal intensity with passage of bolus of paramagnetic contrast material (*Left*, *Top row*). The *shaded area* represents the area used to calculate the rCBV. Data obtained in the time-signal intensity curve are transformed to time-contrast concentration curves (Right, *Top row*) to generate color-coded map that represents rCBV values in brain tissue. Notice the differences between the rCBV parametric maps derived form a SE-EPI and a GE-EPI sequences (*Bottom row*).

fundamental building block of any tracer-kinetic model is the compartment, often defined as a space where the tracer is well mixed or evenly distributed over the space at all times. Following this theory, the residue function can be described as a combination of different compartments:

$$F_{\mathrm{p}}R(t)=\sum_{i=1}^{n}F_i e^{-\frac{t}{\mathrm{T_i}}}, \tag{16.8}$$

where n represents the number of compartments.

Following this compartmental theory, cerebral perfusion can be seen as a single compartment model where the residual function can be expressed as:

$$R(t)=e^{-\frac{t}{\mathrm{MTT}}}. \tag{16.9}$$

In most of the tissues other than brain, standard MRI tracers distribute over two different spaces: the blood plasma P and the extravascular, extracellular space E. The two-compartment exchange model [26–28] is defined by the assumption that (1) P and E are compartments; (2) E does not exchange tracer directly with the environment; (3) the clearances for the outlets connecting P and E are equal; and (4) the clearance for the outlet of P to the environment equals the plasma flow.

There are four different situations where a tissue with this structure can be effectively reduced to a one-compartment model: (1) and (2) when one of the spaces has a negligible volume, (3) if the tracer extravasates slowly, so that, the concentration in the extravascular space is negligible within the acquisition time, and (4) if the tracer extravasates rapidly, so the system

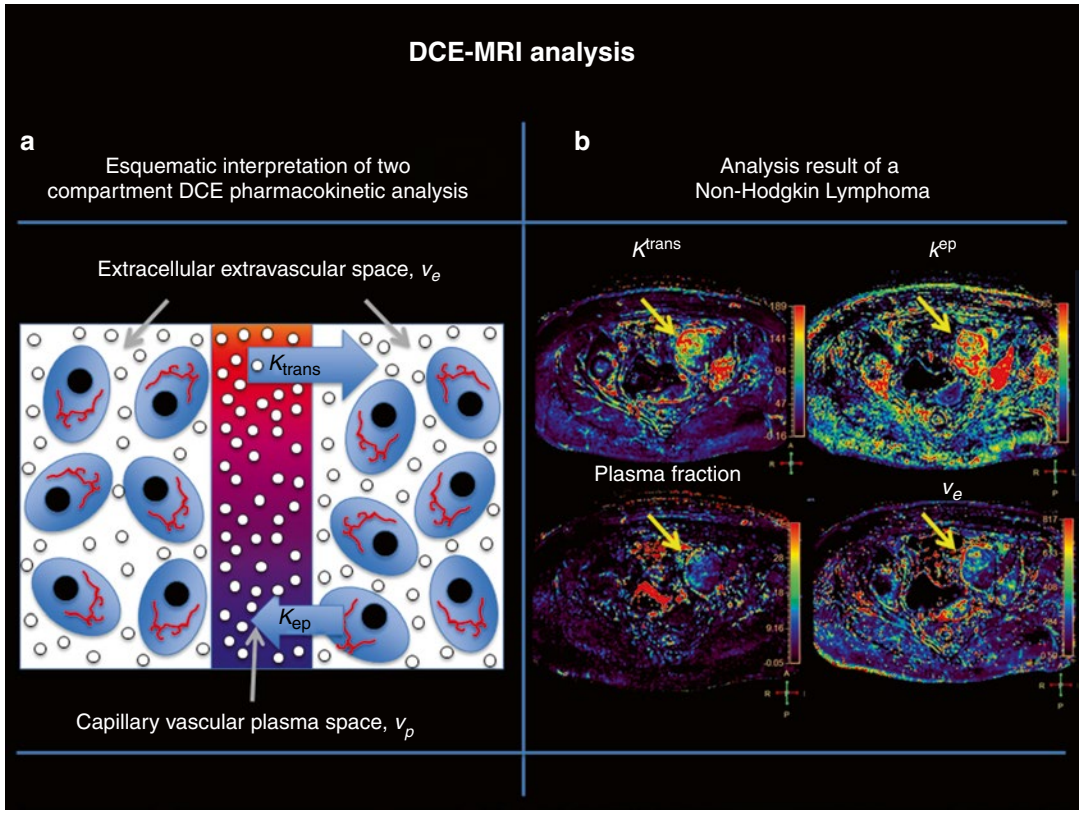

Fig. 16.4 (**a**) A graphical interpretation of the quantification parameters of a two-compartment model and (**b**) K^{trans}, K^{ep}, plasma volume and extraction volume maps obtained according to the quantification process explained in Fig. 16.2. The *yellow arrows* show the pharmacokinetic characteristics of a non-Hodgkin lymphoma, which demonstrates high permeability and perfusion

behaves as a single well mixed space. In each of these regimes, the residue function becomes mono-exponential, but the precise interpretation of the parameters is different. Hence, it is recommended to use an abstract notation K^{trans} and k^{ep} for the model parameters of a one-compartment model:

$$C(t) = K^{trans} e^{-tk_{ep}} \otimes C_A(t). \qquad (16.10)$$

A one-compartment model with these notations is often referred to as a Tofts model [29] or as a modified Tofts model when a term is added to account for the tracer in the vasculature [30]. If prior information regarding the state of the tissue is available, then K^{trans} and k^{ep} can be interpreted in more concrete terms. However, to avoid errors of misinterpretation [31, 32], it is prudent to leave the interpretation open [33, 34].

In those cases where the vascular volume cannot be neglected, it is required to include the plasma contribution in the model with a resulting total contrast concentration equal to:

$$C(t) = v_p C_A(t) + K^{trans} e^{-tk_{ep}} \otimes C_A(t),$$
$$\text{where } k_{ep} = \frac{K^{trans}}{v_e} \qquad (16.11)$$

where v_p represents the volume of plasma inside the voxel and is normally called plasma volume, v_e represents the extravascular-extracellular volume inside the voxel, K^{trans} represents the transfer rate of the blood from the vessels to the extravascular-extracellular space, and k^{ep} the transfer rate of the blood from the extravascular-extracellular space to the vessel. A graphical interpretation of these parameters can be found in Fig. 16.4 and the results of the analysis of a highly vascularized tumor.

16.2.2.3 AIF Selection

For an accurate perfusion estimation, it is necessary to obtain the arterial input function (AIF) of a contrast agent $C^A(t)$; the time-concentration curve in plasma has long presented a problem in MR DCE-MRI and DSC-MRI studies. A poor estimation of the AIF due to insufficient time sampling or signal saturation effects produces substantially increase bias in the estimated hemodynamic and permeability maps [28]. To overcome this limitations, some authors have proposed to use a simplified functional form for the AIF, which is assumed valid for all individuals [35, 36]. However, others have shown that using a simplified standard AIF can lead to large systematic errors in kinetic tracer model output parameters, such as the volume transfer constant K^{trans} and the fractional blood volume [37, 38]. Because interindividual variations in heart rate and kidney function have the potential to lead to differences in the AIF form, the use of an accurately measured AIF for each subject is often the preferred approach, even though it is only attainable in a minority of studies [35, 39]. It is often not possible to perform a reliable AIF measurement due to experimental constraints or due to the lack of a suitable artery in the field of view. Hence, recent published work [40] of a clinical DCE-MRI study has suggested the use of an assumed form of AIF that is sufficiently similar to the true AIF to allow estimation of model parameters. Parker et al. [40] demonstrated that in the presence of measurement errors in an experimentally acquired AIF, there are significant benefits to be gained in the reproducibility of compartmental model parameters by using an assumed form. However, there have been limited studies conducted, so far, to quantify the effects of using an assumed form of AIF in experimental models or in differentiating the effects of varying assumed AIF forms, including population averages.

16.2.3 Contrast Agents and Injection Protocol

DCE-MRI may be performed using low-molecular-weight contrast media or macromolecular contrast media. Most of published DCE-MRI studies in the body have used low-molecular-weight contrast media because of their clinical availability. Due to space constraints, this review will not refer to DCE-MRI with macromolecular contrast agents. Any of the commercially available gadolinium chelates of 0.5 mM concentration are useful to measure first-pass perfusion, but in order to analyze permeability, it is preferable to avoid the use of protein-bound tracers, as they need of a complex specific analysis.

Most commonly, a standard dose of 0.1 mmol/kg body weight is recommended, using an injection rate of at least 3 cc/s flushed with 20–30 ml of saline.

DSC-MRI is usually performed with extravascular-extracellular gadolinium chelates. Some authors advocate for the use of protein-bound tracers or agents with double-gadolinium concentration due to better contrast enhancement and better diagnostic performance in many clinical situations due to higher relaxivity [41]. In DSC-MRI, a dose of 0.1 mmol/kg of gadolinium-based contrast agent is enough for adequate diagnostic performance. Injection protocol requires fast injection rates (ranging from 3 to 5 mL/s bolus injection rate) for stronger arrival effect of the contrast followed by a 20–30 mL saline flush at the same rate.

16.3 Non-Contrast-Based Techniques

16.3.1 Arterial Spin Labeling

Among MRI methods, arterial spin labeling (ASL) techniques have shown their potential for tissue perfusion quantification. The complete noninvasiveness and nonionizing nature of this technique makes ASL a very interesting method for studying perfusion in healthy individuals or patients who require repetitive follow-ups. Furthermore, the use of any radioactive tracers or exogenous contrast agents, which are necessary in most conventional techniques, may be restricted in patients with particular conditions, such as kidney failure, or in pediatric populations. Finally, ASL-based methods are useful for functional studies and evaluations of new therapies, in which physiological changes due

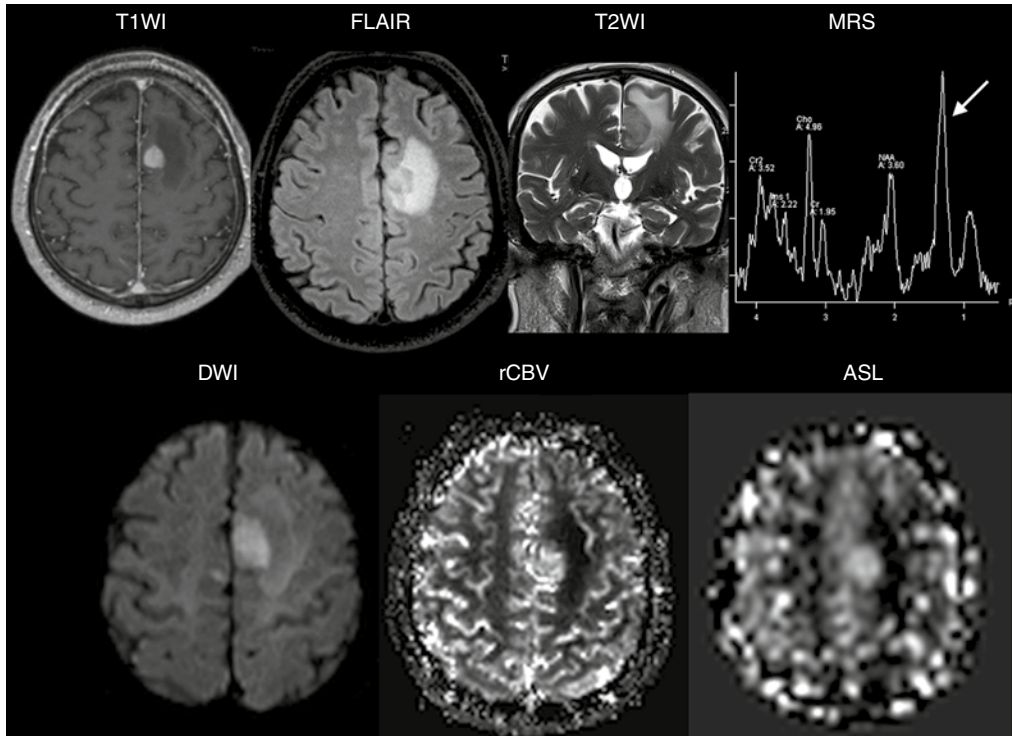

Fig. 16.5 A 47-year-old woman with Hodkgin lymphoma complaining of new onset of seizures. A round-enhancing lesion is demonstrated in the parasagittal aspect of the left frontal lobe, surrounded by vasogenic edema. The lesion also presents restricted diffusion, secondary to its hypercellularity. MR spectroscopy shows elevated picks of choline and lactate/lipids (*arrow*) and reduction of NAA. The lesion demonstrates high perfusion on both rCBV and ASL maps related to brain involvement by lymphoma

to the pharmacological stimuli must be monitored over time. Due to movement artifacts, most of the clinical experience of ASL has been limited to the brain (Fig. 16.5), although recently it has been proven useful in body organ such as kidney.

The common goal of all existing ASL techniques is to produce a flow-sensitized image (also known as a labeled image) and a control image in which the static tissue signals are identical. This is usually performed by inverting or saturating the water protons in the blood supplying the imaged organ. After a delay between labeling and image acquisition, called the inversion delay (TI), the labeled blood spins reach the capillaries, where they exchange with tissue water, giving rise to the perfusion signal. The subtraction of the label from the control yields a difference signal that directly reflects local perfusion, since the signal from stationary tissue is completely eliminated.

There exist two main classes of ASL techniques: continuous ASL (CASL) and pulsed ASL (PASL). In CASL, the supplying blood is continuously labeled below the imaging slab, until the tissue magnetization reaches a steady state. The PASL approach labels a thick slab of arterial blood at a single instance in time, and the imaging is performed after a time long enough to allow the spatially labeled blood to reach the tissue and exchange at the region of interest. Both methods need a control experiment in order to visualize and quantify the perfusion (Fig. 16.6).

16.3.1.1 Continuous Arterial Spin Labeling

The original ASL method proposed by Detre and Williams et al. [42, 43] in 1992 used a continuous flow-driven adiabatic inversion scheme, a method that was previously used for angiography [44]. This type of adiabatic inversion of the arterial

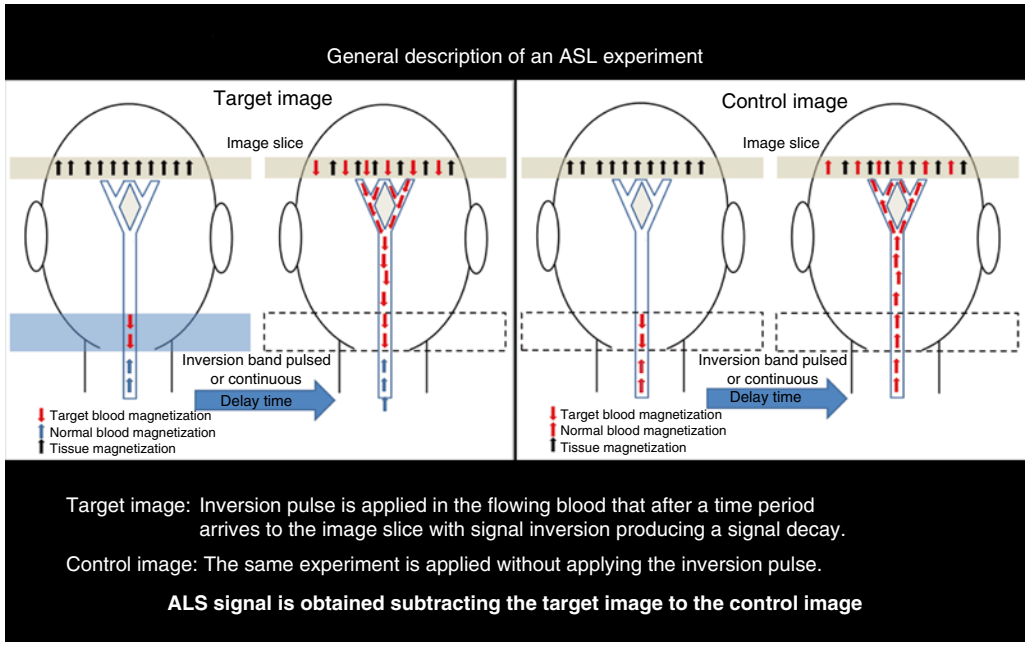

Fig. 16.6 A schematic representation of an ASL experiment is presented where two sets of images are acquired with and without the application of an inversion pulse to the flowing blood. In the first experiment an inversion pulse is applied producing a signal drop in the slice image due to the inverted spins of the target blood. In the second experiment there is no signal drop due as none inversion pulse is applied. The difference between both images provides perfusion information

magnetization is performed using a 2–4 s continuous radiofrequency (RF) pulse, while applying a magnetic field gradient in the flow direction. The moving arterial spins will therefore experience a slow variation of the resonance frequency, which will result in their inversion, while static (tissue) spins will just be saturated. The use of long inversion pulses produces strong magnetization transfer (MT) effect during the labeling procedure that needs to be compensated as well during control image acquisition. In the first implementation, MT effects were compensated by applying a distal labeling during the control experiment. This produces identical saturation effects but, due to the applied gradients during labeling, this is unfortunately valid only for a single slice. For multi-slice acquisition, Alsop et al. [45] proposed the use of two closely spaced inversion planes, also called double adiabatic inversion. In the control experiment, the magnetization gets inverted while traversing the first plane and returns theoretically to its original state during the passage through the second plane.

16.3.1.2 Pulsed Arterial Spin Labeling

In 1994, Edelman et al. [46] proposed the first pulsed ASL scheme. Contrary to CASL, the labeling is performed once in a 10–15 cm slab proximal to the image slices. For the PASL sequences, MT effects have to be considered as well, although these are much smaller compared with CASL. In this first version of the "Echo-Planar MR Imaging and Signal Targeting with Alternating Radio frequency" (EPISTAR) sequence, inversion was performed distal to the image slice during the control experiment to induce identical MT effects in both cases. Again, this truly compensates for a single slice only and, therefore, the sequence was modified for multi-slice acquisition using a single 180° adiabatic pulse for the label experiment and two 180° + 180° pulses of half the power for the control experiment at the same proximal location [46, 47].

Shortly afterwards, an alternative to this asymmetric method of labeling was proposed by Kwong et al. [48] and independently by Kim [49], who named it flow alternating inversion

recovery (FAIR). Here, the label is applied using a nonselective inversion pulse, while the control employs a concomitant slice-selective gradient pulse. The symmetric nature of this sequence automatically compensates for MT effects.

PASL allows inversion of the arterial spins closer to the image slices and the inversion efficiency is improved; however, due to imperfect inversion profiles, a gap between the labeling region and the image slices of typically 1–2 cm is needed, depending on the type of RF pulse used. This increases transit time from the labeling slab to the imaging slices leading to decreased efficiency. In addition, T1 relaxation of all the inverted spins will also result in a theoretically lower signal difference. Nevertheless, the ease of implementation and reduced practical problems, as compared with CASL, has made PASL a popular choice for perfusion imaging.

16.3.1.3 ASL Perfusion Quantification

Having acquired the data using either technique, the subtracted control-label images will be perfusion weighted. The relationship between the ΔM signal and the actual CBF depends mainly on proton density and T1 relaxation rates of tissue and inflowing blood and their respective differences. In addition, the label transit time from the inversion slab to the observed region in the images is also an important factor. Traditionally, quantitative CBF estimation is carried out using the tracer clearance theory originally proposed by Kety and Schmidt [50] which was first adapted to ASL experiments by Detre and Williams et al. [42, 43]. In the original model, it is assumed that the labeled arterial blood water is a free diffusible tracer, implying that the exchange of blood water with tissue water happens instantaneously upon its arrival to the parenchyma. Therefore, this model corresponds to a single compartment tracer kinetic, described by a mono-exponential tissue response function. In the original quantification model, further assumptions about uniform plug flow and equal T1 relaxation of both tissue and arterial blood were made [42]. Buxton et al. [51] proposed a general kinetic model where the magnetization difference between labeled and control measurements were described using the convolution integral between a particular arterial input function and to consider a certain exchange mechanism (CASL and PASL experiments) and the mono-exponential tissue response.

16.3.2 Intravoxel Incoherent Motion

Diffusion-weighted imaging (DWI) is an MRI technique sensible to microscopic mobility of water and is classically referred as Brownian motion. This mobility is due to thermal agitation and is highly influenced by the cellular environment of water. In oncologic imaging, DWI has been linked to lesion aggressiveness and proposed to evaluate tumor response, although the biophysical basis for this is incompletely understood. In biologic tissues, these motions include molecular diffusion of water and microcirculation of blood in the capillary network (perfusion). Molecular diffusion refers to physical properties of tissue that allow tissues to be characterized. The sensitivity to water movement is controlled by a sequence parameter called *b* value. This acquisition parameter controls the water dephasing due to the movement; when this parameter increases, the signal from water molecules with a higher movement disappears, remaining only the signal from those water molecules with restricted movement. In this scenario microcirculation of blood or perfusion can also be considered an incoherent motion due to the pseudorandom organization of the capillary network at the voxel level that can be imaged using low *b* values during the diffusion acquisition.

IVIM imaging is a method initially developed by Le Bihan et al. [52] to quantitatively assess the microscopic translational motions that occur in each image voxel at MRI. Le Bihan et al. [52, 53] demonstrated that both pure molecular diffusion and microcirculation, or blood perfusion, can be distinguished by using IVIM analysis of diffusion signal decay. For this, it is necessary to obtain multiple *b* values to encompass both low *b* values (<200 s/mm^2) and high *b* values (>200 s/mm^2). The low *b* values are used to study the fast water movement associated to the blood flowing

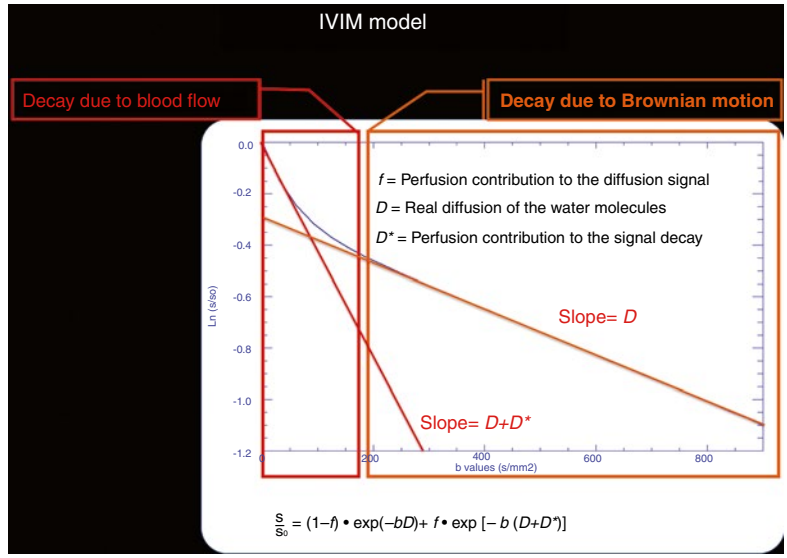

Fig. 16.7 This figure represents a graphical interpretation of IVIM model. In the first part ($b < 200$ s/mm^2) of the diffusion decay curve, there is a fast signal drop related to the blood flowing through the capillary network organized in a random manner. The second part of the curve represents the signal decay due to normal diffusion of the tissue

through the capillary network in a pseudorandom manner. Conversely, for b values over 200 s/mm^2, the signal information from the capillary network is completely dephased obtaining only signal from the extravascular space (Fig. 16.7).

16.3.2.1 IVIM Quantification

Following the diffusion theory the signal variation with the b values can be expressed as:

$$S = S_0 e^{-bD}, \tag{16.12}$$

where S is the acquired signal intensity for each b value; S^0 is the signal intensity when there is no diffusion weighted applied, and D is the diffusion coefficient that represents the water mobility inside the studied voxel.

Under the IVIM theory where the blood flow mimics the diffusion process, the signal is also modeled equivalent to equation to Eq. 16.12

$$F = e^{-bD^*}, \tag{16.13}$$

where D^* represents the fast signal decay due to blood flow and is normally referred as perfusion-related diffusion. Combining the information of both tissues, diffusion territories is obtained:

$$S = S_0 e^{-bD}\left[(1-f)+fe^{-bD^*}\right], \tag{16.14}$$

where f represents the perfusion fraction, which corresponds to the portion of the signal decay explained by the blood. Under this model D represents the free perfusion-diffusion coefficient (Fig. 16.8).

16.4 Clinical Applications in Oncology of perfusion-weighted MRI

16.4.1 Clinical Applications in Brain Tumors

16.4.1.1 Tumor Grading

There is a strong correlation between astrocytoma grading and tumor rCBV. One of the characteristic features of high-grade tumors relative to low grade is a higher degree of vascular proliferation related to neoangiogenesis, which can be assessed by rCBV. Thus, perfusion rCBV maps can provide relevant information regarding tumor grading, as low-grade gliomas have low rCBV (Fig. 16.9) and high-grade gliomas have high rCBV (Fig. 16.10). Some authors also proposed that rCBV measurement has the capability to predict progression and survival [54]. Therefore, a threshold value (1.75) can be proposed to suggest such differentiation, with also the ability to predict progression-free survival (Fig. 16.11) [54].

In a previous publication, rCBV demonstrated a better correlation to progression-free

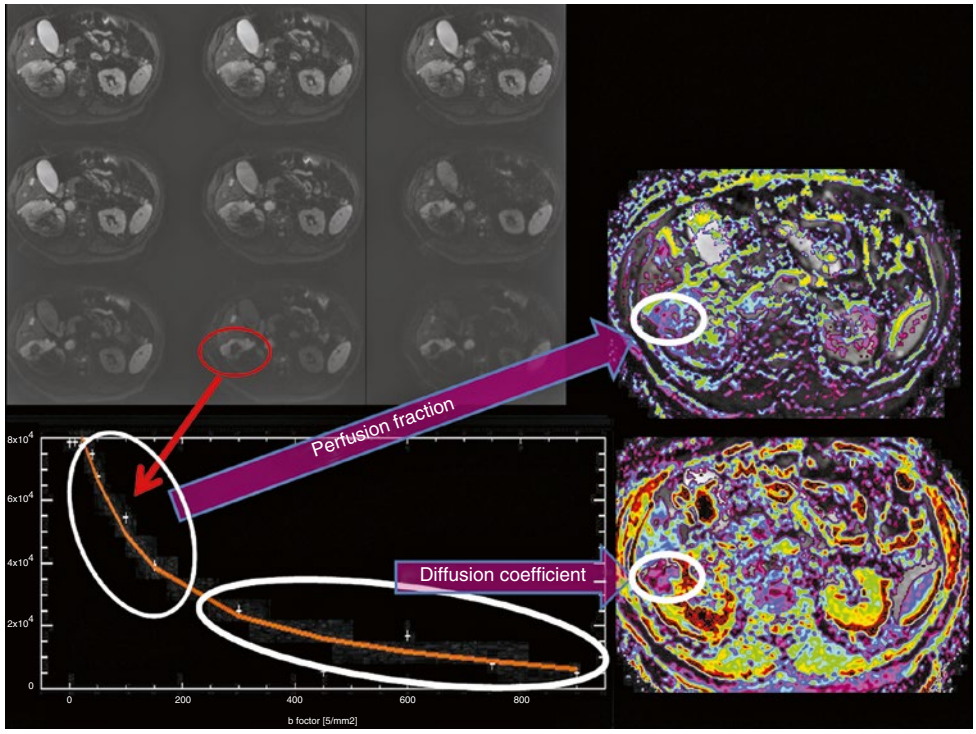

Fig. 16.8 IVIM analysis of round cell carcinoma of the right kidney. Several *b* values under and over 100 s/mm^2 are necessary to model the diffusion-signal decay in a bicompartmental model. The firs fast decay permits to obtain information about tumor moving flow (perfusion fraction map) and posteriorly, the more flattened signal decay of diffusion permits the quantification of tissue diffusivity without perfusion contamination (diffusion coefficient)

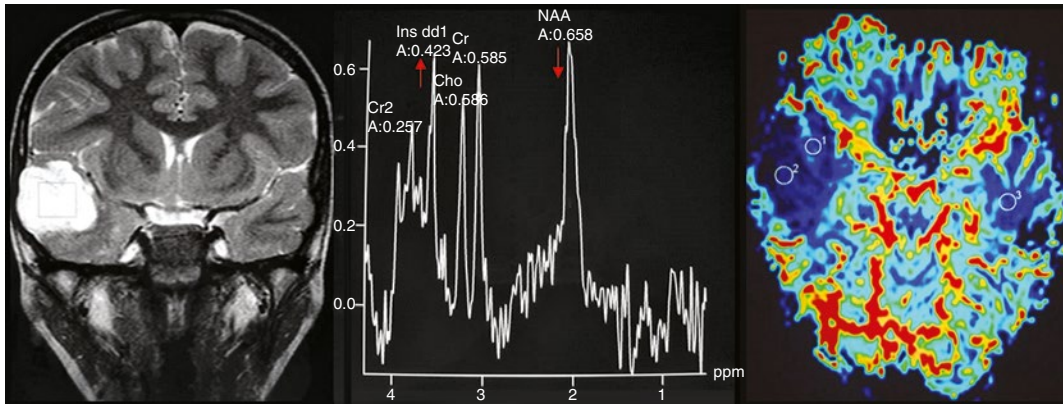

Fig. 16.9 Low-grade glioma. A 5-year-old boy with seizures. An expansive right temporal lobe lesion is demonstrated in the T2-weighted image. MR spectroscopy shows an elevation on myoinositol and a slight elevation of choline. A reduction of NAA is also shown. On DSC-MRI, the lesion presents low rCBV values

survival than the histopathology grading [55]. Potentially rCBV measurements could overcome some limitations of current histological methods, providing additional prognostic factor for tumor biology. Thus, perfusion MRI could also be used to identify the location that demonstrates the highest rCBV values. This allows for a more accurate targeting of stereotactic biopsy in

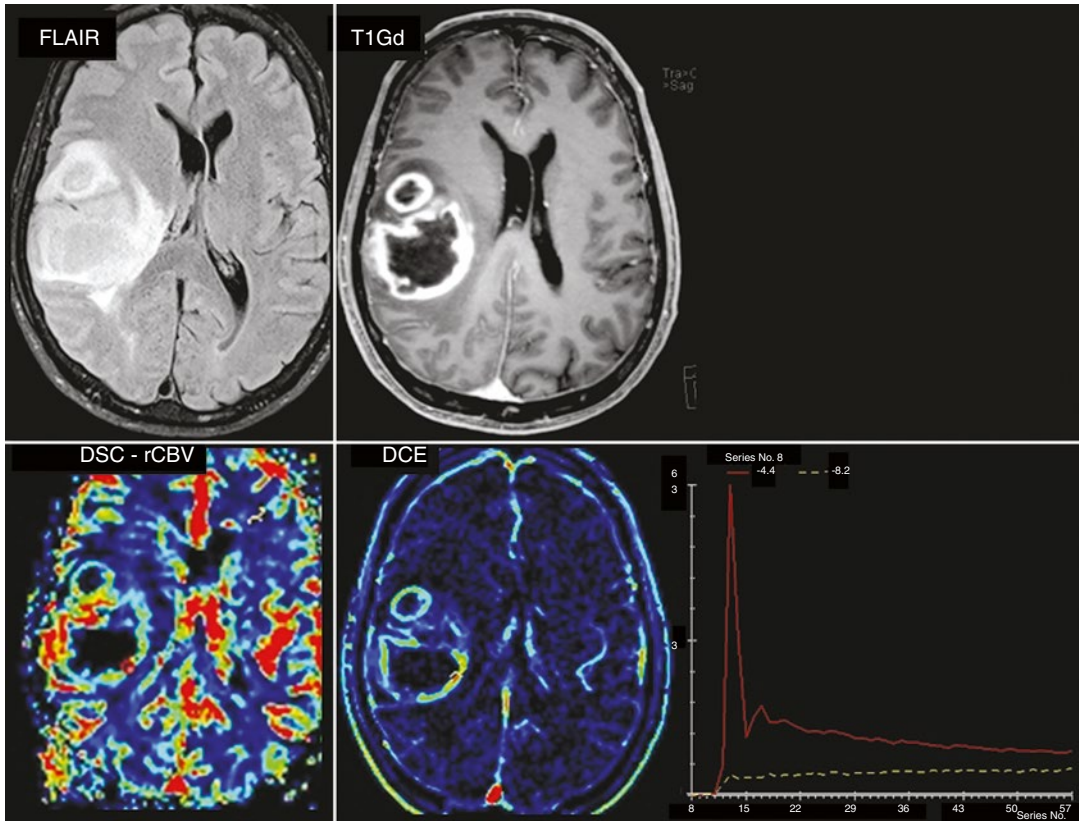

Fig. 16.10 A 58-year-old man with GBM. An expansive, necrotic lesion with irregular and peripheral contrast enhancement surrounded by an abnormal hyperintense area on FLAIR images. The lesion presents high rCBV on DSC-MRI and high permeability on DCE-MRI consistent with high-grade glial tumor

order to avoid an understaged tumor. Not least, rCBV maps can be able to identify within a low-grade lesion areas of malignant transformation or tumor dedifferentiation before they are visible on conventional imaging (Fig. 16.12) [56]. In addition, ASL has also been proposed to predict the difference between high- and low-grade gliomas [57].

On the other hand, the use of rCBV to grade gliomas has in the other hand some limitations. Several low-grade gliomas may have elevated rCBV and therefore can be misclassified as high grade, resulting in a false-positive analysis. Nonfibrillary astrocytoma, like oligodendrogliomas, may have high rCBV regardless of grade [58, 59]. Despite these shortcomings, the WHO classification remains the standard reference system to guide brain tumor management [60].

16.4.1.2 Nonastrocytic Gliomas

Nonastrocytic gliomas, like oligodendrogliomas, may have high rCBV even in low-grade subtypes (Fig. 16.13) and can be, in some cases, misdiagnosed as a high-grade neoplasm [58, 59]. However, there are others MRI features on conventional sequences that might help in the diagnosis of oligodendroglioma, like cortical involvement, frontal lobe predominance, calcification, and intratumoral cysts.

Choroid plexus papilloma is a highly vascular intraventricular glioma, fed by choroid plexus capillaries, which does not contain blood–brain barrier. Thus, this lesion has high contrast enhancement, due to marked gadolinium leakage. On DSC-MRI images, the susceptibility-weighted signal intensity curve never returns towards baseline because neoplasm vasculature lacks of blood–brain barrier and

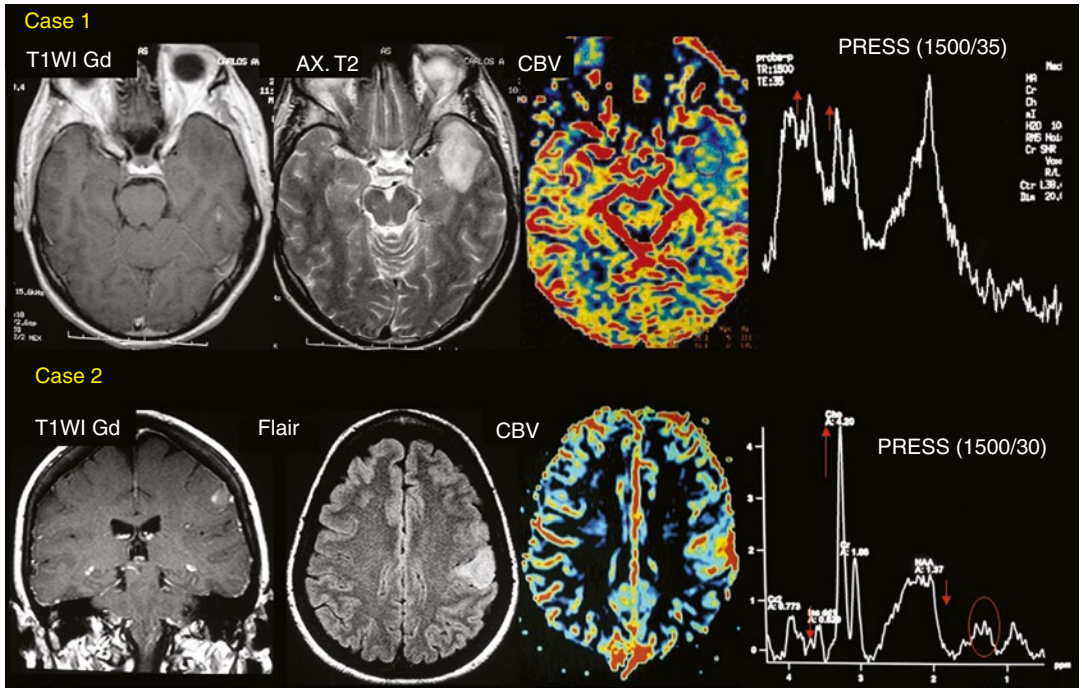

Fig. 16.11 Case 1. A 51-year-old man with a diagnosis of low-grade glioma presented with seizures and headache. The lesion does not enhance after contrast administration and MRS demonstrates elevation of choline and myoinositol and a reduction of NAA. Low rCBV on DSC-MRI suggests a low-grade glial tumor. Case 2. A 51-year-old woman with a diagnosis of high-grade glioma presented with early onset of seizures and right facial palsy. A slightly enhancing cortical lesion with high perfusion is seen. MRS shows a marked elevated choline and reduction of NAA, as well as presence of lipids/lactate. High CBV on DSC-MRI suggests a high-grade glial tumor

a marked contrast leakage occurs during the contrast administration (Fig. 16.14) [58, 59].

16.4.1.3 Non-gliomas Brain Tumors

Metastasis

Some reports suggest that high-grade gliomas have a higher rCBV than metastasis. The vasculature of metastatic lesions contains capillaries that are highly leaky. Then, the susceptibility-weighted signal intensity curve demonstrates a profound leakage of gadolinium during the contrast administration, similar to the observed in the choroid plexus papilloma. The evaluation of the abnormal peritumoral region can also be useful in differentiating primary to secondary brain tumors. The infiltrative edema of gliomas has a higher rCBV than the vasogenic edema surrounding metastatic lesions (Fig. 16.15) [56, 61].

Lymphoma

Distinction between lymphoma and high-grade gliomas can be extremely difficult to neuroradiologists, as these two lesions can have similar imaging features on conventional MRI sequences. Although rCBV can be slightly elevated on lymphoma, rCBV tends to be lower when compared to high-grade lesions (Fig. 16.16). This is likely because neovascularization is not a typical histological feature of this neoplasm [58, 59, 62].

Meningioma

Meningioma can be classified as being benign (WHO grade I) or atypical (WHO grade II). Atypical meningioma tends to be more aggressive and usually recurs after surgical resection. DCE-MRI is considered to be able to determine the meningioma grade. Atypical variants are associated with higher permeability than typical

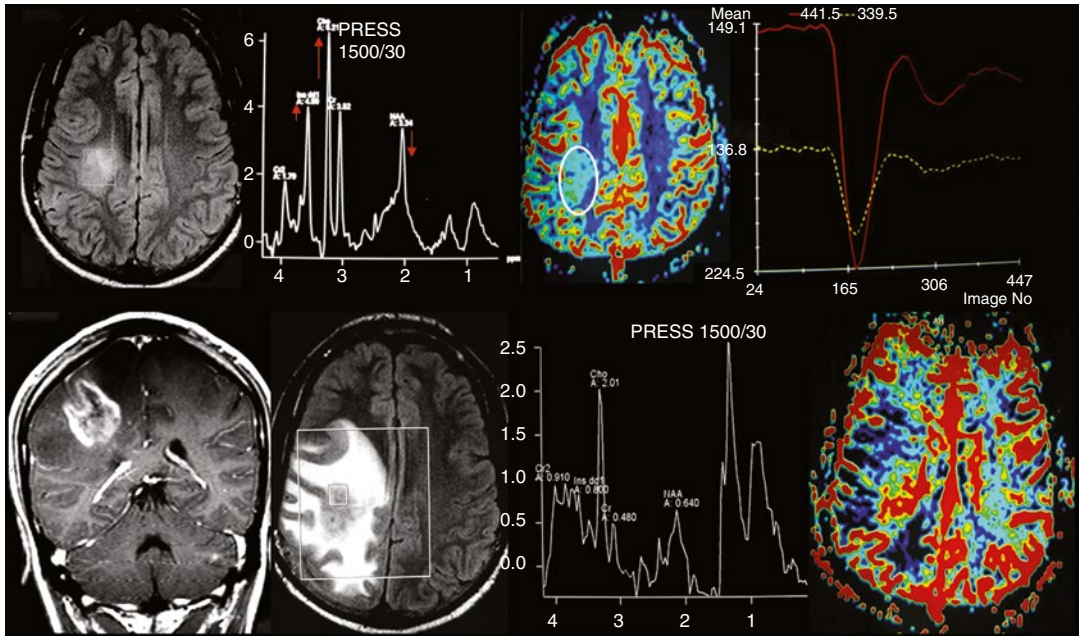

Fig. 16.12 A 21-year-old man with left hemiplegia and seizures, with a biopsy proven low-grade glioma. Presurgical MRI (*top row* images) demonstrated an infiltrative lesion on FLAIR image, with increased perfusion on DSC-MRI. MRS shows elevation of choline and myo-inositol as well as a reduction of NAA, typical of low-grade gliomas. Some months after surgery, the patient got worst clinically and MRI (*bottom row* images) demonstrated progression of both the enhancing portion of the lesion and the surrounding hyperintense area on FLAIR. MRS shows a marked elevation of choline and lipids/lactate and a reduction of NAA. A marked elevation on rCBV values was also demonstrated. A new surgery confirmed the diagnosis of high-grade glioma

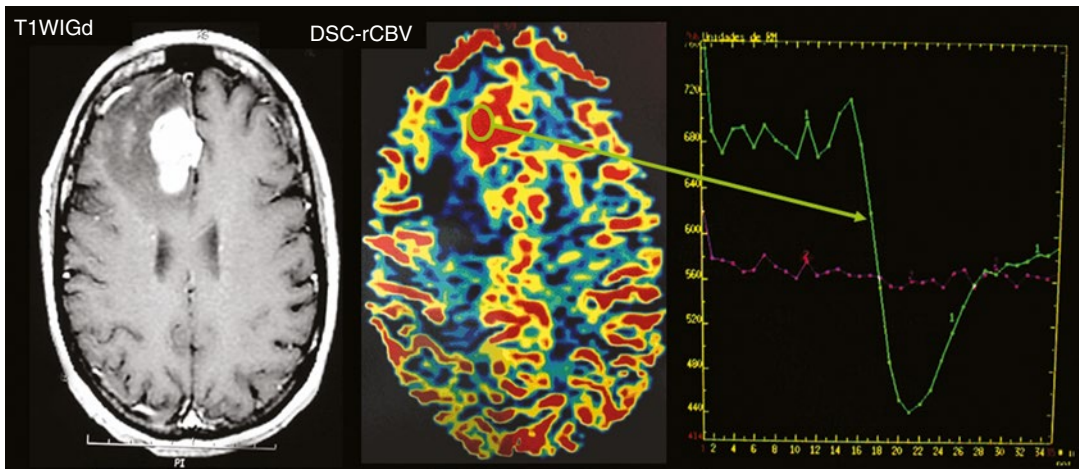

Fig. 16.13 A 52-year-old woman with oligodendroglioma. An expansive-enhancing right frontal lesion with high perfusion (increased rCBV on DSC-MRI) is seen

variants, which have lower permeability [58, 59, 63]. The dynamic perfusion curves generated by using DSC-MRI with respect to the permeability between intravascular and extravascular compartments can provide additional information regarding the differentiation between benign and

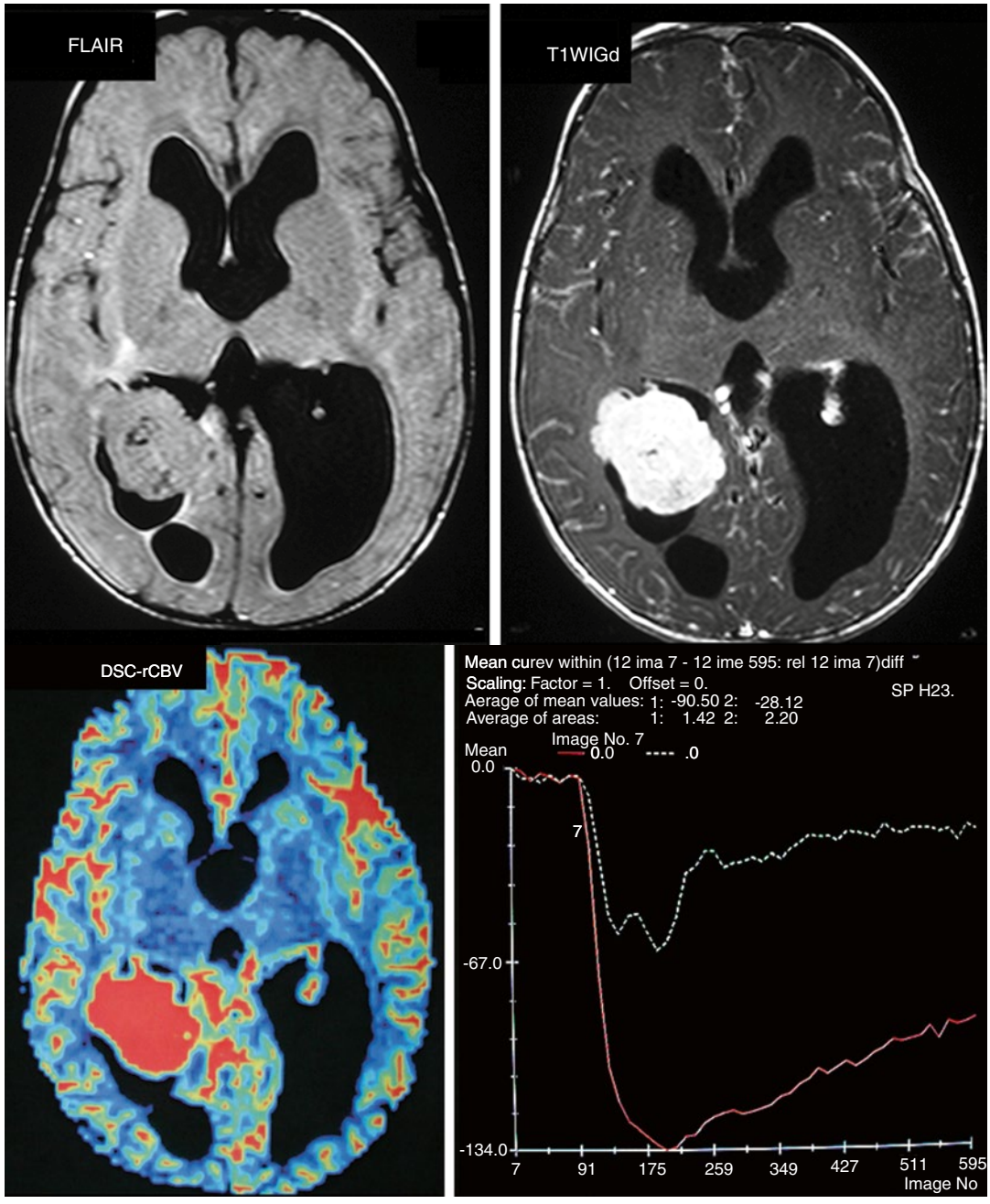

Fig. 16.14 Choroid plexus papilloma. A 22-month-old boy presented with seizures and elevation of the cephalic circumference. An expansive-enhancing lesion is seen at the right posterior choroid plexus topography. The lesion presents a high rCBV value and the time-signal intensity curve (TIC) does not return towards baseline, due to marked contrast leakage

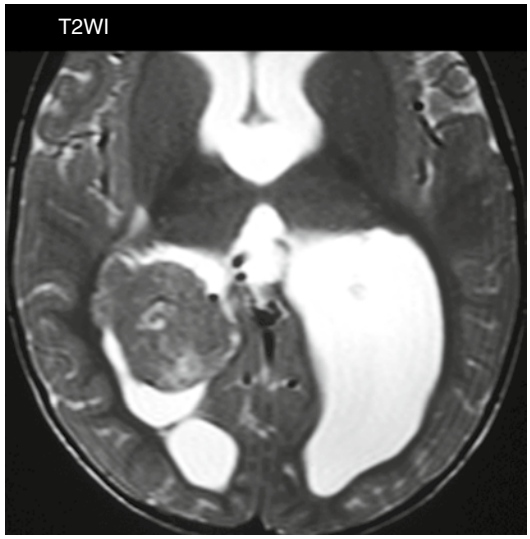

Fig. 16.14 (continued)

atypical meningiomas (Fig. 16.17) [63]. DSC perfusion MRI can also determine the maximal rCBV in the peritumoral edema, what can be useful in the differentiation between benign and malignant meningiomas [64]. Furthermore, ASL may also be useful in distinguishing different subtypes of meningioma [65].

16.4.1.4 Posttreatment Tumor Evaluation

Several studies have demonstrated a relationship between rCBV in gliomas and overall survival. The change in rCBV values measured prior to treatment and after the first 6 weeks of therapy is considered to allow prediction of treatment outcome at 6 months. Changes in rCBV values can be more sensitive than that observed on contrast enhancement tumor size to predict outcome [66, 67].

16.4.1.5 Distinction Between Radiation Necrosis and Tumor Recurrence

The differentiation between radiation necrosis and recurrent or residual tumor remains a challenge in the clinical management. Conventional MRI was unable to predict such difference. Most of the time, these entities coexist when histopathology analysis is performed. Previous reports showed that radiation-induced necrosis has lower rCBV values than the observed in tumor recurrence. Although several studies demonstrated the ability of DSC-MRI to differentiate radiation necrosis from tumor recurrence, to date accurate threshold rCBV values had not yet been validated (Fig. 16.18) [54, 58–60].

16.4.1.6 Tumor-Mimicking Brain Lesions

Abscess

Abscess can be difficult to differentiate from necrotic brain neoplasm based only in conventional MRI sequences. DSC-MRI can demonstrate such difference. Abscess tends to have low rCBV when compared to normal white matter, whereas rCBV values are generally higher in high-grade gliomas and metastasis (Fig. 16.19) [68].

Tumefactive Demyelinating Lesion

DSC-MRI can be useful in differentiating tumefactive demyelinating lesions from brain neoplasms. Demyelinating plaques demonstrate lower rCBV values than brain neoplasms (Fig. 16.20). However, despite the generally decreased cerebral blood flow in inflammatory lesions, a transient increase may be identified in the very early phase of the formation of these lesions [69]. On the source images of DSC-MRI, it is possible to identify vessels within the demyelinating lesion, as the histopathological process consists of perivascular inflammatory infiltration and demyelination (Fig. 16.21).

16.4.2 Clinical Applications in the Body

DCE-MRI in body applications is a broad term that refers to dynamic multiphase contrast-enhanced MRI. It includes two different approaches: (1) low temporal resolution DCE-MRI, which is the heart of almost every abdominopelvic MRI protocol. This approach uses few T1-weighted measurements with high spatial resolution (Fig. 16.22a). (2) Conversely, perfusion MRI needs of multiple fast T1-weighted repetitions with limited coverage and reduced spatial resolution (Fig. 16.22b).

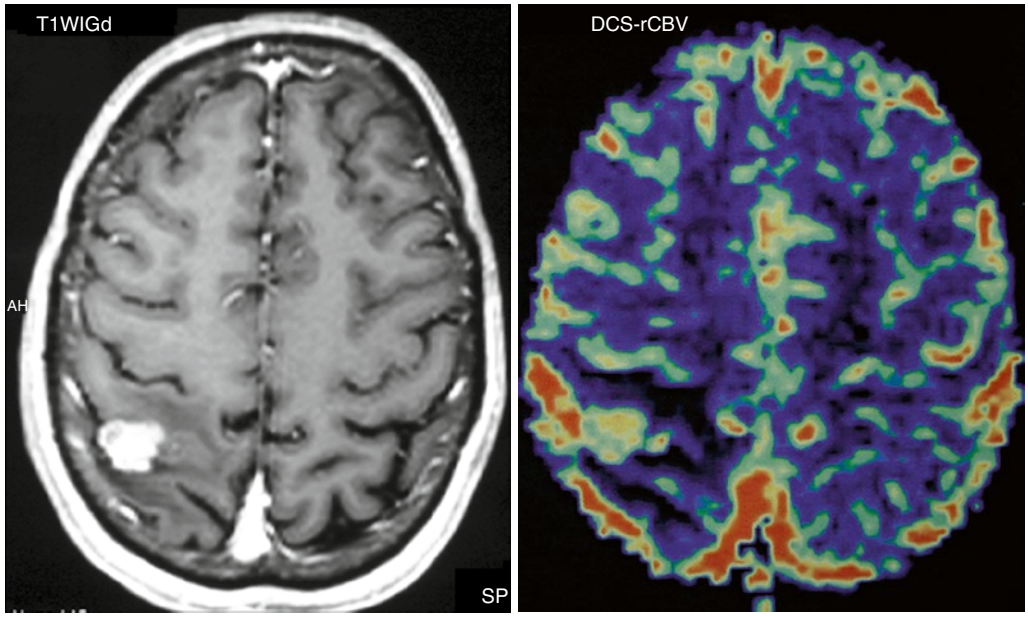

Fig. 16.15 A 37-year-old woman with breast cancer presented early onset of simple partial seizures. A round expansive contrast-enhancing lesion in the post central gyrus is demonstrated. DSC-MRI demonstrated a high rCBV within the lesion, but not at the surrounding area in this brain metastasis

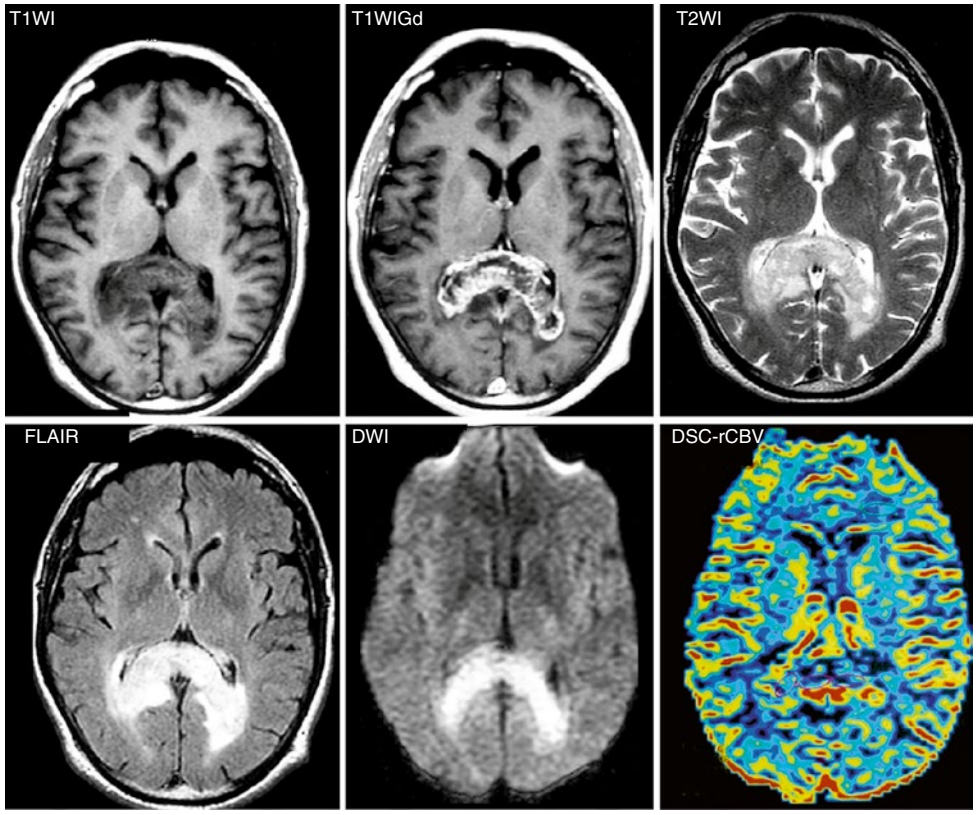

Fig. 16.16 Lymphoma. A 63-year-old man with cognitive impairment. An expansive-enhancing and infiltrating corpus callosum lesion with restricted diffusion and low rCBV

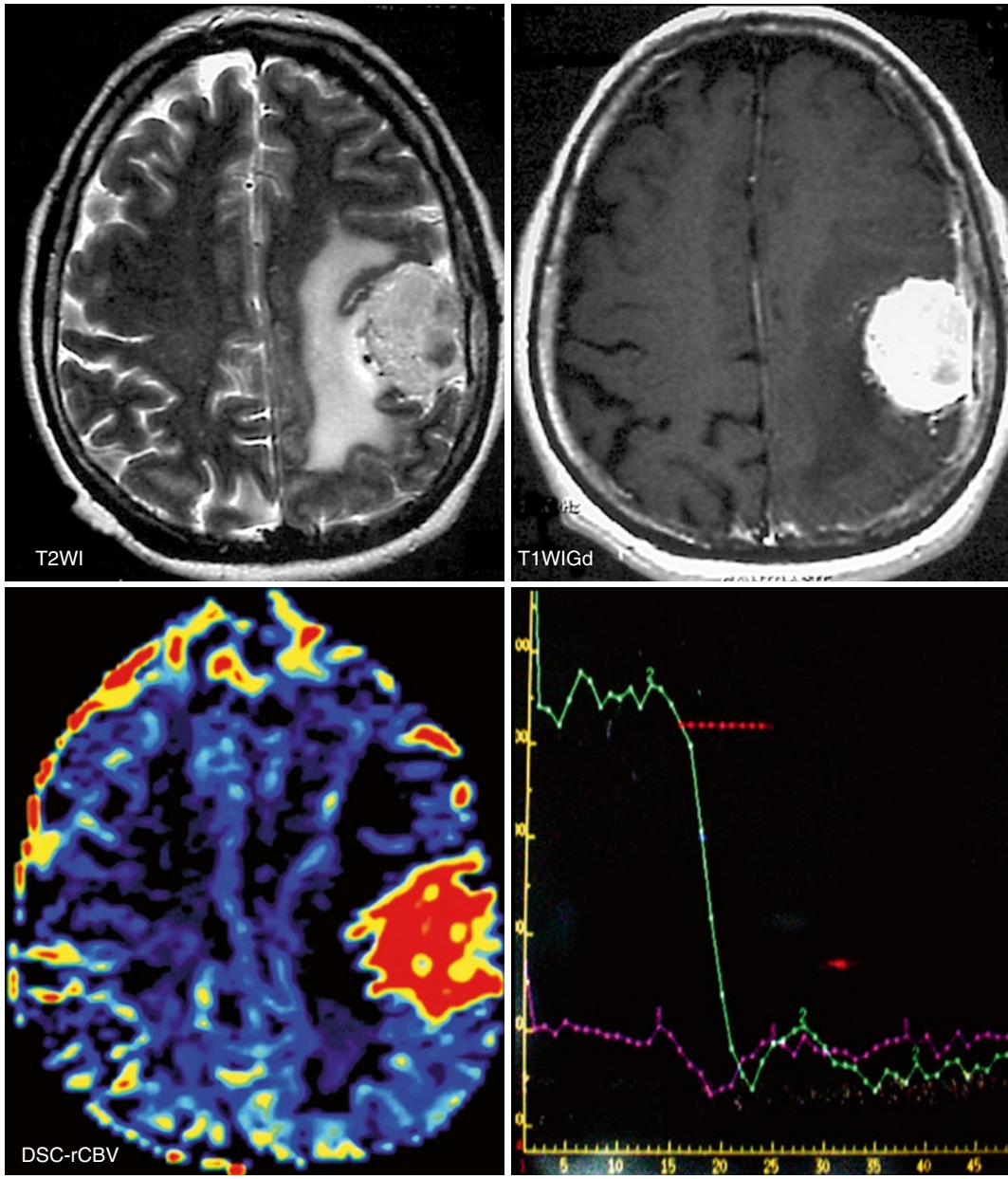

Fig. 16.17 Atypical meningioma in a 52-year-old man that presented with headache and right hemiplegia. DSC-MRI shows a high rCBV value of this lesion. The TIC does not return towards baseline, due to marked permeability

In addition, the use of T2*-weighted DSC-MRI has also been used in research for tumor evaluation outside the brain. Due to very limited available data and space constraints, we will not discuss this approach.

16.4.2.1 Perfusion MRI in Clinical Trials of Body Tumors

Perfusion MRI in the body is still in the research setting, although it is on its way towards the clinical arena. Quantitative vascular parameters

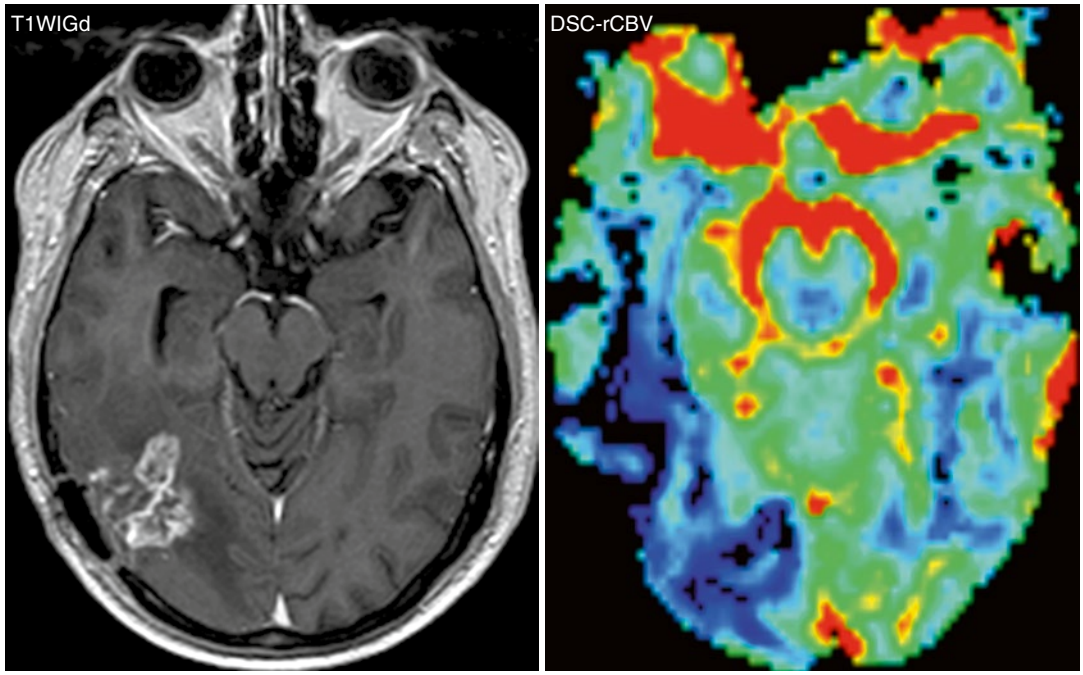

Fig. 16.18 A 56-year-old man with postoperative GBM treated with radiation therapy. The axial T1-weigthed image shows an expansive lesion with irregular and heterogeneous contrast enhancement. DSC-MRI shows low rCBV, consisting with radiation necrosis

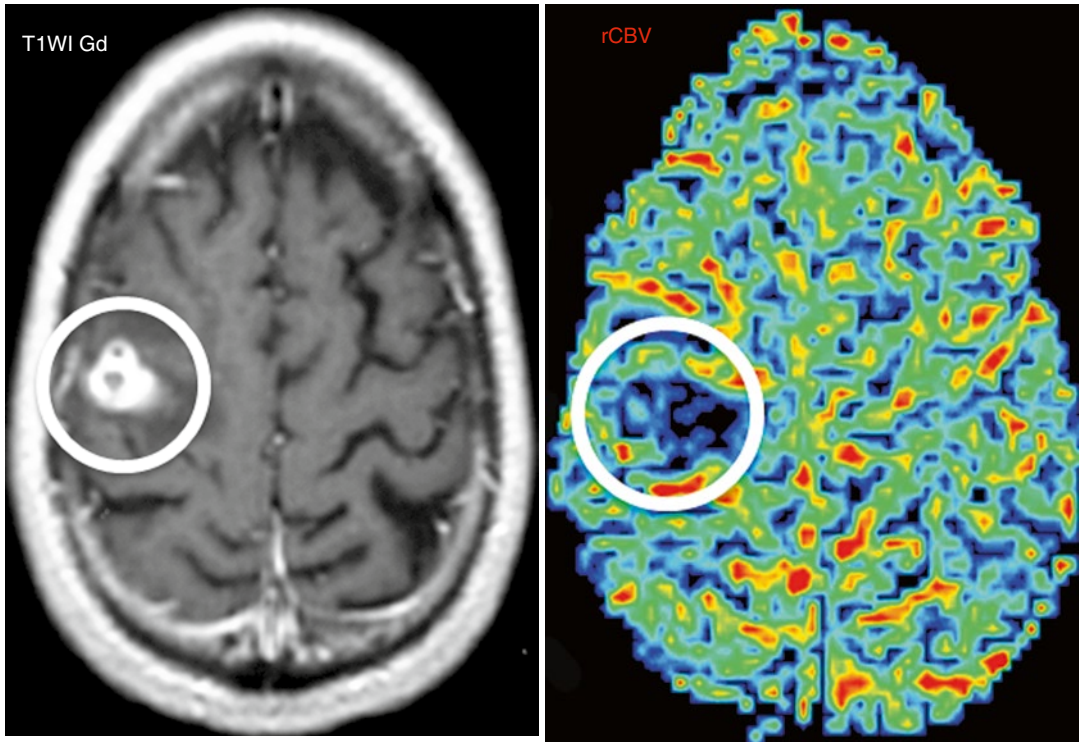

Fig. 16.19 HIV-positive patient with toxoplasmosis presented a round-enhancing lesion (*circle on left image*) that does not present high rCBV on DSC-MRI (*circle on right image*)

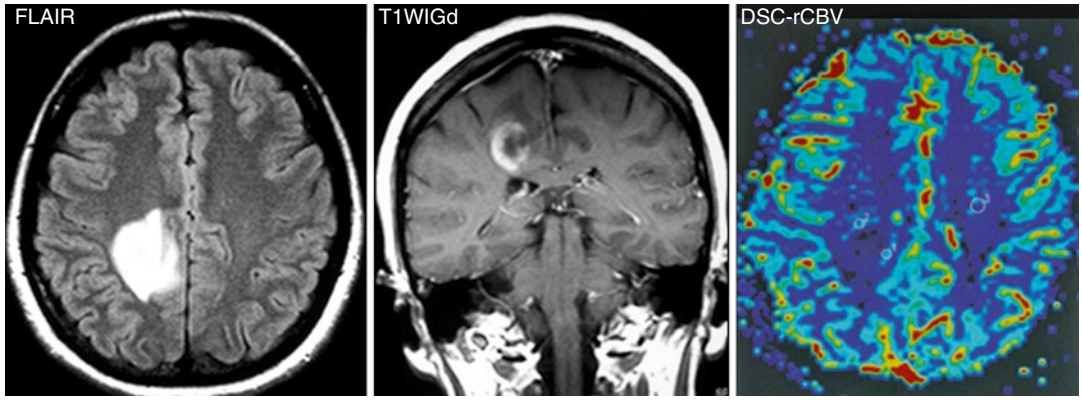

Fig. 16.20 Tumefactive demyelinating lesion. A 50-year-old woman with early onset of left hemiparesthesia. A round lesion surrounded by vasogenic edema in the right subcortical parasagittal parietal white matter is demonstrated. After intravenous contrast administration, the lesion presented an incomplete round enhancement. DSC-MRI does not demonstrate high rCBV

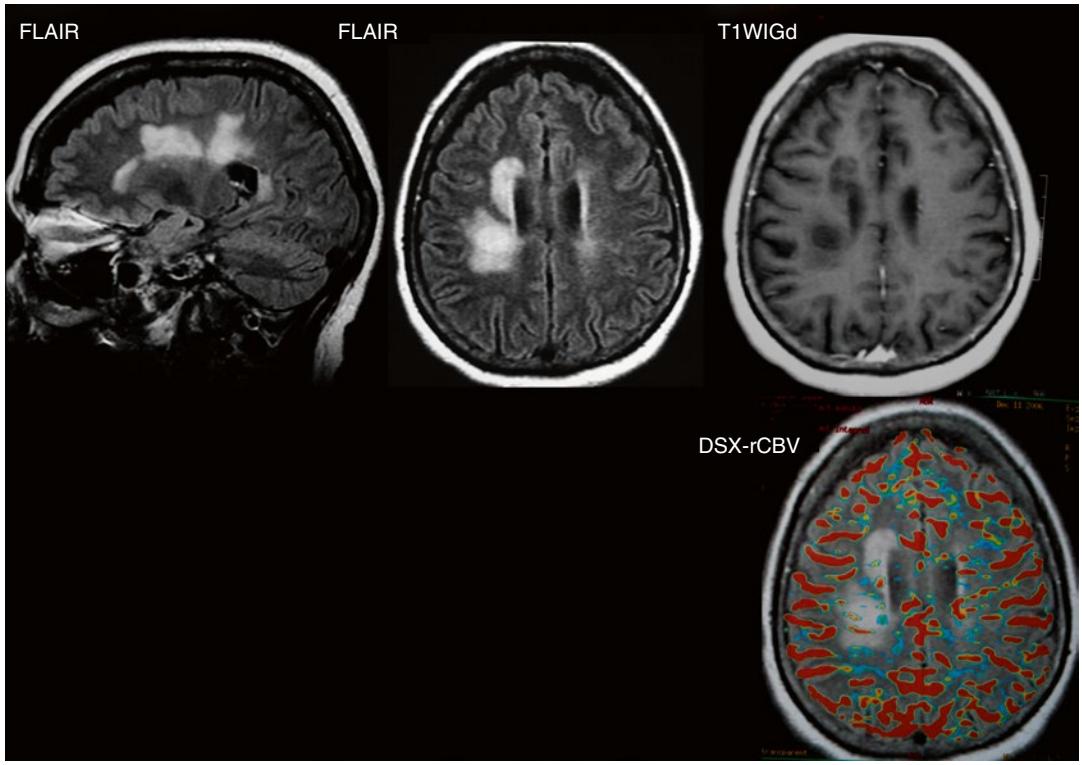

Fig. 16.21 A demyelinating lesion that does not enhances after endovenous contrast administration is seen at the right centrum semiovale in a patient with multiple sclerosis. DSC-MRI demonstrates the presence of vessels within the lesion

derived from DCE-MRI have been usually applied to clinical trials evaluating the effect of drugs on tumor vascularity. In the body, most of the experience comes from the monitorization of rectal cancer [70], hepatocellular carcinoma (HCC), liver metastasis [71], prostate cancer, and renal cell carcinoma (RCC) treated with angiogenic inhibitors or vascular disrupting agents [72] (Fig. 16.23).

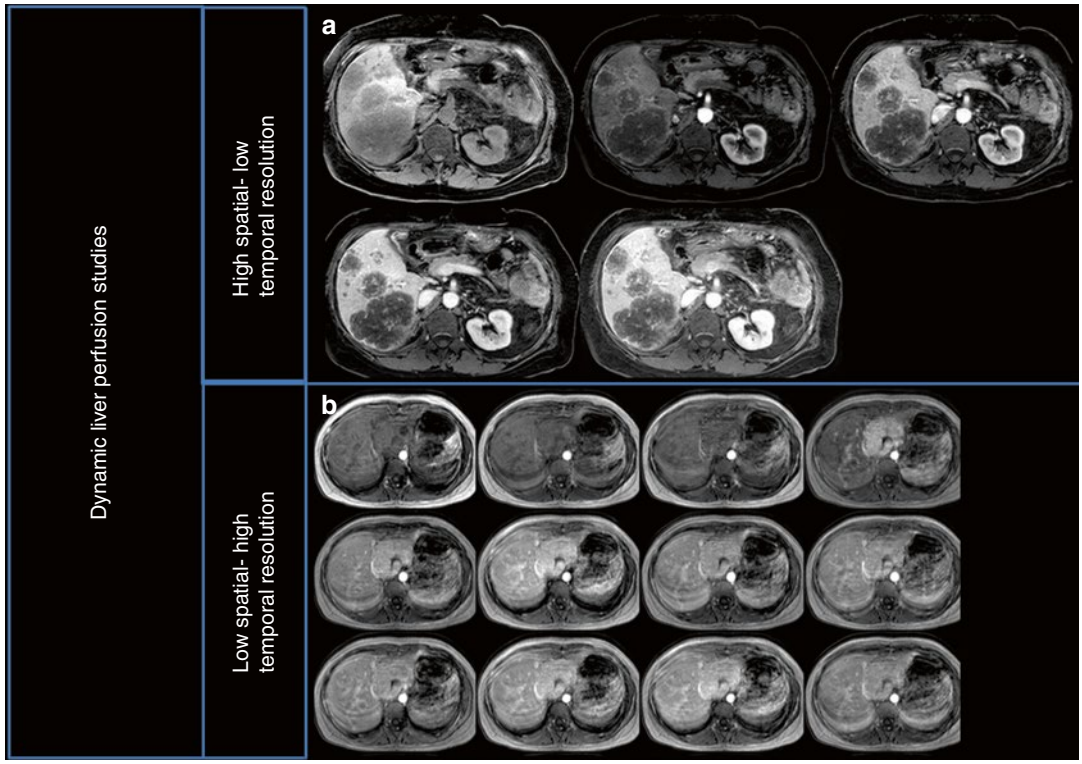

Fig. 16.22 (**a**) Conventional liver DCE-MRI with low temporal resolution and high spatial one in a patient with liver metastases of colon adenocarcinoma. Five acquisitions (pre-contrast, arterial, portal, venous, and equilibrium phases) were acquired. Acquisition time per dynamic: 15 s. (**b**) DCE-MRI using an approach with multiple fast T1-weighted repetitions with limited coverage and reduced spatial resolution in a patient with focal nodular hyperplasia (FNH). Time per dynamic: 3 s. Notice that only the first twelve dynamic series are shown

Several series have linked early reduction of these vascular parameters to treatment response, as early as 2 days after the start of therapy, but further studies are necessary to show its relationship to critical endpoints as patient survival [73].

K^{trans}, the most extended parameter evaluated for this purpose, does not purely measure capillary permeability, and its change with treatment represents a number of different physiological processes. On one hand, K^{trans} is related to tissue perfusion in tissues with flow limitations. On the other hand, if permeability is limited, K^{trans} is related to permeability surface area [74]. Therefore, in flow-limited lesions, K^{trans} will show low values related to negligible microvascular component. v_e is usually diminished in tumors when there is a higher fraction of neovessels in tumor than in surrounding normal tissue.

16.4.2.2 Role of Perfusion MRI in the Liver

Perfusion MRI in the liver is technically demanding, and there is limited literature of its application in oncology. Coronal acquisitions are more commonly acquired to limit inflow artifacts [75]. It is important to perform a whole liver approach in order to avoid missing small lesions. This is of paramount importance in the evaluation of liver metastasis of colorectal carcinoma, as DCE-MRI pharmacokinetic parameters have been proposed as surrogate biomarkers of drug efficacy in colorectal carcinoma metastasis [76]. In the liver, the hepatic perfusion index, a specific semiquantitative-derived parameter, has shown its role in the detection of micrometastases as it appears elevated [77]. Perfusion MRI can also measure perfusion parameters of HCC and can

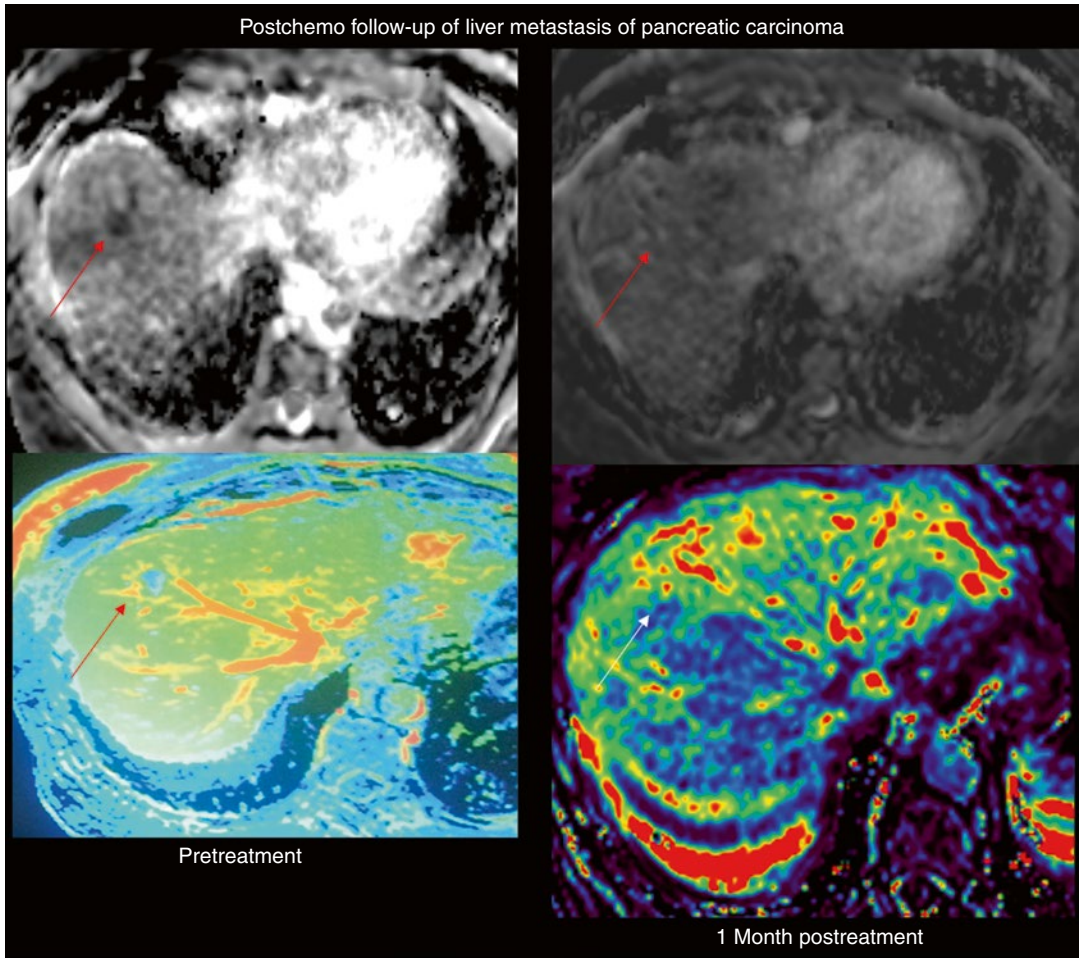

Fig. 16.23 Follow-up functional MRI pre- and post-chemotherapy in a patient with a metastasis (*arrows*) from pancreatic carcinoma. On pretreatment MRI (*left column* images), there is a lesion in segment 8 with very low ADC and increased area under the curve (AUC obtained from DCE-MRI). One month after chemotherapy (*left column* images) the lesion has disappear on ADC map and a drastic reduction on the AUC values indicates complete response

be used for predicting and monitoring treatment response to anti-vascular agents [78].

16.4.2.3 Role of Perfusion MRI in Pancreatic Carcinoma

Initial data of perfusion MRI in the pancreas suggests that derived parameters of bicompartmental model may differentiate pancreatic cancer from normal pancreas tissue, as pancreatic cancer demonstrates significant lower values of K^{trans}, k^{ep}, and AUC [79]. Histologically, pancreatic cancer is a hypovascular tumor due to reduced blood flow, although it has high permeability. Therefore, K^{trans} and AUC of pancreatic cancer represent blood flow as explained before.

Furthermore, there is a significant difference between quantitative parameters of neuroendocrine pancreatic tumors and pancreatic carcinoma [79]. Pretreatment K^{trans} measurement in pancreatic tumors can predict response to antiangiogenic therapy, and decreased of perfusion parameters have been linked to good response after combined chemotherapy and antiangiogenic therapy as soon as 1 month after the start of treatment [80].

16.4.2.4 Role of Perfusion MRI in Renal Cell Carcinoma

Accurate characterization of renal lesions is mainly based on the presence or absence of enhancement to distinguish cystic from solid

lesions. DCE-MRI has shown detection rates of RCC near to 100 %, with low false-positive rates [81]. Furthermore, according to the enhancement pattern, the three most common subtypes of RCC can be distinguished, which is of paramount importance, as the therapeutic approach varies according to the histological type. Clear cell RCC shows early and fast enhancement than other subtypes of RCC during the arterial/corticomedular phases. Conversely, papillary RCC demonstrates poor enhancement in these phases. Chromophobe RCCs usually show an intermediate pattern of enhancement compared to the other most common subtypes. Regarding benign tumors, oncocytomas may overlap with RCCs in terms of degree of enhancement and lipid-poor angyomyolipomas more commonly demonstrate a moderate degree of enhancement overlapping with that of chromophobe RCC [82]. Characterization of renal masses is accurate using a three-point dynamic approach with high spatial and low temporal resolution. However, since the use of new targeted antiangiogenic therapies to clear cell and papillary subtypes of RCC, it is important to assess early response to treatment using functional imaging techniques, such as DCE-MRI or ASL (see Figs. 46.9 and 46.10, respectively) [83].

16.4.2.5 Role of Perfusion MRI in Gynecological Malignancies

Detection and staging of endometrial and cervical uterine carcinomas are improved with the use of DCE-MRI, which is usually included in clinical protocols [84]. There is scarce experience in the posttreatment assessment of endometrial cancer with perfusion MRI. However, it has shown promising results in the early monitoring of response to chemoradiotherapy of cervical cancer. Tumor enhancement or an increase in signal intensity early after initiation of treatment predicts for favorable therapeutic outcome [85]. There are contradictory data about the predictive role of baseline contrast enhancement of cervical cancer with DCE-MRI [86].

16.4.2.6 Role of Perfusion MRI in Ovarian Cancer

DCE-MRI techniques have revealed favorable results in the characterization of ovarian carcinoma. In fact, several studies have suggested a relationship between tumoral grade and pattern of enhancement of solid components. The use of functional DCE-derived parameters, such as wash-in rate, may be helpful to establish a threshold value to determinate or even to predict the risk of invasive malignancy of an ovarian lesion [87]. The use of bicompartmental model derived parameters such as tissue blood flow and AUC are useful to distinguish benign from malignant tumors (Fig. 16.24). In addition, the presence of a shorter lag time, defined as the time required for blood to go from the main arterial reference vessel (usually external iliac) to the tumoral arterioles, has been postulated as a biomarker of potential peritoneal carcinomatosis [88].

16.4.2.7 Role of Perfusion MRI in Prostate Cancer

Evaluation of prostate cancer is probably the most investigated application of perfusion MRI between all abdominopelvic tumors. Most commonly, prostate cancer shows an early, fast and intense enhancement followed by washout, although this is better found in high-grade tumors (Fig. 16.25) [89], and a broad spectrum of different patterns of enhancement have been reported. Furthermore, a recent report suggests that prostate cancer is not associated with increased vascularity [90].

In clinical practice, qualitative and semiquantitative analysis of DCE-MRI is used for prostate cancer management, but they do not represent the true microvascular properties of cancer, as pharmacokinetic parameters do. Most of prostate cancers show elevated K^{trans} due to a mixed effect of increased flow and permeability. In peripheral zone, prostate carcinoma usually demonstrates high vascular permeability and K^{trans} values depend mainly on the tumor flow; whereas; in the central gland, where permeability is the limiting factor, K^{trans} values are related to the permeability surface area. Besides, v_e is commonly decreased in tumors, but it is less useful than K^{trans} to distinguish cancer from normal tissue. Pharmacokinetic MRI is complex in the prostate due to variations in vascularization of the different areas of a normal prostate and vascular heterogeneity of prostate carcinoma. Besides, introduction in the

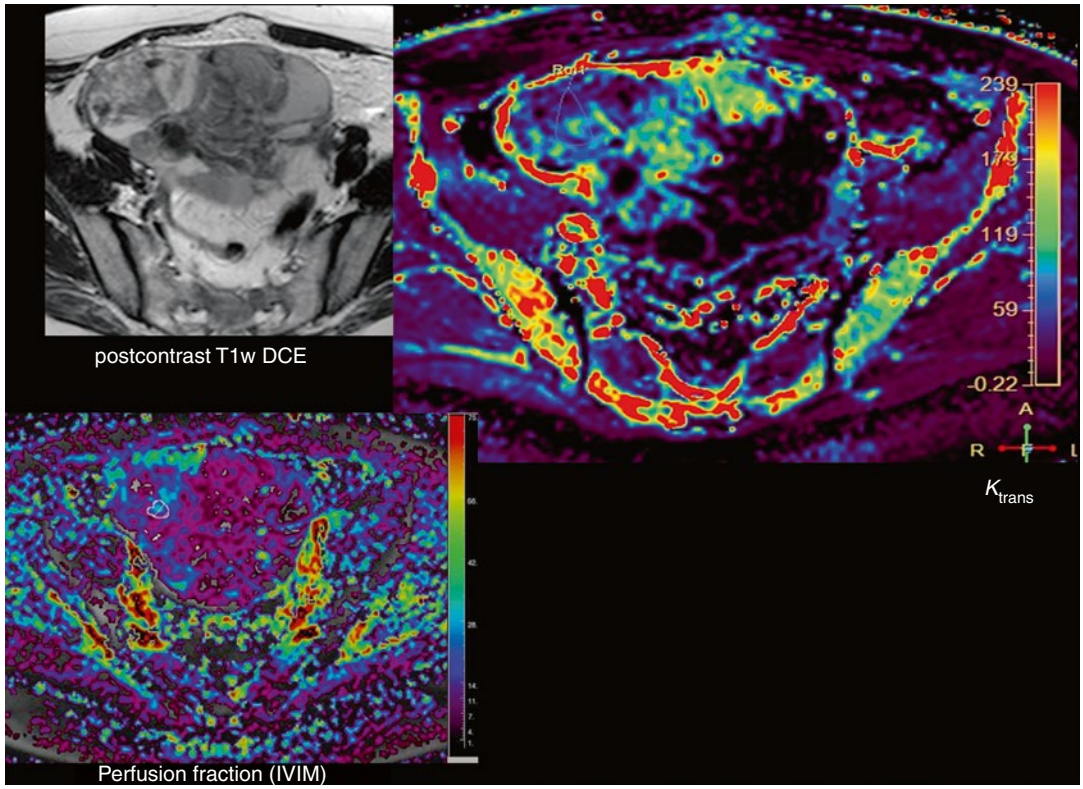

Fig. 16.24 Right ovarian cystoadenocarcinoma. Large heterogenous mass on post-contrast T1-weighted sequence which shows elevated K^{trans} values on solid areas (*green and red colored* areas). Perfusion fraction obtained from IVIM model also demonstrates areas with increased blood flow peripherally (*green colored* areas)

clinical setting has been limited by poor correlation between pharmacokinetic volume and blood flow parameters and histological parameters.

DCE-MRI is superior to T2-weighted sequences alone for detection of prostate cancer, being of interest in patients with previous negative TRUS-guided biopsy and high clinical suspicion of malignancy [91]. Furthermore, DCE-MRI improves detection of prostate cancer when it forms part of a multiparametric analysis, including T2-weighted sequences and other functional MRI techniques [92]. Characterization of hypointense lesions on T2-weighted sequences is a frequent clinical problem. In this setting, the role of DCE-MRI is limited, as it is well-known the overlap in time signal intensity curves (TIC) patterns of chronic prostatitis and prostate carcinoma.

Controversy exists about the role of DCE-MRI in local staging of prostate cancer. DCE-MRI is especially useful in the detection of recurrence in treated prostate with radiotherapy [93], radical prostatectomy [94], androgen-deprivation therapy [95], or multikinase inhibitors [96], being by far the best functional MRI technique for this purpose (Fig. 16.26). DCE-MRI should be included always in prostate imaging protocol along with other functional techniques, for most of clinical indication of prostate MRI, with a central role in the detection of recurrence in the treated prostate.

16.4.2.8 Role of perfusion MRI in Rectal Cancer

DCE-MRI can be used to measure functional vascular changes, and it is well established that parameters obtained significantly correlate with the degree of angiogenesis and microvessel density (Fig. 16.27) [97]. It has been described that the degree of angiogenesis correlates with survival, tumor progression, and liver and lymph

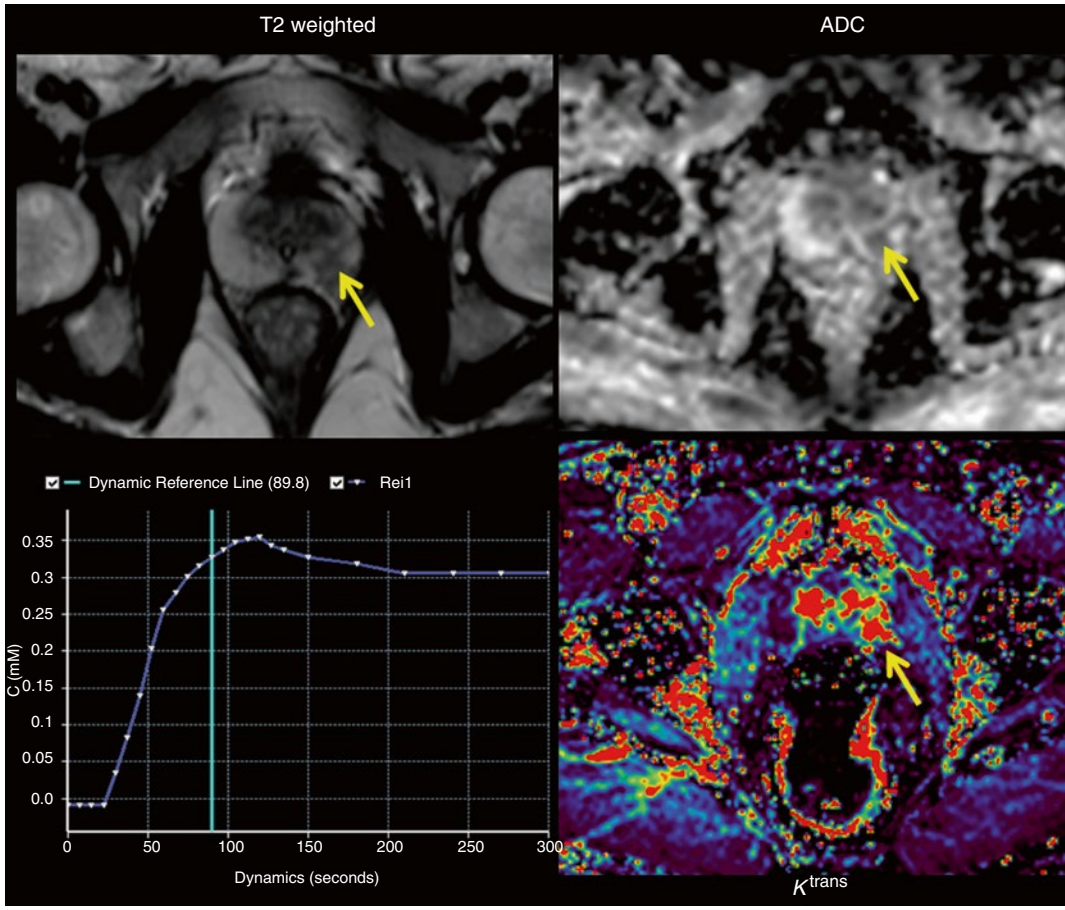

Fig. 16.25 Prostate cancer. Small nodule hypointense on T2-weighted sequence on left peripheral zone demonstrates low ADC values and increased K^{trans} value, indicating a high-grade tumor (*arrows*)

nodes metastasis [98]. Quantitative parameters, such as K^{trans}, can predict response to preoperative treatments, assess response to neoadjuvant chemoradiation, and detect small early recurrence [99, 100]. Rectal tumors with pretreatment higher K^{trans} values respond better to chemoradiation [100]. Elevated K^{trans} in a posttreatment scenario is related to incomplete response and residual active tumor; meanwhile, good responding tumors show decrease of K^{trans} levels. Recurrent rectal cancers also show elevation of K^{trans}. Therefore, limited current data suggest a role for DCE-MRI in rectal cancer management, improving patient selection and potentially clinical outcomes. Recent data also support the capacity for pharmacokinetic MRI to identify complete pathological response after radio and/or chemotherapy, which is a critical endpoint as it is possible to avoid in these patients radical surgical strategies [99].

16.4.2.9 Perfusion MRI in Breast Cancer

DCE-MRI is the basis of every breast MRI study, which is currently a popular MRI examination in clinical practice. Normally, DCE-MRI is performed with a temporal resolution between 40 and 120 s. This approach to DCE-MRI of the breast has a high sensitivity for breast cancer detection (89–100 %) but lacks specificity for characterizing breast tumors (Fig. 16.28). An overlap between the MRI findings of benign and malignant lesions still exists, resulting in variable specificity

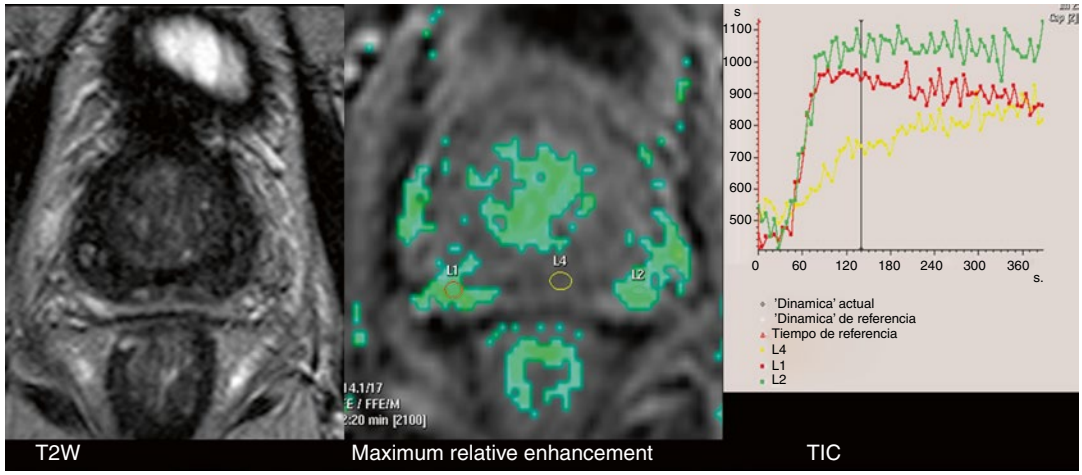

Fig. 16.26 Prostate carcinoma treated with external radiotherapy 9 months ago. Follow-up MRI demonstrates diffuse low signal intensity on T2-weighted image on peripheral zone that prevents tumor detection. Maximum relative enhancement parametric map of DCE-MRI shows two foci of increased enhancement bilaterally on the peripheral zone which show type III TIC (red ROI L1 located in the nodule in right peripheral zone) and type II TIC (green ROI L2 located in the nodule in left peripheral zone). Both nodules corresponded to recurrent prostate carcinoma. Notice differences in enhancement pattern with normal peripheral zone which shows a type 1 TIC (yellow ROI L4)

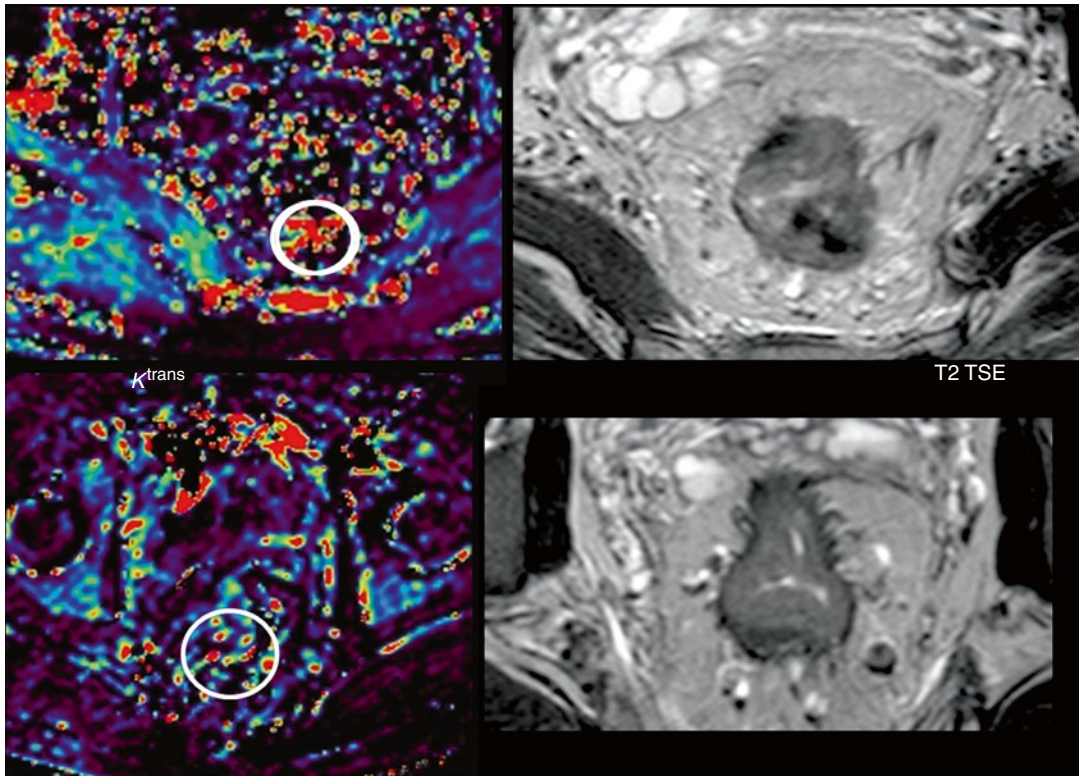

Fig. 16.27 Differences in angiogenesis in rectal carcinoma. *Top row* images show a rectal carcinoma with increased perfusion and permeability (high K^{trans}) and *bottom row* images show another carcinoma with low K^{trans}

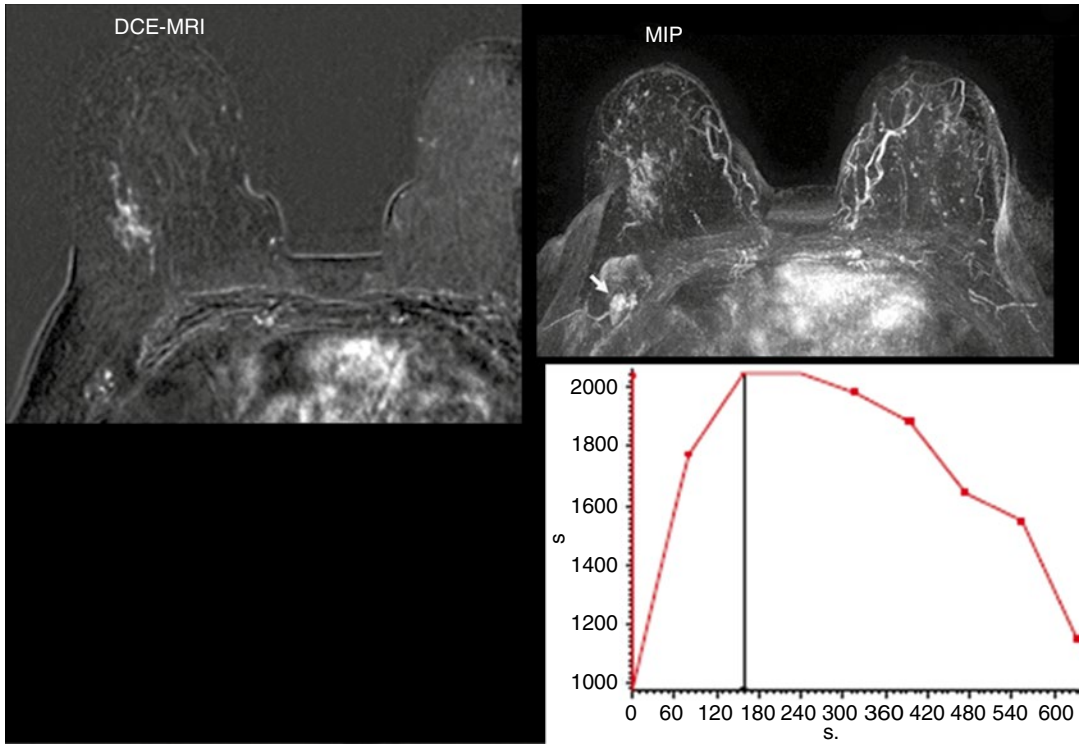

Fig. 16.28 Infiltrating lobular carcinoma. DCE-MRI confirmed a regional enhancement with maximum diameter of 5 cm, whose enhancement pattern (type III TIC) was consistent with malignancy. Axial MIP of the first dynamic post-contrast series better depicted the tumoral extension, the absence of additional foci, and the presence of enlarged right axillary lymph nodes (*arrow*) (With permission from Barcelo et al. [101])

(37–86 %) [101]. In addition, DCE-MRI has been shown useful as a biomarker for assessing overall response to therapy in breast cancer [102]. In this setting, pharmacokinetic MRI (with temporal resolution below 6 s) has been proposed for the early assessment of changes during therapy. The diagnostic accuracy of DCE-MRI to predict pathologic complete response seems to have a high specificity and negative predictive value versus only moderate sensitivity and positive predictive value [103]. In this sense, derived parameters from DCE-MRI pharmacokinetic modeling can be considered as a predictive biomarker to evaluate treatment response to anti-vascular drugs [104]. Preliminary data have shown that IVIM and ASL are technically feasible for breast cancer assessment, although more experience is necessary [105, 106] (Fig. 16.29).

16.4.2.10 Perfusion MRI in Musculoskeletal Malignancies

As a general rule, in DCE-MRI, a malignant tumor shows a rapid wash-in with posterior washout enhancement. However, several studies based on first-pass MRI of musculoskeletal lesions have found a significant overlap of the obtained microcirculatory parameters between highly vascular benign and low vascular malignant lesions. Perfusion MRI may also help in posttreatment monitoring, in the distinction between necrotic and viable tumor tissue and in the differentiation between post-therapeutic soft tissue changes and tumor recurrence [107] (Fig. 16.30).

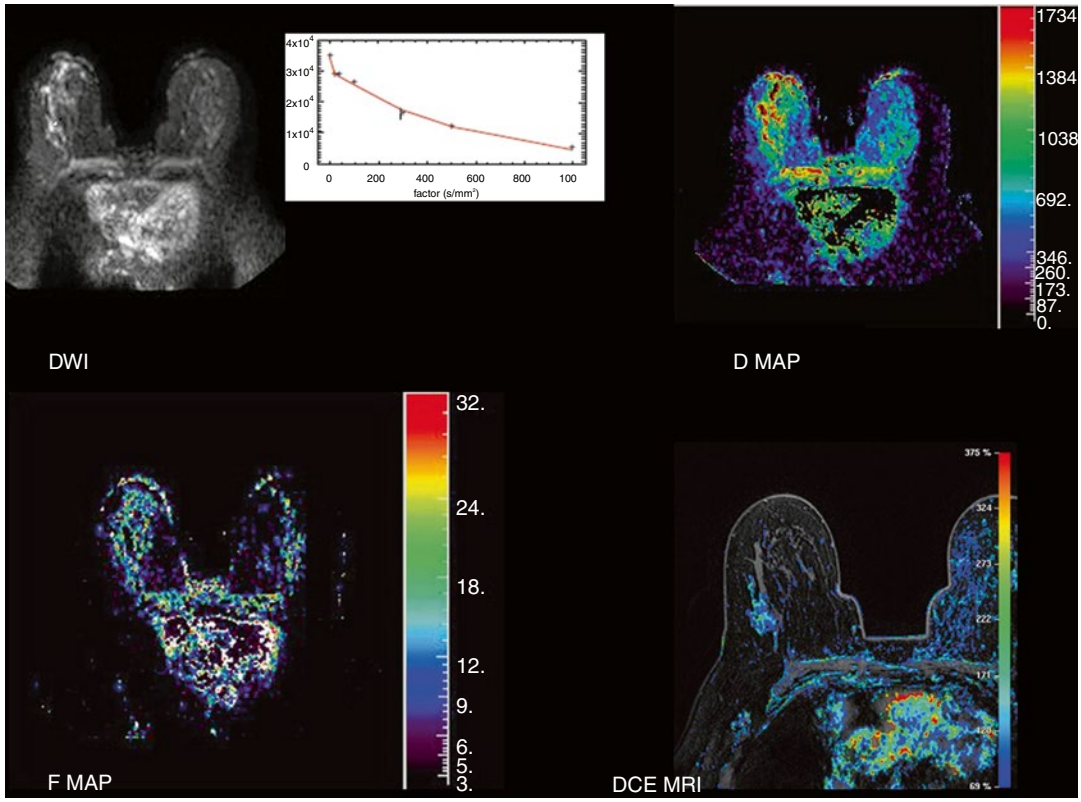

Fig. 16.29 Invasive lobular carcinoma. Axial DWI with a *b* value of 25 s/mm^2 shows a large ill-defined mass on right breast. Graph of the biexponential signal decay of the tumor showed a first fast decay related to tumor perfusion with *b* values under 100 s/mm^2 and a more flattened slope of signal decay with *b* values over 100 s/mm^2 related to true diffusion. Tumor perfusion fraction (*f*) measured with the IVIM approach was that of 12 %. Notice the correlation of the perfusion fraction map with the relative enhancement map derived from a noncompartmental analysis of the DCE-MRI. Tumor *D* value was that of 1.34 × 10–3 mm^2/s. A core biopsy confirmed an infiltrating lobular carcinoma of right breast with right axillary nodal metastases (With permission from Barcelo et al. [101])

Conclusions

Perfusion is a fundamental biological function that refers to the delivery of oxygen and nutrient to tissue by means of blood flow. In the purest sense, perfusion is measured in tissue-specific units of milliliters of blood per unit time and gram of tissue. MRI is able to assess tumor perfusion with different technical approaches. Most commonly, dynamic techniques after contrast injection of contrast material are used with either a T2*-weighed (DSC-MRI) or a T1-weighted (DCE-MRI) sequence. Both approaches are clinically validated for tumor characterization in the brain and body and show promise for early therapy monitoring, being especially interesting if novel-targeted anti-vascular therapies are applied. In addition, non-contrast MR techniques such as ASL or IVIM allow also tumor perfusion analysis. ASL has proved valid for assessment and therapy monitoring of malignancies of brain and kidney, although it needs further validation and it will be tested also in other anatomic regions. IVIM, which measures moving flow, is now being introduced in the clinical arena and its application in oncology still has to be demonstrated.

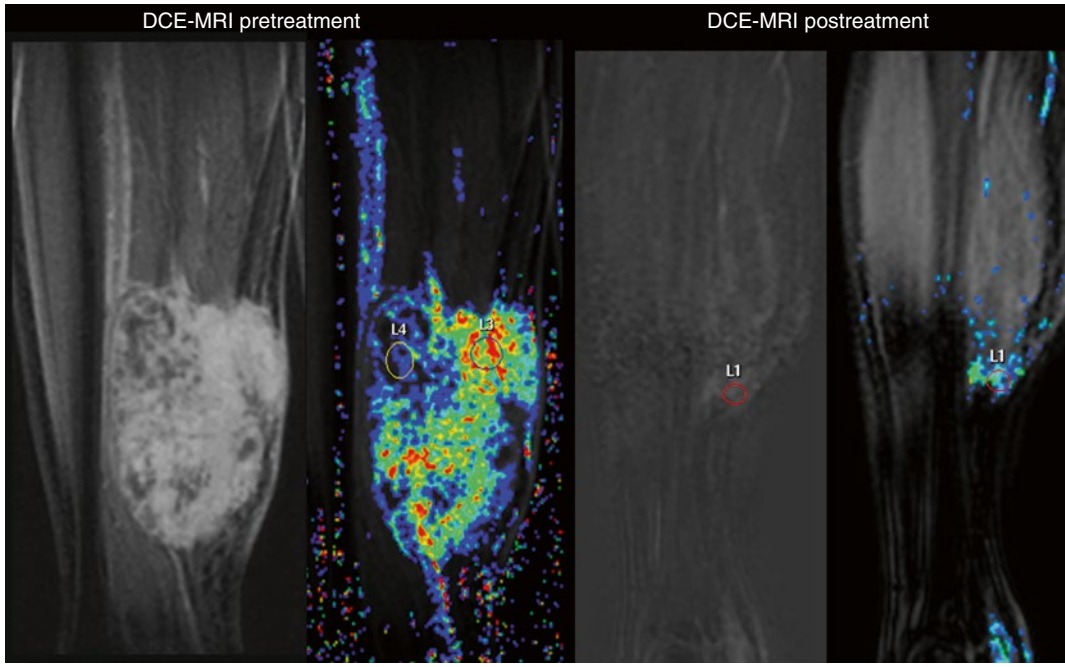

Fig. 16.30 Soft tissue Ewing sarcoma. Pretreatment MRI shows an aggressive soft tissue mass highly vascularized in DCE-MRI acquisition and maximum relative enhancement map. MR performed 3 months after surgery and chemotherapy shows fibrous tissue without evidence of recurrence, which is minimally vascularized

References

1. Østergaard L, et al. High resolution measurement of cerebral blood flow using intravascular tracer bolus passages. Part II: experimental comparison and preliminary results. Magn Reson Med. 1996;36:726–36.
2. Duyn JH, et al. 3D bolus tracking with frequency-shifted BURST-MRI. J Comput Assist Tomogr. 1994;18:680–7.
3. Rempp KA, et al. Quantification of regional cerebral blood flow and volume with dynamic susceptibility contrast-enhanced MR imaging. Radiology. 1994;193:637–41.
4. Speck O, et al. Perfusion MRI of the human brain with dynamic susceptibility contrast: gradient-echo versus spin-echo techniques. J Magn Reson Imaging. 2000;12:381–7.
5. Takeshi Sugahara YK, et al. Perfusion-sensitive MR imaging of gliomas: comparison between gradient-echo and spin-echo echo-planar imaging techniques. AJNR Am J Neuroradiol. 2001;22:1306–15.
6. Troprès I, et al. Vessel size imaging. Magn Reson Med. 2001;45:397–408.
7. Kiselev VG , et al. Vessel size imaging in humans. Magn Reson Med. 2005;53:553–63.
8. Aronen HJ, et al. Cerebral blood volume maps of gliomas: comparison with tumor grade and histologic findings. Radiology. 1994;191:41–51.
9. Edelman RR, et al. Cerebral blood flow: assessment with dynamic contrast-enhanced T2*-weighted MR imaging at 1.5 T. Radiology. 1990;176:211–20.
10. Kassner A, et al. Abnormalities of the contrast recirculation phase in cerebral tumors demonstrated using dynamic susceptibility contrast-enhanced imaging: a possible marker of vascular tortuosity. J Magn Reson Imaging. 2000;11:103–13.
11. Vonken EP, et al. Simultaneous quantitative cerebral perfusion and Gd-DTPA extravasation measurement with dual-echo dynamic susceptibility contrast MRI. Magn Reson Med. 2000;43:820–7.
12. Pettigrew RI, et al. Fast-fieldecho MR imaging with Gd-DTPA: physiologic evaluation of the kidney and liver. Radiology. 1986;160:561–3.
13. Runge VM, et al. Intravascular contrast agents suitable for magnetic resonance imaging. Radiology. 1984;153:171–6.
14. Choyke PL, et al. Dynamic Gd-DTPA-enhanced MR imaging of the kidney: experimental results. Radiology. 1989;170:713–20.
15. Villringer A, et al. Dynamic imaging with lanthanide chelates in normal brain: contrast due to

magnetic susceptibility effects. Magn Reson Med. 1988;6:164–74.
16. Griswold MA, et al. Generalized autocalibrating partially parallel acquisitions (GRAPPA). Magn Reson Med. 2002;47:1202–10.
17. Pruessmann KP, et al. SENSE: sensitivity encoding for fast MRI. Magn Reson Med. 1999;42(5):952–62.
18. Sourbron S. Technical aspects of MR perfusion. Eur J Radiol. 2010;76:304–13.
19. Wang L, et al. Rapid 3D-T1 mapping of cartilage with variable flip angle and parallel imaging at 3.0T. J Magn Reson Med. 2008;27:154–61.
20. De Naeyer D, et al. Flip angle optimization for dynamic contrast-enhanced MRI-studies with spoiled gradient echo pulse sequences. Phys Med Biol. 2011;56(16):5373–95.
21. Michoux N, et al. Analysis of contrast-enhanced MR images to assess renal function. MAGMA. 2006;19:167–79.
22. Jerosch-Herold M, et al. Analysis of myocardial perfusion MRI. J Magn Reson Imaging. 2004;19(6):758–70.
23. Buonaccorsi G, et al. Comparison of the performance of tracer kinetic model-driven registration for dynamic contrast enhanced MRI using different models of contrast enhancement. Acad Radiol. 2006;13:1112–23.
24. Dornier C, et al. Improvement in the quantification of myocardial perfusion using an automatic spline-based registration algorithm. J Magn Reson Imaging. 2003;18:160–8.
25. Song T, et al. Automatic 4-D registration in dynamic MR renography. IEEE Eng Med Biol Soc. 2005;3:3067–70.
26. Brix G, et al. Microcirculation and microvasculature in breast tumors: pharmacokinetic analysis of dynamic MR image series. Magn Reson Med. 2004; 52:420–9.
27. Sourbron S, et al. Quantification of cerebral blood flow, cerebral blood volume, and blood–brain-barrier leakage with DCE-MRI. Magn Reson Med. 2009;62(1):205–17.
28. Thomassin-Naggara I, et al. Dynamic contrast-enhanced MR imaging to assess physiologic variations of myometrial perfusion. Eur Radiol. 2010;20:984–94.
29. Tofts PS, et al. Estimating kinetic parameters from dynamic contrast-enhanced T(1)-weighted MRI of a diffusible tracer: standardized quantities and symbols. J Magn Reson Imaging. 1999;10:223–32.
30. Tofts PS. Modeling tracer kinetics in dynamic Gd-DTPA MR imaging. J Magn Reson Imaging. 1997;7:91–101.
31. Buckley D. Are measurements from two commercial software packages interchangeable? Possibly, if like is compared with like. Radiology. 2008;246:642.
32. van den Hoff J. Assessment of lung cancer perfusion by using Patlak analysis what do we measure? Radiology. 2007;243:907.
33. Ocak I, et al. Dynamic contrast-enhanced MRI of prostate cancer at 3T: a study of pharmacokinetic parameters. Am J Roentgenol. 2007;189:849.
34. Patankar T, et al. Is volume transfer coefficient (Ktrans) related to histologic grade in human gliomas? AJNR Am J Neuroradiol. 2005;26:2455–65.
35. Li KL, et al. Improved 3D quantitative mapping of blood volume and endothelial permeability in brain tumours. J Magn Reson Imaging. 2000;12:347–57.
36. Rijpkema M, et al. Method for quantitative mapping of dynamic MRI contrast uptake in human tumours. J Magn Reson Imaging. 2001;14:457–63.
37. Buckley D, et al. Vascular characteristics of prostate cancer: evaluation with dynamic contrast-enhanced T1-weighted MRI-initial experience. Radiology. 2004;233:709–15.
38. Tofts P, et al. Measurement of the blood–brain barrier permeability and leakage space using dynamic MR imaging. I. Fundamental concepts. Magn Reson Med. 1991;17:357–67.
39. Fritz-Hansen T, et al. Capillary transfer constant of Gd-DTPA in the myocardium at rest and during vasodilation assessed by MRI. Magn Reson Med. 1998;40:922–9.
40. Parker G, et al. Experimentally-derived functional form for a population-averaged high-temporal-resolution arterial input function for dynamic contrast-enhanced MRI. Magn Reson Med. 2006;56:993–1000.
41. Essig M, et al. Perfusion MRI: the five most frequently asked technical questions. AJR Am J Roentgenol. 2013;200(1):24–34.
42. Detre JA, et al. Perfusion imaging. Magn Reson Med. 1992;23:37–45.
43. Williams DS, et al. Magnetic resonance imaging of perfusion using spin inversion of arterial water. Proc Natl Acad Sci U S A. 1992;89:212–6.
44. Dixon WT, et al. Projection angiograms of blood labeled by adiabatic fast passage. Magn Reson Med. 1986;3:454–62.
45. Alsop DC, et al. Multisection cerebral blood flow MR imaging with continuous arterial spin labeling. Radiology. 1998;208:410–6.
46. Edelman RR, et al. Qualitative mapping of cerebral blood flow and functional localization with echo-planar MR imaging and signal targeting with alternating radiofrequency. Radiology. 1994;192:513–20.
47. Golay X, et al. Pulsed star labeling of arterial regions (PULSAR): a robust regional perfusion technique for high field imaging. Magn Reson Med. 2005;53:15–21.
48. Kwong KK, et al. MR perfusion studies with T1-weighted echo planar imaging. Magn Reson Med. 1995;34:878–87.
49. Kim S. Quantification of relative cerebral blood flow change by flow-sensitive alternating inversion recovery (FAIR) technique: application to functional mapping. Magn Reson Med. 1995;34:293–301.
50. Kety S, et al. The nitrous oxide method for the quantitative determination of cerebral blood flow in man: theory, procedure and normal values. J Clin Invest. 1948;27:476.
51. Buxton RB, et al. A general kinetic model for quantitative perfusion imaging with arterial spin labeling. Magn Reson Med. 1998;40:383–96.

52. Le Bihan D, et al. Separation of diffusion and perfusion in intravoxel incoherent motion MR imaging. Radiology. 1988;168:497–505.
53. Le Bihan D, et al. Effects of intravoxel incoherent motions (IVIM) in steady-state free precession (SSFP) imaging: application to molecular diffusion imaging. Magn Reson Med. 1989;10:324–37.
54. Essig M, et al. MR imaging of neoplastic central nervous system lesions: review and recommendations for current practice. AJNR Am J Neuroradiol. 2012;33:803–17.
55. Law M, et al. Comparison of cerebral blood volume and vascular permeability from dynamic susceptibility contrast-enhanced perfusion MR imaging with glioma grade. AJNR Am J Neuroradiol. 2004;25:746–55.
56. Thompson G, et al. Imaging of brain tumors: perfusion/permeability. Neuroimaging Clin N Am. 2010;20(3):337–53.
57. Noguchi T, et al. Perfusion imaging of brain tumors using arterial spin-labeling: correlation with histopathologic vascular density. AJNR Am J Neuroradiol. 2008;29(4):688–93.
58. Cha S. Update on brain tumor imaging: from anatomy to physiology. AJNR Am J Neuroradiol. 2006;27:475–87.
59. Cha S, et al. Comparison of microvascular permeability measurements, K(trans), determined with conventional steady-state T1-weighted and first-pass T2*-weighted MR imaging methods in gliomas and meningiomas. AJNR Am J Neuroradiol. 2006;27:409–17.
60. Lacerda S et al. Magnetic resonance perfusion and permeability imaging in brain tumors. Neuroimaging Clin N Am. 2009;19:527–57.
61. Law M, et al. High-grade gliomas and solitary metastases: differentiation by using perfusion and proton spectroscopic MR imaging. Radiology. 2002;222:715–21.
62. Cha S. Perfusion MR imaging: basic principles and clinical applications. Magn Reson Imaging Clin N Am. 2003;11:403–13.
63. Yang S, et al. Dynamic contrast-enhanced perfusion MR imaging measurements of endothelial permeability: differentiation between atypical and typical meningiomas. AJNR Am J Neuroradiol. 2003;24(8):1554–9.
64. Zhang H, et al. Perfusion MR imaging for differentiation of benign and malignant meningiomas. Neuroradiology. 2008;50(6):525–30.
65. Kimura H, et al. Perfusion imaging of meningioma by using continuous arterial spin-labeling: comparison with dynamic susceptibility-weighted contrast-enhanced MR images and histopathologic features. AJNR Am J Neuroradiol. 2006;27(1):85–93.
66. Essig M, et al. Assessment of brain metastases with dynamic susceptibility-weighted contrast-enhanced MR imaging: initial results. Radiology. 2003;228:193–9.
67. Law M, et al. Gliomas: predicting time to progression or survival with cerebral blood volume measurements at dynamic susceptibility-weighted contrast-enhanced perfusion MR imaging. Radiology. 2008; 247:490–8.
68. Holmes T, et al. Distinction between cerebral abscesses and high-grade neoplasms by dynamic susceptibility contrast perfusion MRI. AJR Am J Roentgenol. 2004;183:1247–52.
69. Cha S, et al. Dynamic contrast-enhanced T2*-weighted MR imaging of tumefactive demyelinating lesions. AJNR Am J Neuroradiol. 2001;22:1109–16.
70. Zhang XM, et al. 3D dynamic contrast-enhanced MRI of rectal carcinoma at 3T: correlation with microvascular density and vascular endothelial growth factor markers of tumor angiogenesis. J Magn Reson Imaging. 2008;27(6):1309–16.
71. Morgan B, et al. Dynamic contrast enhanced magnetic resonance imaging as a biomarker for the pharmacological response of PTK787/ZK 222584, an inhibitor of the vascular endothelial growth factor receptor tyrosine kinases, in patients with advanced colorectal cancer and liver metastases. J Clin Oncol. 2003;21:3955–64.
72. Nathan P, et al. Phase I trial of combretastatin A4 phosphate (CA4P) in combination with bevacizumab in patients with advanced cancer. Clin Cancer Res. 2012;18(12):3428–39.
73. Donaldson SB, et al. Enhancing fraction measured using dynamic contrast-enhanced MRI predicts disease-free survival in patients with carcinoma of the cervix. Br J Cancer. 2010;102:23–6.
74. Bali MA, et al. Tumoral and nontumoral pancreas: correlation between quantitative dynamic contrast-enhanced MR imaging and histopathologic parameters. Radiology. 2011;261(2):456–66.
75. Chandarana H, et al. Diffusion and perfusion imaging of the liver. Eur J Radiol. 2010;76:348–58.
76. Hirashima Y, et al. Pharmacokinetic parameters from 3-Tesla DCE-MRI as surrogate biomarkers of antitumor effects of bevacizumab plus FOLFIRI in colorectal cancer with liver metastasis. Int J Cancer. 2012;130(10):2359–65.
77. Goh V, et al. Functional imaging of the liver. Semin Ultrasound CT MRI. 2013;34:54–65.
78. Lee JM, et al. Diagnosis of hepatocellular carcinoma: newer radiological tools. Semin Oncol. 2012;39(4):399–409.
79. Hyun Kim J, et al. Solid pancreatic lesions: characterization by using timing bolus dynamic contrast-enhanced MR imaging assessment—a preliminary study. Radiology. 2013;266(1):185–96.
80. Akisik MF, et al. Pancreatic cancer: utility of dynamic contrast-enhanced MR imaging in assessment of antiangiogenic therapy. Radiology. 2010;256(2):441–9.
81. Sun MR, et al. Renal cell carcinoma: dynamic contrast-enhanced MR imaging for differentiation of tumor subtypes—correlation with pathologic findings. Radiology. 2009;250:793–802.
82. Vargas AH, et al. Renal cortical tumors: Use of mutiphasic contrast-enhanced MR imaging to

differentiate benign and malignant histologic subtypes. Radiology. 2012;264:779–88.
83. Pedrosa I, et al. Magnetic resonance imaging as a biomarker in renal cell carcinoma. Cancer. 2009;115(10):2334–45.
84. Sala E, et al. The role of dynamic contrast-enhanced and diffusion weighted magnetic resonance imaging in the female pelvis. Eur J Radiol. 2010;76: 367–85.
85. Kim JH, et al. Dynamic contrast-enhanced 3-T MR imaging in cervical cancer before and after concurrent chemoradiotherapy. Eur Radiol. 2012;22:2533–9.
86. Kundu S, et al. Functional magnetic resonance imaging in cervical cancer: current evidence and future directions. J Cancer Res Ther. 2012;8(1):11–8.
87. Bernardin L, et al. Effectiveness of semi quantitative multiphase dynamic contrast-enhanced MRI as a predictor of malignancy in complex adnexal masses: radiological and pathological correlation. Eur Radiol. 2012;22:880–90.
88. Thomassin-Naggara I, et al. Quantitative dynamic contrast-enhanced MR Imaging analysis of complex adnexal masses: a preliminary study. Eur Radiol. 2012;22:738–45.
89. Bonemkamp D, et al. Advancements in MR imaging of the prostate: from diagnosis to interventions. Radiographics. 2011;31:677–703.
90. Tretiakova M, et al. Microvessel density is not increased in prostate cancer: digital imaging of routine sections and tissue microarrays. Hum Pathol. 2013;44(4):495–502.
91. Barentsz JO, et al. ESUR prostate MR guidelines 2012. Eur Radiol. 2012;22(4):746–57.
92. Ren J, et al. Dynamic contrast-enhanced MRI of benign prostatic hyperplasia and prostatic carcinoma: correlation with angiogenesis. Clin Radiol. 2008;63(2):153–9.
93. Yakar D, et al. Feasibility of 3T dynamic contrast-enhanced magnetic resonance-guided biopsy in localizing local recurrence of prostate cancer after external beam radiation therapy. Invest Radiol. 2010;45(3):121–5.
94. Cirillo S, et al. Endorectal magnetic resonance imaging at 1.5 Tesla to assess local recurrence following radical prostatectomy using T2-weighted and contrast-enhanced imaging. Eur Radiol. 2009;19(3):761–9.
95. Barrett T, et al. DCE and DW MRI in monitoring response to androgen deprivation therapy in patients with prostate cancer: a feasibility study. Magn Reson Med. 2012;67(3):778–85.
96. Cyran CC, et al. Perfusion MRI for monitoring the effect of sorafenib on experimental prostate carcinoma: a validation study. Am J Roentgenol. 2012;198(2):384–91.
97. Figueiras RG, et al. The role of functional imaging in colorectal cancer. AJR Am J Roentgenol. 2010;195(1):54–66.
98. Takebayashi Y, et al. Angiogenesis as an unfavorable prognostic factor in human colorectal carcinoma. Cancer. 1996;78:226–31.
99. Gollub MJ, et al. Dynamic contrast enhanced-MRI for the detection of pathological complete response to neoadjuvant chemotherapy for locally advanced rectal cancer. Eur Radiol. 2012;22:821–31.
100. Lim JS, et al. Perfusion MRI for the prediction of treatment response after preoperative chemoradiotherapy in locally advanced rectal cancer. Eur Radiol. 2012;22:1693–700.
101. Barcelo J, et al. DWI of the breast. In: Luna A et al., editors. Diffusion MRI outside the brain. Berlin: Springer; 2012.
102. Woodhams R, et al. Identification of residual breast carcinoma following neoadjuvant chemotherapy: diffusion-weighted imaging – comparison with contrast-enhanced MR imaging and pathologic findings. Radiology. 2010;254(2):357–66.
103. Lobbes MBI, et al. The role of magnetic resonance imaging in assessing residual disease and pathologic complete response in breast cancer patients receiving neoadjuvant chemotherapy: a systematic review. Insights Imaging. 2013;4(2):163–75.
104. Thukral A, et al. Inflammatory breast cancer: dynamic contrast-enhanced MR in patients receiving bevacizumab – initial experience. Radiology. 2007;244(3):727–35.
105. Kawashima M, et al. MR perfusion imaging using the arterial spin labeling technique for breast cancer. J Magn Reson Imaging. 2012;35(2):436–40.
106. Sigmund EE, et al. Intravoxel incoherent motion imaging of tumor microenvironment in locally advanced breast cancer. Magn Reson Med. 2011;65(5):1437–47.
107. Costa FM, et al. Advanced magnetic resonance imaging techniques in the evaluation of musculoskeletal tumors. Radiol Clin North Am. 2011;49(6):1325–58.

DCE-US: Evaluation of Angiogenesis

17

Nathalie Lassau

Contents

Abbreviations

AUC	Area under the curve
AUWI	Area under the wash-in
AUWO	Area under the wash-out
DCE-CT	Dynamic Contrast enhanced Computed Tomography
DCE-MRI	Dynamic Contrast enhanced Magnetic Resonance Imaging
DCE-US	Dynamic Contrast enhanced Ultrasonography
EFSUMB	European Federation of Societies for Ultrasound in Medicine and Biology
ESMO	European Society for Medical Oncology
FDA	Food and Drug Administration
GIST	Gastro-intestinal stromal tumours
HCC	Hepatocellular carcinomas
mTOR	Mammalian Target Of Rapamycin
MTT	Mean transit time
OS	Overall Survival
PDGF	Platelet-derived growth factor
PFS	Progression Free Survival
PI	Peak intensity
RCC	Renal cell carcinoma
RECIST 1.1	Response Evaluation Criteria in Solid Tumours
ROI	Region of interest
SWI	Slope of the wash-in
TIC	Time intensity curve
TKIs	Tyrosine kinase inhibitors
TPI	Time to peak intensity

N. Lassau, MD, PhD
Research Department, IRCIV,
Institut Gustave-Roussy, Villejuif, France

IR4M, UMR8081, Université Paris SUD 11,
Institut Gustave-Roussy, 114 avenue Edouard Vaillant,
94805 Villejuif, France
e-mail: lassau@igr.fr

A. Luna et al. (eds.), *Functional Imaging in Oncology*,
DOI 10.1007/978-3-642-40412-2_17, © Springer-Verlag Berlin Heidelberg 2014

VEGF	Vascular endothelial growth factor
WFUMB	The World Federation for Ultrasound in Medicine and Biology

17.1 Introduction

Currently the Response Evaluation Criteria in Solid Tumours (RECIST 1.1) is the most commonly used international guideline for evaluation of treatment response in solid tumours [1]. Targeted therapy with tyrosine kinase inhibitors (TKIs), vascular endothelial growth factor (VEGF) inhibitors and mammalian target of rapamycin (mTOR) inhibitors have become the standard of care for a variety of malignancies, including renal cell carcinoma (RCC) [2], gastrointestinal stromal tumours (GIST) [3], colorectal cancer, breast cancer and hepatocellular carcinomas (HCC). Sunitinib and sorafenib are US Federal (Food and Drug Administration)-approved TKIs for RCC [4]/GIST [5] and RCC/HCC, respectively. These drugs act on several tyrosine kinases, including receptors for VEGF, platelet-derived growth factor (PDGF) and stem cell factor. Bevacizumab, a humanised monoclonal antibody which inhibits the action of VEGF, is always used with interferon-alpha in RCC or with chemotherapy for colon or breast cancer. These targeted therapies complicate the evaluation of tumour responses, which are frequently underestimated. Despite significant clinical improvement, the radiological response rate using the classical RECIST criteria demonstrated only 15 % partial response and 70 % stable disease in metastatic RCC [6]. Thus, traditional evaluations based on tumour size criteria are no longer effective, as necrosis may occur without reduction in size of the tumour. The goal of functional imaging is to provide adapted tools to monitor patients with earlier surrogate markers.

17.2 How Does DCE-US Work?

17.2.1 What Is a US Contrast Agent?

For dynamic contrast-enhanced ultrasonography (DCE-US), the development of new and effective contrast agents in the form of microbubbles began to open up this application in 2003 (Fig. 17.1) [7]. Microbubbles are 1–10 μm-sized capsules containing an inert gas (Table 17.1) [8], usually chosen to be of high molecular weight so as to slow diffusion through the encapsulating membrane, thus prolonging their life after intravenous injection [9, 10]. Typical gases are perfluorocarbons and sulphur hexafluoride. The shell, again, is biocompatible: denatured albumen and phospholipids are commonly used. Factors influencing their choice are the compromise between stability and flexibility. After injection, they have the same haemodynamics as red blood cells, flooding the entire circulation including the capacious capillary bed. Their size prevents them leaving the circulation, so they behave as true blood pool contrast agents. Eventually (typically after a few minutes), the shell and gas dissolve and the microbubbles disappear. The shell residues are metabolised, mainly in the liver, and the gas is exhaled. Side effects are of the same order of frequency as with gadolinium agents [11].

17.2.2 How to Increase Signal to Noise Ratio

Their contrast behaviour under ultrasound is based on the fact that the gas they contain contracts and expands under the alternating higher and lower pressure phases of the sound beam. Importantly, this contraction and expansion is asymmetric: they resist compression more than expansion (i.e. their response is non-linear), and therefore the echoes they return are distorted compared to the sinusoidal waveform of the transmitted ultrasound beam. This means that the echoes contain harmonics, unlike tissue echoes, and these harmonic components can be detected using multipulse sonication approaches. A very successful choice, known as phase inversion imaging, is to transmit a pair of pulses along each ultrasound line, each with opposite phase [12]. Since tissue's response is broadly linear, when the echoes from such a pulse pair are summed, they cancel out, while the sum of the inverted pair from microbubbles add. Thus, a microbubble-only image can be created, albeit at half the normal frame rate. In the DCE-US studies performed in our institution, a single intravenous

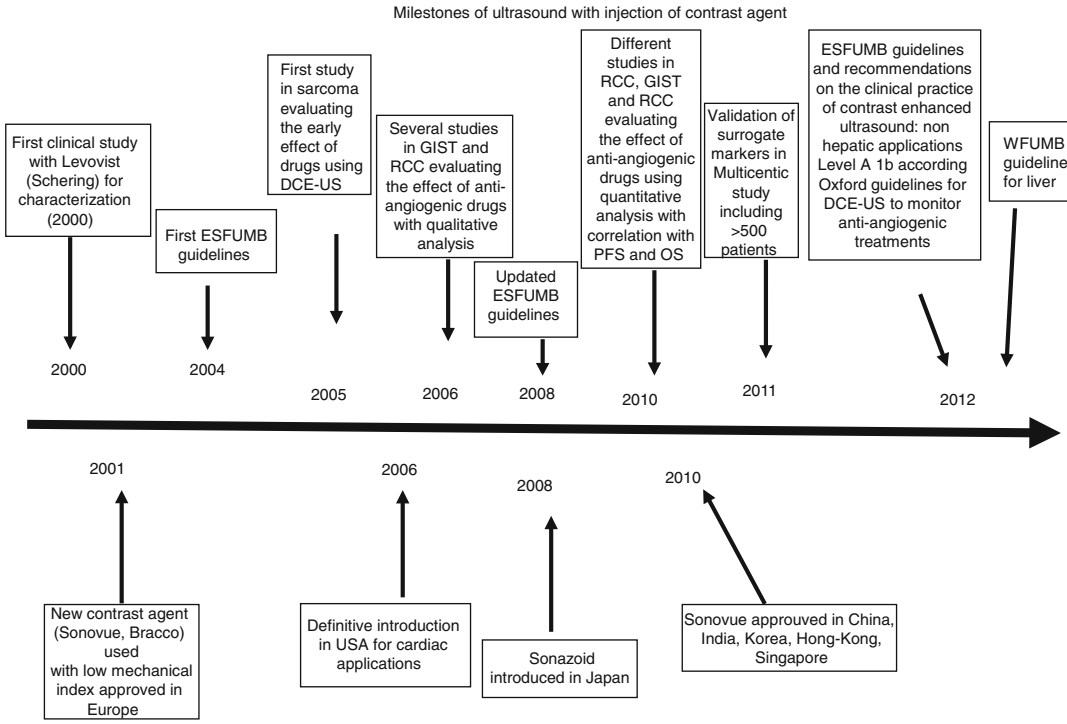

Fig. 17.1 This timeline represents the milestones in the validation process of ultrasound contrast agents for lesion characterization and evaluation of antiangiogenic treatments including guidelines. *Abbreviations*: *EFSUMB* European Federation of Societies for Ultrasound in Medicine and Biology, *WFUMB* World Federation for Ultrasound in Medicine and Biology, *PFS* progression-free survival, *OS* overall survival

Table 17.1 This table summarises the different microbubbles according to the gas and the shell

Ultrasound contrast agents			
Agent	Shell	Gas	Company
Echovist®	Galactose microparticles	Air	Schering
Levovist®	Galactose 99 % + palmitic acid 0.1 %	Air	Schering
Optison®	Human serum albumin	Perflutren (C_3F_8)	GE Healthcare
SonoVue®	Phospholipids	Sulphur hexafluoride (SF_6)	Bracco Imaging
Definity®	Phospholipid bilayer	Perflutren (C_3F_8)	Bristol Meyer Squibb
Sonazoid®	Phospholipids	Perfluorocarbon	GE Healthcare
Imagent®	Surfactant	Perflexane (C_6H_{14}) + air	Imcor Pharmaceuticals
AI-700	Synthetic biodegradable polymers (PLGA)	Perfluorocarbon	Acusphere
CardioSphere®	Polymer bilayer	Nitrogen (N_2)	Point Biomedical

We can classify the different agents that currently exist according to the encapsulated gas

bolus of 4.8 mL of the contrast agent consisting of sulphur hexafluoride-filled microbubbles (SonoVue; Bracco, Milan, Italy) is administered [13] Recording of the investigation together with timing is initiated as soon as the contrast agent is injected. A total of 720 images are acquired during each 3-min examination (Fig. 17.2).

In SonoVue®, the microbubbles are filled with sulphur hexafluoride (SF_6) and stabilised by a shell of amphiphilic phospholipids [8]. The mean diameter of the microbubbles is 3 μm, which means that they are confined to the circulation and they are distributed through the whole blood volume, which is ideal for the evaluation

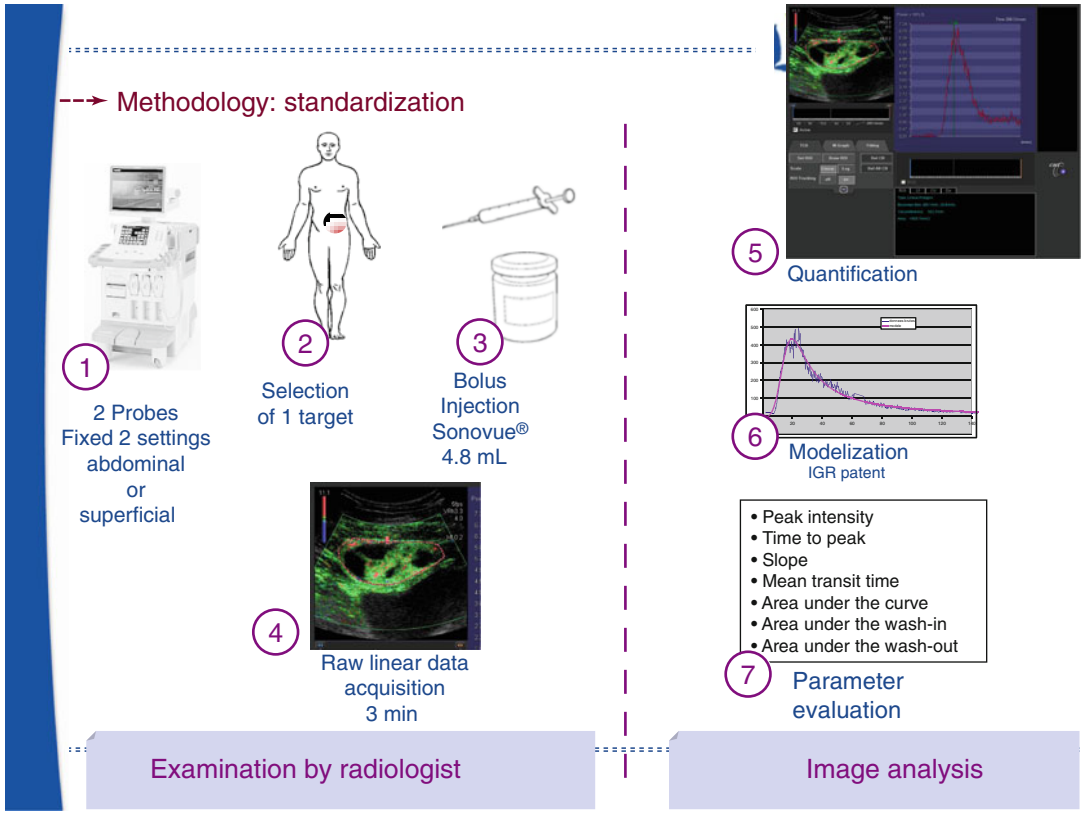

Fig. 17.2 This scheme represents the standardisation of the DCE-US acquisition: with fixed settings of the US machine, the radiologist selects an appropriate target with the best acoustical window. After a bolus injection of SonoVue, raw data are recorded over 3 min. In our institution, the radiologist selects a region of interest and after tracking, the automatic modelisation is applied to calculate 7 vascular parameters

of perfusion. Properties of the SF_6 gas include that it is innocuous, stable and inert. In addition, it is resistant to pressure changes and gives a good nonlinear response when insonated at low acoustic power, providing continuous real-time ultrasonographic (US) imaging without bubble destruction.

17.2.3 Easy to Use

SonoVue® is presented as a vial of SF_6, a powder combining phospholipids and pharmaceutical grade polyethylene glycol, and a syringe prefilled with 5 mL of 0.9 % sodium chloride. Before each ultrasound examination, the contrast agent is reconstructed by introducing the contents of the syringe into the vial followed by manual shaking for at least 20 s. The microbubbles are naturally buoyant and tend to accumulate at the top of the vial after standing for a few minutes: in order to ensure that the preparation is homogeneous for bolus injection, the vial is shaken before each administration. SonoVue® is usable for up to 6 h.

17.3 Qualitative and Quantitative Analysis of DCE-US

The first studies used only qualitative analysis after bolus injection in patients with sarcomas, GIST or RCC [14–16]. The development of perfusion [17] and quantification software, beginning in 2006, enabled quantitative analysis for calculating features linked to blood flow and blood volume. This new methodology, using raw linear ultrasound data [18], has been developed to

produce more robust and quantitative indices. A single intravenous bolus of 4.8 mL of the contrast agent is administered. The recording of the contrast-specific data together with timing is initiated, as soon as the contrast agent is injected.

For the time intensity curve (TIC) analysis, a single-plane imaging is usually performed following each bolus injection at 4 frames per second, which is a very high temporal resolution compared to other functional imaging techniques, over the duration of the ultrasound contrast enhancement. The average intensity within a region of interest (ROI) is displayed as a function of time which describes the wash-in and wash-out of the contrast agent in the ROI. One advantage of this method of quantification is the linear relation [13] between the microbubble concentration and the signal intensity [19]. Tracking software is now available, to correct for breathing movement, and is crucial to allow quantification of acquisitions [20].

Analyses based on the least-squares method can be performed with curve fitting software (Patent: WO/2008/053268 entitled "Method and system for quantification of tumoral vascularization") to derive the coefficients of the fitted curve, including wash-in and wash-out times. This allows functional indices to be determined, of which the most important are the peak intensity (PI), area under the curve (AUC), area under the wash-in (AUWI) and the area under the wash-out (AUWO) (all corresponding to blood volume); time to peak intensity (TPI) and the slope of the wash-in (SWI) (both corresponding to blood flow); and the mean transit time (MTT). A difference between DCE-US and DCE-CT or DCE-MRI is that permeability information cannot be obtained, because microbubbles are confined to the vascular space, behaving as true blood pool agents [21].

17.4 Blood Volume Using DCE-US as Surrogate Marker of Vascularisation

Several studies using quantitative techniques of DCE-US with bolus injection in RCC, HCC and GIST in phase I clinical trials have been published [22–24]. These have shown that indices representing blood volume calculated after 2 weeks of treatment correlated with the RECIST response but were apparent much earlier. In two studies of treatment response of RCC and HCC, the authors demonstrated a good correlation with both progression-free survival (PFS) and overall survival (OS) [22, 23].

In order to strengthen the level of evidence, a French multicentre study was set up to enrol patients with various types of tumours, approximately half of which were located outside the liver, with a majority of metastatic RCC, but also including GIST (Fig. 17.3), colon cancer, melanoma (Fig. 17.4), breast cancer and primary HCC. All patients were treated with antiangiogenic drugs alone or with a combination of two drugs (antiangiogenic + conventional chemotherapy or two antiangiogenic drugs). The preliminary results in this study of 539 patients indicated that the AUC, which is related to the blood volume, is one of the indices that best correlates to response at 6 months in both good and poor responders [25]. It had previously been demonstrated that the variability of this index was less than 15 % in preclinical studies [26], probably explaining the robust results in this study. The AUC at 1 month correlates with the RECIST response at 10 months (European Society for Medical Oncology 2011). The final results with 2 years follow-up will include correlation with PFS and OS.

There is now emerging evidence that DCE-US with appropriate ultrasound hardware and software tools may be used to differentiate between responders and nonresponders at an earlier stage than conventional imaging methods, and this allows tailoring of the treatment regimen, particularly changing treatment for nonresponders or modifying the dose according the toxicity [27]. The AUC promises to form an early surrogate marker to monitor patients. DCE-US offers several advantages over other imaging techniques, including ready repeatability without ionising radiation and lower cost [28, 29]. To the best of our knowledge, a comparable multicentre study with a similar level of standardisation has not been performed with DCE-CT or DCE-MRI.

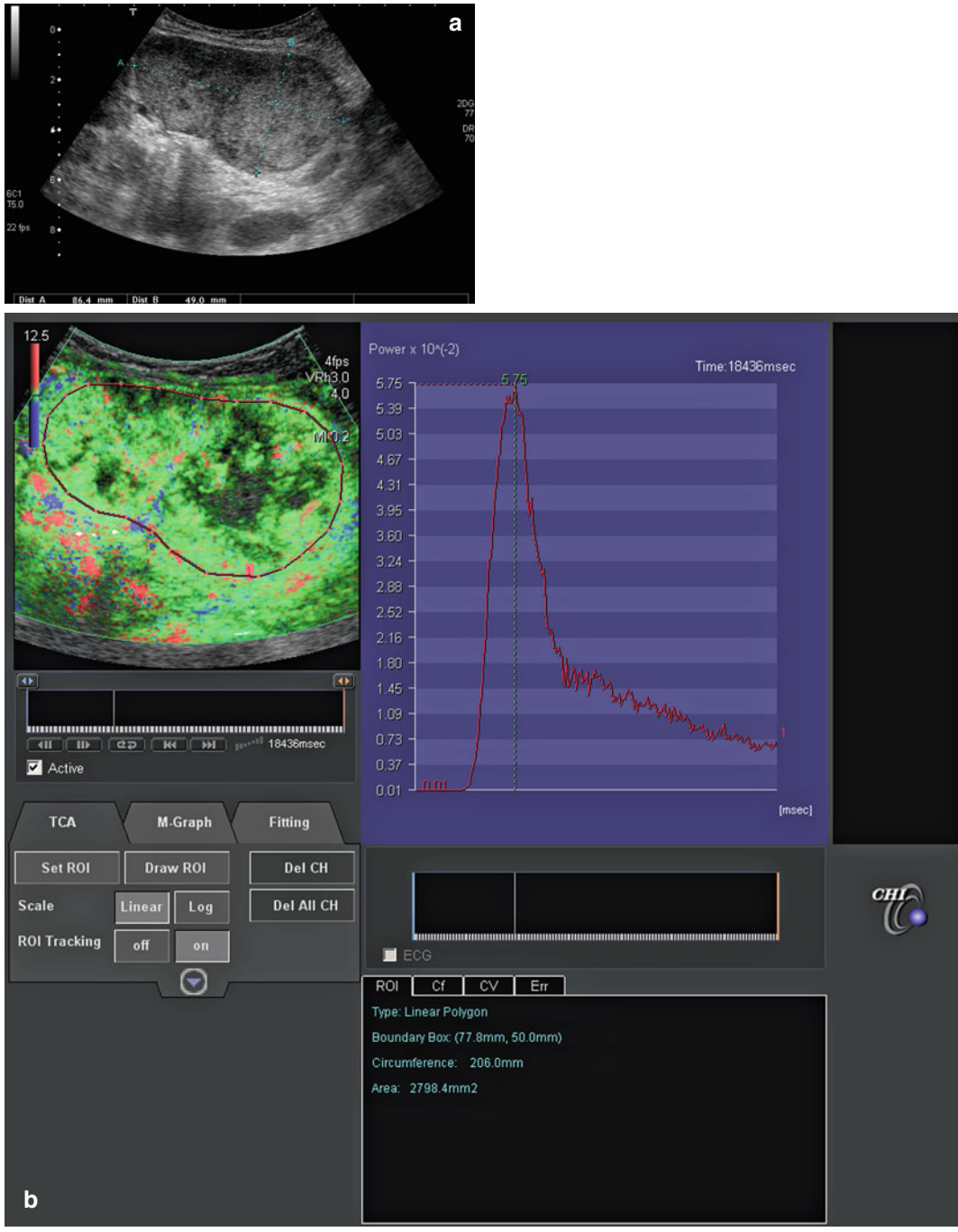

Fig. 17.3 Good responder, 58-year-old female, with metastatic GIST treated with imatinib (400 mg/day) for over 24 months. Target lesion: (**a**) US B-Mode image demonstrates a metastasis in the left iliac fossa, measuring 86 mm in maximum dimension. (**b**) DCE-US at baseline showed intense vascularisation of the mass. DCE-US was repeated at day 7, day 14, 1 (**c**) and 2 months. The *green-coloured* overlay represents the microbubble-specific signals, and the charts on the *right* of each image show the TICs. Note that these are normalised to the PI. (**d**) The corresponding contrast uptake curves demonstrate progressive decrease of the AUC at D7, D14, 1 and 2 months. Conversely to DCE-US, CT scans performed at baseline (**e**) and 2 months (**f**) with matched slices of the target lesion show no change in size (stable disease)

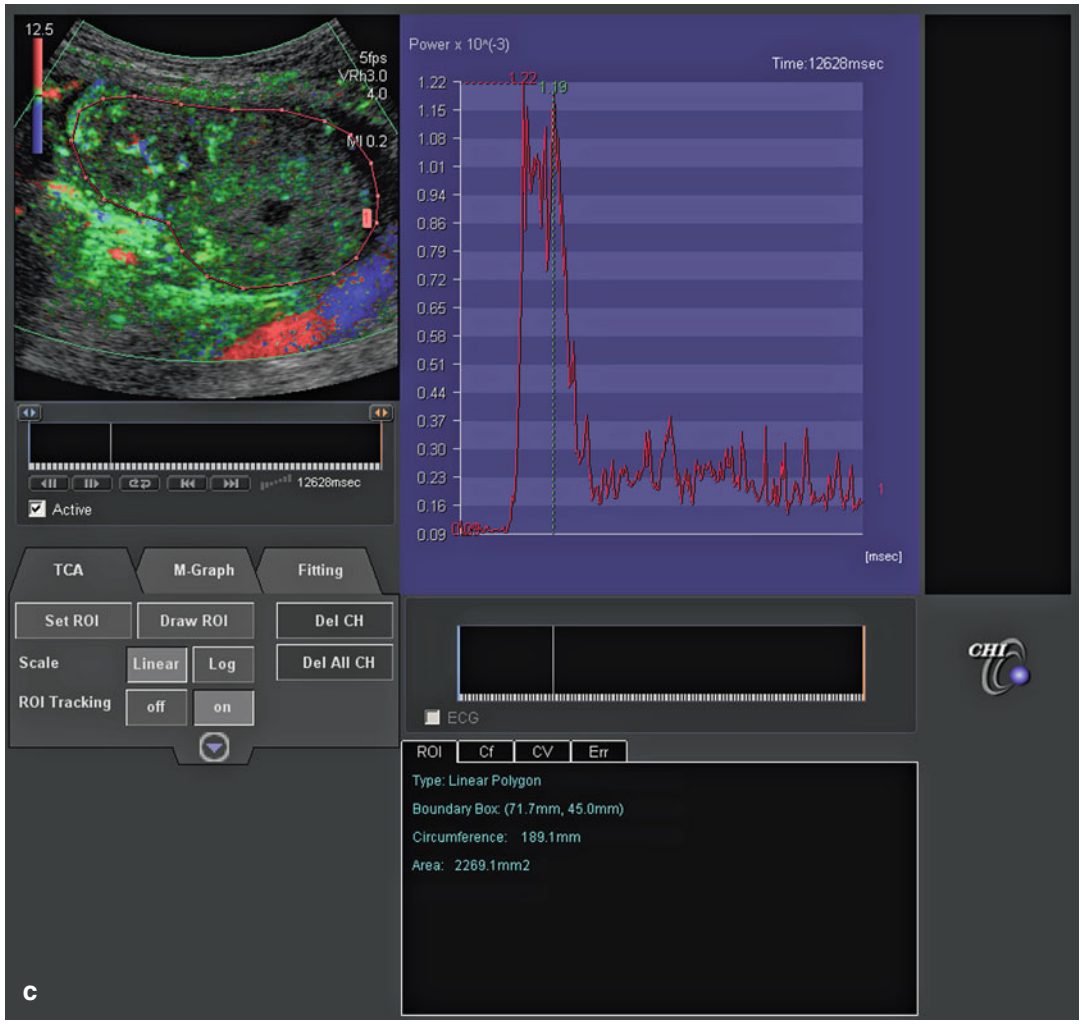

Perfusion curves case 1

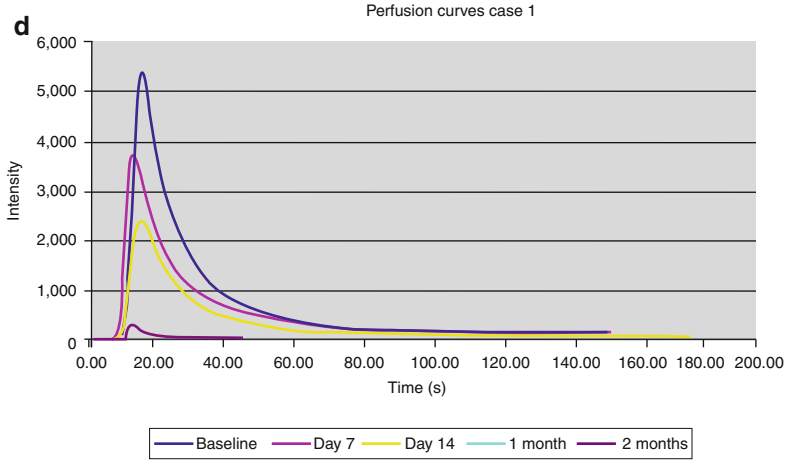

Fig. 17.3 (continued)

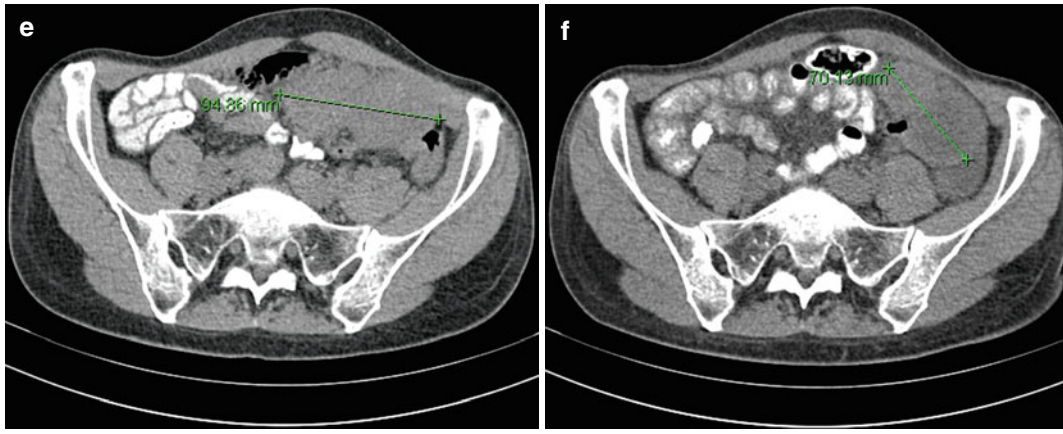

Fig. 17.3 (continued)

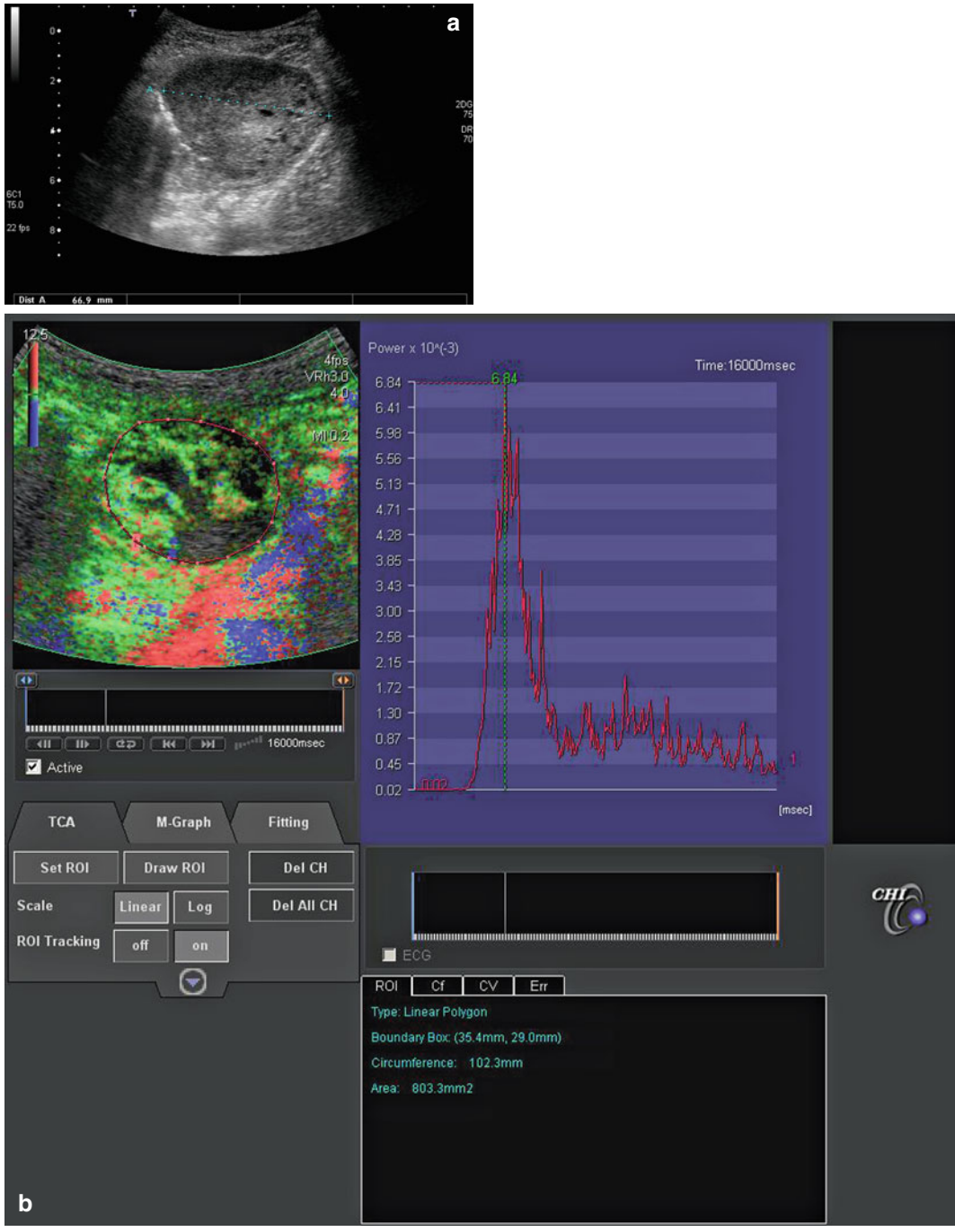

Fig. 17.4 Poor responder, 47-year-old male with melanoma on the left flank, treated with sorafenib and temsirolimus. (**a**) The baseline ultrasound B-Mode image showed a mass measuring 49 mm in largest diameter. (**b**) DCE-US study showed marked enhancement of the mass after contrast administration. (**c**) One month later, the lesion had not changed in size but showed an increase in contrast enhancement, corroborated by an increase in PI and AUC on the TIC (**d**). Unfortunately, the disease progressed uncontrollably at 2 months, and patient died 1 week after stopping the treatment

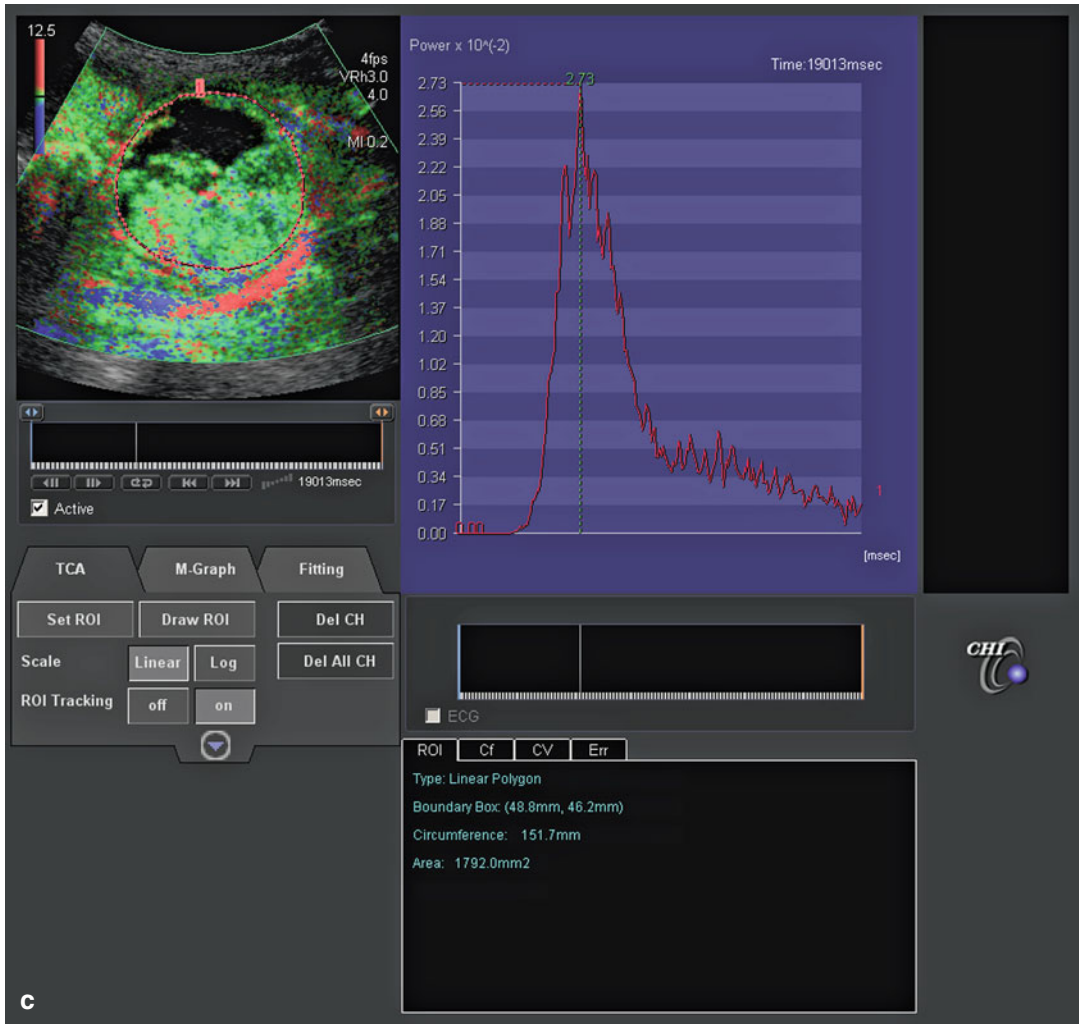

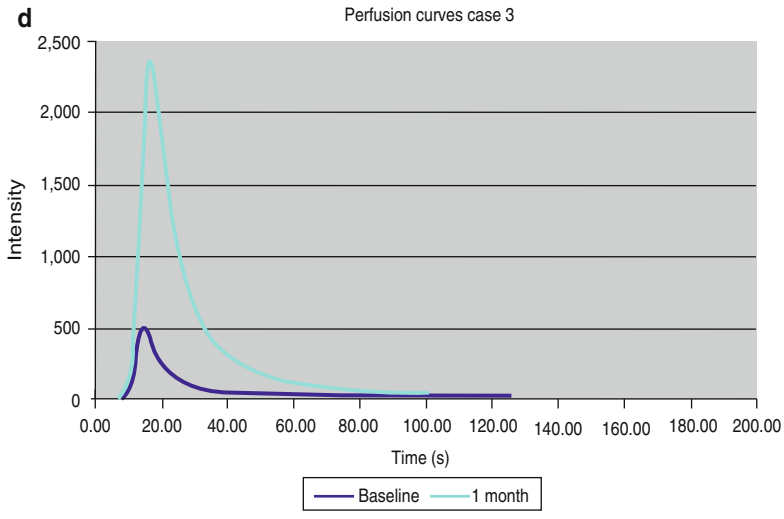

Fig. 17.4 (continued)

17.5 Level of Validation of DCE-US

DCE-US has been endorsed by the European Society for Medical Oncology (ESMO) to assess response to biological therapy for GIST [30], and this technique is also implemented in the European Federation of Societies for Ultrasound in Medicine and Biology (EFSUMB) guidelines for the monitoring of treatments with a high level strength-of-evidence rating (A. 1b) for this indication [31]. It was also included in the World Federation for Ultrasound in Medicine and Biology (WFUMB = international guidelines for contrast ultrasound in the liver) [32].

In the near future, two improvements could become available: 3D acquisition to overcome the sampling errors that are inevitable with single-slice acquisition and the addition of the arterial input to account for variations in the way that contrast bolus is administered [33].

References

1. Eisenhauer EA, et al. New response evaluation criteria in solid tumours: revised RECIST guideline (version 1.1). Eur J Cancer. 2009;45(2):228–47.
2. Rini BI, et al. Renal cell carcinoma. Lancet. 2009;373(9669):1119–32.
3. Demetri GD. Therapeutic monitoring of drug plasma concentrations and improved clinical outcomes in GIST. Clin Adv Hematol Oncol. 2009;7(2):S6–7.
4. Motzer RJ. New perspectives on the treatment of metastatic renal cell carcinoma: an introduction and historical overview. Oncologist. 2011;16 Suppl 2: 1–3.
5. Reichardt P, Reichardt A. Gastrointestinal stromal tumour (GIST): current standards in multimodal management. Zentralbl Chir. 2011;136(4):359–63.
6. van der Veldt AA, et al. Choi response criteria for early prediction of clinical outcome in patients with metastatic renal cell cancer treated with sunitinib. Br J Cancer. 2010;102(5):803–9.
7. Albrecht T, et al. Guidelines for the use of contrast agents in ultrasound. January 2004. Ultraschall Med. 2004;25(4):249–56.
8. Schneider M. Characteristics of SonoVue trade mark. Echocardiography. 1999;16(7 Pt 2):743–6.
9. Cosgrove D. Ultrasound contrast agents: an overview. Eur J Radiol. 2006;60(3):324–30.
10. Cosgrove D, Harvey C. Clinical uses of microbubbles in diagnosis and treatment. Med Biol Eng Comput. 2009;47(8):813–26.
11. Piscaglia F, Bolondi L. The safety of Sonovue in abdominal applications: retrospective analysis of 23188 investigations. Ultrasound Med Biol. 2006;32(9): 1369–75.
12. Phillips P, Gardner E. Contrast-agent detection and quantification. Eur Radiol. 2004;14 Suppl 8:P4–10.
13. Greis C. Technology overview: SonoVue (Bracco, Milan). Eur Radiol. 2004;14 Suppl 8:P11–5.
14. Lassau N, et al. Doppler US with perfusion software and contrast medium injection in the early evaluation of isolated limb perfusion of limb sarcomas: prospective study of 49 cases. Ann Oncol. 2005;16(7):1054–60.
15. Lamuraglia M, et al. To predict progression-free survival and overall survival in metastatic renal cancer treated with sorafenib: pilot study using dynamic contrast-enhanced Doppler ultrasound. Eur J Cancer. 2006;42(15):2472–9.
16. Escudier B, et al. Phase I trial of sorafenib in combination with IFN alpha-2a in patients with unresectable and/or metastatic renal cell carcinoma or malignant melanoma. Clin Cancer Res. 2007;13(6): 1801–9.
17. Burns PN, et al. Pulse inversion imaging of liver blood flow: improved method for characterizing focal masses with microbubble contrast. Invest Radiol. 2000;35(1):58–71.
18. Peronneau P, et al. Contrast ultrasonography: necessity of linear data processing for the quantification of tumor vascularization. Ultraschall Med. 2010;31(4):370–8.
19. Li PC, Yang MJ. Transfer function analysis of ultrasonic time-intensity measurements. Ultrasound Med Biol. 2003;29(10):1493–500.
20. Goetti R, et al. Quantitative perfusion analysis of malignant liver tumors: dynamic computed tomography and contrast-enhanced ultrasound. Invest Radiol. 2012;47(1):18–24.
21. Cosgrove D, Lassau N. Imaging of perfusion using ultrasound. Eur J Nucl Med Mol Imaging. 2010;37 Suppl 1:S65–85.
22. Lassau N, et al. Metastatic renal cell carcinoma treated with sunitinib: early evaluation of treatment response using dynamic contrast-enhanced ultrasonography. Clin Cancer Res. 2010;16(4):1216–25.
23. Lassau N, et al. Advanced hepatocellular carcinoma: early evaluation of response to bevacizumab therapy at dynamic contrast-enhanced US with quantification – preliminary results. Radiology. 2011;258(1):291–300.
24. Lassau N, et al. Quantitative functional imaging by Dynamic Contrast Enhanced Ultrasonography (DCE-US) in GIST patients treated with masatinib. Invest New Drugs. 2012;30(2):765–71.
25. Lassau N, et al. Dynamic contrast-enhanced ultrasonography (DCE-US) and anti-angiogenic treatments. Discov Med. 2011;11(56):18–24.
26. Gauthier M, et al. Estimation of intra-operator variability in perfusion parameter measurements using DCE-US. World J Radiol. 2011;3(3):70–81.

27. Michels J, et al. Sunitinib inducing tumor lysis syndrome in a patient treated for renal carcinoma. Invest New Drugs. 2010;28(5):690–3.
28. Lederle W, et al. Imaging in the age of molecular medicine: monitoring of anti-angiogenic treatments. Curr Pharm Biotechnol. 2012;13(4):595–608.
29. Frampas E, et al. Advanced hepatocellular carcinoma: early Evaluation of response to targeted therapy and prognostic value of perfusion CT and dynamic contrast enhanced-ultrasound. Preliminary results. Eur J Radiol. 2013;82(5):e205–11.
30. Casali PG, Blay JY. Gastrointestinal stromal tumours: ESMO Clinical Practice Guidelines for diagnosis, treatment and follow-up. Ann Oncol. 2010;21 Suppl 5:v98–102.
31. Piscaglia F, et al. The EFSUMB Guidelines and Recommendations on the Clinical Practice of Contrast Enhanced Ultrasound (CEUS): update 2011 on non-hepatic applications. Ultraschall Med. 2012;33(1): 33–59.
32. Claudon M, et al. Guidelines and good clinical practice recommendations for Contrast Enhanced Ultrasound (CEUS) in the liver – update 2012: a WFUMB-EFSUMB Initiative in Cooperation with Representatives of AFSUMB, AIUM, ASUM, FLAUS and ICUS. Ultrasound Med Biol. 2013; 39(2):187–210.
33. Gauthier M, et al. Assessment of quantitative perfusion parameters by dynamic contrast enhanced-ultrasonography using a deconvolution method: an in vitro and in vivo study. J Ultrasound Med. 2012;31(4): 595–608.

Spectroscopy of Cancer

18

Natalie J. Serkova

Contents

Abbreviations

CLL	Chronic lymphatic leukaemia
DNP	Dynamic nuclear polarization
EIC	Extensive intraductal component
FLT	^{18}F-Fluorothymidine
GPC	Glycerophosphocholine
HR-MAS	High-resolution magic angle spinning
Lac	Lactate
MRS	Magnetic resonance spectroscopy
MRSI	MRS and spectroscopic imaging
NAA	*N*-acetyl aspartate
NACT	Neo-adjuvant chemotherapy
NMR	Nuclear magnetic resonance
PC	Phosphocholine
PK	Pharmacokinetics

18.1 Introduction

Nuclear magnetic resonance (NMR) was initially described as a physical phenomenon and initially was developed and used exclusively for chemical and structural analyses [1, 2]. Nowadays, the most commonly used NMR methodologies in biomedicine are based on studying the physical properties of hydrogen nuclei (protons) in tissue water (which is commonly known as magnetic resonance imaging, MRI) followed by proton NMR spectroscopy (or MRS) on other endogenous metabolites and, less frequently, other "magnetically active" nuclei such as ^{31}P, ^{13}C, ^{19}F, and ^{23}Na. The strong external magnetic field aligns the magnetic moments of protons

N.J. Serkova
Departments of Anesthesiology and Radiology, University of Colorado Cancer Center Animal Imaging Core, Anschutz Medical Center, Aurora, CO 80045, USA

A. Luna et al. (eds.), *Functional Imaging in Oncology*,
DOI 10.1007/978-3-642-40412-2_18,

(with spins –½ and ½) parallel and antiparallel to the magnetic field. The population of spins in the parallel orientation (which are of a slightly lower energy level) is larger than in the antiparallel orientation as described by the Boltzmann distribution. This results in a net "magnetization" in the sample aligned with the direction of the external magnetic field. When a radiofrequency (rf) pulse is applied to the sample, the magnetization orientation is changed, and after the pulse is gone, the system relaxes to its original status. Hydrogen nuclei in different tissues have different relaxation properties, which can be detected by rf MR receivers. MR tissue relaxation characteristics following an excitation rf pulse reveal information about the concentration, mobility, and chemical bonding of hydrogen and, less frequently, other tissue elements. The strongest NMR signals in a living system arise from hydrogens in water and fat protons due to their metabolic abundance (water compromises up to 66 % of the body weight). Other endogenous and exogenous metabolites also give signals on ^{1}H-NMR but with much weaker signal-to-noise ratios due to lower concentrations. A significant number of endogenous metabolite signals are usually obscured by the water signal (both in vivo and in vitro), and their detection requires adequate techniques for water suppression (and often lipid or macromolecule suppression).

In 1971, Raymond Damadian discovered that the proton relaxation times of a normal tissue and a tumor differed, which motivated physicians and scientists to consider MRI as a tool for oncologic imaging. Subsequently, in 1973, Paul Lauterbur demonstrated the MRI phenomenon on small test tubes (filled with liquids) using a gradient approach for spatial localization. In 1975, Richard Ernst proposed Fourier Transform, which became the basis for MR phase and frequency encoding allowing for actual image and spectrum creation. The first commercially available MR scanners were introduced to clinical practice in the 1970s, most of them operated at 0.6 Tesla (T, external magnetic field strength). During the following decade, stronger 1.5 T MR systems became available. In 2002, the US Food and Drug Administration approved the use of 3 T for the brain and the whole body. Nowadays, human 7 T brain and whole body scanners are available for human (nonclinical) MRI research. With all technological improvements, it became clear that MR has a great potential in visualizing biochemistry noninvasively (in a precise anatomical location as defined by MRI). This dual ability to provide images as well as highly localized chemical "snapshots" of a lesion noninvasively and in the same experiment is the most unique feature of MR among all other imaging techniques (see as examples Figs. 18.1 and 18.2 for anatomical localizations of MR spectra). The altered tumor metabolic phenotype with its high glucose utilization, high glycolytic activity, and increased membrane biosynthesis can be observed noninvasively by magnetic resonance spectroscopy (MRS), since the hydrogens of different endogenous metabolites (tissue-own small molecules) resonate at slightly different frequencies [6–8]. In general, translational and clinical research intensively utilizes MR spectroscopic approach for biochemical characterization of the tissue of interest either in vivo (using MRS single-voxel or multi-voxel spectroscopic imaging, MRSI) or ex vivo (so-called NMR-based metabolomics) [9, 10]. Other metabolic imaging techniques include positron emission tomography (PET) and single-photon emission computed tomography (SPECT) [11, 12]; with the recent development of integrated PET/MR scanner, new horizons of metabolic and molecular imaging are being recently explored. This review is focused on noninvasive MRS and spectroscopic imaging (MRSI) and their roles in clinical decision-making for cancer diagnosis, staging, and treatment response.

18.2 In Vivo MRS and MRSI

In vivo magnetic resonance spectroscopy (MRS) and spectroscopic imaging (MRSI) have been used for the noninvasive prognosis and diagnosis of tumors for over two decades. Overtime, MRS advanced with the rate of technological improvements such as higher magnetic field, coil design, and advanced pulse sequences. Nowadays,

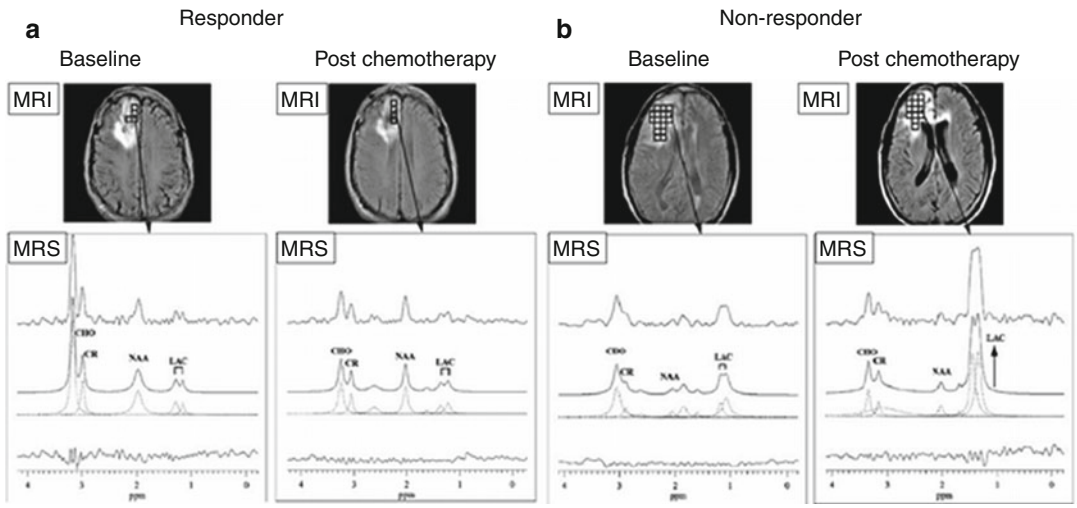

Fig. 18.1 ^{1}H-MRS on brain cancer patients with anatomical localization from gadolinium-enhanced T1-weighted MRI (*top panel*). (**a**) A responder with a mildly enhanced anaplastic oligodendroglioma showed a significant decrease in [tCho/tCr] and a slight improvement in [NAA/tCr] on posttreatment scans (4 months after chemotherapy); (**b**) A nonresponder with an anaplastic astrocytoma revealed unfavorably low NAA levels at the baseline and highly increased [Lac/tCr] levels 4 months after treatment (recurrent disease was confirmed 2 months later by gadolinium-enhanced T1-weighted MRI) (Adapted from [3])

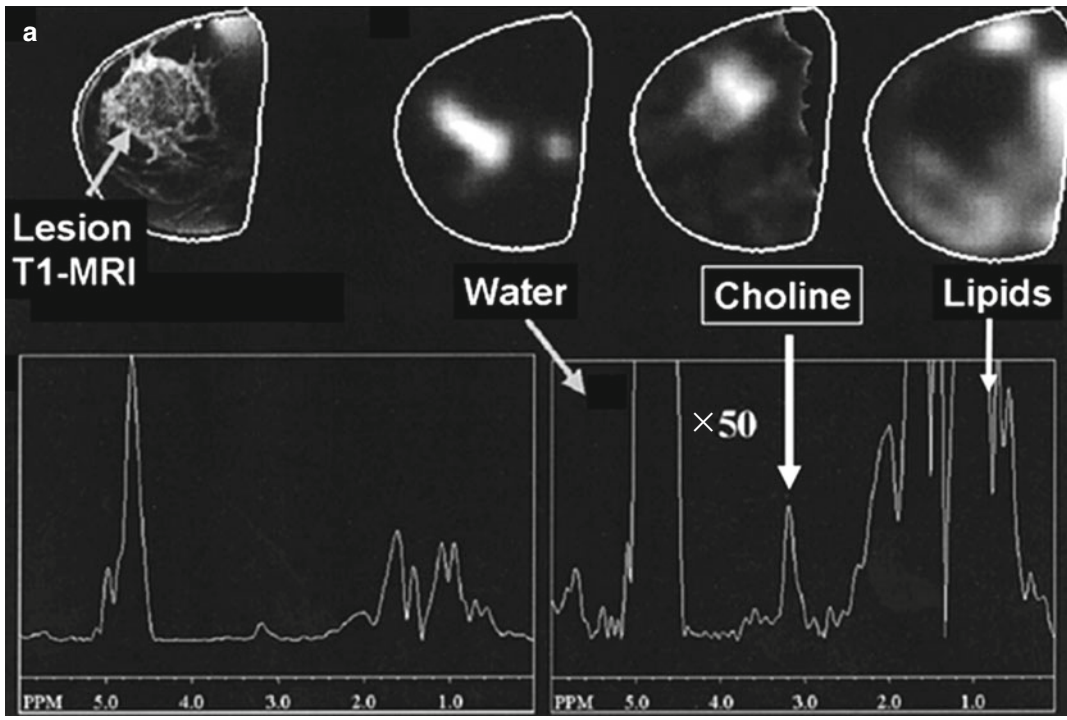

Fig. 18.2 Anatomical MRI and metabolic ^{1}H-MRS/MRSI on patients with breast cancer. (**a**) A patient with infiltrating ductal carcinoma of the breast with spatial co-localization of malignant margins by contrast-enhanced T1-weighted MRI and tCho-^{1}H-MRSI (Adapted from [4]). (**b**) Changes in the lesion size by T2-weighted MRI (*top panel*) and in tCho peak by ^{1}H-MRS (*low panel*) prior and 3 cycles after NACT in a responding and nonresponding patients (Adapted from [5])

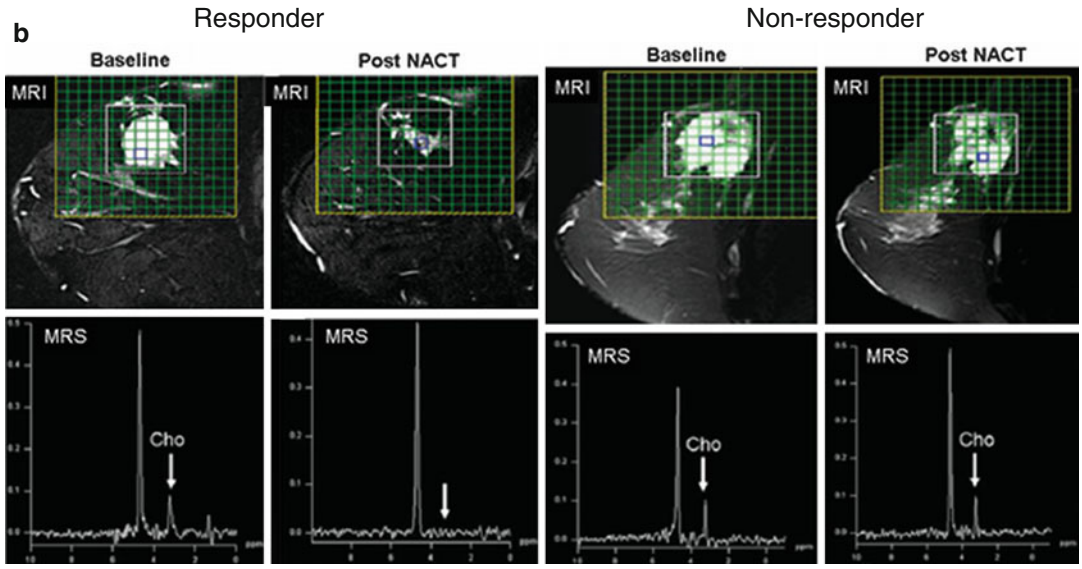

Fig. 18.2 (continued)

clinical MRS data are still most commonly acquired at the field strength of 1.5 T, but the trend is increasing toward the use of clinical 3 T machines (allowing for higher spatial and spectral resolution, doubling of the signal-to-noise, and reducing acquisition times). In order to acquire MR spectra, clinically available MR scanners usually need to be equipped with a set of specifically designed surface coils for precise voxel localization. In some cases, even more sophisticated coil design is required such as endorectal coils for prostate gland MRS or multinuclear resonance channels for ^{31}P- or ^{13}C-MR detection. In clinical applications of MRS, the ^{1}H nuclei have played a dominant role, mainly because proton hydrogens (^{1}H, the most "magnetic sensitive" nucleus) are present in most tissue metabolites and therefore can be detected with high sensitivity. In addition, proton MRS protocols can be employed relatively easily on common clinical MR scanners, which are dedicated to observe the protons of tissue water and fat for conventional MRI. The waste majority of clinically available ^{1}H-MRS protocols has been developed for noninvasive metabolic assessments of brain, breast, and prostate cancers. Modern MRS techniques – such as the point resolved spectroscopy, PRESS – allow for volume localization of 1 μL of tissue ($1 \times 1 \times 1$ mm^3) at the 3 T for, for example, brain MRS scans.

18.2.1 Brain Metabolic ^{1}H-MRS Imaging

Due to its intrinsic soft tissue contrast, MRI is the method of choice for brain imaging. Brain MRI, including gadolinium contrast-enhanced MRI, is the "gold standard" in diagnostic management and treatment planning for brain cancer patients. Historically, ^{1}H-MRS research has been focused mainly on neurological disorders, in part because use of the technique in the brain imposes fewer technical challenges than in other organs. Brain MRS has also pioneered clinical metabolic imaging in oncology by providing unique metabolic information of the lesion to help the diagnosis of tumor type and grade or detection of recurrence [13, 14]. A dedicated brain phased-array coils are used for single-voxel ^{1}H-MRS or multi-voxel ^{1}H-MRSI in the brain. To measure a viable tumor lesion, the voxel is placed by MRI guidance using the well-enhanced part of the tumor (see Fig. 18.1 as an example).

In brain tumors, a relatively high signal is observed at 3.2 ppm on the MRS chemical shift scale, which has been identified (back in the 1990s) as the methyl group of choline-containing compounds (often referred as total choline, tCho, in ^{1}H-MRS). The choline compounds are involved in the biosynthesis and degradation of phospholipids such as phosphatidylcholine, which is required for the buildup and maintenance of cell membranes. A working hypothesis is that elevated tCho is a reflection of increased cellular proliferation and fast membrane turnover in replicating cells. In addition to tCho (increased in most brain tumors), two other brain metabolites – *N*-acetyl aspartate (NAA, a neuronal marker) and total creatine (tCr, energy metabolism) – are usually easily seen in water- and fat-suppressed ^{1}H-MRS of the brain. Changes in tCho, tCr, and NAA can be seen in gliomas, astrocytomas, meningiomas, as well as neuroblastomas. As mentioned above, the most characteristic metabolic feature of brain and CNS tumors is the increase level of tCho as compared to unaffected tissues [14–16]. A reduction in the tCr signal also occurs in gliomas but less consistently than increased tCho. A reduction in NAA is a general observation in adult gliomas. An appearance of lactate (Lac) signals (together with lipids) is often seen in glioblastomas. Recent implementation of high-field magnets (3 T) into a clinical setting allows for expanded metabolic imaging in the brain: Lac [17] and glycine MRSI [18] can easily be performed in glioblastoma patients at a reasonable acquisition time, where significantly increased Lac and glycine might be of a diagnostic value.

Beside diagnostic features with increased tCho/decreased NAA levels, another useful application of ^{1}H-MRS is in stereotactic procedures to obtain biopsies from proper (most malignant) tumor location and to delineate the tumor lesion for surgery planning or radiation treatment [19]. Indeed, ^{1}H-MRS markers have proven of being highly sensitive in assessing the treatment response. An earlier study by UCSF group [15] reported on the treatment response to radiation in glioma patients. Before radiation, there was elevated tCho and decreased tCr and NAA, with a small peak corresponding to Lac + lipids. This characteristic MRS signature was seen for most cases of adult glioma with some level of necrosis. Immediately after radiation, the levels of tCho, tCr, and NAA decreased and the Lac + lipids increased – a typical signature for tumor reduction and radiation-induced necrosis 4 months after radiation. Six months after radiation, all recurrent gliomas were presented with a typical metabolic profile characterized by the high tCho and Lac + lipid levels and the low levels of NAA and tCr [15]. Another ^{1}H-MRSI study was performed on 14 patients with low-grade brain tumors in order to assess the response to chemotherapy [3]. Longitudinal changes of regional levels of tCho, NAA, and Lac relative to tCr were assessed before and after chemotherapy treatment. At baseline, a low [NAA/tCr] was associated with decreased progression-free survival time, as was an increase in [tCho/tCr] during chemotherapy. In responders, a dramatic decrease of tCho and a slight decrease in NAA were seen 4 months after treatment (Fig. 18.1). In nonresponders, an increase in [tCho/tCr] and [Lac/tCr] was noted as a predictor for recurrent disease (2 months before MRI confirmed progressive disease) (Fig. 18.1). ^{1}H-MRS was also applied in animal models for brain tumors, mostly nude rat orthotopic xenograft models of human neuroblastoma and glioblastoma. Animal brain showed a similar metabolic pattern of brain malignancy including increased tCho and decreased NAA and tCr levels [16]. When treated with irinotecan or cisplatin (two commonly used chemotherapeutic drugs), ^{1}H-MRS displayed an abnormal accumulation of mobile neutral lipids and Lac with a simultaneous decrease in tCho in drug-sensitive xenografts [20, 21].

Recent technological advances allow for a multimodality approach for better staging and treatment response assessment. The combination of quantitative MRS/MRSI and highly sensitive PET biomarkers has a lot to offer for brain imaging. Indeed, recent studies showed the correlation between high uptake of ^{18}F-fluoroethyl-tyrosine (FET)-PET (a marker for tumor infiltration) and

neuronal loss by NAA in patients with cerebral gliomas grades II–IV [22]. Conventional FDG-PET and NAA ^{1}H-MRSI detected similar regions in pediatric brain tumors as metabolically active, but (because of high background in glucose uptake in the brain) MRSI proved to be more sensitive [23]. In summary, ^{1}H-MRS remains the most sensitive noninvasive method that can provide the metabolic profile and metabolite levels of a particular brain tumor region. In addition, ^{1}H-MRSI can also be used to establish the spatial distribution of a particular metabolite (with tCho and NAA being the most useful metabolic markers) in the metabolically heterogeneous brain and brain lesions.

18.2.2 Choline ^{1}H-MRS in Breast Cancer

The waste majority of breast ^{1}H-MRS studies so far have been performed at 1.5 T clinical scanners using dedicated multichannel phased-array breast coils (with a patient being in the prone position). Most groups have used single-voxel ^{1}H-MRS to localize metabolite signals, and some groups have explored the use of ^{1}H-MRSI for the spatial distribution of breast metabolites. In both cases, the MRS studies are usually performed immediately after gadolinium-based dynamic contrast-enhanced (DCE)-MRI with fat suppression [24]. ^{1}H-MR spectra from normal breast tissue and breast cancer lesions reveal fewer resonances than generally detected in the brain. Large fat and water resonances are present in the breast tissue and vary in amplitude depending on the amount of fibroglandular and adipose tissues in the voxel. But – as for the brain – one of the metabolic hallmarks of breast cancer is an appearance of choline-containing compounds (tCho) at 3.2 ppm, indicating that this is a general neoplastic phenomenon [24]. Several groups have successfully shown that increased tCho was co-localized with malignant margins on anatomical T1- and T2-weighted MRI (Fig. 18.2a) and the tCho levels that statistically differed between malignant and benign patients ($p < 0.0008$) [4]. Choline-based discrimination of malignant from benign lesions has been reported in various clinical studies with ranges of sensitivity 70–100 % and specificity 67–100 % [24, 25]. A recent 1.5 T clinical ^{1}H-MRS study on 184 breast cancer patients has reported characteristic changes in tCho characterized by different molecular cancer subtypes [26]. The tCho integrals were significantly higher for invasive ductal carcinomas, high-grade cancers, and extensive intraductal component (EIC)-negative cancers than for in situ invasive carcinomas, low-grade cancers, and EIC-positive cancers. Another recent study by Sah et al. [27] has showed that nontriple negative breast cancer patients as well as triple positive have significantly higher tCho levels by ^{1}H-MRS when compared to triple negative cancers, such indicating a potential diagnostic use of tCho-MRS for molecular classification.

Several groups have also shown that the disappearance of tCho is a sensitive indicator for the response success to neoadjuvant chemotherapy (NACT) [5, 28]. In one of these studies, 30 patients with locally advanced breast cancers undergoing three cycles of NACT were monitored by ^{1}H-MRS. The MR response was compared with the clinical response. A strong correlation between the decrease in the lesion size on T2-weighted MRI (average 84 % in responders) and decline in tCho signal (from baseline level of 7.8 to 3.6) was observed for responders at cycle III of NACT (Fig. 18.2b) [5]. The sensitivity and specificity for tCho^{1}H-MRS to detect responders from nonresponders were 86 and 91 %, respectively, while 100 % sensitivity but reduced 73 % specificity were seen for tumor volumes by MRI [5, 28]. Preclinical ^{1}H-MRS studies on cells and animal models of breast cancers have further explored the treatment response to a variety of anticancer drugs in regard to choline metabolism. A significant decrease in tCho was seen for cytotoxic chemotherapeutic drugs (docetaxel), signal transduction inhibitors (MAPK inhibitor), as well as for nonsteroidal antiinflammatory drugs (NSAID, indomethacin) [29–31]. Choline metabolism has also received attention as a therapeutic target – animal studies with choline kinase inhibitors have been performed revealing a moderate inhibition of tumor growth and a significant

decrease in tCho and phosphocholine peaks by ^{1}H- and ^{31}P-MRS, respectively, in treated tumor-bearing animals [32].

In summary, the evidence for abnormal choline metabolism, especially in breast cancer, is so overwhelming that tCho is believed to be a potential biomarker in cancer diagnosis (detection, grading, and staging) and for treatment response [8, 24]. This attracted much attention to develop yet another choline-based imaging platform using a highly sensitive positron emission tomography (PET) approach with ^{11}C- and ^{18}F-choline tracers (such as with ^{18}F-fluoromethyl-choline) [33]. Although still being developed, existing studies of breast tCho^{1}H-MRS/MRSI have shown promising results with the growing number of clinical research groups incorporating these metabolic techniques along with their breast MRI protocols. As for the brain, high fields (3 and 4 T) can potentially improve the quality of breast cancer MRS and provide ability for precise metabolite quantification [34].

18.2.3 Prostate Cancer by ^{1}H-MRS

Since the prostate gland is of a relatively small size and, similarly to the breast, is embedded in adipose tissue, advanced pulse sequences and special endorectal coils need to be used for prostatic ^{1}H-MRS. Multidimensional MRSI and three-dimensional MRS acquisitions can be performed at 1.5 T in about 10–15 min at a spatial resolution down to 0.4 mL. Using these protocols, several groups have demonstrated that ^{1}H-MR spectra of the prostate gland contain tCho and tissue-specific metabolite citrate. As for breast and brain cancers, the increased levels of tCho are indicators of malignancy and disease recurrence in the prostatic gland [35]. Because the prostate gland has physiologic and metabolic functions unique from the rest of the body, the normal prostate gland accumulates remarkably high levels of the metabolite citrate relative to other tissues. This is achieved by the ability to accumulate high cellular levels of zinc in secretory epithelial cells that inhibit citrate oxidation. Citrate can be seen by MRSI [36] and its decreased levels correlate with the Gleason score. The ratios of [citrate/tCho] were also predictive for recurrent prostate cancers after external beam radiation therapy with sensitivity of 89 % and specificity of 82 % [37].

Nowadays, the rapid implementation of 3 T scanners allows for improved multiparametric MRS prostate imaging with faster scans, increased signal-to-noise, and better quantification [38–40]. While the use of an endorectal coil is indispensable at 1.5 T, external phased-array coils might provide adequate signal-to-noise and sufficient spatial and spectral resolution at 3 T [41].

18.2.4 Other Cancers by ^{1}H-MRS

As mention above, increased tCho levels is rather a general neoplastic phenomenon for a variety of cancers. Indeed, extracranial head-and-neck tumors and metastatic lymph nodes have demonstrated increased [Cho:Cr]-ratios at 1.5 T [42]. Patients with head-and-neck squamous cell carcinoma showed not only changes in choline and lipid peaks but also in lactate [43, 44]. In vivo ^{1}H-MRS is still in its infancy for detection of abdominal and pelvic lesions in gynecological cancers. However, a recent study by Italian colleagues has provided an encouraging evidence that three-dimensional ^{1}H-MRS is clinically feasible in ovarian cancer patients even at 1.5 T [45]. A tCho peak was detected in 17 out of 19 malignant tumors (sensitivity 89 %) and absent in 20 out of 21 apparently healthy pelvic tissues. In addition, 3 out of 4 benign lesions revealed a tCho peak resulting in overall specificity of 84 % (21 out of 25 for nonmalignant and benign together) [45].

18.2.5 Introduction of Hyperpolarized ^{13}C Carbon MRS

Unlike hydrogens (100 %), the natural abundance of ^{13}C nuclei is low (1.1 %) which provides this technique with low intrinsic sensitivity. However, it also allows for the use of isotopically

enriched tracers. The use of [1-^{13}C]glucose allowed for ^{13}C-NMR observation of glucose fluxes in perfused cells and organs [46]; however, the low sensitivity of ^{13}C results in very long acquisition times in humans and constitutes a problem for clinical application of ^{13}C-MRS. Yet another technique, called dynamic nuclear polarization (DNP), came to rescue. The technique increases signal-to-noise of the ^{13}C-signal by 50,000-fold by producing hyperpolarized ^{13}C-labeled substrates [47]. Hyperpolarized ^{13}C-tracers have short lifetime, meaning that hyperpolarized ^{13}C-MRS must be completed within a few minutes after preparation of an injectable hyperpolarized ^{13}C-tracer. This technique is still in its infancy and has been almost exclusively used in animals; only selected MR groups have all necessary hyperpolarizer equipment for on-site tracer production. Nevertheless, the approach has its promising features.

The first and, as of today, the major substrate to be proved useful for in vivo ^{13}C-MRS of cancer was [1-^{13}C]pyruvate[48, 49]. Pyruvate is rapidly taken up in the body and its metabolic fate depends on the nature of the organ. In the tissue with high mitochondrial activity (where pyruvate is primarily feeding into the TCA cycle), pyruvate is decarboxylated and produces acetyl-CoA. In tissue with high glycolytic rates (such as the muscle and, of course, in cancerous tissues), [1-^{13}C]pyruvate is metabolized to [1-^{13}C]alanine and, subsequently, to [1-^{13}C]lactate, the end product of glycolysis. Increased aerobic glycolysis and lactate accumulation is the main metabolic hallmark of oncogenesis. As such, using $^{13C\text{-}MRS}$, the conversion rate of [1-^{13}C]pyruvate to [1-^{13}C]lactate has been shown associated with tumor grade [48]. [1-^{13}C]pyruvate studies have been conducted in prostate, liver, and brain cancer and carcinoma animal models. An elegant study from an established UCSF group [50] has recently reported on metabolic glycolytic changes in cMyc-induced liver cancer in the mouse. Metabolic switch to a highly glycolytic profile happened early in tumorigenesis and preceded tumor formation in the liver as seen in increased lactate and alanine formation from pyruvate even during the pre-tumor stage (Fig. 18.3, top panel). Moreover, a metabolic response with decreased pyruvate-to-lactate conversion was detectable as early as 3 days of doxycycline treatment in cMyc-tumor-bearing animals (Fig. 18.3, low panel) [50]. The similar findings have been reported for temozolomide and radiotherapy treatment in glioma brain tumor models with [1-^{13}C]pyruvate [51, 52]. Decreased lactate-to-pyruvate ratios were seen in temozolomide-treated brain tumors at day 1 of treatment, while no reduction in tumor volume was present until day 5–7 of treatment [51]. In a rat C6 glioma tumor model, the ratio of hyperpolarized lactate to pyruvate was decreased from 0.38 to 0.23 ($p<0.05$) by 72 h following whole brain irradiation with 15 Gy [52]. ^{13}C-MRSI measurements of the conversation of hyperpolarized [1-^{13}C]pyruvate into lactate have been used to image tumor LDH activity and its inhibition upon chemotherapy and AKT/PI3K/mTOR pathway inhibition [53–55].

Other ^{13}C hyperpolarized tracers have been recently used. Anti-VEGF therapy in mouse HT29 and LoVo colorectal carcinoma xenografts led to significantly decreased ^{13}C fluxes between hyperpolarized pyruvate and lactate as well as increased production of [1,4-^{13}C]malate from hyperpolarized [1,4-^{13}C]fumarate in parallel with tumor necrosis [56]. The use of hyperpolarized [1-^{13}C]glutamate allowed in vivo detection of α-ketoglutarate, an intermediate in the Krebs cycle, with controls HIF1 stability in a variety of tumors [57, 58]. In addition, intravenous injection of hyperpolarized ^{13}C-bicarbonate can be potentially used for noninvasive pH imaging [59]. There is strong resemblance between two metabolic imaging techniques, ^{13}C-MRS and ^{11}C-PET, and the experience gained during development of PET protocols may be useful in accelerating clinical translation of hyperpolarized ^{13}C-MRS [60]. In summary, hyperpolarized ^{13}C-tracers allow for in vivo ^{13}C-MRS assessment of metabolic transformations. The approach has been successfully applied in several preclinical animal models, and first clinical trials have recently been initiated.

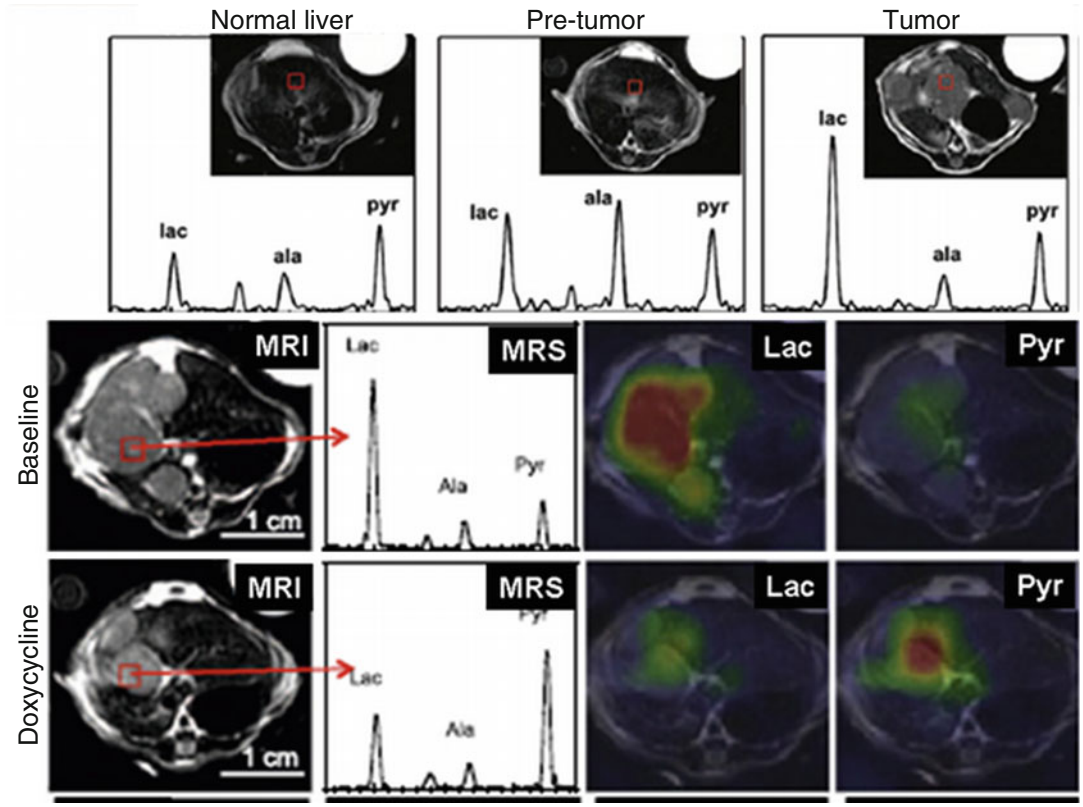

Fig. 18.3 Hyperpolarized in vivo ^{13}C-MRS on mouse xenografts with cMyc-liver cancers. Conversion of hyperpolarized [1-^{13}C]pyruvate to alanine and lactate is increased even in the pre-tumor stage (*top panel*). Doxycycline treatment reverses this glycolytic transformation already 3 days after treatment (*low panel*) (Adapted from [50])

18.2.6 Application of ^{19}F Fluorine MRS

^{19}F-MRS has historically been used for in vivo pharmacokinetics (PK) studies since numerous xenobiotics contain fluorine in their structure. ^{19}F-MR has its advantages such as has high gyromagnetic ratio compared to other non-proton nuclei, no background signal (our organs contain no abundant fluorine-based compounds), and 100 % abundance. The disadvantages of ^{19}F-MR for in vivo PK include low-intensity signals, complex peak shapes that result in further signal loss, long T1 spin–lattice relaxation times, as well as long retention times due to low hydrophilicity or water solubility of most fluorinated compounds. Nevertheless, in vivo ^{19}F-MRS has been successfully applied in the brain to assess delivery of trifluorinated neuroleptics (fluphenazine and trifluoperazine) and trifluorinated antidepressants (fluoxetine and fluvoxamine) [61, 62], in the liver to assess drug metabolism offluorinated compounds [63–65], and in the eye to assess the clearance of corticosteroid drug (triamcinolone acetonide phosphate) [66]. A variety of ^{19}F-MRS PK studies have been performed in animal models and in colorectal cancer patients treated with anticancer compounds such as 5-fluorouracil (5-FU), capecitabine, 3-aminobenzamide, and 4-borono-2-fluorophenylalanine (F-BPA) to assess tumor delivery, biodistribution, and metabolism [63, 67–71]. In addition, tumor metabolism and microenvironment can be investigated by ^{19}F-MRS using

^{19}F-labeled biological reporters [72–74]. However, the recent advances in radiochemistry and PET provide more sensitive approached for in vivo PK when compared to ^{19}F-MRS. Indeed, a single injection of ^{18}F-fluoro-BPA has recently been successfully used in a mouse model of human oral carcinoma in order to assess its biodistribution by micro-^{18}F-PET [75]. The changes in tumor uptake of ^{18}F-labeled 5-FU before and after treatment with bevacizumab were observed in patients with newly diagnosed and untreated metastatic colorectal adenocarcinoma [76]. Novel ^{11}C-labeled drug candidates (such as ^{11}C-erlotinib) are under development for noninvasive PET PK studies [77, 78]. Due to its superb sensitivity and specificity to the target, PET has also multiple advantages (compared to ^{19}F-MRS) while using biological reporters in cancer cells in vivo. ^{18}F-Fluorothymidine (FLT) has become a reliable proliferation marker for PET imaging both in animal models as well as in humans [79, 80].

18.3 High-Resolution Ex Vivo NMR Spectroscopy

In vivo MR spectra of cancer patients (as described above) are performed at "moderate" magnetic field strength (usually from 1.5 to 3 T). These relatively low field strengths and the fixed positions of molecules in the living tissues put limitation on the spectral resolution and low limit of detection. As such, only a small number of high-abundant metabolites can be observed. Ex vivo NMR spectral analyses of tissue specimens can be performed at much higher filed using high-resolution vertical bore NMR spectrometers (from 7 to 21 T) resulting in simultaneous detection and quantification of dozens endogenous metabolites in cells, body fluids, and tissues. As such, high-resolution ex vivo ^{1}H-NMR spectroscopy (often referred as "metabolomics" or "metabonomics") can be seen as a preclinical validation tool and a proof-of-the-principle technique for novel metabolic markers in cancer. Historically, the first pioneering NMR studies on cancer metabolism were performed in cell and tissue extracts. They have confirmed that choline metabolism is significantly altered in a large variety of human [31, 81–86]. Moreover, the well-resolved ^{1}H-NMR spectra of breast cell and tissue extracts have revealed three primary peaks with a trimethylamine moiety [R-$(CH_2)_2$-N^+-$(CH_3)_3$] – namely, phosphocholine (PC), glycerophosphocholine (GPC), and free Cho – as major constituents of the total choline (tCho) signal in in vivo ^{1}H-MRS [83] (Fig. 18.4a–c). These metabolites play a dual role of precursors and products of biosynthesis and catabolism of phosphatidylcholine in the Kennedy cycle (reviewed in [86]). These three resonances PC, GPC, and free Cho can be separated in ex vivo NMR spectra (Fig. 18.4c), but in vivo, these peaks are substantially broadened, and at fields below 4 T, these resonances are generally indistinguishable and termed tCho (Figs. 18.1, 18.2, and 18.4a). Ex vivo ^{1}H- and ^{31}P-NMR spectroscopic studies from several groups [21, 30, 32, 86, 88–90] have reported on reduced phosphocholine levels after treatment with targeted therapies and cytotoxic drugs in leukemia, neuroblastoma, breast cancer, and prostate cancer cell lines. Not only choline metabolism but also decreased in glucose uptake and glycolysis rate by various signal transduction inhibitors have been studied by conventional ^{13}C-NMR in cell cultures [91, 92] and lung tissue extracts [93, 94]. Decreased levels of citrate in patients with prostate cancer (as seen by in vivo ^{1}H-MRS/MRSI) have also been confirmed by high-resolution ^{1}H-NMR on prostatic tissue extracts [95, 96] and prostatic fluids [85, 96–98]. Using recent advances in probe design and pulse sequences, two emerging high-resolution techniques have been introduced into translational biomedicine, namely, unbiased ^{1}H-NMR metabolomics on body fluids and solid-state magic angle spinning ^{1}H-NMR on tissue specimens. The main advantages of both ^{1}H-NMR approaches are their simple and nondestructive sample preparation, fast acquisition times, a large variety of detected and quantifiable metabolite, as well as their reproducibility. Since these ex vivo spectroscopic techniques are highly relevant for clinical cancer research and, potentially, for clinical use, but cannot be seen as

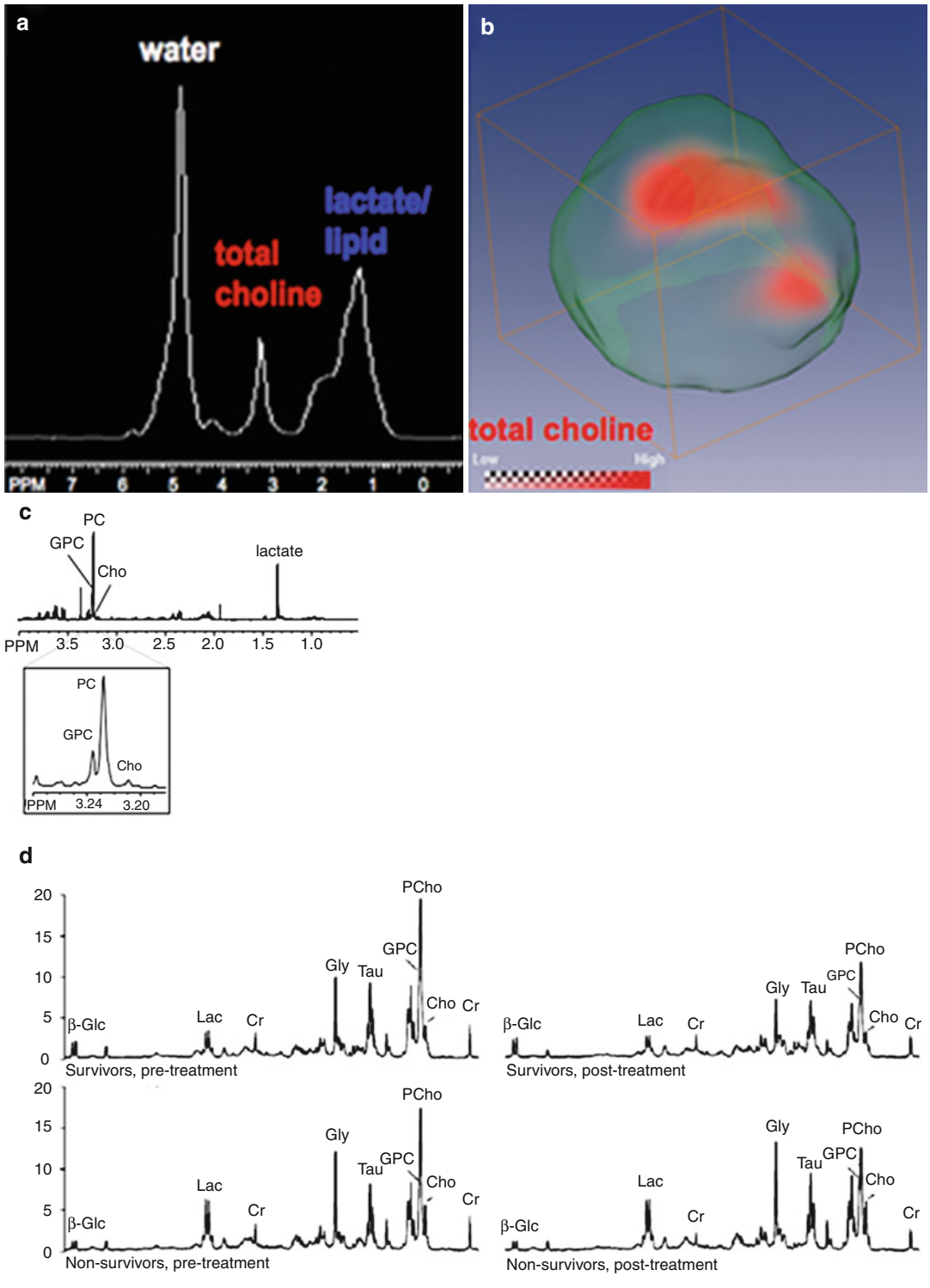

Fig. 18.4 Representative in vivo ^{1}H-MRS (**a**), in vivo ^{1}H-MRSI (**b**), high-resolution ex vivo ^{1}H-NMR spectroscopy on human MDA-MB-231 breast cancer xenografts (**c**) (Adapted from [83]). (**d**) ex vivo HR-MAS ^{1}H-NMR on surgical specimens from breast cancer patients (Adapted from [87])

"imaging technique", only a brief summary on the existing data is provided in this article.

18.3.1 Quantitative ^{1}H-NMR Metabolomics

Quantitative ^{1}H-NMR metabolomics on serum and urine of cancer patients has been recently applied as a cancer biomarker discovery tool [99–101]. Usually 0.1–0.5 mL of a (heparinized) blood product or urine sample is required for quantitative ^{1}H-NMR analysis. One hundred and sixteen serial serum samples from 20 patients with recurrent breast cancer were analyzed by ^{1}H-NMR [102]. Eleven metabolite markers were reported as putative early markers for recurrent breast cancers by using logistic regression and 50-fold cross-validation on NMR data sets. A sensitivity of 86 % and a specificity of 84 % have been reported in this study [102]. Another study has reported on serum metabolic markers for chronic lymphatic leukemia (CLL) in regard to mutational status of disease [103]. Metabolic profiles of CLL patients exhibited higher concentrations of pyruvate and glutamate and decreased concentrations of isoleucine when compared to healthy volunteers. Circulating levels of cholesterol, lactate, glycerol, hydroxybutyrate, and methionine were higher in patients with IGHV-mutated status [103]. The pattern recognition approach on NMR-derived spectroscopic data sets of patients' serum was applied in early stage oral cancer [104–106] and in epithelial ovarian cancer [107]. Plasma and urine of lung cancer patients revealed abnormalities in cholesterol levels and a wide range of other blood and urinary metabolites [108, 109]. Interestingly, urinary metabolome of hepatocellular carcinoma (HCC) appeared to be slightly different in an Egyptian population compared to a Nigerian population. It was not clear if genetic, nutritional, and life style-related factors heavily contributed in metabolic variations [110, 111]. As of today, an enormous amount of metabolic data has been produced, but not a single biomarker is currently being explored for clinical validation. The future translation into the clinic is the highest priority for the field of metabolomics.

18.3.2 Magic Angle Spinning ^{1}H-NMR

NMR is a liquid-based technique, and high-resolution NMR spectra of tissue extracts (dissolved in deuterated solvents) provide detailed information on metabolic fingerprints [99] but at the cost of tissue destruction. The technique called high-resolution magic angle spinning (HR-MAS) NMR decreases the restrictions caused by the fixed position of molecules. HR-MAS NMR has been applied in studies of intact tissue specimens since 1996, but there are some exciting developments in its application. Molecules in tissue have very limited mobility compared to molecules in solutions. The lack of molecular mobility leads to anisotropic interactions, resulting in enormous line broadening in solid-state NMR. In the 1950s, the narrowing of MR lines has been described when a solid sample was spun at a high spinning rate (several kHz) at the "magic angle" of 54.7° to the external magnetic field B_0. Using a HR-MAS probe, non-destructive metabolic analyses on small-volume tissue samples can be performed (at lower temperatures to avoid biochemical degradation of the tissue); subsequently, the tissue can undergo a histopathological examination. The sample size for HR-MAS NMR is in the range of 10–50 mg (for conventional NMR extracts, at least 100 mg tissue is required), allowing for direct metabolic characterization of a needle biopsy [112] or a fine-needle aspirate [113]. But most studies are still performed with surgical clinical specimens.

As with in vivo MRS, some of the very first HR-MAS NMR studies were dedicated to brain tumors [114]. Classification of breast cancer was performed using quantitative HR-MAS [115]. The same group (Dr. Gribbestad's team from Trondheim, Norway) has performed excellent studies to determine treatment response in breast cancer patients receiving neoadjuvant chemotherapy [87, 116] (Fig. 18.4d). Also in animal models, decrease in choline by ex vivo HR-MAS in MCF-7 tumor xenograft treated with docetaxel and in mutant MTLn3E breast cells infected with human CXCR4 cytokine receptor was seen simultaneously with decreased Ki-67 IHC staining for proliferation [29, 117]. Also prostate

cancer biopsies have been intensively used for expanded metabolic profiling by HR-MAS NMR. Not only choline and citrate but also other metabolites such as lactate, alanine, and polyamines (which cannot be detected by in vivo MRS) were discussed as putative biomarkers for prostatic cancers [118–120]. It would be interesting to see characteristic metabolic markers/signatures from other solid tumors; changes in human colorectal cancer metabolome have recently been assessed [121].

18.4 Summary and Future Directions

Magnetic resonance (MR) is often the modality of choice to image cancer patients. In standard-of-care clinical practice, magnetic resonance imaging (MRI) is commonly used to obtain anatomical information based on physical properties of tissue water, but MR techniques are very versatile and can also be applied for functional and metabolic assessment. Metabolic aberrations are common in cancers either as a direct response to altered signal transduction or as a consequence of increased cell proliferation, alterations in blood and substrate supply, tumor necrosis, and hypoxia. Throughout the past years, magnetic resonance spectroscopy (MRS) has been utilized for the noninvasive radiological assessment of the chemical content of a distinct lesion within the body. Next to positron emission tomography (PET), MRS is defined as a metabolic imaging technique. Clinically, proton (^{1}H-) MRS plays a dominant role because of its high sensitivity, high abundance of the ^{1}H nucleus in tissue metabolites, and readily available clinical MR scanners, which are dedicated to observe ^{1}H in water and fat for MRI. A typical feature in ^{1}H-MR spectra of cancer patients is increased concentrations of total choline (tCho) which serve as a diagnostic and prognostic marker for staging and therapy response in brain, breast, prostate, and ovarian cancers. Next to universally increased tCho (membrane phospholipid metabolism), abnormal levels of tissue-specific metabolites have been reported for brain (decreased *N*-acetyl aspartate) and prostate (decreased citrate). Presently, high-field MR magnets (3 T and above) allow for faster acquisition and better resolution of in vivo ^{1}H-MRS in oncology. High-resolution magic angle spinning (HR-MAS) MRS has been successfully applied to small-volume tumor biopsies, needle biopsies, and fine-needle aspirates for fast and nondestructive ex vivo metabolic analysis. Preclinical development of ^{13}C-hyperoplarized MRS in animal models (mostly with [1-^{13}C]pyruvate as a tracer) will soon be translated into clinical ^{13}C-MRS protocols for the assessment of glucose metabolism. This might facilitate the integration of PET and MR into a comprehensive multimodality platform for metabolic imaging in the foreseeable future.

MR technology is a fast developing area in biomedicine, and as it evolves, 3 T MRI studies (as opposed to the conventional 1.5 T field) are increasingly common in the clinical setting. Research 7 T scanners have also been recently installed in various state-of-the-art MR facilities across the US. The higher field strength results in an increase signal-to-noise ratio, increased spatial resolution for MRI and increased spectral resolution for MRS, a smaller voxel size for MRS, and, most importantly for clinical applications of MR, substantially reduced acquisition times. There are still some concerns, while switching to the higher 3 and 7 T magnets, regarding greater amount of noise, changing T1 relaxation properties, and safety concerns (especially at 7 T). Improved acquisition times and standardized data analysis protocols will also be required for in vivo MRS in order to become a standard-of-care imaging technique. High-resolution magic angle spinning (HR-MAS) MRS has been successfully applied to small-volume tumor biopsies, needle biopsies, and fine-needle aspirates for fast and nondestructive ex vivo metabolic analysis of clinical specimens. Preclinical development of ^{13}C-hyperoplarized MRS in animal models (mostly with [1-^{13}C]pyruvate as a tracer) will soon be translated into clinical ^{13}C-MRS protocols for the assessment of glucose metabolism. This might facilitate the integration of PET and MR into a comprehensive multimodality platform for metabolic imaging in the foreseeable future [122] (Fig. 18.5).

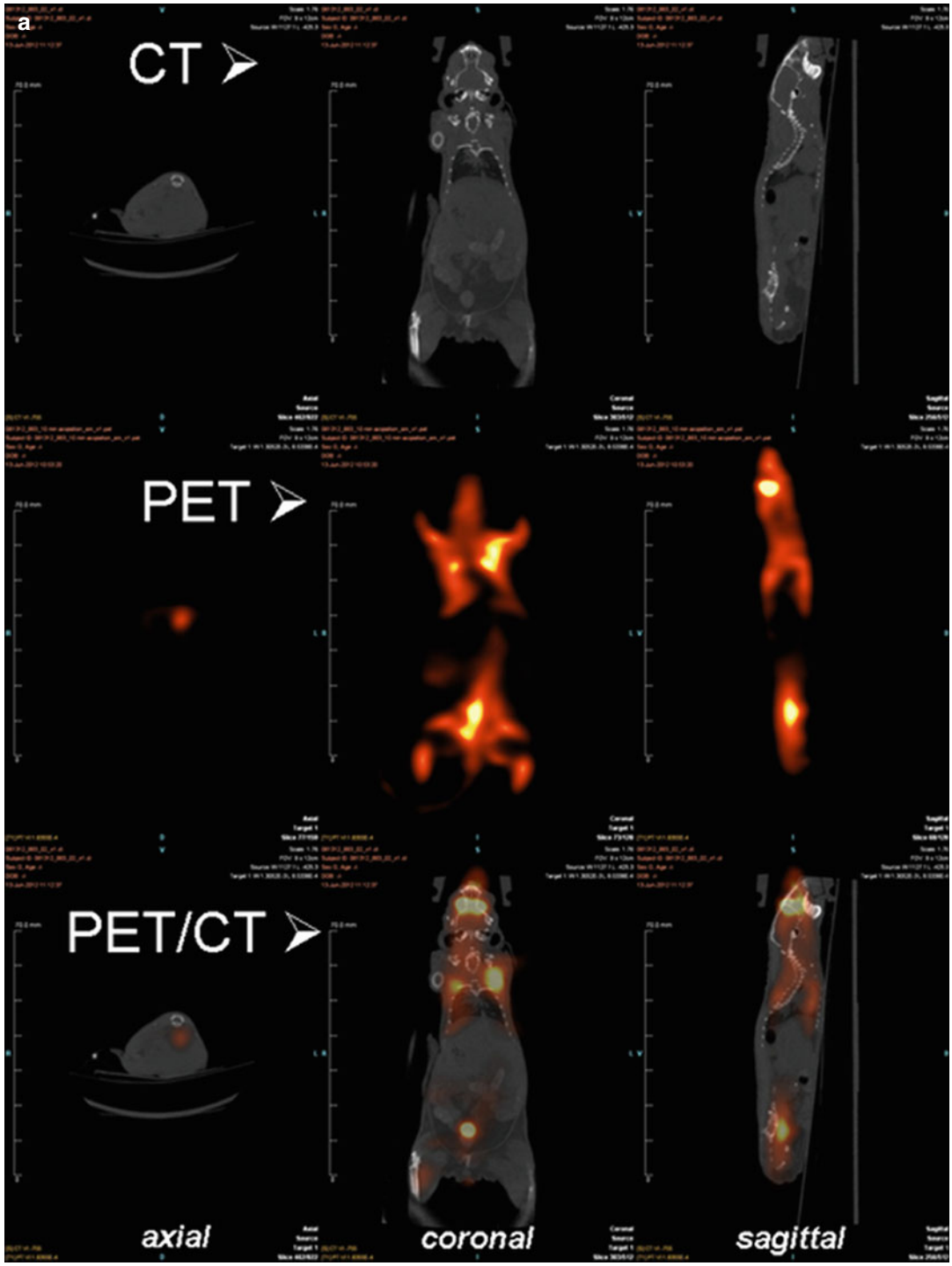

Fig. 18.5 Future multimodality imaging platform will require both an integrated scanner design (mouse ^{18}FDG-PET/CT images from a hybrid microPET/CT scanner, (**a**) mouse ^{18}FES-PET/CT images for estrogen receptor in ovarian cancer model (**b**)) as well as advanced imaging analysis software (fused PET/MRI images of a mouse obtained on a Bruker MRI and a Siemens PET animal scanners (**c**))

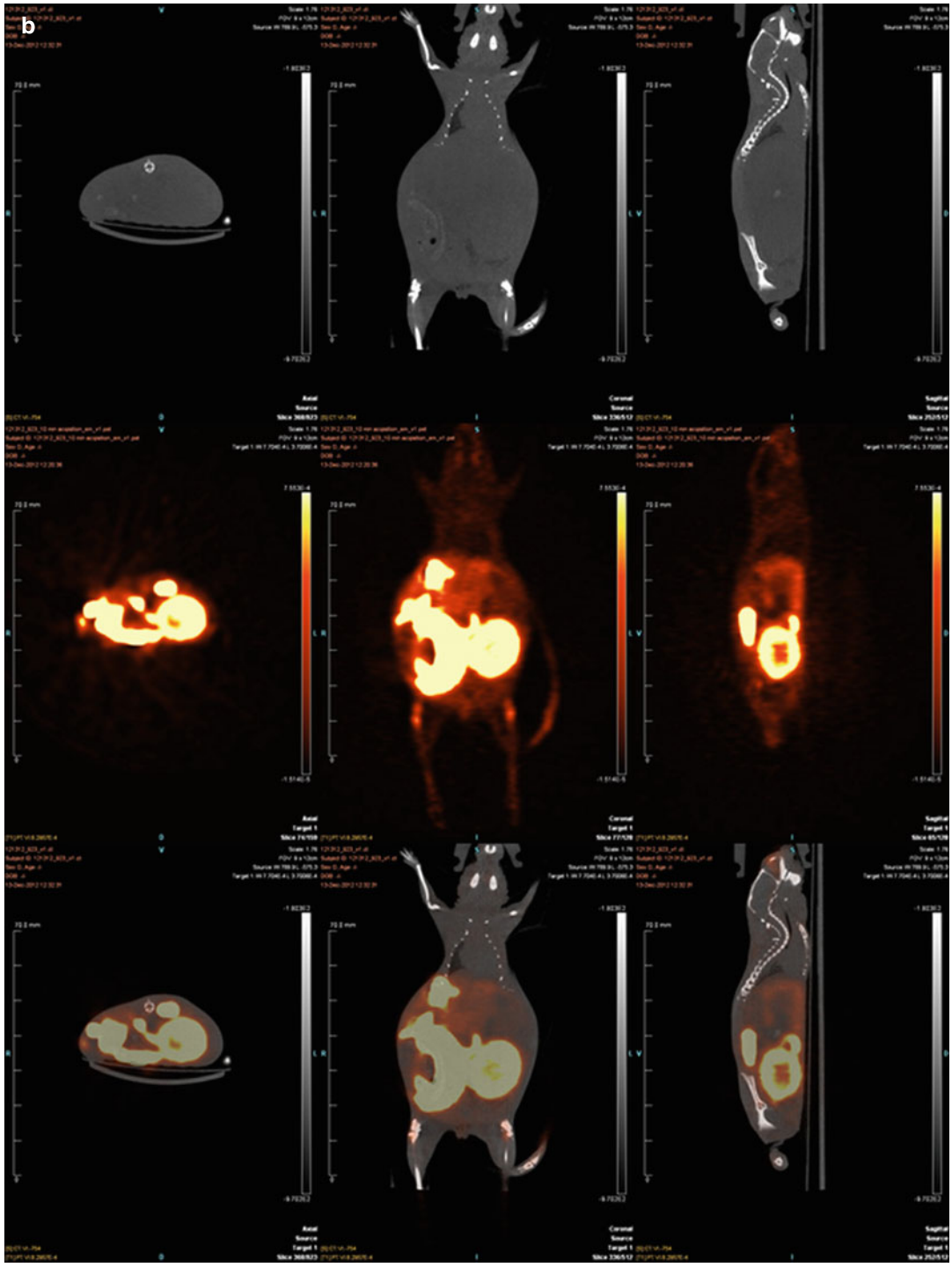

Fig. 18.5 (continued)

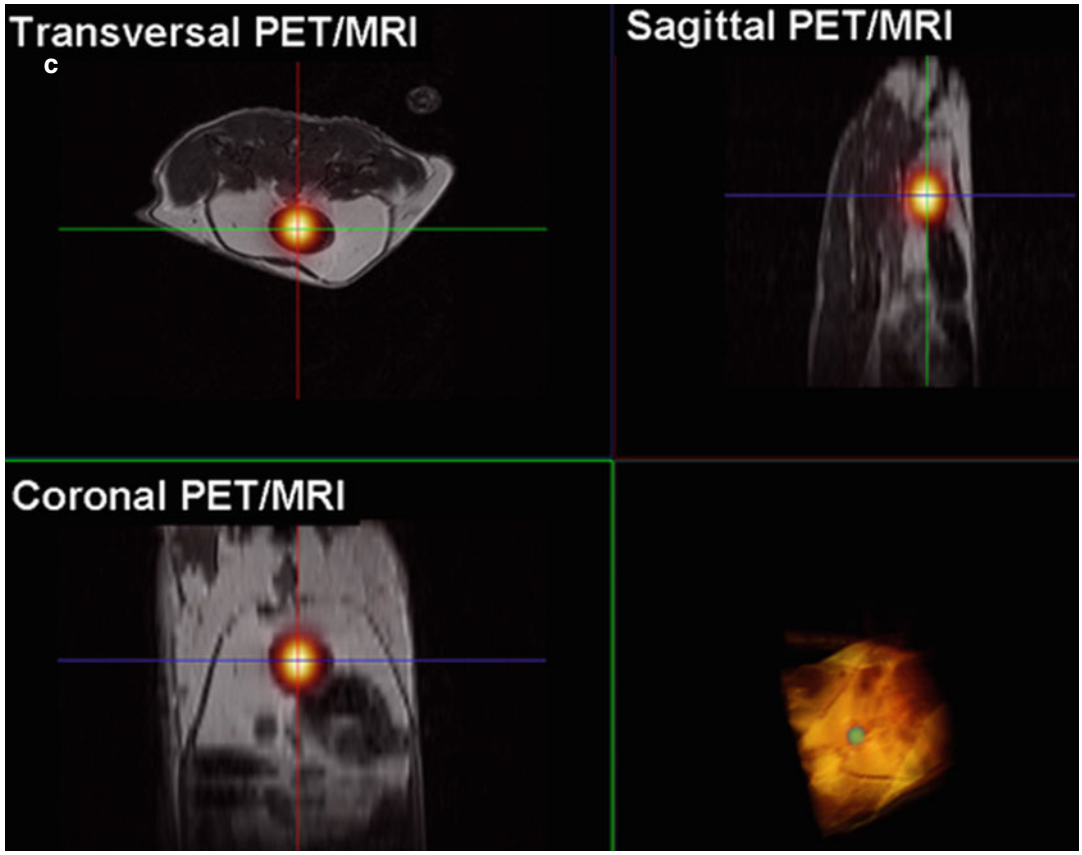

Fig. 18.5 (continued)

References

1. Serkova NJ, et al. Oncologic imaging end-points for the assessment of therapy response. Recent Pat Anticancer Drug Discov. 2009;4(1):36–53. PubMed PMID: 19149687.
2. Serkova NJ, Brown MS. Quantitative analysis in magnetic resonance spectroscopy: from metabolic profiling to in vivo biomarkers. Bioanalysis. 2012;4(3):321–41. PubMed PMID: 22303835.
3. Balmaceda C, et al. Multisection 1H magnetic resonance spectroscopic imaging assessment of glioma response to chemotherapy. J Neurooncol. 2006;76(2):185–91. PubMed PMID: 16151595.
4. Jacobs MA, et al. Proton magnetic resonance spectroscopic imaging of human breast cancer: a preliminary study. J Magn Reson Imaging. 2004;19(1):68–75. PubMed PMID: 14696222.
5. Danishad KK, et al. Assessment of therapeutic response of locally advanced breast cancer (LABC) patients undergoing neoadjuvant chemotherapy (NACT) monitored using sequential magnetic resonance spectroscopic imaging (MRSI). NMR Biomed. 2010;23(3):233–41. PubMed PMID: 20175134.
6. Gillies RJ, Morse DL. In vivo magnetic resonance spectroscopy in cancer. Annu Rev Biomed Eng. 2005;7:287–326. PubMed PMID: 16004573.
7. Glunde K, et al. Choline metabolism in cancer: implications for diagnosis and therapy. Expert Rev Mol Diagn. 2006;6(6):821–9. PubMed PMID: 17140369.
8. Glunde K, et al. MRS and MRSI guidance in molecular medicine: targeting and monitoring of choline and glucose metabolism in cancer. NMR Biomed. 2011;24(6):673–90. PubMed PMID: 21793073. Pubmed Central PMCID: 3146026.
9. Gatenby RA, Gillies RJ. Why do cancers have high aerobic glycolysis? Nat Rev Cancer. 2004;4(11):891–9. PubMed PMID: 15516961.
10. Brindle K. New approaches for imaging tumour responses to treatment. Nat Rev Cancer. 2008;8(2):94–107. PubMed PMID: 18202697.

11. Ma WW, et al. [18F]fluorodeoxyglucose positron emission tomography correlates with Akt pathway activity but is not predictive of clinical outcome during mTOR inhibitor therapy. J Clin Oncol. 2009;27(16):2697–704. PubMed PMID: 19380450. Pubmed Central PMCID: 2689846.
12. Wei LH, et al. Changes in tumor metabolism as readout for Mammalian target of rapamycin kinase inhibition by rapamycin in glioblastoma. Clin Cancer Res. 2008;14(11):3416–26. PubMed PMID: 18519772.
13. Nelson SJ. Analysis of volume MRI and MR spectroscopic imaging data for the evaluation of patients with brain tumors. Magn Reson Med. 2001;46(2):228–39. PubMed PMID: 11477625.
14. Lindskog M, et al. Proton magnetic resonance spectroscopy in neuroblastoma: current status, prospects and limitations. Cancer Lett. 2005;228(1–2): 247–55. PubMed PMID: 15946794.
15. Nelson SJ, et al. In vivo molecular imaging for planning radiation therapy of gliomas: an application of 1H MRSI. J Magn Reson Imaging. 2002;16(4): 464–76. PubMed PMID: 12353260.
16. Doblas S, et al. In vivo characterization of several rodent glioma models by 1H MRS. NMR Biomed. 2012;25(4):685–94. PubMed PMID: 21954105.
17. Park I, et al. Implementation of 3 T lactate-edited 3D 1H MR spectroscopic imaging with flyback echo-planar readout for gliomas patients. Ann Biomed Eng. 2011;39(1):193–204. PubMed PMID: 20652745. Pubmed Central PMCID: 3010202.
18. Choi C, et al. Measurement of glycine in the human brain in vivo by 1H-MRS at 3 T: application in brain tumors. Magn Reson Med. 2011;66(3):609–18. PubMed PMID: 21394775. Pubmed Central PMCID: 3139742.
19. Ganslandt O, et al. Proton magnetic resonance spectroscopic imaging integrated into image-guided surgery: correlation to standard magnetic resonance imaging and tumor cell density. Neurosurgery. 2005;56(2 Suppl):291–8; discussion −8. PubMed PMID: 15794826.
20. Lindskog M, et al. Noninvasive estimation of tumour viability in a xenograft model of human neuroblastoma with proton magnetic resonance spectroscopy (1H MRS). Br J Cancer. 2003;88(3):478–85. PubMed PMID: 12569394. Pubmed Central PMCID: 2747540.
21. Lindskog M, et al. Predicting resistance or response to chemotherapy by proton magnetic resonance spectroscopy in neuroblastoma. J Natl Cancer Inst. 2004;96(19):1457–66. PubMed PMID: 15467035.
22. Stadlbauer A, et al. Metabolic imaging of cerebral gliomas: spatial correlation of changes in O-(2-18F-fluoroethyl)-L-tyrosine PET and proton magnetic resonance spectroscopic imaging. J Nucl Med. 2008;49(5):721–9. PubMed PMID: 18413402.
23. Hipp SJ, et al. Molecular imaging of pediatric brain tumors: comparison of tumor metabolism using (18)F-FDG-PET and MRSI. J Neurooncol. 2012;109(3):521–7. PubMed PMID: 22760419.
24. Bolan PJ, et al. Imaging in breast cancer: magnetic resonance spectroscopy. Breast Cancer Res. 2005;7(4):149–52. PubMed PMID: 15987466. Pubmed Central PMCID: 1175074.
25. Sardanelli F, et al. In vivo proton MR spectroscopy of the breast using the total choline peak integral as a marker of malignancy. AJR Am J Roentgenol. 2009;192(6):1608–17. PubMed PMID: 19457825.
26. Shin HJ, et al. Evaluation of breast cancer using proton MR spectroscopy: total choline peak integral and signal-to-noise ratio as prognostic indicators. AJR Am J Roentgenol. 2012;198(5):W488–97. PubMed PMID: 22528931.
27. Sah RG, et al. Association of estrogen receptor, progesterone receptor, and human epidermal growth factor receptor 2 status with total choline concentration and tumor volume in breast cancer patients: An MRI and in vivo proton MRS study. Magn Reson Med. 2012;68(4):1039–47. PubMed PMID: 22213087.
28. Sharma U, et al. In vivo 1H MRS in the assessment of the therapeutic response of breast cancer patients. NMR Biomed. 2011;24(6):700–11. PubMed PMID: 21793075.
29. Jensen LR, et al. Assessment of early docetaxel response in an experimental model of human breast cancer using DCE-MRI, ex vivo HR MAS, and in vivo 1H MRS. NMR Biomed. 2010;23(1):56–65. PubMed PMID: 19650073.
30. Beloueche-Babari M, et al. Magnetic resonance spectroscopy monitoring of mitogen-activated protein kinase signaling inhibition. Cancer Res. 2005;65(8):3356–63. PubMed PMID: 15833869.
31. Glunde K, et al. Mechanisms of indomethacin-induced alterations in the choline phospholipid metabolism of breast cancer cells. Neoplasia. 2006;8(9):758–71. PubMed PMID: 16984733. Pubmed Central PMCID: 1584299.
32. Al-Saffar NM, et al. Noninvasive magnetic resonance spectroscopic pharmacodynamic markers of the choline kinase inhibitor MN58b in human carcinoma models. Cancer Res. 2006;66(1):427–34.
33. Leyton J, et al. [18F]fluoromethyl-[1,2-2H4]-choline: a novel radiotracer for imaging choline metabolism in tumors by positron emission tomography. Cancer Res. 2009;69(19):7721–8. PubMed PMID: 19773436. Pubmed Central PMCID: 2756457.
34. Haddadin IS, et al. Metabolite quantification and high-field MRS in breast cancer. NMR Biomed. 2009;22(1):65–76. PubMed PMID: 17957820. Pubmed Central PMCID: 2628417.
35. Arrayeh E, et al. Does local recurrence of prostate cancer after radiation therapy occur at the site of primary tumor? Results of a longitudinal MRI and MRSI study. Int J Radiat Oncol Biol Phys. 2012;82(5):e787–93. PubMed PMID: 22331003. Pubmed Central PMCID: 3285390.

36. Nagarajan R, et al. MR spectroscopic imaging and diffusion-weighted imaging of prostate cancer with Gleason scores. J Magn Reson Imaging. 2012;36(3):697–703. PubMed PMID: 22581787.
37. Coakley FV, et al. Endorectal MR imaging and MR spectroscopic imaging for locally recurrent prostate cancer after external beam radiation therapy: preliminary experience. Radiology. 2004;233(2):441–8. PubMed PMID: 15375223.
38. Westphalen AC, et al. Multiparametric 3T endorectal mri after external beam radiation therapy for prostate cancer. J Magn Reson Imaging. 2012;36(2):430–7. PubMed PMID: 22535708.
39. Wright AJ, et al. Quality control of prostate (1) H MRSI data. NMR Biomed. 2013;26(2):193–203. PubMed PMID: 22806985.
40. McLean MA, et al. Prostate cancer metabolite quantification relative to water in 1H-MRSI in vivo at 3 Tesla. Magn Reson Med. 2011;65(4):914–9. PubMed PMID: 21413057.
41. Crehange G, et al. Tumor volume and metabolism of prostate cancer determined by proton magnetic resonance spectroscopic imaging at 3T without endorectal coil reveal potential clinical implications in the context of radiation oncology. Int J Radiat Oncol Biol Phys. 2011;80(4):1087–94. PubMed PMID: 20615624.
42. Bisdas S, et al. In vivo proton MR spectroscopy of primary tumours, nodal and recurrent disease of the extracranial head and neck. Eur Radiol. 2007;17(1):251–7. PubMed PMID: 16703309.
43. Melkus G, et al. Short-echo spectroscopic imaging combined with lactate editing in a single scan. NMR Biomed. 2008;21(10):1076–86. PubMed PMID: 18613250.
44. Le QT, et al. In vivo 1H magnetic resonance spectroscopy of lactate in patients with stage IV head and neck squamous cell carcinoma. Int J Radiat Oncol Biol Phys. 2008;71(4):1151–7. PubMed PMID: 18258377. Pubmed Central PMCID: 2601688.
45. Esseridou A, et al. In vivo detection of choline in ovarian tumors using 3D magnetic resonance spectroscopy. Invest Radiol. 2011;46(6):377–82. PubMed PMID: 21467947.
46. Christians U, et al. Alterations in glucose metabolism by cyclosporine in rat brain slices link to oxidative stress: interactions with mTOR inhibitors. Br J Pharmacol. 2004;143(3):388–96. PubMed PMID: 15339861. Pubmed Central PMCID: 1575349.
47. Ardenkjaer-Larsen JH, et al. Increase in signal-to-noise ratio of > 10,000 times in liquid-state NMR. Proc Natl Acad Sci U S A. 2003;100(18):10158–63. PubMed PMID: 12930897. Pubmed Central PMCID: 193532.
48. Albers MJ, et al. Hyperpolarized 13C lactate, pyruvate, and alanine: noninvasive biomarkers for prostate cancer detection and grading. Cancer Res. 2008;68(20):8607–15. PubMed PMID: 18922937. Pubmed Central PMCID: 2829248.
49. Hu S, et al. Use of hyperpolarized [1-(13)C]pyruvate and [2-(13)C]pyruvate to probe the effects of the anticancer agent dichloroacetate on mitochondrial metabolism in vivo in the normal rat. Magn Reson Imaging. 2012;30(10):1367–72. PubMed PMID: 22819176.
50. Hu S, et al. 13C-pyruvate imaging reveals alterations in glycolysis that precede c-Myc-induced tumor formation and regression. Cell Metab. 2011;14(1):131–42. PubMed PMID: 21723511.
51. Park I, et al. Detection of early response to temozolomide treatment in brain tumors using hyperpolarized 13C MR metabolic imaging. J Magn Reson Imaging. 2011;33(6):1284–90. PubMed PMID: 21590996.
52. Day SE, et al. Detecting response of rat C6 glioma tumors to radiotherapy using hyperpolarized [1–13C] pyruvate and 13C magnetic resonance spectroscopic imaging. Magn Reson Med. 2011;65(2):557–63. PubMed PMID: 21264939.
53. Day SE, et al. Detecting tumor response to treatment using hyperpolarized 13C magnetic resonance imaging and spectroscopy. Nat Med. 2007;13(11):1382–7. PubMed PMID: 17965722.
54. Ward CS, et al. Noninvasive detection of target modulation following phosphatidylinositol 3-kinase inhibition using hyperpolarized 13C magnetic resonance spectroscopy. Cancer Res. 2010;70(4):1296–305. PubMed PMID: 20145128. Pubmed Central PMCID: 2822895.
55. Chaumeil MM, et al. Hyperpolarized 13C MR spectroscopic imaging can be used to monitor Everolimus treatment in vivo in an orthotopic rodent model of glioblastoma. Neuroimage. 2012;59(1):193–201. PubMed PMID: 21807103. Pubmed Central PMCID: 3196046.
56. Bohndiek SE, et al. Hyperpolarized (13)C spectroscopy detects early changes in tumor vasculature and metabolism after VEGF neutralization. Cancer Res. 2012;72(4):854–64. PubMed PMID: 22223844. Pubmed Central PMCID: 3378497.
57. Gallagher FA, et al. 13C MR spectroscopy measurements of glutaminase activity in human hepatocellular carcinoma cells using hyperpolarized 13C-labeled glutamine. Magn Reson Med. 2008;60(2):253–7. PubMed PMID: 18666104.
58. Gallagher FA, et al. Detection of tumor glutamate metabolism in vivo using (13)C magnetic resonance spectroscopy and hyperpolarized [1-(13)C] glutamate. Magn Reson Med. 2011;66(1):18–23. PubMed PMID: 21695718.
59. Gallagher FA, et al. Imaging pH with hyperpolarized 13C. NMR Biomed. 2011;24(8):1006–15. PubMed PMID: 21812047.
60. Gallagher FA, et al. Hyperpolarized 13C MRI and PET: in vivo tumor biochemistry. J Nucl Med. 2011;52(9):1333–6. PubMed PMID: 21849405.
61. Bartels M, Albert K. Detection of psychoactive drugs using 19F MR spectroscopy. J Neural Transm Gen Sect. 1995;99(1–3):1–6. PubMed PMID: 8579798.
62. Bolo NR, et al. Brain pharmacokinetics and tissue distribution in vivo of fluvoxamine and fluoxetine by fluorine magnetic resonance spectroscopy.

Neuropsychopharmacology. 2000;23(4):428–38. PubMed PMID: 10989270.
63. Klomp D, et al. Quantitative 19F MR spectroscopy at 3 T to detect heterogeneous capecitabine metabolism in human liver. NMR Biomed. 2007;20(5): 485–92. PubMed PMID: 17131325.
64. Schneider E, et al. Magnetic resonance spectroscopy for measuring the biodistribution and in situ in vivo pharmacokinetics of fluorinated compounds: validation using an investigation of liver and heart disposition of tecastemizole. J Clin Pharm Ther. 2006;31(3):261–73. PubMed PMID: 16789992.
65. Kimura A, et al. 19F magnetic resonance imaging of perfluorooctanoic acid encapsulated in liposome for biodistribution measurement. Magn Reson Imaging. 2004;22(6):855–60. PubMed PMID: 15234455.
66. Liu X, et al. Ocular pharmacokinetic study of a corticosteroid by 19F MR. Exp Eye Res. 2010;91(3): 347–52. PubMed PMID: 20537996. Pubmed Central PMCID: 2938785.
67. Kamm YJ, et al. 19F-magnetic resonance spectroscopy in patients with liver metastases of colorectal cancer treated with 5-fluorouracil. Anticancer Drugs. 2004;15(3):229–33. PubMed PMID: 15014355.
68. Dresselaers T, et al. Non-invasive 19F MR spectroscopy of 5-fluorocytosine to 5-fluorouracil conversion by recombinant Salmonella in tumours. Br J Cancer. 2003;89(9):1796–801. PubMed PMID: 14583786. Pubmed Central PMCID: 2394413.
69. Doi Y, et al. Quantitative (19)F imaging of nmol-level F-nucleotides/-sides from 5-FU with T(2) mapping in mice at 9.4T. Magn Reson Med. 2009;62(5):1129–39.
70. Brix G, et al. Biodistribution and pharmacokinetics of the (19)F-labeled radiosensitizer 3-aminobenzamide: assessment by (19)F MR imaging. Magn Reson Imaging. 2005;23(9):967–76. PubMed PMID: 16310113.
71. Porcari P, et al. In vivo 19F MR imaging and spectroscopy for the BNCT optimization. Appl Radiat Isot. 2009;67(7–8 Suppl):S365–8. PubMed PMID: 19375924.
72. van Laarhoven HW, et al. Monitoring fluoropyrimidine metabolism in solid tumors with in vivo (19) F magnetic resonance spectroscopy. Crit Rev Oncol Hematol. 2005;56(3):321–43. PubMed PMID: 15982898.
73. Procissi D, et al. In vivo 19F magnetic resonance spectroscopy and chemical shift imaging of tri-fluoro-nitroimidazole as a potential hypoxia reporter in solid tumors. Clin Cancer Res. 2007;13(12): 3738–47. PubMed PMID: 17575240.
74. Ramaprasad S, et al. In vivo 19F MR studies of fluorine labeled photosensitizers in a murine tumor model. Curr Drug Discov Technol. 2007;4(2): 126–32. PubMed PMID: 17691914.
75. Lin YC, et al. Macro- and microdistributions of boron drug for boron neutron capture therapy in an animal model. Anticancer Res. 2012;32(7):2657–64. PubMed PMID: 22753723.
76. Zissen MH, et al. 18F-5-fluorouracil dynamic positron emission tomography/computed tomography shows decreased tracer activity after bevacizumab in colorectal metastases. Nucl Med Commun. 2011;32(5):343–7. PubMed PMID: 21412178.
77. Liu N, et al. PET-based biodistribution and radiation dosimetry of epidermal growth factor receptor-selective tracer 11C-PD153035 in humans. J Nucl Med. 2009;50(2):303–8. PubMed PMID: 19164239.
78. Memon AA, et al. Positron emission tomography (PET) imaging with [11C]-labeled erlotinib: a micro-PET study on mice with lung tumor xenografts. Cancer Res. 2009;69(3):873–8. PubMed PMID: 19155297.
79. Kishino T, et al. Usefulness of 3′-deoxy-3′-18F-fluorothymidine PET for predicting early response to chemoradiotherapy in head and neck cancer. J Nucl Med. 2012;53(10):1521–7. PubMed PMID: 22872738.
80. Li Z, et al. FLT-PET is superior to FDG-PET for very early response prediction in NPM-ALK-positive lymphoma treated with targeted therapy. Cancer Res. 2012;72(19):5014–24. PubMed PMID: 22875026.
81. El-Sayed S, et al. An ex vivo study exploring the diagnostic potential of 1H magnetic resonance spectroscopy in squamous cell carcinoma of the head and neck region. Head Neck. 2002;24(8):766–72. PubMed PMID: 12203802.
82. Bezabeh T, et al. Prediction of treatment response in head and neck cancer by magnetic resonance spectroscopy. AJNR Am J Neuroradiol. 2005;26(8):2108–13. PubMed PMID: 16155166.
83. Amstalden van Hove ER, et al. Multimodal mass spectrometric imaging of small molecules reveals distinct spatio-molecular signatures in differentially metastatic breast tumor models. Cancer Res. 2010;70(22):9012–21. PubMed PMID: 21045154.
84. Lam ET, et al. A phase I study of gefitinib, capecitabine, and celecoxib in patients with advanced solid tumors. Mol Cancer Ther. 2008;7(12):3685–94. PubMed PMID: 19074845. Pubmed Central PMCID: 2813692.
85. Serkova NJ, et al. Use of the 1-mm micro-probe for metabolic analysis on small volume biological samples. J Cell Mol Med. 2009;13(8B):1933–41. PubMed PMID: 19267884.
86. Glunde K, Serkova NJ. Therapeutic targets and biomarkers identified in cancer choline phospholipid metabolism. Pharmacogenomics. 2006;7(7):1109–23. PubMed PMID: 17054420.
87. Cao MD, et al. Predicting long-term survival and treatment response in breast cancer patients receiving neoadjuvant chemotherapy by MR metabolic profiling. NMR Biomed. 2012;25(2):369–78. PubMed PMID: 21823183.
88. Klawitter J, et al. Metabolic characteristics of imatinib resistance in chronic myeloid leukaemia cells. Br J Pharmacol. 2009;158(2):588–600. PubMed PMID: 19663881. Pubmed Central PMCID: 2757699.

89. Klawitter J, et al. Time-dependent effects of imatinib in human leukaemia cells: a kinetic NMR-profiling study. Br J Cancer. 2009;100(6):923–31. PubMed PMID: 19259085. Pubmed Central PMCID: 2661771.
90. Lodi A, Ronen SM. Magnetic resonance spectroscopy detectable metabolomic fingerprint of response to antineoplastic treatment. PLoS One. 2011;6(10):e26155. PubMed PMID: 22022547. Pubmed Central PMCID: 3192145.
91. Gottschalk S, et al. Imatinib (STI571)-mediated changes in glucose metabolism in human leukemia BCR-ABL-positive cells. Clin Cancer Res. 2004;10(19):6661–8. PubMed PMID: 15475456.
92. Kominsky DJ, et al. Abnormalities in glucose uptake and metabolism in imatinib-resistant human BCR-ABL-positive cells. Clin Cancer Res. 2009;15(10):3442–50. PubMed PMID: 19401345.
93. Yokota H, et al. Lactate, choline, and creatine levels measured by vitro 1H-MRS as prognostic parameters in patients with non-small-cell lung cancer. J Magn Reson Imaging. 2007;25(5):992–9. PubMed PMID: 17410583.
94. Guo J, et al. In vitro proton magnetic resonance spectroscopic lactate and choline measurements, 18F-FDG uptake, and prognosis in patients with lung adenocarcinoma. J Nucl Med. 2004;45(8):1334–9. PubMed PMID: 15299058.
95. Raina K, et al. Silibinin feeding alters the metabolic profile in TRAMP prostatic tumors: 1H-NMRS-based metabolomics study. Cancer Res. 2009;69(9):3731–5. PubMed PMID: 19366793. Pubmed Central PMCID: 2679526.
96. Trock BJ. Application of metabolomics to prostate cancer. Urol Oncol. 2011;29(5):572–81. PubMed PMID: 21930089. Pubmed Central PMCID: 3180907.
97. Serkova NJ, et al. The metabolites citrate, myo-inositol, and spermine are potential age-independent markers of prostate cancer in human expressed prostatic secretions. Prostate. 2008;68(6):620–8. PubMed PMID: 18213632.
98. Kline EE, et al. Citrate concentrations in human seminal fluid and expressed prostatic fluid determined via 1H nuclear magnetic resonance spectroscopy outperform prostate specific antigen in prostate cancer detection. J Urol. 2006;176(5):2274–9. PubMed PMID: 17070311.
99. Serkova NJ, Glunde K. Metabolomics of cancer. Methods Mol Biol. 2009;520:273–95. PubMed PMID: 19381962.
100. Spratlin JL, et al. Clinical applications of metabolomics in oncology: a review. Clin Cancer Res. 2009;15(2):431–40. PubMed PMID: 19147747. Pubmed Central PMCID: 2676437.
101. DeFeo EM, et al. A decade in prostate cancer: from NMR to metabolomics. Nat Rev Urol. 2011;8(6):301–11. PubMed PMID: 21587223.
102. Asiago VM, et al. Early detection of recurrent breast cancer using metabolite profiling. Cancer Res. 2010;70(21):8309–18. PubMed PMID: 20959483. Pubmed Central PMCID: 2995269.
103. MacIntyre DA, et al. Serum metabolome analysis by 1H-NMR reveals differences between chronic lymphocytic leukaemia molecular subgroups. Leukemia. 2010;24(4):788–97. PubMed PMID: 20090781.
104. Tiziani S, et al. Early stage diagnosis of oral cancer using 1H NMR-based metabolomics. Neoplasia. 2009;11(3):269–76, 4p following PubMed PMID: 19242608. Pubmed Central PMCID: 2647729.
105. Zhang J, et al. Metabolomics study of esophageal adenocarcinoma. J Thorac Cardiovasc Surg. 2011;141(2):469–75, 75.e1–4. PubMed PMID: 20880550.
106. Zhang J, et al. Esophageal cancer metabolite biomarkers detected by LC-MS and NMR methods. PLoS One. 2012;7(1):e30181. PubMed PMID: 22291914. Pubmed Central PMCID: 3264576.
107. Odunsi K, et al. Detection of epithelial ovarian cancer using 1H-NMR-based metabonomics. Int J Cancer. 2005;113(5):782–8. PubMed PMID: 15499633.
108. Rocha CM, et al. Metabolic signatures of lung cancer in biofluids: NMR-based metabonomics of blood plasma. J Proteome Res. 2011;10(9):4314–24. PubMed PMID: 21744875.
109. Carrola J, et al. Metabolic signatures of lung cancer in biofluids: NMR-based metabonomics of urine. J Proteome Res. 2011;10(1):221–30. PubMed PMID: 21058631.
110. Shariff MI, et al. Urinary metabolic biomarkers of hepatocellular carcinoma in an Egyptian population: a validation study. J Proteome Res. 2011;10(4):1828–36. PubMed PMID: 21275434.
111. Shariff MI, et al. Characterization of urinary biomarkers of hepatocellular carcinoma using magnetic resonance spectroscopy in a Nigerian population. J Proteome Res. 2010;9(2):1096–103. PubMed PMID: 19968328.
112. Martinez-Granados B, et al. Metabolite identification in human liver needle biopsies by high-resolution magic angle spinning 1H NMR spectroscopy. NMR Biomed. 2006;19(1):90–100. PubMed PMID: 16411169.
113. Li M, et al. An HR-MAS MR metabolomics study on breast tissues obtained with core needle biopsy. PLoS One. 2011;6(10):e25563. PubMed PMID: 22028780. Pubmed Central PMCID: 3196497.
114. Tzika AA, et al. Biochemical characterization of pediatric brain tumors by using in vivo and ex vivo magnetic resonance spectroscopy. J Neurosurg. 2002;96(6):1023–31. PubMed PMID: 12066902.
115. Sitter B, et al. Quantification of metabolites in breast cancer patients with different clinical prognosis using HR MAS MR spectroscopy. NMR Biomed. 2010;23(4):424–31. PubMed PMID: 20101607.

116. Cao MD, et al. Prognostic value of metabolic response in breast cancer patients receiving neoadjuvant chemotherapy. BMC Cancer. 2012;12:39. PubMed PMID: 22277092. Pubmed Central PMCID: 3307437.
117. Vermeer LS, et al. NMR metabolomics of MTLn3E breast cancer cells identifies a role for CXCR4 in lipid and choline regulation. J Proteome Res. 2012;11(5):2996–3003. PubMed PMID: 22432781. Pubmed Central PMCID: 3378657.
118. Bertilsson H, et al. Changes in gene transcription underlying the aberrant citrate and choline metabolism in human prostate cancer samples. Clin Cancer Res. 2012;18(12):3261–9. PubMed PMID: 22510345.
119. Tessem MB, et al. Evaluation of lactate and alanine as metabolic biomarkers of prostate cancer using 1H HR-MAS spectroscopy of biopsy tissues. Magn Reson Med. 2008;60(3):510–6. PubMed PMID: 18727052. Pubmed Central PMCID: 2613807.
120. Santos CF, et al. Metabolic, pathologic, and genetic analysis of prostate tissues: quantitative evaluation of histopathologic and mRNA integrity after HR-MAS spectroscopy. NMR Biomed. 2010;23(4):391–8. PubMed PMID: 20033906. Pubmed Central PMCID: 2891902.
121. Chan EC, et al. Metabolic profiling of human colorectal cancer using high-resolution magic angle spinning nuclear magnetic resonance (HR-MAS NMR) spectroscopy and gas chromatography mass spectrometry (GC/MS). J Proteome Res. 2009;8(1):352–61. PubMed PMID: 19063642.
122. Yankeelov TE, et al. Simultaneous PET-MRI in oncology: a solution looking for a problem? Magn Reson Imaging. 2012;30(9):1342–56. PubMed PMID: 22795930. Pubmed Central PMCID: 3466373.

Hybrid Imaging: PET-CT and PET-MRI

19

Barbara Malene Fischer and Johan Löfgren

Contents

Abbreviations

ADC	Apparent diffusion coefficient
APDs	Avalanche photodiodes
ASL	Arterial spin labeling
BGO	Bismuth germinate
BOLD-MRI	Blood oxygen level-dependent MR imaging
Cu-ATSM	^{64}Cu-diacetyl-bis (N4-methylthiosemicarbazone)
DCE	Dynamic contrast enhancement
DOI	Depth-of-interaction
DWI	Diffusion weighted imaging
FDG	Fluorodeoxyglucose
FET	Fluoroethyl-tyrosine
F-FAZA	^{18}F-fluoroazomycin arabinoside
FLT	Fluorothymidine
F-MISO	^{18}F-fluoromisonidazole
fMRI	Functional MRI
GSO	Gadolinium oxyorthosilicate
keV	Kilo electron Volt
kV	Kilo Volt
LBS	Lutetium-based scintillator
LSO	Lutetium oxyorthosilicate
LYSO	Cerium-doped lutetium-yttrium oxyorthosilicate
mA	Milliampere
MET	Methionine
MRS	MR spectroscopy
mSv	Millisievert
NaI(Tl)	Thallium-doped sodium iodide
PERCIST	PET response criteria in solid tumors

B.M. Fischer, MD (✉) • J. Löfgren
Department of Clinical Physiology, Nuclear Medicine and PET, Rigshospitalet, Copenhagen University Hospital, Copenhagen, Denmark
e-mail: malene.fischer@regionh.dk

A. Luna et al. (eds.), *Functional Imaging in Oncology*,
DOI 10.1007/978-3-642-40412-2_19, © Springer-Verlag Berlin Heidelberg 2014

PET-CT	Positron emission tomography – computed tomography
PET-MRI	Positron emission tomography – magnetic resonance imaging
PM	Photomultiplier tubes
ps	Picoseconds
PSF	Point spread function
RECIST	Response evaluation criteria in solid tumors
RF	Radio frequency
SiPMs	Silicon photomultipliers
SNR	Signal-to-noise
SUV	Standardized uptake value
T	Tesla
TOF	Time-of-flight
γPET	Gamma camera PET
μ-map	Attenuation map

19.1 Introduction

Positron emission tomography with computer tomography (PET-CT) and the clinical use of this imaging technology has developed rapidly during the last decade. However, the development of PET possibly confirms rather than disproves the claim that the majority of our recent technological progress is based on old technologies, "barely" adding increased computer power or new combinations of well-known technologies [1]. The increase in computer power and not least the development of a hybrid PET-CT scanner have changed the role of PET from a specialized research tool to a widely available clinical workhorse.

The PET technology is based on the use of proton-rich isotope (e.g., ^{18}F) decaying by positron emission followed by annihilation under emission of two 511 keV photons. Scatter of the positron before annihilation and a slight deviation from 180° of the angle between the two photons are limiting the ultimate spatial resolution of PET to a minimum of 2 mm for whole-body PET systems [2]. Until recently three types of PET scanners have been in use: gamma camera PET (γPET), dedicated stand-alone PET, and integrated PET-CT. The dedicated PET scanner consists of a full ring system with several thousands of scintillation detectors. In γPET, two or three circulating gamma-heads detect the 511 keV photons. γPET was introduced in the mid-1990s and initially gained widespread use due to the lower price and higher availability [3]. However images from γPET have lower resolution and are based on significantly fewer impulses than images from dedicated PET making the examination time consuming and compromising sensitivity; thus, the use of γPET has been abandoned in most places.

The PET technique provides information on tissue function but lacks accurate anatomical information. In order to solve this problem, the integrated PET-CT system was developed. PET-CT makes image fusion more accurate and reduces the examination time, mainly because attenuation correction of the PET scan can be based on the CT data [4, 5]. Moreover, the fusion of PET imaging and modern CT scanners has introduced PET-CT as a valuable technique not only in diagnosing, staging, and therapy evaluation, but also in cancer treatment, e.g., in the planning of radiotherapy. The first PET-CT scanner prototype was introduced in 1998 in the United States. In Europe, the first PET-CT scanner was installed in Zurich followed by a scanner installed in Copenhagen in 2001. Today, summer 2013, there are more than 5,000 PET-CT systems installed worldwide.

Ten years after the introduction of PET-CT, the youngest member of the PET family, PET-MRI, has just entered the scene. Whether PET-MRI will add significant improvement in the diagnosis and staging of cancer patients is uncertain, but it could turn out to be a valuable tool in early evaluation of cancer therapy. Early evaluation of effect by FDG-PET-CT after chemo- or radiotherapy as well as targeted therapy is hampered by the low specificity of FDG, especially with regard to inflammation versus malignancy, and the fact that anatomical shrinkage of the tumor is often a late phenomenon or not a criteria for response as can be seen with some targeted drugs. Using combined PET-MRI could make it possible, by means of, e.g., diffusion-weighted MRI or MRI spectroscopy, to image more specific changes in the tissue together with retention

of FDG or other cancer-specific PET tracers making early therapy evaluation a safer endeavor [6, 7].

19.2 PET-CT

19.2.1 The Technical Evolution from PET to PET-CT

19.2.1.1 PET

The birth of PET for medical imaging took place in the beginning of the 1950s at Massachusetts General Hospital by the work of Gordon Brownell and co-workers [8]. They constructed the first clinical positron-imaging device, a single pair coincidence system. In the late 1960s, PC-I, the first tomographic imaging device, was built [9, 10], but it was in 1975 with the work of Michael E. Phelps, Michel Ter-Pogossian, and co-workers at Washington University School of Medicine the modern PET scanner was first introduced. The design was a ring system surrounding the patient. At the same time, a technical revolution took place within the field of radiology: the introduction of the first CT scanner in 1972 by Sir Godfrey Hounsfield, at EMI Central Research Laboratories. Within 3 years more than 12 companies were marketing, or intending to market, CT scanners. While there was an explosive growth of the CT-market during the 1970s, PET was still in the beginning of its evolution phase, and the first commercial PET scanner dates from around 1980. A prerequisite for the future success of PET was the concurrent development of labeled 2-deoxy-2-(^{18}F)fluoro-D-glucose (FDG) led by Al Wolf and Joanna Fowler [11].

During the 1970s and onwards, there was a continuous refinement of the PET technology. In 1977 bismuth germanate (BGO) was introduced, superseding thallium-doped sodium iodide (NaI(Tl)) as a better scintillator material. Concurrently, improved reconstruction algorithms were developed, and in 1982 Shepp and Vardi [12] introduced an iterative reconstruction technique based on the theory of expectation maximization, which significantly improved image quality compared to the previously used filtered back projection. However, the restricted amount of computer power available at that time made iterative reconstruction immensely time-consuming. Further refinement and optimizations of the reconstruction algorithms together with faster computers speeded up the reconstruction of the PET images [13, 14]. Contrasting the rapid and enormous clinical spread of CT in the 1970s and MRI in the 1980s, the use of PET for diagnosing and staging malignant disease did not gather pace until the US Center for Medicare and Medicaid Services (CMS) approved reimbursement for a number of cancers in 1998 [15].

19.2.1.2 PET-CT

Concurrent reading of PET and CT has been possible for years using adjacent viewing stations or with the help of software registration. By the beginning of the 1990s, a rising interest in the construction of a combined PET-CT scanner emerged, and in 1998 the first combined PET-CT prototype scanner was presented [4], a single-slice spiral CT scanner rotating together with an ECAT ART PET system. This new true image fusion modality, the PET-CT scanner, attributed to David Townsend and Ronald Nutt was named by TIME Magazine as the medical invention of the year in 2000. One of the biggest advantages of hybrid PET-CT, besides the possibility to get the exact anatomical correlate of a focal uptake on PET, is the CT-based attenuation correction. CT-data for attenuation correction was, compared to traditional ^{68}Ge/^{68}Ga positron source or ^{137}Cs gamma-ray source, faster, unaffected by the injected activity, and with significant lower image noise [15].

The first commercial PET-CT system, Discovery LS, was released by GE Healthcare in 2001, a single-slice spiral CT integrated with a PET scanner with BGO detectors. Since then many improvements have been done, and newer generations of PET-CT have emerged, making it possible to shorten the acquisition time and/or to reduce administered activity to the patient. The following provides an overview of selected examples of these advancements:

1. The first PET-CT system had retractable septa making acquisition of data in either 2D or 3D possible. The 3D mode gives higher count rates (higher sensitivity) but requires better computer capacities and a new reconstruction algorithm. The 3D acquisition and reconstruction will result in improved image quality, and all commercial PET-CT systems of today operate in 3D mode only.
2. Increasing the axial field of view results in coverage of a larger area of the body by each scan position, improving sensitivity and decreasing scan time, on the other hand resulting in increased costs.
3. Spiral CT technology has progressed from single to dual-slice, to 4, 8, 16, 64, and, most recently, 128 slices with a transaxial coverage sufficient and optimized for cardiac studies. At the same time CT rotation speed has increased, and these factors have resulted in more rapid CT scans.
4. Radiation dose from CT exams is a matter of increasing concern. However, new CT software technology and reconstruction algorithms (iterative), the possibility to automatically adjust the kilo voltage (kV) and milliampere (mA) related to the body type and region examined, together with increasing awareness on radiation safety, have the potential to significantly reduce the required radiation dose to patients during CT and PET-CT scans, without compromising image quality.
5. The evolution of new and faster scintillator material with higher light output such as gadolinium oxyorthosilicate (GSO), lutetium oxyorthosilicate (LSO), and LYSO (variant of LSO in which some of the lutetium is replaced by yttrium), together with faster acquisition electronics, results in less dead time, improved energy resolution, and therefore better scatter correction and reduced random coincidences, resulting in enhanced whole-body scanning properties.
6. Smaller scintillator crystals have resulted in improved spatial resolution.
7. Faster scintillators with a high stopping power have made it possible to implement time-of-flight (TOF); By means of TOF it is possible to measure the time difference between the two coincidence photons arriving in the detectors, enabling better localization of the annihilation event. This information is incorporated into the reconstruction algorithm leading to improved signal-to-noise (SNR) and improved image quality especially for bigger-sized patients. The first commercial PET-CT system with TOF, Philips Gemini TF (TrueFlight) was released in 2006.
8. Point spread function (PSF) renders it possible to take into account the oblique penetration of photons thru the detectors. The occurrence of oblique penetration varies throughout the field-of-view. By measuring this variability and implementing PSF in the reconstruction algorithm, it is possible to achieve a more consistent spatial resolution throughout the 3D volume.
9. Different approaches have been taken to reduce image blurring due to motion by gating the PET data acquisition (see the section below).
10. Bigger bore size has made the PET-CT systems more patient-friendly and made it possible to scan patients positioned in fixation equipment for radiation therapy, a prerequisite to the now widespread use of PET-CT for radiotherapy planning.
11. In 2013 continuous motion of the patient table was introduced by Siemens, instead of the traditional stop-and-go imaging. Continuous motion of the patient table makes the planning of the PET more flexible in the sense of being able to define exactly where to start and stop the scanning and to more precise differentiate how to scan different regions of the body.

The technical evolution of PET-CT systems will continue despite the introduction of the combined PET-MRI system. The development of PET-MRI has boosted the work with digital semiconductor photo sensors like the Silicon photomultipliers (SiPMs) [16, 17]. This type of photo multipliers offers excellent timing properties and high gain and depth-of-interaction (DOI)

capability making them suitable for time-of-flight (TOF), improving sensitivity and resolution. These features, in combination with the insensitivity of SiPMs to even high magnetic fields, make them attractive for use in future PET systems, both PET-MRI and PET-CT.

Reconstruction algorithms and reconstruction computers will continue to improve. Continuous motion of the patient table will probably become the standard of new PET-CT scanners. Scintillation material will also continue to evolve but probably at a relatively slow pace. The most promising scintillator material with regard to TOF is lanthanum bromide ($LaBr_3$) with the potential of a time resolution down to 375 ps (compared to approximately 550 ps for the current LSO/LYSO) [18]. Even though $LaBr_3$ is expensive and must be hermetically sealed, it is likely that its advantageous properties will result in its introduction in clinical PET systems in the near future.

19.2.2 When and Why Is PET-CT Superior to PET in Oncologic Patients?

FDG-PET provides information on tissue metabolism, but lacks accurate anatomical information. The integrated PET-CT system makes image fusion more smooth and accurate. PET-CT reduces the examination time by approximately 30 % compared to PET alone, mainly because attenuation correction of the PET scan can be based on the CT data [4]. Since the installation of the first clinical PET-CT in 2001, the technology has gained widespread use. The drawbacks concerning PET-CT are costs and radiation dose; adding a diagnostic CT to a whole-body PET scan increases the radiation dose from approximately 8 to 20 mSv. If a nondiagnostic low-dose CT is applied, the radiation dose is only increased from approximately 8 to 10 mSv. Adding this increased amount of radiation dose will, in many oncologic patients, not be a matter of concern; however, using PET-CT (instead of stand-alone PET) in pediatric patients or as a follow-up tool in patients with a favorable prognosis should be a matter of concern and have a clinical impact besides "nicer" images. The published experiences on stand-alone PET compared to integrated PET-CT unequivocally favor PET-CT, of which examples will be given below.

The possibility to accurately correlate anatomical and functional imaging often reduces the false-positive rate, i.e., by pointing out more obvious inflammatory, iatrogenic, or physiologic etiologies. For example, calcifications in tuberculosis [19], structural changes due to iatrogenic procedures, e.g., placement of chest tubes, percutaneous needle biopsy, and radiation pneumonitis or lack of corresponding structural changes as is the case in physiological FDG excretion in the bowel (Fig. 19.1). Detailed knowledge of patient history and the use of integrated PET-CT help distinguish malignant FDG retention from uptake due to benign causes [20, 21]. One of the first results of PET-CT was the description of physiological FDG uptake in brown fat, initially named "USA-fat" [22]. Among the first 359 consecutive patients performing PET-CT at John Hopkins Hospital, Cohade and colleagues found abnormal uptake in the supraclavicular region in 49 patients. Localization to lymph nodes, tumor, or muscles was confirmed in two-thirds of the patients, but in the remaining cases PET-CT revealed that this was caused by previously undescribed uptake in tissue with very low Hounsfield value, namely, brown fat – now well known, but still a potential source of confusion (Fig. 19.2).

Two of the first larger studies comparing the performance of stand-alone PET and integrated PET-CT were published in 2003 by Bar-Shalom and in 2004 by Antoch and colleagues [20, 21]. In a retrospective, blinded analysis of 260 patients with a variety of oncologic diseases, Antoch et al. found that staging by PET-CT was significantly more accurate than staging by PET alone or visually correlated PET and CT [20]. Bar-Shalom et al. evaluated a mixed population of 204 oncologic patients with a total of 586 suspicious lesions [21] finding that PET-CT provided additional information beyond that provided by the separate interpretations of PET and CT in 49 % of the cases and had an impact on patient management in 14 %. The impact of PET-CT

on diagnostic interpretation was significantly greater for patients with abdominal findings compared to patients with findings in other regions, especially by enabling localization of physiologic FDG uptake, avoiding false-positive interpretation (Fig. 19.1). This has been confirmed by later studies focusing on gastrointestinal cancer: PET-CT optimizes localization and characterization of focal FDG uptake improving accuracy and especially specificity [23–26]. Similar findings have been reported in studies on patients with gynecologic malignancy; in a study including 103 consecutive patients with recurrent cervical or endometrial cancer, Kitajima and colleagues found PET-CT to be significantly more accurate compared to PET alone, based on improved sensitivity as well as specificity. This improved diagnostic accuracy had an additional impact on patient management in 16 % of the patients as compared to PET alone [27].

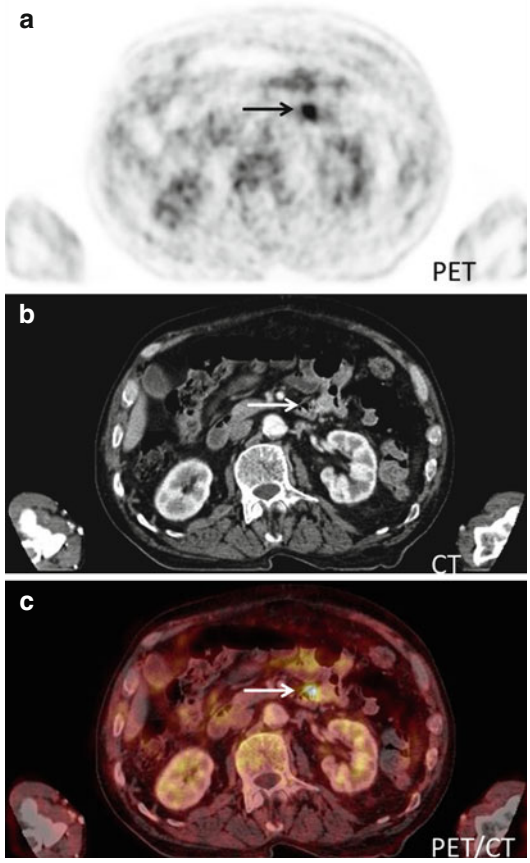

Fig. 19.1 PET-CT showing irregular physiological FDG-uptake commonly seen in the bowels: (**a**) PET shows focal FDG-uptake in the abdomen (*arrow*). (**b**) CT shows high resolution anatomical images of the abdomen. (**c**) Fused PET-CT shows that the focal FDG-uptake correlates to normal configured intestines and therefore interpreted as physiologic FDG-uptake (*arrow*)

In the early study by Bar-Shalom et al., the impact of PET-CT was substantial not only in patients with abdominal foci, but also in characterizing thoracic lesions; almost half (12/28) of the cases in which PET-CT changed patient management had lung cancer or solitary pulmonary nodules, again avoiding false-positive interpretations by characterizing focal FDG uptake as nonmalignant, i.e., vascular structures or FDG embolus (Fig. 19.3). The superiority of combined PET-CT has also been confirmed for the staging of lung cancer, primarily with regard to assigning correct T and N stage, but not for the detection of distant metastases [28, 29]. Whereas no significant difference for the detection of distant metastases could be found in lung cancer, PET-CT was found to be significantly more accurate than PET alone in restaging patients with malignant melanoma primarily as a result of improved sensitivity with regard to M stage (0.99, respectively, 0.89), especially for the detection of visceral metastases, including metastases to the lungs [30]. However, for follow-up of patients previously treated for malignant melanoma, no significant difference between PET and PET-CT could be found.

19.3 PET-MRI

19.3.1 Introduction to PET-MRI

For several decades PET has demonstrated its value in providing noninvasive information of tissue at the molecular level. Although the value of PET lies in its high sensitivity of biomarkers in vivo, it lacks precise anatomical information. As described above this problem was first addressed with the introduction of the PET-CT scanners in 2001. Introducing PET-MRI can, perhaps, approach some of the limitations applying to PET-CT as well as providing a new tool for molecular imaging [6].

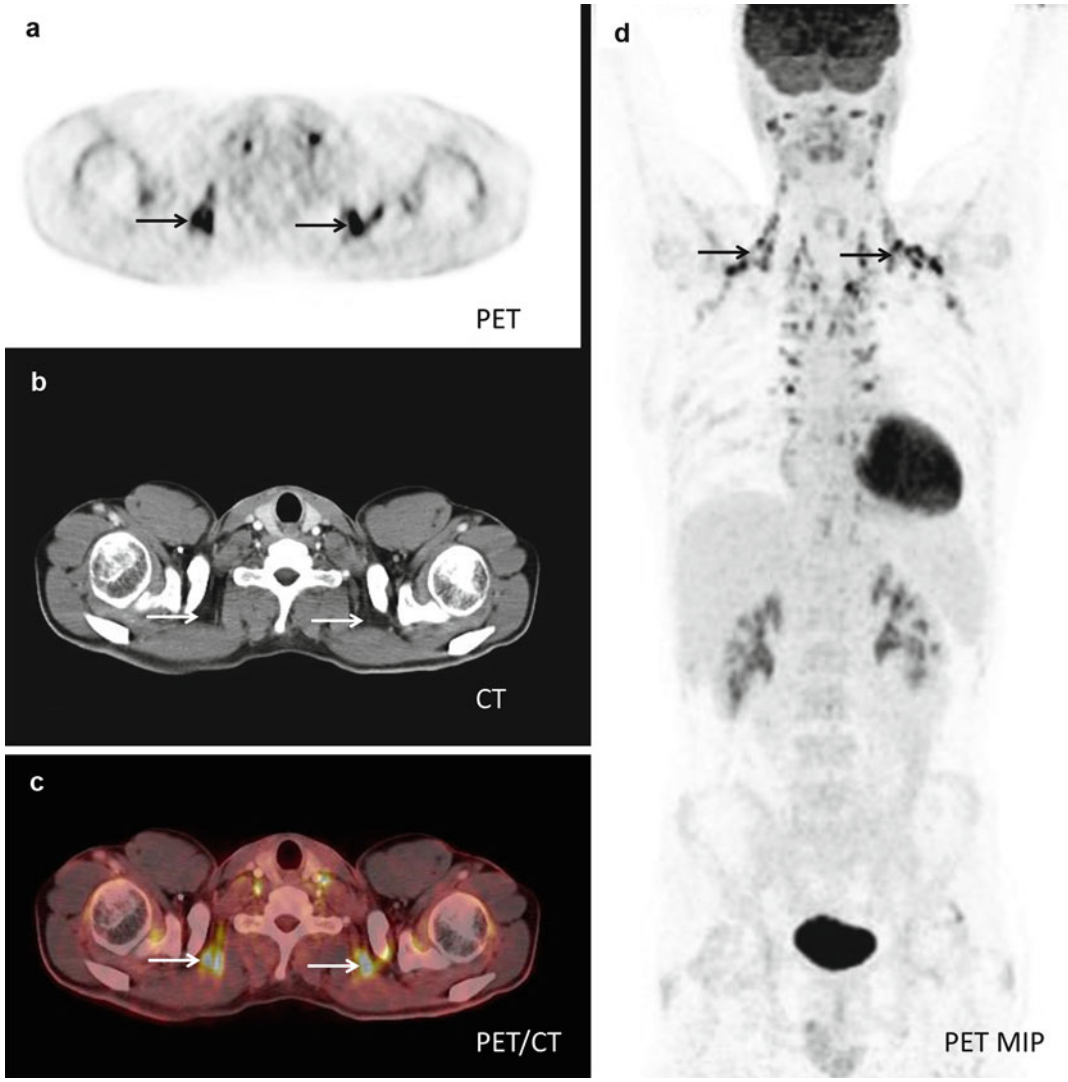

Fig. 19.2 PET-CT showing physiological FDG-uptake in brown fat: (**a**) PET shows intense FDG-uptake especially in the supraclavicular region (*arrows*). (**b**) CT shows high resolution anatomical images of the same region. (**c**) Fused PET-CT shows that the intense FDG-uptake correlates to adipose tissue (*arrows*). (**d**) PET MIP (maximum intensity projection) shows the symmetrical distribution of this metabolic active adipose tissue, aka brown fat

An important limitation on the use of PET-CT is the amount of radiation exposed to the patients during diagnostic workup and follow-up schemes in patients with good prognosis, especially pediatric patients; the amount of ionizing radiation from repeated PET-CT scans is a matter of concern [31, 32] (Fig. 19.4). As CT generally accounts for approximately half of the dose associated with a PET-CT scan, substituting CT with MRI (which is performed without the use of ionizing radiation) will reduce the dose associated with the examination substantially. Thus, the availability of PET-MRI and an increased number of salvage therapies might render the clinicians more amenable, to more frequent follow-up with imaging also in younger patients [6].

CT is a fast and reliable provider of structural information in most scenarios, but with some limitations, especially with regard to soft tissue

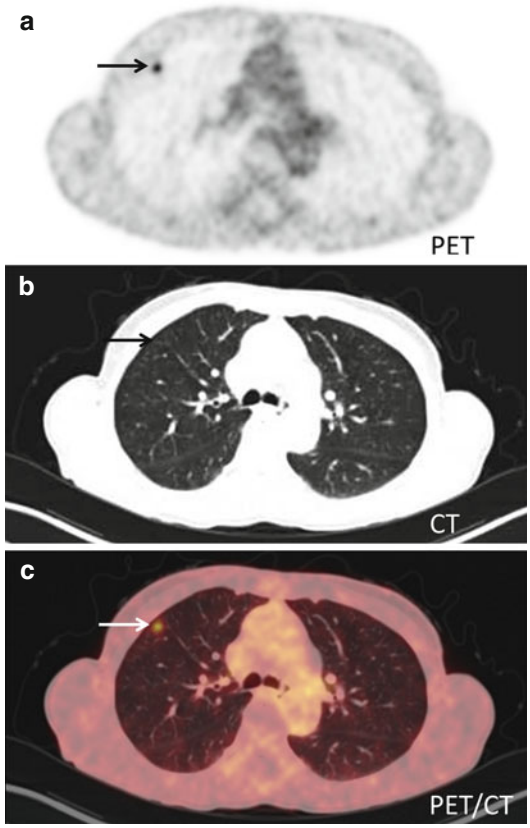

Fig. 19.3 Transaxial PET-CT of a FDG-embolus: (**a**) FDG-PET shows a focal accumulation of isotope (*arrow*) in the anterior part of the right lung. (**b**) CT shows high-resolution anatomical images of the lung parenchyma. (**c**) Fused PET-CT shows that there is no anatomical correlate to the isotope accumulation – this was therefore interpreted as being a FDG-embolus. FDG-embolus is an aggregation of FDG which follows the bloodstream after the injection to the lungs where it is trapped in the capillary bed

and in areas with complex anatomy, i.e., the head and neck area and in the pelvis. MRI on the other hand is often time consuming but provides excellent soft tissue differentiation and in this aspect is considered superior to CT. Using MRI in cancer imaging could allow for more precise radiographic measurements of tumor location, size, and invasion (Fig. 19.5). In addition to routine anatomical MR imaging, a variety of MRI acquisition sequences are available which can yield images of more specific biological or functional properties of the tissue [6].

In PET-CT the duration of the CT scan is typically less than 1–2 min, whereas the PET scan lasts approximately 10–20 min from skull base to thighs. Thus, PET acquisition governs the total scan time. With simultaneously PET-MRI both modalities acquire data, and total scanning time is governed by MR imaging, so that a longer PET acquisition time could be without time loss [33]. This could make it possible to reduce the dose from the PET tracer without hampering sensitivity. Another limitation of PET-CT, not often addressed before the event of PET-MRI, is the sequential acquisition of CT and PET data. Sequential data acquisition and subsequent image fusion can hamper the possibility for accurate quantification and image interpretation due to misalignment. This is especially relevant in abdominal or thoracic studies, due to respiratory movements, bladder filling, and bowel motion [34]. Simultaneous imaging will make it possible to examine the patient in exactly identical metabolic state and condition and allows for essentially perfect temporal correlation of acquired data sets from both modalities.

Thus, combining PET with MRI provides many advantages, which go far beyond simply combining functional PET information with structural MRI information. Some of the challenges will be to adapt the MRI protocols to the PET acquisition time for each bed position and choose the right combination of PET tracer and MR imaging protocols [6]. In the following we will introduce the reader to the technical development of the PET-MRI scanner, together with faults and benefits and the current clinical evidence on the use of PET-MRI in oncology. For a more thorough introduction to specific MRI protocols, the reader should consult one of the chapters dedicated to MR imaging.

19.3.2 The Technical Evolution of PET-MRI

The success of combining PET and CT stimulated the work and interest in trying to combine PET and MRI. MRI with its excellent soft tissue contrast and its possibilities within functional imaging such as diffusion-weighted imaging

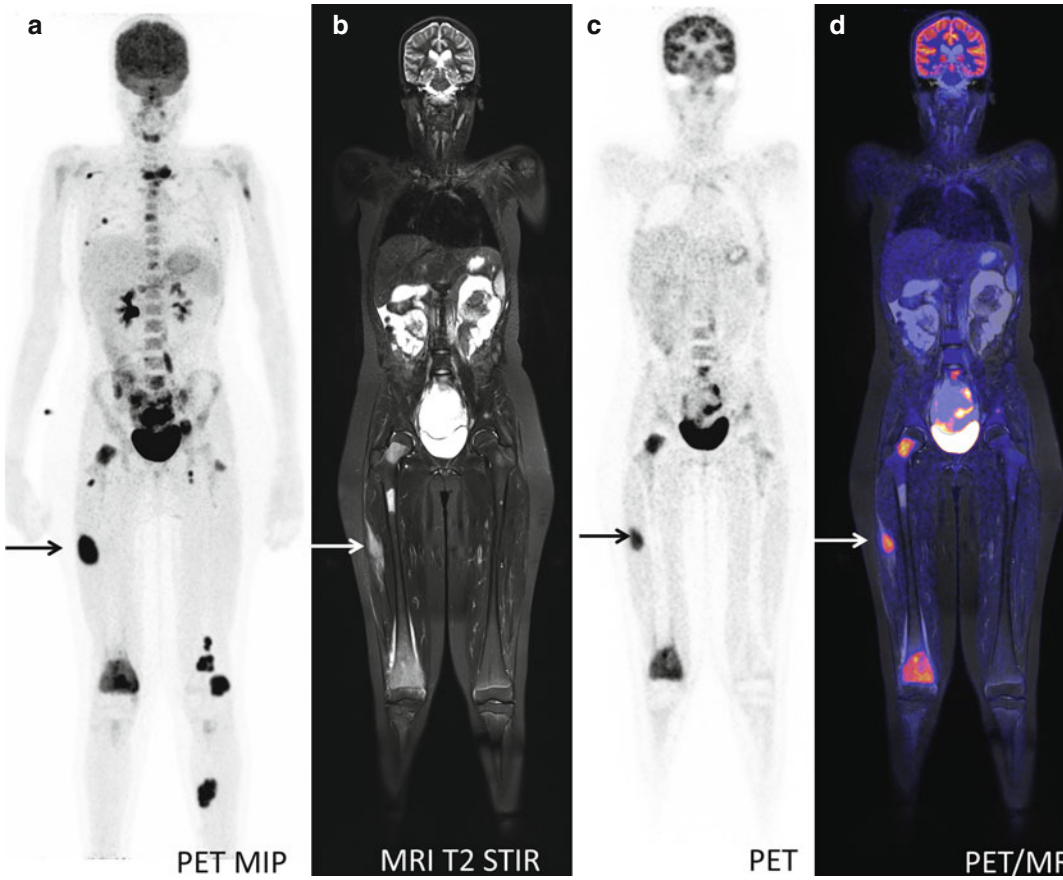

Fig. 19.4 A 13-year-old girl with neurological symptoms and pain in the right knee. FDG-PET for suspected infectious disease: (**a**) PET MIP demonstrates widespread foci of FDG-accumulation suspected for disseminated malignancy. (**b–d**) Sagittal MRI T2 STIR, FDG-PET, and fused PET-MR show soft tissue and bone marrow lesions. Biopsy from lesion in the right thigh (*arrow* on **a-d**) revealed the diagnosis: rhabdomyosarcoma

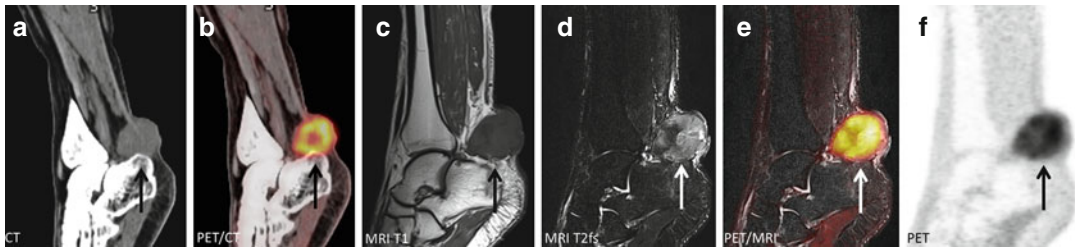

Fig. 19.5 A 50-year-old M with clear cell sarcoma surrounding the Achilles tendon: (**a, b**) CT and fused FDG-PET/CT shows a metabolic active tumor surrounding the Achilles tendon but cannot exclude invasion of the calcaneus bone (*arrow*). (**c–f**) Subsequent FDG-PET/MR could accurately distinguish the tumor from the adjacent bone and showed no infiltration which was confirmed by histology after surgery (*arrow*)

(DWI), dynamic contrast enhancement (DCE), spectroscopy (MRS), functional MRI (fMRI), and arterial spin labeling (ASL), in combination with the molecular information from PET, would result in unparalleled structural, metabolic, and functional information. However, it should take almost a decade to reach the goal of a combined PET-MRI scanner.

Software fusion of PET data and MRI has been used for many years in neurology where MRI is preferred over CT and the registration between the two exams is pretty straightforward. To fuse whole-body PET and MRI exams is more troublesome due to the nonrigid patient motion between the scans and lack of stable landmarks (like the skull for image fusion in neurology imaging). Thus, there was a need for a development of combined acquisition of PET and MRI, preferably simultaneously. Combining MRI and PET in the same gantry for simultaneous imaging has some prerequisites:

1. The PET detectors and electronics must not interfere with the field gradients or the RF signals.
2. The PET detectors should be insensitive to the magnetic field and the RF signals.
3. The coils must be constructed so there is a minimum of interference with RF signals and a minimum of attenuation of the coincidence photons.
4. New strategies for PET attenuation correction have to be developed.

The challenge of combined PET and MR imaging has been approached by three major vendors of hybrid scanners in three different ways (Fig. 19.6):

GE Healthcare has developed a kind of pseudo PET-MRI system – a tri-modality PET-CT+MRI system. This is composed of a 3 T MRI system, a state-of-the art time-of-flight PET-CT system,

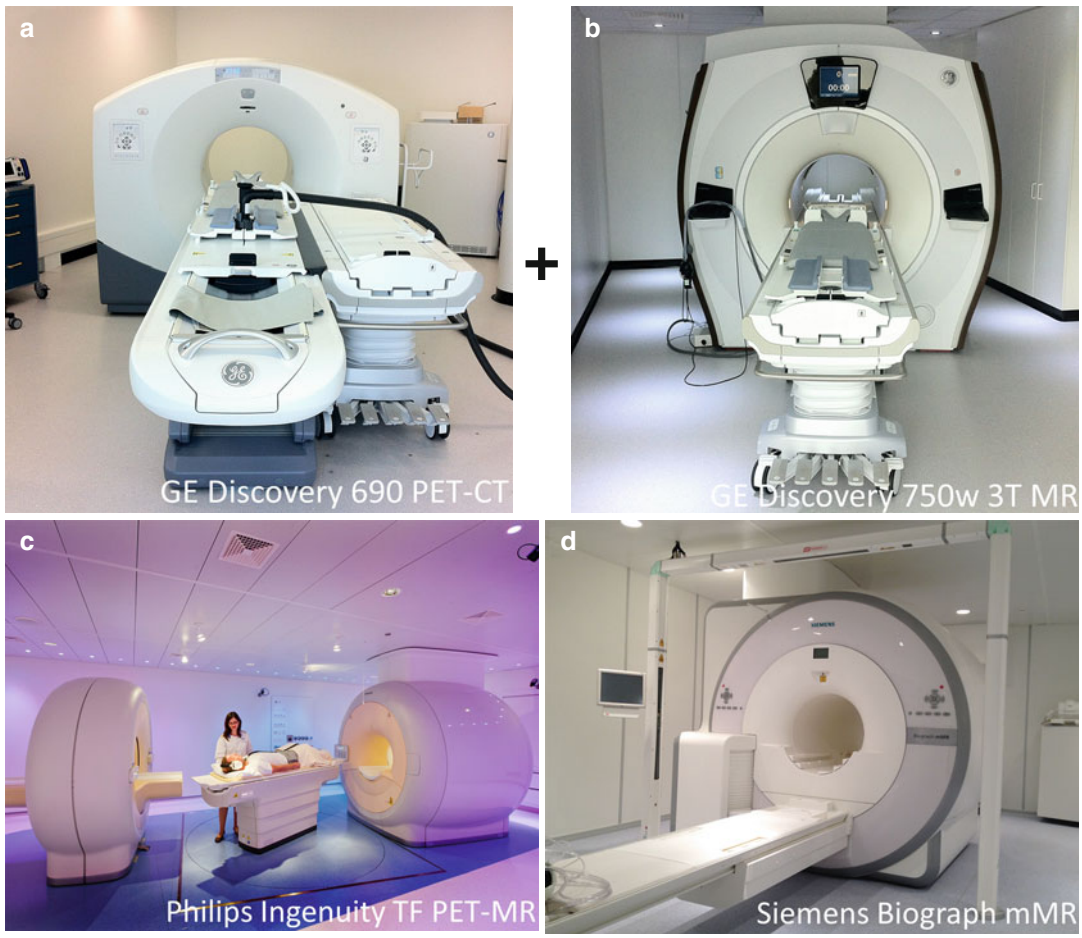

Fig. 19.6 The three commercially available combined PET and MR imaging devices as of today (summer 2013). (**a**) GE Discovery 690 PET-CT with air hovered board mounted onto a mobile shuttle system combined with (**b**) GE Discovery 750w 3 T MR (Courtesy of Patrick Veit-Haibach, MD), (**c**) Philips Ingenuity TF PET-MR (Courtesy of Prof. Otto S. Hoekstra) and (**d**) Siemens Biograph mMR

and a transferable board mounted onto a mobile shuttle system [35]. The shuttle system makes it possible to move the patient without repositioning between the PET-CT and the MRI, placed in separate rooms. This solution has some advantages, for example, the possibility to use the two systems together or as separate stand-alone scanners to optimize the usage. But it still is two sequential scans, and for the patient it is a long acquisition time.

In launching the world's first really integrated PET-MRI system in 2009, Philips Healthcare used another approach [36]: This system is based on an existing 3 T MRI, combined with a PET scanner similar to the one in GEMINI TF PET-CT. The PET scanner was redesigned to be operational inside a standard MRI scanner room by applying magnetic shielding and moving all electronics from the PET gantry to the equipment room. Further, the PET and MRI scanner is placed 3 meter apart. This system acquires PET and MRI sequentially, similar to the workflow in current PET-CT systems. The system suffers some of the same drawbacks as the tri-modality PET-CT+MRI system, but possibly providing better alignment owed to less risk for patient motion between the scans.

The first example of simultaneous PET-MRI system was developed by Marsden and Cherry in 1997 [37]. A single-slice PET was placed in the receiver coil connected to PM tubes outside the magnetic field via long optical fibers. Mainly due to the signal loss in the optical fibers, this approach has never gained commercial success. Instead the work with magnetic insensitive avalanche photodiodes (APDs) prospered. APDs could replace the very magnetic sensitive photomultiplier tubes used in PET detectors, and in 2007 Pichler and colleagues presented a PET insert based on APDs. This insert fits inside a 3 T whole-body MRI scanner with the remaining space in the gantry suitable for scanning brains and extremities [38]. This same approach led to the first clinical and commercially available simultaneous whole-body PET-MRI scanner, the Siemens Biograph mMR. In the Siemens Biograph mMR, optimization of the factors mentioned initially in this section has been attempted, but further development will improve the performance of future generations of simultaneous PET-MRI systems.

19.3.3 Current PET-MRI Systems: Strengths and Weaknesses

Today, summer 2013, there are three commercial available whole-body PET-MRI systems on the market: Discovery PET-CT+MRI (GE Healthcare), Ingenuity TF (Philips Healthcare), and Biograph mMR (Siemens). The performance of these systems is roughly similar (Table 19.1), but as mentioned in the previous section the design is completely different (Fig. 19.6).

Presently, Siemens mMR is the only truly integrated PET-MRI scanner enabling simultaneous imaging possible. However, a PET-CT+MRI system has some obvious advantages, especially regarding the possibility to obtain a CT-based attenuation correction and thereby a reliable PET quantification. Although improvement of the MRI-based attenuation correction has been done, it is still work in progress and with plenty of room for future improvement. Especially the problem of correctly identifying bone in the head and neck region is a serious challenge, together with correct segmentation of tissue in close proximity to metal containing implants and devices. Until this problem is solved, clinical users should routinely review non-corrected and attenuation-corrected emission images together with the diagnostic MR images and the MRI-based attenuation maps (μ-maps) (Fig. 19.7) in order to elucidate and interpret possible image artifacts arising from MRI-based AC [39] (Fig. 19.8). Unfortunately, we do not expect a completely reliable MRI-based attenuation correction method for quantitative whole-body imaging to be developed within the next 2–3 years.

Another advantage of the PET-CT+MRI system is the broader gantry. In the simultaneous system the PET scanner is inserted into the gantry of the MRI scanner, resulting in a narrow and relative long tunnel. This can be a challenge regarding patient comfort, especially for patients with a tendency of claustrophobia and obese

Table 19.1 Design and performance characteristics for today's commercial whole-body PET-MRI systems

	GE Discovery PET-CT+MRI[a]	Philips Ingenuity TF	Siemens Biograph mMR
PET			
Crystal type	LBS	LYSO	LSO
Crystal size (mm^3)	4.2×6.3×25	4×4×22	4×4×20
Axial field of view (cm)	15.7	18.0	25.8
Transaxial field of view (cm)	70	67.6	59.4
Sensitivity (cps/kBq)	7.0	7.0	13.2
Axial resolution 1 cm (mm)	5.6	4.9	4.5
Axial resolution 10 cm (mm)	6.3	5.5	6.7
Transverse resolution 1 cm (mm)	4.9	4.9	4.4
Transverse resolution 10 cm (mm)	6.3	5.5	5.2
Time-of-flight	Yes	Yes	No
MR			
MR field strength	3 T (or 1.5 T)	3 T	3 T
MR field of view (cm^3)	50×50×50	50×50×45	50×50×45
PET-MRI			
Max patient weight (kg)	180	200	200
Min gantry diameter (cm)	70	60	60
Acquisition	Sequential (two separate rooms)	Sequential (same room)	Simultaneous
Attenuation correction	CT based	MRI based	MRI based

Abbreviations: *LBS* Lutetium-based scintillator, *LSO* lutetium oxyorthosilicate, *LYSO* variant of LSO
[a]Possible combinations: Discovery PET-CT 610 or 710 combined with Discovery MR750w (3 T) or Optima MR450w (1.5 T). Data presented are for Discovery PET-CT 710+Discovery MR750w

patients. A bigger gantry will be less claustrophobic and render it possible to scan patients in fixation devices for radiotherapy planning.

The advantages of the truly integrated PET-MRI scanner enabling simultaneous acquisition are however also quite obvious: This method will reduce misalignment, shorten the total acquisition time, potentially reduce radiation burden, make it possible to do synchronized image gating, and to acquire PET and MRI data simultaneously for functional studies under identical physiological conditions. Thus it is our conviction that the development of future PET-MRI scanners will focus on optimization of the truly integrated PET-MRI and gradually abandon the in-line system.

19.3.4 Clinical and Research Application in Oncology

Reported evidence on the use of PET-MRI in oncology is steadily increasing. However the bulk of evidence comes from mixed populations or smaller case series reporting the experience with PET-MRI compared to PET-CT, performing clinical PET-CT in a mixed population followed by PET-MRI on the same injection of FDG [40–45]. As PET-MRI was developed and launched ahead of detailed considerations for practical issues like clinical application, work flow, optimized scan protocols, and attenuation correction [6, 46], this seems to be the logical way to go. But, apart from the small number of patients, this approach causes a number of problems: The sequential acquisition of PET-CT and PET-MRI, often more than an hour apart, makes interpretation and comparison of sensitivity and quantification very difficult – is the difference in focal findings and/or SUV values between the modalities due to different FDG kinetics (dual-time point imaging), technical quality, or different methods for attenuation correction? [40, 43–45, 47]. The sequential acquisition also results in constraints on the duration of the PET-MRI scan as the patient has just undergone a PET-CT scan, making time for evaluation of more functional

Fig. 19.7 MR-based attenuation map (μmap) from Dixon Water Fat segmentation. In- and opposed-phase MR imaging is used for delineation of the four classes of attenuation coefficients: soft tissue, fat, air, and lung (identified by post-processing algorithm) but not bone

MRI sequences together with PET scarce. Finally, PET-MRI should probably not be evaluated as a potential replacement of PET-CT: PET-MRI is, at present, too slow, too expensive, and the workflow too complicated [43]. PET-MRI should instead be seen as a supplement with a huge potential for multiparametric imaging. Whereas PET-CT has been evaluated in numerous studies, including randomized clinical trials and cost-effectiveness studies, PET-MRI is still just "the new kid on the block" with only smaller studies focusing mainly on feasibility and technical evaluation.

19.3.4.1 Diagnosis and Staging

Diagnosing and staging, assessing the anatomical spread and invasion of a malignant tumor, is pivotal in guiding the choice of treatment and estimating patient prognosis. The area where PET-MRI has been most rapidly adopted is in the assessment of brain tumors. MRI has for years been the routine imaging approach of brain tumors, recently supplemented with PET imaging with amino acid tracers such as FET or MET (please refer to Chaps. 24, 25, 26, and 27 for more details). Thus simultaneous PET-MRI combining structural and functional imaging at the same time and under exactly the same physiological conditions is expected to improve management of this group of patients [48].

By combining anatomical MRI, functional MRI, and PET imaging, to obtain concerted information about anatomy and biological activity of the tumor, the sensitivity and specificity in oncology staging, also outside the brain, is likely to be improved. The assessment of tumor invasion into adjacent structures can probably be improved by the combination of MRI anatomy, DW-MRI, and PET, for example, in rectal, bladder, prostate, and gynecological cancers [49–51]. Our experience so far points in that direction (Fig. 19.9), especially regarding gynecologic cancers [41], but clinical studies on PET-MRI in gynecologic and colorectal cancers are still lacking [46]. Whereas DW-MRI has shown some promise for the evaluation of invasion (T stage, as described above), a recent study by Buchbender and colleagues could not demonstrate that adding DWI to FDG-PET-MRI lesion detection (metastases) provided any additional benefit [52].

Secondly, PET-MRI might improve accuracy in the assessment of spread to regional lymph nodes, especially in the pelvic region [53, 54], but also in the mediastinum and head and neck region [55]. Platzek et al. have evaluated the feasibility of PET-MRI (adjacent PET-MRI by Philips) in

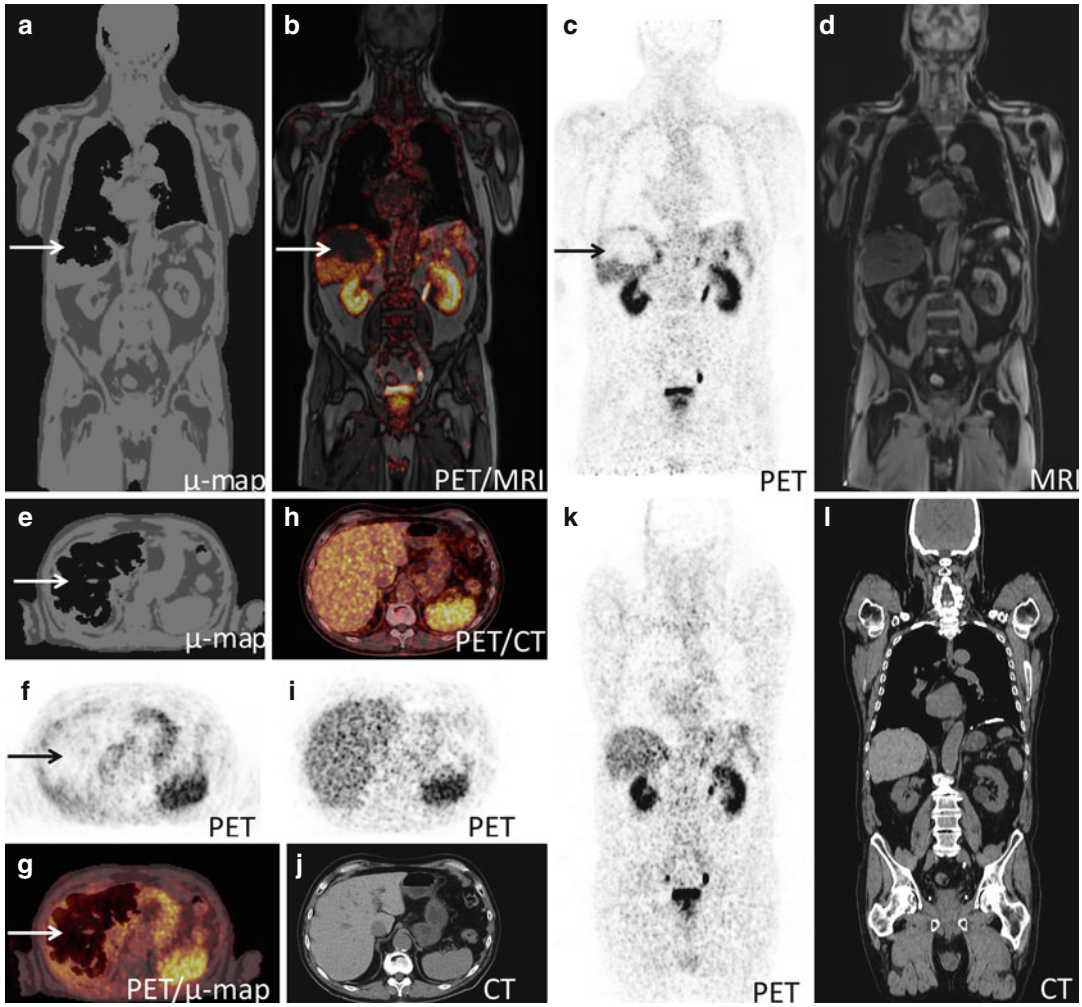

Fig. 19.8 MRI-based attenuation map (**μ**map) from a ^{64}Cu-Dotatate-PET/MRI scan illustrating an artifact in the liver (*arrow*). (**a**–**g**) PET/MRI, (**h**–**l**) PET-CT. (**a** and **e**) MRI-based attenuation map (**μ**map) where the algorithm has falsely segmented a substantial part of the liver as air, (**b** and **g**) attenuation corrected PET fused with MRI erroneous revealing an area in the liver without FDG-uptake, (**c** and **f**) attenuation corrected PET, (**d**) MRI, (**h**–**l**) corresponding images from a subsequent PET-CT with correct attenuation correction

patients with head and neck cancer [43]: They found a significantly higher lesion SUVmax in the PET-MRI examinations compared to dedicated stand-alone PET, and more importantly with regard to staging, the number of lymph nodes with increased FDG uptake detected, using the PET data from PET-MRI was significantly higher than the number detected by the stand-alone PET system. These results are hampered however by the delayed imaging on PET-MRI compared to PET (mean of 177 min, respectively, 64 min post-injection) and the lack of comparison with in-line PET-CT.

19.3.4.2 Planning of Radiotherapy

A fundamental challenge in modern radiotherapy is to balance the prescribed radiation dose between the wish for tumor control and the fear of tissue toxicity. A possible way to increase tumor control, without increasing toxicity, is the dose painting principle [56]. Dose painting relies, in short, on three assumptions: (1) Local recurrences after radiotherapy arise from small areas of the tumor, which are relatively resistant to radiotherapy. (2) This inhomogeneous distribution of radiosensitivity can be mapped by molecular imaging. (3) It is possible to plan and deliver

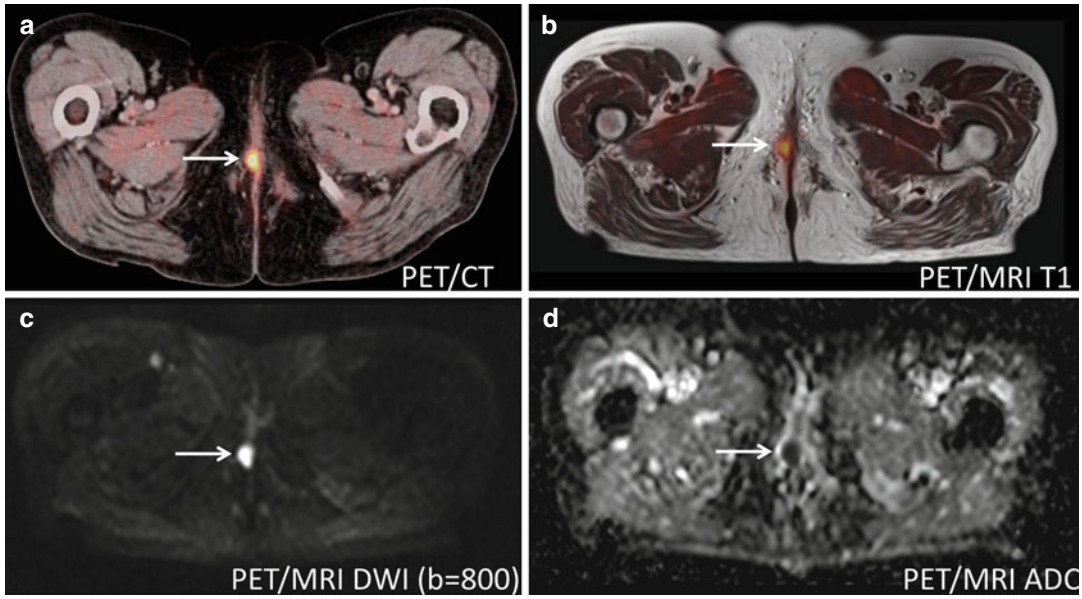

Fig. 19.9 A 73-year-old female with endometrial cancer of the uterus and metastatic spread. FDG-PET for restaging: (**a**) FDG-PET-CT shows focal accumulation of FDG in the labial region (*arrow*) which could represent either metastatic spread or contamination (activity in the urine). (**b–d**) PET-MRI (T1 and DW-MRI) identifies a solid lesion, with low diffusion (high cellularity) representing a metastasis in the labia (*arrow*). In this case PET/MRI increased the reader's confidence in a routine setting

a dose distribution to the tumor, which results in higher doses to the more resistant areas.

Tumor hypoxia is a key mechanism leading to radiotherapy resistance, and a technique for hypoxia mapping to be integrated with radiotherapy planning systems is warranted [57]. PET-based techniques using ^{64}Cu-ATSM, ^{18}F-MISO, or ^{18}F-FAZA can image hypoxia by binding to intracellular macromolecules when $pO_2 < 10$ mmHg. Accumulation of ^{18}F-MISO is less flow dependent, and local oxygen tension is the major determinant of its accumulation [56, 58], enabling imaging of both perfusion, diffusion, and anemic hypoxia. In contrast BOLD-MRI is thought to be most sensitive to perfusion-related hypoxia and thus often correlated with DCE-MRI in order to assess vascularity and perfusion [6].

By simultaneous PET-MRI it will be possible to describe tissue hypoxia by PET hypoxia tracer together with BOLD and/or DCE-MRI to distinguish between perfusion and diffusion as the most dominant cause of tumor hypoxia [6]. This again might be correlated to prognosis and influence treatment planning; Poor perfusion to the tumor area will hamper reoxygenation and thus the effect of radiotherapy. Simultaneous imaging of hypoxia by PET and MRI might also help to address one of the serious drawbacks of hypoxia imaging, namely, the only moderate reproducibility of intratumoral distribution of PET hypoxia tracer [56]. Alternatively, simultaneous FDG or FLT-PET and BOLD or DCE-MRI may result in new knowledge on the relationship between hypoxia, metabolism, proliferation, and radiotherapy resistance [56, 58], paving the way for molecular imaging-based dose painting.

The PET-MRI technology also carries the promise of describing and imaging new tumor characteristics that might be associated with resistance to radiotherapy: Schmidt and colleagues examined the correlation between SUV and ADC (from DWI) on a voxel by voxel analysis in 15 patients with lung tumors, enabling identification of areas within the same tumor with different combinations of metabolism and cellularity [47].

19.3.4.3 Therapy Evaluation

Accurate assessment of tumor response is a cornerstone in clinical patient management as well as in drug development. Currently response is mainly

evaluated by anatomical measures based on a single linear summation of selected target lesions, known as the RECIST criteria (Response Evaluation Criteria In Solid Tumors) [59]. The standardized RECIST criteria take into account differences in slice thickness, minimum tumor sizes, and frequency of evaluations. However, there is a growing concern that response measurements may not be adequately addressed by RECIST, neither when the patient is treated with conventional cytotoxic therapy [60] nor when treated with more recently developed molecularly targeted agents, which can provide therapeutically benefice without significantly reducing the tumor volume [61]. The use of PET-CT, combining metabolic and anatomical information for therapy evaluation, has a huge potential impact on the quality of patient treatment as well as on the evaluation of new therapy regimes [62]. Standardized criteria for response evaluation in solid tumors by PET-CT – PERCIST – were suggested in 2009 [63], and the impact of PET in response evaluation in, e.g., lymphoma is well established, but other tumor types are lacking behind [64]. In parallel with the increasing amount of evidence on FDG-PET as a surrogate marker for response, similar results have emerged for DW-MRI from a broad range of cancer types, suggesting that early changes in tumor diffusion values correlate with response to therapy [65–68]. However, both FDG-PET and DW-MRI suffer some of the very same drawbacks, i.e., lack of specificity in separating malignancy from inflammation. Early comparative studies suggest that the cause for false-positive findings might differ slightly between the two methods, opening a window of opportunity for simultaneous PET-MRI to explore more specific changes in the tissue [7, 65, 66, 69–71]. In this setting, PET-MRI could make early therapy evaluation a safer endeavor [6, 42] and increase our knowledge on the importance of tumor heterogeneity as exemplified on the study by Schmidt and colleagues [47].

19.3.4.4 Motion Compensation and Correction Techniques

Patient motion produces artifacts, due to tissue displacement during and between excitation and data acquisition, leading to blurred images on both PET and MRI. It is crucially important to minimize the negative effects from motion in order to get more precise information, especially when acquiring simultaneous dual modality imaging [6]. In PET-CT the difference in acquisition time between PET and CT can result in misalignment and mislocalization. In PET imaging, as well as in MRI, the acquisition time is relatively long, and the patient respiratory movements will inevitable cause blurring of lesions in the lung and upper abdomen. In PET imaging this blurring may result in an overestimation of the size of the lesion, as well as an underestimation of the lesion SUV (standardized uptake value) [72]. Several methods have been explored in order to minimize these problems by respiratory gating of PET (and CT). These methods mostly depend on external markers or sensors, and longer acquisition time, making it difficult to implement in daily clinical routine [73, 74]. Recently, a markerless structured light 3D surface tracking system has been developed for motion correction in brain studies [75]. The system is independent of external markers on the patient, and designed to fit into narrow spaces, making it highly promising for PET-MRI [6].

With regard to MRI, there are several variants to reduce motion artifacts, some of them independent of external markers. Simultaneous PET-MRI with motion correction has the potential to improve PET quantification in especially tumors of the lung and liver [76], which again will impact both diagnosing, radiotherapy planning, and evaluation. A few recent studies (preclinical) have explored the possibility of MRI-based motion correction of the PET data, finding it to be feasible and resulting in improved image quality [77, 78].

19.4 Conclusion and Future Perspectives

With two different, and likely complementally, hybrid imaging systems, the future of functional oncological imaging seems brighter than ever: PET-CT a relatively well-established modality for diagnosing, staging, restaging, and monitoring response to therapy and the novel PET-MRI

of unexplored potential in management of oncological patient. Based on the few studies available addressing the clinical value of PET-MRI, we conclude that PET-MRI should be seen as a complement and not a replacement of PET-CT. When MRI was initially introduced, it was thought that MRI would replace CT, but instead CT imaging has prospered. In PET it will probably be the same story – both techniques PET-CT and PET-MRI will continue to evolve, and the mission of the research society of functional imaging is to explore, evolve, and validate the role of both PET-CT and PET-MRI in oncology.

There are, however, a number of reasons that PET-MRI will probably never reach the same broad use as PET-CT, and not all patients with an indication for PET will benefit from a PET-MRI rather than a PET-CT.

- There are absolute contraindications to MRI compromising the broader use of this modality.
- CT outperforms MRI in certain areas, e.g., diagnosing small lung lesions.
- Whole-body PET-MRI where MRI governs the total examination time is more time consuming than standard PET-CT.
- Whole-body MRI generates a lot of images and is more time consuming to read than a whole-body CT.
- A PET-MRI scanner will induce patient discomfort more likely than PET-CT beyond claustrophobia.
- Standardization of PET-CT for diagnosis and especially therapy evaluation are not perfect but improving. Standardization of PET-MRI protocols is non-existing and will be a continuous challenge, due to the uncountable possible variations within MRI-protocols.

Based on these considerations we could speculate in three future potential clinical scenarios for PET-MRI (apart from an important and growing role in oncology research):

- A regional PET-MRI scan, e.g., the brain for diagnosing, staging, therapy evaluation, and radiotherapy planning of primary brain tumors where the evident benefit of "one stop shop" and the possibility to do true multiparametric imaging by combining molecular imaging and functional MRI.
- A regional PET-MRI for tumor characterization, tumor delineation, assessment of infiltration, and lymph node staging combined with a whole-body PET-MRI overview for assessment of distant metastases. This approach would be suitable for tumors in regions where CT is suboptimal (e.g., tumors in the pelvic region, musculoskeletal tumors, liver, and head and neck tumors) but also for tumors where response evaluation is expected to be markedly improved by combining PET and functional MRI compared to standard PET-CT. This scenario could consider a supplemental CT of the lung for assessment of small lung lesions.
- A whole-body PET-MRI where PET-CT is suboptimal for other reasons, e.g., all children and young adults in order to reduce radiation dose patients with iodine contrast allergy and patients with thyroid cancer whom should not have iodine contrast.

Introducing PET-MRI in the clinical oncological arena is a challenge, and the biggest challenge will improve MRI-based attenuation, correction, and harmonization of imaging protocols, especially with regard to MRI part. The CT acquisition in a PET-CT exam could basically be performed as a low-dose CT, a diagnostic CT with or without oral and intravenous contrast media and always in the same transaxial plane. The number of possible combinations of MRI sequences, image orientations, and different contrast media is infinite. For a successful implementation the PET-MRI society needs to agree on standardized imaging protocols and evaluate them in well-designed clinical multicenter studies; otherwise, we will fail releasing the full potential of this new and fascinating modality.

References

1. Huebner J. A possible declinig trend for worldwide innovation. Tech Forecasting Soc Change. 2005;72:980–6.
2. Cherry SR, Phelps ME. Positron emission tomography: methods and instrumentation. In: Sandler MP et al., editors. Diagnostic nuclear medicine, vol. 1. Baltimore: Williams & Wilkins; 1995. p. 139–59.

3. Ak I, et al. The clinical value of ^{18}F-FDG detection with a dual-head coincidence camera: a review. Eur J Nucl Med. 2001;28:763–78.
4. Beyer T, et al. A combined PET/CT scanner for clinical oncology. J Nucl Med. 2000;41:1369–79.
5. von Schulthess GK. Cost considerations regarding an integrated CT-PET system. Eur Radiol. 2000;10: S377–80.
6. Balyasnikova S, et al. PET/MR in oncology: an introduction with focus on MR and future perspectives for hybrid imaging. Am J Nucl Med Mol Imaging. 2012;2:458–74.
7. Sauter AW, et al. Combined PET/MRI: one step further in multimodality imaging. Trends Mol Med. 2010;16:508–15.
8. Sweet WH, Brownell GL. Localization of brain tumors with positron emitters. Nucleonics. 1953;11:40–5.
9. Brownell GL, Burnham CA. MGH positron camera. NEREM 1972. Record. 1972;2:117.
10. Burnham CA, Brownell GL. A multi-crystal positron camera. IEEE Trans Nucl Sci. 1972;19:201–5.
11. Ido T, et al. Labeled 2-deoxy-D-glucse analogs. -labeled 2-deoxy-2-fluoro-D-glucose, 2-deoxy-2-fluoro-D-mannose and C-14-2-deoxy-2-fluoro-D-glucose. J Label Compd Radiopharm. 1978;14:175–82.
12. Shepp LA, Vardi Y. Maximum likelihood reconstruction for emission tomography. IEEE Trans Med Imaging. 1982;MI-1:113–22.
13. Hudson HM, Larkin RS. Accelerated image reconstruction using ordered subsets of projection data. IEEE Trans Med Imaging. 1994;13:601–9.
14. Ziessman HA, et al. Nuclear medicine: the requisites. 2014.
15. Shreve P, Townsend DW. Clinical PET-CT in radiology: integrated imaging in oncology. New York: Springer; 2011.
16. Renker D. Geiger-mode avalanche photodiodes, history, properties and problems. Nucl Instrum Meth. 2006;A567:48–56.
17. Renker D. New trends on photodetectors. Nucl Instrum Meth. 2007;A571:1–6.
18. Lecomte R. Novel detector technology for clinical PET. Eur J Nucl Med Mol Imaging. 2009;36:s69–85.
19. Ho Shon I, et al. Positron emission tomography in lung cancer. Semin Nucl Med. 2002;XXXII:240–70.
20. Antoch G, et al. Accuracy of whole-body dual-modality fluorine-18-2-fluoro-2-deoxy-D-glucose positron emission tomography and computed tomography (FDG-PET/CT) for tumor staging in solid tumors: comparison with CT and PET. J Clin Oncol. 2004; 22:4357–68.
21. Bar-Shalom R, et al. Clinical performance of PET/CT in evaluation of cancer: additional value for diagnostic imaging and patient management. J Nucl Med. 2003;44:1200–9.
22. Cohade C, et al. Uptake in supraclavicular area fat ("USA-fat"): description on 18F-FDG PET/CT. J Nucl Med. 2003;44:170–6.
23. Bar-Shalom R, et al. The additional value of PET/CT over PET in FDG-imaging of oesophageal cancer. Eur J Nucl Med Mol Imaging. 2005;32:918–24.
24. Delbeke D, Martin WH. PET and PET-CT for evaluation of colorectal carcinoma. Semin Nucl Med. 2004;XXXIV:209–23.
25. Kim JH, et al. Comparison between 18F-FDG PET, in-line PET/CT, and software fusion for restaging of recurrent colorectal cancer. J Nucl Med. 2005;46: 587–95.
26. Maas M, et al. What is the most accurate whole-body imaging modality for assessment of local and distant recurrent disease in colorectal cancer? A meta-analysis. Eur J Nucl Med Mol Imaging. 2011;38: 1560–71.
27. Kitajima K, et al. Performance of integrated FDG-PET/contrast-enhanced CT in the diagnosis of recurrent uterine cancer: comparison with PET and enhanced CT. Eur J Nucl Med Mol Imaging. 2009;36: 362–72.
28. Cerfolio RJ, et al. The accuracy of integrated PET-CT compared with dedicated PEt alone for the staging of patients with nonsmall cell lung cancer. Ann Thorac Surg. 2004;78:1017–23.
29. Lardinois D, et al. Staging of non-small-cell lung cancer with integrated positron-emission-tomography and computed tomography. N Engl J Med. 2003;348: 2500–7.
30. Reinhardt M, et al. Diagnostic performance of whole body dual modality 18F-FDG PET/CT for imaging N- and M-staging of malignant melanoma: experience with 250 consecutive patients. J Clin Oncol. 2006;24:1178–87.
31. Pearce MS, et al. Radiation exposure from CT scans in childhood and subsequent risk of leukaemia and brain tumours: a retrospective cohort study. Lancet. 2012;380:499–505.
32. Zhang D, et al. Estimated cumulative effective dose from PET/CT in pediatric patients with malignancies. Med Phys. 2008;35:2958.
33. Boss A, et al. Feasibility of simultaneous PET/MR imaging in the head and upper neck area. Eur Radiol. 2011;21:1439–46.
34. Mawlawi O, Townsend DW. Multimodality imaging: an update on PET/CT technology. Eur J Nucl Med Mol Imaging. 2009;36:S15–9.
35. Veit-Haibach P, et al. PET-MR imaging using a tri-modality PET/CT-MR system with a dedicated shuttle in clinical routine. Magn Reson Mater Phys. 2013; 26:25–35.
36. Gagnon D, et al. Hybrid PET-MRI imaging systems. US Patent Application 20080312526; 2008.
37. Shao Y, et al. Simultaneous PET and MR imaging. Phys Med Biol. 1997;42:1965–70.
38. Schlemmer H, et al. Simultaneous MR/PET imaging of the human brain. Radiology. 2008;248:1028–35.
39. Keller SH, et al. Image artifacts from MR-based attenuation correction in clinical, whole-body PET/MRI. Magn Reson Mater Phys. 2013;26:173–81.

40. Chandarana H, et al. Pulmonary nodules in patients with primary malignancy: comparison of hybrid PET/MR and PET/CT imaging. Radiology. 2013;268:874–81.
41. Kjær A, et al. PET/MRI in cancer patients: first experiences and visions from Copenhagen. MAGMA. 2013;26:37–47.
42. Platzek I, et al. PET/MR for therapy response evaluation in malignant lymphoma: initial experience. MAGMA. 2013;26:49–55.
43. Platzek I, et al. PET/MRI in head and neck cancer: initial experience. Eur J Nucl Med Mol Imaging. 2013;40:6–11.
44. Schwenzer NF, et al. Pulmonary lesion assessment: comparison of whole-body hybrid MR/PET and PET/CT imaging – pilot study. Radiology. 2012;264:551–8.
45. Wiesmüller M, et al. Comparison of lesion detection and quantitation of tracer uptake between PET from a simultaneously acquiring whole-body PET/MR hybrid scanner and PET from PET/CT. Eur J Nucl Med Mol Imaging. 2013;40:12–21.
46. Jadvar H, Colletti PM. Competitive advantage of PET/MRI. Eur J Radiol. 2013 [Epub ahead of print].
47. Schmidt H, et al. Correlation of simultaneously acquired diffusion-weighted imaging and 2-deoxy-[18F]fluoro-2-D-glucose positron emission tomography of pulmonary lesions in a dedicated whole-body magnetic resonance/positron emission tomography system. Invest Radiol. 2013;48:247–55.
48. Neuner I, et al. Multimodality imaging utilising MR-PET for human brain tumour assessment. Eur Radiol. 2012;22:2568–80.
49. Hochhegger B, et al. MRI in lung cancer: a pictoral essay. Br J Radiol. 2011;84:661–8.
50. Jansen JFA, et al. Tumor metabolism and perfusion in head and neck squamous cell carcinoma: pretreatment multimodality imaging with 1H magnetic resonance spectroscopy, dynamic contrast-enhanced MRI and [18F]FDG-PET. Int J Radiat Oncol Biol Phys. 2012;82:299–307.
51. Ohno Y, et al. N stage disease in patients with non-small cell lung cancer: efficacy of quantitative and qualitative assessment with STIR Turbo Spin-Echo Imaging, diffusion-weighted MR imaging and fluorodeoxyglucose PET/CT. Radiology. 2012;261:605–15.
52. Buchbender C, et al. Diffusion-weighted imaging as part of hybrid PET/MRI protocols for whole-body cancer staging: does it benefit lesion detection? Eur J Radiol. 2013;82:877–82.
53. Atherly AJ, Camidge DR. The cost-effectiveness of screening lung cancer patients for targeted drug sensitivity markers. Br J Cancer. 2012;106:1100–6.
54. Sequist LV, et al. Implementing multiplexed genotyping of non-small-cell lung cancers into routine clinical practice. Ann Oncol. 2011;22:2616–24.
55. Gerlinger M, et al. Intratumor heterogeneity and branched evolution revealed by multiregion sequencing. N Engl J Med. 2012;366:883–92.
56. Nehmeh SA, et al. Reproducibility of intratumor distribution of 18F-fluoromisonidazole in head and neck cancer. Int J Radiat Oncol Biol Phys. 2008;70:235–42.
57. Padhani AR, et al. Imaging oxygenation of human tumours. Eur Radiol. 2007;17:861–72.
58. Dirix P, et al. Dose painting in radiotherapy for head and neck squamous cell carcinoma: value of repeated functional imaging with 18F-FDG PET, 18F-Fluoromisonidazole PET, diffusion-weighted MRI, and dynam contrast-enhanced MRI. J Nucl Med. 2009;50:1020–7.
59. Therasse P, et al. New guidelines to evaluate the response to treatment in solid tumors. J Natl Cancer Inst. 2000;92:205–16.
60. Jaffe CC. Measurements of response: RECIST, WHO and new alternatives. J Clin Oncol. 2006;24:3245–51.
61. Strumberg D. Preclinical and clinical development of the oral multikinase inhibitor sorafenib in cancer treatment. Drugs Today. 2005;41:773.
62. Weber WA. Use of PET for monitoring cancer therapy and for predicting outcome. J Nucl Med. 2005;46:983–95.
63. Wahl RL, et al. From RECIST to PERCIST: evolving considerations for PET response criteria in solid tumors. J Nucl Med. 2009;50:122S–50.
64. Hutchings M, et al. FDG-PET after two cycles of chemotherapy predicts treatment failure and progression-free survival in Hodgkin Lymphoma. Blood. 2006;107:52–9.
65. Galbán CJ, et al. Evaluation of treatment-associated inflammatory response on diffusion-weighted magnetic resonance imaging and 2-[18F]-fluoro-2-deoxy-d-glucose-positron emission tomography imaging biomarkers. Clin Cancer Res. 2010;16:1542–52.
66. Galbán S, et al. Diffusion-weighted MRI for assessment of early cancer treatment response. Curr Pharm Biotechnol. 2010;11:701–8.
67. Heijmen L, et al. Tumour response prediction by diffusion-weighted MR-imaging: ready for clinical use? Crit Rev Oncol Hematol. 2012;83:194–207.
68. Koh DM, Collins DJ. Diffusion-weighted MRI in the body: applications and challenges in oncology. Am J Roentgenol. 2007;188:1622–35.
69. Boss A, et al. Hybrid PET/MRI of intracranial masses: initial experiences and comparison to PET/CT. J Nucl Med. 2010;51:1198–205.
70. Sauter AW, et al. Letter to the editor re: molecular imaging in oncology: the acceptance of PET/CT and the emergence of MR/PET imaging. Eur Radiol. 2011;5:1–4.
71. Schiepers C, Dahlbom M. Molecular imaging in oncology: the acceptance of PET/CT and the emergence of MR/PET imaging. Eur Radiol. 2011;21:548–54.
72. Werner MK, et al. Respiratory gating enhances imaging of pulmonary nodules and measurement of tracer uptake in FDG PET/CT. Am J Roentgenol. 2009;193:1640–5.

73. Aznar M, et al. Feasibility of breathing-adapted PET/CT imaging for radiation therapy of Hodgkin lymphoma. Cancer Imaging. 2011;Spec No A:S117. Ref Type: Abstract.
74. Nehmeh S, Erdi YE. Respiratory motion in positron emission tomography/computed tomography: a review. Semin Nucl Med. 2008;38:167–76.
75. Olesen OV, et al. Motion tracking for medical imaging: a non-visible structured light tracking approach. IEEE Trans Med Imaging. 2012;31:79–87.
76. Dikaios N, et al. MRI-based motion correction of thoracic PET: initial comparison of acquisition protocols and correction strategies suitable for simultaneous PET/MRI systems. Eur Radiol. 2012;22:439–46.
77. Ouyang J, et al. Magnetic resonance-based motion correction for positron emission tomography imaging. Semin Nucl Med. 2013;43:60–7.
78. Würslin C, et al. Respiratory motion correction in oncologic PET using T1-weighted MR imaging on a simultaneous whole-body PET/MR system. J Nucl Med. 2013;54:464–71.

Dual-Energy and Spectral Energy Computed Tomography: Oncological Body Applications in Clinical Use

20

Alvin C. Silva and Wendy Z. Stiles

Contents

Abbreviations

ASIR	Adaptive statistical iterative reconstruction
CT	Computed tomography
DECT	Dual-energy computed tomography
dsDECT	Dual-source dual-energy computed tomography
FDG-PET	18-fluoro-deoxyglucose positron emission tomography
GIST	Gastrointestinal stromal tumor
HU	Hounsfield units
IV	Intravenous
keV	Kiloelectron volt
kVp	Peak kilovoltage
MR	Magnetic resonance
NSCLC	Non-small-cell lung cancer
PET SUV	Positron emission tomography standardized uptake value
RECIST	Response evaluation criteria in solid tumors
SAFIRE	Sinogram-affirmed iterative reconstruction
SECT	Single-energy computed tomography
ssDECT	Single-source dual-energy computed tomography
SUV_{max}	Maximum standardized uptake value
VNC	Virtual noncontrast

A.C. Silva, MD (✉) • W.Z. Stiles, MD
Department of Radiology, Mayo Clinic,
13400 E Shea Blvd, Scottsdale, AZ 84259, USA
e-mail: silva.alvin@mayo.edu

A. Luna et al. (eds.), *Functional Imaging in Oncology*,
DOI 10.1007/978-3-642-40412-2_20,

20.1 Introduction to DECT

DECT has been investigated since the 1970s because of its potential to improve tissue characterization; however, early deficiencies impeded its implementation in daily clinical practice [1–9]. Recent hardware and software advancements have improved efficiency in CT gantry rotation, x-ray source, and detector arrays. Thus, current multidetector CTs have eliminated earlier misregistration artifact with simultaneous or nearly simultaneous dual-energy acquisition [10]. In addition, excessively noisy images acquired at lower energy (e.g., 80 peak kilovoltage [kVp]) have been overcome by modern detectors [1, 11–13] and iterative reconstruction algorithms [14], whereas improved processors have reduced computational time for analyzing DECT data [12]. DECT's data acquisition and processing have therefore made it competitive with conventional CT [11, 12, 15].

Conventional single-energy CT (SECT) and DECT radiation doses depend on several parameters, including kVp, dual- or single-energy acquisition, number of phases acquired, and manufacturer variations [15]. Although two acquisition energies are needed with DECT, this does not result in twice the dose of conventional SECT. Acquisition at a lower energy, such as 80 kVp, has inherently decreased radiation dose compared to higher energy acquisitions, e.g., 140 kVp [16]. In cases where answering a clinical question would require *multiple* phases on SECT, DECT can simply reduce radiation exposure by acquiring comparable data in only *one* phase [17]. Furthermore, its improved lesion characterization can obviate recommendations for a follow-up examination with additional radiation exposure [18]. Further reductions in effective radiation dose have also been made possible by advancements in newer-generation DECT scanners, such as protocol optimization, tin filter use, and improved post-processing techniques with sinogram-affirmed iterative reconstruction (SAFIRE) and adaptive statistical iterative reconstruction (ASIR) algorithms [19, 20]. Thus, the effective radiation dose is generally dose neutral between DECT and SECT when state-of-the-art technology is used [14, 21, 22].

Commercially available DECT products include single-source dual-energy CT (ssDECT) (GE Healthcare, Piscataway, NJ) that utilizes rapid kVp switching (<250 μs) between two energies from a single x-ray tube and dual-source dual-energy CT (dsDECT) (Siemens Medical Solutions, Erlangen, Germany) that utilizes two independent x-ray tubes to perform an equivalent task [10]. By exploiting attenuation differences at *two* acquisition energies, DECT can more accurately separate different material types than is possible in a *one* acquisition from conventional SECT.

From a DECT acquisition, both the projection-based (ssDECT) and image-based (dsDECT) raw data are used to generate various image displays: material density, computed monochromatic, and effective-z. Material density images, the result of elemental decomposition derived from energy-related attenuation characteristics, are composed as material basis pairs, with the most common pair being water (virtual noncontrast [VNC]) and iodine (an image map of iodine-containing pixels) (Fig. 20.1). The computed monochromatic display represents reconstructed images as if produced by a single monochromatic energy beam, reported in kiloelectron volts (keV). In comparison, conventional SECT images are produced by a polychromatic energy beam and reported in kVp. The virtual monochromatic images are generated from ssDECT source data through a mathematic model [23] (Fig. 20.1), whereas dsDECT uses a nonlinear blending algorithm or a variable weighted average to create images emphasizing benefits at each energy setting [24]. In either case, these DECT images maximize contrast from lower kVp and maintain optimal anatomic resolution with less noise from higher kVp [11, 25], with the use of ssDECT allowing real-time adjustment of monochromatic data from low to high keV [12]. The effective-z display is generated from projection data and differentiates image components on the basis of their atomic numbers (Fig. 20.1).

With the use of an advanced workstation application, ssDECT data can be post-processed

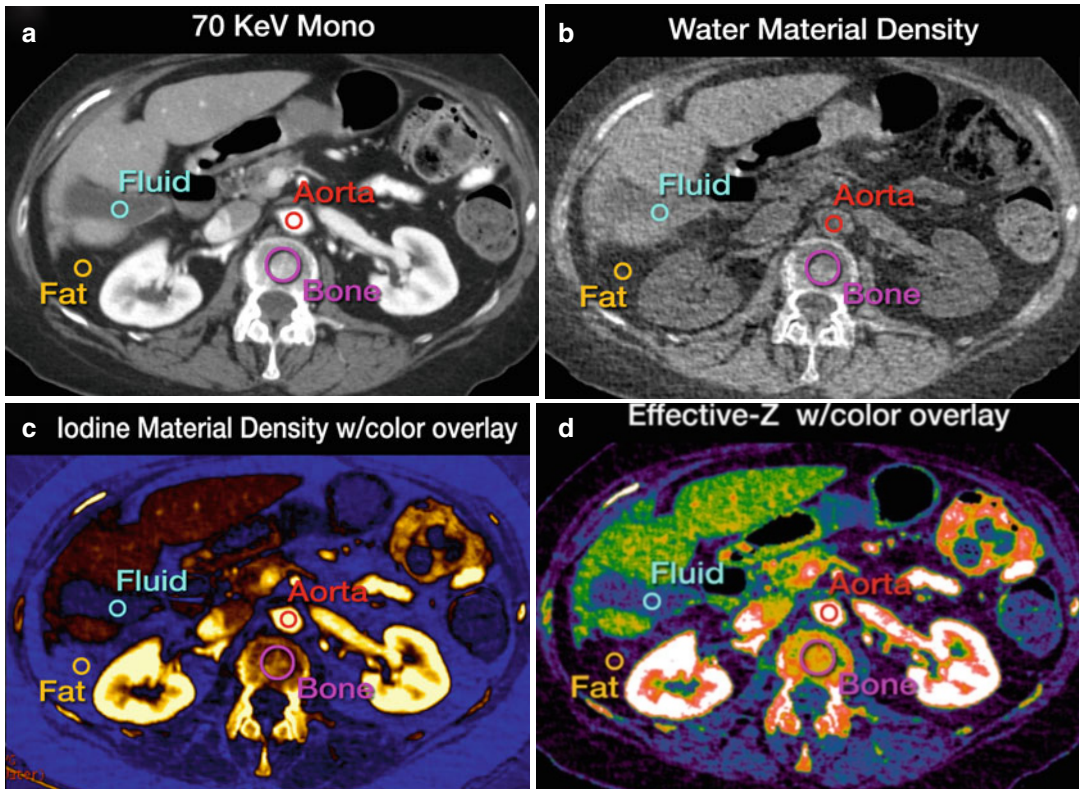

Fig. 20.1 DECT: various image displays. (**a**) 70 keV monochromatic image; (**b**) water material density image; (**c**) iodine material density image with color overlay; and (**d**) effective-Z image with color overlay of regions of interest (ROI) highlighting various materials in the body. The ROI information can be plotted onto different spectral graphs as in Fig. 20.2

to generate spectral Hounsfield units (HU) curves, scatterplots, and histograms (Fig. 20.2). Spectral HU curves are created by plotting attenuation values (HU) for a single material over monochromatic energies spanning from 40 to 140 keV, whereas scatterplots and histograms show pixel-by-pixel information for specific materials. The potential application of these post-processed data sets, as well as those of other specific DECT displays, can vary by organ system, as outlined below.

20.2 Chest

A solitary pulmonary nodule can be imaged to exclude malignancy by proving the presence of a characteristic benign pattern of calcification indicative of prior granulomatous disease exposure. When chest CTs are performed with iodinated intravenous (IV) contrast, a conundrum with SECT arises as to whether a hyperdense solitary pulmonary nodule is calcified or is the result of an enhancing mass. However, with DECT, calcifications have been detected on water basis pair (VNC) images 85–97 % of the time in lung nodules and lymph nodes [26]. In addition, the CT number (HU) on iodine basis pair images from dsDECT has been found to correlate with the degree of enhancement in a solitary pulmonary nodule [26]. Since malignant nodules enhance considerably more than benign nodules, a preliminary study showed that a threshold value of <20 HU on iodine basis pair images can differentiate nodules with an accuracy rate of 82.2 % [26–33]. DECT can detect calcification and measure degree of enhancement in lung nodules, masses, or lymph nodes, allowing accurate classification

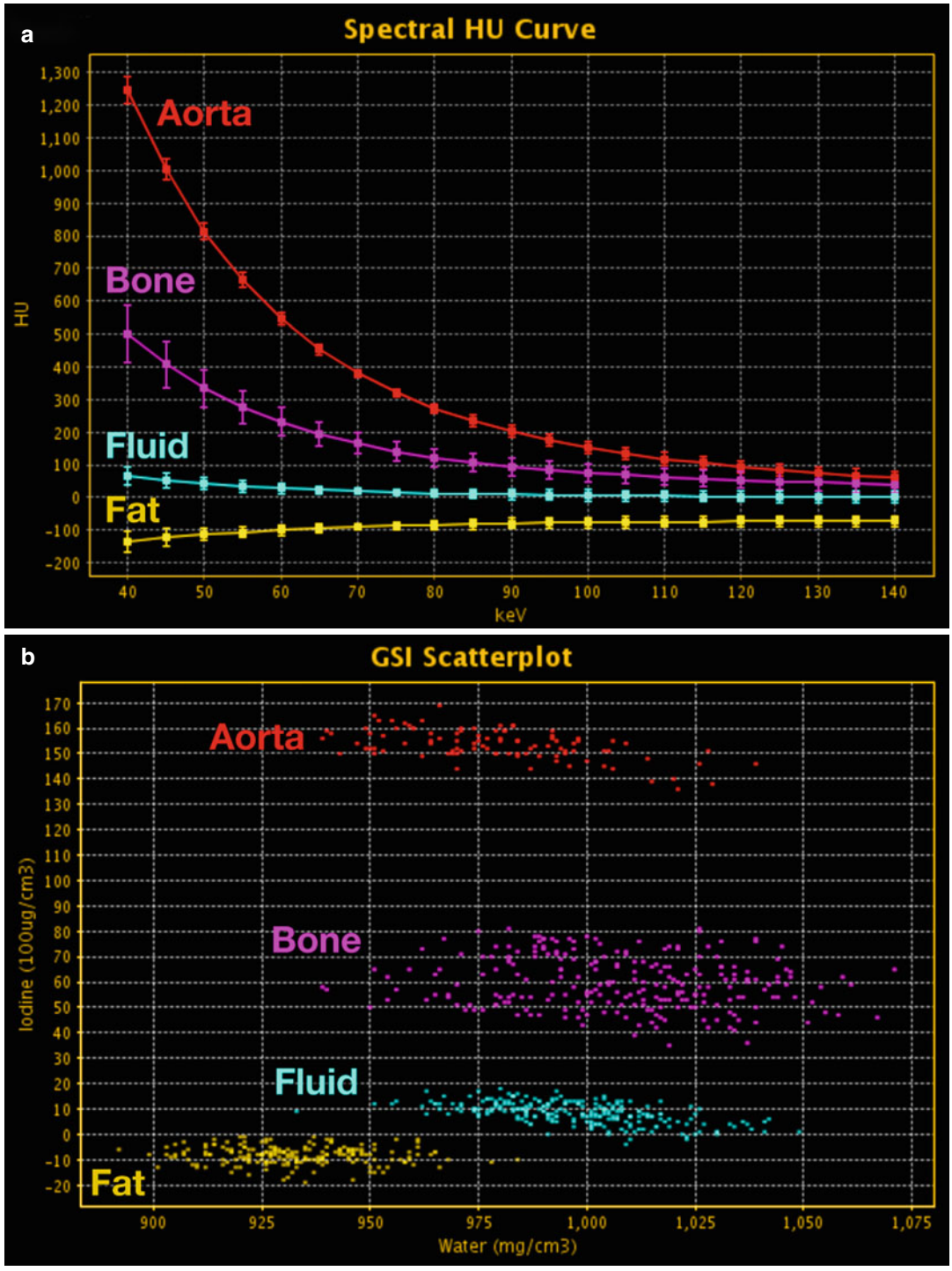

Fig. 20.2 DECT: advanced post-processing displays. (**a**) Spectral HU curves are generated by plotting the attenuation values of a material for every monochromatic energy from 40 to 140 keV. These attenuation curves can help characterize specific materials (e.g., aorta and bone have sharply upward-sloping curves at lower energies due to their specific k-edge, whereas fluid has a relatively flatter curve; and fat has a downward-sloping curve at lower energies). (**b**) DECT scatterplots are generated by plotting material components in a pixel-by-pixel display using various parameters (e.g., concentration of iodine (100 **μ**g/mL) vs. water (mg/mL). The area encompassed by the pixels helps to classify tissue composition within the ROIs. (**c**) Histograms are generated by plotting the percentage of pixels within an ROI rather than by specific DECT parameters, which in this case are HU values as in the 70 keV monochromatic image. Greater separation along the *x*-axis indicates greater differences in composition

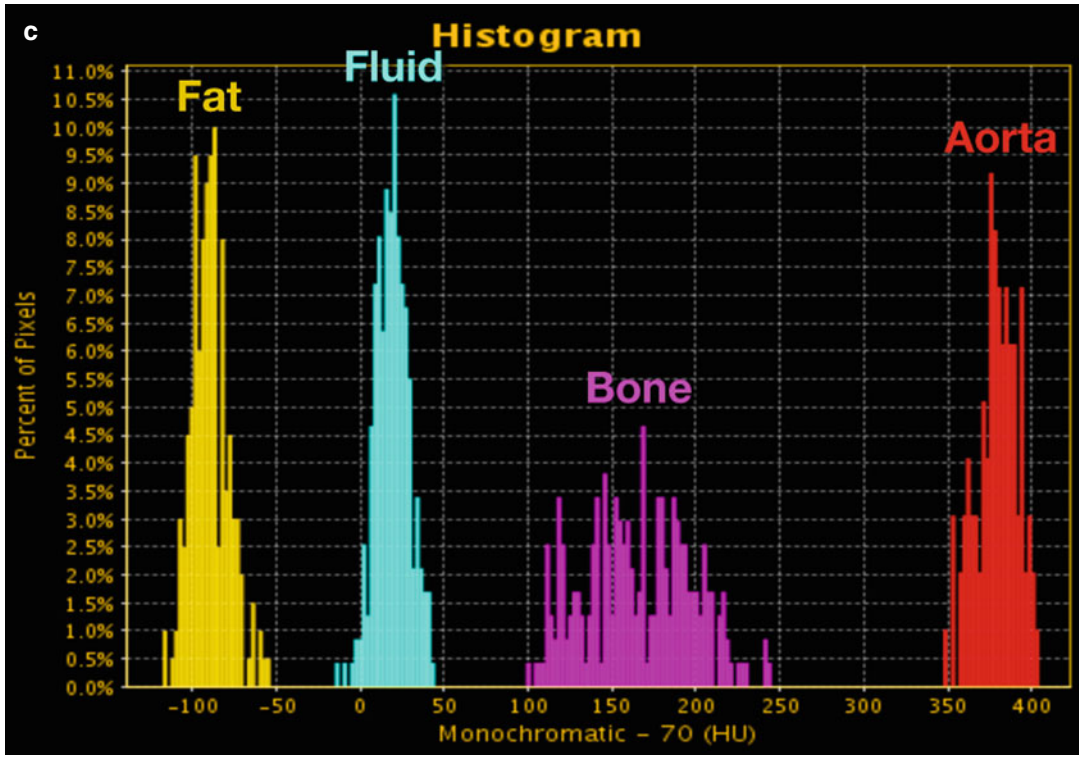

Fig. 20.2 (continued)

on a single enhanced examination, negating the need for a follow-up examination, and decreasing radiation exposure to patients, as well as giving a more streamlined answer to the patient and the referring clinician.

The imaging technique 18-fluoro-deoxyglucose positron emission tomography (^{18}FDG-PET) CT has a proven track record in characterizing pulmonary nodules and in staging lung cancer before and after therapy. Since the maximum standardized uptake value (SUV_{max}) may correlate with tumor aggressiveness [34–41], this imaging study can be an important component of a treatment plan. Unfortunately, ^{18}FDG-PET CT requires more preparation, patient time, and cooperation than DECT, as well as greater radiation exposure. Thus, DECT is being investigated as an alternative. For example, non-small-cell lung cancer (NSCLC) treatment response can be monitored on ^{18}FDG-PET CT by SUV_{max}. However, the degree of viable primary tumor or lymph node enhancement with iodinated contrast (i.e., vascularity) can be measured with maximum iodine-related attenuation, which has been shown to correlate with SUV_{max}, thus indicating that DECT has the potential to replace or become an adjunct imaging study for monitoring NSCLC [42]. Nonetheless, further evaluation is needed to confirm these preliminary results, as well as to investigate the role of DECT for other primary lung cancers.

20.3 Liver

Hypervascular liver lesions, including metastases and hepatocellular carcinomas, are more conspicuous on contrast-enhanced images acquired at lower energy (e.g., 80 kVp) than at higher energy (e.g., kVp) [11, 43–47], but imaging at lower energy with conventional SECT necessitates a specific additional acquisition. However, a range of 101 monochromatic keV displays can be generated from dual-energy data, which combines superior contrast resolution with increased conspicuity of solid organ parenchymal masses from a single DECT acquisition [11, 44] (Fig. 20.3).

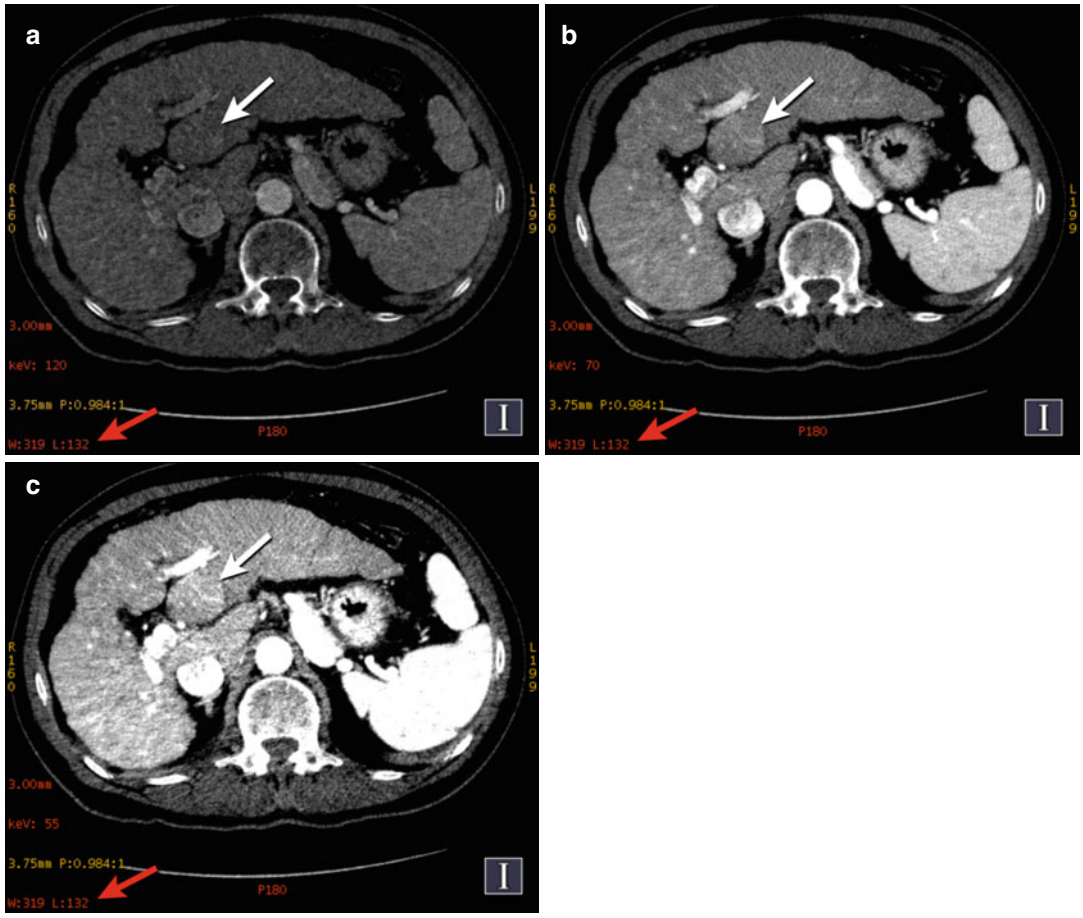

Fig. 20.3 Hepatocellular cancer (HCC). DECT-computed monochromatic images show increasing conspicuity of histologically verified left lobe HCC (**a**–**c**, *white arrows*) as the beam energy ([**a**] 120 keV, [**b**] 70 keV, [**c**] 55 keV) is shifted toward the k-edge of iodine (33.2 keV). Note that each image is depicted using the same window/level settings (**a**–**c**, *white arrows*)

Lv et al. determined that lower energy monochromatic images (40–70 keV) provided the most evident contrast between enhancing liver background and lesions, thus improving detection of hypervascular lesions ≤3 cm [48]. However, the contrast to noise ratio changes with the imaging phase, as well as with energy level. For example, hepatocellular carcinoma is best seen on arterial phase at 50 keV or at portal venous phases at 70 keV, whereas focal nodular hyperplasia is most conspicuous on either arterial or portal venous phase at 50 keV [49]. Furthermore, in addition to the monochromatic images, iodine basis pair images can also improve detection of HCC on portovenous phase on ssDECT [49]. Iodine concentration may also be a differentiating factor in identifying malignancy, because iodine concentration has been found to be statistically higher in focal nodular hyperplasia vs. hepatocellular carcinoma on arterial phase images [49].

The use of spectral HU attenuation curves may be helpful in improving the characterization of indeterminate hepatic lesions (i.e., the differentiation between pseudoenhancement artifact and actual contrast enhancement) [12]. For example, iodine has markedly increased attenuation at lower energy (i.e., near its k-edge of 33.3 keV) and much lower attenuation at higher keV, producing a nonlinear exponential curve with a steeper slope at lower keV. Recent research suggests that enhancing structures demonstrate sharply upward-sloping curves at lower

keV, that mimic iodine's curve, whereas nonenhancing structures have a flatter curve at lower keV, similar to the expected slope of water's curve [12, 50, 51].

With respect to hypovascular liver lesions, the application of DECT for evaluation is evolving. A preliminary study that examined hypovascular liver lesion conspicuity by comparing blended 80/140 kVp data with pure 80 kVp lower energy acquisition failed to illustrate improved detection [52]. However, when hypovascular lesions are detected, DECT may be more helpful than SECT for characterization, particularly of incidental subcentimeter hypoattenuating liver lesions generally deemed too small to characterize. These lesions are presumably benign in asymptomatic patients; however, in patients undergoing oncological evaluation, even such small lesions may be of concern. Additional MR or multiphasic CT imaging increases cost and radiation dose (i.e., in the case of CT), as well as patient and physician unrest until a diagnosis is achieved. In a preliminary study, DECT showed increased sensitivity and specificity compared with conventional CT for differentiating small enhancing masses from cysts with the use of water (virtual unenhanced) and iodine (iodine map) basis pair displays, with spectral HU curve analysis adding further confidence in the characterization of lesions deemed indeterminate on basis pair displays [12, 53] (Fig. 20.4).

Another potential use for the iodine density display is for evaluation of macroscopic portal vein thrombus. Utilizing a threshold iodine density of 11.4 *100 μg/mL*, Qian et al. achieved nearly 92 % specificity in differentiating bland from neoplastic thrombus on portal venous phase DECT [54].

20.4 Urinary

Clinicians are often burdened with follow-up examination(s) to exclude malignant neoplasms when renal lesions are incidentally detected [55, 56]. Although results usually reveal benign cystic lesions, up to 5.5 % are cancerous [57] and 61 % of these cancerous lesions are detected incidentally [55].

Several well-established SECT criteria classify incidentally encountered renal lesions as benign, including attenuation on true unenhanced scan equivalent to water (<20) and lack of enhancement (difference <20 HUs from true unenhanced to enhanced venous phase) [15, 58–61]; however, artifacts such as quantum mottle, beam hardening, and volume averaging have resulted in pseudoenhancement that makes accurate attenuation measurement (HU) less reliable on SECT [62, 63]. In addition, even with multiple phases on SECT (i.e., unenhanced, venous, excretory), accurate evaluation of true enhancement within smaller lesions can be problematic.

HU attenuation on SECT is calibrated with reference to water and depicted in pixels assigned shades of gray. This scheme makes it possible for different materials (e.g., iodinated contrast material, calcium, hemorrhage) to have overlapping HU values on SECT. On the other hand, DECT allocates shades of gray to each pixel by the specific material density (e.g., mg/mL), which may more accurately discriminate different materials [4, 6, 7, 11, 12].

With DECT, material density images are typically reconstructed in pairs, such as water and iodine. The identification and exclusion of iodine-containing pixels from DECT raw data allow construction of the water basis pair (VNC) display, which has the potential to be substituted for the true unenhanced SECT series [64, 65]. Like true unenhanced images, water basis pair images can facilitate diagnosis. For example, the fluid attenuation of benign simple cysts appears hypodense on both true and virtual unenhanced displays. In addition, both displays can be used in the evaluation for solid mass enhancement, as preliminary studies have shown no statistically significant difference in attenuation values between true unenhanced SECT and water basis pair DECT images [15, 66, 67]. For the iodine basis pair, vendor-specific post-processing algorithms facilitates the use of extracted iodine-containing pixels from DECT raw data to generate this display, which looks and functions similar to a subtraction image for MRI [10, 12]. For exam-

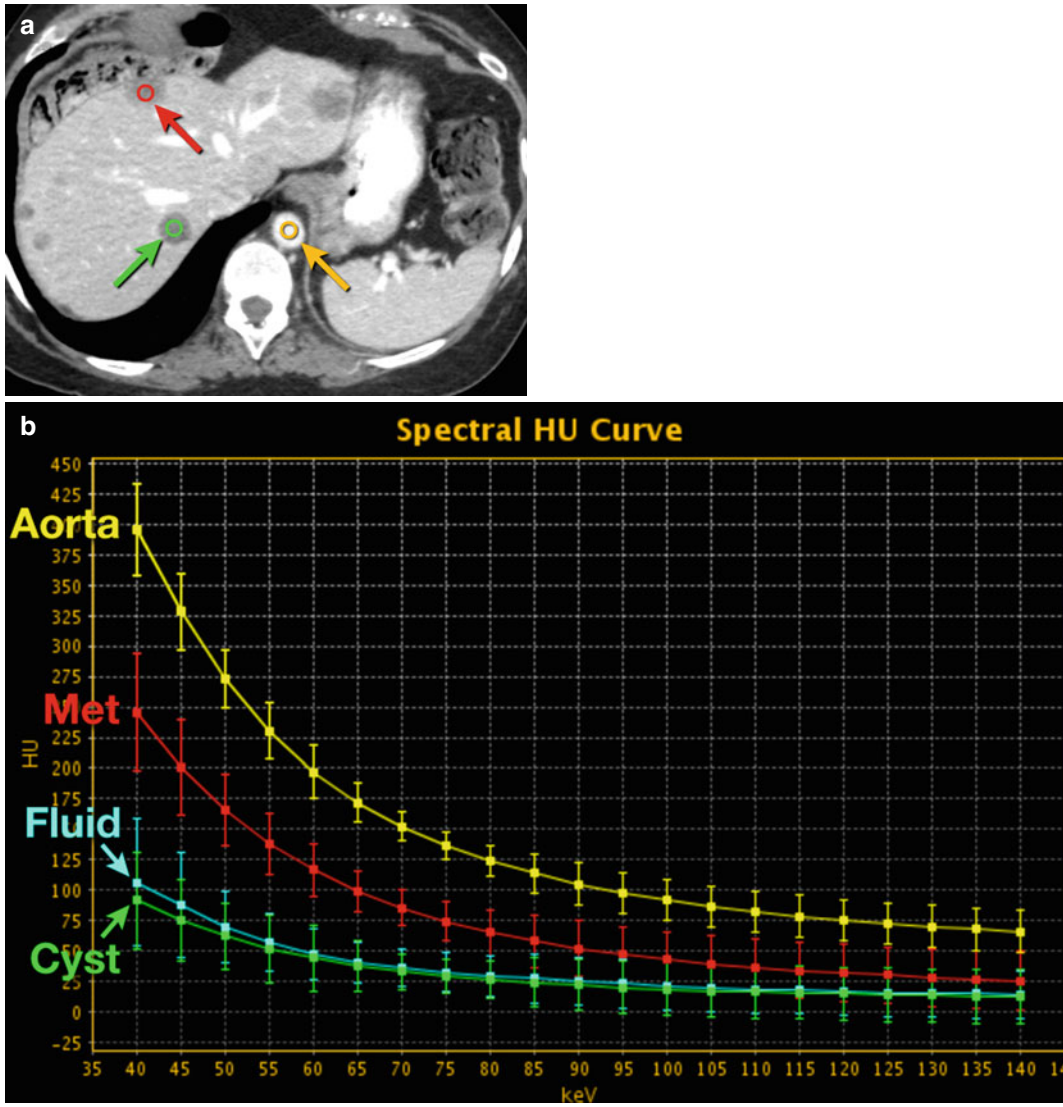

Fig. 20.4 Hepatic cyst and metastasis. (**a**) DECT 70 keV monochromatic image shows multiple hypodense hepatic masses, including two outlined as ROI (*red* and *green circles*). *Yellow circle* indicates aorta. (**b**) DECT spectral HU plot of the two lesions (*red* and *green curves*), the aorta (*yellow curve*) and fluid from gallbladder (*blue curve*; ROI not shown on **a**). Note that the more posterior hepatic lesion, a cyst, has curve attenuation morphology similar to that of nonenhancing fluid, whereas the more anterior lesion, a metastasis (Met), has curve attenuation morphology more in line with that of contrast-enhanced fluid in the aorta

ple, a nonenhancing renal lesion (e.g., a simple cyst) does not contain iodine and appears dark on iodine basis pair images, whereas iodine-enhancing structures (e.g., renal parenchyma) are depicted with various shades of gray, depending on the amount of iodine. Yet a material with a similar attenuation curve (e.g., calcium) will also be depicted on the iodine display, thus comparison with the water basis pair image is necessary for accurate characterization [12].

DECT can thus improve characterization of smaller renal lesions previously considered indeterminate. For example, improved material specificity along with advanced post-processing displays can identify diverse tissue elements within a renal angiomyolipoma (Fig. 20.5).

Other various renal masses (simple cyst, hyperdense nonenhancing cyst, and solid enhancing mass) have a characteristic pattern on water and iodine material density basis pair displays [12, 58, 66]. A simple cyst will appear dark on both displays, whereas a hemorrhagic cyst will appear bright on the first (water) display and dark on the second (iodine). On water basis pair images, a solid mass will appear isodense to hyperdense compared with adjacent solid renal parenchyma, but enhancement with IV iodine contrast will make it brighter than either a simple or a hyperdense cyst on iodine material density basis pair images. Furthermore, supplementary post-processing, such as the addition of color overlay on iodine basis pair display,

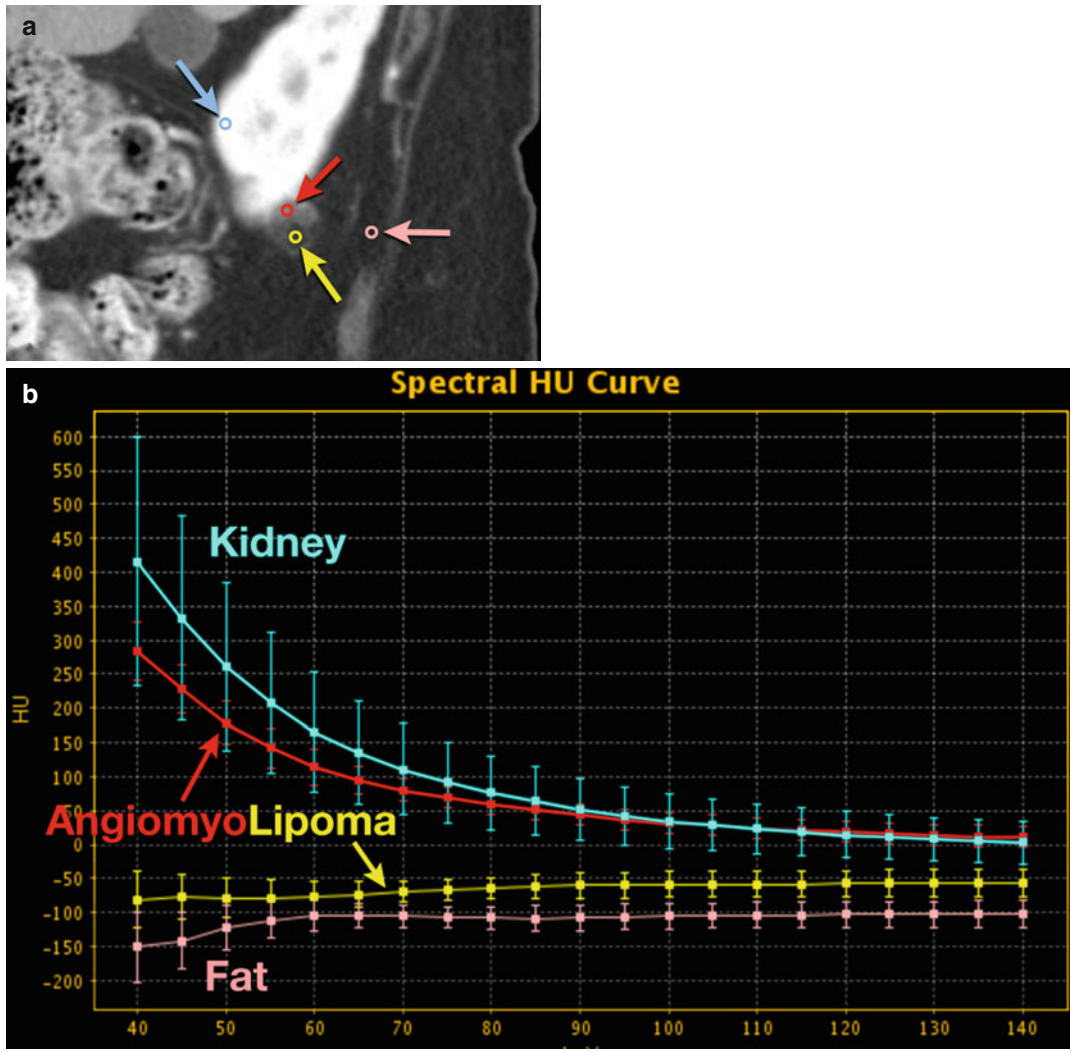

Fig. 20.5 Angiomyolipoma. (**a**) DECT 70 keV monochromatic sagittal image shows a complex right lower pole renal mass with enhancing smooth muscle/vessel (*red circle* and *arrow*) and fat attenuation (*yellow circle* and *arrow*). Additional ROIs performed as internal reference for enhancement (*blue circle* and *arrow*; renal parenchyma) and fat (*pink circle* and *arrow*; adjacent soft tissue fat). (**b**) DECT spectral HU plot also shows that the lesion has enhancing components (*red curve*) that mirror enhancing renal parenchyma (*blue curve*), as well as fat components (*yellow curve*) that closely mimic retroperitoneal fat (*rose curve*). (**c**) Histogram analysis verifies that fat components of the lesion (*yellow bars*) are in the range of retroperitoneal fat (*pink bars*) (i.e., negative HU values)

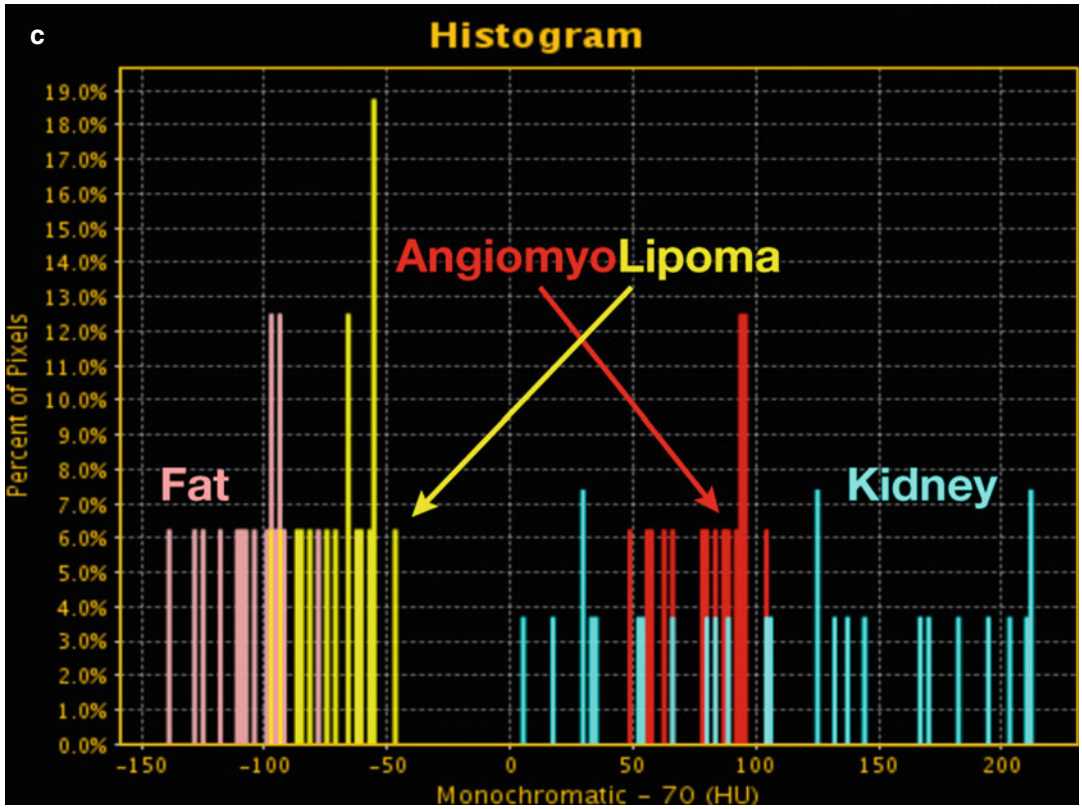

Fig. 20.5 (continued)

can improve visual differentiation of enhancing from nonenhancing structures by assigning color hues. For example, an enhancing, iodine-containing lesion could be displayed with a color ranging from brown to gold, which would help facilitate differentiation from nonenhancing, non-iodine-containing masses such as simple or hemorrhagic cysts, or even pseudoenhancement artifact (Fig. 20.6). In a study comparing SECT with DECT for differentiating enhancing from nonenhancing renal masses, DECT had higher composite sensitivity and specificity than SECT (95 and 93 % vs. 67 and 46 %, respectively), with individual reader confidence rated higher for DECT than SECT image displays [50]. In addition, spectral HU curves can be processed using a workstation to visually illustrate the different attenuation characteristics of iodine (i.e., enhancing masses) vs. non-iodine-containing lesions (i.e., avascular masses), facilitating diagnosis [12, 68] (Fig. 20.4). Iodine can also be used quantitatively as an image biomarker for enhancement in renal lesions [68]. It can be detected and its density obtained from iodine basis pair DECT images, which have had excellent congruence with true iodine amount in a phantom evaluation [69]. In an in vivo study comparing SECT HU vs. DECT *100 μg/mL*, a threshold discrimination of 20 showed an improvement in sensitivity for differentiating cyst from enhancing renal masses from 27 to 95 %, respectively [70].

DECT may also be useful in evaluating urothelial tumors in single-phase examinations. Twelve of fourteen pathologically proven tumors were detected with a CT urography protocol that included an all-in-one approach [71]. The single-phase examination provided synchronous nephrographic and excretory-phase images with administration of 600 mL water orally, 2 boluses (split bolus) of IV contrast material separated by a 7-min delay and scanning at 110 s after the second bolus. Although the superiority of the split bolus protocol has been previously demonstrated [72],

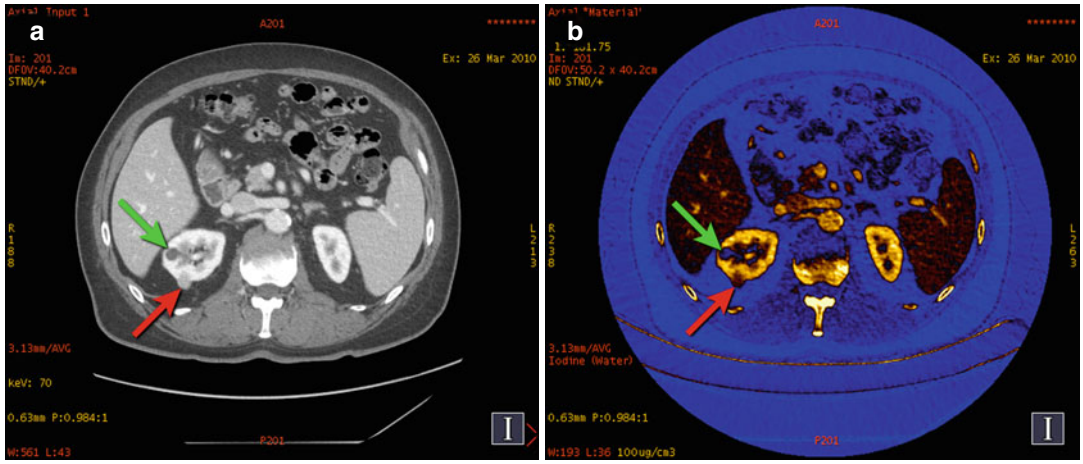

Fig. 20.6 Renal cyst and cancer. (**a**) DECT 70 keV monochromatic image shows two right renal lesions with 24 HU (*green arrow*) and 97 HU (*red arrow*) values. (**b**) Iodine material density image, with color overlay depicting iodine-containing pixels in brown to gold hues, shows that the posterior lesion (*red arrow*) contains iodine and is therefore an enhancing mass (i.e., histologically proven renal cell cancer). The more anterior lesion (*green arrow*) does not contain iodine (i.e., avascular), and thus its >20 HU value in part (**a**) is related to pseudoenhancement artifact

Avanti et al. were the first to combine this technique with single-phase DECT urography, which provided a radiation dose savings of up to 45 % by performing the examination in a single acquisition. This approach was quite sensitive, but failed to detect small lesions (<5 mm) in the urinary bladder. Overall, Ascenti et al. showed sensitivity, specificity, positive predictive value, and negative predictive value in detecting urothelial tumors of 85.7, 98.6, 92.3, and 97.1 %, respectively [71].

20.5 Adrenal Glands

An adrenal nodule is incidentally encountered on 4 % of SECT examinations [73]. Regrettably, when an initial SECT study reveals an indeterminate adrenal lesion, characterization often necessitates another examination, such as adrenal protocol CT or MR imaging. In many cases, nonenhanced or single enhanced-phase DECT could answer the clinical query: adenoma or nonadenoma.

Parameters to differentiate adenoma (or other benign lesion) from metastasis are well documented for SECT [15, 74, 75]. When a lesion has HU ≤10 on conventional unenhanced SECT images, it is consistent with a benign lipid rich adenoma (71 % sensitivity; 98 % specificity [76]. Analogously, with the same HU ≤10 threshold value used with dsDECT VNC images constructed from a single portal venous phase, adrenal lesions of any size can be characterized with 79 % sensitivity, 95 % specificity, and 86 % accuracy) [73]. Furthermore, for adrenal lesions ≥1 cm diameter, single enhanced-phase dsDECT facilitates correct classification 91–95 % of the time compared with true unenhanced images as the reference standard [73]. In a study by Ho et al. [77], no malignant adrenal nodule was misclassified on VNC images.

Investigations have also been performed to evaluate differential low vs. high-energy attenuation to distinguish adrenal lesions, but DECT results have been mixed [15, 78]. Although some adenomas have lower attenuation values at 80 kVp than at 140 kVp, this pattern is not uniformly observed; therefore, the technique is specific but not sensitive. It has been postulated that the variability in attenuation may relate to different quantities of intracellular lipid.

Furthermore, Gupta et al. [78] described novel ways to identify lipid-containing adrenal adenomas. One method evaluated the mean change in attenuation of an adrenal lesion between acquisition energies at 140 and 80 kVp. Despite overlap in the attenuation change for adenomas and metastatic lesions, the change for adenomas at 0.4±7.1 HU

was smaller than that for metastatic lesions, at 9.2±4.3 HU. Another method involved identifying a decrease in the density of an adrenal lesion from 140 to 80 kVp as an indicator of lipid, because it mimicked subcutaneous fat behavior at these two energies. This method obtained 100 % sensitivity and 100 % positive predictive value but only 50 % sensitivity, which indicates that it should be applied as an adjunct to noncontrast evaluation at 140 kVp. Specifically, if a nodule had attenuation >10 HU at 140 kVp, then the attenuation of the nodule should also be assessed at 80 kVp to try to characterize it with the data in hand. Again, no malignant nodule was misclassified, with all such lesions increasing in CT number from lower to higher energy.

20.6 Pancreas

Pancreatic adenocarcinoma is the fourth leading cause of cancer-related mortality in the United States [79], with dismal 5-year survival rates of 1.8–23 %, depending on the extent of disease [80]. Newer chemotherapy regimens are improving these statistics and increasing the necessity for follow-up imaging to monitor treatment response.

Pancreatic adenocarcinoma can appear extremely subtle on CT, but it is typically hypodense at contrast-emhanced pancreatic parenchymal phase images due to fibrosis and desmoplasia [66]. For optimal detection of this subtle neoplasm, 2-phase enhanced SECT (e.g., pancreatic about 40 s; portal venous about 70 s) is generally performed. However, up to 10 % of these neoplasms remain isoattenuating to normal surrounding parenchyma, even during the pancreatic phase when the parenchyma has the greatest enhancement [15, 66, 81–84, 86]. Thus, to facilitate diagnosis, current investigations focus on making pancreatic neoplasms more noticeable on imaging.

In a recent pilot study, dsDECT was used to investigate whether it increased the conspicuity of pancreatic adenocarcinoma [84]. Significant attenuation differences improved the distinction between tumor and normal parenchyma at 80 kVp than at blended 80/120 kVp images, because inherent contrast between tissues is more evident at lower acquisition energies due to differences in the presence of iodine [85]. Using ssDECT to exploit greater iodine contrast resolution on images at low keV provides superior divergence in attenuation of pancreatic lesions than normal parenchymal tissue [12]. These so-called computed monochromatic display images can increase conspicuity of solid organ parenchymal masses (Fig. 20.3), including hypodense pancreatic masses, despite the attendant increase in noise at lower energy.

Enhancing pancreatic parenchyma can be discriminated from acute hemorrhage on DECT water basis pair (virtual unenhanced) display because only the hemorrhage remains hyperdense [10], obviating the need for an additional unenhanced acquisition. Furthermore, this technique is useful for evaluating the extent of hypervascular tumors, such as neuroendocrine or renal cell carcinoma metastases. Iodine basis pair (iodine map) images from ssDECT can help accentuate hypovascular (adenocarcinoma) and hypervascular (islet cell) masses, whereas effective-z images can better delineate their heterogeneity (Fig. 20.7).

On SECT, tumor viability (i.e., vascularity) can be inferred by measuring the attenuation of the mass. Yet, these attenuation measurements can be inaccurate due to pseudoenhancement artifact, and they can be confounded by various materials such as high-density blood products, protein, or calcification [87]. With accurate assessment of tumor viability essential for guiding therapy, particularly with newer targeted chemotherapeutic agents, ^{18}FDG-PET CT is increasingly being used to assess the metabolic activity of pancreatic cancer [88, 89].

However, ^{18}FDG-PET CT is an expensive imaging study, complicated by longer acquisition times, misregistration issues, and relatively less spatial resolution. DECT is therefore an attractive alternative imaging option, because it is fast and relatively inexpensive. DECT acquisition time is <1 min, whereas ^{18}FDG-PET CT can require up to 120 min, with the cost differential between the two examinations up to two to five times greater for ^{18}FDG-PET CT. A preliminary study retrospectively correlating PET standardized uptake value (SUV) with SECT and DECT imaging biomarkers for pancreatic cancer showed by multivariate analysis that DECT had up to 99.9 % correlation (R^2) [90]. In addition, the DECT model appeared to be preferable because of its

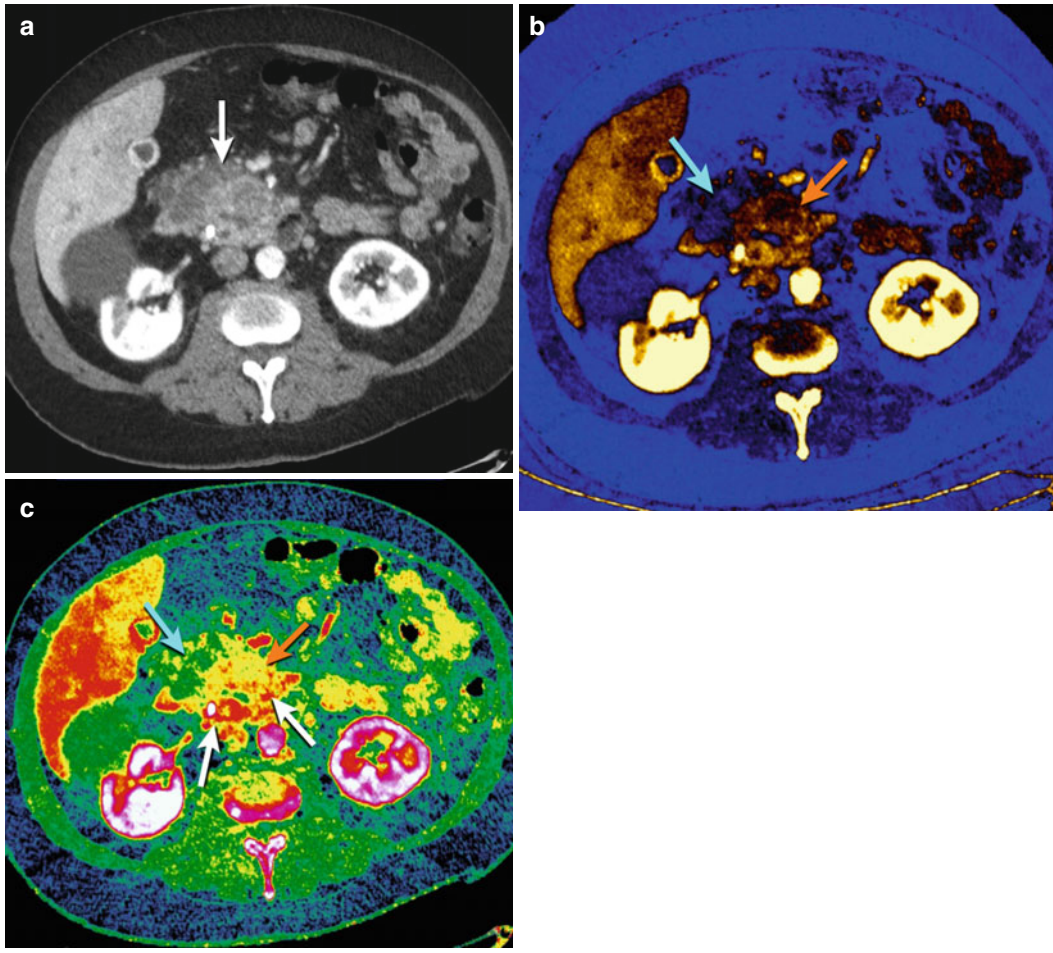

Fig. 20.7 Pancreas ductal adenocarcinoma. (**a**) DECT 70 keV monochromatic axial image shows heterogeneous enlargement of the pancreatic head (*white arrow*) due to an underlying carcinoma. (**b**) DECT iodine basis pair image with color overlay allows for evaluation of tumor perfusion, better differentiating more vascular areas (*orange arrow*) from necrotic areas (*blue arrow*) than would conventional CT. (**c**) DECT effective-z image with color overlay, based on the underlying material's atomic number, gives new insight into the considerable heterogeneity of these tumors (*blue arrow*, *orange arrow*, and *red arrows*)

applicability for predicting future correlation with PET SUV (96 % vs. 64 %) [R^2 predicted], respectively). Thus, it may be feasible for DECT to supplant or become an adjuvant to ^{18}FDG-PET CT.

A not-infrequent pitfall for CT imaging of pancreatic pathology is fatty change, which can be diffuse or focal. Focal cases may be misinterpreted as ductal adenocarcinoma at SECT, compelling follow-up imaging for further characterization, such as chemical shift MR [10]. Hence, ssDECT water basis pair (virtual unenhanced) display may resolve the issue. The area in question would not be isodense to solid pancreatic parenchyma as expected with solid malignancy but would have similar density to adjacent fat.

20.7 Bowel

CT enterography is progressively replacing traditional small-bowel follow-through fluoroscopic examinations because of its robust image quality and performance. When optimally performed using neutral oral contrast to distend the small bowel along with rapid IV contrast bolus, CT enterography has been shown to be more sensitive than

capsule endoscopy for detection of small-bowel masses [85, 91–93]. However, a potential limitation of CTE is the detection of hypoenhancing and nonenhancing masses, which can be better visualized as a filling defect with positive intraluminal oral contrast. Disappointingly, positive luminal contrast can obscure hyperenhancing polyps and bowel mucosa. In this regard, IV contrast-enhanced DECT enterography with oral bismuth contrast may have promise for concurrent detection of hyperenhancing, hypoenhancing, and nonenhancing small-bowel polyps [91] (Fig. 20.8).

CT colonography is a noninvasive, effective option for colorectal cancer screening [94]. A standard protocol requires complete bowel cleansing and fecal/fluid tagging (oral iodinated contrast) before the examination, which is acquired with the patient in supine and prone positions. In a preliminary study with IV contrast enhancement, water (VNC) and iodine basis pair images were obtained to differentiate enhancing polyps from stool [95, 96]. The results suggested that DECT colonography may be technically feasible in a single acquisition, obviating the need for prone images [96], with resultant decreased radiation dose. Furthermore, noncathartic or reduced-catharsis DECT colonoscopy may be possible. Following fecal tagging, electronic "spectral cleansing" is performed by post-processing software to remove iodine-containing material, including tagged residual fecal material [97].

20.8 Tumor Treatment Response

In this new era of targeted therapeutic agents, accurate response assessment remains challenging with conventional imaging and current response evaluation criteria in solid tumors (RECIST) (Fig. 20.9) [98]. For gastrointestinal stromal tumor (GIST) treatment follow-up, a new imaging criteria [99] to evaluate tumor response on SECT was needed because, paradoxically, treated GISTs could increase in size, undermining RECIST criteria and complicating management [99, 100]. Also, a tumor responding positively to treatment can develop foci of necrosis and/or myxoid degeneration [100], resulting in an increase instead of the expected decrease in lesion attenuation [99]. Although an improvement over standard RECIST, Choi's criteria can inaccurately assess response when increased attenuation (HU) is the result of intratumoral hemorrhage [101, 102]. In these cases, DECT can provide a more reliable follow-up examination, since the iodine basis pair display permits selective quantification of iodine and is not affected by hemorrhage [100, 103]. This was validated in another study showing that progressive lesions had significantly higher iodine-related attenuation on dsDECT iodine basis pair images, compared with that of stable or regressive metastatic liver lesions, indicating a poor response to therapy [100]. Thus, compared to SECT, DECT can more robustly assess treatment response in GIST [100] and can better predict overall survival [103].

For nonsurgical patients, or those awaiting liver transplantation, various strategies exist to treat a discovered hepatocellular carcinoma. These include surgical wedge resection, thermal ablation (microwave and radiofrequency), and intra-arterially directed therapies (transcatheter arterial chemoembolization and drug-eluting bead); all of which require follow-up imaging to ensure that no residual or recurrent viable tumor is present. The ability of DECT to produce material-specific images, along with additional post-processing tools to aid visual evaluation, offers a potentially more accurate response assessment than conventional SECT (Fig. 20.10). Furthermore, since the amount of IV-administered iodine contrast depends on vascularity, the iodine content within a tumor, as measured from the DECT iodine basis display, is a potential surrogate for estimation of perfusion and viability (Fig. 20.11) [10, 104]. The use of DECT to quantify iodine as a corollary to vascularity also improves assessment of recurrent or residual tumor after ablation of renal [69, 104, 105] and hepatic [106] masses.

20.9 Pitfalls and Limitations of DECT

Standardized window/level settings for iodine basis pair images with color overlay have not been established. These values can be manipulated to

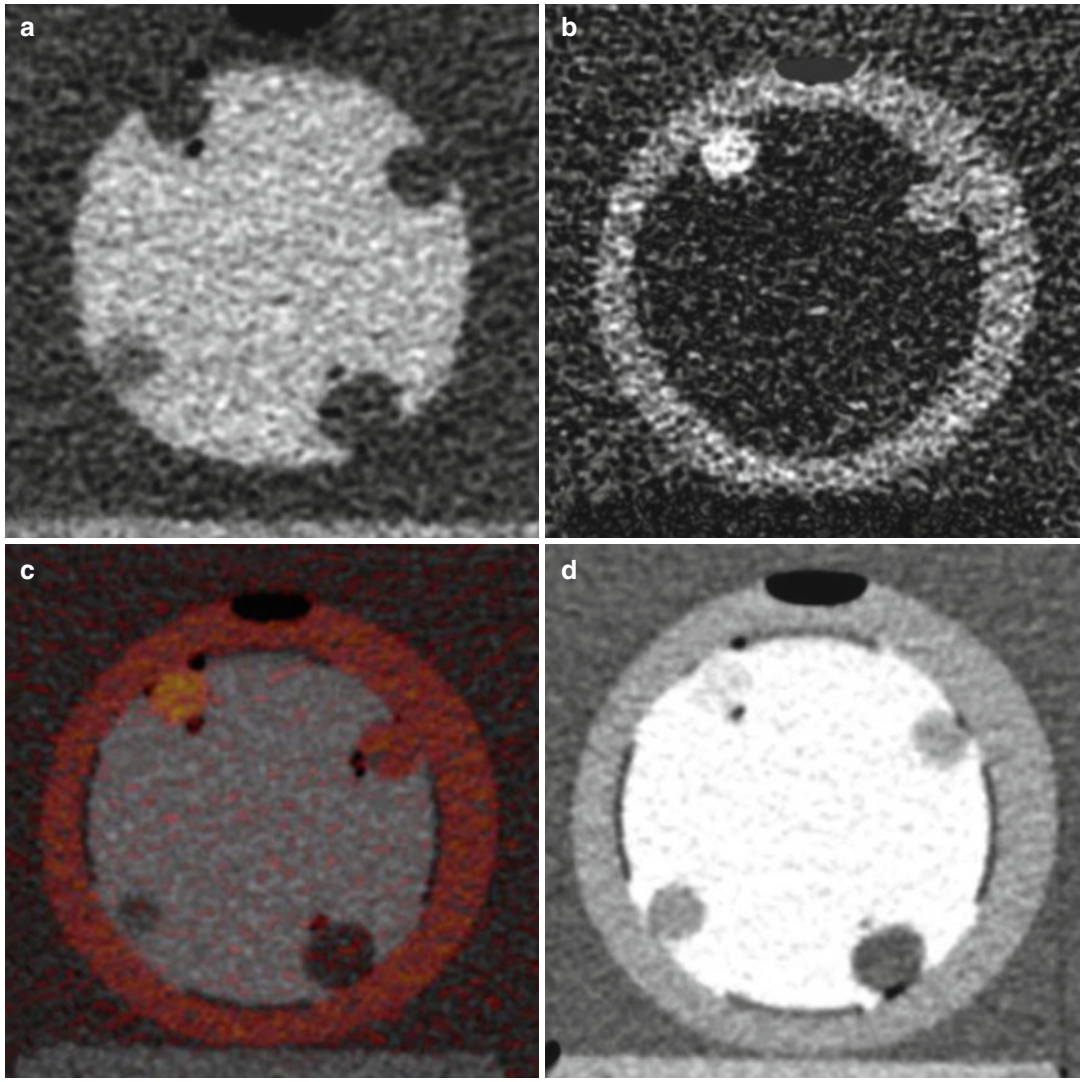

Fig. 20.8 Four different display techniques. (**a**) Bismuth-only image with iodine subtraction showing bowel lumen; (**b**) iodine-only image with bismuth subtraction showing bowel wall; (**c**) iodine-overlay image with color overlay of iodine signal superimposed on iodine image; and (**d**) mixed-kilovoltage image with a 0.5-linear blend of low-kilovoltage and high-kilovoltage images showing routine CT appearance, with both positive enteric contrast and iodine-containing bowel wall and polyps. The "polyps" are latex balloons filled with 6-mg/mL iodine (*upper left*), 3-mg/mL iodine (*upper right*), water (*bottom right*), and tissue equivalent material ball (*bottom left*) (Reprinted with permission from Qu et al. [91])

erroneously make a cyst appear to contain iodine (i.e., enhanced) or to make an enhancing mass appear avascular (Fig. 20.12). Because of the subjectivity of window/level settings, the use of spectral HU curve morphology (Fig. 20.4) or direct iodine quantification (Fig. 20.11) may be a more objective means of distinguishing enhancing from nonenhancing masses.

Additional potential limitations to the qualitative interpretation of the iodine basis pair image include calcium and iodine-containing therapy [12]. Because the mean attenuation curve of calcium falls between those of water and iodine, it is depicted on both types of density images. Thus, when only iodine material density images are reviewed, calcification may be misinterpreted as

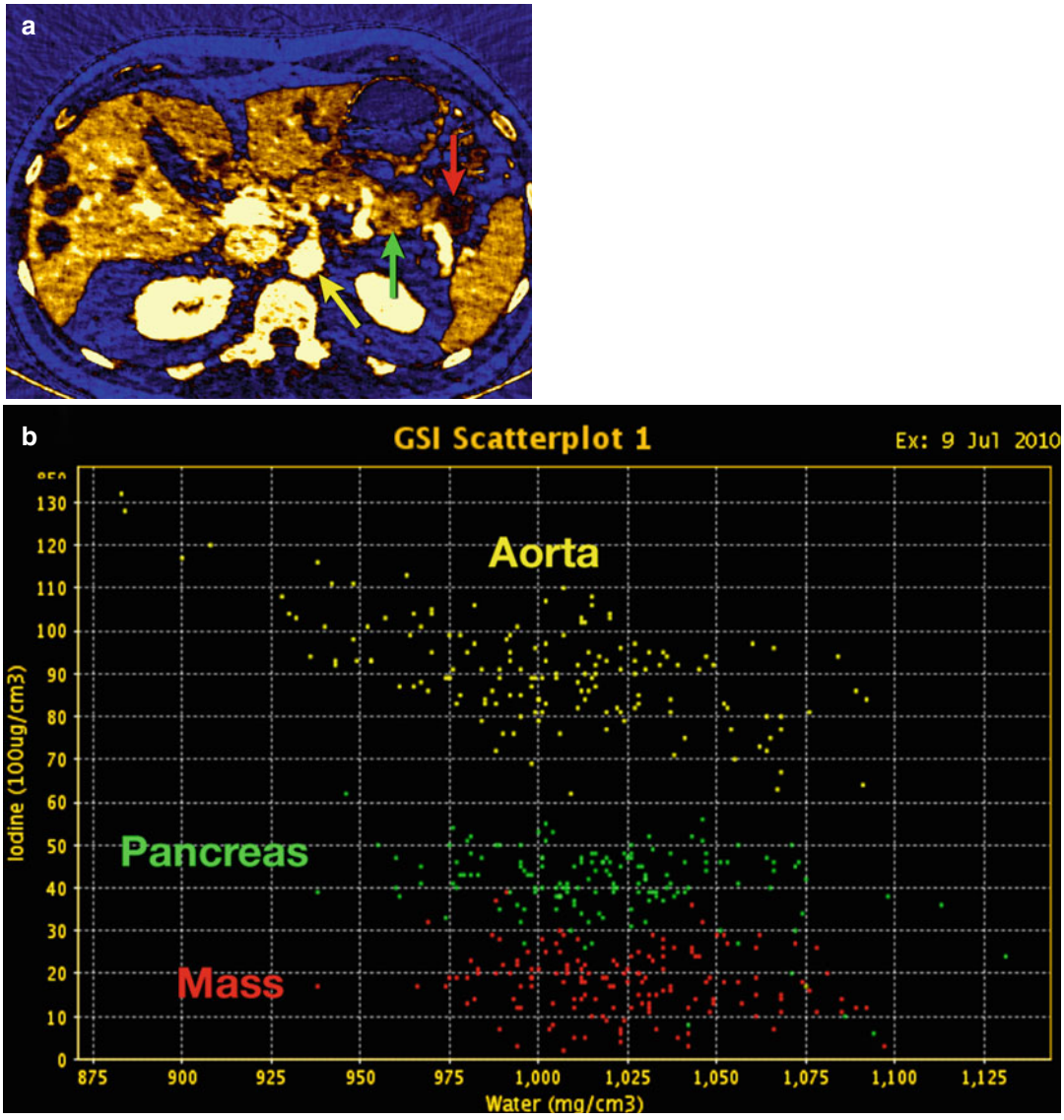

Fig. 20.9 Pancreatic adenocarcinoma with negative response to chemotherapy incorrectly assessed by RECIST. (**a**) Pretreatment DECT iodine material density image shows hypoenhancing pancreatic tail carcinoma (*red arrow*). *Green* and *yellow arrows* indicate placement of additional ROIs to generate scatterplot and spectral HU curves. (**b**) DECT scatterplot shows pixels for hypovascular carcinoma (*red dots*) with predominantly lower iodine concentration than those for normal pancreatic parenchyma (*green dots*). (**c**) DECT spectral HU plot shows pancreatic cancer curve (*red*) below and with a flatter upslope at lower keV than that of normal pancreas curve (*green*). (**d**) Posttreatment DECT iodine material density image shows a decrease in tumor size, which erroneously suggests a positive response to therapy per RECIST. (**e**) However, posttreatment DECT scatterplot shows pancreas cancer pixels (*red dots*) with relatively increased iodine concentration compared to that obtained pretreatment (**b**) and with greater overlap with normal pancreas pixels (*green dots*). (**f**) Posttreatment DECT spectral HU plot likewise shows relatively increased upslope at lower keV of the pancreas cancer curve (*red*) compared to that obtained pretreatment (**c**), now more closely mirroring the normal pancreas parenchyma curve (*green*). These findings are compatible with increased tumor perfusion and viability despite the tumor's decreased size. The patient had contemporaneous PET-CT scans (not shown), which also showed an increase from baseline SUV (4.3) to posttreatment follow-up SUV (6.7)

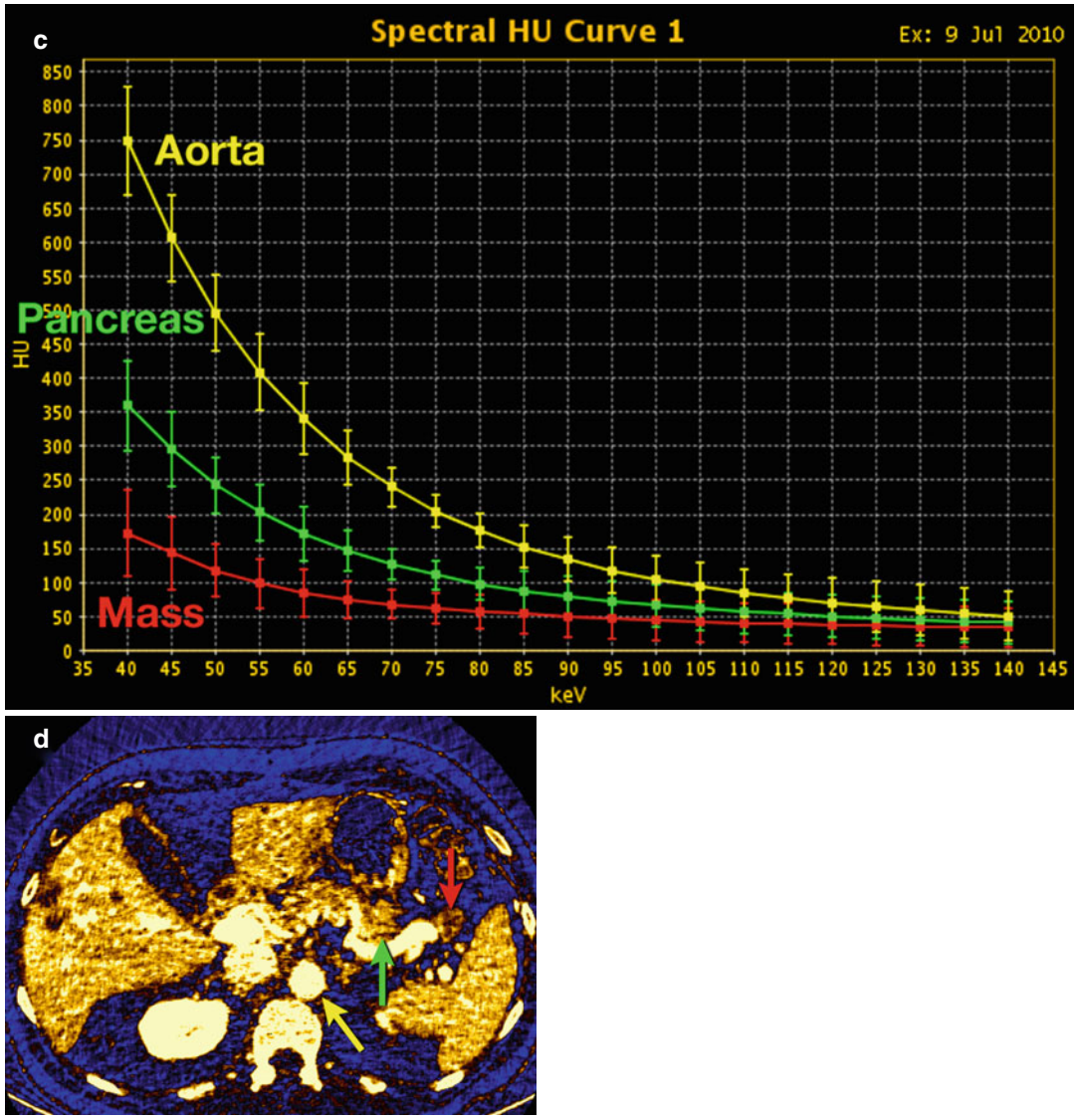

Fig. 20.9 (continued)

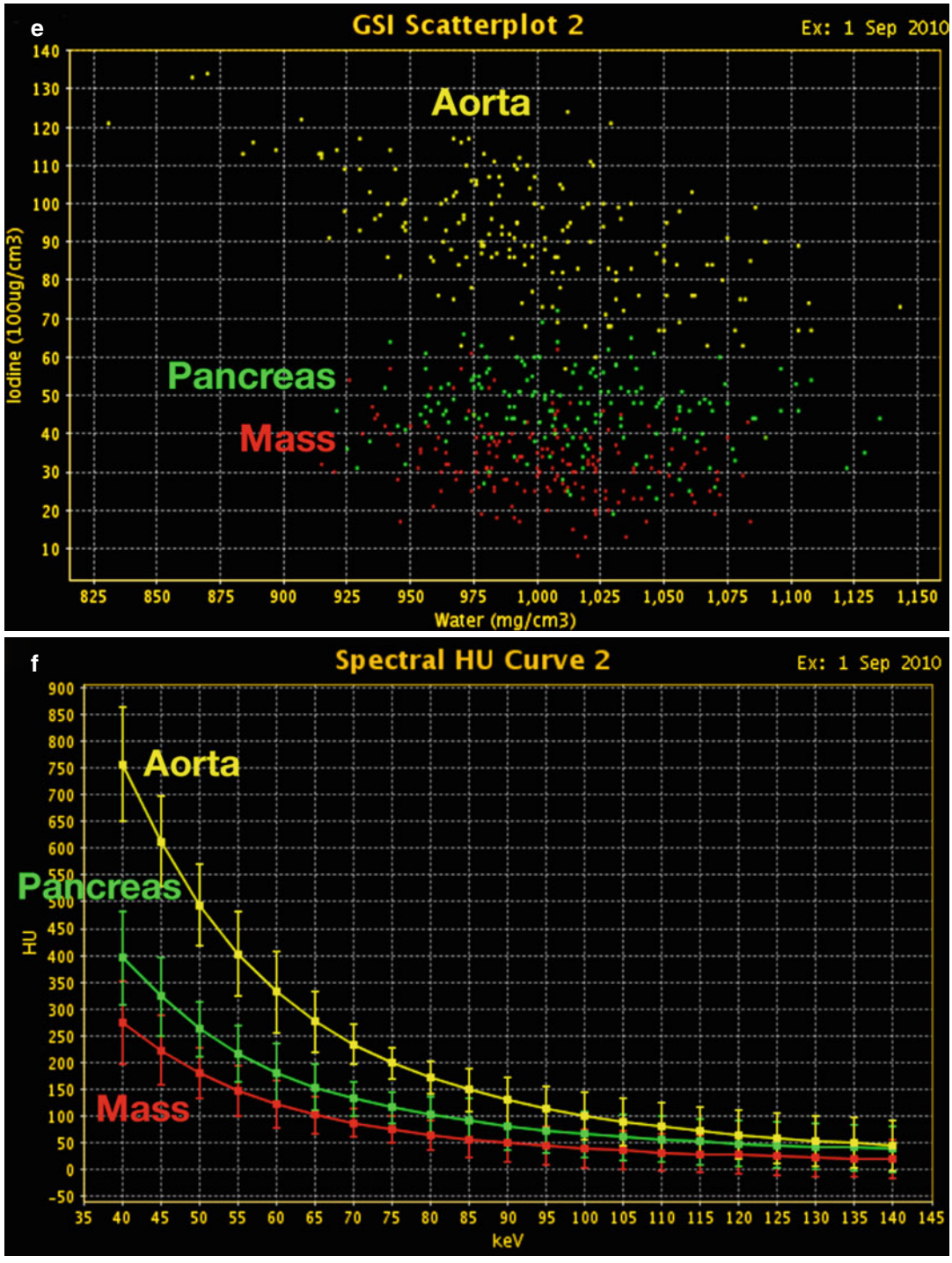

Fig. 20.9 (continued)

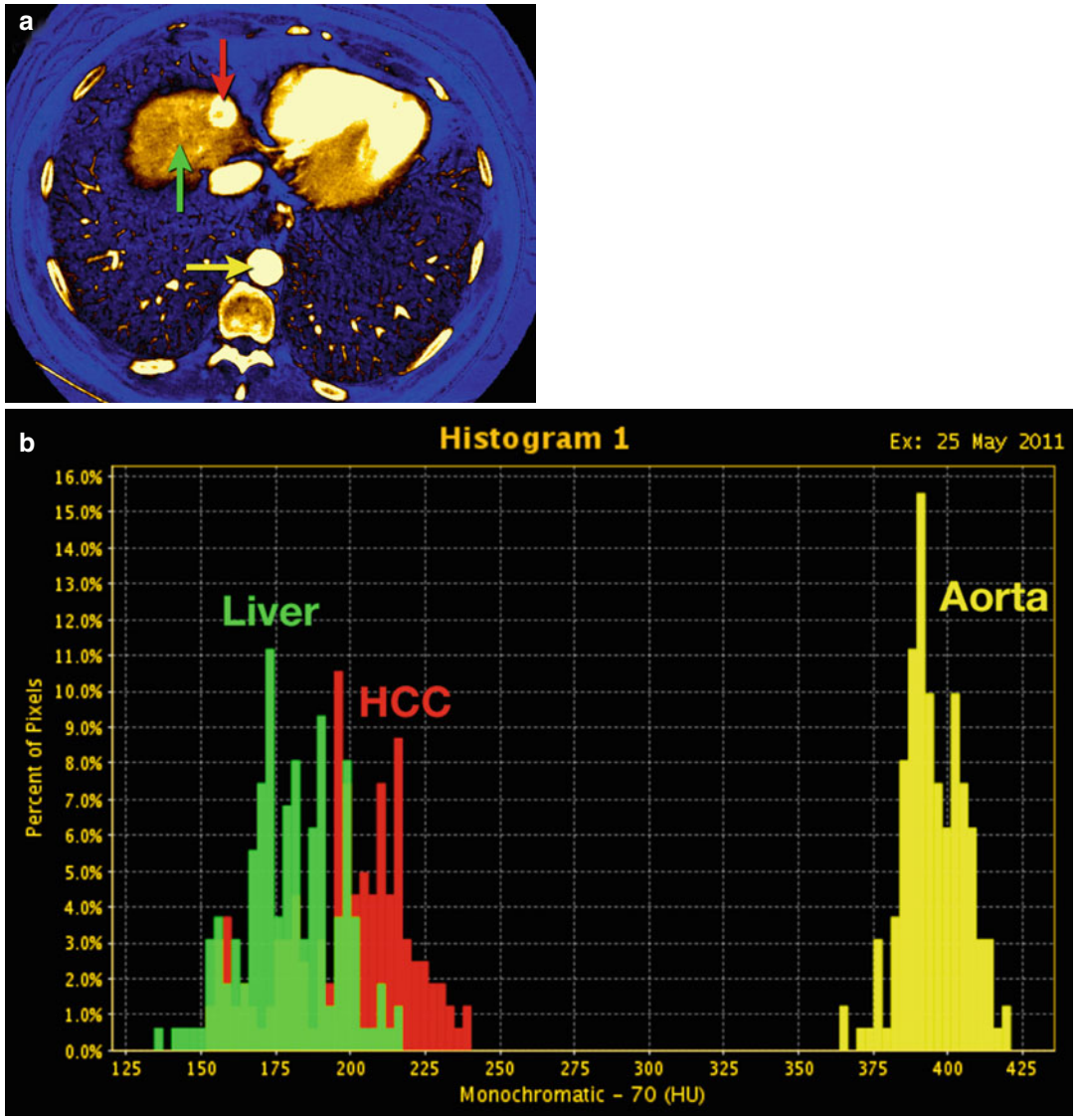

Fig. 20.10 HCC: positive response to drug-eluting bead therapy. (**a**) Pretreatment DECT iodine material density image shows a hypervascular HCC (*red arrow*) that was validated on explant histologic analysis. *Green* and *yellow arrows* indicate additional ROIs placed to generate DECT histograms and spectral HU plot. (**b**) DECT histogram shows overlap of HCC pixels (*red bars*) with normal liver pixels (*green bars*), but the mean for HCC is higher (i.e., farther to right) than that for the liver at baseline (*green bars*). (**c**) DECT spectral HU plot shows HCC curve (*red*) above normal liver curve (*green*) and with steeper upslope at lower keV, which indicates greater iodine concentration/perfusion than the adjacent liver. (**d**) Posttreatment DECT iodine material density image shows tumor (*red arrow*) has not changed in size but appears more heterogeneous. (**e**) Posttreatment DECT histogram shows mean values for HCC pixels (*red bars*) lower (i.e., farther to left) than those for normal liver (*green bars*), which indicates a positive response to therapy. (**f**) Posttreatment DECT spectral HU plot likewise shows that HCC curve (*red*) now below normal liver curve (*green*) and with a relatively flatter upslope at lower keV, which is again a positive response

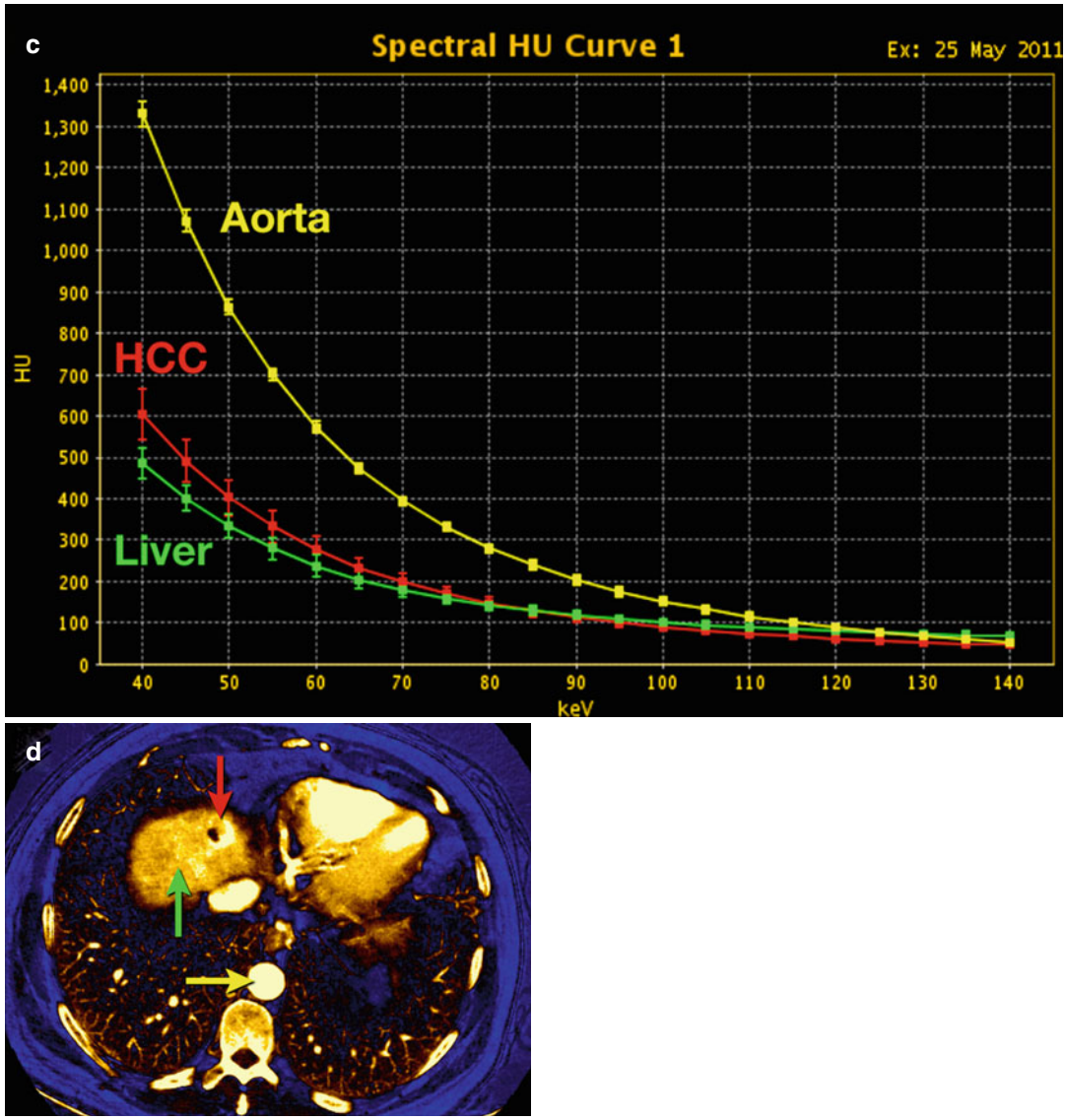

Fig. 20.10 (continued)

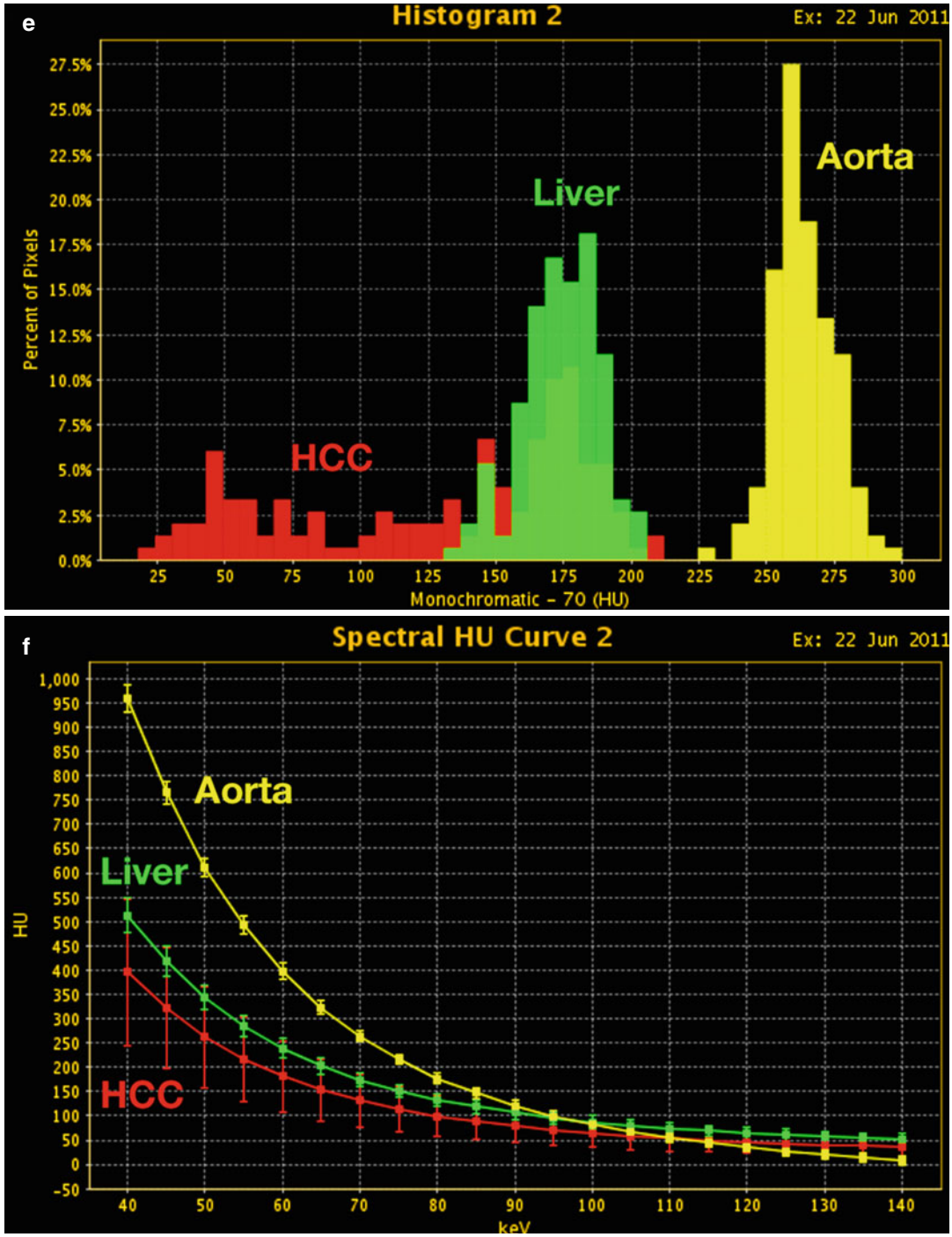

Fig. 20.10 (continued)

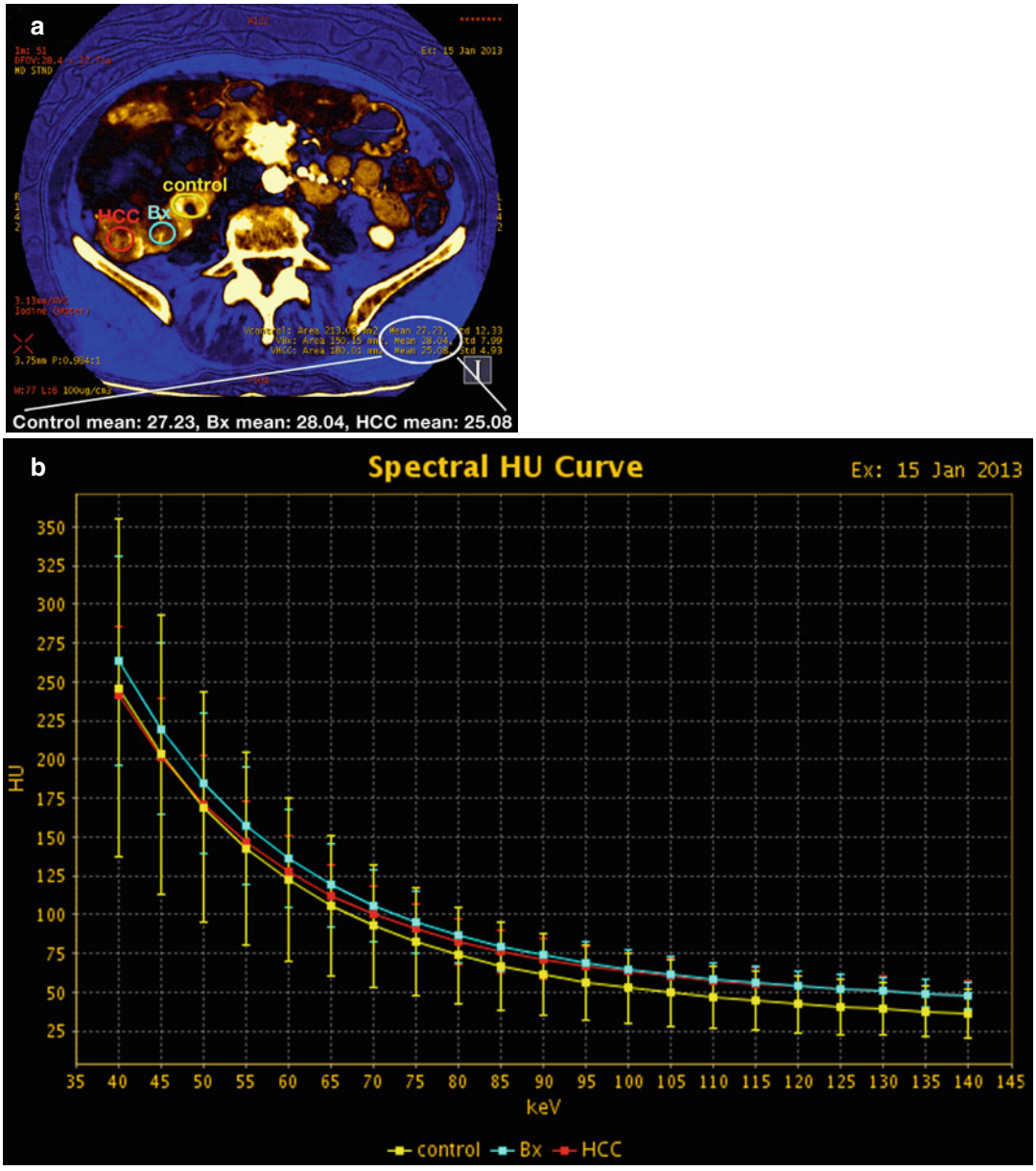

Fig. 20.11 HCC evaluation with direct iodine quantification. (**a**) Pretreatment DECT iodine material density image shows recurrent HCC along posterior margin of previously embolized large HCC. It has three lobulated components ("HCC," "Bx," and "control"), with mean iodine concentrations of 25, 28, and 27 *100 μg*/mL, respectively (*white circle*). (**b**) DECT spectral HU plot shows that all three regions have similar attenuation curve morphology at baseline imaging. (**c**) Posttreatment DECT iodine material density image after direct injection of an investigational therapeutic agent to the most lateral lesion (HCC) shows overall similar size compared to baseline for all three regions, but has a conspicuous change in iodine concentration that is a postulated surrogate for tumor viability. Both the directly treated (HCC) and immediately adjacent regions (Bx) show considerably decreased mean iodine concentration, whereas the furthest region (control), presumably too far to be affected by therapy, conversely has an increased mean iodine concentration (*white circle*). (**d**) Posttreatment DECT spectral HU plot (**b**) confirms the variable response of the three individual regions

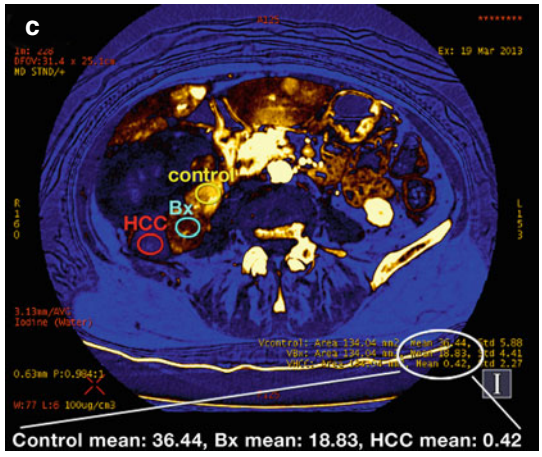

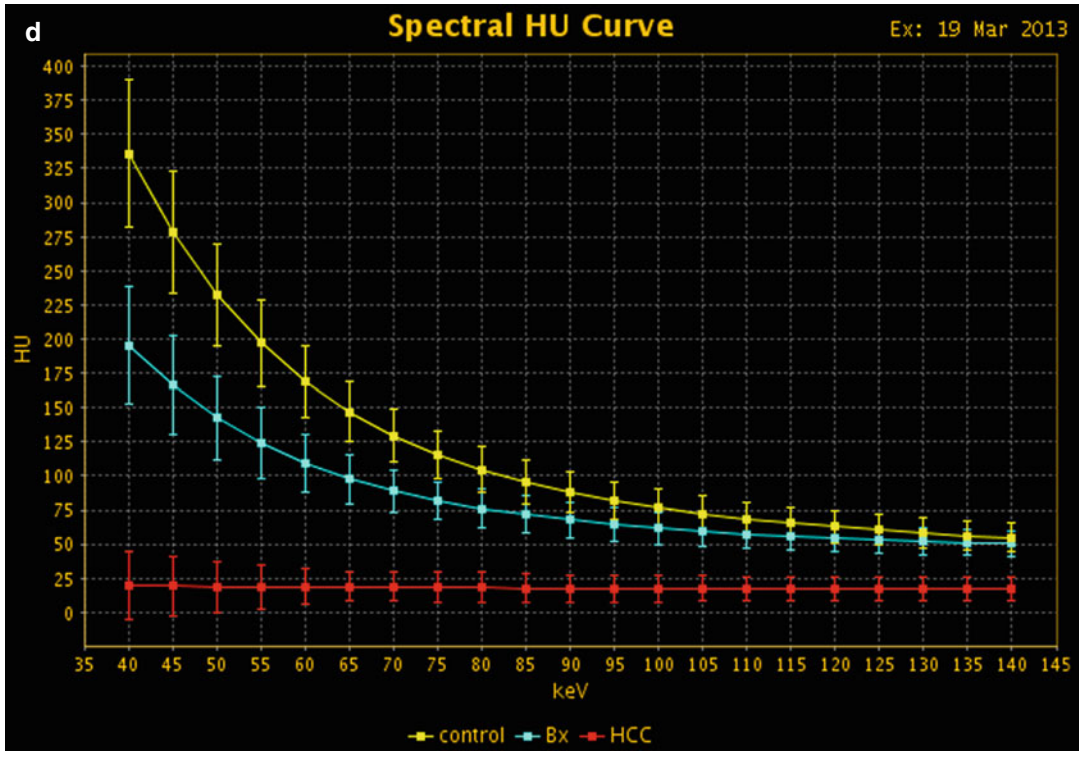

Fig. 20.11 (continued)

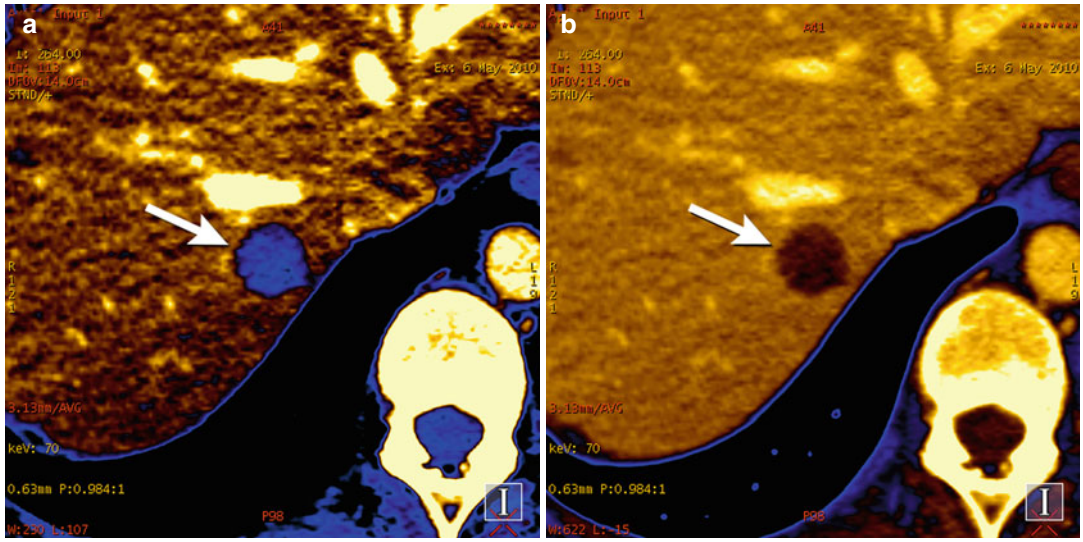

Fig. 20.12 Pitfall. Lack of standardized window/level settings can be problematic for DECT iodine material density images with color overlay. When adjusted toward more extreme settings, the image for this right lobe hepatic cyst (**a**, *red arrow*) can be made artificially to appear to enhance (**b**, *red arrow*). The subjectivity of window and leveling may result in the spectral attenuation curve and direct iodine quantification being more objective means of distinguishing enhancing hepatic masses from cysts

enhancement. The radiologist should therefore interpret water and iodine material density displays concurrently. Iodine is also present in the ethiodized oil/chemotherapeutic agent admixture used in transarterial chemoembolization (TACE) for treatment of hepatic cancer. Thus, apparent findings of focal hepatic enhancement on iodine material density images in treated patients may not indicate a recurrent tumor.

With respect to the water basis pair (virtual unenhanced) series, further validation is required before its routine clinical implementation for quantitative evaluation. For example, inconsistent adrenal adenoma characterization during water basis pair (virtual unenhanced) imaging compared with a true nonenhanced acquisition emphasizes that definitive studies have not yet shown reproducibility [11, 14].

As DECT technology evolves, its technical aspects should improve over time. Potential areas that might benefit from such improvements include image noise reduction, separation of material spectra, partial volume effects, and automated quantitative analysis [12].

Conclusion

Although many applications are still under investigation, DECT shows great promise for augmenting the role of CT in clinical imaging. The added benefit of dual energy exploits the differences in tissue behavior and materials at different energies to allow improved lesion detection and characterization and reduction in radiation dose. For oncological imaging in particular, DECT is at the cusp of a fundamental conceptual change in the evaluation of CT images, with great potential for more accurate tumor staging and assessment of treatment response.

References

1. Kelcz F, et al. Noise considerations in dual energy CT scanning. Med Phys. 1979;6(5):418–25.
2. Takai M, Kaneko M. Discrimination between thorotrast and iodine contrast medium by means of dual-energy CT scanning. Phys Med Biol. 1984;29(8):959–67. 1050 July-August 2010 radiographics.rsna.org.
3. Rutherford RA, et al. Measurement of effective atomic number and electron density using an EMI scanner. Neuroradiology. 1976;11(1):15–21.
4. Rutherford RA, et al. X-ray energies for effective atomic number determination. Neuroradiology. 1976;11(1):23–8.
5. Millner MR, et al. Extraction of information from CT scans at different energies. Med Phys. 1979; 6(1):70–1.
6. Genant HK, Boyd D. Quantitative bone mineral analysis using dual energy computed tomography. Invest Radiol. 1977;12(6):545–51.
7. Goldberg HI, et al. Noninvasive quantitation of liver iron in dogs with hemochromatosis using dual-energy CT scanning. Invest Radiol. 1982;17(4):375–80.
8. Cann CE, et al. Quantification of calcium in solitary pulmonary nodules using single- and dual-energy CT. Radiology. 1982;145(2):493–6.
9. Chiro GD, et al. Tissue signatures with dual-energy computed tomography. Radiology. 1979;131(2): 521–3.
10. Del Gaizo AJ, et al. Utility of dual energy computed tomography in abdominal imaging. Appl Radiol. 2013. [in press, Epub 2013 Nov].
11. Yeh BM, et al. Dual-energy and low-kVp CT in the abdomen. AJR Am J Roentgenol. 2009;193(1): 47–54.
12. Silva AC, et al. Dual-energy (spectral) CT: applications in abdominal imaging. Radiographics. 2011; 31(4):1031–46.
13. Hidas G, et al. Determination of renal stone composition with dual-energy CT: in vivo analysis and comparison with x-ray diffraction. Radiology. 2010; 257(2):394–401.
14. Macari M, et al. Invited commentary of dual-energy multidetector CT: how does it work, what can it tell us, and when can we use it in abdominopelvic imaging? Radiographics. 2010;30(4):1052–5.
15. Coursey CA, et al. Dual-energy multidetector CT: how does it work, what can it tell us, and when can we use it in abdominopelvic imaging? Radiographics. 2010;30(4):1037–51.
16. Vlahos I, et al. Dual-energy computed tomography imaging of the aorta. J Thorac Imaging. 2010; 25(4):289–300.
17. Mileto A, et al. Pancreatic dual-source dual-energy CT: is it time to discard unenhanced imaging? Clin Radiol. 2012;67(4):334–9. Epub 2011 Nov 16.
18. Blake MA. Invited commentary of dual-energy (spectral) CT: applications in abdominal imaging. Radiographics. 2011;31(4):1047–50.
19. Paul J, et al. Dual-source 128-slice MDCT neck: radiation dose and image quality estimation of three different protocols. Eur J Radiol. 2013;82(5):787–96. pii: S0720-048X(12)00569-4.
20. Hwang HJ, et al. Radiation dose reduction of chest CT with iterative reconstruction in image space – part I: studies on image quality using dual source CT. Korean J Radiol. 2012;13(6):711–9. Epub 2012 Oct 12.
21. Schenzle JC, et al. Dual energy CT of the chest: how about the dose? Invest Radiol. 2010;45(6): 347–53.
22. Bauer RW, et al. Dose and image quality at CT pulmonary angiography-comparison of first and second generation dual-energy CT and 64-slice CT. Eur Radiol. 2011;21(10):2139–47. Epub 2011 May 27.
23. Kalender WA, et al. Evaluation of a prototype dual-energy computed tomographic apparatus. I. Phantom studies. Med Phys. 1986;13(3):334–9.
24. Ascenti G, et al. Dual-energy computed tomography (DECT) in renal masses: nonlinear versus linear blending. Acad Radiol. 2012;19(10):1186–93. Epub 2012 Jul 18.
25. Holmes 3rd DR, et al. Evaluation of non-linear blending in dual-energy computed tomography. Eur J Radiol. 2008;68:409–13.
26. Chae EJ, et al. Clinical utility of dual-energy CT in the evaluation of solitary pulmonary nodules: initial experience. Radiology. 2008;249:671–81.
27. Swensen SJ, et al. Solitary pulmonary nodule: CT evaluation of enhancement with iodinated contrast material—a preliminary report. Radiology. 1992; 182:343–7.
28. Swensen SJ, et al. Pulmonary nodules: CT evaluation of enhancement with iodinated contrast material. Radiology. 1995;194:393–8.
29. Yamashita K, et al. Solitary pulmonary nodule: preliminary study of evaluation with incremental dynamic CT. Radiology. 1995;194:399–405.
30. Swensen SJ, et al. Lung nodule enhancement at CT: prospective findings. Radiology. 1996;201:447–55.
31. Zhang M, Kono M. Solitary pulmonary nodules: evaluation of blood flow patterns with dynamic CT. Radiology. 1997;205:471–8.
32. Swensen SJ, et al. Lung nodule enhancement at CT: multicenter study. Radiology. 2000;214:73–80.
33. Jeong YJ, et al. Solitary pulmonary nodule: characterization with combined wash-in and washout features at dynamic multi-detector row CT. Radiology. 2005;237:675–83.
34. Orlacchio A, et al. Solitary pulmonary nodules: morphological and metabolic characterisation by FDG-PET-MDCT. Radiol Med. 2007;112:157–73.
35. Higashi K, et al. Value of whole-body FDG PET in management of lung cancer. Ann Nucl Med. 2003;17:1–14.
36. Eschmann SM, et al. Is standardised (18)F-FDG uptake value an outcome predictor in patients with stage III non-small cell lung cancer? Eur J Nucl Med Mol Imaging. 2006;33:263–9.
37. Higashi K, et al. 18 F-FDG uptake as a biologic prognostic factor for recurrence in patients with surgically resected non-small cell lung cancer. J Nucl Med. 2002;43:39–45.

38. Jeong HJ, et al. Usefulness of whole-body (18) F-FDG PET in patients with suspected metastatic brain tumors. J Nucl Med. 2002;43:1432–7.
39. Pandit N, et al. Prognostic value of [18 F]FDG-PET imaging in small cell lung cancer. Eur J Nucl Med Mol Imaging. 2003;30:78–84.
40. Vansteenkiste JF, Mortelmans LA. FDG-PET in the locoregional lymph node staging of non-small cell lung cancer. A comprehensive review of the Leuven lung cancer group experience. Clin Positron Imaging. 1999;2:223–31.
41. Downey RJ, et al. Preoperative F-18 fluorodeoxyglucose-positron emission tomography maximal standardized uptake value predicts survival after lung cancer resection. J Clin Oncol. 2004; 22:3255–60.
42. Schmid-Bindert G, et al. Functional imaging of lung cancer using dual energy CT: how does iodine related attenuation correlate with standardized uptake value of 18FDG-PET-CT? Eur Radiol. 2012; 22(1):93–103. Epub 2011 Aug 7.
43. Schindera ST, et al. Hypervascular liver tumors: low tube voltage, high tube current multi-detector row CT for enhanced detection—phantom study. Radiology. 2008;246:125–32.
44. Marin D, et al. Hypervascular liver tumors: low tube voltage, high tube current multidetector CT during late hepatic arterial phase for detection—initial clinical experience. Radiology. 2009;251(3):771–9.
45. Yanaga Y, et al. Hepatocellular carcinoma in patients weighing 70 kg or less: initial trial of compact-bolus dynamic CT with low-dose contrast material at 80 kVp. AJR Am J Roentgenol. 2011;196(6):1324–31.
46. Altenbernd J, et al. Dual-energy-CT of hypervascular liver lesions in patients with HCC: investigation of image quality and sensitivity. Eur J Radiol. 2011;21:738–43.
47. Kim KS, et al. Image fusion in dual energy computed tomography for detection of hypervascular liver hepatocellular carcinoma: phantom and preliminary studies. Invest Radiol. 2010;45:149–57.
48. Lv P, et al. Spectral CT in patients with small HCC: investigation of image quality and diagnostic accuracy. Eur Radiol. 2012;22(10):2117–24. Epub 2012 May 23.
49. Yu Y, et al. Hepatocellular carcinoma and focal nodular hyperplasia of the liver: differentiation with CT spectral imaging. Eur Radiol. 2013;23(6):1660–8. PMID: 23306709.
50. Silva AC, et al. Differentiating enhancing vs nonenhancing lesions in the liver and k: comparison of single- and dual-energy CT. In: Radiological Society of North American 96th Scientific Assembly and annual meeting, Chicago, Nov 2011.
51. Silva AC, et al. Quantitative imaging with source dual energy CT (ssDECT): potential applications and how we do it. In: Radiological Society of North American 96th Scientific Assembly and annual meeting, Chicago, Nov 2011.
52. Robinson E, et al. Dual source dual energy MDCT. Comparison of 80 kVp and weighted average 120 kVp data for conspicuity of hypo-vascular liver metastases. Invest Radiol. 2010;45:413–8.
53. Gosalia R, et al. Assessment of liver lesions using single source dual energy CT. In: American Roentgen Ray Society 111th annual meeting, Chicago, May 2011.
54. Qian LJ, et al. Differentiation of neoplastic from bland macroscopic portal vein thrombi using dual-energy spectral CT imaging: a pilot study. Eur Radiol. 2012;22(10):2178–85. Epub 2012 May 24.
55. Berlin LL, The ACR. Strategy for managing incidental findings on abdominal CT. Radiol Clin North Am. 2011;49:237–43.
56. O'Connor SD, et al. Incidental finding of renal masses at unenhanced CT: prevalence and analysis of features for guiding management. AJR Am J Roentgenol. 2011;197:139–45.
57. Parienty RA, et al. Cystic renal cancers: CT characteristics. Radiology. 1984;157:741–4.
58. McClennan BL, et al. CT of the renal cyst: is cyst aspiration necessary? AJR Am J Roentgenol. 1979; 133(4):671–5.
59. Bosniak MA. The use of the bosniak classification system for renal cysts and cystic tumors. J Urol. 1997;157:1852–3.
60. Kaza RK, et al. Distinguishing enhancing from nonenhancing renal lesions with fast kilovoltage-switching dual-energy CT. AJR. 2011;197:1375–81.
61. Isreal GM, Bosniak MA. An update of the bosniak renal cyst classification system. Urology. 2005;66:484–8.
62. Isreal GM, Bosniak MA. Pitfalls in renal mass evaluation and how to avoid them. Radiographics. 2008; 28:1325–38.
63. Bae KT, et al. Renal cysts: is attenuation artifactually increased on contrast enhanced CT images? Radiology. 2000;216:792–6.
64. Scheffel H, et al. Dual-energy contrast-enhanced computed tomography for the detection of urinary stone disease. Invest Radiol. 2007;42(12):823–9.
65. Takahashi N, et al. Dual-energy CT iodine-subtraction virtual unenhanced technique to detect urinary stones in an iodine-filled collecting system: a phantom study. AJR Am J Roentgenol. 2008;190(5):1169–73.
66. Graser A, et al. Dual-energy CT in patients suspected of having renal masses: can virtual nonenhanced images replace true nonenhanced images? Radiology. 2009;252:433–40.
67. Graser A, et al. Single phase DECT allows for characterization of renal masses as benign or malignant. Invest Radiol. 2010;45(7):399–405.
68. Stiles WZ, et al. A novel approach: characterization of renal lesions with dual energy CT. In: American Roentgen Ray Society 113th annual meeting, Washington, DC, Apr 2013.
69. Chandarana H, et al. Iodine quantification with dual-energy CT: phantom study and preliminary experience with renal masses. AJR Am J Roentgenol. 2011;196:W693–700.
70. Bollepalli SD, et al. ssDECT: assessment of renal lesion enhancement with direct iodine quantifica-

tion. In: Abdominal Radiology Course, Scottsdale, Mar 2012.
71. Ascenti G, et al. Single phase dual energy CT urography in the evaluation of haematuria. Clin Radiol. 2013;68(2):e87–94. http://dx.doi.org/10.1016/j.crad.2012.11.001.
72. Takeuchi M, et al. Split-bolus CT-urography using dual-energy CT: feasibility, image quality and dose reduction. Eur J Radiol. 2012;81:3160–5.
73. Gnannt R, et al. Dual-energy CT for characterization of the incidental adrenal mass: preliminary observations. AJR Am J Roentgenol. 2012;198(1):138–44.
74. Song JH, et al. The incidental adrenal mass on CT: prevalence of adrenal disease in 1,049 consecutive adrenal masses in patients with no known malignancy. AJR Am J Roentgenol. 2008;190(5):1163–8.
75. Boland GW, et al. Characterization of adrenal masses using unenhanced CT: an analysis of the CT literature. AJR Am J Roentgenol. 1998;171(1):201–4.
76. Lee MJ, et al. Benign and malignant adrenal masses: CT distinction with attenuation coefficients, size, and observer analysis. Radiology. 1991;179:415–8.
77. Ho LM, et al. Characterization of adrenal nodules with dual-energy CT: can virtual unenhanced attenuation values replace true unenhanced attenuation values? AJR Am J Roentgenol. 2012;198(4):840–5.
78. Gupta RT, et al. Dual-energy CT for characterization of adrenal nodules: initial experience. AJR Am J Roentgenol. 2010;194:1479–83.
79. Conlon KC, et al. Long-term survival after curative resection for pancreatic ductal adenocarcinoma clinicopathologic analysis of 5-year survivors. Ann Surg. 1996;223:273–9.
80. Howlader N, et al. SEER cancer statistics review, 1975–2009. National Cancer Institute cancer statistics review. 2012. Available at http://seer.cancer.gov/csr/1975_2009_pops09/. Accessed 1 Mar 2013.
81. Lu DS, et al. Two-phase helical CT for pancreatic tumors: pancreatic versus hepatic phase enhancement of tumor, pancreas, and vascular structures. Radiology. 1996;199(3):697–701.
82. Boland GW, et al. Pancreatic-phase versus portal vein–phase helical CT of the pancreas: optimal temporal window for evaluation of pancreatic adenocarcinoma. AJR Am J Roentgenol. 1999;172(3):605–8.
83. Prokesch RW, et al. Isoattenuating pancreatic adenocarcinoma at multi–detector row CT: secondary signs. Radiology. 2002;224(3):764–8.
84. Macari M, et al. Dual source dual-energy MDCT of pancreatic adenocarcinoma: initial observations with data generated at 80 kVp and at simulated weighted-average 120 kVp. AJR Am J Roentgenol. 2010;194:W27–32.
85. Graser A, et al. Dual energy CT: preliminary observations and potential clinical applications in the abdomen. Eur Radiol. 2009;19(1):13–23. Epub 2008 Aug 2. Review.
86. Ichikawa T, et al. MDCT of pancreatic adenocarcinoma: optimal imaging phases and multiplanar reformatted imaging. AJR Am J Roentgenol. 2006;187:1513–20.
87. Tkaczyk JE, et al. Quantization of liver tissue in fast-switched dual kVp computed tomography using linear discriminant analysis. In: Samei E, Hsieh J, editors. Proceedings of SPIE: medical imaging 2009—physics of medical imaging, vol. 7258. Bellingham: International Society for Optical Engineering; 2009.
88. Zimny M, et al. Fluorodeoxyglucose positron emission tomography and the prognosis of pancreatic carcinoma. Scand J Gastroenterol. 2000;35:883–8.
89. Bang S, et al. The clinical usefulness of 18-fluorodeoxyglucose positron emission tomography in the differential diagnosis, staging, and response evaluation after concurrent chemotherapy for pancreatic cancer. J Clin Gastroenterol. 2006;40:923–9.
90. Oldan J, et al. Correlation of PET SUV with single and dual energy CT imaging biomarkers. In: Radiological Society of North American 97th Scientific Assembly and annual meeting, Chicago, Nov 2012.
91. Qu M, et al. Toward biphasic computed tomography (CT) enteric contrast: material classification of luminal bismuth and mural iodine in a small-bowel phantom using dual-energy CT. J Comput Assist Tomogr. 2012;36(5):554–9.
92. Hakim FA, et al. CT enterography may identify small bowel tumors not detected by capsule endoscopy: eight years experience at Mayo Clinic Rochester. Dig Dis Sci. 2011;56:291r–9.
93. Huprich JE, et al. Prospective blinded comparison of wireless capsule endoscopy and multiphase CT enterography in obscure gastrointestinal bleeding. Radiology. 2011;260:744–51.
94. Johnson CD, et al. Accuracy of CT colonography for detection of large adenomas and cancers. N Engl J Med. 2008;359(12):1207–17.
95. Karcaaltincaba M, et al. Dual energy virtual CT colonoscopy with dual source computed tomography: initial experience. Rofo. 2009;181:859–62.
96. Karcaaltincaba M, Aktas A. Dual-energy CT revisited with multidetector CT: review of principles and clinical applications. Diagn Interv Radiol. 2011;17:181–94.
97. Eliahou R, et al. Dual-energy based spectral electronic cleansing in non-cathartic computed tomography colonography: an emerging novel technique. Semin Ultrasound CT MR. 2010;31:309–14.
98. De Cecco CN, et al. Dual-energy CT: oncologic applications. AJR Am J Roentgenol. 2012;199(5 Suppl):S98–105. Review.
99. Choi H, et al. Correlation of computed tomography and positron emission tomography in patients with metastatic gastro intestinal stromal tumor treated at a single institution with Imatinib mesylate: proposal of new computed tomography response criteria. J Clin Oncol. 2007;25:1753–9.
100. Apfaltrer P, et al. Contrast-enhanced dual energy CT of gastrointestinal stromal tumors. Invest Radiol. 2012;47:65–70.

101. Reichardt P, et al. Molecular response of gastrointestinal stromal tumour after treatment with tyrosine kinase inhibitor Imatinib mesylate. J Clin Pathol. 2004;57:215–7.
102. Hong X, et al. Gastrointestinal stromal tumor: role of CT in diagnosis and in response evaluation and surveillance after treatment with Imatinib. Radiographics. 2006;26:481–95.
103. Meyer M, et al. CT-based response assessment of advanced gastrointestinal stromal tumor: dual energy CT provides a more predictive imaging biomarker of clinical benefit than RECIST or Choi criteria. Eur J Radiol. 2013;82(6):923–8. pii: S0720-048X(13)00016-8.
104. Dai X, et al. Quantitative therapy response assessment by volumetric iodine-uptake measurement: initial experience in patients with advanced hepatocellular carcinoma treated with Sorafenib. Eur J Radiol. 2013;82(2):327–34. Epub 2012 Dec 12.
105. Davenport MS, et al. MRI and CT characteristics of successfully ablated renal mass: imaging surveillance after radiofrequency ablation. AJR Am J Roentgenol. 2009;192(6):171–8.
106. Lee SH, et al. DECT to assess tumor response to hepatic radiofrequency ablation. Invest Radiol. 2011;46:77–84.

US Elastography: Applications in Tumors

21

Richard G. Barr

Contents

R.G. Barr, MD, PhD, FACR, FSRU
Department of Radiology, Northeastern Ohio Medical College, Rootstown, OH, USA

Department of Radiology,
Surgical Hospital at Southwoods, 7630 Southern Blvd, Youngstown, OH 44512, USA
e-mail: rgbarr@zoominternet.net

Abbreviations

BPH	Benign prostatic hypertrophy
CEUS	Contrast-enhanced ultrasound
DRE	Digital rectal exam
FOV	Field of view
kPa	Kilopascals
M/s	Meters per second
MRS	Magnetic resonance spectroscopy
PC	Prostate cancer
PSA	Prostate-specific antigen
SE	Strain elastography
SWE	Shear wave imaging

21.1 Principals of Ultrasound Elastography

21.1.1 Introduction

Elastography is a new technique in ultrasound which can provide new clinically useful information which was previously not available. Elasticity imaging or elastography is an imaging modality based on tissue stiffness or hardness, rather than anatomy. Palpation has been used to evaluate for a malignancy for over a 1,000 years [1]. Ultrasound elastography can be considered as the imaging equivalent of palpation being able to quantify the stiffness of a lesion, which was previously judged only subjectively by physical exam.

There are two types of elastography: strain elastography (SE) and shear wave imaging (SWE) [2–4]. SE produces an image based on

A. Luna et al. (eds.), *Functional Imaging in Oncology*,
DOI 10.1007/978-3-642-40412-2_21, © Springer-Verlag Berlin Heidelberg 2014

how tissues respond to a displacement force from an external or patient source. This allows for a qualitative assessment of the lesion. SWE applies a special strong low-frequency "push pulse" that results in shear wave propagation that can be measured as a velocity. Because the speed of the shear wave through tissues is dependent on the stiffness of the tissue, a quantitative value of the stiffness can be obtained.

21.1.2 Strain Elastography

SE determines the relative strain or elasticity of tissue within a field of view (FOV) [2–4]. The more an object deforms when a force is applied, the higher the strain and the softer the lesion. To determine the strain of a tissue or lesion, one must evaluate how the lesion deforms when an external force is applied. For example, if we had an almond in a bowl of gelatin (Fig. 21.1) and pushed down on the gelatin, the gelatin would deform indicating it has high strain and is therefore soft. However, the almond would not deform having low strain and is therefore hard.

SE is performed on standard ultrasound equipment with software that evaluates the frame-to-frame differences in deformation in tissue when a force (stress) is applied. The force can be from patient movement, such as breathing, heartbeat, or external compression with rhythmic motion of the ultrasound transducer as the source of the movement [2–4]. In SE the absolute strain modulus value cannot be calculated because the amount of the push (force) cannot be accurately measured. The real-time SE image is displayed with a scale based on the relative strain of the tissues within the FOV.

The technique required to obtain the optimal images varies with the algorithm used by the manufacturer of the system [2–4]. For SE the amount of external displacement needed varies depending on the algorithm used. With some manufactures very little if any manual compression is needed; with others a rhythmic compression release cycle is required. With experience and practice the optimum compression technique to obtain optimal image quality can be learned.

The algorithm used in SE requires the strain changes remain within the imaging plane. The same slice of the lesion needs to remain in the imaging plane during the compression/release cycle. Monitoring of the B-mode image to confirm the lesion is only displaced in depth during scanning, and only moving in the field of view will allow for optimal images. With the displacement technique one cannot be surveying an organ, scanning must be done in one stationary position.

Results can be displayed in gray scale or with various color displays; preference is often

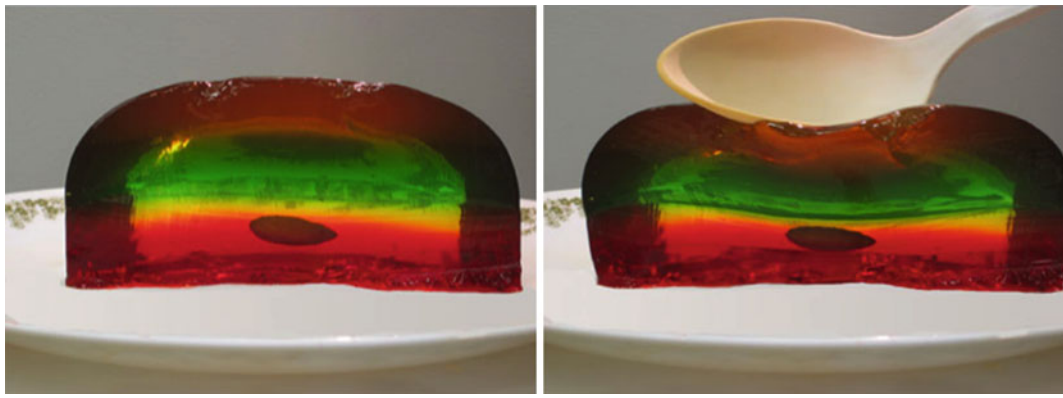

Fig. 21.1 Strain elastography can be explained simply by the following example. An almond is present within a bowl of gelatin. If we apply pressure with a spoon (strain), the gelatin changes shape because it has high strain (soft), while the almond remains unchanged because it has low strain (stiff). The algorithm used in strain elastography evaluates the frame-to-frame changes of tissue occurring when a compression/decompression force is applied. A gray-scale or color map is used to display the relative stiffness of the tissues in the FOV

determined by the user's exposure to elastography and preference in interpretation. In the gray-scale map, soft is coded white, while hard is coded black. It is important to remember that in SE a relative scale is displayed and should not be confused with shear wave imaging where an absolute stiffness value is obtained and color coded on a per pixel basis.

Because SE is a relative technique, a lesion may appear a different shade of gray (or color) depending on the other tissues in the field of view. For example, in a patient with normal dense breast tissue and fat, the fat will appear white (soft) as it is the softest tissue in the field of view. However, if only fat is in the field of view, some of the fat will appear black (hard) because it is the stiffest tissue in the field of view (Fig. 21.2). This can cause difficulty in interpretation. Therefore, a large FOV with multiple tissue types is helpful in image interpretation.

A critical factor in generating a diagnostic elastogram is the amount of pressure you apply when scanning [5]. This is called pre-compression. This is different than the amount of displacement used in generating the elastogram. Scanning with a "heavy hand" compresses the tissues and changes their elastic properties. This pre-compression markedly changes the image quality and can significantly affect results (Fig. 21.3). This is confirmed with SWE where the speed of the shear wave can change by a factor of 10 based on pre-compression. As pre-compression increases the differences in shear wave speed between tissues decrease leading to

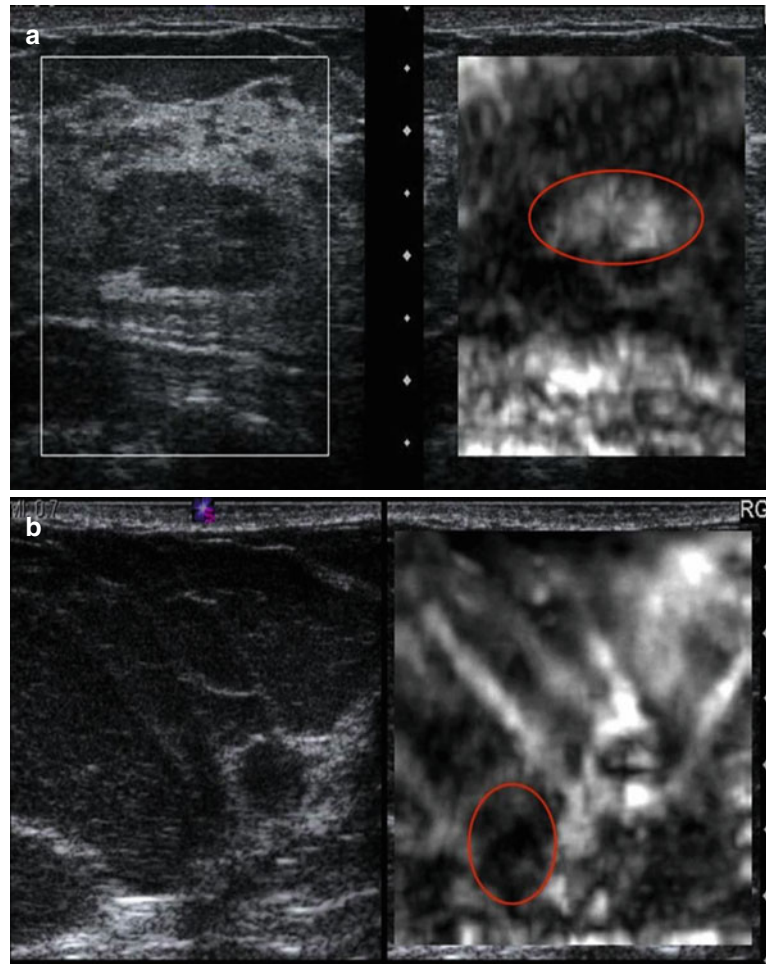

Fig. 21.2 Elastogram of a fat lobule (*red circle*) in fibroglandular breast tissue is presented in (**a**). The conventional B-mode image is on the left and the elastogram is on the right. The fat lobule is white (soft) on the elastogram, while the fibroglandular tissue is black (hard). The scale on the elastogram is based on the stiffness of the tissues in the FOV. In this case the fat is the softest tissue and therefore white, while the fibroglandular tissue is black since it is the stiffest tissue present. In (**b**) almost the entire FOV is fat. Therefore, the algorithm codes the stiffest fat as black (*red circle*) even though it is a very soft tissue. These two cases demonstrate the relative scale used in strain. A given tissue can appear a different shade of gray depending on the other tissues present in the FOV

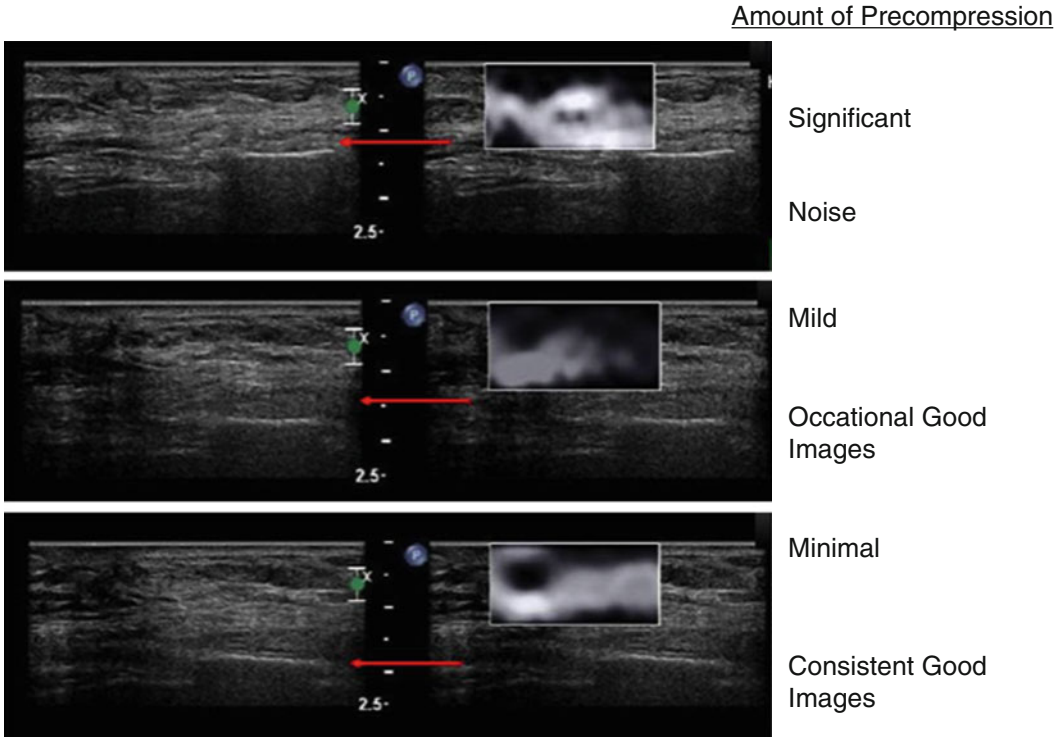

Fig. 21.3 When pre-compression is applied to tissues they become stiffer. The increase in stiffness varies with different tissues. Therefore, the relative stiffness changes between tissues affect the strain elastogram. The increase stiffness is also detected as increased shear wave velocities in shear wave elastography. The effects on ES are demonstrated in this example of a epidermoid cyst. When significant pre-compression is applied, all tissues (*upper frame*) have similar strain and the image is all noise. When mild pre-compression is applied, there are frame-to-frame differences in the appearance of the lesion (*middle frame*). When minimal pre-compression is applied (*lower frame*), the lesion is similar in all frames of the elastogram

less conspicuity between tissues. If enough pre-compression is applied, all tissues are similar and the elastogram changes are mostly noise.

A technique to apply minimal amount of pre-compression reproducibly has been described [5]. Usually a mild amount of pre-compression is used to obtain B-mode images as it improves B-mode image quality. The "quality factor" or "compression bar" used in some manufactures equipment does not assess the amount of pre-compression being applied. It only evaluates the amount of displacement of tissues during the compression and release cycle.

21.1.2.1 Strain Elastography Using an ARFI Pulse

The use of a low-frequency ultrasound pulse (a push pulse) can be used as the source of the displacement. This technique is called acoustic radiation force impulse (ARFI) [6–8]. Using ARFI to create the displacement of tissue and analyzing the displacement changes with the same strain algorithm, an SE image is obtained. Note that this is different than SWE where the speed of the shear wave (Vs) generated from the ARFI pulse is measured. The ARFI pulse power is limited by guidelines of energy input into a body, thus can be limited by depth penetration.

If an ARFI push pulse is used to generate the tissue displacement, no manual displacement should be used. The probe should be held steady and the patient asked to hold their breath and remain motionless during the acquisition. The algorithm used to generate the elastogram is similar to SE on the same system. In general the ARFI push pulse is limited in producing displacement deeper than 4 cm with the breast imaging transducer and up to 9 cm in abdominal applications.

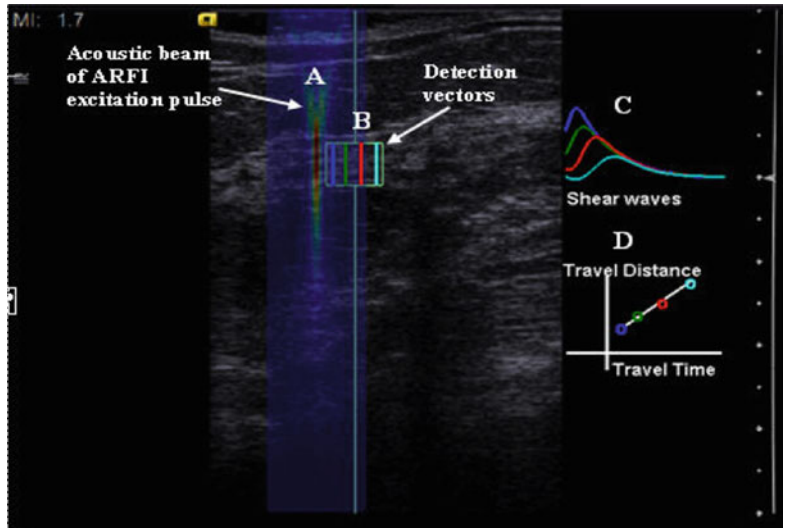

Fig. 21.4 Shear wave elastography is performed by applying a push pulse (*ARFI*). This high-energy pulse (*A*) generates shear waves which propagate perpendicular to the push pulse. Conventional ultrasound is used to monitor the shear waves within the tissue (*B*). The shear waves have higher signal intensity closer to the push pulse and the amplitude of the peak decreases with distance from the push pulse (*C*). (*D*) By plotting the time to peak and the distance from the push pulse, the velocity of the shear wave can be calculated. It can be expressed either as the velocity in m/s or with some assumptions the Young's modulus in kPa

21.1.3 Shear Wave Elastography

A second technique to determine the elastic properties of a tissue is SWE. In this technique an initial ultrasound pulse (push pulse) or ARFI is applied to the tissue that induces a shear wave perpendicular to the ultrasound beam. This is similar to dropping a stone (the push pulse) into a pond of water. The ripples generated correspond to the shear waves. Conventional B-mode ultrasound sampling techniques are used to calculate the speed of the shear wave generated through the tissues. This is diagramed in Fig. 21.4. From the speed of sound through the tissues, the strain modulus can be estimated. The velocity of the shear wave is proportional to stiffness. The hardness of a lesion can be displayed as the speed of the shear wave (Vs, meters/second (m/s)) through the tissue or the strain modulus (kilopascals (kPa)). With SWE a quantitative measure of the lesion stiffness is obtained either in point of interest or in an FOV with pixel-by-pixel color coding of the Vs.

Two shear wave systems are presently available. In the ACUSON S3000™ ultrasound system (Siemens, Mountain View, CA.), a measurement in a small ROI can be obtained (Virtual Touch tissue quantification, VTq) as well as a pixel-by-pixel evaluation of a larger FOV using a color map (Virtual Touch IQ™, VTiq). In VTiq after the initial push pulse, tracking signal vectors are used to detect the tissue displacement as the shear wave passes and thus reconstruct its velocity in a region of interest, which can be displayed as a qualitative image of elasticity or a quantitative image displayed as shear wave speed. A single image is obtained. The tracking vectors with focused transmit results in less noisy and more stable shear wave signal detection. In the Aixplorer (SuperSonic Imagine (SSI), Aix-en-Provence, France), the effect of the push pulses is amplified by sending a series of pulses successively focused at increasing depths faster than the shear wave's velocity, so that a Mach cone front is generated. A high imaging frame rate is achieved by transmitting a plane wave that insonates the entire field of view in a single burst. The result is that the shear wave velocity can be measured and displayed (in m/s or kPa) as a quantitative color overlay image at a frame rate of around 1 frame/s. The SSI technique has been shown to be highly qualitatively reproducible based on shape, homogeneity and color distribution with only 1.6 % of cases being

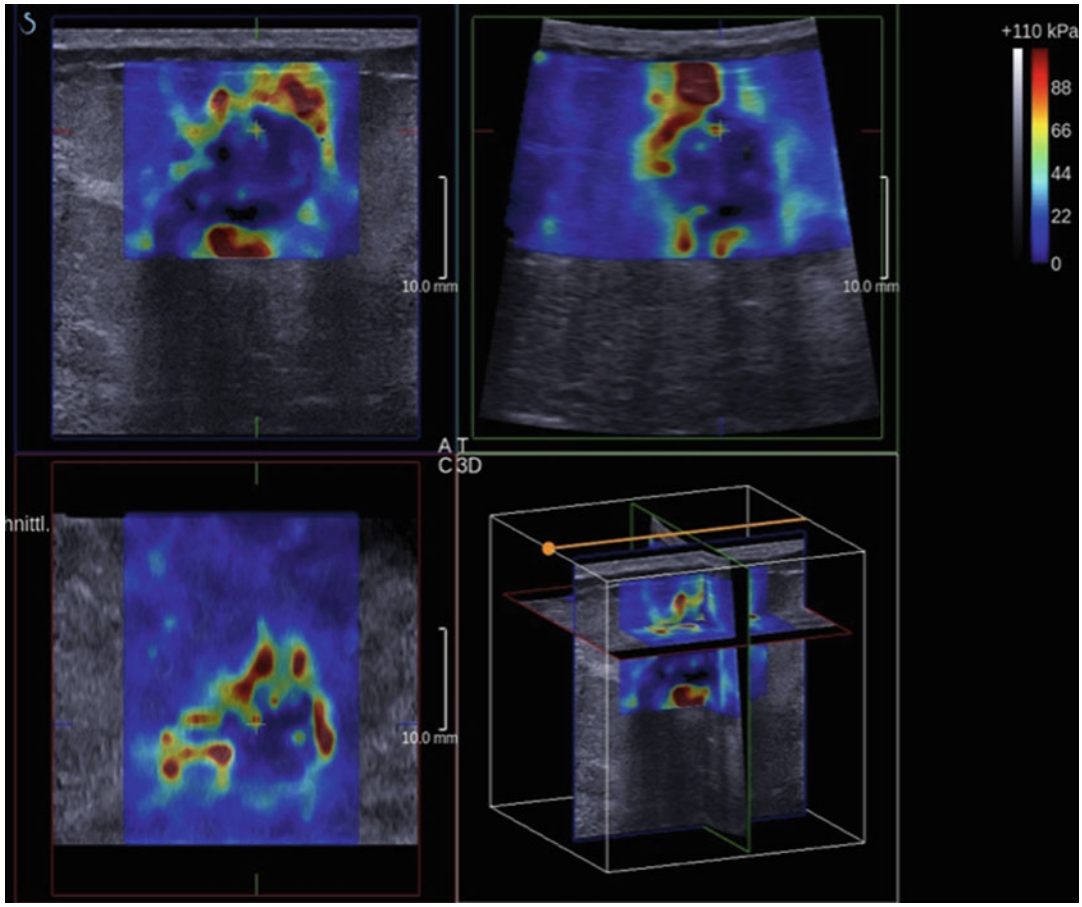

Fig. 21.5 Shear wave imaging can be performed with a 3D technique. The data can be displaced as a volume or selected slices. This example is an invasive ductal cancer. Note the high shear wave velocities surrounding and within the tumor (Courtesy of Dr. D. Amy, Aix-en-Provence, FR)

very dissimilar [9]. Lesion size measurements were highly reproducible (>0.9) and inter-observer reliability for maximum and mean elasticity values were also highly reproducible (>0.8). The E mean value is the most reproducible elasticity measurement [9].

The principles of scanning using SE also pertain to SWE. Pre-compression can change results and it is recommended the same technique discussed above be used to acquire shear wave images. On some systems SWE can be performed in real time; however, to obtain optimal images, remaining in the same plane for several seconds is required for accurate measurements. Shear wave propagation by an ARFI pulse is depth limited. If a shear wave is not generated, a value will not be obtained in the point quantification method and there is no color coding of the area in the FOV method. Repositioning the patient to make the lesion closer to the skin surface can help in these cases. For small parts a 3D probe is now available which allows for a volumetric elastogram (Fig. 21.5).

21.2 Breast

21.2.1 Overview

Although current modalities of breast imaging, including MRI, ultrasound, and mammography, have high sensitivities for detecting breast lesions, they do not have high specificities [10, 11]. This has resulted in close monitoring or

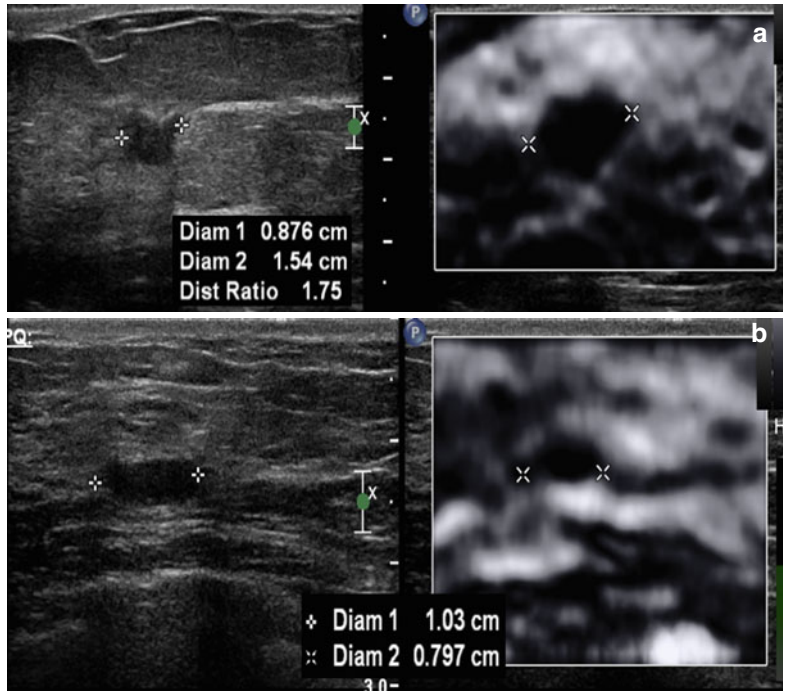

Fig. 21.6 On SE, a unique characteristic occurs in breast lesions. Malignant lesion are larger on the elastogram than on the corresponding B-mode image, while benign lesions are smaller. The EI/B-mode ratio can be used to characterize breast lesions as benign or malignant with high sensitivity and specificity. An example of an invasive ductal cancer in a 69-year-old woman is presented in (**a**). The lesion measures 0.9 mm on the B-mode image and 15.4 mm on the elastogram, a EI/B-mode ratio of 1.7. A biopsy-proven benign fibroadenoma (**b**) had a B-mode length of 1.03 mm and an elastogram length of 0.797 mm giving an EI/B-mode ratio of 0.8

unnecessary biopsies of many benign lesions. An imaging modality with a high specificity for detecting malignant lesions would significantly decrease the amount of unnecessary biopsies.

Ultrasound evaluation of the breast was initially used to determine if a lesion was cystic or solid [12, 13]. With the criteria set forth by Stavros et al. [14], ultrasound has had a more important role in breast lesion characterization. These criteria have been incorporated into the ultrasound BI-RADS lexicon [15] and can be used to distinguish between benign and malignant breast lesions. For thousands of years physicians have used palpation for diagnosis of breast cancer [16]. Ultrasound elastography has the potential to quantify the stiffness of a lesion, which was previously judged only subjectively by physical exam [17–19]. Krouskop et al. [20] determined that in vivo there is significant elastographic contrast between cancerous and noncancerous breast lesions. This suggests that elastography should be an excellent technique for characterizing breast lesions as benign or malignant.

21.2.2 Strain

Three methods of interpreting SE images have been proposed, evaluating the size change between the B-mode image and the elastogram, the relative stiffness based on a color scale, and the ratio of the lesion stiffness to fat, the strain ratio.

21.2.2.1 Length Comparison

Using a real-time dual strain elastography system, Hall et al. [21] demonstrated that there was potential to use this technique to characterize breast lesions as benign or malignant. It was noted on SE elastography that benign lesions measure smaller in size than the corresponding B-mode image, while malignant lesions measured larger (Fig. 21.6). They proposed utilizing

the ratio of the lesion size on elastography to the B-mode size (EI/B-mode ratio) as a diagnostic criteria for benign or malignant. They used an EI/B-mode ratio of >1.2 for a lesion to be malignant. With these criteria they found a sensitivity of 100 % and a specificity of 75.4 %. Barr [22] in a single-center unblinded trial of 123 biopsy-proven cases using an EI/B-mode ratio of <1.0 as benign and equal to or >1.0 as malignant had a sensitivity of 100 % and a specificity of 95 % in distinguishing benign from malignant breast lesions. A large multicenter, unblinded trial evaluating 635 biopsy-proven cases using Barr's criteria had a sensitivity of 99 % and a specificity of 87 % [23].

Either the lesion length ratio or a lesion area ratio can be used. The lesion is measured in the same position on both the elastogram and B-mode image. The use of a copy, shadow, or mirror function in the measurement technique is helpful. As cases of ductal carcinoma in situ (DCIS) and lobular cancer are often poorly visualized on B-mode imaging, this technique should not be used unless they are defined masses that can be measured with true distinguishable borders. Difficulty can occur when measuring the lesion size on the elastogram when a fibroadenoma or fibrocystic lesion is present in dense breast tissue. The strain properties of the fibrocystic change or fibroadenoma are similar to the background dense breast tissue. Therefore, one may visualize the combination of the lesion and normal dense breast tissue as one lesion, creating a false positive [2–4]. This problem can be avoided by comparing the stiffness of the lesion to surrounding tissue; if it is similar to fibroglandular tissue, it is most likely benign. Using the color scale or lesion-to-fat ratio methods may help eliminate this problem. In the multicenter trial [23] this accounted for a large number of the false positives decreasing the specificity. Strain images obtained using the ARFI technique can be interpreted using this technique.

Shadowing which can be seen with some cancers on B-mode is not seen on the accompanying elastogram. Therefore, the inferior border of the cancer can often be identified on the elastogram [2–4]. As long as there is some B-mode signal identified in the shadowing, the algorithm will be able to determine the strain in those pixels. However, if the shadowing is extreme and no returning signal is identified, there is no correlation identified and the pixels will be coded as white [2–4].

Another confounding factor is the presence of two lesions adjacent to each other. These may appear as one lesion on the B-mode image. Close inspection of the elastogram can distinguish the two lesions [2–4]. In these cases care must be taken in performing measurements.

In addition to using the interpretation method previously discussed to determine if a lesion is more likely benign or malignant, asking if the lesion is soft or stiff or visible on SE is clinically helpful in some situations. It is sometimes difficult to determine if a lobular hypoechoic lesion is a fat lobule on conventional ultrasound. If the lesion is a fat lobule, it will appear very soft on the elastogram and similar to the other fat in the image (Fig. 21.2a). Lesions can be isoechoic to background tissue on B-mode imaging and not recognized as a lesion. These lesions may have different strain properties to the background and can be clearly visualized on SE. This is very common with complicated cysts (Fig. 21.7). Evaluation of the EI pattern can also define where to best biopsy a lesion (Fig. 21.8) selecting the hardest location to target the biopsy. The SE pattern can help characterize a complex lesion (Fig. 21.9).

21.2.2.2 5-point Color Scale

A 5-point color scale has been proposed to classify lesions using SE (Fig. 21.10) [24, 25]. This scale combines the ratio changes and degree of stiffness of the lesion. When a lesion is hard and has the same size on elastography as in the B-mode image, the lesion is given a score of 4. If the lesion is hard and larger on elastography, the lesion is classified as 5. It is recommended that lesions that are hard and equal in size to B-mode or larger on the elastogram than B-mode are biopsied. If the lesion is soft, it is classified as a score of 1. If the lesion has a mixed hard and soft pattern, it is classified as a 2. If the lesion is hard but smaller on elastogram, it is given a score of 3.

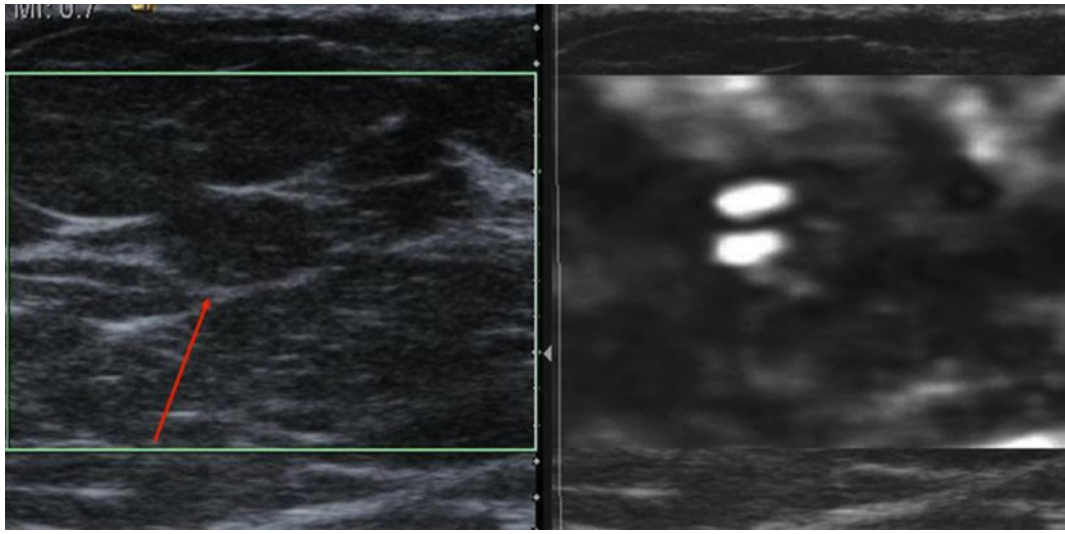

Fig. 21.7 Ultrasound images from a 39-year-old female with a palpable mass and a negative ultrasound examination and mammogram at a different institution. An elastogram taking at the site of the palpable abnormality confirms the presence of an isoechoic complicated cyst (*red arrow*). The lesion has the bull's-eye appearance identified in simple and complicated cysts on certain vendor equipment

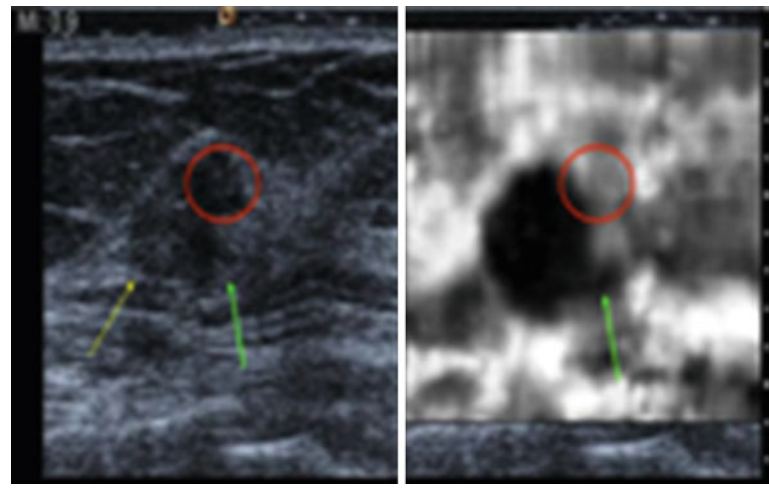

Fig. 21.8 Close evaluation of the elasticity pattern of a lesion can be helpful in characterization and biopsy planning. In this example of an invasive ductal cancer which has a EI/B-mode ratio of >.1 an area (*red circle*) is "soft" on SE. On pathology from surgical resection, the soft area was a benign fibroadenoma which is not distinguishable from the IDC (*yellow arrow*) diagnosed in a 53-year-old woman on the B-mode image. A spicule (*green arrow*) of tumor is better seen on SE

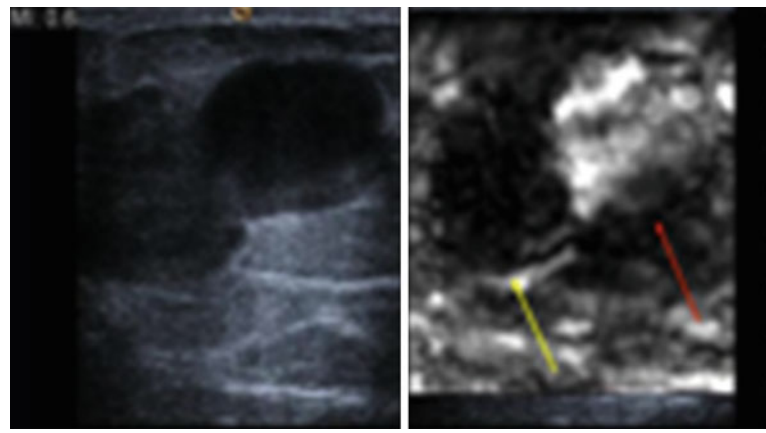

Fig. 21.9 Selected image from an 85-year-old woman presenting with a bloody nipple discharge. On the B-mode image there is a large complex lesion. On SE a hard component (*yellow arrow*) and a soft component (*red arrow*) are identified. On pathology the solid component was a papillary lesion and the soft area was old blood

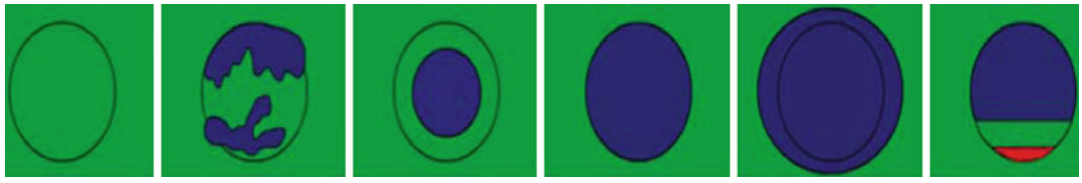

Fig. 21.10 Pictorial display of the Ueno scale for classification of breast lesions when using a color map where *red* is soft and *blue* is hard. For adequate color mapping images should be obtained containing fat, fibroglandular tissue, pectoralis muscle, and the lesion. In grade 1 the lesion is all soft. In grade 2 the lesion has mixed soft and hard components. The lesion is hard and smaller on ES in grade 3, equal in size on SE in grade 4, and larger on SE in grade 5

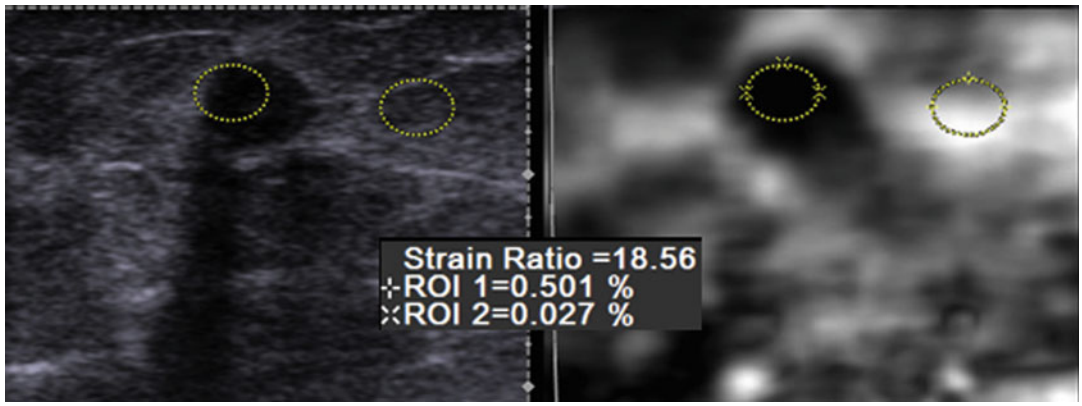

Fig. 21.11 Selected elastogram from a 59-year-old woman with a biopsy-proven invasive ductal cancer. An oval FOV is placed in the lesion and adjacent fat (*yellow ovals*). The strain ratio is calculated by determining the ratio of the strain from the lesion compared to that of fat. In this case the strain ratio is 18.6; that is, the lesion is 18.6 times stiffer than fat. This is highly suggestive of a malignant lesion. The EI/B-mode ratio in this case was 1.2 also suggestive of a malignancy

Scores of 1–3 are classified as benign. This technique has been shown to have moderate to substantial interobserver agreement and substantial to perfect intra-observer agreement [26]. There was no significant difference in inter- and intra-observer agreements according to lesion size.

Using the color scale breast SE has been shown to objectively evaluate tumor or tissue stiffness in addition to morphology and vascularity [24]. Itoh found a sensitivity of 86.5 % and a specificity of 89.8 % using this technique with a cutoff point between 3 and 4. This technique has been shown to correlate well with the ultrasound BI-RADS score [27–29]. SE has also been shown to visualize non-mass lesions or peritumoral ductal lesions [24]. Multiple studies have found similar results [30–34]. This technique has also been used in the evaluation of suspicious microcalcifications on mammography with 97 % sensitivity and 62 % specificity in the differentiation of benign and malignant microcalcifications [30]. Several articles suggest SE may be most helpful in BI-RADS 3 and BI-RADS 4 lesions by upgrading or downgrading them [27, 28, 32].

21.2.2.3 Strain Ratio

In an attempt to semiquantify the measurements, the ratio of lesion stiffness to fat has been suggested. Initial studies [35, 36] have found this technique valuable in determining if a lesion was benign or malignant (Fig. 21.11). This ratio is based on the knowledge that the properties of fat are fairly constant, whereas the properties of other surrounding tissues and lesions are variable. Lesions with densities similar to fat therefore

have smaller ratios. Care must be taken with these measurements as pre-compression can significantly change the strain value of fat [5]. As pre-compression is applied, the stiffness of all tissues increased. However, the stiffness of fat changes more than that of normal breast tissue and lesions. Therefore, with pre-compression the strain ratio of lesion to fat will decrease. Care must also be taken that the FOV for the fat measurement contains only fat. The measurements should be taken at the same depth in the image as the degree of tissue compression varies with depth.

Thomas et al. [35] compared B-mode BI-RADS, the 5-point color scale, and the lesion-to-fat ratio in 227 breast lesions. Based on the ROC curve, they selected a cutoff of 2.455 to distinguish benign from malignant lesions. The mean ratio for malignant lesions was 5.1 ± 4.2 while for benign 1.6 ± 1.0 ($p < 0.001$). They found a sensitivity and specificity of 96 and 56 % for B-mode imaging, 81 and 89 % for the 5-point color scale, and 90 and 89 % for the lesion-to-fat ratio, respectively.

Zhi et al. [37] in a similar study compared the strain ratio and the 5-point color scale in 559 breast lesions. They found the strain ratio of benign lesions was 1.83 ± 1.22, while malignant lesions were 8.38 ± 7.65. These were significantly different ($p < 0.00001$). Based on their ROC curves, they selected a cutoff point of 3.05. The area under the curve for the 5-point color system was 0.885, while that of the strain ratio was 0.944 ($p < 0.05$). In a different study of 408 lesions [38], a lesion-to-fat strain ratio with a cutoff of 4.8 found a sensitivity of 76.6 % and a specificity of 76.8 %.

21.2.2.4 Artifacts

There are several artifacts that can be encountered with SE. Some occur when technique is suboptimal, while some contain diagnostic information. A characteristic elastogram, the bull's-eye artifact, is seen with benign simple and complicated cysts with some systems. This artifact is characterized by a white central signal within a black outer signal and a bright spot posterior to the lesion [39]. This artifact is caused because the fluid is moving and there is decorrelation between images. This artifact has been described in detail [39] (Fig. 21.12). This artifact has a high predictive value for the lesion being a benign simple or complicated cyst. If there is a solid component in the cyst, it will appear as a solid lesion within the pattern (Fig. 21.13). Although limited cases have been reported, this artifact is not seen in mucinous or colloid cancers [39]. This artifact can be used to decrease the number of biopsies performed [39]. In one series 10 % of complicated cysts that appeared solid on B-mode are complicated cysts that can be identified with this technique [39]. If core biopsies are performed, notifying the pathologist that the lesion is a complicated cyst as opposed to a solid mass will lead to better pathology/imaging correlation. If the pathologist is told the lesion is solid, the report may not document that a cyst wall is present and suggest the suspected solid lesion is not in the specimen leading to an indeterminate report. This useful artifact is seen with Siemens (Mountain View, CA) and Philips (Bothell, WA) equipment and may not be seen in other manufacturers' equipment.

The Hitachi system has a different artifact that occurs in cysts (Fig. 21.14). There is a 3-color layered pattern of blue, green, and red identified in cystic lesions [24]. A detailed study evaluating the sensitivity and specificity of this artifact has not been performed.

A white ring or group of waves around a lesion on the elastogram indicates the lesion is moving in and out of the imaging plane while obtaining the elastogram [2–4]. This is called the sliding artifact. This artifact suggests the lesion is freely moveable within the adjacent tissues and is most likely benign. This has been proposed as a method to determine if there is an invasive component to a intraductal malignancy [40].

21.2.3 Shear Wave Elastography

With SWE a quantitative measure of the lesion stiffness can be obtained either in a small fixed ROI (single measurement) or pixel by pixel in an FOV using a color map. The results are color coded usually with red as hard and blue as soft. No studies with the use of 3D SWE have been published. It is unknown if the volumetric data using

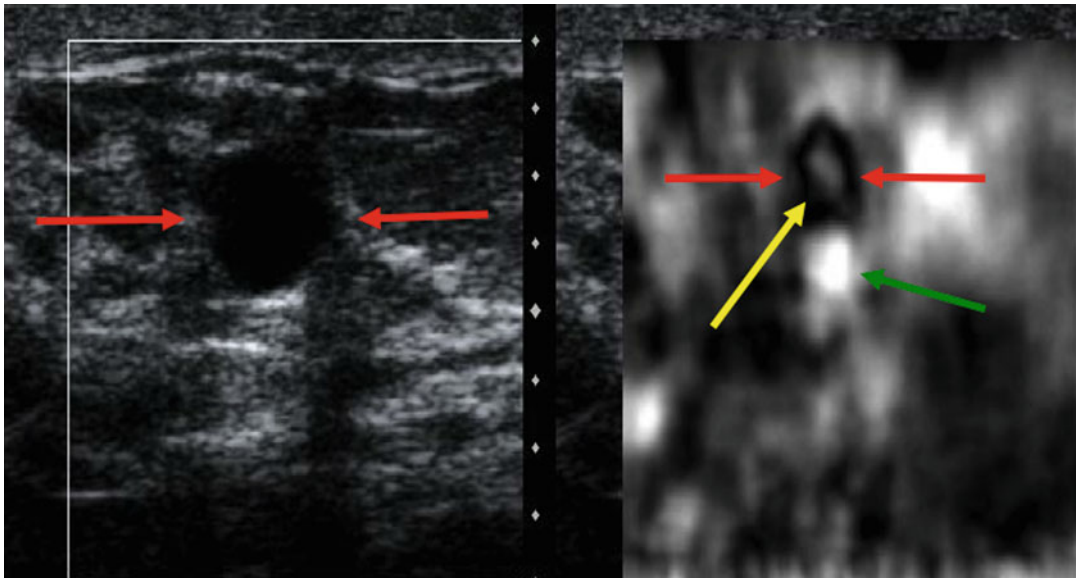

Fig. 21.12 Elastogram of a simple cyst in a 39-year-old woman who presents with a palpable mass. The image on the left in the dual-screen display is the B-mode image, whereas the image on the right is the elastogram. The elastogram shows the characteristic bull's-eye artifact identified in benign simple and complex cysts in selected vendor SE. The artifact is characterized by three components, a *black* area (*red arrow*) with a central bright spot (*yellow arrow*) and posterior bright spot (*green arrow*)

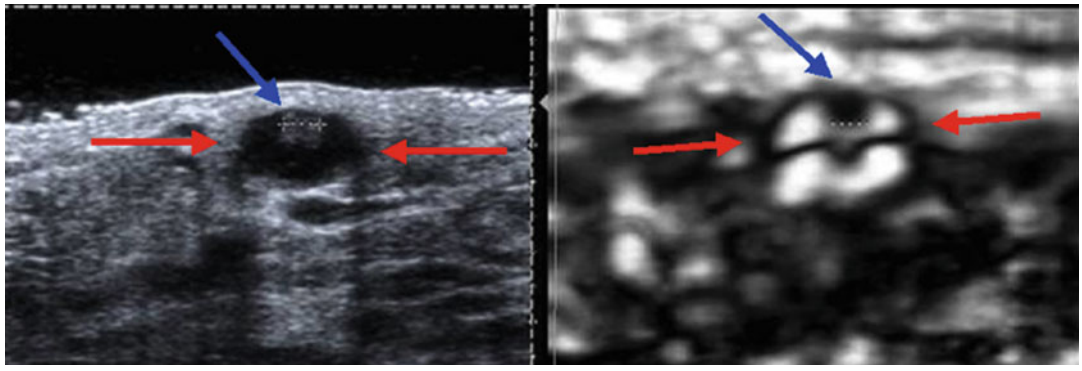

Fig. 21.13 If a solid component is present within a cystic lesion (*red arrow*), the solid component can be identified as a hard area (*blue arrow*) within the bull's-eye artifact. This elastogram is from a patient with a 2 mm benign papilloma with a cystic area (Courtesy of Carmel Smith, Brisbane, Australia)

the 3D technique will provide additional information or allow for breast screening. The principles of scanning technique using SE also pertain to SWE. Pre-compression can change results and the same technique previously discussed above should be used to acquire images using SWE.

21.2.3.1 Quantitative Measurements

Based on a recent large multicenter study, a cut-off value of 80 kPa was determined to distinguish benign from malignant lesions [41]. Examples of a benign and malignant lesion are presented in Fig. 21.15. Tissue measurements in an ROI can be displayed in velocities (m/s) or in pressure/elasticity (kPa). The measurement of stiffness should be obtained from the area of highest stiffness within the lesion or the surrounding tissue. In this large multicenter trial, they demonstrated that when added to BI-RADS classification in B-mode imaging, SWE increases diagnostic

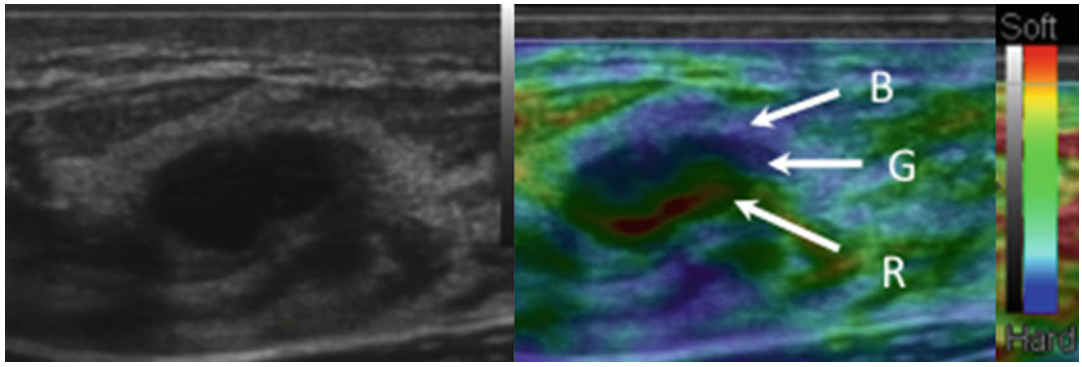

Fig. 21.14 A 3-layered artifact is identified with cysts on some vendor equipment. When using a color map where *red* is soft and *blue* is hard, the artifact has a BGR pattern characterized by a *blue* layer, *green* layer, and *red* layer as depicted in this image

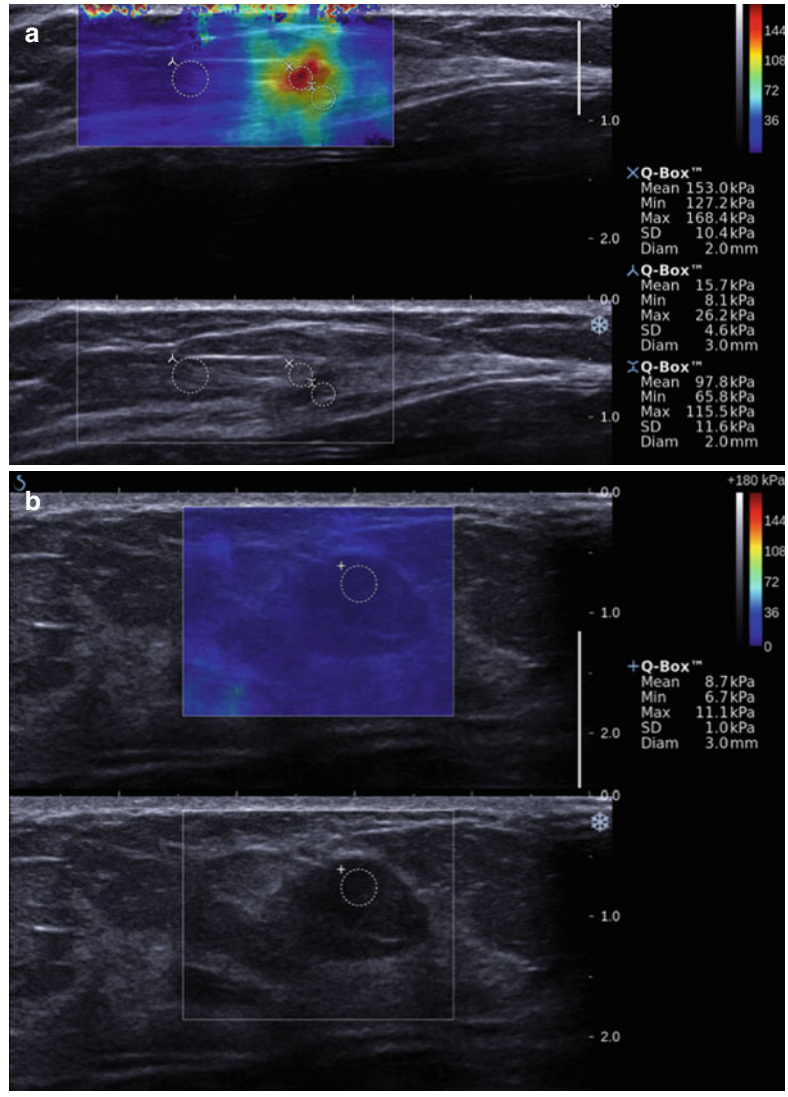

Fig. 21.15 Shear wave image (**a**) of an invasive ductal cancer in a 59-year-old woman demonstrating the elevated shear wave speed in the malignancy. The lesion has a maximum kPa value of 168. The normal background breast tissue has a maximum kPa value of 26. In a benign area of fibrocystic change (**b**) in a 45-year-old woman the maximum kPa value is 11. Different cutoff values between benign and malignant have been proposed ranging from 60 to 80 kPa

accuracy [41]. They found that the evaluation of SWE signal homogeneity and lesion-to-fat ratios were the best differentiators of benign and malignant. The addition of SWE increased the characterization of lesion over BI-RADS alone, with a sensitivity and specificity of 93.1 and 59.4 % in BI-RADS and 92.1 and 76.4 % with the addition of SWE. The authors comment that the major value of the addition of SWE is in BI-RADS 3 and 4a lesions where the SWE results are used to upgrade or downgrade the lesion.

Chang et al. [42] in a study of 158 consecutive patients found the mean elasticity values were significantly higher in malignant masses (153 kPa ± 58) than benign masses (46 kPa ± 43) ($p < 0.0001$). They determined an optimal cutoff value of 80 kPa which resulted in a sensitivity and specificity of 88.8 and 84.9 %. The area under the ROC curve was 0.898 for conventional US, 0.932 for SWE, and 0.982 for the combined data. In a study of 48 breast lesions, Athanasiou et al. [43] found similar results with similar stiffness values for benign lesions (45 ± 41 kPa) and malignant lesions (147 kPa ± 40)($p < 0.001$). There results suggest the addition of SWE to conventional ultrasound could be used to decrease the number of biopsies performed in benign lesions. In a small series Evans et al. [44] found the sensitivity and specificity for SWE (97 and 83 %) to be better than B-mode alone (87–78 %). In their series they used a cutoff value of 50 kPa. They also confirmed that the technique is highly reproducible.

When using Virtual Touch Quantification™ (VTq) (Siemens Ultrasound, Mountain View, CA), where a single measurement is obtained from a small ROI, it is not possible to determine where the area of highest stiffness is located on the B-mode image. Multiple measurements within the lesion and surrounding tissue need to be obtained to acquire optimal measurements. The measurement within the tumor often results in "x.xx" signifying that an adequate shear wave for evaluation was not obtained [2–4]. Bai et al. [45] reported that if a lesion is solid and x.xx is obtained, the lesion is most likely a malignancy. With this assumption they obtained a sensitivity and specificity of 63.4 and 100 %.

Shear waves will not propagate through simple cysts and they too will not be color coded. The shear wave is detected by ultrasonic echo signal. Therefore, when areas in the B-mode image show extremely low signal, it indicates the echo signal is too low for successful detection. These areas are not color coded. This will occur with marked shadowing such as seen with ribs, tumors with significant shadowing, and areas with macrocalcification [2–4].

21.2.3.2 Quality Factor

In very hard lesions such as invasive cancers, the shear wave may not propagate in an orderly fashion. No results are therefore obtained and the area with no results is not color coded (Fig. 21.16). In these areas interpretation is not possible. However, in general the desmoplastic reaction of the tumor will be hard surrounding the tumor and

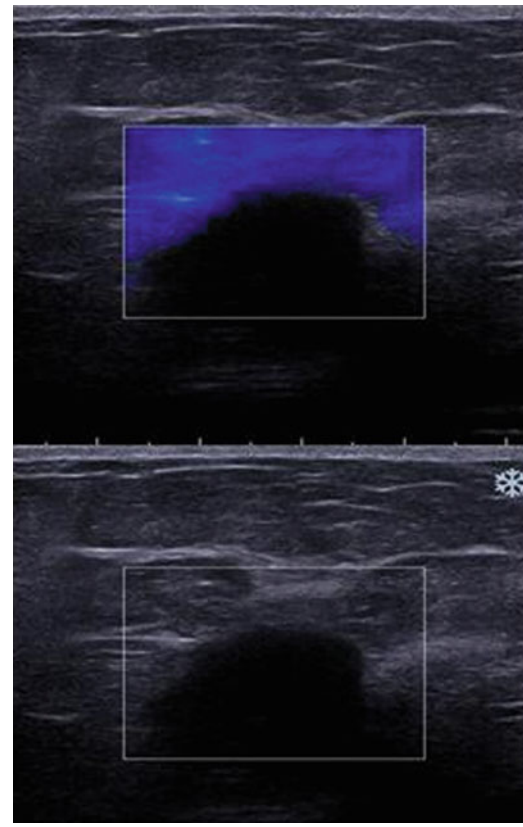

Fig. 21.16 In some cases the push pulse may not generate shear waves. This may be secondary to lesion depth, lesion with simple fluid or very hard lesion. Simple cysts with minimal debris do not support shear wave generation. In this image from a deep invasive ductal cancer, shear waves are not generated and the lesion is not color coded on the elastogram

appear as hard (red) halo surrounding the lesion. Even if the entire mass is not coded as hard, heterogeneity of the SWE is part of the criteria for a suspicious lesion. Care must be taken with precompression as this can also create the same appearance in a benign lesion [5].

In a large number of malignant lesions, the area identified on B-mode as the hypoechoic mass often does not code on SWE because a shear wave is not identified or may code with a low Vs. Bai found that 63 % of breast malignancies have this finding [45]. Preliminary work in the evaluation of this phenomenon suggests that shear waves may not propagate as expected in some malignant lesions [2–4] (Fig. 21.17). Evaluation of the shear waves in these malignant lesions demonstrates significant noise that may be incorrectly interpreted as a low shear wave speed by the algorithm. The addition of a quality measure that evaluates the shear waves generated and determines if they are adequate for an accurate Vs (or kPa) measurement will help in eliminating possible false-negative cases (Barr RG 2012, personal communication) (Fig. 21.18).

21.2.4 Summary

Elasticity imaging of the breast can be performed utilizing several techniques. These techniques all have a high sensitivity and specificity for characterizing breast lesions as benign or malignant. Although the techniques are easy to perform, attention to details are required to obtain optimal images for interpretation. Each of the techniques has advantages and disadvantages. Further comparative studies are needed to determine which technique or combination of techniques is most appropriate for various clinical problems. The bull's-eye artifact seen with SE has been shown

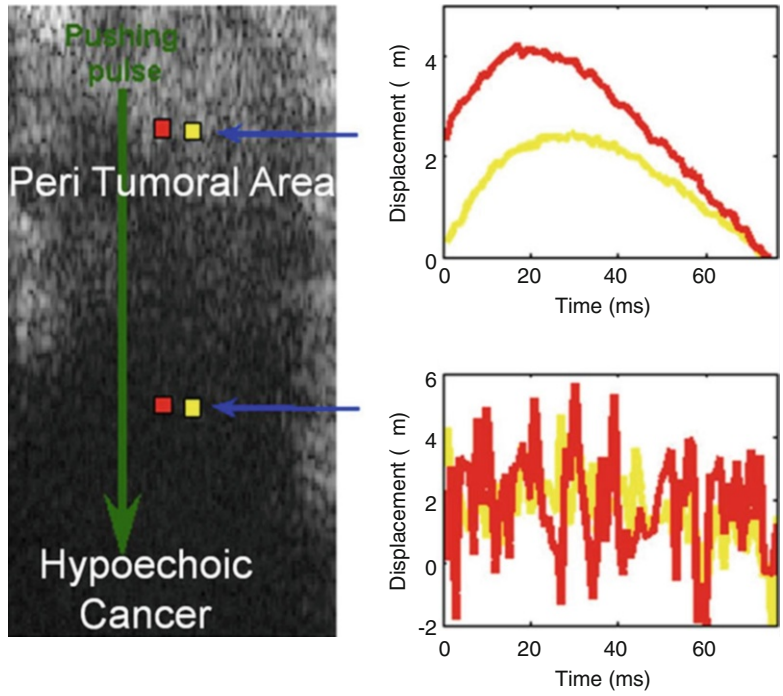

Fig. 21.17 Results from a 57-year-old woman with a palpable mass in her right breast. Mammographic and sonographic workup confirms a BI-RADS 4B lesion. The lesion is a biopsy-proven poorly differentiated invasive ductal cancer. The cancer is the hypoechoic mass in the deeper portion of the image. Two waveforms were obtained using the acoustic radiation force impulse technique. The one taken deeper is from the hypoechoic invasive ductal cancer. The more superficial one is taken in the peritumoral area. The waveform obtained from the cancer is all noise and not interpretable. The waveform in the adjacent peritumoral tissue has more noise than in the fat signals in Fig. 21.2, but the waveform is still able to be interpreted and provide a shear wave speed

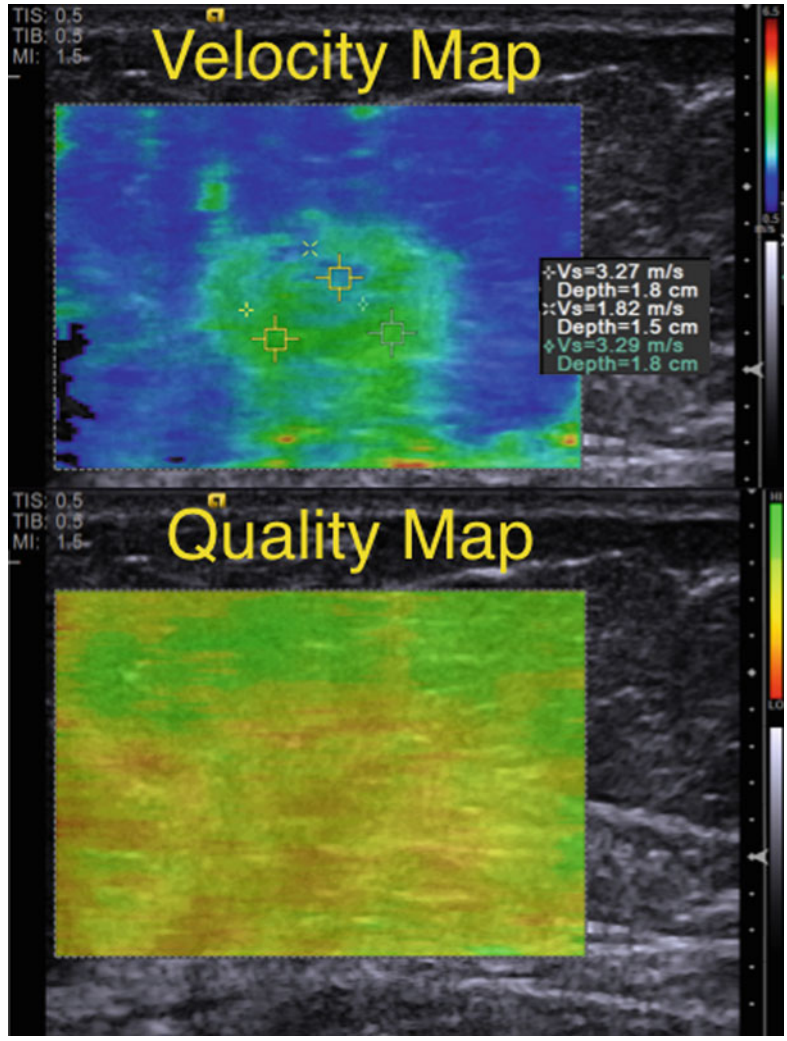

Fig. 21.18 Shear wave elastogram from an invasive ductal cancer. A Velocity Map color codes the shear wave velocity on a pixel-by-pixel base. The Quality Map color codes the quality of the shear wave from that pixel. When the shear waves are not interpretable secondary to weak signal or a large amount of noise, the map codes that area as *red* or *yellow*. In this case the mass has a maximum shear wave speed of 3.2 m/s suggestive of a benign lesion. However, the Quality Map demonstrates that the shear waves are not appropriate for interpretation and the data should not be used in characterizing the mass

to be extremely helpful in characterization of cystic lesions [39]. These techniques are now maturing but continued work on standardizing elastography techniques is required.

21.3 Liver

21.3.1 Focal Liver Lesions

Both SE and SWE can be used to evaluate focal liver lesions. Because SE is qualitative it can be compared to "normal" liver to determine if the lesion is harder or softer than the background liver. However, this technique is limited in that the background liver may have variable stiffness depending on the degree of steatosis or fibrosis. In addition both benign and malignant lesions can be soft or hard compared to normal liver. With SWE we obtain a stiffness measurement; however, because of the wide variability of a given lesions stiffness, characterization of a lesion as benign or malignant is problematic. For example, in a series by Yu and Wilson [46], hemangioma had a range of Vs of 0.87–4.01 m/s with an average of 0.71 m/s, while hepatocellular carcinoma had a range of 0.77–4.34 m/s with an average of 1.01 M/s. Overall, the difference in Vs of malignant 2.57 ± 1.01 m/s and benign lesions 1.73 ± 0.8 was statistically significant ($p < 0.01$);

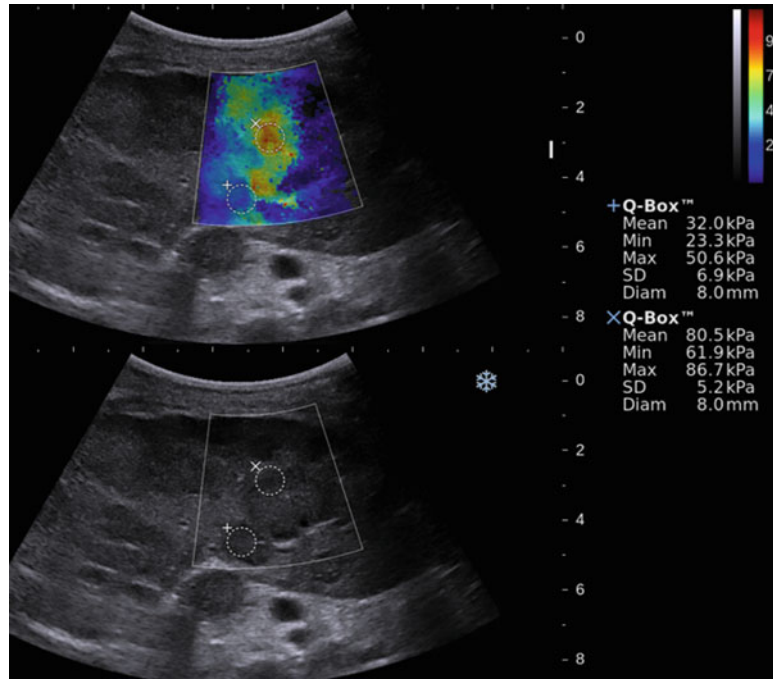

Fig. 21.19 Shear wave elastogram of the liver in a patient with diffuse metastatic disease from colorectal carcinoma demonstrates the marked difference in the stiffness of two metastatic lesions (*white circles*), one with mean kPa value of 32 and the other 81. The wide range of stiffness seen with both benign and malignant lesions overlaps significantly limiting the use of shear wave imaging in characterization of focal liver lesions

however, the large overlap between benign and malignant makes the technique unreliable for focal liver mass characterization in a given case. Figure 21.19 is a selected shear wave elastogram of a patient with multiple metastatic lesions from colorectal carcinoma. There is a wide range of shear wave velocities of the metastatic lesions with some soft and some hard.

21.3.2 Liver Fibrosis

Liver fibrosis is a significant worldwide problem. As fibrosis progresses there is increasing loss of liver function and higher risk of liver cancer. This chronic liver disease is characterized by the deposition of fibrous tissue within the liver. The stage of liver fibrosis is important to determine prognosis, surveillance, and treatment options. Early-stage fibrosis is reversible, while the disease that has progressed to cirrhosis is likely irreversible. Presently the only method of staging the fibrosis has been by liver biopsy [47].

With increasing fibrosis the liver becomes stiffer which can be monitored using shear wave elastography [48, 49]. With this technique an ROI is placed in a region of the liver taking care not to include vasculature. An intercostal approach in segment eight of the liver has been shown to provide more accurate results. Serial measurements are taken while the patient suspends respiration. The average of these measurements is used to estimate degree of liver fibrosis (Table 21.1).

Table 21.1 Correlation of Metavir score and liver stiffness

Liver fibrosis staging	Metavir score	kPa
Normal	F0	2.0–4.5
Normal–mild	F0–F1	4.5–5.7
Mild–moderate	F2–F3	5.7–12.0
Moderate–severe	F3–F4	12.0–21.0
Severe	F4	>21.0

Figure 21.20 shows the results of a 27-year-old with chronic hepatitis C. The stiffness average of 4.77 kPa is consistent with patient's liver biopsy result of mild fibrosis. Figure 21.21 is the image from a patient with marked cirrhosis demonstrating a markedly elevated stiffness of 66 kPa.

How this new technology can be utilized in clinical practice is under extensive investigation [48]. The use of this technique may be able to decrease the number of liver biopsies performed

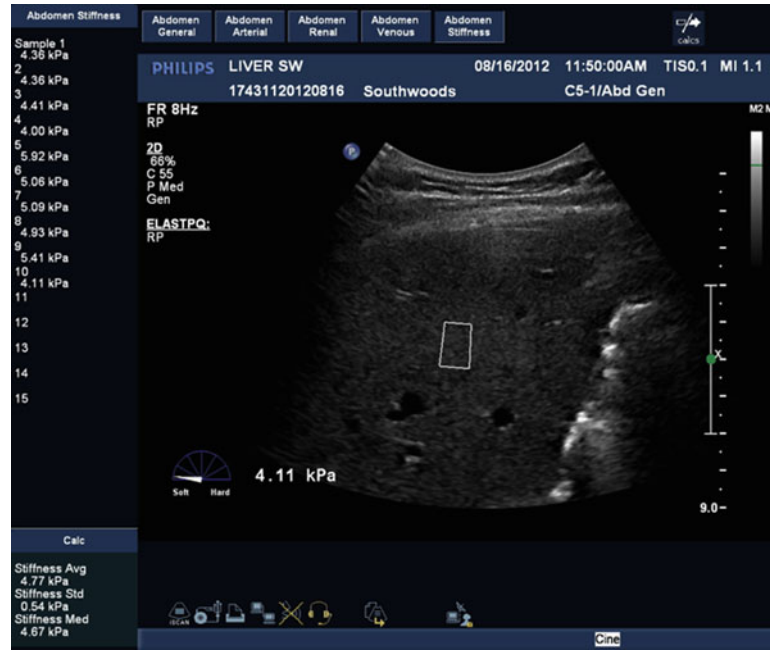

Fig. 21.20 Shear wave elastography of a 28-year-old with chronic hepatitis C infection. The stiffness average of 4.77 kPa is consistent with the patient's liver biopsy result of mild fibrosis. *White rectangle* shows field of view (FOV) where the measurement is taken

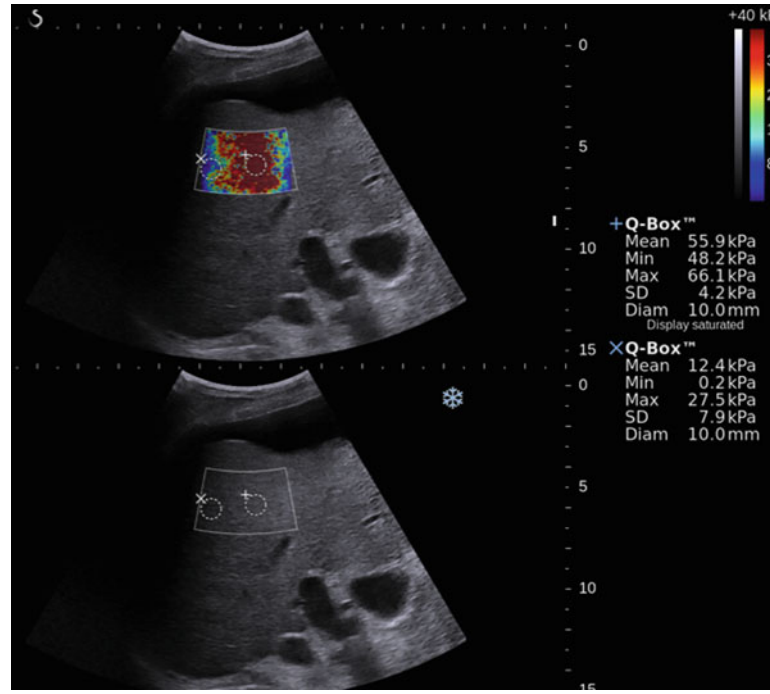

Fig. 21.21 The shear wave elastogram of a 64-year-old male with advanced alcohol-induced cirrhosis confirms a marked stiff liver with a kPa value of 55.9. *White circles* are the field of view (FOV) where the measurement of stiffness is taken

for evaluation of chronic liver disease. Potential uses of this technique include liver cirrhosis suspected but not obvious on B-mode ultrasound, evaluation of patients with chronic hepatitis C, and follow-up of patients to detect a progression of liver disease and initiate treatment.

21.4 Prostate

Prostate cancer (PC), usually adenocarcinoma of the prostate, is the commonest malignancy in American men (excluding skin cancers) and is second only to lung cancer as a cause of cancer-related

death [50]. However, among men diagnosed with the disease, 93 % will survive for at least 5 years and 72 % for at least 10 years [50].

Prostate-specific antigen (PSA), measured in serum, has been used as a screening test for PC, with PSA levels above 4.0 ng/mL considered abnormal. In addition to adenocarcinoma, a variety of benign diseases of the prostate (e.g., acute prostatitis and benign prostatic hypertrophy) as well as prostatic instrumentation will elevate PSA levels, so false-positive PSA results are common. On the other hand, about 20 % of PC will present with PSA <4.0 ng/mL [51, 52]. A commonly used screening protocol for PC combines serum PSA measurement with digital rectal examination (DRE). The positive predictive value (PPV) of this combination is quoted as 60.6 %, an improvement over DRE alone (PPV 31.4 %) or PSA alone (PPV 42.1 %) [51, 53]. Transrectal ultrasound (TRUS)-guided prostate biopsies are then used to evaluate those patients identified as abnormal by this screening protocol. When sextant biopsies are employed, only 25 % of these patients will have at least one positive biopsy, while the biopsy technique will fail to detect tumor in at least 25 % of patients proven subsequently to have PC [54, 55].

T2-weighted MRIs and MR spectroscopy (MRS) are also used to diagnose PC. The weaknesses of MRIs are their low sensitivities and their inability to accurately detect tumors smaller than 1 cm in diameter [56, 57]. MRS also has trouble detecting small tumors due to the relatively small effect on metabolites [58]. Multiparametric MRI (MP-MRI) is increasingly being used for tumor detection and localization [59–63]. However, while its sensitivity is high, its specificity is low, particularly for the detection of small lesions with Gleason scores below 6. Contrast-enhanced ultrasound (CEUS) is also being evaluated for detection and characterization of prostate cancer [64]. The current set of imaging modalities are not sufficient to properly diagnose PC. One possible solution to this problem is arising in the form of elasticity imaging or elastography.

The prostate gland is divided into four zones of anatomy, the peripheral zone, central zone, transitional zone, and periurethral zone. The peripheral zone is disk shaped, is located anterolaterally, and occupies about 70 % of the prostate. In this zone 70–80 % of prostate cancer arises and is the prime target for prostatic surveillance. The central zone is wedge shaped and is located between the urethra and the peripheral zone. It occupies about 25 % of the prostate and is rarely the site of prostate cancer. The transitional zone is made up of two separate lobes adjacent to the anterior prostatic urethra. It comprises only 5 % of the prostate, but is significant because this is the area in which benign prostatic hypertrophy arises in a majority of men later in life. The remaining 10–20 % of prostate cancer arises in the transition zone [65].

21.4.1 Strain Elastography

For SE of the prostate, the FOV should cover the entire gland and surrounding tissue. A strain ratio between normal and abnormal tissue can be used for semiquantitative analysis. Minimal amounts of pressure should be used in performing the exam. Studies using SE have demonstrated a sensitivity and specificity of 55–70 %, PPV of 57–85 %, and a NPV of 72–87 % (11–13). There is controversy of the inability to differentiate PC from chronic prostatitis [66]. SE has been reported to improve biopsy guidance [67]; a well-designed study did not confirm these results [68].

21.4.2 Shear Wave Elastography

In a single-center prospective study [69] of 53 patients using shear wave imaging with 26 foci of cancer detected in 11 of the 53 patients (20.7 %) Barr found excellent result in lesion detection and characterization in the peripheral zone. The kPa value of cancers ranged from 30 to 110 with mean value of 58.0 ± 20.7. Benign lesions had kPa values ranging from 9 to 107 with a mean value of 21.5 ± 11.5. The results are summarized in Table 21.2. Similar results have been obtained by Correas et al. [70, 71]. Based on the ROC curve, a value of 37 kPa was used as the cutoff between benign and malignant. This produced a sensitivity of 96.2 % (25/26), specificity of

Table 21.2 Summary of results

Number	Pathology	Min kPa	Max kPa	Mean kPa	ST. Dev
242	Benign	9	107	21.2	11.8
21	Atypia	14	38	20.6	5.3
26	Cancer	30	110	58.0	20.7
13	Acute inflammation	9	28	19.5	5.5
16	Chronic inflammation	13	63	27.3	15.5

96.2 % (281/292), positive predictive value (PPV) of 69.4 % (25/36), and negative predictive value (NPV) of 99.6 % (281/282). False positives (6/11, 55 %) were secondary to calcifications noted on B-mode in benign tissue.

The kPa value of PC was statistically significant than each of the benign categories: cancer vs. benign ($p<0.0001$), cancer vs. atypia ($p<0.0001$), cancer vs. acute inflammation ($p<0.0001$), and cancer vs. chronic inflammation ($p<0.0001$). The kPa value between benign lesions were all statistically nonsignificant: benign vs. atypia ($p=0.818$), benign vs. acute inflammation ($p=0.606$), benign vs. chronic inflammation ($p=0.0509$), and acute inflammation vs. chronic inflammation ($p=0.096$).

There were 51 nodules noted on B-mode. Of these 6/51 (11.8 %) were malignancies on pathology. 43/45 (95.6 %) benign lesions were classified as benign on SWE and 6/6 (100 %) malignant lesions were classified as malignant on SWE. There were two false positives, both benign lesions with calcifications. This corresponds to a sensitivity of 100 %, specificity of 95.6 %, PPV of 75 %, and NPV of 100 % in SWE predicting malignancy in nodules detected in B-mode.

At the sextant level, to obtain 100 % sensitivity, a cutoff value of 30 kPa is required. At the patient level (patient with cancer of 30 kPa also had two other PC foci with kPa level of 40), if a cutoff of 40 kPa was used, all cancers would have been detected and the positive biopsy rate would be 11/22 (50 %) compared to 11/53 (20.8 %) without SWE, a 140 % increase in the positive biopsy rate.

In the study by Correas et al. [71], he found lesion to background prostate tissue was more discriminatory as it takes into account the increased stiffness of the peripheral zone from calcification and chronic prostatitis. The ratio between the nodule and the adjacent peripheral gland for benign and malignant was 1.5 ± 0.9 and 4.0 +/- 1.9, respectively ($p<0.002$).

One limitation is that shear waves are not generated greater than 3–4 cm. In a large prostate this may not penetrate deep enough to measure the entire peripheral zone. Figure 21.22 is a benign prostate gland in a 74-year-old black male who presented with a PSA of 12.3. His PSA was 8.0 five years earlier. DRE was unremarkable and sextant biopsy was negative. B-mode ultrasound was negative with a prostate volume of 26 cc. On SWE the peripheral zone is blue throughout corresponding to a low (<20 kPa) shear wave velocity.

Figure 21.23 is a selected image from a 65-year-old white male patient who presents with a PSA of 4.6. Firmness on the left side of the gland was present on DRE. No abnormality is identified on B-mode or color Doppler. On SWE there is a lesion with a high shear wave velocity of 119 kPa (red). Image-guided biopsy confirms a Gleason's grade 6 PC.

Figure 21.24 is a selected image from a 54-year-old white patient with a hypoechoic nodule in the peripheral zone. The nodule has a low kPa value of <20 consistent with a benign etiology. However, there is an area of high kPa value of 75 (red) suggestive of a malignancy. On image-guided biopsy, the hypoechoic nodule was benign, while the area of high stiffness was a Gleason's grade 7 prostate cancer. This highlights the clinical strength of elastic imaging. Malignant lesions can be differentiated from BPH or prostatitis as their stiffness often differs by a factor of 3 and can reach a factor of 10 in extreme cases. Elastography can also be used to guide a prostate biopsy. SWE can also be used to evaluate for extracapsular extension of tumor [69].

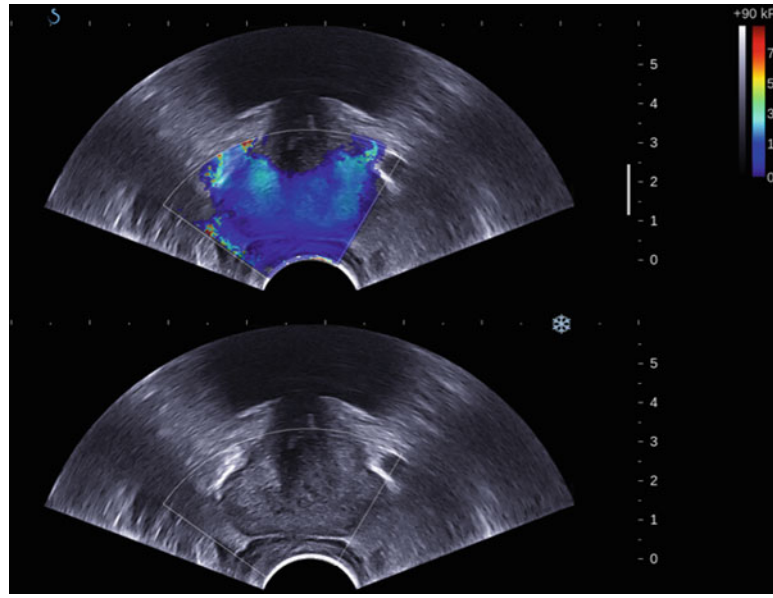

Fig. 21.22 A prostate gland of a patient who recently had an elevation of PSA from 8 to 12.3. While increased PSA may be cause for concern, elastic imaging revealed a benign prostate gland. Note the homogenous blue reading, indicative of uniform low stiffness (<20 kPa) and likely ruling out carcinoma

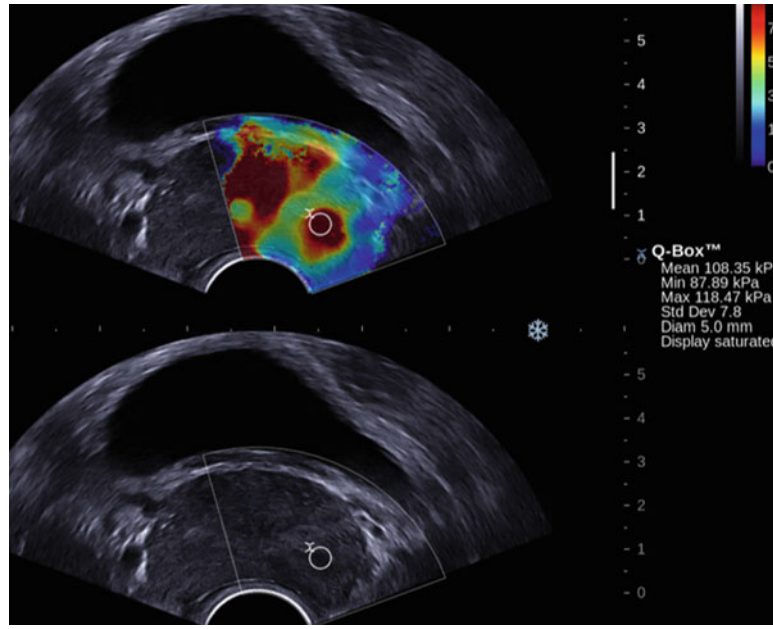

Fig. 21.23 True positive for Gleason 6 carcinoma. This patient presented with a low PSA but firm left side on digital rectal exam. B-mode imaging and color Doppler produced no findings. Shear wave elastography presented this image. Note the posterior high stiffness lesion on the left side. This lesion read at a high stiffness (119 kPa) and was confirmed on biopsy to be a Gleason 6 carcinoma

SWE is a very promising technique for the detection and biopsy guidance of PC. Of particular interest is its high negative predictive value that may reduce the need for invasive procedures such as biopsies. At present only 25–30 % of patients have a positive biopsy. In the study by Barr et al. [69], the use of SWE could have decreased the biopsy rate by 53 %. By assuming lesions with calcifications noted on B-mode are benign, the biopsy rate could have been decreased by 68.8 %.

Transrectal SWE of the prostate has the potential to become the primary first line imaging modality for detection of PC. US elastography has advantages over MRI having lower cost, increased availability, no need for contrast agent,

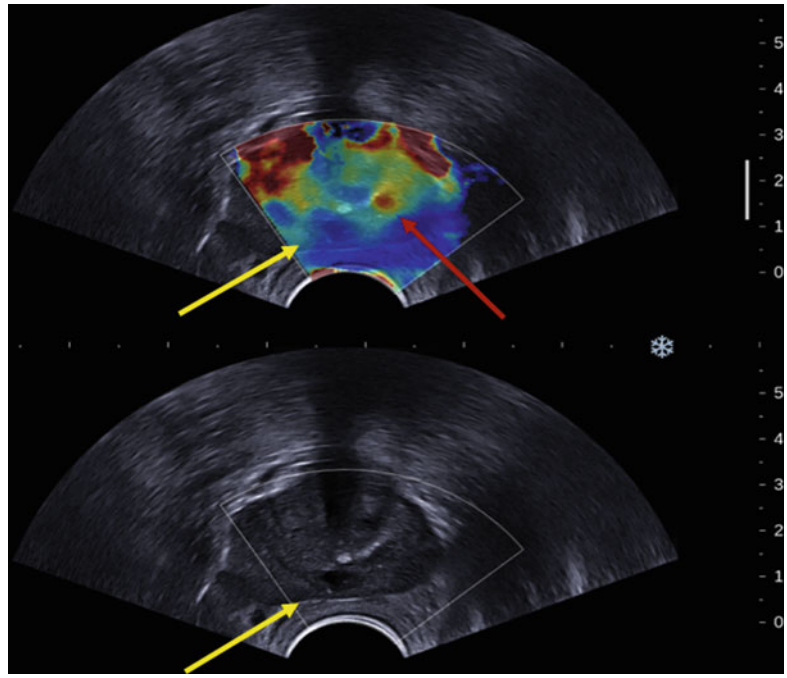

Fig. 21.24 Comparison of US and SWE. This patient presented with a hypoechoic nodule on US (black lesion with *arrow*). SWE was preformed and the nodule was found to be of low stiffness (<20 kPa). Note the blue area with the *yellow arrow*. However, another lesion was found with a high stiffness (75 kPa) and was found 17 upon biopsy to be a Gleason grade 7 prostate cancer. Note the red lesion with the *red arrow*. This highlights the clinical advantages of elastic imaging

and none of the contraindications for MRI. The U. S. Preventive Services Task Force recently advised not to recommend PSA screening because of possible complications of the low positive biopsy rate (20). The concern is that the risk of complications negated any benefit for detection of PC. The addition of SWE to PSA and DRE PC screening has the potential to improve the risk/benefit ratio favoring screening.

21.5 Thyroid

Thyroid nodules are common occurring in up to 68 % of the general population [72]. The majority of thyroid nodules are benign (colloid nodule, follicular adenoma, cyst, thyroiditis), but 5–15 % are malignant (papillary, follicular, medullary, or anaplastic carcinoma). There are four types of malignancies: papillary (86 %), follicular (9 %), medullary (2 %), and anaplastic (1 %).

Conventional B-mode ultrasound is the first procedure to help differentiate benign from malignant nodules. Ultrasound features associated with malignancy are microcalcifications, hypoechogenicity, intra-nodular vascularity, irregular margins, and absent halo sign.

Although all are poorly predictive of malignancy, in combination their specificity increases.

After assessment with ultrasound, suspicious lesions are biopsied under FNA for diagnosis.

FNA provides useful results in 65–75 % of cases. Approximately 60–70 % of aspirates prove to be benign, 5 % are positive for papillary cancer, and 5–15 % remain inconclusive. The remaining 15–25 % remain indeterminate or suspicious.

Both SE and SWE have been shown to improve characterization of thyroid masses.

21.5.1 Strain Elastography

Most benign and malignant thyroid pathology is "stiffer" than normal thyroid. Therefore, most lesions appear stiffer than normal thyroid. The size changes observed in breast cancer do not occur in thyroid masses. Several studies have been performed using different methods to characterize thyroid nodules on strain elastography. Asteria et al. [73] utilized a pattern classification to evaluate thyroid nodules. That classification was performed using a color map of red as soft and blue as hard. The classifications were 1 a

nodule that displays homogeneously green, 2 a nodule that displays predominantly in green with a few blue areas, 3 a nodule that displays predominately in blue with few green areas, and 4 a nodule that displays completely in blue. They found that sensitivity and specificity of the US elastography for thyroid cancer diagnosis were 94.1 (16/17) and 81 % (56/69), respectively. The positive and negative predictive values were 55.2 (16/29) and 98.2 % (56/57), respectively. The accuracy of the technique was 83.7 %. A similar 5-point scale has been proposed by Rago et al. [74]. In their series of 92 patients, they found that the elasticity scores 4–5 were highly predictive of malignancy ($p<0.0001$), with a sensitivity of 97 %, a specificity of 100 %, a positive predictive value of 100 %, and a negative predictive value of 98 %. They suggest elastography is extremely helpful in cases of indeterminate cytology. However, Moon et al. [75] in a study of 703 solid thyroid nodules of which 217 (30.8 %) were malignant found elastography alone, as well as the combination of elastography and gray-scale US, showed inferior performance in the differentiation of malignant and benign thyroid nodules compared to gray-scale US features. In another article Moon et al. [76] determined that a very hard lesion on the color scale was an independent factor for predicting pathologic extra-thyroidal extension on pathology.

In order to semiquantify the stiffness of tissue, the ratio of strain of normal thyroid gland/nodule strain was evaluated by Lyshchik et al. [77]. They determined that a ratio of >4 was the strongest independent factor of malignancy ($p<0.001$) with a 96 % specificity and 86 % sensitivity. The strain ratio is often difficult to obtain if an image with normal thyroid and the mass cannot be obtained secondary to lesion size or if there are multiple.

Vorlander et al. [78] used strain values to evaluate 309 lesions. Three measuring groups were formed: hard (<0.15), intermediate (0.16–0.3), and soft (>0.31). The strain rated from 0.01 to 0.84 (mean 0.26 ± 0.13). A total of 50 thyroid malignancies (35 papillary carcinoma, 9 medullary carcinoma, and 6 follicular carcinoma) were evaluated. Patients (81) were within the hard group, 35 of them (43.2 %) had thyroid cancer (TC) in final histology. Out of 132 patients in the intermediate group, 15 patients had TC (11.4 %). All 96 patients from the soft group showed benign histological results (NPV 100 %). Seventy percent of patients with TC were within the hard group (PPV 42 %). These results were highly significant ($p<0.001$). Coarse calcifications and cystic nodules did not yield reliable measurements and therefore are not suitable for evaluation.

Cantisani et al. [79] evaluated 97 patients with US features, color Doppler pattern, and strain ratio values. Sensitivity and specificity of hypoechogenicity, irregular margins or suspicious halo features, CDUS blood flow pattern, and strain ratio in the diagnosis of malignant nodules were 56.8, 62.2, 54.1 and 97.3 and 71.7, 93.3, 28.3, and 91.7 %, respectively. Elastography was more sensitive and specific than all ultrasonographic features in predicting malignancy of the thyroid nodules ($p<0.0001$). According to elastographic features, the lesions characterized by strain ratio ≥2 were highly likely to be of malignant nature ($p<0.0001$, O.R. 396, 95 %, CI: 44–3530).

Dighe et al. [80] evaluated another method comparing the ratio of highest strain value near carotid artery to the lowest nodule strain. With this technique they determined that a stiffness index of 18 corresponds to a sensitivity of 87.8 % and specificity of 77.5 %.

Bojunga et al. [81] performed a meta-analysis on 8 published studies with 639 nodules. The meta-analysis required FNA or surgical pathology. Various techniques and vendor equipment have been used in the individual studies. 381/639 (59.6 %) had histopathology proof. The mean sensitivity were 92 % (88–96 %) and the mean specificities were 90 % (85–95), with 153/639 (24 %) lesions malignant. This was a highly selected group of patients with a 24 % malignancy rate. The results may not be as significant with a standard population.

An example of SE using strain ratio of a thyroid papillary cancer is presented in Fig. 21.25.

21.5.2 Shear Wave Elastography

Sebag et al. [72] evaluated 146 nodules from 93 patients with SWE of which 29/146 (19.9 %) were malignant. The malignant lesions had a kPa

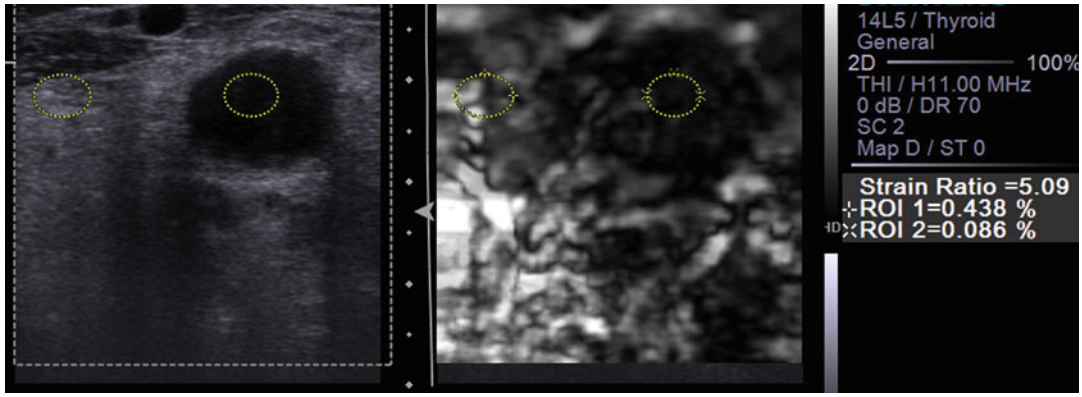

Fig. 21.25 Strain elastogram of a 68-year-old woman with a palpable thyroid mass confirms the presence of nodule that was a papillary carcinoma on FNA. The nodule has a strain ratio of 5. The strain ratio was calculated by placing an FOV (*white dotted circle*) over the nodule and normal thyroid tissue and calculating the ratio of stiffness of the lesion to normal thyroid tissue

value of 150 ± 95 kPa (30–356 kPa), while benign lesions had kPa values of 36 ± 30 kPa (0–200 kPa), $p < 0.001$. Using a cutoff of 65 kPa, there was a sensitivity of 85.2 % and specificity of 93.9 %.

Friedrich-Rust et al. [82] in a study of 60 patients found that the median shear wave velocity of ARFI imaging in the healthy nodule-free thyroid gland as well as in benign and malignant thyroid nodules was 1.98 m/s (range 1.20–3.63 m/s), 2.02 m/s (range 0.92–3.97 m/s), and 4.30 m/s (range 2.40–4.50 m/s), respectively. While no significant difference in median shear wave velocity was found between healthy thyroid tissue and benign thyroid nodules, a significant difference was found between malignant thyroid nodules on the one hand and healthy thyroid tissue ($p = 0.018$) or benign thyroid nodules ($p = 0.014$) on the other hand. Specificity of ARFI imaging for the differentiation of benign and malignant thyroid nodules was comparable with SE (91–95 %).

Both SE and SWE provide additional information on thyroid lesion characterization.

Several methods have been used to determine differences between benign and malignant.

Most studies have been small with small numbers of follicular cancers, medullary cancers, and anaplastic cancers. No studies have compared the various techniques in the same patient population. There is significant overlap of benign and malignant lesions that limits the technique in lesion characteristic. With the overlap of elastography characteristic of benign and malignant lesions, the combination of elastography with B-mode and color Doppler characteristic may be required to improve lesion characterization. Figure 21.26 is an example of a benign thyroid lesion with a maximum kPa of 26.

21.6 Pancreatic Masses

Pancreatic masses have been evaluated using elastography using both an endoscopic and transabdominal approach.

With the endoscopic approach, a classification based on a color scale SE has been used (red as soft and blue as hard). The normal pancreas is soft and homogeneous coded green [83–88]. Benign inflammatory pancreatic pathology can appear as with a honeycomb appearance predominately blue [83, 86, 87], a heterogeneous mixed color pattern with predominately green pattern [83, 86, 87], or a homogeneously green pattern [83, 87]. Adenocarcinoma has a homogeneous blue pattern (stiff) or a heterogeneous predominantly blue lesion [83–87]. Pancreatic neuroendocrine tumors (PNET) have been reported to have a predominantly blue honeycomb pattern, a homogeneous blue pattern, a green central area

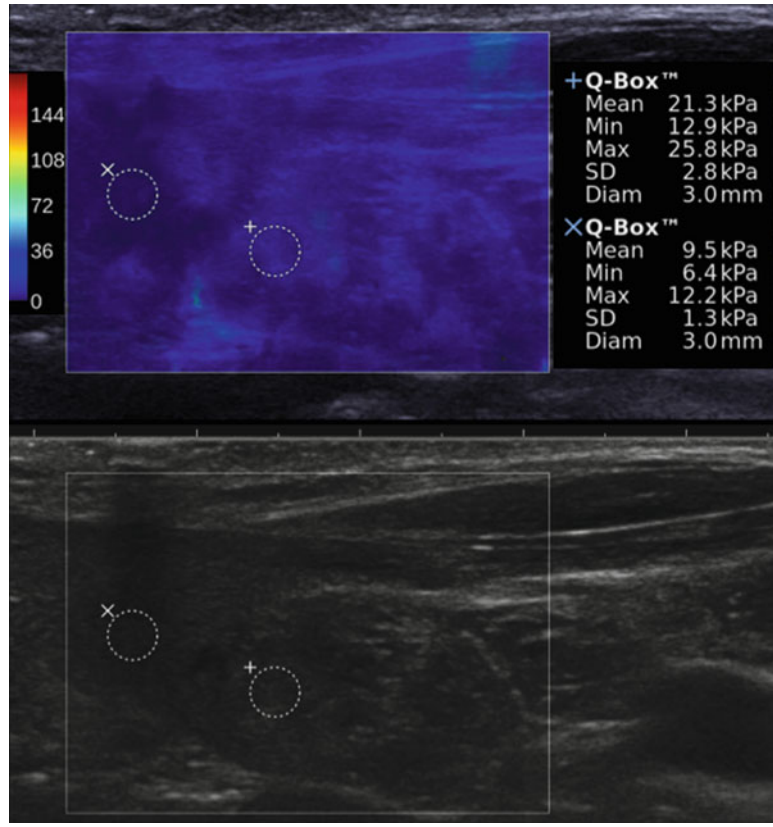

Fig. 21.26 Shear wave elastogram of an FNA-proven benign thyroid nodule which has a low kPa value of 21 suggestive of a benign lesion. *White circles* are the field of view (FOV) where the measurement of stiffness is taken

surrounded by blue tissue, or a homogeneous green pattern [83].

Preliminary studies suggest that a homogeneous green pattern can be used to exclude malignancy [84]. However, the clinical usefulness of this technique in distinguishing benign from malignant pathologies is limited. Inflammatory lesions of the pancreas can be hard or soft depending on the stage of the inflammation. Neoplasms can have necrotic areas that appear soft in contrast to the viable tumor that is hard. Itokawa found the strain ratio (strain of lesion compared to strain of normal pancreas) was 23.7 ± 12.7 for mass-forming pancreatitis and 39.1 ± 20.5 for pancreatic cancer [86].

The use of SWE using the point quantification method may be able to distinguish serous from mucinous malignancies. Serous fluid has low viscosity and does not propagate shear waves. A value of x.xx or 0 is obtained depending on vendor indicating shears waves were not identified in the fluid. However, mucinous cystic lesions have high viscosity that does propagate shear waves. With cystic lesions that contain mucin, a shear wave velocity (expressed in m/s or kPa) will be obtained. Preliminary results using this technique appear promising [89, 90]. The study of D'Onofrio included 14 mucinous cystadenomas, 4 pseudocysts, 3 intraductal papillary-mucinous neoplasms, and 2 serous cystadenomas. The values obtained ranged from XXXX/0 to 4.85 m/s in mucinous cystadenomas, from XXXX/0 to 3.11 m/s in pseudocysts, and from XXXX/0 to 4.57 m/s in intraductal papillary-mucinous neoplasms. In serous cystadenomas all values measured were XXXX/0 m/s. Diagnostic accuracy in benign and non-benign differentiation of pancreatic cystic lesions was 78 %.

Figure 21.27a demonstrates the use of point shear wave quantification and Fig. 21.27b demonstrates the use strain imaging in a patient with acute on chronic pancreatitis.

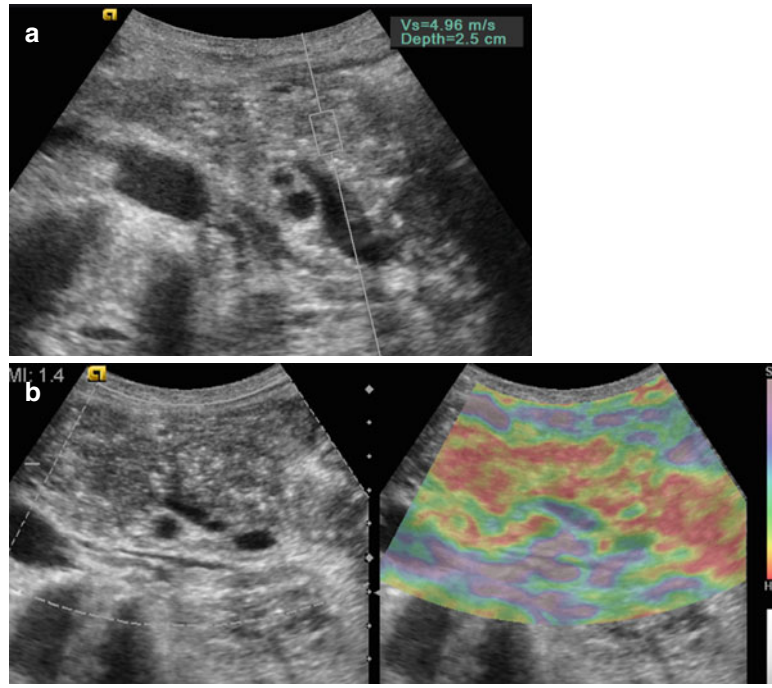

Fig. 21.27 In this patient who presented with abdominal pain, B-mode imaging shows an enlarged pancreas with irregular contour and echotexture, multiple calculi, and mild peripancreatic edema. There is increased shear wave velocity of 4.96 m/s (**a**) suggesting acute pancreatitis. The corresponding strain image (**b**) shows increased stiffness (color scale with *red* as hard) though out the entire pancreatic body and tail also suggestive of acute inflammation (Courtesy of Dr. A. Mateen, Hyderabad, India)

21.7 Gynecological Malignancies

Both strain elastography and shear wave elastography have become recently available on endocavitary probes. No studies evaluating the techniques for characterization of masses as benign or malignant have been published. However, excellent images have been obtained proving proof of concept (Figs. 21.28 and 21.29). Early evaluations are being performed to better define the location and tissue character of uterine fibroids to better determine appropriate treatment

21.8 Testicular Masses

Ultrasound including color Doppler is the imaging modality of choice for evaluating scrotal abnormalities.

A study evaluating testicular lesions identified on B-mode ultrasound found that benign and pseudo-nodules masses of the testes were very soft. Using the Ueno scale they were classified as a score of 1. Malignant lesions were stiff and had scores of 4 or 5. Using this scale they found a 87.5 % sensitivity, 98.2 % specificity, 93.3 % positive predictive value, a 96.4 % negative predictive value, and 95.8 % accuracy in differentiating intratesticular malignant from benign lesions [91]. A small study evaluating epidermoid cysts found all lesions to be very stiff with a strain ratio mean of 43 [92].

21.9 Musculoskeletal Tumors

Elastography has been shown helpful in evaluation of nonmalignant pathology of the musculoskeletal system. Little evaluation of elastography on neoplastic lesions of musculoskeletal system has been performed.

21.10 Lymph Nodes

Ultrasound is frequently used to evaluate lymph nodes particularly if they are in superficial locations. On B-mode ultrasound lymph nodes have a hypoechoic cortex that should be relatively uniform in thickness and has a hyperechoic hilum.

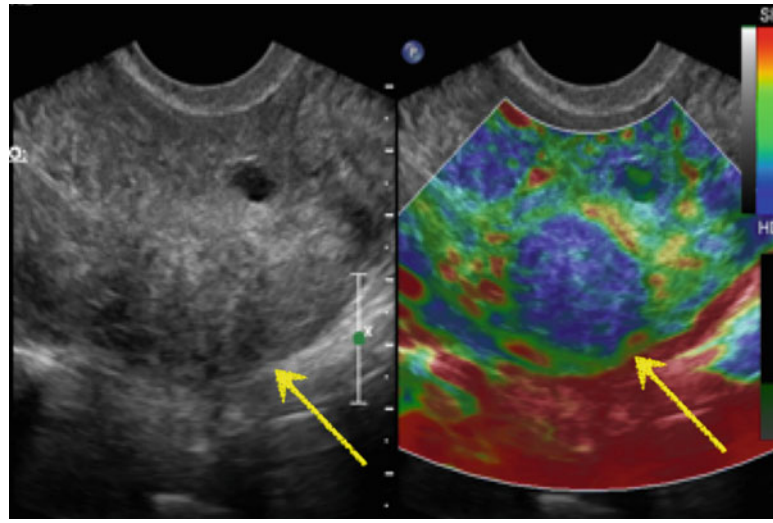

Fig. 21.28 Endocavitary scan of an enlarged uterus. On the B-mode image, there is a subtle uterine fibroid (*yellow arrow*). The fibroid is much better visualized on the SE image. The fibroid is color coded blue (very stiff) compared to the uterus which is coded *red* and *green* (soft)

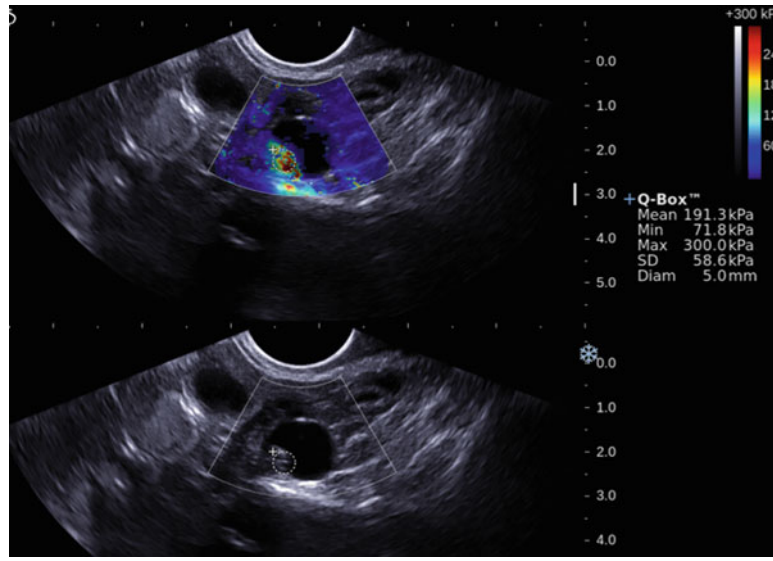

Fig. 21.29 Endocavitary SWE image for a patient with a complex cystic left ovarian mass. The solid component of the lesion has a high kPa value of 191. On surgical pathology, the lesion was a benign cystadenoma of the ovary. *White circles* are the field of view (FOV) where the measurement of stiffness is taken

On color Doppler both the arterial supply and venous supply enter and exit the hilum. Focal thickness or irregularity of the cortex, loss of the fat in the hilum, or if blood flow enter the lymph node at a site other than the hilum are signs suggestive of malignancy.

Several early studies using strain have demonstrated an accuracy of between 73 and 93 % for characterization of lymph nodes as benign or malignant based on their stiffness [93]. These studies have used a color scale to determine relative stiffness and others have used the strain ratio of the lymph node to adjacent muscle. A small study [94, 95] of SWE for cervical lymphadenopathy found that malignant nodes were stiffer (median 25.0 kPa, range 6.9–278.9 kPa) than benign nodes (median 21.4 kPa, range 8.9–30.2 kPa). A cutoff of 30. 2 kPa attained the highest accuracy of 61.8 %, corresponding to 41.9 % sensitivity and 100 % specificity.

Conclusion

There are presently two types of ultrasound elastography, SE and SWE. Both have advantages and disadvantages. Early work suggests that both techniques can have a significant

impact on classification of breast lesions as benign or malignant. The breast has unique elastographic properties as compared to other organs. There is little overlap of elastic properties between benign and malignant breast lesions allowing for high sensitivity and specificity. In other organs (liver, thyroid, prostate) there appears to be some overlap of the elastic properties of benign and malignant lesions decreasing the clinical utility of the technique as compared to breast. In prostate the overlap is small and SWE appears to be a promising method of detection and characterization of PC in the peripheral zone. In the liver and thyroid, the overlap of elastic properties between benign and malignant lesions in early studies appears to be significant enough to limit the clinical utility of the technique.

Ultrasound elastography is a new technique and continues to evolve. The availability of the technology is now becoming widely available and a rapid increase evaluation of this technology for oncologic imaging is expected.

References

1. Emerson K. Diseases of the breast. In: Thorn W, Wintrobe MM, Adams RD, editors. Principals of internal medicine. 7th ed. New York: McGraw-Hill; 1974. p. 582–7.
2. Barr R. Breast. In: Calliada M, Calliada F, Ferraiolo G, Filice C, editors. Sono-elastography main clinical applications. Pavia: Edizioni Medico Scientifiche; 2012. p. 49–68.
3. Barr RG. Shear wave imaging of the breast: still on the learning curve. J Ultrasound Med. 2012;31(3): 347–50.
4. Barr RG. Sonographic breast elastography: a primer. J Ultrasound Med. 2012;31(5):773–83.
5. Barr RG, Zhang Z. Effects of precompression on elasticity imaging of the breast: development of a clinically useful semiquantitative method of precompression assessment. J Ultrasound Med. 2012;31(6):895–902.
6. Fahey BJ, et al. Acoustic radiation force impulse imaging of the abdomen: demonstration of feasibility and utility. Ultrasound Med Biol. 2005;31(9):1185–98.
7. Nightingale K, et al. Acoustic radiation force impulse imaging: in vivo demonstration of clinical feasibility. Ultrasound Med Biol. 2002;28(2):227–35.
8. Rouze NC, et al. Robust estimation of time-of-flight shearwave speed using a radon sum transformation. IEEE Trans Ultrason Ferroelectr Freq Control. 2010;57:2662–70.
9. Cosgrove DO, et al. Shear wave elastography for breast masses is highly reproducible. Eur Radiol. 2012;22(5):1023–32.
10. Bluemke DA, et al. Magnetic resonance imaging of the breast prior to biopsy. JAMA. 2004;292(22):2735–42.
11. Morrow M. Magnetic resonance imaging in breast cancer: one step forward, two steps back? JAMA. 2004;292(22):2779–80.
12. Hilton SV, et al. Real-time breast sonography: application in 300 consecutive patients. AJR Am J Roentgenol. 1986;147(3):479–86.
13. Jellins J, et al. Detection and classification of liquid-filled masses in the breast by gray scale echography. Radiology. 1977;125(1):205–12.
14. Stavros AT, et al. Solid breast nodules: use of sonography to distinguish between benign and malignant lesions. Radiology. 1995;196(1):123–34.
15. ACR. American College of Radiology Breast Imaging Reporting and Data System (BIRADS) Ultrasound. 4th ed. 1st ed. Reston: American College of Radiology; 2003.
16. Tanter M, et al. Quantitative assessment of breast lesion viscoelasticity: initial clinical results using supersonic shear imaging. Ultrasound Med Biol. 2008;34(9):1373–86.
17. Frey H. Realtime elastography. A new ultrasound procedure for the reconstruction of tissue elasticity. Radiologe. 2003;43(10):850–5.
18. Ophir J, et al. Elastography: a quantitative method for imaging the elasticity of biological tissues. Ultrason Imaging. 1991;13(2):111–34.
19. Samani A, et al. Elastic moduli of normal and pathological human breast tissues: an inversion-technique-based investigation of 169 samples. Phys Med Biol. 2007;52(6):1565–76.
20. Krouskop TA, et al. Elastic moduli of breast and prostate tissues under compression. Ultrason Imaging. 1998;20(4):260–74.
21. Hall TJ, et al. In vivo real-time freehand palpation imaging. Ultrasound Med Biol. 2003;29(3):427–35.
22. Barr RG. Real-time ultrasound elasticity of the breast: initial clinical results. Ultrasound Q. 2010;26(2):61–6.
23. Barr RG, et al. Evaluation of breast lesions using sonographic elasticity imaging: a multicenter trial. J Ultrasound Med. 2012;31(2):281–7.
24. Itoh A, et al. Breast disease: clinical application of US elastography for diagnosis. Radiology. 2006;239(2):341–50.
25. Ueno EIA. Diagnosis of breast cancer by elasticity imaging. Eizo Joho Med. 2004;36:2–6.
26. Park JS, Moon WK. Inter and intraobserver agreement in the interpretation of ultrasound elastography of breast lesions. Paper presented at Radiological Society of North America 93rd scientific assembly and annual meeting, Chicago; 2007.

27. Chiorean A, et al. Short analysis on elastographic images of benign and malignant breast lesions based on color and hue parameters. Ultraschall Med. 2008;Suppl 1:OP2.13.
28. Chiorean AD, et al. Real-time ultrasound elastography of the breast: state of the art. Med Ultrason. 2008;10:73–82.
29. Duma M, et al. Breast Lesions: correlations between ultrasound BI-RADS classification and UENO-ITOH elastography score. Ultraschall Med. 2008;Suppl 1:OP2.12.
30. Cho N, et al. Nonpalpable breast masses: evaluation by US elastography. Korean J Radiol. 2008;9(2):111–8.
31. Scaperrotta G, et al. Role of sonoelastography in non-palpable breast lesions. Eur Radiol. 2008; 18(11):2381–9.
32. Tan SM, et al. Improving B mode ultrasound evaluation of breast lesions with real-time ultrasound elastography–a clinical approach. Breast. 2008;17(3): 252–7.
33. Zhi H, et al. Semi-quantitating stiffness of breast solid lesions in ultrasonic elastography. Acad Radiol. 2008;15(11):1347–53.
34. Zhu QL, et al. Real-time ultrasound elastography: its potential role in assessment of breast lesions. Ultrasound Med Biol. 2008;34(8):1232–8.
35. Thomas A, et al. Significant differentiation of focal breast lesions: calculation of strain ratio in breast sonoelastography. Acad Radiol. 2010;17(5):558–63.
36. Waki K, et al. Investigation of strain ratio using ultrasound elastography technique. Paper presented at proceedings of isicE 2007, Kitakyushu. 2007.
37. Zhi H, et al. Ultrasonic elastography in breast cancer diagnosis: strain ratio vs 5-point scale. Acad Radiol. 2010;17(10):1227–33.
38. Ueno E, et al. New quantitative method in breast elastography: fat lesion ratio (FLR). Paper presented at Radiological Society of North America 93rd scientific assembly and annual meeting, Chicago, 25–30 Nov 2007.
39. Barr RG, Lackey AE. The utility of the "bull's-eye" artifact on breast elasticity imaging in reducing breast lesion biopsy rate. Ultrasound Q. 2011;27(3):151–5.
40. Nakashima K, Moriya T. Comprehensive ultrasound diagnosis for intraductal spread of primary breast cancer. Breast Cancer. 2013;20(1):3–12.
41. Berg WA, et al. Shear-wave elastography improves the specificity of breast US: the BE1 multinational study of 939 masses. Radiology. 2012;262(2):435–49.
42. Chang JM, et al. Clinical application of shear wave elastography (SWE) in the diagnosis of benign and malignant breast diseases. Breast Cancer Res Treat. 2011;129(1):89–97.
43. Athanasiou A, et al. Breast lesions: quantitative elastography with supersonic shear imaging–preliminary results. Radiology. 2010;256(1):297–303.
44. Evans A, et al. Quantitative shear wave ultrasound elastography: initial experience in solid breast masses. Breast Cancer Res. 2010;12(6):R104.
45. Bai M, et al. Virtual touch tissue quantification using acoustic radiation force impulse technology: initial clinical experience with solid breast masses. J Ultrasound Med. 2012;31(2):289–94.
46. Yu H, Wilson SR. Differentiation of benign from malignant liver masses with acoustic radiation force impulse technique. Ultrasound Q. 2011;27(4): 217–23.
47. Seeff LB, Hoofnagle JH. National Institutes of Health Consensus Development Conference: management of hepatitis C: 2002. Hepatology. 2002;36(5 Suppl 1):S1–2.
48. Ferraioli G, et al. Diffuse liver diseases. In: Calliada F, Canepari M, Ferraiolo G, Filice C, editors. Sonoelastography main clinical applications. Pavia: Edizioni Medico Scientifiche; 2012.
49. Yu H, Wilson SR. New noninvasive ultrasound techniques: can they predict liver cirrhosis? Ultrasound Q. 2012;28(1):5–11.
50. American Cancer Society. Cancer facts & figures. Atlanta: ACS; 2010.
51. Catalona WJ, et al. Prostate cancer detection in men with serum PSA concentrations of 2.6 to 4.0 ng/mL and benign prostate examination. Enhancement of specificity with free PSA measurements. JAMA. 1997;277(18):1452–5.
52. Gormley GJ, et al. Effect of Finasteride on prostate-specific antigen density. Urology. 1994;43(1):53–8; discussion 58–9.
53. Crawford ED. Prostate cancer awareness week: September 22 to 28, 1997. CA Cancer J Clin. 1997;47(5):288–96.
54. Cookson MM. Prostate cancer: screening and early detection. Cancer Control. 2001;8(2):133–40.
55. Stroumbakis N, et al. Clinical significance of repeat sextant biopsies in prostate cancer patients. Urology. 1997;49(3A Suppl):113–8.
56. Kwek JW, et al. Phased-array magnetic resonance imaging of the prostate with correlation to radical prostatectomy specimens: local experience. Asian J Surg. 2004;27(3):219–24; discussion 225–6.
57. Nakashima J, et al. Endorectal MRI for prediction of tumor site, tumor size, and local extension of prostate cancer. Urology. 2004;64(1):101–5.
58. Zakian KL, et al. Correlation of proton MR spectroscopic imaging with Gleason score based on step-section pathologic analysis after radical prostatectomy. Radiology. 2005;234(3):804–14.
59. Futterer JJ, et al. Prostate cancer localization with dynamic contrast-enhanced MR imaging and proton MR spectroscopic imaging. Radiology. 2006;241(2):449–58.
60. Girouin N, et al. Prostate dynamic contrast-enhanced MRI with simple visual diagnostic criteria: is it reasonable? Eur Radiol. 2007;17(6):1498–509.
61. Lemaitre L, et al. Dynamic contrast-enhanced MRI of anterior prostate cancer: morphometric assessment and correlation with radical prostatectomy findings. Eur Radiol. 2009;19(2):470–80.

62. Lim HK, et al. Prostate cancer: apparent diffusion coefficient map with T2-weighted images for detection–a multireader study. Radiology. 2009;250(1): 145–51.
63. Villers A, et al. Dynamic contrast enhanced, pelvic phased array magnetic resonance imaging of localized prostate cancer for predicting tumor volume: correlation with radical prostatectomy findings. J Urol. 2006;176(6 Pt 1):2432–7.
64. Wink M, et al. Contrast-enhanced ultrasound and prostate cancer; a multicentre European research coordination project. Eur Urol. 2008;54(5):982–92.
65. Amin M, et al. Zonal anatomy of the prostate. Annuals of KEMU. 2010;16:3.
66. Kapoor A, et al. Real-time elastography in the detection of prostate cancer in patients with raised PSA level. Ultrasound Med Biol. 2011;37(9):1374–81.
67. Aigner F, et al. Value of real-time elastography targeted biopsy for prostate cancer detection in men with prostate specific antigen 1.25 ng/ml or greater and 4.00 ng/ml or less. J Urol. 2010;184(3):913–7.
68. Kamoi K, et al. The utility of transrectal real-time elastography in the diagnosis of prostate cancer. Ultrasound Med Biol. 2008;34(7):1025–32.
69. Barr RG, et al. Shear wave ultrasound elastography of the prostate: initial results. Ultrasound Q. 2012;28(1):13–20.
70. Correas JM, et al. Transrectal quantitative shear wave elastography: application to prostate cancer a feasibility study. Vienna: European Congress of Radiology; 2011.
71. Correas JM, et al. Quantitative shear wave elastography of the prostate: correlation to sextant and targeted biopsies. Vienna: European Congress of Radiology; 2012.
72. Sebag F, et al. Shear wave elastography: a new ultrasound imaging mode for the differential diagnosis of benign and malignant thyroid nodules. J Clin Endocrinol Metab. 2010;95(12):5281–8.
73. Asteria C, et al. US-elastography in the differential diagnosis of benign and malignant thyroid nodules. Thyroid. 2008;18(5):523–31.
74. Rago T, et al. Elastography: new developments in ultrasound for predicting malignancy in thyroid nodules. J Clin Endocrinol Metab. 2007;92(8):2917–22.
75. Moon HJ, et al. Diagnostic performance of gray-scale US and elastography in solid thyroid nodules. Radiology. 2012;262(3):1002–13.
76. Moon HJ, et al. Clinical implication of elastography as a prognostic factor of papillary thyroid microcarcinoma. Ann Surg Oncol. 2012;19(7):2279–87.
77. Lyshchik A, et al. Thyroid gland tumor diagnosis at US elastography. Radiology. 2005;237(1):202–11.
78. Vorlander C, et al. Real-time ultrasound elastography–a noninvasive diagnostic procedure for evaluating dominant thyroid nodules. Langenbecks Arch Surg. 2010;395(7):865–71.
79. Cantisani V, et al. Prospective evaluation of multiparametric ultrasound and quantitative elastosonography in the differential diagnosis of benign and malignant thyroid nodules: preliminary experience. Eur J Radiol. 2012;81(10):2678–83.
80. Dighe M, et al. Differential diagnosis of thyroid nodules with US elastography using carotid artery pulsation. Radiology. 2008;248(2):662–9.
81. Bojunga J, et al. Real-time elastography for the differentiation of benign and malignant thyroid nodules: a meta-analysis. Thyroid. 2010;20(10):1145–50.
82. Friedrich-Rust M, et al. Acoustic radiation force impulse-imaging for the evaluation of the thyroid gland: a limited patient feasibility study. Ultrasonics. 2012;52(1):69–74.
83. Giovannini M, et al. Endoscopic ultrasound elastography for evaluation of lymph nodes and pancreatic masses: a multicenter study. World J Gastroenterol. 2009;15(13):1587–93.
84. Hirche TO, et al. Indications and limitations of endoscopic ultrasound elastography for evaluation of focal pancreatic lesions. Endoscopy. 2008;40(11):910–7.
85. Iglesias-Garcia J, et al. EUS elastography for the characterization of solid pancreatic masses. Gastrointest Endosc. 2009;70(6):1101–8.
86. Itokawa F, et al. EUS elastography combined with the strain ratio of tissue elasticity for diagnosis of solid pancreatic masses. J Gastroenterol. 2011;46(6): 843–53.
87. Janssen J, et al. EUS elastography of the pancreas: feasibility and pattern description of the normal pancreas, chronic pancreatitis, and focal pancreatic lesions. Gastrointest Endosc. 2007;65(7):971–8.
88. Lee TH, et al. EUS elastography: advances in diagnostic EUS of the pancreas. Korean J Radiol. 2012;13 Suppl 1:S12–6.
89. D'Onofrio M, et al. Pancreatic mucinous cystadenoma at ultrasound acoustic radiation force impulse (ARFI) imaging. Pancreas. 2010;39(5):684–5.
90. D'Onofrio M, et al. Acoustic radiation force impulse (ARFI) ultrasound imaging of pancreatic cystic lesions. Eur J Radiol. 2011;80(2):241–4.
91. Goddi A, et al. Real-time tissue elastography for testicular lesion assessment. Eur Radiol. 2012; 22(4):721–30.
92. Patel K, et al. Features of testicular epidermoid cysts on contrast-enhanced sonography and real-time tissue elastography. J Ultrasound Med. 2012;31(1):115–22.
93. Bhatia KS, et al. Real-time qualitative ultrasound elastography of cervical lymph nodes in routine clinical practice: interobserver agreement and correlation with malignancy. Ultrasound Med Biol. 2010;36(12): 1990–7.
94. Bhatia K, et al. Reliability of shear wave ultrasound elastography for neck lesions identified in routine clinical practice. Ultraschall Med. 2012;33(5): 463–8.
95. Bhatia KS, et al. Shear wave elasticity imaging of cervical lymph nodes. Ultrasound Med Biol. 2012; 38(2):195–201.

Part IV

Molecular Imaging Techniques in Clinical Use and in Research

New Molecular and Functional Imaging Techniques

22

Vanessa Gómez-Vallejo, María Jiménez-González, Jordi Llop, and Torsten Reese

Contents

Abbreviations

[^{18}F]FDG	2-deoxy-2-[^{18}F]fluoro-D-glucose
ALT	Alanine transaminase
BFCs	Bifunctional chelators
BRET	Bioluminescence resonance energy transfer
CT	Computerized tomography
DNP	Dynamic nuclear polarization
ELISA	Enzyme-linked immunosorbent assay
EPR	Enhanced permeability and retention
FRET	Fluorescence resonance energy transfer
GMP	Good manufacturing practices
HPLC	High-performance liquid chromatography
ID/g	Injected dose per gram
LDH	Lactose dehydrogenase
mAbs	Monoclonal antibodies
MRI	Magnetic resonance imaging
MRS	Magnetic resonance spectroscopy
NIR	Near infrared
NPs	Nanoparticles
PD	Proton density
PDH	Pyruvate dehydrogenase
PEG	Polyethylene glycol
PET	Positron emission tomography
PHIP	Parahydrogen-induced polarization
QDs	Quantum dots

V. Gómez-Vallejo • M. Jiménez-González
J. Llop • T. Reese
Molecular Imaging Unit, CIC biomaGUNE,
San Sebastián, Spain
e-mail: vgomez@cicbiomagune.es;
mjimenez@cicbiomagune.es; jllop@cicbiomagune.es;
treese@cicbiomagune.es

A. Luna et al. (eds.), *Functional Imaging in Oncology*,
DOI 10.1007/978-3-642-40412-2_22,

SELEX	Systematic Evolution by Exponential Enrichment
SPECT	Single photon emission computed tomography
SPIO	Superparamagnetic iron oxide
SWNTs	Single-wall carbon nanotubes
T1	Longitudinal relaxation time
T2	Transverse relaxation time

22.1 Introduction

New molecular and functional imaging technologies emerge from different disciplines in science to address all aspects to diagnose and treat patients. The emerging imaging technologies combine the interest ranging from basic scientists in the field of biology, physics, and chemistry; start-ups, small, medium, and large pharmaceutical industries, as well as engineers and physicians, all thriving for the ultimate aim to improve the quality of life for people affected by cancer. Hereby, the transdisciplinary aspects for medical devices, as a diagnostic tool and ultimately as an approved drug formulation for therapy, affect the individual stakeholder differently. Whereby surrealistic nanocomposites are envisaged by academics to push the limits of technology by creativity, innovation, and curiosity and to attract grant money, pharmaceutical industries as well as regulatory authorities require scientifically sound, batch-controlled safe diagnostics and medications to ensure patient benefit. Like for most other diseases, prevention is envisaged in oncology. Preventive measures are ranging from socioeconomical policies addressing occupational health hazards, which ultimately lead to the current antismoking policies, via vaccinations for cervical cancer in female and male adolescents up to combining family history and genetic markers to outline risk factors, which aims to pretreat "perfectly young and healthy" female patients with radical surgical procedures by mastectomy.

If preventive measures have failed, ultimately, diagnostics and treatment have to result in two distinct positive effects: First, an increased survival rate; second, improvements in the quality of life. Hereby, one can argue that it does not make any sense to diagnose a disease if one is not able to treat it. In cancer research, however, one of the overarching aims in research is to diagnose cancer early, enabling new, potentially already proven therapies or surgical interventions at earlier stages before disease progression for the benefit of the patient. Paired with advances in genetics, proteomics, and metabolomics, imaging biomarkers are promising candidates to make an early differentiated diagnosis. With the power of visualizing directly abnormal tissue types, cancer diagnosis in fact requires imaging and/or surgical resection with histological confirmation. Hereby, ultrasound and chest x-ray are classically used in a setting of a general health service provider or general practitioner. Patient with initial symptoms is referred to specialists: radiologist (computerized tomography (CT) and magnetic resonance imaging (MRI)) and nuclear medicine (single photon emission computed tomography (SPECT) and positron emission tomography (PET)) often with sub-specialization in oncology. Thus, cancer diagnosis is performed using imaging.

Among all compounds with potential application in cancer diagnosis, nanosystems and particularly nanoparticles (NPs) have emerged as promising tools with an enormous potential. Their small size and large surface area give rise to the creation of multifunctional agents, which can be modified with different ligands including targeting moieties or contrast agents.

The enhanced permeability and retention (EPR) effect is an important concept to explain the preferential accumulation of nanoparticles at tumor interstitial spaces. It describes the increased permeability of tumor neovasculature and the dysfunctional lymphatic drainage system [1, 2]. Thus, nanoparticles will accumulate within the tumor (passive targeting) [3]. Liposomes extravasate from blood vessels into tumors at sizes below 400 nm [4], whereas a subsequent study recommends sizes inferior to 200 nm as more efficient [5]. Nanoparticles with sizes smaller than 100 nm should be preferably used to tumor targeting as they are small enough to escape clearance by macrophages from liver and spleen, and thus are able to circulate long enough to reach the tumor [6].

This approach has however several limitations, such as the heterogeneous permeability of the vessel walls to macromolecules throughout the tumors. Moreover, some tumors do not show the EPR effect, and this kind of targeting is quite random as well as difficult to be controlled [7–9]. To overcome these hurdles, active targeting has been increasingly used. This is achieved by conjugating nanoparticles with molecules that bind overexpressed antigens or receptors on target cancer cells [10].

Regarding the cellular uptake of ligand-coated nanoparticles, it has been demonstrated that nanoparticle diameters below 50 nm presented a greater uptake by cells compared with particles with larger diameters [11]. Also Zhang and coworkers theoretically demonstrated that the uptake rate reaches a maximum approximately at diameters of 50 nm, which was in agreement with other experimental studies [12].

22.1.1 Nanocomposites

Multifunctionalized NPs are a priori ideally suited candidates for the design of diagnostic tools with application in cancer [8].

It is clear that a very wide range of NPs which differ in size, shape, chemical composition, etc. can be created. Some NP types are schematized in Fig. 22.1. To perform an exhaustive description of all NP types is beyond the scope of this chapter; however, a brief explanation of the most commonly used NP types in imaging is provided below.

22.1.1.1 Graphene and Carbon Nanotubes

Graphene (Fig. 22.1a) is a 2-D sp^2-bonded one-atom-thick carbon sheet in which carbon atoms are arranged in a regular hexagonal pattern. Graphene can be rolled into 1-D nanotubes (single-wall carbon nanotubes, SWNTs) which

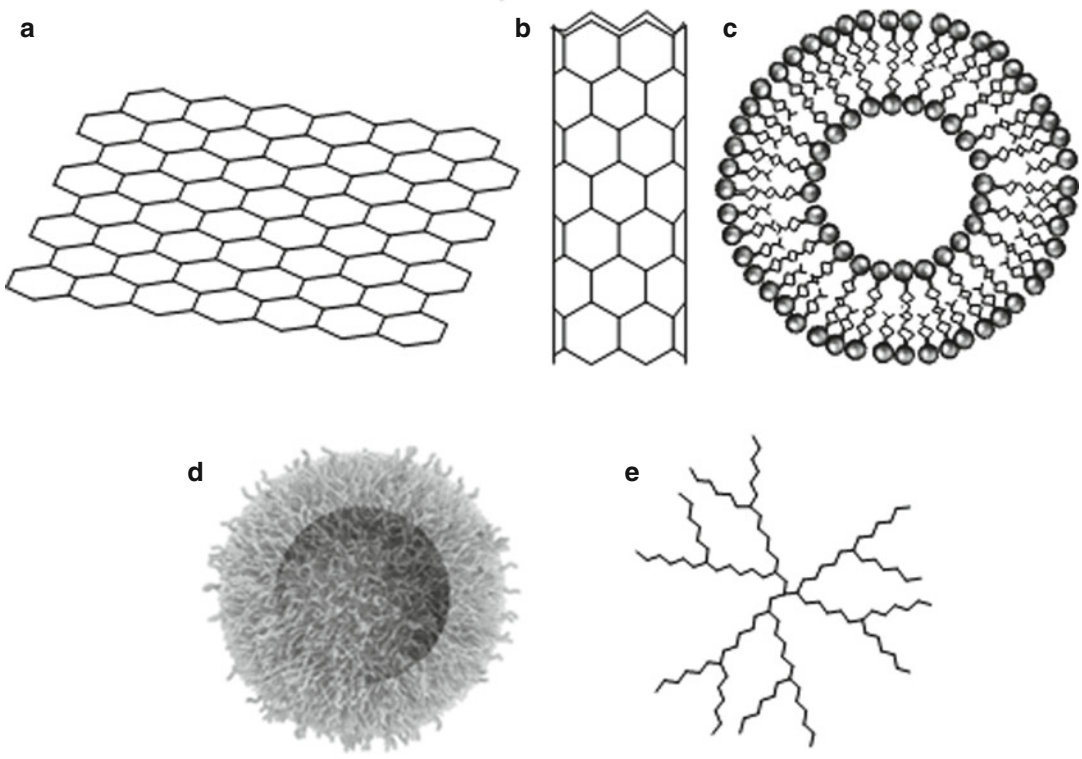

Fig. 22.1 Schematic presentation of: (**a**) graphene, (**b**) single-wall carbon nanotubes, (**c**) liposome, (**d**) core–shell nanoparticle, and (**e**) dendrimer

are just a few nanometers in diameter and several microns long (Fig. 22.1b). Graphene and SWNTs modificable chemistry and large surface area make them excellent candidates for the preparation of multifunctionalized nanosystems.

22.1.1.2 Vesicle-Type Systems

The development of vesicle-type systems like liposomes and micelles allows flexible mechanisms to deliver not only therapeutic-known drugs but other compounds of interest like contrast agents, antibodies and proteins that can be used for therapy and/or diagnosis. Liposomes (Fig. 22.1c) are small vesicles consisting of one or more concentric lipid bilayers enclosing discrete aqueous spaces. They are versatile in terms of size, surface charge, composition, bilayer fluidity, and are able to encapsulate drugs regardless of their solubility. Thus, they have been proposed for a long time as drug carriers with therapeutic purposes and also as potential imaging agents for the visualization of pathological processes.

Alternatively, recent biodegradable polymeric micelles have been developed as new vesicle systems that present remarkable drug delivery potential [13]. Polymeric micelles are formed by self-assembly of block polymers consisting of two or more polymer chains with different hydrophobicity. In aqueous environment, they form a core–shell micellar structure suitable for carrying poorly soluble drugs in its hydrophobic core. Moreover, its hydrophilic shell provides water solubility, protection, and functional groups suitable for further modifications.

22.1.1.3 Core–Shell Nanoparticles

Core–shell NPs (Fig. 22.1d) have a core surrounded by a hydrophilic shell and can be made of a wide variety of materials including quantum dots (QDs), metals, and metal oxides. Direct functionalization of core nanoparticles might be difficult, and, thus, they are often covered with a shell containing natural or FDA-approved biocompatible and degradable polymer(s) (see Table 22.1). An additional effect of embedding the core particle prevents degradation of the particle itself, thus, first, protecting its physicochemical characteristics and second alleviating potential safety concerns that might arise from trace ions. Due to size-dependent properties, low toxicity, large surface to volume ratio, and ease of fabrication and multifunctionalization, gold nanoparticles are the most commonly used in the biomedical field [14], although other materials like iron oxide have been also widely studied.

22.1.1.4 Polymeric Dendrimers

Polymeric dendrimers (Fig. 22.1e) are hyperbranched nanostructures that can be controlled in size by controlling the number of polymerization

Table 22.1 Classification of biodegradable polymers

Biodegradable polymers			
Natural polymers		Synthetic polymers	
Protein-based polymers	Polysaccharides	Approved by *FDA*	Others
Collagen	Agarose	Poly(glycolic) acid (*PGA*)	Poly(propylene fumarate)
Albumin	Alginate	Poly(L-lactic acid) (PLA)	Tyrosine-derived polycarbonate
Gelatin	Carrageenan	Poly(D,L-lactic acid) (*PDLA*)	Poly(glycolide-co-γ-caprolactone)
	Hyaluronic acid	Poly(D,L-lactic-co-glycolic acid) (85/15) (*85/15 DLPLGA*)	Ethylglycinate polyphosphazene
	Dextran	Poly(D,L-lactic-co-glycolic acid) (75/25) (*75/25 DLPLGA*)	
	Chitosan	Poly(D,L-lactic-co-glycolic acid) (65/35) (*65/35 DLPLGA*)	
	Cyclodextrins	Poly(D,L-lactic-co-glycolic acid) (50/50) (*50/50 DLPLGA*)	
		Poly(caprolactone) (*PCL*)	
		Polyethylene glycol (*PEG*)	

generations. As polymerization progresses, a small, planar molecule transforms into a spherical nanostructure, with cavities where therapeutics and contrast agents can be grafted with great loading efficiency [15]. The majority of research into the use of dendrimers in the field of biomedicine has been concentrated on treatment, i.e., dendrimers delivering cytotoxic radiation via radioimmunotherapy. However, they have been eventually evaluated as diagnostic tools with potential applications in cancer.

22.2 Novel Imaging Probes

As outlined in the preceding chapters and section, molecular imaging techniques are in clinical use and applied in research. Hereby, differences between classical drug and contrast agent design on one hand and new, upcoming molecular structures have been described. The reader will be guided through individual aspects of the use of new molecular and imaging technologies in this section. For this, the reviewed examples for novel molecular imaging probes are mainly focused on preclinical in vivo applications in cancer diagnosis. If applicable, a reference to clinical applications has been made. Additionally, to cover the different imaging modalities, we deliberately choose to give each individual imaging modality a different weight. Nuclear imaging is already established, has its own established procedures to validate new molecular probes, and relies on radiochemistry expertise to radiolabel any structure. It has so done in the past, is doing at present and will continue to deliver new molecular probes in the future. New molecular probes in nuclear imaging are often prepared in situ and thus are described in detail, to reflect the special requirements of radiochemical synthesis. MRI was reduced to two applications: smart contrast agent and hyperpolarization of [1-^{13}C]pyruvate. Hereby, smart contrast agents are of special interest as they have the potential to work as functional molecular imaging probes. Hyperpolarization for biomedical applications became recently available, and [1-^{13}C]pyruvate has already reached the clinic as a potential imaging biomarker. Optical imaging, albeit an indispensable tool in cellular studies, was reduced to applications of QDs to cancer models, as they have the potential to build a versatile, sensitive biomedical imaging platform to cover microscopic, cellular, tissues, and in vivo applications.

22.2.1 Nuclear Imaging

Positron emission tomography and single photon emission computerized tomography are ultrasensitive, noninvasive molecular imaging techniques that allow the determination of the space-temporal distribution of a radiotracer after administration into a living organism. The main difference between them is that PET uses positron (β^+)-emitting radionuclides whereas SPECT uses radionuclides that emit gamma (γ) rays. Annihilation of one positron with one electron produces two gamma rays, with equal energy (511 keV) and direction but emitted 180° from each other. Consequently, both techniques rely ultimately in the detection of gamma rays. Due to the high energy of gamma rays, they penetrate tissue almost unaffected and the detection is performed by using detectors located around the imaged organism. The measured photons allow the reconstruction of distribution of radioactivity as an image or sequence of images, which can be analyzed to get quantitative data (Fig. 22.2). Due to the high sensitivity, the radiotracer is usually administered in the sub-micromolar range, facilitating the study of biological systems without disturbing their function; this is, no toxicological, pharmacological, and/or undesired side effects are expected.

The idea behind the application of nuclear imaging (PET and SPECT) for cancer diagnosis is therefore simple: A labeled species (radiotracer) which can provide information related to (1) a biological event (angiogenesis, apoptosis, hypoxia, proliferation, etc.) or (2) the presence of molecular biomarkers (protein kinases, growth factor receptors, specific overexpressed enzymes, or receptors, etc.) occurring uniquely or in a specific way in tumors must be synthesized and

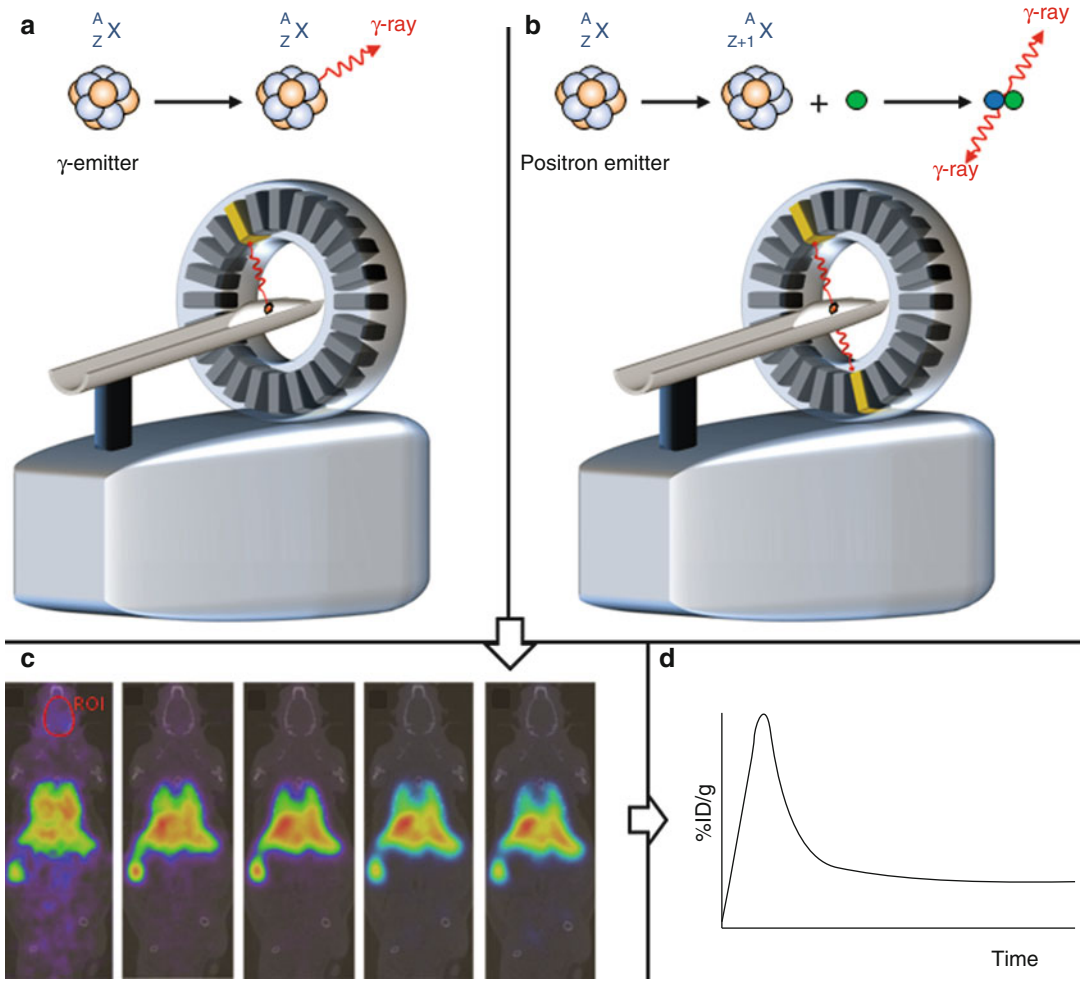

Fig. 22.2 Schematic representation of a single-photon emission computed tomography (SPECT) (**a**) camera and a positron emission tomography (PET) (**b**) camera. In SPECT, one disintegration produces one gamma ray. In the case of PET, the disintegration produces a positron, which annihilates with one electron producing two gamma rays, with equal energy (511 keV) and direction but emitted 180° from each other. In both cases, the detection of hundreds of thousands of photons allows the reconstruction of the distribution of radioactivity as an image or sequence of images (**c**). Regions of interest can be drawn and quantitative information can be obtained (**d**), e.g., as percentage of injected dose per gram of tissue (%ID/g)

administered to the subject under study. Positron Emission Tomography or SPECT images will thus provide information related to the specific biological event or to the presence/absence of a particular biomarker. One classical example is 2-deoxy-2-[^{18}F]fluoro-D-glucose ([^{18}F]FDG), an analog of glucose with an ^{18}F atom in the two position in substitution of an hydroxyl group. [^{18}F]FDG is taken up by cells through the same pathways as glucose, phosphorylated and trapped in the cells (Fig. 22.3); as a result, [^{18}F]FDG concentration increases in proportion to rate of utilization of glucose, and therefore, it can be used as an indirect proliferation marker; [^{18}F] FDG is currently the most commonly used PET tracer in clinical diagnosis. A second example is [^{111}In]pentetreotide (Fig. 22.4), the most widely used radiolabeled somatostatin analog, which binds to somatostatin receptors in the cell surface throughout the body. Tumors containing a high density of somatostatin receptors concentrate this radiotracer via receptor–ligand interaction.

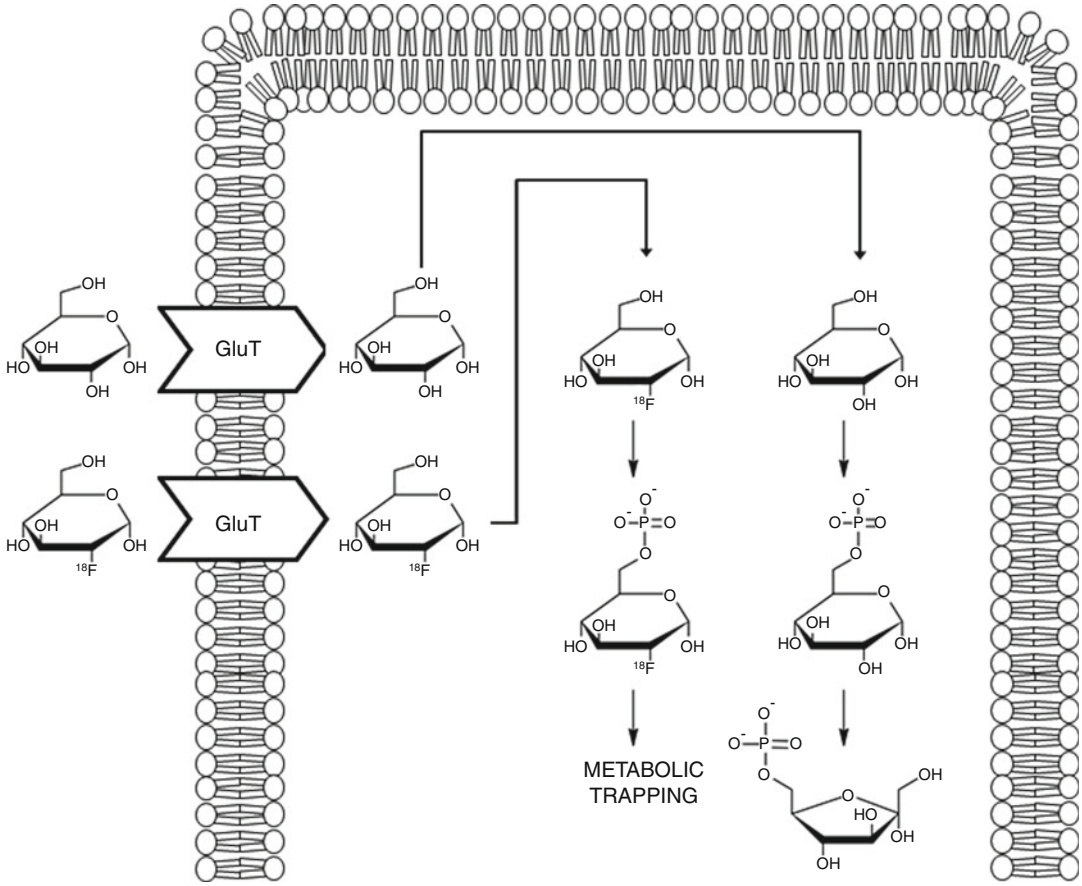

Fig. 22.3 Intracellular metabolism of glucose and [^{18}F]FDG. Both are taken up by cells by means of glucose transporters (GluT). Once into the cell, they are phosphorylated to glucose-6-phosphate and [^{18}F]glucose-6-phosphate, respectively. Unlike glucose, [^{18}F]glucose-6-phosphate does not undergo further metabolism and is trapped in the cell

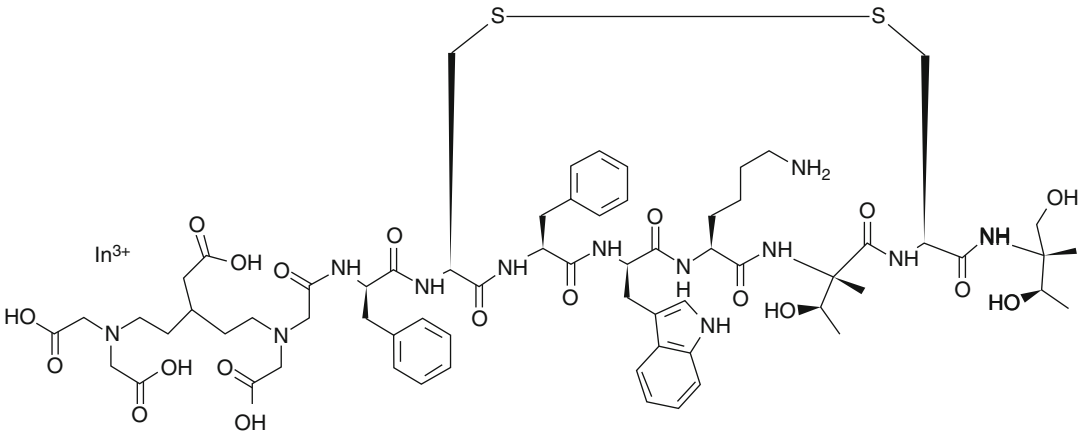

Fig. 22.4 Chemical structure of [^{111}In]pentetreotide. ^{111}In is complexed with the DTPA group on the left of the molecule

Table 22.2 PET and SPECT radiotracers: mechanism of uptake and localization

Radiotracer	Biochemical process	Mechanism of uptake or localization
[^{18}F]FDG	Glucose metabolism	Diffusion via glucose transporters. Substrate for *hexokinase*
[^{18}F]Fluoride	Bone metabolism	Incorporation of the hydroxyapatite crystals in bone
[^{11}C]Choline	Membrane synthesis	Substrates for *choline kinase* in choline metabolism
[^{18}F]Fluorocholine		
[^{18}F]FMISO	Hypoxia	Intracellular reduction and binding
[^{68}Ga]DOTATOC	Receptor binding	Specific binding to somatostatin receptors
[^{68}Ga]DOTANOC		
[^{11}C]L-methionine	Amino acid transport and protein synthesis	Transport into cells involves amino acid carrier protein. Intracellular trapping involves protein synthesis or transmethylation
[^{64}Cu]Annexin V	Apoptosis	Specific binding to phosphatidylserine on cell membrane
[^{18}F]FB-E[c(RGDyK)]2	Angiogenesis	Integrin receptor on endothelial cells of neovasculature
[^{99m}Tc]MDP	Bone metabolism	Incorporation of the hydroxyapatite crystals in bone
[^{99m}Tc]HMDP		

Based on the table in Vallabhajosula [16]

[^{18}F]FDG and [^{111}In]pentetreotide are only two examples of radiotracers which are currently used in the clinical practice. However, the vast amount of information resulting from biomedical research during the last years has enabled the identification of many molecular events that take place during disease processes. As a result, appropriate targets have been selected and a large number of labeled probes for the visualization of such processes in vivo have been developed. Indeed, hundreds of radiotracers based on a wide variety of radionuclides decaying due to β^+ or γ emission have been developed and tested in animal models and/or clinical studies documenting their potential utility as molecular imaging probes. Among them, only a few have become radiotracers with diagnostic applications in the clinical environment. Table 22.2 collates some examples of radiotraces applied in oncology.

A thorough description of all radiotracers used in clinical practice and their applications is far beyond the scope of this chapter. Instead, novel platforms or families of compounds that are currently explored in preclinical studies will be discussed and their labeling strategies utilized for their preparation will be presented. Two main goals lay behind the development of such new imaging agents: (1) the visualization of new molecular processes or biomarkers and (2) to gain specificity/selectivity in the visualization of such processes or biomarkers. Also, in an attempt to bring diagnosis and therapy closer, some newly developed imaging agents move towards the recently coined term theranostics. All these aspects will be covered and examples will be provided for clarity when appropriate.

22.2.1.1 Peptides

Generally, peptides considered as imaging agents have a low molecular weight, containing several to fewer than 50 amino acids. Small peptides have rapid clearance from blood and tissues, good permeability properties, and low toxicity. In addition, they can be usually chemically modified and incorporation of a radioisotope is feasible in most cases. Due to these facts, peptides have been extensively explored as diagnostic and therapeutic agents.

Most peptide-based PET and SPECT probes are designed on the basis of naturally occurring peptides. However, most of natural peptides have a short circulation half-life due to the action of peptidases and proteases. Therefore, identification of the active amino acid sequence and introduction of chemical modifications on the non-active amino acids sequence in order to improve in vivo stability (e.g., attachment of the peptide to a NP, substitution of one or more amino acids) is a commonly followed strategy. Just as an example, somatostatin (Fig. 22.5) is an

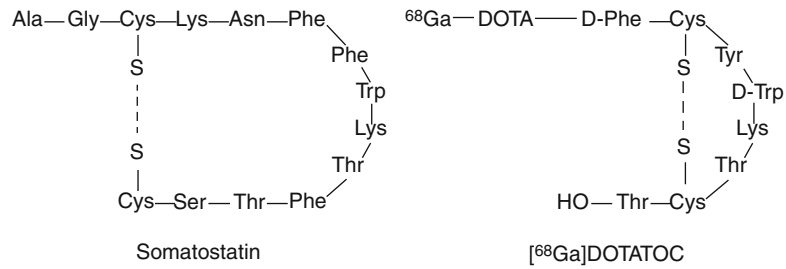

Fig. 22.5 Amino acid sequence of somatostatin and its analog [^{68}Ga]DOTATOC

endogenous peptide hormone that regulates the endocrine system and affects neurotransmission and cell proliferation. Certain subtypes of somatostatin receptors are overexpressed in certain tumor cells, and thus, ligands targeting such receptors may be good candidates to image a wide variety of tumors. However, somatostatin has a very short circulation time (2–3 min) [17], and thus, more stable analogs have been developed, like the abovementioned [^{111}In]pentetreotide or ^{68}Ga-labeled DOTATOC (Fig. 22.5). Additionally to improve stability, chemical modification in inactive sites is used to tune the excretion rate and permeability through membranes.

Radiolabeling of peptides can be achieved by following mainly three different strategies:

- Radioiodination: Incorporation of a radioactive iodine atom (usually, ^{125}I, ^{123}I, or ^{131}I and more recently ^{124}I) is probably the most widely used alternative. Many options for such incorporation have been described in the literature; radioiodine can be incorporated by in situ oxidation of the anionic species (I^-) using an oxidizing agent in solution, e.g., chloramine-T [18] and subsequent electrophilic substitution at the *ortho*- position to the hydroxyl group of a tyrosine residue. Eventually, the iodine atom can be introduced also in a histidine. This methodology provides high incorporation yields. However, not all peptides contain a tyrosine or histidine residue and, in some occasions, these amino acids (if present) might have a significant role in the biological activity of the peptide, which could be affected by the introduction of a bulky atom (notice that iodine is similar in size to a phenyl group and is markedly hydrophobic). Many investigations have also led to the conclusion that the loss of biological activity is dependent on the position of labeling and is sometimes unpredictable [19]. In addition, the peptide might not be stable under strong oxidizing conditions, e.g., oxidative reagents may cause oxidation of sensitive amino acids, like tryptophan to the oxindole and of methionine to the sulfoxide [20]. Finally, this labeling approach is very unspecific, because no control exists on the position in which the iodine atom is incorporated; the product mixture obtained is often complex and requires extensive high-performance liquid chromatography (HPLC) purification [21]. More convenient oxidizing agents have been developed to prevent oxidation of sensitive amino acids, like 1,3,4,6-tetrachloro-3α,6α-diphenyl glycoluril or Iodogen [22], a commercially available water-insoluble oxidizing agent which can be dissolved in an organic solvent and coated on the walls of the glass reaction tube. When Iodogen is used, the reaction can be terminated at any time by simply removing the crude from the reaction tube. Indirect methods, which consist of the covalent attachment of a pre-labeled group to one lysine, have been developed; the most widely used conjugation reagent is radioiodinated *N*-succinimidyl 3-(4-hydroxyphenyl)propionate (Bolton-Hunter reagent) [23]. However, in the indirect method multiple products can be formed by the reaction with the chain end and/or a variety of side chains, and this approach often requires an extensive purification of the resulting product. If the peptide under investigation already contains an iodine atom, isotopic exchange can be conducted [24]. A summary of the most commonly used strategies is schematized in Fig. 22.6.

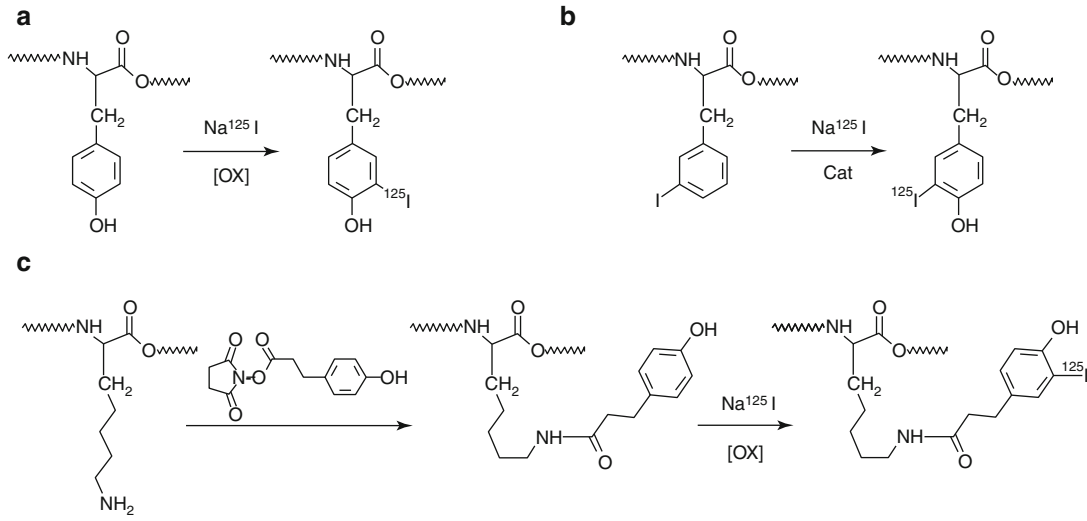

Fig. 22.6 Schematic representation of the main strategies used for the radioiodination of peptides; (**a**) electrophilic substitution, (**b**) isotopic substitution and (**c**) indirect labeling. Examples are shown with ^{125}I; these strategies can be extended to other iodine radioisotopes

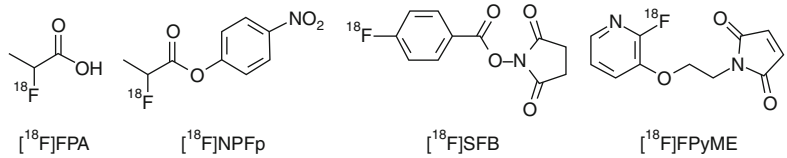

Fig. 22.7 Selected prosthetic groups for ^{18}F labeling of peptides. *FPA* fluoropropionic acid, *NPFP* nitrophenyl fluoropropanoate, *SFB* succinimidyl fluorobenzoate, *FPyME* fluoropyridinyloxypropylmaleimide

- Radiofluorination: Incorporation of an ^{18}F atom can be approached, in general terms, using two different strategies: (1) direct fluorination, in which ^{18}F (as $[^{18}F]F^-$ or $[^{18}F]F_2$) is introduced directly into the target molecule in a single step, and (2) indirect fluorination, in which a prosthetic group is used and multistep synthesis is usually required. Direct fluorination is rarely used in peptide chemistry. However, a large number of ^{18}F-labeled prosthetic groups have been developed (Fig. 22.7), which are used for ^{18}F-fluoroalkylation, ^{18}F-fluoroacylation, or ^{18}F-fluoroamidation of primary amino groups or thiol residues (see Fig. 22.8 for examples). More recently, ^{18}F-labeled fluoroalkynes and azides have been developed and incorporated into proteins via the Huisgen cycloaddition of alkynes to azides ("click chemistry") [25].
- Incorporation of radiometals: This is usually achieved using bifunctional chelators (BFCs), which contain one functional group and a metal-binding moiety function. The first allows for anchoring the BFC to the peptide, while the latter enables the sequestration of the metallic radionuclide. This strategy has been successfully applied to the preparation of ^{64}Cu-, ^{111}In-, ^{68}Ga-, ^{67}Ga-, and ^{99m}Tc-labeled peptides, among others. Interestingly, this approach usually allows incorporation of the radiometal in the last synthetic step. In addition, most radiometals are commercially available or can be produced using generators. Hence, this strategy is becoming more and more popular, and the majority of recent publications related to peptide labeling involve the use of a radiometal.

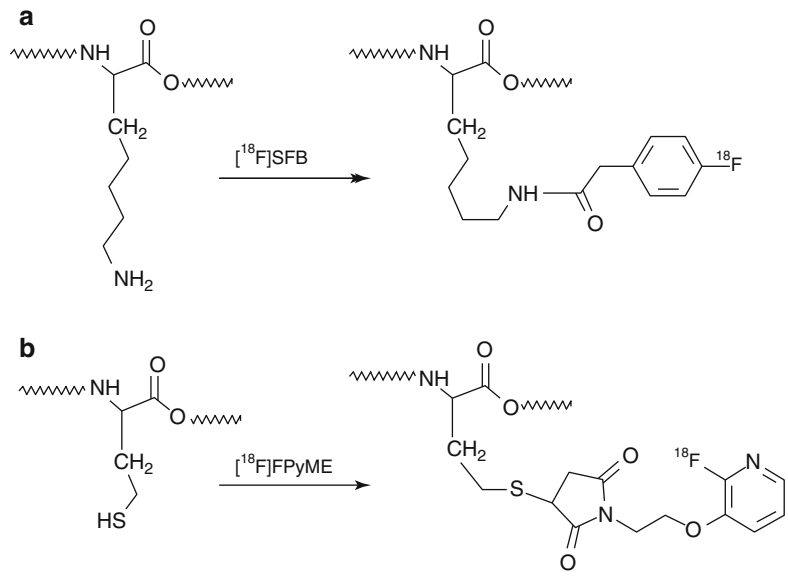

Fig. 22.8 Examples of incorporation of ^{18}F into peptides using ^{18}F-labeled prosthetic groups: (**a**) [^{18}F]SFB and (**b**) [^{18}F]FPyME

As mentioned above, the vast amount of information resulting from biomedical research has enabled the identification of many molecular events that take place during disease processes, appropriate targets have been selected, and a large number of labeled probes for their visualization have been developed. Labeled peptides for the in vivo visualization of the most important targets associated to cancer include integrin receptors, somatostatin receptors (SSTR), gastrin-releasing peptide receptor (GRPR), melanocortin-1 receptor (MC-1R), vasoactive intestinal peptide receptors (VIPRs), glucagon-like peptide-1 receptor (GLP-1R), and neurotensin receptor (NTR). Extensive reviews covering the recent advances in specific delivery of peptide-based probes for PET and SPECT imaging have been recently published [26, 27], and therefore, only a couple of examples will be briefly presented here.

The first example involves the application of gastrin-releasing peptide (GRP) analogs to prostate cancer imaging [28]. In this work, [Lys^3] bombesin ([Lys^3]BBN) was conjugated with 1,4,7,10-tetraazacyclododecane1,4,7,10-tetraacetic acid (DOTA) and labeled with the positron-emitting isotope ^{64}Cu. The labeled peptide was administered to PC-3 androgen-independent (AI) and CRW22 androgen-dependent (AD) prostate cancer tumor models. The peptide had a rapid blood clearance. At 1 h after administration, tumor-to-blood ratios were 13.1 ± 2.3 and 4.1 ± 1.3 for PC-3 and CWR22 tumors, respectively (see Fig. 22.9 for representative PET and autoradiographic images). These results indicated GRP receptor-specific uptake in PC-3 tumor, which was confirmed by in vivo receptor-blocking study at 1-h time point.

In another work, 4-([^{18}F]fluoro)benzoyl-neurotensin(8–13) and two analogs stabilized in one and two positions were synthesized and evaluated in vitro and in vivo as potential candidates to image tumors overexpressing neurotensin receptor 1 (NTR1) by PET. In vitro binding affinity in the low nanomolar range to NTR1-expressing human tumors was found for all analogs. In vivo studies in rats and mice-bearing HT-29 cell tumors showed a moderate uptake of the radiolabeled peptides into the studied tumors, presumingly due to fast elimination by the kidneys. These results suggested that the high binding affinity to NTR1 and the stabilization against proteolytic degradation are not sufficient for tumor imaging by PET [29].

More promising results were obtained with an analog of glucagon-like peptide 1 (GLP-1), the natural ligand of GLP-1 receptors. The analog (exendin-3) was conjugated to DOTA for the

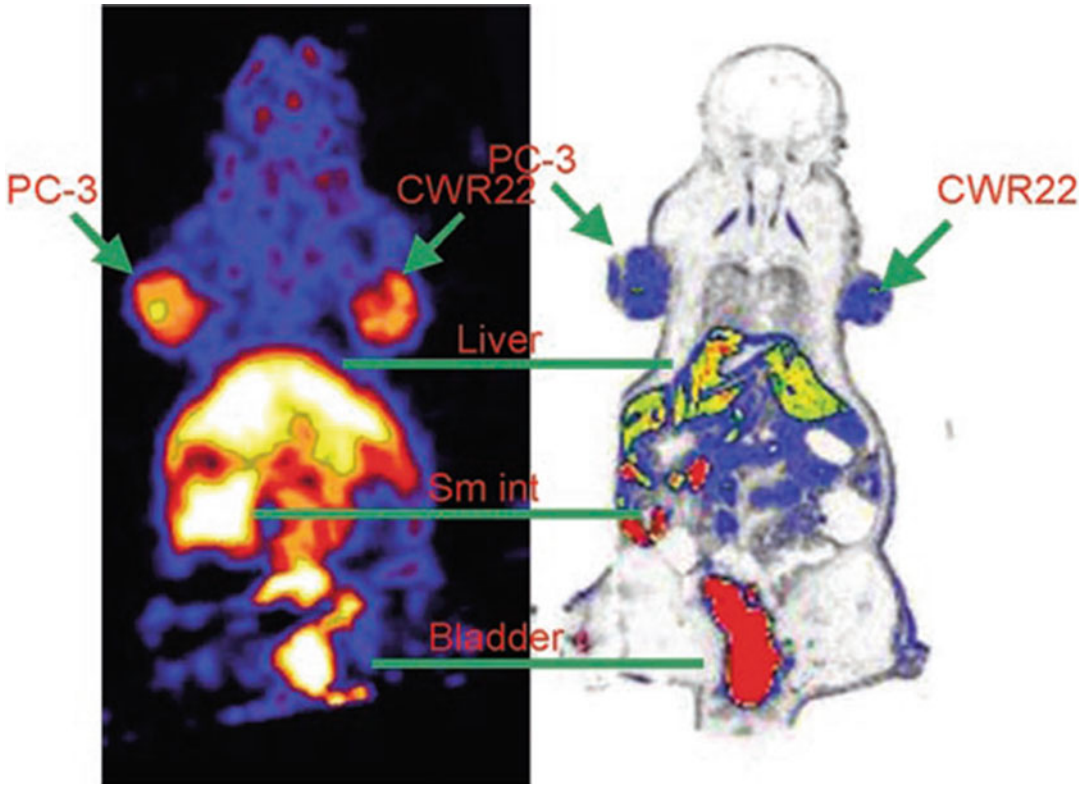

Fig. 22.9 (*Left*) Coronal microPET image of tumor-bearing mouse (PC-3 on left shoulder and CWR22 on right shoulder) 1 h after administration of ^{64}Cu-DOTA-[Lys^{3}]BBN. (*Right*) Digital autoradiograph of section containing tumors. Reprinted by permission of SNMMI from Chen et al. [28]

incorporation of ^{68}Ga and was investigated in vivo in BALB/c nude mice with subcutaneous insulinoma tumor cell (INS-1) tumors [30]. [Lys^{40}(^{111}In-DTPA)]exendin-3 was used as reference. A high uptake of [Lys^{40}(^{111}In-DTPA)] exendin-3 was observed in the tumor (33.5 ± 11.6%ID/g at 4 h after injection, see Fig. 22.10). Remarkably, tumor uptake of ^{68}Ga-labeled [Lys^{40}(DOTA)]exendin-3 was lower than tumor uptake of ^{111}In-labeled [Lys^{40}(DTPA)]exendin-3. This example highlights the potential effect of the BFCs and the radioisotope on the biological behavior of the radiotracers in vivo.

22.2.1.2 Aptamers

At the beginning of the 1990s, it was observed that short ribonucleic acid (RNA) molecules could fold into three-dimensional structures and specifically bind different non-nucleic acid targets. Their surface was perfectly shaped to join them closely; hence, they were named "aptamers" (after the Latin aptus "joined"). Nucleic acid aptamers are capable of forming stable three-dimensional structures in aqueous solution and can be ribo- or deoxyribonucleic acids. In general, RNA offers the possibility of intracellular expression, whereas Deoxyribonucleic Acid (DNA) is more stable. No significant differences in specificity or binding abilities have been observed between these two types. Peptide aptamers, which are proteins that are designed to interfere with other protein interactions inside cells, will not be considered in this chapter.

Nucleic acid aptamers can be synthesized by Systematic Evolution of Ligands by Exponential Enrichment (SELEX) [31]. The SELEX procedure has been extensively described [32] and consists in a succession of 5 steps (See Fig. 22.11

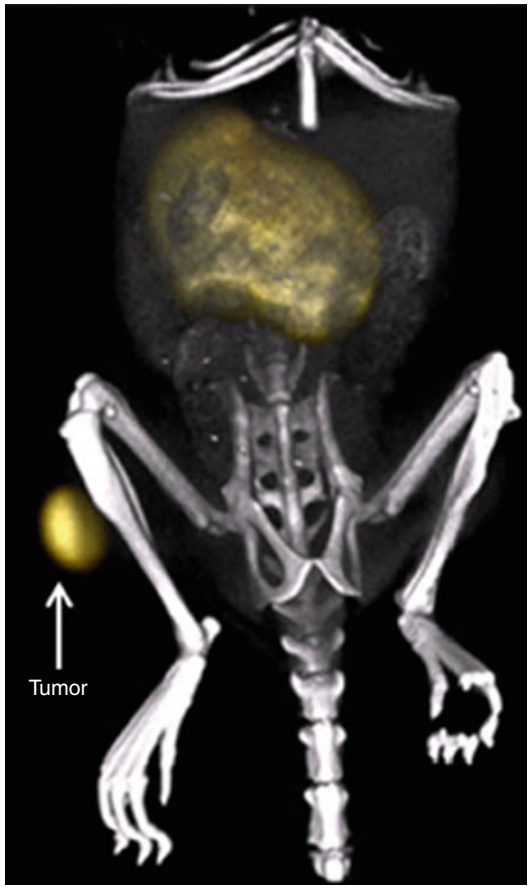

Fig. 22.10 Maximum intensity projection of a PET/CT image of a BALB/c nude mouse with a subcutaneous INS-1 tumor in the right hind limb after injection of 3 MBq HPLC-purified [Lys^{40}(^{68}Ga-DOTA)] exendin-3. The tumor (*arrow*) and kidneys are clearly visible. Due to the low background activity, the additional anatomical information given by the CT image helps to localize the tumor. Reprinted by permission of Springer Science and Business Media from Brom et al. [30])

for scheme) [33]. (1) An oligonucleotide library of sequences (candidates) is produced. All candidates contain two fixed sequences at their extremities to allow polymerase chain reaction (PCR) amplification, flanking a sequence of *n* nucleotides randomly synthesized. (2) The candidates are submitted to an in vitro selection based on their affinities for a specific target or a catalytic activity. (3) Sequences which satisfy the selection criterion are recovered while the others are removed. (4) The winning sequences are then amplified. Steps (2)–(4) are repeated several times. (5) Aptamers are cloned, sequenced, and tested for binding or catalytic activity.

Aptamers have been explored during the last decade as alternatives to monoclonal antibodies (mAbs). Monoclonal antibodies, because of their high affinity, specificity, and wide range of available targets, have been the workhorse of molecular targeting for long time. However, mAbs have a long blood residence, which decreases in vivo image quality. Interestingly, aptamers are comparable to antibodies in specificity and affinity for their target molecule [34]; they are intermediate in size (8–15 kDa) between antibodies (150 kDa) and small peptides (1–5 kDa) and are slightly smaller than single-chain variable-fragment antibodies (25 kDa). Aptamers readily support site-specific modifications that maintain structure and activity and can be coupled to diagnostic or therapeutic agents and to bioconjugates, such as polyethylene glycol (PEG) polymers, that can alter aptamer pharmacokinetics. They possess desirable storage properties, and elicit little or no immunogenicity in therapeutic applications. All these properties, in turn, make aptamers as good candidates to be labeled and used for the visualization of certain receptors in pathological processes. The most convenient way for the incorporation of a radionuclide into aptamers is based in the use of BFCs, which are covalently attached to a non-active site.

One of the first studies with aptamers for SPECT employed NX21909, an aptamer irreversible inhibitor of neutrophil elastase, which was successfully used for diagnostic imaging of inflammation in rats after being labeled with ^{99m}Tc [35]. First application to tumor localization came a few years later. TTA1, an aptamer to the extracellular matrix protein tenascin-C, was prepared and radiolabeled with ^{99m}Tc [36]. First, TTA1 was attached to the chelator 2-Mercaptoacetylglycylglycyl (MAG2) [37] through the 5′ amine for ^{99m}Tc incorporation. Scintigraphic images of U251 tumor-bearing mice were collected at different time points after administration. The images reflected high uptake in bladder and liver after 10 min; at 3 h, the intestines were prominent, with bladder still evident. After 18 h radioactivity had almost

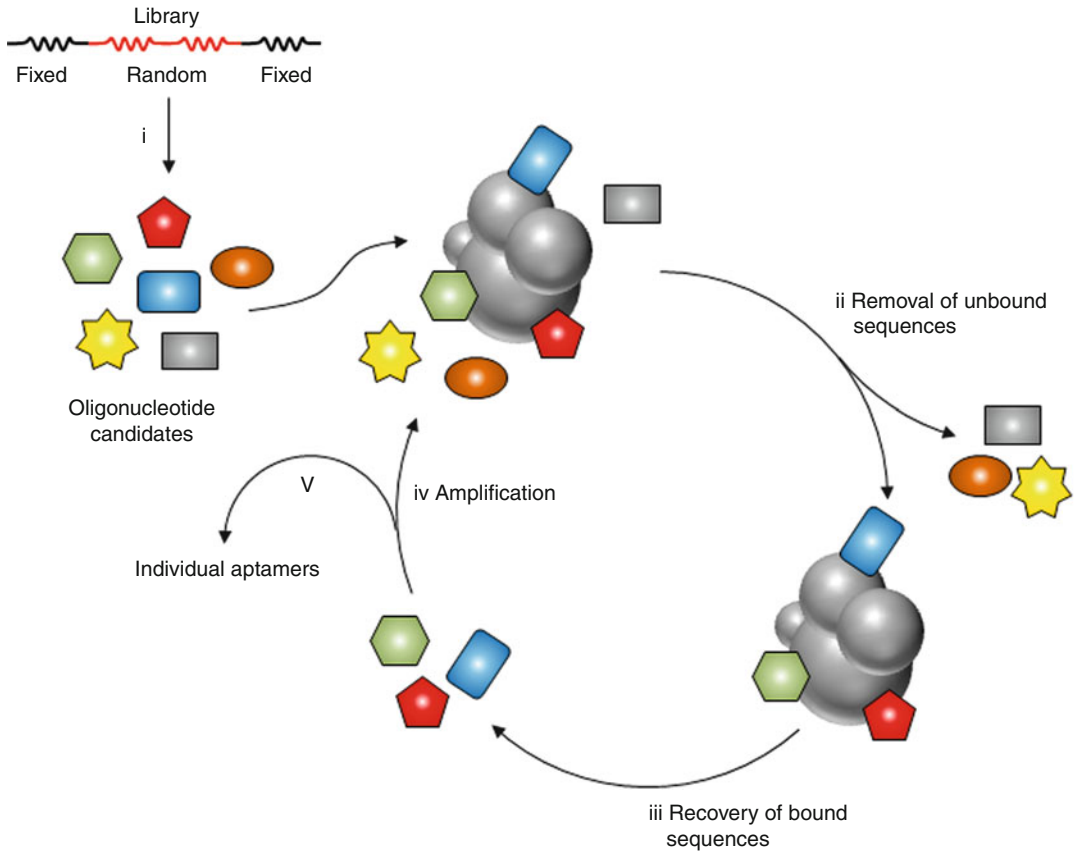

Fig. 22.11 General principle of SELEX. A random pool of oligonucleotides candidates is (*i*) synthesized and (*ii*) incubated with the target. Sequences satisfying the selection criterion are recovered while those that do not are removed. (*iii*) The bound sequences are extracted and (*iv*) amplified. The selected pool can then enter a new round of selection. (*v*) Aptamers are then cloned, sequenced and tested (Based on the drawing included in: Pestourie et al. [33])

entirely cleared the body, and the tumor was the brightest structure visualized. Similar results were obtained with a breast tumor generated using the cell line MDA-MB-435 demonstrating the ability of the aptamer to recognize multiple tumor types. No uptake was observed in the tumor when a control aptamer was used (TTA1.NB). The accumulation in the tumors at different time points after administration can be clearly visualized in Fig. 22.12.

Results obtained with labeled aptamers have not been always successful. In a more recent work, selected aptamers against the protein core (AptA) or the tumor glycosylated (AptB) MUC1 glycoprotein were conjugated to MAG2 and labeled with ^{99m}Tc. The conjugation was achieved in high yield using standard coupling reactions between an amino modification on the aptamer and the activated carboxylic group on the ligands, and the biodistribution of both radiolabeled aptamers was studied in MCF7 xenograft-bearing nude mice at different time points after administration. The tumor uptake and clearance data showed a different behavior between the two aptamers, suggesting a quicker internalization in the tumor cells of AptB than AptA. However, the tumor/tissue ratios were not satisfactory, suggesting that these potential probes still need to be improved before being used as clinical radiolabeled targeting agents [38].

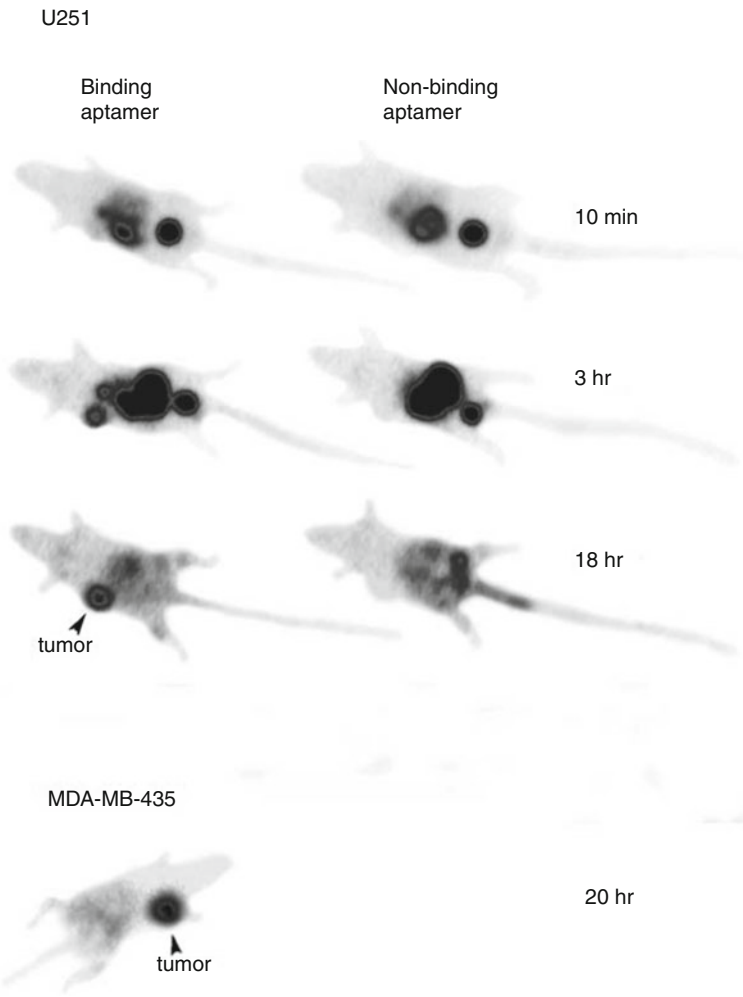

Fig. 22.12 Aptamer-based γ-camera images of tumors. With binding aptamer but not with control aptamer, U251 glioblastoma tumor is faintly visible at 10 min, prominent at 3 h, and the brightest structure at 18 h. Structures prominent at 10 min include bladder and visceral mass. Large intestine, bladder, and tumor are seen at 3 h. Also tested was MDA-MB-435 breast tumor implanted into mammary fat pad of female nude mice and allowed to grow to 400 mg. TTA1 was labeled with ^{99m}Tc, injected intravenously at 3.25 mg/kg, and imaged at 20 h. Reprinted by permission of SNMMI from Hicke et al. [36])

22.2.1.3 Antibodies

Antibodies are glycoproteins that can be made to specifically target the immunizing antigen. Thus, they have a huge potential as specific targeting agents for both diagnosis and therapy. Already in 1948 it was demonstrated that the immunoglobulin fraction containing antibodies to normal rat kidneys could be radiolabeled with ^{131}I and used to specifically target the kidneys in vivo [39]. This work suggested the potential of antibodies for tumor imaging. Many years later, polyclonal antibodies to carcinoembryonic antigen showed that carcinomas can be imaged with radiolabeled anti-CEA antibodies [40]. Since these early works, labeled monoclonal antibodies have been used for imaging different types of tumors, including breast [41], colon [42], lung [43], ovarian [44], etc.

The utility of antibodies for imaging was initially limited by their large size (150 kDa). However, advances in antibody engineering have led to the development of various forms of antibodies, i.e., monovalent fragments (variable fragments, single-chain variable fragments), bivalent or bispecific diabodies, and minibodies. Additionally, improvements have been performed in modulating their immunogenicity, behavior in circulation, and pharmacokinetics. Finally, strategies for the efficient incorporation of radionuclides have been developed. As a result, antibodies

and their modified forms have emerged as preferred agents to target tumor antigens. Currently, several antibodies have been approved by the FDA for imaging (reviewed in [45]). The recent advances in antibody-based oncologic imaging have been recently reviewed [46], and thus, they will not be further discussed in this chapter.

22.2.1.4 Nanocomposites

Due to the different chemical nature of the different NPs (see Sect. 22.1.1), many alternatives have been developed for the incorporation of the radionuclide. However, they can be summarized in 3 main categories:

- Generation of the radioisotope by activation of the NPs, usually achieved by irradiation with ions (protons or deuterons) or neutrons. The radionuclide is thus generated in situ via a nuclear reaction. The activation of Al_2O_3 NPs by irradiation with 16 MeV protons via the $^{16}O(p,\alpha)^{13}N$ nuclear reaction to generate ^{13}N-labeled Al_2O_3 NPs [47], the activation of CeO_2 NPs by deuteron irradiation via the $^{140}Ce(d, p)^{141}Ce$ nuclear reaction [48], and neutron activation of ^{197}Au NPs to generate in situ ^{198}Au-labeled NPs [49] are only a few examples that can be found in the literature. Noteworthy, since neutron capture occurs preferentially at low neutron energies, it can generally be assumed that the activated nucleus remains very close to its original lattice position, this is, in the volume of the NP itself. This allows activation of NPs in solutions, whereas in the case of ion activation, radiolabeling occurs by recoil implantation of an activation product in a second NP, and thus, irradiation of nanoparticulate dry powders is required. In addition, by taking advantage of accelerator-driven neutron sources using the concept of Adiabatic Resonance Crossing, mild activation conditions (lower neutron and gamma-radiation dose rates and sample temperatures) allow the activation of nanoparticles or nanoparticle suspensions that are sensitive to thermal damage or radiation exposure [50–52].
- After-loading or attachment/entrapment of the radionuclide once the NP has been synthesized. This is usually achieved using BFCs, which contain one functional group and a metal-binding moiety function. The first allows for anchoring the BFC to the NP surface, while the latter enables the sequestration of a metallic radionuclide. This strategy has been successfully applied to the preparation of ^{64}Cu-, ^{68}Ga-, and ^{99m}Tc- labeled NPs, among others [53–55]. One clear advantage of this methodology arises from the fact that NPs which already contain the BFC can be prepared and fully characterized. The chelation reaction usually takes place under very mild conditions, and thus, alteration of the NPs properties during labeling can be neglected. Alternatively, the attachment of pre-labeled tags to the NP surface can also be used [56]. Direct surface attachment of radioactive ions [57] and diffusion of radioactive species into the NPs have also been reported [58]. In the particular case of liposomes, transport of the radionuclide through the lipid bilayer and trapping in the aqueous interior are also possible [59].
- Incorporation of the radioisotope during the NP synthesis process, using radioactive precursors [60].

In general terms, the second strategy is the most widely used in the biomedical field. The fact that the radionuclide can be incorporated in a very late stage in the synthetic process and the relatively mild reaction conditions required are definite advantages. Activation of NPs via neutron activation has been also occasionally used, although the number of available neutron sources is scarce, limiting thus its application. Activation of NPs using accelerated ions and incorporation of the radioisotope during the synthesis process have an interesting application field for the detection of inorganic NPs in environmental and toxicological studies.

Despite the number of scientific works reporting the labeling and subsequent utilization of nanoparticulate materials is continuously increasing, there are few concerns to be taken into account during the labeling process as well as during data interpretation. These concerns are not usually discussed in detail, but might lead to complete incorrect or misinterpreted results.

Briefly (1) the term NP is never related to a single species, but to a group of species with very similar (but different) properties. In consequence, the macroscopic, measured biological readout is the sum of different individual actions, and, among those, only the ones derived from radiolabeled NPs will be detected and tracked. Thus, uniform or at least representative labeling must be guaranteed in order to get reliable data. (2) NPs are always altered to some extent during the labeling process. Hence, attention should be paid to characterization of the labeled NPs as well as to the assessment of their biological properties and compared to those of unlabeled ones; (3) nuclear imaging modalities actually track the radioactive atom, independently of its chemical form or environment. Thus, detachment of the radioisotope from the NP might lead to imprecise results and misinterpretation of the data; (4) the physical–chemical and structural properties of the unlabeled and labeled NPs are very similar, and separation of the second from the first is not usually feasible. Thus, the apparent specific activity is often low and the microdosing concept might be lost; (5) the labeling process and further in vivo detection of the labeled NPs require the manipulation of ionizing radioactive species and the use of sophisticated equipment which, in turn, makes the whole process complicated and expensive. These concerns have been recently discussed in detail [61].

Due to the abovementioned pitfalls, it is clear that despite radiolabeling results in an efficient way for the in vivo tracking of NPs after administration/incorporation to/into an organism, such issues need to be carefully considered if the results are to be valid. Noteworthy, the use of radiolabeled NPs becomes more difficult in the clinical environment. It is well known that radiotracers for human use need to be prepared under good manufacturing practices (GMPs), and during the last two decades, most of the radiopharmaceutical laboratories have updated their facilities and have implemented the procedures to accomplish the production under GMPs. However, production of labeled NPs under GMPs can be anticipated to be very challenging. All the equipment involved needs to be qualified. Importantly, because the radiotracer is usually released before sterility tests are finalized, the whole process requires full validation. In addition, radiotracers are usually autoclaved before release for sterility purposes or, alternatively, filtered through 0.22 μm filters. The stability of NPs to autoclaving conditions needs thus to be tested if filtration is not an option due to particle size. Finally, quality control can also become a big issue. Particle size distribution and chemical characterization are usually performed with equipment which is often outside radiation-controlled zones, and NP samples must be allowed to decay to acceptably low activity levels before full characterization can be achieved. All these questions and compliance with regulatory issues need to be carefully addressed before a labeled NP can enter a clinical trial.

Labeled NPs with Diagnostic Applications

As mentioned above, accumulation of NPs in tumor tissue may occur by the EPR effect; indeed, such effect has been exploited in certain occasions, and some examples can be found in the literature. Alternatively, tumor-specificity active targeting using NPs can be accomplished by including a target moiety attached to the surface of the NP, e.g., a ligand such as the RGD peptide [62], epidermal growth factor (EGF) [63], folate [64], transferrin (Tf) [65], or antibodies and antibody fragments, such as a single-chain variable fragment as discussed in previous sections; these moieties recognize a cell surface receptor which is only (or predominantly) expressed in tumor cells [66, 67]. In most cases, these ligand–receptor interactions result in efficient uptake of the NP into the tumor cell by receptor-mediated endocytosis. From this approach, an immediate question may arise: Why should one attach a targeting moiety to an NP, if the targeting moiety is capable to reach the tumor by itself, as explained in previous sections? Actually, there are different reasons that support the use of NPs as vehicles: (1) each NP can incorporate a high number of targeting moieties (multivalency effect); this, in principle, increases the probabilities of targeting moiety–target interactions and enables the simultaneous interaction of various targeting moieties with various binding sites, improving the effective

accumulation of the NP in the targeted tissue; (2) NPs can be multifunctionalized; in other words, the targeting moiety and a therapeutic agent can be simultaneously loaded onto the NP, enhancing the selective accumulation of the therapeutic agent in the targeted tissue; and (3) by being attached to the NP, many bioactive molecules, which could be metabolized or rapidly eliminated, stay longer time in the circulatory system, resulting in an increased bioavailability. For example, attaching a peptide to an NP is expected to have a positive effect, with similar results to those achieved by chemical modification of the peptide. Worth mentioning, alteration of the biological activity due to attachment to the NP should be thoroughly investigated before application.

Given the variety of different cancer types and the multitude of nanoagents designed for their detection and/or treatment, it is impossible to enumerate all of them in this chapter. Thus, we will mention a few examples of some selected targeted and nontargeted nanoagents which have proven efficiency at least in animal models.

PEG-functionalized SWNTs containing c(RGDyK), a potent integrin $\alpha_v\beta_3$ antagonist, and a bifunctional chelator for the incorporation of ^{64}Cu were studied as potential imaging agents in a mouse model bearing subcutaneous integrin $\alpha_v\beta_3$-positive U87MG tumors using PET [68]. The SWNTs were labeled with ^{64}Cu by anchoring the macrocyclic chelator DOTA to the termini of different-sized PEG chains. SWNTs lacking RGD peptides were used as control. Despite the surface PEG chain length significantly affected the blood concentration and biodistribution pattern, SWNTs were found to be highly stable in vivo. PET images with ^{64}Cu-labeled SWNT–PEG_{5400}–RGD showed a high increase in tumor uptake (10–15 % ID g^{-1}, tumor-to-muscle ratio >15) compared to control SWNTs (3–4 % ID g^{-1}) 2 h after administration. Interestingly, ^{64}Cu-labeled PEG–RGD species are known to be rapidly cleared from mice through the renal route in just a few hours; hence, the high tumor accumulation was attributed to the long blood circulation time and the multivalency effect (multiple RGDs loaded in a single SWNT binding to multiple integrin $\alpha_v\beta_3$ simultaneously).

Functionalized nano-graphene has also been assayed for tumor targeting in an animal tumor model [69]. Nano-graphene oxide (NGO) sheets with covalently linked PEG_{10000} chains were conjugated to NOTA (1,4,7-triazacyclononane-1,4,7-triacetic acid) for ^{66}Ga incorporation and TRC105, a human/murine chimeric IgG1 monoclonal antibody which binds to CD105 (endoglin) with high avidity. Endoglin is exclusively expressed on proliferating tumor endothelial cells, and thus, it is potentially an ideal marker for tumor angiogenesis. ^{66}Ga-NOTA-GO-TRC105 accumulated quickly in 4 T1 (murine breast cancer) tumors (5–8 mm), established by subcutaneously injection of cells into the front flank of mice. Administration of a blocking dose of TRC105 2 h before ^{66}Ga-NOTA-GO-TRC105 injection significantly reduced the tumor uptake.

In a very recent study, NGO was conjugated to anti-HER2 antibody (trastuzumab) and was evaluated as imaging agent in two HER2-overexpressing murine models of human breast cancer. ^{111}In was incorporated to the functionalized NGO using diethylenetriaminepentaacetic acid (BnDTPA) and tumor accumulation was evaluated using SPECT [70]. Tumor accumulation amounted to 12.7 ± 0.67 and 15.0 ± 3.7 % of the injected dose/g (% ID/g) of tumor tissue at 72 h, with tumor-to-muscle ratios of 35:1 and 7:1, respectively.

A biodegradable positron-emitting dendritic nanoprobe targeted at $\alpha_v\beta_3$ integrin was developed for the noninvasive imaging of angiogenesis [71]. The nanocarrier consisted of a dendritic core (Pentaerythritol) and a flexible multivalent shell. Pentaerythritol was divergently dendronized by using a derivative of 2,2-bis(hydroxymethyl) propanoic acid to afford a dendrimer with eight branching points. Heterobifunctionality was introduced by coupling eight protected tyrosine moieties, which enabled the introduction of the radioisotope (^{76}Br) on the phenyl moieties. Finally, eight heterobifunctional polyethylene oxide chains (PEO, 2,700 Da) were attached and the amine groups at the terminal ends of PEO were deprotected, coupled to glutaric anhydride, converted to active imidazolides and finally coupled to cRGD peptide moieties (~5 RGD per

dendritic nanoprobe). Nontargeted nanosystems were used as control. In vivo PET experiments were conducted using a mice ischemia model. Image analysis revealed high specific accumulation of targeted ^{76}Br-labeled dendritic nanoprobes in angiogenic muscles, suggesting potential application as angiogenic markers. Worth mentioning, despite their potential as angiogenesis markers in tumor tissue, these nanoprobes were not further tested in animal cancer models.

Starburst dendrimers have also been functionalized with IgG-antibodies [72]; the immunoreactivity of antibodies was unaffected by dendrimer conjugation as determined by enzyme-linked immunosorbent assay (ELISA). Moving towards in vivo imaging, the biodistribution of ^{111}In- and ^{88}Y-labeled polyamidoamine dendrimers (PAMAM) conjugated to humanized anti-Tac IgG (HuTac) was assessed in nude mice. High accumulation was found in the liver, kidney, and spleen; this accumulation significantly decreased when the chelates were saturated with cold radiometals. The biodistribution of the dendrimer-conjugated HuTac in normal organs of tumor-bearing mice was similar to nontumor-bearing mice. Specific tumor (ATAC4) uptake was higher than that in nonspecific tumor (A431).

Liposomes composed of dipalmitoylphosphatidylcholine (DPPC), cholesterol, and charged lipid P-hexadecyl-D-glucuronide (PGlcUA) or PEG-conjugated distearoylphosphatidylethanolamine (DSPE) were labeled with [^{18}F]FDG and administered to mice-bearing Meth A sarcoma 17 days after tumor implantation. PET images were acquired concomitantly with the administration of labeled liposomes. PGlcUA liposomes efficiently accumulated in tumor tissues time dependently from immediately after injection [73]. Because no targeting moiety was attached to the liposomes, this is a good example of the benefits of the EPR effect in passive targeting. The same research group has recently refined their strategy by attaching a targeting moiety covalently anchored to the liposome [74]. Polyethylene glycol (PEG)-modified liposomes were modified with the Ala–Pro–Arg–Pro–Gly (APRPG) motive, which is known to home into angiogenic sites. Liposomes were labeled with 1-[^{18}F]fluoro-3,6-dioxatetracosane (SteP2) and administered to rats 11 days after the implantation of C6 glioma cells. PET images revealed that the positron emitter accumulated in the tumor region, suggesting the penetration of [^{18}F]SteP2-labeled APRPG-liposomes in the tumor tissue. Nontargeted liposomes showed lower specific accumulation. In both cases, low levels of radioactivity in other brain regions were detected due to blood–brain barrier (BBB) protection.

In another work, vasoactive intestinal peptide (VIP) was covalently attached to the surface of sterically stabilized liposomes (SSL) that encapsulated the ^{99m}Tc–hexamethylpropyleneamine oxime complex (^{99m}Tc–HMPAO), and the nanoconstructs were evaluated as imaging agents in a *N*-methyl nitrosourea (MNU)-induced breast cancer rat model. Long-circulating liposomes with and without VIP on their surface significantly accumulated in breast cancer when compared to normal tissue, indicating passive targeting of these constructs to cancer tissues. Importantly, targeted liposomes showed significantly more accumulation than nontargeted ones [75].

In another study, the biodistribution, pharmacokinetics, and imaging of nanotargeted ^{188}Re-*N*,*N*-bis (2-mercaptoethyl)-*N*′,*N*′-diethylethylenediamine (BMEDA)-labeled PEGylated liposomes (RBLPL) and unencapsulated ^{188}Re–BMEDA was evaluated after intraperitoneal injection in a C26 colon carcinoma ascites mouse model [76]. Mice were inoculated intraperitoneally (i.p.) with C26 cells and Micro-SPECT/CT imaging was performed at 10 days after inoculation. The biodistribution studies indicated that the radioactivity in ascites was 69.96 ± 14.0 % of injected dose per gram (% ID/g) at 1 h to 5.99 ± 1.97 % ID/g at 48 h after i.p. administration of RBLPL. Radioactivity progressively accumulated in the tumor to a maximum of 6.57 ± 1.7 % ID/g at 24 h. There was no evidence for the cumulative deposition of ^{188}Re–BMEDA in tumor all along the study.

Core–shell NPs have also been assayed for the in vivo visualization of tumors taking advantage of the EPR effect. Core silica NPs (~120 nm in diameter) covered with a gold shell (8–10 nm)

were functionalized with a mixture of bifunctional chelating agent *S*-2-(4-aminobenzyl)-1,4,7,10-tetraazacyclododecane tetraacetic acid (p-NH_2-Bn-DOTA) and (opyridyldisulfide-polyethylene glycol 2000-*N*-hydroxysuccinimide ester(OPSS-PEG2K-NHS) to enable ^{64}Cu incorporation [77]. NPs were assayed using rats bearing head and neck squamous cell carcinoma (HNSCC), established via subcutaneous inoculation of SCC-4 cells. The complex ^{64}Cu-DOTA and ^{64}Cu-DOTA-PEG were used as controls. The two controls had some weak tumor accumulation starting from 1 h after injection which did not increase over time. In contrast, despite the lack of a targeting unit, ^{64}Cu-labeled NPs tumor accumulation increased over time and reached a plateau at 20 h after injection.

Targeted iron oxide NPs were also used for the in vivo visualization of tumors in a U87MG tumor mice [78]. Polyaspartic acid (PASP)-coated iron oxide (IO) nanoparticles were synthesized and coupled to cRGD peptides and DOTA chelators to enable incorporation of ^{64}Cu. Nontargeted NPs were used as controls. The U87MG tumor was clearly visualized with high contrast relative to the contralateral background from 1 to 21 h after injection of targeted NPs (7.9 ± 0.8 % and 9.8 ± 3.2 % ID/g, respectively), while nontargeted NPs showed significantly lower tumor uptake.

Labeled NPs with Theranostic Applications

NPs, due to their large surface area and their rich chemistry, are ideal candidates to be used as theranostic agents. The therapeutic and the diagnostic agents can be simultaneously loaded onto/attached to the NP for specific release and simultaneous monitoring using nuclear imaging. The therapeutic agent can be a drug; alternatively, the use of α- or β^--emitters can be used for radiotherapeutics.

A detailed explanation and exhaustive revision concerning the theranostic applications of NPs is out of the scope of this chapter. For a recent revision, see [79]. Just as an example, multifunctional and water-soluble superparamagnetic iron oxide (SPIO) NPs were functionalized with cRGD peptides to target integrin $\alpha_v\beta_3$, the therapeutic drug doxorubicin (DOX), and the macrocyclic chelating agent 1,4,7-triazacyclononane-*N*,*N*′,*N*″-triacetic acid (NOTA) for further incorporation of ^{64}Cu [80]. cRGD-free nanocarriers were used as a control. The biodistribution and tumor uptake of these NPs were studied in U87MG tumor-bearing mice. Accumulation of targeted nanocarriers occurred primarily in the tumor and liver but not in most normal tissues. The tumor uptake was clearly visible on the images at 0.5 h postinjection and plateaued after 6 h at around 5 % ID/g. Tumor uptake for nontargeted nanocarriers was significantly lower, proving the positive effect of the targeting moiety.

22.2.2 Magnetic Resonance

Magnetic resonance imaging (MRI) and spectroscopy (MRS) were extensively described in the previous chapters. Excellent books describing the fundamental of MRI and MRS as well as its use in cancer/oncology have been published. Thus, this chapter does not address the general aspect of MR but rather focuses on two emerging fields arising in preclinical research: smart contrast agents [81] and hyperpolarized molecular probes [82].

22.2.2.1 Smart Contrast Agents

Generally, noninvasive MRI contrast between various tissues is produced by the choice of pulse sequence at a given field strength. Hereby the signal that arises from water (protons) is first influenced by the proton density (PD) and second by its surroundings, and thus, differences in the longitudinal relaxation time (T1) and transverse relaxation time (T2) are commonly observed between tissues and during disease evolution. Compared to free water, these relaxation times are reduced in vivo, and thus, one may take the simplified view that the overall tissue composition acts like an endogenous contrast agent mixture. If the composition of the mixture changes significantly, either one or both relaxation times might be affected and thus can be explored for diagnosis.

Contrast agents are used either to reduce the time of an examination or to exaggerate

differences between normal and diseased tissue. However, this renders MRI invasive, and, despite the low potential of anaphylactic shocks, clinician attendance is required. Currently, a little more than 10 contrast agents are approved by the FDA and other western agencies. Nine linear or cyclic complexes of Gadolinium with different physicochemical properties have been approved for different application. Higher molecular weight Gd^{3+} complexes, often bound to macromolecules, can serve as blood pool contrast agents, as their large size prevents the leakage into interstitial space or diffusion through the epithelium. This prolongs the available imaging time from several minutes up to an hour, making these agents ideally suited for MR angiography and perfusion measurements. Having said this, the thermodynamic and kinetic stability of Gadolinium complexes is utterly important, as the contrast agent concentration administered to patients would by far exceed the safe amount if all complexes would degrade into free soluble Gd^{3+}. Thus, besides complex stability, rapid clearance of Gd^{3+}-based contrast agent from the body is paramount. For contrast agents containing superparamagnetic nanoparticles, any safety concern is rarely related to nanoparticle degradation. Thus, longer intravascular circulation times are achieved with SPIO that are larger than 50 nm or ultrasmall (<50 nm) superparamagnetic iron oxide (USPIO) nanoparticles. The circulation time of these agents is concentration dependent and can last several hours. Unfortunately, despite two having successfully passed clinical trials (Endorem and Resovist), both have been stopped being marketed due to economical considerations. Currently, Feredex, an USPIO nanoparticle that has been approved by the FDA to treat anemia, is undergoing clinical trials to explore its use as a contrast agent. Interestingly, a very long half-life, a high-dose (510 mg of Fe), and a fast injection rate of 1 mL/s (30 mg/s) would make it ideally suited for the use as an intravascular contrast agent.

Smart contrast agents differ fundamentally from the above, as they aim to change their influence on relaxation properties within a specific environment. Already in early days of in vivo MRI and MRS, the chemical shift difference between inorganic phosphate and phosphocreatine was measured to determine the pH of various tissues. Another prototypical example in MRI is the transition from oxygenated hemoglobin which has diamagnetic properties to deoxygenated hemoglobin which is paramagnetic. Changes in oxygenation state of hemoglobin build the fundamental basis for functional magnetic resonance imaging (fMRI) by measuring the BOLD (blood oxygen level dependence) effect. Both the chemical shift difference and a transition from a diamagnetic to a paramagnetic compound are found endogenously; thus, one can envisage smart contrast agents that are optimized to measure one specific physiological parameter by following induced changes in an observable MR parameter. In principle, the relaxivity can be modified to be conditionally dependent on certain variables like enzymatic activities, signaling messenger, calcium ion concentration, ion channel functions, receptor systems, degree of glycation of proteins, temperature, pH, pO_2, gene expression, and molecular recognition involved.

Smart MR Contrast Agents as pH Sensors

In cancer tissues there is a reversed pH gradient across the cell membrane. Cancer cells normally have alkaline intracellular pH values (7.12–7.65 compared with 6.99–7.20 in normal tissues) and acidic interstitial extracellular pH values (6.2–6.9 compared with 7.3–7.4) [83]. This pH gradient seems to be present upon cancer cell transformation. The development and maintenance of this gradient is directly due to the ability of the cancer cells to secrete protons and acidify their extracellular environment, which will trigger mechanisms favoring tumor invasiveness and aggressiveness [84]. Indeed, the low extracellular pH of the tumor microenvironment has been shown to promote angiogenesis, accelerate the digestion and remodeling of the extracellular matrix by facilitating the action of acidic proteases that are secreted by tumor cells, and create genomic instability and radiotherapy resistance [85, 86]. Therefore triggering MRI contrast agents by pH variation seems a promising method for highlighting

tumors. Overall pH is an important physiological indicator; many research groups have designed pH-sensitive contrast agents [87].

Different pH-sensitive contrast agents based on a different macrocyclic gadolinium complexing structures have been developed. A pH-sensitive contrast agent with multiple Gd^{3+} chelates and ornithine residues was described [88]: The chelates are conjugated to the amino acid chain via squaric esters, which readily react with amines. This agent is sensitive in the physiological range from pH 4.5 to 8.5. Likewise, a DO3A derivative with a tertiary amine containing side arm has been developed [89]. The side arm amine contains two long alkyl chains. For another compound, an interesting pH sensitivity of a Gd^{3+} complex based on a DOTA-tetramide has been observed [90]. Here, the relaxivity increases with pH from 4 to 6, but subsequently decreases between pH 6 and 8.5. The relaxivity remains constant thereafter at pH 8.5–10.5. Alternatively, a ternary complex between a Gd^{3+} chelate and carbonate ions has been developed [91]. Following a different approach, toluenesulfonamide as a pH-labile ligation group in Gd(DO3A) chelates was proposed; as the pH of a solution is reduced, the sulfonamide becomes protonated and dissociates from the metal center [92]. A similar pH-sensitive dissociation in complexes with one *p*-nitrophenolic ligating group was synthesized [93].

Smart MR Contrast Agents as Sensors for Ions

The use of MRI to detect fluctuations of vital metal ion concentrations has recently received much attention. The pioneering work in this area was conferred by Meade and coworkers who focused on the important role played by intracellular calcium(II) in signal transduction [94, 95]. Zinc(II) is another metal ion that regulates synaptic transmission and cell death and is often used as a nutritional supplement. Selectively sensing Zn^{2+} ions with contrast agents had been previously discussed [96, 97]. Iron-activated GdDO3A-based contrast agents [98] and copper(II)-sensitive contrast agents [99] have been developed recently.

Application to cancer can be envisaged. However, a full in vivo characterization remains challenging, as besides the stability of the complex, other abnormal ion concentrations might influence the relaxivity behavior of the suggested smart contrast agents.

Smart MR Contrast Agents as Sensor for Biomolecules

The sensitivity of MRI contrast agents to specific enzymes depends on the mechanism of their interaction [100]. Provided the interactions between a contrast agent and an enzyme are sufficiently strong, a large increase in relaxivity will be observed due to the increased rotational correlation time of the adduct [101]. Gene expression during an imaging experiment was followed [102, 103]. Alternatively, a magnetic nanoparticle assembly was developed to allow screening of DNA-cleaving agents [104]. The first enzyme activated macrocyclic MR contrast agents was reported [94]; hereby, the enzyme cleavages a molecule to free one coordination position of the Gd^{3+} and thus increases the relaxivity. A DTPA derivative was synthesized which can detect carbonic anhydrase [105]. The gadolinium complex contains a sulfonamide group in place of one of the carboxylic acid arms of the DTPA, helping it to selectively target the enzyme carbonic anhydrase.

Potential Translation of Smart Contrast Agents into Clinics

Smart contrast agents offer the potential to gain insight into the tumor microenvironment with high specificity. As such, the interest to translate them into humans is desirable. Diagnosis would first have to establish that a tumor is present, and as such, MRI diagnosis might require first an administration of the currently marketed contrast agent. Thus, clinical trials would have to establish the time frame when the smart contrast agents might be administered (e.g., 1 week later) without being influenced by the initial one. Ultimately, as a diagnostic agent, it would have to be beneficial for the patient and as such would have to demonstrate suitability in one of the three aspects: (a) a specific imaging biomarker that can replace

surgical resection or sampling; (b) as pharmacological biomarker to assess treatment interaction, and as such, can influence the treatment regimen; or (c) an early diagnostic agent. As large-scale MR clinical studies are not cheap, it remains doubtful if specific agents find a sponsor who can bring a smart contrast agent to the market. Alternatively, following similar approaches of various PET tracers, an approval and thus reimbursement will be not requested, and smart contrast agents may be used as an investigational medicinal products to serve as an imaging biomarker in clinical trials, either as drug response readout or for patient stratification.

22.2.2.2 Hyperpolarization

As outlined in previous chapters, MRI and MRS are powerful tools in biomedicine and clinics. Magnetic resonance imaging offers excellent soft tissue contrast at high temporal spatial resolution. When compared to PET and computerized tomography (CT), it has the main advantage of being noninvasive and thus can be frequently repeated in the same subject. As a molecular imaging methodology, MRS and MRI have one main weakness when compared to the above: a relative low sensitivity. At room temperature, the population of the two energy levels with respect to the applied magnetic field $B_0 = 3$ T differs only by 1 proton in 100,000 (Fig. 22.13a). Other relevant biological nuclei, such as ^{13}C and ^{15}N, have lower gyromagnetic ratios γ, ¼ or 1/10 that of protons. Moreover, as a rule of thumb, sensitivity scales with γ^3, largely due to lower receptivity. Thus, ^{13}C and ^{15}N are rarely used in clinical practice but are valuable exploratory tools in biomedical research [106, 107].

Nuclei with low γ tend to have higher T1, especially if the main relaxation mechanism relies on dipole–dipole interactions. Thus, in vivo selective ^{13}C and ^{15}N relaxation times can increase up to several minutes [108]. To take advantage of long relaxation times, hyperpolarization techniques demonstrated a signal enhancement of up to 100,000 for different ^{13}C- and ^{15}N-containing compounds (Fig. 22.13b) [109–112]. With the use of parahydrogen-induced polarization (PHIP), unsaturated compounds can be hyperpolarized by parahydrogen addition and subsequent spin order transfer to the ^{13}C [111, 112]. Thus, it is ideally suited to hyperpolarize alkenes and alkynes by *cis* addition of parahydrogen using a ruthenium catalyst in water. This makes PHIP methods fast, cost-effective and mobile and requires low maintenance.

Alternatively, dynamic nuclear polarization (DNP) [109, 110] is potentially the general method of choice, as they allow the transfer of polarization through dipolar interactions from electrons of paramagnetic centers (usually stable radicals like trityl) to neighboring nuclear spins of interest at low temperatures down to 1 K. Biomedical applications in general, became only feasible by the introduction of the dissolution method [110], allowing the rapid defrosting of the

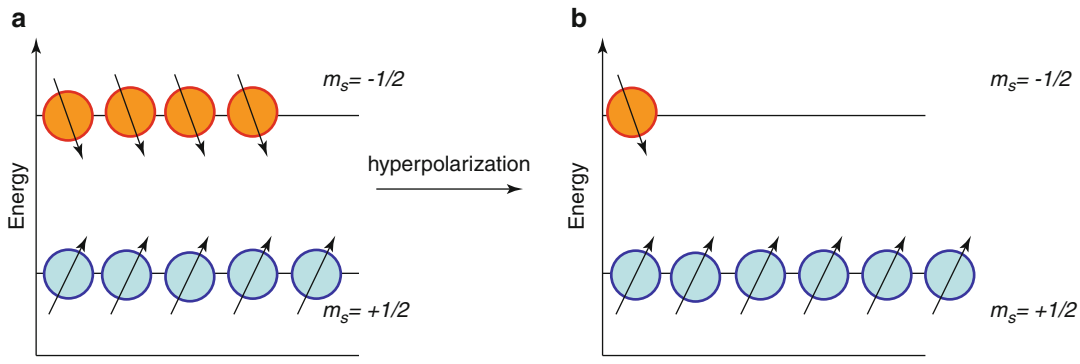

Fig. 22.13 Enhancement of nuclear spin alignment by hyperpolarization

mixture to room temperature while maintaining hyperpolarizations of up to 40 %. Moreover, the technique is generally applicable and has been used to hyperpolarize ^{1}H, ^{6}Li, ^{13}C, ^{15}N, and ^{89}Y in a variety of molecules or nanoparticles [108, 113–120], and in theory any molecule/structure can be hyperpolarized. In practice, relaxation times are often too short to allow sufficient hyperpolarization for in vivo applications. Nevertheless, biomedical molecules of interest like pyruvate, bicarbonate, lactate, and others can be hyperpolarized and have been applied in cancer research [82]. Importantly, most of these are natural products and can be considered inherently safe.

[1-^{13}C] Pyruvate

Fluxes through the LDH (lactate dehydrogenase), ALT (alanine transaminase), and PDH (pyruvate dehydrogenase) catalyzed reaction of hyperpolarized [1-^{13}C] pyruvate are of special interest for cancer (Fig. 22.14). The conversion of the hyperpolarized label from pyruvate to lactate was shown to decrease early after chemotherapy in a murine lymphoma model [121]. A decrease in FDG uptake was found to precede the decrease in flux between pyruvate and lactate [122]. However, 24 h after drug treatment, the magnitude of the decrease in FDG uptake and the decrease in pyruvate to lactate flux was comparable.

Increased levels of lactate following the injection of hyperpolarized [1-^{13}C] pyruvate were observed in a transgenic mouse prostate tumor [123]. Hereby, as the levels of hyperpolarized lactate correlate with increasing tumor grade, the readout might serve as a translatable marker of prostate cancer progression. The reactions catalyzed by both LDH and ALT are readily reversible in the cell, and therefore, the polarized ^{13}C label introduced in [1-^{13}C]pyruvate, [1-^{13}C]lactate, or [1-^{13}C]alanine can effectively exchange with pre-existing pools [124].

An alternative to the lactate–pyruvate ratio, which is critically dependent on the timing of injection and subsequent data acquisition, is to measure the lactate and pyruvate signals over time and fit these to a kinetic model [121, 125–127]. Spatially resolved dynamic data of hyperpolarized pyruvate metabolism and variable

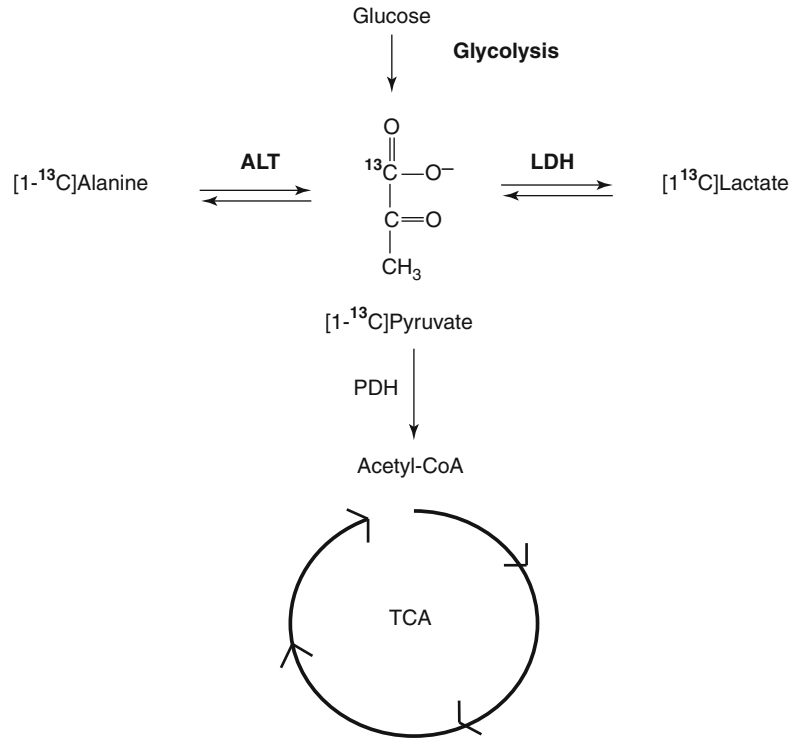

Fig. 22.14 Schematic illustration of [1-^{13}C]pyruvate metabolism. *ALT* alanine transaminase, *LDH* lactate dehydrogenase, *PDH* pyruvate dehydrogenase, *TCA* tricarboxylic acid cycle

uptake of pyruvate and the pyruvate to lactate flux observed in transgenic prostate tumors was consistent with tumor cellularity and necrosis [128].

Potential Translation into Clinics

A translation to the clinic of the PHIP method would require that an interesting molecule that could be hyperpolarized by this method can be identified. Moreover, safety concerns arising from potential contamination of the Rh-catalyst would have to be addressed with high priority. Hospital infrastructures and insurance companies might not appreciate the use of hydrogen to perform chemical reactions.

Unlike microdosing in PET, hyperpolarization still requires high concentrations of a compound, and thus, parent compound and its metabolites pose potential dose-dependent safety concerns. As such, hyperpolarized [1-^{13}C]pyruvate, for example, is being developed for clinical studies of prostate cancer. In preparation for human studies, initial dose-escalation safety and tolerability studies were performed preclinically and nonhyperpolarized [1-^{13}C]pyruvate in human volunteers [129]. To date, no significant adverse effects have been reported, and hyperpolarized [1-^{13}C] pyruvate has investigational medicinal product status approval for initial use in prostate cancer patients, with a phase 1 clinical trial started in Oct. 2010 with an anticipated completion date of Dec. 2015 (*ClinicalTrials.gov Identifier*: NCT01229618).

Theoretically, following an approval of a hyperpolarized compound, validated GMP-certified hyperpolarizer would be required to dispose the polarized product steril, and at an acceptable temperature and pH. As the hyperpolarized compound must be delivered to the subject quickly, the MR scanner and the polarizer should be placed within the same environment. Similar to PET/radiochemistry facility, the GMP production of hyperpolarized compounds within an imaging unit will undoubtedly increase the administrative burden and thus, might be only reserved for specialized centers.

From the MR acquisition side, no technical challenges are paramount that would prevent the translation of specific hyperpolarized compounds in the clinics. Initial proof of concept experiments of hyperpolarized compounds like [1-^{13}C] pyruvate can be conducted in specialized centers that have multinuclear MR capabilities. Hereby, ^{13}C is commonly available;^{15}N potentially might require new hardware in the form of radiofrequency coils (rf-coils) and filters. As always in MR optimizations, depending on the organ of interest, a special rf-coil might be required to improve the signal to noise ratio. New pulse sequences would have to be implemented, and thus, the user requires access to the data acquisition software, which, with a proper research agreement with MR manufacturers, hardly poses a problem. If a research agreement is not in place, intellectual property (IP)-related issues concerning new software developments would have to be negotiated. This is potentially a time-consuming process that could last several years and might still be unresolved, as MR manufactures tend to impose potentially unacceptable conditions concerning the transfer of IP. As such, the purchase of a hyperpolarizer with a dedicated MR system may circumvent any potential IP issues, but may restrict price competition.

22.2.3 Optical Imaging

Bioluminescence imaging requires illumination arising from within the body, whereby fluorescence imaging requires an external light for excitation, followed by the release of a longer wavelength, lower energy light for imaging. Importantly, light propagation in biological samples depends on the wavelength; the most favorable spectral window in terms of depth penetration is situated in the near-infrared range (wavelengths between [600 and 1,000] nm).

Currently, we use QDs as a general biomedical platform description, to highlight the almost-endless possibilities of nanoscale systems in imaging applications, as well as the challenges that currently prevent an easy translation into the clinical environment.

Unfortunately, currently hot topics that relate to fluorescence [130] or bioluminescence resonance energy transfer (FRET and BRET) as well as new

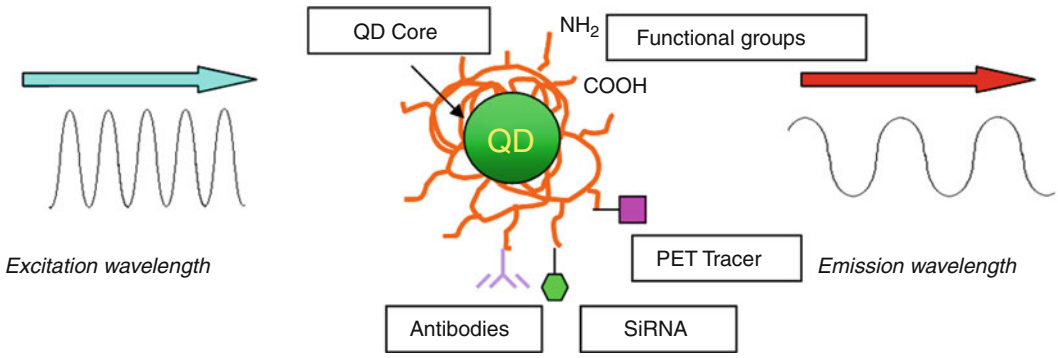

Fig. 22.15 Schematic illustration of a multifunctionalized quantum dot

Table 22.3 Comparison of the different properties between traditional fluorophores and quantum dots

Property	Traditional organic fluorophores	Quantum dots
Size scale	Molecular <0.5 nm	Colloidal 1.5–10 nm diameter
Hydrodynamic radius	Small <0.6 nm	Variable 1.4–40 nm
Absorption spectra	Discrete bands, FWHM*, 35 nm to 80 nm to 100 nm	Strong and broad
Emission spectra	Broad, red-tailed, and asymmetric FWHM*, 35 nm to 70 nm to 100 nm	Narrow symmetric FWHM* 30–90 nm
Fluorescence lifetime	Short <5 ns. Mono-exponential decay	Long >10 ns, typically multi-exponential decay
Photostability	Usually poor	Resistance to photobleaching, observation time of minutes to hours
Multifunctionality	Difficult and few	Great potential
Toxicity	Variable, based on dye	Related to the heavy metal

FWHM full width at half height of the maximum. Based on the table in Fang [133]

developments in photoacoustic imaging are out of the scope of the chapter. The interested reader is directed to excellent books [131, 132] addressing technological fundamental and advances as well as giving a detailed overview of optical and endoscopic imaging applied to cancer.

22.2.3.1 Quantum Dots

With chemical advantages in preparation of QDs, QD-based nanotechnology is helpful in constructing a biomedical imaging platform for cancer, covering cell studies to preclinical applications [133]. The physicochemical characterization of QDs such as size, shape, composition, and surface features yield unique optical properties; besides the possibility of working as an ideal core for adding coating structures and functionalization with target ligand of interest (Fig. 22.15). QDs offer multiple advantages over traditional organic fluorescent dyes as summarized in Table 22.3. Importantly, a shift of light excitation and ultrabright fluorescence emission towards near-infrared (NIR) of NIR-QDs would be able to penetrate "deep" tissues (approximately 1 cm below the skin surface), making them suitable for in vivo imaging with high signal to background ratio [134–136]. Additionally, endogenous tissue autofluorescence in conventional in vivo fluorescence imaging might be overcome by using bioluminescence or BRET as they do not require extrinsic excitation. BRET–QDs with various emission wavelength have been developed [137]. The BRET–QDs were evaluated for lymphatic imaging and compared to conventional bioluminescence and fluorescence imaging [138].

As described earlier, the EPR effect has inspired the development of a variety of

nanotherapeutics and nanoparticles for the imaging and treatment of cancer by passive targeting. Thus, many nontargeted QDs can be used for cell trafficking [139], vasculature imaging [140], sentinel lymph node mapping [141–143], and neural imaging [144].

Given the potential toxicity of the heavy metals in QDs (e.g., Cd, Se, Zn), traditional QDs might require modification in size, valences, composition, and surface coating. Hereby, special consideration should be given to potential degradation of the coating polymer and its biocompatibility not to exert toxicological effects on its own (see Sect. 22.1). However, generally, it is assumed that QDs below 5.5 nm in diameter are cleared via the kidney [145]. Larger QDs are circulating longer in the blood and thus would be able to reach the tumor, but will be also scavenged by the reticuloendothelial system. Thus, despite the potential toxicity, newly developed functionalized QDs will continue to find in vitro and preclinical applications to foster our understanding about basic applications of optics, cellular mechanism, targets, and transport. Unfortunately, the heavy metal exposure remains a concern and is a large hurdle to translate QDs into clinics.

22.2.3.2 Multimodal Quantum Dots

The combination of multiple molecular imaging modalities can offer synergistic advantages over any modality alone, mainly with respect to temporal spatial resolution and sensitivity. As such, ultrasound, MRI, PET, SPECT, MRS, optical fluorescence, and bioluminescence imaging can be either sequentially or, depending on the hardware, simultaneously employed. The creation of multimodular probes is often facilitated by the use of a "core" nanoparticle structure (e.g., iron oxide for MRI, QDs for optical imaging) with a subsequent functionalization and incorporation of a tracer that is sensitive to an alternative technology of choice (e.g., metal chelating macrocyclic to complex a PET or SPECT radionuclei).

Constructs can be created with ease in the laboratory, leading to potentially indefinite number of combinations. Nevertheless, the feasibility of multimodular probes was demonstrated successfully [146, 147]. Hereby, the MR-fluorescence bimodal QDs were used to study targeted tumor angiogenesis. To improve the biocompatibility, the QDs bimodal probes were incorporated in a silica nanoparticle [148]. QD-based probes enabled PET after chelation with ^{64}Cu [149].

To summarize, QDs are one example that can be used in nanomedicine to combine therapeutic components and multimodality imaging, thus addressing the ultimate goal of nanomedicine by monitoring the efficient targeted drug delivery noninvasively. As purely diagnostic agents, the hurdles concerning toxicity and traditional request for PK/PD profiles, metabolite analysis, stability, etc. might be just too high to justify an investment towards a selected diagnostic biomarker.

22.3 New Perspectives and Conclusions

In this chapter we have collected a relatively high amount of information regarding the use of the new molecular and functional imaging techniques in oncology. Though the first impression of the reader could be that the new technologies reflect a very variable and complex set of possibilities in diagnostic and therapy, the truth is that all that has been developed is just the implementation of the past and present knowledge of basic scientist fields such as biology, physics, and chemistry in a way that we can combine a discrete number of properties of the matter in order to find the best solution for the detection of the lesion in the organism (in this case cancer) or its possible cure.

In order to achieve these purposes, the new technologies presented here have to deal with different aspects ranging from scientific to economical and social issues. First of all, there is a considerable amount of strategies under research due to the possible combination of disciplines. Then, the selection of real promising solutions becomes more difficult. Additionally, the cost of clinical and preclinical research becomes higher, so a deep consideration about the candidate technique must be made.

Current methodologies tend to go further and deal with the theranostics, trying to find a simultaneously diagnosis and therapy. In this case, the difficulties increase as efficacy of both aspects has to be taken into account.

References

1. Matsumura Y, Maeda H. A new concept for macromolecular therapeutics in cancer chemotherapy: mechanism of tumoritropic accumulation of proteins and the antitumor agent smancs1. Cancer Res. 1986;46:6387–92.
2. Rhyner M, et al. Quantum dots and targeted nanoparticle probes for in vivo tumor imaging. In: Bulte J, Modo M, editors. Nanoparticles in biomedical imaging – emerging technologies and applications. London: Springer Science; 2008. p. 413–25.
3. Kairemo K, et al. Nanoparticles in cancer. Curr Radiopharm. 2008;1:30–6.
4. Yuan F, et al. Vascular permeability in a human tumor xenograft: molecular size dependence and cutoff size. Cancer Res. 1995;55:3752–6.
5. Hobbs S, et al. Regulation of transport pathways in tumor vessels: role of tumor type and microenvironment. Proc Natl Acad Sci U S A. 1998;95:4607–12.
6. Couvreur P, Vauthier C. Nanotechnology: intelligent design to treat complex disease. Pharm Res. 2006;23:1417–50.
7. Daldrup H, et al. Correlation of dynamic contrast enhanced MR imaging with histologic tumor grade: comparison of macromolecular and small-molecular contrast media. AJR Am J Roentgenol. 1998;171:941–9.
8. Peer D, et al. Nanocarriers as an emerging platform for cancer therapy. Nat Nanotechnol. 2007;2:751–9.
9. Yuan F, et al. Microvascular permeability and interstitial penetration of sterically stabilized (stealth) liposomes in a human tumor xenograft. Cancer Res. 1994;54:3352–6.
10. Torchilin VP. Micellar nanocarriers: pharmaceutical perspectives. Pharm Res. 2007;24(1):1–16.
11. Gao H, et al. Mechanics of receptor-mediated endocytosis. Proc Natl Acad Sci. 2005;102(27):9469–74.
12. Zhang S, et al. Size-dependent endocytosis of nanoparticles. Adv Mater. 2009;21:419–24.
13. Zhang L, et al. Nanoparticles in medicine: therapeutic applications and developments. Clin Pharmacol Ther. 2008;83(5):761–9.
14. Muthu MS, Singh S. Targeted nanomedicines: effective treatment modalities for cancer, AIDS and brain disorders. Nanomedicine. 2009;4:105–18.
15. Surendiran A, et al. Novel applications of nanotechnology in medicine. Indian J Med Res. 2009;130:689–701.
16. Vallabhajosula S. Molecular imaging: radiopharmaceuticals for PET and SPECT. Berlin/Heidelberg: Springer; 2009.
17. Peters GE. Distribution and metabolism of exogenous somatostatin in the rat. Regul Pept. 1982;3:361–9.
18. Hunter WM, Greenwood FC. Preparation of iodine-131 labelled human growth hormones of high specific activity. Nature. 1962;194:495–6.
19. Hofmann K, et al. Radioactive probes for adrenocorticotropic hormone receptors. Biochemistry. 1986;25:1339–46.
20. Regoeczi E. Iodine-labeled plasma proteins. Boca Raton: CRC Press; 1984.
21. Leidy JW. Reversed-phase high performance liquid chromatographic purification of ^{125}I-labeled rat growth hormone-releasing hormone for radioimmunoassay. J Chromatogr A. 1989;483:253–62.
22. Fraker PJ, Speck Jr JC. Protein and cell membranes iodinations with a sparingly soluble chloroamide, 1,3,4,6-tetrachloro-3α,6α-diphenyl glycoluril. Biochem Biophys Res Commun. 1978;80:849–57.
23. Bolton AE, Hunter WM. The labeling of proteins to high specific radioactivities by conjugation to a ^{125}I-containing acylating agent. Biochem J. 1979;111:529–39.
24. Breslav M, et al. Preparation of radiolabeled peptides via an iodine exchange reaction. Anal Biochem. 1996;239:213–7.
25. Kolb HC, et al. Click chemistry: diverse chemical function from a few good reactions. Angew Chem Int Ed. 2001;40:2004–21.
26. Chen K, Conti PS. Target-specific delivery of peptide-based probes for PET imaging. Adv Drug Deliv Rev. 2010;62:1005–22.
27. Gomes CM, et al. Molecular imaging with SPECT as a tool for drug development. Adv Drug Deliv Rev. 2011;63:547–54.
28. Chen X, et al. microPET and autoradiographic imaging of GRP receptor expression with ^{64}Cu-DOTA-[Lys3]bombesin in human prostate adenocarcinoma xenografts. J Nucl Med. 2004;45:1390–7.
29. Bergmann R, et al. Biodistribution and catabolism of (18)F-labeled neurotensin(8–13) analogs. Nucl Med Biol. 2002;29:61–72.
30. Brom M, et al. ^{68}Ga-labelled exendin-3, a new agent for the detection of insulinomas with PET. Eur J Nucl Med Mol Imaging. 2010;37:1345–55.
31. Tuerk C, Gold L. Systematic evolution of ligands by exponential enrichment: RNA ligands to bacteriophage T4 DNA polymerase. Science. 1990;249:505–10.
32. Fitzwater TB, Polisky B. A SELEX primer. Method Enzymol. 1996;267:275–301.
33. Pestourie C, et al. Aptamers against extracellular targets for in vivo applications. Biochimie. 2005;87:921–30.
34. Gold L, et al. Diversity of oligonucleotide functions. Annu Rev Biochem. 1995;64:763–97.

35. Charlton J, et al. In vivo imaging of inflammation using an aptamer inhibitor of human neutrophil elastase. Chem Biol. 1997;4(11):809–16.
36. Hicke BJ, et al. Tumor targeting by an aptamer. J Nucl Med. 2006;47(4):668–78.
37. Hilger CS, et al. Tc-99m-labeling of modified RNA. Nucleosids Nucleotides. 1999;18:1479–81.
38. Pieve CD, et al. Anti-MUC1 aptamers: radiolabelling with (99m)Tc and biodistribution in MCF-7 tumour-bearing mice. Nucl Med Biol. 2009;36(6):703–10.
39. Pressman D, Keighley G. The zone of activity of antibodies as determined by the use of radioactive tracers; the zone of activity of nephrotoxic antikidney serum. J Immunol. 1948;59:141–6.
40. Mach JP, et al. Tumor localization of radiolabeled antibodies against carcinoembryonic antigen in patients with carcinoma. N Engl J Med. 1980;303:5–10.
41. Rainsbury RM, et al. Localization of metastatic breast carcinoma by monoclonal antibody chelate labeled with In-111. Lancet. 1983;1:934–8.
42. Chatal JF, et al. Immuno-scintigraphy of colon carcinoma. J Nucl Med. 1984;25:307–14.
43. Kramer EL, et al. Radioimmunodetection of non-small cell lung cancer using technetium-99m-anticarcinoembryonic antigen IMMU-4 Fab9 fragment. Preliminary results. Cancer. 1994;73(3 Suppl):890–5.
44. Epenetos AA, et al. I-123 radio- iodinated antibody imaging of occult ovarian cancer. Cancer. 1985;55:984–7.
45. van Dongen GA, et al. Immuno-PET: a navigator in monoclonal antibody development and applications. Oncologist. 2007;12:1379–89.
46. Kaur S, et al. Recent trends in antibody-based oncologic imaging. Cancer Lett. 2012;315:97–111.
47. Pérez-Campaña C, et al. Biodistribution of different sized nanoparticles assessed by positron emission tomography: a general strategy for direct activation metal oxide particles. ACS Nano. 2013;7(4):3498–505.
48. Simonelli F, et al. Cyclotron production of radioactive CeO_2 nanoparticles and their application for in vitro uptake studies. IEEE Trans NanoBiosci. 2011;1:44–50.
49. Lipka J, et al. Biodistribution of PEG-modified gold nanoparticles following intratracheal instillation and intravenous injection. Biomaterials. 2010;31(25):6574–81.
50. Häfeli UO, et al. Stability of biodegradable rhenium (Re-186 and Re- 188) microspheres after neutron activation. Appl Radiat Isot. 2001;54:869–79.
51. Hamoudeh M, et al. Dirhenium decacarbonyl-loaded PLLA nanoparticles: influence of neutron irradiation and preliminary in vivo administration by the TMT technique. Int J Pharm. 2008;348:125–36.
52. Thrash TP, et al. Towards fullerene-based radiopharmaceuticals: high-yield neutron activation of endohedral 165Ho metallofullerenes. Chem Phys Lett. 1999;308:329–36.
53. Albernaz MD, et al. Radiolabelled nanohydroxyapatite with ^{99m}Tc: perspectives to nanoradiopharmaceuticals construction. Artif Cells Nanomed Biotechnol. 2013 (in press).
54. Locatelli L, et al. Biocompatible nanocomposite for PET/MRI hybrid imaging. Int J Nanomedicine. 2012;7:6021–33.
55. Rossin R, et al. In vivo imaging of ^{64}Cu-labeled polymer nanoparticles targeted to the lung endothelium. J Nucl Med. 2008;49(1):103–11.
56. Rojas S, et al. Biodistribution of amino-functionalized diamond nanoparticles: in vivo studies based on ^{18}F radionuclide emission. ACS Nano. 2011;5(7):5552–9.
57. Jauregui-Osoro M, et al. Biocompatible inorganic nanoparticles for [^{18}F]-fluoride binding with applications in PET imaging. Dalton Trans. 2011;40(23):6226–37.
58. Hildebrand H, Franke K. A new radiolabeling method for commercial Ag0 nanopowder with 110mAg for sensitive nanoparticle detection in complex media. J Nanopart Res. 2012;14(10): 1142–8.
59. PhillipsWT RAS, et al. A simple method for producing a technetium-99m-labeled liposome which is stable in vivo. Nucl Med Biol. 1992;19:539–47.
60. Cydzik I, et al. A novel method for synthesis of ^{56}Co-radiolabelled silica nanoparticles. J Nanopart Res. 2012;14(10):1185–93.
61. Llop J, et al. Quantitative determination of the biodistribution of nanoparticles: could radiolabeling be the answer? Nanomedicine. 2013;8(7):1–4.
62. Garanger E, et al. Tumor targeting with RGD peptide ligands design of new molecular conjugates for imaging and therapy of cancers. Anticancer Agents Med Chem. 2007;7:552–8.
63. de Bruin K, et al. Cellular dynamics of EGF receptor-targeted synthetic viruses. Mol Ther. 2007;15:1297–305.
64. Hilgenbrink AR, Low PS. Folate receptor-mediated drug targeting: from therapeutics to diagnostics. J Pharm Sci. 2005;94:2135–46.
65. Xu L, et al. Transferrin-liposome-mediated systemic p53 gene therapy in combination with radiation results in regression of human head and neck cancer xenografts. Hum Gene Ther. 1999;10:2941–52.
66. Dass CR, Choong PF. Selective gene delivery for cancer therapy using cationic liposomes: in vivo proof of applicability. J Control Release. 2006;113:155–63.
67. Xu L, et al. Systemic tumor-targeted gene delivery by antitransferrin receptor scFv-immunoliposomes. Mol Cancer Ther. 2002;1:337–46.
68. Liu Z, et al. In vivo biodistribution and highly efficient tumour targeting of carbon nanotubes in mice. Nat Nanotechnol. 2007;2(1):47–52.
69. Hong H, et al. In vivo targeting and positron emission tomography imaging of tumor vasculature with ^{66}Ga-labeled nano-graphene. Biomaterials. 2012;33(16):4147–56.

70. Cornelissen B, et al. Nanographene oxide-based radioimmunoconstructs for in vivo targeting and SPECT imaging of HER2-positive tumors. Biomaterials. 2013;34(4):1146–54.
71. Almutairi A, et al. Biodegradable dendritic positron-emitting nanoprobes for the noninvasive imaging of angiogenesis. Proc Natl Acad Sci. 2009;106(3):685–90.
72. Kobayashi H, et al. Evaluation of the in vivo biodistribution of indium-111 and yttrium-88 labeled dendrimer-1B4M-DTPA and its conjugation with anti-Tac monoclonal antibody. Bioconjug Chem. 1999;10:103–11.
73. Oku N, et al. In vivo trafficking of long-circulating liposomes in tumour-bearing mice determined by positron emission tomography. Biopharm Drug Dispos. 1996;17:435–41.
74. Oku N, et al. PET imaging of brain cancer with positron emitter-labeled liposomes. Int J Pharm. 2011;403:170–7.
75. Dagar S, et al. V IP grafted sterically stabilized liposomes for targeted imaging of breast cancer: in vivo studies. J Control Release. 2003;91:123–33.
76. Chen LC, et al. Biodistribution, pharmacokinetics and imaging of ^{188}Re-BMEDA-labeled pegylated liposomes after intraperitoneal injection in a C26 colon carcinoma ascites mouse model. Nucl Med Biol. 2009;34:415–23.
77. Xie H, et al. In vivo PET imaging and biodistribution of radiolabeled gold nanoshells in rats with tumor xenografts. Int J Pharm. 2010;395:324–30.
78. Lee HY, et al. PET/MRI dual-modality tumor imaging using arginine-glycine-aspartic (RGD)–conjugated radiolabeled iron oxide nanoparticles. J Nucl Med. 2008;49:1371–9.
79. Janib SM, et al. Imaging and drug delivery using theranostic nanoparticles. Adv Drug Deliv Rev. 2010;62:1052–63.
80. Yang X, et al. cRGD-functionalized, DOX-conjugated, and 64Cu-labeled superparamagnetic iron oxide nanoparticles for targeted anticancer drug delivery and PET/MR imaging. Biomaterials. 2011;32:4151–60.
81. Lowe MP. Activated MR contrast agents. Curr Pharm Biotechnol. 2004;5:519–28.
82. Kurhanewicz J, et al. Analysis of cancer metabolism by imaging hyperpolarized nuclei: prospects for translation to clinical research. Neoplasia. 2011;13(2):81–97.
83. Gillies R, et al. MRI of the tumor microenvironment. J Magn Reson Imaging. 2002;16(4):430–50.
84. Cardone R, et al. The role of disturbed pH dynamics and the Na+/H+ exchanger in metastasis. Nat Rev Cancer. 2005;5:786–94.
85. Gatenby R, Gillies R. Why do cancers have high aerobic glycolysis? Nat Rev Cancer. 2004;4:891–9.
86. Orive G, et al. Hydrogen ion dynamics and the Na+/H + exchanger in cancer angiogenesis and antiangiogenesis. Br J Cancer. 2003;89:1395–9.
87. Gerweck LE, Seetharaman K. Cellular pH gradient in tumor versus normal tissue: potential exploitation for the treatment of cancer. Cancer Res. 1996;56:1194–8.
88. Mikawa M, et al. An intelligent MRI contrast agent for tumor sensing. In: Proceedings of the 26th international symposium on Controlled Release of Bioactive Materials and the Second Consumer and Diversified Products Conference. Boston Marriott Copley Place, Boston, MA, USA. June 20–23, 1999, p. 1158–9
89. Aime S, et al. A macromolecular Gd(III) complex as pH-responsive relaxometric probe for MRI applications. Chem Commun. 1999;38:1577–8.
90. Zhang S, et al. A novel pH-Sensitive MRI contrast agent. Angew Chem Int Ed Engl. 1999;38:3192–4.
91. Aime S, et al. Dependence of the relaxivity and luminescence of gadolinium and europium aminoacid complexes on hydrogen carbonate and pH. Chem Commun. 1999;11:1047–8.
92. Lowe MP, et al. pH-dependent modulation of relaxivity and luminescence in macrocyclic gadolinium and europium complexes based on reversible intramolecular sulfonamide ligation. J Am Chem Soc. 2001;123:7601–9.
93. Woods M, et al. Synthesis, relaxometric and photophysical properties of a new pH-responsive MRI contrast agent: the effect of other ligating groups on dissociation of a p-nitrophenolic pendant arm. J Am Chem Soc. 2004;126:9248–56.
94. Li WH, et al. A calcium-sensitive magnetic resonance imaging contrast agent. J Am Chem Soc. 1999;121:1413–4.
95. Li WH, et al. Mechanistic studies of a calcium-dependent MRI contrast agent. Inorg Chem. 2002;41:4018–24.
96. Hanaoka K, et al. Selective sensing of zinc ion with a novel magnetic resonance imaging contrast agent. J Chem Soc [Perkin 1]. 2001;2:1840–3.
97. Trokowski R, et al. Selective sensing of zinc ions with a PARACEST contrast agent. Angew Chem Int Ed Engl. 2005;44:6920–3.
98. Comblin V, et al. Designing new MRI contrast agents: a coordination chemistry challenge. Coord Chem Rev. 1999;185–186:451–70.
99. Que EL, Chang CJ. A smart magnetic resonance contrast agent for selective copper sensing. J Am Chem Soc. 2006;128:15942–3.
100. Moats R, et al. A smart magnetic resonance imaging contrast agent that reports on enzymatic activity. Angew Chem Int Ed Engl. 1997;36:726–8.
101. Rudin M. Target watching with a beady eye. Nat Biotechnol. 2000;18:383.
102. Jacobs RE, et al. Looking deeper into vertebrate development. Trends Cell Biol. 1999;9:73–6.
103. Louie AY, et al. In vivo visualization of gene expression using magnetic resonance imaging. Nat Biotechnol. 2000;18:321–5.
104. Perez JM, et al. DNA-based magnetic nanoparticle assembly acts as a magnetic relaxation nanoswitch allowing screening of DNA-cleaving agents. J Am Chem Soc. 2002;124:2856–7.

105. Anelli PL, et al. Sulfonamide-functionalized gadolinium DTPA complexes as possible contrast agents for MRI: a relaxometric investigation. Eur J Inorg Chem. 2000;4:625–30.
106. Bohndiek SE, et al. Hyperpolarized ^{13}C spectroscopy detects early changes in tumor vasculature and metabolism after VEGF neutralization. Cancer Res. 2012;72:854–64.
107. Gruetter R, et al. Localized in vivo 13C NMR spectroscopy of the brain. NMR Biomed. 2003;16:313–38.
108. Gabellieri C, et al. Therapeutic target metabolism observed using hyperpolarized 15Ncholine. J Am Chem Soc. 2008;130:4598–9.
109. Abragam A, Goldman M. Principles of dynamic nuclear polarisation. Rep Prog Phys. 1978;41(3):395–9.
110. Ardenkjaer-Larsen JH, et al. Increase in signal-to-noise ratio of >10,000 times in liquid-state NMR. Proc Natl Acad Sci. 2003;100(18):10158–63.
111. Bowers CR, Weitekamp DP. Transformation of symmetrisation order to nuclear-spin magnetization by chemical reaction and nuclear magnetic resonance. Phys Rev Lett. 1986;57(21):2645–8.
112. Bowers CR, Weitekamp DP. Parahydrogen and synthesis allow dramatically enhanced nuclear alignment. J Am Chem Soc. 1987;109:5541–2.
113. Aptekar JW, et al. Silicon nanoparticles as hyperpolarized magnetic resonance imaging agents. ACS Nano. 2009;3:4003–8.
114. Ardenkjaer-Larsen JH, et al. Hyperpolarized 13C magnetic resonance imaging—principles and applications. In: Weissleder R, Ross BD, Rehemtulla A, editors. Molecular imaging: principles and practice. Shelton: People's Medical Publishing House; 2009. p. 377–88.
115. Jamin Y, et al. Hyperpolarized (13)C magnetic resonance detection of carboxypeptidase G2 activity. Magn Reson Med. 2009;62(5):1300–4.
116. McKnight TR, et al. Correlation of magnetic resonance spectroscopic and growth characteristics within grades II and III gliomas. J Neurosurg. 2007;106(4):660–6.
117. Mishkovsky M, Frydman L. Progress in hyperpolarized ultrafast 2D NMR spectroscopy. Chemphyschem. 2008;9:2340–8.
118. Sarkar R, et al. Proton NMR of (15)N-choline metabolites enhanced by dynamic nuclear polarization. J Am Chem Soc. 2009;131:16014–5.
119. vanHeeswijk RB, et al. Hyperpolarized lithium-6 as a sensor of nanomolar contrast agents. Magn Reson Med. 2009;61(6):1489–93.
120. Wolber J, et al. Generating highly polarized nuclear spins in solution using dynamic nuclear polarization. Nucl Instrum Meth Phys A. 2004;526(1–2):173–81.
121. Day SE, et al. Detecting tumor response to treatment using hyperpolarized 13C magnetic resonance imaging and spectroscopy. Nat Med. 2007;13:1382–7.
122. Witney T, et al. A comparison between radiolabeled fluorodeoxyglucose uptake and hyperpolarized C-13–labeled pyruvate utilization as methods for detecting tumor response to treatment. Neoplasia. 2009;6:574–82.
123. Albers MJ, et al. Hyperpolarized 13C lactate, pyruvate, and alanine: noninvasive biomarkers for prostate cancer detection and grading. Cancer Res. 2008;68(20):8607–15.
124. Kettunen MI, et al. Magnetization transfer measurements of exchange between hyperpolarized [1-13C] pyruvate and [1-13C]lactate in a murine lymphoma. Magn Reson Med. 2010;63(4):872–80.
125. Keshari KR, et al. Hyperpolarized (13)C spectroscopy and an NMR-compatible bioreactor system for the investigation of real-time cellular metabolism. Magn Reson Med. 2010;63(2):322–9.
126. Ward CS, et al. Noninvasive detection of target modulation following phosphatidylinositol 3-kinase inhibition using hyperpolarized 13C magnetic resonance spectroscopy. Cancer Res. 2010;70(4):1296–305.
127. Zierhut ML, et al. Kinetic modeling of hyperpolarized 13C1-pyruvate metabolism in normal rats and TRAMP mice. J Magn Reson. 2009;202(1):85–92.
128. Larson PE, et al. Investigation of tumor hyperpolarized [1-(13)C]-pyruvate dynamics using time-resolved multiband RF excitation echo-planar MRSI. Magn Reson Med. 2010;63(3):582–91.
129. Nelson S, et al. DNP-hyperpolarized 13C magnetic resonance metabolic imaging for cancer applications. Appl Magn Reson. 2008;34:533–44.
130. Richards CI, et al. FRET – enabled optical modulation for high sensitivity fluorescence imaging. J Am Chem Soc. 2010;132(18):6318–23.
131. Azar FS, Intes X. Translational multimodality optical imaging. Norwood: Artech House; 2008.
132. Liang R. Optical design for biomedical imaging. Bellingham: SPIE; 2010.
133. Fang M, et al. Quantum dots for cancer research: current status, remaining issues and future perspectives. Cancer Biol Med. 2012;9:151–63.
134. Bentolila LA, et al. Quantum dots for in vivo small-animal imaging. J Nucl Med. 2009;50:493–6.
135. He X, et al. Near-infrared fluorescent nanoprobes for cancer molecular imaging: status and challenges. Trends Mol Med. 2010;16:574–83.
136. Hilderbrand SA, Weissleder R. Near-infrared fluorescence: application to in vivo molecular imaging. Curr Opin Chem Biol. 2010;14:71–9.
137. So MK, et al. Self-illuminating quantum dot conjugates for in vivo imaging. Nat Biotechnol. 2006;24:339–43.
138. Kosaka N, et al. Self-illuminating in vivo lymphatic imaging using a bioluminescence resonance energy transfer quantum dot nanoparticle. Contrast Media Mol Imaging. 2011;6(1):55–9.
139. Dubertret B, et al. In vivo imaging of quantum dots encapsulated in phospholipid micelles. Science. 2002;298:1759–62.

140. Smith JD, et al. The use of quantum dots for analysis of chick CAM vasculature. Microvasc Res. 2007;73:75–83.
141. Kim S, et al. Near-infrared fluorescent type II quantum dots for sentinel lymph node mapping. Nat Biotechnol. 2004;22:93–7.
142. Kim SW, et al. Engineering InAs(x)P(1-x)/InP/ZnSe III-V alloyed core/shell quantum dots for the near-infrared. J Am Chem Soc. 2005;127:10526–32.
143. Zimmer JP, et al. Size series of small indium arsenide-zinc selenide core-shell nanocrystals and their application to in vivo imaging. J Am Chem Soc. 2006;128:2526–7.
144. Thorne RG, Nicholson C. In vivo diffusion analysis with quantum dots and dextrans predicts the width of brain extracellular space. Proc Natl Acad Sci. 2006;103:5567–72.
145. Choi HS, et al. Renal clearance of quantum dots. Nat Biotechnol. 2007;25:1165–70.
146. Mulder WJ, et al. Molecular imaging of tumor angiogenesis using alphavbeta3-integrin targeted multimodal quantum dots. Angiogenesis. 2009;12:17–24.
147. Mulder WJ, et al. Quantum dots with a paramagnetic coating as a bimodal molecular imaging probe. Nano Lett. 2006;6:1–6.
148. Koole R, et al. Paramagnetic lipid-coated silica nanoparticles with a fluorescent quantum dot core: a new contrast agent platform for multimodality imaging. Bioconjug Chem. 2008;19:2471–9.
149. Cai W, et al. Dual-function probe for PET and near-infrared fluorescence imaging of tumor vasculature. J Nucl Med. 2007;48:1862–70.

Multiparametric Imaging

23

Luis Martí-Bonmatí, Ángel Alberich-Bayarri,
Gracián García-Martí, and Roberto Sanz-Requena

Contents

L. Martí-Bonmatí (✉)
Department of Radiology, Hospital Quirón Valencia, Valencia, Spain

Radiology, Department of Medicine, Universitat de Valencia, Valencia, Spain
e-mail: marti_lui@gva.es

Á. Alberich-Bayarri • R. Sanz-Requena
Department of Radiology, Hospital Quirón Valencia, Valencia, Spain

G. García-Martí
Department of Radiology, Hospital Quirón Valencia, Valencia, Spain

Department of Neuroimaging, CIBERSAM, ISCIII, Madrid, Spain

Abbreviations

ADC	Apparent diffusion coefficient
CHO	Choline
CIT	Citrate
CNMF	Convolutive non-negative matrix factorization
CR	Creatine
CT	Computed Tomography
D	Diffusion coefficient
DCE	Dynamic contrast-enhanced
DICOM	Digital imaging and communications in medicine
DW	Diffusion-weighted
FDG	Fluorodeoxyglucose
HER2/Neu	Human epidermal growth factor receptor
HIF-1	Hypoxia-inducible transcription factor
IVIM	Intra-voxel incoherent motions
K^{trans}	Permeability coefficient
LDA	Linear Discriminant Analysis
MR	Magnetic Resonance
PCA	Principal Components Analysis
PET	Positron Emission Tomography
R2	Relaxivity of the transverse magnetization
ROI	Region of interest
SPECT	Single Photon Emission Computed Tomography
SR	Structured Report
TIMP-1	Tissue inhibitor of metalloproteinases

A. Luna et al. (eds.), *Functional Imaging in Oncology*,
DOI 10.1007/978-3-642-40412-2_23, © Springer-Verlag Berlin Heidelberg 2014

US	Ultrasound
VEGF	Vascular Endothelial Growth Factor
VOI	Volume of interest

23.1 Introduction

Conventional imaging plays a pivotal role in cancer diagnosis and follow-up. Technical developments in image acquisition and display are changing the way radiologists interact with the oncological problem. Nowadays, the development of new imaging techniques and the optimisation of image quality facilitate the understanding of the mechanisms, causes and factors related to different oncological diseases. The main objective of these developments is the improvement of tumour diagnosis, grading and staging, as well as the precise treatment definition, monitoring and prediction of the therapeutic response.

Developed countries have reached high penetration indexes of different imaging modalities, both for preclinical and clinical purposes. Nowadays, researchers and clinicians can have access to a wide range of techniques, including long-standing modalities that are continuously improved and upgraded and the most advanced developments in the molecular imaging armamentarium [1]. In this context, the amount of available data has increased exponentially, and choosing the most suitable modality or sequence is becoming more and more difficult. This has led to the development of multimodality imaging, which tries to combine different imaging modalities or sequences in order to improve the sensitivity and specificity of each independent component [2–4].

Imaging offers the possibility of noninvasively assessing multiple facets of pathophysiological processes that exist simultaneously. Different imaging modalities will give complementary information on a specific tumour-related aspect. In most oncological centres, multimodal co-registered imaging is routinely used in tumour staging and treatment evaluation [5]. Combining multiple imaging contrasts that reflect different aspects of pathophysiological processes may provide additional insight over what can be gleaned from a single imaging parameter. Multimodal imaging can be defined as the combination of the information given by two different imaging modalities in the same subject and close in time. In multimodality imaging, the need to chain morphofunctional information is solved by the synchronous acquisition of images from the different sources and merging them automatically to guarantee consistency in time and space. Clear examples of this type of examination are PET-CT and SPECT-CT procedures where final images are the voxel-by-voxel combination of the PET/SPECT and CT images. Both images contribute to the final visualisation, although there is no post-acquisition signal modelling apart from registration and overlay.

Next steps are under active development and investigation in multimodal imaging. The development of efficient detector systems and electronics capable of detecting the two modalities signal at once, and the combination of new different source images such as MR-PET or US-optical fluorescence, will surely improve the capabilities of multimodality imaging in the oncological field.

A completely different approach is to extract multiple relevant tissue parameters by modelling the relationship between a set of registered medical images (raw data) obtained using the same imaging modality. A model is a simplified description of a system or process to assist calculations and predictions. A voxel-based approach will identify spatially heterogeneous changes on the analysed tissue properties that are not readily discernible. By doing this, data dimensionality reduction will generate intuitive interpretable maps with potential applications in the daily clinical routine. The answer to a simple clinical question in a personalised medicine environment, such as ‘do I have a prostate cancer?’ or ‘do I have to worry about my prostate cancer?’, must be also simple and understandable and not a complex display of different maps of cancer-related aspects such as permeability, cellularity and choline maps that radiologists have to subjectively integrate in their readings. This is the base of the combined multiparametric imaging development.

The objective of this chapter is to properly define and evaluate the contribution of multiparametric imaging in oncology.

23.2 Imaging Biomarkers and Data

Parametric imaging and their multiparametric derivatives are based on signal modelling, processing and quantitation. Although the conventional image-based diagnostic, based on the radiologist's integration and qualitative assessment of imaging findings, is the most important process in the daily workflow, there is additional information that needs to be quantitatively extracted, processed and analysed for the radiologists to achieve a better monitoring about what is happening in the specific patient-disease interaction. These quantitative measures help to determine whether there are structural, functional or molecular changes caused by the presence of the tumour, modifying its biological boundaries. These predictive markers help to envisage the outcome of cancer and to establish the best use of available drugs to determine the efficacy of the different therapies.

According to the *National Institute of Health*, a biomarker is defined as 'a characteristic that is objectively measured and evaluated as an indicator of normal biological processes, pathogenic processes, or pharmacologic responses to a therapeutic intervention' [6]. This approach has two main advantages. First, numeric measurements represent quantitative variables that characterise and measure several different normalised parameters, which can be associated to a specific oncological process. Second, parametric maps are generated and used to show the topological distribution of the abnormal biomarkers in the affected area by a voxel-based analysis and display.

This quantitative information, obtained to analyse a lesion or a biological process that is not qualitatively evident, is calculated by analysing different tissue properties whose values may then be combined and simplified into a multivariate model that include the relevant information. The potential to spatially display and qualitatively measure a wide range of biological and physiological tumour-related variables makes imaging biomarkers one of the most active fields in cancer research.

To Control data redundancy and improve data relevance are the most important aspects of medical imaging biomarkers implementation and quality assurance. As several parameters may be obtained and represented as parametric images from the same organ or lesion, the contribution of each one to the final answer must be clearly evaluated and weighted. Multiparametric imaging is a type of multivariate analysis and data display dealing with the statistical definition and pattern combination of data reduction and data relevance increments. With the help of computing, statistical modelling, data mining and image representation, multiparametric maps will give a simple answer about the disease: is it present, where is it located, how aggressive is it and how will it respond to therapy.

23.2.1 Biomarker Definition: Main Steps

The biomarker extraction methodology and clinical implementation require a careful imaging acquisition process, data normalisation, extraction, analysis, measurement and visualisation of the obtained results. Figure 23.1 shows the different stages in the pipeline steps and data flow. The use of biomarkers in clinical practice and clinical trials must consider several implementation aspects, including:

- *Sensitivity*. The relationship between the dynamic variability of the biomarker and the variable to be measured has to be appropriate in order to detect the desired effects.
- *Specificity*. The probability of obtaining a negative result has to be large when the target is not present.
- *Reproducibility*. The variability calculated after repeating the same measurement must be minimal in order to allow replication of the findings. These precision values must be smaller than those differences intended to be detected by the biomarker.
- *Accuracy*. The degree of closeness of the measurement to the quantity's true value.

A clinical methodology is valid if it is both sensitive and specific. A measurement methodology is valid if it is both reproducible and accurate. Taking into account these principles, the

definition of a new biomarker should involve the following steps [7, 8]:

- *Proof of concept*. Evaluate if a specific biological process can be observed with the available imaging and computational techniques.
- *Proof of mechanism*. To study the effect that a specific disease or therapeutic strategy exerts on the biomarker.
- *Proof of principle*. To perform a validation of the proofs of concept and mechanism in a small data set, before using a large number of subjects in a clinical trial.
- *Proof of efficacy*. Analyse the ability of the biomarker in large sample sizes to achieve correct measurements controlling all the steps involved in their calculation.
- *Proof of effectiveness*. Analyse the sensitivity of the biomarker to a specific clinical endpoint.

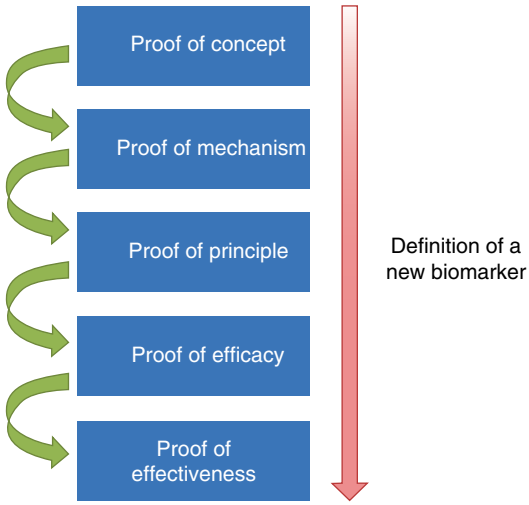

Fig. 23.1 Stages during the definition of a new biomarker

23.2.2 Biomarkers in Oncology

Cancer is a complex entity that affects several systems including metabolism, gene expression, functional proteins, vascular recruitment and cell growth [9]. The role of quantitative imaging signal biomarkers and sample biomarkers in cancer involves many fields (Fig. 23.2), including mainly cancer diagnosis, prognosis, therapeutic response and oncological drug development.

- *Diagnosis*. The use of biomarkers can help in the diagnosis of cancer by determining, for example, whether a tumour located in the brain is primary or not. This aspect can be tested by evaluating the chromosomal alterations in the affected area, which are different in primary tumours and metastases [10] or by the in vivo MR spectroscopy of the lesion [11].
- *Prognosis*. Biomarkers can also predict the course of cancer. This helps in estimating the outcome of the illness in order to establish the most effective (more or less aggressive) patient-specific treatment. For example, some studies have demonstrated that an increased level of TIMP-1 (tissue inhibitor of metalloproteinases) has a good correlation and predicts for poor survival in patients with advanced myeloma [12] and that quantitative pharmacokinetic assessment of dynamic contrast-enhanced MR parametric images of hepatocellular carcinoma can separate lesions

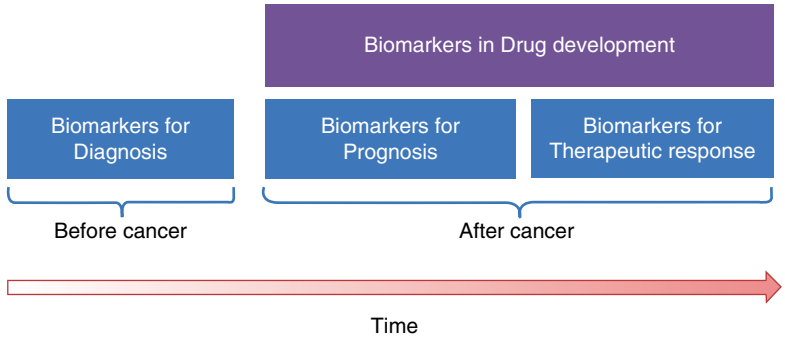

Fig. 23.2 Use of biomarkers in the oncological workflow

with different microvascular properties and biological evolution [8].

- *Therapeutic response*. Biomarkers may help to predict response to treatments, analysing the effects that a particular therapy has in a specific patient. For instance, the oncogene HER2/Neu (human epidermal growth factor receptor) has been validated as a predictor of response to HER2-targeting therapy [13], as the HER2 over-expression is detected when there is a significant increment in the cellular growth and division, showing a more aggressive cancer. It is also known that functional imaging techniques such as diffusion-weighted (DW) and dynamic contrast-enhanced (DCE) MR imaging have the ability to depict important tumoural biological features and are able to predict therapy response based on assessments of cellularity and tumour vascularity, which often precede morphologic alterations [14].
- *Drug development*. The use of biomarkers may decrease the duration of the clinical trials by earlier showing the relevant changes to the tumour and the evaluated drug effect. Many oncological treatments have promising results in phase 1 and phase 2 trials but nevertheless do not achieve the desired success level in phase 3 trials. For example, PET imaging with $Carbon^{11}$ radiotracers is useful to study the pharmacokinetics in new anticancer drugs obtaining information about the metabolic processes and active molecules [15], which can be potentially useful to improve the development times. Also emerging evidence indicates that multiparametric analysis of DCE-MRI data offers greater insight into the mechanism of drug action in early-phase trial design than studies measuring a single parameter, such as the blood vessel permeability K^{trans} value [16].

23.3 Parametric Imaging

One of the key factors in the clinical acceptability and success of an imaging biomarker is the way it is represented and the amount of information provided to the specialist interpreting the results and integrating them into the patient-specific status. Images are treated as raw data by post-processing techniques and computational models. Imaging biomarkers are calculated from specific mathematical models applied to the signal obtained in the acquisition modality. In this sense, the extraction of the biomarker can be performed either from the application of the model to the averaged intensities contained in a certain region of interest (ROI) or from a voxel-by-voxel basis. The first method ignores any information regarding the spatial distribution of the signal variations, obviating the heterogeneous distribution of the biomarker (e.g. as it occurs in cancerous tissue, where different physiologic and biological scenarios coexist). Therefore, the voxel-by-voxel parametric approach is preferable.

Parametric imaging consists in the generation of synthetic maps representing the spatial distribution of imaging biomarkers and is the most suitable tool to analyse the heterogeneity of the distribution of the biomarker at the examined lesions, organ or tissue. This quantitative approach tends to be as automated as possible, reducing user interaction to maximise reproducibility. The output is a series of colour parametric images and, as these biomarkers often show functional information, they are superimposed on anatomical images to help user interpretation.

The main advantage of multiparametric imaging is that images do not represent arbitrary intensity units but quantitative biological-related data obtained by the analysis of a model and usually represented in a colour scale (compared to the greyscale of the original source images) [17]. These parametric images are also widely considered as univariate maps, since they represent a certain variable or parameter that has been extracted from a model and has, usually, a specific measurement unit (e.g. the apparent diffusion coefficient obtained from DW MR images; parameter: ADC; units: mm^2/s).

23.3.1 From Source Data and Redundancy to Parameters

The generation of parametric images can be understood not only as the process to obtained

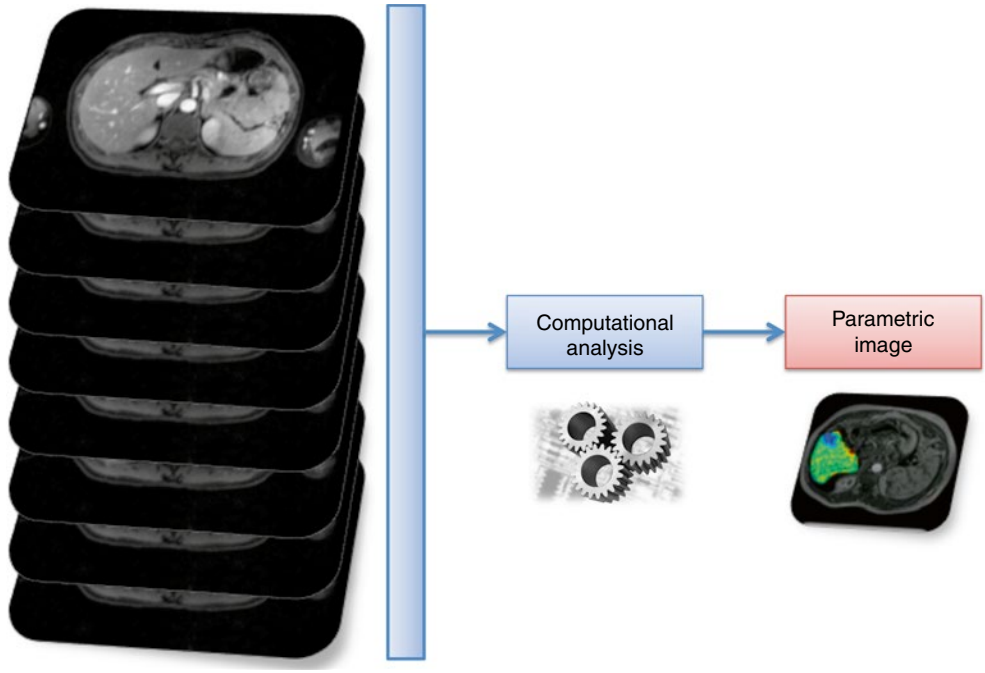

Fig. 23.3 Data reduction for the parametric image generation in the extraction of an imaging biomarker of perfusion from a dynamic study

hidden tissue properties by signal modelling but also as a process of data reduction, passing from a huge amount of acquired data in the obtained images to the spatial parametric representation of the imaging biomarker that is relevant to the disease (Fig. 23.3). As an example, several temporal acquisitions are performed in perfusion studies ending up with a high number (typically hundreds) of images containing information that is not directly relevant to the radiologists, while the application of the proper pharmacokinetic model to the enhancement curves allows the extraction of the relevant parametric distribution of the vascular permeability coefficient (K^{trans}) in all the slices of the acquired volume (tens of images).

23.3.2 Synthesizing Matrices and Volumes

In the data reduction process, in order to synthesize parametric images, a mathematical function included in a computational algorithm processes the image intensities in each voxel to produce the measurable values of the imaging biomarker, P_{im} (Eq. 23.1)

$$P_{im}(i,j) = f_b\left[I_k(i,j)\right] \qquad (23.1)$$

where I_k represent the intensities of different images, k is the type of image and *i, j* are the positions of the pixel in the planar image matrices.

Although parametric images obtained from the processing of medical images can be directly related to the 2D dimension due to the concept 'image', the reasoning in Eq. 23.1 can be perfectly extrapolated to 3D information data sets in order to generate parametric volumes.

There are different types of parametric imaging extraction techniques, depending on the type of functions applied for the extraction of the imaging biomarker. The main ones are the following:

- Voxel-wise curve fitting: A mathematical model is applied to signals built from images of an anatomical region acquired repeated times with the variation of a certain parameter (e.g. temporal variation in dynamic perfusion studies or *b*-value changes in MR DW imaging studies).

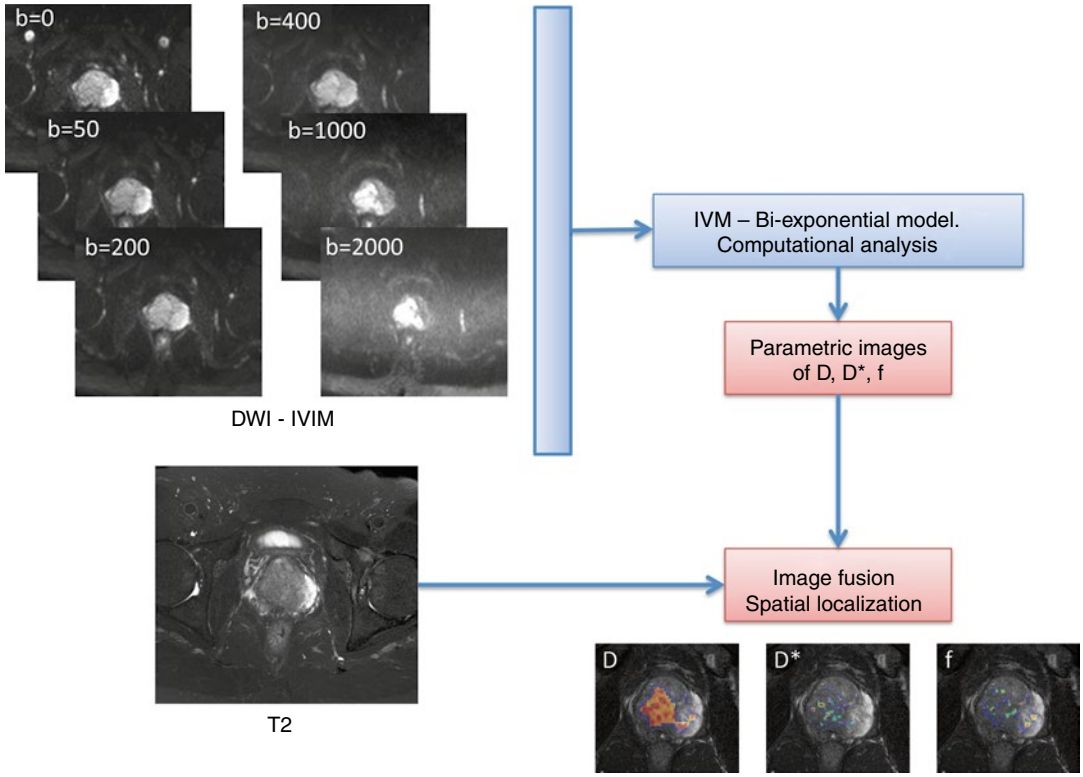

Fig. 23.4 Calculation of diffusion parametric maps and registration to anatomical T2 by the application of a biexponential mathematic model to diffusion images acquired with different *b*-values

- Static morphology-texture analysis: Direct morphology or texture characteristics are extracted from the images acquired in a specific anatomical region (e.g. cortical thickness from high spatial resolution MR).
- 3D model simulation: Generation and simulation of 3D models of organs or tissues from a set of images acquired in a specific anatomical region (e.g. computational fluid dynamics analysis in a model of the aorta extracted from CT images).

23.3.3 The 2D and 3D Spatial Localisation of Biomarkers

It is important not only to generate parametric images containing the spatial distribution of a biomarker but also to identify the exact spatial position of its major alterations and pathological changes. As tumours are highly heterogeneous tissues, it is desirable that the generated parametric images are spatially registered to anatomical images, improving the quality of the quantitative data available for the accurate diagnosis and also guiding the biopsy and/or therapeutic procedures. An example of registration and image fusion of DW parametric maps calculated after the application of the intra-voxel incoherent motions (IVIM) theory [18] can be observed in Fig. 23.4.

Parametric volume reconstructions can also be generated from the 3D source data set. These images may be obtained, after the proper segmentation of any organ or volume of interest (VOI), from the selected tissue, reducing the computational burden. In this case, the biomarker is also calculated voxel-base and then the 'cloud' of values superimposed to the reconstructed VOI. An example of a parametric volume reconstruction of the metabolic profile in a prostate can be appreciated in Fig. 23.5.

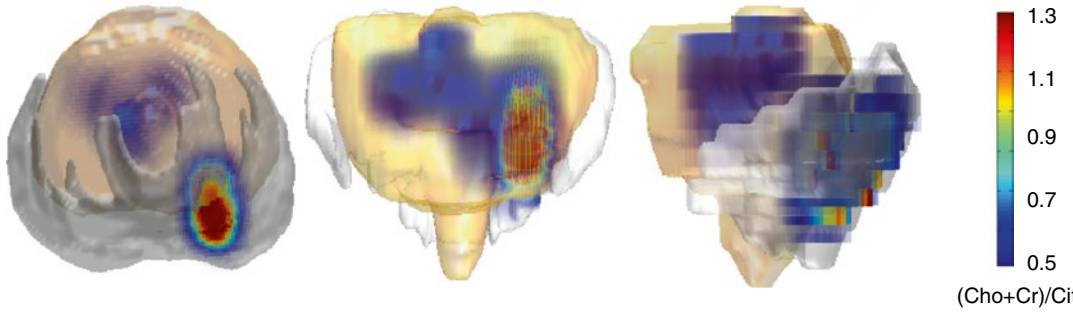

Fig. 23.5 Parametric volume reconstruction of the Choline-Creatine to Citrate (Cho+Cr/Cit) ratio in a prostate, extracted from the processing of MR spectroscopy data

23.4 Multiparametric Imaging

Combining multiple imaging quantitative parameters that reflect different aspects of pathophysiological processes will provide new insight over what can be collected from single parametric maps. As noticed, the advances in imaging technology have boosted the availability and specificity of imaging modalities. Following the modern tendencies of medicine to provide tailored diagnosis and treatments, a whole variety of imaging-derived quantitative measures compete to be the gold standard for each piece of the cancer management items and hallmarks' evaluation. However, it seems that there are not single winning candidates comparing different protocols inside particular modalities. As this race needs to take into account many factors, including clinical and technical aspects, researchers are interested not only in developing advanced imaging tools but also in making the most of what is currently available in conventional clinical centres.

An interesting new approach, currently work in progress, is the multiparametric imaging. Some approaches involve evaluating different imaging data sets that are typically acquired at the same imaging session, while other approaches concentrate on the evaluation of longitudinally acquired single parametric maps [19]. One clear example of the first way is the MR study of the prostate using perfusion, diffusion and spectroscopy. In this case, different sequences from the same imaging modality are used and combined, but there are still several issues that need to be addressed for this approach to be standardised and widely used [20, 21]. The longitudinal multiparametric approach is given by the change in time of the relevant parameters, which typically evaluate the treatment effect in a given disease. The statistical analysis of large image series can also provide secondary images that minimise any redundant data [22].

Multiparametric imaging biomarkers extracted by post-processing manipulation can also be considered secondary images to be further analysed and included in the multidimensional imaging workflow. Figure 23.6 shows a theoretical framework in which several imaging modalities, protocols and biomarkers can be used and where multiparametric imaging can be applied at different levels.

The levels described above may release a significant number of images, describing either gross alterations or different biological behaviours at a group of pixels. However, these results may be difficult to summarise in a single report and it becomes necessary to reduce the amount of data to just the relevant, mainly by statistical regression. At this level, statistics or pattern recognition-based techniques play an essential role to determine which images (either original images or computationally derived imaging biomarkers) and with which weights provide the most useful information about the clinical question being evaluated.

The final output can be considered as a nosological image that shows on a pixel-by-pixel

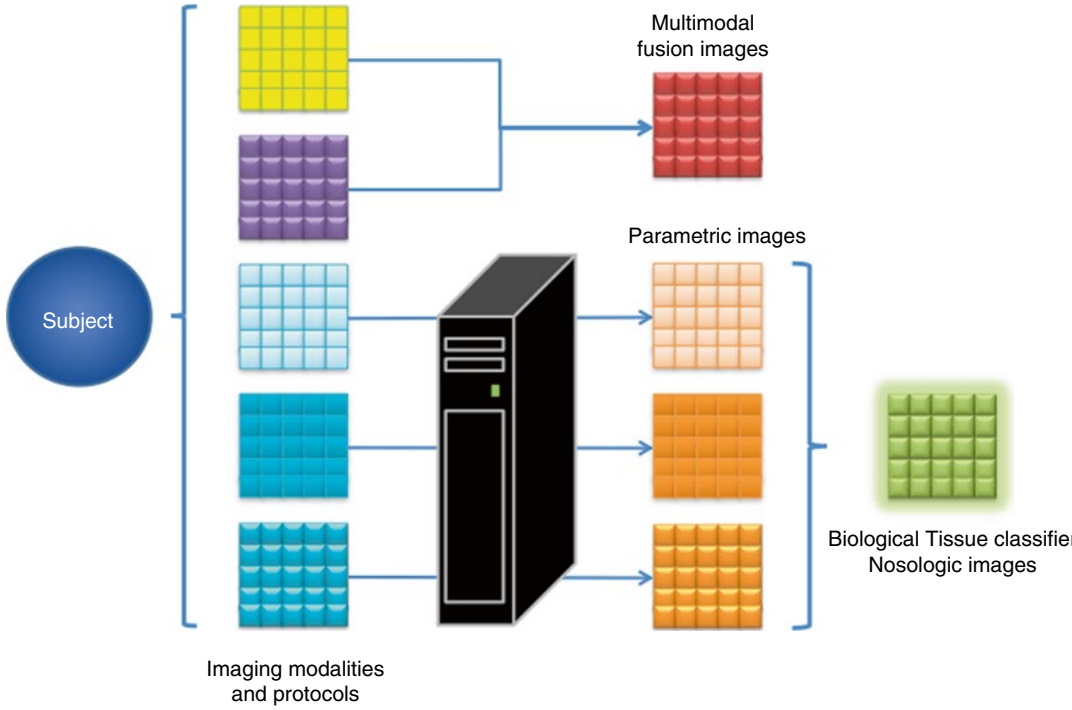

Fig. 23.6 Diagram showing the different levels of multiparametric imaging. Multimodal images are acquired from the subject and they can be directly combined to obtain descriptive fusion multiparametric images. If post-processing algorithms are applied on the original images, imaging biomarkers can be extracted and combined in new multiparametric images. Finally, if there is enough data and proof, statistic models can be built to generate multiparametric nosological images

basis the probability of a disease or any other biological condition the model takes into account [23]. For localisation purposes, it is again common to show the nosological image superimposed on an anatomical image.

Obtaining nosological images in multiparametric imaging is not a simple task, and the techniques used to compute these images vary greatly depending on the output information that the nosological image should include. Nosological images may be based on rules or models based on statistical studies (as in the case of the creation of nosological images for prostate tumours from MR spectroscopy imaging based on ratios between metabolites) or may be based on pattern recognition approaches (Fig. 23.7).

Techniques based on pattern recognition analyse voxel-wise or region similarities between image biomarkers in order to establish mathematical relations between them. There are two main approaches for creating an image from different parametric biomarkers using pattern recognition techniques. The first and most common is the supervised classification approach. The supervised classification is a specific case of pattern recognition task where the goal is identifying a relationship between observations and a set of known categories so that new, previously unseen observations of unknown categorisation can be assigned a category or class label [24, 25]. On the other hand, it can occur that we do not have the pixels labelled in order to train a supervised classifier or that our goal is to obtain a blind segmentation of the different tissues existing in the parametric image according only to the biomarkers values. In this case we can use unsupervised classification methods [26].

It is important to note that in most cases, the biomarkers included in the multiparametric imaging studies present a high degree of

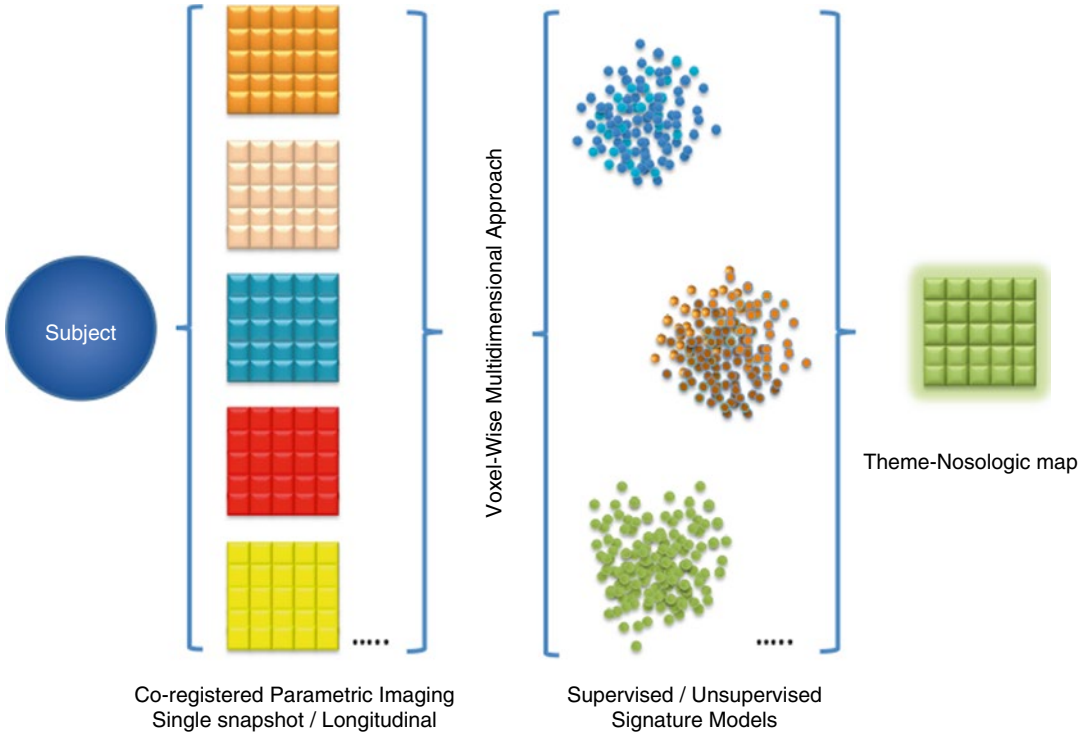

Fig. 23.7 Stepwise process in the development of multiparametric nosological images through signature models

redundancy. Therefore, it is desirable to use dimensionality reduction techniques over the set of biomarkers to reduce the input variables of the model in which the nosological image is based. Dimensionality reduction techniques can be based on feature selection techniques (relief, stepwise, statistical selection), multivariate projections algorithms (PCA, LDA, CNMF) or manifold learning techniques (isomap, locally linear embedding, semi-definite embedding).

Statistically or pattern recognition-derived multiparametric images are based on data-driven models and therefore need even larger databases to build significant knowledge models that minimise bias from different sources. This demand for standard methodologies and large databases has set a hotspot for research taskforces both in preclinical and clinical oncology studies.

It is important to know that while descriptive multimodality images only need to take into account a correct registration of the images so that the functional information is correctly overlaid on the anatomical image, multiparametric images need more robust standardised acquisition protocols and image processing workflows. Also, it is necessary to previously evaluate how accurate and reproducible the biomarker is (i.e. with large databases of samples and subjects) to ensure a standard methodology. Finally, it is also important to notice that adequate visualisation tools are required, as radiologists and physicians need to interpret the resulting images accurately. False colour images overlaid on greyscale anatomic images are usually the best option, so that a colour bar indicates the value of the parameter or nosological output at each pixel (Fig. 23.8).

23.5 Examples of Multiparametric Imaging in Oncology

Despite the direct clinical utility of the spatial distribution of an imaging biomarker in a parametric map or combined biomarkers in a

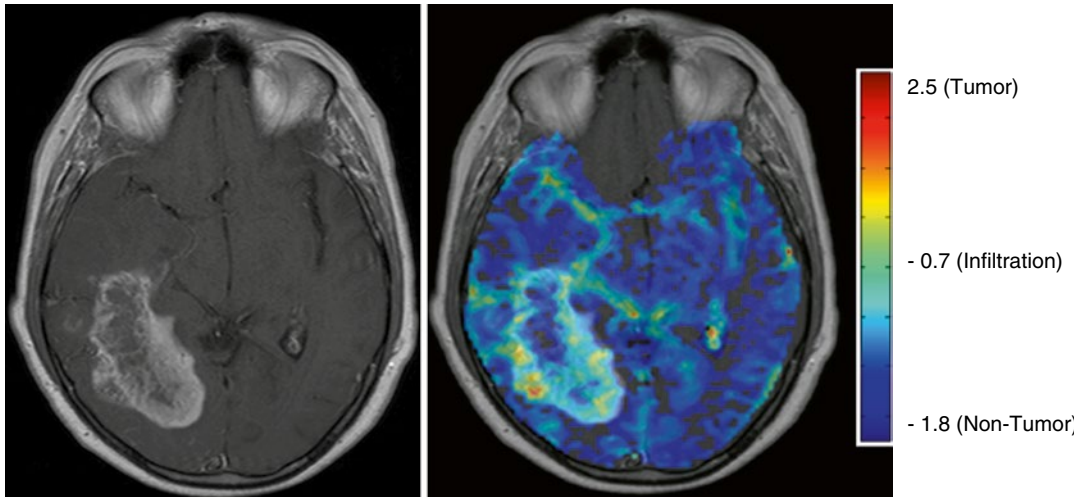

Fig. 23.8 Nosological image obtained after the multiparametric analysis of dynamic susceptibility-weighted MR images of a glioblastoma. The *colorbar* shows the value of a discriminant function obtained from a linear combination of different quantitative perfusion parameters. The centroids of tumour, infiltration and nontumoural regions are indicated

multiparametric nosological image, its integration in the clinical routine is an issue of current concern. Nowadays, the DICOM Structured Reporting (DICOM-SR) is being established as the main way to complement the traditional qualitative reports in medical imaging with new quantitative information that may improve not only the diagnosis but also the treatment response and follow-up.

As mentioned, the display of too many imaging biomarkers also presents a saturation risk, as the amount of parameters that can be calculated today may become a confounding factor for appropriate clinical use. That is why many of these parameters, spatially represented by parametric images, may be further analysed in conjunction with data reduction techniques that permit the generation of multivariate parametric maps, more oriented to the simplified management of the clinical endpoints of the disease.

Multiparametric imaging combines quantitative information from a number of techniques to provide a multidimensional-multispectral, spatial and temporally resolved, depiction of tumour morphology and biology [27]. In oncology, multiparametric imaging enables complex and multifaceted depiction of tumour phenotype, improved characterisation of lesion pathology and more accurate assessment of the therapeutic response [28].

MRI biomarkers of tumour oedema, vascular permeability, blood volume and average vessel calibre are increasingly being employed to assess the efficacy of tumour therapies.

The main biomarkers evaluated by imaging that can be related to the different tumour hallmarks are cell density, interstitial space volume, perfusion changes (such as blood flow, blood volume, mean transit time, contrast transfer coefficients and vascular fractions), oxygen and choline concentration. However, the dependence of these biomarkers on a number of physiological factors can compromise their sensitivity and complicate the assessment of therapeutic efficacy [29].

Tumour cellularity can be approached by the apparent diffusion coefficients (ADCs) calculated from diffusion MR imaging. A decrease in ADC has been shown to correlate with an increase in tumour cellularity, while an increased ADC correlates with a decrease in cellularity as a result of successful treatment and/or radiation-induced necrosis [30]. Even more precisely, the slow component (D) of the biexponential behaviour of the signal decay in a multiple *b*-values DW IVIM experiment more closely relates to cell density.

Measurements of tumour perfusion are based on the temporal analysis of the signal behaviour after the administration of a contrast agent. Although the acquisition techniques may be different (DCE-US, DCE-CT, DCE-MRI), the dynamic analysis reflects tumour vascular density (typically correlates with peak enhancement, blood volume and/or permeability-surface area product). Vascular density is related to tumour oxygenation and hypoxia-inducible transcription factor (HIF-1) activity, which increases angiogenesis via vascular growth factors, thereby supporting tumour growth and survival [28].

Even more, oxygen parametric maps can be obtained by the extraction of the transverse relaxation time (R2) in a multi-echo MR sequence. Multivoxel MR spectroscopy gives information on the local concentration of choline, having the potential to perform truly quantitative tissue characterisation.

Although several examples of parametric assessment of tumours are now being evaluated, the relevance of multiparametric imaging has not been exploited. The most advanced case in multifunctional imaging is prostate cancer in tumour detection and grading. These data can also be extrapolated to understand targeted therapy definition and response, personalising diagnosis and therapy. However, nosological images are not implemented already.

Also, combined imaging of glucose metabolism (FDG-PET) and angiogenesis (DCE-CT) can allow vascular-metabolic phenotyping of rectal tumours. A mismatch between tumour vascularity and metabolism reflects adaptation to hypoxia and adverse tumour biology. The high metabolic/low vascularity phenotype is common in colorectal tumours with greater expression of VEGF and HIF-1, suggesting an adaptation to hypoxia via angiogenesis. Even more, high blood flow and blood volume in rectal cancer has strong predictive value in response to either adjuvant or neo-adjuvant chemo/radiotherapy.

Finally, in the brain and breast, multiparametric images can be used to predict tumour aggressiveness and response to treatment. Perfusion, metabolic and cellularity images, as well as elastograms, have proved their efficiency in this matter, although their combination is still work in progress.

23.6 Texture-Based Imaging

Tumour tissue properties can be also analysed by the examination of the texture characteristics. These texture-based techniques permit the characterisation of the imaging findings in terms of touch properties like smoothness, uniformity, roughness and granularity. Furthermore, texture analysis methods can be applied both to original and parametric or multiparametric images.

The main methodology for the application of texture analysis is based on the use of co-occurrence matrices in order to analyse repetition patterns in the image. If a certain voxel of the image is taken as the reference, the co-occurrence matrix is then generated by the analysis of the neighbouring voxels that have similar intensity values and the distance between them. In other words, a texture mapping is a measure of the relationship between different signal intensities. The co-occurrence matrix needs to be normalised in order to calculate concrete parameters which represent some texture characteristics like the correlation, contrast, entropy, energy and homogeneity [31].

Regarding oncological analysis, the correlation is increased when the difference or distance of the tumour voxels to the average tumour value is smaller. The texture contrast properties detect abrupt signal intensity changes within the analysed region. Contrast can be mathematically analysed by the distance of elements to the main diagonal of the co-occurrence matrix, which contains the elements with similar intensities; thus, the contrast is higher if the corresponding elements are distant from the diagonal. In terms of imaging, when the probabilities of having specific intensities are similar, high entropy values are obtained since there is uncertainty. However, the entropy value will be lower if we have high probabilities of having a specific intensity in a uniform texture. The energy can be extracted from the convolution of the image of the tumour

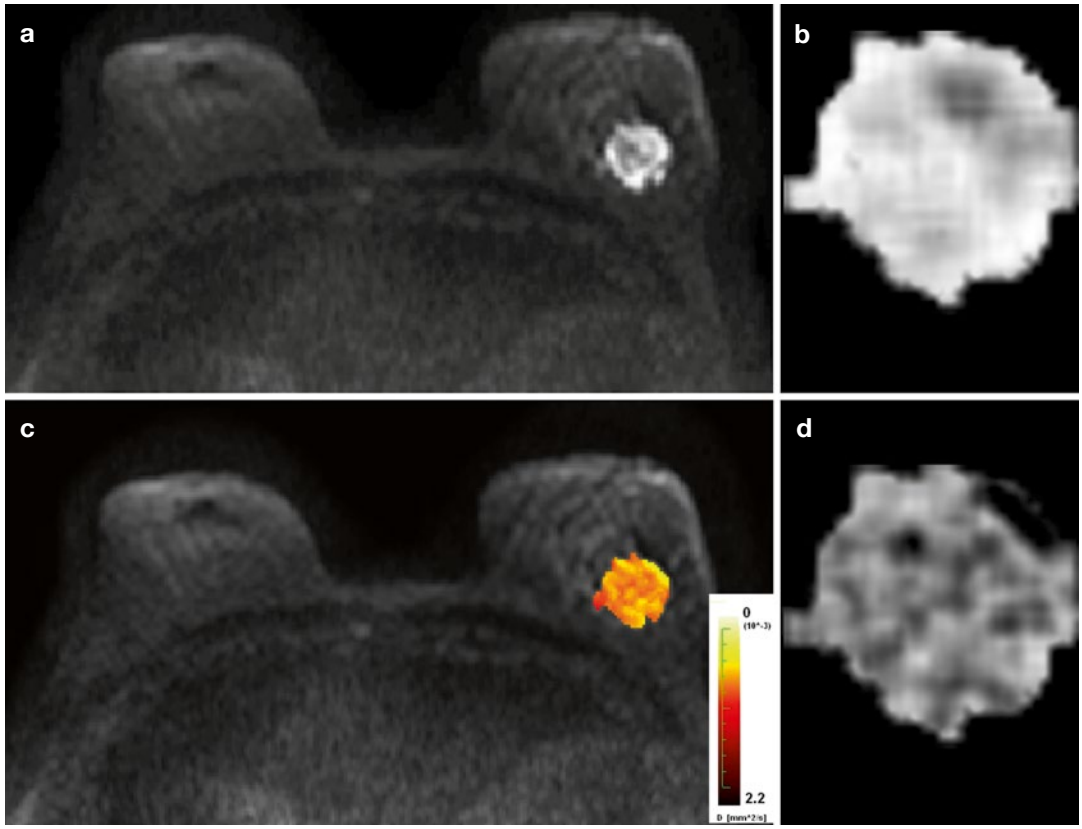

Fig. 23.9 Texture analysis of a mammary ductal carcinoma. In (**a**), MR diffusion-weighted acquisition with a *b*-value of 1,000 s/mm^2 clearly depicting the lesion zones restricting water molecules movement. In (**b**), textural entropy calculated in the lesion, a high entropy is observed in all the lesion corresponding to a high-diffusion heterogeneity, with the exception of a darker and small area with low entropy. In (**c**), diffusion coefficient (*D*) map of the lesion as extracted from the IVIM theory. In (**d**), entropy analysis applied to the map in (**c**) showing a better contrast between the different regions of the tumour

with filters for specific spatial frequencies. Finally, homogeneity is a marker of texture similarity in a certain region and is higher as probabilities of occurrence increase.

The study of tumour heterogeneity through textures analysis can be directly performed on the original images, parametric images or multiparametric images. As an example, such texture analysis techniques can be applied to simple MR diffusion images acquired at a *b*-value of 1,000 s/mm^2 or to the resulting parametric maps of the diffusion coefficient (D) extracted from the application of the intra-voxel incoherent motion (IVIM) theory [18] (Fig. 23.9). By this approach, we can quantitatively analyse the degree of heterogeneity in the cell density within the lesion.

References

1. Wessels JT, et al. In vivo imaging in experimental preclinical tumor research – a review. Cytometry A. 2007;71:542–9.
2. Estorch M, Carrio I. Future challenges of multimodality imaging. Recent Results Cancer Res. 2013;187:403–15.
3. Kaijzel EL, et al. Multimodal imaging and treatment of bone metastasis. Clin Exp Metastasis. 2009;26:371–9.
4. Wolf G, Abolmaali N. Preclinical molecular imaging using PET and MRI. Recent Results Cancer Res. 2013;187:257–310.
5. Martí-Bonmatí L, et al. Multimodality imaging techniques. Contrast Media Mol Imaging. 2010;5:180–9.
6. Biomarkers Definitions Working Group. Biomarkers and surrogate endpoints: preferred definitions and conceptual framework. Clin Pharmacol Ther. 2001;69:89–95.

7. Martí Bonmatí L, et al. Imaging biomarkers, quantitative imaging, and bioengineering. Radiologia. 2012;54:269–78.
8. Martí-Bonmatí L, et al. Magnetic resonance pharmacokinetic imaging clusterization of hepatocellular carcinomas as a means to grade tumor aggressiveness. Expert Rev Gastroenterol Hepatol. 2012;6:711–6.
9. Vucic EA, et al. Translating cancer 'omics' to improved outcomes. Genome Res. 2012;22:188–95.
10. Popławski AB, et al. Frequent genetic differences between matched primary and metastatic breast cancer provide an approach to identification of biomarkers for disease progression. Eur J Hum Genet. 2010;18:560–8.
11. García-Gómez JM, et al. Multiproject-multicenter evaluation of automatic brain tumor classification by magnetic resonance spectroscopy. MAGMA. 2009;22:5–18.
12. Terpos E, et al. High levels of serum TIMP-1 correlate with advanced disease and predict for poor survival in patients with multiple myeloma treated with novel agents. Leuk Res. 2010;34:399–402.
13. Weigel MT, Dowsett M. Current and emerging biomarkers in breast cancer: prognosis and prediction. Endocr Relat Cancer. 2010;17:245–62.
14. Li SP, Padhani AR. Tumor response assessments with diffusion and perfusion MRI. J Magn Reson Imaging. 2012;35:745–63.
15. Tu Z, Mach RH. C-11 radiochemistry in cancer imaging applications. Curr Top Med Chem. 2010;10:1060–95.
16. O'Connor JP, et al. Dynamic contrast-enhanced MRI in clinical trials of antivascular therapies. Nat Rev Clin Oncol. 2012;9:167–77.
17. Todd-Prokoprek A, Di Paola R. The use of computers for image processing in nuclear medicine. IEEE Trans Nucl Sci. 1982;4:1299–309.
18. Le Bihan D, et al. MR imaging of intravoxel incoherent motions: application to diffusion and perfusion in neurologic disorders. Radiology. 1986;161:401–7.
19. Wu O, et al. Multiparametric magnetic resonance imaging of brain disorders. Top Magn Reson Imaging. 2010;21:129–38.
20. Hoeks CMA, et al. Prostate cancer: multiparametric MR imaging for detection, localization and staging. Radiology. 2011;261:46–66.
21. Panebianco V, et al. Conventional imaging and multiparametric magnetic resonance (MRI, MRS, DWI, MRP) in the diagnosis of prostate cancer. Q J Nucl Med Mol Imaging. 2012;56:331–42.
22. Nattkemper TW. Multivariate image analysis in biomedicine. J Biomed Inform. 2004;37:380–91.
23. De Vos M, et al. Fast nosologic imaging of the brain. J Magn Reson. 2007;184:292–301.
24. De Edelenyi FS, et al. A new approach for analyzing proton magnetic resonance spectroscopic images of brain tumors: nosologic images. Nat Med. 2000;6:1287–9.
25. Luts J, et al. Nosologic imaging of the brain: segmentation and classification using MRI and MRSI. NMR Biomed. 2009;22:374–90.
26. Li Y, et al. Unsupervised nosologic imaging for glioma diagnosis. IEEE Trans Biomed Eng. 2013;60(6):1760–3.
27. Padhani AR, Miles KA. Multiparametric imaging of tumor response to therapy. Radiology. 2010;256:348–64.
28. Singh D, Miles K. Multiparametric PET/CT in oncology. Cancer Imaging. 2012;12:336–44.
29. Farrar CT, et al. Sensitivity of MRI tumor biomarkers to VEGFR inhibitor therapy in an orthotopic mouse glioma model. PLoS One. 2011;6:e17228.
30. Ellingson BM, et al. Validation of functional diffusion maps (fDMs) as a biomarker for human glioma cellularity. J Magn Reson Imaging. 2010;31:538–48.
31. Mahmoud-Ghoneim D, et al. Three dimensional texture analysis in MRI: a preliminary evaluation in gliomas. Magn Reson Imaging. 2003;21:983-7.

Index

A. Luna et al. (eds.), *Functional Imaging in Oncology*,
DOI 10.1007/978-3-642-40412-2, © Springer-Verlag Berlin Heidelberg 2014